

Upper Limb Joint Angle Tracking with Inertial Sensors

Mahmoud El-Gohary, Lars Holmstrom, Jessie Huisinga, Edward King, James McNames, and Fay Horak

Abstract—Wearable inertial systems have recently been used to track human movement in and outside of the laboratory. Continuous monitoring of human movement can provide valuable information relevant to individual’s level of physical activity and functional ability. Traditionally, orientation has been calculated by integrating the angular velocity from gyroscopes. However, a small drift in the measured velocity leads to large integration errors that grow with time. To compensate for that drift, complementary data from accelerometers are normally fused into the tracking systems using the Kalman or extended Kalman filter (EKF). In this study, we combine kinematic models designed for control of robotic arms with the unscented Kalman filter (UKF) to continuously estimate the angles of human shoulder and elbow using two wearable sensors. This methodology can easily be generalized to track other human joints. We validate the method with an optical motion tracking system and demonstrate correlation consistently greater than 0.9 between the two systems.

I. INTRODUCTION

Measurement and analysis of human movement has many applications including assessment of neurological movement disorders, rehabilitation from injury, and enhancement of athletic performance. Movement can be measured using a wide variety of techniques and sensors. Wearable inertial sensors enjoy the advantages of being simple, unobtrusive, and self-contained. They are well suited to recording long-term monitoring while the subject performs normal activities of daily life at home. A typical wearable inertial sensor is a compact wearable device that contains a triaxial accelerometer and triaxial gyroscope. Fig. 1 shows an example of Opal sensor (APDM, Inc., Portland, OR) used in this study. Traditionally, the orientation of a body segment is estimated by integrating the angular velocity measured by gyroscopes, and position is obtained by double integration of the translational acceleration measured by accelerometers. A significant problem with integration, however, is that inaccuracies inherent in the measurements quickly accumulate in the integrated estimation, resulting in an unacceptable levels of position error in as little as 10–60 s [1]. Roetenberg

M. El-Gohary and J. McNames (Director) are with the Biomedical Signal Processing Laboratory in the Department of Electrical and Computer Engineering at Portland State University (PSU), Portland, Oregon. Email: mahmoud@pdx.edu, mcnames@pdx.edu.

L. Holmstrom is Chief Information Officer at APDM, Inc. Email: lars@apdm.com.

J. Huisinga, E. King, and F. Horak (Director) are members of the Balance Disorders Laboratory in the Department of Neurology at Oregon Health & Science University (OHSU). Email:huisinga@ohsu.edu, kinged@ohsu.edu, horakf@ohsu.edu.

J. McNames, L. Holmstrom, F. Horak, OHSU, and PSU have a significant financial interest in APDM, a company that may have a commercial interest in the results of this research and technology. The potential individual and institutional conflicts of interest have been reviewed and managed by OHSU and PSU.



Fig. 1. Example of an Opal inertial sensor (APDM, Inc.).

showed that integration of gyroscope data resulted in a drift between $10 - 25^\circ$ after one minute [2]. One approach to reducing integration drift is to fuse the gyroscope data with complementary data from other sensors. Luinge *et al.* estimated orientation by fusing gyroscope and accelerometer data [3]. The difference between tilt computed from gyroscope and that from accelerometer sensors was used as an input to a Kalman filter to obtain a better tilt estimate. The estimate was then combined with the rotation around the vertical axis to produce a better orientation estimate. However, the estimation was accurate for only brief periods when the subject was not moving and when the acceleration measurements were only due to gravity. Luinge *et al.* developed a method that used constraints in the elbow to measure the orientation of the forearm with respect to the upper arm [4]. They reported an average orientation error of 20° . Giansanti *et al.* combined gyroscopes with accelerometers to track position and orientation during three tasks; stand-to-sit, sit-to-stand and gait-initiation [5]. Estimation error was minimal, however they restricted the application to short periods of 4 s.

Bachmann *et al.* investigated the effect of electrical and ferromagnetic materials on the accuracy of orientation tracking using a triaxial accelerometer, gyroscope and magnetometer sensors [6]. They observed errors that ranged from 12° to 16° and stated that these errors can be avoided by maintaining an approximate distance of two feet from any source of disturbance. This restricts the use of their tracking system to custom laboratory environment. Yun *et al.* used a quaternion-based EKF to track human body motion. A rotary tilt table with two DOF’s was used to assess the performance

of the tracker [7]. The error for the pitch angle was not reported, and an error of 9° in less than 2 s was obtained for the roll angle. Zhou *et al.* successfully estimated elbow orientation using inertial sensors mounted on the wrist and elbow joints. They integrated the rotational rate to localize the wrist and elbow, and smoothed the abrupt amplitude changes to reduce overshoots of the inertial measurement due fast movements to reduce error in position estimation. They attained a high correlation between position estimates from the inertial tracker and estimates from a reference optical tracking system, ≥ 0.91 . However, all the reported correlations were not statistically significant [8].

In this paper we combine kinematic models designed for control of robotic arms with state space methods to directly estimate human joint angles of a multi-segment limb. Estimated joint angles are computed from measured inertial data as a function of time in a single step using a nonlinear state space estimator. The estimator utilizes the unscented Kalman filter which incorporates state space evolution equations based on a kinematic model of the multi-segment limb. The proposed algorithm can be applied to any combination of sensors to track any limb movement in either real-time or off-line processing mode with higher accuracy for slow and fast motion with a minimal number of sensors.

II. THEORY

In the analysis and control of robotic manipulators, a robot arm is normally represented as a sequence of links connected by joints [9]. This convention has also been successfully applied in addressing human motion and is based upon characterizing the configuration between consecutive links by a transformation matrix. If each pair of consecutive links is related via a matrix, then using the matrix chain-rule multiplication, it is possible to relate any segmental link (e.g., between the wrist and elbow) to another (e.g., between the elbow and shoulder).

To obtain a systematic method for describing position and orientation of each pair of consecutive links, we generate a transformation matrix between the links using the Denavit and Hartenberg (D-H) method, starting with attaching frames or coordinate systems to each link [10]. Each frame $\{X_i, Y_i, Z_i\}$ is then related to the previous one using a 4×4 homogeneous transformation matrix. This matrix depends on four parameters associated with each link. The first parameter is the link length a_i which is the distance from Z_i to Z_{i+1} measured along the X_i axis. The second parameter is the link twist α_i which is the angle from Z_i to Z_{i+1} measured about the X_i axis. The distance from X_{i-1} to X_i measured along the Z_i axis is known as the link offset d_i . The fourth parameter is the joint angle θ_i , which is the angle from X_{i-1} to X_i measured about the Z_i axis.

A. Link Transformations

Four transformations are needed to relate the i^{th} frame to its neighboring $(i-1)^{th}$ frame. First, rotate about X_i an angle α_{i-1} to make the two coordinate systems coincide. Next, translate along X_i a distance a_{i-1} to bring the two

origins together. Third, rotate about Z_i an angle θ_i to align X_i and X_{i-1} . Finally, translate along Z_i a distance d_{i-1} to bring X_i and X_{i-1} into coincidence. Each of these four operations can be expressed by a basic homogeneous rotation-translation matrix and the product of these four transformation matrices yields a composite matrix ${}^{i-1}_i T$, known as the D-H transformation matrix which defines frame i to its adjacent $i-1$

$${}^{i-1}_i T = \begin{bmatrix} c(\theta_i) & -s(\theta_i) & 0 & a_{i-1} \\ s(\theta_i)c(\alpha_{i-1}) & c(\theta_i)c(\alpha_{i-1}) & -s(\alpha_{i-1}) & -s(\alpha_{i-1})d_i \\ s(\theta_i)s(\alpha_{i-1}) & c(\theta_i)s(\alpha_{i-1}) & c(\alpha_{i-1}) & c(\alpha_{i-1})d_i \\ 0 & 0 & 0 & 1 \end{bmatrix}$$

where $s(\alpha_{i-1}) = \sin(\alpha_{i-1})$, $c(\theta_i) = \cos(\theta_i)$, etc.

B. Shoulder and elbow joint angle tracker example

As an example, we present a model for forearm movement with shoulder and elbow joints. Fig. 2 shows the base reference frame 0 at the center of the shoulder joint. Frames 1 through 3 represent shoulder flexion/extension, abduction/adduction and internal/external rotation, respectively. Frames 4 through 5 represent the elbow flexion/extension and pronation/supination of the forearm. The two inertial sensors are placed near the wrist and on the upper arm between the shoulder and elbow as shown in Fig. 3. Table I shows the

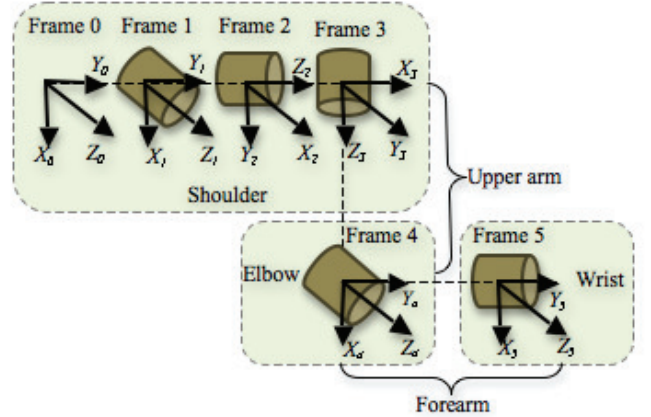


Fig. 2. Kinematics diagram of the arm model with Frame 0 as the reference frame. Frames 1 through 3 represent shoulder flexion/extension, abduction/adduction and internal/external rotation, respectively. Frames 4 through 5 represent the elbow flexion/extension and pronation/supination.

D-H parameters, where α_{i-1} is the angle to rotate to make the two coordinate systems coincide, the length of the upper arm l_u , is the distance from Z_3 to Z_4 along the X_4 axis, l_f is the length of the forearm, and θ_i is the i^{th} angle of rotation.

C. Velocity and acceleration propagation from link to link

At any instant, each link of the arm in motion has some linear and angular velocity. The linear velocity is that of the origin of the frame. The angular velocity describes the rotational motion of the link. The velocity of link $i+1$ is

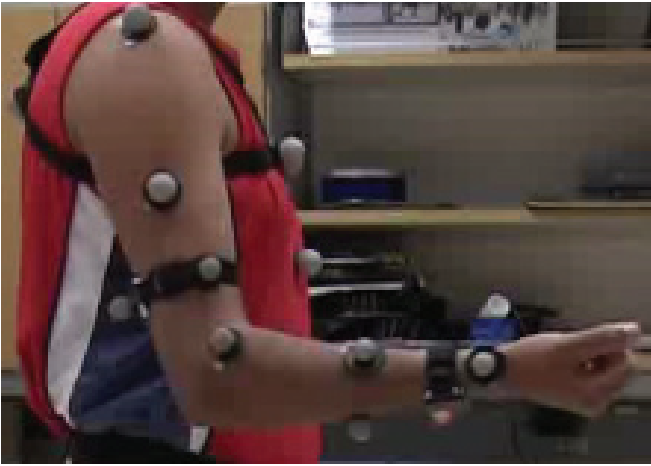


Fig. 3. Subject performing elbow flexion, with one inertial sensor attached with a black band on the wrist and another on the upper arm. Ten reflective markers were attached to the arm, and three were attached to the sternum.

TABLE I
DENAUVIT-HARTENBERG PARAMETERS FOR THE ARM MODEL.

Frame	α_{i-1}	a_{i-1}	d_i	θ_i
1	0	0	0	θ_1
2	$-\frac{\pi}{2}$	0	0	θ_2
3	$-\frac{\pi}{2}$	0	0	θ_3
4	$\frac{\pi}{2}$	l_u	0	θ_4
5	$-\frac{\pi}{2}$	0	l_f	θ_5

that of link i plus the new velocity component added by joint $i + 1$

$${}^i\omega_{i+1} = {}^i\omega_i + {}^{i+1}R \dot{\theta}_{i+1} {}^{i+1}Z_i, \quad (1)$$

where ${}^{i+1}R$ is the rotation matrix that relates frame i to frame $i + 1$, and is used to represent added rotational components due to motion at the joint in frame i . If we multiply both sides of the equation by ${}^{i+1}R$, we find the description of the angular velocity of link $i + 1$ with respect to frame $i+1$

$${}^{i+1}\omega_{i+1} = {}^{i+1}R {}^i\omega_i + \dot{\theta}_{i+1} {}^{i+1}Z_{i+1}$$

The linear velocity of the origin of frame $i + 1$ is the same as that of the origin of frame i plus a new component caused by the rotational velocity of link i

$${}^{i+1}v_{i+1} = {}^{i+1}R({}^i v_i + {}^i\omega_i \times {}^i P_{i+1})$$

where ${}^i P_{i+1}$ is the position vector of the frame $i + 1$ and is the upper right 3×1 vector of the D-H matrix. The angular acceleration from one link to the next is

$${}^{i+1}\dot{\omega}_{i+1} = {}^{i+1}R {}^i\dot{\omega}_i + {}^{i+1}R {}^i\omega_i \times \dot{\theta}_{i+1} {}^{i+1}Z_{i+1} + \ddot{\theta}_{i+1} {}^{i+1}Z_{i+1}$$

The linear acceleration of each link frame origin is

$${}^{i+1}\dot{v}_{i+1} = {}^{i+1}R [{}^i\dot{\omega}_i \times {}^i P_{i+1} + {}^i\omega_i \times ({}^i\omega_i \times {}^i P_{i+1}) + {}^i\dot{v}_i]$$

where the single and double dot notation is used to represent first and second derivatives with respect to time. The rotation matrices R can be obtained by taking the transpose of the upper left 3×3 D-H transformation matrix, and the D-H

parameters shown in Table I. We initialize $\omega_0 = \dot{\omega}_0 = (0, 0, 0)^T$, and $\dot{v}_0 = (g_x, g_y, g_z)^T$, where g is gravity. These equations are part of what is known as Newton-Euler equations of motion. They are forward recursive equations that propagate linear and angular velocity and acceleration from the reference coordinate system to the last link.

D. State Space Model

Having defined the kinematic model of the arm, we now formulate the relationship between the measured data and the biomechanical states using a state space model. The general discrete time statistical state-space model is of the form,

$$x(n+1) = f_n[x(n), u(n)] \quad (2)$$

$$y(n) = h_n[x(n), v(n)] \quad (3)$$

where n is the discrete time index, $x(n)$ is the unobserved state of the system, $y(n)$ is the observed or measured data, $f_n[\cdot]$ and $h_n[\cdot]$ are nonlinear state and observation equations, $u(n)$ is process noise, and $v(n)$ is an observation noise. Both $u(n)$ and $v(n)$ are assumed to be white noise processes with zero mean. The state model equations which describe the evolution of the states with time are given by

$$\theta_i(n+1) = \theta_i(n) + T_s \dot{\theta}_i(n) + \frac{1}{2} T_s^2 \ddot{\theta}_i(n) \quad (4)$$

$$\dot{\theta}_i(n+1) = \dot{\theta}_i(n) + T_s \ddot{\theta}_i(n) \quad (5)$$

$$\ddot{\theta}_i(n+1) = \alpha \ddot{\theta}_i(n) + u_{\ddot{\theta}_i}(n) \quad (6)$$

where $i = \{1, \dots, 5\}$, $\theta_i(n)$ is the i^{th} angle at time n , $\dot{\theta}_i(n)$ is the angular velocity of the i^{th} angle at time n , $\ddot{\theta}_i(n)$ is the angular acceleration of the i^{th} angle at time n , $u_{\ddot{\theta}_i}(n)$ is a white noise process with zero mean, α is a process model parameter, and $T_s = 1/f_s$ is the sampling period. These are standard equations for a physical object traveling at a constant acceleration. In this case the model assumes the acceleration is constant for the duration of a sampling interval, which is short enough (approximately 8 ms) for this approximation to be sufficiently accurate for tracking. The model of angular acceleration is a first-order autoregressive process with zero mean. Typically the value of α will be assigned an intermediate value that represents typical patterns of human motion in joint angles.

The observation model describes the relationship of the states to the observed data obtained from the inertial sensor. We assume that the inertial sensor includes triaxial accelerometers and triaxial gyroscopes. This simple model assumes the sensor noise is additive and white, but could be easily generalized to include drift, which is common to MEMS inertial sensors.

$$y(n) = \begin{bmatrix} \omega_x(n) \\ \omega_y(n) \\ \omega_z(n) \\ \dot{v}_x(n) \\ \dot{v}_y(n) \\ \dot{v}_z(n) \end{bmatrix} + \begin{bmatrix} v_{gx}(n) \\ v_{gy}(n) \\ v_{gz}(n) \\ v_{ax}(n) \\ v_{ay}(n) \\ v_{az}(n) \end{bmatrix}, \quad (7)$$

where ω_x , ω_y and ω_z are the angular velocities along the x , y and z axes, respectively. The gyroscope noise along the

different axes is described by v_{gx} , v_{gy} and v_{gz} . Similarly, the translational accelerations along the three axes are \dot{v}_x , \dot{v}_y and \dot{v}_z , and the accelerometer noise is given by v_{ax} , v_{ay} and v_{az} . The acceleration measurement vector includes translational accelerations and the effects of gravity.

E. Nonlinear state estimator

The arm model introduced above exhibits nonlinearities. The use of the linear Kalman filter in a highly nonlinear dynamics introduces estimation errors. The most common approach to solving the nonlinear estimation problem is the extended Kalman filter (EKF), which is based upon linearizing the state and observation models with a first-order Taylor expansion. However, this linearization leads to poor performance if the dynamics are highly nonlinear and the simple linearized model based on the gradient is an inaccurate approximation. The EKF also requires Jacobian matrices and inverse matrix calculation. Alternatively, sequential Monte Carlo methods (i.e., particle filters), which are applicable to highly nonlinear and non-Gaussian estimation problems, allow for a complete representation of the density function of the unobserved states using a finite number of samples. However, particle filters require much more computation. The unscented Kalman filter (UKF) has nearly the same computational requirements as the EKF, but uses a more accurate method to characterize the nonlinear effects. The results in this paper were generated with a UKF [11].

III. RESULTS

To evaluate the performance of the inertial tracking system in monitoring arm movement, the joint angles calculated by the inertial tracker were compared to those obtained by an optical tracking system, used as a reference system. The study was conducted in the Balance Disorders Laboratory at OHSU, which is equipped with an optical motion tracking system that comprises eight high-speed, infrared cameras (Eagle Analog System, Motion Analysis Corporation, California). The cameras record position of reflective markers placed on the upper arm, forearm, shoulder and wrist. Optical relative joint angles were calculated from three-dimensional markers positions using Grood's method [12]. One subject performed a set of tasks described in Table II. Each articulation was performed for 15 s while keeping the rest of the body still. The correlation coefficients between the angle estimates from the inertial tracker and estimates from the reference optical tracking system were all statistically significant ($p < .05$) and ≥ 0.91 .

TABLE II
CORRELATION BETWEEN OPTICAL AND INERTIAL ANGLES OF
SHOULDER AND ELBOW OF A SUBJECT PERFORMING A SET ARM
MOVEMENT.

Task	R (normal speed)	R (fast speed)
Elbow Flexion/Extension	0.92	0.89
Elbow Supination/Pronation	0.96	0.93
Shoulder Flexion/Extension	0.97	0.94
Shoulder Abduction/Adduction	0.94	0.91

One of the limitations of previous tracking methods is that they performed well only during slow movements. To determine the capability of the proposed algorithm of tracking fast activities, the subject was instructed to repeat the same activities as fast as they could. On average, the subject reached from initial anatomical position to maximum joint movement range in 0.5 s, compared to 1.0 s during normal speed activities. Although, the correlation was slightly lower than that for the regular speed, the correlation coefficients were still statistically significant ($p < .05$) and were all ≥ 0.89 .

IV. CONCLUSION

This paper described a new method for estimating joint angles of a multi-segment limb using inertial sensors. Estimated joint angles are computed from measured inertial data as a function of time in a single step using a nonlinear state space estimator. The estimator utilizes the unscented Kalman filter which incorporates state space evolution equations based on a kinematic model of the multi-segment limb. The algorithms outlined in this paper can be applied to any combination of sensors, and could be generalized to track any limb movement in either real-time or off-line with higher accuracy for slow and fast motion with a minimal number of sensors.

REFERENCES

- [1] O. Woodman, "An introduction to inertial navigation," Computer Laboratory, University of Cambridge, UK, Tech. Rep., August 2007.
- [2] D. Roetenberg, "Inertial and magnetic sensing of human motion," Ph.D. dissertation, University of Twente, Enschede, The Netherlands, 2006.
- [3] H. J. Luinge, "Inertial sensing of human motion," Ph.D. dissertation, University of Twente, Enschede, The Netherlands, December 2002.
- [4] H. J. Luinge, P. H. Veltink, and C. T. M. Baten, "Ambulatory measurement of arm orientation," *Journal of Biomechanics*, vol. 40, pp. 78–85, 2007.
- [5] D. Giansanti, G. Maccioni, and V. Macellari, "The development and test of a device for the reconstruction of 3-d position and orientation by means of a kinematic sensor assembly with rate gyroscopes and accelerometers," *IEEE Transactions on Biomedical Engineering*, vol. 52, no. 7, pp. 1271–1277, 2005.
- [6] E. R. Bachmann, X. Yun, and C. Peterson, "An investigation of the effects of magnetic variations on inertial magnetic orientation sensors," in *Proceedings of the 2004 IEEE International Conference on Robotics and Automation*, 2004, pp. 1115–1122.
- [7] X. Yun and E. R. Bachmann, "Design, implementation, and experimental results of a quaternion-based kalman filter for human body motion tracking," *IEEE Transaction on Robotics*, vol. 22, pp. 1217–1227, 2006.
- [8] H. Zhou and H. Hu, "Upper limb motion estimation from inertial measurements," *International Journal of Information Technology*, vol. 13, no. 1, pp. 1–14, 2007.
- [9] J. J. Craig, *Introduction to Robotics, Mechanics and Control*, ser. Electrical and Computer Engineering: Control Engineering. Addison-Wesley, 1989.
- [10] J. Denavit and R. S. Hartenberg, "A kinematic notation for lower-pair mechanisms based on matrices," *Applied Mechanics*, vol. 23, pp. 215–221, 1955.
- [11] S. J. Julier and J. K. Uhlmann, "Unscented filtering and nonlinear estimation," in *Processings of The IEEE*, vol. 92, March 2004, pp. 401–422.
- [12] E. S. Grood and W. J. Suntay, "A joint coordinate system for the clinical description of three-dimensional motions: Application to the knee," *ASME*, vol. 105, pp. 136–142, 1983.

Measuring Walking and Running Cadence using Magnetometers

Umran A. Abdulla
School of Engineering & IT
UNSW@ADFA
Canberra, Australia
Umran.Abdulla@student.adfa.edu.au

Ken Taylor
ICT Center
CSIRO
Canberra, Australia
Ken.Taylor@csiro.au

Michael Barlow
School of Engineering & IT
UNSW@ADFA
Canberra, Australia
M.Barlow@adfa.edu.au

Khushnood Z.
Naqshbandi
Khushnood.Zn@gmail.com

Abstract— Several smart phone connected devices are becoming popular as replacements for pedometers for monitoring human activity and exercise levels. Most of them, including Fitbit and Nike Fuel Band measure step cadence using accelerometers. It would be advantageous to obtain this data using smart phone sensors without additional devices but smart phones produce varying accelerometer signal patterns when carried in different locations on the body. Magnetometers are an alternative low power sensor on most smart phones that could potentially be used for cadence estimation. We provide an algorithm that derives walking and running cadence from magnetometer readings that is robust to the location on the body that the smart phone is carried. The algorithm has been tested with data gathered from twenty one subjects while walking and running, in several body locations that should comprehensively represent body movements. A high accuracy was achieved when the estimated cadence was verified against an accelerometer worn on the subject's thigh. The algorithm is robust in dealing with sudden changes in direction while walking or running which is also likely to make it robust against magnetic field fluctuations that are common in urban environments.

Keywords—magnetometer, compass, candance, activity-recognition, energy-expenditure, smart phone, body sensor network, sensor localization

I. INTRODUCTION

Several smart phone connected devices are becoming popular as replacements for pedometers for monitoring human activity and exercise levels. Most of them, including Fitbit and Nike Fuel Band measure step cadence using accelerometers. It would be advantageous to obtain this data using smart phone sensors without additional devices.

Smart phones are an excellent platform for context-aware computation and pervasive health applications. This arises from the large number of sensors integrated into the phone, the large processing resources available, the relatively low cost and availability, and the internet connection available. On the other hand, smart phones face different challenges from purpose-built sensors, in that: they can be carried in many different orientations and locations on the human body with each different location producing different signal patterns; may have little connectivity to the body itself (such as when in a loose pocket or handbag); have to deal with issues originating from platform design (such as inconsistent

sampling) and algorithms have to be power efficient so as not to exhaust the phone's battery too quickly [1].

Among the sensors available on smart phones are accelerometers, magnetometers and gyroscopes. At the time of writing this paper, gyroscopes are still new and few in number, but almost all smart phones come with accelerometers and magnetometers.

Among the three sensors accelerometers are becoming widely accepted for human motion studies in free-living environments [2]. The signal from the accelerometer, among other things, depends on the location it is placed on [2].

Much research has been done in measuring cadence or step-counts. Although the algorithms used by most commercial pedometers are unavailable, several papers have gone into verifying the results of commercial step-counters that were then common, without considering how the devices work internally or the fact that the devices get phased out and replaced with new devices after a few years. One published algorithm by Oliver and Flores-Mangas [3] requires the accelerometer to be worn on the chest, and an adaptive threshold is used to detect steps from magnitude of the accelerometer signal. Similarly, Barralon, Vuillerme and Noury [4] worked on detecting periods of walking in elderly people and used frequency analysis on the subject's vertical acceleration for chest-mounted accelerometers.

Yumono, Su, Moulton and Nguyen [5] looked into detecting walking and measuring gait parameters by extracting the periodicity in torso pitch angle, which in turn is extracted from signals from chest-worn accelerometers and gyroscopes.

Instead of using the accelerometer and gyroscope as done by [5] and [6], we use the orientation given by the magnetometer and extract the period of each gait cycle. Magnetometers are an alternative low power sensor on most smart phones that could potentially be used for cadence estimation. Magnetometers easily provide the orientation angle (as has been extracted from accelerometer and gyroscope data by [5]) hence reducing the required processing. On the other hand, magnetometers face the problem that they get attracted to magnetic and ferrous materials in the subject's vicinity.

Magnetometers have been used in dead-reckoning for indoor navigation [7][8] and estimation of body segment orientations [6][9][10]. We found no research has been done into examining magnetometer readings for pervasive health applications.

In the following sections, we discuss how we collected the data, our method of extracting cadence from magnetometer readings, the results we got when we compared the cadence extracted from magnetometer readings and the cadence extracted from an accelerometer worn on the subject's thigh, and future work we hope to do.

II. DATA COLLECTION

To avoid issues originating from mobile platform design (e.g. inconsistent sampling due to multitasking, and low sampling rates), an Opal System from APDM [11] was used in wireless buffering mode to capture data. Each sensor module has a triaxial accelerometer (range: $\pm 6g$, noise: $0.0012 \text{ m/s}^2 / \sqrt{\text{Hz}}$), a triaxial magnetometer (range: ± 6 Gauss, noise: $0.5 \text{ mGauss} / \sqrt{\text{Hz}}$) and a triaxial gyroscope (range: $\pm 2000 \text{ deg/s}$, noise: $0.05 \text{ deg/s} / \sqrt{\text{Hz}}$). Sampling was done at 128Hz ($\leq 10\mu\text{s}$ synchronized sample timing difference).

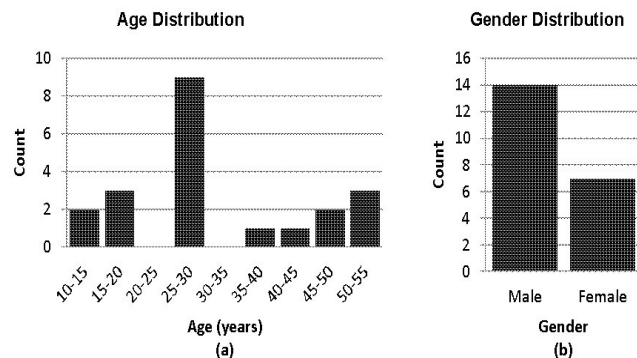


Figure 1. Subject age and gender distributions. (a) shows the age distribution, while (b) shows the age distribution.

Fig. 1 above shows the age and gender distributions of the subjects.

Sensor modules were strapped onto 21 able-bodied subjects on 3 locations: thigh, trunk, and palm. For 4 of the subjects, additional modules were strapped on the ankle, upper arm, and on the navel (near the body's center of gravity [12]). The placement is illustrated in the Fig. 2.

The sensors were strapped onto the locations, because we wanted to avoid artifacts caused by the sensor module moving in the pocket so as to obtain the best-case performance of our algorithm.

The subjects were asked to walk 20 meters on flat ground, turn and walk back. Each subject did this 3 times for each activity, making a total distance of 120 meters recorded per subject-activity session. Two activities were recorded: walking and running. No speed or time constraints were set to avoid any effects the constraints might have on the walking and running styles. For running, the subjects were instructed to do a "light run", and were left to decide what that meant to them. The turns made at the end of every 20 meter straight were included in the data recording. The subjects took the turns in different ways; some took sharper turns while some took wider turns. In addition, to cover

multiple walking surfaces, for 4 of the subjects, data was taken on both hard (pavement) and soft (grass) surfaces.

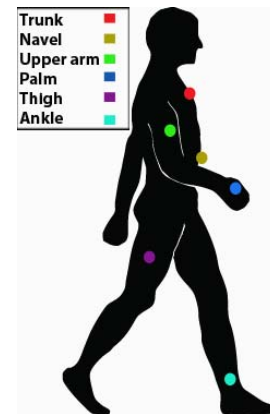


Figure 2. Sensor placement on the subjects.

The data collection method was selected so as to allow the subjects to walk and run naturally, at their own natural pace, while at the same time, allow us to observe and accurately label the dataset.

III. METHOD

The algorithm we propose for extracting cadence is based on the assumption that when we analyze the orientation at a point on the body, while walking or running, each body part completes one cycle in every two steps (one right step and one left step, equivalent to one complete gait cycle). Based on this assumption we attempted to extract the time-taken by the gait cycle (the period) and hence derive the cadence of the activity.

In order to extract the subject's cadence our method includes the following steps: conversion from 3D space to 2D space, signal filtering, and cadence extraction.

A. Conversion from 3D space to 2D space

Data sampled from the magnetometer is in the form of 3D vectors pointing to the direction of magnetic North. We can reduce the data's dimensions from 3 to 2 while still maintaining the important attributes in the data that allow the period of the cycles to be extracted, by removing the length of the vector (normalizing) then converting the orientation of the vectors as the latitude and longitude. Whether or not the magnetometer was pointing towards the magnetic North is not important, as long as it points towards a stationary external (off the subject's body) point. The actual direction they point to is also not important, since we discard this but maintain the relative angles between the vectors.

By using the relative direction to any fixed point instead of to the magnetic North, we avoid errors that would have been caused had the magnetometer been attracted to a magnetic or ferrous material in the subject's vicinity.

The 3D vectors are converted to points on a 2D Cartesian plane representing the longitude and latitude of the given magnetometer vector with relation to a given equator. The direction and magnitude of the change in the longitude and

latitude from one vector to the next vector must be maintained in the conversion process. This means avoiding the wrapping of angles to the range $[-\pi \text{ rad}, \pi \text{ rad}]$ that happens because of trigonometric equations, and the π rad flip that occurs when the vectors cross the north and south poles. The following algorithm was used to do this:

1. Normalize the 3D vectors gathered.
2. Compute the mean vector, m .
3. Find the furthest vector, f , which has the largest angle to the mean vector, m .
4. Compute vector u , such that: $u = m * f$, where $*$ represents the cross product. u is then taken as the vector that points to the north pole of the sphere, of which m and f lie on the equator.
5. For each of the normalized 3D vectors extract:
 - a. Change in longitude from the previous vector along the equator. The longitude of a vector can then be obtained as the cumulative change of longitude from the first vector to the current vector. The longitude of the first vector would be zero.
 - b. Latitude from the sphere's equator, positive towards the direction of vector u , and negative in the opposite direction.

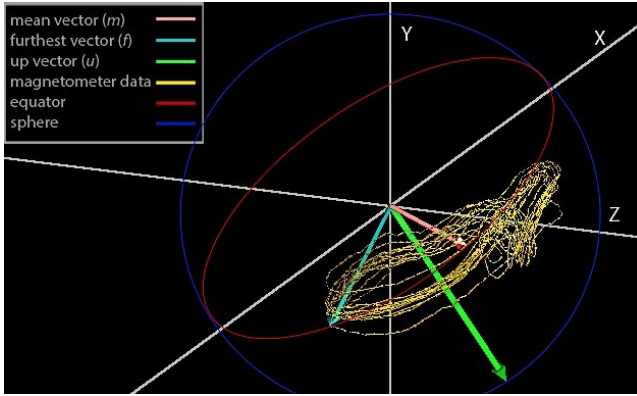


Figure 3. A 3D rendering of some sample data taken from the thigh while the subject was walking. The mean vector m and the furthest vector f lie on the equator of the unit sphere. The points on which the normalized magnetometer data intersect with the surface of the sphere are shown in yellow. The up vector u points to the north of this sphere. The longitudes extracted are degrees along the sphere's equator while the latitudes extracted are the angles between the sphere's equator and the normalized magnetometer vectors, positive in the direction of the up vector u , and negative away from it.

B. Filtering

We assume the highest cadence for a human being while running is 10 steps per second. To reduce noise we filter the signal using an FFT-based FIR low pass filter, removing any signal components above 5Hz. We then again use FFT to split the signal into low frequency components and high frequency components. We used a cutoff threshold of 0.5Hz. Since the frequencies reflect half of the cadence, 0.5Hz equates to 1 step per second, which is lower than the slowest

walking speed, 95% confidence level, for a person that is walking [13].

The split removes any effect of sharp changes of direction (e.g. when the magnetometer suddenly gets attracted to a different item in the subject's vicinity, or when the subject turns sharply) in the high frequency signal and leaves the gradual change in direction reflected in the low frequency signal.

Samples of data before and after the 5Hz low pass filter are shown in the Fig. 4. Fig. 5 shows a sample containing a subject walking towards, turning around a cone and walking back and its low frequency signal. The arc is a result of the turn, while the clusters on either side of the arc represent the subject's walk towards the cone, and return. In addition, Fig. 5 shows the low frequency component which tracks the arc and hence shows the greatest change for the turn section.

C. Cadence Extraction

In this step we extract the gait cycle frequency in the data (i.e. the smallest period at which gait cycles exist). We based the process on the assumption that, as a cycle repeats, the Euclidean distance of a point to a similar point on the previous cycle is minimized.

To do this, we define the distance function d of the point at index i and time period τ , as:

$$d(i, \tau) = \sqrt{((x_i - x_{i+\tau})^2 + (y_i - y_{i+\tau})^2)} \quad (1)$$

Where x and y are the longitude and latitude.

We then define the mean distance function h for time period τ , based on $d(i, \tau)$, as the mean of the distances for i in the range of $[1, N]$ where N are the number of points in the given window.

$$h(\tau) = \frac{\sum_{i=1}^N d(i, \tau)}{N} \quad (2)$$

We then find the first time offset with local minima (m) that occurs after a local maxima (n), such that $(m - n) > a$. Where a is a threshold value that is experimentally determined and set to avoid selecting local minima caused by noise. The time offset at which m occurs corresponds to the period of the gait cycle.

$$(m, n) = (\tau_i, \tau_j) \mid \left((\tau_j < \tau_i) \wedge (h(\tau_j) > h(\tau_i)) \wedge (h(\tau_i) < h(\tau_{i-1})) \wedge (h(\tau_{i+1}) > h(\tau_i)) \wedge (h(\tau_j) > h(\tau_{j-1})) \wedge (h(\tau_{j+1}) < h(\tau_j)) \wedge (h(\tau_j) - h(\tau_i) > a) \right) \quad (3)$$

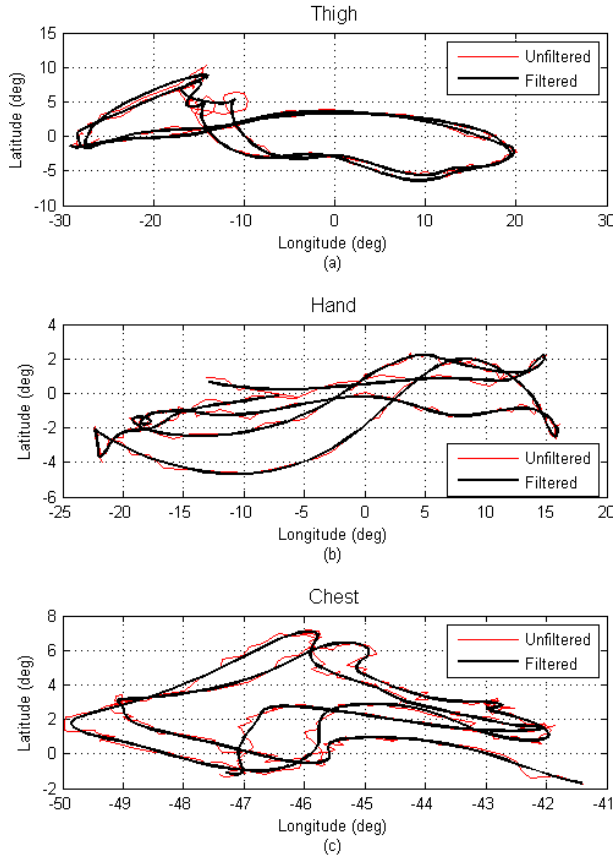


Figure 4. Sample data after conversion from 3D space to 2D space, then filtered using a low band pass of 5Hz. (a) Shows data from a thigh mounted sensor, (b) from a hand mounted sensor, and (c) from a chest mounted sensor. Each graph shows the data before the 5Hz low band pass filter, and after the filter.

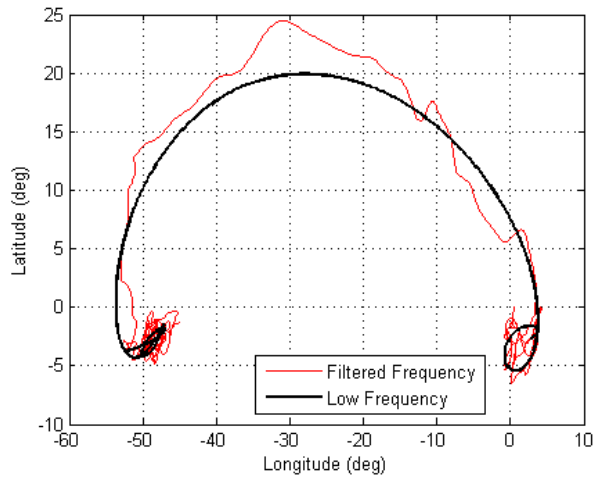


Figure 5. A sample of chest data with the subject taking a corner showing the data after the 5Hz low pass filter and low frequency signal ($< 0.5\text{Hz}$). The arc represents the corner, and the two clusters on either side of the arc represent the signal as the subject walks into the corner and later out of the corner.

While analyzing the signals, we found that because of the noisy chaotic nature of the signals (especially the chest signals) this method works better than the autocorrelation of the complex signal (longitude and latitude). Fig. 6 shows an example where the function $h(\tau)$ performs better than autocorrelation.

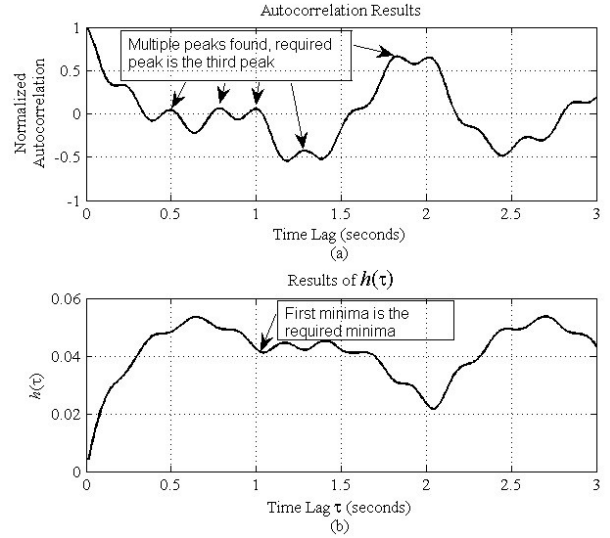


Figure 6. Results of the function $h(\tau)$ for $\tau=[0,3]$ seconds compared to autocorrelation results of the same walking data. The peak/minima of the actual measured cadence is expected at approximately 1 second, equivalent to the period of a single gait cycle for this subject at this point in time. (a) Shows the autocorrelation of the complex signal, while (b) shows results of function $h(\tau)$. Autocorrelation gives several peaks, of which the closest to measured cadence is the third, while the first minima of $h(\tau)$ gives the required minima.

IV. RESULTS ANALYSIS

In this section we validate the cadence extracted using our method against the actual cadence. The actual cadence that we used to verify our results was extracted using a method similar to that of [3], except we made use of the autocorrelation of the vertical component extracted from accelerometer data from the thigh-mounted sensor, which we then visually verified to be correct.

We measured the accuracy of our method based on the deviation from the actual cadence (estimated – actual). We then manually fit a Gaussian cluster over the data and extracted two sets of values:

1. the mean and standard deviation of the main cluster; and
2. the percentage of samples outside the main cluster (outliers).

The reason for doing this is that the results had a majority of the estimated cadences distributed close to the actual cadence, while some were distributed far from the actual cadence. These outlying points affect our results by increasing the standard deviation and hence giving the impression of a wider Gaussian distribution.

The results are given in Table 2 for the three body locations and two activities. For each location-activity combination, the mean and standard deviation (S. D.) of the main cluster is given, together with the percentage of samples outside the cluster. Data from sensors on the ankle, upper arm and navel, gave similar results to thigh, hand and chest respectively.

TABLE I. DEVIATION OF ESTIMATED CADENCE FROM ACTUAL CADENCE (STEPS PER SECOND) FOR THREE BODY LOCATIONS, AND TWO ACTIVITIES STUDIED. MEAN AND STANDARD DEVIATION (S. D.) OF THE MAIN CLUSTER DISTRIBUTION IS GIVEN, TOGETHER WITH PERCENTAGE OF DATA OUTSIDE THE CLUSTER.

Location	Walking			Running		
	Mean	S. D.	% outliers	Mean	S. D.	% outliers
Thigh	0.00	0.04	1.69	0.00	0.04	0.55
Hand	0.00	0.02	4.04	-0.02	0.06	1.99
Chest	-0.04	0.04	21.31	0.00	0.06	2.44

From the results in Table 2, we can see that for the main clusters the magnetometer results are close to the thigh accelerometer results (maximum standard deviation of 0.06 for chest and hand running). However there are a number of samples for the chest location while walking that were outside the main cluster. The error causing this effect is shown on Fig. 7. It can be noticed that each gait cycle (loop) has a chaotic period in which an inner loop forms. The chaotic period results in another peak occurring at half the time period (twice the cadence).

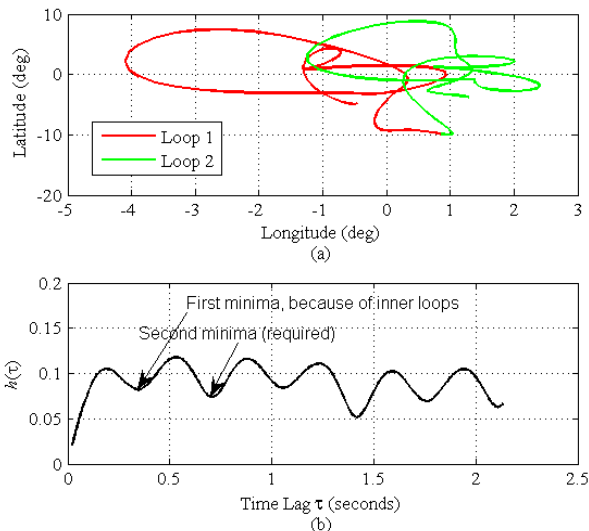


Figure 7. Example of cycles with chaotic periods forming inner loops. This particular sample was obtained from the chest sensor. (a) Shows the graph cycles (b) Graph of the output of $h(\tau)$ (eq. 2); even though the actual cadence (1.4 cycles/sec or 2.8 steps/sec) is found as the second trough, a significant first trough is also found resulting to it's selection instead of the actual cadence.

V. CONCLUSION

Magnetometers have largely been used in dead-reckoning and less in context-aware computation and pervasive health applications. The closest work is that of body segment orientation, of which most has been done using gyroscopes and accelerometers. Although there have been relatively few publications pertaining to the usage of magnetometers in context-aware computation, we have shown that magnetometer data can be used for measuring walking and running cadence. Our algorithm involves converting the magnetometer vectors to 2D space, filtering, and then estimating the period at which cycles repeat in the 2D signals. This period is equal to the period of the gait cycle, hence the inverse has to be multiplied by two to obtain the cadence in steps per second. Our algorithm is able to extract the cadence from the chaotic patterns and has led to results comparable to those of a thigh-mounted accelerometer. In the future, we hope to implement the algorithm on a smart phone so that the cadence can serve as a parameter in activity-recognition and ubiquitous energy-expenditure estimation in our day-to-day lives.

REFERENCES

- [1] K. Taylor, U. A. Abdulla, R. J. Helmer, J. Lee, I. Blanchonette, "Activity classification with smart phones for sports activities," *Procedia Engineering*, vol. 13, pp. 428-433, Jul. 2011.
- [2] M. J. Mathie, A. C. Coster, N. H. Lovell, B. G. Celler, "Accelerometry: providing an integrated, practical method for long-term, ambulatory monitoring of human movements," *Physiological measurement*, vol. 25, no. 2, pp R1-R20, Apr. 2004.
- [3] N. Oliver, F. Flores-Mangas, "MPTrain: a mobile, music and physiology-based personal trainer," in *Proceedings of the 8th conference on Human-computer interaction with mobile devices and services*, Espoo, Finland, 2006, pp. 21-28.
- [4] P. Barralon, N. Vuillerme, and N. Noury, "Walk detection with a kinematic sensor: frequency and wavelet comparison," in *28th Annual International Conference of the IEEE Engineering in Medicine and Biology Society (EMBS '06)*, New York, NY, 2006, pp. 1711-1714.
- [5] M. Yuwono, S. W. Su, B. D. Moulton, and H. T. Nguyen, "Gait cycle spectrogram analysis using a torso-attached inertial sensor," in *Annual International Conference of the IEEE Engineering in Medicine and Biology Society (EMBC)*, San Diego, Cal., 2012, pp. 6539-6542.
- [6] C. Mazzà, M. Donati, J. McCamley, P. Picerno, and A. Cappozzo, "An optimized Kalman filter for the estimate of trunk orientation from inertial sensors data during treadmill walking," *Gait & Posture*, vol. 35, no. 1, pp. 138-142, Jan. 2012.
- [7] E. Foxlin, "Pedestrian tracking with shoe-mounted inertial sensors," *Computer Graphics and Applications*, vol. 25, no. 5, pp. 38-46, Dec. 2005.
- [8] X. Yun, E. R. Bachmann, H. Moore, and J. Calusdian, "Self-contained position tracking of human movement using small inertial/magnetic sensor modules," in *IEEE International Conference on Robotics and Automation*, Roma, Italy, 2007, pp.2526-2533.
- [9] D. Roetenberg, H. J. Luinge, C. T. M. Baten, and P. H. Veltink, "Compensation of magnetic disturbances improves inertial and magnetic sensing of human body segment orientation," *IEEE Trans. on Neural Syst. and Rehabil. Eng.*, vol. 13, no. 3, pp. 395-405, Sept. 2005.
- [10] D. Roetenberg, C. T. M. Baten, and P. H. Veltink, "Estimating body segment orientation by applying inertial and magnetic sensing near ferromagnetic materials," *IEEE Trans. on Neural Syst. and Rehabil. Eng.*, vol 15, no. 3, pp. 469-471, Sept. 2007.

- [11] *Opal* by APDM, inc. [Online]. Available: <http://apdm.com/products/movement-monitors/opal/>
- [12] S. Gambino, M. Mirochnik, and S. Schechter. (2006). *Center of mass of a human* [Online]. Available: <http://hypertextbook.com/facts/2006/centerofmass.shtml>
- [13] T. Öberg, A. Karsznia, and K. Öberg, "Basic gait parameters: reference data for normal subjects, 10-79 years of age," *Journal of Rehabilitation Research and Development*, vol. 30, no. 2, pp. 210-223, 1993.
- [14] D. Mizell, "Using gravity to estimate accelerometer orientation," *Proceedings of the 7th IEEE International Symposium on Wearable Computers*, White Plains, NY, 2003, pp. 252.

Distinguishing Near-Falls from Daily Activities with Wearable Accelerometers and Gyroscopes using Support Vector Machines

Omar Aziz, Edward J. Park, *IEEE, Member*, Greg Mori and Stephen N. Robinovitch

Abstract—Falls are the number one cause of injury in older adults. An individual’s risk for falls depends on his or her frequency of imbalance episodes, and ability to recover balance following these events. However, there is little direct evidence on the frequency and circumstances of imbalance episodes (near falls) in older adults. Currently, there is rapid growth in the development of wearable fall monitoring systems based on inertial sensors. The utility of these systems would be enhanced by the ability to detect near-falls. In the current study, we conducted laboratory experiments to determine how the number and location of wearable inertial sensors influences the accuracy of a machine learning algorithm in distinguishing near-falls from activities of daily living (ADLs).

I. INTRODUCTION

Falls are the leading cause of injuries in older adults with a substantial impact on health and healthcare costs. Approximately one in three persons over the age of 65 falls at least once each year [1-3]. An individual’s risk for falls depends on his or her frequency of imbalance episodes, and ability to recover balance following these events [4-6]. For example, investigators have found that older adults who report multiple “near-falls” (missteps or stumbles) are more likely to go on to fall [7]. An accurate quantification of near-falls during daily activities could assist clinicians in assessing balance and developing strategies to prevent future falls [7, 8]. However, our current knowledge of near-falls in older adults is based on self-reports, which are often unreliable and likely underestimate the true occurrence of such events [6, 9].

Wearable inertial sensors, such as miniature accelerometers and/ or gyroscopes represent a promising technology for objectively quantifying balance, mobility and falls in older adults. Sensor hardware is rapidly advancing in terms of size, accuracy and cost. However, challenges remain in developing software to derive accurate, reliable and clinically relevant outcomes from sensor data. At present, the primary application for these systems is to detect the occurrence of a fall and alert care providers to this event [1, 10, 11].

Our goal is to enhance the utility of wearable fall monitoring systems beyond fall detection, to distinguish near-

falls from activities of daily living (ADLs). In particular, the current paper describes efforts to test, through laboratory experiments, how the number and location of sensors (3D accelerometers and gyros) influence the accuracy of a machine learning algorithm in distinguishing near-falls from ADLs.

II. METHODOLOGY

A. Participants

Ten healthy adults participated in this study, ranging in age between 22 and 32 years. All subjects were students at Simon Fraser University (SFU), recruited through advertisements posted on university notice boards. All participants provided informed written consent and the experiment protocol was approved by the research and ethics committee at SFU.

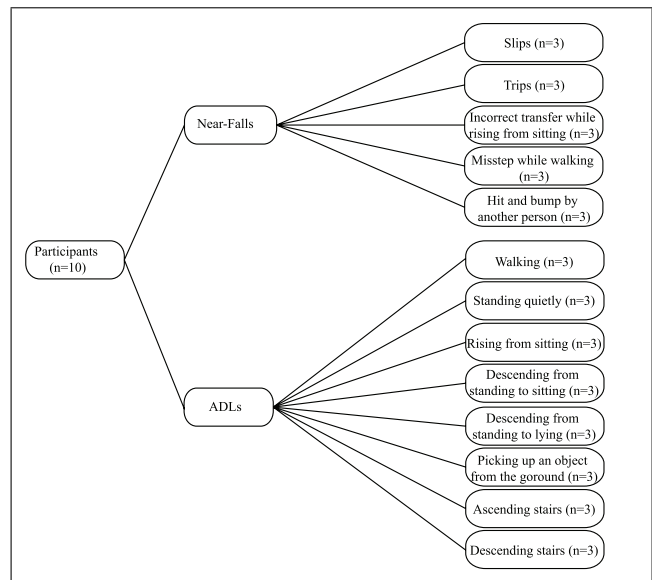


Fig. 1. Experiment protocol, indicating various types of near-falls and Activities of Daily Living (ADLs) simulated by each participant.

B. Experimental Design

During the experiment, participants underwent five types of near-falls and eight different activities of daily living (ADLs) (Fig. 1). These near-fall scenarios were selected as being representative of those emerging as most common from a study analyzing video-captured real life falls in long term care. All participants viewed falls from this library were then asked to act out the scenarios [12]. All near-fall trials were performed on a 30 cm thick gymnasium mattress, into which we inserted a 13 cm top layer of high density

O. Aziz is with the School of Engineering Science, Simon Fraser University, Burnaby, BC, V5A 1S6 Canada. oaziz@sfu.ca

E. J. Park is with Mechatronics Systems Engineering, School of Engineering Science, Simon Fraser University, Burnaby, BC, V5A 1S6 Canada. ed_park@sfu.ca

G. Mori is with the School of Computing Science, Simon Fraser University, Burnaby, BC, V5A 1S6 Canada. mori@cs.sfu.ca

S. N. Robinovitch is with the School of Engineering Science, Simon Fraser University, Burnaby, BC, V5A 1S6 Canada, and also with the Department of Biomedical Physiology and Kinesiology, Simon Fraser University, Burnaby, BC, V5A 1S6 Canada. stever@sfu.ca

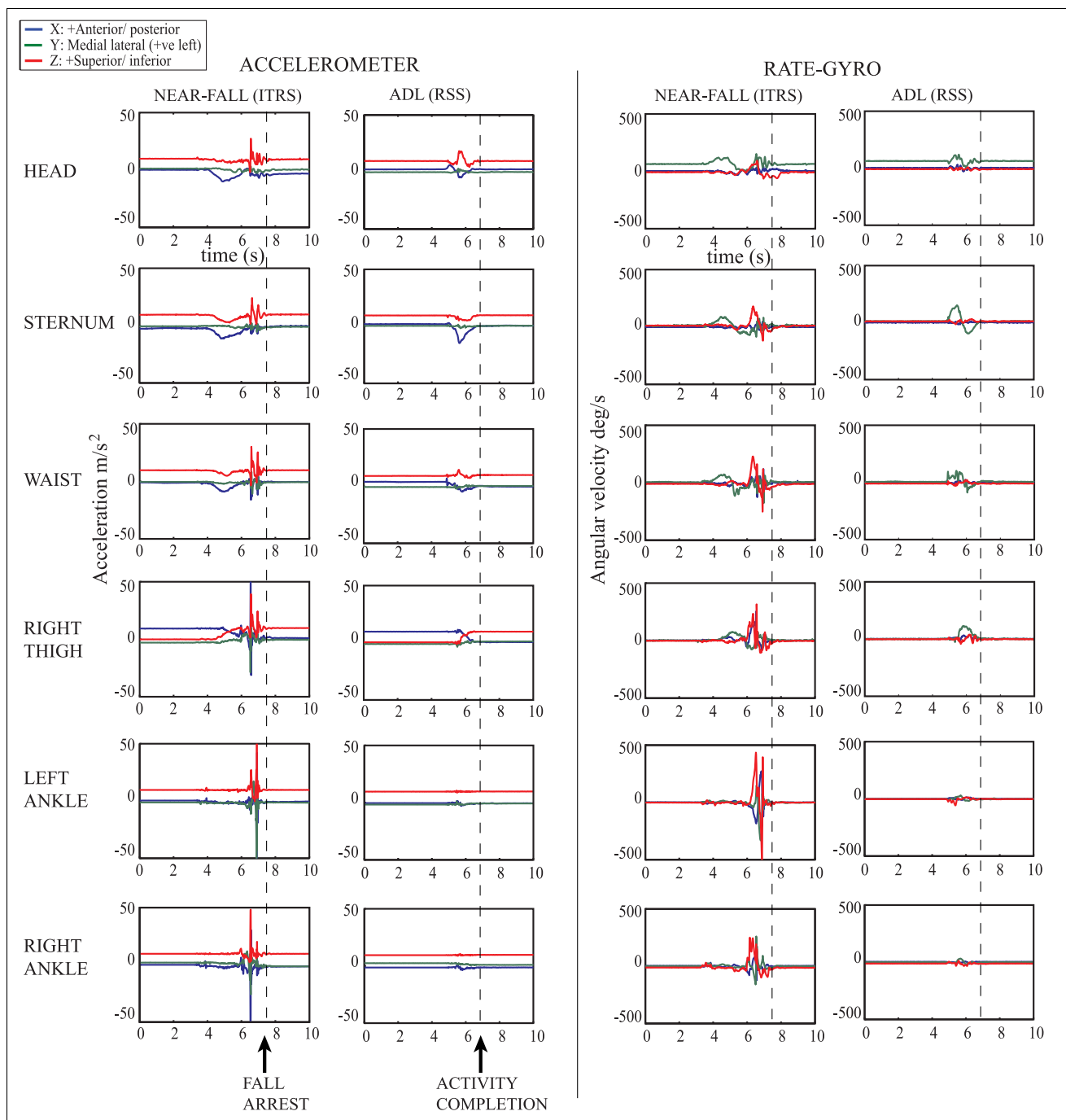


Fig. 2. Acceleration and rate-gyro traces in X, Y and Z direction from a typical participant in near-fall (Incorrect Transfer while Rising from Sitting (ITRS)) and ADL (Descending from Standing to Sitting (DSS)). The two vertical dotted lines show the completion of fall arrest in near-falls and the completion of activity in ADL.

ethylene vinyl acetate foam so the composite structure was stiff enough to allow for stable standing and walking, but soft enough to reduce the impact force to a safe level in case of a fall. In the near-falls, the participants were subjected to five different scenarios: (i) slips, (ii) trips, (iii) incorrect transfer while rising from sitting to standing (iv) misstep while walking, and (v) hit and bump by another person. For ADLs, eight scenarios were included: (i) walking, (ii) standing quietly, (iii) rising from sitting, descending from

(iv) standing to sitting and (v) standing to lying, (vi) picking up an object from the ground, (vii) ascending and (viii) descending stairs. All participants performed three trials in each category. Accordingly, over the ten participants, a total of 150 near-falls and 240 ADLs were recorded.

C. Data Acquisition

In each trial, we used seven inertial sensors (triaxial accelerometers having a range of $\pm 6g$ and triaxial gyros having a range of ± 1500 deg/s, APDM, Inc. Opals) worn

bilaterally on ankles and thighs, and at the waist, sternum and head recording at 128 Hz to acquire synchronized measures of the 3D accelerations and angular velocities.

III. DATA ANALYSIS

Data analysis focused on determining how the number and location of sensors influenced the ability of our classification algorithm to distinguish near-falls from ADLs. In the single sensor category, head, sternum, waist and both thigh sensors were included but not right or left ankle, based on the consideration that asymmetry in foot movements could necessitate bilateral placement in any real life application of our sensor technology. Moreover, in all three or more sensor categories, only one of the thigh sensors (i.e. right thigh) was used in the analysis. Thigh sensors are particularly useful for identifying transitions in movement, for example, descending from standing to sitting or lying position and vice versa, and one thigh sensor is deemed sufficient to capture such transition movements [13].

For each trial, we identified the approximate instant of fall-arrest (for near-fall trials) and activity completion (for ADL trials) by visual inspection of the sensor data. We then selected a 2.5 s time window prior to this instant to calculate the means and variances of the X, Y and Z signals for each accelerometer and gyroscope sufficient to capture the near-fall event from the initiation to arrest phase (Fig 2).

We used the Support Vector Machine (SVM) implementation in LIBSVM [14] with Radial Basis Function (RBF) kernel to distinguish near-falls from ADLs. The features (i.e. means and variances) were then split into training and testing sets of equal size by choosing the data from the first five subjects for training and the following five for testing. The SVM constructs a hyper-plane or a set of hyper-planes in a high or infinite-dimensional space, which can be used for classification. However, the effectiveness of the SVM depends on the selection of kernel and the kernel's parameters. In this study we used SVMs with RBF kernel which required two parameters, C and γ . The best combination of C and γ was selected by a grid-search with exponential growing sequences of C and γ (i.e. $C \in \{2^{-5}, 2^{-4}, \dots, 2^{14}, 2^{15}\}$; and $\gamma \in \{2^{-15}, 2^{-14}, \dots, 2^2, 2^3\}$). Each combination of parameter choices was checked using a 10-fold cross-validation and the parameter with the best cross-validation accuracy was picked. The final model, which was used for classifying test data, was then trained on the whole training set using the selected parameters. The procedure was conducted on the data from each sensor, and for each possible combination of 2, 3, 4, 5 and 6 sensors. In each case, we then calculated the sensitivity and specificity as:

$$Sensitivity = \frac{TruePositive}{TruePositive + FalseNegative} \quad (1)$$

$$Specificity = \frac{TrueNegative}{TrueNegative + FalsePositive} \quad (2)$$

TABLE I
SENSITIVITY AND SPECIFICITY OF 3D ACCELEROMETER AND RATE-GYRO ARRAYS IN SEPARATING NEAR-FALLS FROM ACTIVITIES OF DAILY LIVING

Sensor Combination	No. of FP	No. of FN	Sensitivity	Specificity
Single sensor				
Head	11	7	90.66	90.83
Sternum	6	9	88.00	95.00
Waist	5	15	80.00	95.83
L.thigh	11	3	96.00	90.83
R.thigh	1	6	92.00	99.16
Two sensors				
L.foot+R.foot	2	3	96.00	98.33
L.thigh+R.thigh	7	2	97.33	94.16
R.thigh+Waist	0	18	76.00	100.00
R.thigh+Sternum	1	12	84.00	99.16
R.thigh+Head	3	12	84.00	97.50
Waist+Sternum	3	7	90.66	97.50
Waist+Head	6	20	73.33	95.00
Sternum+Head	5	11	85.33	95.83
Three sensors				
L.foot+R.foot+R.thigh	1	3	96.00	99.16
L.foot+R.foot+Waist	1	0	100.00	99.16
L.foot+R.foot+Sternum	1	0	100.00	99.16
L.foot+R.foot+Head	5	2	97.33	95.83
R.thigh+Waist+Sternum	1	10	86.66	99.16
R.thigh+Waist+Head	2	18	76.00	98.33
R.Thigh+Sternum+Head	3	7	90.66	97.50
Four sensors				
L.foot+R.foot+R.thigh+Waist	1	2	97.33	99.16
L.foot+R.foot+R.thigh+Sternum	1	1	98.66	99.16
L.foot+R.foot+R.thigh+Head	1	0	100.00	99.16
L.foot+R.foot+Waist+Sternum	1	0	100.00	99.16
L.foot+R.foot+Waist+Head	2	0	100.00	98.33
L.foot+R.foot+Sternum+Head	1	0	100.00	99.16
R.thigh+Waist+Sternum+Head	2	20	73.33	98.33
Five sensors				
L.foot+R.foot+R.thigh+Waist+Sternum	1	1	98.66	99.16
L.foot+R.foot+R.thigh+Waist+Head	0	0	100.00	100.00
L.foot+R.foot+R.thigh+Sternum+Head	1	1	98.66	99.16
Six sensors				
L.foot+R.foot+R.thigh+Waist+Sternum+Head	2	1	98.66	98.33

False Positive (FP) = ADLs, incorrectly identified as near-falls

False Negatives (FN) = Near-falls, incorrectly identified as ADLs

IV. RESULTS

We found that our SVM algorithm showed good sensitivity and specificity in distinguishing near-falls from ADLs with various sensor combinations (Table 1). With a single sensor, the sensitivity and specificity of the system was at least 88% except for the waist sensor, which had 80% sensitivity.

With two sensors, the least number of false positives (FP) and false negatives (FN) was provided by the left ankle + right ankle combination, which distinguished near-falls and ADLs with 96% sensitivity and 98% specificity.

With three sensors, the highest sensitivity and specificity was provided by (a) left foot + right foot + sternum and (b) left foot + right foot + waist. Both combinations showed 100% sensitivity and 99% specificity.

The best overall performance was observed with the five sensor combination of left foot + right foot + right thigh + waist + head, which did not result in any false positive or false negative, and provided 100% sensitivity and specificity in distinguishing near-falls and ADLs. Sensitivity and specificity were no better with four and six sensor combinations

than with three.

V. DISCUSSION

In this study, we conducted lab based experimental trials with young adults to examine the utility of a wearable sensor array for distinguishing near-falls from ADLs. Our results indicated that the data from various combinations of three or more sensors, when input in our Support Vector Machine algorithm, provided sensitivity and specificity higher than 99% in distinguishing near-falls from ADLs. We also found that sensor placement at the feet considerably decreased false negatives indicating that lower extremity body kinematics was essential to identify near-falls.

There are important limitations to this study. First, our participants were healthy young adults, and they were aware of the external perturbations being applied to disturb their balance. An important unanswered question is the extent to which our classification procedure and results will transfer to unexpected near-falls in real-life scenarios by older adults, including those with specific disease conditions or neuromuscular impairment. Ultimately, this issue can only be addressed by testing the system with older adults as they go about their daily activities. However, several aspects of our experimental design enhance the validity of our results for older adults. Most importantly, before commencing a given series of trials, each of our participants studied representative video clips of real-life falls experienced by older adults residing in long-term care, and were instructed to “act out” a similar fall and near-fall [12]. Despite the inevitable variability in the acting style of participants, we believe this approach substantially enhanced the validity of our results for older adults.

Second, given the current size of self-contained wearable 3D sensors with on-board data storage and power supply (which are at least the size of large wrist watches), there is a legitimate concern that routine wear may be met with low user compliance in the target population. However, given the rapid rate of miniaturization of these components, one might expect that sufficient performance will soon be achieved with units the size of plasters.

This study demonstrates the utility of a wearable sensor system in distinguishing near-falls from ADLs with high accuracy. Incorporation of this application in fall monitoring systems should substantially enhance their utility for health professionals in assessing and monitoring the effectiveness of strategies in reducing fall risk.

ACKNOWLEDGMENT

This work was supported by team grants from the Canadian Institutes of Health Research (CIHR; grant numbers AMG-100487 and TIR-103945).

REFERENCES

- [1] W. H. Organization, “Global Report on Falls Prevention in Older Age”, World Health Organization, Geneva 2008.
- [2] V. Scott, S. Peck, and P. Kendall, “Prevention of Falls and Injuries Among the Elderly: A Special Report from the Office of the Provincial Health Officer”. Victoria BC: Provincial Health Office, BC Ministry of Health Services, 2004.
- [3] M. E. Tinetti and M. Speechley, “Prevention of falls among the elderly”, *New England Journal of Medicine*, vol. 320, pp. 1055-1059, 1989.
- [4] J. W. Ryan, J. L. Dinkel, and K. Petrucci, “Near falls incidence. A study of older adults in the community”, *Journal of Gerontological Nursing*, vol. 19, pp. 23-28, 1993.
- [5] Y. Nilsagard, C. Lundholm, E. Denison, and L. G. Gunnarsson, “Predicting accidental falls in people with multiple sclerosis a longitudinal study”, *Clinical Rehabilitation*, vol. 23, pp. 259-269, March 1, 2009 2009.
- [6] J. M. Srygley, T. Herman, N. Giladi, and J. M. Hausdorff, “Self-Report of Missteps in Older Adults: A Valid Proxy of Fall Risk?”, *Archives of Physical Medicine and Rehabilitation*, vol. 90, p. 786, 2009.
- [7] J. Teno, D. P. Kiel, and V. Mor, “Multiple stumbles: a risk factor for falls in community-dwelling elderly. A prospective study”, *Journal of the American Geriatrics Society*, vol. 38, pp. 1321-1325, 1990.
- [8] C. Arnold and R. Faulkner, “The history of falls and the association of the timed up and go test to falls and near-falls in older adults with hip osteoarthritis”, *BMC Geriatrics*, vol. 7, p. 17, 2007.
- [9] L. Mackenzie, J. Byles, and C. D’Este, “Validation of self-reported fall events in intervention studies”, *Clinical Rehabilitation*, vol. 20, pp. 331-339, April 1, 2006 2006.
- [10] N. Noury, A. Galay, J. Pasquier, and M. Ballussaud, “Preliminary investigation into the use of Autonomous Fall Detectors”, in *Engineering in Medicine and Biology Society, 2008. EMBS 2008. 30th Annual International Conference of the IEEE*, 2008, p. 2828.
- [11] M. N. Nyan, F. E. H. Tay, A. W. Y. Tan, and K. H. W. Seah, “Distinguishing fall activities from normal activities by angular rate characteristics and high-speed camera characterization”, *Medical Engineering & Physics*, vol. 28, p. 842, 2006.
- [12] O. Aziz and S. N. Robinovitch, “An Analysis of the Accuracy of Wearable Sensors for Classifying the Causes of Falls in Humans”, *Neural Systems and Rehabilitation Engineering*, *IEEE Transactions on*, vol. 19, pp. 670 - 676, 2011.
- [13] H. Gjoreski, M. Lustrek, and M. Gams, “Accelerometer Placement for Posture Recognition and Fall Detection”, in *2011 Seventh International Conference on Intelligent Environments*, 2011, pp. 47-54.
- [14] C.-C. Chang and C.-J. Lin, “LIBSVM: A library for support vector machines”, *ACM Transactions on Intelligent Systems and Technology*, vol. 2, pp. 1-27, 2011.

Enhancing clinical measures of postural stability with wearable sensors*

Priyanka M. Deshmukh, Colin M. Russell, Lisa E. Lucarino and Stephen N. Robinovitch

Abstract—About 30% of individuals over the age of 65, and 50% over age 80, fall at least once per year [1]. Fall-related injuries cost the Canadian health care system \$2.8 billion annually [2]. Risk for falls in older adults is commonly assessed in the clinical environment using tools such as the Short Physical Performance Battery (SPPB) [3], which include subjective assessments of postural sway while standing under various sensory conditions. This study uses wearable accelerometers and a force plate to quantify measures of postural stability during these tasks. Four participants were asked to maintain quiet stance in six different conditions, while their center of pressure (COP) and accelerations from six accelerometers were recorded. Standard deviations in signals were used as measures of postural sway. The sway observed in all sensors increased with the difficulty of the stance condition. Manipulation of vision and surface stiffness caused greater changes in sway in the AP than ML direction, while changes in stance configuration were more evident in the ML direction. Furthermore, the ankle sensor was the most sensitive in registering changes in sway when manipulating vision and surface stiffness (showing an increase of 236% over baseline values in AP sway with eyes closed and standing on foam), while the thigh was most sensitive to changes in stance width (showing an increase of 336% over baseline values in ML sway in the tandem stance condition). This study contributes in establishing the utility of wearable sensors for quantifying postural stability under various stance configurations in future studies with high-risk older adults.

I. INTRODUCTION

Falls are a major cause of injury in older adults. An individual's risk for falls associates with their postural stability during daily activities. In the clinical environment, postural stability is often assessed using tools such as the Short Physical Performance Battery (SPPB) [3] the timed Get-Up-and-Go [4], and the Physiological Balance Profile [5]. However, such tools rely on subjective classifications of performance.

In the laboratory environment, postural stability is commonly assessed by measuring the variability in the location of the centre-of-pressure (COP) between the feet and ground from a force plate [6]. Miniature wearable sensors represent a lower-cost alternative to force plates for quantifying postural

stability both within and outside of the clinical environment [7]. However, previous studies have not validated sensor-based measures of postural stability through comparison with force plate data.

Accordingly, the primary goal of this study was to compare COP-based measures of postural stability to those acquired by miniature inertial sensors worn at various body sites. A second goal was to examine the effect on these measures of alterations in vision, floor stiffness and stance configuration (manipulations typically incorporated into clinical tests). Our results illustrate how wearable sensors provide information on postural stability that correlates with COP measures, is sensitive to task conditions, and conveys underlying postural control mechanisms. These results support the value of this portable technology as an attractive option to force plates in quantifying postural stability during stance.

II. METHOD

A. Study participants

Study participants consisted of 4 healthy young individuals (1 male, 3 female), all of whom provided informed consent.

B. Stance Conditions

Participants were instructed to stand as quietly as possible while adopting different stance configurations, with eyes open and closed, and while standing on a firm surface or foam. The conditions were as follows:

- 1) Normal stance (feet shoulder width apart), eyes open, on rigid surface;
- 2) Semi-tandem (ST) stance (right foot in front of left, with narrow stance width), eyes open, on rigid surface;
- 3) Tandem (T) stance (right foot in front of left, with zero stance width), eyes open, on rigid surface;
- 4) Normal stance, eyes closed, on rigid surface;
- 5) Normal stance, eyes open, on compliant surface (10 cm thick foam pad);
- 6) Normal stance, eyes closed, on compliant surface.
- 7) Normal stance, eyes open, rigid surface, exaggerated anterior-posterior (heel-toe) rocking.

C. Data collection and analysis

In each trial, data were collected from miniature wireless sensors (tri-axial accelerometers $\pm 6g$, Opals, APDM Inc.) secured at six body sites (Fig. 1): sternum, waist (posterior aspect), right and left thighs and right and left ankles (lateral aspects). An additional sensor was placed on a mallet drop synchronization system. Sensor data were sampled at 128 Hz (the maximum sampling frequency offered by the sensors).

*Research supported by the Canadian Institutes of Health Research (CIHR)

Priyanka M. Deshmukh is with Simon Fraser University, Burnaby, BC V5A 1S6 Canada. Phone: 778-782-6679; e-mail: pmd1@sfu.ca

Colin M. Russell is with Simon Fraser University, Burnaby, BC V5A 1S6 Canada. Phone: 778-782-6679; e-mail: crussell@sfu.ca

Lisa E. Lucarino is with Simon Fraser University, Burnaby, BC V5A 1S6 Canada. Phone: 778-782-6679; e-mail: lel18@sfu.ca

Stephen N. Robinovitch is with Simon Fraser University, Burnaby, BC V5A 1S6 Canada. Phone: 778-782-3566; e-mail: stever@sfu.ca

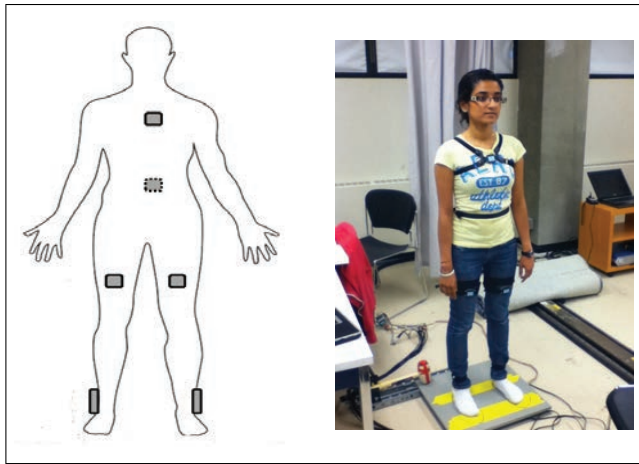


Fig. 1. Location of inertial sensors on the body.

We also acquired foot reaction forces and moments from a force plate (Accusway, AMTI) at 1280 Hz via LabVIEW. COP in the x and y directions was calculated from ground reaction forces (F_x , F_y , F_z) and moments (M_x , M_y , M_z) as follows: $COP_{x_direction} = \frac{-M_y}{F_z} \times 1000$ and $COP_{y_direction} = \frac{M_x}{F_z} \times 1000$.

The APDM data collection software allowed for synchronized measures from each of the 7 sensors. To synchronize these sensor data with data from force plate, a hinged mallet, having a sensor attached to its head, was raised a fixed height and released to strike the force plate, providing a distinct time stamp for synchronization of sensor and force data. Force

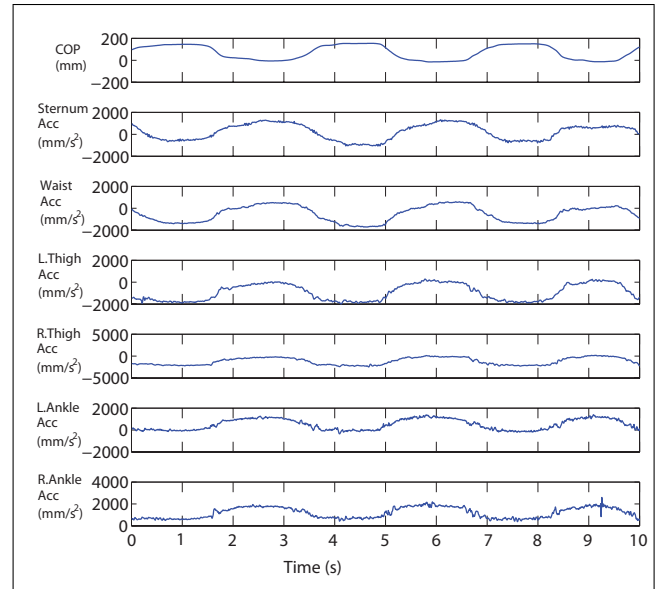


Fig. 2. COP and acceleration traces in the AP direction (7) - exaggerated heel-toe rocking.

plate and sensor data were filtered using a fourth-order low-pass Butterworth filter, having a 10Hz cut-off frequency [8]. Fig. 2 illustrates an example of COP and acceleration data acquired under condition (7), exaggerated heel-toe rocking.

In each trial, we characterized postural sway as the standard deviation (SD) in acceleration (from the sensors) or COP (from the force plate) in both the anterior-posterior (AP)

TABLE I
EFFECT OF CONDITION ON POSTURAL SWAY

	Sternum	Waist	Thigh	Ankle	COP
AP Direction					
Normal stance	54.1 (20.6)	43.9 (13.3)	40.6 (11.6)	22.5 (8.1)	2.3 (0.8)
Semi tandem	56.9 (13.4)	50.4 (6.3)	46.8 (5.8)	30.7 (5.7)	2.7 (0.4)
Tandem	73.2 (11.2)	72.7 (19.4)	84.9 (16.0)	78.8 (22.0)	3.5 (0.9)
Eyes closed, rigid surface	75.3 (11.6)	70.7 (21.1)	55.3 (15.7)	41.2 (11.6)	4.2 (0.9)
Eyes open, foam surface	84.3 (26.8)	70.1 (22.2)	65.6 (17.6)	59.4 (19.9)	4.9 (1.5)
Eyes closed, foam surface	91.3 (19.0)	86.1 (21.0)	86.1 (25.6)	74.4 (23.4)	6.6 (1.9)
Heel-toe-rocking	860.3 (234.5)	792.9 (275.4)	616.8 (169.3)	414.0 (21.7)	58.4 (8.5)
ML Direction					
Normal stance	33.5 (10.7)	19.8 (2.6)	23.4 (2.8)	12.7 (3.6)	1.0 (0.2)
Semi tandem	45.7 (9.9)	34.7 (5.3)	32.7 (2.3)	31.1 (10.2)	2.6 (0.3)
Tandem	110.6 (18.6)	68.6 (9.7)	103.3 (22.0)	82.8 (24.8)	5.5 (1.2)
Eyes closed, rigid surface	38.4 (9.7)	21.7 (4.1)	26.5 (6.6)	20.9 (8.6)	1.2 (0.3)
Eyes open, foam surface	42.5 (7.6)	32.3 (8.1)	34.2 (6.5)	32.7 (7.0)	2.3 (0.6)
Eyes closed, foam surface	42.1 (7.4)	34.2 (6.7)	40.8 (8.8)	43.4 (14.6)	2.9 (0.8)
Heel-toe-rocking	122.5 (51.8)	98.2 (37.1)	141.2 (16.2)	129.3 (53.5)	6.9 (2.4)

Notes: Cell entries show mean values of the standard deviations (SD's) in acceleration and COP location, averaged over all subjects, across right and left sides for thigh and ankle sensors. SD's of the SD's are shown in parentheses. Units are mm/s² for sensor accelerations and mm for COP position.

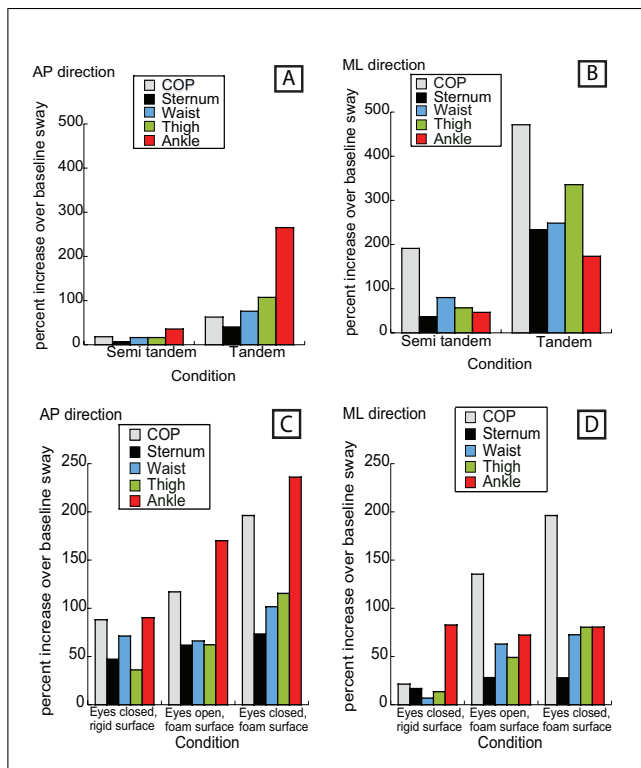


Fig. 3. Percent change in postural sway (signal SD) over baseline (condition (1)) condition following manipulations in stance configurations (A and B) or vision and surface stiffness (C and D).

and medial-lateral (ML) directions, over 10 seconds. We also examined the correlation between sensor accelerations and COP, after down-sampling the latter (from 1280 to 128 Hz) using a shape-preserving piecewise cubic interpolation.

III. RESULTS

As the difficulty of the task increased (from 1 to 6), there was an increase in the SD's of both COP and acceleration signals (Table 1). In the AP direction, the largest SD's occurred in condition 6 (eyes closed, compliant surface), except for the ankle sensor, where the largest SD's occurred in condition 3 (tandem stance). In the ML direction, the largest SD's in COP and acceleration occurred in condition 3 (tandem stance).

Alterations in stance configuration caused larger changes in sway in the ML than AP direction, with the largest changes observed at the thigh and waist sensors (Figs. 3A and 3B). When compared to baseline conditions, tandem stance (condition 3) involved increases in ML sway of 336% at the thigh, and 249% at the waist. Conversely, changes in vision and surface stiffness yielded larger changes in sway in the AP than ML direction (Figs. 3C and 3D), with the largest changes observed at the ankle (increases of 90%, 170% and 236% over baseline values for conditions 4, 5 and 6, respectively).

IV. DISCUSSION

In this study, we examined the utility of wearable sensors in characterizing postural sway under various clinical testing

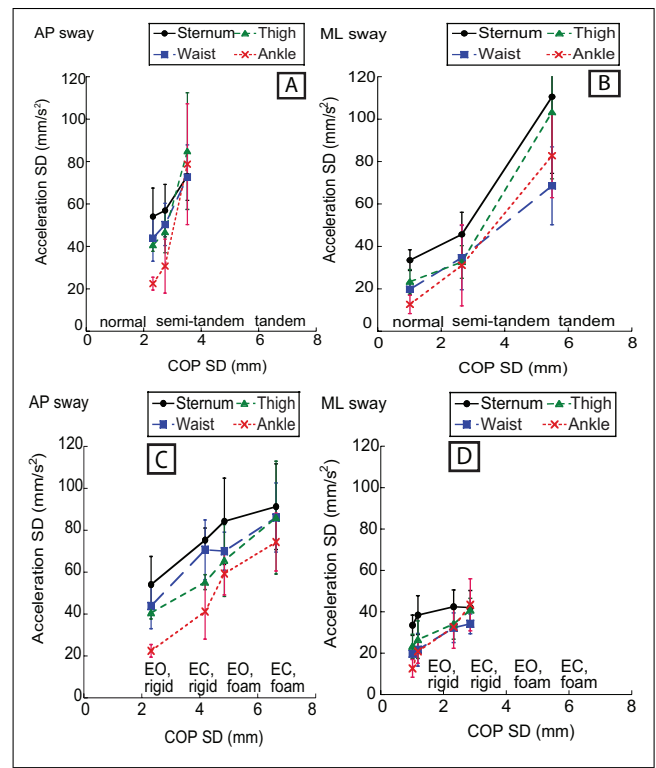


Fig. 4. Combinations of COP and acceleration for various sensor locations following manipulations in stance configurations (A and B) or vision and surface stiffness (C and D).

conditions. We found that the variance (standard deviation) from all sensors increased as the base of support decreased, as vision was removed, or when moving from a rigid to compliant ground. We also found that the ankle sensor was most sensitive in registering changes in sway when manipulating vision and surface stiffness, while the waist and thigh sensors were most sensitive to changes in stance width.

Furthermore, manipulation in vision and surface stiffness caused greater changes in sway in the AP than ML direction, while changes in stance configuration had a larger effect on sway in the ML than AP direction. These results guide the design of a minimum sensor array for future clinical use.

They also illustrate the value of wearable sensors in providing insight on the postural control strategies (e.g., hip versus ankle strategy) used under various sensory and support conditions [9,10]. An important limitation of this study is that our participants were young healthy individuals, and an essential next step is to repeat the experiment with older adults.

V. CONCLUSION

We instructed human participants to stand as quietly as possible under various sensory and support conditions, and compared measures of postural sway from miniature accelerometers mounted at various body locations, to those acquired with a force plate. Of all the signals we examined, AP sway at the ankle was most sensitive to alternations in

vision and surface stiffness, while ML sway at the waist or thigh was most sensitive to changes in stance width.

While inertial sensors have previously been used to assess postural stability, to our knowledge, there have been no previous studies that compare COP measures to information provided through wearable sensors across a wide range of static task conditions (that not only include normal quiet stance, but also alter the base of support, vision and somatosensory input). Furthermore, we employed a novel approach by using sensors to identify the relationship between various task conditions and direction (AP vs. ML) of greatest instability. Lastly, study findings can guide in the identification of a minimum sensor array system to help understand underlying postural control mechanisms. Overall, the study results contribute to the development of a cost effective wearable sensor system for providing accurate and meaningful measures of postural stability.

ACKNOWLEDGMENT

This work was supported by team grants from the Canadian Institutes of Health Research (CIHR; grant numbers AMG-100487 and TIR-103945).

REFERENCES

- [1] J. L. O'Loughlin, Y. Robitaille, J. F. Boivin, S. Suissa, "Incidence of and risk factors for falls and injurious falls among the community-dwelling elderly". *American Journal of Epidemiology*, vol. 137, pp.342-354, 1993.
- [2] Public Health Agency of Canada. "Cost and Saving associated with falls." Internet: http://www.phac-aspc.gc.ca/seniors-aines/publications/pro/healthysante/haging_newvision/vision-rpt/falls-chutes-eng.php , Oct. 01, 2009 [March 12, 2012].
- [3] J. M. Guralnik, E. M. Simonsick, "A short physical performance battery assessing lower extremity function: Association with self-reported disability and prediction of mortality and nursing home admission". *Journal of Gerontology: Med Sciences*, vol. 49, pp.M85-M94, 1994.
- [4] D. Podsiadlo, S. Richardson, "The times 'Up & Go': a test of basic functional mobility for frail elderly persons". *Journal of American Geriatric Society*, vol. 39, pp. 142-148, 1991.
- [5] S.R. Lord, R.D. Clark, "Simple physiological and clinical tests for the accurate prediction of falling in older people". *Gerontology*, vol. 42, pp. 199-203, 1996.
- [6] T.E. Prieto, J. B. Myklebust, R.G. Hoffmann, E.G Lovett, B.M. Myklebust, "Measures of postural steadiness: differences between healthy young and elderly adults", *IEEE Transactions on Biomedical Engineering*, vol.43, pp. 956-966, 1996.
- [7] A. Salarian, F. Horak, C. Zampieri, P. C. Kuhta, J. G. Nutt, K. Aminian, "iTUG, a Sensitive and Reliable Measure of Mobility", *IEEE Trans. Neural Systems and Rehabilitation Engineering*, vol.18, pp. 303-310, 2010.
- [8] K. Nomura, K. Fukada, T. Azuma, T. Hamasaki, S. Sakoda, T. Nomura, "A quantitative characterization of postural sway during human quiet standing using a thin pressure distribution measurement system", *Gait and Posture*, vol. 29, pp. 654-657, 2009.
- [9] I. G. Amiridis, V. Hatzitaki, F. Arabatzi, "Age-induced modifications of static postural control in humans", *Neuroscience Letters*, vol. 350, no.3, pp. 137-140, 2003.
- [10] F. Horak, L.M. Nashner, "Central programming of postural movements: adaptation to altered support-surface configurations", *Journal of Neurophysiology*, vol. 55, no.6, pp. 1369-1381, 1986.

Shoulder and Elbow Joint Angle Tracking With Inertial Sensors

Mahmoud El-Gohary* and James McNames

Abstract—Wearable inertial systems have recently been used to track human movement in and outside of the laboratory. Continuous monitoring of human movement can provide valuable information relevant to individuals' level of physical activity and functional ability. Traditionally, orientation has been calculated by integrating the angular velocity from gyroscopes. However, a small drift in the measured velocity leads to increasing integration error over time. To compensate that drift, complementary data from accelerometers are normally fused into tracking systems using the Kalman or extended Kalman filter. In this study, we combine kinematic models designed for control of robotic arms with state-space methods to continuously estimate the angles of human shoulder and elbow using two wearable inertial measurement units. We use the unscented Kalman filter to implement the nonlinear state-space inertial tracker. Shoulder and elbow joint angles obtained from 8 subjects using our inertial tracker were compared to the angles obtained from an optical-tracking reference system. On average, there was an RMS angle error of less than 8° for all shoulder and elbow angles. The average correlation coefficient for all movement tasks among all subjects was $r \geq 0.95$. This agreement between our inertial tracker and the optical reference system was obtained for both regular and fast-speed movement of the arm. The same method can be used to track movement of other joints.

Index Terms—Elbow, inertial sensors, joint angle tracking, kinematics, shoulder, wearable devices.

I. INTRODUCTION

MEASUREMENT and analysis of human movement has many applications including diagnosis of neurological movement disorders, rehabilitation from injury, and enhancement of athletic performance. Movements can be measured using a wide variety of techniques and sensors. Optical systems have been widely used to assess leg, elbow, and shoulder kinematics noninvasively. They rely on measurements of reflected or emitted light [1]. Motion is captured by placing reflective markers on the body and cameras are used to record the markers positions. Optical systems are the most common and accurate in tracking movement [2]. However, they require a clear line of sight between the source and the sensor, are costly, and can only be used in a laboratory environment.

Manuscript received May 6, 2012; revised June 26, 2012; accepted July 10, 2012. Date of publication July 13, 2012; date of current version August 16, 2012. Asterisk indicates corresponding author.

*M. El-Gohary is with the Biomedical Signal Processing Laboratory, Department of Electrical and Computer Engineering, Portland State University, Portland OR 97201, USA (e-mail: mahmoud@pdx.edu).

J. McNames (Director) is with the Biomedical Signal Processing Laboratory, Department of Electrical and Computer Engineering, Portland State University, Portland OR 97201, USA (e-mail: mcnames@pdx.edu).

Color versions of one or more of the figures in this paper are available online at <http://ieeexplore.ieee.org>.

Digital Object Identifier 10.1109/TBME.2012.2208750

A typical inertial measurement unit (IMU) is a compact wearable device that contains a triaxial accelerometer and a triaxial gyroscope. Accelerometers measure the translational acceleration and acceleration due to gravity. Gyroscopes measure angular velocities. Wearable inertial sensors are simpler, unobtrusive, and self-contained. They are suitable for continuously monitoring over long periods while the subject performs normal activities of daily life at home. Fig. 2 shows an example of Opal sensor (Ambulatory Parkinsons Disease Monitoring, Inc., Portland, OR) used in this study.

Traditionally, orientation of a segment has been estimated by integrating the angular velocities measured by gyroscopes, and position is obtained by double integration of the translational acceleration measured by accelerometers. A significant problem with integration, however, is that inaccuracies inherent in the measurements quickly accumulate and rapidly degrades accuracy. Roetenberg showed that integration of noisy gyroscope data resulted in a drift of 10° – 25° after 1 min [3].

One approach to reducing integration drift is to fuse the gyroscope data with complementary data from other sensors. Luinge *et al.* estimated orientation of body segments by fusing gyroscope and accelerometer data [4], [5]. The orientation obtained by integrating angular rate was spilt into tilt and orientation around the global vertical axis. The difference between gyroscope and accelerometer tilt was fused with a Kalman filter to more accurately estimate the tilt. This was then combined with the rotation around the vertical axis to produce a better orientation estimate. However, the estimation was accurate for only brief periods when the subject was not moving and when acceleration was only due to gravity.

To alleviate the cumulative drift around the vertical axis encountered in their earlier system [6], Luinge *et al.* developed a method that used constraints in the elbow to measure the orientation of the forearm with respect to the upper arm [7], [8]. They used one inertial measurement unit near the wrist and another near the elbow. Heading error between the two arm segments was minimized using the knowledge that the elbow joint does not permit abduction/adduction. The filter estimated the orientation in a way that sets the adduction angle to zero. Although they reported an improvement in estimating the orientation, the average orientation error was 20° .

Giansanti *et al.* combined gyroscopes with accelerometers to track position and orientation during three tasks: stand-to-sit, sit-to-stand, and gait initiation [9]. Error in estimation was minimal. However, they restricted the application to simple tasks and limited the measurements to a time duration of 4 s.

In a series of studies, Bachmann *et al.* used accelerometers and magnetometers in a quaternion-based complementary filter to compensate the drift of the orientation produced by

integrating the angular velocity [10], [11]. The system combined a triaxial accelerometer, a triaxial gyroscope and a triaxial magnetometer assembled to produce a sensor module referred to as Magnetic, Angular Rate and Gravity sensor (MARG). In a later study, Bachmann *et al.* investigated the effect of electrical appliances and furniture made of ferromagnetic materials on the accuracy of orientation tracking using MARG systems [12]. They observed errors that ranged from 12° to 16° and stated that these errors can be avoided by maintaining an approximate distance of two feet from the source of disturbance. This limits the success of their tracking system and restricts its use to custom laboratory environment.

Roetenberg *et al.* argued that errors due to magnetic-field disturbance may be compensated by adequate model-based sensor fusion [13]. They developed a Kalman filter that operated on two inputs. The first was the difference between inclination from the accelerometer and gyroscope. The second input was the difference inclination from the magnetometer and gyroscope. The states of the model included the gyroscope bias error, orientation error, and magnetic disturbance. The filter was tested under quasi-static and dynamic conditions with ferromagnetic materials close to the sensor for less than a minute. The results show that the orientation estimates improved significantly when the magnetic interference correction was used. However, the accuracy could decrease if the magnetic disturbance was due to varying sources that are present during longer periods of testing. In a subsequent study, Roetenberg *et al.* combined a body-mounted magnetic system with gyroscopes and accelerometers to track position and orientation using a complementary Kalman filter [14]. Orientation and position were obtained by single and double integration of gyroscope and accelerometer data, respectively. These were then updated with magnetometer data to improve accuracy. The tracker was tested without metals in the vicinity, and errors were expected to grow if ferromagnetic materials were anywhere close to the magnetic system.

Yun *et al.* used MARG modules and a quaternion-based extended Kalman filter (EKF) to track human body motion. A Gauss–Newton iteration method was used to preprocess accelerometer and magnetometer data to produce quaternion input to the EKF [15]. A rotary tilt table with two DOF's was used to assess the performance of the tracker [16], [17]. The pitch angle error was not reported, and an error of 9° in less than 2 s was obtained for the roll angle. In a recent study, Yun *et al.* presented a simplified algorithm for orientation estimation using only accelerometers and magnetic field measurements [18]. Although the system was suitable for tracking slow movements, the gyroscope-free system is not suited for normal or fast movements, resulting in large orientation errors.

In a series of studies by Zhou *et al.* orientations of wrist and elbow were estimated by fusion of the signals from MARG modules mounted on the wrist and elbow joints [19], [20]. They integrated the rotational rate to localize the wrist and elbow, and smoothed the abrupt amplitude changes to reduce overshoot during fast movements. Three subjects performed a set of tasks that lasted 20 s and was repeated three times with a resting period of 30 s in between. The tasks included reaching a target, drinking, lifting the arm, and flexing the elbow while keeping the

shoulder still. They attained a high correlation between position estimates from the inertial tracker and estimates from a reference optical tracking system ≥ 0.91 [21].

In summary, other groups have used accelerometers and magnetometers to compensate for the orientation error that occurs when integrating the angular rate from gyroscopes, but all of these methods were only applicable under limited circumstances. Some groups restricted the application to simple tasks and short tracking periods. In other studies, the estimation was accurate for only brief periods when the acceleration measurements were only due to gravity. Others reported large orientation errors due to magnetic field disturbances.

In this paper, we combine kinematic models designed for control of robotic arms with state-space methods to directly and continuously estimate human joint angles from inertial sensors. We investigate the performance of our unscented Kalman filter (UKF)-based method by first validating our statistical models using synthetic data. We then investigate the performance of our inertial tracking algorithm by comparing the estimated inertial angles to those obtained from an optical reference system during normal and fast movement of eight subjects performing both simple planar and complex arm movement.

II. THEORY

We use an established method of biomechanical modeling based on a sequence of links connected by joints. This type of model could represent any part of the human body. To systematically describe the position and orientation of each pair of consecutive links, a method was proposed by Denavit and Hartenberg in 1955. The method is widely used in the analysis and control of robotic manipulators [22] and has also been successfully applied to characterize human motion [23]. The method is based on characterizing the relationship between links and joints with a (4×4) transformation matrix. This matrix depends on four parameters associated with each link. The first parameter is the link length a_i , which is the distance from the rotation axis Z_i to Z_{i+1} measured along their common normal axis X_i . The second parameter is the link twist α_i , which is the angle from Z_i to Z_{i+1} measured about the X_i -axis. The distance from X_{i-1} to X_i measured along the Z_i -axis is known as the link offset d_i . The fourth parameter is the joint angle θ_i , which is the angle from X_{i-1} to X_i measured about the Z_i -axis. These four parameters are known as the Denavit–Hartenberg (D-H) parameters and will be specified for the shoulder and elbow in the following section. To describe the location and orientation of each link relative to the one next to it, we attach a frame to each link. The convention of attaching reference frames to upper arm and forearm segments was detailed in [23].

A. Shoulder and Elbow Joint Angles

We present a model for shoulder and elbow movement with five degrees of freedom (DOFs). The shoulder and the shoulder girdle make up one of the most complex joint groups of the human body [24]. This complex joint is typically simplified as a ball-and-socket joint with three DOFs. When a joint has n -DOFs, it can be modeled as n joints of one DOF connected with $n - 1$ links of zero length [22]. Fig. 1 shows the arm

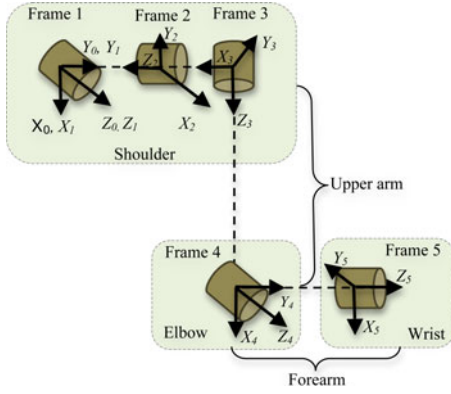


Fig. 1. Kinematics diagram of the arm model with Frame 0 as the static reference frame. Frames 1 through 3 represent shoulder flexion/extension, abduction/adduction and internal/external rotation, respectively. Frames 4 through 5 represent the elbow flexion/extension and forearm pronation/supination.

TABLE I
DENAVIT–HARTENBERG PARAMETERS FOR THE ARM MODEL

Frame	α_{i-1}	a_{i-1}	d_i	θ_i
1	0	0	0	θ_1
2	$\pi/2$	0	0	$\theta_2 + \pi/2$
3	$\pi/2$	0	l_u	$\theta_3 + \pi/2$
4	$\pi/2$	0	0	$\theta_4 + \pi/2$
5	$-\pi/2$	0	l_f	θ_5

model with static base reference frame 0 at the center of the shoulder joint. Frames 1 through 3 represent shoulder flexion/extension, abduction/adduction, and internal/external rotation, respectively. The elbow joint is a hinge joint that allows movement in one plane, flexion/extension, represented by frame 4. The radioulnar joint is a pivot joint that allows for forearm pronation/supination, represented by frame 5 [25].

Table I shows the D-H parameters, where α_{i-1} is the angle to rotate to make the two coordinate systems coincide, l_u is the length of the upper arm, l_f is the length of the forearm, and θ_i is the i th angle of rotation.

B. Propagation of Velocity and Acceleration

To formulate the dynamic equations for the arm IMUs during movement, we use three of the Newton–Euler equations of motion. These forward recursive equations are used to propagate angular velocity, and angular and linear acceleration from the reference coordinate system through the links of upper arm, forearm, and wrist. Each link of the arm in motion has some angular velocity, and angular and linear acceleration ($\omega, \dot{\omega}, \dot{v}$). The velocity ${}^{i+1}\omega_{i+1}$ of link $i+1$ is that of link i plus the new velocity component added by joint $i+1$. Similarly, the angular and linear acceleration of each link are related by the following recursive equations:

$${}^{i+1}\omega_{i+1} = {}^i R^i \omega_i + \dot{\theta}_{i+1} {}^{i+1} Z_{i+1}$$

$${}^{i+1}\dot{\omega}_{i+1} = {}^i R^i \dot{\omega}_i + {}^i R^i \omega_i \times \dot{\theta}_{i+1} {}^{i+1} Z_{i+1} + \ddot{\theta}_{i+1} {}^{i+1} Z_{i+1}$$

$${}^{i+1}\dot{v}_{i+1} = {}^i R^i [\dot{\omega}_i \times {}^i P_{i+1} + \omega_i \times ({}^i \omega_i \times {}^i P_{i+1}) + \dot{v}_i]$$

where ${}^i R^i$ is the rotation matrix between the i th and $(i+1)$ th link, \times represents the cross product operation, $\dot{\theta}_i$ is the angular

velocity, ${}^i P_{i+1}$ is the position vector of frame $i+1$, which is the upper-right 3×1 vector of the D-H matrix. The rotation matrices R , can be obtained by taking the transpose of the upper left 3×3 transformation matrix with parameters shown in Table I. Single and double dot notation represents first and second derivatives with respect to time. We initialize $\omega_0 = \dot{\omega}_0 = (0, 0, 0)^T$, and $\dot{v}_0 = (g_x, g_y, g_z)^T$, where g is gravity.

C. State-Space Model

The general discrete time state-space model is of the form

$$x(n+1) = f_n [x(n), u(n)] \quad (1)$$

$$y(n) = h_n [x(n), v(n)] \quad (2)$$

where $x(n)$ is the unobserved state, $y(n)$ is the measured data, $f_n[\cdot]$ and $h_n[\cdot]$ are nonlinear state and observation equations, $u(n)$ and $v(n)$ are the state and observation white noise with zero mean. Our state model equations are given by

$$\theta_i(n+1) = \theta_i(n) + T_s \dot{\theta}_i(n) + \frac{1}{2} T_s^2 \ddot{\theta}_i(n) \quad (3)$$

$$\dot{\theta}_i(n+1) = \dot{\theta}_i(n) + T_s \ddot{\theta}_i(n) \quad (4)$$

$$\ddot{\theta}_i(n+1) = \alpha \ddot{\theta}_i(n) + u_{\ddot{\theta}_i}(n) \quad (5)$$

where $i = \{1, \dots, 5\}$ of the five angles, $\theta_i(n)$ is the i th angle at time n , $\dot{\theta}_i$ is the angular velocity, $\ddot{\theta}_i$ is the angular acceleration, $u_{\ddot{\theta}_i}(n)$ is a white noise process with zero mean, α is a process model parameter, and $T_s = 1/f_s$ is the sampling period. These are standard equations for a physical object moving at a constant acceleration. The model assumes the acceleration is constant for the duration of a sampling interval. This is sufficient for our data, which was acquired with a sample rate of $f_s = 128$ Hz. The angular acceleration is modeled as a first-order autoregressive process with zero mean. Depending on the choice of α , this model ranges from a random walk ($\alpha = 1$) to a white noise model ($\alpha = 0$). For values of $\alpha < 1$ the estimated angular accelerations are biased toward 0, but for human motion this bias is reasonable and may improve performance.

The observation equations were created with an algorithm that algebraically applies the Newton–Euler recursive equations with the parameters in Table I. Equations of the upper arm IMU are

$$\dot{\omega}_z = \dot{\theta}_3 + \dot{\theta}_1 s \theta_2$$

$$\dot{\omega}_x = \dot{\theta}_1 c \theta_2 s \theta_3 - \dot{\theta}_2 c \theta_3$$

$$\dot{\omega}_y = \dot{\theta}_1 c \theta_2 c \theta_3 + \dot{\theta}_2 s \theta_3$$

$$\dot{v}_x = -l_u [\dot{\theta}_1^2 c \theta_2^2 + \dot{\theta}_2^2] - g c \theta_1 c \theta_2$$

$$\dot{v}_y = l_u [c \theta_2 s \theta_2 s \theta_3 \dot{\theta}_1^2 - 2 \dot{\theta}_2 c \theta_3 s \theta_2 \dot{\theta}_1 + \ddot{\theta}_2 s \theta_3 + \ddot{\theta}_1 c \theta_2 c \theta_3] + g [c \theta_3 s \theta_1 + c \theta_1 s \theta_2 s \theta_3]$$

$$\dot{v}_z = l_u [c \theta_2 c \theta_3 s \theta_2 \dot{\theta}_1^2 + 2 \dot{\theta}_2 s \theta_2 s \theta_3 \dot{\theta}_1 + \ddot{\theta}_2 c \theta_3 - \ddot{\theta}_1 c \theta_2 s \theta_3] - g [s \theta_1 s \theta_3 + c \theta_1 c \theta_3 s \theta_2]$$

where $(\omega_x, \omega_y, \omega_z, \dot{v}_x, \dot{v}_y, \dot{v}_z)$ are the gyroscope, and accelerometer data at time n . The time index n was dropped for

ease of readability. Measurement equations for the forearm IMU are too long to be shown in this paper.

D. Nonlinear State Estimator

The state-space arm model introduced earlier has a nonlinear relationship between the joint angles and observed sensor measurements. The EKF is the most common method of nonlinear state estimation. It is based on linearizing the state and observation models with a first-order Taylor series expansion. It models the state variables with first- and second-order moments, which is most appropriate when the distribution is Gaussian. The linearization leads to poor performance if the dynamics are highly nonlinear and the local linearization insufficiently characterizes the relationship. The EKF also requires calculation of Jacobian matrices, which can be difficult, tedious, error prone, and time consuming.

Sequential Monte Carlo methods, which are also known as particle filters, can overcome the performance and implementation limitations of the EKF [26]. These algorithms can be applied to highly nonlinear and non-Gaussian estimation problems, has computational requirements that are orders of magnitude larger than the EKF. While the methods described in this article could be implemented with any of these nonlinear tracking algorithms, in this study we used the UKF [27].

Before the algorithms can be applied, the variance of the measurement noise and the variance of the noise driving the acceleration of the joint angles must be specified. We approximated the measurement noise of the accelerometers and gyroscopes based on short recordings while the sensors were stationary. We used 0.001 and 0.01 for gyroscope and accelerometer noise variance. The variance of the noise driving the acceleration of the joint angles is the primary user-specified tuning parameter. This controls the tradeoff between the smoothness of the estimated angles and how precisely the model tracks the data recorded from the accelerometers and gyroscopes. For all of the results reported here, we used a process noise variance of 1. The joint angle acceleration were modeled as a random walk process ($\alpha = 1$).

E. Performance Assessment

To evaluate the performance of the inertial tracking system, we compared the joint angles calculated by the inertial tracker with those from an optical tracking reference system. We collected two datasets from a total of eight subjects performing tasks described in Table II. The study was conducted in the Balance Disorders Laboratory at Oregon Health and Science University, which is equipped with a motion capture system with eight high-speed, infrared cameras (Motion Analysis Corporation, Santa Rosa, CA). The cameras recorded the position of 14 reflective markers placed on the sternum, upper arm, forearm, shoulder and wrist (see Fig. 2). Elbow and forearm angles were obtained from the 3-D positions of the markers placed on the upper arm and forearm based on the algorithm described in [28]. Similarly, shoulder angles were obtained from positions of the reflective markers placed on the shoulder and upper arm. Two IMUs, containing a triaxial accelerometer and gyroscope, were placed on the upper arm and forearm. Each IMU was attached

TABLE II
AVERAGE CORRELATION r , RMSE, AND PEAK-TO-PEAK ERROR BETWEEN OPTICAL AND INERTIAL ANGLES OF SHOULDER AND ELBOW

Task	r	RMSE($^{\circ}$)	Peak Error($^{\circ}$)
Elbow Flexion/Extension	0.98	6.5	9.8
Forearm Supination/Pronation	0.95	5.5	7.8
Shoulder Flexion/Extension	0.98	5.5	7.9
Shoulder Abduction/Adduction	0.99	4.4	8.1



Fig. 2. Reflective markers and Opal inertial sensors (APDM, Inc.) placement on the arm of one of the subjects.

to the arm with a strap band, in the center of a cluster of four markers. A stationary calibration period of 3 s at the initial pose preceded each movement task. The calibration period served two purposes. The first was to align the inertial and optical reference systems. The second was to calculate the gyroscope constant bias. This bias was removed from the gyroscope data before calculating the joint angles. Optical and inertial systems were synchronized to start and stop recording simultaneously. The inertial data was originally sampled at 128 Hz, and the Vicon data at 60 Hz. The angles calculated from inertial sensors were then resampled to 60 Hz for comparison to the Vicon optical angles.

III. RESULTS

To validate our statistical models, used to generate the state and observation equations, we first investigate the performance of the UKF-based tracker on synthetic data generated by these statistical models. On average, the root-mean-squared error (RMSE) between the synthetic and estimated angles and was less than 0.6° for all five arm angles. Fig. 3 shows the true (solid lines) and estimated (dotted lines) synthetic shoulder angles, and the very small-tracking error in bold gray line.

In the rest of this section, we present results for tracking real data using the inertial and optical systems. In the first dataset, four subjects repeated simple planar articulations three times. Each time lasted 18 s, including a stationary calibration period of 3 s at initial pose. The subjects performed each task at a normal daily life movement speed, at an approximate average of $180^{\circ}/s$, while keeping the rest of the body stationary. Fig. 4 shows forearm supination/pronation angles, and Fig. 5 shows shoulder abduction/adduction angles estimated by the inertial and optical

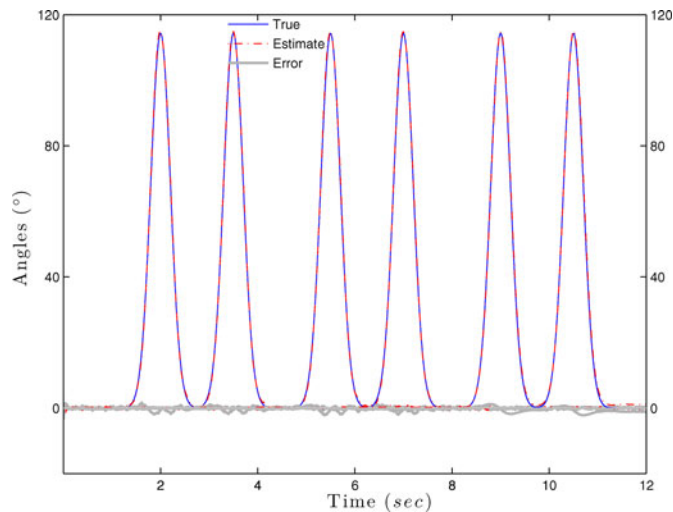


Fig. 3. Synthetic shoulder angles (solid lines), their estimate (dashed), and error (grey). The first two bumps represent flexion/extension. The third and fourth are shoulder abduction/adduction. The last two are internal/external rotation.

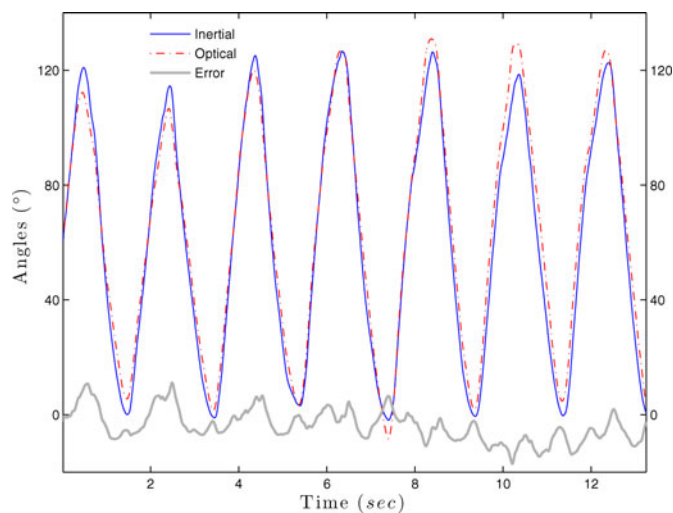


Fig. 4. Forearm supination/pronation estimates by the optical system (dashed line) compared to inertial angles estimate (solid line), and the error in gray.

tracking systems, and the difference between estimates in gray lines.

We calculated the correlation coefficient r , and the RMSE between angle estimates from the inertial and optical tracking system. On average, the correlation coefficient was $r \geq 0.97$ for all tasks among all subjects. Table II shows the correlation coefficient, RMSE average across subjects for all tasks, and the peak-to-peak error between inertial and optical angles.

In the second dataset, the other four subjects performed the same tasks described earlier continuously without stopping the recording. Starting with simple planar articulation, and ending with free movement to mimic touching the nose with the index finger, and reaching for a doorknob. The continuous recording lasted approximately 2 min for each subject. Fig. 6 shows an example of shoulder flexion/extension angles estimated by the

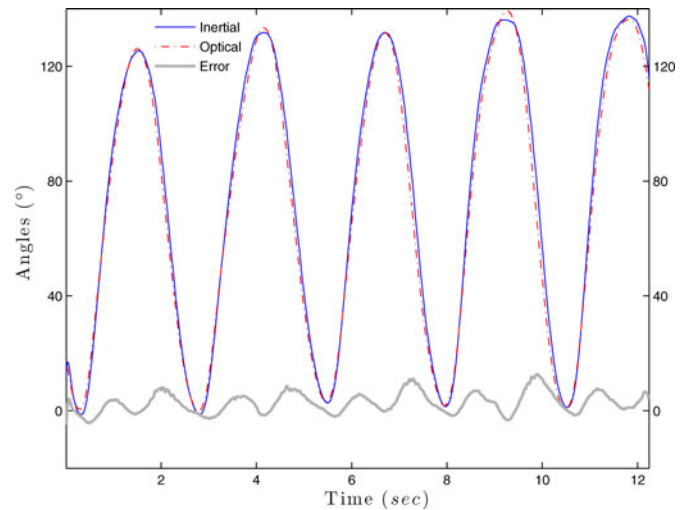


Fig. 5. Shoulder abduction/adduction angle estimates by the optical system (dashed line) compared to inertial angles estimate (solid line), and the error in gray.

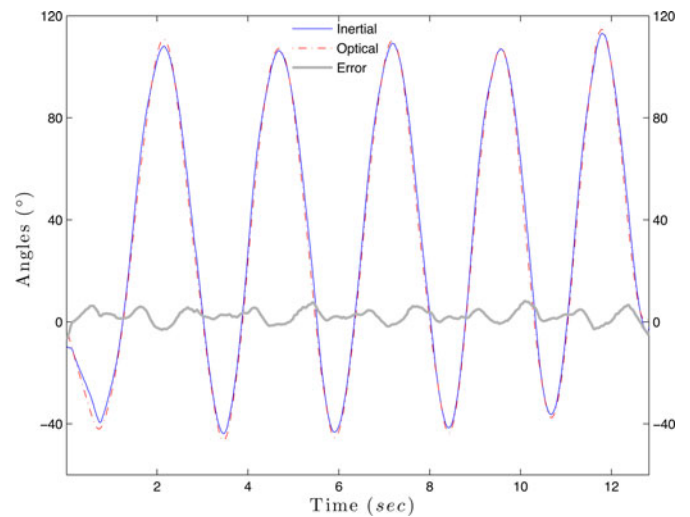


Fig. 6. Shoulder flexion/extension estimates by the optical system (dashed line) compared to inertial angles estimate (solid line), and the error in gray.

inertial and optical tracking systems. The average RMSE for all tasks among the four subjects was less than 7° .

To determine the performance of the inertial tracker when subjects performed more complex movements than simple articulation around one axis, each subject was asked to mimic touching nose with the index finger, and to mimic reaching for the doorknob to open a door. Each movement was repeated five times, lasting about 10s. Both tasks were performed around the end of second minute of recording. Table III shows the average correlation coefficient r among subjects for each task, RMSE, and the peak-to-peak error between inertial and optical angles.

To verify the performance of our inertial system in tracking fast movement, we asked the eight subjects to perform the tasks described in Table II at a fast pace. The articulation was performed at an approximate average rate of $420^\circ/\text{s}$. Fig. 7 shows the estimated inertial elbow flexion/extension angles compared to the angles obtained from the optical system. Average RMSE

TABLE III
AVERAGE CORRELATION r AND RMSE BETWEEN OPTICAL AND INERTIAL
ANGLES OF SHOULDER AND ELBOW

Task	r	RMSE($^{\circ}$)	Peak Error($^{\circ}$)
Touching nose	0.94	6.5	9.8
Reaching for a doorknob	0.95	5.5	8.8

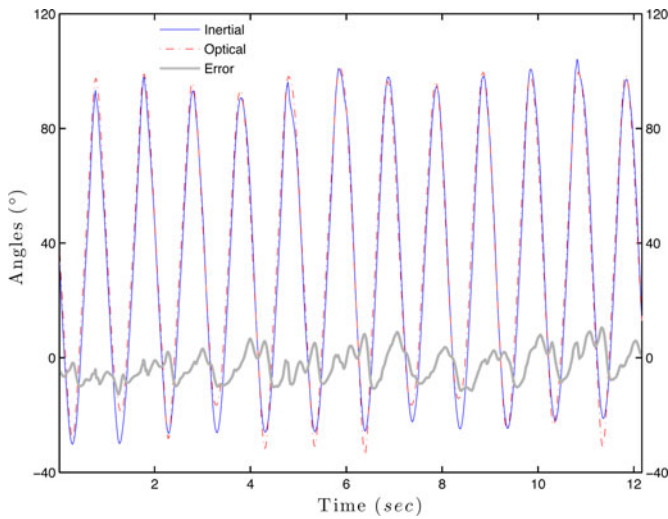


Fig. 7. Elbow flexion/extension during fast arm movement. Inertial estimates (solid line) compared to estimates from the optical system (dashed line).

among the eight subjects for all tasks was less than 8° , and the average peak-to-peak error was less than 12° .

IV. DISCUSSION

We combined kinematic models with state-space methods to estimate human joint angles using IMUs containing a triaxial accelerometer and a triaxial gyroscope. To estimate shoulder and elbow joint angles, we used the UKF which provides a few advantages over the most commonly used EKF. The UKF uses a more accurate method to characterize the propagation of the state variable distribution through the nonlinear models, and it does not require the calculation of Jacobian matrices. In some applications, including the one presented in this study, the calculation of the Jacobian matrices is tedious and error prone due to the structure and dimension of the process and measurement equations.

We compared joint angles estimated by the inertial system to those estimated by an optical tracking reference system. Two different datasets from a total of eight subjects were used to evaluate the performance. In the first dataset, each subject performed 15 s of shoulder and elbow planar articulations at a daily life movement speed with an approximate average rotation rate of $180^{\circ}/s$. RMS angle error between the two systems ranged from 4.4° to 6.5° , with a correlation coefficient $r \geq 0.97$. This is a very reasonable error range compared to what was achieved by Bachmann *et al.* who reported error range of 12° – 16° [12]. Based on the recursive measurement equations, distal segment angles are affected by the accuracy of proximal segments. In other words, error in shoulder angles might result in added error

in elbow angles. Table II shows that maximum estimation error occurred at elbow angles.

The majority of tracking algorithms discussed in the introduction limit their performance assessment to slow movement. We evaluated the performance of our inertial algorithm in tracking fast movement of the eight subjects. Each subject performed the same planar movement at a fast pace, with an approximate average rotation rate of $420^{\circ}/s$. On average, we obtained an RMS angle error of less than 8° for shoulder and elbow angles, with an excellent average correlation coefficient $r \geq 0.95$. During all movement tasks, subjects were instructed to keep the trunk fixed without moving. If the trunk moves, the shoulder and elbow angles will be underestimated or overestimated.

Although errors between optical and inertial angle estimates are minimal, performance is reduced by the noise, bias, and drift of MEMS inertial sensors. Bias generally consists of two parts: a deterministic part called bias offset and a random part. The bias offset refers to the offset in the measurement provided by the inertial sensor, is deterministic in nature. Gyroscope bias offset was determined from a 3-s calibration period of stationary movement at the initial pose. This offset was removed from the gyroscope data before calculating the joint angles. The random drift refers to the rate at which the error in an inertial sensor accumulates with time. Gyroscope and accelerometer random drift can be modeled as a stochastic process; increasing the dimension of the process model by adding six more states for each IMU.

Some of the estimation errors might also be attributed to markers moving independently of each other, especially during fast movements. Fig. 7 shows that maximum errors occurred when the elbow reached its peak flexion or extension. Marker placement over anatomical landmarks can create skin artifacts. The motion of the skin-mounted markers are usually greater than bone markers [29]. Soft-tissue artifact is caused by the relative displacement of markers mounted on the skin surface, and is a major source of error in the kinematic measurement of human movement. Another common problem in motion capture is marker occlusion. When a significant proportion of markers data was missing in any of the recordings, the recording had to be discarded. Six of 56 recordings were discarded due to missing marker data. Vicon data was sampled at 60 Hz. When one or two markers were nonvisible for six frames or less, the occluded marker positions were estimated from neighboring markers using interpolation.

An excellent agreement was also maintained between inertial and optical angle estimates during target reaching and touching nose with the index finger. Table III shows an average RMSE among all subjects that is less than 7° , and an average peak-to-peak error less than 10° .

Because the state-space model includes both the translational and gravitational components of acceleration, the algorithm is accurate during both fast and slow movements. However, one of the limitations of this study, and of all of tracking algorithms discussed in the introduction, is the use of short periods of movement for performance assessment. Although, we used longer periods than most of other studies, our continuous recordings lasted only 2 min for four of the eight subjects. To mitigate the effect of sensors drift on the estimated angles during longer

periods of movement, we plan to use a modified state model. The model will incorporate prior knowledge of physical constraints and human natural range of motion, as well as the gyroscope and accelerometer random drift. The combined effect of imposing physical constraints on state estimates and modeling the sensor random drift are expected to result in better joint angle estimates by our tracking system which does not utilize magnetometer measurements. This could eliminate the need to using magnetic sensors in other systems, which leads to large errors due to magnetic field disturbances [12]. We also plan to compare the performance of the EKF to that of the UKF in estimating the joint angles, given the nonlinear relationship between the joint angles and the observed sensor measurements.

V. CONCLUSION

We combined kinematic models designed for control of robotic arms with state-space methods to directly and continuously estimate human shoulder and elbow joint angles using wearable inertial sensors containing a triaxial accelerometer and gyroscope. These algorithms can be applied to any combination of synchronized sensors and can be generalized to track any limb movement. The implementation can use tracking algorithms that are either causal, real-time or non-causal, offline smoothing with higher accuracy. The agreement between our inertial tracker and a traditional optical motion capture reference system was excellent. This agreement was obtained for both regular and fast speed, and for simple planar and more complex movement of the arm. However, unlike optical systems which require fixed cameras in a controlled environment and suffer from problems of occlusion, wearable inertial sensors can be used anywhere, cannot be occluded, and are low cost. They are suitable for continuous monitoring over long periods while the subject performs normal activities of daily life at home.

ACKNOWLEDGMENT

J. McNames and Portland State University (PSU), Portland, OR, have a significant financial interest in Ambulatory Parkinsons Disease Monitoring, Inc., Portland, OR, a company that may have a commercial interest in the results of this research and technology. The potential individual and institutional conflicts of interest have been reviewed and managed by PSU.

REFERENCES

- [1] G. Welch and E. Foxlin, "Motion tracking: No silver bullet, but a respectable arsenal," *IEEE Comput. Graphics Appl.*, vol. 22, no. 6, pp. 24–38, Nov/Dec. 2002.
- [2] N. L. Keijsers, M. W. Horstink, and S. C. Gielen, "Online monitoring of dyskinesia in patients with Parkinson's disease," *IEEE Eng. Med. Biol. Mag.*, vol. 22, no. 3, pp. 96–103, May/June. 2003.
- [3] D. Roetenberg, "Inertial and magnetic sensing of human motion," Ph.D. dissertation, University of Twente, Enschede, The Netherlands, 2006.
- [4] H. J. Luinge, P. H. Veltink, and C. T. M. Baten, "Estimating orientation with gyroscopes and accelerometers," *Technol. Health Care*, vol. 7, no. 6, pp. 455–459, Jan. 1999.
- [5] H. J. Luinge, "Inertial sensing of human motion," Ph.D. dissertation, University of Twente, Enschede, The Netherlands, Dec. 2002.
- [6] H. J. Luinge and P. H. Veltink, "Measuring orientation of human body segments using miniature gyroscopes and accelerometers," *Med. Biol. Eng. Comput.*, vol. 43, no. 2, pp. 273–282, Mar. 2005.
- [7] H. J. Luinge, P. H. Veltink, and C. T. M. Baten, "Ambulatory measurement of arm orientation," *J. Biomechanics*, vol. 40, pp. 78–85, 2007.
- [8] H. J. Luinge, D. Roetenberg, and P. J. Slycke, "Motion tracking system," U.S. Patent 2008/0285805 A1, Nov. 2008.
- [9] D. Giansanti, G. Maccioni, and V. Macellari, "The development and test of a device for the reconstruction of 3-D position and orientation by means of a kinematic sensor assembly with rate gyroscopes and accelerometers," *IEEE Trans. Biomed. Eng.*, vol. 52, no. 7, pp. 1271–1277, Jul. 2005.
- [10] E. R. Bachmann, "Inertial and magnetic tracking of limb segment orientation for inserting humans in synthetic environments," Ph.D. dissertation, Naval Postgraduate School, Monterey, CA, 2000.
- [11] E. R. Bachmann and R. B. McGhee, "Inertial and magnetic posture tracking for inserting humans into networked virtual environments," in *Proc. ACM Symp. Virtual Reality Softw. Technol.* New York, NY: ACM, 2001, pp. 9–16.
- [12] E. R. Bachmann, X. Yun, and C. Peterson, "An investigation of the effects of magnetic variations on Inertial/Magnetic orientation sensors," in *Proc. IEEE Int. Conf. Robot. Autom.*, 2004, pp. 1115–1122.
- [13] D. Roetenberg, H. J. Luinge, C. T. M. Baten, and P. H. Veltink, "Compensation of magnetic disturbances improves inertial and magnetic sensing of human body segment orientation," *IEEE Trans. Neural Syst. Rehabil. Eng.*, vol. 13, no. 3, pp. 395–405, Sep. 2005.
- [14] D. Roetenberg, P. J. Slycke, and P. H. Veltink, "Ambulatory position and orientation tracking fusing magnetic and inertial sensing," *IEEE Trans. Biomed. Eng.*, vol. 54, no. 5, pp. 883–890, May 2007.
- [15] X. Yun, M. Lizarraga, E. R. Bachmann, and R. B. McGhee, "An improved quaternion-based Kalman filter for real-time tracking rigid body orientation," in *Proc. IEEE/RSJ Int. Conf. Robot. Syst.*, 2003, vol. 2, pp. 27–31.
- [16] X. Yun, C. Aparicio, E. R. Bachmann, and R. B. McGhee, "Implementation and experimental results of a quaternion-based Kalman filter for human body motion tracking," in *Proc. IEEE Int. Conf. Robot. Autom.*, 2005, pp. 317–322.
- [17] X. Yun and E. R. Bachmann, "Design, implementation, and experimental results of a quaternion-based Kalman filter for human body motion tracking," *IEEE Trans. Robot.*, vol. 22, pp. 1217–1227, 2006.
- [18] X. Yun, E. R. Bachmann, and R. B. McGhee, "A simplified quaternion-based algorithm for orientation estimation from earth gravity and magnetic field measurements," *IEEE Trans. Instrum. Meas.*, vol. 57, no. 3, pp. 638–650, 2008.
- [19] H. Zhou and H. Hu, "Inertial motion tracking of human arm movements in stroke rehabilitation," in *Proc. IEEE Int. Conf. Mechatronics Autom.*, 2005, pp. 1306–1311.
- [20] H. Zhou, H. Hu, and Y. Tao, "Inertial measurements of upper limb motion," *Med. Biological Eng. Comput.*, vol. 44, pp. 479–487, 2006.
- [21] H. Zhou and H. Hu, "Upper limb motion estimation from inertial measurements," *Int. J. Inf. Technol.*, vol. 13, no. 1, pp. 1–14, 2007.
- [22] J. J. Craig, *Introduction to Robotics, Mechanics and Control*, (Electrical and Computer Engineering: Control Engineering Series). Boston, MA: Addison-Wesley, 1989.
- [23] M. El-Gohary, L. Holmstrom, J. Huisinga, E. King, and J. McNames, "Upper limb joint angle tracking with inertial sensors," in *Proc. IEEE Ann. Int. Conf. Eng. Med. Biol. Soc.*, 2011, pp. 5629–5632.
- [24] J. L. Pons, R. Ceres, and L. Calderon, *Wearable Robots: Biomechanical Exoskeletons*, J. L. Pons, Ed., 2nd ed. Hoboken, NJ: Wiley, 2008.
- [25] J. Hamill and K. M. Knutzen, *Biomechanical Basis of Human Movement*, P. Darcy, Ed., 2nd ed. Baltimore, MD: Lippincott Williams & Wilkins, 2003.
- [26] O. Cappé, S. Godsill, and E. Moulines, "An overview of existing methods and recent advances in sequential monte carlo," *Proc. IEEE*, vol. 95, no. 5, pp. 899–924, May 2007.
- [27] S. J. Julier and J. K. Uhlmann, "Unscented filtering and nonlinear estimation," *Proc. IEEE*, vol. 92, Mar. 2004, pp. 401–422.
- [28] E. S. Grood and W. J. Suntay, "A joint coordinate system for the clinical description of three-dimensional motions: Application to the knee," *American Soc. Mechanical Eng.*, vol. 105, pp. 136–142, 1983.
- [29] A. G. Cutti, C. Troncossi, A. Davalli, and R. Sacchetti, "Soft tissue artefact assessment in humeral axial rotation," *Gait Posture*, vol. 21, pp. 341–349, 2005.

Authors' photographs and biographies not available at the time of publication.

HIERARCHICAL DYNAMIC MODEL FOR HUMAN DAILY ACTIVITY RECOGNITION

Blanca Florentino Liaño, Niamh O'Mahony, Antonio Artes Rodríguez

Departamento de Teoría de la Señal y Comunicaciones, Universidad Carlos III de Madrid, Spain
{blanca, niamh, antonio}@tsc.uc3m.es

Keywords: Activity Recognition, Inertial sensors

Abstract: This work deals with the task of human daily activity recognition using miniature inertial sensors. The proposed method is based on the development of a hierarchical dynamic model, incorporating both inter-activity and intra-activity dynamics, thereby exploiting the inherently dynamic nature of the problem to aid the classification task. The method uses raw acceleration and angular velocity signals, directly recorded by inertial sensors, bypassing commonly used feature extraction and selection techniques and, thus, keeping all information regarding the dynamics of the signals. Classification results show a competitive performance compared to state-of-the-art methods.

1 INTRODUCTION

The task of human activity recognition using wearable inertial sensors is becoming popular in applications which require context-aware monitoring, such as ambulatory monitoring of elderly patients and home-based rehabilitation. In such applications, knowledge of the activity being carried out by the patient is vital for providing the context within which the patient is being monitored and this context-awareness can help to overcome the limitations associated with the use of self reporting in medical assessment. One of the major advantages of such systems is that they can reduce the frequency of patients' visits to medical centers, improving their quality of life and reducing medical costs.

There are two main methods for human activity recognition: vision-based, e.g. (Moeslund et al., 2006), and inertial sensor-based, e.g. (Sabatini et al., 2005). The main disadvantages of vision-based systems are that they can only be used in a confined space, they interfere with the privacy of the individual and they produce an excessive amount of information that must be processed. On the other hand, due to recent advances in sensor technologies, inertial sensor devices have become compact and portable enough to be unobtrusively attached to the human body. For this reason, wearable miniature inertial sensors, incorporating accelerometers and gyroscopes, have become the ideal platform for human movement moni-

toring (Sabatini et al., 2005), falls detection (Wu and Xue, 2008), medical diagnosis and treatment (Powell et al., 2007), and tele-rehabilitation (Winters and Wang, 2003).

Nowadays, the main challenge in activity recognition is the development of a system for real-life monitoring applications using wearable sensors. Long term recording capabilities and unobtrusiveness are the primary requirements of such systems. The main constraint for the long term recording capabilities requirement is the battery life of the sensor devices. This drawback is even more important in real-time applications, such as fall detection systems. The processing of the data in real time can either be done by the sensor, if it has an on-board processor, or by transmitting the data wirelessly from the sensor to an external processor. Both cases result in high battery consumption and the latter case also requires the patient to be confined within the range of the wireless communication system. In order to make the system as unobtrusive as possible, the number of sensors placed on the body should be kept to a the minimum despite the fact that the larger the number of sensors, the more activities the system can recognize (Bao and Intille, 2004). Thus, choosing the number of sensors is a trade off between performance and usability.

Further to simply identifying which activities a subject is carrying out, this work proposes to also provide information regarding of the dynamics of the activity itself. There are two benefits to this approach:

(1) the intra-activity dynamics can aid the classification task and (2) additional contextual information could be gained from characteristics of the dynamic behaviour. With this in mind, we propose a hierarchical dynamical model which takes into account two levels of dynamics: inter-activity and intra-activity. The model aims to represent the activities as intuitively as possible in terms of the patterns present in the raw data from the sensors. Thus, not only are different activities recognized, but the “events” within a given activity are also distinguished, for example, the steps in the case of walking. Three different dynamic models are described, each one pertaining to a particular type of activity: the first is for stationary activities like standing, sitting and lying; the second, for active movements like walking and running, whilst the third deals with short-time motions like jumping and falling.

A further advantage of the proposed system is that it uses raw signals directly from the sensor, thus avoiding computationally expensive techniques such as feature extraction and selection. Because the system is designed to capture directly the dynamics of the signals, activity recognition is achieved with high accuracy whilst eliminating costly processing techniques.

The paper is organized as follows: in Section 2 the activity recognition literature is reviewed. Section 3 describes the proposed hierarchical dynamic model. The test procedure is outlined in Section 4, whilst in Section 5 the results obtained with our model are presented. Finally, in Section 6, conclusions and future lines of work are discussed.

2 BACKGROUND AND RELATED WORK

2.1 Sensors and Feature Extraction

The previously published literature in the area of human activity recognition using inertial sensors is quite extensive. Most of the published work follows a similar approach of data collection and processing, as outlined in this section.

Perhaps the first consideration in any activity recognition system, is the selection of the type and the number of sensors, as well as the positions on the human body where they will be worn. The simplest sensor used in the recent literature is a triaxial accelerometer (Han et al., 2010; Krishnan et al., 2008; He and Jin, 2008; Khan et al., 2010). In (Frank et al., 2010; Altun and Barshan, 2010; Zhu and Sheng, 2010), in-

ertial measurement units (IMU), combining triaxial accelerometers and triaxial gyroscopes, are used to provide measurements of specific force and angular rate, respectively. As has been previously mentioned, the larger the number of sensors used, the more activities the system can recognize. Similarly, the choice of sensor positions on the body is crucial. In the case of a single sensor, the most popular place is the waist, on the belt or in the pocket of the trousers (Frank et al., 2010; Han et al., 2010; He and Jin, 2008). In this work, a single IMU placed on either the left or right hip is considered for testing purposes, although the model is not limited to this configuration.

The first processing step is, typically, focused on the construction of a feature vector derived from the raw signals of the sensor. In the literature, a large number of different features have been reported as being suitable for the classification task considered in this work; (Preece et al., 2009) provides a comparison of the most popular features. A common approach is to extract many features (for example in (Krishnan et al., 2008) thirty-nine features are extracted); then, dimensionality reduction techniques such as Principal Component Analysis (PCA) or Linear Discriminant Analysis (LDA) are used to reduce the size of the feature vector before classification.

In addition to the processing required for feature extraction and selection, another disadvantage of this approach is that a predefined window length must be determined to compute the features. Furthermore, an overlap is often used between consecutive windows. The selection of such parameters is somewhat arbitrary and there is a lack of agreement on the best choice; in the literature, the window length varies widely (e.g. from 16 msec (Han et al., 2010) to 6 sec (Bao and Intille, 2004)), whilst a 50% overlap is common.

Once the feature vector has been computed from the windowed signals, the next step is the development of a model that is able to discriminate among activities. The most popular methods that have been used to solve this sequential supervised learning problem are batch supervised learning algorithms and Dynamic Bayesian Networks (DBN).

In (Altun and Barshan, 2010), a comparison of classification results using various batch supervised learning algorithms, including Bayesian Decision Making (DBM), Least-Squares Method (LSM), k -Nearest Neighbor (k -NN), Support Vector Machines (SVM) and Artificial Neural Networks (ANN) can be found. Batch supervised learning algorithms, which ignore the dynamics of the signals, are not considered in this work. One reason for this is to bypass the feature extraction step and, furthermore, it will be

seen that consideration the dynamics of the signals can give useful information about the type of activity that is being performed.

In the case of DBN, Hidden Markov Models (HMM) are the most frequently used. The model proposed in this work is based on HMMs and, so, the next section will describe, briefly, the theory governing HMMs and discuss, in detail, their use in the task of daily human activity recognition.

2.2 Hidden Markov Models

2.2.1 Background

A HMM (Rabiner, 1990) is a probabilistic model that represents the joint distribution of the observations and the unobserved (hidden) variable. In this work the observations are continuous signals of acceleration and angular velocity. The unobserved variable must be discrete and its possible values are called states. The proposed hierarchical model in this work, defines two different unobserved variables: the activities (e.g. walking, running, etc.) and the events within each activity. This will be explained in more detail in the Section 3.

A first order HMM is characterized by the following:

- N , the number of states in the model. The individual states are denoted as $S = \{S_1, S_2, \dots, S_N\}$, and the state at time t as q_t .
- The state transition probability distribution matrix, $A = \{a_{ij}\}$. This is an $N \times N$ matrix where the element, a_{ij} , is the probability of making a transition from state S_i to state S_j :

$$a_{ij} = P(q_{t+1} = S_j | q_t = S_i). \quad (1)$$

- The emission distribution vector, $B = \{b_j(\mathbf{O})\}$, where, for state j :

$$b_j(\mathbf{O}) = \sum_{m=1}^M c_{jm} \mathfrak{N}(\mathbf{O}, \boldsymbol{\mu}_{jm}, \mathbf{U}_{jm}), \quad (2)$$

where \mathbf{O} is the vector to be modeled, M is the number of mixtures, c_{jm} is the mixture coefficient for the m th mixture in state j and \mathfrak{N} is any log-concave or elliptically symmetric density (in our case we have selected a Gaussian density) with mean vector $\boldsymbol{\mu}_{jm}$ and covariance matrix \mathbf{U}_{jm} for the m th mixture component in state j .

- The initial state distribution $\pi = \{\pi_i\}$ where

$$\pi_i = P(q_0 = S_i) \quad (3)$$

Thus, the HMM is defined by $\lambda = (A, B, \pi)$.

For HMMs, the problem of learning the model parameters is solved by the Baum-Welch algorithm (Rabiner and Juang, 1993). The Viterbi algorithm (Viterbi, 1967) is used to compute the most likely sequence of states, $Q = q_0 q_1 \dots q_T$, from time $t = 0$ to $t = T$ and its probability, given the model and an observation sequence, $O = O_0 O_T \dots O_t$.

2.2.2 HMMs and Activity Recognition

In the literature, there are two main approaches to solving the activity recognition task using HMMs. In the first approach (Zhu and Sheng, 2010), only the temporal dependency among activities is modeled and there is just one HMM, whose number of states is equal to the number of activities. This model is very simple and is usually combined with batch supervised learning algorithms. Modeling the temporal dependencies among the activities allows the system to model human behavior by forbidding impossible transitions like, for example, a direct transition from running to lying down. An example of this approach can be found in (Zhu and Sheng, 2010) where the classification is done in two steps; first, two ANNs are used for determining whether or not the feature vector corresponds to a dynamic activity and whether the movement is vertical or horizontal; then, the fusion of these two outputs becomes the input to a HMM where the states are the activities.

In the second approach (Han et al., 2010), one HMM per activity is modeled. The number of states of each HMM is a design parameter. The inference step consists of computing the likelihood of a test sequence with each of the HMMs. The activity corresponding to the HMM with the highest likelihood is the chosen activity. The main drawback of this approach is that it is necessary to define a sequence size in order to learn the models and to infer the test sequence. Well-defined sub-units do not exist in the recorded IMU signals, since human activities are continuous and any given activity can have a highly variable duration. The sequence size is often selected taking into account the time interval during which only one activity exists. In (Han et al., 2010), this is set to 2 seconds. Some disadvantages of this approach are the requirement to define the sequence size, that the temporal dependency among activities is not modeled and that the HMM of each activity does not represent the activity itself but a sequence of, for example, 2 seconds of the activity. Thus, dynamic information is lost by truncating movement patterns and rhythmic movements.

To overcome this problem, (Oliver et al., 2002) develop a Layered Hidden Markov Model (LHMM),

in which each layer of the architecture is connected to the next layer via its inferential results. This representation segments the problem into distinct layers that operate at different temporal granularities. But, again, the parameters of the HMMs do not give any intuitive information about how the person is performing the activity and it is necessary to arbitrarily define these temporal granularities.

As has been shown in this section, there is no consensus on the most discriminative features for use in an activity recognition system. For this reason, it is usual to extract a large number of features and, then, use a dimensionality reduction technique. The major drawback of this approach is the computational cost. Moreover, it has been mentioned that the window length used to compute the features is another design parameter that varies widely among previous studies. With this in mind, this work aims to bypass the feature extraction step and work directly with the raw data produced by the sensor.

3 PROPOSED METHOD

The method proposed in this work consists of a hierarchical dynamical model based on HMMs whose inputs are the raw signals given directly by the sensor. This model takes into account the temporal dependencies among activities and models each activity in terms of acceleration and angular velocity signals. The hierarchical scheme concept has been mentioned before in the activity recognition literature (Khan et al., 2010). In this work, the term hierarchical is used because the learning process is done in two steps. First, the type of the activity (static, dynamic or transition) is recognized, using an ANN, and, then, the activity itself is determined.

3.1 Hierarchical Dynamical Model

The final result of our hierarchical dynamical model is a single HMM ($\lambda^F = (A^F, B^F, \pi^F)$). This final HMM is built up of “sub”-HMMs, one for each activity, which are joined to yield the final HMM. The learning process is performed in two stages. In the first stage the intra-activity dynamics are taken into account, modeling each activity separately with a unique “sub”-HMM and learning its parameters, as described in Section 3.1.1. The second stage concatenates these HMMs, modeling inter-activity dynamics, as outlined in Section 3.1.2.

3.1.1 Intra-Activity Dynamics

At this level, the hidden variable represents the significant events occurring during the activity. These events are the internal states of the sub-HMMs of each activity. The individual events, or states, of activity, Z , are denoted by $E^Z = \{E_1^Z, \dots, E_{K^Z}^Z\}$ where K^Z is the number of states of activity, Z , and the state at time t is denoted by e_t .

In this first stage of the learning process, the joint probability distribution of the observations, \mathbf{O} , and the events, e , given the activity, Z , ($p(e, \mathbf{O}|Z)$) are modeled:

$$p(e, \mathbf{O}|Z) = \prod_{t=1}^l p(\mathbf{O}_t|e_t, Z)p(e_t|e_{t-1}, Z). \quad (4)$$

Each activity can have a different number of events and a different topology, as detailed in the following.

We propose three different topologies, depending on the type of the activity. All of them have in common that they have two transient states (the first and the last), that describe the transition from one activity to another. Each activity must begin in the first state, and once this state is left it cannot be returned to from within the activity. The only possible transition from the last state is to itself. This is achieved by forcing the values of the model parameters to be:

- The transition matrix A^Z of the activity Z :

$$A^Z = \begin{pmatrix} a_{11}^Z & a_{12}^Z & 0 & \dots & 0 \\ 0 & a_{22}^Z & a_{23}^Z & \dots & a_{2K^Z}^Z \\ 0 & 0 & a_{33}^Z & \dots & a_{3K^Z}^Z \\ \vdots & \vdots & \vdots & \ddots & \vdots \\ 0 & 0 & 0 & \dots & 1 \end{pmatrix} \quad (5)$$

- The initial state distribution vector:

$$\pi^Z = [1 \quad 0 \quad \dots \quad 0] \quad (6)$$

For stationary activities like standing, sitting and lying, a left-right model with three states is proposed (Figure 1). The first and the last states are the transient states and the state in the middle models the permanent state of being seated, for example.

The second model is designed for active movements like walking and running (Figure 2). In this case there are two intermediate states which represent the pattern of stepping. These two states are fully inter-connected in order to model the periodicity of walking or running.

The last topology models short-time motions like jumping and falling. This model is made up only of transient states since there is neither a permanent action nor a rhythmic movement (Figure 3).

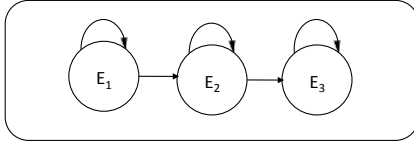


Figure 1: HMM topology for stationary activities.

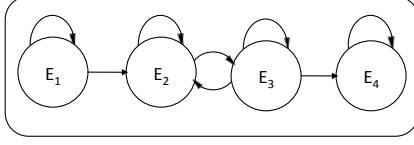


Figure 2: HMM topology for active movements.

3.1.2 Inter-Activity Dynamics

Once the models of each activity have been defined, they can be concatenated by means of their transient states (Figure 4) defining the transition probabilities among activities. These transition probabilities model human behavior; for example, the transition probability from walking to standing is higher than the transition probability from walking to running. Nevertheless, if the activity recognition system is used to monitor the elderly, the transition probability between walking and running would be lower than that in the case of monitoring children.

The result of the concatenation is a single HMM, $\lambda^F = (A^F, B^F, \pi^F)$, with twenty-one states, corresponding to all events of all activities as follows: running (states 1-4), walking (5-8), standing (9-11), sitting (12-14), lying (15-17), jumping (18-19) and falling (20-21). The state transition probability matrix of the final model, A^F , is built up following the steps below:

- (i) Set the transition probability matrixes of the sub-HMMs in the diagonal transition probability matrix of the final HMM:

$$A^F = \begin{bmatrix} A^{Run} & 0 & 0 & 0 & 0 & 0 & 0 & 0 \\ 0 & A^{Wlk} & 0 & 0 & 0 & 0 & 0 & 0 \\ 0 & 0 & A^{Std} & 0 & 0 & 0 & 0 & 0 \\ 0 & 0 & 0 & A^{Sit} & 0 & 0 & 0 & 0 \\ 0 & 0 & 0 & 0 & A^{Lie} & 0 & 0 & 0 \\ 0 & 0 & 0 & 0 & 0 & A^{Jmp} & 0 & 0 \\ 0 & 0 & 0 & 0 & 0 & 0 & A^{Fill} & 0 \end{bmatrix}. \quad (7)$$

- (ii) Connect the sub-HMMs. This step is straightforward, thanks to the definition of transient states, since all the activities must begin at the first state and end at the last state of their sub-HMM. Thus, we set:

$$\begin{aligned} a_{ij}^F &= P(e_{t+1} = S_j | e_t = S_i) \\ &= P(act_{t+1} = Z' | act_t = Z), \end{aligned} \quad (8)$$

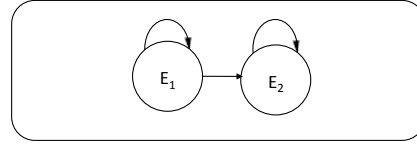


Figure 3: HMM topology for short-time motions.

for all $i \neq j$ which satisfy the condition that S_i is the last state of any activity, Z , and S_j is the first state of any other activity, Z' . For example, to connect the sub-HMM of running to the sub-HMM of walking, the value of the parameter $a_{45}^F = P(e_{t+1} = E_1^{walk} | e_t = E_4^{run})$ of the final HMM will be set to $P(act_{t+1} = walk | act_t = run)$.

- (iii) Reset the self-transition probabilities corresponding to the last event of each activity, i.e. set:

$$a_{jj}^F = 1 - \sum_{m=1, m \neq j}^{21} a_{jm}^F \quad (9)$$

for each j which satisfies the condition, $S_j \in \{E_4^{run}, E_4^{wlk}, E_3^{Std}, E_3^{Sit}, E_3^{Lie}, E_2^{Jmp}, E_2^{Fill}\}$

The emission probabilities of the final HMM, B^F , are the corresponding emission probabilities of each sub-HMM, defined in the first stage of the learning process.

Finally, the initial state distribution of the final HMM, π^F , is defined. In general, the value π_j^F is set to zero if S_j does not correspond to the first event of any sub-HMM. In this work, standing is always considered as the first position.

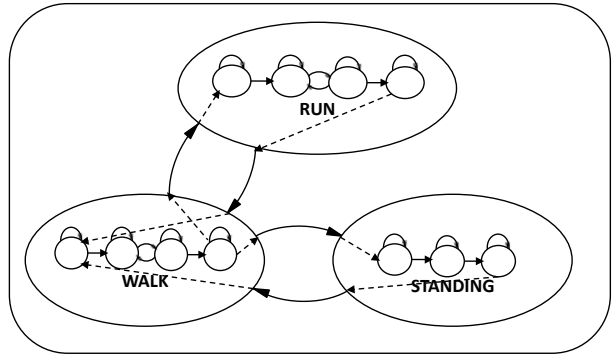


Figure 4: Concatenation of the HMMs.

4 TEST PROCEDURE

4.1 Database Description

In order to facilitate comparison of results with state-of-the-art results, the database available in (Frank

et al., 2010) has been used for testing the proposed method. This database consists of 4 hours and 30 minutes of activity data from 16 subjects (6 females and 10 males) aged between 23 and 50 years. Data were recorded in semi-naturalistic conditions. The IMU was placed on a belt, either on the right or left hip, providing 3-axis acceleration and 3-axis angular velocity signals at a sampling rate of 100 Hz.

The activities labelled in the database are running, walking, standing, sitting, lying, jumping, falling, ascending (from sitting to standing and from lying to standing), descending, accelerating (from walking to running) and decelerating (from running to walking). In the database, there are both training sequences and benchmark sequences. There are two benchmark sequences from two different subjects (Emil and Sinja). Emil has the IMU placed on his right side and Sinja, on her left side. These benchmark sequences consist of a succession of activities. More details of the data collection and labeling can be found in (Frank et al., 2010).

4.2 Training

For the purposes of learning the model for each activity, sequences corresponding to one single activity were extracted from the database, to be used as training data. Therefore, for each activity there are a different number of sequences with different lengths. Each HMM learned its parameters using the Baum-Welsh algorithm. The emission distributions were defined as mixtures of two gaussian distributions with diagonal covariance matrix.

4.3 Evaluation

The hierarchical dynamic model was tested, using the benchmark sequences, which were decimated by a factor of 4. This means that the model can be used with acceleration and angular velocity signals recorded at a sampling rate of 25 Hz, allowing the sensor device to consume less battery. In order to compute the most likely sequence of events given the observation sequence, the Viterbi algorithm was used. Using the knowledge of which set of events correspond to each activity, finally, the sequence of activities was obtained.

5 RESULTS

5.1 Classification

Figure 5 shows the sequence of events for the benchmark sequence of Emil. The blue crosses correspond to the events inferred by the Viterbi algorithm. Events 1 to 4 belong to the activity running, 5 to 8 to the activity walking and so on, as listed in Section 3.1.2. The red circles are the true, labelled activities and they are aligned in the graph with the last event of each activity. It should be remembered, here, that the model proposed in this work does not consider as activities, the “transition” activities labelled in the database (i.e. ascending, descending, accelerating and decelerating), since these events are inherently dealt with by means of the transient events in the hierarchical dynamic model. It can be seen from Figure 5 that the transition activities have, indeed, been incorporated by the proposed algorithm into the inferred intra-activity events. The figure shows good agreement between true and inferred activities.

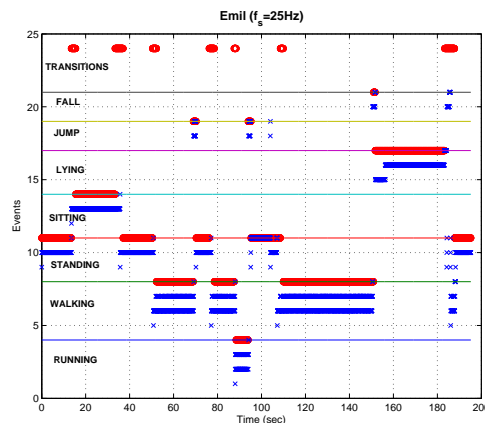


Figure 5: Sequence of events inferred for Emil’s benchmark sequence.

Tables 1 and 2 show the precision and recall values of each activity for the benchmark sequences of Emil and Sinja, respectively. The precision of activity, Z , is measured as number of samples classified correctly as activity, Z , divided by the total number of samples with inferred label equal to Z . The recall parameter is the number of samples correctly classified as activity, Z , divided by the number of samples whose true label is Z .

For comparison, Table 3 shows the performance reported in (Frank et al., 2010), relative to which the performance of the proposed algorithm is seen to be competitive. The results obtained for Sinja are lower than those for Emil because our model does not

deal specifically with the location of the sensor. The number of training sequences recorded with the sensor placed on the right side was greater than those recorded on the left side, so the model has learned, more accurately, the models for a sensor on the right. In the case of Sinja, the sensor was on the left side. Nevertheless, the results achieved are considered acceptable.

Table 1: Recall and precision for Emil’s benchmark sequence (IMU placed on the right side).

Activity	Recall (%)	Precision (%)
Running	100	95
Walking	99	97
Standing	96	99
Sitting	100	100
Lying	99	100
Jump	72	96
Fall	100	60

Table 2: Recall and precision for Sinja’s benchmark sequence (IMU placed on the left side).

Activity	Recall (%)	Precision (%)
Running	100	89
Walking	99	88
Standing	92	100
Sitting	100	100
Lying	100	96
Jump	34	100
Fall	59	82

Table 3: Recall and precision results reported by (Frank et al., 2010).

Activity	Recall (%)	Precision (%)
Running	93	100
Walking	100	98
Standing	98	100
Sitting	100	97
Lying	98	96
Jump	93	93
Fall	100	80

5.2 Intra-Activity Dynamics

In order to show, more clearly, the operation of the algorithm in terms of intra-activity dynamics, Figure 6 shows the acceleration signals and the events inferred during the activity of walking. The rhythmic transitions between events 2 and 3 are seen to correspond

with the stepping pattern in the acceleration signals. Not only has the definition of the hierarchical dynamic model proposed in this work allowed accurate classification of activities without preprocessing of the raw sensor signals, but the information regarding the dynamics within the activity itself could also be used to further characterise the subject’s behavioural patterns and provide useful contextual awareness for the monitoring system.

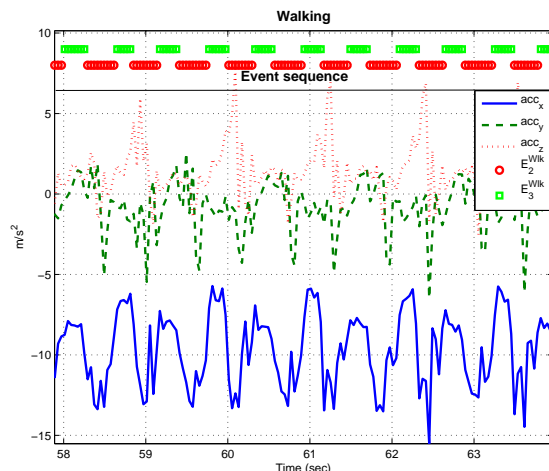


Figure 6: Events inferred for walking and acceleration signals.

6 CONCLUSIONS AND FUTURE WORK

This work has proposed a new approach to the task of human daily activity recognition using wearable inertial sensors. The method presented has two dynamic levels, augmenting the information provided by activity classification alone, through the provision of supplementary information regarding the dynamics within the activity. In an activity such as walking, for example, this level of dynamics could be analysed to give postural patterns for use in rehabilitation science.

Additionally, our bypasses the typically used feature extraction process, which is a computational bottleneck in current activity recognition methods. Working directly with the raw signals from the IMU sampled at a low sampling rate, the inherent dynamic nature of human motion is exploited. With this novel method, results with high precision and recall rates have been obtained.

Future research plans include developing more sophisticated models to take into account variations in

sensor placement as well as implementing the algorithm in real-time.

ACKNOWLEDGEMENTS

This work has been partly supported by Ministerio de Educación of Spain (projects ‘DEIPRO’, id. TEC2009-14504-C02-01, and ‘COMONSENS’, id. CSD2008-00010).

REFERENCES

- Altun, K. and Barshan, B. (2010). Human activity recognition using inertial/magnetic sensor units. In *Proceedings of the First International Conference on Human Behavior Understanding*, HBU’10, pages 38–51, Berlin, Heidelberg. Springer-Verlag.
- Bao, L. and Intille, S. S. (2004). Activity Recognition from User-Annotated Acceleration Data. *Pervasive Computing*, pages 1–17.
- Frank, K., Nades, M. J. V., Robertson, P., and Angermann, M. (2010). Reliable real-time recognition of motion related human activities using MEMS inertial sensors. In *ION GNSS 2010*.
- Han, C. W., Kang, S. J., and Kim, N. S. (2010). Implementation of HMM-based human activity recognition using single triaxial accelerometers. *IEICE Transactions*, 93-A:1379–1383.
- He, Z. Y. and Jin, L. W. (2008). Activity recognition from acceleration data using AR model representation and SVM. *Machine Learning and Cybernetics*.
- Khan, A. M., Lee, Y.-K., Lee, S. Y., and Kim, T.-S. (2010). A triaxial accelerometer-based physical-activity recognition via augmented-signal features and a hierarchical recognizer. *IEEE Transactions on Information Technology in Biomedicine*, 14:1166–1172.
- Krishnan, N. C., Colbry, D., Juillard, C., and Panchanathan, S. (2008). Real time human activity recognition using tri-axial accelerometers. In *Sensors Signals and Information Processing Workshop (SENSIP)*.
- Moeslund, T. B., Hilton, A., and Krüger, V. (2006). A survey of advances in vision-based human motion capture and analysis. *Computer Vision and Image Understanding*, 104:90–126.
- Oliver, N., Horvitz, E., and Garg, A. (2002). Layered representations for human activity recognition. In *Proceedings of the 4th IEEE International Conference on Multimodal Interfaces*, ICMI ’02, pages 3–, Washington, DC, USA. IEEE Computer Society.
- Powell, H., Hanson, M., and Lach, J. (2007). A wearable inertial sensing technology for clinical assessment of tremor. In *IEEE Biomedical Circuits and Systems Conference, BIOCAS 2007*, pages 9–12.
- Preece, S. J., Goulermas, J. Y., Kenney, L. P. J., and Howard, D. (2009). A comparison of feature extraction methods for the classification of dynamic activities from accelerometer data. *IEEE Transactions on Biomedical Engineering*, 56(3):871–879.
- Rabiner, L. and Juang, B.-H. (1993). *Fundamentals of Speech Recognition*. Prentice Hall, united states ed edition.
- Rabiner, L. R. (1990). Readings in speech recognition. In Waibel, A. and Lee, K.-F., editors, *Readings in speech recognition*, chapter A tutorial on hidden Markov models and selected applications in speech recognition, pages 267–296. Morgan Kaufmann Publishers Inc., San Francisco, CA, USA.
- Sabatini, A., Martelloni, C., Scapellato, S., and Cavallo, F. (2005). Assessment of walking features from foot inertial sensing. *IEEE Transactions on Biomedical Engineering*, 52(3):486–494.
- Viterbi, A. (1967). Error bounds for convolutional codes and an asymptotically optimum decoding algorithm. *IEEE Transactions on Information Theory*, 13(2):260–269.
- Winters, J. and Wang, Y. (2003). Wearable sensors and tele-rehabilitation. *IEEE Engineering in Medicine and Biology Magazine*, 22(3):56–65.
- Wu, G. and Xue, S. (2008). Portable preimpact fall detector with inertial sensors. *IEEE Transactions on Neural Systems and Rehabilitation Engineering [see also IEEE Trans. on Rehabilitation Engineering]*, 16(2):178–183.
- Zhu, C. and Sheng, W. (2010). Recognizing human daily activity using a single inertial sensor. In *Proceedings of the 8th World Congress on Intelligent Control and Automation (WCICA)*, pages 282–287.

Human Activity Recognition using Inertial Sensors with Invariance to Sensor Orientation

Blanca Florentino-Liaño, Niamh O’Mahony, Antonio Artés-Rodríguez

Department of Signal and Communications Theory, Universidad Carlos III de Madrid,
Avenida de la Universidad, 30, Leganés, 28911, Spain
Email: {blanca, niamh, antonio}@tsc.uc3m.es,

Abstract—This work deals with the task of human daily activity recognition using miniature inertial sensors. The proposed method reduces sensitivity to the position and orientation of the sensor on the body, which is inherent in traditional methods, by transforming the observed signals to a “virtual” sensor orientation. By means of this computationally low-cost transform, the inputs to the classification algorithm are made invariant to sensor orientation, despite the signals being recorded from arbitrary sensor placements. Classification results show that improved performance, in terms of both precision and recall, is achieved with the transformed signals, relative to classification using raw sensor signals, and the algorithm performs competitively compared to the state-of-the-art. Activity recognition using data from a sensor with completely unknown orientation is shown to perform very well over a long term recording in a real-life setting.

I. INTRODUCTION

Human activity recognition has recently become a popular topic of research interest due to the growth of applications based on context-aware monitoring, including home-based rehabilitation, independent living solutions for the elderly and ambulatory monitoring of patients with psychiatric or other disorders. Knowing the activity being carried out by the patient throughout their day-to-day life provides context-awareness for the physiological or other measurements that are being monitored, allowing a more accurate analysis of the measurements than in a stand-alone monitoring system.

The two main methods for human activity recognition are vision-based, e.g. [1], and inertial sensor-based, e.g. [2]. Vision-based systems suffer from limitations such as only being usable in a confined space, interfering with the privacy of the individual and producing an excessive amount of information that is costly to process. On the other hand, due to recent advances in sensor technologies, inertial sensor devices have become compact and portable enough to be unobtrusively attached to the human body. For this reason, wearable miniature inertial sensors, incorporating accelerometers and gyroscopes, have become the ideal platform for human movement monitoring [2], falls detection [3], medical diagnosis and treatment [4], and tele-rehabilitation [5].

Recently, the authors presented a novel algorithm for the classification of human activities based on a hierarchical dynamic model (HDM) [6]. This method was shown to give competitive classification results, compared to state-of-the-art methods, whilst avoiding the computational bottleneck of

traditional feature extraction methods, by basing the entire algorithm on the raw signals measured by the sensors. One drawback of this method, due, in part, to not extracting features, is that the raw sensor signals are sensitive to the placement of the sensor on the subject’s body, in terms of position and orientation. For applications in real life situations, control of the exact placement of the sensor is not feasible and adverse effects of variations due to body shape, clothing and other factors must be eliminated from classification algorithms.

This work proposes a novel transformation of sensor measurements, before classification, which renders the collected signals insensitive to the position and orientation of the sensor on the subject’s body. The proposed algorithm allows the sensor to be placed in any fixed location within a region approximately bounded by a belt at the waist and a trouser pocket, as illustrated in Fig. 1. The only restriction is that the sensor should be fixed such that its movement during the day is limited to a few millimeters. All measurements are transformed to a ‘virtual’ sensor placement, defined at the approximate center of mass of the subject’s body and with a known orientation, with respect to the body in a standing position, as illustrated in Fig. 1.

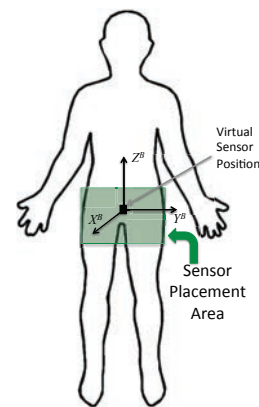


Fig. 1. Allowable Sensor Placement and Virtual Sensor Position

This simple transformation, in conjunction with the HDM, is shown to result in an improved classification performance (in terms of both precision and recall) compared with the HDM using raw sensor signals. These results are based on a database available in [7]; as such, the authors have no information

regarding the sensor position and orientation for each subject, other than the side of the hip on which it was placed, and this information is not made available to the algorithm.

The rest of this paper is laid out as follows: in Section II, a brief introduction to the background theory of inertial sensors, coordinate systems and the HDM is provided. Section III describes the proposed transform. The experimental procedure is outlined in Section IV and classification results are presented in Section V. These results are followed by a discussion in Section VI and finally conclusions and future work are outlined in Section VII.

II. BACKGROUND

A. Inertial Sensors

The inertial sensors used in this work are each equipped with a triaxial accelerometer and triaxial gyroscope. The accelerometers measure, in m/s^2 , the total inertial force acting on the sensor. This inertial force includes both linear accelerations in each of the three sensor axes and a gravitational force component in each axis. The gyroscopes measure the angular velocity of the sensor in rad/s .

The signals measured by the sensors can be modeled as follows: the accelerometer measurement vector, α_t , at time, t , is given by:

$$\alpha_t = \mathbf{a}_t + \mathbf{g}_t + \boldsymbol{\mu}_{a,t}, \quad (1)$$

where \mathbf{a}_t is the linear acceleration component due to sensor motion, \mathbf{g}_t is the component due to the Earth's gravitational force and $\boldsymbol{\mu}_{a,t}$ is a noise term. Similarly, the gyroscope signal, ω_t , is given by:

$$\omega_t = \mathbf{w}_t + \boldsymbol{\mu}_{w,t}, \quad (2)$$

where \mathbf{w}_t is the angular rotation and $\boldsymbol{\mu}_{w,t}$ is a noise term. The measurement noise terms, $\boldsymbol{\mu}_{a,t}$ and $\boldsymbol{\mu}_{w,t}$, are assumed to be zero mean Gaussian random processes. Signals from both accelerometers and gyroscopes also contain bias components but, for the purposes of classification, these can be considered negligible.

B. Coordinate Systems

The signals recorded by the inertial sensors are measured in a three-dimensional coordinate system which is fixed to and moves with the sensor, both linearly and rotationally. This frame is referred to as the sensor frame (S) and is defined by an orthogonal set of unit vectors, $\{\vec{x}^S, \vec{y}^S, \vec{z}^S\}$. A fixed frame (F) can also be defined, in which the gravitational component of the force of acceleration is constant; for example, in the frame, $\{\vec{x}^F, \vec{y}^F, \vec{z}^F\} = \{\text{North, West, Up}\}$, acceleration due to gravity is given by $\mathbf{G}^F \approx [0, 0, 9.81] \text{ m/s}^2$.

During epochs of little or no linear acceleration (i.e. $\mathbf{a}_t \approx 0$ for $t_1 \leq t \leq t_2$), comparing the mean of the measured acceleration vector in the sensor frame, $\bar{\alpha}^S = \text{mean}(\alpha_{t_1:t_2}^S)$, to the gravitational vector in the fixed frame, \mathbf{G}^F , allows the orientation of the sensor frame, relative to the fixed frame, to be partially resolved. The inclination of the sensor, given by the angles of roll, θ_x , (the angle between the y^S -axis and the

x^F - y^F plane) and pitch, θ_y , (the angle between the x^S -axis and the x^F - y^F plane), can be estimated by means of ratios of the gravitational acceleration component in each sensor axis [8]:

$$\theta_x = \arctan\left(\frac{\bar{\alpha}_y^S}{\bar{\alpha}_z^S}\right), \quad (3)$$

$$\theta_y = \arcsin\left(\frac{-\bar{\alpha}_x^S}{\sqrt{(\bar{\alpha}_x^S)^2 + (\bar{\alpha}_y^S)^2 + (\bar{\alpha}_z^S)^2}}\right). \quad (4)$$

With just accelerometers and gyroscopes, there is not sufficient information to resolve the angle of yaw, θ_z , (the angle between the projection of the x^S -axis onto the x^F - y^F plane and the x^F -axis), since the gravitational component in both the x^F - and y^F -axes is zero, resulting in an infinite number of possible solutions in the range $\{0, 2\pi\}$. Fortunately, for the purposes of activity recognition, it is irrelevant whether a subject is facing due North or in any other direction whilst carrying out a particular activity and it will be seen in Section III that a yaw estimate is not required for the proposed method.

The final coordinate system to be introduced is the body frame (B), which is fixed to and moves with the center of mass of the subject's body (approximately located at the waist). This is the frame of the virtual sensor to which all of the sensor measurements will be transformed and is shown in Fig. 1. The directions of each axis, relative to the subject's body in a standing position, can be described as: $\{\vec{x}^B, \vec{y}^B, \vec{z}^B\} = \{\text{Forward, Left, Up}\}$. It should be remembered that as the subject changes position, these directions will change with respect to the fixed frame; for example, if the subject is lying down, the z^B -axis will no longer point upwards, but along the x^F - y^F plane. This is the key to the operation of the transform.

C. Hierarchical Dynamic Model with HMM

In previous work by the authors [6], a Hierarchical Dynamic Model (HDM) with HMM was proposed for the task of activity recognition. In that paper, the raw signals of the sensor were directly used as the inputs of the activity recognition algorithm. In order to evaluate the effectiveness of the transformation proposed, the same model is used in this work, but in this case, transforming the input signals. This section briefly reviews the HDM with HMM, for details see [6].

The HDM with HMM constructs a model taking into account two levels of dynamics: inter-activity and intra-activity. The inter-activity dynamics refer to the temporal dependency among activities. This level of dynamics helps in the recognition task because the current activity depends on which activity the subject was doing in the previous time step. This is modeled by transition probabilities among activities.

On the other hand, the amplitude of the signals and how they evolve in time, both give valuable information for the recognition of the activity. This level of dynamics is referred to as intra-activity dynamics. This is modeled by constructing a HMM for each of the activities. Various different dynamic

models are proposed, each with a different topology. For example, for stationary activities like standing, sitting and lying, a left-right model with three states is defined. The first and the last states are transient states and the state in the middle models the permanent state of, for example, being seated. This can be seen within the activity “LYING” in Fig. 2.

The final result of the HDM is a single HMM built up of “sub”-HMMs, one for each activity, which are interconnected by means of their transient states according to the transition probabilities defined by the inter-activity level. Fig. 2 shows an example of these interconnections.

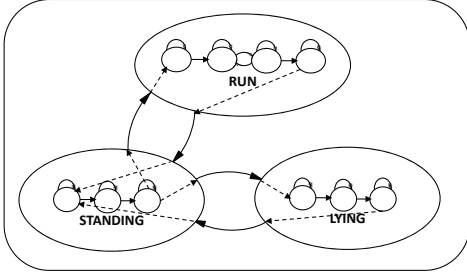


Fig. 2. Example of HDM hierarchy with “sub”-HMMs.

III. TRANSFORM

Knowledge of the orientation of a body segment can be very useful for activity recognition, especially for distinguishing between different “low-motion” activities, such as standing still, sitting and lying down. For all of these activities, the linear acceleration and angular rotation are close to zero throughout the activity and, so, the classification algorithm must rely on only the acceleration due to gravity to recognize the activities by determining the orientation or pose of the subject’s body. The measurement of the gravitational acceleration component, g_t^S , directly in the sensor frame, does not give any information about the orientation of the subject’s body, relative to the fixed frame, because it depends on the initial placement of the sensor. This can be observed in Fig. 3a and 4a, which show accelerometer observations recorded during two similar sequences of activities, carried out by the same subject, but with the sensor at different positions and orientations, namely, attached to a belt at the left hip and in the right trouser pocket. The activities are labelled above the signals (‘STD’ - standing, ‘SIT’ - sitting, ‘WLK’ - walking, ‘LYING’ - lying down). The values of the acceleration in each axis in the sensor frame, during, for example, standing, can be seen to be highly dependent on sensor orientation and, thus, not comparable across multiple sequences or epochs of the same activity.

Using the roll and pitch, estimated by (3) and (4), respectively, and assuming a yaw of zero, a rotation matrix can be defined to partially transform the measurements from the sensor frame to the fixed frame, such that the z -component of the transformed measurement is aligned with the z^F -axis and the x^S - y^S plane is aligned with the x^F - y^F plane. Once the initial orientation has been calculated in this manner, the angular velocity can be integrated over time to update the rotation

matrix between the sensor and the fixed frame at each time instant. In this coordinate system, the gravitational component of acceleration is independent of sensor orientation. However, it is always contained in the same axis (z^F), regardless of whether the subject is lying down, sitting, standing, etc. Thus, always transforming the data to an Earth fixed frame does not help to distinguish between the low-motion activities.

With this in mind, the virtual sensor in the body frame is introduced. When the subject is in a standing position (a duration of two seconds is sufficient), the roll and pitch are estimated using (3) and (4) and the rotation matrix is calculated once by:

$$R(\theta_x, \theta_y) = \begin{bmatrix} \cos(\theta_y) & \sin(\theta_x) \sin(\theta_y) & \cos(\theta_x) \sin(\theta_y) \\ 0 & \cos(\theta_x) & -\sin(\theta_x) \\ -\sin(\theta_y) & \sin(\theta_x) \cos(\theta_y) & \cos(\theta_x) \cos(\theta_y) \end{bmatrix}. \quad (5)$$

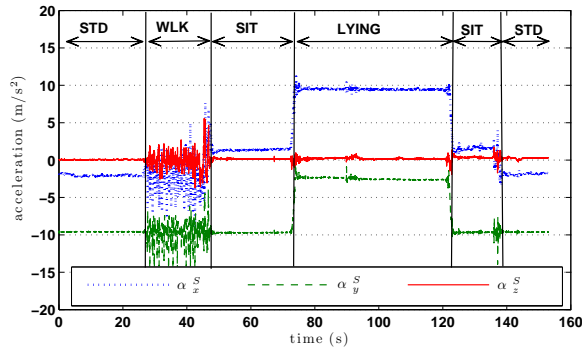
Using (5), the measured signals are all transformed by the same constant rotation at each time instant, such that it appears that all measurements have been recorded from the virtual sensor position. The transformation of the acceleration, for example, is given by:

$$\alpha_t^{B'} = R(\theta_x, \theta_y) \alpha_t^S, \quad (6)$$

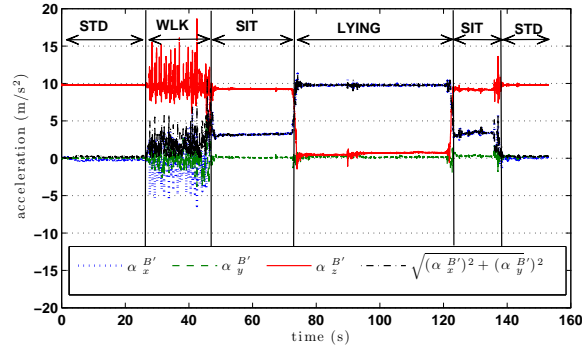
where the frame, B' , denotes the body frame with an arbitrary yaw angle. The gyroscope signals are transformed in the same way. One of the benefits of using a constant rotation matrix is that the transform is insensitive to the accumulation of biases in the sensors as the orientation does not need to be updated by integrating the gyroscope signals over time. Furthermore, the computational load requirement for multiplication of the signals by a constant matrix is low.

Fig. 3b and 4b show that the $z^{B'}$ -components of the transformed acceleration signals are very similar despite the significant differences in sensor placement and orientation, observed in Fig. 3a and 4a. Clearly, there are some remaining variations from one sequence to the next, which depend on the subject’s exact behavior, whether they are seated upright or slouching, whether they are lying face down or on their side, among many other variable factors. The $x^{B'}$ - and $y^{B'}$ -components remain dependent on the initial yaw. However, the modulus of the acceleration in the $x^{B'}$ - $y^{B'}$ plane, $\sqrt{(\alpha_x^{B'})^2 + (\alpha_y^{B'})^2}$, can be seen to behave similarly for both sequences, i.e independently of sensor orientation, suggesting that it may be a suitable signal for classification.

In the body frame, the orientation of the gravitational acceleration is the distinguishing signal characteristic for low-motion activities, whilst specific periodic patterns in acceleration and angular velocity characterize movement activities, such as walking, running, jumping, etc. This periodicity can be observed independently of the sensor orientation, as shown in Fig. 3 and 4. More importantly, the modulus of the $x^{B'}$ - and $y^{B'}$ -components of acceleration and angular velocity conserves the periodicity of the signals while making their joint magnitude invariant to the yaw angle.

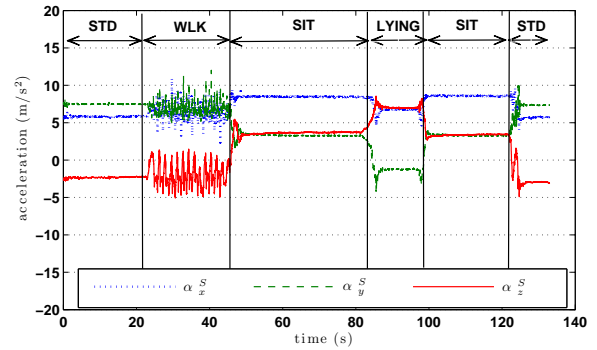


(a) Observed acceleration in sensor frame

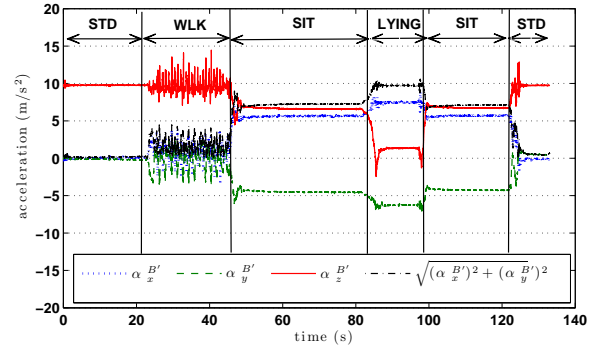


(b) Transformed acceleration in body frame

Fig. 3. Sensor attached to belt at the left hip



(a) Observed acceleration in sensor frame



(b) Transformed acceleration in body frame

Fig. 4. Sensor in right trouser pocket

IV. EXPERIMENTAL PROCEDURE

A. Database Description

In order to evaluate the effectiveness of the proposed transformation, the results obtained with the transformed signals will be compared with the results obtained without any transformation. For this purpose we use the same database as was used in [6], which can be found in [7]. This database consists of 4 hours and 30 minutes of activity data from 16 subjects (6 females and 10 males) aged between 23 and 50 years. The sensors used were Xsens MTx-28A53G25 inertial measurement units (IMUs).

The IMU was placed on a belt, either on the right or left hip, providing 3-axis acceleration and 3-axis angular velocity signals at a sampling rate of 100 Hz. The activities labelled in the database are running, walking, standing, sitting, lying, jumping, falling, and transient activities. In the database, there are both training sequences and benchmark sequences, recorded in semi-naturalistic conditions. There are three benchmark sequences from three different subjects. Two of the subjects have the IMU placed on the lefthand side of the waist and the third, on the righthand side. More details of the data collection and labeling can be found in [7].

In addition, to further test the generality of the method, data was collected with an APDM [9] Opal sensor placed at the subject's waist, during their normal work day. More than six hours of data were collected, including mainly the

following activities: sitting, standing and walking. The subject was requested to very roughly report their activities, in terms of time of day and what they were doing (working at desk, walking to a meeting, eating lunch, etc.) These data were collected for the purposes of algorithm evaluation only and were not used for training.

B. Training

As every training sequence in the database starts with the activity, “standing”, the rotation matrix for transformation was computed using the two first seconds of the acceleration signals. Sequences corresponding to one single activity were extracted from the database, to be used as training data for that activity. Each HMM learned its parameters using the Baum-Welsh algorithm [10]. The emission distributions were defined as mixtures of two gaussian distributions with diagonal covariance matrix. Training was carried out, in the same way, for both transformed and raw data sequences, separately.

C. Evaluation

Activity estimates were calculated for each benchmark sequence from [7], after resampling the signals to a frequency of 25 Hz. Each benchmark sequence was evaluated using the models for the HDM with HMM, obtained in the training phase for both transformed and raw data. In the case of the transformed model, acceleration and angular velocity signals of the benchmark sequences were transformed using the same

process as described for training. In order to compute the most likely sequence of activities, given the observation sequence, the Viterbi algorithm [11] was used.

The algorithms reported by Frank et al. [7] produce activity estimates at a rate of 4 Hz. To provide a “like-with-like” comparison, the final outputs of our system are given by the mode of each set of 6 consecutive activity estimates (i.e. at 4.17 Hz). The data from the APDM sensor were evaluated in the same way, using the models trained by the Xsens sensor data.

V. CLASSIFICATION RESULTS

Tables I and II show the recall and precision values of each activity for the benchmark sequences of Emil, Sinja and Paula from [7], with and without transformation. The average recall and average precision are also shown in these tables. The precision of activity, Z , is measured as the number of samples classified correctly as activity, Z , divided by the total number of samples with inferred label equal to Z . The recall parameter is the number of samples correctly classified as activity, Z , divided by the number of samples whose true label is Z .

TABLE I
RECALL RESULTS

Transformation	Emil		Sinja		Paula	
	YES	NO	YES	NO	YES	NO
Running	100%	100%	96%	100%	100%	100%
Walking	100%	99%	100%	100%	100%	99%
Standing	96%	96%	92%	92%	91%	90%
Sitting	100%	100%	100%	100%	85%	0%
Lying	100%	100%	100%	100%	100%	36%
Jump	75%	67%	39%	38%	73%	92%
Fall	100%	100%	60%	60%	75%	100%
Average	96%	95%	84%	84%	89%	74%

TABLE II
PRECISION RESULTS

Transformation	Emil		Sinja		Paula	
	YES	NO	YES	NO	YES	NO
Running	100%	96%	89%	84%	76%	90%
Walking	97%	97%	88%	89%	89%	87%
Standing	100%	100%	100%	100%	95%	97%
Sitting	100%	100%	100%	100%	100%	0%
Lying	100%	100%	97%	97%	94%	33%
Jump	100%	100%	100%	100%	100%	100%
Fall	100%	60%	100%	75%	100%	22%
Average	100%	93%	96%	92%	93%	61%

Fig. 5 shows the estimated activities obtained by evaluating the long-term data collected with the APDM sensor. The figure shows estimates obtained both with and without transformation. The time periods identified by the vertical lines on the graph signify epochs labeled by the subject as follows:

- 1) Walking to canteen (includes descending stairs).
- 2) Heating lunch in microwaves (waiting on foot).
- 3) Sitting down to eat.
- 4) Returning to the lab (includes ascending stairs).
- 5) Sitting at desk discussing work with a colleague.

VI. DISCUSSION

As Table I and II show, in every benchmark sequence we have achieved equal or higher average recall and average precision using transformed signals, compared to the raw sensor signals. For activities, such as running, walking and lying, the HDM with HMM, even without transformation, was capable of achieving good results, especially for the benchmark sequences of Emil and Sinja. However, sitting, for example, suffered from a precision and recall of zero for Paula, without transformation. With transformation, the average recall and precision show an improvement, relative to the results without transformation, of 15% and 32%, respectively, for Paula, and are equal or up to 7% better for both Emil and Sinja.

The result of transforming the signals to the virtual sensor orientation was shown, in Section III, to improve the uniformity of the signals prior to classification. With the original training sequences, some of which were recorded on the right side and some on the left, the classification algorithm essentially has to learn two models for each activity. By transforming the signals to the virtual sensor orientation, all of the training sequences contribute to a single unified model, hence providing better classification results.

It should be noted that the database used for the experiments in this work contained only a small amount of data for the short-term activities, jumping and falling. This may be part of the reason why the classification of such activities performs worse than the others. Another factor, which was taken into account by [7], is human error in labeling, which will have a more significant effect in activities with a very short duration. However, it may also be the case that the models for short-term activities need to be modified to better capture the dynamics of the activities. This remains as future work.

To compare our results with those reported by Frank et al., the average precision and recall obtained by our method (with transformation) for Emil and Sinja were calculated (results for Paula were not included in the average, as results for this subject were not mentioned in [7]). Overall average precision for our method is 98%, compared to 95% in [7], whilst overall average recall for our method is 90%, compared to 97.9% in [7]. Thus, it can be seen that our method performs better, in terms of precision, with some loss in recall performance. It should also be remembered that our method is computationally very fast, consisting of only a constant matrix multiplication of each signal, whilst the feature extraction and dynamic unrestricted Bayesian network recognition algorithm reported by [7] will be computationally more expensive.

For the data collected using the ADPM sensor (Fig. 5), it can be seen that the estimated activities with transformation represent quite well the activities described by the subject. For example, epoch 1 consists mainly of standing and walking, as would be expected in this case. The jumping and running estimates are thought to occur because the subject was descending stairs. Similarly, during epoch 3, sitting is predominant with some samples estimated as lying - possibly due to slouching in

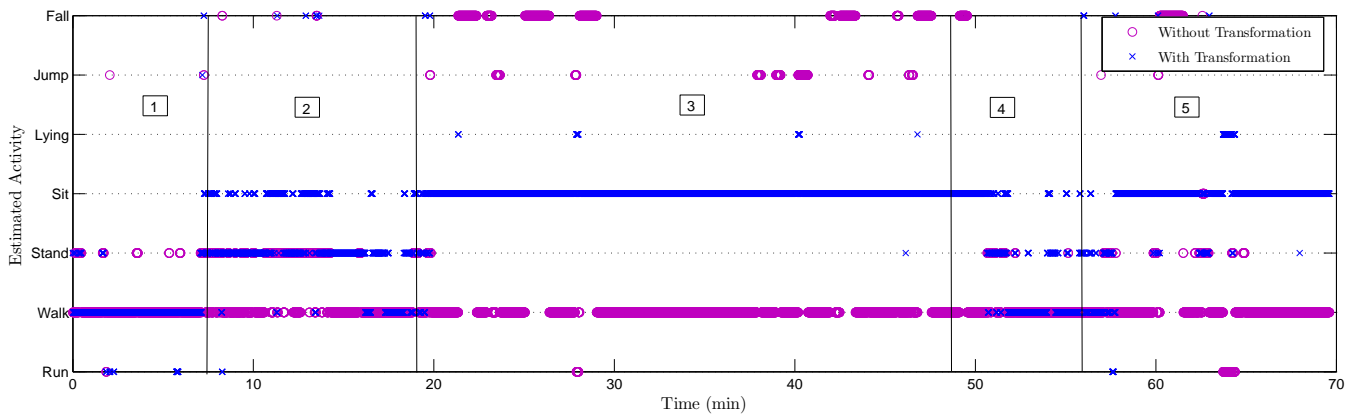


Fig. 5. Long-term activity estimation using APDM sensor: with and without transformation

the seat. Throughout the entire period shown in the figure, the estimates without transformation have no relation to the labels, as would be expected given that the sensor orientation was the subject's arbitrary choice, and not one of the options used in the training sequences. These results are very promising as they indicate invariance, not only to sensor orientation, but also to the brand of sensor used.

The transformation proposed in this work can be used also in approaches in which there is a previous stage of feature extraction. One of the advantages of feature extraction is to make the inputs of the recognition algorithm more robust, but many commonly-used features are not invariant to the sensor orientation, for example, the modulus of the acceleration and angular velocity in the horizontal and in the vertical planes of the sensor. In general, these planes correspond to different frames in each subject, depending on the orientation of the sensor. Calculating similar features using transformed signals would ensure uniformity across subjects and, as such, produce classifiers with a better generalization capability.

VII. CONCLUSIONS AND FUTURE WORK

In this work, in order to compare, fairly, the results using transformed signals and non-transformed signals, exactly the same classification model, the HDM with HMM, was used for both sets of results. For this purpose each activity has been modeled in the same way as in the previous work by the authors [6], i.e. with the same number of states for each activity and with emission distributions defined as mixtures of two gaussians. Nevertheless, thanks to the transformation proposed in this work, very similar signal amplitudes for each particular activity, have been achieved, independently of sensor orientation. With this in mind, it might be interesting to identify more representative topologies for some activities, modeling the emission distributions as a single Gaussian distribution, instead of a mixture model.

Furthermore, in order to improve the estimation of inter-activity dynamics in real life situations, a database will be constructed by the authors. It is intended to collect data in more naturalistic circumstances than in existing databases and

the database will contain data from a very large number of subjects for both training and test purposes.

ACKNOWLEDGEMENTS

This work has been partly supported by Ministerio de Educación of Spain (projects 'DEIPRO', id. TEC2009-14504-C02-01, and 'COMONSENS', id. CSD2008-00010).

REFERENCES

- [1] T. B. Moeslund, A. Hilton, and V. Krüger, "A survey of advances in vision-based human motion capture and analysis," *Computer Vision and Image Understanding*, vol. 104, pp. 90–126, November 2006.
- [2] A. Sabatini, C. Martelloni, S. Scapellato, and F. Cavallo, "Assessment of walking features from foot inertial sensing," *IEEE Transactions on Biomedical Engineering*, vol. 52, no. 3, pp. 486–494, 2005.
- [3] G. Wu and S. Xue, "Portable preimpact fall detector with inertial sensors," *IEEE Transactions on Neural Systems and Rehabilitation Engineering*, vol. 16, no. 2, pp. 178–183, 2008.
- [4] H. Powell, M. Hanson, and J. Lach, "A wearable inertial sensing technology for clinical assessment of tremor," in *IEEE Biomedical Circuits and Systems Conference, BIOCAS 2007.*, November 2007, pp. 9–12.
- [5] J. Winters and Y. Wang, "Wearable sensors and telerehabilitation," *IEEE Engineering in Medicine and Biology Magazine*, vol. 22, no. 3, pp. 56–65, May–June 2003.
- [6] B. Florentino-Liaño, N. O'Mahony, and A. Artés-Rodríguez, "Hierarchical dynamic model for human daily activity recognition," in *Proceedings of BIOSIGNALS 2012 (BIOSTEC)*, Vilamoura, Portugal, 1–4 February 2012.
- [7] K. Frank, M. J. V. Nades, P. Robertson, and M. Angermann, "Reliable real-time recognition of motion related human activities using MEMS inertial sensors," in *ION GNSS 2010*, September 2010.
- [8] S.-h. Won, W. Melek, and F. Golnaraghi, "A Kalman/particle filter-based position and orientation estimation method using a position sensor/inertial measurement unit hybrid system," *IEEE Transactions on Industrial Electronics*, vol. 57, no. 5, pp. 1787–1798, May 2010.
- [9] APDM, Inc. <http://www.apdm.com/>.
- [10] L. R. Rabiner, "A tutorial on hidden markov models and selected applications in speech recognition," in *Readings in speech recognition*, A. Waibel and K.-F. Lee, Eds. San Francisco, CA, USA: Morgan Kaufmann Publishers Inc., 1990, pp. 267–296.
- [11] A. Viterbi, "Error bounds for convolutional codes and an asymptotically optimum decoding algorithm," *IEEE Transactions on Information Theory*, vol. 13, no. 2, pp. 260–269, April 1967.

IAC-12-A1.6.6

USING INERTIAL MEASUREMENT UNITS FOR MEASURING SPACESUIT MOBILITY AND WORK ENVELOPE CAPABILITY FOR INTRA-VEHICULAR AND EXTRA-VEHICULAR ACTIVITIES

Ryan L. Kobrick, PhD

Massachusetts Institute of Technology, USA, kobrick@mit.edu / ryan@yurisnight.net

Christopher E. Carr, ScD, Forrest Meyen, Ana R. Domingues, and Prof. Dava J. Newman

Massachusetts Institute of Technology, USA, chrisc@mit.edu, meyen@mit.edu, ritadom@mit.edu, and dnewman@mit.edu

Shane E. Jacobs, PhD

David Clark Company, USA, SJacobs@davidclark.com

Human spaceflight destinations are expanding to include a multitude of environments that will offer different mobility challenges to explorers due to varying gravity levels and surface operations. Intravehicular Activities (IVA) suits might include a basic “get-me-down” suit for suborbital spaceflight, or a high performance pressurized pilot suit where arm mobility and field of vision are particularly important. Future Extravehicular Activities (EVA) will likely accommodate various spacesuit architectures including: a microgravity station/craft maintenance suit where hand dexterity is critical; a close proximity operation suit for asteroid missions where manoeuvrability and visibility are critical; and a planetary surface suit for the Moon or Mars where leg mobility is a key requirement. Spacesuit kinematics are currently measured using video motion capture or photographic analysis systems. Although these methods measure the external motion of the suit, they do not capture the physical body motions within the suit and in the case of motion capture, they are restricted to a laboratory setting with significant overhead for camera calibration and set-up. Inertial Measurement Units (IMUs) use accelerometers and gyroscopes to estimate relative translation and rotation. IMU systems are mobile, low-powered, and offer an economical and efficient kinematic tracking capability for use in a laboratory or in the field. In this study, we applied IMU sensors to study space-suited motion. To first validate the use of IMUs for motion tracking, we tracked knee flexion angle while walking using both IMUs and a Vicon motion-capture system, which is considered the industry gold standard for kinematic analysis. The IMU knee joint angle average root-mean-square error with respect to the Vicon system was $5.4 \pm 2.4^\circ$, demonstrating the potential of the new system. We then used the IMUs, in conjunction with a Contingency Hypobaric Astronaut Protective Suit (CHAPS), to measure elbow flexion/extension, shoulder flexion/extension, and shoulder abduction/adduction motions for unsuited, suited and unpressurized, and suited and pressurized conditions. Results from the elbow study demonstrate our ability to capture joint angles in a laboratory environment with the goal of being used in any environment. In general, the internal IMU angle on the subject’s body was approximately 25° larger than the external CHAPS IMU external angle measured. A brief discussion summarizes key findings and identifies limitations in the test configuration. Recommendations for future implementation and testing are outlined, and conclusions are drawn on the usability of IMUs to investigate astronaut mobility and to provide work envelope results.

I. INTRODUCTION

The new human spaceflight market in suborbital space tourism and research flights as well as new crew capabilities to the International Space Station (ISS) will mix customer needs with high-powered vehicles that lack extensive flight history. It is important to monitor passenger comfort and safety and inform future improvements to mission elements such as spacesuits, personal cabin space, and throttling profiles. The fast pace of commercial orbital vehicle development will benefit from novel mobility measurement techniques, especially if they can be taken within the vehicles during operational development. Inertial measurement units (IMUs), sensors that integrate data from

orthogonal gyroscopes, accelerometers, and magnetometers, can aid in these assessments.

The goal of this research is to develop novel applications for IMU technology in characterization of human motion, such as estimating orientation, acceleration, velocity, and position during restrained or natural movement. In particular, this work focuses on spacesuit mobility and how IMU data can be used to construct range of motion joint angles and eventually work envelope definitions in a realistic test environment. This data can aid in the development of future space suits and improve knowledge of current suit performance and limitations.

Systems of inertial sensors may also have many terrestrial applications where enhanced monitoring of

human movement is beneficial. These areas include estimation of ambulatory joint kinematics¹⁻⁴, injury rehabilitation^{5,6}, assessment of neurological movement disorders⁷, and enhancement of athletic performance^{8,9}.

II. SPACESUIT MOBILITY TESTING BACKGROUND

Pressure suits are worn by pilots and astronauts to protect them from a variety of hazards including low-pressure environments and thermal extremes. Pressure suits worn inside the vehicle during dynamic phases of flight, such as launch, entry, and docking are primarily designed to protect the crewmember in the event of an emergency. During nominal unpressurized operations, the crewmember must be comfortable and have the mobility to perform mission tasks, such as ingressing the vehicle and performing flight operations. During an emergency, the suit must enable the crewmember to perform any operations necessary to return to safety while protecting the crewmember from hazards. To that end, launch and entry suits often incorporate bailout systems, fire protection, cold-water immersion protection and integrated flotation, which are all dependent on the requirements and interfaces of the vehicle¹⁰. The current set of requirements outlined by NASA for commercial vehicles is in the ISS Crew Transportation and Services Requirements Document CCT-REQ-1130. It does not specifically mandate a pressure suit, but the NASA Astronaut Office considers it mandatory¹¹.

Similarly, pressure suits for the emerging commercial spaceflight industry will be primarily worn unpressurized, but in the event of an emergency, the suit must ensure the crewmember survives and, if necessary, can continue to perform the necessary functions to return to safety. It is important to note though that pressure suit needs vary amongst the different mission profiles, as differing levels of mobility will be required of passengers in different vehicles. Even within a single vehicle, the mobility requirements are varied, as pilots must be able to continue to fly the spacecraft while pressurized (in the event of a cabin depressurization), while suits for passengers must simply ensure their survival.

Understanding and quantifying exactly how much mobility a crewmember needs to perform each task is critical to derive requirements that will not over constrain the design. It is important to recognize that increases in pressurized mobility often come at a cost, such as a mass penalty, detriment to unpressurized comfort, or increased development costs^{11,12}. The mobility requirements therefore must not drive a design beyond that which is absolutely necessary, as other desirable characteristics of the suit may be sacrificed.

Additionally, as NASA prepares for exploration missions outside of low earth orbit, it is increasingly

important to be able to quantify, communicate, and validate, space suit mobility for suits worn outside the spacecraft. These suits are always worn pressurized, and as such pressurized mobility becomes far more critical. One of the long term goals of space suit design is to design suits that approach as close as possible to “shirt-sleeve mobility”, such that an astronaut in a pressurized space suit could perform all the same tasks, with the same ease, as a geologist on earth in a t-shirt and shorts. Research at MIT in the Man-Vehicle Laboratory (MVL) has been moving towards this mobility goal with incremental subsystem design of a mechanical counterpressure BioSuitTM¹³. In order to achieve this goal, the mobility enabled by various joint designs must be well understood and quantified. Improvements to the joints can then in turn be quantified, by measuring the reduction in mobility, and understanding the physical principles responsible for the reduction. Without continuous benchmarking and iteration, the suit designer cannot make progress towards a highly mobile joint.

It is evident then that proper characterization of mobility requirements – how much mobility is needed to perform all mission tasks – as well as mobility capabilities – how much mobility a certain space suit enables – is absolutely essential for both government space programs and the commercial spaceflight industry.

Spacesuit Environments: IVA and EVA

There are essentially two key working environments that must be considered for suit mobility design. Intravehicular Activities (IVA) suits might include a basic “get-me-down” suit for suborbital spaceflight, or a high performance pressurized pilot suit where arm mobility and field of vision are particularly important. Future Extravehicular Activities (EVA) will likely accommodate various spacesuit architectures including: a microgravity station/craft maintenance suit where hand dexterity is critical; a close proximity operation suit for asteroid missions where manoeuvrability and visibility are critical; and a planetary surface suit for the Moon or Mars where leg mobility is a key requirement.

Mobility Methodologies

Several methodologies have been used to measure mobility, though two methods have emerged as the most common within the spacesuit community¹⁴. Unfortunately each has its drawbacks. Photogrammetry, the process of measuring joint angles from pictures of a subject in the suit at the extremes of a joint’s range, has been used to quantify pressure suit mobility dating back at least to the Apollo program¹⁵, and through various space suit development programs^{16,17} including the most recent prototype suits developed for NASA’s project Constellation^{12,18,19}. This method only quantifies

isolated joint movements, making it difficult to properly characterize the suit's mobility for complex tasks. Additionally, this method requires the subject to hold a joint at "maximum" angles, which can be very workload intensive, and as a result tends to underestimate a suit's full range of mobility.

The second method commonly used, developed more recently with advances in technology, involves three dimensional video motion capture technology. Subjects in suits are outfitted with reflective markers, and systems of multiple cameras are used to track the markers as the subject performs various functional tasks. The coordinates of the markers can be used to measure individual joint angles using inverse kinematics software. This method was used extensively for the derivation of requirements for project Constellation²⁰. Motion capture methodology is advantageous as it captures mobility during functional movements and tasks, but it is costly both in terms of equipment needed and in post-processing time. Additionally, it requires line of sight for several (2-3 minimum) cameras on each marker at all times, restricting it to a laboratory environment and making it difficult to track motions within a mock-up. This drawback was at least partially alleviated in a 2011 study through the use of a somewhat transparent mock-up of the Orion vehicle^{21,22}. The mock-up allowed the cameras to see "through" the vehicle, and motions could be tracked as subjects performed all the mission tasks, such as ingressing/egressing the vehicle, attaching the harnesses and umbilical, and other tasks. The mock-up was an innovative solution to the problems associated with motion capture using reflective markers and cameras, however it demonstrated the need for the ability to capture mobility data in non-laboratory environments, as it would have been ideal to use a higher fidelity mock-up of Orion.

Recently, a new method of implementing IMUs has become feasible, which has the potential to enable mobility characterization during functional tasks in all environments, without the need for line of sight from expensive camera systems. Two initial studies have recently been performed^{23,24} demonstrating the potential for this methodology, which involves placing small inertial measurement units (IMUs) onto the subject. These trials have shown that data from the IMUs can be converted into joint angle measurements as a subject performs various tasks in various environments. This methodology enables mobility measurement outside the laboratory environment, captures motion data in three dimensions during functional tasks, and eliminates the need for additional vehicle mock-ups.

Inertial Measurement Units (IMUs)

In order to understand the motion of the human body within a relevant environment (spacecraft habitable area

or spacesuit), IMUs are selected to demonstrate a novel way of collecting data. IMUs use accelerometers and gyroscopes to estimate relative translation and rotation. Desirable IMU characteristics include:

- Sized to fit application (minimal mass or specific shape);
- Low power consumption / long battery life;
- Dynamic range, resolution, bandwidth, Sampling Rate, Noise, Sensitivity;
- Connection to other recording infrastructure versus data logging / standalone;
- Comfort and/or unobtrusiveness;
- Long-term monitoring; and
- Affordable price.

This research effort has evolved from a lineage of projects at MIT's MVL. In order to compare the use of IMUs for estimation of lower limb joint angles against the standard motion capture methodology and inverse kinematics software, a study was conducted using commercial IMUs to capture three-dimensional acceleration and angular velocity data generated during human walking. Preliminary results using an extended Kalman filter to estimate both knee and ankle joint angles were encouraging³. Collaborators at MIT and the Instituto Superior Técnico (Portugal) demonstrated the efficacy of IMUs as sensory systems for gait analysis replacing the standard motion capture camera method. Through the use of different processing tools and custom filtering, it was possible to improve the data provided by the IMUs to be used for prosthetic and orthotic devices to estimate joint kinematics during walking^{25,26}. On-going research implements IMU joint kinematics in real-time for the design of ankle-foot smart orthotics^{27,28}.

For an array of experimental medical and space applications, the authors have selected IMUs that include a set of three magnetometers, gyroscopes, and accelerometers each. These IMUs (Opals™, APDM, Portland, OR) are low mass wristwatch-sized devices enabled by real-time wireless data capture or storage for later download (see Fig. 1).

To assess IMU capabilities for human spaceflight applications, a pilot study was conducted in a car on a relatively smooth highway looking at constant velocity motion and acceleration profiles. The aims of the study were to examine ideal IMU positions and operational protocol for data collection using a car and seat interface as an analogue to suborbital spaceflight keystone events simulating a seated launch²³. Preliminary results indicated that IMUs can be used to characterize the human body's motion in an analogue situation and the vehicle's vibrational environment.



Fig. 1: APDM IMUs are small wearable devices. Axes are shown for IMU body reference frame.

III. PRELIMINARY VALIDATION OF IMUS VS. MOTION CAPTURE GOLD STANDARD

To validate this data collection method we tested the accuracy of the APDM IMUs during normal walking. The IMUs were compared to the “gold standard” of kinematic data collection, the Vicon motion capture system in the Wyss Institute’s motion capture laboratory. This system uses an array of eight T-series cameras to track reflective markers illuminated by infrared light.

IMUs were strapped to the subject’s legs and a plaque labelled with reflective markers was attached (Fig. 2).

The locations of the reflective markers aligned with the Y and X axis of the IMU and enabled the 8-camera Vicon motion capture system in interpret the rotation of the IMUs strapped to the lateral side of the upper and lower leg. The subject was instructed to walk the length of the motion capture volume. Limb segment rotation in the sagittal plane was recorded with the Vicon and APDM IMU system. Knee rotation was determined by subtracting the rotation of the lower leg from the reference rotation of the upper leg. A representative trial is shown in Fig. 3.



Fig. 2: IMU placement and reflective marker locations.

Knee Flexion IMU and Vicon Comparison (RMS Error = 2.188 Degrees)

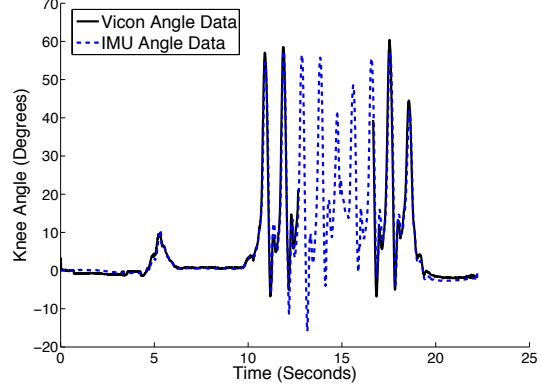


Fig. 3: IMU-Vicon Knee walking comparison.

Areas in Fig. 3 where the Vicon data disappears from the plot is where the subject stepped outside the collection volume. Data was collected for 13 trials. The average RMS error (relative to the Vicon system) throughout the samples was 5.4 degrees with a standard deviation of 2.4 degrees. This analysis shows that the IMUs can be used as a substitute for a Vicon motion capture system when an optical system is unavailable. It also demonstrates potential advantages of the IMU approach: freedom of movement without the restriction of a specific motion capture volume.

El-Gohary et al. (2011)²⁹ investigated the use of APDM IMUs for estimating joint angles of a multi-segment limb using a custom unscented Kalman filter algorithms and compared data to an optical tracking system (Eagle Analog System, Norwood, MA). All elbow and shoulder motions analysed were found to have IMU data correlate with greater than 0.9 to the motion tracking system, and all cases were statistically significant for both normal (rate not specified) and fast (as fast as user could bend elbow) speed motions.

Another study found the APDM IMU system to have a high Pearson's R correlation while compared to a Vicon system ($R > 0.90$) for gait cadence, head rate of rotation, and torso rate of rotation. These measurements are typically used to test patients with mild traumatic brain injury³⁰.

IV. CHAPS MEASUREMENT METHODOLOGY

Testing at David Clark Company

The APDM IMU system was brought to the David Clark Company (Worcester, MA) to test basic mobility in the Contingency Hypobaric Astronaut Protective Suit (CHAPS). Before testing, it was decided to focus on the elbow joint motion. The motion of the entire arm could potentially be used to generate a point cloud of tracking data to generate a work envelope, which is further explored in the recommendations in section VII.

IMUs were placed on the forearm and bicep both directly on the subject’s body and on the external

surface of the CHAPS (two external IMUs are indicated on Fig. 4 on the CHAPS). Additional IMUs were placed on the fingertips (outside of glove) and on a fixed position on the wall. Three sets of motion were recorded including: elbow flexion/extension; shoulder flexion/extension; and shoulder abduction/adduction. The IMUs were used to data log the motion for both scenarios of the suit unpressurized and with the suit pressurized to 1 psig. Two different methods were examined for conducting the motion. The first method had the subject tap the fixed wall IMU before each arm motion (tap), and the second method had the subject move in a continuous motion (continuous). For every trial, three complete arm motions were conducted and the trials were repeated twice for all sixteen scenarios (the two methods were only used for the elbow motion).

The elbow starting position of a straight arm (locked) of 0° was used in every elbow trial (see Fig. 4 “zero angle”). Flexion, or elbow bend, was considered positive rotation according to the Standardization and Terminology Committee of the International Society of Biomechanics³¹.

A similar study at the University of Maryland Space Systems Laboratory²⁴, investigated outfitting IMUs internal to a spacesuit, using the CHAPS as a demonstration of the technology. The Body Pose Measurement System (BPMS) uses 18 IMUs on a conformal garment worn under the suit to track body motion by measuring the attitude of the major long bones.

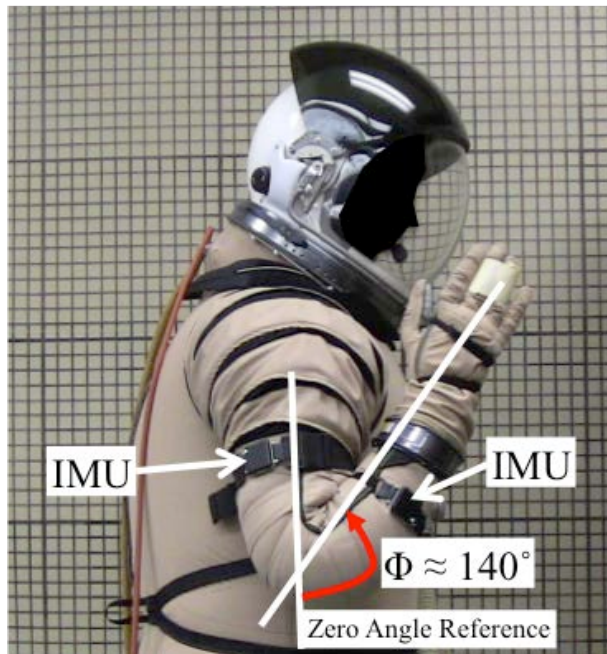


Fig. 4: IMU Placement on CHAPS with elbow flexion measurement (used with Permission from David Clark Company).

Results: Euler Angle Calculations

The following is an overview of the code developed in MATLAB (The Mathworks, Natick, MA) to reduce the acquired IMU data and find the final three Euler angles for a pair of IMUs about a given body joint. The basic approach is to calculate a rotation matrix that transforms one IMU frame into another IMU frame, and then determine the Euler angles for that rotation matrix, which represent the 3dof rotations of the joint between the two IMU frames. In more detail, the approach is:

1. Import data from IMU csv file to Matlab
2. Convert Quaternions to Euler Angles using Matlab’s “quat2angle” (Aerospace tool box)
 - Angles are in body reference frame X, Y, Z with respect to North, West, Up (NWU) world frame that the IMUs use.
3. Generate rotation matrices for both IMUs in joint angle couple, from Bong Wie Equation 5.13 on 311³²:

$$R^{B/A} \equiv R_1(\theta_1)R_2(\theta_2)R_3(\theta_3)$$

$$= \begin{bmatrix} c_2c_3 & c_2s_3 & -s_2 \\ s_1s_2c_3 - c_1s_3 & s_1s_2s_3 + c_1c_3 & s_1c_2 \\ c_1s_2c_3 + s_1s_3 & c_1s_2s_3 - s_1c_3 & c_1c_2 \end{bmatrix}$$

where,

$R^{B/A}$ is the rotation matrix to B (NWU frame) from A (body frame of individual IMU – A1 and A2 are used in this paper to illustrate the two matrices for a joint angle couple as described below)

R_i are rotation matrices about Euler angles θ_1 , θ_2 , and θ_3 that are not shown in this summary.

$$c_i = \cos\theta_i$$

$$s_i = \sin\theta_i$$

4. Rotate the first IMU to NWU frame and then to second IMU body reference frame using two rotation matrices. This is done by the following matrix chain-rule multiplication of the transpose (inverse) of IMU-A1:

$$R^{B/A1} = \text{rotation matrix from A1 to NWU}$$

$$R^{B/A2} = \text{rotation matrix from A2 to NWU}$$

$$R^{A1/A2} = R^{B/A2} \left(R^{B/A1} \right)^{-1}$$

5. Compute the final three Euler angles from the double rotation ($R^{A1/A2}$) using methodology such as G.G. Slabaugh’s white paper³³. The pseudo code to

find both possible solutions* for each angle is as follows³³:

```

if (R31 ≠ ±1)
    θ1 = -asin(R31)
    θ2 = π - θ1
    ψ1 = atan2 (  $\frac{R_{32}}{\cos \theta_1}, \frac{R_{33}}{\cos \theta_1}$  )
    ψ2 = atan2 (  $\frac{R_{32}}{\cos \theta_2}, \frac{R_{33}}{\cos \theta_2}$  )
    φ1 = atan2 (  $\frac{R_{21}}{\cos \theta_1}, \frac{R_{11}}{\cos \theta_1}$  )
    φ2 = atan2 (  $\frac{R_{21}}{\cos \theta_2}, \frac{R_{11}}{\cos \theta_2}$  )
else
    φ = anything; can set to 0
    if (R31 = -1)
        θ = π/2
        ψ = φ + atan2(R12, R13)
    else
        θ = -π/2
        ψ = -φ + atan2(-R12, -R13)
    end if
end if
end if

```

where,

θ₁, ψ₁, φ₁ and θ₂, ψ₂, φ₂ are the two Euler angle solutions for the double rotation

R_{ij} is the element in the *i*th row and *j*th column of the 9x9 R^{A1/A2} matrix.

6. Data may jump from π to -π in the solution space so “unwrap” is recommended in Matlab.
7. Zero the starting point if necessary for given joint angle set.
8. Plot rotation about primary axis (in the case of the elbow, this was the Z axis of the IMU body frame or Φ from the double rotation to A2 reference frame).

V. RESULTS: CHAPS ELBOW JOINT ANGLE

The data from the four IMUs measuring the elbow flexion inside the suit on the body and on the outside of the CHAPS were calculated and the final z-axis Euler angle was analysed for trends. A typical output plot is shown in Fig. 5 that shows the internal angles of the elbow flexion with larger values than the CHAPS. This sample plot is from the elbow in continuous motion with the CHAPS pressurized to 1 psig. Fig. 6 is a cross-sectional rendering of the CHAPS and human subject, which was developed to visually demonstrate the angular differences.

*There are two solutions because of properties where $\sin(\pi - \theta) = \sin(\theta)$ and $\cos(\theta) \neq 0$. Slabaugh explains how to handle these in his paper.

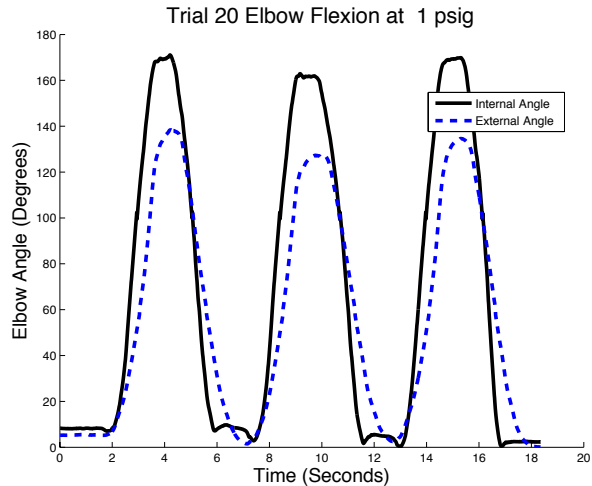


Fig. 5: Elbow flexion data showing internal angle of subject’s motion larger than motion of the CHAPS.

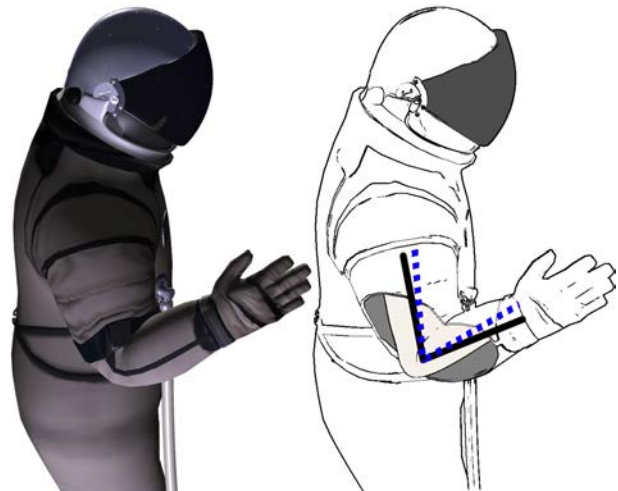


Fig. 6: Rendering of the CHAPS and human user showing approximate differences in elbow joint values.

Assuming the arm started in a perfectly straight position before every elbow flexion, the peak-to-valley difference was measured for both internal (on the subject’s body) and external (on the CHAPS) angles. These maximum movement values were subtracted to find a final difference value. Video data was also used to compare the CHAPS external data and was found to be similar within a few degrees (see Fig. 1 for snapshots of elbow straight and fully bent under 1 psig conditions from video). Video was not shot of all trials so it was not statistically analysed. The CHAPS maximum angle lags the internal body, but these values were not investigated in this study.

Table 1 summarizes the statistical tests that compared the different methodologies and suit pressure results. If a scenario has a P value of less than 5% it is

considered significant (* denotes value is significant), meaning that the data closely match. For example, it was found from the measurement of the internal angle, that the two methodologies of tap versus continuous yielded similar results ($P=0.005$) and that the measurements were similar regardless of the CHAPS pressure ($P=0.002$). This was not true for the external angle, as the results of the methodology differed enough to be not significant ($P=0.128$). However, the final values of angle differences were found to be similar regardless of method ($P=0.000$), but dependent on suit pressure ($P=0.349$).

Table 1: Statistical P-Values calculated to investigate spacesuit pressure and test methodology significance

	Method (Tap/Continuous)	Suit Pressure (0/1 psig)
Internal Body Angle	0.005**	0.002**
External Suit Angle	0.128	0.001**
Difference of Angles	0.000**	0.349

**Significant value

To distinguish some of the calculated averages of all of these cases, values are presented in Table 2. Since the method for the final angle data is significant (not much difference between two methods) we can look at final results and standard deviations by averaging all of the unpressurized ($26.2 \pm 6.7^\circ$) versus pressurized values ($24.2 \pm 7.1^\circ$). We see that the pressurization of the suit leads to slightly reduced angle values of the overall elbow flexion. The final results also show a different story, that the continuous motion led to bigger angle differences regardless of pressure.

Table 2: Peak angles calculated to investigate spacesuit pressure and test methodology significance

	Internal Body Angle ($^\circ$)	External Suit Angle ($^\circ$)	Difference of Angles ($^\circ$)
Tap 0 psig	152.1 ± 5.5	130.1 ± 4.2	22.0 ± 3.6
Tap 1 psig	158.0 ± 3.5	138.4 ± 1.3	19.5 ± 3.5
Continuous 0 psig	157.3 ± 4.5	126.8 ± 7.3	30.5 ± 6.4
Continuous 1 psig	163.8 ± 3.6	134.9 ± 6.8	28.8 ± 6.9

Some key observations from this data are that the internal angle of the human body is always larger than the CHAPS angle (total average of all tests was $25.2 \pm 6.8^\circ$) as seen in Fig. 6; larger internal and external

angles were observed in the pressurization data versus unpressurized; and the continuous method had larger angles for the internal angle and smaller for the external.

VI. LIMITATIONS OF IMUS

IMU systems have limitations and the optimal system must be selected for the right job. Typical limitations are in g-range, sensitivity, lag, filtering, and accuracy. A few issues were identified with the selected APDM system for this application and are described in this section.

The investigators found that the magnetometers were susceptible to magnetic interference, even from metal tabletops, which changes the orientation of the NWU coordinate frame. For the CHAPS testing there was little magnetic interference, but this should be monitored in all testing environments and can be displayed with custom Matlab code to show the data in real time. A study by Bachmann et al. in 2004 developed a guideline that errors can be avoided by maintaining an approximate distance of two feet from any source of disturbance²⁹.

For the elbow joint, the positioning of the IMUs was closely matched internally and externally, but as seen in Fig. 1, the IMUs are not exactly on the rotation axes of the arm. For this reason, it was desired to find the final three Euler angles before reducing any data. The final rotation axis data may therefore have some twist associated with the values and this data should be used as a proof of concept.

The CHAPS was not sized specifically for the subject in this test, and the suit is designed to be used nominally in the seated position. Had the experiments been performed with a perfectly fitting suit in the seated position, it is possible that the internal and external measurements would be more similar.

Dead reckoning is a technological issue for IMUs as they do not know their exact positions at any given time. This is why the “tap” methodology was tested, to try and have a reset point in physical space. The advancement of this technique is further explored in the next section. A common indicator of the difficulty of position tracking is from the occurrence of drift.

Pseudo markers can be estimated from video analysis. However, in future testing it would be ideal to have arm markers for validation in photos or videos.

VII. RECOMMENDATIONS FOR FUTURE SPACESUIT TESTING

The following are recommendations for future improved data acquisition testing with IMU systems for applications like spacesuit mobility.

IMU data could be verified by constructing a simple non-ferrous rig to test one degree of freedom at a time with known angles and potentially known rotation rates (motor activated).

Real time acquisition of Euler angles can be generated with Matlab code. The signal will be slightly lagged, but the instant validation of motion would be useful and more insightful. This could also be used for real time monitoring of a variety of spacesuit joints.

Position estimation would be a valuable addition to the capabilities of the IMU. The performance of the ADPM IMUs is marginal for position estimation, due to drift, without regular position fixes. ADPM has unreleased code that uses frequent position fixes (every 5 seconds) and velocity nulling to track IMU position; performance figures have not been released but a comparison of the estimate to video of an IMU is compelling. We attempted some trials using arm motion in which position fixes were provided using a tap between two IMUs. These events can be identified and used as position fixes. Analysis of these trials is ongoing. If adequate performance can be demonstrated, either through position fixes and careful software correction, or via future hardware improvements, IMU position estimation would enable a variety of applications such as:

- Generating a point cloud that maps out space suit workspace envelopes using natural motions.
- Tracking displacement in all directions for standardized tasks such as using a tool, useful for tool and task optimization.
- Enabling more general motion capture without the cost and constraints of a vision-based system.

It is also recommended that future work in spacesuit motion tracking incorporate El-Gohary et al.'s (2011) linkage method.

VIII. CONCLUSIONS

This proof of concept research met the goal of demonstrating that measurements of the human body within a spacesuit can be taken in a novel method using inertial measurement units (IMUs). With IMUs it is possible to track internal versus external angles to figure out optimal spacesuit fit, energy expenditure, and work envelope. Refinement of the method should prove to be valuable while testing in analogue environments or out in the field without the need for a visual motion capture system. Future data could be collected during spaceflight and lead to improved spacesuit design.

IX. ACKNOWLEDGMENTS

The authors would like to acknowledge support from the Man-Vehicle Laboratory and Dr. Alan Natapoff, the David Clark Company, especially Donald B. Tufts, the Wyss Institute for Biologically Inspired Engineering at Harvard, Gabe Montague for CHAPS renderings and animations, and Massimiliano Di Capua for reviewing this manuscript. This research was made possible in part by the MIT Portugal Program.

X. REFERENCES

1. Favre, J., Aissaoui, R., Jolles, B.M., Guise, J.A., and Aminian, K. (2009): "Functional calibration procedure for 3D knee joint angle description using inertial sensors". *Journal of Biomechanics*. Vol. 42, Pp. 2330-2335.
2. Schepers, H.M., Koopman, H.F.J.M., and Veltink, P.H. (2007): "Ambulatory Assessment of Ankle and Foot Dynamics". *IEEE Transactions on Biomedical Engineering*. Vol. 54, Pp. 8995.
3. Young, D., D'Orey, M.S.R., Opperman, R., Hainley, C., and Newman, D.J. (2010): "Estimation of Lower Limb Joint Angles During Walking Using Extended Kalman Filtering". *6th World Congress of Biomechanics. IFMBE Proceedings*. Vol. 31, Pp. 1319-1322.
4. Young, D., and Newman, D.J. (2011): "Chapter: Augmenting Exploration: Aerospace, Sea and Self. Wearable Monitoring Systems". Eds. Annalisa Bonfiglio and Danilo De Rossi. Springer Science.
5. Moreno, J.C., Lima, E.R., Ruiz, A.F., Brunetti, F.J., and Pons, J.L. (2006): "Design and implementation of an inertial measurement unit for control of artificial limbs: Application on leg orthoses." *Sensors and Actuators B: Chemical*. Vol. 118, Pp. 333-337.
6. Tee, K.S., Awad, M., Dehghani, A., Moser, D., and Zahedi, S. (2011): "A Portable Gait Monitoring System for Lower Limb Prosthetic Alignment". *World Congress on Engineering*. Vol. 3, Pp. 2131-2134.
7. Teskey, W.J.E., Elhabiby, M., and El-Sheimy, N. (2012): "Inertial Sensing to Determine Movement Disorder Motion Present before and after Treatment". *Sensors*. Vol. 12, Pp. 3512-3527.
8. Callaway, A.J., Cobb, J.E., and Jones, I. (2009): "A Comparison of Video and Accelerometer Based Approaches Applied to Performance Monitoring in Swimming". *International Journal of Sports Science & Coaching*. Vol. 4, Pp. 139-153.
9. Lapinski, M. (2009): "A Distributed Wearable, Wireless Sensor System for Evaluating Professional Baseball Pitchers and Batters". *13th IEEE International Symposium on Wearable Computers*. Pp. 131-138.
10. Klaus, D.M., Metts, J., Kobrick, R., Mesloh, M., Monk, T., Gauthier, E., Eberhart, K., Baca, D., Wright, C., Gustafson, A., Oryshchyn, L., and Massey, D (2007): "Space Suit Concepts and Vehicle Interfaces for the Constellation Program". *SAE Technical Paper 2007-01-3088*.
11. Lee, G.R., Graziosi, D., Splawn, K., and Ferl, J. (2011): "Enhancing Capability in Launch, Entry, and Abort Style Spacesuits Fro ISS and Commercial Use". *41st International Conference on Environmental Systems. AIAA 2011-5032*.

12. Jacobs, S.E., and Tufts, D.B. (2011): "Follow-On Development of the Demonstrator Suit for Post-Shuttle Operations". 41st International Conference on Environmental Systems. AIAA 2011-5030.
13. Newman, D.J., Canina, M., and Trotti, G.L. (2007): "Revolutionary Design for Astronaut Exploration – Beyond the Bio-Suit System". 4th Symposium on New Frontiers and Future Concepts, Space Technology and Applications International Forum. American Institute of Physics. Pp. 975-986.
14. Aitchison, L.T. (2012): "A Comparison of Methods for Assessing Space Suit Joint Ranges of Motion". 42nd International Conference on Environmental Systems. AIAA 2012-3534.
15. Jones, R.L. (1966): "Evaluation and Comparison of Three Space Suit Assemblies." NASA Technical Note D-3482.
16. Ross, A. (2000): "Advanced Space Suit Isolated Joint Mobility Test for the Space Suit Comparative Technology Evaluation Test" JSC-39522 (CTSD-ADV-387).
17. Abramov, I., Moiseyev, N., and Stoklitshy, A. (2004): "Some Problems of Selection and Evaluation of the Martian Suit Enclosure Concept". *Acta Astronautica*, 57, 901-909.
18. Tufts, D.B., Jacobs, S.E., and Barry, D.M. (2010): "The Demonstrator Suit: Incorporating Waist, Hip and Shoulder Mobility in a Full Pressure Suit" 40th International Conference on Environmental Systems. AIAA 2010-6178.
19. Ripps, T.B., Garcia, J.M., Macleod, S.M., and Jacobs, S.E. (2011): "The Demonstrator Suit: Evaluating a Full Pressure Suit through Manned and Unmanned Testing". 41st International Conference on Environmental Systems. AIAA 2011-5106.
20. England, S., Benson, E., and Rajulu, S. (2010): "Functional Mobility Testing: Quantification of Functionally Utilized Mobility among Unsuiting and Suited Subjects". Report No. NASA/TP-2010-216122.
21. Jacobs, S.E., and Tufts, D.B. (2012): "Space Suit Development for the Multi-Purpose Crew Vehicle". 42nd International Conference on Environmental Systems. AIAA 2012-3550.
22. Ripps, T.B., Garcia, J.M., and Macleod, S.M. (2012): "Evaluating Suited Ingress and Egress of a Space Vehicle (Orion) Seat". 42nd International Conference on Environmental Systems. AIAA-2012-3551.
23. Kobrick, R.L., Carr, C.E., Meyen, F., Domingues, A.R., and Newman, D.J. (2012): "Using inertial measurement units for space vehicle safety, comfort, design, and performance optimization" (abstract and presentation). Next-Generation Suborbital Researchers Conference 2012. Session: Life Sciences. Palo Alto, California, USA. Paper Registration ID: 38594404.
24. Di Capua, M., and Akin, D. (2012): "Body Pose Measurement System (BPMS): An Inertial Motion Capture System for Biomechanics Analysis and Robot Control from Within a Pressure Suit". 42nd International Conference on Environmental Systems. AIAA-2012-3643.
25. D'Orey, M.S.R., Martins, J.M., Silva, M.T., and Newman, D.J. (2011): "Detection of Gait Cycle Events Through Fourier Series Expansion of Kinematic Data". EUROMECH Colloquium 511 on Biomechanics of Human Motion.
26. D'Orey, M.S.R. (2012): "Passive Dynamic Walkers and Sensory Systems for Gait Analysis". Ph.D. Thesis, Instituto Superior Técnico and Massachusetts Institute of Technology (MIT Portugal Program).
27. Domingues, A.R., Marreiros, S.P., Martins, J.M., Silva, M.T., and Newman, D.J. (2011): "Skin Strain Field Analysis of the Human Ankle Joint", 4^o Congresso Nacional de Biomecânica (CNB2011).
28. Domingues, A.R., Marreiros, S.P., Martins, J.M., Silva, M.T., and Newman, D.J. (2012): "Analysis of Ankle Skin Deformation for the Development of Soft Orthotics" (abstract). 18th Congress of the European Society of Biomechanics (ESB2012). Paper ID: 01713.
29. El-Gohary, M., Holmstrom, L., Huisinga, J., King, E., McNames, J., and Horak, F. (2011): "Upper limb joint angle tracking with inertial sensors". Conference Proceedings, 33rd Annual International Conference of the IEEE Engineering in Medicine and Biology Society. Pp. 5629-5632.
30. Simoes, M.A. (2011): "Feasibility of Wearable Sensors to Determine Gait Parameters". Master's Thesis. University of South Florida, Graduate School Theses and Dissertations. Paper 3346.
31. Wu, G., van der Helm, F.C.T., Veeger, H.E.J., Makhsous, M., Van Roy, P., Angling, C., Nagels, J., Karduna, A.R., McQuade, K., Wang, X., Werner, F.W., and Buchholz, B. (2005): "ISB recommendation on definitions of joint coordinate systems of various joints for the reporting of human joint motion—Part II: shoulder, elbow, wrist and hand". *Journal of Biomechanics*, 38, Pp. 981-992. doi:10.1016/j.jbiomech.2004.05.042.
32. Wie, B. (1998): "Space Vehicle Dynamics and Control". Page 311, Equation 5.13. AIAA Educational Series, Reston, VA.
33. Slabaugh, G.G. (1999): "Computing Euler angles from a rotation matrix". Report from personal website. Available online (last accessed 5 July 2012): <http://www soi.city.ac.uk/~sbbh653/publications/euler.pdf>.



MEASURING UPPER LIMB PROSTHETIC DEVICE USAGE FOR MANIPULATIVE AND NON-MANIPULATIVE TASKS

Amanda L. Martori¹, Stephanie L. Carey¹, Derek J. Lura¹, Samuel L. Phillips²
University of South Florida, Tampa, Florida¹, James A Haley Veterans Medical Center, Tampa, FL²

INTRODUCTION

Despite the high rejection rate of upper limb prostheses (Biddiss & Chau, 2007), few studies have attempted to distinguish between upper limb prosthetic wear time and usage during manipulative tasks. Therefore, in this preliminary study, a wearable sensor was used to collect acceleration data in order to differentiate between a non-manipulative task and a manipulative task. The ability to monitor the task-related usage of an upper limb prosthesis will provide a better representation of its usage and may lead to improved prosthetic design and training practices (Bouwsema et al, 2010).

METHOD

Subjects: One healthy female subject 23 years old.

Apparatus: A wearable Opal sensor (APDM Inc., Portland, OR), the size of a wristwatch, was placed on the subject's right wrist. The Opal sensor includes a triaxial accelerometer, a triaxial gyroscope and a triaxial magnetometer, but only the accelerometer component was used in this study. One major benefit of the Opal sensor is that it can collect data for an entire day on one charge and store up to 28 days worth of data. Therefore, it can be used outside of a laboratory setting and during a person's normal activities of daily living.

Procedures: The subject was asked to walk at a comfortable speed for 20 seconds. The subject was also asked to sit in a chair with their arm resting on a table while holding a glass, and to drink from the glass every 10 seconds, for a total of 50 seconds. Both tasks were repeated 5 times.

Data Analysis: The data from the Opal sensors was exported into MATLAB (MathWorks, Natick, MA). A program was used to filter the raw data with a moving weighted average digital filter, plot the acceleration in the x-direction (which corresponds to anterior-posterior for walking and up and down for drinking) and count the number of actions (tasks) above a threshold acceleration of 6 m/s^2 .

RESULTS

An example of the results from one trial is shown in Figures 1 and 2. During walking (Figure 1), all acceleration values were below the threshold and the program did not detect any manipulative tasks. During the drinking task, the program detected five

manipulative tasks as shown by the number of peaks above the threshold in Figure 2. These results accurately corresponded to the actual tasks performed by the subject.

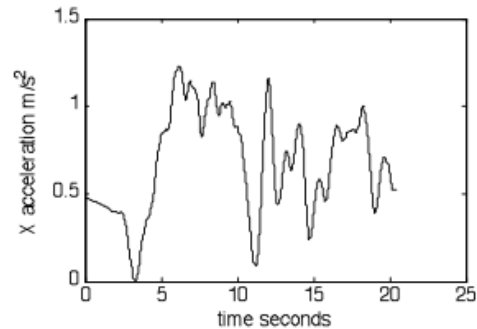


Figure 1 x-acceleration during walking

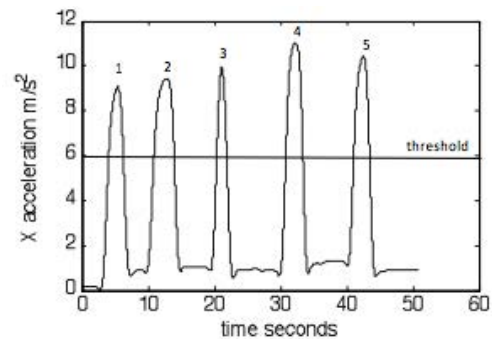


Figure 2: x-acceleration while drinking from a glass

DISCUSSION

The accelerations during walking were all significantly below the threshold and did not yield any false positive readings. Each of the manipulative tasks was well above the threshold and correctly identified by the MATLAB program. Future work will involve more subjects, additional manipulative tasks, prosthetic users and monitoring outside of a laboratory setting.

CONCLUSION

The preliminary results provided a clear differentiation between the manipulative and non-manipulative tasks, demonstrating the effectiveness of a wearable Opal sensor in monitoring the usage of an upper limb prosthesis for manipulative tasks.

REFERENCES

- Biddiss & Chau, *Prosthet. Orthot. Int.* 31, 236-257, 2007.
- Bouwsema et al. *Clin. Biomech.* 25, 523-529, 2010.

VALIDATION OF A COMMERCIAL WEARABLE SENSOR SYSTEM FOR ACCURATELY MEASURING GAIT ON UNEVEN TERRAIN

Mark Tyler Rigsby and Kimberly Edginton Bigelow

University of Dayton, Dayton, OH, USA
email: Kimberly.Bigelow@udayton.edu

INTRODUCTION

Wearable sensor systems comprised of accelerometers and/or gyroscopes have gained popularity in recent years as a means of collecting physical activity and gait data in real-world environments [1,2]. Such systems open up a whole realm of possibilities for better understanding and determining true patient abilities and habits without the constraints associated with traditional motion analysis evaluations [1,2]. Though these systems have great promise, there is believed to be some trade-off in accuracy for the benefits of real-world monitoring [1,2]. Validation of such systems is paramount to ensure that the data collected appropriately reflects the subject's true gait.

Of particular interest is the validation of turn-key systems developed with clinical user-friendliness in mind. Unlike basic sensors, where raw accelerometer or gyroscope data can be manipulated and processed according to the user's expertise, many of these turn-key systems automate the post-processing of the data, showing only the ultimate outcome measures. If such systems produce highly accurate results, this has the potential to change practice as clinicians of all backgrounds would be able to utilize motion capture-type data. Unfortunately research to validate such systems has shown mixed results as related to their accuracy [e.g. 3,4]. The purpose of this study was therefore to validate one such commercially available wearable sensor system (MiniSun IDEEA) in outdoor environments over a span of age ranges.

METHODS

A total of 32 subjects participated in this study: 16 comprising the younger adult group (ages 18 – 38, mean age: 21.6 ± 2.3) and 16 comprising the

middle-aged adult group (ages 45 – 65, mean age: 53.6 ± 5.0). All subjects were free of any injury, disease, or disorder that would affect their ability to walk. Subjects gave written informed consent and all procedures were approved by the university's IRB.

Each subject performed six 50 meter walking trials in an outdoor park: 3 on a paved, well maintained path and 3 across an area of mown grass to replicate uneven terrain that might be encountered during daily ambulation. Subjects were encouraged to walk at their natural pace and to wear their normal, comfortable walking or tennis shoes.

Data for each trial was collected with two systems: the commercially available wearable sensor system of interest (Intelligent Device for Energy Expenditure and Physical Activity (IDEEA), MiniSun LLC) and an inertial measurement system (Opal IMU, APDM Inc.) used for comparison. The IDEEA system consists of five bi-axial accelerometers placed on the feet, thighs, and sternum wired together to a data logger worn on the subject's waistband. The Opal IMU was placed on the L3 spinal process with an elastic belt and the tri-axial accelerometer feature was utilized for data collection.

The data from the IDEEA system was processed using the system's proprietary software. The data from the Opal IMU accelerometer was processed according to a published algorithm proposed by Moe-Nilssen [5], which has been used successfully to study gait, including in outdoor environments. Paired t-tests were performed to investigate the differences between the mean values of gait speed, cadence, step length, and gait duration obtained from the tri-axial accelerometer and the MiniSun

IDEEA for each age group, walking upon each surface ($p < 0.05$).

RESULTS AND DISCUSSION

Statistically significant differences ($p < 0.05$) were found between the systems for gait speed, cadence, and step length in both age groups and for both the even, paved path and the uneven terrain. In all cases the commercially available system underestimated the gait parameters as compared to standard raw accelerometer method. Table 1 provides the results for the trials occurring on the uneven terrain.

These results suggest that there is an accuracy trade-off using this system and its' automated proprietary post-processing software. Others who have investigated the validity of the IDEEA have reported similar underestimations, even when other gold standard comparisons are used [e.g. 3, 6]. However, these studies have been done over shorter distances, and it was hoped that better validity would be found when the distances better matched typical ambulation tasks. This was not the case, and as such researchers and clinicians should be cautious in extracting gait parameters from this particular system.

In contrast, however, gait cycle duration showed no statistically significant differences in any condition, suggesting good accuracy of this particular measure. If the IDEEA uses this information to calculate gait speed and cadence, similar to the estimation of gait parameters done using the raw acceleration data from the Opal, it would make sense for the IDEEA to be more accurate in calculating these parameters than it was. Though the proprietary nature of the IDEEA post-processing software prevents identification of why these values may be

underestimated, this finding does suggest that there may be a refinement that can be done to the IDEEA algorithm to improve the device's accuracy.

There is a need to similarly examine other commercially available systems, particularly those like the IDEEA whose turn-key nature prevent comprehensive understanding of how the system functions. This will provide insight into which systems might be most ideal for clinical real-world monitoring of gait.

CONCLUSIONS

It was found that though easy to use, the commercially available MiniSun IDEEA wearable sensor system consistently underestimated measures of gait, other than cycle duration. This suggests it may not have the accuracy needed for motion analysis studies.

REFERENCES

1. Aminian K, et al. *Comput Animat Virtual Worlds* **15**, 79-94, 2004.
2. Yang C and Hsu Y. *Sensors* **10**, 7772-7788, 2010.
3. Maffiuletti NE, et al. *Gait Posture* **27**, 160-163, 2008.
4. Gardner MJ, et al. *Arch Orthop Traum Su* **127**, 223-227, 2007.
5. Moe-Nilssen R. *Clin Biomech* **13**, 328-335, 1998.
6. Gorelick ML, et al. *J Clin Physiol Funct Imaging* **29**, 271-276, 2009.

ACKNOWLEDGEMENTS

This work was supported by funds from the University of Dayton Graduate School (MTR) and the University of Dayton Research Council (KEB).

Table 1: Summary of Mean \pm Standard Deviation Gait Parameters for Uneven Terrain, ** $p < 0.01$, *** $p < 0.001$

Age Group	18-38		45-65	
	Tri-axial Accelerometer	IDEEA	Tri-axial Accelerometer	IDEEA
Gait Speed (m/s)	1.32 \pm 0.15	1.17 \pm 0.12 ^{***}	1.52 \pm 0.21	1.36 \pm 0.20 ^{***}
Cadence (step/min)	104.93 \pm 6.09	104.38 \pm 6.24 ^{**}	117.10 \pm 9.98	115.71 \pm 9.85 ^{***}
Step Length (m)	0.76 \pm 0.07	0.69 \pm 0.05 ^{***}	0.76 \pm 0.06	0.72 \pm 0.06 ^{**}
Gait Cycle Duration (s)	1.14 \pm 0.07	1.15 \pm 0.07	1.03 \pm 0.09	1.03 \pm 0.09

Ambulatory measurement of elbow kinematics using inertial measurement units

Wei Sin Ang, I-Ming Chen, *Fellow, IEEE*, Qilong Yuan

Abstract— Using inertial measurement unit (IMU) to measure human body kinematics has gained popularity because of its low-cost and ease of handling, compared to optoelectronic and electromagnetic systems. However, its usage has to be supported by post-processing protocols that integrate the data with reliable kinematic model to improve the accuracy. In this paper, a method to calculate the rotation axes and angles of the elbow joint from IMU data is presented. The method makes use of product of exponential (POE) representation and an optimization process to decompose the rotation matrix into angles along the two rotation axes without introducing the carrying angle and assuming orthogonality of the two axes. Using the method, the estimated errors of the calculated axes of rotation are comparable to published results, and the rotation angles yield an orientational deviation of less than 1.5°.

Keywords—kinematics; IMU; elbow; optimization

I. INTRODUCTION

The recent advancements in the development of IMU make these sensors a serious contender against the widely used optoelectronic and electromagnetic systems in capturing motion data in vivo. It is cheaper, portable, less cumbersome to setup, and can be used in a non-laboratory environment [1]. The data captured can be used in biomechanical models that provide musculoskeletal information. This is especially attractive to clinicians and therapists working in the field of rehabilitation, where operations are constrained by costs and manpower. One drawback is, however, its accuracy compared to the optoelectronic and electromagnetic systems which have many protocols proven to be effective [2]. The solution to this is to develop algorithms that can apply the information captured by the IMUs onto accurate models of the human anatomy. One useful and illustrative example is using IMUs to estimate the elbow flex/extension and pro/supination axes and angles.

The methods to find the elbow rotation axes described in [3-5] required the precise locations of several bony landmarks with respect to a reference. These landmarks were either located using cadaver data or in vivo by using electromagnetic tracking devices with proper palpation techniques. The electromagnetic systems are too expensive and cumbersome for practical use of the kinematic data in a clinic or rehabilitation facility. And proper palpation requires the skills of trained therapists, which may not be readily available. The discrepancy in the definitions of palpated

locations of the landmark among different therapists is also a problem.

In general, the flex/extension axis, S_{FE} , is not orthogonal to the longitudinal axis of the humerus, y_H . S_{FE} and the pro/supination axis, S_{PS} , are also non-intersecting and not orthogonal to each other [5, 6]. This introduces a third angle, the carrying angle, when we want to obtain the rotation angles in S_{FE} and S_{PS} from decomposing the rotation matrix of the forearm relative to the upper arm. The definition of the carry angle is inconsistent [2], but in this context it is viewed as the angular offset between the orthogonal of S_{FE} and S_{PS} . For the ease of finding the rotation angles in S_{FE} and S_{PS} , the two axes are often taken to be orthogonal and the carrying angle is often conveniently regarded as a constant [1, 7]. However, the carrying angle varies significantly among individuals [8], and it is dependent on the two elbow rotation angles [9]. In this study, we propose a method to decompose the rotation angles, obtained from the data captured by IMUs, in S_{FE} and S_{PS} directly using product of exponentials (POE) and optimization without making any assumption on the carrying angle and the orthogonality of S_{FE} and S_{PS} .

II. METHODS

A. Measurement Device

The APDM Opal™ wireless inertial measurement units system is used in this study (APDM Inc., Portland, OR, USA). It has an accelerometer, a gyroscope, and a magnetometer all encased into a small unit of 48.4 x 36.5 x 13.4 mm, and weighs 22 g. The static and dynamic accuracy of the measured angle is 1.5° and 2.8° respectively. It is shown to correlate well with optical sensors [10]. The device local coordinate system, with x-axis pointing downwards, y-axis pointing to the side, and z-axis pointing forwards, is with respect to an earth-based global coordinate system. The system calculates and gives the quaternion representation of the orientation as the output. In this study, data was acquired at 128 Hz.

B. Subjects and Experimental Set-up

Four healthy male subjects (mean age 26.5 years, with SD 2.65 years) volunteered for the experiment after informed consent was obtained from them. All subjects do not have any known upper limb disorder.

Three IMUs were attached to the subject's body. The first is positioned at the sternum, just below the neck, using double sided tape, with the IMU frame (x_I, y_I, z_I) shown in Fig. 1. This IMU is used to measure the orientation of the thorax (which is expected to have very small changes throughout the experiment). The second and third IMUs are strapped to the centre of the right upper arm, and to the right lower arm near the wrist, respectively, using elastic straps.

This work was supported in part by the Agency for Science, Technology and Research, Singapore, under SERC Grant 092 149 0082.

All authors are with School of Mechanical and Aerospace Engineering, Nanyang Technological University, Singapore 597627 (Corresponding author: Wei Sin Ang; e-mail: wsang3@e.ntu.edu.sg). Wei Sin Ang is on leave from Nanyang Polytechnic, Singapore.

The frames of the two IMUs (x_2, y_2, z_2) and (x_3, y_3, z_3) are shown in Fig. 1.

There were two sets of experiment done in this study. The first was to find the two axes of rotation of the forearm (S_{FE} , flexion-extension, and S_{PS} , pronation-supination) with respect to the humerus frame. As the sensors were wireless, the subjects were able to stand at a clearing in the lab, away from any metallic objects that might affect the measurements. To find S_{FE} , the subject stood upright with both arms resting naturally by the sides. During the experiment, the subject flexed the forearm completely at a controlled speed, and then extended back to the initial position. To find S_{PS} , the subject fully pronated the forearm from the initial position, and then supinated the forearm fully at a controlled speed. Both motions were performed three times by the subjects.

The second experiment was designed to test the accuracy of the methods proposed in this study. The subjects stood upright with their arms resting naturally by the sides. Then they performed the following two motions: (1) raising the whole arm in the sagittal plane to above the head at a controlled speed; (2) moving the hand towards the mouth as if drinking water from a cup and returned to the initial position.

C. Estimation of the Rotation Axes of the Forearm

The global coordinate system is defined as: X_G – north, Y_G – east, and Z_G – down. The local coordinate systems of the thorax, humerus and forearm when the arm is resting are defined as: x_T, x_H, x_F – left, y_T, y_H, y_F – up, and z_T, z_H, z_F – front. With the help of a compass, the initial local z -axes were aligned with the north during the experiments, so that the orientations of the local systems are known with respect to global. Unlike in [7, 11], we do not assume that the thorax frame to be stationary, and the local coordinate systems are independent of the positions and orientations of the IMUs, so that the kinematic data can be compared among subjects and used without ambiguity.

To find S_{FE} with respect to the humerus frame, the orientations of the IMUs strapped to the upper and lower arm between two consecutive positions were calculated. The orientation of the lower arm IMU in the upper arm IMU frame at the current (initial) position and the next (final) position are given by [12, 13]

$$R_{UL}^i = (R_{GU}^i)^T R_{GL}^i \quad (1)$$

$$R_{UL}^f = (R_{GU}^f)^T R_{GL}^f \quad (2)$$

where the superscripts i and f denote initial and final positions; the subscripts G, U and L denote global, upper arm IMU and lower arm IMU frames respectively. The rotation matrix R_{XY} represents orientation of frame Y in frame X . The rotation matrix of the final position relative to the initial position in the lower arm IMU frame is

$$R_L^{if} = (R_{GL}^i)^T R_{GL}^f \quad (3)$$

The skew-symmetric matrix, W_L^{if} , that represents the rotation axis of R_L^{if} is [14]

$$W_L^{if} = R_L^{if} - (R_L^{if})^T \quad (4)$$

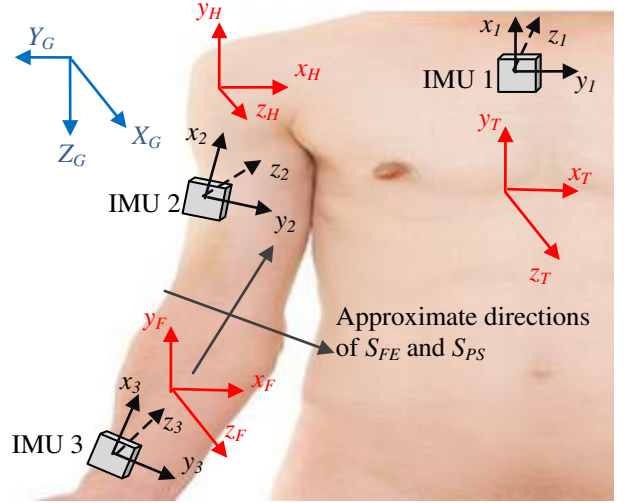


Fig. 1. The IMU frames, global frame and the local frames.

The rotation axis in the lower arm IMU frame is calculated as

$$S_L = [w_1, w_2, w_3]^T / \sqrt{w_1^2 + w_2^2 + w_3^2} \quad (5)$$

where $w_1, w_2,$ and w_3 are the independent components of W_L^{if} .

The rotation axis can be represented in the upper arm IMU frame using

$$S_U = R_{UL}^i S_L \quad (6)$$

And the rotation axis, when represented in the humerus frame, H , is

$$S_{FE} = (R_{GH}^i)^T R_{GU}^i S_U \quad (7)$$

The procedures to find S_{PS} is exactly the same. In the first experiment, both S_{FE} and S_{PS} were calculated for ten times for the duration of the experiment. These axes are the Instantaneous Helical Axes (IHA) [15] during the motion of the elbow. The optimal axes were then calculated closest to the IHAs using least-squared method as

Minimize $J(S_{opt})$, where

$$J(S_{opt}) = \sum_{i=1}^{10} \|S_{opt} - S_i\| \quad (8)$$

where S_i are the IHAs in either flexion/extension or pronation/supination motions.

D. Decomposition of Joint Angles at the Elbow

After finding the orientations of the rotation axes of the forearm relative to the humerus, we can make use of the IMU data during arm motion to estimate the flexion/extension and pronation/supination angles of the elbow at each time-step.

The orientations of the humerus frame in the upper arm IMU frame and the forearm frame in the lower arm IMU frame are constant matrices, given as

$$R_{UH}^0 = (R_{GU}^0)^T R_{GH}^0 \quad (9)$$

$$R_{LF}^0 = (R_{GL}^0)^T R_{GF}^0 \quad (10)$$

where the superscript 0 denotes initial position when the arm is resting by the side. The orientations of the humerus

and the forearm in the global frame at time-step n can be calculated as

$$R_{GH}^n = R_{GU}^n R_{UH}^0 \quad (11)$$

$$R_{GF}^n = R_{GL}^n R_{LF}^0 \quad (12)$$

Next, we can calculate the orientation of the forearm frame in the humerus frame as

$$R_{HF}^n = (R_{GH}^n)^T R_{GF}^n \quad (13)$$

The rotation matrix that represents the transformation of the forearm frame at time-step n relative to $n-1$ in the humerus frame is

$$R_H^{n-1,n} = (R_{HF}^{n-1})^T R_{HF}^n \quad (14)$$

The rigid body rotation about a fixed axis, $R \in \text{SO}(3)$, where $\text{SO}(3) = \{R \in \mathbb{R}^{3 \times 3}; RR^T = I, \det R = 1\}$ [14]. The skew-symmetric matrix that corresponds to the axis of rotation is

$$\hat{W} = R - R^T = \begin{bmatrix} 0 & -w_z & w_y \\ w_z & 0 & -w_x \\ -w_y & w_x & 0 \end{bmatrix} \quad (15)$$

In the exponential form, $R = e^{\hat{W}q}$, where $q \in \mathbb{R}$ is the angle of rotation. In a more explicit form [16],

$$R = e^{\hat{W}q} = I + \sin q \frac{\hat{W}}{\|\hat{W}\|} + (1 - \cos q) \frac{\hat{W}^2}{\|\hat{W}\|^2} \quad (16)$$

In the context of the elbow joint which has two DOF, the joint motion can be represented by two consecutive rotations, one about S_{FE} axis, followed by one about S_{PS} axis:

$$R_{\text{elbow}} = e^{\hat{W}_{FE}q_{FE}} e^{\hat{W}_{PS}q_{PS}} \quad (17)$$

where \hat{W}_{FE} and \hat{W}_{PS} are the skew-symmetric matrices that correspond to S_{FE} and S_{PS} respectively; q_{FE} and q_{PS} are the respective rotation angles.

The rotation matrices $R_H^{n-1,n}$ and R_{elbow} describe the same motion at the elbow if q_{FE} and q_{PS} are the change in angle about the respective axes from time-step $n-1$ to n . To calculate q_{FE} and q_{PS} from the rotation matrices without having to induce a third non-DOF angle (the carrying angle), we introduce an optimization routine:

Minimize $J(q_{FE}, q_{PS})$, where

$$J(q_{FE}, q_{PS}) = \sum_{i=1}^3 \|e_i \times r_i\|^2 \quad (18)$$

where r_i and e_i are the i^{th} column of $R_H^{n-1,n}$ and R_{elbow} respectively. The optimization routine ensures the respective column vectors of $R_H^{n-1,n}$ and R_{elbow} are optimally in the same directions. We do not attempt to match all nine components of the matrices because it may cause convergence issues in the optimization process. The routine is implemented in Matlab® using the function *fsolve* with the ‘trust-region-dogleg’ algorithm.

By adding a third IMU at the thorax, the humerus frame can be represented in the thorax frame. This permits an extension to the usage of the methods described in this paper to provide the humerothoracic motion information for the purpose of modeling the whole arm.

III. RESULTS

A. Results for Experiment 1

The calculated S_{FE} and S_{PS} of one subject are shown in Fig. 2. The dashed lines show the axes of rotation of the twenty segments throughout the duration of the experiment. The solid lines are the optimal axes. The view is presented in the frontal plane where the relative orientation between S_{FE} and S_{PS} is most apparent. The results of all four subjects are shown in Table 1. The error estimations of the optimal axes are calculated as [4]:

$$e_S = \frac{1}{N} \sum_{i=1}^N \cos^{-1}(S_{opt} \cdot S_i) \quad (19)$$

where S_i are the IHAs in either flexion/extension or pronation/supination motions, and S_{opt} is the optimal axes.

The average optimal axes and error estimations of S_{FE} and S_{PS} of all the subjects in the humerus frame are $[0.967, -0.180, -0.097]$ and 6.37° , and $[0.198, 0.974, -0.084]$ and 3.05° respectively. The results from [4] and [15] are included for comparison. The axes calculated and the corresponding errors in this study are very similar to that published in [4]. The axes calculated in [15] are closer to the axes in the humerus frame. This may be due to the fact that the results were calculated from cadaveric data where the sensors were fixed directly to the bones. Whereas in living subjects there are always some disturbances caused by soft tissue movements and involuntary motions from other parts of the body, there are no such issues in cadavers.

B. Results for Experiment 2

The trajectories of the flexion/extension angle, q_{FE} and the pronation/supination angle, q_{PS} of a subject performing the arm motions are presented in Fig. 3. For Fig. 3a and 3b, the subject flexed his arm fully from initial position. The q_{FE} started from 0° and decreased steadily to -118° .

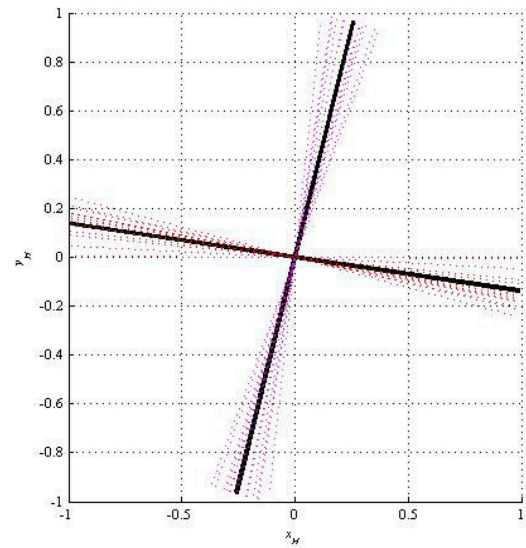


Fig. 2. The calculated S_{FE} and S_{PS} of one subject shown in the frontal plane. The dashed lines are the axes calculated between two consecutive positions. The solid lines are the optimal axes. The axes are dimensionless as only the directions of the axes are plotted.

TABLE I. CALCULATED S_{FE} AND S_{PS}

Subject	S_{FE}				S_{PS}			
	x_{opt}	y_{opt}	z_{opt}	e_s (°)	x_{opt}	y_{opt}	z_{opt}	e_s (°)
1	0.968	-0.229	-0.103	5.45	0.274	0.957	-0.097	4.39
2	0.918	-0.251	-0.307	6.00	0.240	0.968	-0.073	3.45
3	0.996	-0.087	-0.035	8.77	0.176	0.984	-0.034	2.09
4	0.987	-0.151	0.058	5.24	0.103	0.985	-0.132	2.28
Mean (sd)	0.967 (0.035)	-0.180 (0.075)	-0.097 (0.155)	6.37 (1.64)	0.198 (0.075)	0.974 (0.014)	-0.084 (0.041)	3.05 (1.08)
Ref [4] ^a	0.965 (0.035)	-0.134 (0.032)	-0.212 (0.118)	4.12 (0.670)				
Ref [15]	0.992 (0.007)	-0.084 (0.066)	-0.018 (0.083)	4.72 (0.073)	0.02 (0.088)	0.996 (0.004)	-0.022 (0.027)	4.59 (0.039)

^aStokdijk et al. [4] only provided results for S_{FE} .

As the subject was told to flex the arm naturally, the forearm supinated slightly during the flexion.

The subject pro/supinated the forearm from the initial natural resting position in the second motion, and the angles are shown in Fig. 3c and 3d. The range of the q_{PS} is from -50° to 50° . As no external constraint was used on the subject's body during the experiment, the arm flexed slightly during movement. The subject raised his arm from initial position to above his head. As expected, both angles have only small variations during this movement, as shown in Fig. 3e and 3f. In the last movement, the subject was told to pick up a bottle from a table in front of him, drink from it, and put it back. The q_{FE} nearly reached its maximum at about -100° as shown in Fig. 3g. It is apparent from Fig. 3h that the movement invoked mainly pronation.

All subjects have similar ranges and patterns in q_{FE} and q_{PS} in the first three movements, but not in the drinking motion, as shown in Fig. 4. This is due to the differences in the trajectory taken by each subject in more complicated movements.

The accuracy of obtaining the flexion/extension angle, q_{FE} and the pronation/supination angle, q_{PS} using the optimization method with respect to the measurements by the sensors is tested by an error estimation [16]. We define the logarithm of a rotation matrix, $R \in SO(3)$, as

$$\log[R] = \frac{\phi}{2 \sin \phi} (R - R^T) \quad (20)$$

where $2 \cos \phi = \text{trace}(R) - 1$, and $\log[R]$ is skew-symmetric. The average quantified orientational deviations between the calculated and measured poses is defined as

$$\Delta R = \frac{1}{m} \sum_{i=1}^m \|\log(R_{mi}^{-1} R_{ci})^V\| \quad (21)$$

where m is the number of time-steps, R_m is the measured rotation matrix (in this case $R_H^{n-1,n}$), and R_c is the calculated matrix (in this case R_{elbow}). The notation $(\cdot)^V$ refers to the \mathfrak{R}^3 vector that represents $\log[R]$. The results of ΔR of each subject performing each movement are shown in Table 2. It can be seen that the deviations are small, and this means that the optimization gives reliable results.

IV. DISCUSSION

Many of the methods developed to make use of the kinematic data of human body captured by sensors thus far require careful palpation of the bony landmarks or sophisticated protocols and setups [2]. The former has to be done by trained therapists, and small therapist to patient ratio in many ageing societies poses a challenge in making rehabilitation cheaper and more accessible. The reliability and repeatability of palpation is also a concern [17]. The expensive and cumbersome setups in the latter are often only possible in laboratories, and this is also a hindrance in promoting rehabilitation.

The method described in this paper demonstrates that finding elbow rotation angles using IMUs can be performed easily and with accuracy comparable to protocols that require palpation and more expensive devices. It also avoids complex and costly minimization computations that involve partial derivatives and integrals [18]. Comparing the errors in the calculations of S_{FE} and S_{PS} with [4] and [15], we see that the proposed method yields reasonably accurate results. Although attaching IMUs to the arm and body is susceptible to the problems faced by every non-invasive methods [2], like measurement noise and noise caused by soft tissue movements and involuntary rotations of other body joints by the subjects during experiments, the results can be made more reliable by low-pass filtering the raw IMU data before processing.

The mean angle between S_{FE} and S_{PS} among the four subjects is 88.6° with a standard deviation of 3.67° . This justifies our choice of not using Euler decomposition which assumes orthogonality of the two axes to find q_{FE} and q_{PS} . The effect of the non-orthogonality of S_{FE} and S_{PS} will be more apparent if the method is used in a whole arm model that aims to estimate muscle strengths. In these types of complex musculoskeletal model, the lines of action of the muscles with respect to the joints are very important. The assumption of orthogonality will compromise the accuracy in these models.

TABLE II. Orientational Deviation Between The Calculated And Measured Poses, ΔR

Subject	ΔR ($^{\circ}$)			
	Flexion	Pro/Supination	Raise Arm	Drinking
1	0.756	0.344	0.141	0.250
2	2.05	0.412	0.303	0.604
3	2.26	0.571	0.603	0.557
4	0.622	0.101	0.194	0.527
Mean (<i>sd</i>)	1.42 (0.853)	0.357 (0.195)	0.310 (0.207)	0.485 (0.160)

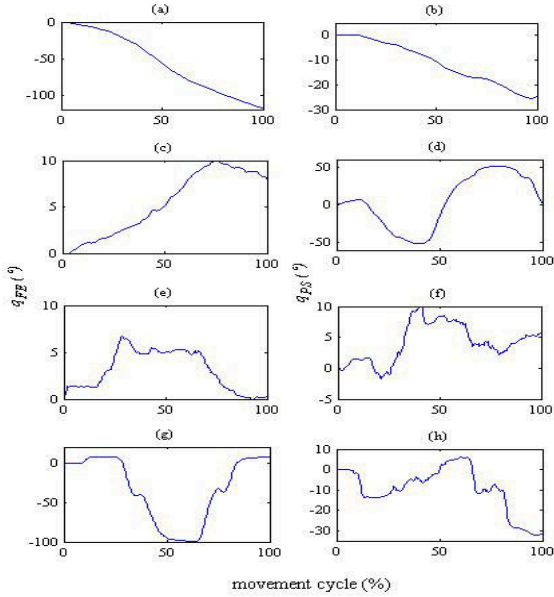


Fig. 3. The plot of the trajectories of q_{FE} (left column) and q_{PS} (right column) versus the percent of movement cycle of one subject: (a) & (b) flexion; (c) & (d) supination/pronation ; (e) & (f) arm raised in the sagittal plane; and (g) & (h) drinking water.

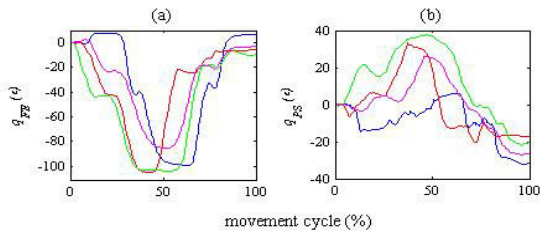


Fig. 4. Comparison of (a) q_{FE} and (b) q_{PS} during the drinking movement among subjects.

Notwithstanding the accuracy issues of the IMU itself, the optimization routine used in calculating q_{FE} and q_{PS} yields results that have very small deviation from the measured data. The cost of computation is low since there are only two variables. This eliminates the need to introduce the carrying angle which is not a DOF at the elbow.

The third IMU attached to the thorax was not used in the computations of the results in this study. However, it was to illustrate that the motions of the forearm and the humerus can be represented more accurately with respect to the thorax instead of the global frame, since the torso of a subject will inevitably move during any arm movements. In a more complete arm model, q_{FE} and q_{PS} calculated using the method can be viewed as the joint angles of the elbow which can be modeled by two revolute joints.

The ease of use of the method is an advantage but it is also its limitation. Without making references to bony landmarks, the angles calculated are presented in the initial frame of the humerus, which in turns is referenced to the global frame. To improve the accuracy of the method when used in a more complete and comprehensive model, one should establish a relationship between the humerus frame to anatomic landmarks. This can be done by palpation (which we have tried to avoid) or by using published anatomic data that can be scaled according to the subject's measurable parameters [19].

V. CONCLUSION

The advantages of using IMU over the more popular sensor systems in capturing kinematics of human body lie in its low-cost and ease of handling. However, it has to be supported by reliable algorithms and protocols to increase its accuracy.

In this study, the rotation axes and angles of the elbow joint were calculated from the IMU data of the forearm and the humerus, using a novel method of decomposing the rotation matrix by a POE representation and an optimization process. Results have shown that the accuracy of the method is comparable to those using more expensive sensor systems. It also has the characteristic of not having to introduce the carrying angle and assume orthogonality of the two DOFs at the elbow. However, since locating bony landmarks as references was not done, one has to be cautious when integrating the method into a comprehensive musculoskeletal arm model.

ACKNOWLEDGMENT

Wei Sin Ang would like to thank Nanyang Polytechnic for the PhD scholarship.

REFERENCES

- [1] H. J. Luinge, P. H. Veltink, and C. T. M. Baten, "Ambulatory measurement of arm orientation," *Journal of Biomechanics*, vol. 40, pp. 78-85, 2007.
- [2] C. Anglin and U. P. Wyss, "Review of arm motion analyses," *Proceedings of the Institution of Mechanical Engineers Part H-Journal of Engineering in Medicine*, vol. 214, pp. 541-555, 2000.
- [3] M. Stokdijk, M. Biegstraaten, W. Ormel, Y. A. de Boer, H. E. J. Veeger, and P. M. Rozing, "Determining the optimal flexion-extension axis of the elbow in vivo - a study of interobserver and intraobserver reliability," *Journal of Biomechanics*, vol. 33, pp. 1139-1145, Sep 2000.
- [4] M. Stokdijk, C. G. M. Meskers, H. E. J. Veeger, Y. A. de Boer, and P. M. Rozing, "Determination of the optimal elbow axis for evaluation of placement of prostheses," *Clinical Biomechanics*, vol. 14, pp. 177-184, Mar 1999.
- [5] H. E. J. Veeger, B. Yu, K. N. An, and R. H. Rozendal, "Parameters for modeling the upper extremity," *Journal of Biomechanics*, vol. 30, pp. 647-652, Jun 1997.
- [6] V. M. Zatsiorsky, "Kinematics of human motion. 1998," *Human Kinetics*, 2002.
- [7] A. G. Cutti, A. Giovanardi, L. Rocchi, A. Davalli, and R. Sacchetti, "Ambulatory measurement of shoulder and elbow kinematics through inertial and magnetic sensors," *Medical & Biological Engineering & Computing*, vol. 46, pp. 169-178, Feb 2008.
- [8] R. Shiba, C. Sorbie, D. W. Siu, J. T. Bryant, T. D. V. Cooke, and H. W. Wevers, "Geometry of the humeroulnar joint," *Journal of orthopaedic research*, vol. 6, pp. 897-906, 1988.
- [9] E. Chao and B. Morrey, "Three-dimensional rotation of the elbow," *Journal of Biomechanics*, vol. 11, pp. 57-73, 1978.
- [10] M. El-Gohary, L. Holmstrom, J. Huisinga, E. King, J. McNames, and F. Horak, "Upper limb joint angle tracking with inertial sensors," in *Engineering in Medicine and Biology Society, EMBC, 2011 Annual International Conference of the IEEE*, 2011, pp. 5629-5632.
- [11] C. Quental, J. Folgado, J. Ambrosio, and J. Monteiro, "A multibody biomechanical model of the upper limb including the shoulder girdle," *Multibody System Dynamics*, vol. 28, pp. 83-108, Aug 2012.
- [12] Q. Yuan, I.-M. Chen, and S. P. Lee, "SLAC: 3D localization of human based on kinetic human movement capture," in *Robotics and Automation (ICRA), 2011 IEEE International Conference on*, 2011, pp. 848-853.
- [13] Q. Yuan and I.-M. Chen, "Simultaneous Localization and Capture with velocity information," in *Intelligent Robots and Systems (IROS), 2011 IEEE/RSJ International Conference on*, 2011, pp. 2935-2940.
- [14] J. M. McCarthy, *Introduction to theoretical kinematics*, 1990.
- [15] H. E. J. Veeger and B. Yu, "Orientation of axes in the elbow and forearm for biomechanical modelling," *Proceedings of the 1996 Fifteenth Southern Biomedical Engineering Conference*, pp. 377-380, 1996.
- [16] I. M. Chen, G. L. Yang, C. T. Tan, and S. H. Yeo, "Local POE model for robot kinematic calibration," *Mechanism and Machine Theory*, vol. 36, pp. 1215-1239, Nov-Dec 2001.
- [17] L. Chaitow, "The palpation reliability debate: the experts respond," *Journal of Bodywork and Movement Therapies*, vol. 6, p. 18, 2002.
- [18] E. V. Biryukova, A. Roby-Brami, A. A. Frolov, and M. Mokhtari, "Kinematics of human arm reconstructed from spatial tracking system recordings," *Journal of Biomechanics*, vol. 33, pp. 985-995, Aug 2000.
- [19] P. De Leva, "Adjustments to Zatsiorsky-Seluyanov's segment inertia parameters," *Journal of Biomechanics*, vol. 29, pp. 1223-1230, 1996.

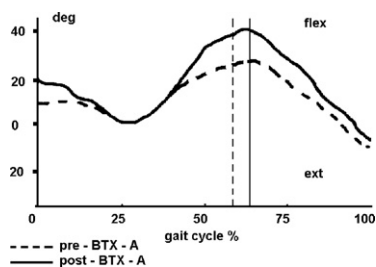


Fig. 1.

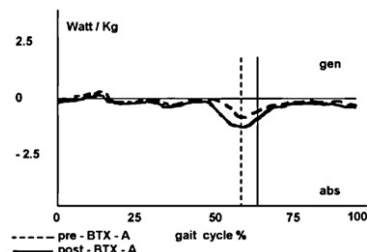


Fig. 2.

botulinum toxin was always combined with appropriate intensive physiotherapy (90 min per session, 5 times/wk). Gait analysis and a clinical and functional evaluation were carried out on two occasions: at inclusion and 1 month after botulinum toxin injection.

Results: Post-BTX-A there was a significant improvement of 9° in maximum swing phase knee flexion and 7° in total range of knee motion (Fig. 1). Average peak hip flexion in swing phase significantly increased by 8. Post-BTX-A the maximum negative of knee joint power reached at the end of the stance phase increased significantly (Fig. 2).

Dynamic electromyography recorded slightly decreasing vastus medialis activity, whereas those of the vastus lateralis, rectus femoris, biceps femoris and soleus were more markedly reduced.

Discussion: As a result of BTX-A treatment, elimination of high rectus femoris activity led to large increases in peak knee flexion. The knee extension moment, which is influenced by rectus femoris activity, prior to toe-off, rather than after toe-off, may be a more prevalent contributor to stiff-knee gait.

The gait analysis data have shown that BTX-A treatment facilitates more normal swing pattern in patients post-stroke [2].

This study confirm the importance of the rectus femoris in the physiopathology of stiff knee gait, suggesting that rectus femoris overactivity should decrease knee flexion.

We believe that the BTX-A treatment provides a “window of normal tone” of opportunity to retrain the rehabilitative program. We suggest that perhaps a combination of botulinum toxin injection and specific physiotherapy would have yielded more significant results regarding the functional benefit of the therapy in patients with a stiff-knee gait after stroke, particularly with some flexion [3].

References

Table 1
Median, 25th and 75th percentiles of evaluated gait parameters for each tested period of gait maturation.

	1st week			1st month			2nd month			3rd month			6th month		
	Median	25th perc	75th perc	Median	25th perc	75th perc	Median	25th perc	75th perc	Median	25th perc	75th perc	Median	25th perc	75th perc
strT	0.81	0.75	1.06	0.71	0.65	0.72	0.68	0.66	0.71	0.71	0.71	0.75	0.75	0.67	0.79
swT	0.31	0.30	0.34	0.33	0.31	0.33	0.35	0.34	0.35	0.36	0.34	0.37	0.36	0.34	0.37
stanceT	0.42	0.41	0.70	0.38	0.33	0.39	0.34	0.32	0.37	0.38	0.34	0.38	0.39	0.32	0.42
dsT	0.35	0.35	0.35	0.33	0.33	0.34	0.34	0.33	0.35	0.35	0.34	0.37	0.38	0.37	0.38
stepR	0.48	0.31	0.50	0.34	0.33	0.38	0.26	0.21	0.33	0.39	0.28	0.41	0.36	0.33	0.39
strP	0.29	0.20	0.29	0.33	0.25	0.38	0.37	0.32	0.40	0.31	0.24	0.35	0.29	0.26	0.32
stepS	1.66	1.44	1.72	1.43	0.90	1.48	0.95	0.55	1.57	0.96	0.93	1.52	1.19	1.09	1.40

- [1] Goldberg SR, Ounpuu S, Arnold AS, Gage JR, Delp SL. Kinematic and kinetic factors that correlate with improved knee flexion following treatment for stiffknee gait. *J Biomech* 2006;39:689–98.
- [2] Stoquart GG, Detrembleur C, Palumbo S, Deltombe T, Lejeune TM. Effect of botulinum toxin injection in rectus femoris on stiff-knee gait in people with stroke. *Arch Phys Rehabil* 2008;89:56–61.
- [3] Sheehan GL. Botulinum treatment of spasticity: why is it so difficult to show a functional benefit? *Curr Opin Neurol* 2001;14:771–6.

<http://dx.doi.org/10.1016/j.gaitpost.2012.12.021>

C4

A longitudinal study to evaluate the development of independent walking in infants using inertial sensors: Preliminary results

M.C. Bisi, R. Stagni

DEIS, University of Bologna, Italy

Introduction: Many studies have been observing infants at the onset of walking in order to evaluate the development of different strategies and coordination [1–3]. These studies regard most of the times small groups (<10) and only few studies observed longitudinally the evolution of independent walking (on 2 or 5 subjects) [4,5]. To the author knowledge, these observations were always made using optoelectronic or video-based data. The use of wireless inertial sensors is more practical when aiming at the measurements of large populations. Moreover, inertial sensors can be worn under the clothes facilitating the experiments with infants who are not distracted by markers and can freely walk in any environment. The aim of the present study is to observe longitudinally a large group of infants using inertial sensors over a 6-month period after onset of independent walking (period in which the most dramatic changes of maturation of many gait parameters occurs [6]). This database will allow evaluating the changes in gait temporal parameters, postural stability and coordination at the beginning of independent walking.

Methods: Twenty healthy infants (77 ± 2 cm, 9.3 ± 0.8 kg, 13 ± 2 months) were included in the study. All of the infants had no known developmental delays. The tests were scheduled once a month after the onset of independent walking for three months, and one after six months. When possible, a test was performed during the very first week of independent walking. Three tri-axial wireless inertial sensors (OPALS, Apdm, USA) were mounted on the lower back and on the right and left legs, respectively. The participants were asked to walk straight in the room. Heel-strike and toe-off instants were estimated from the angular velocity of the lower limbs [7]. Median stride (strT), swing (swT), stance (stanceT) and double support (dsT) times were calculated. Step-, stride-regularity (stepR and strR) and step symmetry (stepS) were evaluated using trunk vertical acceleration [8]. Up to now only five infants completed all the scheduled tests, thus the presented results are preliminary.

Results: Up to now no significant trends were shown in the evaluated parameters even if, generally, the swT showed an increase with months of experience. In Table 1, median (and 25th-, 75th

percentile) strT, swT, stanceT, dsT, stepR, strR, stepS, calculated on the five infants are shown for each tested period of gait maturation.

Discussion: The increased swT with months of experience evidenced the fear of falling of the infants during the beginning of independent walking. Gait regularity was low in all the infants, as expected. StepS is higher than 1, showing high symmetry but it is calculated as stepR/strideR, which values are close to 0, therefore it is not a reliable value.

References

- [1] Kubo M, Ulrich BD. *J Mot Behav* 2006;38(3):229–37.
- [2] Roncesvalles MN, et al. *J Mot Behav* 2000;32(1):100–11.
- [3] Ivanenko YP, et al. *J Neurophysiol* 2005;94(1):754–63.
- [4] Brill B, Breniere Y. *J Mot Behav* 1992;24(1):105–16.
- [5] Ivanenko YP, et al. *J Exp Biol* 2004;207(21):3797–810.
- [6] Ivanenko, et al. *Exerc Sport Sci Rev* 2007;35:67–73.
- [7] Aminian, et al. *J Biomech* 2001;35:689–99.
- [8] Moe-Nilssen, et al. *J Biomech* 2004;37:121–6.

<http://dx.doi.org/10.1016/j.gaitpost.2012.12.022>

C5

Quantitative gait analysis in parkin disease

A. Castagna^{1,2}, S. Frittoli¹, F. Del Sorbo¹, A. Elia¹, L. Romito¹, B. Reggiori¹, A. Albanese^{2,3}

¹ *Istituto Neurologico Carlo Besta, Milan, Italy*

² *Istituto Santa Maria Nascente, Fondazione Don Gnocchi, Milan, Italy*

³ *Università Cattolica del Sacro Cuore, Milan, Italy*

Introduction: The typical clinical phenotype of parkin disease (PARK2, OMIM 602544) shows early onset of parkinsonian features, benign clinical course, often dystonia at onset. Multifactorial recording of gait analysis has been already used to investigate gait disturbances in Parkinson Disease (PD) in comparison with normal subjects [1–3]. However, PARK2 differs from idiopathic PD because of early onset, associated dystonia and other motor differences. No information is yet available on gait parameters for PARK2. The aim of the study is to compare gait parameters in parkin disease during the off (OFF) and on-phase (ON) of oral medication with those of healthy age-matched control subjects.

Methods: We performed a group-comparison study in the gait analysis laboratory of our movement disorder unit. Ten PARK2 patients and ten healthy controls (HC) performed 5 walking trials at a self-selected speed. Main outcome measures were spatiotemporal, kinematic, and kinetic gait parameters acquired with an integrated system (SMART-D, BTS bioengineering, Italy). Data collection was performed over two sessions, in the ON and OFF condition. The parameters were computed bilaterally for each participant and the mean and standard deviation values of all indexes were calculated for each group (PARK2-ON, PARK2-OFF and HC). We used the Kruskal–Wallis test to assess the more-affected side for each subject and the Mann–Whitney *U*-test for comparing PARK2-ON/PARK2-OFF and HC. A statistically significant difference was accepted as $p < 0.05$ (STATISTICA 6.0, StatSoft).

Results: The PARK2 group gait spatial and temporal data showed a significant reduction of walking velocity, stride length, increased step width in OFF and ON compared with controls. Cadence was reduced and the duration of gait cycle was increased only in OFF condition. In the kinematics, the main features of the PARK2 group were: at the knee an increased flexion at the initial contact and loading response in OFF and ON, increased ROM in stance and flexion in swing; at hip increased flexion at the initial contact and terminal swing; reduced extension in stance and at toe-off in OFF; at pelvis increased antiversión. Kinetics data showed increased knee and hip

power generation in stance in OFF and ON and reduced ankle power generation and absorption in ON.

Discussion: PARK2 patients have an abnormal gait patterns that partially differs from that of PD, patients. Whereas ROM is usually reduced in all joints in PD, PARK2 patients have increased ROM at the knee and hip in the sagittal plane. There is not a significant typical kinematic pattern at the ankle as seen in PD patients (reduction of plantarflexion at push off, reduction of ROM in stance and swing). These features are likely related to the variability of the dystonic component. Kinetic data show increased power generation at hip in OFF and ON in comparison with controls which is, on the contrary, reduced in PD patients; also increased power generation at knee in OFF and ON and ankle power absorption and generation are reduced in ON like is described in PD patients.

References

- [1] Ferrarin M, Carpinella I, Rabuffetti M, Calabrese E, Mazzoleni P, Nemni R. Locomotor disorders in patients at early stages of Parkinson's disease: a quantitative analysis. *Conf Proc IEEE Eng Med Biol Soc* 2006;1:1224–7.
- [2] Sofuwa O, Nieuwboer A, Desloovere K, Willems AM, Chavret F, Jonkers I. Quantitative gait analysis in Parkinson's disease: comparison with a healthy control group. *Arch Phys Med Rehabil* 2005;86(5):1007–13.
- [3] Morris ME, McGinley J, Huxham F, Collier J, Iansek R. Constraints on the kinetic, kinematic and spatiotemporal parameters of gait in Parkinson's disease. *Hum Mov Sci* 1999;18:461–83.

<http://dx.doi.org/10.1016/j.gaitpost.2012.12.023>

C6

Achilles tendon percutaneous repair with tenolog: Quantitative analysis of postural control and gait pattern

S. Mezzarobba¹, S. Bortolato², A. Giacomazzi¹, R. Valentini², R. Marcovich¹, G. Fancellu²

¹ *Physiotherapy Degree University of Trieste, Italy*

² *Clinica Ortopedica e Traumatologica, Università di Trieste, Cattinara Hospital, Trieste, Italy*

Introduction: Surgical approach in Achilles tendon rupture has involved during the last years becoming safer and less invasive as possible. Lots of studies investigate the outcomes of the minimally-invasive technique with Tenolog proving its good results [1,2], but never in a long-term period. Our study wants to emphasize the effectiveness of this surgical approach exploring the postural and gait patterns in a 24 months follow up.

Materials and methods: We enrolled as volunteers 22 patients (21 male and 1 female) aged 42.81 (± 7.91), with a average body weight of 81.75 \pm 10.61 kg (BMI of 25.31 \pm 2.95), and average height (1.80 \pm 0.05 m), treated with percutaneous technique with Tenolog in the previous two years. In the postoperative period, patients did not undergo to a specific rehabilitation program but only to a specific self training exercises finalized to the gait cycle and postural control where triceps surae muscle has its greatest implication. The clinical sample was compared to a control group of 19 healthy volunteers matched by age (40.31 \pm 6.12), physical constitution (average body weight 77.5 \pm 7.51, BMI 23.4 \pm 1.88, height 1.80 m \pm 2.1), and sport activities. After a clinical examination, we did an instrumental analysis including a measurement on barometric footboard and an optokinetic gait analysis. This study used an experimental scheme, where both limbs of each group were measured and the results were compared between the limbs of the case group (injured and uninjured) and the control group (difference between limbs).

Results: Clinical measures show a significantly increased ROM in ankle's dorsal flexion in the case group ($p = 0.006$). Gait analysis data show no differences with control group in time-distance parameters, despite an altered propulsion phase data, confirmed



Published in final edited form as:

Conf Proc IEEE Eng Med Biol Soc. 2013 July ; 2013: 6341–6344. doi:10.1109/EMBC.2013.6611004.

Classification of Stand-to-Sit and Sit-to-Stand Movement from Low Frequency EEG with Locality Preserving Dimensionality Reduction

Thomas C. Bulea [Member, IEEE],

Functional and Applied Biomechanics Section at the National Institutes of Health, Bethesda, MD 20892 and the University of Houston, Houston, TX 77204. (thomas.bulea@nih.gov)

Saurabh Prasad [Member, IEEE],

University of Houston, Houston, TX 77204

Atila Kilicarslan, and

University of Houston, Houston, TX 77204

Jose L. Contreras-Vidal [Senior Member, IEEE]

University of Houston, Houston, TX 77204

Saurabh Prasad: sprasad2@uh.edu; Atila Kilicarslan: akilica2@uh.edu; Jose L. Contreras-Vidal: jlcontreras-vidal@uh.edu

Abstract

Recent studies have demonstrated decoding of lower extremity limb kinematics from noninvasive electroencephalography (EEG), showing feasibility for development of an EEG-based brain-machine interface (BMI) to restore mobility following paralysis. Here, we present a new technique that preserves the statistical richness of EEG data to classify movement state from time-embedded low frequency EEG signals. We tested this new classifier, using cross-validation procedures, during sit-to-stand and stand-to-sit activity in 10 subjects and found decoding accuracy of greater than 95% on average. These results suggest that this classification technique could be used in a BMI system that, when combined with a robotic exoskeleton, can restore functional movement to individuals with paralysis.

I. Introduction

Electroencephalography (EEG) is a method for imaging brain activity by measuring the electrical activity of pyramidal neurons in the superficial layers of the brain from electrodes placed on the scalp. While EEG recordings possess high temporal resolution, the potentials are a linear combination of many current sources, resulting in poor spatial resolution (volume conduction). Yet, the noninvasive nature of scalp EEG makes it an attractive candidate for use in brain-machine interfaces (BMIs). BMIs have been the subject of intensifying research over the past decade [1–3] and have been deployed in a wide range of applications, including control of computer cursors, powered wheelchairs, and assistive robots. BMIs are incorporated into rehabilitation therapy to either train the central nervous system to produce more normal activity, or to control a device that assists movement thereby producing sensory input that induces plasticity to restore motor control [2]. Finally, BMIs can be used to control prosthetic limbs or powered exoskeletons to restore functional mobility to amputees or individuals with paralysis.

The key component of a BMI for restoration of movement is the algorithm that translates brain signals into useful commands. One approach is to infer limb movement from the recorded neural signals. Many techniques have been investigated for this decoding task [4]

including the Weiner filter, Kalman Filter, unscented Kalman filter, particle filter, artificial neural networks, and finite state approaches. A majority of these studies have applied these techniques to decoding motion of the upper extremity, such as reaching and grasping, from invasive neural recording such as electrocorticographic (ECoG) or local field potentials [5–7], while some studies demonstrate the feasibility of utilizing noninvasive EEG for these purposes in humans [8,9]. Extension of noninvasive neural decoding to the lower extremity offers great potential to BMIs for rehabilitation, since recovery of independent mobility after paralysis can greatly improve quality of life. Recent work has demonstrated the ability to decode lower extremity limb motion from scalp EEG [10,11]. While such decoding is useful for rehabilitation and motor recovery, individuals with paralysis or amputations could benefit from methods that classify the desired action in a more discrete fashion. For example, a BMI for controlling a robotic exoskeleton that restores walking mobility need not decode the exact desired trajectory of the limb; instead, the BMI must only decode the intent of the user (e.g., stand, walk, turn, stop, etc.). Once intent is established, internal controls of the exoskeleton can execute the desired movement.

Here we present a new strategy for EEG classification to infer user action from brain activity during sit-to-stand and stand-to-sit tasks. We employ a locality preserving dimensionality reduction technique coupled with a statistical classifier to determine the current state of the user from offline analysis of scalp EEG recordings.

II. Methods

A. Classifier Algorithm

A Gaussian mixture model (GMM) seeks to represent arbitrary statistical distributions in the feature space via a summation of multiple Gaussian distributions, termed components or modes. The shape of the resulting probability density function depends on the number of mixture components (K), and the mixing weight, mean, and covariance matrix of each component. The determination of K is critical to successful implementation of GMMs for classification. The Bayes information criterion (BIC) has been reported as an effective metric for determining K [12]. Once the value of K has been determined, the other parameters of the GMM can be estimated by the expectation-maximization algorithm [13].

One drawback for use of GMMs is the size of the parameter space that must be learned, which can be calculated as $K^*(1 + d^*(d-1)/2) + K*d$, where d is the dimensionality of the data to be fit. It is common to include 10 lags of past EEG data in the feature matrix for neural decoding [10,11]. To fit a GMM with $K = 10$ components to a feature matrix constructed from 32 channels of EEG requires learning a parameter space of dimension 6.2×10^5 , a task which is often impractical given the limited time and training data available from EEG studies. Many techniques for dimensionality reduction have been evaluated in BMI, with the most popular being genetic algorithm (GA), principal component analysis (PCA) and linear discriminant analysis (LDA) [4]. These methods have shown promising results, however these data reduction techniques have some limitations. In the case of PCA and LDA, the underlying assumption is that class-conditional data are Gaussian. Yet, scalp recorded EEG data represent a mixture of millions of neural inputs. Thus, it is likely that EEG data recorded for the purpose of determining user intent (e.g. sit or stand) will be contaminated by other neural activity. Therefore, we hypothesize that the statistical distribution of a given class will be multimodal, and thus, classifiers such as GMMs are well suited to classify user intent from EEG data. Evidence from prior studies indicates that utilization of a locality preserving dimensionality reduction, such as local Fisher's discriminant analysis (LFDA), improves performance of GMMs compared to traditional data reduction techniques [12]. LFDA combines LDA with a linear manifold learning technique to obtain between-class separation in the reduced dimension projection space

while preserving the within class structure found in the original space. LFDA seeks to find a projection that preserves local neighborhood information, thereby ensuring that the underlying structure of the data distribution is preserved in a lower dimensional subspace. This is accomplished by deploying local between-class and within-class scatter matrices which are scaled by the distance between a given data point and its k_{nn} -nearest neighbor (the value of k_{nn} must be optimized for a given data set). These local scatter matrices are used to define Fisher's ratio. The transformation matrix T_{lfda} , which projects the original data set into the reduced dimensional space, is then found by maximizing a modified form of Fishers ratio as in [12].

B. Experimental Setup and Data Collection

Ten healthy adults (6 male, 4 female) with no history of neurological disease participated in the study after giving informed consent. This study protocol was approved by the Institutional Review Board at the University of Houston. Participants were asked to complete sit-to-stand and stand-to-sit tasks as follows. Participants were asked to stand quietly in an upright posture for 15 seconds. Next, an audio cue (beep) was given at which point the participant transitioned from the standing to a seated posture. The seated posture was held for a period ranging from 3–10 seconds, after which a second audio cue was given to initiate the transition from sit-to-stand. The standing posture was held for 3–10 second interval, at which point the process was repeated until 20 transitions (10 of each) were completed.

Time-locked kinematic, electromyography (EMG), and EEG data were collected simultaneously using a previously developed data collection system [14]. Inertial sensing units (APDM, Inc., Portland, OR) containing triaxial magnetometers, accelerometers, and gyroscopes sampled at 128 Hz were mounted bilaterally on the foot, shank, and thigh, and on the lower back, sternum, and head. Surface EMG (Biometrics, Ltd, Ladysmith, VA) was recorded at 1000 Hz bilaterally from the tibialis anterior, gastrocnemius, biceps femoris, and vastus lateralis. Whole scalp, active electrode, 64-channel EEG (Brain Products, GmbH, Morrisville, NC) were collected at 1000 Hz and labeled by the 10–20 international system.

C. Signal Preprocessing

All data analysis, classifier optimization and evaluation were performed off-line using custom software in Matlab (Mathworks, Natick, MA). Peripheral EEG channels susceptible to eye blinks and facial/cranial muscle activity were removed for offline analysis (all channels labeled Fp, AF, FT, T, TP, O, and P7–8, PO7–10). Time traces of the remaining channels were visually inspected to assure no irregularities were present. EEG signals were decimated to 100 Hz and then band pass filtered with a zero phase, 3rd order Butterworth filter from 0.1–2 Hz. The EEG data were then standardized by channel by subtracting the mean and dividing by the standard deviation. Finally, a time-embedded feature matrix was constructed from 10 lags, corresponding to 100 ms in the past, of EEG data. The embedded time interval was chosen based on previous studies demonstrating accurate decoding of lower extremity kinematics from EEG [10,11]. The feature vector for each time point was constructed by concatenating the 11 lags (the current time point plus the 10 prior) for each channel into a single vector of length $11 \times N$, where N is the number of EEG channels. To avoid the problem of missing data, the feature matrix was constructed starting at the 11th EEG sample of the trial.

EEG data are used to classify the current motor activity of the participant into one of three classes: quiet, stand-to-sit, or sit-to-stand. The true state of the participant was assessed from the linear envelope of the lower extremity EMG. To attain the envelope the EMG data was detrended, band pass filtered (15 – 300 Hz), rectified, and low pass filtered (3 Hz). A simple

threshold detection algorithm identified the class as 0 (quiet), 1 (stand-to-sit), or 2 (sit-to-stand) based on the linear envelope. Classes 1 and 2 were identified as time periods when the linear envelope value exceeded three standard deviations from the mean of the quiet phase value.

D. Classifier Optimization

The parameters of the LFDA-GMM classifier (k_{nn} and the dimensionality of the projected subspace (r)) were optimized for each subject using a set of training and testing data randomly selected from each class. This optimization was performed using a grid search technique while varying the values of k_{nn} and r from 1–99 and 1–100, respectively. Mutually exclusive training and testing data sets for optimization were randomly selected from each class. For the optimization, the number of samples selected from each class was equal for both training and testing (50% of the least populated class). The LFDA-GMM classifier was then trained and tested at all points of the parameter space for k_{nn} and r . The optimal parameter set for each subject was selected as the one that produced the highest overall accuracy from the testing data set.

D. Classifier Performance

The performance of the LFDA-GMM classifier with the optimal parameter set was analyzed for each subject by randomly selecting a subset of data points to serve as the training set. The number of samples in the training subset was equal to 20% of the least populated class. After training, the LFDA-GMM classifier was then tested on all data remaining in the set for that given subject. To avoid training bias, the experiment was repeated 20 times and the accuracy reported is the average classification accuracy. We also investigated the effect of the size of the training data set by varying the size of the training set between 10%–90% of the least populated class.

III. Results

A representative optimization surface of overall classifier accuracy as a function of parameters k_{nn} and r is given in Fig. 1. The contour was similar for all subjects. Accuracy plateaus at moderate r values (~15–40). In some subjects, accuracy remained nearly constant for increasing values of r while in other cases accuracy dipped slightly as r increased beyond 40. Generally, the value of k_{nn} had little impact on accuracy beyond a peak at ~11. The optimized LFDA-GMM parameters for each subject are given in Table I. The number of components (K), estimated from BIC, demonstrate that stand-to-sit (class 1) and sit-to-stand (class 2) distributions are multi-modal for at least half of the participants.

Fig. 2 shows the average classification accuracy with the optimal parameter set for each subject. The mean accuracy across the ten subjects was $95.2 \pm 1.3\%$. Fig. 3 shows a representative example of the LFDA-GMM classifier performance for 65 seconds of the sit-to-stand and stand-to-sit experimental protocol, including the true class, predicted class, and EMG envelope of the left vastus lateralis.

IV. Discussion

Previous studies have shown promising results for decoding of lower extremity kinematics during walking activity [10,11]. These studies and others from upper extremity [6–9] demonstrate that critical information pertaining to limb motion can be extracted from smooth amplitude modulated brain waves in the delta band (0.1 – 4 Hz). Collectively, these studies show that limb motion can be reconstructed from EEG. Such reconstruction could be used as a control signal for a noninvasive BMI for restoration of movement. However, we

postulate that state-based EEG classifiers, serving as a BMI with a robotic exoskeleton or other assistive device, can provide functional recovery of movement to impaired individuals. This study shows that time-domain EEG signals from the lower delta band can be effectively used to classify movement state in healthy individuals with a very high level of accuracy, providing impetus for its use in a BMI.

Our underlying hypothesis for this study was that because spatially coarse EEG signals are combinations of many neural sources, the within-class statistical distribution of data can be multi-modal, and thus a classification scheme that can handle such non-Gaussian distributions will accurately classify the movement state. The results presented support this hypothesis. Optimization of classifier parameters for each subject is critical. For every subject peak accuracy was attained in a reduced dimensional space of less than 25% of the original, indicating LFDA was able to significantly reduce dimensionality while preserving the statistical features necessary for accurate classification. Furthermore, the GMMs for the stand-to-sit (class 1) and sit-to-stand (class 2) classes contain more than one mixture component for over half the subjects, supporting our assumption of multi-modal within class data.

In a similar manner as previous studies [15], we introduced a control group during classifier optimization to strengthen our conclusion regarding classification accuracy. The control group was created by randomly shuffling original EEG data within each channel for each subject. The highest overall accuracy for LFDA-GMM optimization was significantly higher for original EEG than control ($p < 10^{-6}$). Across subjects, the maximum accuracy during optimization for the control EEG was $35.5 \pm 5.8\%$, which does not compare favorably to chance value of 33%.

We also found that training set size had little impact on classifier performance. Even when trained using a set of length equal to 10% of the least populated class (comprising approximately 2% of the total data set), mean accuracy was $88.7 \pm 6.4\%$ across subjects. The length of the 10% training set was $7.8N$ on average, where N is the size of the original feature space (number of EEG channels). This finding agrees with previous studies of LFDA-GMM classifiers that found similar accuracy levels at the same training abundance [12]. Furthermore, these high accuracies with relatively low number of training samples demonstrate robustness of the LFDA-GMM classifier to EEG artifacts since the training data are taken randomly in time from each class.

In this study, LFDA-GMM demonstrated high accuracy for prediction of current motor state during one experimental session. For real time application, within-class statistical data distribution can be expected to vary between sessions, and thus the classifier may need to be optimized before each use. Despite feature reduction by LFDA, the optimal parameter set (Table I) can still result in a relatively large learning space for the GMMs as described in section II. This is a potential hindrance for real-time deployment of this classifier. However, careful examination of subject specific surfaces like the one in Fig. 2 shows that gains in accuracy level-off at values of approximately 20 and 11 for r and k_{nn} , respectively, with only small gains in accuracy for parameters exceeding these levels. These results suggest online application of the LFDA-GMM classifier to be reasonable. Future work will focus on its implementation in combination with a robotic exoskeleton [16].

Acknowledgments

This work was supported by the National Institute of Neurological Disorders and Stroke (NINDS) grant # R01NS075889-01.

References

1. Daly JJ, Wolpaw JR. Brain-computer interfaces in neurological rehabilitation. *Lancet Neurol.* 2008; vol. 7(no. 11):1032–1043. [PubMed: 18835541]
2. Gramann K, Gwin JT, et al. Cognition in action: imaging brain/body dynamics in mobile humans. *Rev. Neurosci.* 2011; vol. 22(no. 6):593–608. [PubMed: 22070621]
3. Lebedev MA, Tate AJ, et al. Future developments in brain-machine interface research. *Clinics.* 2011; vol. 66(no. S1):25–32. [PubMed: 21779720]
4. Bashashati A, Fatourehchi M, et al. A survey of signal processing algorithms in brain-computer interfaces based on electrical brain signals. *J. Neural. Eng.* 2007; vol. 4(no. 2):R32–R57. [PubMed: 17409474]
5. Carmena JM, Lebedev MA, et al. Learning to control a brain-machine interface for reaching and grasping by primates. *PLoS Biol.* 2003; vol. 1(no. 2):e42. [PubMed: 14624244]
6. Acharya S, Fifer MS, et al. Electrocorticographic amplitude predicts finger positions during slow grasping motions of the hand. *J Neural. Eng.* 2010; vol. 7(no. 4):046002. [PubMed: 20489239]
7. Ince NF, Gupta R, et al. High accuracy decoding of movement target direction in non-human primates based on common spatial patterns of local field potentials. *PLoS One.* 2010; vol. 5(no. 12):e14384. [PubMed: 21200434]
8. Bradberry TJ, Gentili RJ, Contreras-Vidal JL. Reconstructing three-dimensional hand movements from noninvasive electroencephalographic signals. *J. Neurosci.* 2010; vol. 30(no. 9):3432–3437. [PubMed: 20203202]
9. Muralidharan A, Chae J, Taylor DM. Extracting attempted hand movements from EEGs in people with complete hand paralysis following stroke. *Frontiers in NeuroSci.* 2011; vol. 5(no. 39)
10. Presacco A, Goodman R, Forrester L, Contreras-Vidal JL. Neural decoding of treadmill walking from noninvasive electroencephalographic (EEG) signals. *J. Neurophysiol.* 2011; vol. 106:1875–1887. [PubMed: 21768121]
11. Presacco A, Forrester LW, Contreras-Vidal JL. Decoding intra-limb and inter-limb kinematics during treadmill walking from scalp electroencephalographic (EEG) signals. *IEEE Trans. Neur. Sys. Rehab.* 2011; vol. 20(no. 2):212–219.
12. Li W, Prasad S, et al. Locality-preserving dimensionality reduction and classification for hyperspectral image analysis. *IEEE Trans. Geosci. Remote Sens.* 2012; vol. 50(no. 4):1185–1198.
13. Vlassis N, Likas A. A greedy EM algorithm for Gaussian mixture learning. *Neural Proc. Let.* 2002; vol. 15(no. 1):77–87.
14. Bulea TC, Kilicarslan A, Ozdemir R, Paloski WH, Contreras-Vidal JL. Simultaneous electroencephalography (EEG), electromyography (EMG), and whole-body segmental inertial recording for multi-modal neural decoding. *J. Vis. Exp.* in press.
15. Liu J, Perdoni C, He Bin. Hand movement by phase-locking low frequency EEG signals. *Proc. IEEE Eng. Med. Biol. Soc.* 2011:6335–6338.
16. Kilicarslan A, Prasad S, et al. High accuracy decoding of user intentions using EEG to control a lower-body exoskeleton. *Proc. IEEE Eng. Med. Biol. Soc.* 2013 submitted for publication.

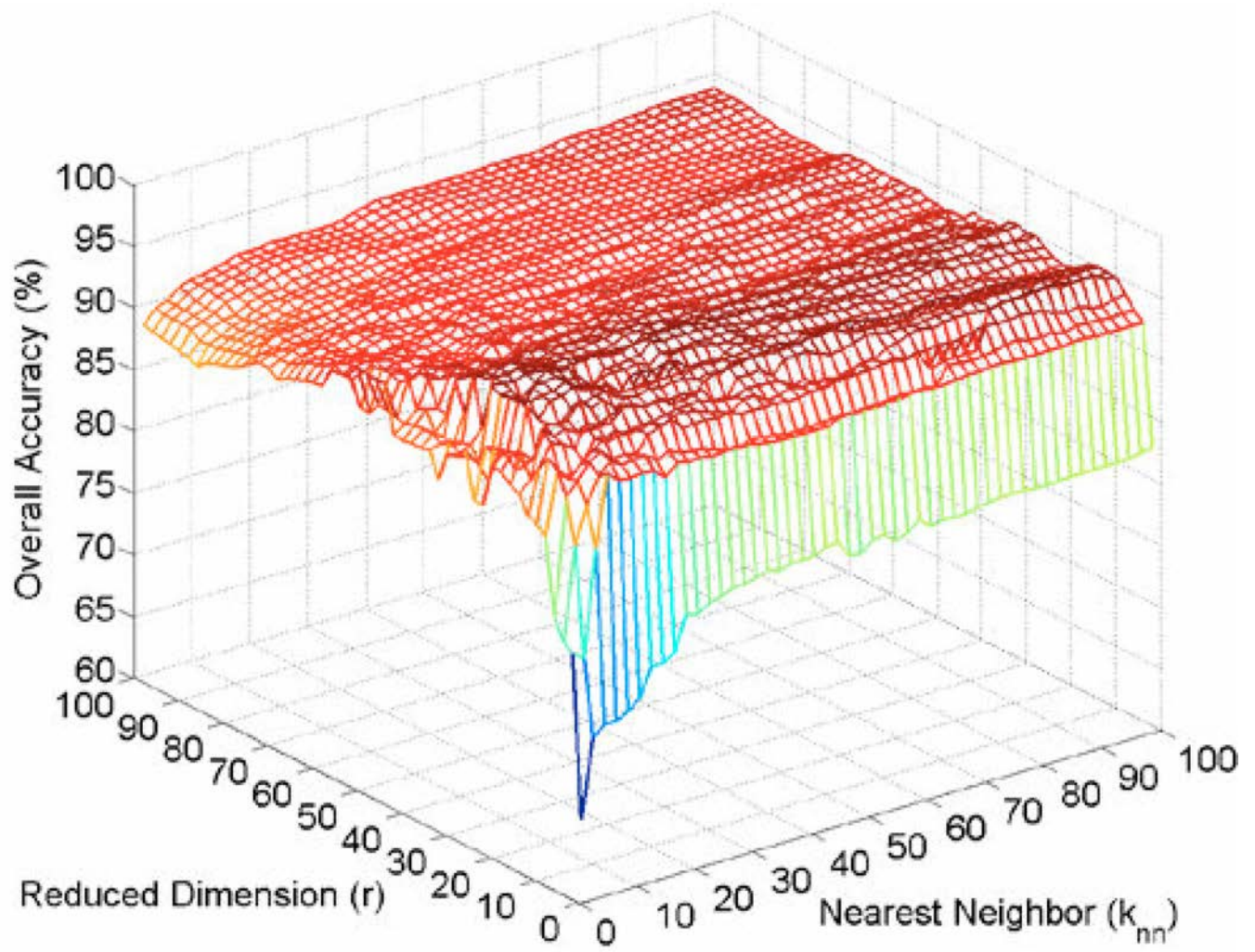


Fig. 1.
A representative example (S5) of overall LFDA-GMM accuracy for optimization of parameters r and k_{nn} .

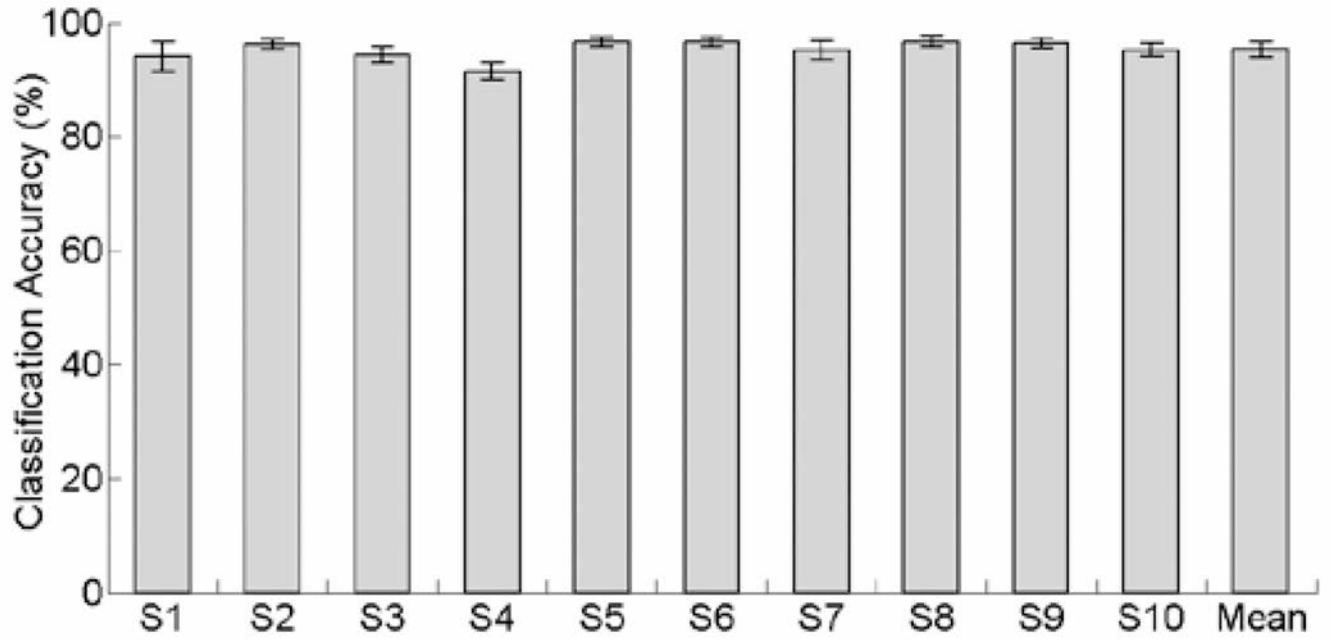


Fig. 2.
Average ($n = 20$) LFDA-GMM classifier accuracy across subjects.

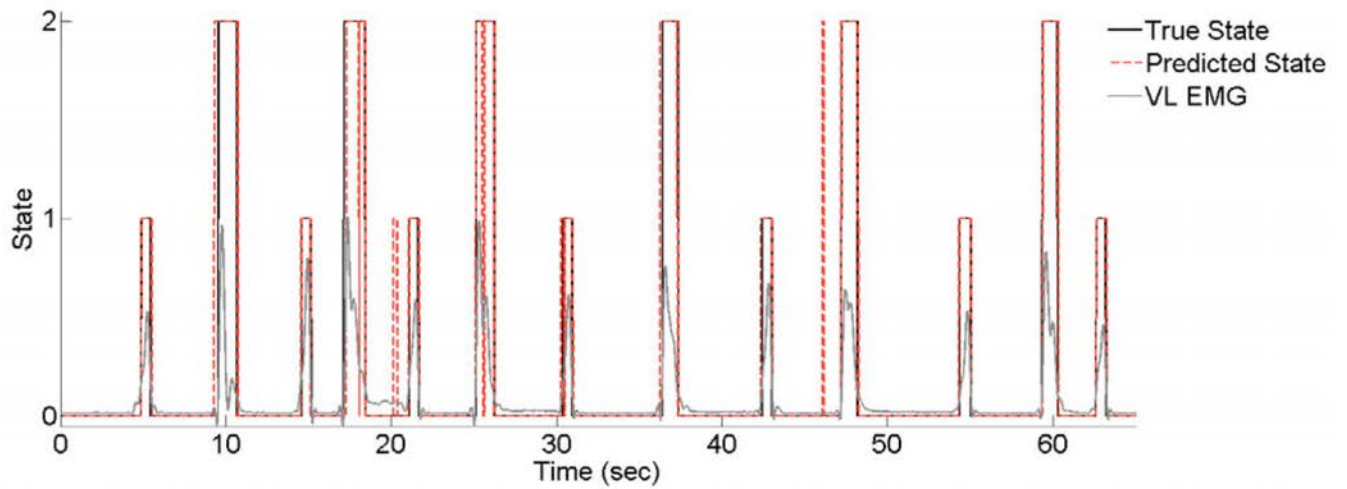


Fig. 3. Representative example of LFDA-GMM classification of user action from EEG: quiet (0), stand-to-sit (1), or sit-to-stand (2). Predicted and true states of the participant are shown with the EMG of left vastus lateralis (VL) as a reference.

Table 1

Optimal Parameters and Number of Mixture Components by Subject

Subject	k_{opt}	Reduced Dimension (r)	Mixture Components (K)		
			Class 0	Class 1	Class 2
S1	41	19	1	2	1
S2	11	21	2	2	2
S3	57	15	1	2	3
S4	97	37	1	1	1
S5	35	25	1	3	7
S6	25	43	1	2	1
S7	33	39	1	1	1
S8	37	71	1	1	3
S9	23	35	1	1	1
S10	29	45	1	1	1

THE ROLE OF MOTION ANALYSIS IN BIOMEDICAL ENGINEERING EDUCATION AND INTERDISCIPLINARY RESEARCH

Stephanie L.Carey, Derek J. Lura, Rajiv V. Dubey

University of South Florida
Department of Mechanical Engineering
Tampa, FL 33612
USA

This is copy is maintained as a self-archive.
Please see below to obtain a copy from the publisher.

<http://proceedings.asmedigitalcollection.asme.org/proceeding.aspx?articleID=1819841>

INTRODUCTION

The purpose of this paper is to summarize current motion analysis techniques and described their role in biomedical engineering education as well as in interdisciplinary research. At the University of South Florida (USF), various methods of motion analysis are used for collaborative research in fields such as prosthetics, robotics, rehabilitation, and injury prevention. The motion analysis laboratory is also used in course work in a variety of fields promoting interdisciplinary exchanges among students and faculty.

MOTION ANALYSIS

Analyzing motion has a long history and has evolved since Eadweard Muybridge captured horse motion in 1878 using multiple cameras. There are currently many techniques for studying motion including image based analysis, active and passive marker systems, inertial measurement units (IMU), as well as two and three dimensional type systems. The motion analysis laboratory that is part of the University of South Florida's Center for Assistive, Rehabilitation and Robotics Technologies has several modes of motion capture and analysis capabilities.

Video based optical motion analysis systems have recently been used to study athletes[1], to compare gait in patients with anterior cruciate ligaments problems [2] and squat performance of physical therapists[3]. The main motion analysis system at USF consists of an 8 camera Vicon optical passive marker based system. These cameras offer high speed (up to 690 Hz.), high resolution (2 megapixel) and accuracy (0.5 mm). Each camera has powerful infrared strobe lights that allows for smaller markers to be identified over a large capture volume. Passive reflective markers are placed on landmarks to capture movement data (Figure 1). The USF motion



Figure 1. Reflective markers

analysis laboratory also has two force platforms (AMTI, Watertown, MA) and a 6 degree of freedom ATI (Apex, NC) force transducer that can be integrated with the Vicon system to collect and analyze kinetic data.

IMUs another popular method of motion analysis have recently been used to study baseball pitches[4] and fall risks[5]. The motion analysis laboratory at USF also has 6 IMUs (Opal sensors, APDM, Inc. Portland, OR) that each include a triaxial accelerometer, gyroscope, and magnetometer. A watch-like size, a 22 g weight, a battery life of 16 hours, and 16 GB of on-board storage enable these Opal sensors to provide wearable, unobtrusive sensing. For real-time data access, a wireless access point can connect up to eight sensors with a computer for integrated data collection.

The Microsoft Kinect for Windows (Microsoft, Redmond, WA) can also be used as a motion capture system. The Kinect device includes a standard RGB camera, a multi-array microphone, and a depth sensor. It captures 30 frames per second at a distance of 0.8 to 4 meters in front of the camera.

EDUCATION

The motion analysis laboratory is used as an educational tool across disciplines at USF. Students that experience the laboratory learn that the various methods of data collection and analysis differ and part of the process is to determine which technique is appropriate for which application. As part of the physical therapy doctoral program, in the Movement Science III course, students learn about analyzing movement in a "hands on" setting in the motion analysis laboratory. Students study gait deviations, sports injuries, exercises (Fig. 2), injury prevention techniques and various rehabilitation methods. Engineering students work together with physical therapy students to collect and analyze data while comparing it to current literature.

The Human Factors, an industrial engineering required course, first learns about motion capture through lectures, and then also spends time in the laboratory experiencing data collection and analysis to help with human factors based design projects.

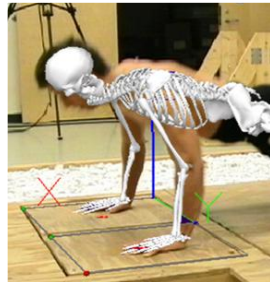


Figure 2. Analysis of a push up

The students from the Dance Kinesiology course, from the College of the Arts are also exposed to the motion analysis laboratory.

Various dance movements are collected and analyzed and the students learn about injury prevention and how motion analysis can be used to study rehabilitation programs. This also allows engineering students and performing artists to interact and learn from each other.

The motion analysis laboratory is also used for outreach purposes by exposing K-12 students to this movement technology. The authors often take the wearable sensors and Kinect to schools around the community demonstrating the purpose of motion analysis. The various methods of motion capture are presented in hands on exhibits at the Engineering Expo on campus, a free event that educates K-12 students on the importance of math, science, engineering and technology. The "Minds for Design" week long summer day camp for girls in Grades 6-12 sponsored by the Girl Scouts of West Central Florida also incorporates the technology of the motion analysis laboratory. Members of the laboratory also work with the Museum of Science and Industry to promote science education and help develop interactive exhibits.

INTERDISCIPLINARY RESEARCH

The motion analysis laboratory at USF provides a creative center for researchers from multiple disciplines to develop projects. Recent projects have allowed biomedical and mechanical engineers to collaborate with computer scientists, physical therapists, musicians, dancers, and psychologists. Having a laboratory with several options for motion capture allows for many different research opportunities.

In collaboration with the School of Physical Therapy, the gait, sit to stand motions, and upper limb activities of daily living of persons using a prosthesis have been studied [6-8]. A robotic human body model (RHBM) to predict human upper motion and compensatory motion of prosthetic users has been developed with the collaboration of biomedical, mechanical and electrical engineers, computer scientists, physical therapists, prothetists and amputees as well as movement data collected and analyzed in the laboratory [9]. The kinematics of instrumentalists before and after an intervention program have also been analyzed at USF's motion analysis lab [10].

Recently in the motion analysis lab, data were collected from a biomorphic quadrupedic robot to determine the optimal control algorithms. Motion data were collected on board a modified Boeing 727 (Zero-G) during parabolic arcs creating a weightless environment using a Microsoft Kinect. During the flight, a task sequence was completed for 1 parabola representing Martian gravity, 2 parabolas representing lunar gravity and 23 parabolas in zero gravity. A project looking at the practice techniques of dancers in order to prevent injury is currently under way (Figure 3). A testing protocol for the analysis of softball pitching in the typical outdoor game setting is in development. Marker placements to compare tortoise movement to

the motion of a new robot are being researched.

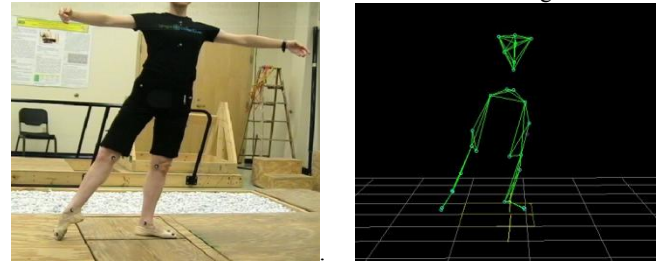


Figure 3. Dance movements

CONCLUSION

Motion analysis technologies are important educational and research tools for biomedical engineers as well as other professionals. The many methods of motion analysis at USF's laboratory have been used to enrich coursework on campus, encourage K-12 STEM learning, and for development of interdisciplinary research projects. We plan to add electromyography and virtual reality components to the lab in the near future. The laboratory also encourages collaboration between different levels of students and professionals as well as communication across disciplines allowing for creative innovation. The people of USF motion laboratory continue to work on campus, around the community and across the country to further develop the role of motion analysis in biomedical engineering education and interdisciplinary research.

REFERENCES

- [1] D. Whiteside, B. Elliott, B. Lay, and M. Reid, "The Effect of Age on Discrete Kinematics of the Elite Female Tennis Serve," *Journal of applied biomechanics*, Dec 27 2012.
- [2] K. Zuka-Nowak, K. Ogrodzka, W. Chwala, L. Niedzwiedzki, and T. Niedzwiedzki, "Kinetic and kinematic characteristics of natural velocity gait in anterior cruciate ligament-deficient patients," *International Journal of Rehabilitation Research*. Dec 12 2012.
- [3] B. K. Weeks, C. P. Carty, and S. A. Horan, "Kinematic predictors of single-leg squat performance: a comparison of experienced physiotherapists and student physiotherapists," *BMC musculoskeletal disorders*, vol. 13, p. 207, 2012.
- [4] R. S. McGinnis and N. C. Perkins, "A highly miniaturized, wireless inertial measurement unit for characterizing the dynamics of pitched baseballs and softballs," *Sensors*, vol. 12, pp. 11933-45, 2012.
- [5] J. Liu, X. Zhang, and T. Lockhart, "Fall risk assessments based on postural and dynamic stability using inertial measurement unit," *Saf Health Work*, vol. 3, p. 7, Sept 2012 2012.
- [6] S. L. Carey, M. J. Highsmith, M. E. Maitland, and R. V. Dubey, "Compensatory movements of transradial prosthesis users during common tasks," *Clin Biomech (Bristol, Avon)*, vol. 23, pp. 1128-35, Nov 2008.
- [7] S. L. Carey, R. V. Dubey, G. S. Bauer, and M. J. Highsmith, "Kinematic comparison of myoelectric and body powered prostheses while performing common activities," *Prosthet Orthot Int*, vol. 33, pp. 179-86, Jun 2009.
- [8] M. J. Highsmith, J. T. Kahle, S. L. Carey, D. J. Lura, R. V. Dubey, K. R. Csavina, and W. S. Quillen, "Kinetic asymmetry in transfemoral amputees while performing sit to stand and stand to sit movements," *Gait & Posture*, vol. 34, pp. 86-91, May 2011.
- [9] D. J. Lura, S. L. Carey, M. J. Highsmith, and R. V. Dubey, "Robotic model for simulating upper body movement," presented at the IEEE International Conference on Robotics and Biomimetics, Bangkok, Thailand, 2009.
- [10] S. H. Lee, S. Carey, R. Dubey, and R. Matz, "Intervention program in college instrumental musicians, with kinematics analysis of cello and flute playing: a combined program of yogic breathing and muscle strengthening-flexibility exercises," *Medical problems of performing artists*, vol. 27, pp. 85-94, Jun 2012.



ISB 2013
BRAZIL

XXIV CONGRESS OF THE INTERNATIONAL
SOCIETY OF BIOMECHANICS

XV BRAZILIAN CONGRESS
OF BIOMECHANICS

THREE-DIMENSIONAL KINEMATIC ANALYSIS OF SHOULDER THROUGH WEARABLE INERTIAL AND MAGNETIC SENSORS DURING SWIMMING STROKES SIMULATION

¹Fabrizio Anício Magalhães, ²Andrea Giovanardi, ²Matteo Cortesi, ²Giorgio Gatta and ^{1,2}Silvia Fantozzi

¹Department of Electrical, Electronic and Information Engineering, University of Bologna, Bologna, Italy;

²School of Pharmacy, Biotechnology, and Sport Science, University of Bologna, Bologna, Italy

Corresponding e-mail: fanicio@me.com

SUMMARY

Wearable inertial and magnetic measurement units (IMMUs) have recently gained much attention in investigations approaching human kinematic analysis in sports scenario. Running, tennis, baseball, snowboarding, rowing, and swimming are some examples of sports already approached. In swimming, many studies proposed several methods to identify the temporal phases of a single swimming stroke or the swimming style. However, this temporal information alone does not provide any joint kinematic data like joint angles. Therefore, the present study aimed to verify the accuracy of a protocol, previously developed for ambulatory joint kinematic analysis through IMMUs, in measure the shoulder kinematics during swimming strokes simulation. A stereo-photogrammetric system was considered the gold standard. Three trained swimmers realized 3 trials of breaststrokes simulation and 3 trials of front-crawl strokes simulation in dry condition. As first verification, the relative motion of both the segments thorax and arm with respect to the first-synchronized frame (automatically detected by an ad-hoc algorithm) was compared by means of root mean square error (RMSE) and correlation coefficient (r) between the two systems. The RMSE was 5° and 7° , and the r was 0.85 and 0.91 for breaststroke and front-crawl stroke, respectively, indicating a good relationship between both methods in measuring the body segments' orientation. As second verification, the shoulder flexion/extension, abduction/adduction and internal/external rotation angles were computed, and no significant difference was found ($p < 0.05$) between both systems. In conclusion, a protocol previously implemented for joint measurement in ambulatory settings is also suitable and accurate to estimate the shoulder kinematics during swimming strokes simulation when using wearable inertial and magnetic measurement units.

INTRODUCTION

The use of technology in swimming played an important role in acquiring reliable performance data to provide greater understanding of the swimming biomechanics and enable swimmers to perform to their highest potential.

Recently, several authors examined the difference of movement patterns and the evaluation of the athlete's technique using sensors composed by accelerometers, gyroscopes and magnetometers, also known as IMMUs, covering a large range of disciplines, including: ambulatory measurements, physical activity, gait analysis, and improvement of the athlete's performance [1]. Thus, the use of IMMUs has been presented as a useful tool for monitoring human movement kinematics.

In swimming, wearable IMMUs were used to measure several variables regarding athletes' performance including lap time, stroke identification, stroke count, stroke rate, stroke length, wall push off, forward speed, swimmer's proficiency, energy expenditure, and swimming velocity [2, 3]. However, to the knowledge of the present authors, no previous investigation performed a three-dimensional kinematic analysis of the shoulder joint, that is, by far, the most demanded joint during swimming [4]. As a consequence, investigations approaching the shoulder kinematics analysis can aid coaches and therapists in identifying risk factors for injuries as well as in planning injuries prevention programs. Therefore, the aim of this study was to verify the suitability and accuracy of a protocol previously developed for the shoulder joint kinematic analysis through IMMUs in ambulatory settings in measure the shoulder joint kinematics during swimming.

METHODS

The protocol implemented was described and validated by Cutti and co-workers [5]. Whereas the protocol was developed to measure the upper-limbs kinematics in ambulatory settings, the present work proposes to verify its applicability also in swimming.

From a biomechanical point of view, the shoulder joint was modeled as an open kinematic chain composed by 2 rigid segments (thorax and arm), with 3 degrees of freedom. Two clusters composed of one IMMU and four retro-reflective passive markers fixed on a wooden plate (15x15x1cm) were used, one placed on the right arm and the other on the thorax. Basically the protocol consisted in positioning the clusters on the body segments and in calculating joint angles according to the appropriate Euler's conventions.

The evaluation of the IMMUs' estimation of the orientation was performed during swimming strokes simulation on a bench in dry condition. A wireless IMMUs system (APDM, Opal, USA, 2 nodes, 128Hz) and a stereo-photogrammetric system (BTS Smart DX, Italy, 8 cameras, 200Hz) recorded the trials. Data from both systems were posteriorly synchronized and resampled at the IMMUs' frequency rate. Three trained swimmers were laid facing down on a bench and their lower-limbs were held tight by a person. Each subject performed 2 trials (one breaststroke and one front-crawl stroke) during 10s, trying to simulate the movements in the swimming pool. The relative motion of the segments thorax and arm with respect to the first-synchronized frame was compared by means of root mean square error (RMSE) and correlation coefficient (r) between the two methods.

RESULTS AND DISCUSSION

The goal of the present study was to verify the accuracy of a protocol previously developed for ambulatory joint kinematic analysis through IMMUs in measure the shoulder kinematics during swimming strokes simulation in comparison with a gold standard system. The results of the first verification are presented in table 1.

Table 1: Root mean square error and correlation coefficient for both measurement systems.

	Breaststroke		Front-Crawl	
	RMSE (°)	r	RMSE (°)	r
Mean	5	0,85	7	0.91
Minimum	3	0.76	5	0.82
Maximum	8	0,97	10	0.97

The mean RMSE was 5° and 7° for the breaststroke trials and for the front-crawl stroke trials, respectively, in accordance with other investigations that performed human joint angle measurement. In addition, the mean r was 0.85 for the breaststroke trials and 0.91 for the front-crawl stroke trials indicating a good relationship between both systems in estimating the body segments' orientation with respect to the first frame.

Figure 1 shows the three shoulder angles for one subject's trial representative of all trials. Five strokes normalized by

its percentage of the duration were plotted overlapped. No significant difference was found ($p < 0.05$) between both systems in the estimation of the shoulder flexion/extension, abduction/adduction and internal/external rotation angles. Nonetheless, these values are comparable to the three-dimensional joint kinematics estimated using underwater kinematics video analysis [6].

For our analysis, only the shoulder was considered because it is the most demanded joint during swimming. Further investigations in other joints such as elbow, wrist, hip, knee and ankle can be addressed in order to get a full body kinematic analysis during swimming.

In this work we intended to perform shoulder kinematic analysis in dry condition because the protocol proposed by Cutti and co-workers [5] was implemented in an ambulatory environment. The dry condition has two main advantages: 1) the stereo-photogrammetric system is more accurate with respect to the underwater one, and 2) the whole swimming stroke cycle can be analyzed: the aerial phase (recovery) as well as the "underwater" phases. Finally, the joint kinematic analysis in real condition (i.e. underwater) during swimming will be aimed in the next future.

CONCLUSIONS

The protocol implemented previously for joint measurement in ambulatory settings is also suitable and accurate to estimate the shoulder kinematics during swimming strokes simulation using wearable inertial and magnetic measurement units.

REFERENCES

1. Callaway, A.J. et al., *International Journal of Sports Science & Coaching*. **4**(1):139-153, 2009.
2. Dadashi, F., et al., *Sensors*. **12**(10):12927-12939, 2012.
3. Ohgi, Y. *Proceedings of IEEE on Sensors*, 2002.
4. Heinlein, S.A. and Cosgarea, A.J. *Sports Health*, **2**(6):519-525, 2010.
5. Cutti, A.G., et al., *Medical & Biological Engineering & Computing*. **46**(2):169-178, 2008.
6. Cecon, S. et al., *Journal of Sports Science*. 1-12, 2012.

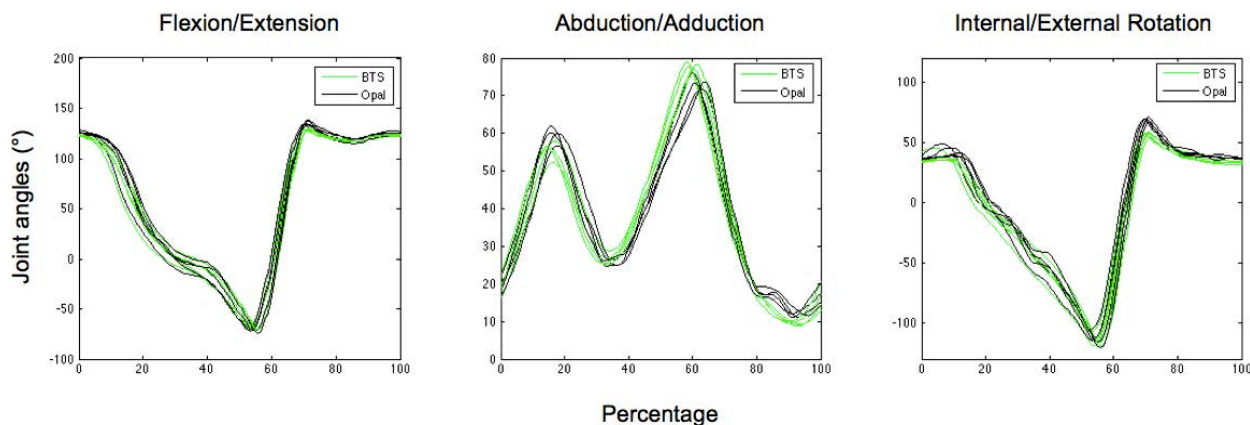


Figure 1: Shoulder flexion/extension, abduction/adduction and internal/external rotation. Lines green for the stereo-photogrammetric system (BTS) and lines black for the inertial and magnetic measurement units (Opal).

January 2013

A Wearable Motion Analysis System to Evaluate Gait Deviations

Amanda Lynn Martori

University of South Florida, martori@mail.usf.edu

Follow this and additional works at: <http://scholarcommons.usf.edu/etd>



Part of the [Mechanical Engineering Commons](#)

Scholar Commons Citation

Martori, Amanda Lynn, "A Wearable Motion Analysis System to Evaluate Gait Deviations" (2013). *Graduate Theses and Dissertations*. <http://scholarcommons.usf.edu/etd/4724>

This Thesis is brought to you for free and open access by the Graduate School at Scholar Commons. It has been accepted for inclusion in Graduate Theses and Dissertations by an authorized administrator of Scholar Commons. For more information, please contact scholarcommons@usf.edu.

A Wearable Motion Analysis System to Evaluate Gait Deviations

by

Amanda Lynn Martori

A thesis submitted in partial fulfillment
of the requirements for the degree of
Master of Science in Mechanical Engineering
Department of Mechanical Engineering
College of Engineering
University of South Florida

Major Professor: Stephanie L. Carey, Ph.D.
Rajiv Dubey, Ph.D.
Kevin Hufford, M.S.

Date of Approval:
July 3, 2013

Keywords: IMU, APDM, Sensors, Knee Angle, Quaternion

Copyright © 2013, Amanda Lynn Martori

DEDICATION

I would like to dedicate this thesis to my parents, Sam and Debbie, my brother Scotty and my cousin Debra Marrano-Lucas.

ACKNOWLEDGMENTS

I would like to thank my advisor Stephanie Carey, as well as my committee members Rajiv Dubey and Kevin Hufford for their support and guidance. I would also like to thank all the members of the Rehabilitation Robotics and Prosthetics Testbed (RRT) for their participation in the study, as well as their help with many aspects of this project.

I would also like to thank my family for their continuous encouragement and support throughout this whole process. Without their constant love I would not have been able to complete this thesis. Mom, Dad, Scotty and Debbie, you guys were a major part of this accomplishment.

TABLE OF CONTENTS

LIST OF TABLES	iv
LIST OF FIGURES	v
ABSTRACT	viii
CHAPTER 1: INTRODUCTION	1
CHAPTER 2: BACKGROUND	4
2.1 Gait.....	4
2.2 Traumatic Brain Injury	4
2.2.1 Mild Traumatic Brain Injury.....	5
2.2.2 Prevalence and Statistics of TBI and mTBI.....	5
2.2.3 Effect on Gait and Balance	6
2.2.4 Current Diagnostics	8
2.2.5 What’s Missing in TBI Research/Diagnosis?	9
2.3 Gait Analysis Methods.....	9
2.3.1 Optical System	10
2.3.2 Inertial Measurement Unit	10
2.3.2.1 Previous Work	10
CHAPTER 3: METHODS	18
3.1 WMAS Testing.....	18
3.1.1 Institutional Review Board Approval	18
3.1.2 Participants.....	18
3.1.3 WMAS Instrumentation.....	19
3.1.3.1 Sensor Locations.....	21
3.1.4 Vicon Instrumentation	21
3.1.4.1 Reflective Marker Locations.....	22
3.1.4.2 Subject Measurements	23
3.1.4.3 Camera Calibration	23
3.1.5 Testing Protocol.....	25
3.1.5.1 WMAS	25
3.1.5.2 Vicon Motion Analysis System	26
3.1.5.3 Timed Up and Go Test.....	27
3.2 Verification Testing	27

3.2.1 Movement Analysis Using a Programmed Robotic Motion.....	28
3.2.1.1 Instrumentation	29
3.2.1.2 Testing Protocol	31
3.2.1.3 Data Analysis	32
3.2.2 Range of Motion	34
3.2.3 Sit to Stand.....	35
CHAPTER 4: DATA ANALYSIS	36
4.1 WMAS	36
4.1.1 Knee Angle	36
4.1.2 Stride Length.....	37
4.1.3 Cadence.....	39
4.1.4 Graphical User Interface Development	39
4.2 Vicon.....	40
4.2.1 Visual 3D Model.....	40
4.2.2 Visual 3D Pipeline	40
4.3 Statistics	41
CHAPTER 5: RESULTS.....	43
5.1 Verification Tests.....	43
5.1.1 Movement Analysis Using a Robotic Motion	43
5.1.2 Range of Motion Tests.....	57
5.1.3 Sit to Stand Tests	59
5.2 WMAS	60
5.2.1 Knee Angle	61
5.2.2 Stride Length.....	66
5.2.3 Cadence.....	68
5.2.4 Graphical User Interface	69
CHAPTER 6: DISCUSSION.....	70
6.1 Verification Tests.....	70
6.2 Comparison Between Vicon and WMAS	73
6.3 Comparison Between WMAS and Previous Work.....	76
6.4 Graphical User Interface	78
6.5 Limitations of this Research	79
6.6 Applications of WMAS	79
CHAPTER 7: CONCLUSION	80
CHAPTER 8: FUTURE WORK	81
8.1 Use with mTBI and TBI Subjects.....	81
8.2 Robotic Arm.....	81
8.3 Testing Outside of Laboratory	81
8.4 CAREN.....	82
8.5 Sports Concussion.....	82
REFERENCES	84

APPENDICES	91
Appendix A: WMAS Data Collection Checklist.....	92
Appendix B: Instructions for WMAS Data Collection.....	93
B.1 APDM Instructions	93
B.2 Vicon Set Up	94
B.3 APDM Sensors Data Collection Steps.....	95
B.4 Vicon Data Collection Steps	95
Appendix C: Visual 3D Pipeline.....	96
C.1 Joint Angle Calculations	96
C.2 Stride Length Calculations.....	97
Appendix D: IRB Approval.....	102

LIST OF TABLES

Table 1 Subject Information	19
Table 2 Plug-In Gait Marker Set.....	22
Table 3 Subject Measurements Required for Plug-In Gait.....	23
Table 4 RMSE Between Vicon and APDM Sensors	51
Table 5 RMSE for 3 Methods of Knee Angle Calculation.....	53
Table 6 Angular Velocity.....	53
Table 7 RMSE and R Values for 3D Motion Trials 1 & 2	57
Table 8 RMSE and R Values For Range of Motion Tests.....	58
Table 9 RMSE and R Values For Sit To Stand Testing	60
Table 10 RMSE and R Values For Knee Flexion Angle	63
Table 11 RMSE For Maximum Knee Flexion.....	63
Table 12 Average Stride Length	66
Table 13 Stride Length Statistics	66
Table 14 Average Cadence	68

LIST OF FIGURES

Figure 1 Abnormalities That Occur During the Gait of a Person with a TBI.....	7
Figure 2 APDM Instrumentation Setup	20
Figure 3 Sensor Locations	21
Figure 4 Vicon Calibration L-Frame and Wand.....	24
Figure 5 Vicon Static Trial T-Pose.....	24
Figure 6 Motion Studio Screen During Streaming Prior to Data Collection.....	26
Figure 7 Wheelchair Mounted Robot Arm (WMRA).....	29
Figure 8 Locations of IMUs on WMRA.....	30
Figure 9 Reflective Markers and IMUs on WMRA	31
Figure 10 Range of Motion Tests	34
Figure 11 Sit to Stand Test.....	35
Figure 12 Shank Angular Velocity & Toe-Off (Rectangle) and Heel-Strike (Circle) Events.....	37
Figure 13 Parameters for Stride Length Calculation	38
Figure 14 V3D Model.....	40
Figure 15 Joint 1 Hip Flexion A	43
Figure 16 Joint 1 Hip Flexion B	44
Figure 17 Joint 1 Hip Flexion C	44
Figure 18 Joint 1 Hip Extension A	45

Figure 19 Joint 1 Hip Extension B.....	45
Figure 20 Joint 1 Hip Extension C.....	46
Figure 21 Joint 3 Hip Internal Rotation A	46
Figure 22 Joint 3 Hip Internal Rotation B	47
Figure 23 Joint 3 Hip External Rotation A	47
Figure 24 Joint 3 Hip External Rotation B	48
Figure 25 Joint 4 Knee Flexion A.....	48
Figure 26 Joint 4 Knee Flexion B.....	49
Figure 27 Joint 4 Knee Flexion C.....	49
Figure 28 Joint 4 Knee Extension A.....	50
Figure 29 Joint 4 Knee Extension B.....	50
Figure 30 Joint 4 Knee Extension C	51
Figure 31 Comparison Between Algorithm and Sensor On Joint 4.....	52
Figure 32 Joint 1 3D Motion 1.....	54
Figure 33 Joint 1 3D Motion 2.....	54
Figure 34 Joint 3 3D Motion 1.....	55
Figure 35 Joint 3 3D Motion 2.....	55
Figure 36 Joint 4 3D Motion 1.....	56
Figure 37 Joint 4 3D Motion 2.....	56
Figure 38 Range of Motion Test.....	57
Figure 39 Left Knee Angle Range of Motion WMAS and Vicon.....	58
Figure 40 Sit To Stand Test in Vicon Workstation.....	59
Figure 41 Right Knee Angle During Sit To Stand.....	60

Figure 42 Right Knee Flexion Angle During One Slow Gait Cycle	61
Figure 43 Right Knee Flexion Angle During One Normal Gait Cycle	62
Figure 44 Right Knee Flexion Angle During One Fast Gait Cycle.....	62
Figure 45 Bland Altman Plot: Maximum Knee Flexion During Slow Gait	64
Figure 46 Bland Altman Plot: Maximum Knee Flexion During Normal Gait	65
Figure 47 Bland Altman Plot: Maximum Knee Flexion During Fast Gait.....	65
Figure 48 Bland Altman Plot: Stride Length During Slow Gait.....	67
Figure 49 Bland Altman Plot: Stride Length During Normal Gait.....	67
Figure 50 Bland Altman Plot: Stride Length During Fast Gait	68
Figure 51 Knee Angle GUI.....	69
Figure 52 Knee Angle GUI Comparing Two Knee Angles.....	69

ABSTRACT

A Wearable Motion Analysis System (WMAS) was developed to evaluate gait, particularly parameters that are indicative of mild traumatic brain injury. The WMAS consisted on six Opal IMUs attached on the sternum, waist, left and right thigh and left and right shank. Algorithms were developed to calculate the knee flexion angle, stride length and cadence parameters during slow, normal and fast gait speeds. The WMAS was validated for repeatability using a robotic arm and accuracy using the Vicon motion capture system, the gold standard for gait analysis. The WMAS calculated the gait parameters to within a clinically acceptable range and is a powerful tool for gait analysis and potential concussion diagnosis outside of a laboratory setting.

CHAPTER 1: INTRODUCTION

Current methods of measuring gait parameters involve expensive optical motion capture systems, time intensive setup, wires, complicated filtering techniques, and a laboratory setting. A wearable and wireless motion analysis system would allow gait analysis to be performed outside of a laboratory setting during activities of daily living, in a clinical setting or on a football field or battlefield. Mild traumatic brain injury (mTBI), or concussion, and traumatic brain injury (TBI) have become a major problem in both the sports and military as well as the general population from car accidents and other traumatic events. There is a major need for a quick and accurate method to diagnose mTBI and TBI, and other gait deviations outside of a laboratory setting.

A review paper by Bergmann and McGregor investigated both clinicians and users' preferences about wearable sensors. Both clinicians and users stated that wearable sensors must be "compact (light and small), available alongside the work of health professionals, and simple to operate and maintain. User's also wanted wearable sensors that were "low-invasive and that did not affect normal daily behavior," while clinicians wanted sensors that "have real-time data function, minimal time to familiarize with the device, follow/monitor a patient's progress, low cost, simple interface, long battery life, large storage capacity and are not restricted to one location or room." [1] These preferences were considered in both the selection of a sensor and the development of the wearable motion analysis system (WMAS).

The Opal sensor by APDM (APDM Inc., Portland OR) is an inertial measurement unit (IMU) that consists of a tri-axial accelerometer, tri-axial gyroscope and tri-axial magnetometer. Each Opal sensor is about the size of a wristwatch and weighs less than 22 grams. One major benefit of the Opal sensor is it can collect data for an entire day (up to 16 hours) on one charge and store up to 28 days worth of data [2]. Therefore the Opal sensor is small and compact, has a long battery life and large storage capacity, and thus can be used outside of a motion analysis laboratory setting and during a person's activities of daily living. Wireless streaming, and visualization of real-time data is also possible with the Opal sensor. Since the Opal sensor meets both the user and clinician's preferences, it was selected as the wearable sensor for the WMAS.

The goal of this project was to continue to develop and validate a wearable motion analysis system (WMAS) that can provide clinically relevant information for researchers, physical therapists and physicians. The parameters stride length, cadence and knee flexion were collected. The WMAS knee flexion angles must have less than 5 degrees of error relative to the Vicon system. The stride length calculations also need to be improved from Simoes [3]. As a result, the WMAS could be used to detect gait deviations, particularly indicators of mild traumatic brain injury (mTBI); provide instant feedback on a person's gait; and as an evaluation tool for rehabilitation plans and outcomes.

Data were collected from ten healthy subjects. The WMAS consisted of six Opal IMU sensors located on the sternum, waist, right and left thigh and right and left shank. There was also simultaneous data collection with the Vicon motion analysis system using the Plug in Gait marker set [4]. The subjects performed a timed up and go test (TUG): sit in a chair, stand up, walk to the end, turn around, walk back to the chair and sit down. Each subject performed

fifteen trials: five at a normal (comfortable) speed, five at a very slow speed, and five at a fast speed.

The WMAS data from the Opal sensors were processed and analyzed in MATLAB, while the Vicon data were processed in Visual 3D. The parameters that were analyzed were stride length, cadence and knee flexion. The WMAS data was compared to the Vicon data in order to validate the WMAS. Root mean square error (RMSE), Pearson's R correlation and Bland Altman plots were used to compare the WMAS to the Vicon system.

CHAPTER 2: BACKGROUND

2.1 Gait

Gait is a cyclic, repetitive motion. There are many parameters that can affect a person's gait from a disease to their footwear. A gait cycle is the movement of one limb from heel-strike of one foot to successive heel strike of the same foot. The gait cycle is divided into two phases: stance and swing. The stance phase occurs when the foot is touching the ground and begins at heel-strike, while the swing phase begins at toe-off and occurs when the foot is moving forward not touching the ground. Double support is also part of the gait cycle and occurs when both feet are in contact with the ground [5]. Step length and stride length are gait parameters that are often confused or used interchangeable but are two different measurements. Step length is the distance between heel-strike of the one foot to the heel-strike of the opposite foot. Whereas stride length is the distance between heel-strikes of the same foot [5]. Cadence is another gait parameter that is the measure of the number of steps per minute. During gait analysis, kinematic parameters such as stride length; cadence and joint angles are calculated.

2.2 Traumatic Brain Injury

A traumatic brain injury (TBI) can occur from a battlefield trauma, fall, car accident, or other illnesses, and is one of the leading causes of disability [6, 7]. The Center for Disease Control (CDC) defines a traumatic brain injury (TBI) as:

“A TBI is caused by a bump, blow or jolt to the head or a penetrating injury that disrupts the function of the brain. The severity of a TBI may range from ‘mild’ (a brief change in mental status or consciousness) to ‘severe’ (an extended period of consciousness or amnesia after the injury).” [8]

TBI can result in behavioral, cognitive and physical disabilities. A mild traumatic brain injury can also occur and may go undiagnosed [9].

2.2.1 Mild Traumatic Brain Injury

Mild traumatic brain injuries (mTBI), also known as concussions, are a major focus in both the military and sports communities. Similar to TBI, mTBI can result in behavioral, cognitive and physical disabilities. Furthermore, mTBI can affect a person’s ability to walk or gait, as well as their activities of daily living [9].

2.2.2 Prevalence and Statistics of TBI and mTBI

According to the CDC, every year approximately 1.7 million people are diagnosed with TBI, of which 75% are classified as mild [10]. Sports-related brain injuries are also especially prevalent accounting for at least 1.6 million concussions annually [11]. In addition to having a major impact on the civilian population, TBI and mTBI are among the most common injuries to members of the military. The Department of Defense (DoD) reported that from 2000-2012 service members have sustained approximately 266,810 TBI, of which 82.4% were classified as mTBI. Last year alone, the DoD diagnosed 29,668 service members with TBI, of which 85.5% were classified as mTBI [12].

In order to address the growing number of mTBI, the National Football League (NFL) provided \$30 million in funding for traumatic brain injury research to the National Institutes of Health [13]. Similarly, the Department of Defense and Veterans Affairs provided \$100 million

to research new methods to identify and evaluate mTBI [14]. The military and NFL have also partnered together to combat mTBI in their players and soldiers [15]. Dr. Jonathan Woodson depicts the importance of mTBI research,

“PTSD and mTBI are two of the most-prevalent injuries suffered by our war fighters in Iraq and Afghanistan, and identifying better treatments for those impacted is critical.” -Dr. Jonathan Woodson, Assistant Secretary of Defense for Health Affairs [14]

2.2.3 Effect on Gait and Balance

Many researchers have shown there are several parameters that often occur during the gait of a person with TBI and mTBI when compared to a healthy individual. The most common abnormalities are reduced stride length and cadence [7, 9, 16-20] and slower gait speed [9, 16-19, 21-23]. Other gait parameters that affected by TBI include: wider base of support [16], stiff-legged gait [24-26] and increased double support time [19, 27]. TBI also has a significant effect on the trunk, pelvis and lower limbs [16, 28]. The center of mass (COM), hip, knee and ankle are the most affected parts of the body and these abnormalities are summarized in Figure 1.

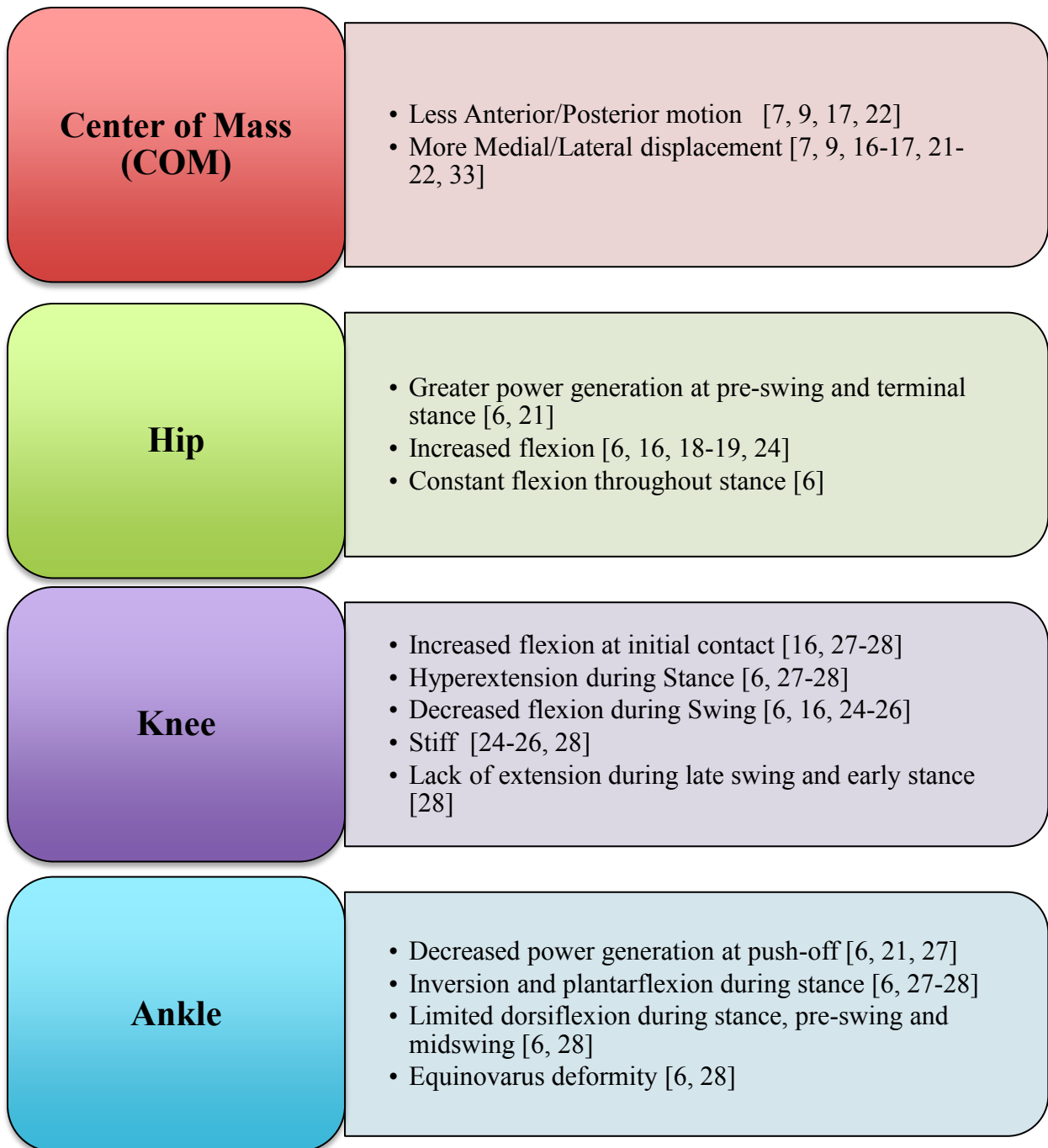


Figure 1 Abnormalities That Occur During the Gait of a Person with a TBI

The vestibular system, which is responsible for balance control, head movement and maintaining posture, can also be affected by TBI. Imbalance, dizziness, and vertigo can all be consequences of TBI [9, 22, 25, 29-33]. It has also been shown that at high head rotation speeds the vestibular-ocular reflex (VOR), used to stabilize gaze, does not work properly, causing issues with gait and balance in a person with TBI [3, 34].

2.2.4 Current Diagnostics

Several methods are used to diagnose and determine the severity of a TBI. The Glasgow Coma Scale (GCS) is one of the common diagnostic tests used to determine the severity of TBI and is particularly useful for determining the presence of a severe brain injury. The scale ranges from 3-15, where the low end of the scale represents a severe brain injury and 14-15 a mild brain injury. The GCS involves a combination of motor, eye and verbal tests to determine a person's consciousness [11]. The most common method for diagnosing sports-related mTBI is the Sports Concussion Assessment Tool (SCAT2), which involves motor and visual tests, a set of questions relating to memory or orientation, balance testing and a symptom checklist. However, the SCAT2 and other concussion tests are mostly subjective and rely on the evaluator (coach, trainer, etc.) to make the ultimate decision of whether to take the player or soldier off the field. The results are also often dependent on honest responses by the injured person, who is likely to represent their symptoms as better than they are in order to return to action [11]. Currently there is not a standardized test or method that is used universally to identify mTBI, especially in the field. There is a significant need for an accurate, simple, fast and objective method to identify and diagnose mTBI [11].

Current technology, such as the Vicon motion analysis system, used to evaluate gait parameters that are indicative of TBI is expensive, limited to a laboratory setting and time-consuming [9]. Previous work by Simoes analyzed parameters that are present during TBI including cadence, stride length, torso and head rotation using two systems: an industry standard optical tracking system and a wearable motion analysis system containing five inertial measurement units (IMUs) (APDM, Portland, OR). Correlations for cadence, head rate of rotation and torso rate of rotation were high between both systems [35].

2.2.5 What's Missing in TBI Research/Diagnosis?

TBI and mTBI research is lacking a quick, accurate and easy diagnostic test that can be performed outside of a laboratory setting. According to Dziemianowicz et al,

“While each test can be helpful in diagnosis or management, a single test that can reliably detect the presence of a concussion or complete recovery from a concussion has not been developed...There still is a need for further research into a quick and reliable test validated by scientific investigation.” [11]

There is a need for a test that can evaluate a TBI outside of a laboratory setting because someone may walk well in a confined environment where their only focus is on the task of walking, but when other factors are added such as a curb, lots of people around or other distractions the issues may arise [36].

2.3 Gait Analysis Methods

Gait analysis is the study of how a person walks. It can be as simple as how fast they walk or as complicated kinematic and kinetic parameters. There are two main methods of gait analysis: optical systems and inertial measurement units. Another method for gait analysis include the GAITRite mat, which uses pressure sensors in the walkway to determine gait parameters [37].

2.3.1 Optical System

The gold standard for gait analysis is optical motion capture systems. Optical motion capture systems use infrared cameras to track the motion of passive reflective or active light emitting markers in 3D space. While optical motion capture systems have high accuracy, they are very expensive and must be confined to a small laboratory setting.

2.3.2 Inertial Measurement Unit

In order to address the problems with optical motion capture systems for gait analysis, inertial measurement units (IMUs) have recently been a popular alternative for gait analysis. Gait parameters such as stride length, cadence, center of mass movement, range of motion, joint angles, and gait speed to name a few have been investigated [38-41].

An IMU typically consists of two sensors: an accelerometer, and a gyroscope. The accelerometer is used to measure acceleration or how fast something moves and the gyroscope is used to measure angular velocity rate of rotation. IMUs can also contain a magnetometer. The magnetometer is used to measure the orientation relative to the earth's magnetic field. These three components are combined to track the motion of an object [41, 42].

2.3.2.1 Previous Work

Many studies have used inertial measurement units (IMUs) or other sensors to measure knee, hip or ankle flexion angle, as well as other gait parameters such as stride length, gait speed, stance time, etc.

Guo et al. used two sets of IMUs on the thigh, shank and foot to calculate knee and foot flexion and differentiate between hemiplegia and healthy subjects. The subjects walked for five meters at their own comfortable pace and were recorded by a video camera. The angles were calculated using quaternions and a Kalman filter. The knee flexion angle was calculated using

the inverse of the quaternion from the shank sensor multiplied by the quaternion from the thigh sensor. While the results between the sets were accurate relative to a video camera based analysis, the data were not validated by an optical motion capture system [43].

Another study by Toffola et al. involved a wearable knee sleeve with an electrogoniometer and accelerometer to monitor knee flexion. This study involved one subject walking on a treadmill and compared the data from the sleeve to a Vicon system with a RMSE of 2.1 degrees [44].

Schiefer et al. used accelerometers and gyroscopes to calculate knee flexion during several activities of daily living, however not during gait, and compared the data to an optical camera system with a RMSE between 4.6 and 7.1 degrees [45].

Watanabe et al. used an IMU based system to calculate stride length and knee angles during treadmill and walking for several meters. This study used 7 IMUs with accelerometer and gyroscope components. Knee angles were calculated from the integration of the angular velocity from the thigh and shank gyroscopes. A Kalman filter was also applied to the data. An IMU on the foot was used to calculate the stride length using the accelerometer. An optical motion capture system was used to assess the accuracy of the data calculated from the IMUs. The data were reported with and without the Kalman filter. The average RMSE for the knee angle calculations was between 4 and 5 degrees. However, the average RMSE for the knee angle without the Kalman filter was 7 degrees and between 8 and 14 degrees for the several meter walking and treadmill walking respectively. The stride length calculations from the IMU on the foot were within 7% error relative to the optical system for slow walking, 8% error for normal walking and 5% error for fast walking [46].

Cloete and Scheffer evaluated the Xsens Moven full body inertial suit, which consisted of 16 IMUs. The IMUs have wires but communicate with a laptop via a wireless connection. The accuracy of the suit was validated using the Vicon motion capture system. The eight subjects walked and ran at several different speeds. The Xsens software, similar to the APDM software, exports a quaternion for each of the sensors. Knee angles were calculated by multiplying the quaternion from the shank by the complex conjugate of the quaternion from the thigh and then the resulting quaternion was converted to an Euler angle. Pearson's R correlations were 0.9 between the Xsens and Vicon systems for the knee flexion angle at normal speed. Even though the R correlation was high, the RMSE was 9.58 degrees for the right knee and 13.47 degrees for the left knee. The knee angles were also filtered and the bias was removed which resulted in knee flexion angle RMSE of 7.61 and 9.53 degrees for the right and left knees. The authors suggested that high RMSE may have been caused by movement of the suit during testing [47].

Another study by Pochappan et al. used 5 IMUs called Orient Specks, which contain accelerometers, gyroscopes and magnetometers. The IMUs were placed on the feet, shanks, thighs and the lower back. Knee flexions were calculated using a Latent Space Algorithm and the accelerometer data was used to identify gait events. The testing involved several trials in which the subjects walked 30 meters, however the analysis only looked at a few trials in which only one gait cycle was analyzed per trial. The data from the IMUs were compared to a Vicon system. The RMSE for the knee flexion angle was 9.12 degrees with a R correlation of 0.86. The error between the Vicon and IMU system for stride length was 0.17 meters. The authors suggested that the force plates on the floor may have interfered with the magnetometer signals and resulted in errors in the calculations [48].

Chen et al. used TEMPO inertial sensors, which contain an accelerometer and gyroscope component, to calculate the knee angle during treadmill walking. The tilt angle of the thigh and shank was calculated from the acceleration data. The angular velocity was integrated to calculate the knee angle during walking. Several different calibration methods and high pass filtering were used to remove error and drift. During slow, medium and fast walking on the treadmill the RMSE for the knee angle with the linear calibration method were 2.75, 3.03 and 3.15 degrees. The RMSE with the piecewise calibration method were 3.59, 3.88 and 4.01 degrees for the slow, medium and fast speeds [49].

Kun et al. and Lui et al. used a physical sensor and virtual sensor difference method in which the shank rotational acceleration was subtracted from the thigh rotational acceleration. This method did not involve integration of the accelerometer or gyroscope signals [50, 51]. The average RMSE reported by Kun et al. was 2.52 degrees [50]. Liu et al. reported an average RMSE of 3.07 degrees for the knee flexion angle during walking trials [51]. However, both of these studies used wired systems [50, 51].

Favre et al. conducted several studies that investigated the calibration, alignment and calculation of knee angles using IMUs [52-55]. The IMUs contained accelerometer and gyroscope components. The method used quaternions to calculate the knee angle and combined both the integration of the angular velocity from the gyroscope and the acceleration data from the accelerometer [53]. Several alignment procedures were also used to calibrate the IMUs and drift was filtered out [54]. The knee angle from the IMUs was compared to a magnetic tracking system during level walking with a RMSE less than 2 degrees and a high R correlation near 1 [52].

Dejnabadi et al. used filtered gyroscope and accelerometer data to calculate knee angles during treadmill walking. The IMUs were attached to metal plates and attached to the shank and thigh. The knee angle calculated by the IMUs was compared to an ultrasound motion capture system. At slow, medium and fast speeds the RMSE was 1.1, 1.25 and 1.6 degrees [56].

Bergmann et al. used Xsens MTx IMUs to investigate the knee flexion angle while walking up and down stairs. This is a wired system that calculates the knee angle using the rotation matrices from the thigh and shank IMUs. The data from the Xsens system was compared to an active marker Codamotion system with a RMSE of 4 degrees and a standard deviation of 3 degrees [57].

Schulze et al. calculated the knee angle by integrating the filtered angular velocity from the gyroscope. The IMUs were placed on the outer thigh and inner shank during treadmill walking at three different speeds. The knee angle calculated from the IMUs was compared to a video camera based analysis method. This study involved only one subject. The RMSE was 2.6 degrees for slow speed, 1 degree for normal speed and 6.3 degrees for fast speed [58].

Cooper et al used wired IMUs and a treadmill to calculate knee flexion angle from gyroscope and accelerometer signals. The IMU data were compared to an optical motion capture system. The authors reported a low RMSE of between 0.7 degrees for the slow speed and 4.1 degrees for the fast speed [59].

Takeda et al. used accelerometers and gyroscopes to calculate the knee flexion angle during gait. The system contained a data logger connected via wires to the IMUs. The inclination angle of the thigh and shank were calculated by the accelerometer, which was combined with the integrated angular velocity to calculate the knee angle. The average RMSE reported was 6.79 degrees, while the correlation coefficient was 0.93 [60].

Saito et al. also used accelerometers and gyroscopes to calculate the knee flexion angle during treadmill and 4-meter walk tests. In addition to using the accelerometer to determine inclination and the integrated angular velocity from the gyroscope, a Kalman filter was used. The data from the IMUs were compared to an optical motion capture system. The RMSE for the 4-meter walk tests with the Kalman filter was 2.98 degrees and without the Kalman filter was 5 degrees. The RMSE with the Kalman filter for the treadmill walking was 4.19 degrees [61].

Miyazaki et al. used a simplified gait model and a single gyroscope on the thigh to calculate the stride length and velocity during walking. The angular velocity from the gyroscope was integrated to get the angle of the thigh. The angle of the thigh and leg length was used to calculate the stride length. The error for the stride length calculation was 15% [62].

Aminian et al. compared spatio-temporal parameters from footswitches and a gyroscope system. The footswitches were placed under the heel and toe in order to detect heel-strike and toe-off gait events. The angular velocity measured by the gyroscope on the shank was used to identify the heel-strike and toe-off events. Sharp negative peaks in the angular velocity signal were shown to represent the heel-strike and toe-off events. A double pendulum and inverted double pendulum gait model was used to calculate the spatio-temporal parameters from the gyroscope system. The RMSE for stride length was 0.07 meters or 7.2% for the footswitch and gyroscope gait model [38].

Salarian et al. also used gyroscopes to calculate gait parameters. The gyroscope on the shank was used to calculate the gait events and temporal parameters. A data logger was connected with wires to the gyroscopes. The angular velocity signal was integrated to calculate the angle of the shank segment and the signal was filtered. The gait events were detected

similar to Aminian et al. [38]. However, a different peak detection algorithm was used to identify the maximum or mid-swing peaks and used an interval of 1.5 seconds to identify the local minimum peaks or gait events. A double and inverse pendulum model were used to calculate stride length, similar to Aminian et al [38]. A timed up and go (TUG) test was used for the gait trials. The error for the stride length calculations between the reference system and gyroscope algorithm was 3.5 centimeters [39].

Doheny et al. also used a single gyroscope to calculate gait parameters relative to the GAITRite electronic walkway. The angular velocity and detection of gait events were similar to Salarian et al [39]. The stride length was calculated using a scale factor, the height of the subject and the range of the shank angle. Data were collected at slow, normal and fast speeds. Stride length had a RMSE of 0.09 meters and an R correlation of 0.84 relative to the GAITRite walkway [63].

Previous work by Simoes analyzed cadence, stride length, torso and head rotation between two systems: an industry standard optical tracking system and a wearable motion analysis system containing five IMUs (APDM, Portland, OR). The gait parameters were calculated using APDM's iTUG plug in which is based on work by Aminian et al. [38] and Salarian et al. [39]. Cadence, head rate of rotation and torso rate of rotation had high Pearson's R correlation values. The R correlation values for stride length were 0.776, 0.8 and 0.817 for normal, fast and slow speeds, with an overall correlation of 0.86 [3, 35].

Shanshan et al. used IMUs to calculate stride length and gait speed. The angular velocity of the shank from the gyroscope signal was integrated to determine the angle of the shank. The angular velocity was low pass filtered and a peak detection algorithm was used to detect the gait events. The range of rotation of the shank during the gait cycle was used to

calculate stride length by a compass gait model. A refined model was also used, which added the range of rotation of the thigh in addition to the range of rotation of the shank [64].

Zexi et al. used gyroscopes to calculate step length and distance travelled. The angular velocity was integrated to determine the angle of the leg. The law of cosines was then used to calculate the step length based on the angle of the leg and the leg length. The distance travelled was calculated using three methods, the waist gyroscope, the thigh gyroscope, and the gyroscope on the foot. The error was lowest using the gyroscope on the thigh to calculate the step length and distance travelled [65].

CHAPTER 3: METHODS

3.1 WMAS Testing

3.1.1 Institutional Review Board Approval

This research study “Feasibility of Wearable Sensors to Determine Gait Parameters” was approved by the University of South Florida (USF) Institutional Review Board (IRB) as an adult minimal risk research study #Pro00003205 (see Appendix D). The principal investigator of the study was Dr. Stephanie Carey, and the research staff included Amanda Martori and Matt Wernke. Before participating in the study, each participant was briefed about the following using the IRB informed consent form: the purpose of the study, procedures, benefits, risks, disclosures, privacy, how the information will be used, their rights and how to withdraw from the study. After the briefing and participant’s questions were answered, the participant and the research staff member both signed the informed consent form.

3.1.2 Participants

Ten participants, eight men and two women (average age 27) were recruited to participate in the study. All of the participants were over the age of 18 and healthy, with no known pathologies that would affect their gait. The subject identification number, age, height and weight of each subject is listed in Table 1.

Table 1 Subject Information

Subject ID	Age	Height (m)	Weight (kg)
WMAS01	22	1.815	76
WMAS02	22	1.81	83
WMAS03	25	1.845	102
WMAS04	28	1.79	74.5
WMAS05	22	1.86	72.4
WMAS06	21	1.695	59.5
WMAS07	54	1.74	92.3
WMAS08	24	1.83	85.2
WMAS09	25	1.63	76
WMAS10	22	1.89	95

3.1.3 WMAS Instrumentation

The Wearable Motion Analysis System (WMAS) was composed of six Opal inertial measurement units (APDM Inc., Portland, OR). Each wearable Opal IMU sensor includes a triaxial accelerometer, a triaxial gyroscope and a triaxial magnetometer. The Opal sensors also include precision temperature calibration and a docking station. Each sensor is about the size of a wristwatch and weighs 22 grams, has a battery life of 16 hours, wireless connectivity, latency recovery and 16 GB of on-board storage. The APDM system can utilize up to eight sensors transmitting data to a computer or the sensors can record data directly onboard. The real-time data can then be viewed once a wireless connection is detected and the on board data can be accessed once the sensors are connected to the docking station. In this study, the sensors transmitted real time data to a laptop via a wireless access point. Motion Studio software (APDM Inc., Portland, OR) was used to view the IMU data in real-time and save the data as comma separated value files (CSV).

The APDM instrumentation includes a Macbook Pro laptop, Motion Studio software, docking station, access point, two USB cables, an external power adapter, six Opal IMUs, a chest harness, belt, and two small Velcro straps. The external power adapter was used to plug the docking station into a power outlet. The access point and docking station were both plugged into the laptop. Each Opal IMU sensor was plugged into a separate dock on the docking station. The setup during sensor configuration (prior to data collection) is shown in Figure 2.

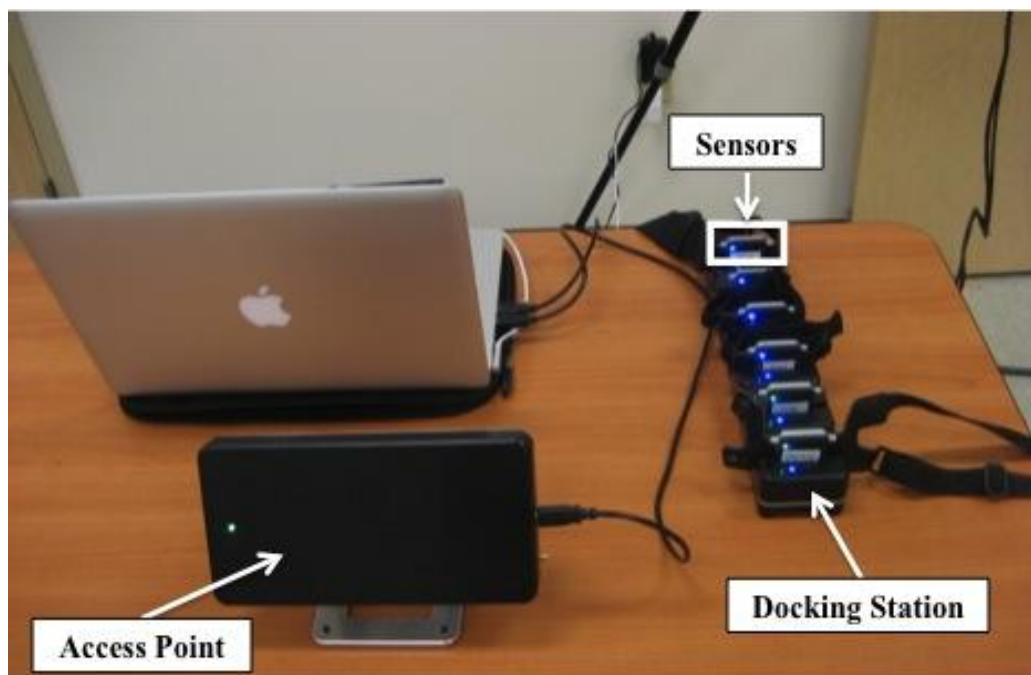


Figure 2 APDM Instrumentation Setup

The Motion Studio software was used to calibrate and configure the sensors. The sensors were calibrated according to the manufacturer’s specifications. During configuration, the accelerometer with a range of $\pm 6g$, gyroscope and magnetometer sensors were enabled, the sampling rate was set to 128 Hertz and the recording configuration was “Robust Synchronized Streaming.” After the configuration was complete, the sensors were removed from the docking station and attached to the subject.

3.1.3.1 Sensor Locations

The sensors were attached to the subject using the manufacturer's chest harness, belt, and small Velcro straps. In order to reduce the movement of the thigh sensors during walking, the sensors were attached with Velcro to two Neoprene sleeves that were then wrapped tightly around each thigh. The locations of the six sensors were the sternum, lower back, right thigh (RThigh), left thigh (LThigh), right shank (RShank) and left Shank (LShank) as shown in Figure 3.

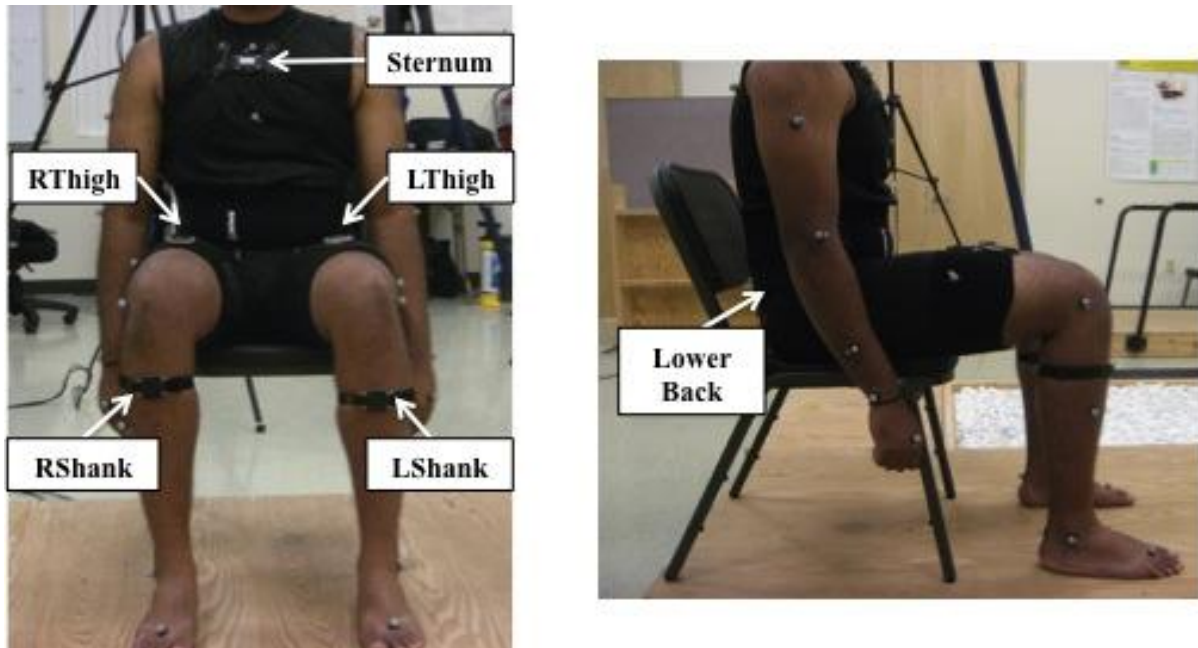


Figure 3 Sensor Locations

3.1.4 Vicon Instrumentation

A Vicon optical motion analysis system consisting of eight infrared cameras was used to track the motion of passive reflective markers placed on the subject. Vicon Workstation was used to calibrate the cameras, auto label the model, collect and check the gait trials. In addition, a Canon digital camcorder was used to simultaneously record each trial.

3.1.4.1 Reflective Marker Locations

Prior to data collection, thirty-five spherical reflective markers 14 millimeters in diameter were placed on subjects' skin at key bony landmarks, according to the Vicon Plug-In Gait marker set [4]. The marker labels, anatomical locations and descriptions for the Plug-In Gait marker set are listed in Table 2. Each body segment requires three markers to define its three-dimensional local coordinate system.

Table 2 Plug-In Gait Marker Set

Body Segment	Marker Label	Anatomical Location	Description of Location
Torso	C7	7th Cervical Vertebrae	Spinous process of the 7th cervical vertebrae on back of neck
	T10	10th Thoracic Vertebrae	Spinous process of the 10th thoracic vertebrae
	CLAV	Clavicle	Jugular notch where the clavicle meets the sternum, below base of neck and between the collar bones
	STRN	Sternum	On the bone above the Xiphoid process in the middle of the ribcage
	RBAK	Right Back	Right scapula, assymetrical, used for labeling purposes
Right Arm	RSHO	Right Shoulder	Right acromio-clavicular joint
	RUPA	Right Upper Arm	Right upper arm in between the shoulder and elbow markers
	RFRA	Right Forearm	Right forearm between the elbow and wrist markers
	RELB	Right Elbow	Right lateral epicondyle, approximating the elbow joint axis
	RWRA	Right Wrist A	Thumb side of the right wrist
	RWRB	Right Wrist B	Pinkie side of the right wrist
	RFIN	Right Finger	On the dorsum of the right hand below the third metacarpal
Left Arm	LSHO	Left Shoulder	Left acromio-clavicular joint
	LUPA	Left Upper Arm	Left upper arm in between the shoulder and elbow markers, assymetrical from the RUPA
	LFRA	Left Forearm	Left forearm between the elbow and wrist markers, assymetrical from the RFRA
	LELB	Left Elbow	Left lateral epicondyle, approximating the elbow joint axis
	LWRA	Left Wrist A	Thumb side of the left wrist
	LWRB	Left Wrist B	Pinkie side of the left wrist
	LFIN	Left Finger	On the dorsum of the left hand below the third metacarpal
Pelvis	RASI	Right Anterior Iliac Spine	On top of the anterior iliac spine
	LASI	Left Anterior Iliac Spine	
	RPSI	Right Posterior Iliac Spine	On top of the bony locations where the spine joins the pelvis
	LPSI	Left Posterior Iliac Spine	
Right Leg	RTHI	Right Thigh	Lower 1/3 of the lateral surface of right thigh
	RKNE	Right Knee	Lateral epicondyle of the right knee
	RTIB	Right Tibia	Lower 1/3 of the lateral surface of the right shank
	RANK	Right Ankle	Lateral malleolus on the right foot
	RTOE	Right Toe	Second metatarsal head on the right foot
	RHEE	Right Heel	Right calcaneous, height is level with the right toe marker
Left Leg	LTHI	Left Thigh	Lower 1/3 of the lateral surface of left thigh
	LKNE	Left Knee	Lateral epicondyle of the left knee
	LTIB	Left Tibia	Lower 1/3 of the lateral surface of left shank
	LANK	Left Ankle	Lateral malleolus on the left foot
	LTOE	Left Toe	Second metatarsal head on the left foot
	LHEE	Left Heel	Left calcaneous, height is level with the left toe marker

3.1.4.2 Subject Measurements

The Vicon Plug-In Gait model requires several anatomical measurements for each subject; these are listed in Table 3. The subject's height and weight was measured using a professional scale, in centimeters (cm) and kilograms (kg) respectively. The other measurements were taken by hand using a cloth measuring tape, and recorded in cm.

Table 3 Subject Measurements Required for Plug-In Gait

Measurement	Description	Units
Mass	Weight of the subject	kg
Height	Height of the subject	cm
ASIS Distance	Distance between RASI and LASI markers	cm
Leg Length	Distance from ASIS narker to medial malleolus	cm
Knee Width	Medio-lateral knee width about flexion axis	cm
Ankle Width	Distance between the lateral and medial malleolus	cm
Elbow Width	Distance between the lateral and medial epicondyle	cm
Wrist Width	Distance between the two wrist markers	cm
Hand Thickness	Thickness between the dorsum and palm of hand	cm
Shoulder Offset	Vertical distance between the SHO marker and shoulder joint center	cm

3.1.4.3 Camera Calibration

An L-frame with four passive reflective markers (shown in Figure 4) was used for calibration of the Vicon cameras. It was placed on the floor at the corner of the first force plate and was used to define the laboratory's global coordinate system, axes and the location of the origin. The data collection volume was also defined by moving a wand with two reflective markers (shown in Figure 4) in various directions over the entire walkway.



Figure 4 Vicon Calibration L-Frame and Wand

After the static and dynamic camera calibration was completed, a static trial was collected in which the participant was asked to stand still on the force plates in a T-pose (shown in Figure 5) in order to define and label the locations of the reflective markers.

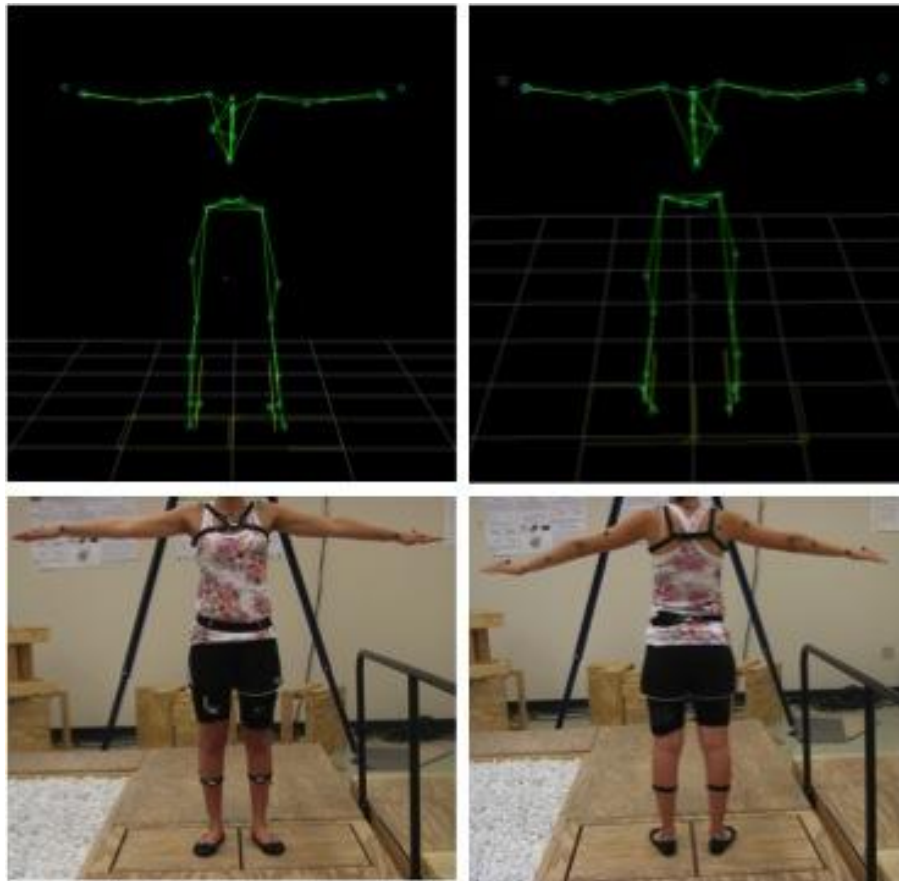


Figure 5 Vicon Static Trial T-Pose

3.1.5 Testing Protocol

This study was conducted in the Rehabilitation Robotics & Prosthetics Testbed (RRT) motion analysis laboratory at the University of South Florida. The eight Vicon cameras were focused on a 3-meter wooden walkway with two AMTI force platforms. A chair was placed at the beginning of the walkway. Both the WMAS and Vicon systems were configured and calibrated per the manufacturer's instructions prior to the beginning of the testing as described previously and in more detail in Appendix B. After the configuration of both systems, data were collected simultaneously from the WMAS and Vicon systems during the gait trials. One member of the research staff was needed to run the WMAS, and another staff member was needed to run the Vicon system. The start of the recording for each trial was coordinated verbally by one of the staff members.

3.1.5.1 WMAS

The Motion Studio software was used to record the data from the WMAS during the gait trials. After the sensors were configured in "Robust Synchronized Streaming Mode" at 128 hertz and removed from the docking stations, the stream button was pressed and a new window popped up on the screen as shown in Figure 6. The data from the WMAS was streamed to the laptop via the wireless access point and displayed in a real time strip chart from each of the sensors. The strip chart displayed the accelerometer, gyroscope and magnetometer readings, shown on the left hand side of Figure 6. Before each trial, the research staff member responsible for the WMAS was required to select the record duration as indeterminate, the file format as CSV and name the trial according to the format "Subject ID_Type of Trial_Trial Number." For each trial, the record button was pressed to begin the trial and the stop button

was pressed at the end of the trial. For detailed instructions on how the Motion Studio program was used see Appendix B.

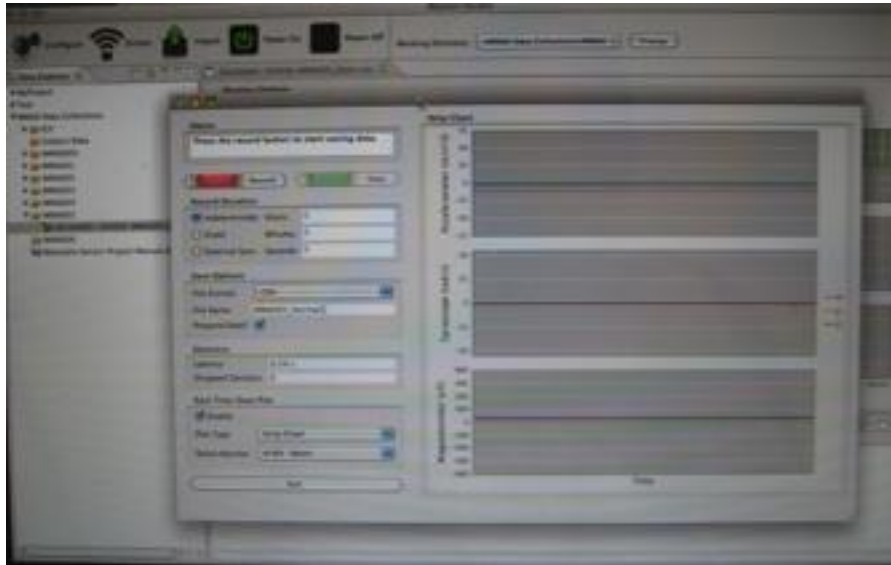


Figure 6 Motion Studio Screen During Streaming Prior to Data Collection

3.1.5.2 Vicon Motion Analysis System

The Vicon Workstation software was used to collect data from the Vicon optical motion analysis system. The static trial described previous was used to label each of the markers according the plug-in gait marker set (Table 2) and define an auto label pipeline. When the model was completed a stick figure of the subject was created based on the position of the markers and the defined segments (shown in Figure 5). The auto labeling was used to automatically define the stick figure for each of the trials, however due to occasional marker dropout it did not always work properly. As a result, after the data collection each trial needed to be checked to make sure all the markers were labeled properly and all the markers were present. Before the start of the each trial, the new trial icon was selected and named according to the WMAS data collection checklist (Appendix A). The start and stop buttons were used to

capture each trial. Each gait trial was checked briefly to make sure all the markers were present and there were no issues prior to the start of the next trial.

3.1.5.3 Timed Up and Go Test

A timed up and go (TUG) test [66] was used for all gait trials in this study. A TUG test is a common test used during gait analysis and physical therapy evaluation. The TUG test began with the subject sitting in a chair at one end of the walkway with their knees bent to approximately 90 degrees and hands on their lap. When asked to go, the subject stood up, walked to the other end of the walkway and when they reached a line on the floor, turned around, walked back to the chair and sat back down. The subjects were asked to walk at three different speeds: normal, slow and fast. Each subject completed five trials at each of the three speeds. The slow speed was used to correspond to mTBI patients.

3.2 Verification Testing

Three different verification tests were performed with the WMAS and APDM IMUs:

1. Movement analysis using a robotic motion.
2. Range of motion
3. Sit to stand

In the movement analysis testing, a wheelchair mounted robotic arm (WMRA) was used to provide a repeatable movement at varying speeds, with the sensors securely attached in order to investigate the accuracy of the APDM Opal IMUs for kinematic analysis relative to an optical motion analysis system without any filtering and to identify the sources of error. The range of motion and sit to stand movements were used to determine the accuracy of the knee angle calculation algorithm.

3.2.1 Movement Analysis Using a Programmed Robotic Motion

In order to verify the accuracy of the WMAS and its algorithms, the joint angles and velocities measured with the wearable IMU sensors were compared to measurements from a Vicon optical motion-tracking system while a robotic arm completed various predetermined paths. The robotic arm was used to test the repeatability of the measurements as it could provide the same movement over and over again for longer trials than is possible with human subject testing. The sensors were also running for a much longer period of time with the robotic arm testing than with the human subject testing. A 7 Degree of Freedom wheelchair mounted robotic arm (WMRA), developed at the University of South Florida was used. The robotic arm uses incremental encoders at each joint to measure and calculate its Cartesian motion relative to a reference frame using inverse kinematics [67]. Motion profiles of the robotic arm were tracked using an eight-camera Vicon motion-tracking system with passive retro-reflective markers, and four wearable APDM IMUs. In order to better isolate various types of contributing errors, linear, planar, and 3-dimensional robot motions were used. Data were collected from the sensors over several hours, which provided insight into time-based effects as well as management of large amounts of data for future long-term tracking applications. In addition, acquisition errors with high-speed gaits were found previously, thus robotic arm trajectories of varying velocities were used to provide further insight into these rate-based effects. Angular velocity and joint angles were compared for the Vicon and APDM systems and used to investigate the accuracy of the IMUs and algorithms during motion tracking. Effects on IMU performance due to the application of filtering algorithms were not investigated.

3.2.1.1 Instrumentation

The WMRA is shown in Figure 7, where the circles indicate the locations of the joints, the lines indicate the links or segments and the boxes indicate the locations of the sensors. The robotic arm was used to represent a person’s leg, where joints 1 and 3 represent the “hip” joint, link 1 represents the “thigh” segment, joint 4 represents the “knee” joint and link 2 represents the “shank” segment. Two APDM sensors were placed on the “knee” joint, and one sensor was placed on each segment or link connected to the “knee” joint.

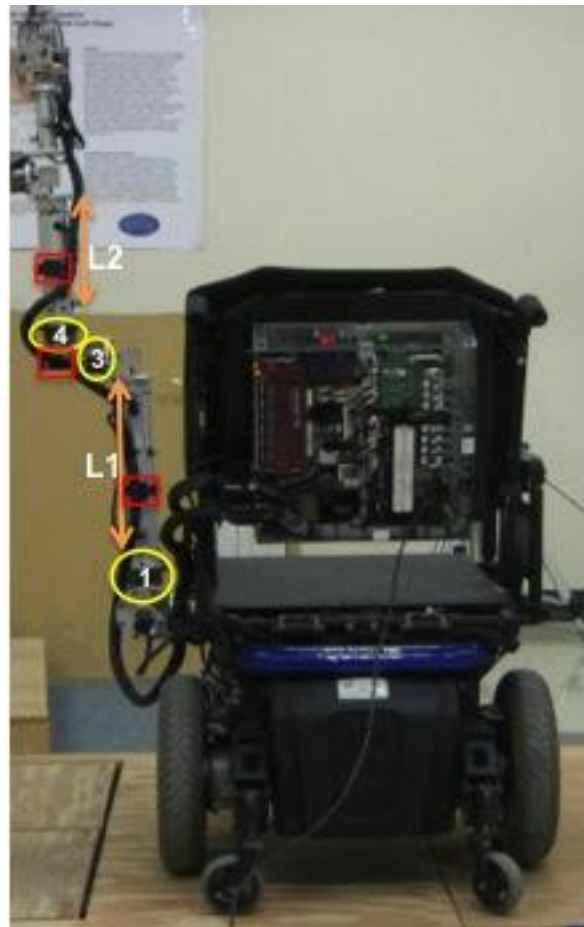


Figure 7 Wheelchair Mounted Robot Arm (WMRA)

Four Opal IMU units were placed on the robotic arm as shown by the red boxes in Figure 7 and Figure 8: one on link 1 (L1), one on link 2 (L2) and two on joint 4 coaxially.



Figure 8 Locations of IMUs on WMRA

An eight-camera Vicon optical motion analysis system was also used simultaneously to capture the movement of the robotic arm by tracking the position of passive reflective markers. A total of 16 spherical reflective markers were placed on the robotic arm (Figure 9). Each segment requires three markers to define its 3-dimensional local coordinate system. Redundant markers were used to avoid marker dropout due to the wheelchair blocking cameras from seeing markers.



Figure 9 Reflective Markers and IMUs on WMRA

3.2.1.2 Testing Protocol

The robotic arm was programmed to complete range of motion movements at particular joints and a 3-dimensional motion of all three joints. Data from each movement (trial) were collected from the APDM Opal sensors and the Vicon motion analysis system simultaneously. The following movements were recorded:

Joint 1: Hip flexion and extension

Joint 3: Hip internal and external rotation

Joint 4: Knee flexion and extension

The flexion and extension linear movements were collected at three different speeds, and the internal and external rotation movements were collected at two different speeds. The robotic arm was then programmed to continue simultaneous three-dimensional movement of all three joints for five complete cycles. A total of eighteen trials were recorded over the course of

several hours. The starting position of the WMRA for the flexion and internal rotation movements, and the ending position of the WMRA for the extension and external rotation movements was defined as zero degrees for the Vicon and APDM systems.

3.2.1.3 Data Analysis

The Vicon data were analyzed using Visual3D (C-Motion Inc., Germantown, MD). A model was created in Visual3D that used the positions of the reflective markers to define segments for link 1 (“thigh”) and link 2 (“shank”). The joint angles were calculated from the model using the rotation of one segment relative to a reference segment (in some cases the laboratory coordinate frame) and followed by an X-Y-Z Euler sequence.

MATLAB was used to process and analyze the data from the APDM sensors. An algorithm was created to calculate the angle between link 1 and link 2 (joint 4) or “knee” angle between the two APDM sensors. Anatomically the knee angle is calculated using Equation 1 but an algorithm was used to calculate the knee angle from the sensors. This algorithm identified the quaternion “q” (Equation 2), which comes from the APDM sensors. The quaternion provides the orientation of the sensor and is calculated from a combination of the accelerometer, gyroscope and magnetometer readings as well as the temperature correction feature of the IMUs [68]. After the quaternion was identified, the norm of the quaternion was calculated (Equation 3). Next the quaternion was normalized using “w, x, y and z” (Equation 4). The knee angle quaternion was calculated by using Equation 5, in which the inverse of the shank quaternion was multiplied by the normalized thigh quaternion. Lastly, the knee angle quaternion was then converted into Y-X-Z Euler angles (Equation 6). This process was used to obtain the flexion angle for both the “thigh and “shank” sensors, which represent Link 1 and

Link 2 respectively. The Y-X-Z rotation is the sensor equivalent to the Vicon X-Y-Z rotation [10, 43, 69, 70].

$$\theta_{Knee} = \theta_{Thigh} - \theta_{Shank} \quad (1)$$

$$q = q_0 + q_1 + q_2 + q_3 \quad (2)$$

$$q_{norm} = \sqrt{q_0^2 + q_1^2 + q_2^2 + q_3^2} \quad (3)$$

$$w = \frac{q_0}{q_{norm}}; x = \frac{q_1}{q_{norm}}; y = \frac{q_2}{q_{norm}}; z = \frac{q_3}{q_{norm}}; \quad (4)$$

$$q_{Knee} = q_{Shank}^{-1} \otimes q_{Thigh} \quad (5)$$

$$q_{Knee} \text{ Euler Angles } YXZ = \begin{bmatrix} \text{atan2}(-2xz + 2wy), z^2 - y^2 - x^2 + w^2 \\ \text{asin}(2yz + 2wx) \\ \text{atan2}(-2xy + 2wz, y^2 - z^2 + w^2 - x^2) \end{bmatrix} \quad (6)$$

For the two sensors located directly on joint 4 and to calculate joint angles 1 and 3, which represent the “hip” angle, Equation 1 and Equation 2 were used to identify and normalize the quaternion. Then the quaternion was converted directly to Euler angles. The joint angle calculated by the sensor located directly on the joint was compared to the joint angle calculated by the two-sensor algorithm (Equations 1-5).

In order to compare the Vicon and APDM systems, the joint angles were calculated from for each trial and were plotted in degrees versus time in seconds on the same graph. The Vicon and APDM systems collected data at 120 Hz and 128 Hz respectively. Therefore in order to compare the two systems, the data were down-sampled. The root mean square error (RMSE) and Pearson’s R correlation were calculated in order to compare the joint angles from the Vicon and APDM sensors. The angles calculated by the two-sensor algorithm and the Vicon system were also compared to the angles calculated by the sensors located directly on joint 4 using the

RMSE. The average angular velocities for each trial were also compared in degrees per second for all three systems. The angular velocity measured by the APDM sensor's gyroscopes was compared to the calculated angular velocity from both the Vicon and WMRA systems.

3.2.2 Range of Motion

The range of motion tests were performed using the WMAS and Vicon motion analysis systems simultaneously in order to validate the knee angle algorithm created in Matlab for the WMAS. Both the WMAS and Vicon motion analysis systems were set up and calibrated according to methods previously discussed in sections 3.1.3 and 3.1.4. For all of the tests the subject was seated and asked to flex and extend their leg. Several tests were performed including knee extension from 90 degrees to 45 degrees (shown in the top two pictures of Figure 10), knee flexion from 45 degrees to 90 degrees, full knee flexion and extension (shown in the bottom two pictures of Figure 10).

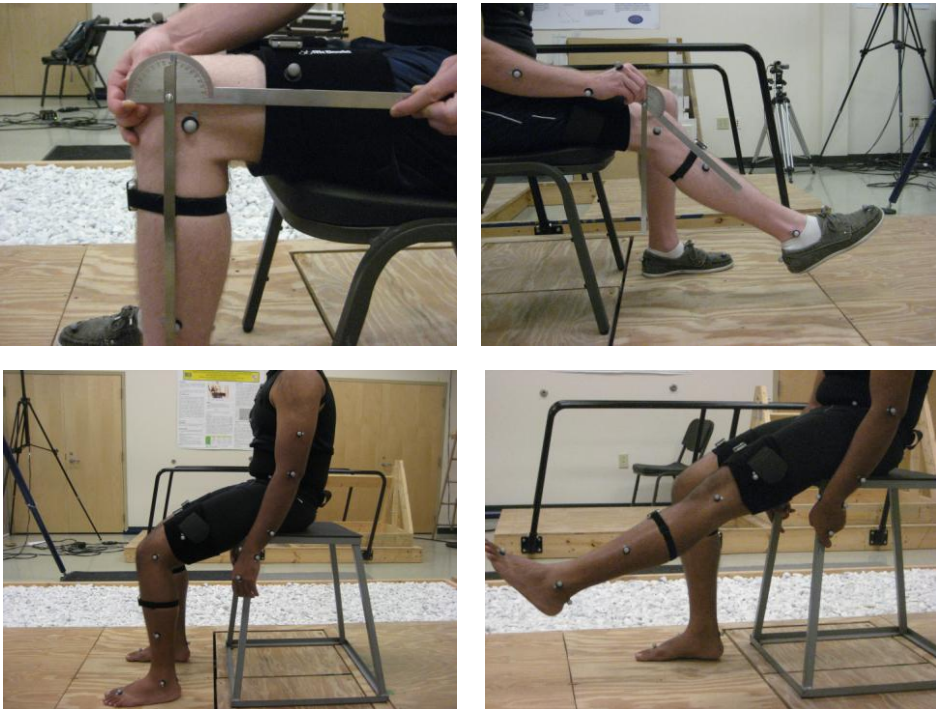


Figure 10 Range of Motion Tests

3.2.3 Sit to Stand

Sit to stand tests (shown in Figure 11) were performed using the same procedures as the range of motion testing. For these trials subject began in a seated position and was asked to stand up, and sit back down. These trials were also used to validate the knee angle calculation algorithm of the WMAS.



Figure 11 Sit to Stand Test

CHAPTER 4: DATA ANALYSIS

4.1 WMAS

The WMAS analysis was performed in Matlab. Algorithms were developed and adapted from previous work with quaternions [69, 70] to calculate knee flexion angle, stride length and cadence.

4.1.1 Knee Angle

The knee angle was calculated from the previously mentioned Equations 2-6 (also shown below) in Matlab. Before the calculations were performed, the csv file was imported into Matlab as column vectors with headings “RTQScalar, RTQX, RTQY, RTQZ, RSQScalar, RSQX, RSQY, RSQZ, LTQScalar, LTQX, LTQY, LTQZ, LSQScalar, LSQX, LSQY and LSQZ,” representing the quaternion components of the right thigh, right shank, left thigh and left shank respectively. Equations 2-4 were performed for each of the four sensors: right thigh, right shank, left thigh and left shank. Equations 2-4 was used to define the quaternion calculate the norm of the quaternion, and to normalize the quaternion (Equation 4). Equation 5 was used to calculate the knee angle quaternion by multiplying the inverse of the shank quaternion by the thigh quaternion. Equation 6 was then used to convert the knee angle quaternion to Euler angles. The Y-X-Z rotation is the sensor equivalent to the Vicon X-Y-Z rotation, where angle 1 corresponds to flexion/extension, angle 2 corresponds to internal/external rotation and angle 3 corresponds to abduction/adduction [10, 43, 69-71].

$$q = q_0 + q_1 + q_2 + q_3 \quad (2)$$

$$q_{norm} = \sqrt{q_0^2 + q_1^2 + q_2^2 + q_3^2} \quad (3)$$

$$w = \frac{q_0}{q_{norm}}; x = \frac{q_1}{q_{norm}}; y = \frac{q_2}{q_{norm}}; z = \frac{q_3}{q_{norm}}; \quad (4)$$

$$q_{Knee} = q_{Shank}^{-1} \otimes q_{Thigh} \quad (5)$$

$$q_{Knee} \text{ Euler Angles } YXZ = \begin{bmatrix} \text{atan2}(-2xz + 2wy), z^2 - y^2 - x^2 + w^2 \\ \text{asin}(2yz + 2wx) \\ \text{atan2}(-2xy + 2wz, y^2 - z^2 + w^2 - x^2) \end{bmatrix} \quad (6)$$

4.1.2 Stride Length

Aminian et al. found that the heel-strike and toe-off events can be identified using the angular velocity signal from the shank sensor. The toe-off and heel-strike events are evident in the minimum peaks of the shank angular velocity signal on either side of the maximum peaks (greater than 100 deg/s). The rectangles and circles in Figure 12 represent the toe-off and heel-strike gait events during one of the slow gait trials [38].

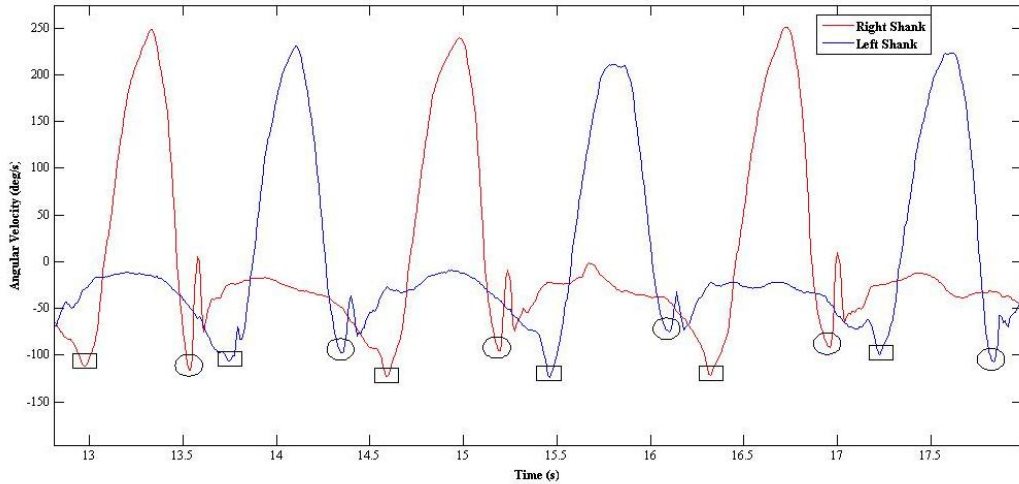


Figure 12 Shank Angular Velocity & Toe-Off (Rectangle) and Heel-Strike (Circle) Events

The toe-off and heel strike events were detected from the angular velocity signal using a peak detection algorithm in Matlab that located the minimum and maximum peaks of the signal [72]. Prior to stride length calculation the events were checked to make sure the points were the actual heel-strike and toe-off events and not a peak due to noise in the signal.

Stride length was calculated using the law of cosines, similar to the Zexi et al calculation of step length [65]. The stride length was equal to the sum of the right and left step. This consists of the sum of the distance from right heel-strike to left heel-strike and the distance from left heel-strike to subsequent right heel-strike. According to the law of cosines, if you have two sides of a triangle and the angle between them you can calculate the length of the third side [73]. As shown by s_1 in Figure 13, the right step (RHS to LHS) includes the two sides or leg lengths and the angles of the right shank and left shank at heel-strike. These two angles are then added together to determine the angle between the right and left leg. The first step (s_1) in Figure 13 is from right heel-strike to the left heel-strike, and the second step (s_2) is from left heel-strike to the subsequent right heel-strike.

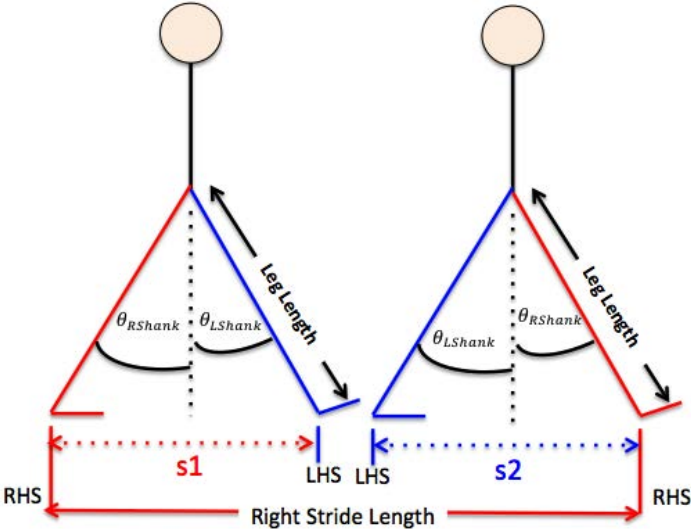


Figure 13 Parameters for Stride Length Calculation

Equation 7 was used to determine step length (s) based on the law of cosines [73].

Equation 8 was used to calculate the stride length by adding s1 and s2.

$$s = LegLength\sqrt{2 - (\cos(\theta_{RShank} + \theta_{LShank}))} \quad (7)$$

$$Stride Length = s_1 + s_2 \quad (8)$$

4.1.3 Cadence

Cadence or number of steps per minute was calculated using Equation 9. The heel-strike events were used to determine each step as defined previously. The number of steps before the turn and the total time from the beginning of the first step to the end of the last step was used in the calculation. This process was also repeated for the steps that occurred after the turn. The cadence before the turn and after the turn was averaged to determine the cadence for that trial.

$$Cadence = \frac{Steps}{Minute} = \# Steps \times \frac{60}{Total Time (s)} \quad (9)$$

4.1.4 Graphical User Interface Development

A graphical user interface was developed in Matlab using the GUIDE tool. The graphical user interface will allow the user to view the knee angle calculations and results by simply loading the CSV file from the sensors and running the program. The GUI needs to be easy to use and run by a clinician. The GUI was partially developed in this study, future work will involve adding the other gait parameters and the ability to collect and analyze the data directly rather than using another software program for data collection.

4.2 Vicon

The data from the Vicon system was first inspected using the BodyBuilder software, and was then exported into Visual 3D (C-Motion, Germantown, MD) software for further analysis.

4.2.1 Visual 3D Model

In Visual 3D, a model was created that identified the locations of the reflective markers and defined the bone segments based on the plug in gait marker set, static trial and subject measurements. The model was based on the C-Motion Visual 3D Tutorial: Building a Conventional Gait Model [74] and is shown in Figure 14.

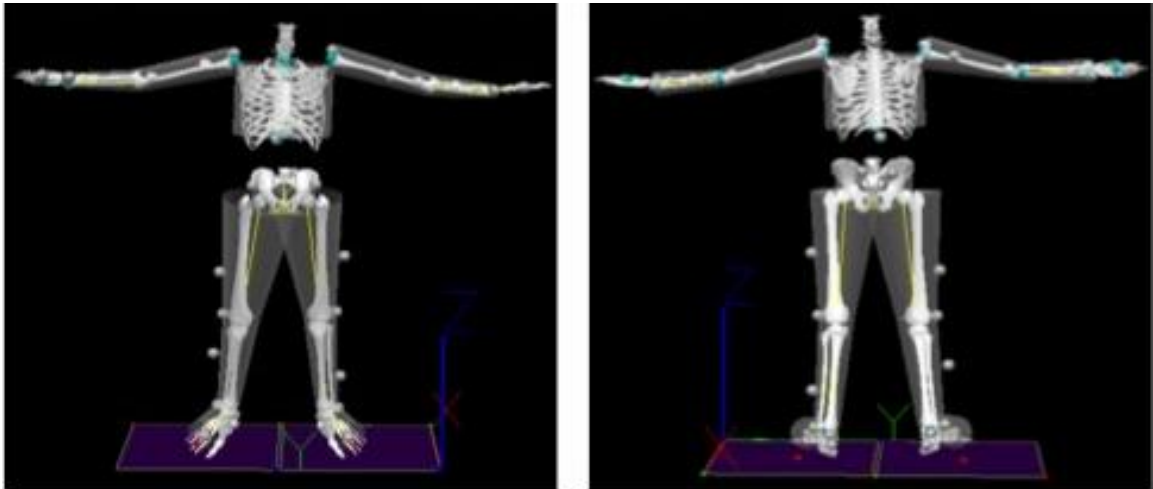


Figure 14 V3D Model

4.2.2 Visual 3D Pipeline

A pipeline was created in Visual 3D (V3D) to calculate the knee joint angle [75] and stride length [76, 77] (See Appendix C). The thigh and shank segments were used to calculate the angle of the shank relative to the thigh, or the knee flexion angle during the gait trials [75]. The position of the heel with respect to the pelvis was used to determine the heel-strike events.

4.3 Statistics

Three types of statistics were used to compare the WMAS and Vicon systems: Pearson's R Correlation, Root Mean Square Error (RMSE) and Bland Altman plots. Pearson's R Correlation was calculated using Equation 10 [78]. RMSE was calculated using Equation 11 [79]. In both Equations 10 and 11, X was the results from the WMAS system, Y was the results from the Vicon system and n is the number of samples.

$$R = \frac{n \sum XY - (\sum X)(\sum Y)}{\sqrt{[n \sum X^2 - (\sum X)^2][n \sum Y^2 - (\sum Y)^2]}} \quad (10)$$

$$RMSE = \sqrt{\frac{\sum (X-Y)^2}{n}} \quad (11)$$

Pearson's R Correlation is used to compare two variables by determining on a scale of positive to negative 1 the strength of their linear relationship. The closer the value is to 1, the stronger the correlation. If the value is close to zero, there is a weak linear relationship between the two variables [78]. Root mean square error (RMSE) is often used to compare two methods of measurement, or a model to a reference measurement. The RMSE is a measure of fit between two methods [79]. Another way to compare two measurement techniques is with a Bland Altman plot. The average of the two methods is the x-axis of the plot and the difference between the two methods is the y-axis of the plot. The center dashed line on the plot is the mean and the upper and lower dashed lines are the mean +/- two standard deviations. The upper and lower dashed lines are called the limits of agreement, and are used to determine if the two methods are similar. If the limits of agreement are within an acceptable range of error then the two methods are similar. The advantage of a Bland Altman plot is the outliers, bias and similarities between the two methods are easy to identify [80, 81]. Bland Altman plots were

used in addition to R correlation values because an R correlation assumes a linear relationship, and it is possible for two methods to have a linear relationship but not be similar.

CHAPTER 5: RESULTS

5.1 Verification Tests

5.1.1 Movement Analysis Using a Robotic Motion

There were six trials recorded during the movement of joint 1. The hip flexion and hip extension angles calculated by the Vicon and APDM systems at speeds A, B and C are shown in the following graphs in degrees versus time in seconds. The Vicon system is shown in the plots by the blue lines and the red lines show the APDM system. Figure 15 shows the angles for both the Vicon and APDM system during the movement of joint 1, representative of hip flexion at speed A. Joint 1 hip flexion B and joint 1 hip flexion C are shown in Figure 16 and Figure 17.

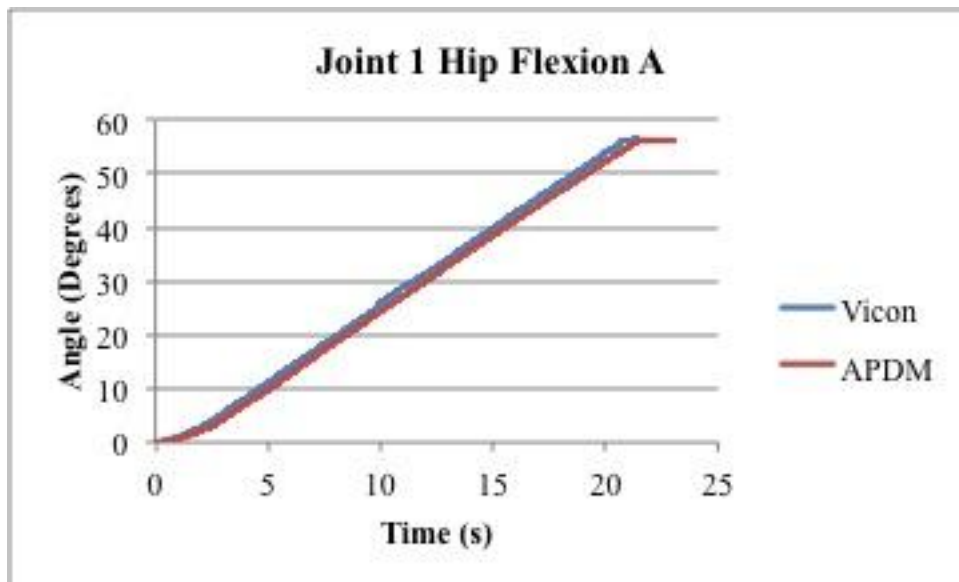


Figure 15 Joint 1 Hip Flexion A

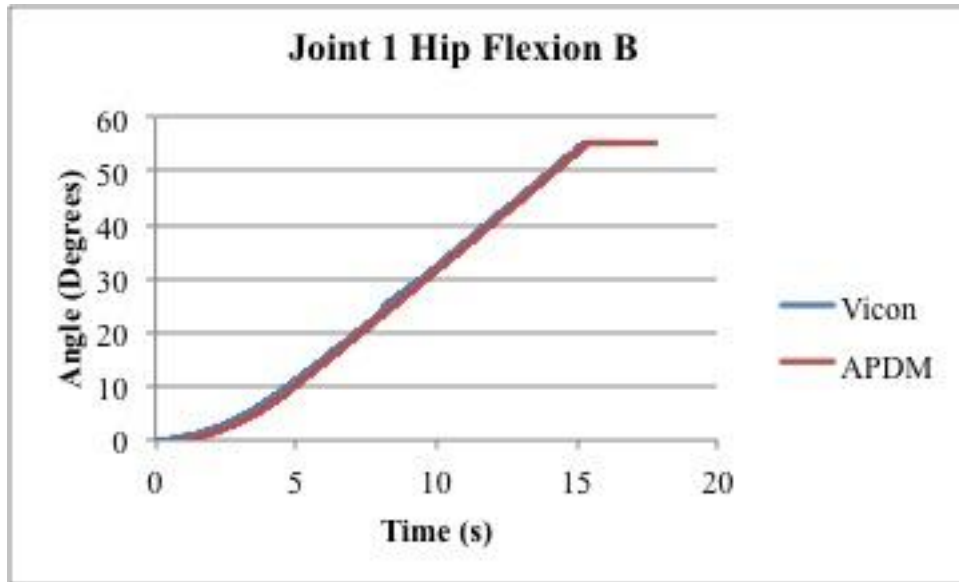


Figure 16 Joint 1 Hip Flexion B

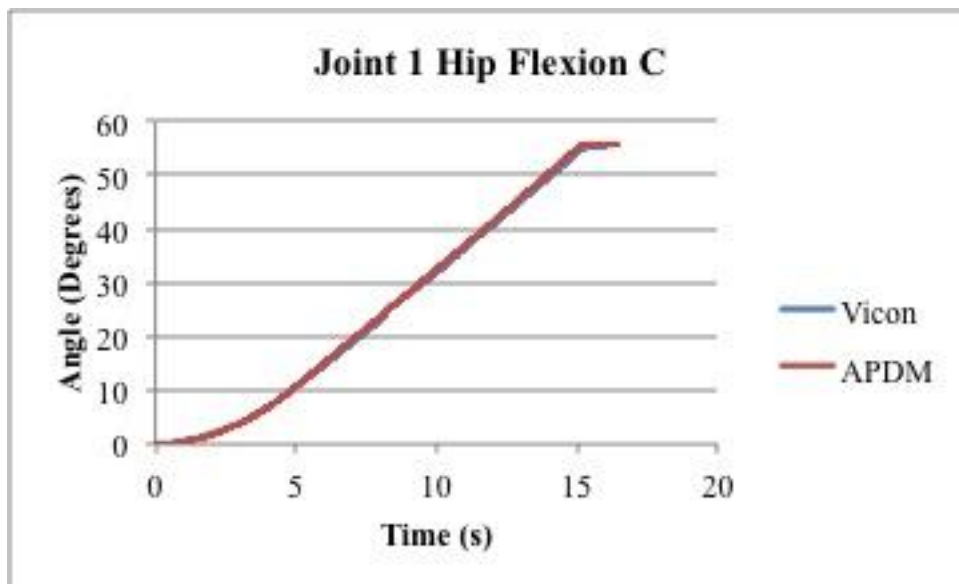


Figure 17 Joint 1 Hip Flexion C

The comparison of the angle measured by the Vicon system and the APDM system for joint 1 hip extension A is shown in Figure 18. The movement of joint 1 hip extension B is shown in Figure 19. The movement of joint 1 hip extension at speed C is shown in Figure 20.

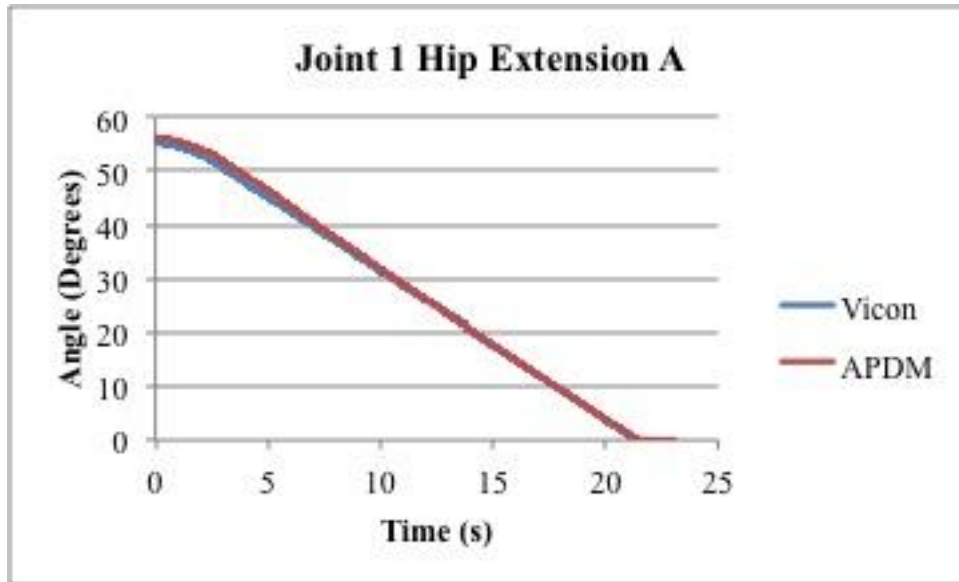


Figure 18 Joint 1 Hip Extension A

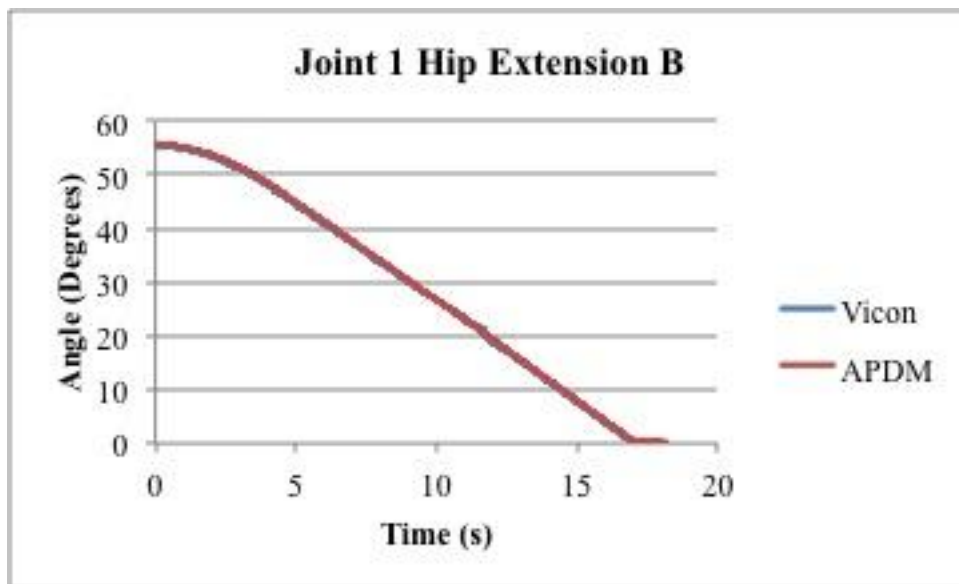


Figure 19 Joint 1 Hip Extension B

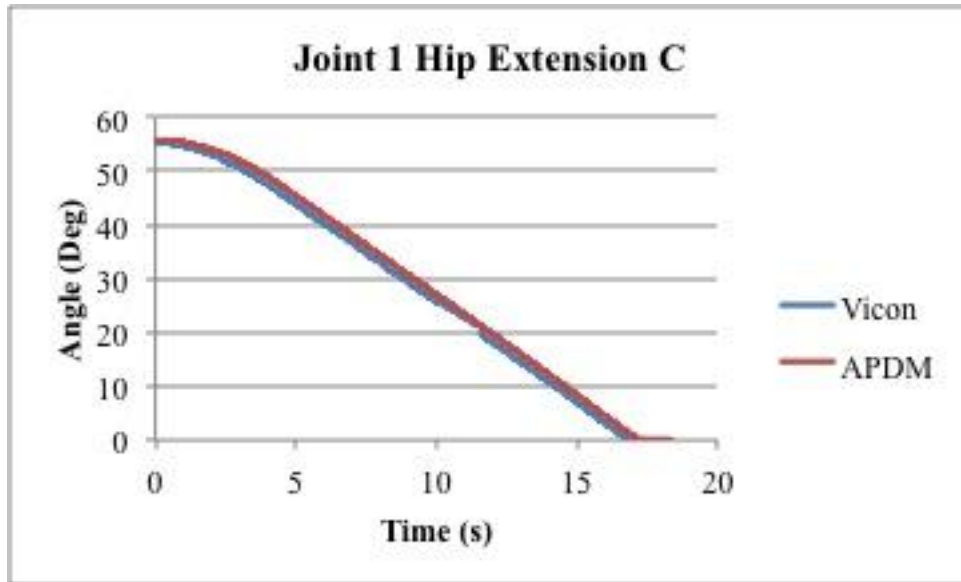


Figure 20 Joint 1 Hip Extension C

Four trials were recorded during the movement of joint 3, representative of internal and external rotation, at speeds A and B. Figure 21 and Figure 22 shows the movement of joint 3 hip internal rotation at speeds A and B respectively.

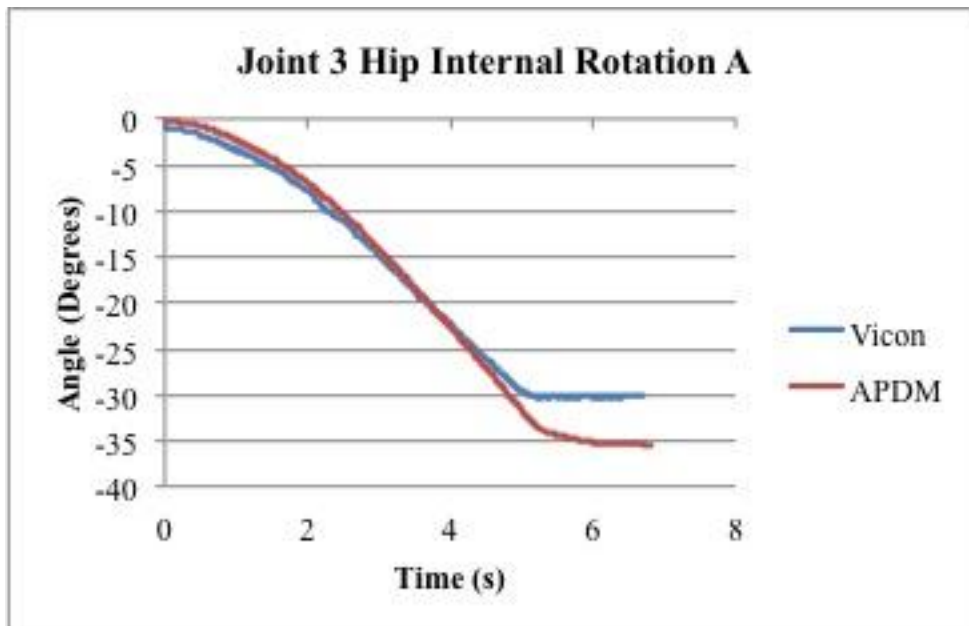


Figure 21 Joint 3 Hip Internal Rotation A

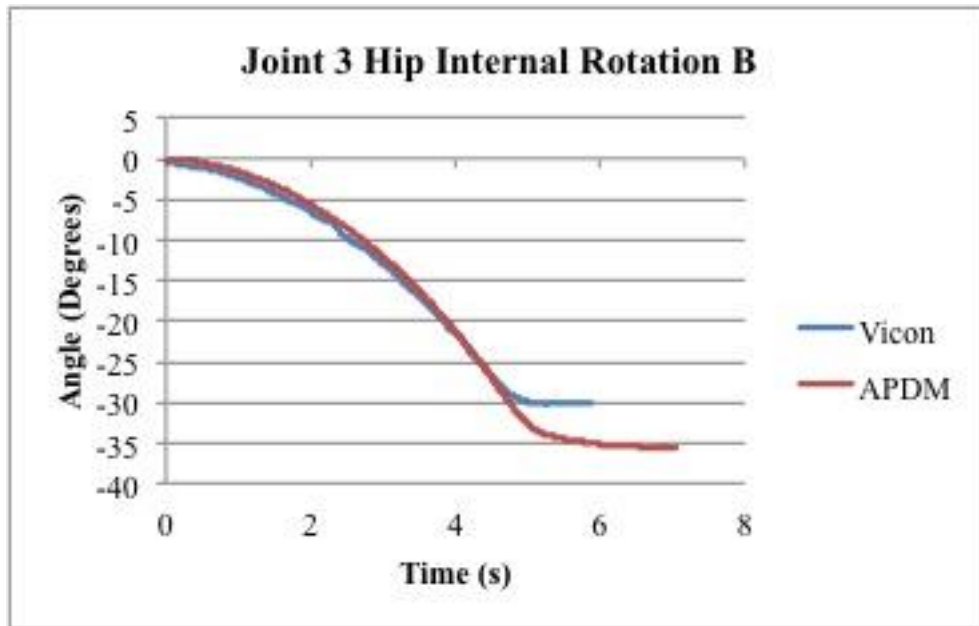


Figure 22 Joint 3 Hip Internal Rotation B

The movement of joint 3 hip external rotation at speeds A and B is shown in Figure 23 and Figure 24.

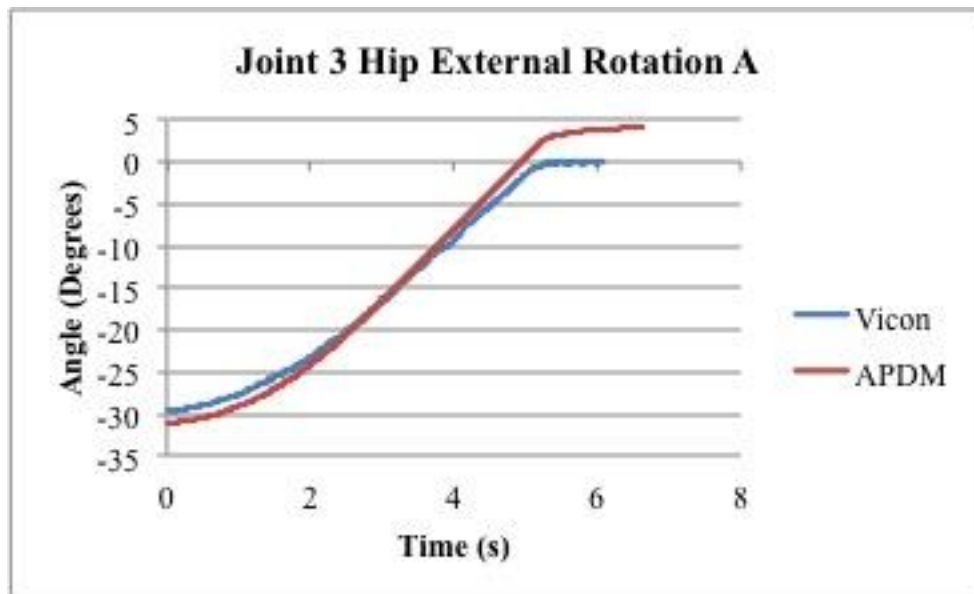


Figure 23 Joint 3 Hip External Rotation A

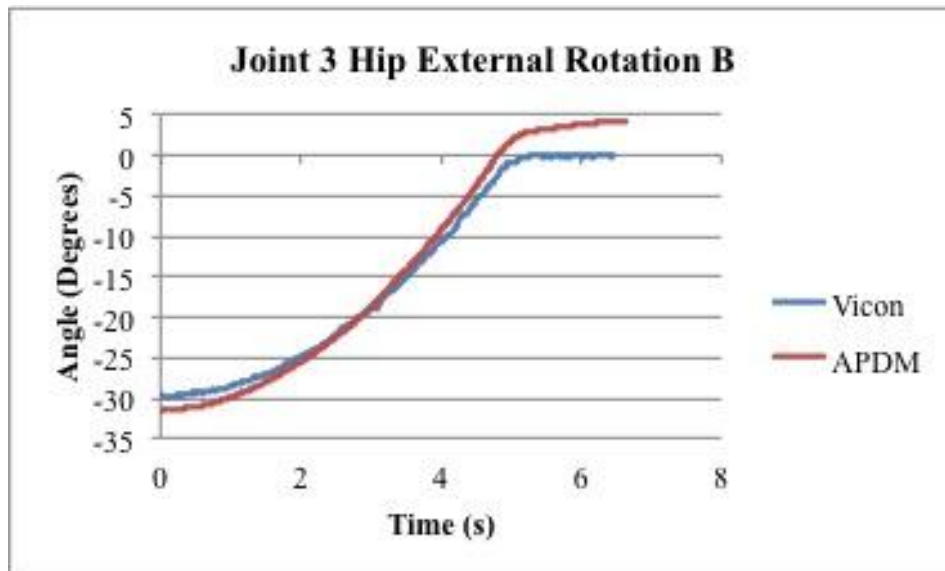


Figure 24 Joint 3 Hip External Rotation B

There were six trials recorded for joint 4, representative of knee flexion and extension at speeds A, B and C. The Vicon and systems are shown in the plots by the blue and red lines respectively. Figure 25, Figure 26 and Figure 27 show joint 4 knee flexion at speeds A, B and C.

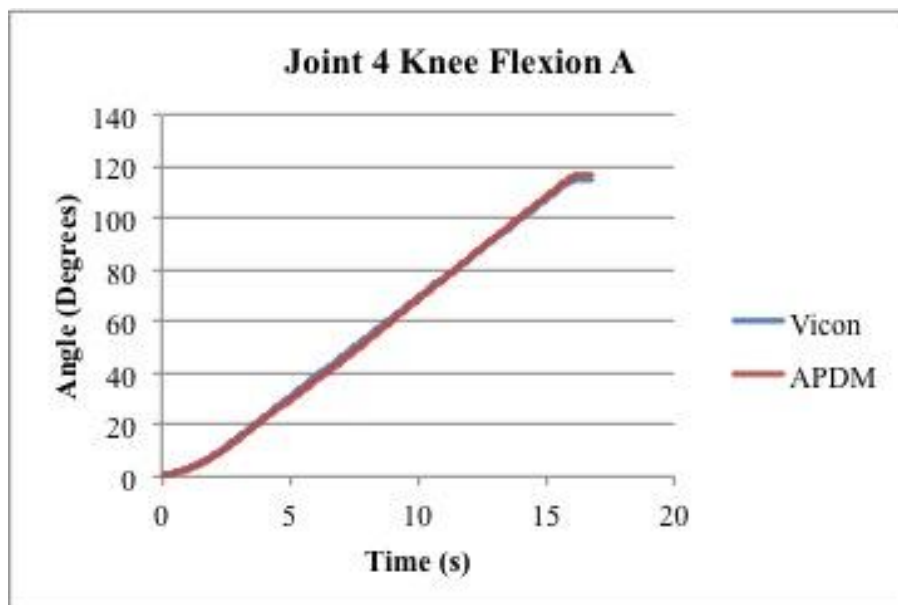


Figure 25 Joint 4 Knee Flexion A

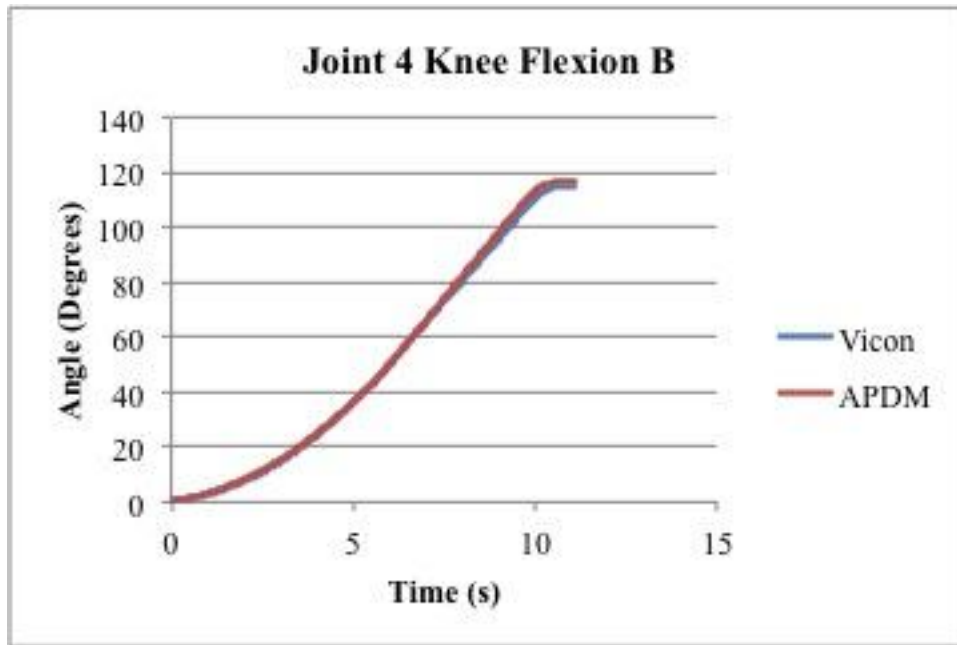


Figure 26 Joint 4 Knee Flexion B

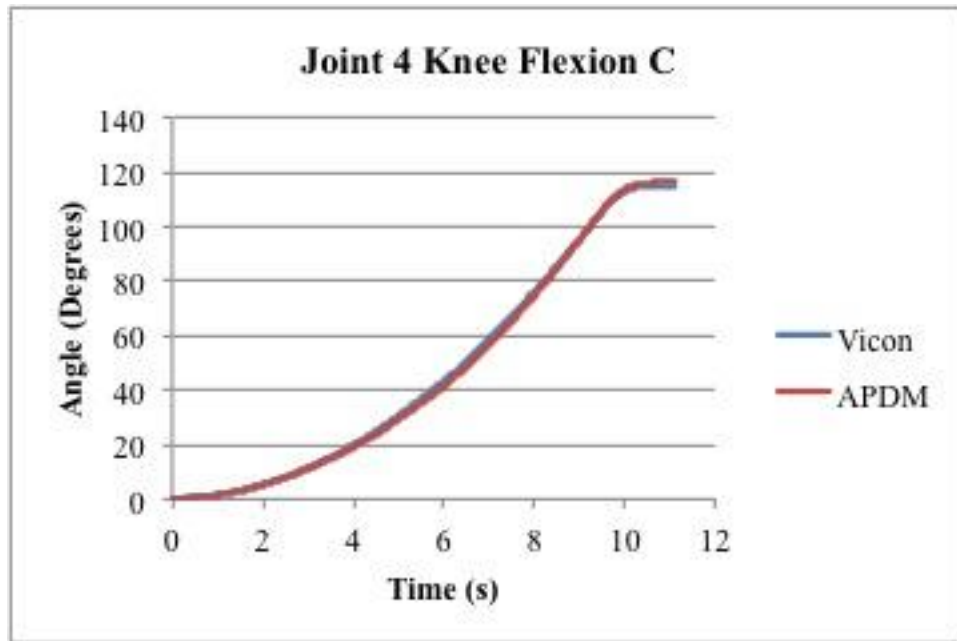


Figure 27 Joint 4 Knee Flexion C

Joint 4, representative of knee extension, at speeds A, B and C are shown in Figure 28, Figure 29 and Figure 30.

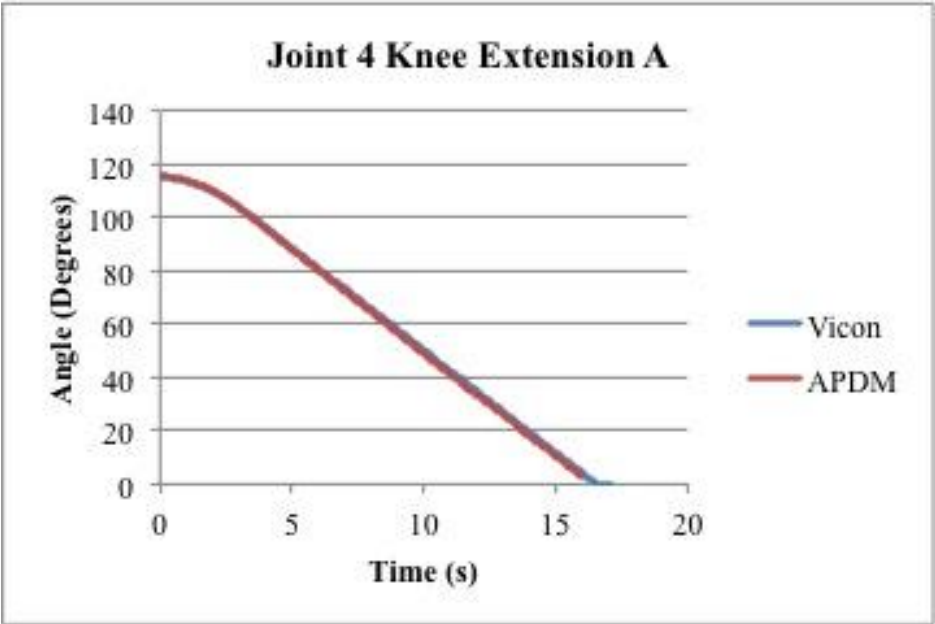


Figure 28 Joint 4 Knee Extension A

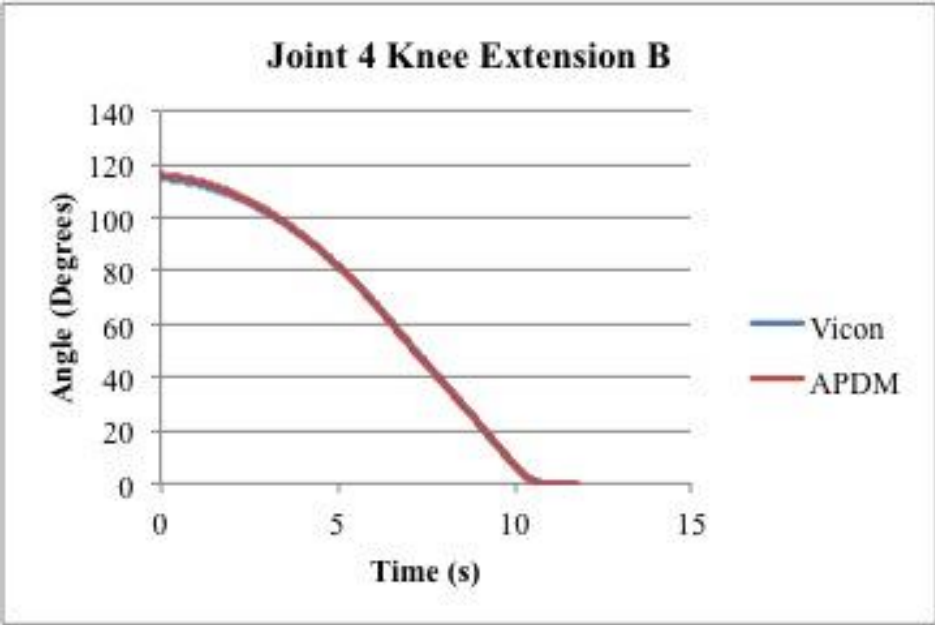


Figure 29 Joint 4 Knee Extension B

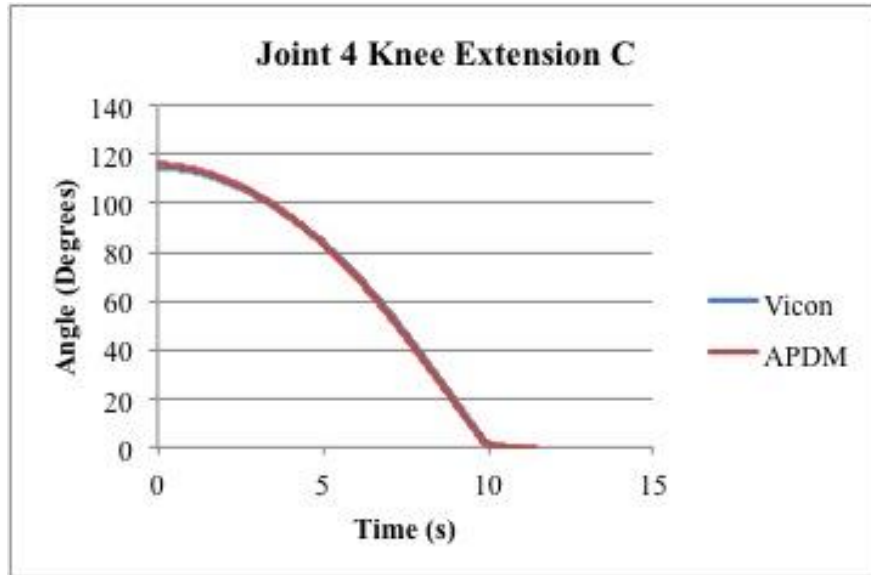


Figure 30 Joint 4 Knee Extension C

Table 4 shows the RMSE in degrees between the Vicon and APDM joint angle calculations for the single joint movements. The joint 4 “knee” angles for the APDM sensors were calculated using the two-sensor algorithm (Equations 2-6). The Pearson’s R correlation values were all 0.999 except joint 3 hip internal rotation B which was 0.996.

Table 4 RMSE Between Vicon and APDM Sensors

Joint	Movement	RMSE (Degrees)
Joint 1	Hip Extension A	0.8
	Hip Extension B	0.4
	Hip Extension C	1.4
	Hip Flexion A	1.3
	Hip Flexion B	0.9
	Hip Flexion C	0.5
Joint 3	Hip External Rotation A	2.1
	Hip External Rotation B	2.1
	Hip Internal Rotation A	2.4
	Hip Internal Rotation B	1.8
Joint 4	Knee Extension A	1.0
	Knee Extension B	0.8
	Knee Extension C	0.9
	Knee Flexion A	1.0
	Knee Flexion B	1.4
	Knee Flexion C	1.1

The knee angle or joint 4 angle was calculated three different ways: the Vicon system, with the two-sensor algorithm and the sensor directly on the joint. An example of the comparison between the angles calculated by the Vicon system, two-sensor algorithm and the sensor on joint 4 are shown in Figure 31. The blue line represents the Vicon system, the red line is the two-sensor algorithm and the orange line is the sensor directly on joint 4.

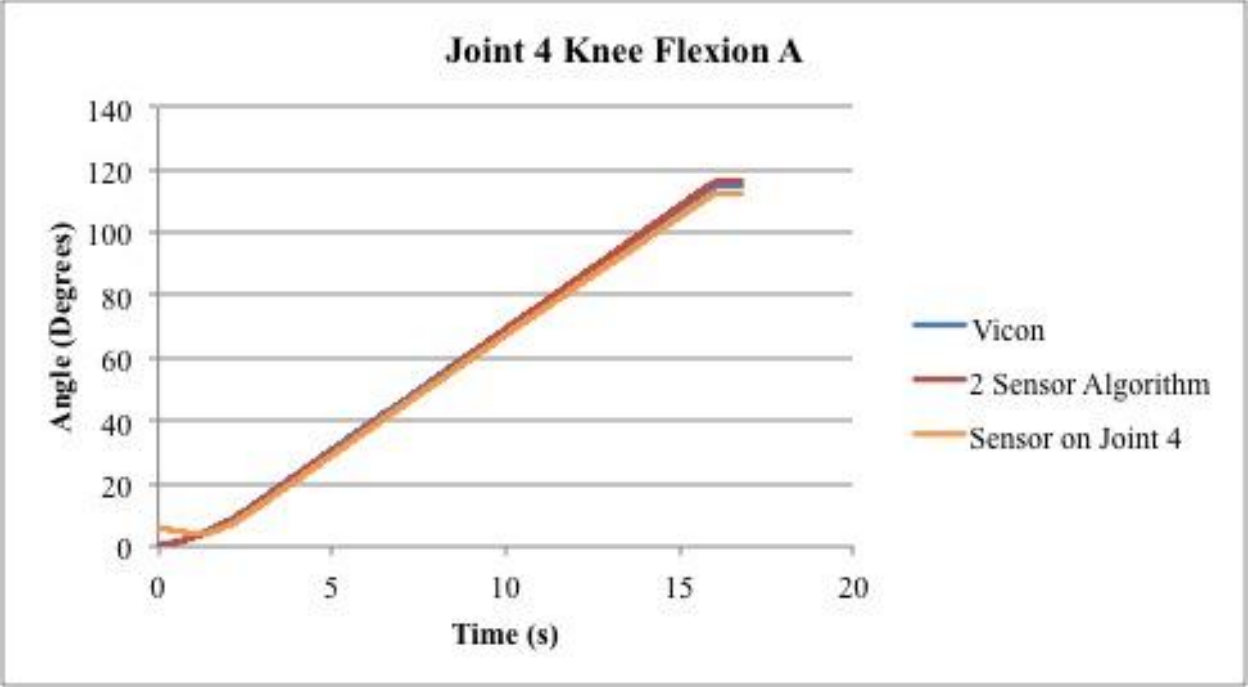


Figure 31 Comparison Between Algorithm and Sensor On Joint 4

The RMSE between the Vicon and the two-sensor algorithm, between the Vicon and the sensor on joint 4 and the two-sensor algorithm and the sensor directly on the joint 4 is shown in Table 5. The Pearson’s R correlation values were all 0.999.

Table 5 RMSE for 3 Methods of Knee Angle Calculation

	Movement	RMSE (Degrees)		
		Vicon and 2 Sensor Algorithm	Vicon and Sensor on Joint	2 Sensor Algorithm and Sensor on Joint
Joint 4	Knee Flexion A	1.0	2.0	2.2
	Knee Flexion B	1.4	1.2	1.9
	Knee Flexion C	1.1	2.2	2.2
	Knee Extension A	1.0	2.3	2.5
	Knee Extension B	0.8	3.9	4.2
	Knee Extension C	0.9	2.1	2.7

Table 6 shows the angular velocity in degrees per second for each of the three systems:

Vicon, APDM and WMRA.

Table 6 Angular Velocity

Link	Movement	Angular Velocity (deg/s)		
		Vicon	APDM	WMRA
Link 1	Hip Flexion A	2.6	2.7	2.6
	Hip Flexion B	3.4	3.3	3.5
	Hip Flexion C	3.5	3.6	3.6
	Hip Extension A	-2.5	-2.0	-2.5
	Hip Extension B	-3.1	-2.8	-3.2
	Hip Extension C	-3.2	-2.9	-3.2
Link 2	Hip Internal Rotation A	-4.3	-4.1	-5.2
	Hip Internal Rotation B	-4.5	-4.4	-5.7
	Hip External Rotation A	4.9	4.5	5.2
	Hip External Rotation B	4.7	4.7	6.0
	Knee Flexion A	6.8	6.3	6.8
	Knee Flexion B	10.3	9.7	10.2
	Knee Flexion C	10.2	10.1	10.8
	Knee Extension A	-6.7	-6.7	-6.8
	Knee Extension B	-9.6	-9.5	-10.1
Knee Extension C	-10.2	-10.1	-10.7	

All three joints were moved simultaneously during the 3-dimensional motion for five cycles, and two separate trials. The two trials for joint 1 are shown in Figure 32 and Figure 33.

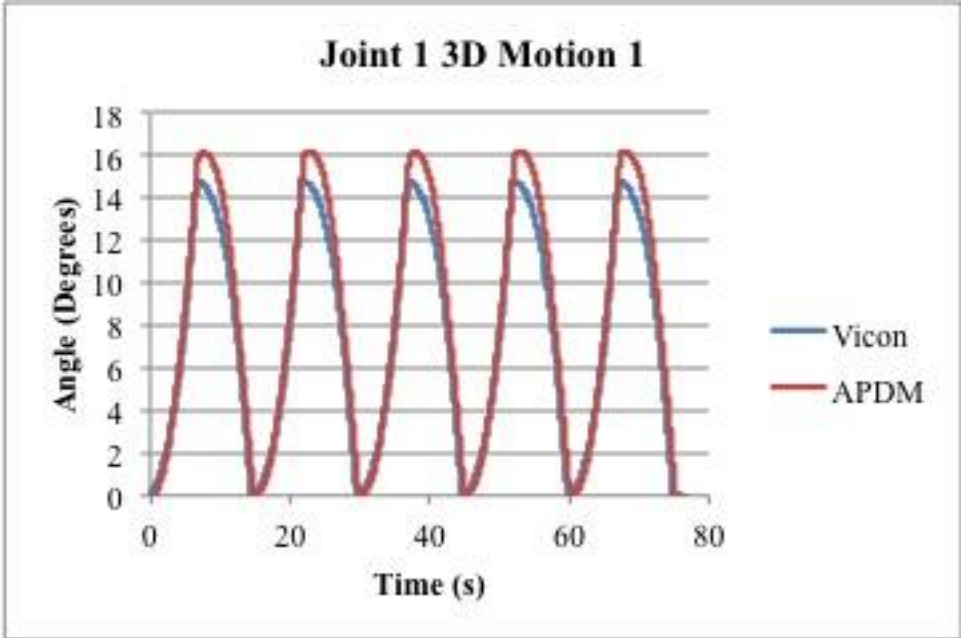


Figure 32 Joint 1 3D Motion 1

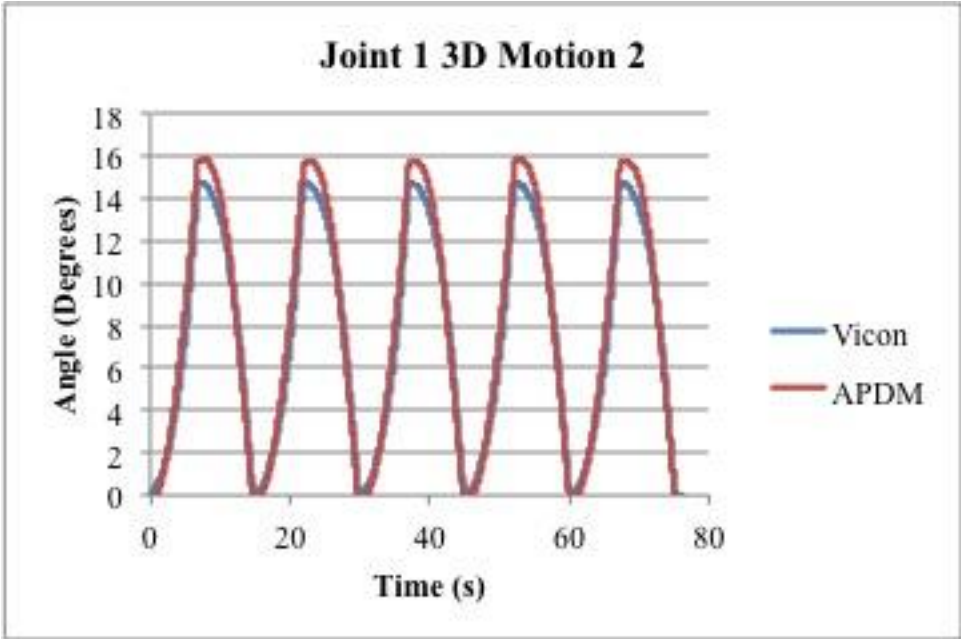


Figure 33 Joint 1 3D Motion

The movement of joint 3 during the 3-D trials is shown in Figure 34 and Figure 35.

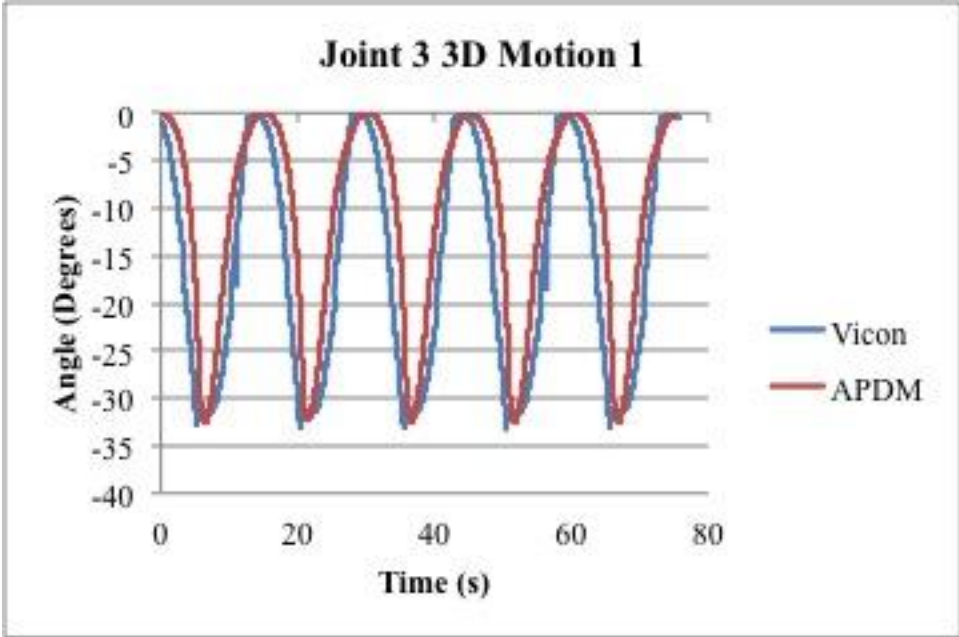


Figure 34 Joint 3 3D Motion 1

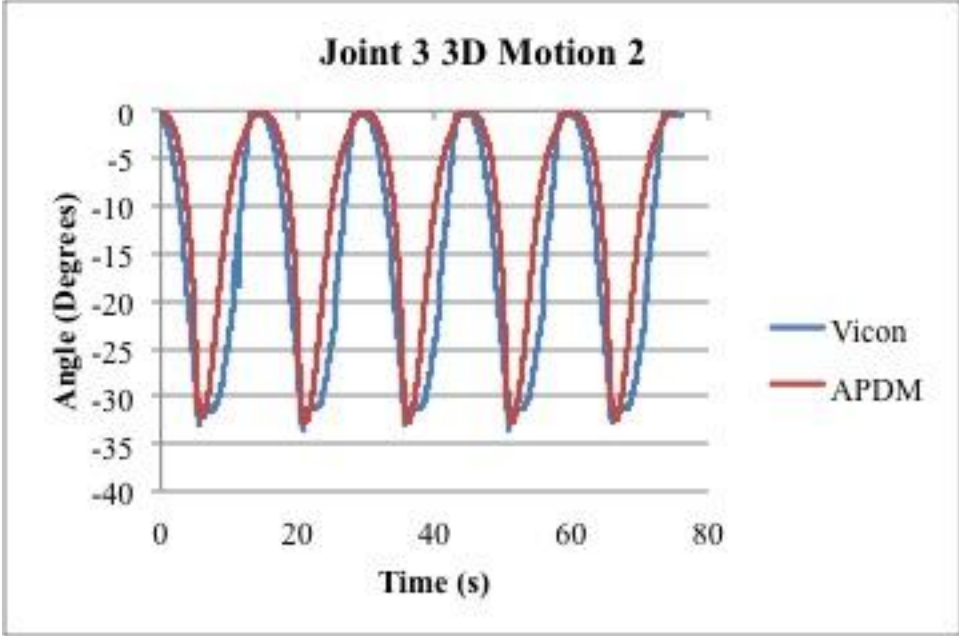


Figure 35 Joint 3 3D Motion 2

The movement of joint 4 during the 3-D trials is shown in Figure 36 and Figure 37.

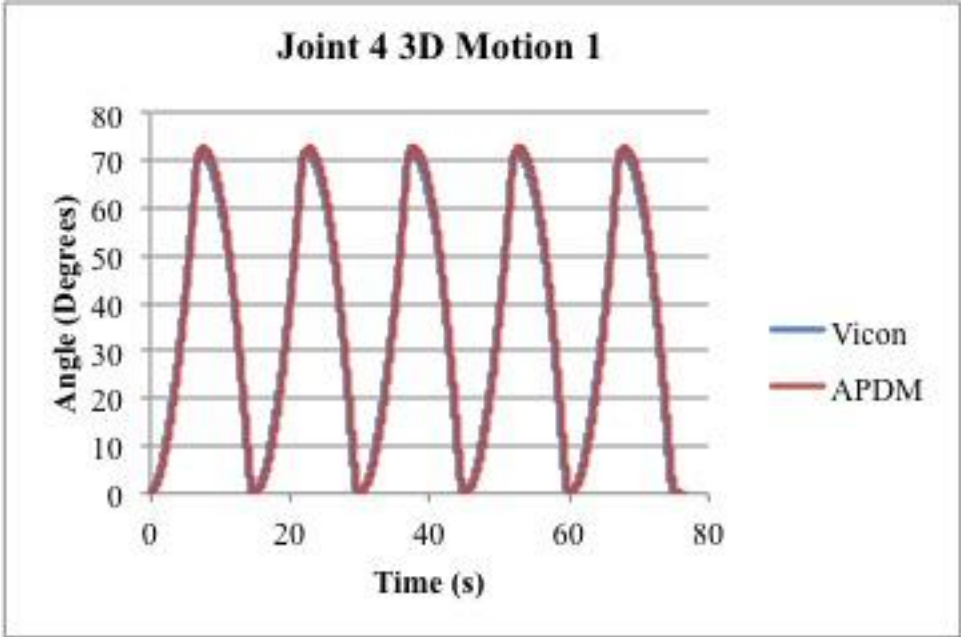


Figure 36 Joint 4 3D Motion 1

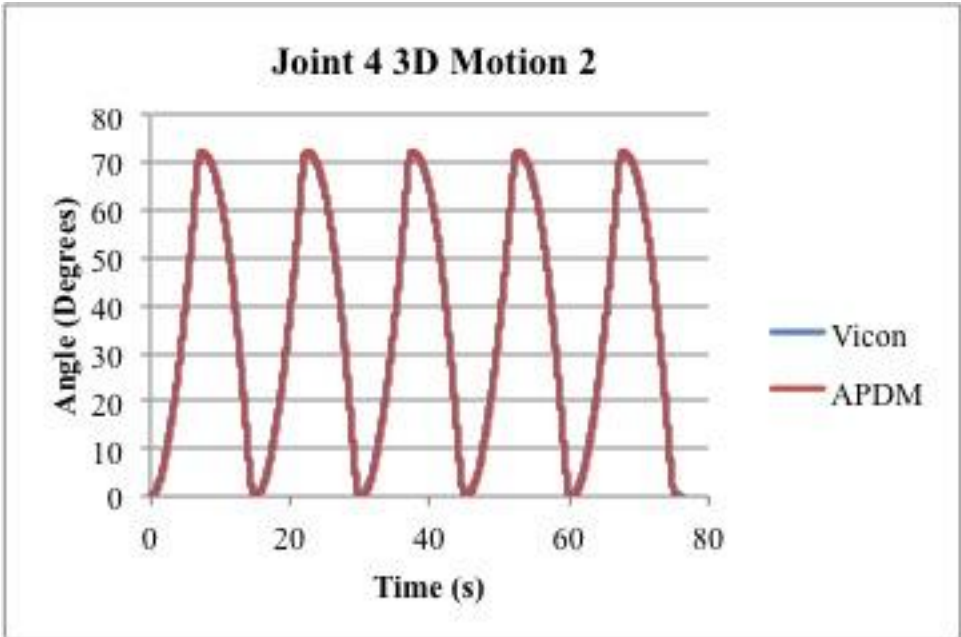


Figure 37 Joint 4 3D Motion 2

The RMSE and Pearson's R correlation between the APDM and Vicon calculations for 3D motion trials 1 and 2 are shown in Table 7.

Table 7 RMSE and R Values for 3D Motion Trials 1 & 2

APDM vs Vicon				
Joint	3D Motion 1		3D Motion 2	
	RMSE (Deg)	Pearson's R	RMSE (Deg)	Pearson's R
Joint 1	1.1	1.0	0.8	1.0
Joint 3	7.0	0.9	6.8	0.9
Joint 4	4.0	1.0	0.8	1.0

5.1.2 Range of Motion Tests

Figure 38 shows the range of motion test during the Vicon data collection.

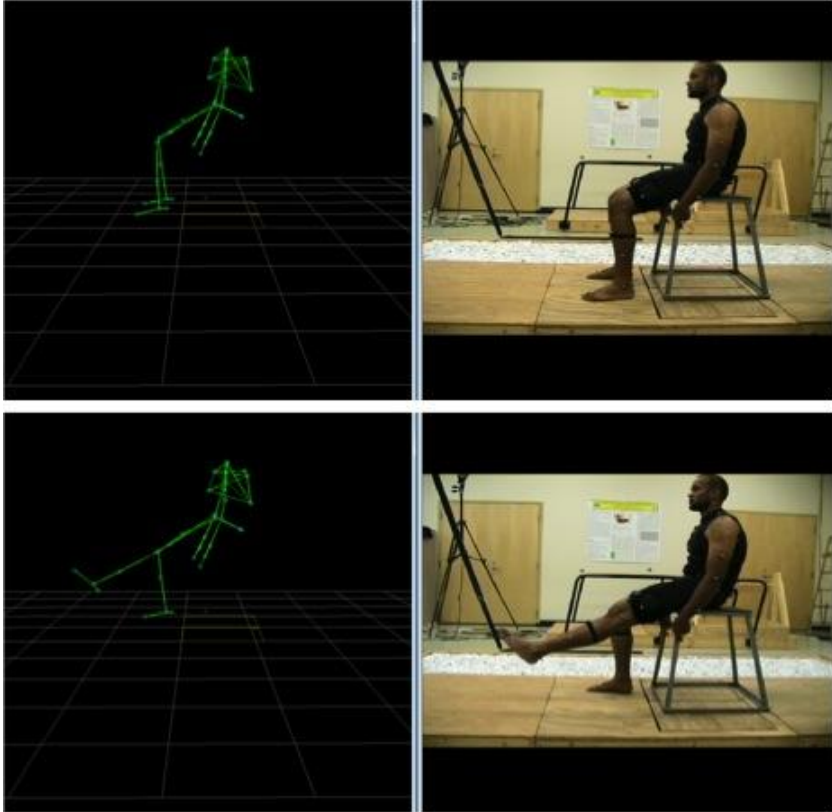


Figure 38 Range of Motion Test

The comparison between the knee flexion angle calculated by the WMAS and the Vicon system during the range of motion test is shown in Figure 39.

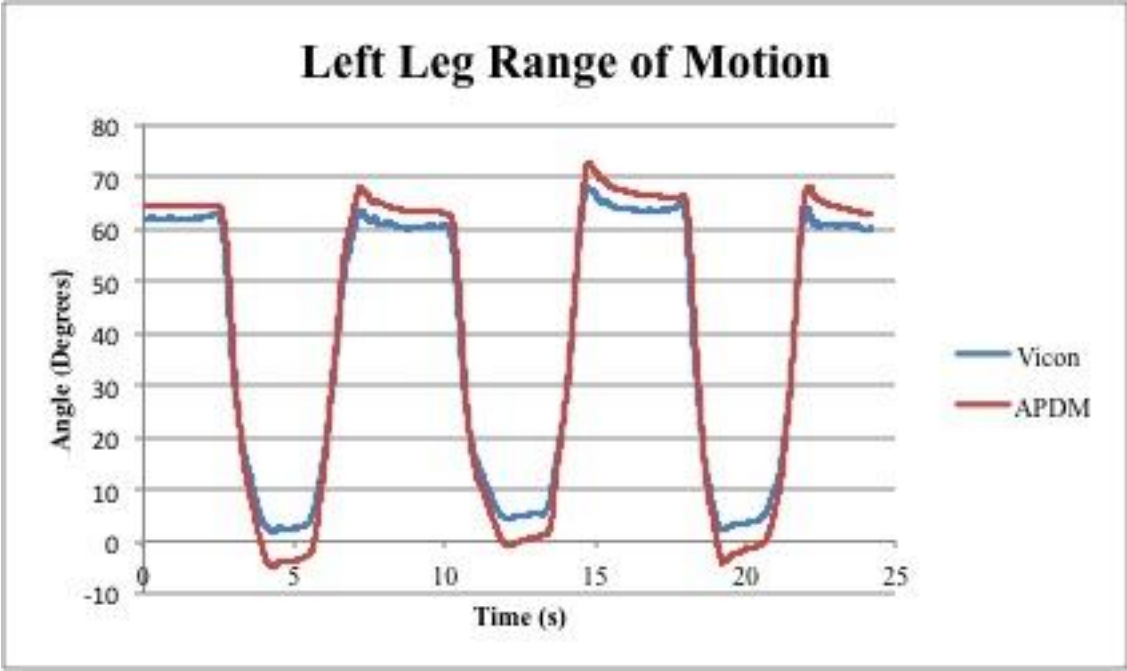


Figure 39 Left Knee Angle Range of Motion WMAS and Vicon

The RMSE and R Correlation for the range of motion tests are shown in Table 8.

Table 8 RMSE and R Values For Range of Motion Tests

Trial	Left Knee Angle	
	RMSE (Degrees)	R
ROM L1	4.0	0.998
ROM L2	4.1	0.998
ROM L3	4.3	0.998
Overall	4.1	0.998

5.1.3 Sit to Stand Tests

The sit and stand positions, as well as the Vicon plug in gait model and autolabel are shown in Figure 40. Figure 41 shows the comparison between the WMAS and Vicon calculated right knee angles during the sit to stand test.

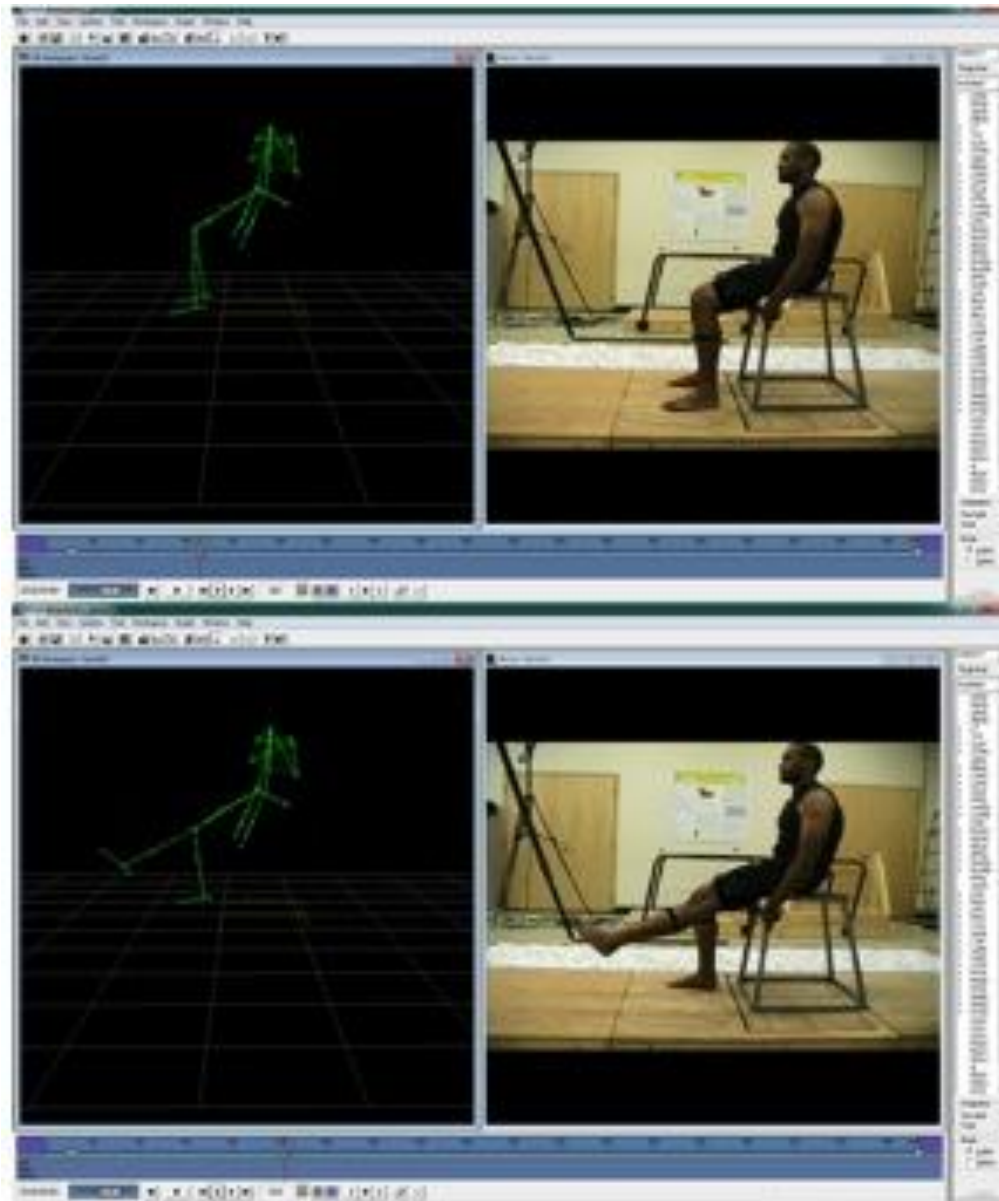


Figure 40 Sit To Stand Test in Vicon Workstation

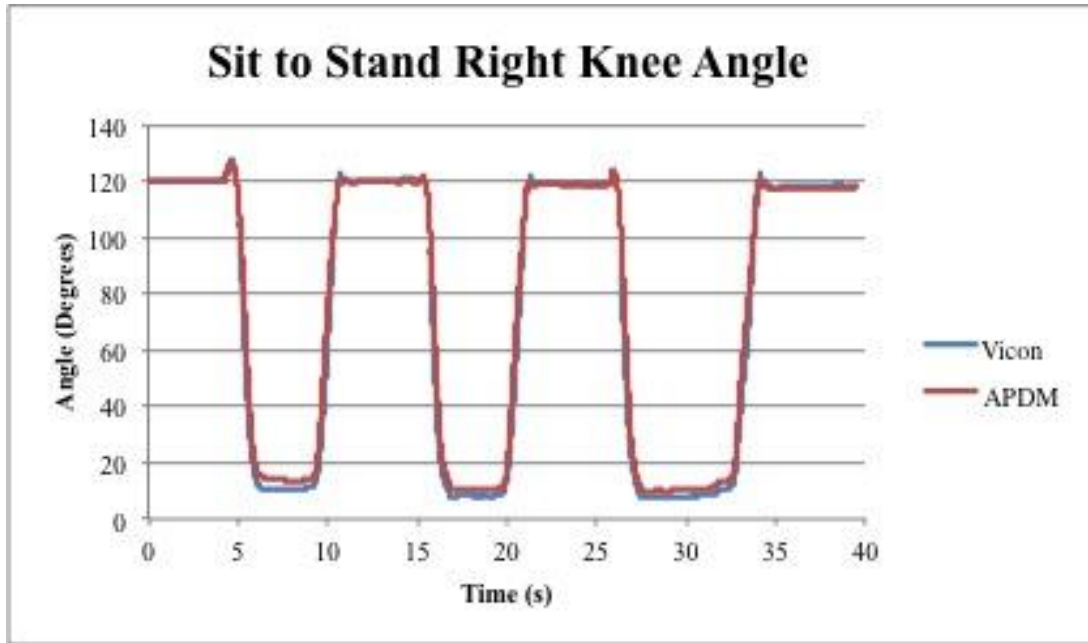


Figure 41 Right Knee Angle During Sit To Stand

The RMSE and R Values are shown in Table 9.

Table 9 RMSE and R Values For Sit To Stand Testing

Trial	Right Knee Angle		Left Knee Angle	
	RMSE (Degrees)	R	RMSE (Degrees)	R
STS 2	4.0	0.999	4.0	0.998
STS 4	5.2	0.999	5.4	0.999
STS 5	4.1	0.998	4.2	0.998
Overall	4.4	0.999	4.5	0.998

5.2 WMAS

The WMAS calculates knee flexion angle, stride length, and cadence. The results for each of these parameters are in sections 5.2.1, 5.2.2 and 5.2.3 respectively. The graphical user interface is also shown in section 5.2.4.

5.2.1 Knee Angle

Examples of the right knee flexion angle with the WMAS and Vicon system overlaid are shown in the following figures. An example of the right knee flexion angle during one slow gait cycle is shown in Figure 42. The knee flexion angle in degrees is shown as percent gait cycle. The WMAS angle is shown in red and the Vicon angle is shown in blue.

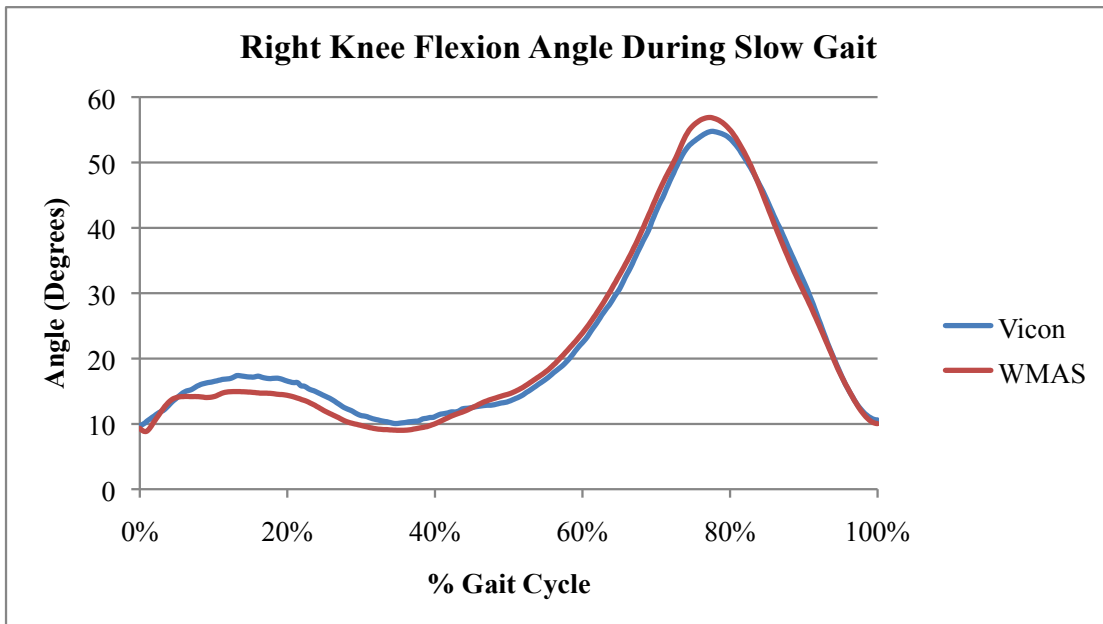


Figure 42 Right Knee Flexion Angle During One Slow Gait Cycle

An example of the right knee flexion angle during one normal gait cycle is shown in Figure 43. The blue line represents the knee flexion angle in degrees calculated by the Vicon system and the red line is the knee flexion angle calculated by the WMAS.

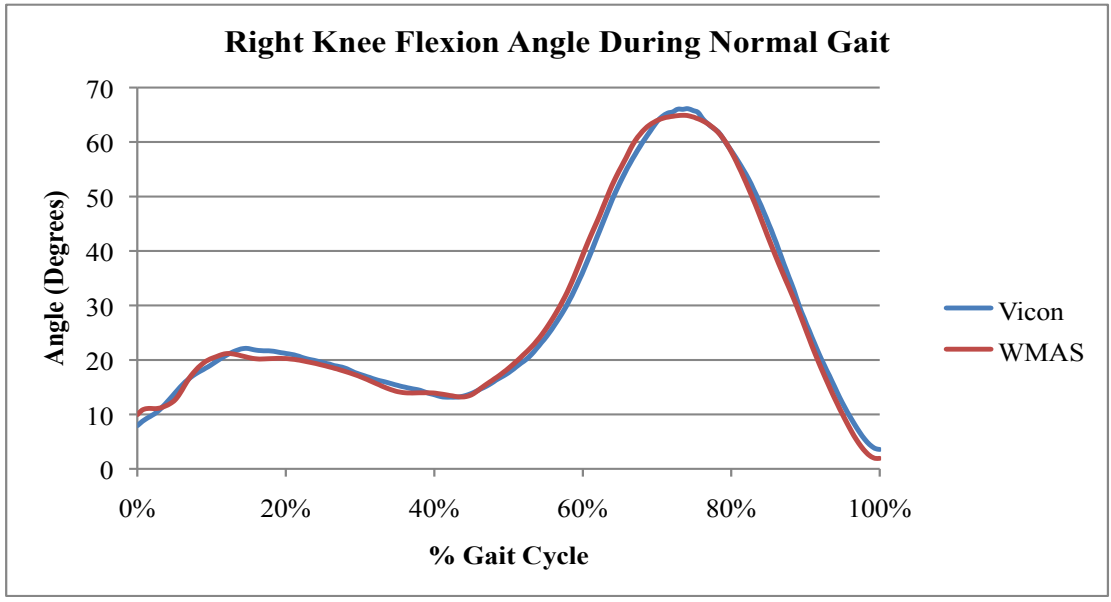


Figure 43 Right Knee Flexion Angle During One Normal Gait Cycle

Figure 44 shows an example of the right knee flexion angle calculated by both the WMAS and Vicon systems during one fast gait cycle.

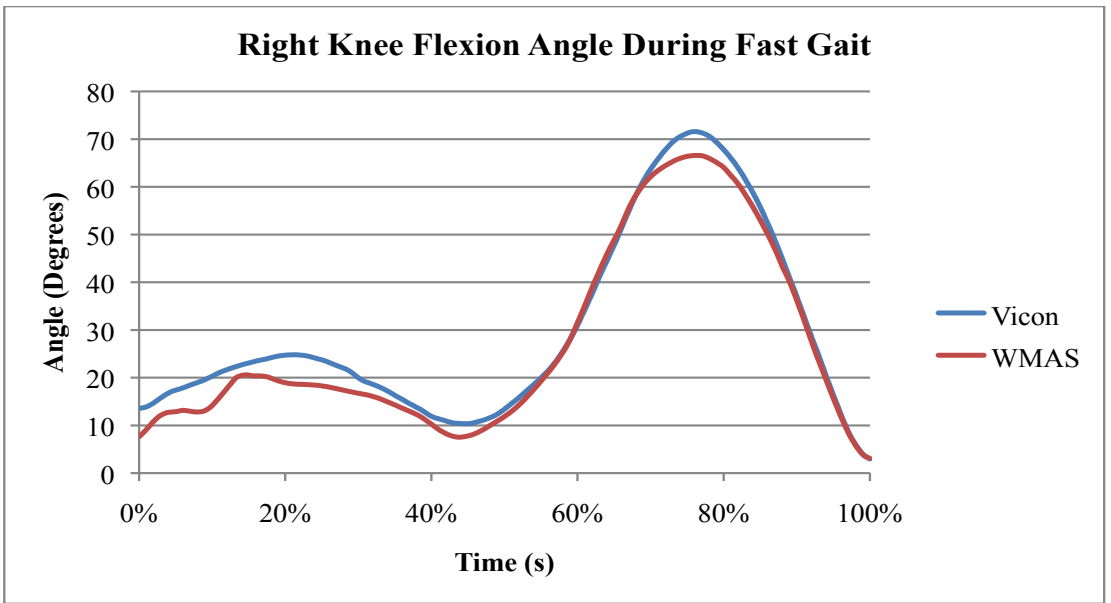


Figure 44 Right Knee Flexion Angle During One Fast Gait Cycle

The WMAS and Vicon knee flexion angles were compared for the all of the gait trials. The RMSE and R correlations values the knee flexion angle for the slow, normal and fast speeds is shown in Table 10.

Table 10 RMSE and R Values For Knee Flexion Angle

Speed	RMSE Right Knee Flexion (Degrees)	Pearson's R Right Knee Flexion	RMSE Left Knee Flexion (Degrees)	Pearson's R Left Knee Flexion
Slow	3.3	0.992	3.9	0.983
Normal	3.3	0.989	3.9	0.988
Fast	4.1	0.978	4.4	0.987
Overall	3.5	0.988	3.3	0.986

Each gait trial was separated in gait cycles and the maximum knee flexion angle was identified. The maximum knee flexion angle from the WMAS compared to the Vicon maximum knee flexion for each gait cycle. The RMSE for both the right and left knees at each of the three speeds is shown in Table 11.

Table 11 RMSE For Maximum Knee Flexion

Speed	RMSE Right Knee Max Flexion (Degrees)	RMSE Left Knee Max Flexion (Degrees)
Slow	2.6	2.3
Normal	2.6	2.8
Fast	3.5	3.4
Overall	2.8	2.8

The maximum knee flexion angle for one subject during slow gait as calculated by the WMAS and Vicon systems are compared in the Bland Altman plots shown in Figure 45. The top dashed line represents the mean of the APDM angle (degrees) minus the Vicon Angle (degrees) plus two standard deviations. The bottom dashed line represents the mean minus two

standard deviations. The upper and lower dashed lines are the limits of agreement. The center dashed line represents the mean for the maximum knee flexion angle in degrees. The Bland Altman plot for the maximum knee flexion during normal gait is Figure 46. The Bland Altman plot for the maximum knee flexion during fast gait is Figure 47.

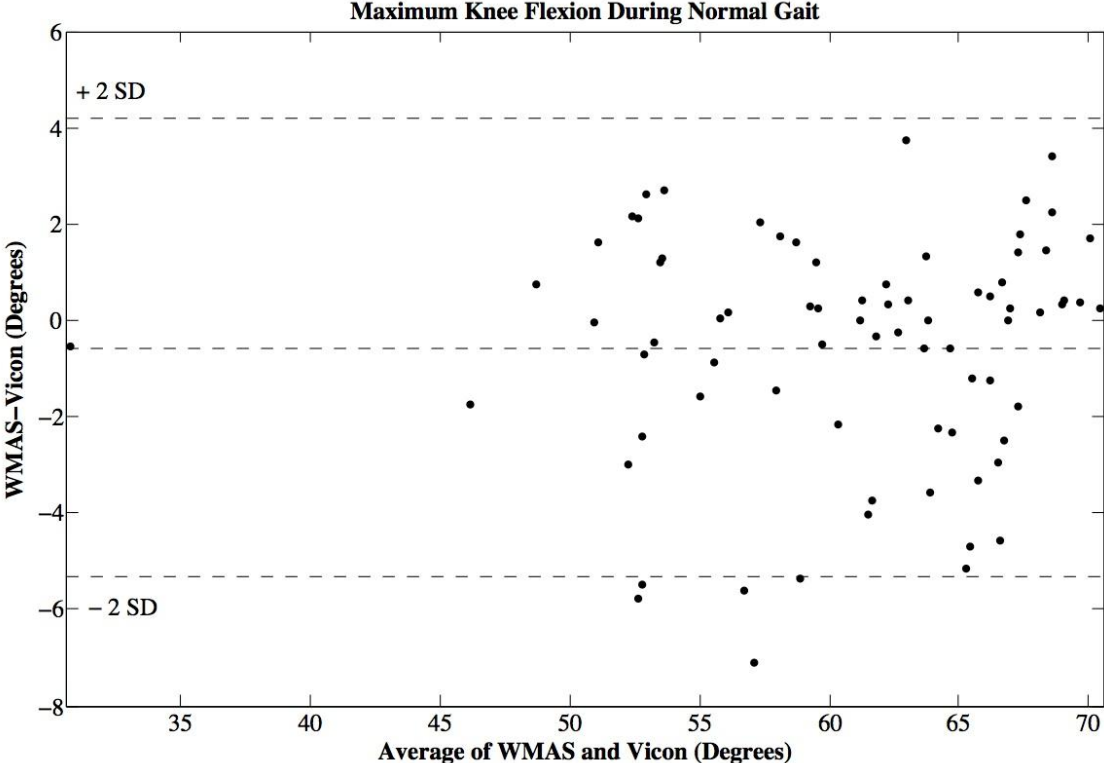


Figure 45 Bland Altman Plot: Maximum Knee Flexion During Slow Gait

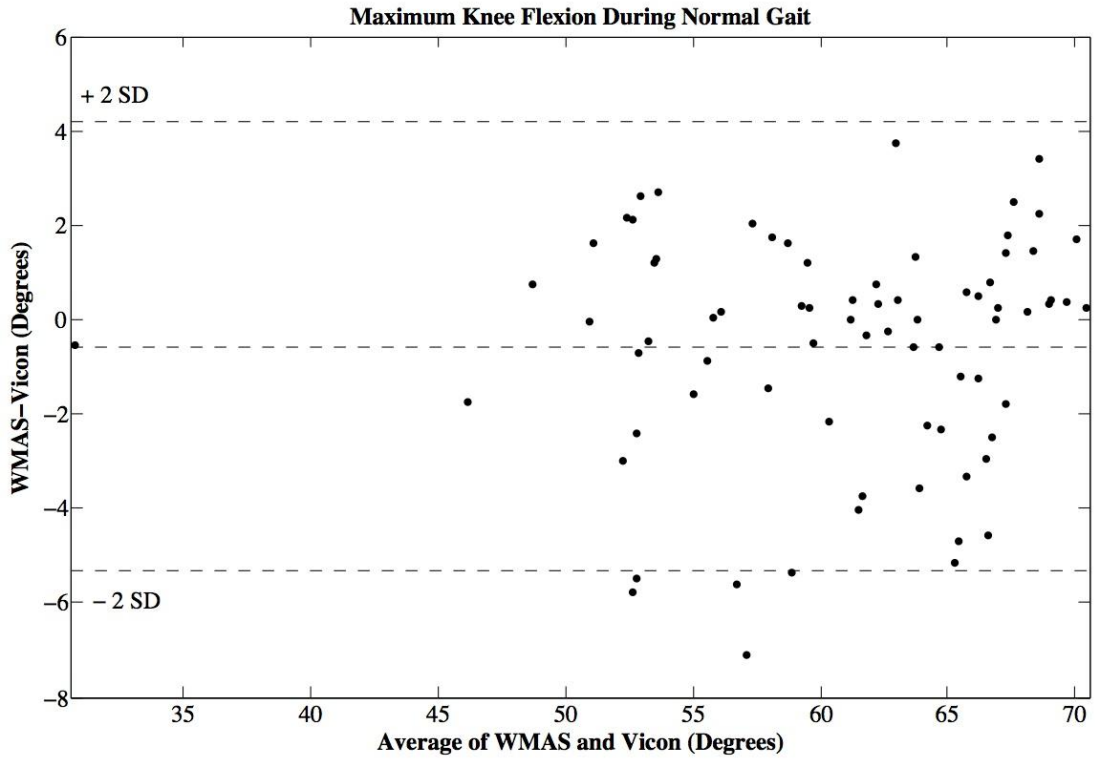


Figure 46 Bland Altman Plot: Maximum Knee Flexion During Normal Gait

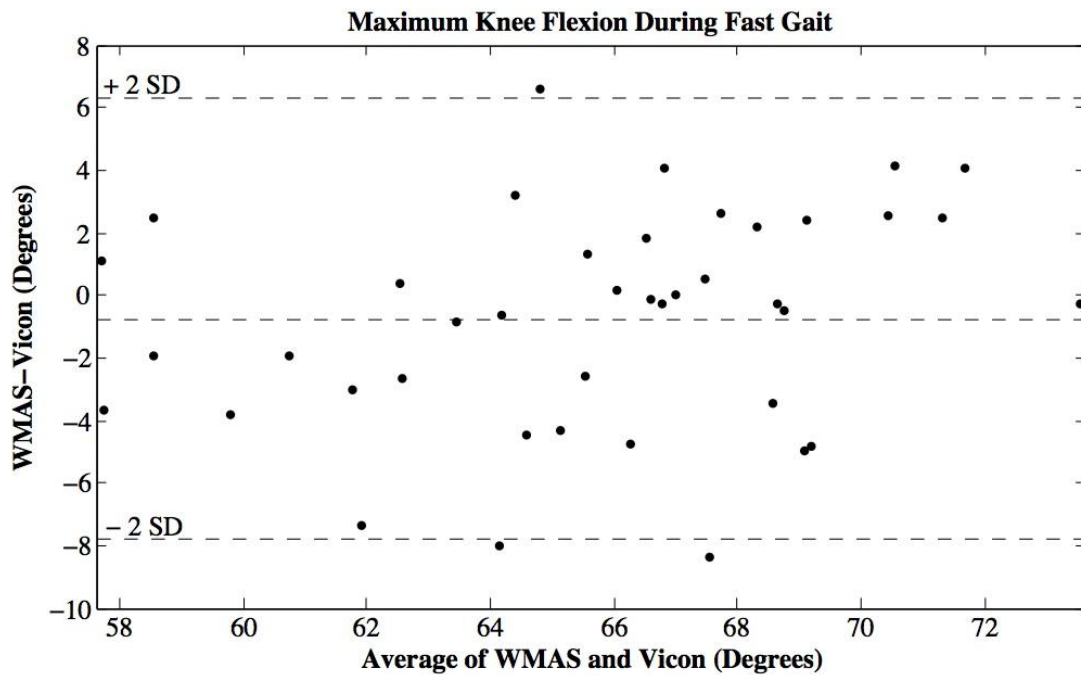


Figure 47 Bland Altman Plot: Maximum Knee Flexion During Fast Gait

5.2.2 Stride Length

The average stride length in meters at the slow, normal and fast speeds is shown in Table 12. The Pearson's R correlation values, RMSE and percent difference for stride length between the WMAS and Vicon system is shown in Table 13.

Table 12 Average Stride Length

Average Stride Length (m)		
Speed	Vicon	APDM
Slow	1.08	1.11
Normal	1.29	1.25
Fast	1.54	1.48
Overall	1.30	1.27

Table 13 Stride Length Statistics

Speed	Pearson's R	RMSE (m)	Percent Difference
Slow	0.91	0.056	1.96%
Normal	0.88	0.067	0.37%
Fast	0.87	0.136	5.31%
Overall	0.89	0.091	2.11%

Bland Altman plots for stride length are shown for the slow, normal and fast gait speeds for one subject in Figure 48, Figure 49 and Figure 50.

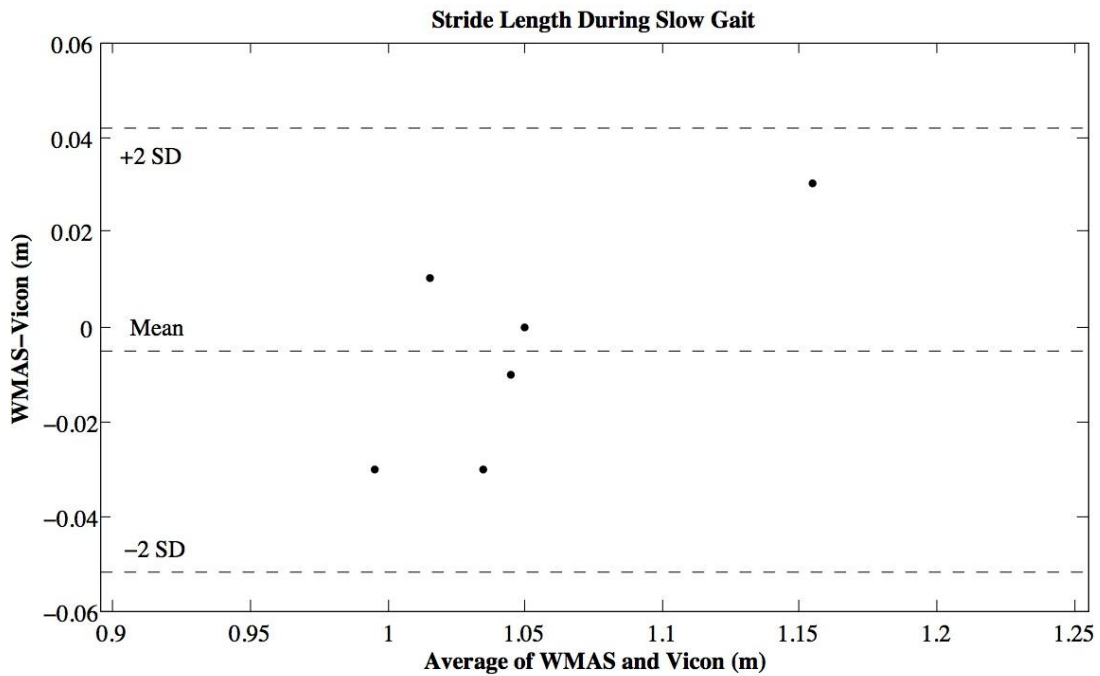


Figure 48 Bland Altman Plot: Stride Length During Slow Gait

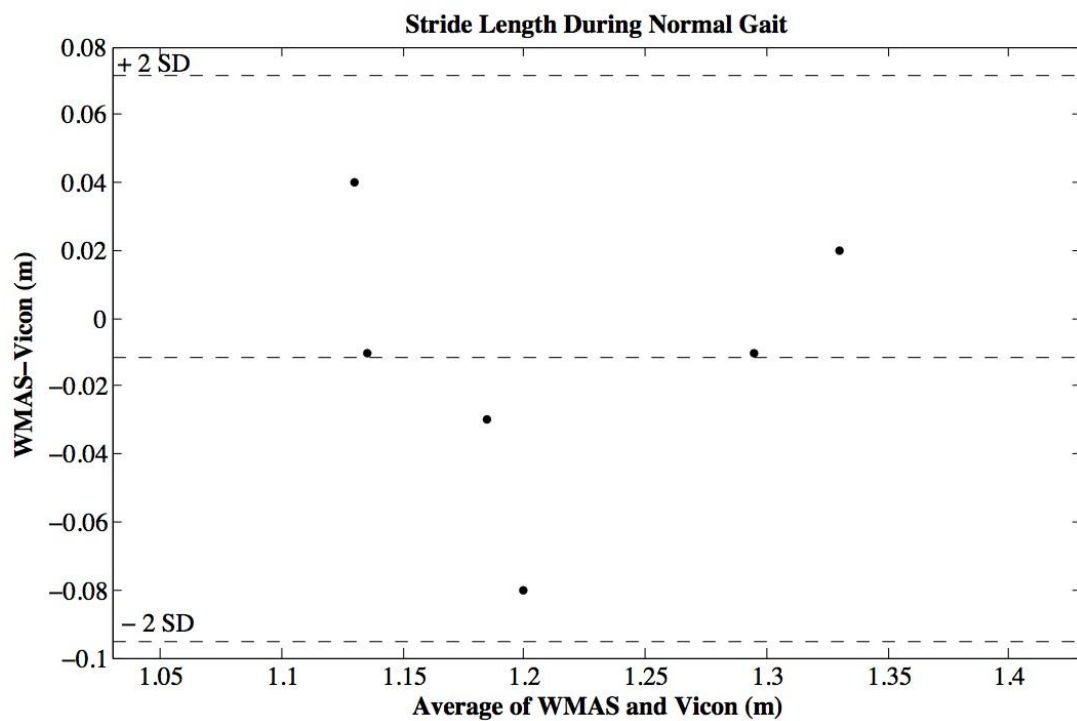


Figure 49 Bland Altman Plot: Stride Length During Normal Gait

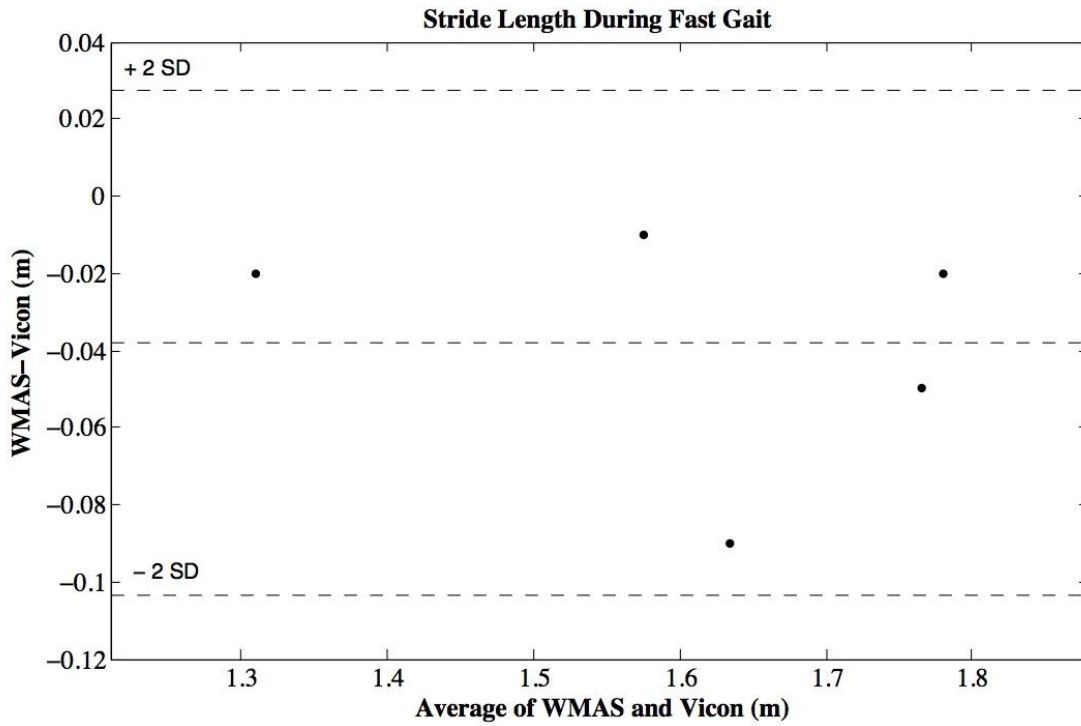


Figure 50 Bland Altman Plot: Stride Length During Fast Gait

5.2.3 Cadence

Cadence was calculated from the WMAS and Vicon system and the results are shown in Table 14. The average cadence is reported in steps per minute at each of the three speeds.

Table 14 Average Cadence

Speed	WMAS (steps/min)	Vicon (steps/min)	Pearson's R
Slow	70	71	0.951
Normal	96	94	0.933
Fast	123	120	0.908
Overall	96	95	0.931

5.2.4 Graphical User Interface

A graphical user interface (GUI) was created in Matlab to display the knee angle analysis as shown in Figure 51. The GUI has a drop down menu to select which trial to plot.

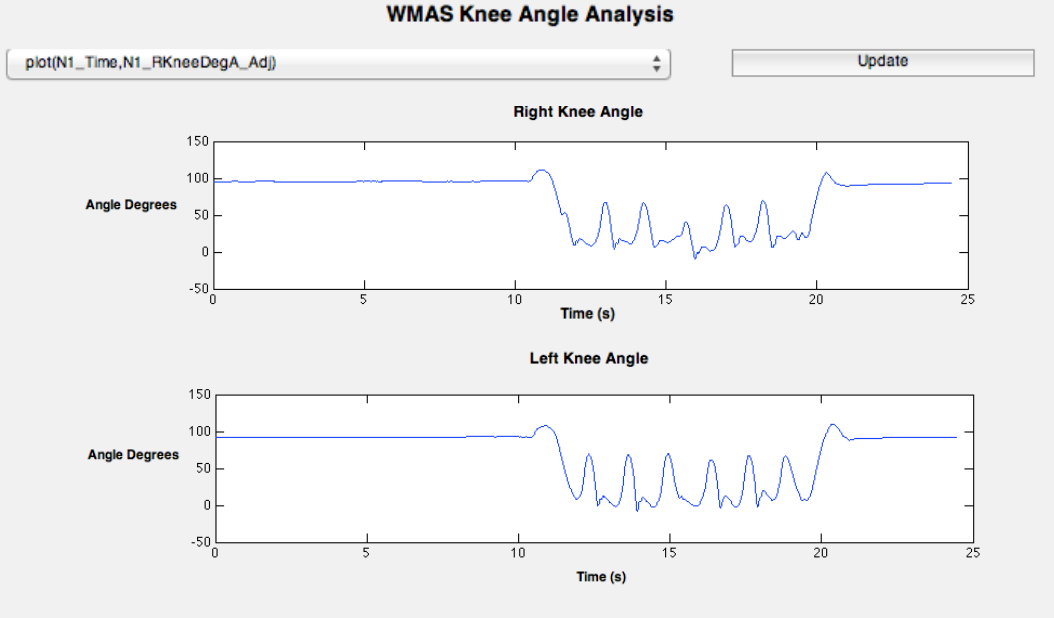


Figure 51 Knee Angle GUI

The GUI can also display two knee angle trials on top of each other as shown in Figure 52. This is a useful feature if you want to compare two separate trials, or a new to a baseline trial.

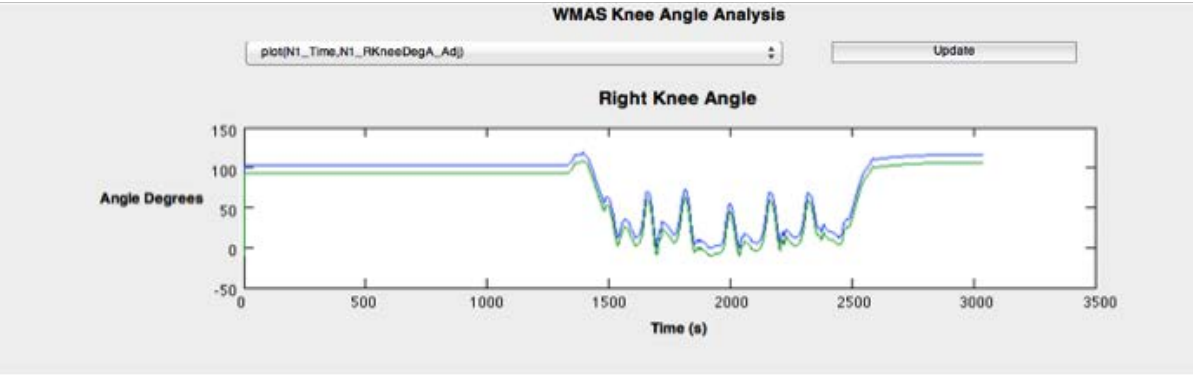


Figure 52 Knee Angle GUI Comparing Two Knee Angles

CHAPTER 6: DISCUSSION

6.1 Verification Tests

The purpose of the verification tests was to show that the WMAS algorithm calculated the knee flexion angle within 5 degrees of error relative to the gold standard Vicon motion capture system.

The first step of the verification testing used a robotic arm to provide a repeatable movement. These movements allowed for the comparison between the Vicon optical motion capture system and the APDM Opal IMU system in terms of joint angle calculation, angular velocity and trajectory recognition.

During the linear or single joint movements, the calculated joint angles from the Vicon, APDM and WMRA systems shown in Figures 4-6 were very similar. The three speeds did not seem to have a significant effect on the joint angle calculations. The joint angles calculated by the Vicon and APDM systems for the linear movements had an average RMSE of 1.2 degrees. The Vicon and APDM systems were also strongly correlated with a Pearson's R correlation value of 0.998. According to manufacturer, the APDM Opal sensors have a static roll/pitch orientation accuracy of 1.15 degrees, a static heading orientation accuracy of 1.50 degrees and dynamic orientation accuracy of 2.80 degrees [82]. Therefore, the quaternion-based algorithm improved the accuracy of the APDM sensors. The largest deviations in joint angle between the three systems were most apparent in the joint 3 hip internal and external rotation movements.

The APDM sensor begins to drift towards the end of each trial. Joint 3 hip internal and external rotation trials have an average RMSE between the Vicon and APDM sensors of 2.1 degrees; nearly double the average RMSE for all linear movements. This is because the APDM sensors begin to drift at the end of each trial.

When the Vicon system and two-sensor algorithm was compared the average RMSE for the knee flexion angle was 1.0 degree. Since the Vicon system is considered the gold standard for gait analysis, this shows that the two-sensor algorithm accurately calculates the knee flexion angle within a clinically acceptable range. The RMSE was less than the results reported by Schiefer et al. and Toffola et al [44, 45] and the manufacturer's specifications. The comparison between the Vicon system and sensor directly on joint 4 had a RMSE of 2.3, which was nearly double the error calculated by the two-sensor algorithm. The RMSE between the two-sensor algorithm and the sensor directly on the joint was 2.6 degrees.

The angular velocity measurements from the APDM sensors came directly from the data from the gyroscope sensor and the manufacturer's calibration, whereas the Vicon and WMRA angular velocities were calculated using the time and angle measurements. The correlation between the Vicon system and APDM average angular velocities was the highest with a Pearson's R-value of 0.999 and RMSE of 0.29 degrees per second. The WMRA and Vicon had a correlation value of 0.997 and an average RMSE of 0.57 degrees per second. The WMRA and Vicon systems had an R-value of 0.997 and an average RMSE of 0.69 degrees per second. Since the APDM sensor directly measures the angular velocity, it makes sense that the APDM and Vicon comparison has the highest correlation and lowest RMSE, followed by the APDM and WMRA comparison. The APDM angular velocity towards the end of each trial the measurements did not drift significantly, the signals were a little noisy but remained relatively

constant. This is likely due to the calibration of the gyroscope data. The raw gyroscope data was noisier than the calibrated data, and contained some drift. When the joint angles were calculated by integrating the gyroscope signal, the drift continually increased and the error was compounded over time. However, the manufacturer's calibration seems to correct the gyroscope drift, so drift was not a significant problem in this study.

The last trials collected were the two three-dimensional trials where all three joints moved simultaneously for five complete cycles. All three systems had been running for several hours and the calibration files were not reset for any of the systems. The largest differences between the three systems joint angles, particularly the WMRA, were evident in the 3-dimensional motion trials. These trials also had some of the highest RMSE, particularly for joint 3. Before beginning the study, time-based effects were expected to be a factor and source of error. Knee angle calculations using the two-sensor algorithm for both 3-D trials 1 and 2 were still within a clinically acceptable range, even after several hours of data collection.

The management of several hours of IMU data in this study was possible due to the MATLAB (Mathworks, Natick, MA) algorithm and the ability to save each trial separately in the Motion Studio program. However, the APDM Opal sensors are capable of on board data storage, which would allow for continuous data collection outside of a laboratory setting during activities of daily living. The calculations of the joint angles would be similar to having separate trials, however the processing time of the MATLAB algorithm would be increased. The problems with data management would arise when attempting to separate different activities.

The manufacturer's calibration of the APDM sensor gyroscopes limited the drift and time-based effects. As a result, the APDM sensor algorithm accurately calculated the joint angles well within a clinically acceptable range relative to the gold standard Vicon gait analysis system.

The range of motion and sit to stand tests were an additional method used to verify the WMAS knee angle calculation algorithm. Both the range of motion and sit to stand tests had a RMSE of less than 5 degrees when compared to the Vicon system. A potential source of error in these tests was the height of the stool that the subject sat on. The stool did not allow the subject to begin with their legs at a 90-degree angle and it was difficult for the subject to sit completely upright. However, the stool was used rather than the chair used during the rest of the gait trials because the RPSI and LPSI markers were blocked from the view of the cameras by the back of the chair. Since three markers are needed to define a segment, the pelvis could not be defined at the start of the trials due to drop out of two of the four pelvis markers. The pelvis is used as a reference segment for the legs, and as a result the knee angles could not be calculated using the chair. Another potential source of error was movement of the pelvis markers during the trial. The pelvis markers were attached to the elastic belt on the APDM strap, and moved slightly during the trials. However, these tests showed that WMAS was able to accurately measure the knee flexion angle within the goal of 5 degrees error relative to the Vicon system and within clinically acceptable range.

6.2 Comparison Between Vicon and WMAS

The Vicon and WMAS were compared for three gait parameters: knee flexion angle, stride length and cadence. The three verification tests were the first methods that were used to compare the WMAS and Vicon system. As mentioned previously, the Vicon motion analysis

system is the gold standard for gait analysis and was used to validate the algorithms and accuracy of the WMAS.

The goal of the WMAS knee angle calculations was to have less than 5 degrees of error relative to the Vicon system. The RMSE for the WMAS was less than 5 degrees for both the entire trial comparisons and the maximum knee flexion angle comparison. For the entire gait trial comparisons, the RMSE for the right knee during the slow, normal and fast speeds was 3.3 degrees, 3.3 degrees and 4.1 degrees respectively. The left knee flexion RMSE were slightly higher than those calculated for the right knee. Slow, normal and fast RMSE for the left knee were 3.9 degrees, 3.9 degrees and 4.4 degrees. For both the left and right knee flexion angles, the R correlation values were between 0.983 and 0.992. The overall RMSE and Pearson's R correlation values for the right knee were 3.5 degrees and 0.988, whereas the left knee was 3.3 degrees and 0.986.

The maximum knee flexion angles were also well within under the goal of 5 degrees of error with an overall RMSE of 2.8 degrees. Analysis of the bland altman plot shows that the maximum flexion angles were well with an error of 5 degrees, with the exception of a few outliers. The bland altman plot was used to show a comparison between the Vicon and WMAS measurements, and to validate if the WMAS is an acceptable alternative to the gold standard. Unlike Pearson's R correlation, the bland altman plot does not assume a linear relationship between the values. The limits of agreement are the top and bottom dashed lines in the figure representing the mean +/- two standard deviations. Since the limits of agreement fall within a clinically acceptable range, it can be assumed that the WMAS is a reliable alternative to the Vicon system.

There are several potential sources of error for the knee angle calculations. The potential error sources related to the Vicon system include misplacement of the knee markers. These markers are difficult to locate properly, and a slight offset could affect the location of the knee joint center. An additional source of error related to the Vicon system is the movement of the pelvis markers during the trials due to their placement on an elastic belt on the waist and the movement of the subjects shirt and in turn the reflective markers. The potential error sources related to the WMAS include misalignment of the APDM sensor with the axes of the thigh and shank, magnetic interference and movement of the sensors during the trials. Magnetic interference may have occurred due to the force platforms, solo step, cameras and computer system, but did not seem to have a major effect on the results. Lastly, the sensors were not calibrated before each data collection. The Motion Studio software has been updated since the collections for this study were completed and now includes a calibration feature that can recalibrate the gyroscopes and magnetometers before beginning data collection. It is expected that recalibrating the sensors before every data collection would improve the results.

Another goal of this study was to improve the stride length calculations in a previous study using the APDM sensors by Simoes. Simoes reported stride length R correlations of 0.776, 0.8 and 0.817, which correspond to normal, fast and slow speeds, and an overall correlation of 0.861 [3, 35]. In this study the stride length calculations were improved at all three speeds as well as in the overall correlation. The highest correlation value for stride length in this study was 0.91 at slow speed. The normal and fast correlation values were 0.88 and 0.87 respectively. Overall the stride length correlation was 0.89. In addition to the correlation values, the overall average RMSE was 0.091m, with the slow speed having the lowest RMSE at 0.056m. The limits of agreement from the stride length Bland Altman plot for slow gait also

show that the error between the two methods at slow speed was approximate 0.05m. Since the literature has shown that subjects with TBI tend to walk slower, so the WMAS will be able to calculate the TBI parameters accurately. The overall percentage difference between the WMAS and Vicon stride length calculations was 2.11%.

In the WMAS, a peak detection method was used to identify the heel-strike and toe-off gait events from the angular velocity signal. However, manual inspection was necessary to avoid selection of noise in the signal rather than a peak or gait event. A filtering technique should be used in the future to eliminate the need for manual inspection of the locations of the gait events.

The WMAS was able to achieve the goals of 5 degrees or less of error in the knee flexion measurements and improve upon previous stride length results.

6.3 Comparison Between WMAS and Previous Work

There are several differences between the WMAS and the previous work with IMUs mentioned in Chapter 2. One significant difference is a lot of the systems contain wires connected to a data logger, and are not small or practical for a person to wear during their activities of daily living. Another difference between previous work and the WMAS is the gait parameters were calculated directly not from integrating gyroscope or accelerometer signals. This resulted in a smaller error due to the elimination of error propagation and drift accumulation during integration. The WMAS was also validated against a gold-standard, industry leading, Vicon optical motion capture system rather than a video camera based, magnetic or ultrasound system. No extensive filtering, such as Kalman filtering, was used in the WMAS but was popular in previous work. The WMAS is different from the iTUG plug-in used by Simoes because the data is based off individual subject measurements rather than a

normative database, the data is output into columns and graphs that are editable rather than a standard template report that cannot be edited, and the equations and calculations are known to the user rather than a “black box” type software. The other major advantage to the WMAS is the gait parameters and knee angles are calculated directly from the orientation data rather than the integration of the sensor data. In addition the WMAS can be used for other activities and gait tests, other than just the TUG test, which is the only test Simoes was able to perform [3, 35].

The WMAS RMSE for knee flexion angle was 3.3 degrees for the normal and slow speeds and 4.1 degrees for the fast speed during gait, which were lower than those reported in the literature. For example, Schiefer et al. used accelerometers and gyroscopes to calculate knee flexion during several activities of daily living compared the data to an optical camera system with a RMSE between 4.6 and 7.1 degrees [46]. Watanabe reported RMSE of 4-5 degrees, and 7 degrees without a Kalman filter, which are also higher than those from the WMAS [46]. Pochappan reported a RMSE of 9.12 degrees, nearly triple the error calculated by the WMAS [48]. The Xsens MTx sensors are a similar product to the APDM Opal sensors, however Cloete and Scheffer reported RMSE of 7.6 degrees for the knee flexion angle using the Xsens software [47]. RMSE from the WMAS were not as small as Dejnabadi [83] or Cooper [59], however, these systems were not validated with an optical motion capture system. Lastly, Favre reported lower average RMSE for knee flexion angle but used several calibration and alignment procedures prior to data collection [52, 54, 55], which were not used with the WMAS.

The work by Aminian [38] and Salarian [39] was used in the WMAS to identify the gait events or heel-strike and toe-off from the angular velocity signal from the shank IMU. However, unlike Aminian [38] and Salarian [39], the gyroscope data was not integrated to get

the segment angles that are necessary to calculate parameters such as stride length. The WMAS calculations for stride length were similar to Zexi, however their equations were used to calculate step length and the segment angles were calculated by integrating the angular velocity [65]. Aminian reported RMSE of 0.07 meters and 7.2% error for stride length calculations [38], which are slightly higher than the WMAS. The WMAS has a RMSE of 0.056 meters and 0.067 meters for slow and normal gait speeds, and an average error of 2.11%. Salarian reported lower stride length RMSE than the WMAS with 3.5 centimeters, however Salarian used filtering and a more complex gait double pendulum and inverse double pendulum gait model [39]. Doheny reported a RMSE of 0.09 meters and an R correlation of 0.84 for stride length calculations [63]. The WMAS performed better during slow and normal speeds, and had about the same average RMSE for all three speeds (0.091 meters) with an R correlation of 0.89. Lastly, as previously mentioned the stride length calculations were improved with the WMAS relative to the work by Simoes with the APDM Opal sensors [3].

6.4 Graphical User Interface

A graphical user interface was also created in Matlab for use with the knee angle analysis during gait. The user is able to select the data which they have previously collected and plot both the right and left knee flexion angles, or compare a knee flexion angle to one collected previously as a baseline. This will allow for visual analysis of the knee angle during gait. A future improvement includes adding the values for maximum knee flexion. Future work could also involve adding the stride length parameters. The GUI could also be programmed to collect the data directly from the sensors rather than from Motion Studio. This would allow for collection and analysis in one easy to use tool.

6.5 Limitations of this Research

There are several limitations of this research in addition to the previously discussed sources of error. The main limitation is a small sample size of only healthy; generally young subjects participated in the study. Ten healthy individuals with an average age of 27 participated in the study. The ultimate application of the study is for mTBI and TBI research, as well as concussion or return to duty diagnosis, which would require an additional validation study. Another limitation is the use of a short gait lane in a defined laboratory setting. However, despite these limitations the WMAS showed it was able to calculate gait parameters within a clinically acceptable range to the gold standard Vicon motion capture system.

6.6 Applications of WMAS

The WMAS has several applications including use in a physical therapy or rehabilitation clinic, data collection outside of a laboratory setting during a person's normal activities of daily living, on the sidelines at sporting events or in the battlefield to analyze concussion injuries, and to determine return to duty or return to play after a head injury.

CHAPTER 7: CONCLUSION

The purpose of this study was to develop a wearable motion analysis system to evaluate gait parameters that are indicative of gait deviations, particular those relevant to mTBI and TBI. In addition to developing the WMAS, one of the goals of this project was to calculate knee flexion angle within 5 degrees of error of the Vicon optical motion capture system. The other goal was to improve the stride length calculations from Simoes [3]. Both of these goals were met as the RMSE of the knee flexion angle was 3.5 degrees relative to the Vicon system and the stride length correlations were increased to strong correlation values of 0.91, 0.88 and 0.87 corresponding to slow, normal and fast speeds. The WMAS is a powerful clinical tool for gait analysis, especially outside of a laboratory setting. A future study will include mTBI patients, and test the validity of the WMAS for evaluating and rehabilitating mTBI.

CHAPTER 8: FUTURE WORK

8.1 Use with mTBI and TBI Subjects

The next phase of this project should involve testing the validity and accuracy of the WMAS with mTBI and TBI subjects. Similar testing to this study could be used, with an addition of treadmill walking. The data from the mTBI and TBI subjects can be compared to the data collected in this study from healthy subjects.

8.2 Robotic Arm

Future work with the robotic arm will also include the development of algorithms to detect gait abnormalities such as those seen in patients with mild traumatic brain injury (mTBI). To complement human subject testing with gait pathology, controlled introduction of gait deviations into this robotic testing framework will allow for well-characterized unit testing, providing more robust algorithm development.

8.3 Testing Outside of Laboratory

Future studies will involve collecting data continuously on board the sensors outside of a laboratory setting. After the data collection, there would be a large amount of data to process, and would test the ability to extract only the relevant parameters.

8.4 CAREN

The CAREN or Computer Assisted Rehabilitation Environment and WMAS system could be used together for return to duty testing for subjects with mTBI or PTSD. The testing could begin in the gait laboratory with the WMAS and Vicon motion capture system for analysis of level walking, stairs and gravel. The testing framework could also include noises and visual distractions during the gait trials. The next phase would involve testing on the CAREN for several weeks with visual distractions, varying terrain and noises. The final phase would involve retesting in the gait laboratory to determine if the rehabilitation training improved the gait and could result in return to duty. A benefit of using the WMAS and the CAREN would be the ability to control the environment and the movement of the platform. The CAREN could provide perturbations and obstacles, as well as distractions that cannot be provided during gait analysis on a flat walkway in a laboratory setting. Someone may walk well when the only focus is walking, but when other factors are introduced gait deviations may occur. This would allow the WMAS to be tested with closer to real life situations than the traditional gait lane testing, but still in a controlled and known environment.

8.5 Sports Concussion

The WMAS has the potential to identify the growing number of concussion and mTBIs that occur during sports such as football, hockey and baseball. As mentioned previously, the current on field diagnostic tools for concussions are subjective. There is a major need for an objective, portable method to determine whether a player can return to play or has suffered a concussion on the field. Baseline gait measurements with the WMAS could be collected prior to the start of the season for each player, and used to compare to the gait measurements after a potential concussion. Treadmill walking should be tested, in addition to the regular gait trials

because if there is a correlation between slow speed and concussion players may be able to outsmart the system by walking slower. If a treadmill was used, the speed would be controlled, and the gait deviations would be evident and not dependent on gait speed.

REFERENCES

- [1] Bergmann, J. H., and McGregor, A. H., 2011, "Body-worn sensor design: what do patients and clinicians want?," *Ann Biomed Eng*, 39(9), pp. 2299-2312.
- [2] APDM, 2010, "Opal Technical Specifications," <http://apdm.com/products/movement-monitors/opal/>.
- [3] Simoes, M. A., 2011, "Feasibility of Wearable Sensors to Determine Gait Parameters," Master of Science, University of South Florida, Graduate School Theses and Dissertations.
- [4] 2010, "Plug-In Gait Product Guide Foundation Notes (Rev. 2.0)," http://www.vicon.com/support/downloads/cef70cc8dbcc7149988652bf7dff8ff84cc6bc77302948.73654482/Plugin_Nexus_PluginGait_ProductGuide_Foundation_Rev2.0_2010April.pdf.
- [5] Perry, J., and Burnfield, J. M., 2010, *Gait Analysis: Normal and Pathological Function*, SLACK Incorporated, Thorofare, NJ.
- [6] Esquenazi, A., 2004, "Evaluation and management of spastic gait in patients with traumatic brain injury," *J Head Trauma Rehabil*, 19(2), pp. 109-118.
- [7] Williams, G., Galna, B., Morris, M. E., and Oliver, J., 2010, "Spatiotemporal Deficits and Kinematic Classification of Gait Following a Traumatic Brain Injury: A Systematic Review," *The Journal of Head Trauma Rehabilitation*, 25(5), pp. 366-374.
- [8] Faul, M., Xu, L., Wald, M., and Coronado, V., 2010, "Traumatic Brain Injury in the United States: emergency department visits, hospitalizations, and deaths," Center for Disease Control and Prevention, National Center for Injury Prevention, Atlanta, GA.
- [9] Basford, J. R., Chou, L. S., Kaufman, K. R., Brey, R. H., Walker, A., Malec, J. F., Moessner, A. M., and Brown, A. W., 2003, "An assessment of gait and balance deficits after traumatic brain injury," *Arch Phys Med Rehabil*, 84(3), pp. 343-349.
- [10] Stevens, B. L., and Lewis, F. L., 2003, *Aircraft Control and Simulation*, Wiley.
- [11] Dziemianowicz, M., Kirschen, M., Pukenas, B., Laudano, E., Balcer, L., and Galetta, S., 2012, "Sports-Related Concussion Testing," *Current Neurology and Neuroscience Reports*, 12(5), pp. 547-559.

- [12] Center, D. a. V. B. I., 2013, "DoD Worldwide Numbers for TBI," <http://www.dvbic.org/dod-worldwide-numbers-tbi>.
- [13] 2012, "The National Football League Commits \$30 Million Donation to the Foundation for the National Institutes of Health to Support Medical Research."
- [14] 2012, "VA, DOD to Fund \$100 Million PTSD and TBI Study," Department of Veterans Affairs Washington, DC.
- [15] Lopez, C. T., "Army, NFL report to Congress on brain-injury initiatives," <http://www.army.mil/article/87297>.
- [16] Williams, G., Morris, M. E., Schache, A., and McCrory, P. R., 2009, "Incidence of Gait Abnormalities After Traumatic Brain Injury," *Archives of Physical Medicine and Rehabilitation*, 90, pp. 587-593.
- [17] Chou, L. S., Kaufman, K. R., Walker-Rabatin, A. E., Brey, R. H., and Basford, J. R., 2004, "Dynamic instability during obstacle crossing following traumatic brain injury," *Gait Posture*, 20(3), pp. 245-254.
- [18] McFadyen, B. J., Swaine, B., Dumas, D., and Durand, A., 2003, "Residual Effects of a Traumatic Brain Injury on Locomotor Capacity: A First Study of Spatiotemporal Patterns During Unobstructed and Obstructed Walking," *The Journal of Head Trauma Rehabilitation*, 18(6), pp. 512-525.
- [19] Ochi, F., Esquenazi, A., Hirai, B., and Talaty, M., 1999, "Temporal-spatial feature of gait after traumatic brain injury," *J Head Trauma Rehabil*, 14(2), pp. 105-115.
- [20] Scherer, M. R., and Schubert, M. C., 2009, "Traumatic brain injury and vestibular pathology as a comorbidity after blast exposure," *Phys Ther*, 89(9), pp. 980-992.
- [21] Williams, G., Morris, M. E., Schache, A., and McCrory, P. R., 2010, "People Preferentially Increase Hip Joint Power Generation to Walk Faster Following Traumatic Brain Injury," *Neurorehabilitation and Neural Repair*, 24(6), pp. 550-558.
- [22] Kaufman, K. R., Brey, R. H., Chou, L.-S., Rabatin, A., Brown, A. W., and Basford, J. R., 2006, "Comparison of subjective and objective measurements of balance disorders following traumatic brain injury," *Medical Engineering & Physics*, 28(3), pp. 234-239.
- [23] Paul F. Pasquina, M. D., Cooper, R. A., United States. Dept. of the Army. Office of the Surgeon, G., and Borden, I., 2009, *Care of the combat amputee*, Office of the Surgeon General, United States Army.
- [24] Horn, L. J., and Zasler, N. D., 1996, *Medical rehabilitation of traumatic brain injury*, Hanley & Belfus.

- [25] Hutin, E., Pradon, D., Barbier, F., Gracies, J.-M., Bussel, B., and Roche, N., 2011, "Lower limb coordination patterns in hemiparetic gait: Factors of knee flexion impairment," *Clinical Biomechanics*, 26(3), pp. 304-311.
- [26] Kerrigan, D. C., Bang, M. S., and Burke, D. T., 1999, "An algorithm to assess stiff-legged gait in traumatic brain injury," *J Head Trauma Rehabil*, 14(2), pp. 136-145.
- [27] Williams, G. P., and Schache, A. G., 2010, "Evaluation of a Conceptual Framework for Retraining High-Level Mobility Following Traumatic Brain Injury: Two Case Reports," *The Journal of Head Trauma Rehabilitation*, 25(3), pp. 164-172
110.1097/HTR.1090b1013e3181dc1120b.
- [28] Hsu, J. D., Michael, J. W., Fisk, J. R., and Surgeons, A. A. o. O., 2008, *AAOS atlas of orthoses and assistive devices*, C V MOSBY Company.
- [29] Fausti, S. A., Wilmington, D. J., Gallun, F. J., Myers, P. J., and Henry, J. A., 2009, "Auditory and vestibular dysfunction associated with blast-related traumatic brain injury," *J Rehabil Res Dev*, 46(6), pp. 797-810.
- [30] Sosnoff, J., Broglio, S., and Ferrara, M., 2008, "Cognitive and motor function are associated following mild traumatic brain injury," *Experimental Brain Research*, 187(4), pp. 563-571.
- [31] Bland, D. C., Zampieri, C., and Damiano, D. L., 2011, "Effectiveness of physical therapy for improving gait and balance in individuals with traumatic brain injury: a systematic review," *Brain Inj*, 25(7-8), pp. 664-679.
- [32] Gottshall, K. R., Sessoms, P. H., and Bartlett, J. L., 2012, "Vestibular physical therapy intervention: utilizing a computer assisted rehabilitation environment in lieu of traditional physical therapy," *Engineering in Medicine and Biology Society (EMBC), 2012 Annual International Conference of the IEEE*, pp. 6141-6144.
- [33] Clark, R. A., Williams, G., Fini, N., Moore, L., and Bryant, A. L., 2012, "Coordination of Dynamic Balance During Gait Training in People With Acquired Brain Injury," *Archives of Physical Medicine and Rehabilitation*, 93(4), pp. 636-640.
- [34] Whitney, S. L., Marchetti, G. F., Pritcher, M., and Furman, J. M., 2009, "Gaze stabilization and gait performance in vestibular dysfunction," *Gait Posture*, 29(2), pp. 194-198.
- [35] Carey, S., Hufford, K., Martori, A., Simoes, M., Sinatra, F., and Dubey, R., "Development of a Wearable Motion Analysis System for Evaluation and Rehabilitation of Mild Traumatic Brain Injury (mTBI)," *Proc. ASME Summer Bioengineering Conference*.
- [36] Moseley, A. M., Lanzarone, S., Bosman, J. M., van Loo, M. A., de Bie, R. A., Hassett, L., and Caplan, B., 2004, "Ecological validity of walking speed assessment after traumatic brain injury: a pilot study," *J Head Trauma Rehabil*, 19(4), pp. 341-348.

- [37] Greene, B. R., Foran, T. G., McGrath, D., Doheny, E. P., Burns, A., and Caulfield, B., 2012, "A Comparison of Algorithms for Body-Worn Sensor-Based Spatiotemporal Gait Parameters to the GAITRite Electronic Walkway," *J Appl Biomech*, 28(3), pp. 349-355.
- [38] Aminian, K., Najafi, B., Bula, C., Leyvraz, P. F., and Robert, P., 2002, "Spatio-temporal parameters of gait measured by an ambulatory system using miniature gyroscopes," *J Biomech*, 35(5), pp. 689-699.
- [39] Salarian, A., Russmann, H., Vingerhoets, F. J., Dehollain, C., Blanc, Y., Burkhard, P. R., and Aminian, K., 2004, "Gait assessment in Parkinson's disease: toward an ambulatory system for long-term monitoring," *IEEE Trans Biomed Eng*, 51(8), pp. 1434-1443.
- [40] Bonato, P., 2009, "Clinical applications of wearable technology," *Engineering in Medicine and Biology Society, 2009. EMBC 2009. Annual International Conference of the IEEE*, pp. 6580-6583.
- [41] Zeng, H., and Zhao, Y., 2011, "Sensing Movement: Microsensors for Body Motion Measurement," *Sensors*, 11(1), pp. 638-660.
- [42] Madgwick, S. O. H., Harrison, A. J. L., and Vaidyanathan, R., 2011, "Estimation of IMU and MARG orientation using a gradient descent algorithm," *Rehabilitation Robotics (ICORR), 2011 IEEE International Conference on*, pp. 1-7.
- [43] Guo, Y., Wu, D., Liu, G., Zhao, G., Huang, B., and Wang, L., 2012, "A Low-Cost Body Inertial-Sensing Network for Practical Gait Discrimination of Hemiplegia Patients," *Telemed J E Health*.
- [44] Toffola, L. D., Patel, S., Ozsecen, M. Y., Ramachandran, R., and Bonato, P., 2012, "A wearable system for long-term monitoring of knee kinematics," *Biomedical and Health Informatics (BHI), 2012 IEEE-EMBS International Conference on*, pp. 188-191.
- [45] Schiefer, C., Kraus, T., Ochsmann, E., Hermanns, I., Ellegast, R., and Duffy, V., 2011, "3D Human Motion Capturing Based Only on Acceleration and Angular Rate Measurement for Low Extremities Digital Human Modeling," *Springer Berlin / Heidelberg*, pp. 195-203.
- [46] Watanabe, T., Saito, H., Koike, E., and Nitta, K., 2011, "A preliminary test of measurement of joint angles and stride length with wireless inertial sensors for wearable gait evaluation system," *Comput Intell Neurosci*, 2011, p. 975193.
- [47] Cloete, T., and Scheffer, C., 2008, "Benchmarking of a full-body inertial motion capture system for clinical gait analysis," *Engineering in Medicine and Biology Society, 2008. EMBS 2008. 30th Annual International Conference of the IEEE*, pp. 4579-4582.
- [48] Pochappan, S. S., Arvind, D. K., Walsh, J., Richardson, A. M., and Herman, J., 2012, "Mobile Clinical Gait Analysis Using Orient Specks," *Wearable and Implantable Body Sensor Networks (BSN), 2012 Ninth International Conference on*, pp. 172-177.

- [49] Chen, S., Brantley, J. S., Kim, T., and Lach, J., "Characterizing and minimizing synchronization and calibration errors in inertial body sensor networks," Proc. Proceedings of the Fifth International Conference on Body Area Networks, ACM, pp. 138-144.
- [50] Kun, L., Tao, L., Shibata, K., and Inoue, Y., 2009, "Ambulatory measurement and analysis of the lower limb 3D posture using wearable sensor system," Mechatronics and Automation, 2009. ICMA 2009. International Conference on, pp. 3065-3069.
- [51] Kun, L., Yoshio, I., and Kyoko, S., 2010, "Visual and quantitative analysis of lower limb 3D gait posture using accelerometers and magnetometers," Mechatronics and Automation (ICMA), 2010 International Conference on, pp. 1420-1425.
- [52] Favre, J., Jolles, B. M., Aissaoui, R., and Aminian, K., 2008, "Ambulatory measurement of 3D knee joint angle," J Biomech, 41(5), pp. 1029-1035.
- [53] Favre, J., Jolles, B. M., Siegrist, O., and Aminian, K., 2006, "Quaternion-based fusion of gyroscopes and accelerometers to improve 3D angle measurement," Electronics Letters, 42(11), pp. 612-614.
- [54] Favre, J., Aissaoui, R., Jolles, B. M., Siegrist, O., de Guise, J. A., and Aminian, K., 2006, "3D joint rotation measurement using MEMs inertial sensors: Application to the knee joint," Ninth International Symposium on the 3D Analysis of Human Movement, International Society of Biomechanics (ISB) Technical Group on the 3-D Analysis of Human Movement, France.
- [55] Favre, J., Aissaoui, R., Jolles, B. M., de Guise, J. A., and Aminian, K., 2009, "Functional calibration procedure for 3D knee joint angle description using inertial sensors," Journal of Biomechanics, 42(14), pp. 2330-2335.
- [56] Dejnabadi, H., Jolles, B. M., and Aminian, K., 2005, "A new approach to accurate measurement of uniaxial joint angles based on a combination of accelerometers and gyroscopes," Biomedical Engineering, IEEE Transactions on, 52(8), pp. 1478-1484.
- [57] Bergmann, J. H., Mayagoitia, R. E., and Smith, I. C., 2009, "A portable system for collecting anatomical joint angles during stair ascent: a comparison with an optical tracking device," Dyn Med, 8, p. 3.
- [58] Schulze, M., Liu, T.-H., Xie, J., Zhang, W., Wolf, K.-H., Calliess, T., Windhagen, H., and Marschollek, M., 2012, "Unobtrusive ambulatory estimation of knee joint angles during walking using gyroscope and accelerometer data - a preliminary evaluation study," Biomedical and Health Informatics (BHI), 2012 IEEE-EMBS International Conference on, pp. 559-562.
- [59] Cooper, G., Sheret, I., McMillian, L., Siliverdis, K., Sha, N., Hodgins, D., Kenney, L., and Howard, D., 2009, "Inertial sensor-based knee flexion/extension angle estimation," Journal of Biomechanics, 42(16), pp. 2678-2685.
- [60] Takeda, R., Tadano, S., Todoh, M., Morikawa, M., Nakayasu, M., and Yoshinari, S., 2009, "Gait analysis using gravitational acceleration measured by wearable sensors," J Biomech, 42(3), pp. 223-233.

- [61] Saito, H., Watanabe, T., Arifin, A., Dössel, O., and Schlegel, W. C., 2009, "Ankle and Knee Joint Angle Measurements during Gait with Wearable Sensor System for RehabilitationWorld Congress on Medical Physics and Biomedical Engineering, September 7 - 12, 2009, Munich, Germany," R. Magjarevic, ed., Springer Berlin Heidelberg, pp. 506-509.
- [62] Miyazaki, S., 1997, "Long-Term Unrestrained Measurement of Stride Length and Walking Velocity Utilizing a Piezoelectric Gyroscope," *IEEE Transactions on Biomedical Engineering*, 44(8), pp. 753-759.
- [63] Doheny, E. P., Foran, T. G., and Greene, B. R., 2010, "A single gyroscope method for spatial gait analysis," *Engineering in Medicine and Biology Society (EMBC), 2010 Annual International Conference of the IEEE*, pp. 1300-1303.
- [64] Shanshan, C., Cunningham, C. L., Lach, J., and Bennett, B. C., 2011, "Extracting Spatio-Temporal Information from Inertial Body Sensor Networks for Gait Speed Estimation," *Body Sensor Networks (BSN), 2011 International Conference on*, pp. 71-76.
- [65] Zexi, L., and Won, C.-H., 2010, "Knee and waist attached gyroscopes for personal navigation: Comparison of knee, waist and foot attached inertial sensors," *Position Location and Navigation Symposium (PLANS), 2010 IEEE/ION*, pp. 375-381.
- [66] Salarian, A., Horak, F. B., Zampieri, C., Carlson-Kuhta, P., Nutt, J. G., and Aminian, K., 2010, "iTUG, a sensitive and reliable measure of mobility," *IEEE Trans Neural Syst Rehabil Eng*, 18(3), pp. 303-310.
- [67] Schrock, P., Farelo, F., Alqasemi, R., and Dubey, R., 2009, "Design, simulation and testing of a new modular wheelchair mounted robotic arm to perform activities of daily living," *Rehabilitation Robotics, 2009. ICORR 2009. IEEE International Conference on*, pp. 518-523.
- [68] Almeida, E. C. V. d., 2012, "Development of a wearable sensor system for real-time control of knee prostheses," Linköping.
- [69] Isenberg, D. R., 2009, "Quaternion and Euler-angle based approaches to the dynamical modeling, position control, and tracking control of a space robot," Ph.D, The University of North Carolina at Charlotte.
- [70] Tincknell, M., 2013, "Matlab quaternion class."
- [71] Diebel, J., 2006, "Representing Attitude: Euler Angles, Unit Quaternions, and Rotation Vectors."
- [72] Billauer, E., 2012, "peakdet: Peak detection using MATLAB," <http://www.billauer.co.il/peakdet.html>.
- [73] Stewart, J., Redlin, L., and Watson, S., 2011, *Trigonometry*, 2nd ed, Brooks Cole Publishing Company.

- [74] C-Motion, 2013, "Tutorial: Building a Conventional Gait Model," http://www.c-motion.com/v3dwiki/index.php?title=Tutorial:_Building_a_Conventional_Gait_Model.
- [75] C-Motion, 2013, "V3D Wiki: Joint Angle," http://www.c-motion.com/v3dwiki/index.php?title=Joint_Angle.
- [76] C-Motion, 2012, "V3D Wiki: Events Example 6," http://www.c-motion.com/v3dwiki/index.php?title=Events:Example_6.
- [77] C-Motion, 2012, "V3D Wiki: Metric Vector Between Events," http://www.c-motion.com/v3dwiki/index.php?title=Metric_Vector_Between_Events.
- [78] Randolph, K. A., and Myers, L. L., 2013, Basic Statistics in Multivariate Analysis, Oxford University Press, USA.
- [79] Mould, R. F., 2010, Introductory Medical Statistics, 3rd edition, Taylor & Francis.
- [80] Bland, J. M., and Altman, D. G., 1999, "Measuring agreement in method comparison studies," *Statistical Methods in Medical Research*, 8(2), pp. 135-160.
- [81] Bland, J. M., and Altman, D. G., 2007, "Agreement Between Methods of Measurement with Multiple Observations Per Individual," *Journal of Biopharmaceutical Statistics*, 17(4), pp. 571-582.
- [82] 2013, "APDM Movement Monitors," <http://apdm.com/Wearable-Sensors/inertial-sensors>.
- [83] Dejnabadi, H., Jolles, B. M., Casanova, E., Fua, P., and Aminian, K., 2006, "Estimation and visualization of sagittal kinematics of lower limbs orientation using body-fixed sensors," *Biomedical Engineering, IEEE Transactions on*, 53(7), pp. 1385-1393.

APPENDICES

Appendix A: WMAS Data Collection Checklist

WMAS Data Collection Checklist

Subject ID: _____ Name: _____ Date: _____

- Subject sign informed consent
- Measure and record subject measurements for plug-in gait (see attached measurement sheet)
- Attach Opal Sensors before Vicon markers
 - Attach sternum harness with sensor #165
 - Attach waist sensor #160 on lower back
 - Right thigh sensor #163
 - Left thigh sensor #162
 - Right shank sensor #164
 - Left shank sensor #161

Attach marker set for plug in gait

Torso	Pelvis	Right Arm	Left Arm	Left Leg	Right Leg
<input type="checkbox"/> C7	<input type="checkbox"/> LASI	<input type="checkbox"/> RSHO	<input type="checkbox"/> LSHO	<input type="checkbox"/> LKNE	<input type="checkbox"/> RKNE
<input type="checkbox"/> T10	<input type="checkbox"/> RASI	<input type="checkbox"/> RUPA	<input type="checkbox"/> LUPA	<input type="checkbox"/> LTHI	<input type="checkbox"/> RTHI
<input type="checkbox"/> CLAV	<input type="checkbox"/> LPSI	<input type="checkbox"/> RFRA	<input type="checkbox"/> LFRA	<input type="checkbox"/> LANK	<input type="checkbox"/> RANK
<input type="checkbox"/> STRN	<input type="checkbox"/> RPSI	<input type="checkbox"/> RELB	<input type="checkbox"/> LELB	<input type="checkbox"/> LTIB	<input type="checkbox"/> RTIB
<input type="checkbox"/> RBAK		<input type="checkbox"/> RWRA	<input type="checkbox"/> LWRA	<input type="checkbox"/> LTOE	<input type="checkbox"/> RTOE
		<input type="checkbox"/> RWRB	<input type="checkbox"/> LWRB	<input type="checkbox"/> LHEE	<input type="checkbox"/> RHEE
		<input type="checkbox"/> RFIN	<input type="checkbox"/> LFIN		

- Calibrate Cameras and Force Plates
- Static Trial

Trials:

Subject will sit in a chair then asked to walk to the end of the walkway turn around, walk back and sit back down in the chair. The trials will be done at normal speed, very slow speed and fast speed.

- | | | |
|---------------------------------------|--|-------------------------------------|
| <input type="checkbox"/> Normal Speed | <input type="checkbox"/> Very Slow Speed | <input type="checkbox"/> Fast Speed |
| <input type="checkbox"/> 1 | <input type="checkbox"/> 1 | <input type="checkbox"/> 1 |
| <input type="checkbox"/> 2 | <input type="checkbox"/> 2 | <input type="checkbox"/> 2 |
| <input type="checkbox"/> 3 | <input type="checkbox"/> 3 | <input type="checkbox"/> 3 |
| <input type="checkbox"/> 4 | <input type="checkbox"/> 4 | <input type="checkbox"/> 4 |
| <input type="checkbox"/> 5 | <input type="checkbox"/> 5 | <input type="checkbox"/> 5 |

Appendix B: Instructions for WMAS Data Collection

B.1 APDM Instructions

1. Plug access point USB into laptop
2. Plug docking station into outlet using power adapter
3. Connect USB cord into docking station and plug into laptop
4. Go to Programs and open Motion Studio
5. Plug Opal sensors into docking station. The light on each sensor should turn blue
6. Under "Working Directory" specify which folder data will go into
7. Press New at top of Motion Studio
8. It will say "plug in all hardware that you wish to configure" Click Ok
9. It will check the firmware and calibration
10. Choose the "Systems tab":
 - a. Under "Attached hardware" it should show: 1 access point, 6 docking stations and 6 monitors
 - b. Under "Recording configuration" it should be Robust Synchronized Streaming, wireless channel 90 and sample rate 128.
11. Choose the "Monitors" tab:
 - a. Make sure the sensors that you connected are shown in the "Select Monitor" drop down menu
 - b. Make sure the boxes next to Enable Accelerometer, Enable Gyroscope and Enable Magnetometer are all checked
 - c. Accelerometer range should be 6g
 - d. Select Do Nothing for Spin Mode

Appendix B (Continued)

12. Click Configure, it will configure for the channel selected
13. Once its finished it will say Configuration Complete. Click Ok
14. Undock the sensors from the docking station.
15. Put the sensors on the subject (prior to placing the markers on the subject). Make sure the sensor number (located on the back of the sensor case) corresponds accordingly to where the sensors are placed on the subject as specified previously in the "Monitors" tab
16. Attach the sensors with the USB port facing toward the ground
17. Adjust the straps so that they are snug but not uncomfortable on the subject
18. Click the Stream button at the top of the toolbar
19. A window will show up with the strip charts on the right and a list of menu options down the left side.

B.2 Vicon Set Up

1. Place the Plug-in-Gait marker set on the subject
2. Open Workstation on the computer
3. Calibrate the cameras and force plates
4. Create a folder for your data
5. Press the turquoise "New Trial" icon
6. Under Trial Types check mark the Static Trial option
7. Capture a static trial
8. Make sure marker set is Plug in Gait
9. Label the markers and apply autolabel

Appendix B (Continued)

B.3 APDM Sensors Data Collection Steps

1. Click "Stream"
 - a. Under "Record Duration" choose Indeterminate
 - b. Under "Save Options" choose CSV for the file format and the file name should follow the following format: subjectid_typeoftrial_trialnumber
 - c. Press Record
 - d. Under "Real Time Data Plot" different plot types of each sensor can be picked
 - e. Press Stop
 - f. Repeat 5 times for each of the 3 trial types
 - g. Click Exit
2. Take the sensors off of the subject
3. Dock the Sensors in the docking station
4. Click "Power Off"
5. Undock the Sensors

B.4 Vicon Data Collection Steps

1. Press the turquoise New Trial icon
2. Make sure the Static Trial box is unchecked
3. Capture a trial by pressing Start and Stop

Appendix C: Visual 3D Pipeline

C.1 Joint Angle Calculations

Calculate Right Knee Angle [75]:

```
Compute_Model_Based_Data
/RESULT_NAME=Right Knee Angle
/FUNCTION=JOINT_ANGLE
/SEGMENT=RSK
/REFERENCE_SEGMENT=RTH
/RESOLUTION_COORDINATE_SYSTEM=
!/USE_CARDAN_SEQUENCE=FALSE
!/NORMALIZATION=FALSE
!/NORMALIZATION_METHOD=
!/NORMALIZATION_METRIC=
/NEGATEX=TRUE
/NEGATEY=TRUE
/NEGATEZ=TRUE
!/AXIS1=X
!/AXIS2=Y
!/AXIS3=Z;
```

Calculate Left Knee Angle [75]:

```
Compute_Model_Based_Data
/RESULT_NAME=Left Knee Angle
/FUNCTION=JOINT_ANGLE
/SEGMENT=LSK
/REFERENCE_SEGMENT=LTH
/RESOLUTION_COORDINATE_SYSTEM=
!/USE_CARDAN_SEQUENCE=FALSE
!/NORMALIZATION=FALSE
!/NORMALIZATION_METHOD=
!/NORMALIZATION_METRIC=
/NEGATEX=TRUE
/NEGATEY=TRUE
/NEGATEZ=TRUE
!/AXIS1=X
!/AXIS2=Y
!/AXIS3=Z;
```

Appendix C (Continued)

C.2 Stride Length Calculations

Calculate the Position of the Right Heel with Respect to the Pelvis [76]:

```
Compute_Model_Based_Data
/RESULT_NAME=RHEEL_WRT_PELVIS
/FUNCTION=TARGET_PATH
/SEGMENT=RHEE
/REFERENCE_SEGMENT=RPV
/RESOLUTION_COORDINATE_SYSTEM=RPV
!/USE_CARDAN_SEQUENCE=FALSE
!/NORMALIZATION=FALSE
!/NORMALIZATION_METHOD=
!/NORMALIZATION_METRIC=
!/NEGATEX=FALSE
!/NEGATEY=FALSE
!/NEGATEZ=FALSE
!/AXIS1=X
!/AXIS2=Y
!/AXIS3=Z;
```

Calculate the Position of the Left Heel with Respect to the Pelvis [76]:

```
Compute_Model_Based_Data
/RESULT_NAME=LHEEL_WRT_PELVIS
/FUNCTION=TARGET_PATH
/SEGMENT=LHEE
/REFERENCE_SEGMENT=RPV
/RESOLUTION_COORDINATE_SYSTEM=RPV
!/USE_CARDAN_SEQUENCE=FALSE
!/NORMALIZATION=FALSE
!/NORMALIZATION_METHOD=
!/NORMALIZATION_METRIC=
!/NEGATEX=FALSE
!/NEGATEY=FALSE
!/NEGATEZ=FALSE
!/AXIS1=X
!/AXIS2=Y
!/AXIS3=Z;
```

Appendix C (Continued)

Calculate the Position of the Right Toe with Respect to the Pelvis [76]:

```
Compute_Model_Based_Data
/RESULT_NAME=RTOE_WRT_PELVIS
/FUNCTION=TARGET_PATH
/SEGMENT=RTOE
/REFERENCE_SEGMENT=RPV
/RESOLUTION_COORDINATE_SYSTEM=RPV
!/USE_CARDAN_SEQUENCE=FALSE
!/NORMALIZATION=FALSE
!/NORMALIZATION_METHOD=
!/NORMALIZATION_METRIC=
!/NEGATEX=FALSE
!/NEGATEY=FALSE
!/NEGATEZ=FALSE
!/AXIS1=X
!/AXIS2=Y
!/AXIS3=Z;
```

Calculate the Position of the Left Toe with Respect to the Pelvis [76]:

```
Compute_Model_Based_Data
/RESULT_NAME=LTOE_WRT_PELVIS
/FUNCTION=TARGET_PATH
/SEGMENT=LTOE
/REFERENCE_SEGMENT=RPV
/RESOLUTION_COORDINATE_SYSTEM=RPV
!/USE_CARDAN_SEQUENCE=FALSE
!/NORMALIZATION=FALSE
!/NORMALIZATION_METHOD=
!/NORMALIZATION_METRIC=
!/NEGATEX=FALSE
!/NEGATEY=FALSE
!/NEGATEZ=FALSE
!/AXIS1=X
!/AXIS2=Y
!/AXIS3=Z;
```

Appendix C (Continued)

Find the Right Heel Strikes [76]:

```
Event_Maximum
/SIGNAL_TYPES=LINK_MODEL_BASED
/SIGNAL_NAMES=RHEEL_WRT_PELVIS
!/SIGNAL_FOLDER=ORIGINAL
/EVENT_NAME=RHS
!/SELECT_X=FALSE
/SELECT_Y=TRUE
!/SELECT_Z=FALSE
!/FRAME_WINDOW=8
!/START_AT_EVENT=
!/END_AT_EVENT=
/EVENT_INSTANCE=0;
```

Find the Left Heel Strikes [76]:

```
Event_Maximum
/SIGNAL_TYPES=LINK_MODEL_BASED
/SIGNAL_NAMES=LHEEL_WRT_PELVIS
!/SIGNAL_FOLDER=ORIGINAL
/EVENT_NAME=LHS
!/SELECT_X=FALSE
/SELECT_Y=TRUE
!/SELECT_Z=FALSE
!/FRAME_WINDOW=8
!/START_AT_EVENT=
!/END_AT_EVENT=
/EVENT_INSTANCE=0;
```

Find the Right Toe-offs [76]:

```
Event_Minimum
/SIGNAL_TYPES=LINK_MODEL_BASED
/SIGNAL_NAMES=RTOE_WRT_PELVIS
!/SIGNAL_FOLDER=ORIGINAL
/EVENT_NAME=RTO
!/SELECT_X=FALSE
/SELECT_Y=TRUE
!/SELECT_Z=FALSE
!/FRAME_WINDOW=8
!/START_AT_EVENT=
```


Appendix C (Continued)

```
! /END_AT_EVENT=  
/EVENT_INSTANCE=0;
```

Find the Left Toe-Offs [76]:

```
Event_Minimum  
/SIGNAL_TYPES=LINK_MODEL_BASED  
/SIGNAL_NAMES=LTOE_WRT_PELVIS  
! /SIGNAL_FOLDER=ORIGINAL  
/EVENT_NAME=LTO  
! /SELECT_X=FALSE  
/SELECT_Y=TRUE  
! /SELECT_Z=FALSE  
! /FRAME_WINDOW=8  
! /START_AT_EVENT=  
! /END_AT_EVENT=  
/EVENT_INSTANCE=0;
```

Calculate the Right Stride Length [77]:


```
Metric_Vector_Between_Events  
/RESULT_METRIC_NAME=RStride  
! /RESULT_METRIC_FOLDER=PROCESSED  
/GENERATE_VECTOR_LENGTH_METRIC=TRUE  
/START_SIGNAL_TYPE=TARGET  
/START_SIGNAL_NAME=RHEEL  
! /START_SIGNAL_FOLDER=ORIGINAL  
/END_SIGNAL_TYPE=TARGET  
/END_SIGNAL_NAME=RHEEL  
! /END_SIGNAL_FOLDER=ORIGINAL  
/EVENT_SEQUENCE=RHS+RTO+RHS  
/EXCLUDE_EVENTS=  
/GENERATE_MEAN_AND_STDDEV=FALSE  
! /APPEND_TO_EXISTING_VALUES=FALSE  
! /RETAIN_NO_DATA_VALUES=FALSE;
```

Appendix C (Continued)

Calculate the Left Stride Length [77]:

```
Metric_Vector_Between_Events
/RESULT_METRIC_NAME=LStride
!/RESULT_METRIC_FOLDER=PROCESSED
/GENERATE_VECTOR_LENGTH_METRIC=TRUE
/START_SIGNAL_TYPE=TARGET
/START_SIGNAL_NAME=LHEEL
!/START_SIGNAL_FOLDER=ORIGINAL
/END_SIGNAL_TYPE=TARGET
/END_SIGNAL_NAME=LHEEL
!/END_SIGNAL_FOLDER=ORIGINAL
/EVENT_SEQUENCE=LHS+LTO+LHS
/EXCLUDE_EVENTS=
/GENERATE_MEAN_AND_STDDEV=FALSE
!/APPEND_TO_EXISTING_VALUES=FALSE
!/RETAIN_NO_DATA_VALUES=FALSE;
```

Appendix D: IRB Approval

 UNIVERSITY OF SOUTH FLORIDA	DIVISION OF RESEARCH INTEGRITY AND COMPLIANCE Institutional Review Boards, PWA No. 00001668 12801 Bruce B. Downs Blvd., MDC015 • Tampa, FL 33613-4799 © 13 974-9650 • FAX 013 974-9653
---	--

March 30, 2011

Stephanie Carey
Mechanical Engineering
4202 E. Fowler Ave. ENB 118

RE: **Expedited Approval** for Initial Review
IRB#: Pro00003205
Title: Feasibility of Wearable Sensors to Determine Gait Parameters

Dear Dr. Carey:

On 3/29/2011 the Institutional Review Board (IRB) reviewed and **APPROVED** the above referenced protocol. Please note that your approval for this study will expire on 3/29/2012.

Approved Items:
Protocol Document(s):

Feasibility of Wearable Sensors_Study Protocol.docx	1/12/2011 11:37 AM	0.01
---	--------------------	------

Consent/Assent Documents:

Name	Modified	Version
3205_ICF.docx.pdf	3/30/2011 10:18 AM	0.01

It was the determination of the IRB that your study qualified for expedited review which includes activities that (1) present no more than minimal risk to human subjects, and (2) involve only procedures listed in one or more of the categories outlined below. The IRB may review research through the expedited review procedure authorized by 45CFR46.110 and 21 CFR 56.110. The research proposed in this study is categorized under the following expedited review category:

(6) Collection of data from voice, video, digital, or image recordings made for research purposes.

Please note, the informed consent/assent documents are valid during the period indicated by the official, IRB-Approval stamp located on the form. Valid consent must be documented on a copy of the most recently IRB-approved consent form.

As the principal investigator of this study, it is your responsibility to conduct this study in accordance with IRB policies and procedures and as approved by the IRB. Any changes to the approved research must be submitted to the IRB for review and approval by an amendment.

We appreciate your dedication to the ethical conduct of human subject research at the University of South Florida and your continued commitment to human research protections. If you have any questions regarding this matter, please call 813-974-9343.

Sincerely,

Janelle Perkins, PharmD, Chairperson
USF Institutional Review Board

UNIVERSITY OF MIAMI

TOWARD AN EMOTIONALLY INTELLIGENT PIANO: REAL-TIME
EMOTION DETECTION AND PERFORMER FEEDBACK VIA
KINESTHETIC SENSING IN PIANO PERFORMANCE

By

Matan Ben-Asher

A THESIS PROJECT

Submitted to the Faculty
of the University of Miami
in partial fulfillment of the requirements for
the degree of Master of Science in Music Engineering Technology

Coral Gables, Florida

May 2013

UNIVERSITY OF MIAMI

A Thesis Project submitted in partial fulfillment of
the requirements for the degree of
Master of Science in Music Engineering Technology

TOWARD AN EMOTIONALLY INTELLIGENT PIANO: REAL-TIME
EMOTION DETECTION AND PERFORMER FEEDBACK VIA
KINESTHETIC SENSING IN PIANO PERFORMANCE

Matan Ben-Asher

Approved:

Dr. Colby N. Leider
Associate Professor of Music Engineering

Dr. Shannon K. de l'Etoile
Associate Dean of Graduate Studies

Dr. Christopher L. Bennett
Research Assistant Professor of Music En-
gineering

Dr. Daniel S. Messinger
Professor of Psychology

Toward an Emotionally Intelligent Piano: Real-Time Emotion Detection and Performer Feedback via Kinesthetic Sensing in Piano Performance

Abstract of a Master's Research Project at the University of Miami

Research Project supervised by Dr. Colby N. Leider

Number of Pages in Text: [124]

This research employs an agglomeration of knowledge from the fields of electrical engineering, digital signal processing, physics, computer music, music performance, music psychology, machine learning, and pattern recognition. The integration of this knowledge is applied to the technology of inertial measurement sensors in an attempt to detect musical expression and emotion in intuitive gestures based solely on kinesthetic data from piano players in real-time. A system is presented for detecting common gestures, musical intentions and emotions of pianists in real time using kinesthetic data retrieved by wireless inertial measurement sensors. The algorithm is implemented using the gesture recognition toolbox in EyesWeb software and employs the lens model of communication of emotions in music. The algorithm can detect common Western musical structures such as chords, arpeggios, scales, and trills as well as musically conveyed emotions such as cheerful, mournful and vigorous, completely and solely based on motion sensor data. The algorithm can be trained per performer in real time or can work based on previous training sets. The system presents feedback to the user by mapping the emotions to a color set and projecting them as a flowing emotional spectrum on the background of a piano roll. The detected emotion is also shown as an object floating in the two-dimensional emotion space of the adjective circle. The system was tested on a study group of pianists, detected and displayed structures and emotions, and it provided some insightful results and conclusions.

DEDICATION

In loving memory of my grandfather, emeritus supreme court justice professor Menachem Elon, who passed away while I was writing this thesis. He inspired me to strive for the very truth and towards great achievements, but to forever maintain a practice of solidarity, justice, and human dignity. He knew very little about music and even less about engineering, but he knew a great deal about emotion.

PREFACE

Hence, again, it becomes possible for motion in music to imitate the peculiar characteristics of motive forces in space, that is, to form an image of the various impulses and forces which lie at the root of motion. And on this, as I believe, essentially depends the power of music to picture emotion. [Helmholtz, 1863].

TABLE OF CONTENTS

DEDICATION	iii
PREFACE	iv
LIST OF TABLES	ix
LIST OF FIGURES	x
CHAPTER	
1 Introduction	1
2 Background	8
2.1 Inertial Measurement Units (IMUs)	8
2.1.1 Overview	8
2.1.2 Accelerometers	9
2.1.3 Gyroscopes	10
2.1.4 The APDM Software Development Kit	12
2.2 Motion Analysis and Gesture Recognition	12
2.2.1 Motion Capture Data	12
2.2.2 Similarity Measures	14
2.3 Bayes Decision Theory	15
2.4 Expressive Notation	17
2.4.1 Dynamic Markings	18
2.4.2 Articulation	19
2.5 Expression and Communication of Emotion in Music Performance	22
2.5.1 Philosophical Problems and Theories of Emotions	22

	Page
2.5.2 Hevner’s Adjective Circle	29
2.5.3 The GERMS Model	31
2.5.4 The Functionalist Perspective	33
2.5.5 The Standard Paradigm	35
3 Previous Work	38
3.1 Computational and Perceptual Models	38
3.1.1 The Todd Model	38
3.1.2 The KTH Rule System	40
3.1.3 The Lens Model	43
3.2 Real-Time Machine Learning Tools	47
3.2.1 The Wekinator	47
3.2.2 EyesWeb and The Gesture Recognition Toolbox	49
3.3 Previous Applications	50
3.3.1 The Fuzzy Analyzer	50
3.3.2 Mapping Emotions to Colors in Musical Performance	53
3.3.3 IMUs in Piano Teaching	54
4 Proposed System	58
4.1 System Design	58
4.1.1 System Specifications	58
4.1.2 Setup and Top-Level Design	60
4.1.3 Data Collection and Storage	63
4.2 Algorithm Description	63
4.2.1 Feature Extraction	64

	Page
4.2.2 Classification	71
4.3 Post Processing and Visual Feedback	78
4.3.1 Post Processing	78
4.3.2 Visual Feedback	79
5 Evaluation	82
5.1 Evaluation and Research Goals	82
5.2 Subjects	83
5.3 Experiment Procedure	84
5.3.1 Stage 1 – The Standard Paradigm, One Piece Different Emotions	84
5.3.2 Stage 2 – Different Pieces, Different Emotions	85
5.3.3 Stage 3 – Free Playing, Self-report, and Listener Evaluation	86
5.4 Tools for Classifier Evaluation	86
5.4.1 Confusion Matrix	87
5.4.2 Precision, Recall, Accuracy, and Specificity	87
5.4.3 RMS Error	88
5.4.4 χ^2 Test	89
5.4.5 Cohen’s κ test and weighted κ test	91
5.5 Results	93
5.5.1 Stage 1 - The Standard Paradigm, One Piece Different Emotions	93
5.5.2 Stage 2 – Six Pieces, Different Emotions, testing on Free- playing and Self-report	97
5.5.3 Stage 3 – Performer vs. Listener vs. Algorithm	101

	Page
6 Discussion	107
6.1 System Performance, Limitations, and Possible Improvements .	107
6.2 Research Discoveries and Ideas for Future Research	112
LIST OF REFERENCES	118

LIST OF TABLES

Table		Page
1	Test Subjects Description	84
2	Stage 1 – Classification results per subject over all categories in the Standard Paradigm	94
3	Precision, Recall, Specificity, and Accuracy per category for Stage 1	96
4	χ^2 test results per category for Stage 1	97
5	κ test results for Stage 1	97
6	Precision, Recall, Specificity, and Accuracy per category for Stage 2	100
7	χ^2 test results per category for Stage 2	100
8	κ test results for Stage 2	101

LIST OF FIGURES

Figure		Page
1	Diagram of accelerometer design	9
2	Diagram of MEMS gyroscope tuning fork design	11
3	Opal monitors on hands.	11
4	First measures of Beethoven Sonata No. 8 <i>Pathetique</i>	20
5	Excerpt from Schubert Impromptu 142 D 935.	21
6	Hevner’s Adjective Circle.	30
7	Five components of performance expression, the GERMS model.	33
8	Todd simulation results.	39
9	Summary of KTH rule system.	42
10	Portraying emotions with the KTH rules.	42
11	Modified Lens Model.	43
12	Naïve Bayes Classification in EyesWeb.	50
13	Fuzzy Analyzer for Estimating Emotions.	52
14	Mapping Colors to Emotions.	54
15	IMU Data in Piano Playing Patterns.	56
16	System Diagram Illustration.	61
17	Tempo from Motion Algorithm.	68
18	Dynamics from Motion Algorithm.	70
19	Articulation from Motion Algorithm.	72
20	Tempo, Dynamics, and Articulation displayed in EyesWeb. . . .	72
21	Display of piano roll with emotion colored background.	80

Figure	Page
22	Adjective Circle on HSV Color Wheel. 81
23	Overall Confusion Matrix Stage 1. 95
24	Overall Confusion Matrix for Stage 2 99
25	Three dimensional confusion cube 102
26	Emotion paths of Performer, Listeners, and Algorithm though one minute of Classical piece 103
27	Emotion paths of Performer, Listeners, and Algorithm though one minute of Jazz improvisation 105
28	Emotion paths of Performer, Listeners, and Algorithm though 20 seconds of a Contemporary improvisation 106
29	<i>Intensity, tempo, and articulation</i> 3D scatter plot 110
30	3D scatter of linear combination of features projected to three dimensions using MDA 111

1

Introduction

“Music exists only at the moment of its performance” [Kierkegaard, 1843]. Although nearly two centuries have passed since this statement was first made, it seems that it is still well established that live performance is in fact the paramount musical experience. It is in live performance that the dyad between performer and audience creates that intimate setting where extreme emotions manifest in music and gestural expressions. And it is the integration and interaction of senses – sound, sight, and even touch – that the performer exploits in order to convey the verbally ineffable. It seems therefore, that while investigating the emotions aroused by music it is only reasonable to explore the relationship of motion to the musical experience.

The expressions and emotions communicated and aroused by music have been addressed from a wide range of directions, some of which are quite distinct and some that overlap. These include the fields of philosophy, music psychology, musicology, computer music, artificial intelligence, machine learning, and music information retrieval.

From a philosophical and psychological perspective, emotions in music have been of core interest for centuries and have attempted to define, model, and justify the problematic, controversial but yet undeniable expressive power of music. Some of the influential works were those of [Helmholtz, 1863],

[Seashore, 1938], and [Meyer, 1956]. However, a significant majority of this research was based on the acoustical phenomena and structural compositional elements. It is only recently that the performance aspect of music has become of interest to this kind of exploration [Juslin and Timmers, 2010]. I will review some of this in the *background* section.

More recently, from the motivation of expressive performance in computer music, there have been ongoing attempts to quantify and objectify the way in which human expression can be embedded in what otherwise would be a stale performance. The KTH rule-system developed at the KTH Royal Institute of Technology [Friberg et al., 2006], describes a set of rules to employ on a musical score in order for it to sound lively and expressive while being played back by a computer. This research led to an enhanced understanding of how expression is conveyed in the audio of a music performance. But it is reasonable to assume that these realizations might not be limited to the analysis of the acoustical property of music, since many of these insights describe performance rules that can possibly be picked up in the motion of the performer. Thus, the motion can be analyzed using some of the same rules that are employed on musical audio analysis. This is explained in more detail in the *previous work* and *proposed system* sections.

The more recent burst of development and utilization of machine-learning algorithms has spawned research in human gesture recognition aimed at the control of musical instruments and audio effects [Dillon et al., 2006],

[Toyoda, 2007], [Höfer et al., 2009], and [Odowichuk et al., 2011]. These publications mostly describe novel controllers and games employing gesture recognition. Utilizing the motion in musical performance has also been attempted in some studies. Friberg [Friberg, 2004] implemented a *fuzzy logic analyzer* that uses audio data as well as video stream of a performer to map the performance to specific expressions. This is also reviewed in detail in the *previous work* section. More recently, Nicholas Gillian and Benjamin Knapp [Gillian et al., 2011a] have developed a gesture recognition toolbox for the EyesWeb¹ environment that enables use of a variety of machine-learning algorithms in real-time. This environment was specially designed to explore interactive multidimensional musical interfaces and displays. For additional related work that has been performed with EyesWeb and this toolbox see [Camurri et al., 2000], [Camurri et al., 2004], [Camurri et al., 2007], [Varni et al., 2010] and [Gillian et al., 2011b]. The gesture-recognition toolbox in EyesWeb is a major infrastructure in the present research. I will go into more detail regarding some of these in the *background* and *previous work* sections. However, at this point, it is important to note that all of these developments indicate that we are approaching a point where machines can recognize and detect human intentions in a real-time environment to a level of accuracy that can make the computer an active and live participant in the music-making process.

There is a history of the study of motion of performers in the past century,

¹http://www.infomus.org/eyesweb_eng.php

but in the recent decades this is traditionally carried out by use of video-tracking systems employing passive or active markers. This setup is referred to as motion capture (*mocap*) and is mostly used for animation. I will review it in the *background* section. In addition and in parallel to these, during the past decade, the technology of inertial measurement units (IMUs) has become commercially available and accessible at any budget and scope. Sensors such as accelerometers, gyroscopes, and magnetometers are commonly integrated in almost all mobile devices, and much research is carried out with these sensors in a variety of fields from medical devices, computer games, and musical controllers.

However, to this day, and despite these advances, the use of these novel technologies has not yet been adopted by most musicians, and most performers still use instruments employing technology from decades ago. A common justification to this phenomenon is that many performers lack the bandwidth required to master additional controls [Cook, 2001], or in other words, they have their hands “tied”. This implies that these technologies have still not been implemented in musical controllers in a way that can actually be useful to create music that can be mastered, widely adopted and appreciated.

A possible reason for the deficiency of motion sensor-based controllers could be the knowledge gap in the understanding of the optimal way to employ motion-sensor technology into musical controllers in a way that a greater majority of musicians would accept. A musical controller might be easy to adapt to if instead of having to master it, the device would employ machine-learning

algorithms to detect the musicians' intentions. This way mastering it would impose a minor requirement on the musician in terms of how much they need to alter their movements. Such a controller could be trained to detect various types of musical intentions such as patterns of playing, expression and musical emotions. Therefore, it seems that the missing link between utilizing motion sensor technology in music controllers, machine learning and interactive computer music composing and performance is some theory in the ability of a machine to detect musical intentions (just like a fellow performer does) in intuitive expressive musical gestures.

But how much information is actually conveyed through a musician's motions, and how detailed is this information? Are these motions direct expressions of emotions, or are they merely a side effect of the physicality in controlling the instrument? Since it is reasonable to assume that it is not one or the other but rather a combination of the two, by tracking a musician's motions, how much information can we retrieve about the musical content being displayed? Could we track musical structures such as chords and arpeggios, crescendos and diminuendos? Could we detect emotions such as anger or cheerfulness? At what resolution and accuracy could we detect this information? And moreover, assuming the musician is *moved* by his or her's own performance, how would this influence our observations, and how much would this information correlate with the musical interpretation of the piece being played? These are all questions this research attempts to address.

The applications of answering these questions aside from pleasing our curiosity would enable us to design artificially intelligent musical controllers that could interact with the musician by detecting the musician's intuitive gestures and using them to augment and control the music. This could also be used in music pedagogy and music therapy as a feedback system for expressive performance. Moreover, the evolution path of emotions through a musical piece has interest in other communities such as music informatics/retrieval, musicology, music composition and music psychology. For example, following the emotional path through a Beethoven sonata might help us better understand the tracks of the emotional "rollercoaster" we experience while listening to this exhilarating music.

In this research, I will employ an agglomeration of knowledge from the fields of electrical engineering, digital signal processing, physics, computer music, music performance, music psychology, machine learning, and pattern recognition. I will attempt to combine the knowledge in order to use the rather recent technology of inertial measurement sensors to detect musical expression and emotion in intuitive gestures based solely on kinesthetic data of piano players in real time. While preparing for this research I noticed that much of the published work in the fields of engineering is engaged in the tasks of circuit design, programming, mechanical design, and other technical issues of "getting stuff to work", which does not leave much time for the research itself. It was therefore my secondary goal to utilize existing technology as much as possible in order to

minimize the time lost on development and maximize that spent on the research.

2

Background

The ordering of the sections in this chapter is one of several possible alternatives that exist. Nevertheless, I have chosen a layout in a bottom-up approach, from the finest physical inspection in the details of particle motion to the large-scale abstract observations and reflections on human emotions. I feel that this should make the reading experience flowing and insightful to the reader.

2.1 Inertial Measurement Units (IMUs)

In this section, I will review the topic of inertial measurement units, describe those used in this research and provide a brief overview of how they operate.

2.1.1 Overview

The inertial measurement units used in this project are body worn monitors named *Opals*, manufactured by *APDM*¹. Each IMU consists of a 3-axis accelerometer, a 3-axis gyroscope, and a 3-axis magnetometer. The Opals transmit the measurements from these sensors wirelessly to a receiver connected to a computer at a rate of 64 samples per second. These units will be explained in the sections that follow.

¹For more information about the Opal sensors, see the APDM web site. <http://www.apdm.com/>.

2.1.2 Accelerometers

Accelerometers typically measure *proper acceleration* which is the physical acceleration experienced by an object in the frame of an observer in free-fall. Therefore, an accelerometer on the earth's surface and in no motion will measure a constant positive 9.8 SI (m/sec^2) upwards and an accelerometer in free-fall towards earth will measure zero acceleration. A more general explanation to this behavior is the *equivalence principle* from relativity theory [Einstein et al., 1920] that shows how the effects of gravity on an object are indistinguishable from acceleration. In fact, the design concept of accelerometers is based on this equivalence since what is actually measured in them is force and not position. In order to measure the movement acceleration that is the second derivative of the body position relative to earth, this constant can be corrected by a simple calibration, by subtracting its value from our measurements.

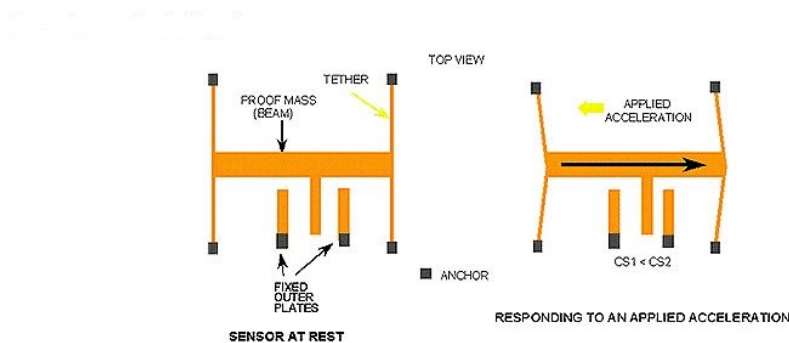


Figure 1: **Diagram of typical accelerometer design.** A moving proof mass hung between two tethers and connected to a capacitive plate that moves between two anchored plates creates a capacitance divider. Diagram from [Analog Devices, 2008].

The modern design of accelerometers and also that of our Opals is a *micro electro-mechanical system* (MEMS). A typical design is based on a proof mass

connected to a tether that is anchored at the edges. The mass is free to move in a constant range between those edges. The proof mass is also connected to some capacitive plate that moves along with it between two anchored capacitive plates. This creates two sets of capacitive plates that modify their capacitance as a result of the mass's movement. See figure 1.

2.1.3 Gyroscopes

Gyroscopes measure angular velocity in units of degrees per second. The theory behind their operation is employing the phenomena of the *Coriolis effect* that a mass in motion experiences when angular rotation is applied to it. This force is always perpendicular to both the motion vector and the angular velocity vector ² [Feynman et al., 1963]. The Coriolis force causes a displacement that can be measured by a capacitive sensing structure, similar to that in a MEMS accelerometer. Typically, in a method called *tuning fork configuration*, two masses are positioned in a way that they constantly oscillate in opposite directions. The masses are attached to capacitive plates that are also in motion with them. Then, when an angular velocity is applied to the two-mass system, the Coriolis force pushes each of the masses in opposite directions. This causes a displacement between the masses that is measured in a change in the capacitance between the plates connected to them.

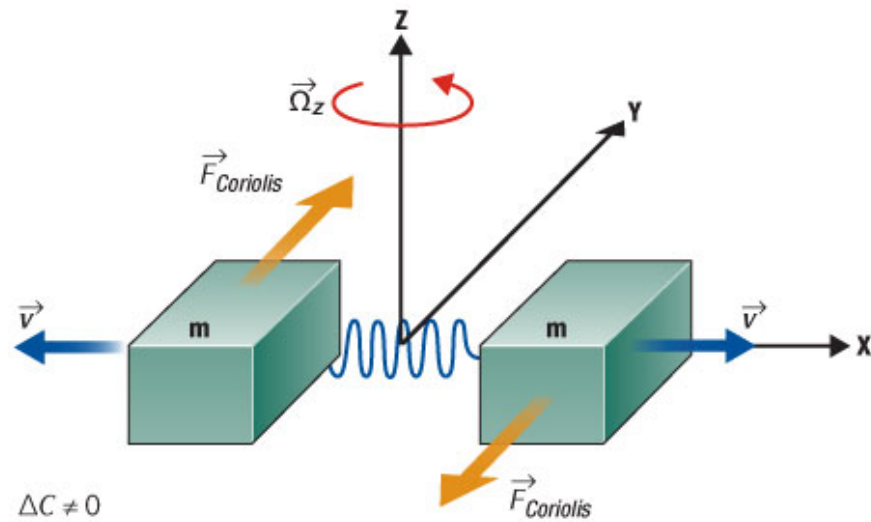


Figure 2: **Diagram of MEMS gyroscope tuning fork design.** Two masses oscillate in opposite directions. Applying angular velocity to the two-mass system causes them to displace in opposite directions. This displacement is measured in a capacitance change between them. Diagram from [Solid State Technology, 2010].



Figure 3: **Opal monitors on hands.**

2.1.4 The APDM Software Development Kit

The APDM access point is read utilizing a set of library functions in MATLAB in a dedicated SDK. This includes functions for reading the data buffers in the access point per monitor or for all monitors at once, clearing the buffers, setting parameters such as sample rate, streaming configuration modes and data synchronization. The SDK can be used in Matlab or C++. For detailed information on the SDK and its functions see [APDM, 2011] and [APDM, 2012b]

2.2 Motion Analysis and Gesture Recognition

2.2.1 Motion Capture Data

Motion capture (AKA *mocap*) and motion analysis algorithms have been of deep interest in the fields of computer science and specifically computer animation for military, sports and entertainment applications for over two decades. A majority of the development in this field is image-processing-based and is engaged in detecting human activities in video streams. The most common technique of collecting motion capture [Müller, 2007] is with the use of several dozen (40–50) retro-active optical markers attached to a subject’s suit and a set of 6–12 cameras detecting their location at up to 240 frames per second. Each camera generates a 2D data stream of the marker locations. By knowing the location and orientation of the different cameras, alignment algorithms can collect the multiple sets of 2D data and reconstruct the 3D image of the motion that was tracked. The data set created by such a system can be either used immediately for animation purposes or referred to further processing such as

²it is a *vector cross product* of the two.

detecting gait deviations and other movements for physical therapy. In some applications, the marker data must be converted to a *skeletal kinematic chain* by using fitting algorithms. This is useful for robustness and enables using different sensor configurations, but it is limited by the skeletal model's accuracy in its approximation of the human body that does not always account for possible variances.

One way or another, most mocap systems produce some kind of *kinematic chain* that consists of body segments connected by joints. For a proper mathematical description of mocap data, we let J denote a set of joints (such as {left ankle, right knee}). Then we define the *motion capture data stream* as a set of frames (also called *poses*). Each pose can be described as a matrix

$$P \in \mathbb{R}^{3 \times |J|} \tag{1}$$

where $|J|$ is the number of joints. Thus, the j th column of P is denoted P^j and is in effect the 3D coordinates of that joint in that frame. So, the complete data stream can be described by

$$D : [1 : T] \rightarrow \mathcal{P} \subset \mathbb{R}^{3 \times |J|} \tag{2}$$

Now T is the number of poses and \mathcal{P} is the set of poses. A subsequence of frames is also referred to as a *motion clip* and the curve described by a single body joint is referred to as *3D trajectory*.

2.2.2 Similarity Measures

While observing mocap data, probably the most fundamental element is finding suitable similarity measures that can be calculated by an algorithm and used to compare two or more motion clips. Now, the definition of similarity of course varies per application according to the requirements on the performance of the system. For example if the system needs to detect a state of running versus walking but disregard the subtleties of gait then we shall define all types of walking as similar as opposed to running. However, if the system is required to detect an emotional intention in motion such as *aggressive* or *shy*, then it would have to distinguish between different types of walking but not necessarily between running and walking if they were to fall under the same category (for example, vigorous walking and running would both fall under the *aggressive* category).

A good general rule for defining similarity is to regard two motions as similar if and only if they can be projected to have the same representation via a *global transformation*. The simplest example of a similarity such as this is a body performing the same motion at two different locations relative to the center of a room. By projecting both motions to an axis system centered on the body itself, the dissimilarity is eliminated and the motions can be regarded as similar.

However, this measure could also be extended to any global rotation about an axis, or, in the case where size and speed are not of interest, (for example in detecting an element in sign language), the transformation could include scaling in time and space, making the similarity measure spatially and temporally

invariant.

In the scope of this project, I intend to detect emotions and intended expressions in piano-playing motion. In mocap nomenclature, this falls under the category of *motion style* or *motion content*. Various techniques such as Fourier Expansion, Principle Component Analysis (PCA) and Hidden Markov Models are employed in order to address the complex task of analyzing and synthesizing motion styles. For a comprehensive overview of how motion content and style are treated in literature see [Müller, 2007].

2.3 Bayes Decision Theory

Bayes decision theory is one of the most efficient and straightforward methods in pattern classification. It is a stochastic approach that assumes that the decision problem can be solved based on probabilistic considerations [Duda et al., 1995a]. A Bayes classifier relies on the fundamental *Bayes Theorem* from probability theory dating back to Reverend Bayes himself. The theorem, [Bayes and Price, 1763] determines the probability of occurrence of event ω_j given the fact that another event x has occurred. This rule is an inverse version of the conditional probability rule and is depicted in Equation 3.

$$P(\omega_j|x) = \frac{p(x|\omega_j)P(\omega_j)}{p(x)} \quad (3)$$

Here, the lower case p is the probability *density function* and the upper case P is the *probability mass function*. Notice that the denominator in equation 3 does not depend on ω_j and is actually the sum of all density functions weighted by their

probabilities and is a constant scaling factor. Therefore, because we will only be comparing and not interested in evaluating the probabilities, in practice we can ignore the denominator and use the numerator to classify the event ω_j . In order to further understand how we can apply the Bayes rule to make decisions and predict future events, we can express it informally in English as in equation 4:

$$posterior = \frac{likelihood \times prior}{evidence} \quad (4)$$

So, by measuring the value of x , knowing the probability density of $p(x|\omega_j)$ and knowing the prior probability $P(\omega_j)$ we can evaluate the posterior probability $P(\omega_j|x)$, which is the probability of the occurrence of ω_j given that the value x has been measured.

Now, let us assume a uniform distribution of the class state ω_j , i.e. without prior knowledge it could be any state at equal probability³. Then, all we need to do is get a good approximation of the likelihood $p(x|\omega_j)$. One way to do this is to assume a distribution function for x (for example a Gaussian distribution), and then estimate its parameters by performing measurements of x in different ω_j conditions (i.e. for all j) [Duda et al., 1995b]. These training measurements will give us estimations of the mean and standard deviation of our variable and that is all we need in order to calculate the Gaussian probability density function for any x . And since we already assumed that $P(\omega_j)$ is constant, this Gaussian function will give us the likelihood of event ω_j occurring given the

³More knowledge however, could improve our approximation, and I will discuss this in later chapters.

value of x . Now, by choosing the event with the highest likelihood, we can classify which is the most likely event ω_j .

Moreover, by comparing the likelihood of the different events at a given x we can calculate the probability error which is, in the case of two categories, equal to the probability of the category not chosen. Thus, by selecting the category with the higher probability, we de facto minimize the error. Therefore, our final decision and error for the two-category case with equal probabilities can be given by

$$\text{Given } x : \text{decide } \omega_1 \text{ if } P(x|\omega_1) > P(x|\omega_2); \text{ otherwise decide } \omega_2 \quad (5)$$

and

$$P(\text{error}|x) = \min[P(\omega_1|x), P(\omega_2|x)], \quad (6)$$

I will review the Naive Bayes Classifier in more detail in the *proposed system* section including a generalization for the multivariate d dimensional feature space and N categories. For a comprehensive mathematical description of Bayesian theory and see [Duda et al., 1995a] and [Duda et al., 1995b].

2.4 Expressive Notation

Modern Western music notation has evolved for over 400 years and has realized stages of varying levels of detail in terms of how descriptive composers have conveyed their intentions in scores. The basic score representation describes only the technical aspect of music, namely, which note is played at what time and for how long. Thus, in their primal form, music scores depicted just this. The

Baroque period was in fact characterized with very few expressive markings in the notes and often employed tablature in the form of figured bass. However, as musical instruments evolved and were perfected through the Classical and Romantic periods, as seen in the evolution from the harpsichord to the fortepiano and then on to the piano [Fletcher and Rossing, 1998], the expressive bandwidth of musicians expanded and along with it the expressive markings on piano score sheets. These markings incorporated various forms and will be discussed to an extent in this introduction. For more details and an insightful reading experience about the history and evolution of music notation see [Read, 1979a].

2.4.1 *Dynamic Markings*

Dynamic markings were introduced in sheet music at the beginning of the seventeenth century. The first indications were the Italian words *piano* (soft) and *forte* (loud). Further on, with the development of symphonic writing during the eighteenth century in the works of Mozart and Haydn, the dynamic markings evolved from the binary form to more of discrete degrees of loudness such as *mezzo forte* and *pianissimo*. The romantic composers of the nineteenth century (such as Wagner, Tchaikovsky and Mahler) followed by the avant-garde twentieth century composers (e.g. Berio and Stockhausen) with their demand for extreme subtlety ultimately transformed the markings to a practically continuous spectrum of dynamics. This leaves us with a very wide range from *fortissississimo* (**ffff**) (used by Tchaikovsky in the *1812 Overture*) all the way down to *pianissississississimo* (**pppppp**) (used by Tchaikovsky in the *Pathetique*

Symphony).

In addition to the above absolute and somewhat obscure scale, the more commonly used and comprehensible dynamic markings are the relative markings *crescendo* and *diminuendo* which direct a gradual increase or decrease in loudness. When a relatively short increase or decrease is required (over just a few notes), the word markings are often replaced by the dynamic symbols $>$ and $<$. These symbols are often accompanied by descriptors *molto* (much) and *poco* (little).

More specifically, due to its unique design, piano notations are even more complex and are often combined in intriguingly sophisticated ways such as the sign ***fp*** on a single note. This marking is a direction to attack with *forte* and then an immediate *piano*. This type of marking appears in various forms such as ***ffpp***; ***ffmp***; ***mfp***; and ***fppp***. Finally, accent terms are also often merged in with dynamic notation, forming marking such as ***fzp*** which means *forzando* followed by *piano*, or ***sfmp*** which means *sforzando* followed by *mezzo piano*, all variations of the ***fp*** sign. See figure 4 for an example on the use of combined dynamic markings. For more details, see [Read, 1979b]

2.4.2 Articulation

A second fundamental variant that makes music more than just a mechanical stream of sounds are the patterns of accents on which the musical expression is conveyed. An accent is an exaggerated stress upon any beat or portion of a beat. Even without extra markings, all Western music has an innate

The image shows the first two systems of a musical score for Beethoven's Sonata No. 8, Pathétique. The first system is marked 'Grave' and contains three measures. The second system starts at measure 4 and contains two measures. The score is written for piano and includes various dynamic markings such as *fp*, *sf*, *p*, *cresc.*, and *ff*. It also features articulations like accents and slurs, and complex rhythmic patterns in both the treble and bass staves.

Figure 4: **First measures of Beethoven Sonata No. 8. *Pathétique*.** Emphasizing the composers extended use of combined dynamic markings to direct the performer on his precise expressive intention.

pattern of accent or stress that is emphasized by the meter of the piece which is set up by the bar lines. Thus, the initial beat of any measure receives an accent, regardless of the time signature. In order to direct an accent in a place other than this, a composer uses the accent mark ($>$) below or above the note opposite to where the stem is.

Accent markings are divided into two categories: *percussive* attack and *pressure* attack. Percussive accents are typically used for higher dynamic levels (*mf* and louder) while pressure accents are used with lower levels of dynamics (*mp* and softer). This is comes from pragmatic reasons that accenting a note with a sharp percussive attack will naturally create a loud dynamic level whereas accenting while keeping a low dynamic level will produce a pressured accent with a soft percussive attack. The percussive accents are marked either by $>$ or by a wedge \wedge . The wedge typically directs a forceful accent and is used with only high dynamic levels (*f* and up). The pressure accents are usually marked by $>$ or $-$.

played in a *legato-staccato* fashion, thus, stressing each note but also merging them and somehow emphasizing that they are a group. For an example see figure 5. The result of performing such accentuation is more perceptual than physical and therefore it will be quite interesting to see how much of it can be detected with inertial sensors. For more details on accents and slurs see [Read, 1979c].

2.5 Expression and Communication of Emotion in Music Performance

The emotional aspect of music has been studied for over a century and has been approached by researchers in the fields of music psychology, philosophy, musicology, music pedagogy, and music performance. In this section, I will attempt to review and summarize only that research that I intend to employ or observations that seem relevant to me in the context of this dissertation. Namely, the research that involves the understanding of communication of emotions in music performance and specifically that which relates to human motion. For a comprehensive review, see [Juslin and Timmers, 2010], [Gabrielsson and Lindström, 2010], and [Davies, 2010].

2.5.1 *Philosophical Problems and Theories of Emotions*

Before commencing this short expedition, I feel it is appropriate to point out some philosophical difficulties in the topic itself. The first obstacle that arises immediately when discussing emotions in music is the following: When we say that something expresses an emotion, we mean that it reflects a state that it feels. For example, a person's tears could express their sadness if they are actually feeling it. So how could music, being merely organized sound and by

definition a non-sentient object, express emotion? There are, of course, several answers to this question, but there are also various consequent questions that would follow [Davies, 2010].

Addressing these problems requires a basic understanding of theories regarding the phenomenon of emotions. The core debates regarding emotions in the world of philosophy and psychology have historically been over the extent of emotions being bodily sensations, a notion dating as far back as Descartes's awareness of perturbations of animal spirits [Descartes, 1649], or rather cognitive realizations as developed in the cognitive theory in the 20th century.

The first attempts to discuss emotions in the science of the modern age were through a biological-physiological perspective. In Darwin's "The Expression of the Emotions in Man and Animals" [Darwin, 1874], he discussed the role of emotions in human communication for the purpose of survival. This was then followed later by the *James-Lange Theory of Emotions* [James, 1884] and [Lange, 1885]. These theorists maintain that emotions are perceptual experiences corresponding to triggered activities in the autonomic nervous system, and that they are caused only by physiological changes in the body. In the words of William James: "we feel sad because we cry, angry because we strike, afraid because we tremble, and neither we cry, strike, nor tremble because we are angry, or fearful, as the case may be". These theories, and modified versions of them, are still held today to an extent, especially in the fields of neuroscience and in biofeedback research. Since the current research is of proximity to the latter, I

shall refer to it in later sections.

The developments in the fields of biology and psychology during the 20th century lead to a more complex interpretation described in the *Cannon-Bard Theory* [Cannon, 1929]. It was claimed and even proven to an extent that although physiological responses could cause some of the experienced emotions such as fear through the *fight-or-flight* mechanism, they could not account for the variety and the rapidness in which emotions are perceived. Moreover, [Bard, 1928] proved that all physiological sensations including motor information had to pass through the thalamus before being processed and interpreted to consequential actions. This makes it impossible for certain sensations to trigger direct physiological responses and then emotions without first being consciously perceived. It was therefore established that cognition generates both the physiological and perceptual manifestations of at least some of the emotions.

Another research that is important to mention here is that which initiated the *Two-factor Theory of Emotion* [Schachter and Singer, 1962]. This observed the emotional state of subjects that were injected with epinephrine. The epinephrine typically causes a state of arousal and bodily sensations. It was observed that in the presence of emotion evoking cues, (for example, from an actor in the room), the subjects who were unaware of the expected effects of epinephrine, attributed the physiological responses to emotions, while the subjects who were informed about the effect did not, and some of them did not even display any of the typical physiological manifestations of emotions (such as

tremors or increased pulse). This research led to an understanding that although physiological changes play a role in experiencing emotions, the role is to allow a cognitive appraisal to an event, but the interpretation of this event is what defines the subjective emotional experience. Thus, being at a high state of arousal could lead a subject to euphoria just as well as anger, depending on the cues that are available. This research was then followed by [Erdmann and Janke, 1978] and criticized in [Marshall and Zimbardo, 1979].

More topics discussed and specifically regarding emotions experienced in music, are if the existence of emotions requires an external object (real or imaginary) to which they are directed. Moreover, a distinction is made between emotions and moods that I will not go into in this framework. It is however, important to summarize that emotions in and out of the musical context are generally observed as a phenomenon that is more cognitive than mere physiological reactions such as increased heartbeat and tremors, but is not completely and solely a cognitive process. It is also important at this point, to note that even though we are addressing emotions in the musical context, we are still constrained to assign terms such as *sad* and *happy* with their usual meanings, otherwise we cannot refer to them as emotions. Therefore, when we describe an emotion expressed in music in terms of regular emotions we must also account for how it relates to its normal application. This constraint is actually quite helpful, because it rules out some approaches to the topic.

It follows that music's expressiveness can no longer be reduced to simple

technical compositional elements such as a minor chords, since the term *minor key* cannot not equate to *sounds sad* until it is explained how the music's modality can make true the manifestation of something actually pertaining to sadness and misfortune. Another approach that is ruled out is that which refers to music as a metaphor of expressive nature. This too is not inductive to claim anymore because a metaphor by definition is a linguistic device based on semantic relations. But music in its core cannot contain these semantics unless they are defined that way (i.e. the term *minor key* is not defined as *sad* even if it can trigger that emotion). Otherwise, it is like suggesting that music is a metaphor by metaphor, which does not really lead anywhere. The third approach that cannot hold is the theory of *sui generis*, which claims that music's expressiveness is of its own kind. This is now clearly not offering a theory because based on this we cannot refer to the expressions in music as emotions. Of course, music is unique in its expressiveness, which is only to be expected due to its manifestation in a different medium than other communications, but in order to analyze this phenomenon one must address the existence of any equivalence to other biological expressiveness [Davies, 2010].

Music as a Symbol

There are however still various possible explanations to our problem. The first one is suggesting that music operates as a symbol [Cooke, 1959]. Thus, it can refer to an emotion and characterize it similar to the way a language does. For this to be possible, music must encompass a sort of vocabulary for expressing

emotions. Although there have been attempts to describe such as system [Jackendoff and Lerdahl, 1983] and it is clear that music is highly formed and organized, it still does not consist of the basic elements required in a meaningful language such as predications and propositional logic. Another symbolic explanation is that music refers to emotions by association due to linking of phrases and sounds to certain texts or ceremonies such as relating the organ to religion and spirituality and the trumpet to majesty and war. This might explain some referral to emotions but still cannot account for how music characterizes emotions. There are more semiotic theories regarding music's expressive nature, but they all fail in the same way because they lack a proper account for the direct and immediate manner that music affects us. Moreover, [Raffman, 1991] claims that whatever the meaning conveyed in music turns out to be, it will not be the *garden-variety* of emotions. She supports this with the claim that most traditional musical theories and grammars do not consist of elements attempting to convey emotions, in contrast with linguistics and other semantic languages that are designed to portray the meanings they offer.

Another topic addressed in length, since we have defined that emotion must exist in a sentient being, is who is therefore experiencing the emotions? There are of course three main candidates: the composer, the performer and the listener, and there are theories assigning the emotions to each of these and research supporting and refuting these claims. There is also an interesting theory describing an *imagined persona* to which we relate the emotions expressed in

music [Walton, 1988]. This theory is widely accepted but also has some objections, again relating to the level of detail that instrumental music can convey to be enough to imagine a story contrary to film or literature. For a full review see [Davies, 2010].

The Contour Theory

This seems to be the most promising theory and it is fortunate because it is highly consistent with the scope of this research. The *Contour Theory*, [Kivy, 1980], [Kivy, 1989], [Davies, 1994] and also [Nussbaum, 2007] does not attempt to connect the expression in music to occurring emotions. Instead, it suggests that certain patterns, shapes or movements are experienced as expressive without manifesting actual emotions. It is observed that faces and gait can appear happy or sad without actually feeling it or even intending to convey it. Furthermore, even still images of a weeping willow seem to express an emotion. The manner in which this is carried out according to the contour theory is by secondary side effect to a primary emotion that it often accompanies. The weeping willow looks like a person bent over in sorrow. In most cases, this appeals to us as a person actually expressing and feeling sorrow and we are wired to identify to this sorrow because it serves an evolutionary purpose, as I explain in later sections.

The contour theory notion with regard to music is that it can present emotion characteristics in a similar fashion. These manifest in the dynamic structures of music, which resemble those of human behavior and movement that

are related to emotions. This is different from the previous theories, since it does not suggest that music refers or symbolizes something beyond itself. The ability to be expressive is in the features of the music itself because they resemble the features of human motion that in many cases reflect emotion!

The emotion expressed in music is not immediate like the picture of the weeping willow, because music is a temporal phenomenon, and its expressiveness unfolds with the piece. This however, makes it more powerful in expressing emotions because they too, have a temporal aspect to them. Emotions are continuous, and they evolve in time. It is therefore, this innate sensitivity that composers and performers have mastered over the years to control (or one might say, exploit and manipulate), but the expressive nature inherently lies in our ability to animate music characteristics as motion.⁴

2.5.2 *Hevner's Adjective Circle*

In order to have a solid working definition to the emotions we wish to observe, we must look at some emotion categories. An inclusive and thorough work that laid the ground for further understanding and is still considered a sort of *ground truth* when it comes to musical emotions is Kate Hevner's *Adjective Circle* [Hevner, 1936]. It classifies the emotions portrayed in music into eight categories located on a circle where the distance between two categories on the circle implies their *proximity* in terms of the emotional meaning. Hence, for example, the categories *merry* and *mournful* are on opposite sides of the circle

⁴Davies addresses two more problems, which I will not review in this context. For more thoughts and analyses such as these, see [Davies, 2010].

whereas *dreamy* and *serene* are adjacent categories. See figure 6. The circle was

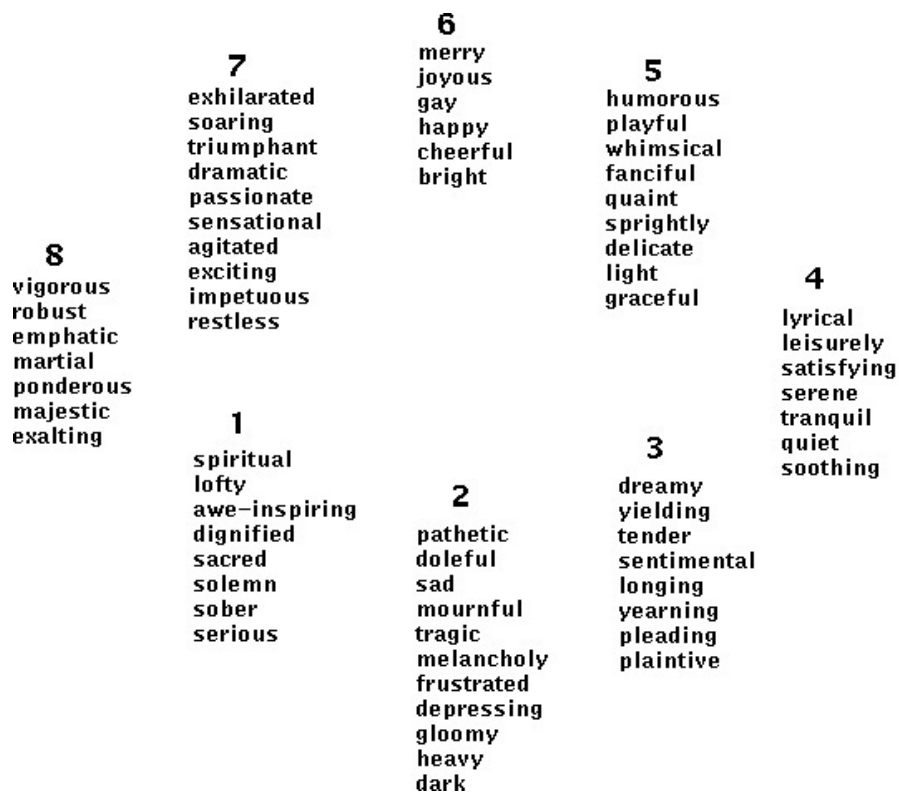


Figure 6: **Hevner's Adjective Circle.** The distance between categories on the circle implies their *proximity* in the context of their emotional meaning.

later updated by Schubert [Schubert, 2003] to have more categories, and some of the terms were adjusted to fit more modern English. Another common measurement of emotions is using Russell's *Circumplex Model of Affect* where the musical emotion is mapped in two-dimensional space of valence vs. arousal [Russell, 2003]. However, the emotion categories in this model were not tailored for musical emotions, and some are difficult to convey in music (such as sleepy or disgust). Moreover, it is possible to map Hevner's circle to a dimensional model similar to Russell's [Gabrielsson and Lindström, 2010]. In this study, I will utilize this implicit dimensionality by addressing adjacent categories as *close* in the

emotional context.

2.5.3 *The GERMS Model*

Since the release of the seminal work *Emotion and Meaning in Music* [Meyer, 1956], the study of music and emotion expanded dramatically. This brought with it many advances in our understanding of how and why music moves us the way it does as well methods for measuring and evaluating the emotions aroused by music in listeners and psychological models of the techniques used by composers to stimulate these emotions. However, most of the research over the last century focused on the structure and compositional aspects of music that allow it to convey emotions. More recently and with the rapid development of computational technology that allowed a musical score to be accurately performed by a computer, an understanding has evolved that musical expression is largely in the hands of the performer and in many ways more than the composer or arranger. A computer performing a dictated score in a precise manner will still sound mechanical and unnatural such that it would, in many cases, fail to trigger the musical emotions to the same extent as an expert performer will. This implies that the performer has a crucial role in shaping the musical experience in listeners [Widmer and Goebel, 2004]. The many other manifestations of music are mere coding or other technical representations. This brings us back to the imperative comprehension that “music exists only in the moment of its performance”. Therefore, to fully understand the phenomenon of music experience we must capture and analyze the performance and not only the

score or other representations.

The current opinion regarding music expression in performance is that is a multi-dimensional phenomenon that can be decomposed into subcomponents each influencing the expressive character of the performance. It is very difficult to pinpoint the exact nature of each component and its contribution and their reciprocal relations. Juslin suggests a model known as the *GERMS model*, [Juslin, 2003] in which he describes expressive performance as deriving from five main sources:

- *Generative rules (G)* are variations in timing, dynamics, and articulations that allow a performer to highlight, accentuate or group notes and harmonic structures in a musically pleasing manner.
- *Emotional expression (E)* is the manipulation of large-scale performance features such as tempo or loudness that the performer uses in order to communicate emotions to listeners.
- *Random fluctuations (R)* reflect human motor precision limitations, even expert performers attempting to play perfectly even intervals will present minor fluctuations in timing [Gilden, 2001].
- *Motion principles (M)*. This is the notion that tempo and dynamic changes should follow natural patterns of human movement and locomotion to convey a musically pleasing shape [Shove and Repp, 1995]
- *Stylistic unexpectedness (S)* is the intentional deviation from stylistic

expectation of the performance. The performer uses this to surprise the audience, thus adding tension and unpredictability [Meyer, 1956]

These components are utilized by the performer and merged together to create an expressive and meaningful performance. It is interesting to note that each component originates from a different source, is characterized by different features and is even processed in a different region of the brain [Juslin, 2003].

Figure 7 describes these observations.

Characteristic	Component				
	G	E	R	M	S
Origin of pattern	Generative transformations of the musical structure	Emotion-specific patterns of acoustic cues deriving from vocal expression	Internal timekeeper and motor delay variance reflecting human limitations	Biological motion; distinct patterns of movement typical of human beings	Deviations from expected performance conventions
Nature of pattern	Local expressive features related to the structural interpretation	Mainly overall levels of multiple uncertain, partly redundant cues that are compensatory	Semi-random patterns 1/f noise and white noise; very small in magnitude, irregular	Dynamic, non-compensatory patterns; smooth and global	Local; not predictable from the structure
Salient brain regions	Left hemisphere (adjacent to Broca's area)	Right hemisphere (the basal ganglia)	Lateral and medial parts of the cerebellum, plus the motor cortex	Left hemisphere (adjacent to the superior temporal sulcus)	Anterior cingulate cortex
Perceptual effects	Clarifies structure; affects the inherent expression of a piece	Expresses emotions and moods (mainly in broad categories of emotion)	Generates a 'living' and natural quality	Yields expressive form that is similar to human gestures	Heightens tension and unpredictability
Knowledge dependence	Medium	Low	None	Low	High
Aesthetic contribution	Beauty, order, coherence	Recognition, arousal, personal expression	Unevenness, novelty	Balance, unity, recognition	Novelty, arousal
Under voluntary control	Yes, mostly	Yes	No	Yes, partly	Yes

Figure 7: **Five components of performance expression according to the GERMS model.** The components are analyzed by origin, features, processing brain region, perceptual effects, knowledge dependence, aesthetics contribution, and voluntary controllability. From [Juslin, 2003].

2.5.4 The Functionalist Perspective

As mentioned above, the fact that music can communicate emotions from a performer to an audience is a complex psychological and anthropological phenomenon and explaining the process that enables this is problematic to say

the least. There have not been many models addressing this issue, nevertheless [Juslin, 1997] suggested a framework inspired by Herbert Spencer [Spencer, 1875]. The reason we call this a functionalist approach is that it assumes the same ideas explaining other non-verbal communications and their function in human survival.

The functionalist approach attributes the expression of emotions in music to two factors. The first factor is evidence of the existence of innate programs for vocal expression of basic emotions. According to this, humans possess an expressive code that originates from involuntary physiological changes that are associated with emotional reactions. These reactions strongly influence different aspects of voice production, see [Juslin and Scherer, 2005]. The notion assumes that the decoding and encoding of emotions is designed to account for a discrete and limited number of emotion categories. The reason for this is the requirement for accuracy in decoding the correct emotion on the expense of high resolution of emotions. The ability to quickly and correctly interpret an emotional expression is a strong advantage for survival because only then can it act as a guideline for action in essential life problems such as danger (*fear*), competition (*anger*), loss (*sadness*), cooperation (*happiness*) and caregiving (*love*). It is also reasonable to assume that these vocal expressions of emotion were later used in ancient ceremonies of festivals, funerals, wars, and caregiving and reflected *happiness*, *sadness*, *anger*, and *love* and through this music obtained its expressive nature. This realization has a significant implication on music performance since it

indicates that these basic emotions will be *privileged* over other intended emotions in our perception of music due to our biological preparedness for their effective communication. In other words, we are evolutionarily programmed to be very sensitive in detecting these emotions and are constantly searching for their patterns.

The second factor that characterizes music's emotional expression is related to social learning. This begins in very early childhood and some research suggests even before birth [Parncutt, 2006]. But definitely a process of imprinting happens when mothers talk to their infants while trying to calm them by reducing the tempo and intensity of speech or if they want to scold or warn them using a sharp staccato and louder voice. Later on, expressive skills of actual music performance will also develop but often the performers adapt the basic expressive codes to their performing style [Timmers, 2007]. For a list of consistencies endorsing the functionalist approach of the existence of an innate code for vocal expression of basic emotions, see [Juslin and Timmers, 2010]. Juslin also suggested a model for capturing these functional relationships of decoding and encoding emotions [Juslin, 2000]. This is called the *Lens Model* and I will review it in the *previous work* section.

2.5.5 *The Standard Paradigm*

It is important to note here that when it comes to the exploration of musical performance, the literature dates back as far as the 18th century. Much of the first work during these periods was done by the performers and composers

themselves, stating their personal view on musical expression and even detailed description on how to enhance performance. For example, see [Bach, 1778] who wrote the *Essay on the true art of playing keyboard instruments*. This type of literature describes techniques for expression such as tempo, dynamics and ornamentation and structural composition techniques to enhance musical expression. However, all of this information concludes to personal opinions of musical experts. It is only in the past few decades that scientific research methods have been developed to actually measure and analyze the music-psychological effects of performance.

The most well developed line of research is based on the *Standard Paradigm*. Some claim that this research method originated with Seashore and his famous quote that “deviation from the exact is the medium for the creation of the beautiful, for the conveying of emotion” [Seashore and Metfessel, 1925]. Later on he suggested a paradigm used on actors who were required to express various emotions in speech. Following that, the speech was analyzed acoustically to understand the coding of these emotions. Seashore claimed this could be done for music back in the 1940s but this was not attempted until the early 90s [Juslin and Timmers, 2010].

In the *Standard Paradigm*, performers are requested to play melodies while attempting to express certain emotions selected by the researcher. The performances are recorded and later played to listeners in order to assess if they can recognize the intended emotion. Typically, the performances are presented to

the listeners in random order. The judgments are measured in terms of *forced choice*, *adjective ratings*, *free labeling*, or *continuous response*. The acoustical recording of the performance is then analyzed to discover the cues used by the performer to convey the emotions.

A well accepted technique is to ask the performer play the same melody in different expressions in order to factor out the compositional effect of the melody in conveying the expression and focus on the performance itself. However, due to the interaction of the melody with the performer and the performance, it is not always reasonable to request a performer to play with a certain expression that does not fit the melody. In addition, because this research is mainly interested in the detection of emotion by a computer and not by a human listener, and because the music itself will not be analyzed but rather the motion, the effect of different melodies is less problematic (since no one and nothing is listening to the melody). In this research, I will therefore, employ both techniques. The performers will play the same melodies in different emotions but also play different melodies that match typical emotions in order assure that they can completely engage in the emotion they are expressing.

3

Previous Work

3.1 Computational and Perceptual Models

In this section, I will review some of the computational and perceptual models related to expression of emotions in performance. I have used a combination of the knowledge gained in these models in the final design of my system.

3.1.1 *The Todd Model*

Presented by [Todd, 1985], this model is one of the first to attempt to design a timing structure in expressive computer performance. The model was entirely based on empirical measurement of performances and model of tonal music generation. Later on the model was modified to reflect relationships between dynamics and tempo [Todd, 1992] and is most well-known for the quote “the faster, the louder, the slower the softer”.

The main assumption in this model is based on the observation that a performer has control only over two characteristics of the music and those are duration and intensity. The pitch and musical structure are controlled by the composer, and the timbre is determined by the physics of the instrument at hand. Nevertheless, the performer manages to create an expressive performance with these two variables. The model therefore assumes that there are direct links between tempo variations (*rubato*) and dynamics variations to expressive performance and that these links can be drawn out by simple rules. The rules

designed are based on the *Generative Theory* by [Jackendoff and Lerdahl, 1983]. This theory describes points of stability in the structure of music, and it is on these points that the performer leans in order to emphasize the expressive musical structure to the listener. These points are in many cases the edges of musical groupings, where it is observed that the tempo significance is minimal. This is very similar to the *phrase arch* rule in the KTH rule system described ahead. The rules of this model are rather simple. The tempo is related to

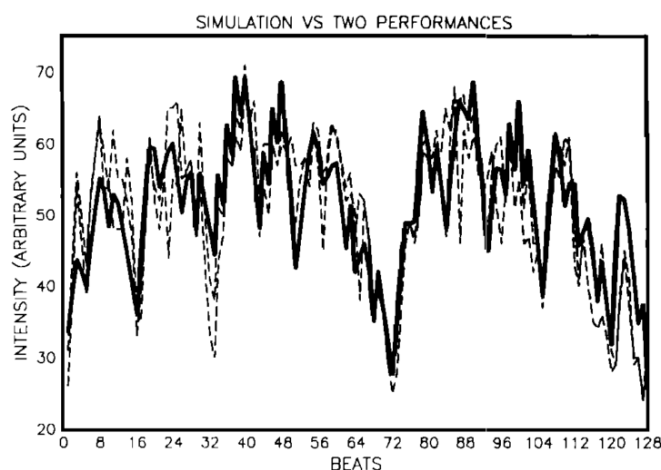


Figure 8: **Todd simulation results.** Comparison of intensity in computer generated simulation to two human performances. The average intensity in each beat is plotted vs. the beat number (the beats are constant time frames measuring temporal metrical distances from the beginning of the piece). The bold line is the computer-generated intensity and the dotted lines are the human performances. Figure from [Todd, 1992].

dynamics in a power relationship, i.e. intensity is proportional to the squared tempo. The tempo on the other hand varies in a *rubato* according to the phrasing and hierarchical grouping of the piece. Thus, the tempo is minimal at the edges of arches (beginnings and endings of groups) while accelerating toward the center and retarding toward the end. The dynamics, in turn, follow the

tempo in the square rule mentioned above. The rules were implemented in the LISP language to produce artificially generated expressive performances of Haydn and Mozart and compared it to human generated performances. The comparison can be seen in figure 8.

It is also interesting to note that the model analogizes tempo changes and dynamics in musical expression to that of physical movement and extends this to concepts of energy and mass. There is even a suggestion that this is more than an analogy and that it originates from a neuro-physiological source in the inner ear and the vestibular cortex. See [Todd, 1992] for more details.

Todd's model was later on evaluated by other researchers (see [Widmer and Goebel, 2004] for a summary of this) some of whom showed it was not successful in generating a performance similar to pianists. Regardless, the model was used by some to understand what cannot be explained by these simple rules and to assess some idiosyncrasies in human performance.

3.1.2 *The KTH Rule System*

In contrast to the empirical nature of the Todd model, the KTH rule system is based on the concept of *analysis by synthesis*. Hence, the rules are first designed based on theoretical framework, then the music is synthesized with them, then it is evaluated by expert listeners and the rules are adjusted accordingly. The system was initially designed by Gabrielson [Gabrielsson, 1985] and then refined and extended by Friberg and Bresin [Friberg et al., 2006]. It consists of a greater set of rules compared to the Todd model, all intended to

transform a stale technical stream of notes into an expressive musical performance. The rules depict instructions to alter timing, dynamic levels and articulations of specific events in the piece. The top-level rule scheme is a block of performance rules and its input is the nominal score and k values. These k values set the level of expression required for each rule. The rules are grouped in eight categories and are described in Figure 9. Each category consists of a set (one or more) rules that are designed to alter the corresponding aspect of the perceived performance.

It is also interesting to see how these rules fall into the categories of the GERMS model described in the background section [Juslin, 2003]. For example, the *phrasing* rule probably corresponds to the *Generative rules* component, whereas the *Performance noise* rule falls under the *Random fluctuations* category.

In order to generate a specific emotion or expression in a performance, a combination of rules must be applied with appropriate k values. There are no “correct” k values. It is entirely dependent on the requirement of the composer or arranger as to the level of expressivity and accentuation through the piece. For a detailed description of each of the groups see [Friberg et al., 2006]. There has however, been some research done on how to generate certain emotional categories using the rule set. Figure 10 depicts the qualitative ranges on some of the rules to create the emotions *Happy*, *Sad*, *Angry*, and *Tender*.

Phrasing	
Phrase arch	Create arch-like tempo and sound level changes over phrases
Final ritardando	Apply a ritardando in the end of the piece
High loud	Increase sound level in proportion to pitch height
Micro-level timing	
Duration contrast	Shorten relatively short notes and lengthen relatively long notes
Faster uphill	Increase tempo in rising pitch sequences
Metrical patterns and grooves	
Double duration	Decrease duration ratio for two notes with a nominal value of 2:1
Inégales	Introduce long-short patterns for equal note values (swing)
Articulation	
Punctuation	Find short melodic fragments and mark them with a final micropause
Score legato/staccato	Articulate legato/staccato when marked in the score
Repetition articulation	Add articulation for repeated notes.
Overall articulation	Add articulation for all notes except very short ones
Tonal tension	
Melodic charge	Emphasize the melodic tension of notes relatively the current chord
Harmonic charge	Emphasize the harmonic tension of chords relatively the key
Chromatic charge	Emphasize regions of small pitch changes
Intonation	
High sharp	Stretch all intervals in proportion to size
Melodic intonation	Intonate according to melodic context
Harmonic intonation	Intonate according to harmonic context
Mixed intonation	Intonate using a combination of melodic and harmonic intonation
Ensemble timing	
Melodic sync	Synchronize using a new voice containing all relevant onsets
Ensemble swing	Introduce metrical timing patterns for the instruments in a jazz ensemble
Performance noise	
Noise control	Simulate inaccuracies in motor

Figure 9: **Summary of KTH rule system.** The rules are grouped into eight categories. Musical expression can be altered by varying combinations of rules. Table from [Friberg et al., 2006].

	Happy	Sad	Angry	Tender
Overall changes				
Tempo	somewhat fast	slow	fast	slow
Sound level	medium	low	high	low
Articulation	staccato	legato	somewhat staccato	legato
Rules				
Phrase arch	small	large	negative	small
Final ritardando	small	-	-	small
Punctuation	large	small	medium	small
Duration contrast	large	negative	large	-

Figure 10: **Portraying emotions with the KTH rules.** Qualitative changes of overall performance and rule quantities for portraying four different emotional expressions. Table from [Friberg et al., 2006].

3.1.3 The Lens Model

In order capture the functional relationship and the manner in which emotion is encoded and decoded in music, [Juslin, 2000] employs a model originally designed for visual perception and cognitive studies based on Brunswik's *Lens Model* [Brunswik, 1956]. This model must account for some intriguing and somewhat confusing findings related to emotional communication in music. For example, how it is that that different performers using dissimilar instruments manage to successfully communicate emotions despite the fact that the sounds they produce vary drastically and thus offer diverse perceptual sonic cues? The technique suggested is called the *Modified Lens Model* and is shown in figure 11. On the left side of the lens, the model depicts how a performer encodes

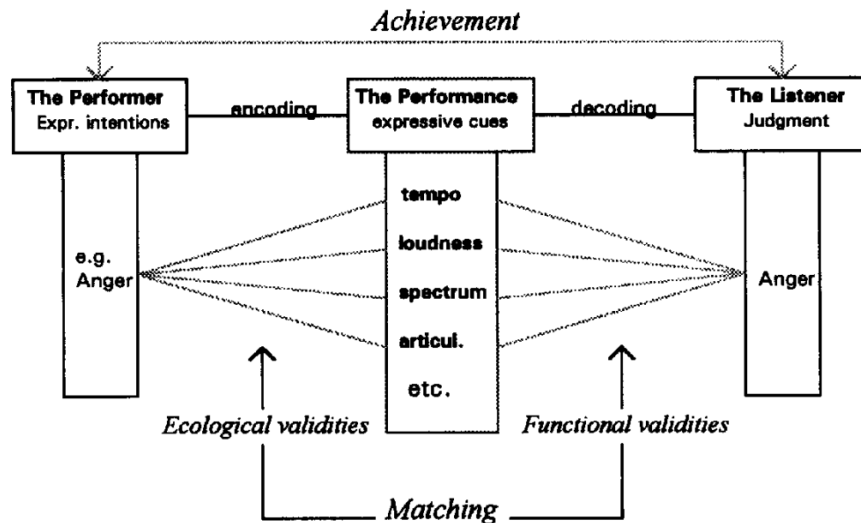


Figure 11: **Modified Lens Model of communication of emotions in musical performance.** Figure from [Juslin, 2000].

emotions in performance by manipulating a set of cues (e.g. variations in dynamics, tempo, and timbre). On the other side of the lens, the listener decodes

the expressed emotion by identifying the cues and classifying the emotion they convey. It is important to note that the employment and characteristics of the cues in the performer and listener are probabilistic and redundant. They are probabilistic in that a specific emotion will be expressed by the same cues only to the extent that the performer is consistent in using those cues and that the sampled set of cues is a sufficient representation of the performer's expressivity that can encapsulate this distribution. They are redundant in that many times more cues are used to express an emotion than necessary in order to guarantee that the message is properly conveyed and not misinterpreted. This redundancy is crucial because of the probabilistic nature of this nonverbal communication. For example a fast tempo will not always represent *happiness*, since it could also in some cases occur in *anger*. The way to distinguish between them is by adding more cues.

Thus, performers and listeners combine several cues together in order to successfully communicate emotions. The more cues, the more reliable the communication. It is interesting to note the analogy of this redundancy to that of the sounds of musical instruments. For example, a strong attack on the piano will produce a loud sound but also a sharper timber. I mentioned this in the difference of accent notations between the case of *forte* and *piano* where the former implies a *percussive* accent and the latter a *pressure* accent. This correlation and redundancy is shown by Juslin [Juslin, 2000] by calculating a multiple regression analysis between both sides of the lens.

The lens model is also described by some numeral factors that help further understand the nature of this communication. These factors are:

- *Achievement* (r_a) is the correlation between the performer's intention and the listener perceived emotion. This is an overall measure of the success of the communication.
- *Cue weight* (β_i) is the significance of cue i in the encoding on the performer's side or decoding on the listener's side relative to the other cues. In other words, these are the "coefficients" used by the performer or listener in the communication. It is by this weighted combination that these cues are utilized and interpreted.
- *Matching* (G) is the similarity between the use of cues on the performer's side and the listener's side. It is calculated by correlating the predicted values of the performer's regression model to that of the listener's regression model. This is essentially an upper limit to the *Achievement* rate since if the performer and the listeners are not using the same cues, the communication is bound to fail.
- *Consistency* (R_e, R_s) is the degree of consistency in the performer's and listener's use of the cues. This is calculated by a multiple correlation of the performer's intention or listener's perception and cues. This too, sets an upper limit to the *Achievement* rate, since an inconsistent behavior on either of the side is likely to be difficult to interpret on the other side unless

by extreme chance the inconsistency is similar on both sides and this factor is dealt with later.

The Lens Model Equation

By employing regression models on performers and listeners, Juslin [Juslin, 2000] showed a mathematical relationship between intended and perceived emotions via the *Lens Model Equation* (LME). This equation was originally designed by Hursch and Hammond [Hursch et al., 1964] for describing cognitive judgment. The studies attempt to model the cognitive system as a statistical decision making process. The LME is described in equation 7.

$$r_a = GR_eR_s + C\sqrt{(1 - R_e^2)}\sqrt{(1 - R_s^2)} \quad (7)$$

The equation relates the factors of consistency and matching to the final achievement in communicating emotions. The first component, also called the *linear* component, is a simple multiplication of the matching factor by the consistencies of the performer and the listener. If the communication is unsuccessful we can look which one of these three variables is the most significant in its influence on the result and then determine whether: (a) the performer and listeners are using different codes (low G value), (b) the performer is applying the code inconsistently (low R_s value) or (c) the listener is applying the code inconsistently (low R_e value). As mentioned above, these three factors set the upper limit of achievement.

The second component, also call the *unmodelled* component, is intended

to correct for the unsystematic and systematic variance that cannot be accounted for in the linear component. This could be the result of inconsistencies, order effects, distractions, memory, omission of relevant cues, and configurationally cue utilization. The $(1 - R^2)$ factors are the residual variances of the regression models and C is a factor that represents the correlation between these residuals. A high C value could imply either a common reliance on acoustical cues that was not accounted for in the model, a chance agreement in model errors, cue interaction common to both models, or non linear cue functions common to both models. It turns out however, that the unmodelled matching factor is small in music performance [Juslin and Madison, 1999].

In this research, I will use the lens model to decide on the features to calculate from the pianist motions to decode the emotions. I will then use the Bayesian decision theory to model the cue utilization process that enables the communication of emotions in music.

3.2 Real-Time Machine Learning Tools

In this section, I will review some of the existing platforms that allow the use of real-time machine learning algorithms.

3.2.1 The Wekinator

In her doctoral thesis, [Fiebrink, 2011] researched the application of supervised learning algorithms to music performance and composition and implemented the Wekinator, a real-time interactive data mining environment

based on the *Weka*¹ software from the University of Waikato and the *Chuck*² environment developed at Princeton university.

The Wekinator is a software program that is designed to enable machine-learning algorithms to be trained and employed in real time and with a rather simple interface. It offers two main options to the user, either classification of discrete categories using AdaBoost or K-nearest neighbors or continuous output control using neural networks. The goal of this project was to allow end users to design interactive applications for performance and composition of computer music by employing supervised machine-learning algorithms.

It can handle various input sources such as a web cam, the tilt sensors in a laptop and external inputs such as audio and joysticks. The user trains the program based on selected features that are calculated on the input data and uses this to control audio or video output. The software comes with sample projects such as Max/MSP feature extraction and synthesis, Kinect and GameTrak.

The Wekinator, however, is not a comfortable environment for the development of new applications or exploration of techniques that do not already exist in it. The user has little control over the features and almost no information on the algorithms that are employed. Hence, it is more of an interactive game for playing with controllers and an introduction to machine learning rather than a research and development environment. Therefore, I have chosen not to use it in this project.

¹<http://www.cs.waikato.ac.nz/ml/weka/>

²<http://chuck.cs.princeton.edu/>

3.2.2 *EyesWeb and The Gesture Recognition Toolbox*

The EyesWeb environment was developed by a team led by Antonio Cammuri in the infoMus lab at the University of Genoa [Camurri et al., 2000]. It is a visual programming, open software research platform similar to Simulink and Max but dedicated to the design and development of real-time multimodal systems and interfaces. It supports a large number of input systems including audio, video, and motion sensors as well as various standards such as MIDI, OSC, VST plugins and MATLAB.

A rather recent addition to EyesWeb is the machine-learning toolbox that was designed by a team at the Queens University Belfast [Gillian et al., 2011a]. The toolbox features an exhaustive list of machine learning and pattern recognition algorithms including *Adaptive Naïve Bayes*, *Artificial Neural Networks*, *Hidden Markov Models*, *Dynamic Time Warping*, *Fuzzy C Means*, *K Means*, *K-Nearest Neighbor*, and *Support Vector Machines*.

Each algorithm is designed as a set of blocks for data collection, training, and predicting. The inputs to the collection blocks (called *training tool*) are the data features their respective weight vector. This block merely collects the data and stores it to a file upon user request. The training block (called *train*) loads this file upon startup or user request and calculates a training model according to the algorithm it implements. This model is also stored to a file. Finally, the *predict* block loads the model upon startup or user request and classifies newly received data based on the model.

The simplicity of this design and its ease of use makes the gesture recognition toolbox an extremely handy tool while trying to rapidly develop and evaluate pattern-recognition algorithms. The fact that it works in real time makes it even more efficient for research because an algorithm can be optimized by modifying the various parameters while the data is streaming in and the feedback is immediate. An example of a Naïve Bayes Classification layout is shown in figure 12.

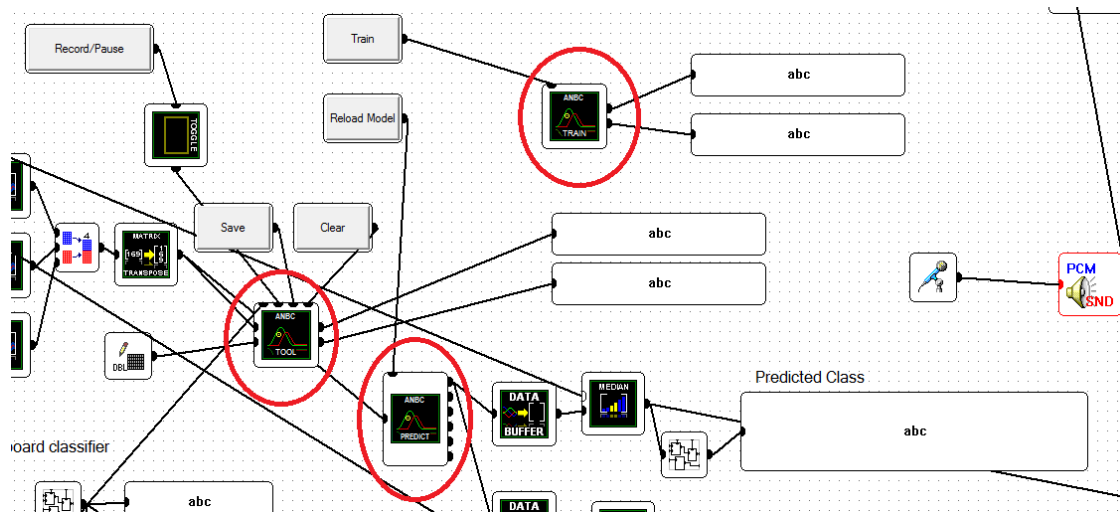


Figure 12: **Naïve Bayes Classification in EyesWeb.** Notice the three major blocks marked in red: *ANBC training tool*, *ANBC train*, and *ANBC Predict*.

3.3 Previous Applications

In this section, I will describe some implementations and applications that are similar or closely related to the current research.

3.3.1 The Fuzzy Analyzer

The Fuzzy analyzer is a system designed by Andres Friberg [Friberg, 2004] that implements a real-time algorithm for analyzing emotional expression in

music performance and body motion. It is mainly intended for artistic human computer performance. The algorithm uses both acoustical information and motion capture information from a camera to assess the emotional content of the performance.

The audio input is analyzed for cues similar to those in the KTH system such as tempo, sound level and articulation. This is done by calculating the RMS after applying a *Hanning* window to the audio signal. Then two envelopes are created by filtering this signal with a bank of cut offs of 40Hz and 1Hz. These two filters extract single tones and phrases. The crossing of envelopes defines tone onsets and offsets. On each tone, five cues are calculated: *sound level* (dB), *instant tempo* (tones/second), *articulation* (relative pause duration), *attack rate* (dB/ms), and *high-frequency content* (high/low energy). These cues were selected based on multiple regression analysis results performed by [Juslin, 2000].

The motion signal is evaluated for a parameter called *Quantity of Motion* (QoM) which is an evaluation of the total difference between frames, indicating a change and hence motion. In addition, two other motion cues are calculated, *width peak to peak* and *height peak to peak*. These reflect the extent of motion in two dimensions of the video frame.

The second step in the algorithm is a calibration step to account for variances in the instrument and performer. This is merely a normalization that verifies that the mean of the cues is zero and the standard deviation is one.

The third and final step is mapping from cues to emotions. This is done

via a *Fuzzy Logic* rules set based on data collected in previous research [Juslin, 2000]. Fuzzy logic means that the discrete threshold decision process is performed on continuous values of cues. Based on the data collected linking these cues to emotions most of the continuous cues were assigned a value of high or low, however in some cases, they were assigned three discrete levels: high, medium and low. Then, a standard logic (truth table) process is applied to decide on a classification. Figure 13 specifics the complete process on three audio cues only.

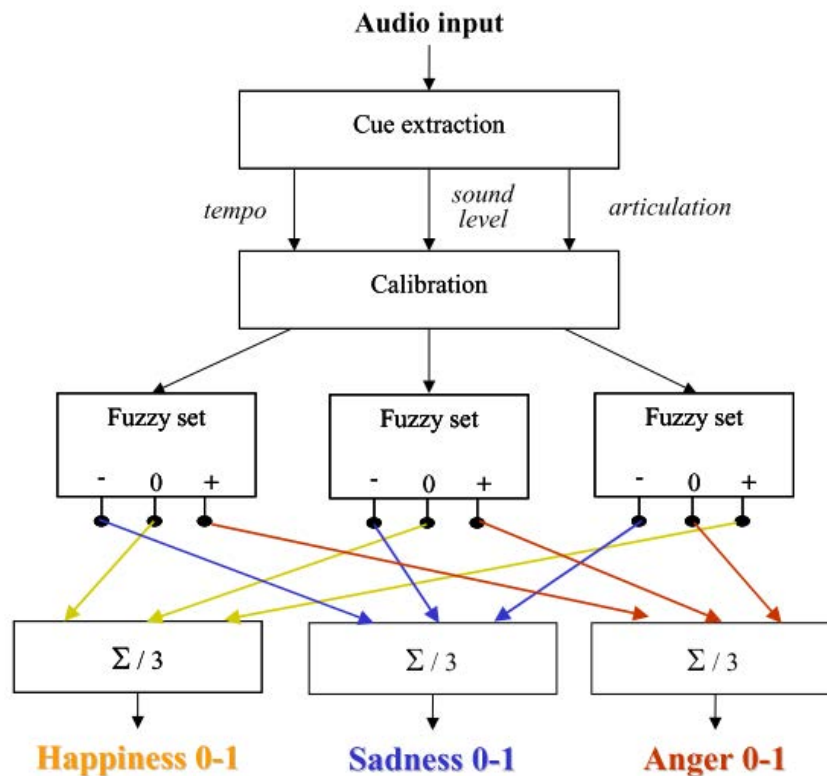


Figure 13: **Fuzzy analyzer for estimating emotions.** An audio input is analyzed in terms of tempo, sound level and articulation. The resulting prediction of emotional expression is output in terms of three functions ranging from zero to one. Figure from [Friberg, 2004].

The system detected three categories of emotions: *happiness*, *sadness*, and *anger*. It was demonstrated in a number of installations such as *Ghost in the*

Cave and *Expressiball*. The system was not evaluated for validity because of difficulties in establishing a ground truth and in simulating the motion in a performance. However, the authors do suggest ways to evaluate the system in future research. See [Friberg, 2004] for details.

3.3.2 *Mapping Emotions to Colors in Musical Performance*

This research, performed by [Bresin, 2005], explored the relationship between colors and the perceived emotion in musical performance. The aim of the research was to come up with a mapping of HSB (Hue Saturation Brightness) coloring the different emotions aroused in music. This knowledge could help design pedagogic feedback systems for music students by providing them with live expressive evaluation of their performance. Subjects were presented with 12 music performances expressing different emotions and were asked to rate how well each of a set of eight colors and their nuances corresponded with the emotions perceived in those performances.

The emotion categories selected were: *happiness, love, contentment, pride, curiosity, indifference, sadness, fear, shame, anger, jealousy* and *disgust*. It is not clear why these emotions were selected since they do not reflect the emotions expressed in musical research and the author does not explain this. Nine musicians were asked to express these emotions in music by Haydn and Brahms played on piano, guitar, and saxophone. Then these recordings were evaluated through listening tests to find the best match for each emotion. The final set of music excerpts were

12 (*emotions*) \times 3 (*instruments*) \times 2 (*melodies*) = 72 (*performances*).

The colors presented were *red, orange, yellow, green, cyan, blue, violet, and magenta*, their brightness and saturation variances (saturation and brightness set to 1 or 0.5 respectively). Thus, $8 \times 3 = 24$ total colors were used.

The subjects were presented with the music and the colors in randomized order and asked to set a slider based on how well the colors were associated with the music on a scale of 1 to 10. The results show some significant correlations between colors and emotional intention in the music. A summary of the results for the hue parameter are displayed in figure 14.

Emotion	Hue
Happiness	0.167 (Yellow)
Love	0.667 (Blue), 0.75 (Violet)
Pride	0.167 (Yellow)
Tenderness	0.75 (Violet)
Curiosity	0.5 (Cyan)
Contentment	0.083 (Orange)
Anger	0 (Red)
Sadness	0.75 (Violet)
Fear	0.667 (Blue)
Disgust	0.75 (Violet)
Shame	0.083 (Orange)
Jealousy	0 (Red)

Figure 14: **Mapping colors to emotions.** Results for hue values that received the highest mean rating for each emotional expression. Figure from [Bresin, 2005].

3.3.3 IMUs in Piano Teaching

Research in the field of music pedagogy has also examined the option of tracking a pianist's motion with IMUs. With the goal of enhancing piano teaching systems, currently based mainly on MIDI data, [Hadjakos et al., 2008]

explored the use of an accelerometer in a setup quite similar to what this research suggests. They designed a prototype IMU with an accelerometer and a gyroscope. They attached the sensor to three locations: the upper arm, the wrist and the hand of the right arm only. The aim of the research was only to present how piano playing patterns such as trills and scales appear in inertial measurement data.

The research focused on examining the following patterns:

- Rotation patterns displaying *supination* and *pronation* (clockwise and counterclockwise rotation of the right ulna), *Tremoli and Trills* (the rapid repetition of two distant or adjacent notes) and *scales*.
- Jump patterns displaying vertical forearm motion and flexible or rigid arm.

Some of the interesting results are displayed in figure 15. *Trills* and *Tremoli* can be played using only the fingers or using the forearm. Another variant of trills is using the upper arm. All three techniques were clearly observed in the results. Detecting these differences in performance could be useful for music information retrieval because they are often employed in specific settings. For example, finger-tremolo is generally used in soft gentle parts in contrast to forearm tremolo that is used in louder, more dramatic parts.

The data from scales playing is also interesting, the high peaks correspond to thumb crossings, in which there is either a pronation or supination of the forearm. This typically happens in groups of three and four notes (e.g. in the C

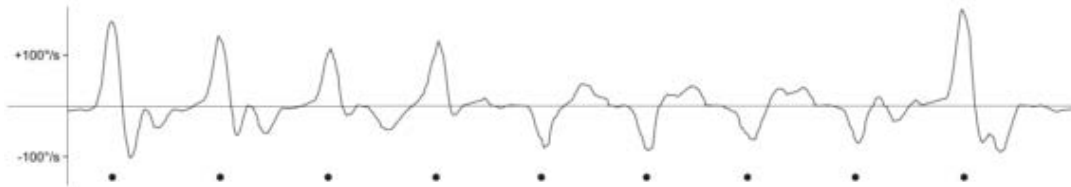


Figure 2. Wrist, x-rate, pronation and supination



Figure 3. Wrist, x-rate, finger vs. forearm tremolo



Figure 4. Upper arm, x-rate, forearm vs. upper arm tremolo

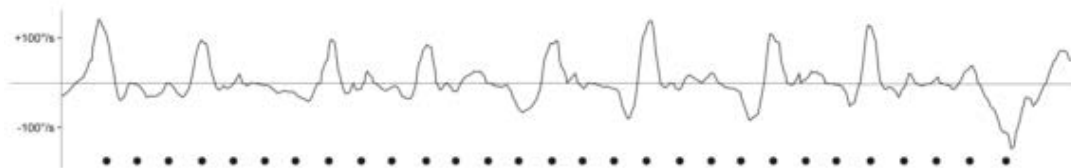


Figure 5. Wrist, x-rate, scale

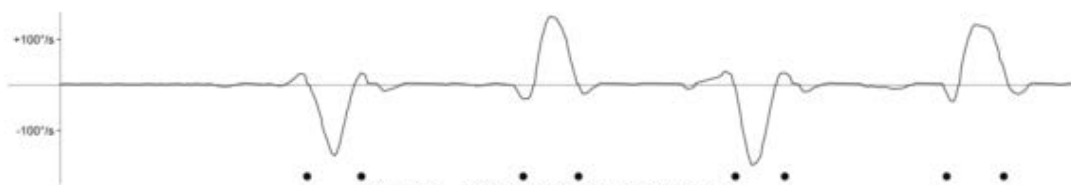


Figure 6. Upper arm, x-rate, jumps

Figure 15: **IMU Data in Piano Playing Patterns.** The dots indicate the *note on* events from the MIDI data. Playing patterns are clearly distinguishable such as pronation and supination, finger, forearm, and upper arm tremolo, scales and jumps. Figure from [Hadjakos et al., 2008].

major scale). Nonetheless, most of the single notes are also observed in the signal. Also, notice the negative drop at the end of the scale. This indicates a supination on the little finger when the player finished the scale, which is a typical expressive gesture pertaining to pianists.

Vertical forearm movement is often used by pianists to connect loud note to a soft note in the case of a *resolved dissonance*. This is also a very basic expressive gesture and is clearly observed in the data. Although none of this is very surprising or novel, the results of this research seem encouraging in regard to what could be accomplished with the use of inertial measurement units in piano performance.

4

Proposed System

4.1 System Design

In this section, I will review the system structure including the required specifications, the top-level block diagram of the solution, and the system setup with regard to hardware and software implementation platforms and data structures.

4.1.1 System Specifications

The system is required to function as a real-time musical gesture expression classifier that can detect intended musical expression and emotions performed by a pianist. The inputs to the system are kinesthetic data from two wrist-worn IMUs each transmitting 3-axis acceleration and 3-axis angular velocity.

Requirements

- Collect kinesthetic data from APDM sensors at a rate of 64 samples per second.
- Record data to files and use to train an algorithm and enable playback mode for demonstration and algorithm development.
- Detect and Classify in real-time the following common musical structures from each hand:

1. *scales*

2. *chords*

3. *arpeggios*

4. *trills*

- Detect and Classify in real-time the following expressions in Western notation [Read, 1979b], [Read, 1979c]:

1. Tempo: *ritardando* and *accelerando*

2. Dynamics: *crescendo* and *diminuendo*

3. Articulation: *staccato* and *legato*.

- Detect and Classify in real-time the following emotion categories from Hevner's adjective circle [Hevner, 1936]:

1. *sad/mournful*

2. *dreamy/tender*

3. *lyrical/serene*

4. *humorous/playful*

5. *cheerful/merry*

6. *vigorous/dramatic*

- Display all expression evaluations as feedback to the performer in real-time to enable an intuitive interactive musical experience.

4.1.2 Setup and Top-Level Design

In order to perform the required tasks, I have designed a system comprised of the following hardware and software elements. Most of the elements could be substituted with similar functioning parts. However, the real-time performance and stability of the algorithm might be affected by the processing power of the PC and the operating system. Moreover, the IMU data must be synchronized at 64 samples per second with a lag of less than 50 ms to allow for proper tempo alignment and response time.

- Hardware

IMU system including 2 Opal sensors and one access point.

Celviano AP-220 Digital Piano (from Casio).

Mini Super computer with 16G RAM and 2 Intel Xeon co-processor CPUs.

- Software

Windows 7, 64 bit operating system.

Matlab environment version 7.10 including the APDM SDK.

EyesWeb environment version 5.2.1.

An illustrative block diagram of the system setup is presented in Figure 16.

The Opals [APDM, 2012a] are small wireless wrist worn inertial sensors that feature triaxial accelerometers, gyroscopes, and magnetometers transmitting 9 values 64 times per second. The values transmitted are:

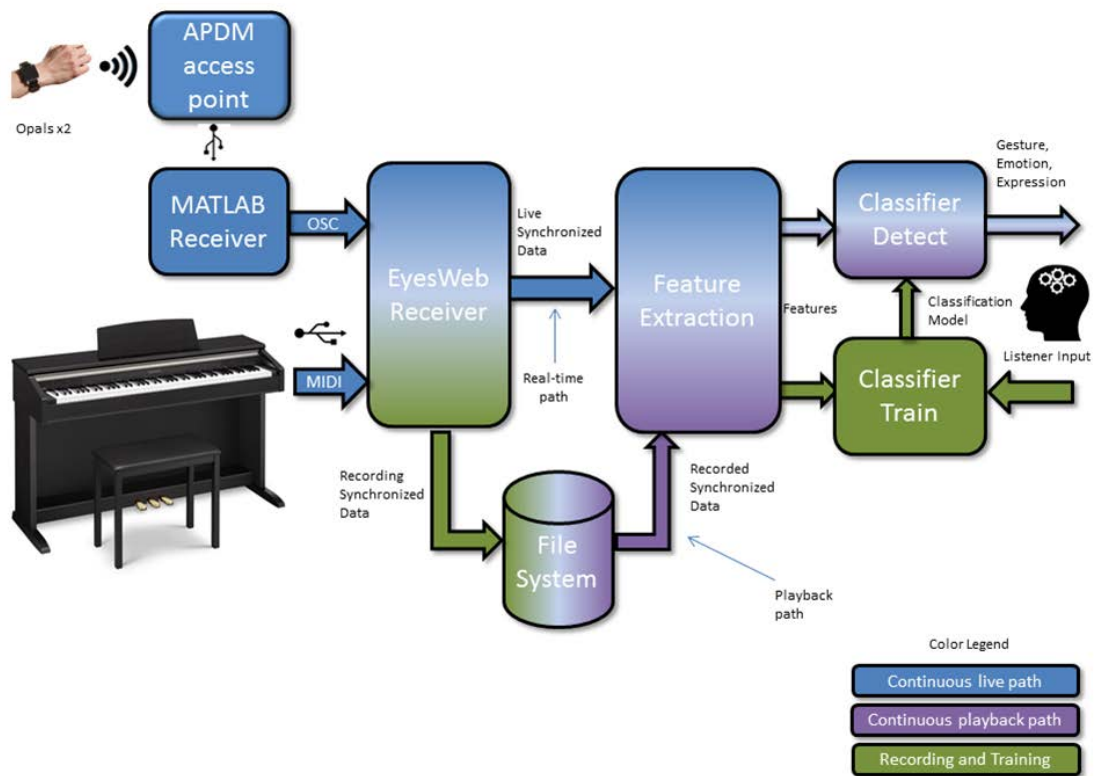


Figure 16: **System Diagram Illustration.** The system is designed to work in real-time or playback mode.

- 3 axis proper acceleration in SI units relative to x, y, z .
- 3 axis angular velocity in radians per second units around x, y, z .
- 3 axis magnetic field projection in μT units on x, y, z .

The magnetometer values are ignored in this project because they would make the training data based on orientation relative to the North and thus make the algorithm sensitive to the pianist's position. Therefore, they will not be discussed here or henceforth.

The data arrives at the receiver via multiple ports. The motion signal data from the sensors is transmitted wirelessly to an access point for synchronization. The access point is read utilizing a set of functions in MATLAB [MATLAB, 2010] in a dedicated SDK. The MIDI data from the piano is transferred via USB to the receiver. The synchronization of Opal and MIDI data is implemented via a combined system in MATLAB and EyesWeb. The MATLAB receives the data from the Opals through the APDM access point and transmits them via OSC messages to EyesWeb. The EyesWeb receiver acquires these data from MATLAB in addition to the MIDI and Audio data directly from the piano. The MIDI and motion data are synchronized at 64 samples per second and stored to a file system. While the data are being collected, it is also passed to the classification algorithms for training and prediction. All of this happens simultaneously on parallel processors and in real-time.

4.1.3 Data Collection and Storage

The MIDI and sensor data are collected in two formats; The EyesWeb native format (.ebf), and a text file. Each row consists of sample of data (IMU measurements and MIDI commands) along with a time stamp. The .ebf files can be read directly in EyesWeb and enable the playback of data just as it was collected simulating a real-time environment. This allows for developing and evaluating the algorithm while running it on real subjects' data. The text files can be read in any other software platform for additional offline analysis.

4.2 Algorithm Description

Six dimensional data from two sensors are collected by the system at 64 samples per second. These data are buffered into three consecutive frames of one second each. This windowing of data corresponds to the *Gestalt* theory of music psychology which describes how music is perceived in groups rather than single notes [Narmour, 1992]. Determining the optimal size of these chunks is not trivial and with the aim avoiding a deeper dive into the studies of music perception and auditory scene analysis, it was currently chosen by trial and error. Also, it most likely varies between musical pieces and performances. Nevertheless, a window size of 1 second corresponds to a tempo of 60 BPM, and should allow for capturing several notes in rapid playing or single notes in slower playing. It is also reasonable to assume that in most cases the musical mood will not change during this period. The reason three frames are buffered is due to short term memory considerations. It is assumed that the emotions expressed

and experienced in music preserve some continuity, evolve gradually and are influenced by recent emotional states [Meyer, 1956]. Therefore it make sense to record the data from the recent past in order to make a decision regarding the emotional state of the present. The degree of the past influence on the present is also a parameter of the algorithm and is reflected in the weight assigned to the features in the classifier. The features are calculated on each frame, except for the *tempo* feature which is continuous. The features from each frame are weighed and passed to the classifier for training or prediction. I will discuss the weighing considerations in the sections that follow.

4.2.1 *Feature Extraction*

For each frame, the following features are calculated on the incoming signals:

- mean motion intensity (per hand per axis)
- RMS motion intensity (per hand per axis)
- variance of acceleration (per hand per axis)
- mean spin intensity (per hand per axis)
- RMS spin intensity (per hand per axis)
- variance of angular velocity (per hand per axis)
- dynamics
- tempo

- articulation (per hand)

In the following subsections, I will describe how each of these features is calculated.

Motion Intensity

Motion intensity is calculated on each hand over each axis separately via sum of squares over an entire frame, i.e. the average of the sum of squares over all accelerations as described in equation 8, per dimension (per hand per axis). This feature over the z axis should be a good estimator of the audio intensity since the acceleration is proportional to the force exerted on the keys, which is proportional to the squared velocity of the hammers striking the strings which is proportional to the kinetic energy converted into acoustic energy [Fletcher and Rossing, 1998]. The factor of two compensates for adding the absolute value of the positive and negative accelerations, which should cancel out in the case of zero total distance traveled.

$$\text{motion intensity} = I_{a_j} = \frac{1}{N} \sum_{i=1}^N a_{i,j}^2 \quad (8)$$

Where N is the number of samples in a frame and j is the dimension column (i.e. which hand which axis).

Variance of Acceleration

The variance of acceleration σ_a^2 is calculated in the unbiased estimator definition as described in equation 9. It is an indicator of the variation in intensity during a frame a might point to certain expressive elements such as

legato vs. *staccato* playing as well as rapidly changing vs. monotonic performance. The feature is calculated per hand per axis.

$$\text{variance of acceleration} = \sigma_{a_j}^2 = \frac{\sum_{i=1}^N (a_{i,j}^2 - I_{a_j})^2}{N - 1} \quad (9)$$

Spin Intensity

The spin intensity feature is extracted from the angular velocities measured by the gyroscopes. It is calculated via sum of squares over an entire frame, i.e. the average of the sum of squares over all angular velocities as described in equation 10, per dimension. It is an estimation of total *supination* and *pronation* as well as *forearm tremolo*.

$$\text{spin intensity} = I_{g_j} = \frac{1}{N} \sum_{i=1}^N g_{i,j}^2 \quad (10)$$

Variance of Angular Velocity

As with motion intensity, the variance is calculated in the unbiased estimator definition. It is an indication of the change in articulation style within a frame with regards to *tremolo*, *supination*, and *pronation*.

$$\text{variance of angular velocity} = \sigma_{g_j}^2 = \frac{\sum_{i=1}^N (g_{i,j}^2 - I_{g_j})^2}{N - 1} \quad (11)$$

Tempo

For extracting tempo out of motion, one must consider the phenomena of tempo perception in piano playing. Bruno Repp shows some insightful concepts in this specific area [Repp, 1994] and the algorithm is mostly based on his findings. The assumption is that the perception of tempo evolves from an

accumulation of temporal cues derived from the audio in the form of varying intensities. Therefore, using this, a real-time running tempo estimator can be attempted as follows. First, the envelope of the signal is calculated via RMS. Then, two thresholds are calculated based on the standard deviation of a half-second frame. For both thresholds, crossings are detected and their times registered in to a buffer. For the low thresholds the crossings are weighed by the intensity of the peak in that crossing, this is to account for the stronger pulses having a more significant influence on the perception of tempo. Then a weighted average is performed on the buffer. For the high threshold, the timing of the crossing are only registered to buffer and a median filter is applied to account for extreme outliers. Finally, the average of the two tempo estimations is calculated to provide an overall perceived tempo. The implementation of this algorithm in EyesWeb is depicted in Figure 17.

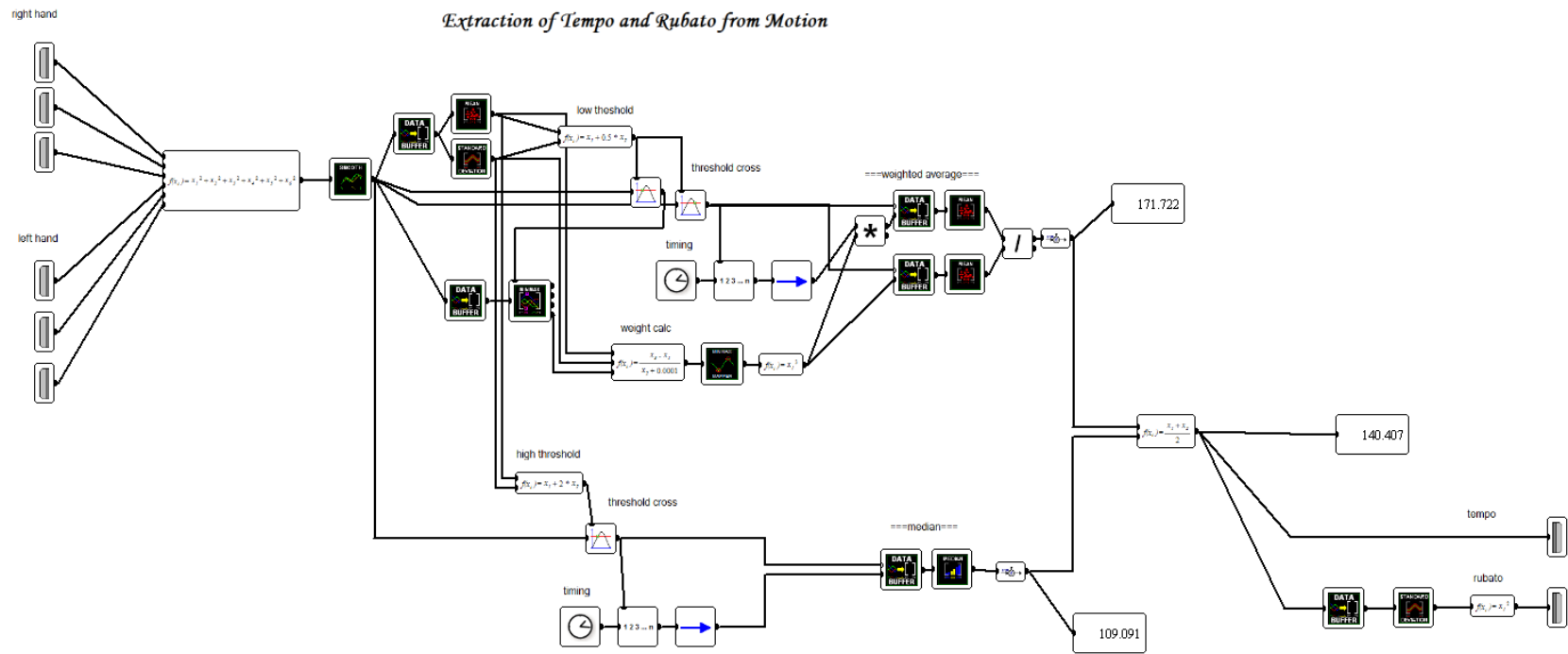


Figure 17: **Tempo from Motion Algorithm** . A perceptual model based on averaging of temporal cues.

It is important to note that the tempo feature it is not calculated separately on each hand since both hands contribute to one performance and there should only be one perceived tempo. Thus, the input to this algorithm is a Pythagorean sum of all six accelerations from both hands. Using this approach, the algorithm can detect a joint tempo created with accents from both hands. For example, if a waltz in three fourths is played at 60 BPM playing the bass with the left hand and two accents with the right, then the tempo may vary depending on how this is articulated. If the bass is accentuated significantly stronger than the following notes then only the downbeat will be detected as a threshold crossing and the tempo will be assigned 60 BPM. However, if the right hand part is articulated with equal intensity then the tempo algorithm might detect those as crossings and measure 180 BPM. Intuitively this makes sense because the perceived tempo of the audio would also probably be affected by these differences in articulation and so will the expressive nature of the piece. See [Repp, 1994], [Levitin and Cook, 1996], and [Scheirer, 1998] for a broader review of the problems with definitions and perceptions of tempo and in establishing a ground truth.

Dynamics

The dynamics features are extracted by estimating a corollary to the acoustic energy. Thus, we calculate features that are proportional to mean acoustic energy, gradient of mean acoustic energy, and variance of acoustic energy. This is done by first summing the squares on the two z axis components

of the accelerations from the left and right hand. Then an envelope of that signal is calculated and buffered over time frame of one second. Then we calculate the mean and the variance. In order to detect *crescendo* and *diminuendo* we also compute the derivative of the mean. A positive derivative for a long enough time is a continuous increase in energy and therefore a *crescendo*. Similarly a steady negative derivative is a *diminuendo*. The EyesWeb implementation of extracting dynamics from motion is shown in Figure 18.

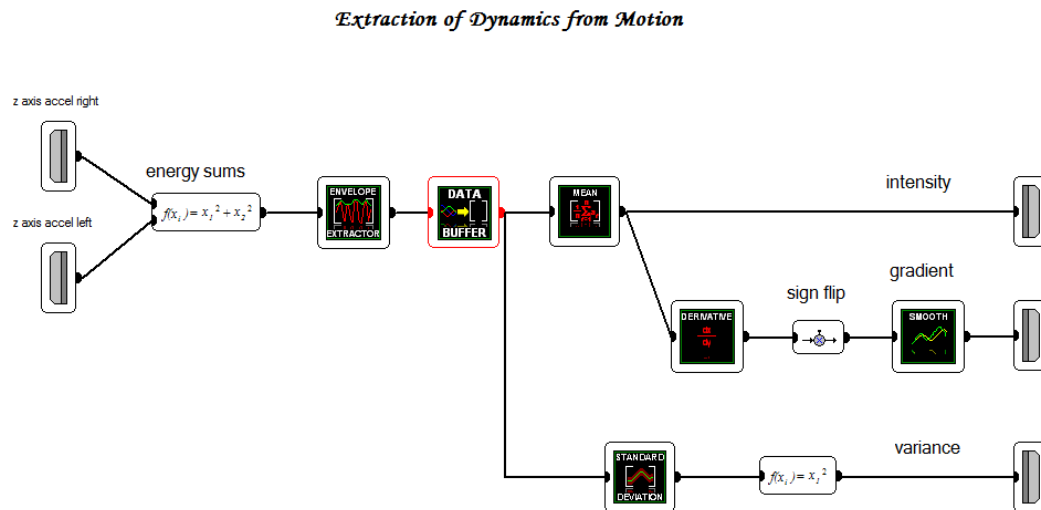


Figure 18: **Dynamics from Motion Algorithm.** Estimating acoustic energy levels, variance, and gradient from acceleration in the z axis.

Articulation

Articulation is defined in [Juslin, 2000] and [Bresin and Battel, 2000] as the ratio between the note duration and the inter onset interval. It is an estimation of the *legato* in a phrase. To calculate this, two values are defined:

d_{ii} the duration from the onset of a note until the onset of the next note.

d_{io} the duration from the onset of the note to its offset.

Then, note articulation is defined as:

$$Articulation = \frac{d_{io}}{d_{ii}} \quad (12)$$

In engineering terms this could be viewed as the *duty cycle* of the note in a phrase. Detecting articulation from motion in this manner would require us to detect precise note onsets and offsets from motion. Since this is difficult to achieve and although intriguing, is not in the context of this research, I have designed a different but similar approach. Instead of finding note onsets we find temporal regions of activity in the z axis signal. Since the z axis is in the direction of the key down and up, this should closely correspond to note onset and offset behavior. We count the number of activity occurrences in a time frame of half a second and divide it by the total time. An articulation value close to one represents *legato* and an articulation value close to zero corresponds to *staccato* articulation. The implementation of the articulation algorithm in EyesWeb is described in Figure 19. The display of tempo, dynamics, and articulation in EyesWeb is shown in figure 20.

4.2.2 Classification

Following feature extraction, the features are fed to an Adaptive Naïve Bayes Classifier (ANBC) along with a weight matrix that defines the weight for each feature. The ANBC is a part of the gesture recognition toolbox in EyesWeb [Gillian et al., 2011b]. In this section, I will review how this block operates,

Extraction of Articulation from Motion

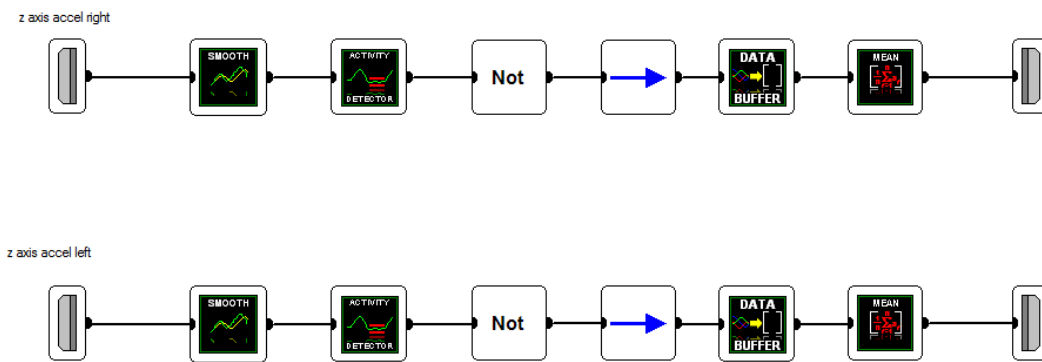


Figure 19: **Articulation from Motion Algorithm.** Utilizing high and low activity detection on the z axis as estimations of note onsets and offsets.

Expression and Emotion from Motion in Piano Performance

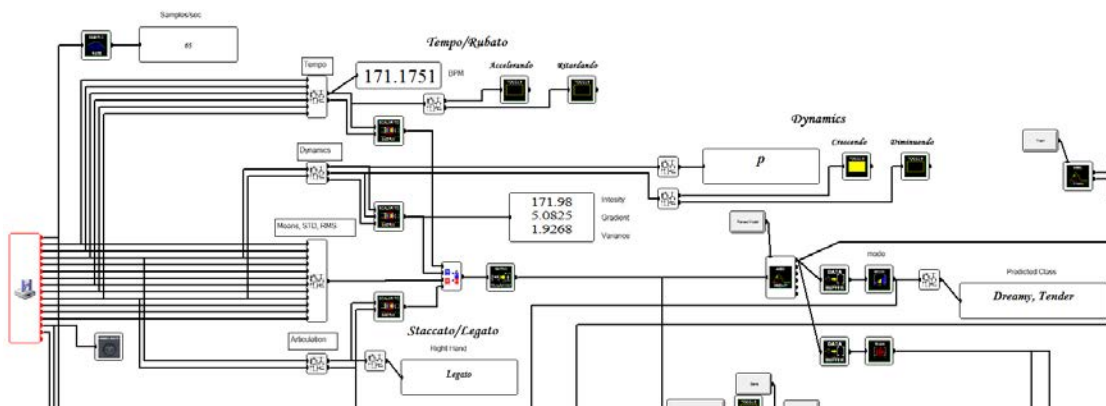


Figure 20: **Tempo, Dynamics, and Articulation** displayed in EyesWeb

including its features and some of its advantages and drawbacks.

As described in the background section, the design of any classifier employing the Bayes decision theory is structured on the Bayes theorem (equation 3) and some naïve assumptions regarding the probabilistic nature of the features and classes. One assumption is that the features are independent random variables. Another assumption is that their distribution (i.e. their probability density function) can be approximated to be of Gaussian nature. Note that neither of these assumptions is prerequisite for Bayes decision theory to be optimum. Bayes theory is general and optimum for any random variables in any distribution as long as the distribution is correct. However, assuming these distributions and independent variables significantly simplifies calculations and programming complexity.

Rewriting the Bayes theorem for gesture recognition we define the likelihood (or conditional probability) of gesture g_k being the state of nature out of G gestures given an observation of the input feature vector $\mathbf{x} = \{x_1, x_2, \dots, x_N\}$ in equation 13.

$$P(g_k|\mathbf{x}) = \frac{p(\mathbf{x}|g_k)P(g_k)}{\sum_{i=1}^G p(\mathbf{x}|g_i)P(g_i)} \quad (13)$$

Notice that just as in equation 3, the denominator is constant because it sums over all gestures and therefore can be ignored for classification purposes. Also note that because \mathbf{x} is a vector of N variables, $p(\mathbf{x}|g_k)$ is a function of N parameters. If we assume that the features abide to a normal distribution then this function becomes the multivariate Gaussian distribution function

[Duda et al., 1995a] defined in equation 14.

$$p(\mathbf{x}|g_k) \sim \mathcal{N}(\mathbf{x}|\boldsymbol{\mu}, \boldsymbol{\Sigma}) = \frac{1}{(2\pi)^{N/2}|\boldsymbol{\Sigma}|^{1/2}} \exp\left(-\frac{1}{2}(\mathbf{x} - \boldsymbol{\mu})^t \boldsymbol{\Sigma}^{-1}(\mathbf{x} - \boldsymbol{\mu})\right) \quad (14)$$

Where $\boldsymbol{\mu}$ is an N dimensional mean vector of the features in a class defined in equation 15.

$$\boldsymbol{\mu} \equiv \mathcal{E}(\mathbf{x}) = \int \mathbf{x}p(\mathbf{x})d\mathbf{x} \quad (15)$$

$\boldsymbol{\Sigma}$ is an $N \times N$ covariance matrix of the features defined in equation 16.

$$\boldsymbol{\Sigma} \equiv \mathcal{E}[(\mathbf{x} - \boldsymbol{\mu})(\mathbf{x} - \boldsymbol{\mu})^t] = \int (\mathbf{x} - \boldsymbol{\mu})(\mathbf{x} - \boldsymbol{\mu})^t p(\mathbf{x})d\mathbf{x} \quad (16)$$

$\boldsymbol{\Sigma}$ is always symmetric and semidefinite, $|\boldsymbol{\Sigma}|$ is its determinant and $\boldsymbol{\Sigma}^{-1}$ is its inverse matrix. To simplify this, we observe that the components of the covariance matrix are the single pair covariances $\sigma_{i,j}^2$. Also, we note that the expected value of a vector is found by taking the expected value of its components. Thus, our individual scalar components are:

$$\mu_i = \mathcal{E}[x_i] \quad (17)$$

And,

$$\sigma_{i,j}^2 = \mathcal{E}[(x_i - \mu_i)(x_j - \mu_j)] \quad (18)$$

Now, if we assume statistically independent features then the covariance matrix becomes diagonal where $\sigma_{i,j}^2 = 0$ when $i \neq j$. In this case, the multivariate Gaussian distribution simplifies to a multiplication of single variable distributions as in equation 19.

$$p(\mathbf{x}|g_k) \sim \mathcal{N}(\mathbf{x}|\boldsymbol{\mu}, \boldsymbol{\Sigma}) = \prod_{i=1}^N \frac{1}{\sqrt{2\pi}\sigma_i} \exp\left(-\frac{(x_i - \mu_i)^2}{2\sigma_i^2}\right) \quad (19)$$

Therefore, under these assumptions what we need is to calculate the μ_i and σ_i^2 of each feature in each class condition during the training phase. This will give us the conditional probability density function $p(\mathbf{x}|g_k)$ for every gesture g_k .

Finally, looking back at equation 13, one last assumption is made, and it is that prior distributions of the gestures $P(g_k)$ are equal. This implies that prior to any knowledge there is an equal chance for any gesture to occur. This assumption seems reasonable to make considering the complexity and randomness of emotional responses in music. If this is not the case, and we have some prior knowledge such as the composer's or performer's inclination for specific expressive gestures, then adjusting this factor could improve the performance of the classifier.

Therefore, for every input feature vector \mathbf{x} we compute the conditional probability density $p(\mathbf{x}|g_k)$ for all G gestures. And based on our assumptions and equation 13, this is proportional to the posterior probability $P(g_k|\mathbf{x})$. Thus, the gesture with the highest prior is the one that will be predicted by the classifier. This is the simplest case of Bayes classification. However, the ANBC block has some additional features to enable flexibility in its application that make it a powerful tool for musical gesture recognition.

Feature Weighting

The training block of the ANBC has a weight parameter for every for each feature. This allows certain features to be more significant than others in the classification process. The weighting works as follows. For each gesture class k , a

discrimination function is created from vectors of mean, variances, and the weight vector:

$$\Phi_k = \Phi\{\boldsymbol{\mu}_k, \boldsymbol{\sigma}_k^2, \boldsymbol{\phi}_k\} \quad (20)$$

The function is defined such that if the weight ϕ_n is greater than zero, then the Gaussian function is multiplied by the weight, otherwise the function is forced to 1, thus not affecting the classification process. Then, the product of all these functions is computed as before. To prevent underflow of precision due to many multiplications, a log is taken over each distribution, followed by an addition.

In our implementation, the features are weighed such that those from the current frame are weighed 1.0, those from the previous frame are weighed 0.6 and those from the frame before are weighed 0.3. This allows for a diminishing significance of the past features.

Rejection Threshold

A second important feature of the ANBC is allowing for a null class without having the user explicitly define and train it. This is carried out by computing a *rejection threshold* for each gesture under which the classifier will not choose the gesture even if it is with the highest probability. Therefore, if none of the gestures pass the *rejection threshold*, the classifier will choose the null gesture. This feature is especially important for the case of continuous data that may or may not contain gestures, and this is the case when we are presented with IMUs in piano performance.

The rejection threshold is calculated using a confidence measure in the

form of a log likelihood confidence and standard deviation. The threshold is set by:

$$\tau_k = \mu_k^* - (\sigma_k^* \gamma) \quad (21)$$

Where μ_k^* is the mean log likelihood, σ_k^* is the standard deviation log likelihood, and γ is a scalar set by the user. For an overview on how these are calculated, see [Gillian et al., 2011b].

Adaptive Real-time Training

The third powerful feature of the ANBC is the ability to add training samples to improve the model while classifying in real time. This enables an initial relatively small training set, then more data could be recorded for refining the classifier during the performance. The adaptive training feature is controlled by three parameters: maximum training buffer size, model update rate, and the scalar number of standard deviations for the rejection threshold. Based on these parameters, every time the rejection threshold is crossed a new sample is added to the buffer, discarding the oldest one, and a counter is incremented. Once the counter crosses the update rate, the model is recalculated based on the new samples and the counter is set to zero. The adaptive training feature can be powerful for improving accuracy and adapting to performers, however it is also inherently sensitive to errors, especially at the beginning of a trial. If the first samples are classified incorrectly (despite crossing the rejection threshold) then a run-away model will be created which will get worse at every step.

4.3 Post Processing and Visual Feedback

This section describes the operations performed after the Bayes classification. The classifier generates a prediction 64 times per second. These predictions are then further processed for display and feedback.

4.3.1 Post Processing

Since the output of the classifier is a discrete class from 1 to 6 and it is updated every sample, some post processing is required in order to exclude outliers and smooth the transition between emotions. This is meant to create the effect of a human listener perceiving the music and responding emotionally to it. To do this, two main assumptions are laid:

- Emotions change slowly at intervals of at least several seconds (or several notes) and have a similarly long minimum duration. This is based on short term memory for objects [Miller, 1956] and on phonological working memory research [Baddeley and Hitch, 1974].
- While shifting from one emotion to another, the emotional path should be as continuous as possible and follow the implicit dimensionality in Hevner's adjective circle [Gabrielsson and Lindström, 2010]. Hence, while jumping from sad and *mournful* to *humorous* and *playful* must first pass through *tender* and then *serene*.

These assumptions make the flow of the algorithm more human like in its real-time behavior while following an emotionally varying performance. In order

to account from these assumptions the last few seconds of the classifier output are buffered into a mode filter in order to remove occasional erroneous outliers. Then, then a running average is employed on the output to smooth the transition from one state to another. This creates intermediate categories between the adjectives that can describe transient emotions.

4.3.2 *Visual Feedback*

The data are collected, trained and classified in real time. The emotions are predicted as discrete integers 1–6 and displayed as text on the screen. To make the display more intuitive and to smooth the behavior of the algorithm, a moving average is computed over the previous several seconds. The working memory for sound, known as the *phonological loop* is generally known to be 1–2 seconds [Baddeley and Hitch, 1974]. However, following several trials in the development of this display I observed that musical emotions change less rapidly than this and a three second buffer was found to be more appropriate. This creates a continuous flow that is used for two displays as follows.

Piano Roll Display

The piano roll display maps the MIDI *note on* and *note off* events to colored locations on an image. The color of the notes is set by the velocity of the *note on* event. The background color of this piano roll is mapped from the continuous emotion number generated by the classifier. The mapping of emotional musical performances to colors is based on [Bresin, 2005] as described in the background section and was used as a reference for our color mapping.

Displaying the emotions predictions this way allows for the feeling of a continuous flow in the music along with the musical emotion coloring that evolves in a natural rate similar to how we experience emotional responses in music. The emotional piano roll implementation is shown in Figure 21.

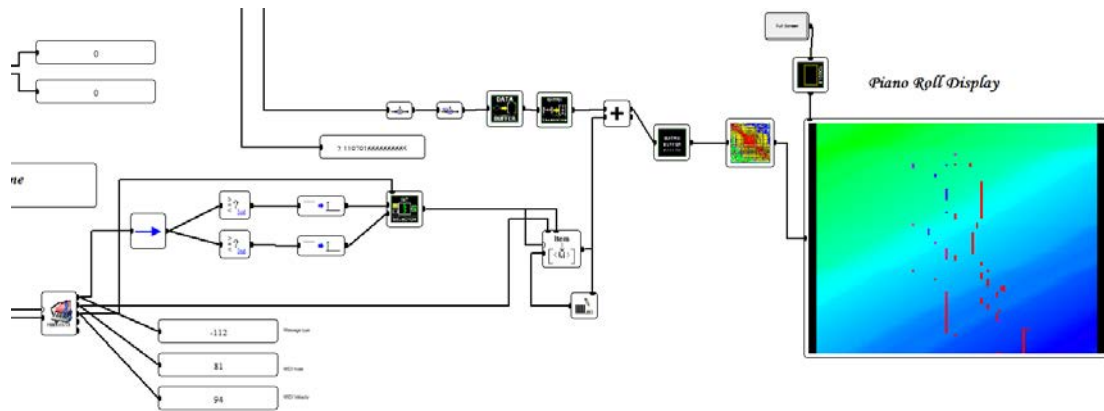


Figure 21: **Display of piano roll with emotion colored background.** The colors change continuously based on the emotion detected providing naturally flowing visual feedback to the performer.

Color Wheel Display

The second display is the Adjective circle projected on an HSV color wheel. The current state of emotion is represented by a moving, circle-shaped object followed by a tracer (tail). The head of the object is located on the current emotion predicted by the algorithm and the tail on the recent trajectory of emotional states. This display provides a feedback that is motion-like and can serve as a motive indication to the pianist similar to a dancer responding to the music. The emotional color wheel implementation in EyesWeb is shown in Figure 22.

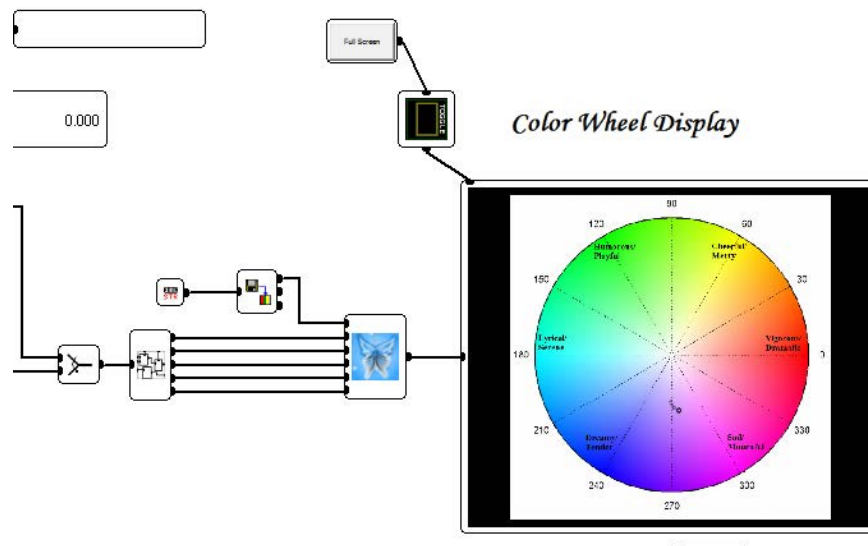


Figure 22: **Adjective Circle on HSV Color Wheel.** The head of the circle shaped object tracks the current emotional state tracked by the algorithm, providing the performer with dance-like feedback responding to the music. The emotion-to-color mapping is based on [Bresin, 2005] the adjectives are from [Hevner, 1936].

5

Evaluation

5.1 Evaluation and Research Goals

The evaluation section has two goals:

- To assess the accuracy in the system's performance with regards to detecting emotions.
- To provide an understanding of the detail of information that can be obtained from kinesthetic data of musicians and to attempt to identify the reasons and possible solutions for limitations.

Assessing the performance of a classifier is carried out by training it with a training sample set and then classifying using a different known test set. In order to do this, the training and data must include each of the classified categories. This is challenging to accomplish when dealing with live performance since it implies either requesting the musician to perform in a certain fashion (all of the expressions and emotions) or having the musician self-report on the performance. In both cases, the experiment is sensitive to bias and subjectivity.

Moreover, as mentioned earlier, the *standard paradigm* in experiments such as these is to play the same piece in different emotions thus eliminating the factor of the composition. However, in my pilot study it was observed that it is difficult to express an emotion in a composition that was not meant to convey it. This causes a dissonance in the performance, rendering it more of a technical

attempt at acting an emotion than a successful communication of it. For this reason, I have decided to add to the standard paradigm a test where each emotion is portrayed via a dedicated piece. Because the algorithm is completely deaf to the music the composition factor diminishes in its significance compared to that of analyzing the audio signal.

Finally, it is also in the scope of this project to follow the patterns in which performers shift from one emotion to the other during a performance. This could reveal some interesting observations regarding live performance as well as a musicological understanding of the structure of a piece. Therefore, a third section was added to the test in which the performers were requested to play freely either from a long score or through improvisation while self-reporting on their emotional intentions.

5.2 Subjects

The test subjects for this evaluation were a homogenous group of 13 pianists, with an average playing experience of $\mu = 12.6 \pm 4.8(\text{yrs})$. The age group statistic was $\mu = 21.8 \pm 3.0(\text{yrs})$. Four subjects described their genre as Classical, three as Jazz , four Contemporary, and two Rock/Pop. The subjects were from a variety of academic backgrounds and academic levels, this was not considered an affecting factor in this research since the subjects were not required to perform any academically related task other than piano performance. The details of the subject group are described in Table 1.

Table 1: Test Subjects Description

Subject	age (yrs)	experience (yrs)	genre
1	18	12	Classical
2	30	5	Contemporary
3	21	14	Classical
4	19	11	Pop/Rock
5	23	17	Classical
6	20	15	Contemporary
7	24	8	Pop/Rock
8	20	12	Jazz
9	22	5	Classical
10	25	23	Jazz
11	21	12	Jazz
12	20	13	Contemporary
13	21	17	Contemporary

5.3 Experiment Procedure

As described above, because the system is required to detect various patterns and due to the complexity of the different affecting factors in this condition, the experiment was divided to three sections.

5.3.1 Stage 1 – The Standard Paradigm, One Piece Different Emotions

In this section, the performers played the first few measures of Bach’s Minuet in G major, BWV 841 from the *Notebook of Anna Magdalena Bach*. The piece was played six times in the six different emotion categories based on the *standard paradigm* [Juslin and Timmers, 2010] to create the training data. The performers were only allowed to make variations in intensity, tempo, accents and slight pitch variations (major/minor and decorations). This was repeated twice while randomizing the order for training and testing. The algorithm classified emotion categories were tested against the intended emotion categories.

5.3.2 Stage 2 – Different Pieces, Different Emotions

In this section, the performers chose six different pieces with the intention to convey the six different emotion categories. The hypothesis in this section is that it would be more intuitive for the performers to express the emotions that matched the piece. An example of the six pieces played (per category) by the performers were:

- *sad/mournful* Nocturne in E Minor, Chopin
- *dreamy/tender* Clair de Lune, Debussy
- *lyrical/serene* Songs without Words, Mendelson
- *playful/humorous* Maple Leaf Rag, Joplin
- *cheerful/merry* Sonata in C Major, Mozart
- *vigorous/dramatic* Sonata no. 8 movement 1, Beethoven

The data from this stage was used as training data for stage 3. The primary hypothesis was that training based on this data would achieve improved generality of the classifier compared to that of the standard paradigm in stage 1. This hypothesis was clearly observed while attempting to classify the stage 2 results based on training from stage 1. The reason for this is that training on one song severely limits the expressivity that can be conveyed and thus it yielded poor results in classifying other pieces with a wider range of expressiveness. In

other words, more training data was needed displaying a wider range of expressivity. This proved successful as seen in the *Results* section.

5.3.3 Stage 3 – Free Playing, Self-report, and Listener Evaluation

In this section, the performers were asked to play freely for several minutes while continuously self-reporting on their intended emotions. They played either from a selected score or improvisation. The algorithm had been trained before based on the previous section. However, in this section the classified emotion categories were tested against the intended emotion categories as well as against listener evaluation. The listener evaluation was carried out by four musically trained listeners. Thus, a three-way comparison was performed between the intended emotion, the algorithm’s classification, and the average of the listeners’ perceived emotion.

5.4 Tools for Classifier Evaluation

There are several methods and techniques to evaluate a classifier that vary with the application, the implementation, and the purpose of the evaluation. In this research, the classification results were evaluated using a *Confusion Matrix*, *Precision*, *Recall*, *Specificity*, and *Accuracy* parameters, *RMS error*, χ^2 test, and Cohen’s κ test to assess the statistical validity of the results. The following is a brief overview of these tools and how they were used in the context of this research.

5.4.1 *Confusion Matrix*

The confusion matrix is the simplest way to provide a qualitative but comprehensive evaluation on the performance of a classifier. It displays the total classification in an $c \times c$ matrix where c is the number of categories. The rows represent the labeled (true) categories and the columns represent the classified (estimated) categories. As the classification improves, the matrix becomes diagonal (with higher values on the main diagonal and zeros in the remaining fields). The confusion matrix is also useful for understanding the limitations and weaknesses of the classifier, i.e. which categories are classified incorrectly and which categories they are confused with, hence the name, confusion matrix.

5.4.2 *Precision, Recall, Accuracy, and Specificity*

Precision and Recall are single parameters that evaluate the performance of an algorithm in detecting an occurrence of an event [Powers, 2007]. These can be extracted directly from the confusion matrix. In order to define precision and recall, four terms are defined:

- True Positive – the prediction of a category in its presence.
- False Positive – the prediction of a category in its absence.
- False Negative – the non-prediction of a category its presence.
- True Negative – the non-prediction of a category in its absence.

Then, *Precision* and *Recall* are defined in equations 22 and 23 respectively:

$$Precision = \frac{TP}{TP + FP} \quad (22)$$

$$Recall = \frac{TP}{TP + FN} \quad (23)$$

Looking again at these definitions, we can observe that *Precision* is an evaluation of the positive predictions while *Recall* is an evaluation of the true positive rate and it is also referred to as *Sensitivity*. In other words, *Precision* is an evaluation of the correctness of classifications generated by the algorithm while *Recall* is an estimation regarding the ability of the classifier to detect an event in its occurrence. A third term that is useful is *Accuracy* and it is defined in equation 24:

$$Accuracy = \frac{TP + TN}{TP + TN + FP + FN} \quad (24)$$

Another term for classifier evaluation is *specificity* as defined in equation 25. It is an estimation of the probability of a negative prediction of a class in its absence.

$$Specificity = \frac{TN}{TN + FP} \quad (25)$$

In this research, the *Precision*, *Recall*, *Accuracy*, and *Specificity* parameters are calculated on each of the six categories.

5.4.3 RMS Error

This evaluation metric is based on our assumption that there exists a dimensionality in the category space of the adjective circle[Gabrielsson and Lindström, 2010]. Thus, two adjacent emotion categories

are also *close* in their expressive content. Moreover, the ground truth is set by the emotion category the performer was requested to play; however, it was observed that the pianists drifted between categories based on their self-report. Therefore, the binary relation of *true/false* is an incomplete description of the algorithm's behavior. Instead, we measure the RMS distance of the classification from the intended emotion. The RMS error is defined in by:

$$RMS\ error = \sqrt{\frac{1}{N} \sum_{i=1}^N (\omega_c - \omega_i)^2} \quad (26)$$

Where ω_c is the classified emotion, and ω_i is the intended emotion.

Another aspect of the assumed dimensionality is that the categories are set on circular space. Therefore the difference between categories is the distance on the circle. In other words, there is a wrapping of the classes, where the actual distance between two categories is the shortest path around the adjective circle. For example, the distance from *vigorous/dramatic* to *dreamy/tender* is two, and so is the distance to *humorous/playful*. The distance error is therefore an *angular RMS error* and can be measured in units of degrees.

5.4.4 χ^2 Test

The χ^2 test is a common statistical method used to evaluate a null hypothesis when a sample set consists of several events or categories that are mutually exclusive and have a total probability of 1. The purpose of the test is to examine the rejection of the null hypotheses. The null hypothesis in the case of this research would be that the classification outputs of the algorithm are a

random variable and uniformly distributed with equal probability.

The test is performed by separating the data into category bins and comparing the observed and expected rates at which each bin occurs. Then, the χ^2 is calculated by:

$$\chi^2 = \sum_{i=1}^M \frac{(O_i - E_i)^2}{E_i} \quad (27)$$

Where

- M – number of categories or bins.
- E_i – expected number of occurrences in category i .
- O_i – observed number of occurrences in category i .

Then the χ^2 is mapped to a p value indicating the probability of the observed data given the null hypothesis. If p is below a threshold we say that we can reject the null hypothesis.

For the purpose of this research, we shall define a sample as one instance of classification or categorization. Therefore, for every subject, and for every intended emotion category we have N instances of categorizations into one of six bins (the six emotion categories). The null hypothesis is that the algorithm is randomly guessing with equal probability (uniform distribution one out of six), therefore the expected samples in each of the six bins are $\frac{N}{6}$. We then plug in our observed classifications for that trial and compute the χ^2 based on equation 27. Our number of bins is six and therefore we have five degrees of freedom. This is used to map the χ^2 to a p value. The p value represents the probability that, had

the null hypothesis been true, we would get our observations. Therefore the lower p is, the more unlikely the null hypothesis.

5.4.5 Cohen's κ test and weighted κ test

The κ test, [Cohen et al., 1960], is a statistical measure of agreement between two judges in a multicategorization problem. In the context of this research one judge would be the performer's intended emotion and the other judge is the algorithm's classification. The κ test accounts for the chance-expected agreement, thus evaluating the actual proportion of agreement after chance is removed from consideration. For this, two quantities are defined:

- p_o - the proportion of units in which the judges agreed.
- p_c - the proportion of units for which agreement is expected by chance.

The purpose of the test is to evaluate the extent to which p_o exceeds p_c .

Therefore, κ is defined by:

$$\kappa = \frac{p_o - p_c}{1 - p_c} \quad (28)$$

We can compute this directly from the frequencies in the confusion matrices for each emotion category by:

$$\kappa = \frac{f_o - f_c}{N - f_c} \quad (29)$$

Where, f_o are the observed classifications and f_c are the expected classifications, i.e $N/6$. Thus, a high κ implies a good agreement between the judges. There is no one criteria scale for interpreting the κ values. In this research we use the scale suggested by [Landis and Koch, 1977].

However, the simple κ test assumes that all misclassifications are equally costly. In order to account for categories that are ordered in dimensionality (similar to our case where adjacent categories are considered “close” in the emotional aspect), the *weighted κ test* was developed [Cohen, 1968]. In order to compute a the weighted κ we define a $c \times c$ weight matrix, where c is the number of categories. Typical weights are linear or quadratically decaying values as a function of the distance from the main diagonal. Then, f_o and f_c are computed by multiplying the frequencies by the weights as in equations 30 and 31.

$$\text{weighted } f_o = \sum_{i=1}^c \sum_{j=1}^c w_{ij} O_{ij} \quad (30)$$

$$\text{weighted } f_c = \sum_{i=1}^c \sum_{j=1}^c w_{ij} E_{ij} \quad (31)$$

Where O is the observed matrix and E is the expected (chance) matrix.

In this research we will look at the unweighted, linearly weighted, and quadratically weighted κ values. The reason for this is that we do not have a priori knowledge regarding the form of dimensionality in the emotional space, or in other words, how close is *sad* to *dreamy* relative to *sad* and *lyrical* or *cheerful* to *playful* and so on. Thus, as shown the results section, experimenting with different weight techniques might give us an understanding of the dimensionality of the emotion space in the adjective circle.

5.5 Results

This section presents the results followed by a brief interpretation. A more thorough inquiry is carried out in the discussion chapter.

5.5.1 Stage 1 - The Standard Paradigm, One Piece Different Emotions

The initial classification results per subject on all categories are summarized in Table 2. The *correct* and *off by one* values are calculated as a percentage of the total number of classification samples. Each trial consisted of 3000–6000 classifications, distributed evenly to 500–1000 classifications per emotion. It is important to note that the emotion categories are organized on the adjective circle in a way that adjacent emotions are close to each other in concept and those who are across are different. This is the implicit dimensionality mentioned earlier in [Gabrielsson and Lindström, 2010] and it is for this reason that we do not completely ignore incorrect classifications but also look at those that are *one off*. The *total* column shows the sum of *correct* and *1 off* predictions. For example many times the emotions *sad/mournful* are confused with *dreamy/tender*. This confuses performers as well as the algorithm and the listeners as observed in the following sections. The percentage of correct classifications is approximately 50% and including those that are *off by one* we get to over 80% mean total classification accuracy. Also, the results are quite stable (*std* = 6.7%).

Furthermore, the RMS angular error is displayed in the most right column. This is calculated as explained in the previous section and is an

Table 2: **Classification results per subject over all categories in the Standard Paradigm**

Subject	Correct (%)	Off by 1 (%)	Total (%)	Angular RMS error (°)
1	49.37	35.082	84.452	61.884
2	46.128	39.319	85.447	61.279
3	59.03	17.893	76.923	63.496
4	67.531	18.904	86.436	51.321
5	23.917	45.002	68.919	78.292
6	39.626	32.532	72.158	76.615
7	28.828	49.545	78.373	71.144
8	47.981	27.019	75	81.163
9	67.899	18.133	86.031	51.616
10	61.576	15.117	76.693	70.392
11	59.21	14.983	74.193	74.952
12	60.97	27.931	88.9	51.028
13	49.301	39.263	88.564	55.319
population mean	50.8743	29.2864	80.1607	65.2693
population std	13.8282	11.8183	6.7427	10.8732

indication of the mean accuracy angle when a classification is made. Thus, while the algorithm is classifying an emotion, this predicts the error range in degrees in which the emotion is expected to be found. The angular distance between adjacent emotions is 60° . We get a mean angle accuracy of approximately 65° which implies that the predictions are within one emotion on the adjective circle.

The overall confusion matrix is calculated by the sum of all confusion matrices and is displayed in Figure 23. The results show high performance in detecting most of the intended emotions. A clear diagonal is observed in the confusion matrix, with the main discrepancies occurring between the *sad*, *dreamy*, and *serene* categories.

In order to understand the confusion matrix more, one should observe it in varying levels of resolution. First, four major blocks are clearly seen, the two

on the main diagonal are bright and the two on the remaining are dark. This is an indication of the algorithm's strong ability in distinguishing between high and low arousal in emotions. The *sad*, *dreamy*, and *serene* are low arousal and the *humorous*, *cheerful*, and *vigorous* are high arousal categories.

Second, the inner diagonals are observed, this is an indication of the algorithm's ability in distinguishing valence. The *sad* and *vigorous* categories are considered low in valence while the *lyrical*, *humorous*, and *cheerful* are in high valence. The *dreamy* category is generally assumed neutral in valence (there are good dreams and bad dreams). Perhaps this is why it gets confused the most.

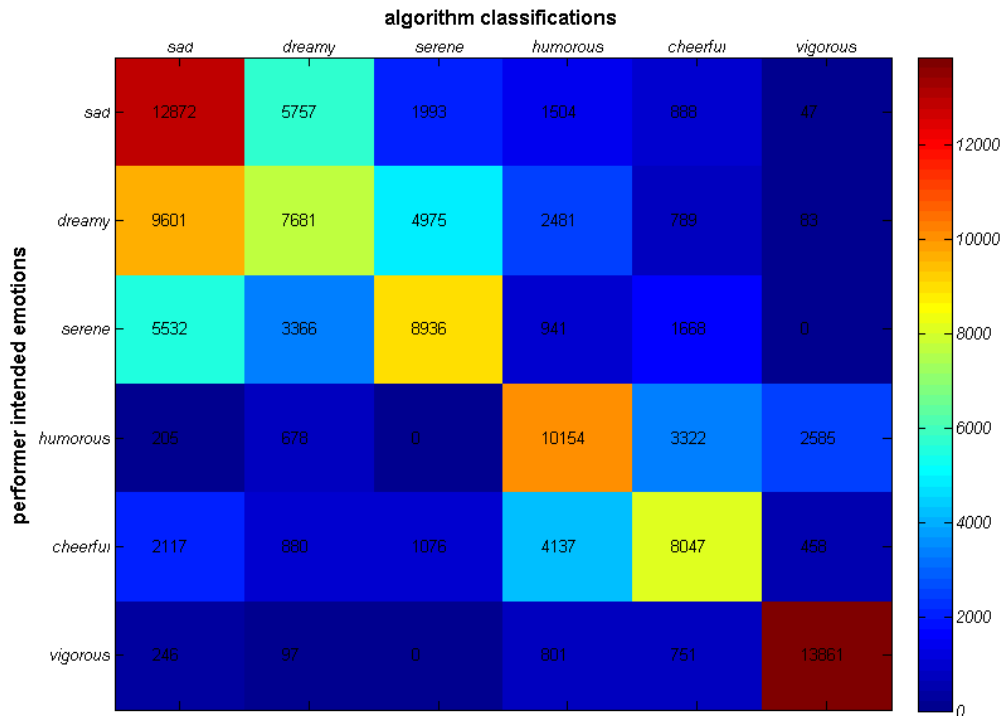


Figure 23: **Overall Confusion Matrix Stage 1.** A clear diagonal is observed, the main discrepancies are between *dreamy/tender*, *sad/mournful*, and *lyrical/serene* .

Based on the total confusion matrix, the results for *Precision*, *Recall*,

Table 3: **Precision, Recall, Specificity, and Accuracy per category for Stage 1**

Category	Precision	Recall	Specificity	Accuracy
<i>sad/mournful</i>	0.5582	0.421	0.8842	0.7647
<i>dreamy/tender</i>	0.2999	0.4161	0.8208	0.7578
<i>lyrical/serene</i>	0.4371	0.5263	0.8867	0.8351
<i>humorous/playful</i>	0.5993	0.5072	0.9311	0.8595
<i>cheerful/merry</i>	0.4814	0.5203	0.9159	0.8643
<i>vigorous/dramatic</i>	0.8797	0.8137	0.9813	0.9572

Specificity, and *Accuracy* are be obtained per category and displayed in Table 3.

The results show that the *vigorous* emotion has the highest precision, recall, specificity, and accuracy. This is expected since the vigorous playing is very different and easily distinguishable from the other emotions. This is also consistent with the functionalist perspective [Juslin, 1997], i.e. that we are programmed to be sensitive to emotions that can be life threatening and are imperative to our survival.

The *humorous* and *cheerful* categories had similar results, both were lower in precision and recall because they were confused between each other. Their accuracy however, is still relatively high because when detected they were not confused with other categories.

The *sad* and *lyrical* also had similar results but lower than the other categories because they were often not only confused between each other but also with *dreamy*. The *dreamy* category had the lowest achievement in all categories. This too, matches our expectation regarding its neutral valence as explained in the analysis of the confusion matrix.

The results for the χ^2 test per emotion category are displayed in Table 4.

Table 4: χ^2 test results per category for Stage 1.

category	N	dof	χ^2	p
<i>sad/mournful</i>	38	5	27.895	0.0000382
<i>dreamy/tender</i>	42	5	32	0.00000594
<i>lyrical/serene</i>	32	5	21.875	0.000553
<i>humorous/playful</i>	29	5	19.897	0.001307
<i>cheerful/merry</i>	29	5	18.655	0.002228
<i>vigorous/dramatic</i>	25	5	17.32	0.003931

Table 5: κ test results for Stage 1. The agreement criteria is taken from [Landis and Koch, 1977]

weighting	p_o	p_c	κ	agreement
unweighted	0.5193	0.1667	0.4231	moderate
linearly weighted	0.8460	0.6107	0.6044	substantial
quadratically weighted	0.9361	0.7662	0.7269	substantial

The method of calculation is explained in the previous section. $p < 0.01$ is observed for all categories, clearly rejecting the null hypothesis. Thus, the system is obviously performing much better than guessing one category out of six.

The results for the κ test on the complete confusion matrix are displayed in Table 5. The method of calculation is explained in the previous section. The agreement criteria is taken from [Landis and Koch, 1977]. As expected, it is observed that using the weighted κ produces a better agreement criteria. However, it is interesting to observe that the quadratic weighting is better than the linear. This will be discussed further in the next section.

5.5.2 Stage 2 – Six Pieces, Different Emotions, testing on Free-playing and Self-report

In this section, the algorithm was trained on the performers playing six different pieces that were chosen to express the six emotion categories. Following that, they were asked to play freely and self-report on their intended emotion.

The first analysis is the overall confusion matrix of the self-reported intended emotion vs. the algorithm classification. The overall confusion matrix is calculated by the sum of all confusion matrices and is displayed in Figure 24. The main diagonal is still observed. However, the *sad* and *dreamy* categories were often misclassified as *serene*. Also, the *humorous* category was misclassified as *cheerful* and *vigorous*. Misclassifying all three low-arousal categories with *serene* implies that the system in this test performed less accurately in distinguishing valence in the low-arousal categories. Once again, if valence cannot be distinguished, there is really no difference between *sad*, *dreamy*, and *serene*. Misclassifying *humorous* with *cheerful* and *vigorous* implies that there is a dimension in emotions we are not considering. Humor is typically thought of as high in valence but there is also dark and sarcastic humor. Moreover, humor in many cases by definition is a case of contradiction (such as the contradiction between the literal and actual meaning in the definition of irony) this type of contraction can easily throw off an algorithm trained to detect only the literal. Such is the case in many scherzo portions of pieces by Beethoven and Schubert which are often played in a playful manner but convey dark drama attributed to Beethoven's growing deafness and Schubert's decaying health [Ringer, 2009]. That said, perhaps there are other ways of detecting hidden meanings in motion that could be explored in future research.

Still, these results are quite promising considering the difficulty in detecting emotions from a much broader range compared to that of the standard

paradigm test in the previous section. The purpose of this section was to evaluate the performance of the algorithm in real-life scenarios where the system is presented with an unknown piece that it had not been trained on, and attempt to predict the intended emotions in it. Considering the difficulty in this, and the fact that it has not been attempted before in such conditions, the results of this section are satisfying.

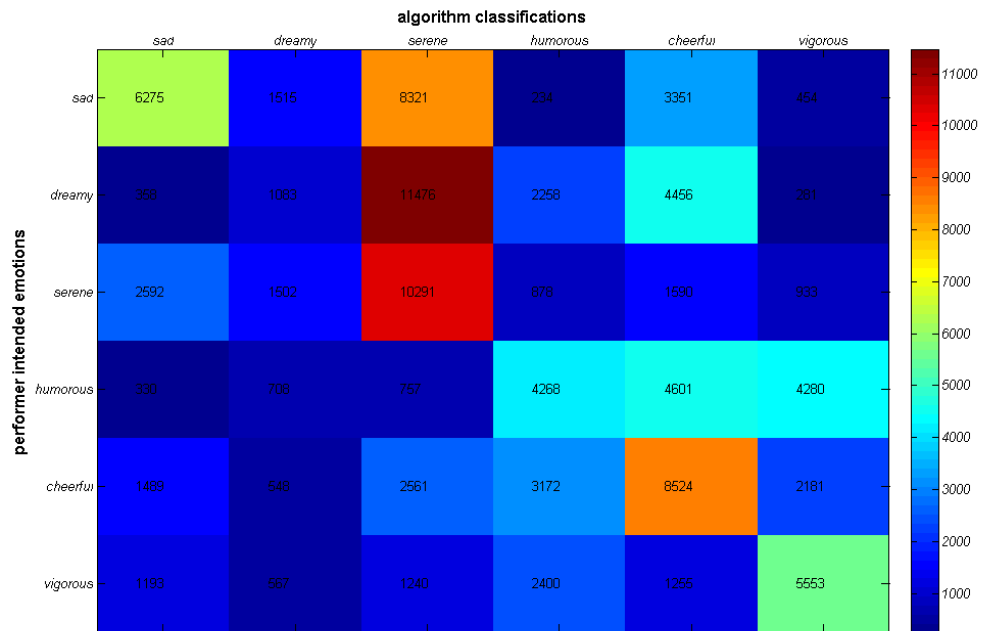


Figure 24: **Overall Confusion Matrix for training on different pieces and test on free playing and self-report** Rows represent labeled emotions while columns represent algorithm classified emotions. The main diagonal is still observed. However, the *sad* and *dreamy* categories were often misclassified as *serene*. Also, the *humorous* category was misclassified as *cheerful* and *vigorous*.

Based on the total confusion matrix, the results for *Precision*, *Recall*, *Specificity*, and *Accuracy* are be obtained per category and displayed in table 6. The results for the χ^2 test per category are displayed in table 7. The precision and recall rates are lower than before but the accuracy and specificity are still

Table 6: **Precision, Recall, Specificity, and Accuracy per category for Stage 2**

Category	Precision	Recall	Specificity	Accuracy
<i>sad/mournful</i>	0.2992	0.4822	0.8473	0.8039
<i>dreamy/tender</i>	0.0561	0.189	0.8037	0.7679
<i>lyrical/serene</i>	0.5604	0.2865	0.89	0.6917
<i>humorous/playful</i>	0.3202	0.3422	0.886	0.8123
<i>cheerful/merry</i>	0.4426	0.3547	0.8741	0.7599
<i>vigorous/dramatic</i>	0.4846	0.4298	0.9264	0.8575

Table 7: χ^2 test results per category for Stage 2.

category	N	dof	χ^2	p
<i>sad/mournful</i>	34	5	24.471	0.000176
<i>dreamy/tender</i>	35	5	25.4	0.000117
<i>lyrical/serene</i>	29	5	18.655	0.002228
<i>humorous/playful</i>	23	5	14.652	0.011957
<i>cheerful/merry</i>	33	5	22.818	0.000366
<i>vigorous/dramatic</i>	25	5	15.4	0.008783

quite high. The results of the χ^2 still show $p < 0.05$ value, rejecting the null hypothesis. However, it is seen now that the *playful* category achieved the least significant results ($p = 0.012$). This can be seen in the confusion matrix where *playful* was often confused with *cheerful* and *vigorous*.

The results for the κ test for Stage 2 on the complete confusion matrix are displayed in table 8. The method of calculation is explained in the previous section. The agreement criteria is taken from [Landis and Koch, 1977]. Here too, it is observed that better agreement is achieved with the weighted κ test and especially with the quadratically weighted κ . It seems that there exists a pattern here which could imply the form of the dimensionality in the emotion space. This form is a falling quadratic where adjacent categories are very similar but the similarity drops rapidly after one category. For example, *dreamy* is very similar

Table 8: κ test results for Stage 2. The agreement criteria is taken from [Landis and Koch, 1977].

weighting	p_o	p_c	κ	agreement
unweighted	0.3466	0.1667	0.2159	fair
linearly weighted	0.7448	0.6122	0.3419	fair
quadratically weighted	0.8723	0.7680	0.4495	moderate

to *sad* and *lyrical* which are immediately adjacent to it but very different from *playful* and *vigorous* which are two steps from it. Likewise, *playful* is similar to *cheerful* and *lyrical* but very different from *vigorous* and *dreamy*. This fits a falling quadratic form more than a linear form and it is also pleasingly consistent with our initial justification for adding the “one off” column in the results of Stage 1.

5.5.3 Stage 3 – Performer vs. Listener vs. Algorithm

In this section, three pieces from the free-playing self-report part were selected for listener evaluation. The pieces were selected one from each genre, Classical, Jazz, and Contemporary. Four listeners evaluated the perceived emotion and compared to the performers’ intentions and the algorithm classification. This three-way comparison allows for interesting qualitative observations of what the system is doing. First, instead of looking at a 2D confusion matrix we present a 3D confusion matrix or a *Confusion Cube*. The confusion cube of the total algorithm performance on the three performers is presented Figure 25.

Each of the small cubes represents a bin of classifications corresponding to the emotion a coordinate of the cube. The colors in each cube are mapped the

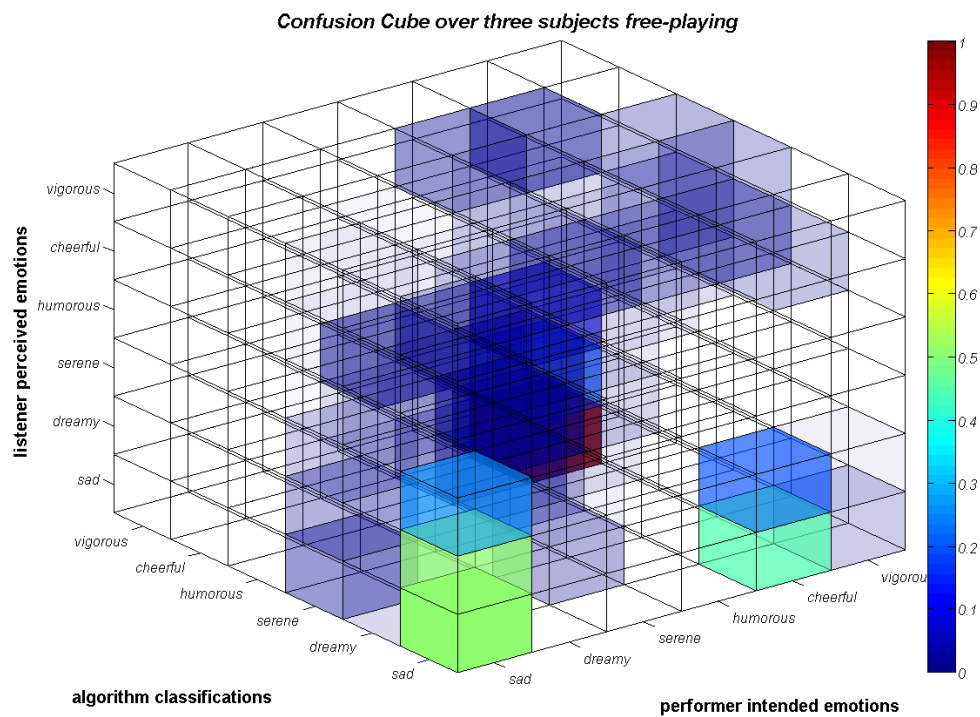


Figure 25: **Three dimensional confusion cube.** The intended emotions are compared with the listener perceived emotions and the algorithm classification through a complete piece.

number of classifications via the jet color mapping. The α transparency factor is also adjusted according to the number of classifications. Hence, empty bins will remain colorless, bins with only few classifications in them will be colored in blue transparent colors, and fuller bins will be colored yellow and then in dark red. The main diagonal is still observed but is it wider now, and there are disagreements especially regarding the *sad*, *dreamy*, and *serene* categories. It is still observed though, that most of the classifications occur around the main diagonal and in the center of the cube and most of the remaining edges are empty.

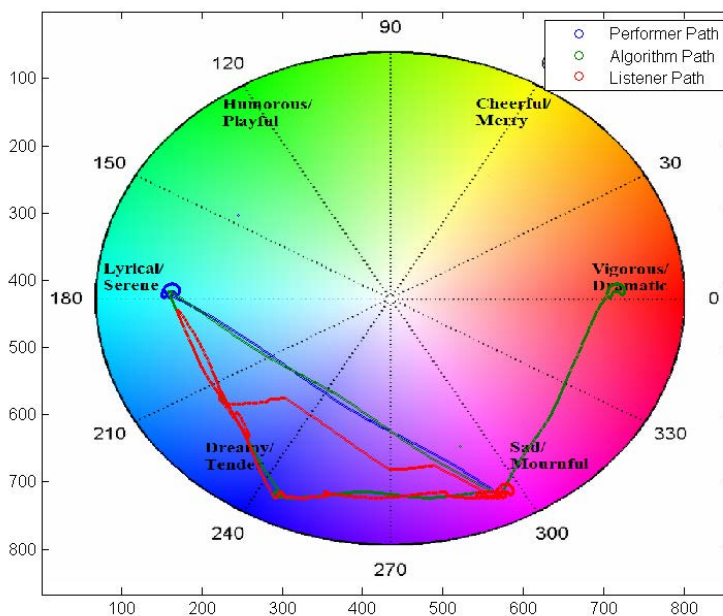


Figure 26: **Emotion paths of Performer, Listeners, and Algorithm through 10 seconds of Classical piece played by subject No. 9.** The piece was Chopin Nocturne Posthumous in $C\sharp$ Minor. The performer, algorithm, and audience in agreement, but the algorithm is detecting *vigorous* at some point.

Next, while the confusion cubes are fun to look at, they can only tell us about the accuracy of detection at every point in time through the piece.

However, we would also like to observe the emotional path through longer sections of the piece. Thus, we can draw the emotion paths of the performer, listener, and the algorithm projected on the color wheel. This provides some interesting insights regarding communication of emotions during a performance. Figure 26, shows the emotion path of a 10 second section during the Chopin Nocturne Posthumous in $C\sharp$ Minor. It is observed that the performer, algorithm, and audience are in agreement, but the algorithm is detecting *vigorous* at some point in disagreement with the listeners and performer intentions.

Figure 27 shows a 20 second section of a Jazz improvisation. Here, we observe a general agreement that the section is centered between the humorous and *vigorous* emotions. The algorithm decides on *cheerful* at some point in disagreement with the performer and audience.

Figure 28 portrays the emotion paths through 20 seconds the contemporary piece. Here while the performer is attempting to convey *humorous* and *lyrical*, the *lyrical* is mostly detected by the algorithm and audience, but the *humorous* is perceived as *cheerful* by both. Moreover, the listeners and the algorithm detected a *dreamy* and even *sad* mood that the performer did not intend to convey.

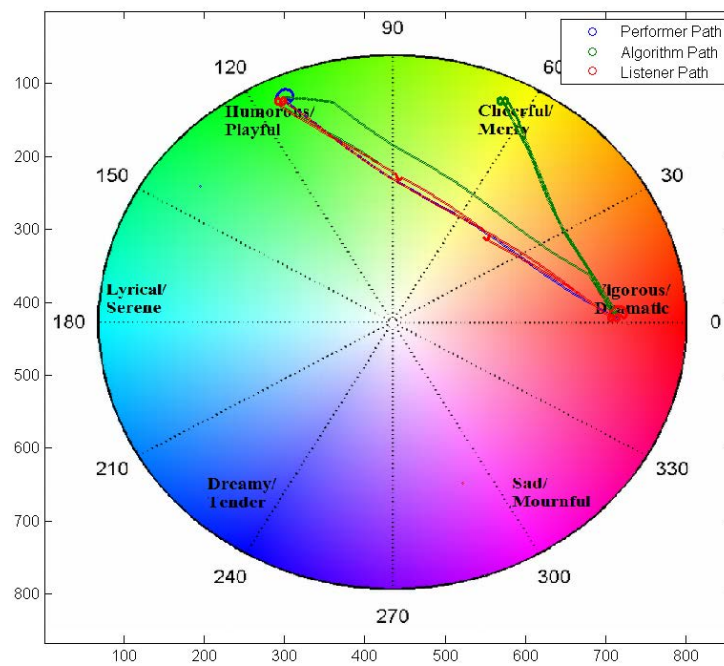


Figure 27: **Emotion paths of Performer, Listeners, and Algorithm through one minute of Jazz improvisation played by subject No. 11.** There is a general agreement that the piece is centered on the *humorous* emotion.

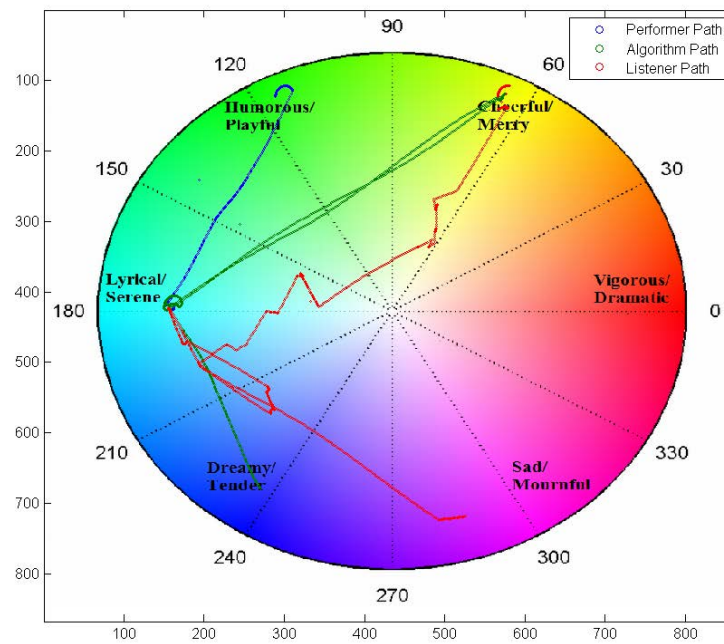


Figure 28: **Emotion paths of Performer, Listeners, and Algorithm through 20 seconds of a Contemporary improvisation played by subject No. 12.** An agreement is observed at the *lyrical* emotion but the humorous is detected as *cheerful* and there is an unintended drift to *dreamy* and *sad*.

6

Discussion

6.1 System Performance, Limitations, and Possible Improvements

The system presented is a first attempt at musical expression recognition based solely on kinesthetic sensing. It is successful in detecting basic expressions such as dynamics and articulation as well as the performer intended emotions and even listener perceived emotions. Moreover, the system can function as a performance feedback system via its various displays, the piano roll and the emotion color wheel. Using this, a musician can be presented with continuous feedback while practicing for a performance or while composing a piece. Moreover, this type of detection can also be used to augment musical instruments by adding musical and emotional intelligence to them and using the predictions of the algorithm to control various audio parameters in correspondence with the musical mood and performers intentions.

The system performed well in the standard paradigm where it was tested on the same piece played in six different emotions. However, in the second section where a more realistic situation was tested, the system was introduced to an unknown piece and expected to detect the expressions in it. In this case the system still succeeded in detecting the obvious emotions *sad*, *vigorous*, and *cheerful*. However, the system was limited in the prediction of ambiguous emotions such as *lyrical* and *dreamy*. Moreover, the *humorous* emotion is often confused with *cheerful* and *vigorous*. This could be explained by the notion that

these emotions differ mainly in valence and are similar in arousal. While it is quite straightforward to detect high and low arousal via motion, it is not the case for valence. There is some equivalence with the findings of [Schachter and Singer, 1962] and their research with epinephrine that is quite intriguing. The epinephrine alters the physiological state of arousal but it does not alter valence, therefore it was difficult in some cases to establish the emotional state. It was thus their conclusion that some emotional experiences could not be generated and via physiological changes because they require cognitive processing. This could be the case of some of the musical emotions as well. When we measure motion, we measure a physiological state. This could be used to carry some of the cues that convey emotions but possibly not enough for those that are complex and require more cognitive processing. Perhaps the *dreamy* and *lyrical* emotions fall under this category.

Other limitations of the system and this research include the discrepancy between performer intention and listener perception. Since this is the case, it is difficult to establish a ground truth on which to evaluate the system or assign a goal it must achieve. However, this is precisely the phenomena in which this system can be helpful in addressing, as I will explain in the future research section.

There are many ways in which the system could be improved. First, the obvious way to obtain more information would be to add more sensors. Sensors could easily be added to the legs and torso of a performer, measurements such as

these would add more independent features. It is generally shown that increasing the number of independent features improves the performance of a classifier [Duda et al., 1995a]. It is however, important to mention that it also increases the number of dimensions and can lead to the requirement of a large training data set. This limitation is referred to as *the curse of dimensionality* where it is generally claimed that the required training data grows exponentially with the dimensionality of the problem. However, this too could be overcome by use of dimensionality reduction techniques such as *Principle Component Analysis* and *Multiple Dimension Analysis* [Duda et al., 1995b]. Figure 29 shows on the *intensity*, *tempo*, and *articulation* features per class projected on a three-dimensional scatter plot. The classification problem is apparent and it is observed that although the classes occupy different spaces, the shape seems quite erratic and a decision rule would not take the form of a simple plane or curve. Figure 30 shows all of the features after they have been projected to a three-dimensional space using multiple discriminant analysis. Now the clusters are clearly observed and even though there is still some overlap, the decision boundaries are now easier to establish.

Second, in this research, the system was only trained per performer. This is because the performers differed in their ranges and expression styles. However, this severely limits the generality of the system and therefore its usability in real-life scenarios. The training data from this research, could be used along with proper reference to the inter-performer differences to obtain a scaled data set

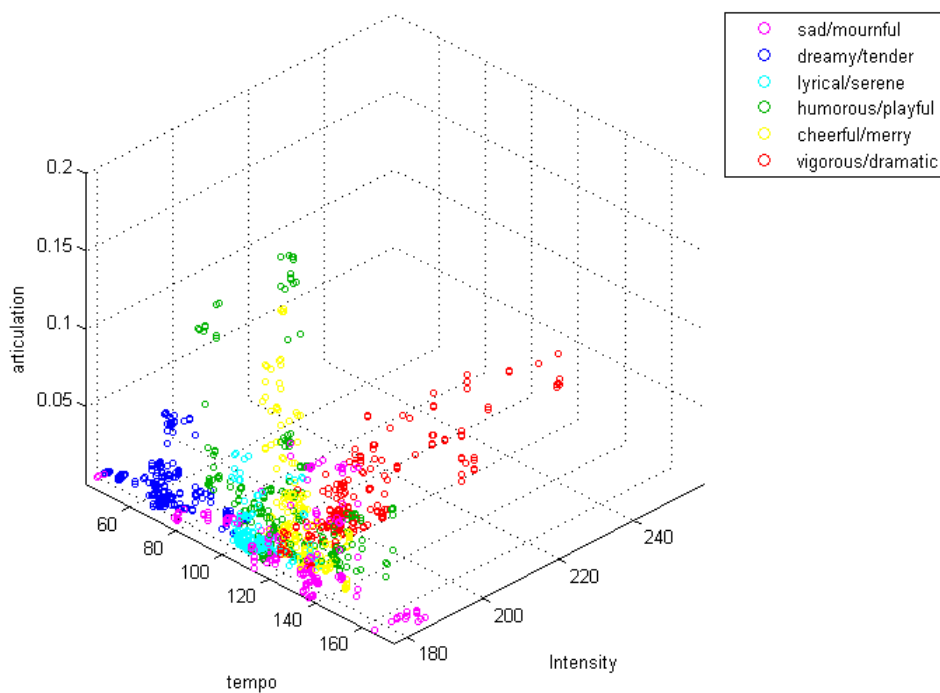


Figure 29: [*Intensity, tempo, and articulation* 3D scatter plot. Although the classes occupy different spaces, the shape seems quite erratic and a decision rule would not take the form of a simple plane or curve.

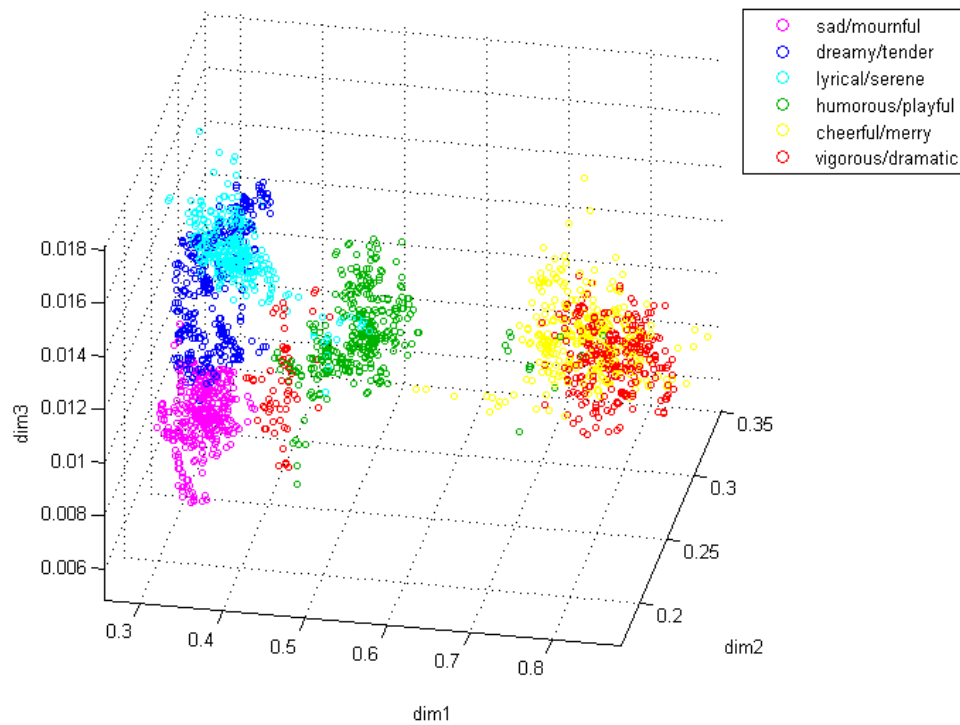


Figure 30: **3D scatter of linear combination of features projected to three dimensions using MDA.** Clusters are clearly observed and even though there is still some overlap, the decision boundaries are now easier to establish.

such that the system could be trained on multiple subjects. This might prove successful since the number and variety of training samples will grow significantly, and will therefore address the problem of dimensionality mentioned above.

Third, the system was only evaluated using a Bayes classifier. Other classifiers such as Hidden Markov Models could perhaps perform with better results. This assumption is based on the observation that music is a temporal phenomenon, and so are the emotions portrayed and perceived in it. Classifiers such as Hidden Markov Models are specifically designed to handle such time evolving systems in which the current state is influenced by previous states, and thus it is reasonable to assume that they might perform better at this task [Duda et al., 1995b].

Finally, the limiting of kinesthetic data was for the purpose of this research to answer the question, of how much we can achieve by looking only at motion. However, for further applications in which better classification performance is of main interest, using the audio signal in real time could reveal more information. Specifically information regarding major and minor tonality could, in many cases, help in distinguishing valence [Hevner, 1935].

6.2 Research Discoveries and Ideas for Future Research

We have seen that musically relevant information regarding a performance and specifically musically conveyed emotions can be detected by using real-time kinesthetic data. This observation is of importance for several reasons. First, it highlights the manifestation of emotions in musical performance and it serves to

show that they can be perceived and distinguished not only subjectively by humans, but also by a machine. Moreover, since the acoustic detailed musical information regarding pitch and tonality cannot be conveyed in these motions, it is only the envelope that is observed, and it is shown to be enough to classify to some extent. This is consistent with the *Contour Theory* discussed in [Kivy, 1980], [Kivy, 1989], [Davies, 1994] and also [Nussbaum, 2007].

However, it is also interesting to look at where the classification was less successful. These were generally the categories *dreamy* and *serene* that were in many cases confused with *sad*. It was observed that even in cases where there was an agreement between the performer and listeners, the algorithm had difficulty distinguishing between them. This of course could imply a weakness of the algorithm, which as engineers, is always the first assumption. Nevertheless, it could also imply that the fine differences between these categories cannot be explained by the contour theory because they require more detail than the contour can carry. In other words, perhaps the distinction between some emotions requires a higher sample-rate than the musical contour carries. This means that some other carrier is at work for this information which could be the musical grammar and semantics referred to and devised by [Cooke, 1959] and [Jackendoff and Lerdahl, 1983]. Thus, the findings of this research might help determine the boundary in which the contour and the semiotic theories meet. Furthermore, since the semiotic theory generally requires some musical training and the contour theory does not, this could have implications on understanding

the borders on which a trained listener and an untrained listener would be able to determine the emotional content of a musical piece.

Moreover, this research shows that emotions not only manifest in motion but also that (for some of the performers) they manifest consistently and repeatedly in the same gestures such that a machine would be able to detect and classify them. Also, in the standard paradigm test it was noticed that because playing an instrument forces the performer to repeat the same motions somewhat accurately, it is a good tool to detect minor deviations in motion style that could be used to infer on the emotional and possibly physiological changes. Thus, tracking a performer playing an instrument could be used as a measurement tool for subtle physiological responses to emotional states. In addition to this, it could be used as a non-intrusive bio-feedback setting devised to help a subject regulate physiological and emotional states.

In a related topic but closer to music pedagogy, we have also seen that the successful communication of emotion is a challenge for performers. We have observed that by simply asking the performer to play in a certain emotion or report the emotion they are expressing we challenge them to not only play and feel but also control what is felt and be aware of it. This awareness is a primary key in successful communication, since if one is not aware of what one is transmitting, how is the information expected to be conveyed to the other? This is where our system can really come into play. Using a system such as this while performing or practicing, forces the performer to become aware of the emotion

and mood of the performance and thus adjust the performance accordingly via feedback. In this research, the system was only trained based on the emotions the performers were instructed to play in the first and second sections. However, using the results of the listening tests and performing more listening evaluations on the rest of the recorded data, the algorithm could be trained based on an average audience perception. This could then better represent the audience in a performance feedback scenario. Using this and training on the complete data set could create a system that is trained on many samples and is quite intelligible regarding the audience perception of emotion in a variety of performances.

Moreover, the displays designed in the evaluation of this research are novel ways at observing the phenomena of communication in performance. The idea of the *Confusion Cube* represents the interaction that exists between performer, listener, and model. This is complementary to the *Lens model* and *Lens equation* described in [Juslin, 2000] and [Juslin and Timmers, 2010]. However, in contrast to the lens model and the lens equation that numerically evaluate and describe the overall success rate of a performance, the confusion cube describes which emotion categories fail in communication and which succeed. It could also show where in the “optic” path of lens model the failure occurred, whether it was between the performer and the model, the performer and the listener, or the listener and the model, thus pointing to one of the three factors: G , R_e or R_s in the lens equation as described in the background section. Finally, it could show which emotion it was confused with and then possibly allow a correction. The

emotion paths add to this and describe the communication success through a temporal window during the performance. In this research, a window of 10–20 seconds proved to be a good time to observe deviations between performer, audience, and algorithm. During a window shorter than this, it was sometimes difficult to establish a meaningful observation and a longer window seemed to average out the local deviations that occurred during the performance.

The display of emotion paths is also interesting from a musicological perspective. If the algorithm is trained to accurately represent the audience in determining the emotional path, then one could obtain an average musical mood as well as the general musical path of a piece simply by playing it with the system. This again, comes down to the matter of awareness. A composer or songwriter might think that his piece conveys a certain emotion due to the lyrics or the emotion he is currently feeling. But the algorithm (and perhaps audience) might think otherwise and this feedback is important to any composer. Even the mere fact that during the entire piece the algorithm is stuck on one emotion could alert the composer that the piece is not evolving and might need some modifications.

Finally, from a music-engineering point of view, an obvious future research that should be carried out is, now that we know this information regarding our performance, how do we use this to augment the musical experience in real time? An immediate application could be displaying objects or videos on a screen in a performance, corresponding to the musical mood, similar to the background

coloring of the piano roll in our system. Another option could be continuously controlling and adjusting audio effects or synthesized sounds that correspond to detected expressions. Future research should address questions regarding the relationship between certain effects such as *reverb* or *vibrato* and emotions and the use of these correlations in live performance. This would render the system not only emotionally intelligent but also musically competent.

LIST OF REFERENCES

- [Analog Devices, 2008] Analog Devices, I. (2008). Accelerometer Design and Applications. Technical report, AD.
- [APDM, 2011] APDM, I. (2011). APDM SDK Developer Guide. Technical report, APDM Inc.
- [APDM, 2012a] APDM, I. (2012a). APDM Opal Sensor White Paper. Technical report, APDM Inc.
- [APDM, 2012b] APDM, I. (2012b). Host Libraries API Documentation. Technical report, APDM Inc.
- [Bach, 1778] Bach, C. (1778). *Essay on the true art of playing keyboard instruments*. New York, W. W. Norton.
- [Baddeley and Hitch, 1974] Baddeley, A. D. and Hitch, G. (1974). Working memory. *The psychology of learning and motivation*, 8:47–89.
- [Bard, 1928] Bard, P. (1928). A diencephalic mechanism for the expression of rage with special reference to the sympathetic nervous system. *American Journal of Physiology; American Journal of Physiology*.
- [Bayes and Price, 1763] Bayes, M. and Price, M. (1763). An essay towards solving a problem in the doctrine of chances. by the late rev. mr. bayes, frs communicated by mr. price, in a letter to john canton, amfrs. *Philosophical Transactions (1683-1775)*, pages 370–418.
- [Bresin, 2005] Bresin, R. (2005). What is the color of that music performance. In *Proceedings of the International Computer Music Conference*, pages 367–370.
- [Bresin and Battel, 2000] Bresin, R. and Battel, G. (2000). Articulation strategies in expressive piano performance analysis of legato, staccato, and repeated notes in performances of the andante movement of mozarts sonata in g major (k 545). *Journal of New Music Research*, 29(3):211–224.
- [Brunswik, 1956] Brunswik, E. (1956). *Perception and the representative design of psychological experiments*. Univ of California Press.
- [Camurri et al., 2007] Camurri, A., Coletta, P., Varni, G., and Ghisio, S. (2007). Developing multimodal interactive systems with EyesWeb XMI. *Proceedings of the 7th international conference on New interfaces for musical expression - NIME '07*, page 305.

- [Camurri et al., 2000] Camurri, A., Hashimoto, S., Ricchetti, M., Ricci, A., Suzuki, K., Trocca, R., and Volpe, G. (2000). Eyesweb: Toward gesture and affect recognition in interactive dance and music systems. *Computer Music Journal*, 24(1):57–69.
- [Camurri et al., 2004] Camurri, A., Mazzarino, B., and Volpe, G. (2004). Analysis of expressive gesture: The eyesweb expressive gesture processing library. In Camurri, A. and Volpe, G., editors, *Gesture-Based Communication in Human-Computer Interaction*, volume 2915 of *Lecture Notes in Computer Science*, pages 460–467. Springer Berlin Heidelberg.
- [Cannon, 1929] Cannon, W. B. (1929). Organization for physiological homeostasis. *Physiological Reviews*, 9(3):399–431.
- [Cohen, 1968] Cohen, J. (1968). Weighted kappa: Nominal scale agreement provision for scaled disagreement or partial credit. *Psychological bulletin*, 70(4):213.
- [Cohen et al., 1960] Cohen, J. et al. (1960). A coefficient of agreement for nominal scales. *Educational and psychological measurement*, 20(1):37–46.
- [Cook, 2001] Cook, P. (2001). Principles for designing computer music controllers. In *Proceedings of the 2001 conference on New interfaces for musical expression*, pages 1–4. National University of Singapore.
- [Cooke, 1959] Cooke, D. (1959). *The language of music*. Oxford University Press London.
- [Darwin, 1874] Darwin, C. (1874). *The expression of the emotions in man and animals*. Oxford University Press, USA.
- [Davies, 1994] Davies, S. (1994). *Musical meaning and expression*. Cornell University Press.
- [Davies, 2010] Davies, S. (2010). Emotions expressed and aroused by music. In Juslin, P. N. and Sloboda, J. A., editors, *In Music and Emotion: Theory and Research.*, pages 454–489. New York: Oxford University Press.
- [Descartes, 1649] Descartes, R. (1649). *The passions of the soul*. Hackett Publishing Company Incorporated.
- [Dillon et al., 2006] Dillon, R., Wong, G., and Ang, R. (2006). Virtual orchestra: An immersive computer game for fun and education. In *Proceedings of the 2006 international conference on Game research and development*, pages 215–218. Murdoch University.

- [Duda et al., 1995a] Duda, R., Hart, P., and Stork, D. (1995a). *Pattern Classification and Scene Analysis 2nd ed.*, chapter Bayesian Decision Theory, pages 20–84.
- [Duda et al., 1995b] Duda, R., Hart, P., and Stork, D. (1995b). *Pattern Classification and Scene Analysis 2nd ed.*, chapter Maximum-Likelihood and Bayesian Parameter Estimation, pages 128–138.
- [Einstein et al., 1920] Einstein, A., Lawson, R., Geroch, R., and Cassidy, D. (1920). *Relativity: The special and general theory*. Pi Pr.
- [Erdmann and Janke, 1978] Erdmann, G. and Janke, W. (1978). Interaction between physiological and cognitive determinants of emotions: Experimental studies on schachter’s theory of emotions. *Biological Psychology*, 6(1):61–74.
- [Feynman et al., 1963] Feynman, R., Leighton, R., and Sands, M. (1963). *The Feynman Lectures on Physics, Vol. I: Mainly Mechanics, Radiation, and Heat*, volume 1, chapter 19, pages 245–246. Narosa.
- [Fiebrink, 2011] Fiebrink, R. (2011). *Real-time Human Interaction with Supervised Learning Algorithms for Music Composition and Performance*. PhD thesis, Princeton University, Princeton, NJ, USA.
- [Fletcher and Rossing, 1998] Fletcher, N. and Rossing, T. (1998). *The physics of musical instruments*, chapter The Piano. Springer Verlag.
- [Friberg, 2004] Friberg, A. (2004). A fuzzy analyzer of emotional expression in music performance and body motion. *Proceedings of Music and Music Science*, i:1–13.
- [Friberg et al., 2006] Friberg, A., Bresin, R., and Sundberg, J. (2006). Overview of the KTH rule system for musical performance. *Advances in Cognitive Psychology*, 2(2):145–161.
- [Gabrielsson, 1985] Gabrielsson, A. (1985). Interplay between analysis and synthesis in studies of music performance and music experience. *Music Perception*, pages 59–86.
- [Gabrielsson and Lindström, 2010] Gabrielsson, A. and Lindström, E. (2010). The influence of musical structure on emotional expression. In Juslin, P. N. and Sloboda, J. A., editors, *In Music and Emotion: Theory and Research.*, pages 367–400. New York: Oxford University Press.
- [Gilden, 2001] Gilden, D. (2001). Cognitive emissions of 1/f noise. *Psychological review*, 108(1):33.

- [Gillian et al., 2011a] Gillian, N., Knapp, R., and O’Modhrain, S. (2011a). A machine learning toolbox for musician computer interaction. In *Proceedings of the 2011 International Conference on New Interfaces for Musical Expression (NIME11)*.
- [Gillian et al., 2011b] Gillian, N., Knapp, R. B., and OModhrain, S. (2011b). An adaptive classification algorithm for semiotic musical gestures. In *the 8th Sound and Music Computing Conference*.
- [Hadjakos et al., 2008] Hadjakos, A., Aitenbichler, E., and Mühlhäuser, M. (2008). Potential use of inertial measurement sensors for piano teaching systems: Motion analysis of piano playing patterns. In *Proceedings of the 4th i-Maestro Workshop on Technology-Enhanced Music Education*, pages 61–68.
- [Helmholtz, 1863] Helmholtz, H. (1863). *On the sensations of tone*. Dover Publications.
- [Hevner, 1935] Hevner, K. (1935). The affective character of the major and minor modes in music. *The American Journal of Psychology*, 47(1):pp. 103–118.
- [Hevner, 1936] Hevner, K. (1936). Experimental studies of the elements of expression in music. *American Journal of Psychology.*, 48(2):246–268.
- [Höfer et al., 2009] Höfer, A., Hadjakos, A., and Mühlhäuser, M. (2009). Gyroscope-based conducting gesture recognition. *NIME09*.
- [Hursch et al., 1964] Hursch, C., Hammond, K., and Hursch, J. (1964). Some methodological considerations in multiple-cue probability studies. *Psychological Review*, 71(1):42.
- [Jackendoff and Lerdahl, 1983] Jackendoff, R. and Lerdahl, F. (1983). *A generative theory of tonal music*. Cambridge, Mass.: MIT Press.
- [James, 1884] James, W. (1884). What is an emotion? *Mind*, (34):188.
- [Juslin, 1997] Juslin, P. (1997). Emotional communication in music performance: A functionalist perspective and some data. *Music perception*, pages 383–418.
- [Juslin, 2000] Juslin, P. (2000). Cue utilization in communication of emotion in music performance: Relating performance to perception. *Journal of Experimental Psychology: Human perception and performance*, 26(6):1797.
- [Juslin and Madison, 1999] Juslin, P. and Madison, G. (1999). The role of timing patterns in recognition of emotional expression from musical performance. *Music Perception*, pages 197–221.
- [Juslin and Scherer, 2005] Juslin, P. and Scherer, K. (2005). The new handbook of methods in nonverbal behavior research. chapter Vocal expression of affect. Oxford University Press, Oxford, UK.

- [Juslin and Timmers, 2010] Juslin, P. and Timmers, R. (2010). Expression and communication of emotion in music performance. In Juslin, P. N. and Sloboda, J. A., editors, *In Music and Emotion: Theory and Research.*, pages 454–489. New York: Oxford University Press.
- [Juslin, 2003] Juslin, P. N. (2003). Five Facets of Musical Expression: A Psychologist’s Perspective on Music Performance. *Psychology of Music*, 31(3):273–302.
- [Kierkegaard, 1843] Kierkegaard, S. (1843). *Either/or: A fragment of life.* ePenguin.
- [Kivy, 1980] Kivy, P. (1980). *The corded shell: Reflections on musical expression.* Princeton University Press Princeton.
- [Kivy, 1989] Kivy, P. (1989). *Sound sentiment.* Temple University Press.
- [Landis and Koch, 1977] Landis, J. R. and Koch, G. G. (1977). The measurement of observer agreement for categorical data. *biometrics*, pages 159–174.
- [Lange, 1885] Lange, C. G. (1885). The mechanism of the emotions. *The Classical Psychologists.* Boston: Houghton Mifflin, 1912.
- [Levitin and Cook, 1996] Levitin, D. J. and Cook, P. R. (1996). Memory for musical tempo: Additional evidence that auditory memory is absolute. *Attention, Perception, & Psychophysics*, 58(6):927–935.
- [Marshall and Zimbardo, 1979] Marshall, G. D. and Zimbardo, P. G. (1979). Affective consequences of inadequately explained physiological arousal.
- [MATLAB, 2010] MATLAB (2010). *version 7.10.0 (R2010a).* The MathWorks Inc., Natick, Massachusetts.
- [Meyer, 1956] Meyer, L. (1956). *Emotion and meaning in music.* University of Chicago Press.
- [Miller, 1956] Miller, G. (1956). The magical number seven, plus or minus two: some limits on our capacity for processing information. *Psychological review*, 63(2):81.
- [Müller, 2007] Müller, M. (2007). *Information retrieval for music and motion*, volume 6, chapter Fundamentals on Motion Capture Data. Springer Berlin.
- [Narmour, 1992] Narmour, E. (1992). *The analysis and cognition of melodic complexity: The implication-realization model.* University of Chicago Press.
- [Nussbaum, 2007] Nussbaum, C. O. (2007). *The musical representation: meaning, ontology, and emotion.* Mit Press.

- [Odowichuk et al., 2011] Odowichuk, G., Trail, S., Driessen, P., Nie, W., and Page, W. (2011). Sensor fusion: Towards a fully expressive 3d music control interface. In *Communications, Computers and Signal Processing (PacRim), 2011 IEEE Pacific Rim Conference on*, pages 836–841. IEEE.
- [Parncutt, 2006] Parncutt, R. (2006). The child as musician. chapter Prenatal Development. Oxford University Press.
- [Powers, 2007] Powers, D. M. (2007). Evaluation: From precision, recall and f-factor to roc, informedness, markedness & correlation. *School of Informatics and Engineering, Flinders University, Adelaide, Australia, Tech. Rep. SIE-07-001*.
- [Raffman, 1991] Raffman, D. (1991). The meaning of music. *Midwest Studies in Philosophy*, 16(1):360–377.
- [Read, 1979a] Read, G. (1979a). *Music notation: A manual of modern practice*, chapter Brief History of Music Notation. Taplinger Publishing Company.
- [Read, 1979b] Read, G. (1979b). *Music notation: A manual of modern practice*, chapter Dynamic Markings. Taplinger Publishing Company.
- [Read, 1979c] Read, G. (1979c). *Music notation: A manual of modern practice*, chapter Accents and Slurs. Taplinger Publishing Company.
- [Repp, 1994] Repp, B. (1994). On determining the basic tempo of an expressive music performance. *Psychology of Music*, 22:157–157.
- [Ringer, 2009] Ringer, M. (2009). *Schubert's theater of song*. Amadeus Pr.
- [Russell, 2003] Russell, J. A. (2003). A circumplex model of affect. *Journal of Personality and Social Psychology.*, 39(6):1161–1178.
- [Schachter and Singer, 1962] Schachter, S. and Singer, J. (1962). Cognitive, social, and physiological determinants of emotional state. *Psychological Review; Psychological Review*, 69(5):379.
- [Scheirer, 1998] Scheirer, E. (1998). Tempo and beat analysis of acoustic musical signals. *The Journal of the Acoustical Society of America*, 103:588.
- [Schubert, 2003] Schubert, E. (2003). Update of the Hevner adjective checklist. *Perceptual and motor skills*, 96(3 Pt 2):1117–22.
- [Seashore, 1938] Seashore, C. (1938). *Psychology of music*. Dover Publications.
- [Seashore and Metfessel, 1925] Seashore, C. E. and Metfessel, M. (1925). Deviation from the regular as an art principle. *Proceedings of the National Academy of Sciences of the United States of America*, 11(9):538.

- [Shove and Repp, 1995] Shove, P. and Repp, B. (1995). Musical motion and performance: Theoretical and empirical perspectives. *The practice of performance*, pages 55–83.
- [Solid State Technology, 2010] Solid State Technology, I. (2010). Introduction to MEMS gyroscopes. Technical report, Solid State Technology.
- [Spencer, 1875] Spencer, H. (1875). The origin and function of music.
- [Timmers, 2007] Timmers, R. (2007). Vocal expression in recorded performances of schubert songs. *Musicae Scientiae*, 11(2):237–268.
- [Todd, 1985] Todd, N. (1985). A model of expressive timing in tonal music. *Music Perception*, pages 33–57.
- [Todd, 1992] Todd, N. (1992). The dynamics of dynamics: A model of musical expression. *The Journal of the Acoustical Society of America*, 91:3540.
- [Toyoda, 2007] Toyoda, S. (2007). Sensillum: an improvisational approach to composition. In *NIME*, volume 7, pages 254–255. Citeseer.
- [Varni et al., 2010] Varni, G., Mancini, M., Volpe, G., and Camurri, A. (2010). A System for Mobile Active Music Listening Based on Social Interaction and Embodiment. *Mobile Networks and Applications*, 16(3):375–384.
- [Walton, 1988] Walton, K. L. (1988). What is abstract about the art of music? *Journal of Aesthetics and Art Criticism*, pages 351–364.
- [Widmer and Goebel, 2004] Widmer, G. and Goebel, W. (2004). Computational models of expressive music performance: The state of the art. *Journal of New Music Research*, 33(3):203–216.

Influence of Input Parameters on Dynamic Orbital Stability of Walking: In-Silico and Experimental Evaluation

Federico Riva^{1*}, Maria Cristina Bisi¹, Rita Stagni^{1,2}

1 Department of Electrical, Electronic, and Information Engineering 'Guglielmo Marconi', University of Bologna, Bologna, Italy, **2** Health Sciences and Technologies – Interdepartmental Center for Industrial Research (HST-ICIR), University of Bologna, Bologna, Italy

Abstract

Many measures aiming to assess the stability of human motion have been proposed in the literature, but still there is no commonly accepted way to define or quantify locomotor stability. Among these measures, orbital stability analysis via Floquet multipliers is still under debate. Some of the controversies concerning the use of this technique could lie in the absence of a standard implementation. The aim of this study was to analyse the influence of i) experimental measurement noise, ii) variables selected for the construction of the state space, and iii) number of analysed cycles on the outputs of orbital stability applied to walking. The analysis was performed on a 2-dimensional 5-link walking model and on a sample of 10 subjects performing long over-ground walks. Noise resulting from stereophotogrammetric and accelerometric measurement systems was simulated in the in-silico analysis. Maximum Floquet multipliers resulted to be affected by both number of analysed strides and state space composition. The effect of experimental noise was found to be slightly more potentially critical when analysing stereophotogrammetric data than when dealing with acceleration data. Experimental and model results were comparable in terms of overall trend, but a difference was found in the influence of the number of analysed cycles.

Citation: Riva F, Bisi MC, Stagni R (2013) Influence of Input Parameters on Dynamic Orbital Stability of Walking: In-Silico and Experimental Evaluation. PLoS ONE 8(11): e80878. doi:10.1371/journal.pone.0080878

Editor: Pedro Antonio Valdes-Sosa, Cuban Neuroscience Center, Cuba

Received: May 24, 2013; **Accepted:** October 7, 2013; **Published:** November 15, 2013

Copyright: © 2013 Riva et al. This is an open-access article distributed under the terms of the Creative Commons Attribution License, which permits unrestricted use, distribution, and reproduction in any medium, provided the original author and source are credited.

Funding: This research was funded by the project "Fall risk estimation and prevention in the elderly using a quantitative multifactorial approach" (project ID number 2010R277FT) managed by Italian Ministry of Education, University and Research (Ministero dell'Istruzione, dell'Università e della Ricerca). The funders had no role in study design, data collection and analysis, decision to publish, or preparation of the manuscript.

Competing interests: The authors have declared that no competing interests exist.

* E-mail: f.riva@unibo.it

Introduction

Stability, in terms of capability to walk without falling or stumbling, is a crucial feature of gait [1,2]. Loss of dynamic stability while walking can lead to falls, which represent a major problem for community and public health, with large clinical and economic consequences [3,4]. Moreover, the majority of fall-related injuries in older adults occur during walking [5–7]. The possibility to detect a loss of stability, offline or in real-time, would represent an improvement in the understanding of the mechanisms related to falls. The capability to quantify decreased dynamic stability could lead to the development of devices alerting the subject (or the clinician) of potentially critical situations in order to prevent the fall, particularly in the case of long walks. Moreover, subjects with low gait stability could be selected for fall prevention programs.

Several stability indices have been proposed in the literature for clinical application [2,7–10], among them, measures coming

from nonlinear analysis of dynamical systems are particularly interesting.

Many human tasks are structurally cyclic, and show a periodic-like behaviour. A motor task can be treated as a nonlinear dynamic system: biomechanical variables (e.g. joint angles, accelerations) vary during the temporal evolution of the task, defining a system whose kinematics continuously changes over time according to a controlled pattern. Techniques for nonlinear stability analysis basically consist in the quantification of the tendency of an orbit (defined by the temporal evolution of a set of variables called *state space*) to diverge from (or converge to) the previous orbit or a repelling/attracting limit cycle.

Two main approaches for nonlinear stability analysis in biomechanics are proposed in the literature: local and orbital stability analysis. These nonlinear measures of dynamic stability quantify different properties of system dynamics [11].

In particular, orbital stability analysis can be applied to periodic systems with a limit cycle behaviour; it has been

extensively used in the study of passive dynamic walking robots [12] and, in recent years, it has been applied to biomechanics also [2,11,13–16]. Fundamental indicators of orbital stability are Floquet multipliers (FM). FM quantify, discretely from one cycle to the next, the tendency of the system's states to return to the periodic limit cycle orbit. If FM have magnitude < 1 , perturbations tend to shrink by the following repetition, and the system remains stable [11]. Smaller FM's imply higher stability [17].

Despite the lack of evidence of a direct correlation between maxFM and fall risk [10], still FM were found to be higher in fall-prone older adults than in healthy subjects [1], and capable to detect perturbations during walking [18]. For this reason, FM could be used in the detection of real time short-term potentially critical variations in stability.

Deriving from the nonlinear analysis of dynamic systems, orbital stability analysis finds its main application in robotics. When assessing the stability of a robot (e.g. a walker), the equations of motion and the nature of the controllers are known, allowing an adequate selection of the variables that properly characterize the system and the implementation of the analysis in an analytical or semi-analytical way [19]. However, when dealing with human biomechanical time series, equations of motion and control laws are unknown. FM must hence be calculated numerically, and with no a-priori knowledge on the more appropriate variables that define the system. This lack of knowledge makes the implementation not straightforward.

Beyond the mathematical implications, it is however important to highlight that applying this analysis to human gait implies several assumptions: i) human gait is an inherently stochastic system, while Floquet theory applies to deterministic limit cycle systems; ii) walking trajectories are continuously "re-perturbed" by stochastic perturbations that are often internal to the system. Since one of the main assumptions behind the application of this technique is the existence of a limit cycle trajectory, a reference trajectory for human stable walking has to be chosen. To cope with this situation, the average trajectory during the motor task is assumed as limit cycle, although the likely asymmetrical nature of the basin of attraction of human walking.

Orbital stability analysis preliminarily resulted to detect gait instability [1,18], suggesting its effectiveness despite the many theoretical assumptions, but reference values for orbital stability of stable human walking are not known and, in the literature, incoherent results are reported [20]. This incoherence is likely to result from the absence of a standard implementation of the technique. In particular, the influence to experimental input noise, state space construction, and analysed cycles has not been characterized yet. No unique way of defining the state space of a given motor task was defined in the literature: which and how many variables should be included in the state space and how this choice affects the results of the numerical calculation of orbital stability analysis have not been analysed yet. A similar problem was examined in the literature [21]: the performance of local dynamic stability was analysed when applied to a Lorentz attractor and an experimental sewing task, but this did not allow to draw clear conclusions about locomotion. Another relevant issue is the

minimum and optimum number of task cycles to be analysed in order to obtain reliable orbital stability results: this issue was addressed before [22], but only for experimental treadmill walking. Moreover, it is not clear yet how the experimental noise can affect FM calculation.

In this scenario, the analysis of physiological signals of gait (e.g. accelerations, joint angles) from a walking stable model can allow the assessment of the influence of i) experimental noise, ii) state space variables and iii) number of analysed cycles on FM values.

In order to obtain indications applicable in experimental conditions, model data must be comparable with experimental data. Signals extracted from a stable walking model are hence required.

Some authors performed simulation studies on orbital stability of 1 or 2-link walking models related to fall risk [19,23,24]. However, these are simplified models and simulate very peculiar walking conditions. Simplicity is both the strength and the limitation of these models: their walking conditions can be easily manipulated, but they generate signals that significantly differ from physiologic human gait. Stability analysis on a more complex model can better describe human walking, allowing the comparison between model and experimental results. In order for the model to produce kinematics as similar as possible to stable human gait, the required conditions for the model are a continuous walk and the absence of falls or stumbles, regardless of control laws and implementation details.

The aim of the present study was to analyse, from an applicative point of view, the influence on the final results of orbital stability analysis applied to walking of i) experimental measurement noise, ii) selection of the variables for the reconstruction of the state space iii) number of analysed cycles on a 2-dimensional 5-link walking model [25], providing walking patterns of known stability. Results of in-silico analysis were compared to those obtained experimentally on 10 subjects performing long overground walks.

Methods

Overview

In-silico orbital stability analysis of a 5-link stable walking model [25] was performed. The model showed continuous walking, free of falls or stumbles, for all the simulation period (300 strides). This was also assured by a check on step variability, which was minimal following visual inspection of the phase portraits. In order to properly calculate orbital stability, model was slightly perturbed. The analysis was performed for increasing number of cycles (from 10 to 300), based on differently composed state spaces (including different joint angles and/or accelerations). Semi-analytical value of the maxFM of the model was also calculated for reference. Simulated experimental error and noise were added to the segmental kinematics of the model and the sensitivity of orbital stability analysis was evaluated. Orbital stability analysis was also performed on data collected experimentally on 10 subjects; given the impossibility to use a stereophotogrammetry system on a long outdoor road, only



Figure 1. Schematic representation of the 5-link 2-dimensional model (Solomon et al., 2010).

doi: 10.1371/journal.pone.0080878.g001

acceleration data were acquired experimentally. Orbital stability was calculated using an established technique [13].

In-silico data

The 2-dimensional, 5-link biped walking model analysed [25] consisted of a trunk, two thigh and two shank segments (Figure 1). The model orientation was described by stance and swing knee angles, stance and swing hip angles and upper body angle ($\varphi_{k,sw}$, $\varphi_{k,st}$, $\varphi_{h,st}$, $\varphi_{h,sw}$, φ_{ub} , all referred to gravity direction). The dynamics of the model consisted of a continuous swing phase during which the swing leg smoothly swung past the stance leg, and an instantaneous, fully inelastic heel strike when the swing foot touched the floor. The swing leg knee contained a hyper-extension stop and a latch that was activated upon full extension to hold the leg straight. There were a total of four control torques on the model, at the stance/swing knee and at the stance/swing hip. All control torques were implemented with fixed gain proportional-derivative (PD) controllers (with $k_p = 100$ Nm and $k_d = 10$ Nms).

Small random perturbations were added to the state variables at each heel strike event as uniformly distributed random numbers having maximum amplitude $\pm 10^{-4}$. This maximum amplitude was chosen based on the maximum perturbation that the model could tolerate without falling.

The model was adapted to perform 315 consecutive strides. The first 15 strides of the simulation were discarded in order to assure stable walking condition. The simulation was performed using a MATLAB's (Mathworks, Natwick, NA) fourth- and fifth-order variable time-step Runge-Kutta solver (ode45, with relative error tolerance set to 10^{-12}). Joint angles were expressed using Grood and Suntay approach [26]. Accelerations of the trunk segment at the level of the fifth lumbar vertebra (L5) were obtained by the second derivative of the position of a point located at 1/8 of the trunk segment.

Segmental kinematics data obtained from the model were used to reconstruct experimental data from a stereophotogrammetric system (joint angles) and a single inertial sensor located on the trunk (accelerations). Simulated experimental noise and errors were superimposed to segmental kinematics signals obtained from the model.

Clusters of 4 markers were virtually applied to all the segments of the model (trunk, thighs and shanks, for a total of 20 markers) and simulated instrumental normally distributed noise with a standard deviation of 0.2 mm was added to the marker position in 2-d space. Technical reference frames were calculated from the cluster positions, and the position of the segment extremities relative to these frames was estimated. A mis-localization error of anatomical landmark positions (Table 1) was also added to the estimate of the position of segment extremities [27]. Joint angles were then calculated from the relative orientation of the anatomical reference frames [28].

Table 1. Precision of the palpable anatomical landmark position (in millimeters) in the relevant mean anatomical frame obtained by Della Croce et al., 1999.

Anatomical landmark	x	y
Greater trochanter (GT)	12.2	11.1
Medial Epicondyle (ME)	5.1	5.0
Lateral Epicondyle (LE)	3.9	4.9
Medial Malleolus (MM)	2.2	2.6
Lateral Malleolus (LM)	2.6	2.4

For ME, LE and MM, LM the mean value between the two was used in the analysis.

doi: 10.1371/journal.pone.0080878.t001

Instrumentation noise (white noise with an SNR of 10 dB and alignment errors with a normal distribution and a standard deviation of 0.1 degrees), compatible with use of commercial accelerometers, was added to acceleration signals of the trunk segment at the level of L5. Smaller magnitudes of noise were also analysed that led to comparable results, therefore, only the most potentially critical conditions were reported.

Experimental data

10 healthy participants [age 28 ± 3 years, height 174 ± 11 cm, weight 67 ± 13 kg] were included in the study. Two synchronized tri-axial inertial sensors (Opal, APDM, Portland, OR, USA) were placed on the participants at the level of L5 and of the right shank, for measuring angular velocity of the lower leg. Accelerations and angular velocities were recorded. The range of the accelerometers was $\pm 2G$ and sampling rate was 128 samples/second. The participants were instructed to walk straight at self-selected speed on a 250 m dead-end long road.

Ethics Statement

The Bioethical Committee of the University of Bologna approved this study (July 7, 2012). Written informed consent was obtained from the participants.

Data processing

Orbital stability analysis was implemented according to methodology described in the literature [13,23,24,29].

Seven state spaces (six for model-data and one for experimental data) were analysed (Table 2), based on the literature about orbital stability of human gait [11,15,16]. Two approaches were used. Five state spaces were constructed directly including time series into the state space. These state spaces (Table 2) included model knee flexion-extension joint angles (WMk), model hip flexion-extension joint angles (WMh), model knee+hip+trunk flexion-extension joint angles (WMhkt)

and experimental accelerations in the V and AP directions (EXPa). Two state spaces were constructed using delay embedding [30,31] of model AP (WMAp) and V (WMAv) trunk acceleration signals. An embedding dimension of $d_E = 5$ was chosen, as several published studies supported this delay dimensions appropriate for gait data [22,31,32]. A fixed time delay $\tau = 10$ was chosen [22,32].

For both model and experimental data, a stride cycle was considered as the interval between two consecutive right heel strikes. For experimental data, right heel strike instants were estimated from the angular velocity of the lower limb with a method based on wavelet analysis [33]. Strides were resampled to 101 samples, because Floquet theory requires a strictly periodic system. Experimental data were analysed without filtering, to prevent complications resulting from linear filtering of nonlinear signals [34]. A Poincaré section was defined at each percentage of the gait cycle (0% = right heel strike).

The Poincaré map:

$$S_{k+1}FS_k \tag{1}$$

defines the evolution of the state S_k to the state S_{k+1} at each Poincaré section, for each stride k .

The limit cycle trajectory was defined as the average trajectory across all strides, defining a fixed point in each Poincaré section:

$$S^*FS^* \tag{2}$$

A linear approximation of equation (1):

$$S_{k+1}S^* \approx JS^*S_kS^* \tag{3}$$

allows to calculate how system states diverge from or converge to fixed points. The FM are the eigenvalues of the Jacobian matrix $J(S^*)$. The maximum FM (maxFM) is believed to govern the dynamics of the system, and hence to be the most representative in terms of instability. If the maxFM have magnitude < 1 , the system is stable, otherwise, the system tends to diverge from the limit cycle and is unstable. maxFM were calculated for each Poincaré section (0 – 100% of the gait cycle), and the overall mean value of maxFM across the gait cycle was calculated and used in this analysis.

Orbital stability analysis on model-data was performed on the seven different state spaces (Table 2). Both noise-free and noisy conditions were analysed, as well as experimental data. Mean values of maxFM along the gait cycle were calculated for increasing number of strides (from 10 to 300 for model-data, from 10 to 160 for experimental data).

In order to perform a sanity check of the results obtained from numerical calculation of maxFM on model time series, semi-analytical calculation of the FM was performed. The full 10-dimensional state space (composed of angular velocities and accelerations) was considered for this analysis. Instead of estimating S^* , the stable period one solution was taken. Ten strides were then simulated (being the state space 10-dimensional), each one with a small perturbation of one of the state variables at the heel strike instant. States at heel strike after the perturbation were then put in matrix form; S^* was then subtracted from said matrix, obtaining the right hand side of Eq.

Table 2. Description of the state spaces.

Acronym	Description	Composition
WMk	Swing+stance knee flexion/extension joint angles (model)	$WMk(t) = [\phi_{k,st}(t), \phi_{k,sw}(t)] \in \mathbb{R}^2$
WMh	Swing+stance hip flexion/extension joint angles (model)	$WMh(t) = [\phi_{h,st}(t), \phi_{h,sw}(t)] \in \mathbb{R}^2$
WMhkt	Knees, hips and trunk flexion/extension joint angles (model)	$WMhkt(t) = [\phi_{k,st}(t), \phi_{k,sw}(t), \phi_{h,st}(t), \phi_{h,sw}(t), \phi_t(t)] \in \mathbb{R}^5$
WMAp	5-dimensional delay embedding of AP accelerations of L5 (model)	$WMAp(t) = [a_{AP}(t), a_{AP}(t + \tau), \dots, a_{AP}(t + (d_E - 1)\tau)] \in \mathbb{R}^5$
WMAv	5-dimensional delay embedding of V accelerations of L5 (model)	$WMAv(t) = [a_V(t), a_V(t + \tau), \dots, a_V(t + (d_E - 1)\tau)] \in \mathbb{R}^5$
WMA	Accelerations in the AP and V direction of L5 (model)	$WMA(t) = [a_{AP}(t), a_V(t)] \in \mathbb{R}^2$
EXPa	Accelerations in the AP and V direction of L5 (experimental)	$EXPa(t) = [a_{AP}(t), a_V(t)] \in \mathbb{R}^2$

$\phi_{k,st}$ and $\phi_{k,sw}$ are flexion/extension knee angles for stance and swing limb; similarly, $\phi_{h,st}$ and $\phi_{h,sw}$ are flexion/extension hip angles. ϕ_t is flexion/extension trunk angle. a_{AP} and a_V are accelerations of the trunk at the level of L5 in anterior-posterior and vertical directions. For delay-embedded state spaces, τ is time delay and d_E is the embedding dimension ($\tau = 10$, $d_E = 5$).

doi: 10.1371/journal.pone.0080878.t002

3. This matrix was then divided by the magnitude of the initial perturbation in order to obtain J matrix [19,35].

Results

Semi-analytical calculation of the FM of the model led to a value of $\max FM_{sa} = 0.23$.

Experimental noise had a slight but non-negligible influence on maxFM for state spaces composed by joint angles (WMhkt, WMk and WMh). Analysis on these state spaces in noise-free conditions led to mean values of maxFM along the gait cycle that decay with the increase of the analysed stride cycles, until reaching the values 0.27, 0.15 and 0.22 respectively. For all state spaces about 130 strides were needed to reach steady values. Standard deviation slightly decreased with the increase of the number of stride cycles (Figure 2). State spaces composed by noise-affected signals showed a similar overall trend, but seemed to reach slightly different steady values, especially for WMhkt state space (Figure 3).

MaxFM calculated on noise-free acceleration state spaces, both 2- and 5-dimensional (WMA, WMAp and WMAv), behaved similarly: values of maxFM gradually decreased, starting from values between 0.5 and 0.9, until stabilizing around values a little lower to the ones previously found for non noise affected joint angle state spaces (0.13 - 0.19) with a standard deviation of about 0.04 (Figure 4). About 130 strides were needed in order to reach steady values. Results coming from analysis of noisy accelerations signals were practically identical to those obtained from noise-free signals for overall trend, number of required strides and numerical values (Figure 5).

MaxFM calculated on experimental acceleration state space (EXPa) showed decreasing value for increasing number of



Figure 2. maxFM obtained for model state spaces WMhkt, WMk and WMh (clean signals) for increasing number of stride cycles. Error bars represent standard deviation calculated over the stride cycle. The dotted line (SA) represents the semi-analytical value of the maxFM.

doi: 10.1371/journal.pone.0080878.g002



Figure 3. maxFM obtained for model state spaces WMhkt, WMk and WMh (noisy signals) for increasing number of stride cycles. Error bars represent standard deviation calculated over the stride cycle. The dotted line (SA) represents the semi-analytical value of the maxFM.

doi: 10.1371/journal.pone.0080878.g003



Figure 4. maxFM obtained for model state spaces WMa, WmaAP and WMaV (clean signals) for increasing number of stride cycles. Error bars represent standard deviation calculated over the stride cycle. The dotted line (SA) represents the semi-analytical value of the maxFM.

doi: 10.1371/journal.pone.0080878.g004



Figure 5. maxFM obtained for model state spaces WMa, WmaAP and WMaV (noisy signals) for increasing number of stride cycles. Error bars represent standard deviation calculated over the stride cycle. The dotted line (SA) represents the semi-analytical value of the maxFM.

doi: 10.1371/journal.pone.0080878.g005



Figure 6. maxFM obtained for experimental state space EXPa for increasing number of stride cycles. Error bars represent standard deviation calculated over the stride cycle.

doi: 10.1371/journal.pone.0080878.g006

cycles analysed, reaching values close to 0.4 from 80 cycles on, with a standard deviation of about 0.1 (Figure 6).

Discussion

The possibility to have a reliable locomotor stability index is of fundamental importance in early identification and treatment of older adults with high predisposition to fall, and possibly in real-time gait instability detection also. However, still there is no unique definition of locomotor stability in the literature. Orbital stability analysis via maxFM seems promising for the analysis of cyclic locomotor tasks. However, when dealing with biomechanical time series, the equations of motion are unknown, excluding the possibility to calculate maxFM in an analytical or semi-analytical way. Numerical calculation of maxFM from experimental time series is hence required, but it

is not clear yet how different implementations of this analysis can influence the stability estimations.

In this explorative study, orbital stability analysis was applied to a 5-link stable walking model. The walking model was used in order to produce signals (joint angles and trunk accelerations) as similar as possible to real human gait signals. Stability was assumed, since the model didn't show any fall or stumble during the simulation period. Different implementations of numerical orbital stability analysis were then performed on the biomechanical signals obtained from the model. As a reference, semi-analytical calculation of FM of the model was performed. The aim was to better understand the influence of number of analysed cycles, state space composition and experimental noise on the stability outputs.

The magnitude of maxFM obtained in this study was lower than values obtained in previously published simulation studies

[19,23,24]. Whereas those studies analysed the behavior of 1- or 2-link walking models, in our study walking of a 5-link model was analysed. A possible explanation is that the higher model complexity allows for a higher number of state variables to compensate for perturbations, thus leading to higher stability. However, as also explicitly stated by Roos and Dingwell [24], the main aim of the previous published works was to show the general relationship between fall risk and stability measures, and not to give exact numerical values.

According to the results of the present study, the number of cycles analysed plays a fundamental role. From a theoretical point of view, the number of analysed cycles cannot be smaller than the dimension of the state space otherwise the set of equations would be underdetermined. Once the dimension of the state space is reached, the analysis of more gait cycles leads to a better estimate of the true attractor [22] in presence of physiological gait variability and experimental noise.

Orbital stability analysis performed on noise-free signals from the stable walking model resulted in maxFM values close to the reference value of $\text{maxFM}_{\text{sa}} = 0.23$, as provided by the semi-analytical calculation of maxFM, for both state spaces composed by joint angles and L5 accelerations. The coherence between these results is encouraging, as it seems to indicate that a repeatable value of the maxFM can be obtained analysing different state spaces. Another similarity among these results was the dependence on the number of analysed cycles, since for all state spaces composed by non noise-affected signals steady results were obtained from about 130 strides on.

For a few number of cycles, maxFM values resulted to be high and inconsistent, hence probably unreliable. Moreover, for shorter time series (15 strides), analysis conducted upon stereophotogrammetric data led to a lower overestimation of the maxFM with respect to the analysis conducted upon acceleration data.

Whereas the analysis performed on 5-dimensional state space WMhkt led to value very close to the semi-analytical value, 2-dimensional state spaces performed comparably, and sometimes slightly better (as it is the case for WMh state space, composed by hip joint angles time series). Whereas a 2-dimensional representation of a complex system may seem insufficient to provide a proper characterization, compared to a 5-dimensional state space, it may serve the applicative purpose of obtaining a repeatable index of stability with a simpler representation of the system dynamics. The relationship with the stability index obtained with this implementation and the actual fall risk remains, however, still undetermined.

Results from the analysis of noisy signals led to slightly different results between acceleration and stereophotogrammetric data. Analysis of noisy accelerations of L5 led basically to the same results obtained for noise-free signals, for all the state spaces: simulated experimental noise on inertial sensor data did not influence maxFM calculation. This can lead to the conclusion that orbital stability analysis performed on state spaces composed by accelerations coming from inertial sensors is robust to noise, and that again a high dimensional (5) reconstruction of the state space may not be

necessary, as a lower dimension (2) state space led basically to the same results. Analysis of joint angles showed an influence of experimental noise and mis-localization error, leading to lower steady values for the maxFM, with the exception of WMh which remained practically unvaried (and very close to the reference value of $\text{maxFM}_{\text{sa}} = 0.23$).

These results are in agreement with Bruijn et al. [16], who found a correlation of 0.66 between maxFM obtained from two measurement systems (accelerometers and optoelectronics).

Experimental trial results on the accelerations-based state space showed a similar trend with respect to the ones obtained from the analysis of the same variables derived from the model; nevertheless, the value of maxFM obtained was slightly higher, and so the standard deviation. A limitation of this experimental session was the relatively short length of the walks (160 strides) with respect to the model-data; given the high handiness and portability of inertial sensor, however, future studies can analyse orbital stability of very long overground walks. On the other hand, 160 strides seem to be sufficient to reach a steady value for the maxFM.

Based on these results, a reliable implementation of orbital stability analysis could be obtained from an acceleration-based state space (reconstructed with delay-embedding or including in the state space accelerations in different directions) and a number of stride cycles not lower than 130.

In conclusion, the exploration of the influence of experimental input parameters in orbital stability analysis led to interesting results. One of the main issues relative to this technique is the necessity to properly describe the dynamical system, in order to obtain a reliable orbital stability index; hence, the definition of the state space is of crucial importance for the outputs. The coherence between the results obtained with differently composed state spaces showed that the same stability output can be obtained with different implementations and experimental setup. The number of gait cycles necessary to obtain these results is also practically identical among these setups. For the peculiarity of the instrumentation features, however, stereophotogrammetry system is only suitable for acquiring such long gait trials when a treadmill is used.

Experimental noise and operator errors have an impact, although small, on the results when using orbital stability analysis based on joint angles obtained from stereophotogrammetric systems. Further studies are needed to determine if the stability measures obtained from analysis on these state spaces are really capable to discriminate between known stability conditions. Experimental noise on accelerometer data showed no particular influence on the stability results.

Experimental results were also coherent with the model results in terms of number of cycles required, supporting the validity of the stability outcomes. This result confirms the possibility to obtain reliable orbital stability measures with a single inertial sensor and could lead to advantages in the development of a simple and fast data acquisition protocol, confirming what was found in literature for treadmill walking [16].

Acknowledgements

The authors gratefully thank Dr. Martijn Wisse for his contribution in the implementation of the model.

Author Contributions

Conceived and designed the experiments: FR RS. Performed the experiments: FR. Analyzed the data: FR MCR. Contributed reagents/materials/analysis tools: FR MCR RS. Wrote the manuscript: FR RS.

References

- Granata KP, Lockhart TE (2008) Dynamic stability differences in fall-prone and healthy adults. *J Electromyogr Kines* 18(2): 172–178. doi: 10.1016/j.jelekin.2007.06.008. PubMed: 17686633.
- Hurmuzlu Y, Basdogan C (1994) On the measurement of dynamic stability of human locomotion. *J Biomech Eng* 116(1): 30–36. doi: 10.1115/1.2895701. PubMed: 8189711.
- Fuller GF (2000) Falls in the elderly. *Am Fam Physician* 61(7): 2159–2168, 2173–2174 PubMed: 10779256.
- Heinrich S, Rapp K, Rissmann U, Becker C, König HH (2009) Cost of falls in old age: a systematic review. *Osteoporos Int* 21: 891–902. PubMed: 19924496.
- Campbell AJ, Borrie MJ, Spears GF (1989) Risk factors for falls in a community-based prospective study of people 70 years and older. *J Gerontol* 44(4): 112–117. doi:10.1093/geronj/44.4.M112.
- Rubenstein LZ, Robbins AS, Schulman BL, Rosado J, Osterweil D et al. (1988) Falls and instability in the elderly. *J Am Geriatr Soc* 36(3): 266–278. PubMed: 3276771.
- Hausdorff JM, Rios DA, Edelberg HK (2001) Gait variability and fall risk in community-living older adults: a 1-year prospective study. *Arch Phys Med Rehabil* 82(8): 1050–1056. doi:10.1053/apmr.2001.24893. PubMed: 11494184.
- Hof AL, Gazendam MGJ, Sinke WE (2005) The condition for dynamic stability. *J Biomech* 38(1): 1–8. doi:10.1016/j.jbiomech.2004.03.025. PubMed: 15519333.
- Holt KJ, Jeng SF, Ratcliffe R, Hamill J (1995) Energetic Cost and Stability During Human Walking at the Preferred Stride Velocity. *J Mot Behav* 27(2): 164–178. doi:10.1080/00222895.1995.9941708. PubMed: 12736125.
- Hamacher D, Singh NB, Van Dieën JH, Heller MO, Taylor WR (2011) Kinematic measures for assessing gait stability in elderly individuals: a systematic review. *J R Soc Interface* 8(65): 1682–1698. doi:10.1098/rsif.2011.0416. PubMed: 21880615.
- Dingwell JB, Kang HG (2007) Differences between local and orbital dynamic stability during human walking. *J Biomech Eng* 129(4): 586–593. PubMed: 17655480.
- McGeer T (1990) Passive Dynamic Walking. *Int J Robot Res* 9(2): 62–82. doi:10.1177/027836499000900206.
- Hurmuzlu Y, Basdogan C, Stoianovici D (1996) Kinematics and dynamic stability of the locomotion of post-polio patients. *J Biomech Eng* 118(3): 405–411. doi:10.1115/1.2796024. PubMed: 8872264.
- Kang HG, Dingwell JB (2009) Dynamics and stability of muscle activations during walking in healthy young and older adults. *J Biomech* 42(14): 2231–2237. doi:10.1016/j.jbiomech.2009.06.038. PubMed: 19664776.
- Van Schooten KS, Sloat LH, Buijn SM, Kingma H, Meijer OG et al. (2011) Sensitivity of trunk variability and stability measures to balance impairments induced by galvanic vestibular stimulation during gait. *Gait Posture* 33(4): 656–660. doi:10.1016/j.gaitpost.2011.02.017. PubMed: 21435878.
- Buijn SM, Ten Kate WRT, Faber GS, Meijer OG, Beek PJ et al. (2010) Estimating dynamic gait stability using data from non-aligned inertial sensors. *Ann Biomed Eng* 38(8): 2588–2593. doi:10.1007/s10439-010-0018-2. PubMed: 20354902.
- Dingwell JB, Robb RT, Troy KL, Grabiner MD (2008) Effects of an attention demanding task on dynamic stability during treadmill walking. *J Neuroeng Rehabil* 5: 12. PubMed: 18426571.
- McAndrew PM, Wilken JM, Dingwell JB (2011) Dynamic stability of human walking in visually and mechanically destabilizing environments. *J Biomech* 44(4): 644–649. doi:10.1016/j.jbiomech.2010.11.007. PubMed: 21094944.
- Buijn SM, Bregman DJJ, Meijer OG, Beek PJ, van Dieën JH (2011) The validity of stability measures: A modelling approach. *J Biomech* 44(13): 2401–2408. doi:10.1016/j.jbiomech.2011.06.031. PubMed: 21762919.
- Riva F, Bisi MC, Stagni R (2013) Orbital stability analysis in biomechanics: A systematic review of a nonlinear technique to detect instability of motor tasks. *Gait Posture* 37(1): 1–11. doi:10.1016/j.gaitpost.2012.06.015. PubMed: 22795784.
- Gates DH, Dingwell JB (2009) Comparison of different state space definitions for local dynamic stability analyses. *J Biomech* 42(9): 1345–1349. doi:10.1016/j.jbiomech.2009.03.015. PubMed: 19380140.
- Buijn SM, van Dieën JH, Meijer OG, Beek PJ (2009) Statistical precision and sensitivity of measures of dynamic gait stability. *J Neurosci Methods* 178(2): 327–333. doi:10.1016/j.jneumeth.2008.12.015. PubMed: 19135478.
- Su JL, Dingwell JB (2007) Dynamic stability of passive dynamic walking on an irregular surface. *J Biomech Eng* 129(6): 802–810. doi: 10.1115/1.2800760. PubMed: 18067383.
- Roos PE, Dingwell JB (2011) Influence of simulated neuromuscular noise on the dynamic stability and fall risk of a 3D dynamic walking model. *J Biomech* 44(8): 1514–1520. doi:10.1016/j.jbiomech.2011.03.003. PubMed: 21440895.
- Solomon JH, Wisse M, Hartmann MJ (2010) Fully interconnected, linear control for limit cycle walking. *Adap Behav* 18(6): 492–506. doi: 10.1177/1059712310389624.
- Grood ES, Suntay WJ (1983) A joint coordinate system for the clinical description of three-dimensional motions: Application to the knee. *J Biomech Eng* 105(2): 136–144. doi:10.1115/1.3138397. PubMed: 6865355.
- Della Croce U, Cappozzo A, Kerrigan DC (1999) Pelvis and lower limb anatomical landmark calibration precision and its propagation to bone geometry and joint angles. *Med Biol Eng Comput* 37(2): 155–161. doi: 10.1007/BF02513282. PubMed: 10396818.
- Cappozzo A, Catani F, Della Croce U, Leardini A (1995) Position and orientation in space of bones during movement: anatomical frame definition and determination. *Clin Biomech* 10(4): 171–178. doi: 10.1016/0268-0033(95)91394-T. PubMed: 11415549.
- Kang HG, Dingwell JB (2009) Dynamic stability of superior vs. inferior segments during walking in young and older adults. *Gait Posture* 30(2): 260–263. doi:10.1016/j.gaitpost.2009.05.003. PubMed: 19502060.
- Takens F (1981) Detecting strange attractors in turbulence. In: D Rand LS Young. *Dynamical Systems and Turbulence*. Warwick 1980. Springer Berlin / Heidelberg. pp 366–381
- Dingwell JB, Cusumano JP (2000) Nonlinear time series analysis of normal and pathological human walking. *Chaos* 10(4): 848–863. doi: 10.1063/1.1324008. PubMed: 12779434.
- England SA, Granata KP (2007) The influence of gait speed on local dynamic stability of walking. *Gait Posture* 25(2): 172–178. doi:10.1016/j.gaitpost.2006.03.003. PubMed: 16621565.
- Aminian K, Najafi B, Büla C, Leyvraz PF, Robert P (2002) Spatio-temporal parameters of gait measured by an ambulatory system using miniature gyroscopes. *J Biomech* 35(5): 689–699. doi:10.1016/S0021-9290(02)00008-8. PubMed: 11955509.
- Kantz H, Schreiber T (2004) *Nonlinear time series analysis*. Cambridge University Press.
- Hobbelen DG, Wisse M (2007) A Disturbance Rejection Measure for Limit Cycle Walkers: The Gait. *Sensitivity Norm*. *IEEE T Robot* 23(6): 1213–1224. doi:10.1109/TRO.2007.904908.

ALMA MATER STUDIORUM
UNIVERSITÀ DEGLI STUDI DI BOLOGNA

DEPARTMENT OF ELECTRICAL, ELECTRONIC AND INFORMATION
ENGINEERING "GUGLIELMO MARCONI" - DEI

SCUOLA DI DOTTORATO IN BIOINGEGNERIA - CICLO XXV
SETTORE CONCORSUALE: 09/G2
SETTORE SCIENTIFICO DISCIPLINARE DI AFFERENZA:
ING-INF/06

**METHODS FOR THE
QUANTIFICATION OF MOTOR
STABILITY FOR THE
ASSESSMENT OF FALL RISK**

Federico Riva

Supervisor

Rita Stagni, Ph.D.

Co-Supervisor

Luca Cristofolini, Ph.D.

Reviewers

Aurelio Cappozzo, Ph.D.

Harinderjit Gill, D.Phil.

Ph.D. Coordinator

Angelo Cappello, Ph.D.

Esame Finale Anno 2013

ALMA MATER STUDIORUM
UNIVERSITÀ DEGLI STUDI DI BOLOGNA

DEPARTMENT OF ELECTRICAL, ELECTRONIC AND INFORMATION
ENGINEERING “GUGLIELMO MARCONI” - DEI

SCUOLA DI DOTTORATO IN BIOINGEGNERIA - CICLO XXV
SETTORE CONCURSALE: 09/G2
SETTORE SCIENTIFICO DISCIPLINARE DI AFFERENZA:
ING-INF/06

**METHODS FOR THE
QUANTIFICATION OF MOTOR
STABILITY FOR THE
ASSESSMENT OF FALL RISK**

Federico Riva

Supervisor

Rita Stagni, Ph.D.

Co-Supervisor

Luca Cristofolini, Ph.D.

Reviewers

Aurelio Cappozzo, Ph.D.

Harinderjit Gill, D.Phil.

Ph.D. Coordinator

Angelo Cappello, Ph.D.

Esame Finale Anno 2013

Ai miei genitori

There are these two young fish swimming along, and they happen to meet an older fish swimming the other way, who nods at them and says, 'Morning, boys, how's the water?' And the two young fish swim on for a bit, and then eventually one of them looks over at the other and goes, 'What the hell is water?'

[...]

The real value of a real education [...] has almost nothing to do with knowledge, and everything to do with simple awareness. Awareness of what is so real and essential, so hidden in plain sight all around us, all the time, that we have to keep reminding ourselves over and over: 'This is water. This is water.'

David Foster Wallace, commencement speech to a graduating class at Kenyon College, Ohio, May 21 2005.

We are at the very beginning of time for the human race. It is not unreasonable that we grapple with problems. But there are tens of thousands of years in the future.

Our responsibility is to do what we can, learn what we can, improve the solutions, and pass them on.

Richard P. Feynman

ABSTRACT

The research field of the Thesis is the evaluation of motor variability and the analysis of motor stability for the assessment of fall risk. Since many falls occur during walking, a better understanding of motor stability could lead to the definition of a reliable fall risk index aiming at measuring and assessing the risk of fall in the elderly, in the attempt to prevent traumatic events. Several motor variability and stability measures are proposed in the literature, but still a proper methodological characterization is lacking. Moreover, the relationship between many of these measures and fall history or fall risk is still unknown, or not completely clear.

The aim of this thesis is hence to: i) analyze the influence of experimental implementation parameters on variability/stability measures and understand how variations in these parameters affect the outputs; ii) assess the relationship between variability/stability measures and long- short-term fall history.

Several implementation issues have been addressed. Following the need for a methodological standardization of gait variability/stability measures, highlighted in particular for orbital stability analysis through a systematic review, general indications about implementation of orbital stability analysis have been showed, together with an analysis of the number of strides and the test-retest reliability of several variability/stability numbers. Indications about the influence of directional changes on measures have also been provided. Association between measures and long/short-term fall history has also been assessed. Of all the analyzed variability/stability measures, Multiscale entropy and Recurrence quantification analysis demonstrated particularly good results in terms of reliability, applicability and association with fall history. Therefore, these measures should be taken in consideration for the definition of a fall risk index.

SUMMARY

I. Introduction.....	13
II. Orbital stability analysis in biomechanics: a systematic review of a nonlinear technique to detect instability of motor tasks	20
III. Influence of input parameters on dynamic orbital stability of walking: in-silico and experimental evaluation	39
IV. Reliability of stability and variability measures.....	51
V. Estimating fall risk with inertial sensors using gait stability measures that do not require step detection.....	57
VI. Are gait variability/stability measures influenced by directional changes?.....	65
VII. Stability of walking and long-short term fall-history	69
VIII. Conclusions	73
IX. Appendix	75
X. References	81
XI. Scientific writing.....	91

I. INTRODUCTION

I.1. FALLS IN THE ELDERLY

“A fall [...] is an event which results in a person coming to rest unintentionally on the ground or lower level, not as a result of a major intrinsic event (such as a stroke) or overwhelming hazard.” [1]

Considered to be one of the so-called *geriatric giants*, falls place a heavy economic burden on society, and are also responsible for a considerable loss of life quality. In 2009 alone, falls led to costs ranging between 0.85 and 1.5 per cent of the total healthcare expenses within the USA, Australia, EU and the UK [2]. Falls also have a critical influence on health status, with approximately 81-98% of hip fractures caused by falls [3,4], and are the leading cause of injury-related visits to emergency departments in the USA [5].

Risk of a falling increases with age [6,7]; falls are and the primary etiology of accidental deaths in persons over the age of 65 years. The mortality rate for falls increases dramatically with age, with falls accounting for 70 percent of accidental deaths in persons 75 years of age and older [5]. The main associated costs therefore tend to occur in higher age groups and in the wake of fractures, a problem that is further exacerbated by the increasing proportion of elderly among the population [8].

There are currently over 400 known risk factors for falls [9], classified into extrinsic (or environmental), intrinsic (or personal) and task-related factors [10,11]. Extrinsic factors comprise all external influences and might include factors such as poor lighting, surface elevation, surface roughness, obstacles, clothing/footwear, lack of equipment or aids, or external perturbations. Task-related factors include task complexity and speed, fatigue, load handling. Intrinsic factors reflect individual differences in, among others, age and gender, muscular strength, reaction time, visual impairment (e.g. glaucoma, macular degeneration, retinopathy), ethnicity, use of drugs and medications (e.g. polypharmacy, sedatives, cardiovascular medications), living alone, sedentary behavior, psychological status, impaired cognition (e.g. dementia), cardiovascular issues and foot problems. In addition, history of falls as well as impaired stability and mobility (e.g. as a result of stroke, parkinsonism, arthritic changes, neuropathy, neuromuscular disease or vestibular disease) can be considered as higher level factors owing to their interdependency with both intrinsic and extrinsic factors. While knowledge of the environment is known to play

a role in minimizing the effect of intrinsic and task-related factors on instability, extrinsic factors cannot generally be controlled, tested or accounted for in clinical assessment. Intrinsic factors have also been identified as major risk factors for falling. In particular, gait instability is considered to be a major fall risk factor, particularly in geriatric patients [12–14]; however, the quantification of gait stability is still an issue [8].

Several interventions to prevent falling (and associate injuries) have been proposed [15], but in order to correctly select individuals to which prescribe appropriate interventions, a reliable identification of individuals at risk of falling is needed [16]. Since many falls in the elderly occur during walking [17,18], assessment of gait stability represents a fundamental aspect.

I.2. ASSESSMENT OF GAIT STABILITY

The most established techniques to quantify fall risk are (i) motor function tests, (ii) questionnaires, and (iii) biomechanical laboratory-based measurements. However, since motor function tests and questionnaires are generally not capable of providing a quantitative predictive assessment of gait stability or fall risk [19,20], biomechanical laboratory-based measurements can help defining subject-specific methods with high sensitivity and specificity for gait stability assessment [8].

As said above, assessment of gait stability can allow the identification of subjects at risk of falling, being an important and necessary precondition for walking without falling. However, while stability is a well-defined concept in mechanics, there still is no complete consensus on how to measure stability of gait. Several methods are currently available, each one having advantages and disadvantages.

The term gait stability is comprehensive of both *indirect* as well as *direct* biomechanical aspects of stability during gait. These aspects can be measured and quantified, and hence could contribute to the definition of a subject-specific fall risk index. *Indirect* assessment of gait stability is represented by kinematic variability measures; when error corrections during a motor task become less effective, variability increases. It can therefore be assumed that variability is related to fall risk, because increased variability may bring the dynamic state of the person closer to the limit of stability [8]. On the other hand, *direct* stability measures not only provide information regarding the disturbances in the motor task performance, but also explicitly quantify the performance of the dynamic error correction. In addition, other *stability-related measures* have been recently associated with gait stability.

Mathematical details about *indirect*, *direct* and *stability-related* measures can be found in Chapter IX (Appendix).

I.2.1. Indirect assessment of gait stability

Kinematic variability measures represent the magnitude of variability of a certain kinematic parameter over strides during gait. One of the most established variability

measure is stride time variability, expressed in terms of Standard deviation (SD) or Coefficient of variation (CV) [17].

Somehow complementary measures of stride-to-stride variability are the Inconsistency of the variance of the stride time (IV) and the Nonstationary index (NI) [21], which measure the fluctuation dynamics of the stride time.

The Poincaré plot is a widely accepted method for the analysis of 2-D dynamic systems [22]; it has been extensively applied in the study of heart rate variability as a qualitative visualization tool, but can also be applied to other physiological signals (for example stride time). Stride time data plots between successive gait cycles show variability of stride time. Plots are used to extract indices, such as length (PSD2) and width (PSD1) of the long and the short axes describing the elliptical nature of the plots.

Whereas variability measures have been shown to be positively correlated with the probability of falling in the elderly [17,23], decreased variability has also been reported for mobility-impaired subjects, suggesting that these subjects are less stable due to a less flexible system [24,25]. Moreover, analyzing the effects of walking speed on stability and variability, no relationship between variability and the time needed to recover from a perturbation has been found, leading to the conclusion that locomotion variability measures may not be dependable indicators of locomotion stability [26] and are not able to quantify how the locomotor system responds to perturbations [27]. Hence, the relationship between gait variability and stability is not as straightforward as it may seem.

1.2.2. Direct assessment of gait stability

Human locomotion is, in all respects, a dynamical system. To test the stability of a dynamical system, several tools have been developed, since dynamical systems are often nonlinear and complex, and human locomotion definitely is. For this reason, some authors applied methods coming from stability analysis of nonlinear dynamic systems to biomechanics [8].

In theoretical mechanics, stability is defined by how the system state responds to perturbations [28]; similarly, an appropriate definition for the stability of a motor task should be based on the quantification of the tendency of a subject to recover from small (natural or artificial) perturbations occurring during the execution of a structurally cyclic task (e.g. gait [29]). However, in mechanics and robotics a state variable is deterministic and can predict the future state of the mechanical system: while the behaviour of walking robots under perturbation conditions can quite easily be predicted [30], dealing with biomechanical time series of human locomotion variables is not as straightforward as in robotics. In fact, when dealing with human locomotion the equations of the system are not known, and such nonlinear techniques have to be applied in a numerical (rather than analytical) fashion.

A motor task can hence be treated as a nonlinear dynamic system: biomechanical variables (e.g. joint angles, angular velocities or accelerations, marker positions, muscle

activations and others) vary during the temporal evolution of the task, defining a system that continuously changes over time. In a repetitive task, like walking, biomechanical variables have a cyclic behavior and recur iteratively with almost the same pattern; this pseudo-periodic behavior can be exploited for nonlinear analysis. For example, plotting the temporal evolution of knee angle against hip angle will design an orbit, which will vary dynamically in time but will maintain almost the same trend. In mechanical dynamics, the set of the variables that describe this orbit (two or more) is called *state space*, which can be defined as a vector space where the dynamical system can be defined at any point [31]. The number of task cycles (e.g. strides, commonly defined as the interval of time that starts at the heel strike of one foot and ends at the following heel strike of the same foot [32,33]) will determine how many times the variables will travel around the orbit. The locomotor pattern will force those variables to roughly travel around a fixed orbit, in a sort of limit cycle behavior. If a perturbation occurs during the motor task, the orbit will instantaneously move away from the limit cycle; in case of stability, the orbit will then tend back to the limit orbit, otherwise will diverge from it. For example, if a significant variation in knee angle occurs during walking (because of an obstacle), a coherent variation in hip angle will take place: simply observing the trend of one of these variables during the task could bring to misleading conclusions regarding stability, whereas embedding the two in the state space gives a more complete characterization of the system behavior. If a measure of only one of these time series is available, a proper way to obtain a characterization of the system is to embed in the state space the variable (e.g. knee angle) and its time-delayed copies; again, if an obstacle causes a sudden variation of knee angle, the orbits will reveal if the subject recovered stability after getting ahead of the obstacle, getting back to the limit cycle orbit after the destabilizing time event. Techniques of nonlinear stability analysis consist then in the quantification of the tendency of an orbit to diverge from or converge to the previous one or to an attracting limit cycle. Two main approaches for nonlinear stability analysis are present in literature: local and orbital stability analysis. These measures of orbital and local dynamic stability quantify different properties of system dynamics [34].

Local stability is used for systems that do not necessarily exhibit a discernable periodic structure, and therefore does not exploit the previously described pseudo-periodicity of some motor tasks. It is defined using short-term (sLE) and long-term (ILE) local divergence exponents (Lyapunov exponents). These indicators quantify how the system state responds to very small (local) perturbations continuously in real time [34]; many studies using this approach are present in literature [14,24,27,35–38]. Recently, an association between local stability and fall history have been found [39].

Orbital stability is defined for periodic systems with a limit cycle behavior, and can then be applied to cyclic motor tasks. This approach is extensively used in the study of passive dynamic walking robots [30], and in the last years it has been applied also to biomechanics [40]. Orbital stability analysis can be applied under the hypothesis of periodicity and assuming that motor dynamics (e.g. walking dynamics) are governed by central pattern generator processes yielding repetitive limit cycle behavior [41].

Fundamental indicators of orbital stability are Floquet multipliers (FM) which quantify, discretely from one cycle to the next, the tendency of the system state to return to the periodic limit cycle orbit after small perturbations [34]. If maximum Floquet Multipliers (maxFM) have magnitude < 1 , perturbations tend to shrink by the next repetition, and the system remains stable. Every point on the orbit represents an instant of the task cycle. To calculate FM, a section must be defined in some point along the orbit (Poincaré section). In theory, the orbital stability of a deterministic limit cycle process should be the same, regardless of where along the trajectory the Poincaré section is made; however, human walking is not strictly periodic and people respond to perturbations differently during different phases of the gait cycle [34]. Hence, many authors put the Poincaré section in the most significant phases of the motor task (e.g., for gait, maximum sagittal knee flexion, toe off etc.) along the orbit, in order to obtain information about stability in the task phases that are more likely affected by perturbations. According to the literature, orbital stability analysis seems a promising approach for the definition of a reliable motor stability index; it can represent a novel way to predict risk of fall and to identify the most unstable phases of a motor task, in order to plan appropriate rehabilitation therapies. The most interesting feature of this method is the possibility to account for the whole task cycle dynamics, including more variables in the state space characterising the system. With a proper choice of Poincaré section, that is a proper choice of interesting instants during the task, the stability of every phase of the task cycle can be calculated. However, still the use of maxFM as a fall risk index is deemed to be controversial [8].

I.2.3. Stability-related measures

Other measures are present in literature that, whereas not representing a direct assessment of gait stability *per se*, are considered to be related with gait stability as they quantify strictly gait-correlated characteristics (such as smoothness, complexity, recurrence).

Some measures, such as the Index of Harmonicity (IH) and Harmonic Ratio (HR), involve decomposing signals into harmonics by means of Discrete Fourier Transform and then analyze their spectral components [42,43], in order to obtain a measure of smoothness and rhythm of the gait pattern.

HR, derived from trunk acceleration signals and based on amplitudes in frequency spectra, is an indication of smoothness of acceleration patterns and provides information on how smoothly subjects control their trunk during walking and gives an indication of whole body balance and coordination [42,44].

Similarly to HR, IH assesses the contribution of the oscillating components to the observed coordination patterns by means of spectral analysis [43]. It quantifies the contribution of the stride frequency to the signal power relative to higher harmonics.

Other methods that have been associated with gait stability are Multiscale Entropy (MSE) [45,46] and Recurrence Quantification Analysis (RQA) [47,48].

MSE quantifies the complexity or irregularity of a time series. Time series derived from complex systems, like biological systems, are likely to present structures on multiple spatio-temporal scales [45], and MSE has been introduced to this aim.

RQA is a nonlinear technique that has been applied recently to various biological time series, including walking [47]. Based on local recurrence of data points in the reconstructed phase space, it provides a characterization of a variety of features of a given time series, including a quantification of deterministic structure and non-stationarity [48].

I.3. AIM OF THE THESIS

In the last paragraph, several measures of gait variability and stability proposed in the literature have been illustrated; the aim of such measures is quantifying subject specific gait characteristics such as gait impairment, degree of neuromotor control and balance disorders, in both pathologic and healthy subjects.

However, still there is no methodological standardization on how to properly implement variability/stability analysis measures. These measures often come from the analysis of dynamical systems, and depend on many input parameters. The implementation in movement analysis is hence not straightforward, and a methodological standardization is needed in order to obtain reliable, repeatable and easily interpretable outcomes for a fall risk index definition.

Moreover, the relationship between many of these measures and fall history or fall risk is still unknown, or not completely clear. Loss of dynamic stability during gait may be caused by structural changes in gait patterns or by temporary modifications in balance control that could not be displayed while the subject is being tested. An assessment of the association between these measures and the two aforementioned conditions is hence needed, in order to define the capability of the measures to detect long- and short-term stability modification in relation to fall risk.

The aim of this thesis is hence to:

- i) analyze the influence of experimental implementation parameters on variability/stability measures and understand how variations in these parameters affect the outputs;
- ii) assess the relationship between variability/stability measures and long/short-term fall history.

OUTLINE OF THE THESIS

In Chapter II, a systematic review of orbital stability analysis in biomechanics [49] is presented, to provide an overview of the state of the art and of the questions raised by this relatively new approach. In Chapter III a model- and experimental-based study on the influence of the experimental input of orbital stability analysis is presented, with the aim to analyze the influence of experimental noise and of several implementation parameters on the outputs of orbital stability applied to human gait. Chapter IV is dedicated to the assessment of the number of required strides and the test-retest reliability of variability/stability measures proposed in the literature. In Chapter V an assessment of the association between fall history and several step detection independent nonlinear measures is presented. Chapter VI is dedicated to the influence of directional changes during gait on variability/stability measures. Chapter VII are dedicated to and the association between such measures with long/short-term fall risk. Finally, in Chapter VIII a general conclusion is drawn, and directions for future research are explored.

II. ORBITAL STABILITY ANALYSIS IN BIOMECHANICS: A SYSTEMATIC REVIEW OF A NONLINEAR TECHNIQUE TO DETECT INSTABILITY OF MOTOR TASKS¹

II.1. INTRODUCTION

The use of maxFM in the assessment of fall risk has been deemed controversial [8], because of some discrepancy and incoherence in the results found in the literature. A possible cause of this controversy could lie in the lack of a “standard” implementation of this technique, being the technique relatively novel in biomechanics. Considering the motor task as a dynamic nonlinear system, orbital stability analysis implies the definition of a state space characterising the system. No unique way of defining the state space of a given motor task (e.g. gait) has been shown in the literature; the most crucial point seems to be the choice of which and how many biomechanical variables (e.g. joint angles, trunk accelerations) have to be inserted into the space. Even the choice of the position of the Poincaré section represents a critical issue when trying to obtain reliable information about orbital stability of a motor task. Another criticality is represented by the minimum and optimum number of task cycles that should be included in the analysis to obtain reliable stability results.

With the aim to summarize the various applications of this approach in biomechanics and to analyse the solution proposed in the literature about the methodological issues stated above, in this paper a systematic review and a critical evaluation of the literature on the application of orbital stability analysis in biomechanics are provided, with particular focus to its application in gait analysis.

II.2. METHODS

II.2.1. Search strategy

In October 2011 an electronic search was performed by one reviewer to find all articles on the topic of orbital stability analysis in biomechanics. The databases included MEDLINE (1966 - October 2011), ISI Web of Knowledge (1986 - October 2011), and Scopus (2004 - October 2011). Keywords used in the search strategy included "orbital stability", "floquet", "biomechanics" and "movement". "And" and "Or" conjunction were

¹ Published. Riva F, Bisi MC, Stagni R. Orbital stability analysis in biomechanics: A systematic review of a nonlinear technique to detect instability of motor tasks. *Gait & Posture* 2013; 37: 1–11.

used. Only English language articles were considered. Some articles investigated other forms of stability in addition to orbital stability; only details from orbital stability analysis were considered. A manual, targeted search of reference lists of relevant studies and other publications from the authors of the electronically found articles was also performed.

II.2.2. Inclusion and exclusion criteria

A single reviewer assessed the titles and abstract of the articles. The articles included in the study satisfied the following criteria: i) investigation of gait, locomotor or functional tasks, ii) clear and documented purpose of the application of orbital stability analysis and iii) full scientific papers. Since this study focused on the application of orbital stability analysis to biomechanics, reports related to robotics were excluded. Studies published only as conference proceedings were excluded from the review.

II.2.3. Data extraction

A customised data extraction form was developed, based on previous systematic reviews on associated areas [50–53]. The data extraction themes were selected to give an exhaustive overview of each article for analysis and assessment of the quality of the scientific literature. Data extraction themes included the description of the sample, details of the experimental and analytical protocol and the key results of the study (Table II.1). Data were obtained independently by three reviewers. In order to compare results from different articles, 95% confidence intervals for each maxFM calculation in preferred/normal gait condition were extracted (when available).

Table II.1 – Data extraction results

Ref	Article	Subjects	Age	Body Mass Index (BMI)	Motion analysis	State space definition	Motor task
[54]	Arellano et al.	23	23.8 ± 4.5	22.1	3d stereophotogrammetry	Angular positions and velocities on the sagittal plane of the right ankle, knee and hip	Treadmill walking
[55]	Arellano et al.	23	23.8 ± 4.5	22.1	3d stereophotogrammetry	Angular positions and velocities on the sagittal plane of the right ankle, knee and hip	Treadmill walking
[56]	Bruijn et al.	9	25.5 ± 3.6	23	3d stereophotogrammetry	First derivatives of anterior posterior, medio lateral and vertical position time-series of the average movements of the thorax markers (delay reconstruction of individual states)	Treadmill walking
[57]	Bruijn et al.	9	–	–	3d stereophotogrammetry, tri-axial accelerometer	Time-normalized 3D acceleration and 3D rotational velocities time series, each with their sample delayed copies, coming from the inertial sensor and the 3d stereophotogrammetry system	Treadmill walking
[34]	Dingwell and Kang	10	27.1 ± 3.2	22	Electrogoniometers, tri-axial accelerometer	Trunk acceleration data (AP, ML, VT) and right leg sagittal plane joint angles (delay reconstruction of individual states)	Overground walking, treadmill walking
[58]	Dingwell et al.	37	61 ± 6.6 (NP), 57.6 ± 7.7 (CO), 27.9 ± 5.1 (young)	30.3 ± 4.4 (NP), ± 2.2 (CO), (young)	Electrogoniometers, 3d stereophotogrammetry	1: sagittal joint angles of hip, knee and ankle joints of the right leg; 2: T1 marker motions in the AP, ML and VT directions (delay reconstruction of individual states)	Overground walking, treadmill walking

Table II.1 – (Continued)

Ref	Article	Subjects	Age	Body Mass Index (BMI)	Motion analysis	State space definition	Motor task
[59]	Dingwell et al.	13	24.5 ± 3.4	25	3d stereophotogrammetry	Anterior-posterior, medio-lateral and vertical velocity of a marker attached to the skin over C5/T1 (delay reconstruction of individual states)	Treadmill walking
[60]	Gates & Dingwell	20	25.5 ± 2.2	24	3d stereophotogrammetry	Three rotational angles and angular velocities for each joint (shoulder, elbow, wrist)	Saw task, lift task
[61]	Gates & Dingwell	10	27.9 ± 2.2	24	3d stereophotogrammetry	Three rotational angles and angular velocities for each joint (shoulder, elbow, wrist)	Sawing-like task
[13]	Granata et al.	12	26.3 ± 2.1 (young), 71.3 ± 6.5 (elderly); 71.0 ± 3.0 (fall-prone elderly)	23 (young), 26 (elderly), 30 (fall-prone elderly)	3d stereophotogrammetry	3d position and velocity of a point mid-way between the ASIS and the location of the heel-markers (surrogate CoP relative to CoM)	Treadmill walking
[62]	Hidler and Rymner	4	26 ± 4	–	Precision potentiometer and tachometer	Ankle position and ankle velocity	Clonus initiated in the plantar flexor muscles
[40]	Hurmuzlu and Basdogan	20	28 (19-49)	–	Electrogoniometers	Joint angles of ankle, knee and hip of the dominant side, and their time-derivatives	Overground walking
[63]	Hurmuzlu et al.	26	26 ± 4 (healthy), 52 ± 10 (polio survivors)	25 (healthy), 24 (polio survivors)	Electrogoniometers	Bilateral rotations and velocities at the hip, knee and ankle	Overground walking

Table II.1 – (Continued)

Ref	Article	Subjects	Age	Body Mass Index (BMI)	Motion analysis	State space definition	Motor task
[64]	Kang and Dingwell	35	23.3 ± 2.6 (young), 6.0 (elderly)	23.8 (young), 25.3 (elderly)	SEMG	SEMG signals from 4 muscles of the left leg, and their time-derivatives	Treadmill walking
[65]	Kang and Dingwell	35	23.3 ± 2.6 (young), 6.0 (elderly)	23.8 (young), 25.3 (elderly)	3d stereophotogrammetry	Linear velocities and accelerations of the three coordinates of a virtual center marker representing the trunk; angular velocities and accelerations of three dimensional trunk rotations	Treadmill walking
[66]	Kang and Dingwell	35	23.3 ± 2.6 (young), 6.0 (elderly)	23.8 (young), 25.3 (elderly)	3d stereophotogrammetry	Linear and angular velocities of a virtual center marker, defined as the average location of the markers on each segment (delay reconstruction of individual states)	Treadmill walking
[67]	Marghita and Hobatho	6	41.464	–	Video-based 2d motion analysis system	Rotations of the hip joint, the knee joint, the ankle joint and their corresponding angular velocities on the sagittal plane	Overground walking
[68]	Marghita et al.	5	–	–	Video-based 2d motion analysis system	Joint angular displacements (coxo femoral angle, femoro tibial angle, tarsal angle) and velocities	Overground walking
[69]	McAndrew et al.	12	29 ± 7.5	24	3d stereophotogrammetry	Delay embedding of the AP, ML and vertical velocities of a C7 vertebral marker	Walking in a CAREN system

Table II.1 – (Continued)

Ref	Article	Subjects	Age	Body Mass Index (BMI)	Motion analysis	State space definition	Motor task
[70]	Schabowski and Gerner	10	–	–	3d stereophotogrammetry	Joint angles and velocities (ankle, knee, hip)	Treadmill walking
[71]	Scott-Pandorf et al.	10	22.4 ± 2.2	23	3d stereophotogrammetry	Angular positions and velocities of the right ankle, knee and hip	Treadmill walking
[72]	Scott-Pandorf et al.	10	24.6 ± 6.5	24	3d stereophotogrammetry	Angular positions and velocities of the right ankle, knee and hip	Treadmill walking
[73]	van Schooten et al.	12	23.7 ± 2.4	23	Inertial sensors	Linear acceleration and angular velocities of the trunk in all three directions and their time-delayed copies	Treadmill walking

II.2.4. Quality

Quality assessment was performed to limit bias, minimise errors and improve reliability of findings [74]. The quality of a study relates to aspects of the study's design, methods of sample recruitment, the execution of the tests, and the completeness of the study report. It is essential that the quality of the studies included in the review is assessed and reported, so that appropriately cautious inferences can be drawn [75]. Quality can be described as "the extent to which all aspects of a study's design and conduct can be shown to protect against systematic bias, non-systematic bias, and inferential error" [76]. Some checklists which assist in the assessment of the quality of studies are present in literature [75,77], but no quality assessment tool existed for the evaluation of articles in this field. Therefore, a customised quality assessment tool was developed (Table II.2), based upon general systematic reviews principles and guidelines from other systematic reviews [50,51,77,78]. The tool consisted of 16 questions that concerned the major research purposes. A scoring system was developed to perform an overall evaluation of each article. Each question coming from the questionnaire was scored as follows: 2 = Yes; 1 = Limited detail; 0 = No. Three reviewers (FR, MCB and RS) scored each paper independently.

Table II.2 – Quality analysis form

Question
1. Is the aim of the study clearly described?
2. Is the design of the study clearly described?
3. Are participant characteristics adequately described?
4. Is sampling methodology appropriately described?
5. Is sample size used justified?
6. Are state space definitions accurately described?
7. Is the choice of the variables set justified?
8. Are equipment and setup clearly described?
9. Are motor tasks clearly defined?
10. Is the analytical technique clearly described?
11. Are appropriate statistical analysis methods used?
12. Are the main findings of the study clearly described?
13. Are key findings supported by the results?
14. Are limitations of the study clearly described?
15. Are key findings supported by other literature?
16. Are conclusions drawn from the study clearly stated?

II.3. RESULTS

II.3.1. Search yield

The initial search of the databases, containing all the keywords, yielded 46 results. Eight more articles [13,54,60,63,64,67,71,72] were identified from the manual targeted search. After the application of the inclusion and exclusion criteria, 23 articles related to orbital stability analysis in biomechanics were selected for review. Details of reviewed articles are summarized in Table II.1 and Table II.5.

II.3.2. Quality

Table II.3 summarizes the quality of the reviewed articles. The overall quality of the articles was high, particularly in the areas of aim and design of the study, equipment and setup description, motor task description, reporting of main findings and the drawn conclusions. Participant characteristics were generally well reported, but in many cases information about body mass index (BMI) were not available. Methods for participant sampling were rarely reported. Many articles had limited details about the choice of the variable set and the analytical technique. Also, many articles had limited statistical analysis. Meta-analysis was not performed in this review.

Table II.3 – Quality analysis results. Each question coming from the questionnaire (Table II.2) was scored as follows: 2 = Yes; 1 = Limited detail; 0 = No. Three reviewers (FR, MCB and RS) scored each paper independently.

Ref	Article	Question number															
		1	2	3	4	5	6	7	8	9	10	11	12	13	14	15	16
[54]	Arellano et al.	2	2	1,3	0,3	0,3	2	1,3	2	2	1,3	2	1,3	2	1,3	2	1,6
[55]	Arellano et al.	2	2	2	1	0,6	2	1,3	2	2	1,3	2	1,6	2	2	1,3	1,3
[56]	Bruijn et al.	1,3	2	1,3	1	0,6	2	1	2	2	1,3	1,3	2	1,3	2	1,6	2
[57]	Bruijn et al.	2	1,3	1,3	0,3	0,3	1,6	1	2	2	1,6	2	2	2	1,3	1,3	1,3
[34]	Dingwell and Kang	2	2	1,6	0,6	0,3	1,3	1,3	2	2	1,6	1,6	2	2	2	1,6	2
[58]	Dingwell et al.	2	2	1	0,3	0,6	1,3	1,6	1,3	2	1,3	2	1,6	2	1,3	2	1,3
[59]	Dingwell et al.	2	2	1,3	1,3	0,6	2	1,6	2	2	1,3	2	2	2	1,6	1,3	1,3
[60]	Gates & Dingwell	2	2	2	1,6	0,3	2	1,3	2	2	1,6	2	2	2	2	1,3	2
[61]	Gates & Dingwell	2	1,3	1,3	1,3	0,6	2	1,3	2	2	1,6	2	2	2	2	1,6	2
[13]	Granata et al.	2	2	2	1	0,6	1,3	1,6	2	2	1,6	2	2	2	2	2	2
[62]	Hidler and Rymer	2	2	2	1,6	0,3	1,6	1	1,3	2	1,3	0,3	2	2	1	1	1,6
[40]	Hurmuzlu and Basdogan	2	2	1	0,3	0,3	2	1,3	2	1,3	1,3	2	1,3	2	2	0,6	1,3
[63]	Hurmuzlu et al.	2	2	2	1,3	0,3	2	1,3	2	2	1,3	1,6	2	2	0,6	1	1,6
[64]	Kang and Dingwell	2	2	1,3	1,6	0,6	2	1,3	2	2	1,6	2	2	2	1	2	2
[65]	Kang and Dingwell	2	2	2	1,3	0,6	2	1	2	2	1,3	1,3	2	2	0,6	1,6	2
[66]	Kang and Dingwell	2	2	1,3	1	0,6	2	1	1,6	1,3	1,3	1,3	2	2	2	2	2
[67]	Marghita and Hobatho	1	1	1	0,3	0,6	2	1,3	1	1	1,6	0	1	1,3	0,3	0,3	1
[68]	Marghita et al.	1,3	1,3	1	1	0,3	1,6	1,3	2	0,6	1,3	0	1	1,3	1,3	0	1,3
[69]	McAndrew et al.	2	2	1,3	0	0,3	2	1,3	1,3	1,3	1,6	2	2	2	1	2	1,6
[70]	Schabowski and Gerner	1,3	1	0,3	0	0,6	1	1,3	1	1,6	1,3	0,6	1,6	2	0,6	1	1,6
[71]	Scott-Pandorf et al.	2	2	2	1,3	1,3	2	1,6	2	2	1,3	2	2	2	1,3	1,3	2
[72]	Scott-Pandorf et al.	2	2	2	1,6	1,3	2	1,6	2	2	1,3	2	2	2	2	2	2
[73]	van Schooten et al.	2	2	1,6	1,3	0,6	1,3	1	2	2	1	2	2	2	1,6	1	2

II.3.3. Participants

The reviewed articles tested participants with different ages and physical characteristics. Some articles provided insufficient data regarding the physical characteristics of tested participants. The reviewed articles tested different sized groups of participants; the largest group consisted of 37 [58] participants, the smallest group of four participants [62]. Ten articles tested ten subjects or less. Age was mostly restricted to young (mean age 25.4 years) or old adults (mean age 71.7). One article involved children (aged 7-9, [67]), another one dogs [68]. Some articles involved pathologic subjects [58,62]. BMI was used to estimate the body composition of participants. The majority of participants had a BMI value lower than 25, indicating that they had a healthy weight in respect to their height. Where not explicitly reported, mean BMI of the participants was calculated.

II.3.4. Orbital stability analysis

All the subjects analyzed in the articles showed orbitally stable motor patterns ($\max FM < 1$). Hurmuzlu & Basdogan [40] found that normal individuals possess stability measures that are substantially less than unity, confirming the theory regarding the stability of normal gait. Hurmuzlu et al. analyzed gait of post-polio patients [63]; their gait resulted significantly less stable than the gait of normal individuals. Pathologic subjects were involved also in a study by Hidler & Rymer [62]: they examined ankle clonus in spastic subjects, concluding that the periodic motion exhibited during clonus is in fact a stable limit cycle. In two studies orbital dynamic stability was found to be unaffected by small changes in walking velocity, and the authors stated that slowing down does not lead to a higher orbital stability [13,58]. Conversely, a study [64] reported that both younger and older adults exhibited decreased instability by walking slower, in spite of increased variability. Schablowski & Gerner [70] reported a not very strong, yet nevertheless significant, dependence of orbital stability on walking speed, with a weak local minimum at intermediate speeds. One of these studies [13] indicated also that fall-prone elderly show poorer stability of dynamic walking than young adults and healthy old adults. Of the four articles that confronted orbital stability of walking in young and old adults, three concluded that healthy active older adults exhibit significantly increased orbital dynamic instability (kinematic and muscular), independent of walking speed [64–66]. The other one found no significant difference between the healthy old and young adult groups in terms of $\max FM$ [13]. One study [59] showed that performing an attention demanding task while walking on a treadmill does not affect dynamic stability. One study [66] analyzed muscle activation during walking, and found that $\max FM$ measures were only slightly correlated between electromyography (EMG) and kinematics. However, older adults exhibited greater inter-stride dynamic instability of muscle activation patterns. Two studies analyzed sawing task [60,61], concluding that muscle fatigue does not lead to instability of movement. Some works analyzed the orbital stability of walking with an added mass, with contradictory results: one article concluded that walking with an external load of 30% body weight does not influence the stability of the gait pattern in the sagittal plane [54], while the other one stated that increasing body mass alone would lead to a decrease in the stability of the sagittal plane leg kinematics during steady-state

walking [55]. Scott-Pandorf et al. [71,72] concluded that added load have little effect on the sagittal dynamic stability while in simulated Martian gravity, but the gait pattern is more dynamically stable with loads (e.g. Portable Life Support Systems) at the side of the torso and low on the body.

Trunk motion dynamics appeared to provide a more sensitive marker of the decline in gait function in healthy older adults compared to other body segments [65]. Trunk segment is known to play a critical role in regulating gait-related oscillations in all directions [79], hence it might also be responsible for major compensation mechanisms aimed to maintain stability of gait.

One study [69] had the purpose to determine if exposing subjects to different types of continuous perturbations would evoke changes in orbital stability; subjects exhibited direction-specific responses perturbations. A study [73] tested whether (combinations of) measures of variability, and local and orbital dynamic stability were sensitive to experimentally induced impaired gait stability, during treadmill walking at several different speeds, concluding that FM cannot be used to assess balance control in gait. In the opinion of the authors this may be due to compensatory changes, and this claim would require additional research. Orbital stability results for young subjects walking at normal or preferred speed are reported in a forest plot (Figure II.1).

Different methods and instruments of movement analysis lead to the acquisition of different locomotor variables; hence, the composition of the state space strongly depends from the chosen method of movement analysis. Different movement analysis techniques were used in the manuscripts. For kinematic measures, 15 articles used 3d stereophotogrammetry [13,54–59,64,65,70–72], two articles used 2d video motion analysis [67,68], four used electrogoniometer systems [34,40,59,63], three articles used tri-axial accelerometers [34,57,73], one article used surface electromyography [66], one used potentiometers and tachometers [62]. Some articles used two or more techniques.

Orbital stability analysis in literature has been applied to different kinds of cyclic motor tasks. Almost every reviewed article involved overground or treadmill walking, at different speeds with/without carrying loads. One article analyzed subjects walking in a Computer Assisted Rehabilitation ENvironment (CAREN) system (Motek, Amsterdam, Netherlands) and exposed to continuous, pseudo-random oscillations of the support surface or visual field [69]. Two articles analyzed sewing task [60,61], one analyzed lifting task [60]. One article was about dogs trotting [68], another one analyzed a subject who was seating while clonus was stimulated [62]. Although the conclusions drawn by these study are hardly exploitable outside their specific research field, we decided to include them in the review as an application example, as some author might want to apply the technique to different biomechanical-related research areas.

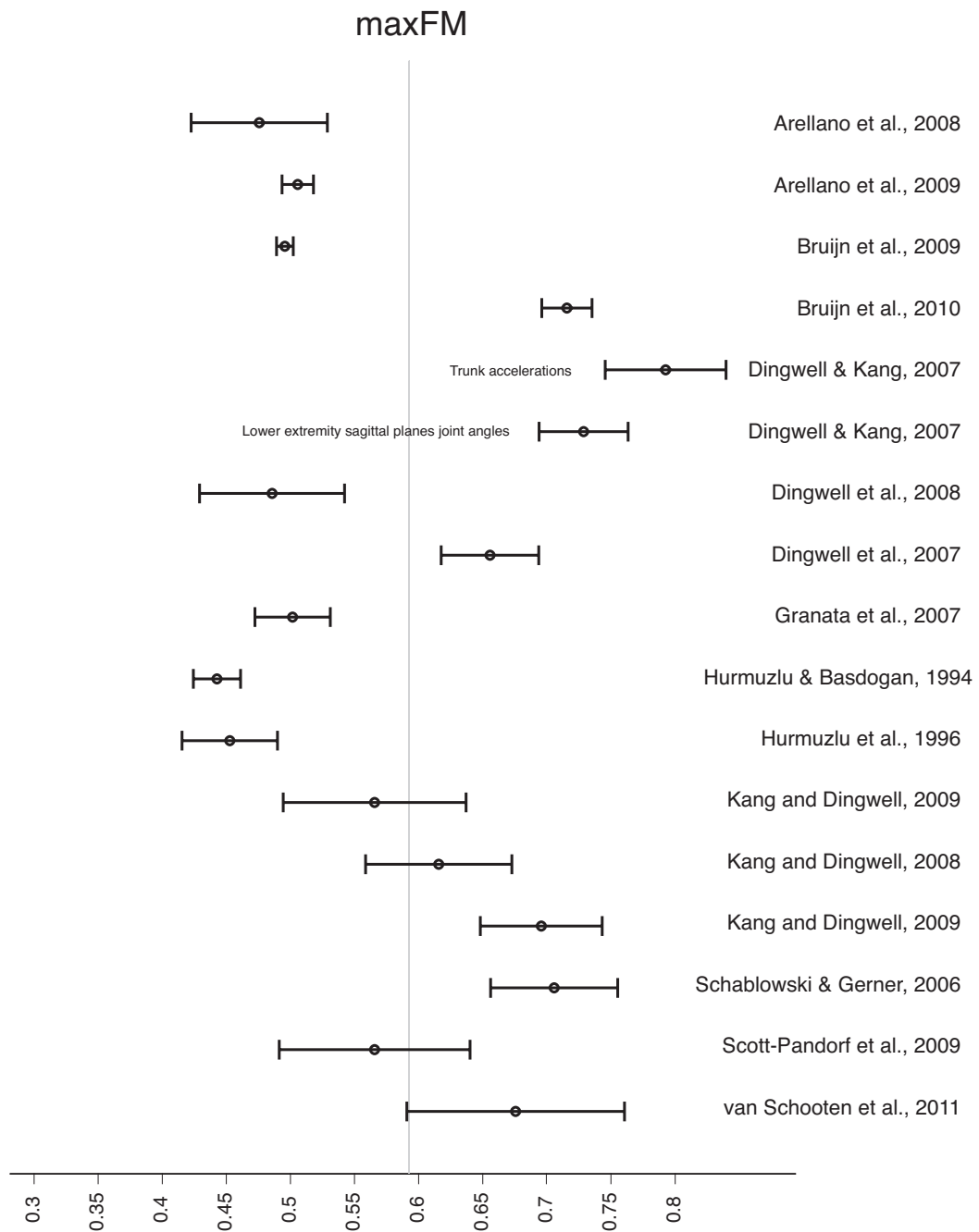


Figure II.1 - maxFM for young healthy subjects walking at preferred (or normal) walking speed. Error bars represent 95% of confidence interval.

All the reviewed articles used the same numerical method for maxFM calculation from time series, referring to the established method by Hurmuzlu et al. [63]. Some articles calculated the dependence on speed of maxFM.

Different state spaces were used in reviewed articles. Many articles included in the state space different combinations of joint angles and their derivatives, including or not their time-delayed copies. Some articles used virtual marker positions, velocities and/or accelerations instead of physical markers [13,64,65]. One article included EMG signals in the state space, and their time derivatives [66]. Articles involving tri-axial accelerometers included in the state space linear acceleration data [34,57,73]. Some articles included in the state space variables coming from both sides, some others just from the dominant side.

Different choices of Poincaré sections were made in the studies. Four articles [63,67,71,72] used maximum sagittal knee flexion to mark the first return data. Two articles [13,40] put Poincaré section at the instant of different foot strike events (left-step, right-step, stride [13] and heel strike, foot flat, heel off, toe off [40]). Two articles [34,58] analyzed the values of maxFM all over the gait cycles, while one [70] took the average values of the maxFM over all the points of the gait cycle. Three articles calculated multipliers at different percentage of the gait cycle [59,64,66]. Five articles calculated all the multipliers in the task cycle; four [56,57,61,69] considered for statistical analysis only the largest FM across all different phases in the cycle, two [69,73] considered the average maxFM value across the cycle. Two articles [54,55] computed maxFM in the instances of heel strike and maximum knee flexion. One article involving spasticity [62] choose the point in the clonus cycle where the ankle acceleration is zero. One article involving dogs trotting [68] put Poincaré maps at the instant of paw strike. Some authors [40] stated that the stability measures are fairly insensitive to the choice of Poincaré section, while other authors stated that the magnitudes of maxFM vary across the gait cycle [34].

Just a few articles [56,63,67,69] stated explicitly the number of cycles upon which the analysis was conducted (Table II.4). The number of cycles analyzed in the articles varied from 4 [63] to 300 [56]. The majority of the articles only indicated the time duration of the trials. One article about precision and sensitivity of orbital stability measures [56] stated that an acceptable value of maxFM for human walking can be estimated within 300 strides; viewing the multiplier as a measure of convergence towards an attractor, using less data could lead to less accurate estimates of the true attractor.

Table II.4 – Number of analyzed cycles

Reference	Article	Cycles number
[54]	Arellano et al.	6 mins walking
[55]	Arellano et al.	6 mins walking
[56]	Bruijn et al.	from 30 to 300 strides
[57]	Bruijn et al.	5 mins walking
[34]	Dingwell and Kang	200 m walkway (overground), 10 mins walking (treadmill)
[58]	Dingwell et al.	10 minutes walking
[59]	Dingwell et al.	3 mins walking
[60]	Gates & Dingwell	-
[61]	Gates & Dingwell	-
[13]	Granata et al.	50s walking (minimum of 35 consecutive steps)
[62]	Hidler and Rymer	-
[40]	Hurmuzlu and Basdogan	pass on a twenty meter walkway (all the gait cycles)
[63]	Hurmuzlu et al.	first 4 gait cycles
[64]	Kang and Dingwell	5 mins walking
[65]	Kang and Dingwell	5 mins walking
[66]	Kang and Dingwell	5 mins walking
[67]	Marghitu and Hobatho	a minimum of 5 gait cycles
[68]	Marghitu et al.	-
[69]	McAndrew et al.	150 continuous strides
[70]	Schablowski and Gerner	90 seconds walking
[71]	Scott-Pandorf et al.	3 mins walking
[72]	Scott-Pandorf et al.	3 mins walking
[73]	van Schooten et al.	2.5 mins / 3 mins / 3.5 mins walking

Table II.5 – Limitations and conclusions reported by the authors

Ref	Article	Limitations	Conclusions
[54]	Arellano et al.	–	Walking with an external load of 30% body weight about the waist did not influence the stability of the gait pattern in the sagittal plane.
[55]	Arellano et al.	The vest may have assisted with the stability of the leg dynamics by providing additional torso control. It is also possible that small horizontal forces were introduced if the subject did not stay directly below the fixed pulley. Potentially, these horizontal forces may have influenced our measures of stability. The vertical lifting forces were more variable as additional mass was added to the subject.	Added mass reduces the stability of the leg kinematics during steady state walking. These results indicate that the inertial state of the body plays a role in the stability of the leg kinematics and may be related to how the body is redirected and accelerated during walking.
[56]	Bruijn et al.	Fatigue and/or boredom may have affected the walking patterns; we cannot exclude the possibility that the observed increase in precision reported was, at least in part, due to the increase in overlap in the samples.	The dependence of the estimates of local and orbital dynamic stability upon the number of strides included in the analysis implies that when estimating stability at different walking speeds, or in different patient groups, a fixed number of strides should be analyzed. The increase in precision with increasing data series length indicates the need to use long data series. The gain in precision tends to be limited when using more than 150 strides.
[57]	Bruijn et al.	The poincaré sections were not sampled at exactly the same time.	The two measurement methods lead to comparable results and thus may be used interchangeably. Inertial sensors may be used as a viable and valid alternative for optoelectronic measurement systems.
[34]	Dingwell and Kang	The additional "states" created were not aligned during the same "phase" of the gait cycle. It is possible this may have led to "averaging out" of differences at individual phases of the gait cycle.	All subjects exhibited orbitally stable walking kinematics during both overground and treadmill walking; the variability inherent in human walking, which manifests itself as local instability, does not significantly adversely affect the orbital stability of walking.
[58]	Dingwell et al.	–	All subjects exhibited orbitally stable walking kinematics, even though these same kinematics were previously shown to be locally unstable. Neuropathic patients do not gain improved orbital stability as a result of slowing down.
[59]	Dingwell et al.	Subjects walked on a motorized treadmill; treadmill walking can reduce the natural variability and enhance the local and orbital stability.	The decreased movement variability associated with the strop task did not translate to greater dynamic stability.

Table II.5 – (Continued)

Ref	Article	Limitations	Conclusions
[60]	Gates & Dingwell	Despite our attempt to make the tasks as similar as possible for the different subjects, significant differences in their responses remained, particularly for the MVC measures. As this task was inherently redundant, subjects could compensate for fatigue by using different muscles or strategies that might allow them to maintain their stability. Different subjects fatigued to different degrees.	When performing multijoint redundant tasks, humans can compensate for muscle fatigue in ways that maintain task precision while increasing movement stability.
[61]	Gates & Dingwell	It was not possible to perform maximum voluntary contractions during this test due to the continuous nature of the task. As such, we were not able to directly quantify decreased force-generating-capacity of subjects' muscles using this protocol. In this paper, we quantified a large number of parameters. It is likely that not all of these were parameters are independent. As such, some caution is likely warranted in interpreting the degree of statistical significance present in some cases.	Subjects significantly altered their kinematic patterns in response to muscle fatigue. These changes were more pronounced when the task was performed at a higher height. Subjects also exhibited increased variability of their movements post-fatigue. Increases in variability and altered coordination did not lead to changes in local or orbital dynamic stability, however. Local stability of the shoulder was lower when movements were performed at a lower height. In contrast, orbital stability of the shoulder and elbow was lower for movements at the higher height. This research showed that people continuously adapt their strategies in multi-joint redundant tasks and maintain stability in doing so.
[13]	Granata et al.	The data represent a pilot study with a small sample size; data were collected while walking on a treadmill; analyses were limited to kinematics of foot-strike with respect to the CoM.	The fall-prone group demonstrated poorer stability of dynamic walking than the other groups.
[62]	Hidler and Rymer	–	The involuntary rhythmic oscillatory movements commonly observed in spastic subjects are driven by peripheral stretch reflexes rather than by a central pattern generator, and the system under these conditions is acting as a stable limit cycle.
[40]	Hurmuzlu and Basdogan	Fewer number joint measurements can be made compared to more advanced optical data acquisition system; it was assumed that the human body is composed of seven segments.	Normal individuals possess stability measures that are substantially less than unity.
[63]	Hurmuzlu et al.	–	With the measure of dynamic stability the gait of post-polio patients is seen to be significantly less stable than the gait of normal individuals.
[64]	Kang and Dingwell	Since muscle activations measured using EMG do not represent muscle forces, it is not yet clear how these muscle activation dynamics result in the muscle forces that lead to the observed kinematics.	Older adults exhibited greater inter-stride variability of muscle activation patterns during gait; multi-dimensional dynamics of muscle activations are reflected in that of kinematics.

Table II.5 – (Continued)

Ref	Article	Limitations	Conclusions
[65]	Kang and Dingwell	This study only quantified responses to local perturbations. These results may or may not extend to global stability, where responses to large perturbations, like tripping or slipping would be assessed. The motorized treadmill may not properly reflect overground walking.	Even active older adults who walk at the same preferred speeds as younger adults still exhibit significantly increased orbital dynamic stability, independent of walking speed.
[66]	Kang and Dingwell	–	Superior segments exhibited less local instability but greater orbital instability compared to inferior segments. The superior segments are less sensitive to very small initial perturbations and thus its motion is initially less affected by these small perturbations, compared to inferior segments. Trunk motion dynamics appears to provide a more sensitive marker of the decline in gait function in healthy older adults compared to other body segments.
[67]	Marghitsu and Hobatho	–	The techniques of nonlinear dynamics used in this study provide an analytical tool that is easy to use in the clinical diagnosis of human gait abnormalities.
[68]	Marghitsu et al.	The 3-angle model for the animal body is a highly simplified model.	The stability index and the measures used will help to clarify and localize the source of the instability and serve to document changes in severity of the condition.
[69]	McAndrew et al.	-	Subjects experienced decreased orbital and short- term local dynamic stability in a direction-specific manner when walking during the continuous pseudo-random perturbations applied in the present study
[70]	Schablowski and Gerner	–	Two different mechanisms regarding dynamic stability of locomotion seem to exist. The increasing instability at higher speeds may be one reason for the transition from walking to running.
[71]	Scott-Pandorf et al.	True martian gravity cannot be created on the earth's surface; offloading the center of mass of an individual is not likely to be the same as true reduced gravity. Additionally, the body weight suspension system may supply some stabilizing forces.	Adding weight to the walking system while walking in simulated Martian gravity had no effect on the sagittal dynamic stability of the walking pattern.
[72]	Scott-Pandorf et al.	It is possible that the body weight support system may have provided additional stabilizing forces in the frontal plane.	Portable life support system loads at the side of the torso and low on the body improve dynamic stability of the gait pattern in simulated martian gravity.
[73]	van Schooten et al.	The time-normalization that was used was different between the walking speeds. A treadmill was used to control walking speed.	Variability and FM of trunk kinematics cannot be used to assess balance control in gait.

II.4. DISCUSSION

Although the problem of falls in the elderly is gaining increasing clinical and economical attention, assessment methods designed to identify fall-prone individuals remain controversial; biomechanical approaches for assessing gait stability seem to be able to quantify the dynamic stability of locomotion, but they have not been taken up as routine procedures in clinical settings [8]. In particular, orbital stability analysis via FM revealed effective identification of fall-related and age-related differences, but its use in the assessment of fall risk remains controversial [8]. A possible cause of this controversy could be the lack of a “standard” procedure for implementing this kind of analysis in experimental trials; different implementations could in fact lead to different results, and introduce difficulties in their interpretation.

This paper provides a systematic review of the literature in the field of orbital stability analysis application in biomechanics, with particular focus to methodological aspects. 15 articles out of 23 were of very high quality, proving the excellent level of the literature in the field.

MaxFM resulted < 1 for all the analyzed motor tasks (human gait, sewing, dog trotting); hence, those tasks were demonstrated to be orbitally stable. These results showed that the analyzed periodic motor tasks reached a stable condition when equilibrium was attained. MaxFM resulting for young subjects walking at preferred or normal speed, showed in Figure 1, confirm this aspect. Gait of pathologic subjects like post-polio patients, fall-prone elderly, or children with torsional anomalies of the lower limb joints have also been demonstrated to be orbitally stable, even if less stable than gait of healthy young subjects [13,63,67]. On the contrary, subjects with diabetic peripheral neuropathy did not experience any loss of orbital stability as a result of their sensory loss [58]. The increase in risk of falling of these patients may be due to their inability to develop and execute appropriate avoidance and/or response strategies when subjected to large-scale perturbations while walking [58]. Several studies showed how slowing down while walking does not improve orbital stability [13,58] but can eventually worsen it [70]. Only one study reported that older adults exhibited decreased instability by walking slower, in spite of increased variability [64]. These results suggest that the reduction of walking velocity, commonly observed in the elderly, may not be caused by the need to enhance orbital stability [13]. Comparison between orbital stability of gait in young and elderly subjects seems to confirm that old adults tend to be less stable while walking, partially explaining the tendency to fall. The incoherence in the results about walking with added mass does not allow drawing clear conclusions.

In general, a lack of uniformity in the methodological approaches used by the authors was found; this could also explain the different results reported by different authors for basically the same task (Figure 1). Methodological quality of the studies included in this review was in general sufficient, but articles included in the review implemented orbital stability analysis in different manners. Three main factors suffered a general lack of

homogeneity between the analyzed studies: state space definition, Poincaré section location and number of cycles analyzed (Tables 3, 4).

Whereas state space composition have been satisfactorily described by most of the manuscripts, the choice of the variables for the state space definition often lacked justification. All the state space defined in the articles seemed appropriate to adequately describe the analyzed dynamical systems; however, an "optimal" set of variables for the definition of state space for orbital stability analysis purposes have not emerged from the analyzed literature. A standardization of the variable set to be used for orbital stability analysis purposes would contribute to the interpretation of stability results and would allow to better compare stability results under different motor conditions.

As stated in the introduction, the orbital stability of a deterministic limit cycle process should be theoretically the same, regardless of the position of Poincaré section along the trajectory. This is not verified when dealing with human cyclic tasks: human cyclic movements are not strictly periodic, and consequently the response to perturbations during different phases of the task is different [34]. This aspect was confirmed by experimental results: different choices for Poincaré section position led to different values of maxFM. All the authors seem to agree that positioning the section in different instants over the task cycle allows to obtain information about orbital stability of the different phases of the task, and that mean value of maxFM across the task cycle give global information about the stability of the task.

One of the most critical issues regarding orbital stability analysis of human locomotion was found to be the number of task cycles necessary to obtain reliable orbital stability results. One article [56] stated that the "true" value of maxFM for human walking could be estimated within 300 strides; most of the articles did not report the number of cycles analyzed, or performed the analysis on a number of task cycles inferior to 300 (Table 4). When dealing with human locomotion (e.g. gait) in a movement analysis laboratory, it is possible to reach a similar number of cycles only by treadmill walking; however, whereas the use of motorized treadmill is generally justified, treadmill walking differs significantly from overground walking [80] and it is also known to enhance orbital stability [58]. Hence, conclusions obtained from treadmill walking, whereas they can be significant and useful in some context, cannot directly be transferred to overground walking.

One of the main goals of research about stability of motor tasks is to understand the mechanisms that underlie motion, particularly in case of falls. Studies included in this review showed the state-of-art in the application of orbital stability analysis via FM calculations in biomechanics.

In summary, the main explanation to the incoherence between some of the results and to the differences in the implementation of the method is believed to be the absence of a generalized methodological procedure to perform orbital stability analysis on biomechanical time series data. This kind of analysis could have a major impact in the

prevention of falls. Future research should look for a standardized methodological procedure to implement this kind of analysis, identifying the best experimental setup and analytical procedure to obtain maxFM. In order to obtain more insights on the magnitude of maxFM during human gait, analytical orbital stability analysis of the equations of a full human rigid body model can also represent a promising approach. Another fundamental issue will be the evaluation of the capability of maxFM to predict falls in the elderly.

III. INFLUENCE OF INPUT PARAMETERS ON DYNAMIC ORBITAL STABILITY OF WALKING: IN-SILICO AND EXPERIMENTAL EVALUATION²

III.1. INTRODUCTION

The analysis of modelled physiological signals of gait (accelerations, joint angles) could contribute to the assessment of the influence of implementation parameters on FM, in relation to experimental results also. Given the similarity of the signals, influences of different implementations on the stability results are likely to be analogous between model and experimental data analysis. In order to compare model and experimental results, stability in both conditions must be assured. Signals extracted from a stable walking model are hence required.

Some authors performed simulation studies on orbital stability of 1- or 2-link walking models related to fall risk [81–83]. However, these models are rather simple and simulate very peculiar walking condition. Simplicity is both the strength and the limitation of these models: their walking conditions can be easily manipulated, but they generate signals that are far from physiologic conditions of human walking. Stability analysis on a more complex model can give better insight on the orbital stability conditions of human walking, allowing the comparison between model and experimental results. In order to allow adequate comparison, stability condition must be assured for the walking model. The required conditions for the model are hence a continuous walk and the absence of falls or stumbles, in order for the model to produce kinematics as similar as possible to stable human gait.

The aim of the present study was to analyse, from an applicative point of view, the influence on the final results of orbital stability analysis applied to walking of: 1) number of analyzed cycles; 2) selection of the variables for the reconstruction of the state space; 3) experimental measurement noise on a 2-dimensional 5-link walking model [84], providing walking patterns of known stability. Results of in-silico analysis were compared to those obtained experimentally on 10 subjects performing long overground walks.

² Under review. Riva F, Bisi MC, Stagni R. Influence of Input Parameters on Dynamic Orbital Stability of Walking: In-silico and Experimental Evaluation. Submitted to Journal of Biomechanical Engineering.

III.2. MATERIALS AND METHODS

III.2.1. Overview

In-silico orbital stability analysis of a 5-link stable walking model [84] was performed. The model showed continuous walking, free of falls or stumbles, for all the simulation period (300 strides). This was also assured by a check on step variability, which was minimal following visual inspection of the phase portraits. The analysis was performed for increasing number of cycles (from 10 to 300), based on differently composed state spaces (including different joint angles and/or accelerations). Simulated experimental error and noise were added to the segmental kinematics of the model and the sensitivity of orbital stability analysis was evaluated. Orbital stability analysis was also performed on data collected experimentally on 10 subjects; given the impossibility to use a stereophotogrammetry system on a long outdoor road, only acceleration data were acquired experimentally. Orbital stability was calculated using an established technique [63].

III.2.2. *In-silico* data

The 2-dimensional, five-link biped walking model analyzed [84] consisted of a trunk, two thigh and two shank segments (Figure III.1). The model orientation was described by supporting and swinging knee angles, supporting and swinging hip angles and upper body angle ($\phi_{k,sw}$, $\phi_{k,st}$, $\phi_{h,st}$, $\phi_{h,sw}$, ϕ_{ub} , all referred to gravity direction).

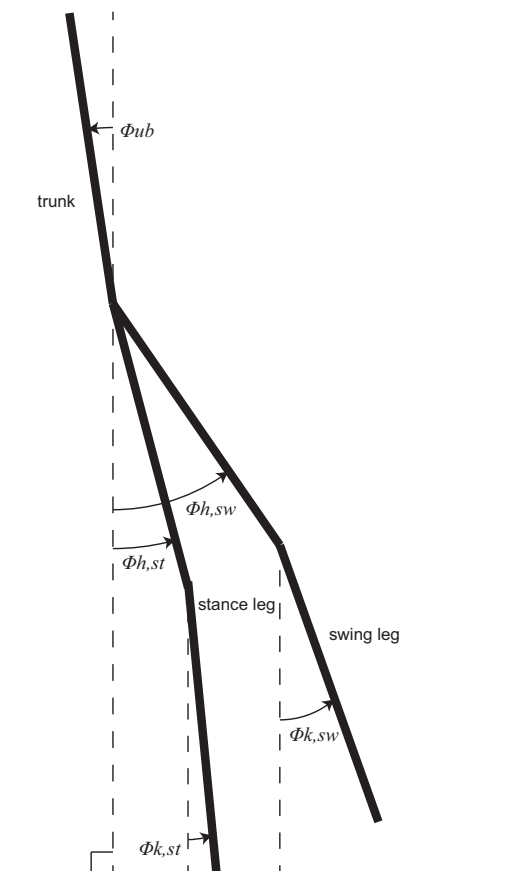


Figure III.1 - Schematic representation of the 5-link 2-dimensional model (Solomon et al., 2010).

In addition to the mentioned joint angles, the model included also the corresponding joint angular velocities. The model was adapted to perform 315 consecutive strides. The first 15 strides of the simulation were discarded in order to assure stable walking condition. The simulation was performed using a MATLAB's (Mathworks, Natwick, NA) fourth- and fifth- order variable time-step Runge-Kutta solver (ode45, with relative error tolerance set to 10^{-12}). Accelerations of the trunk segment at the level of the fifth lumbar vertebra (L5) were obtained as the second derivative of the time history of the position of a point located at 1/8 of the length of the trunk segment.

Table III.1 – Precision of the palpable anatomical landmark position (in millimeters) in the relevant mean anatomical frame obtained by Della Croce et al., 1999. For ME, LE and MM, LM the mean value between the two was used in the analysis.

Anatomical landmark	<i>x</i>	<i>y</i>
Greater trochanter (GT)	12.2	11.1
Medial Epicondyle (ME)	5.1	5.0
Lateral Epicondyle (LE)	3.9	4.9
Medial Malleolus (MM)	2.2	2.6
Lateral Malleolus (LM)	2.6	2.4

Segmental kinematics data obtained from the model were processed to simulate experimental data from a stereophotogrammetry system (joint angles) and a single inertial sensor located on the trunk (accelerations). Simulated experimental noise and errors were superimposed to segmental kinematics signals obtained from the model.

Clusters of 4 markers were virtually applied to all the segments of the model (trunk, thighs and shanks, for a total of 20 markers) and simulated instrumental normally distributed noise with a standard deviation of 0.2 mm was added to the marker trajectories (or coordinate time histories) in 2-D space. Technical reference frames were calculated from the cluster positions, and the position of the segment extremities relative to these frames was measured. A mislocation error of anatomical landmark positions (Table III.1) was also added to the estimate of the position of segment extremities [85]. Joint angles were then calculated from the relative orientation of the anatomical reference frames [86].

Instrumentation noise (white noise with an SNR of 10 dB and alignment errors with a normal distribution and a standard deviation of 0.1 degrees), compatible with the use of commercial accelerometers, was added to the acceleration signals of the trunk segment at the level of L5. Analyses on lower amounts of noise were also performed, which led to comparable results; hence, we chose to show results in the most potentially critical condition.

III.2.3. Experimental data

10 healthy participants [28 ± 3 years, 174 ± 11 cm, 67 ± 13 kg] were included in the study. Subjects gave informed consent before participating. Two synchronized tri-axial inertial sensors (Opal, APDM, Portland, OR, USA) were placed on the participants at the level of L5 and of the right shank. The range of the accelerometers was $\pm 2g$ and sample rate was 128 Hz. The participants were instructed to walk straight at self-selected speed on a 250 m dead-end long road.

III.2.4. Data processing

For both model and experimental data, stride cycles were considered as the time between consecutive right heel strikes and were resampled to be 101 samples long, because Floquet theory assumes that the system is strictly periodic. For experimental data, right heel strike instants were estimated from the angular velocity of the lower limb with a method based on wavelet analysis [87]. Angular velocity of the lower limb was measured with the inertial sensor placed on the right shank. Experimental data were analyzed without filtering, in order to avoid the complications associated with the application of linear filtering to nonlinear signals [88]. Orbital stability analysis on model data was performed on six different state spaces (Table III.2). The analysis was conducted for both noise-free and noisy condition. The same analysis was conducted on experimental data. Mean values of maxFM across the gait cycle were calculated on increasing number of strides (from 10 to 300 for model data, from 10 to 160 for experimental data).

III.3. RESULTS

The presence of noise resulted to be critical for state spaces composed by joint angles (WMhk, WMk and WMh). Analysis on WMhk in noise-free conditions led to mean values of maxFM across the gait cycle that decay with the increase of the analyzed stride cycles, until reaching the value 0.3 (for about 250 stride cycles). Standard deviation decreased with the increase of stride cycles. WMk and WMh led to values of 0.34, with low standard deviation (about 0.07), independent of the number of cycles upon which the analysis was conducted (Figure III.2); values of mean maxFM remained stable from 10 to 300 cycles. State spaces composed by noise-affected signals showed a different behavior. For WMhk, maxFM values increased until reaching the value of about 0.7, for 100 stride cycles. For WMk and WMh, mean maxFM value slowly decayed towards zero instead of stabilizing around a fixed value (Figure III.3).

Table III.2- Description of the state spaces. $\phi_{k,st}$ and $\phi_{k,sw}$ are flexion/extension knee angles for supporting and swinging limb; similarly, $\phi_{h,st}$ and $\phi_{h,sw}$ are flexion/extension hip angles. ϕ_t is flexion/extension trunk angle. a_{AP} and a_V are accelerations of the trunk at the level of L5 in anterior-posterior and vertical directions. For delay-embedded state spaces, τ is time delay and d_E is the embedding dimension ($\tau = 10$, $d_E = 5$).

Acronym	Description	Composition
WMk	Swinging+supporting knee flexion/extension joint angles (model)	$WMk(t) = [\phi_{k,st}(t), \phi_{k,sw}(t)] \in \mathfrak{R}^2$
WMh	Swinging+supporting hip flexion/extension joint angles (model)	$WMh(t) = [\phi_{h,st}(t), \phi_{h,sw}(t)] \in \mathfrak{R}^2$
WMhk	Knees, hips and trunk flexion/extension joint angles (model)	$WMhk(t) = [\phi_{k,st}(t), \phi_{k,sw}(t), \phi_{h,st}(t), \phi_{h,sw}(t), \phi_t(t)] \in \mathfrak{R}^5$
WMAp	5-dimensional delay embedding of AP accelerations of L5 (model)	$WMAp(t) = [a_{AP}(t), a_{AP}(t + \tau), \dots, a_{AP}(t + (d_E - 1)\tau)] \in \mathfrak{R}^5$
WMAV	5-dimensional delay embedding of V accelerations of L5 (model)	$WMAV(t) = [a_V(t), a_V(t + \tau), \dots, a_V(t + (d_E - 1)\tau)] \in \mathfrak{R}^5$
WMA	Accelerations in the AP and V direction of L5 (model)	$WMA(t) = [a_{AP}(t), a_V(t)] \in \mathfrak{R}^2$
EXPa	Accelerations in the AP and V direction of L5 (experimental)	$EXPa(t) = [a_{AP}(t), a_V(t)] \in \mathfrak{R}^2$

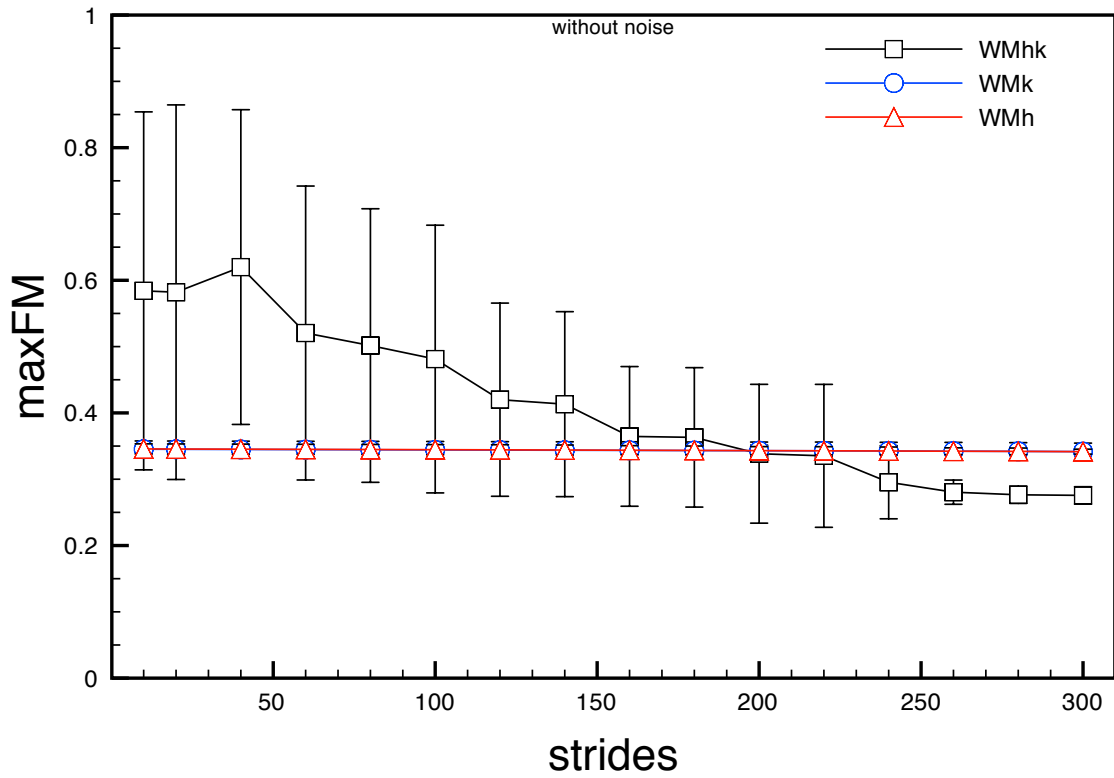


Figure III.2 - Mean maxFM values across the stride cycle calculated on state spaces WMhk, WMk and WMh (clean signals) for increasing number of stride cycles.

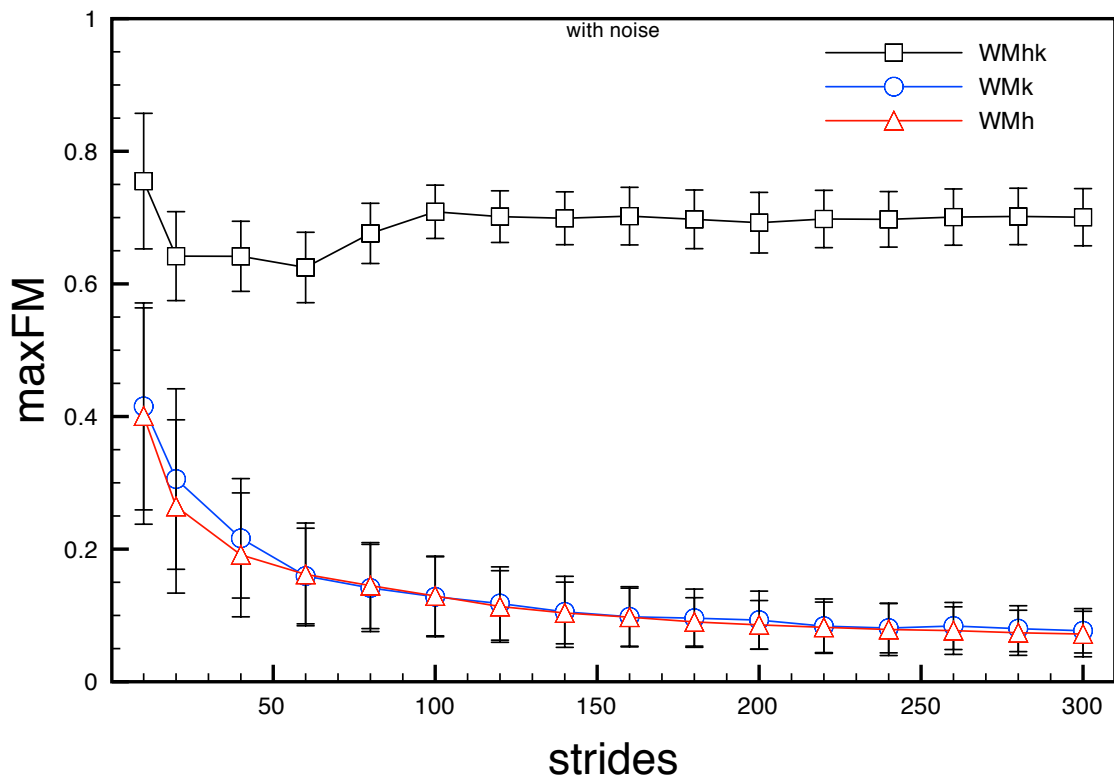


Figure III.3 - Mean maxFM values across the stride cycle calculated on state spaces WMhk, WMk and WMh (noisy signals) for increasing number of stride cycles.

MaxFM calculated on noise-free acceleration state spaces, both 2 and 5 dimensional (WMa, WMaAP and WMaV), behaved similarly: for less than 30 cycles, values of maxFM gradually decreased, starting from values near (or above) one. Starting from about 30 cycles, values of maxFM stabilized around the value previously found for joint angle state spaces (0.34 – 0.4) with a standard deviation of about 0.09 (Figure III.4). Results coming from analysis of noisy accelerations signals were very similar to those obtained from noise-free signals (Figure III.5).

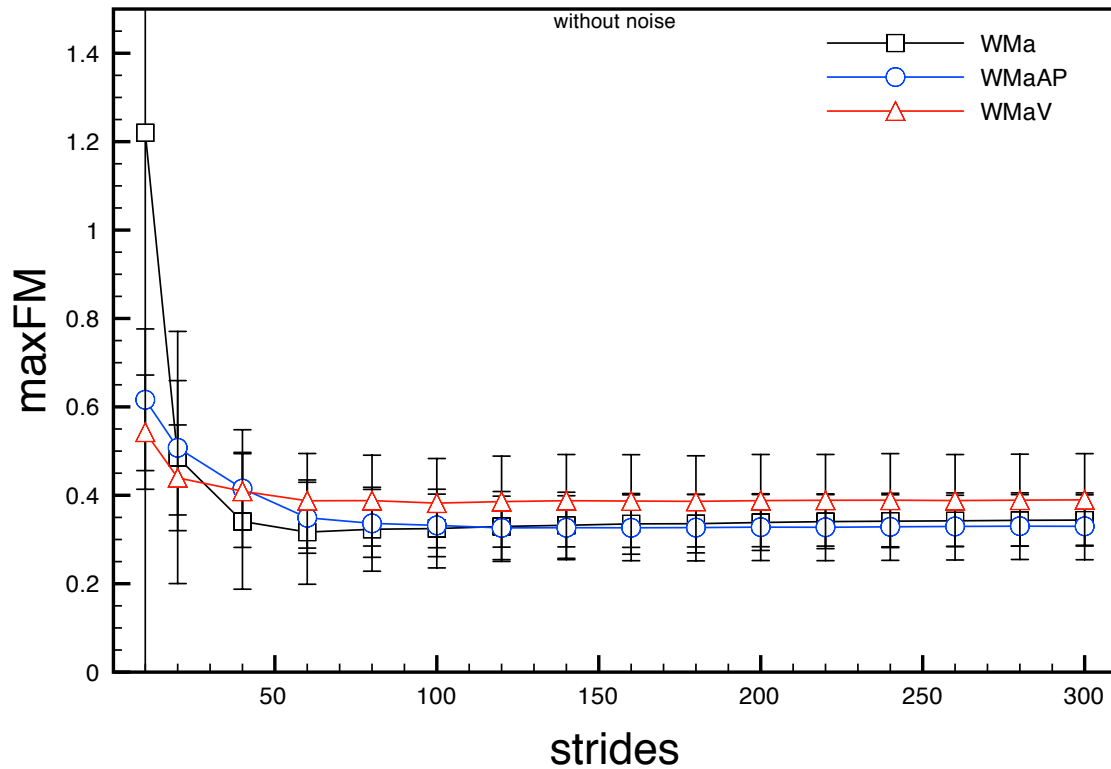


Figure III.4 - Mean maxFM values across the stride cycle calculated on state spaces WMa, WmaAP and WMaV (clean signals) for increasing number of stride cycles.

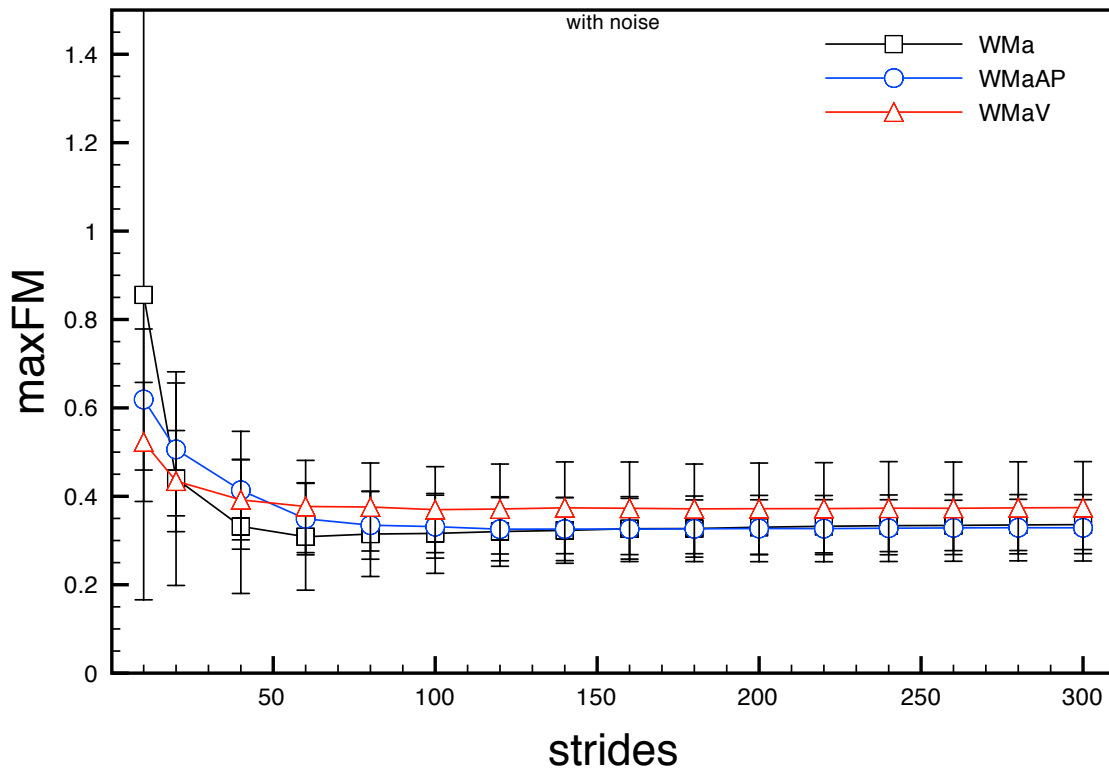


Figure III.5 - Mean maxFM values across the stride cycle calculated on state spaces WMa, WmaAP and WMaV (noisy signals) for increasing number of stride cycles.

MaxFM calculated on experimental acceleration state space (EXPa) showed decreasing value for increasing number of cycles analyzed, reaching values close to 0.4 from 80 cycles on, with a standard deviation of about 0.1 (Figure III.6).

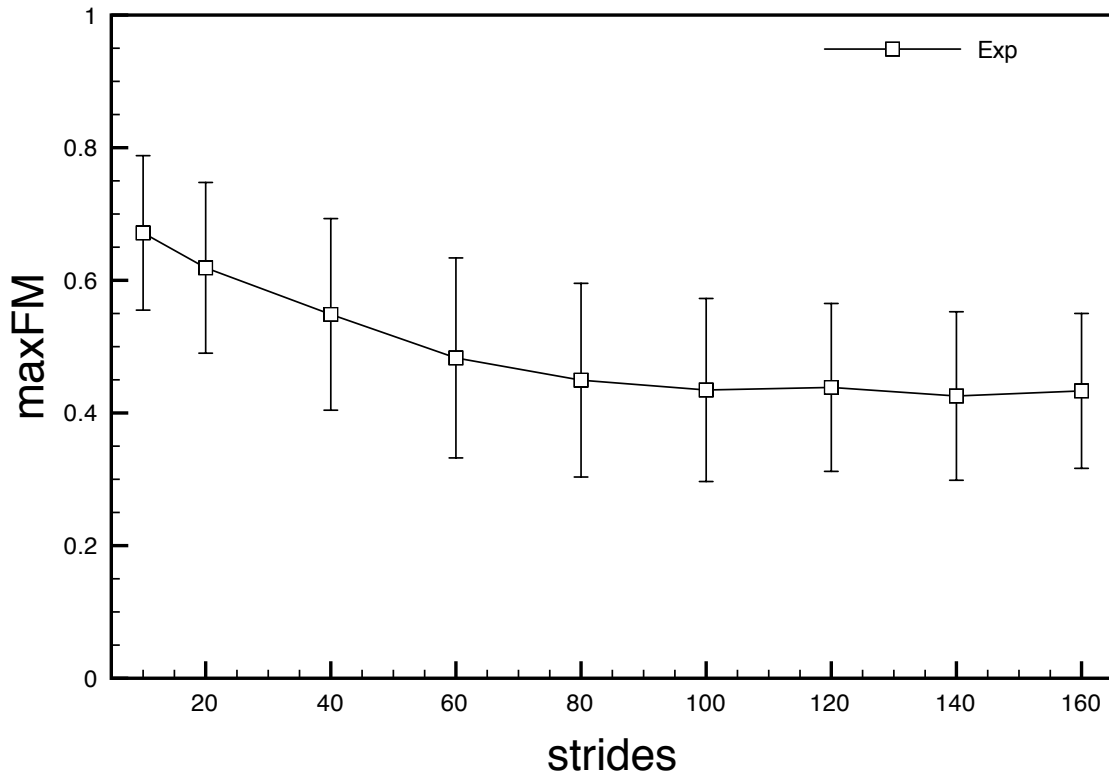


Figure III.6 - Mean maxFM values across the stride cycle calculated on state space EXPa for increasing number of stride cycles.

III.4. DISCUSSION

The possibility to have a reliable locomotor stability index is of fundamental importance in early identification and treatment of older adults with high predisposition to fall, and possibly in real-time gait instability detection also. However, still there is no unique definition of locomotor stability in literature.

Orbital stability analysis via maxFM seems promising for the analysis of cyclic locomotor tasks. When dealing with biomechanical time series, the equations of motion are obviously unknown, thus excluding the possibility to calculate maxFM in an analytical or semi-analytical way. Numerical calculation of maxFM from experimental time series is hence required, but still it is not clear how different implementations of this analysis can influence the stability measure.

Beyond the mathematical implications, it is however important to highlight that applying this analysis to human gait implies several assumptions. Human gait is an inherently stochastic system, while Floquet theory applies to deterministic limit cycle systems. Walking trajectories are continuously being "re-perturbed" by stochastic perturbations, which often are internal to the system. In order to overcome this, the average trajectory is considered to be the limit cycle, but given the likely asymmetrical nature of the basin of

attraction of human walking, this is obviously an assumption. However, orbital stability analysis was found to detect gait instability [13,69], hence proving usefulness despite the many theoretical assumptions that must be made.

In this explorative study, orbital stability analysis was applied to a 5-link stable walking model. The walking model was used in order to produce signals (joint angles and trunk accelerations) as similar as possible to real human gait signals. Stability was assumed, since the model didn't show any fall or stumble during the simulation period. Different implementations of numerical orbital stability analysis were then performed on the biomechanical signals obtained from the model. The aim was to better understand the influence of number of analyzed cycles, state space composition and experimental noise on the stability outputs. Given the similarity between model signals and real human gait data, relationships between implementations and stability results are likely to be transferrable to experimental analysis. As a comparison, experimental data of trunk accelerations during gait have also been analyzed.

The magnitude of maxFM obtained in this study was lower than values obtained in simulation studies present in literature [81–83]. Whereas those studies analyzed the behavior of 1- or 2-link walking models in presence of external/internal perturbations, in our study unperturbed walking of a 5-link was analyzed. These two aspects (the absence of perturbations and the higher complexity of the model) are likely to be the major cause of differences in the results. However, as also explicitly stated by Roos and Dingwell [82], the main aim of the cited articles was to show the general relationship between fall risk and stability measures, and not to give exact numerical values.

According to the results of the present study, the number of cycles included in the analysis played a fundamental role when trying to obtain a reliable orbital stability measure from differently composed state spaces. This influence is also correct from a theoretical point of view: for example the number of analyzed cycles cannot be lower than the dimension of the state space otherwise the set of equations would be underdetermined. A possible explanation might be that analyzing more data leads to a better estimate of the true attractor [56]. Orbital stability analysis performed on noise-free signals from the stable walking model resulted in maxFM values that tended to the value of about 0.34 for state spaces composed by joint angles and L5 accelerations. The coherence between these results is encouraging, as it seems to lead to indicate that a repeatable value of the maxFM can be obtained analyzing different state spaces. The main difference between these results was the dependence from the number of cycles considered: a limited number of cycles (about 10) was sufficient to obtain the value 0.34 with WMh and WMk, but at least 30 cycles were necessary to obtain the same result with WMa, WmaAP and WMaV. Using these state spaces for less than 30 cycles, maxFM values resulted to be high (close to or even above 1) and inconsistent, and hence are not believed to be reliable. The number of stride cycles needed to reach the value 0.34 was even higher when analyzing WMhk; it is possible that including a higher number of variables in the joint angle state space introduced redundancy, negatively influencing the results, instead of leading to a better characterization of the system. Whereas a 2-

dimensional representation of a complex system may seem insufficient in order to provide a proper characterization, it may serve the applicative purpose of obtaining a repeatable index of stability. The relationship with the stability index obtained with this implementation and the actual fall risk is, however, still to be determined.

Results coming from the analysis of noisy signals showed again a strong influence of number of cycles and state space composition on the maxFM, with different results between acceleration and kinematic data. Analysis of noisy accelerations of L5 led basically to the same results obtained for noise-free signals, for all the state spaces: simulated experimental noise on inertial sensor data did not influence maxFM calculation. This can lead to the conclusion that orbital stability analysis performed on state spaces composed by accelerations coming from inertial sensors is robust to noise, and that a high dimensional (5) reconstruction of the state space may not be necessary, as a lower dimension (2) state space led basically to the same results for the maxFM. WMk and WMh showed a very different behavior: maxFM tended to gradually decrease towards zero for increasing number of cycles, suggesting that stereophotogrammetric experimental noise and misplacement errors could dramatically influence maxFM calculation, significantly affecting their reliability. Analysis of WMhk led to the same conclusion, even though maxFM showed a different trend: maxFM values seemed to settle around the value 0.7 in about 100 strides. This value indicates very poor stability and is not coherent with results obtained from the analysis of clean signals. This suggests that the influence of noise may have had a negative impact on this result.

A possible explanation for this could be that the peculiar simulated stereophotogrammetric noise characteristics may contribute in hiding the information relative to the distance between the orbits, due to close proximity of the orbits to the limit cycle. This might not happen in an experimental trial, as the orbits defined by joint angles are likely to be less repeatable than those obtained from the model; further experimental analysis on state spaces composed by joint angles obtained from different data acquisition techniques (e.g. inertial sensors) are needed to clarify this aspect. These results are in agreement with Bruijn et al. [57], who found a correlation of 0.66 (defined “low” by the authors) between maxFM obtained from two measurement systems (accelerometers and optoelectronics).

Experimental trial results on the accelerations-based state space showed a similar trend with respect to the ones obtained from the analysis of the same variables derived from the model; nevertheless, the value of maxFM obtained was slightly higher, and so the standard deviation. A limitation of this experimental session was the relatively short length of the walks (160 strides) with respect to the model data; given the high handiness and portability of inertial sensor, however, future studies can analyze orbital stability of very long overground walks. On the other hand, 160 strides seem to be sufficient to reach a steady value for the maxFM.

Based on these results, a reliable implementation of orbital stability analysis could be obtained from an acceleration-based state space (reconstructed with delay-embedding or

including in the state space accelerations in different directions) and a number of stride cycles not inferior to 30.

In conclusion, the exploration of the influence of experimental input parameters in orbital stability analysis led to interesting results. One of the main issues relative to this technique is the necessity to properly describe the dynamical system, in order to obtain a reliable orbital stability index; hence, the definition of the state space is of crucial importance for the outputs. The coherence between the results obtained with differently composed state spaces showed that the same stability output can be obtained with different implementations and experimental setup, despite the fact that different numbers of gait cycles are necessary. On the other hand, the number of gait cycles necessary to obtain this result is different among these setups; in particular, analysis conducted on accelerometer data required more gait cycles with respect to analysis conducted on joint angles obtained from stereophotogrammetric data.

Experimental noise and operator errors could represent a critical issue when using orbital stability analysis based on joint angles obtained from stereophotogrammetric systems. Further studies are needed to determine if the stability measures obtained from analysis on these state spaces are really capable to discriminate between known stability conditions. Experimental noise on accelerometer data showed no particular influence on the stability results.

Experimental results were also coherent with the model results supporting the validity of the stability outcomes. This result confirms the possibility to obtain reliable orbital stability measures with a single inertial sensor and could lead to advantages in the development of a simple and fast data acquisition protocol, confirming what was found in literature for treadmill walking [57].

III.5. ACKNOWLEDGMENTS

The authors gratefully thank Dr. Martijn Wisse for his contribution in the implementation of the model.

IV. RELIABILITY OF STABILITY AND VARIABILITY MEASURES³

IV.1. INTRODUCTION

In order to perform a proper evaluation of gait variability and stability, standardization of implementation parameters is necessary, as outputs can be influenced by implementation differences (e.g. number of strides). Moreover, the consistency of results in the same experimental conditions between the measures must be ensured. The aim of this study is to assess the minimum number of required strides and the test-retest reliability of 11 temporal variability/stability measures proposed in the literature. Analysis was performed on trunk accelerations acquired on a sample of 10 healthy young participants performing an overground walking task. In general, the overall number of strides necessary to obtain a reliable measure was larger than those conventionally used. For some measures (ILE and RQA max/diverg in the vertical direction) 150 strides were not sufficient to obtain a steady value. MSE and RQA showed excellent reliability.

IV.2. METHODS

Ten healthy participants [28 ± 3 years, 174 ± 11 cm, 67 ± 13 kg] walked straight at self-selected natural speed on a 250 m long dead-end road (about 180 strides), wearing two synchronized tri-axial inertial sensors (Opal, APDM, Portland, OR, USA), one on the trunk at the level of the fifth lumbar vertebra and one on the right ankle. The range of the accelerometers was $\pm 6g$ and sampling rate 128 Hz. Right foot strikes were obtained from the angular velocity measured by the sensor on the ankle with wavelet analysis based method[87]. The first and the last ten strides (time intervals between two consecutive right heel strikes) were excluded from the analysis, in order to exclude gait initiation and termination phases. The Review Board Committee of the authors' institution approved this study, and informed consent was obtained from the participants.

The following variability measures were applied to stride time:

- i. SD [89];
- ii. CV [89];
- iii. IV [21];
- iv. NI [21];
- v. PSD1, PSD2 [22].

³ Under review. Riva F, Bisi MC, Stagni R. Gait variability and stability measures: minimum number of strides and test-retest reliability. Submitted to Gait & Posture.

The following stability measures were calculated on trunk accelerations in vertical (V) medio-lateral (ML) and anterior-posterior (AP) directions.

- vi. maxFM [34,49]. Four different state spaces were constructed: one 3-dimensional state space composed by acceleration signals in the V, ML and AP direction and three (one per direction) 5-dimensional state spaces composed by delay-embedding of each acceleration component (delay = 10).
- vii. sLE, ILE [34]. The same state spaces constructed for maxFM were analyzed.
- viii. RQA [47]. Same state space construction as for maxFM and LE was used. Recurrence rate (rr), determinism (det), averaged diagonal line length (avg), maximum diagonal line length (max) and divergence (diverg) were calculated from the recurrence plot (radius = 40%).
- ix. MSE [45]. Sample entropy (consecutive data points $m = 2$, distance $r = 0.2$) was calculated on six consecutively more coarse-grained (scale factor $\tau = 1, \dots, 6$) time series.
- x. HR [42]. HR was not calculated stride by stride, but decomposing the whole signal into its harmonics.
- xi. IH [43].

For the quantification of the **minimum number of strides**, measures were calculated on windows of decreasing length (from 150 to 10 strides, 1 stride resolution). Percent interquartile/median ratio (*imr*) was calculated for all the windows, starting from the 150 strides window (which gave the lowest ratio) and proceeding backwards. Thresholds for the *imr* were fixed at 10%, 20%, 30%, 40% and 50%. The required number of strides was defined as the smallest one at which the ratio remained below the lowest possible threshold. The minimum number of strides was first calculated per index and per subject, then for each index the largest number of strides over subjects was selected.

The assessment of **test-retest reliability** was performed calculating variability/stability measures on a window sliding (with 1 stride steps) along the trial. The sliding window was sized at 85 strides because this number of strides comprised the minimum number of strides for most measures (51 out of 57). ILE (tot, V, ML, AP) and RQA V (max, diverg) didn't satisfy this criterion. Interquartile and median values of the measures over the windows were calculated, and the percent *imr* for each measure was calculated. Measures were grouped in five reliability categories, ranging from very poor (*imr* > 40%) to excellent (*imr* < 10%). The maximum inter-subject *imr* was considered for grouping.

IV.3. RESULTS

Measures reached steady values for different number of strides, depending on the threshold. For MSE V ($\tau = 1, \dots, 4$) and RQA (AP rr, det, avg, ML rr and V rr, det, avg), 10 strides were sufficient to reach a 10% threshold. MSE (AP, ML, V $\tau = 5,6$), RQA (ML det, avg) and sLE V reached a 20% threshold within 10 strides. Other measures showed lower stride number requirement with the increasing of the threshold. ILE required a high number of strides (> 110) even for the 50% threshold. RQA (V max, diverg), never

reached steady values in the analyzed range (150 strides). Detailed results are shown in Table IV.1.

Table IV.1 - Number of required strides for each measure at each threshold.

Variability/stability	Thresholds				
	10%	20%	30%	40%	50%
SD	125	59	20	15	10
CV	127	59	49	15	10
NI	143	97	89	78	70
IV	143	91	44	35	29
PSD1	127	52	16	15	10
PSD2	120	106	74	25	19
MSE AP $\tau = 1$	19	10	10	10	10
MSE AP $\tau = 2$	19	10	10	10	10
MSE AP $\tau = 3$	18	10	10	10	10
MSE AP $\tau = 4$	15	10	10	10	10
MSE AP $\tau = 5$	35	10	10	10	10
MSE AP $\tau = 6$	17	10	10	10	10
MSE ML $\tau = 1$	10	10	10	10	10
MSE ML $\tau = 2$	30	10	10	10	10
MSE ML $\tau = 3$	63	10	10	10	10
MSE ML $\tau = 4$	31	10	10	10	10
MSE ML $\tau = 5$	10	10	10	10	10
MSE ML $\tau = 6$	32	10	10	10	10
MSE V $\tau = 1$	10	10	10	10	10
MSE V $\tau = 2$	10	10	10	10	10
MSE V $\tau = 3$	10	10	10	10	10
MSE V $\tau = 4$	10	10	10	10	10
MSE V $\tau = 5$	12	10	10	10	10
MSE V $\tau = 6$	15	10	10	10	10
RQA AP (\bar{r})	10	10	10	10	10
RQA AP (det)	10	10	10	10	10
RQA AP (avg)	10	10	10	10	10
RQA AP (max)	121	75	74	37	36
RQA AP (diverg)	107	95	74	74	74
RQA ML (\bar{r})	10	10	10	10	10
RQA ML (det)	78	10	10	10	10
RQA ML (avg)	55	10	10	10	10
RQA ML (max)	136	129	73	29	29
RQA ML (diverg)	136	135	79	29	29
RQA V (\bar{r})	10	10	10	10	10
RQA V (det)	10	10	10	10	10
RQA V (avg)	10	10	10	10	10
RQA V (max)	150	150	150	150	150
RQA V (diverg)	150	150	150	150	150
HR AP	141	26	15	10	10
HR ML	137	30	10	10	10
HR V	66	29	10	10	10
IH AP	143	141	137	75	10
IH ML	145	141	49	10	10
IH V	140	127	120	18	11
maxFM tot	137	135	23	10	10
maxFM AP	138	137	132	10	10
maxFM ML	137	131	14	10	10
maxFM V	137	51	20	10	10
sLE tot	105	70	10	10	10
sLE AP	90	17	10	10	10
sLE ML	72	10	10	10	10
sLE V	63	10	10	10	10
ILE tot	139	132	130	128	124
ILE AP	141	135	132	131	129
ILE ML	146	125	119	114	110
ILE V	138	123	121	116	113

Table IV.2 - Values of the maximum inter-subjects *imr* with corresponding reliability grouping. Measures have been grouped based on the maximum inter-subject percentage *imr*. Reliability has been labeled as Very poor (*imr* > 40%), Poor (*imr* = 30-40%), Average (*imr* = 20-30%), Good (*imr* = 10-20%), Excellent (*imr* < 10%). As an indication of reference values for the measures, median values of inter-subjects medians and interquartile ranges for variability/stability measures are also shown.

	Variability/stability measures	Median inter-subject value of the medians	Median inter-subject interquartile value	Maximum inter-subject <i>imr</i>
Excellent	MSE AP $\tau = 1$	0.38	0.01	0.07
	MSE AP $\tau = 2$	0.56	0.02	0.07
	MSE AP $\tau = 3$	0.65	0.02	0.06
	MSE AP $\tau = 4$	0.76	0.02	0.07
	MSE AP $\tau = 5$	0.81	0.02	0.08
	MSE AP $\tau = 6$	0.85	0.02	0.07
	MSE ML $\tau = 1$	0.59	0.01	0.08
	MSE ML $\tau = 2$	0.86	0.02	0.08
	MSE ML $\tau = 3$	1.09	0.03	0.07
	MSE ML $\tau = 4$	1.31	0.03	0.06
	MSE ML $\tau = 5$	1.46	0.04	0.06
	MSE ML $\tau = 6$	1.55	0.04	0.06
	MSE V $\tau = 1$	0.46	0.01	0.05
	MSE V $\tau = 2$	0.63	0.02	0.05
	MSE V $\tau = 3$	0.74	0.02	0.07
	MSE V $\tau = 4$	0.84	0.03	0.09
	MSE V $\tau = 5$	0.92	0.03	0.07
	MSE V $\tau = 6$	1.00	0.03	0.09
	RQA AP (rr)	15.65	0.06	0.07
	RQA AP (det)	69.3	1.1	0.05
	RQA AP (avg)	8.94	0.12	0.07
	RQA ML (rr)	8.50	0.12	0.03
	RQA ML (det)	49.7	0.8	0.09
	RQA ML (avg)	6.67	0.12	0.07
RQA V (rr)	13.76	0.22	0.06	
RQA V (det)	81.9	0.5	0.03	
RQA V (avg)	13.58	0.28	0.08	
Good	HR AP	3.70	0.14	0.15
	HR ML	2.21	0.11	0.13
	HR V	4.68	0.24	0.16
	PSD1	0.021	0.001	0.14
Average	sLE AP	0.67	0.14	0.26
	sLE ML	0.81	0.14	0.20
	sLE V	0.89	0.19	0.28
	SD	0.02	0.002	0.23
	CV	1.94	0.14	0.23
Poor	IH ML	0.15	0.02	0.37
	PSD2	0.021	0.002	0.34
	sLE tot	0.44	0.10	0.39
	NI	0.52	0.10	0.30
	IV	0.32	0.06	0.37
Very poor	maxFM tot	0.36	0.09	0.57
	maxFM AP	0.43	0.08	0.45
	maxFM ML	0.39	0.06	0.44
	maxFM V	0.48	0.08	0.44
	IH AP	0.04	0.01	0.50
	IH V	0.022	0.003	0.55
	RQA AP (max)	399	51	0.66
	RQA AP (diverg)	0.0025	0.0003	1.64
	RQA ML (max)	281	39	0.88
	RQA ML (diverg)	0.0036	0.0004	0.69
	RQA V (max)	1986	481	0.96
	RQA V (diverg)	0.0005	0.0002	1.76
	ILE tot	0.035	0.007	0.89
	ILE AP	0.035	0.008	1.12
ILE ML	0.014	0.004	0.52	
ILE V	0.041	0.007	0.57	

MSE and RQA (rr, det, avg) showed excellent reliability. HR and sLE demonstrated average to good reliability, with the exception of sLE (tot) that performed poorly. Temporal variability measures (SD, CV, IV, NI and PSD) showed from poor to good reliability. IH showed poor reliability, particularly in AP and V directions. ILE, maxFM and RQA (max, diverg) showed very poor reliability. Reliability results are shown in Table IV.2. Median values of inter-subjects medians and interquartile ranges for variability/stability measures, together with maximum *imr* values, are also shown. These values are meant to give an indication of reference values for the measures.

IV.4. DISCUSSION

The aim of this study was to investigate the minimum number of strides required and the test-retest reliability of a number of gait variability/stability measures. In general, measures showed comparable performances between the reliability indication and the threshold reached for a corresponding number of strides (85).

MSE (ML $\tau = 1, 5$ and V $\tau = 1, \dots, 4$) and RQA (AP rr, det, avg, ML rr and V rr, det, avg) reached a steady value for a 10% threshold within 10 strides. MSE and RQA (rr, det, avg) also showed excellent reliability. sLE (ML, V) showed that the 10% threshold could be reached for 85 strides, but inter-subject *imr* was slightly higher (0.20 and 0.28 respectively); this is likely due to the influence of the inherent variability of the trial. SD and CV showed average reliability and a quite high number of strides (respectively 125 and 127) to undergo the 10% threshold. This confirms findings from other studies stating that a few number of strides may not be sufficient to obtain reliable measures. While other studies in the past tested the reliability of variability gait parameters, the instrumentation used was different, making it hard to directly extrapolate results from those studies to other instruments. A high number of required strides was found for ILE and RQA (V max, diverg). The former measure required at least 110 strides to reach the 50% threshold, while the latter never reached steady values in the analyzed range. IH, maxFM, sLE and RQA (max, diverg) showed poor or very poor reliability.

In conclusion, of the 11 variability/stability measures that were tested, only MSE and RQA (rr, det, avg) showed excellent reliability. In general, the number of strides necessary to obtain a reliable measure was larger than those conventionally used.

V. ESTIMATING FALL RISK WITH INERTIAL SENSORS USING GAIT STABILITY MEASURES THAT DO NOT REQUIRE STEP DETECTION⁴

V.1. INTRODUCTION

Many gait stability measures proposed in the literature are based on the identification of gait cycles [17,22,34,90,91]. Several methods for step detection have been presented in the literature [87,92,93], based on different techniques and sensor positioning. Errors in step detection can, however, critically affect stability outcomes, making step detection a possible intrinsic source of error for stability calculations; examples are present in the literature of inability in the detection of gait events due to irregular acceleration patterns [94] and incorrect identification of acceleration peaks in correspondence of foot strike [95]. Other temporal parameters detection systems, such as foot switches or pressure sensors attached to the sole, suffer from difficulties in sensor attachment when assessing subjects with abnormal gait; even when correctly done, several problems limit their applicability [87]. Step detection can hence be invalidated by unexpected gait behaviour resulting in atypical signals, which can reflect possible informative gait characteristics or anomalies in the execution of the motor task, such as a shuffling gait. Assuming that such anomalies are more common among people with a high fall risk, such errors may even cause a bias when calculating gait stability measures. To overcome this possible source of error, nonlinear analysis techniques may offer a powerful tool. In particular, some of these stability related measures do not depend on step detection and can provide insights into the mechanisms underlying dynamic stability of walking. In this study the HR [42,44], the IH [43], MSE [45], and RQA measures [48] of trunk accelerations during gait were calculated [42–45,47,48]. The relationship between these measures and fall risk has not been analyzed and reported yet.

The aim of the present study was to investigate the association between fall history and the aforementioned measures during treadmill walking in a large sample of older subjects. The data used have been described earlier in a paper on local dynamic stability and stride variability of gait [39]. Both of these measures were shown to be associated with fall risk, but do rely on step detection.

⁴ In press. SIAMOC methodological award 2012. Riva F, Toebes MJP, Pijnappels M, Stagni R, van Dieën JH. Estimating fall risk with inertial sensors using gait stability measures that do not require step detection. *Gait & Posture*, in press.

V.2. MATERIALS AND METHODS

V.2.1. Participants

A total of 131 healthy subjects (age 62.4 ± 6.1 years; height 171 ± 8 cm; body mass 74 ± 10 kg) aged between 50 and 75 participated in the study, after giving informed written consent. Subjects were recruited and tested at a fair aimed at people of 50 years and older. Subjects were included if they were aged between 50 and 75 years and able to walk on a treadmill without aids. Additional details have been reported by Toebe et al. [39]. Three subjects from the original data set were excluded from the analysis due to technical problems during data acquisition.

V.2.2. Protocol

Participants walked on a treadmill at 4 km/h for 12-17 minutes, wearing an inertial sensor (Dynaport Hybrid, McRoberts B.V., The Hague, The Netherlands) located on the trunk, below the shoulder blades. Sensing range was $\pm 2g$ and sample frequency was 100 Hz. The first 5-10 minutes of walking were excluded from the data collection, to allow the subject to familiarize with treadmill walking. Data of the subsequent 3 minutes of walking were acquired. Fall history was obtained by self-report; a subject was classified as a faller if at least one fall had occurred in the 12 months prior to the measurements. 42 subjects (32.1%) experienced at least one fall in the year previous to the experiment. To estimate the habitual physical activity in daily life, the Longitudinal Aging Study Amsterdam Physical Activity Questionnaire (LAPAQ) was used. The LAPAQ data were used to calculate the total physical activity score (in MET·minutes·per day) [96]. Subjects were classified as experienced treadmill walkers if they had walked on a treadmill at least two times previously.

V.2.3. Data analysis

Accelerations of the trunk in the anterior-posterior (AP) and medio-lateral (ML) directions were analyzed. Vertical acceleration signals showed clipping artefacts (on average 0.34% of the signal) in 52% of the subjects, and were therefore not considered in the analysis. HR, IH, MSE and RQA were calculated on AP and ML accelerations of the trunk.

V.2.4. Statistical analysis

To assess differences in demographics, treadmill experience and physical activity between fallers and non-fallers, Mann-Whitney U-test, independent samples t-test and chi-square test were used. SPSS Statistics 20.0 (IBM, Armonk, NY, USA) was used for all statistical tests. Statistical significance for all statistical tests was declared if $p < 0.05$.

A factor analysis was performed to assess to what extent the resulting 24 different measures (HR, IH, MSE at 6 different scales and 4 RQA measures, both in AP and ML directions) reflect different properties of the dynamics. To correct for non-normality, all measures were log transformed and then used as input for factor analysis. The scree plot

was used to determine the number of extracted factors, and VariMax rotation was used to optimize the loading of variables onto factors.

Log transformed measures were then used as inputs for univariate logistic regression models, to test if measures were able to classify subjects as fallers or non-fallers, considering self-report as the gold standard. The resulting regression models were then checked for confounders (demographic variables, treadmill experience and physical activity score). In addition, a multivariate, forward step-wise logistic regression model was constructed using the most representative variables of each factor as predictors, i.e. the variable with the highest factor loading for each factor. Potential confounders were added to the models one by one and retained when they changed the coefficients by more than 10%.

V.3. RESULTS

Factor analysis on the 24 log transformed measures led to 7 factors (Table 1), accounting for 89% of the variance (all eigenvalues > 0.8). In general, absolute factor loading values were > 0.5 , with the exception of HR in AP direction, which had cross loading on 3 factors and was considered non-specific to a factor. RQA parameters in AP direction showed quite high (absolute value > 0.4) loading on two factors. Parameters of MSE, IH, RQA in the ML direction and HR in the ML direction showed loadings on different factors, reflecting the description of different system dynamics. Furthermore, parameters for the trunk kinematics in the ML and AP were largely independent as reflected in the factor loadings. In summary, Factor 1 mainly reflected AP entropy and recurrence characteristics, Factor 2 reflected ML entropy, Factor 3 reflected ML recurrence characteristics, Factor 4 reflected ML harmonicity, Factor 5 reflected AP harmonic ratio, Factor 6 reflected AP harmonicity, and Factor 7 reflected ML harmonic ratio.

Univariate associations with fall history were found for MSE and RQA measures in the AP direction (Table 2). The best classification results were obtained for MSE with scale factor $\tau = 2$ ($p < 0.001$) and for maximum length of diagonals in RQA ($p = 0.002$), which correctly classified 72,5% (sensitivity 21.4%, specificity 96.6%) and 71% (sensitivity 16.7%, specificity 96.6%) of cases, respectively. All MSE measures in AP direction showed correlations $> 70\%$. Other measures showed no significant association with fall history (Figure V.1, Table V.2). The multivariate model retained only AP direction MSE with $\tau = 3$, and this model yielded slightly worse classification than the model using MSE with $\tau = 2$. All models were checked for possible confounders (demographics, physical activity score, treadmill experience); none of the variables changed the coefficients by more than 10%.

As reported previously by Toebe et al. [39], no significant differences were found between fallers and non-fallers regarding demographic variables, physical activity score and treadmill experience.

Table V.1 - Loading of log transformed variables after factor analysis. Absolute loadings > 0.4 are shown.

Stability measure	Factor 1	Factor 2	Factor 3	Factor 4	Factor 5	Factor 6	Factor 7
HR ML							0.951
HR AP	-0.498				0.790		
MSE ML ($\tau = 1$)		0.938					
MSE ML ($\tau = 2$)		0.946					
MSE ML ($\tau = 3$)		0.970					
MSE ML ($\tau = 4$)		0.961					
MSE ML ($\tau = 5$)		0.899					
MSE ML ($\tau = 6$)		0.823					
MSE AP ($\tau = 1$)	0.913						
MSE AP ($\tau = 2$)	0.960						
MSE AP ($\tau = 3$)	0.968						
MSE AP ($\tau = 4$)	0.960						
MSE AP ($\tau = 5$)	0.947						
MSE AP ($\tau = 6$)	0.919						
IH ML				0.860			
IH AP						0.901	
RQA ML rr				0.884			
RQA ML det			0.716				
RQA ML avg			0.848				
RQA ML max			0.764				
RQA AP rr	-0.837						
RQA AP det	-0.721						
RQA AP avg	-0.725	0.448					
RQA AP max	-0.701	0.437					

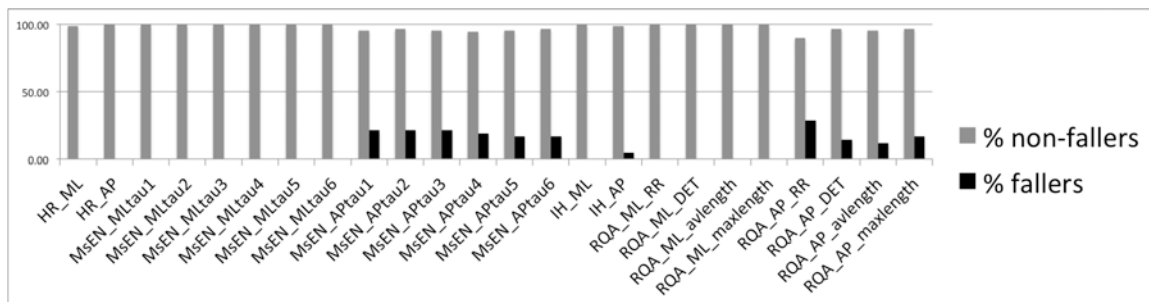


Figure V.1 – Classification results

Table V.2 - Result of the univariate logistic regression models. Regression coefficient (β), p-value (p) and 95% confidence interval of β (95% CI $_{\beta}$) are shown.

Stability measure	β	p	95% CI $_{\beta}$
HR ML	3.135	0.113	-0.74 – 7.01
HR AP	-2.016	0.183	-4.98 – 0.95
MSE ML ($\tau = 1$)	1.579	0.689	-6.15 – 9.31
MSE ML ($\tau = 2$)	0.208	0.951	-6.44 – 6.86
MSE ML ($\tau = 3$)	1.119	0.75	-5.78 – 8.02
MSE ML ($\tau = 4$)	1.915	0.63	-5.87 – 9.70
MSE ML ($\tau = 5$)	3.861	0.376	-4.68 – 12.41
MSE ML ($\tau = 6$)	4.525	0.312	-4.25 – 13.30
MSE AP ($\tau = 1$)	8.994	0.002	3.34 – 14.65
MSE AP ($\tau = 2$)	9.138	0.001	3.68 – 14.60
MSE AP ($\tau = 3$)	9.191	0.001	3.82 – 14.56
MSE AP ($\tau = 4$)	8.594	0.001	3.39 – 13.80
MSE AP ($\tau = 5$)	7.750	0.002	2.80 – 12.70
MSE AP ($\tau = 6$)	7.010	0.004	2.26 – 11.76
IH ML	-3.102	0.105	-6.85 – 0.65
IH AP	-4.072	0.128	-9.32 – 1.17
RQA ML rr	-2.688	0.14	-6.26 – 0.89
RQA ML det	-0.470	0.843	-5.11 – 4.17
RQA ML avg	0.106	0.959	-3.94 – 4.16
RQA ML max	-0.001	0.999	-0.94 – 0.94
RQA AP rr	-8.510	0.999	-13.12 – -3.61
RQA AP det	-4.197	0.001	-7.34 – -1.05
RQA AP avg	-6.485	0.009	-11.04 – -1.94
RQA AP max	-2.410	0.005	-3.90 – -0.92

V.4. DISCUSSION

Nonlinear measures can provide useful insights in the dynamics of gait, and in particular of gait stability. Currently, fall risk is mainly inferred from fall incidence, but this method obviously provides information only after the fact and has proven to be unreliable, especially when dealing with subjects with memory impairments [97]. Alternative fall risk measures are hence needed, and quantitative nonlinear dynamic measures applied to acceleration signals could represent a viable alternative to more traditional fall risk assessment methods; accelerometric systems are very useful for clinical purposes, as they are small, light and portable. Some of these measures (HR, IH, MSE and RQA were analyzed in the present study) do not require stride detection, excluding a possible source of error. This study aimed to explore the relationship of such measures (HR, IH, MSE and RQA were analyzed in the present study) with fall history.

In the literature, one study[39] assessed the association between 'linear and nonlinear measures (namely gait variability and Lyapunov exponents), concluding that these

parameters were, individually and combined, positively associated with fall history. Another study [14] investigated the association between Lyapunov exponents and tendency to fall in older adults, but on a significantly smaller sample. The nonlinear measures implemented in our study have already been applied to gait parameters [42,43,45,47], but their relationship with fall history has, to authors' knowledge, not been investigated yet.

The factor analysis on the analyzed measures highlighted a quite sharp separation (Table V.1), supporting the hypothesis that the techniques describe different aspects of the system dynamics; each one of these aspects can reflect different aspects of locomotion features, and could contribute information related to fall risk.

Although previously effects of age were shown for HR in AP direction [98], HR and IH did not show any correlation with fall history in our sample. Harmonicity of oscillations and rhythmicity of the accelerations of the trunk hence seem not to provide useful information for fall risk assessment.

Costa et al. found that the spontaneous output of the human locomotor system during usual walking is more complex than walking under slow, fast or metronome paced protocols [45]. The association between MSE and fall history found in the present study seems to suggest that complexity can also be related to fall risk. Modifications in complexity could reflect alterations in locomotor strategy that affect stability. In particular, MSE with a scale factor $\tau = 2$ led to the best classification results, suggesting that frequencies in the band of 17-25 Hz contribute the most; in fact, operating two coarse graining procedures on gait acceleration signal would filter frequencies higher than 25 Hz, while operating three would filter frequencies higher than 17 Hz.

The present findings seem to suggest higher complexity of gait kinematics in subjects with a fall history, while previous studies have associated higher entropy with better health [46,99]. This is perhaps not surprising, since nonlinear time series analysis often showed contradictory results also when applied in the same context, as it has been demonstrated for FM [49]. Also, non-monotonic relationships could exist. Moreover, results of nonlinear time series analysis of gait accelerations also strongly depend on sensor placement [42].

A previous study [47] used RQA to differentiate healthy and hypovestibular subjects; our findings extend this result, showing that RQA can discriminate between healthy subjects and fall-prone subjects. In the present study, RQA measures, and in particular the maximum length of diagonal structures in recurrence plots, were found to correlate with fall history. RQA (max) is strictly related to the mechanical concept of stability in terms of Lyapunov exponents; in fact, its inverse (called divergence) can roughly reflect the largest Lyapunov exponent [48,100,101]. These results are in line with the existing literature showing an association between short term Lyapunov exponents and fall history [39]. Whereas these two measures express theoretically similar concepts, the calculation

process is different; in particular, as stated above, the RQA algorithm does not depend on stride detection.

For all gait variables, specificity of the associations with fall history was low (maximally 21.4%). This may imply that the present methods are not yet suitable to identify individuals at risk of falling and thus the target group for interventions. Combinations with other variables in a multivariate prediction model, e.g. variables that reflect physical capacity, may be necessary. On the other hand, fall history may comprise a substantial number of incidental falls in subjects, exposed to high-risk events, who may not necessarily have an increased risk due to intrinsic factors.

A possible limitation of the present study is the fact that subjects walked on a treadmill; hence, conclusions cannot be directly transferred to over-ground walking, due to the differences between the two motor tasks [38,102]. Moreover, no procedure was applied to precisely standardize the acceleration signals direction, in terms of sensor placement; however, due to the intrinsic nature of the task and the instrumentation, straight walking was assured. Another limitation is the use of self-report as a gold standard for the classification; despite the disadvantages, this method represents the most established technique for fall risk assessment [8], and hence this choice is unavoidable.

In the literature, a standard implementation for the measures studied here is lacking. Due to the lack of methodological studies, there is no consensus on how to deal with methodological aspects such as sample frequency of the signal, instrumentation noise and trial length. For this reason, comparison of results from different implementations of the same measures is not straightforward. With respect to the length of the trials, these measures, particularly RQA, have often been applied to short trials (a few steps). In the opinion of the authors, the analysis of longer trials is preferable for several reasons: effects of long range dynamics, acclimatization time and the probability that occasional gait anomalies show up during the acquisition. On the other hand, also transfer from our results to less controlled acceleration data obtained during daily activities, in which stride detection is a major problem, needs further exploration.

Further research should address the physiological correlates of these measures; whereas the analysis of acceleration time series give useful information about gait dynamics and fall risk, the physiological conditions leading to differences in complexity or recurrence of locomotion acceleration signals are yet unknown. The identification of the physiological correlates could lead to the development of proper targets for therapies or rehabilitation programs aiming at fall prevention.

In conclusion, nonlinear dynamic measures, in particular MSE and RQA are positively associated with fall history and could contribute to the selection of individuals at risk for participation in fall prevention programs.

VI. ARE GAIT VARIABILITY/STABILITY MEASURES INFLUENCED BY DIRECTIONAL CHANGES?⁵

VI.1. INTRODUCTION

Directional changes represent an essential aspect of gait, since 20-50% of steps performed during daily activity are reported to be turns [24]. As a methodological characterization, an assessment of the influence of directional changes on variability/stability measures is needed in order to evaluate the applicability of the measures, both in controlled laboratory trials and in daily life activity analysis. In this study, nine variability/stability measures were calculated on trunk acceleration data of a sample of healthy young subjects walking in straight walking condition and in presence of directional changes. Since large differences in sampling are believed to affect stability measures [37], the influence of sampling frequency of trunk acceleration data on the results was also analyzed.

The aim of this study was to assess the influence of directional changes on variability/stability measures calculated on trunk acceleration data acquired at different sampling frequencies during gait.

VI.2. METHODS

Fifty-one healthy young adults (23 ± 3 years, 172 ± 11 cm, 68 ± 14 kg) volunteered for this study. All subjects were physically active and self-reported no musculoskeletal or neurological disorders that could affect their performance and/or behavior.

Participants were asked to perform one 6-minute walk test [103]. In particular, they were asked to walk back and forth for 6 minutes along a 30m straight pathway, turning by 180 deg at each end of the pathway, and to cover the maximum possible distance over the 6 minutes and, thus, walking as fast as possible. A 180 deg turn was considered in order to test the limit condition, as it represents the most sharp and potentially hazardous directional change. The Review Board Committee of the authors' institution approved this study, and informed consent was obtained from the participants.

An inertial measurement unit (FreeSense, Sensorize s.r.l) was fixed to the lower trunk of the subjects. Only acceleration data was taken into consideration.

⁵ Submitted. Riva F, Grimpampi E, Mazzà C, Stagni R. Are gait variability/stability measures influenced by directional changes?. Submitted to Gait & Posture.

Twenty-six trials were acquired with a sampling frequency equal to 100 Hz and twenty-five trials were acquired at 200 Hz. A third set of data was then obtained from the second group, down-sampling acceleration signals from 200 Hz to 100 Hz, and added to the 100 Hz group. Foot strikes were detected from the vertical acceleration using the algorithm proposed by McCamley et al. [104]. Two portions of signals (about 20 strides each) were extracted for each subject and divided in two groups: straight walking (SW) and walking with directional change (DCW). The number of strides was chosen as the maximum number of strides reachable by the subjects in completely straight walking conditions.

Nine variability/stability measures were calculated. Three temporal variability measures were applied to stride time: SD [21], CV [21] and Poincaré plots (PSD1, PSD2) [22]. Stride times were obtained as the time intervals between two consecutive strikes of the same foot. Six stability measures were calculated on trunk acceleration signals in the vertical (V), medio-lateral (ML) and anterior-posterior (AP) directions: maxFM [34], sLE [34], RQA [47], MSE [45], HR [42] and IH [43]. IV [21], NI [21], ILE [34] and RQA (max, diverg) [47] were also considered, but 20 strides were not deemed to be sufficient to draw accurate conclusions having an intrinsic variability > 50%, based on the results illustrated in Chapter IV. Details on the implementation can be found in Chapter IX (Appendix).

In order to assess the influence of directional changes on the measures, significant differences in results between SW and DCW conditions were calculated. Z-scores between the two conditions were calculated for each measure for the two sampling groups (100 Hz and 200 Hz). Bonferroni-corrected p-values for each measure at each sampling condition were then calculated based on the z-scores. Measures were selected based on the capability to discriminate between the two conditions ($p < 0.05$) for the majority (> 20 for 200 Hz group, > 40 for 100 Hz group) of subjects. The increasing or decreasing effect of directional changes has also been assessed, based on the sign of the mean value of the difference between measures obtained in SW and DCT conditions.

VI.3. RESULTS

Only HR was found to be affected by directional changes, both at 200 Hz and at 100 Hz. HR decreased when a directional change was present in the task. HR was affected in the AP and V directions for the 200Hz, but only in AP direction for the 100Hz group.

Other measures (SD, CV, PSD1, PSD2, MSE, RQA, maxFM and sLE) were not found to be affected by directional changes in the walk.

VI.4. CONCLUSION

Variability measures based on stride time were generally found to be not affected by directional changes. It is likely that the stride times suffered minor modifications during the 180 deg turn, hence not significantly influencing measures based on its variability.

HR was the only measure found to be affected by directional change. In particular, it was affected when applied to AP and V accelerations, but not when ML accelerations were analyzed.

IH, maxFM, sLE and RQA were not found to be affected by directional changes. MSE, sLE and RQA also recently proved to be related to fall history in treadmill walking tests [39,105].

The sampling frequency had effects on the measures, but only related to the direction of the acceleration. At 100 Hz, only HR in the AP direction was found to be affected by directional change, while at 200 Hz AP and V directions were affected. This is likely caused by the loss of information induced by the lower sampling frequency.

In conclusion, temporal variability measures were not affected by directional changes. IH, MSE, sLE and RQA were not affected by of directional changes. In particular, MSE, sLE and RQA could contribute to the definition of a fall risk index in free-walking conditions, based on their previously demonstrated association with fall history [39,105]. Further research is needed to assess the capability of these measures to identify fall-prone subjects in an overground walking task.

VII. STABILITY OF WALKING AND SHORT TERM FALL-HISTORY

VII.1. INTRODUCTION

The assessment of the association between variability/stability measures and fall history should highlight if these indicators are capable to detect any eventual *structural* alteration in gait patterns. The application of such measures to portions of acceleration signal that are located in the proximity of a fall should instead assess the capability of such indicators to detect if the gait pattern undergo a particular modification which may cause a critical loss of stability. The detection of this *temporary* modification may become particularly evident in the case of fall-prone pathological subjects, which can experience several falls even in a short period of time.

Ten variability/stability measures were applied to a database of trunk acceleration data acquired during a 24 hour monitoring of 20 parkinsonian fall-prone subjects affected by progressive supranuclear palsy. The subjects experienced a fall during the monitoring, hence allowing to know the temporal distance from the fall episode and the analyzed walking window. The aim of the study was to test if variability/stability measures can i) discriminate between the close-to-a-fall and the far-from-a-fall conditions; ii) discriminate between unfrequent faller and frequent faller subjects; iii) discriminate between the pre-fall and the post-fall conditions. In addition, a case study was analyzed in order to iv) observe the behavior of variability/stability measures in the very proximity (< 30 minutes) of a fall episode compared to a far-from-a-fall condition.

VII.2. METHODS

Twenty elderly subjects (7 unfrequent fallers, 13 frequent fallers) affected by Progressive supranuclear palsy (PSP) were monitored in daily activity for 24h, using an accelerometer located on the trunk (data were supplied by Bagalà et al., University of Bologna). A subject was classified as frequent faller if his fall rate was ≥ 1 fall/month.

Five subjects fell during the registrations. For some subjects, more than one 24h registration was available, and thus were considered to be additional subjects. This led to a total of ten subjects who fell during the registrations that were considered for the analysis. Trunk acceleration signals relative to three windows containing only walking activity were extracted. Each window included a number of strides comprised between 30 and 70. In order to obtain comparable results among the subjects, 30 strides for each window were used for the analysis.

Ten variability/stability measures were calculated on the three windows. Six temporal variability measures were applied to stride time: SD [21], CV [21], IV [21] and Poincaré plots (PSD1, PSD2) [22]. Stride times were obtained as the time intervals between two consecutive strikes of the same foot, detected from the AP trunk acceleration with a peak detection method [92]. Four stability measures were calculated on trunk acceleration signals in the vertical (V), medio-lateral (ML) and anterior-posterior (AP) directions: Recurrence quantification analysis (RQA) [47], Multiscale entropy (MSE) [45], Harmonic ratio (HR) [42] and Index of harmonicity (IH) [43]. NI [21], ILE [34] were also considered, but the number of strides included in the windows (30 strides) was not deemed to be sufficient to draw accurate conclusions, having an intrinsic variability > 50% based on the results illustrated in Chapter IV. Based on the same results, for RQA (max, diverg) [47] only ML direction was considered. Details on the implementation can be found in Chapter IX (Appendix).

Four different analyses were performed on the sample: i) a comparison between the close-to-a-fall (CF) and the far-from-a-fall (FF) conditions; ii) a comparison between variability/stability measures calculated on unfrequent fallers (UnF) and frequent fallers (FrF); iii) an overall analysis on the pre-fall (PrF) and post-fall (PoF) condition; iv) a case study analysis on a subject for which the walking windows were extracted particularly close to a fall (< 30 minutes).

VII.2.1. Close to a fall / Far from a fall

In order to define the CF and FF conditions, a threshold equal to 8 hours was set, being the median of the time distances from the nearest fall of all the extracted windows. Two windows for each subject were considered, one close to the fall and one far from the fall, disregarding if the fall episode occurred before or after the extracted window. Three subjects satisfied this criterion, and hence were selected for the analysis.

Z-scores for each subject were calculated between the results of the measures in the two conditions (CF and FF), using as variance the between-subjects median value of the interquartile obtain in a previous study (see Chapter IV). Bonferroni-corrected p-values were then obtained.

VII.2.2. Unfrequent fallers / Frequent fallers

Two groups were created. The first was composed by measures calculated on unfrequent fallers windows (UnF). The second was composed by measures calculated on the windows that were considered to be far from a fall (time distance > 8 hours) of frequent fallers that experienced a fall during the registrations (FrF). To assess the differences between the two groups, a t-test was performed.

VII.2.3. Pre-fall / Post-fall

Measures calculated on the windows for all the subjects were re-grouped, disregarding the information relative to the subjects, in two groups (PrF and PoF), based only on the

sign of the time distance from the nearest fall. To assess the differences between the two groups, a t-test was performed.

VII.2.4. Single subject case study

A single subject with a favorable location of the time windows with respect to the fall episode was analyzed. The three time windows extracted were located at 18m before the fall episode (PrF), 30m (PoF) and 20h after the fall episode (FF).

Z-scores of measures between the PrF/PoF and the FF condition were calculated, using as variance the between-subjects median value of the interquartile obtain in a previous study (see Chapter IV). Bonferroni-corrected p-values of the two conditions in relation to the FF condition were then obtained.

VII.3. PRELIMINARY RESULTS

VII.3.1. Close to a fall / Far from a fall

HR, MSE AP ($\tau = 2, \dots, 6$), RQA ML (diverg) and IV didn't highlight any difference between the CF and the FF condition for all the three subjects. SD, CV, IH (ML, V), PSD1, PSD2, MSE V ($\tau = 2, 3, 5$), RQA AP (rr, det, avg), RQA ML (rr, det, avg) and RQA V (det) found statistically significant differences between the two conditions for all the three subjects. Results are illustrated in Table VII.1.

VII.3.2. Unfrequent fallers / Frequent fallers

HR (AP, V), IH (AP, V) and RQA (AP det, ML det, V diverg) found statistically significant differences between the UnF and the FrF groups. Other measures didn't find any difference.

VII.3.3. Pre-fall / Post-fall

Only PSD1 was found to be significantly different between the PrF and the PoF condition. Other measures didn't highlight any difference.

VII.3.4. Single subject case study

HR, MSE AP ($\tau = 4, \dots, 6$) and RQA V (max) didn't highlight any difference between the PrF/PoF and the FF condition. RQA V (avg, diverg) and NI didn't find differences between the PrF condition and the FF condition. MSE AP ($\tau = 1, \dots, 3$), RQA ML (diverg), RQA V (rr) and IV didn't find any differences between the PoF condition and the FF condition. All other measures were found to be significantly different between the PrF/PoF and the FF condition.

Table VII.1 – Significance of measures between the CF and FF condition

Significantly different for 3/3 subjects	Significantly different for 2/3 subjects	Significantly different for 1/3 subjects	Non significantly different
IH (ML, V)	IH (AP)	MSE AP ($\tau = 1$)	HR (AP, ML, V)
PSD1	MSE ML ($\tau = 1, \dots, 6$)	RQA ML (max)	MSE AP ($\tau = 2, \dots, 6$)
PSD2	MSE V ($\tau = 1, 4, 6$)		RQA ML (diverg)
MSE V ($\tau = 2, 3, 5$)	RQA V (rr, avg)		IV
RQA AP (rr, det, avg)			
RQA ML (rr, det, avg)			
RQA V (det)			
SD			
CV			

VII.4. CONCLUSION

A possible limitation of the studies i) and ii) is the large temporal threshold (8 hours) that had to be fixed in order to separate subjects in the CF and FF conditions. Temporal variability measures (SD, CV, PSD1, PSD2) were found to be different in proximity of a fall episode. In particular, PSD1 was also capable to highlight differences between the pre- and post-fall conditions. HR, IH and RQA showed to be sensitive to the frequency of the falls experienced by the subjects, being capable to discriminate between frequent and infrequent fallers, although not for all acceleration directions. MSE and RQA showed different behaviors, highly influenced by the direction of the trunk acceleration. Particularly interesting is the result of MSE AP ($\tau = 1, \dots, 3$), which performed poorly in discriminating between CF and FF when the threshold was high, but was able to discern between the two conditions in the very few minutes before a fall. Having been associated with fall history [105], this measure seems capable to reflect potentially critical changes in the gait pattern. However this result has been obtained from a single subject, and conclusions must hence be drawn carefully.

VIII. CONCLUSIONS

Falls in the elderly pose a serious problem in society, both clinically and economically. From a clinical point of view, falls are often associated with injuries (e.g., hip fractures) [4], and have a negative psychological impact on patients [106]. Moreover, older adults may restrict their activities in response to a fall, leading to a loss of independence and ability to carry out life's routine tasks [107].

In this context, reliable methods for quantifying fall risk are needed, in order to adequately select subjects to include in fall prevention programs. Since falls often occur during walking [17,18], assessment of gait stability represents a crucial indicator for fall risk. Many methods (*direct*, *indirect* and *stability-related*) to quantify gait stability are presented in literature; however, the relationship between many of these stability measures and fall history/fall risk is still unknown, and there is still no consensus in the literature on how to correctly interpret the stability indicators and how to effectively implement stability analysis methods to obtain reliable stability outcomes.

The aim of this thesis was to analyze the influence of experimental implementation parameters on stability measures and to understand how variations in these parameters affect the outputs. The assessment of the relationship between dynamic stability measures and long/short-term fall risk was also an objective of this thesis.

In Chapter II a systematic review of the literature on the topic of biomechanical applications of a nonlinear dynamic stability measure (namely orbital stability analysis via maximum Floquet multipliers) is presented. The review highlighted an incoherence among the results of the studies present in the literature, believed to be due mainly to the absence of a generalized methodological procedure to implement orbital stability analysis on biomechanical time series data [49] and confirming the uncertainty regarding how to properly apply stability measures in biomechanics and the association of these measures with risk of fall.

As a consequence of the results obtained from the review, an experimental- and model-based study on the influence of experimental input parameters in orbital stability analysis was performed. The results are presented in Chapter III. One of the main issues relative to this technique is the necessity to properly describe the dynamical system, in order to obtain a reliable orbital stability index; hence, the definition of the state space is of crucial importance for the outputs. The coherence between the results obtained with differently composed state spaces shows that the same stability output can be obtained with different implementations and experimental setup, despite the fact that different numbers of gait cycles are necessary. On the other hand, the number of gait cycles necessary to obtain this result is different among these techniques; in particular, analysis conducted on

accelerometer data requires more gait cycles. Experimental noise and operator errors could represent a critical issue when using orbital stability analysis based on joint angles obtained from stereophotogrammetric systems, while experimental noise on accelerometer data showed no particular influence on the stability results. Experimental results were also coherent with the model results, supporting the validity of the stability outcomes.

In Chapter IV, an assessment of the minimum number of strides needed and a test-retest reliability analysis performed on several temporal variability/stability measures is presented. Multiscale entropy and Recurrence Quantification Analysis showed excellent reliability. In general, the number of strides necessary to obtain a reliable measure was larger than those conventionally used.

An analysis of the association between nonlinear stability measures and fall history is presented in Chapter V. In particular, in this study measures independent from stride detection were tested, in order to avoid a potentially critical implementation process. Multiscale entropy and Recurrence Quantification Analysis were found to be positively associated with fall history.

In Chapter VI, the influence of directional changes on variability/stability measures was assessed. Only Harmonic ratio was found to be influenced by directional changes, while measures such as short-term Lyapunov exponents, Multiscale entropy and Recurrence quantification analysis were not.

In Chapter VII, the association of variability/stability measures with short-term risk of fall is presented. Preliminary results showed that Multiscale entropy in the AP direction seems to be able to detect modification in the gait pattern immediately before a fall episode.

In conclusion, several implementation issues have been addressed. Following the need for a methodological standardization of gait variability/stability measures, highlighted in particular for orbital stability analysis through a systematic review, general indications about implementation of orbital stability analysis have been shown, together with an analysis of the number of strides and the test-retest reliability of several variability/stability numbers. Indications about the influence of directional changes on measures have also been provided. Association between measures and long/short-term fall history has also been assessed. Of all the analyzed variability/stability measures, Multiscale entropy and Recurrence quantification analysis demonstrated particularly good results in terms of reliability, applicability and association with fall history. Therefore, these measures should be taken in consideration for the definition of a fall risk index.

IX. APPENDIX

IX.1. STANDARD DEVIATION

Standard deviation (SD) of stride time was simply calculated as the standard deviation of the stride times in the analyzed time-window [17].

IX.2. COEFFICIENT OF VARIATION

Coefficient of variation (CV) was calculated as the SD normalized to each subject's mean stride time [21]:

$$CV = \frac{SD \times 100}{mean_stride_time} \quad \text{IX.1}$$

IX.3. INCONSISTENCY OF THE VARIANCE

Each time series was first normalized with respect to its mean and SD, yielding new time series each with mean = 0 and SD = 1, but with different dynamic properties. This normalized time series was then divided into blocks of five strides each, and in each segment the (local) average and (local) SD were computed. The inconsistency of the variance (IV) is the SD of the local SD [21].

IX.4. NONSTATIONARY INDEX

Similarly to the IV, the nonstationary index (NI) is defined as the SD of the local averages of the normalized time series's five strides blocks. The nonstationary index provides a measure of how the local average values change during the walk, independent of the overall variance (the fluctuation magnitude) of the original time series. A higher nonstationary index indicates greater range among the local averages [21].

IX.5. POINCARÉ PLOTS

Stride time data plots between successive gait cycles, known as Poincaré plots, show variability of stride time data. Brennan *et al.* [108] provided mathematical expressions that relate each measure derived from Poincaré plot geometry to well-understood existing heart rate variability indexes. Using the method described by Brennan [108], these plots

were used to extract indices, such as length (PSD2) and width (PSD1) of the long and short axes describing the elliptical nature of the Poincaré plot images. Statistically, the plot displays the correlation between consecutive stride times data in a graphical manner. Points above the line-of-identity indicate strides that are longer than the preceding, and points below the line of identity indicate shorter strides than the previous ones. The Poincaré plot typically appears as an elongated cloud of points oriented along the line-of-identity. The dispersion of points perpendicular to the line-of-identity reflects the level of short-term variability [108]. The dispersion of points along the line-of-identity is shown to indicate the level of long-term variability [22].

IX.6. ORBITAL STABILITY ANALYSIS

The first step of orbital stability analysis via maximum Floquet multipliers (maxFM) is the state space reconstruction. Two approaches were used: direct inclusion of acquired variables (joint angles/acceleration time series) into the state space, delay-embedding reconstruction. Delay embedding is a technique to reconstruct a dynamical system from a sequence of observations. Standard embedding techniques were used [27,109]; an appropriate state space was reconstructed from each time series and its time delayed copies. An embedding dimension of $d_E = 5$ was always chosen; many studies in literature agree in considering this to be an appropriate dimension for gait data [27,37,56]. A fixed time delay $\tau = 10$ was always used [37,56].

Stride cycles were considered as the time between consecutive right heel strikes and were resampled to be 101 samples long, because Floquet theory assumes that the system is strictly periodic. A Poincaré section was defined at each percentage of the gait cycle (0% = right heel strike).

The Poincaré map:

$$S_{k+1} = F(S_k) \tag{IX.2}$$

defines the evolution of the state S_k to the state S_{k+1} at each Poincaré section, for each stride k .

The limit cycle trajectory was defined as the average trajectory across all strides. This produces a fixed point in each Poincaré section:

$$S^* = F(S^*) \tag{IX.3}$$

A linear approximation of Eq. IX.1:

$$[S^{k-1} - S^*] \approx J(S^*)[S^k - S^*] \quad \text{IX.4}$$

allows calculating how system states diverge from or converge to fixed points. The FM are the eigenvalues of the Jacobian matrix $J(S^*)$. The maximum FM (maxFM) is believed to govern the dynamics of the system, and hence to be the most representative in terms of instability. maxFM was calculated for each Poincaré section (0 – 100% of the gait cycle). If the maxFM have magnitude < 1 , the system remains stable; otherwise, the system tends to diverge from the limit cycle and become unstable. The overall mean value of maxFM across the gait cycle was calculated and used in the analyses.

IX.7. LOCAL STABILITY ANALYSIS

The first step for local stability analysis is the state space reconstruction (see description in Section IX.6). Local dynamic stability of walking is quantified by estimating the average exponential rates of divergence of initially neighboring trajectories in state space as they evolve in real time. These local divergence exponents provide a direct measure of the sensitivity of the system to extremely small (i.e., local) perturbations. Positive exponents indicate local instability, with larger exponents indicating greater sensitivity to local perturbations. Nearest neighbor points on adjacent trajectories in the reconstructed state space represent the effects of small local perturbations to the system. Euclidean distances between neighboring trajectories in state space were computed as a function of time and averaged over all original pairs of initially nearest neighbors. Local divergence exponents were estimated from the slopes of linear fits to these exponential divergence curves:

$$y(i) = \frac{1}{\Delta t} \langle \ln d_j(i) \rangle \quad \text{IX.5}$$

where $d_j(i)$ is the Euclidean distance between the j th pair of initially nearest neighbors after i discrete time steps (i.e., $i\Delta t$ seconds) and $\langle . \rangle$ denotes the average over all values of j . Since the intrinsic time scales were different for each subject (i.e., different average stride times), the time axes of these curves were rescaled by multiplying by the average stride frequency for each subject. Short-term exponents (sLE) were calculated from the slopes of linear fits to the divergence curve between 0 and 1 stride. Long-term exponents (lLE) were calculated as the slope between 4 and 10 strides [34].

IX.8. HARMONIC RATIO

The Harmonic ratio (HR) was calculated by decomposing the AP and ML acceleration signals into harmonics using a discrete Fourier transform [42]; the summed amplitudes of

the first 10 even harmonics were then divided by the summed amplitudes of the first 10 odd harmonics for the AP accelerations, and vice-versa for the ML accelerations. This difference is due to the fact that whereas the AP accelerations have two periods every stride, showing a dominance of the second harmonic, representing step frequency and subsequent even harmonics, ML accelerations have only one period per stride, reflecting a dominance of the first (and subsequent odd) harmonics [42]. In order to avoid errors that might be introduced by step-detection, HR was not calculated stride by stride, but decomposing the whole signal into its harmonics. A higher HR is an indication of increased smoothness of gait, which can be interpreted as increased stability.

IX.9. INDEX OF HARMONICITY

Index of harmonicity (IH) was calculated according to Lamoth et al. [43]. The power spectra of the AP and ML acceleration signals were estimated by means of discrete Fourier transform. The peak power at the first six harmonics was estimated and IH was defined as:

$$IH = \frac{P_0}{\sum_{i=0}^5 P_i} \quad \text{IX.5}$$

where P_0 is the power spectral density of the first harmonic and P_i the cumulative sum of power spectral density of the fundamental frequency and the first five super-harmonics. Values close to 1 indicate high harmonicity (e.g. a sine wave has a power ratio of 1, indicating perfect harmonicity). Power spectral density of each peak was averaged over a range of $[-0.1 \dots + 0.1]$ Hz around the peak frequency value

IX.10. MULTISCALE ENTROPY

Multiscale entropy (MSE) was implemented constructing consecutively more coarse-grained time series; this procedure implies averaging increasing numbers of data points in non-overlapping windows of length τ . Sample entropy (SE) [110] was then calculated for each coarse-grained time series, in order to obtain entropy measures at different scales; SE quantifies the conditional probability that two sequences of m consecutive data points similar (distance of data points inferior to a fixed radius r) to each other will remain similar when one more consecutive point is included, thus reflecting the regularity of the time series [45]. SE at each time scale τ is hence a function of m and r and is expressed as the negative of the natural logarithm of the conditional probability $C(r)$ that two sequences that are close within a tolerance $r\delta$ for m consecutive points remain close at the next point [111], where δ is the standard deviation of the original series:

$$SE = -\ln \frac{C^{m+1}(r)}{C^m(r)} \quad \text{IX.6}$$

MSE was hence calculated for values of τ ranging from 1 to 6, $m = 2$ and $r = 0.2$, as suggested by Pincus [112] and later applied by Richman and Moorman to biological time series [110].

IX.11. RECURRENCE QUANTIFICATION ANALYSIS

The first implementation step of Recurrence quantification analysis (RQA) is the reconstruction of the phase space by means of delay embedding [109]. In this study, an embedding dimension of 5 and a delay of 10 samples were used, based on previous studies [14,56,113]. A distance matrix based on Euclidean distances between normalized embedded vectors was then constructed; the recurrence plot was obtained by selecting a radius of 40% of the max distance, and all cells with values below this threshold were identified as recurrent points. A radius of 40% was chosen to make sure that recurrence rate (rr) responded smoothly and was not too high, and that determinism (det) did not saturate at the floor of 0 or the ceiling of 100, as approaching these limits would tend to suppress variance in the measure [48].

A number of measures can then be obtained by RQA; in this study, rr, det, averaged diagonal line length (avg) and maximum diagonal line length (max) were calculated (Eq. IX.7, IX.8, IX.9, IX.10), reflecting different properties of the system.

$$rr = \frac{1}{N^2} \sum_{i,j=1}^N R_{i,j} \quad \text{IX.7}$$

where N is the number of points on the phase space trajectory;

$$\det = \frac{\sum_{l=4}^N lP_l}{rr} \quad \text{IX.8}$$

where l is the length of diagonal lines, represented through a histogram (P_l);

$$\text{avg} = \frac{\sum_{l=4}^N lP_l}{\sum_{l=4}^N P_l} \quad \text{IX.9}$$

$$\text{max} = (\{l_i; i = 1 \dots N_l\}) \quad \text{IX.10}$$

where N_l is the number of diagonal lines in the recurrence plot.

SE was calculated using MATLAB (Mathworks, Natick, MA) software available on Physionet [114]. All other measures were calculated through custom self-made MATLAB (Mathworks, Natick, MA) scripts.

X. REFERENCES

- [1] Tinetti ME, Williams TF, Mayewski R. Fall risk index for elderly patients based on number of chronic disabilities. *The American Journal of Medicine* 1986; 80: 429–34.
- [2] Heinrich S, Rapp K, Rissmann U, Becker C, König H-H. Cost of falls in old age: a systematic review. *Osteoporosis International* 2009; 21: 891–902.
- [3] Parkkari J, Kannus P, Palvanen M, Natri A, Vainio J, Aho H, et al. Majority of Hip Fractures Occur as a Result of a Fall and Impact on the Greater Trochanter of the Femur: A Prospective Controlled Hip Fracture Study with 206 Consecutive Patients. *Calcified Tissue International* 1999; 65: 183–7.
- [4] Tinetti ME. Preventing Falls in Elderly Persons. *New England Journal of Medicine* 2003; 348: 42–9.
- [5] Fuller GF. Falls in the elderly. *American Family Physician* 2000; 61: 2159–68, 2173–4.
- [6] Alexander BH, Rivara FP, Wolf ME. The cost and frequency of hospitalization for fall-related injuries in older adults. *American Journal of Public Health* 1992; 82: 1020–3.
- [7] Mathers LJ, Weiss HB. Incidence and Characteristics of Fall-related Emergency Department Visits. *Academic Emergency Medicine* 1998; 5: 1064–70.
- [8] Hamacher D, Singh NB, Dieën JH Van, Heller MO, Taylor WR. Kinematic measures for assessing gait stability in elderly individuals: a systematic review. *Journal of The Royal Society Interface* 2011; 8: 1682–98.
- [9] Masud T, Morris RO. Epidemiology of falls. *Age and Ageing* 2001; 30: 3–7.
- [10] American Geriatrics Society, British Geriatrics Society and American Academy of Orthopaedic Surgeons Panel on Falls Prevention. Guideline for the Prevention of Falls in Older Persons. *Journal of the American Geriatrics Society* 2001; 49: 664–72.
- [11] Oliver D, Daly F, Martin FC, McMurdo MET. Risk factors and risk assessment tools for falls in hospital in-patients: a systematic review. *Age and Ageing* 2004; 33: 122–30.
- [12] Buzzi UH, Stergiou N, Kurz MJ, Hageman PA, Heidel J. Nonlinear dynamics indicates aging affects variability during gait. *Clinical Biomechanics* 2003; 18: 435–43.

- [13] Granata KP, Lockhart TE. Dynamic stability differences in fall-prone and healthy adults. *Journal of Electromyography and Kinesiology: Official Journal of the International Society of Electrophysiological Kinesiology* 2008; 18: 172–8.
- [14] Lockhart TE, Liu J. Differentiating fall-prone and healthy adults using local dynamic stability. *Ergonomics* 2008; 51: 1860–72.
- [15] Costello E, Edelstein JE. Update on falls prevention for community-dwelling older adults: review of single and multifactorial intervention programs. *Journal of Rehabilitation Research and Development* 2008; 45: 1135–52.
- [16] Bloem BR, Boers I, Cramer M, Westendorp RG, Gerschlager W. Falls in the elderly. I. Identification of risk factors. *Wiener Klinische Wochenschrift* 2001; 113: 352–62.
- [17] Hausdorff JM, Rios DA, Edelberg HK. Gait variability and fall risk in community-living older adults: a 1-year prospective study. *Archives of Physical Medicine and Rehabilitation* 2001; 82: 1050–6.
- [18] Berg WP, Alessio HM, Mills EM, Tong C. Circumstances and consequences of falls in independent community-dwelling older adults. *Age and Ageing* 1997; 26: 261–8.
- [19] Laessoe U, Hoeck HC, Simonsen O, Sinkjaer T, Voigt M. Fall risk in an active elderly population – can it be assessed? *Journal of Negative Results in BioMedicine* 2007; 6: 2.
- [20] Furnham A. Response bias, social desirability and dissimulation. *Personality and Individual Differences* 1986; 7: 385–400.
- [21] Hausdorff JM, Nelson ME, Kaliton D, Layne JE, Bernstein MJ, Nuernberger A, et al. Etiology and modification of gait instability in older adults: a randomized controlled trial of exercise. *J Appl Physiol* 2001; 90: 2117–29.
- [22] Khandoker AH, Taylor SB, Karmakar CK, Begg RK, Palaniswami M. Investigating Scale Invariant Dynamics in Minimum Toe Clearance Variability of the Young and Elderly During Treadmill Walking. *IEEE Transactions on Neural Systems and Rehabilitation Engineering* 2008; 16: 380–9.
- [23] Maki BE. Gait changes in older adults: predictors of falls or indicators of fear. *Journal of the American Geriatrics Society* 1997; 45: 313–20.
- [24] Segal AD, Orendurff MS, Czerniecki JM, Shofer JB, Klute GK. Local dynamic stability in turning and straight-line gait. *Journal of Biomechanics* 2008; 41: 1486–93.
- [25] Horak FB, Nutt JG, Nashner LM. Postural inflexibility in parkinsonian subjects. *Journal of the Neurological Sciences* 1992; 111: 46–58.
- [26] Li L, Haddad JM, Hamill J. Stability and variability may respond differently to

changes in walking speed. *Human Movement Science* 2005; 24: 257–67.

[27] Dingwell JB, Cusumano JP. Nonlinear time series analysis of normal and pathological human walking. *Chaos (Woodbury, N.Y.)* 2000; 10: 848–63.

[28] Nayfeh AH, Balachandran B. *Applied Nonlinear Dynamics: Analytical, Computational, and Experimental Methods*. Wiley-VCH; 1995.

[29] Pecoraro F, Mazzà C, Zok M, Cappozzo A. Assessment of level-walking aperiodicity. *Journal of NeuroEngineering and Rehabilitation*; 3: 28.

[30] McGeer T. Passive Dynamic Walking. *The International Journal of Robotics Research* 1990; 9: 62–82.

[31] Abarbanel HDI. *Analysis of observed chaotic data*. Springer; 1996.

[32] David A. W. Kinematic and kinetic patterns in human gait: Variability and compensating effects. *Human Movement Science* Marzo; 3: 51–76.

[33] Jacquelin Perry, Perry J. *Gait Analysis: Normal and Pathological Function*. [[Thorofare, New Jersey]]: SLACK Incorporated; 1992.

[34] Dingwell JB, Kang HG. Differences between local and orbital dynamic stability during human walking. *Journal of Biomechanical Engineering* 2007; 129: 586–93.

[35] Dingwell JB, Marin LC. Kinematic variability and local dynamic stability of upper body motions when walking at different speeds. *Journal of Biomechanics* 2006; 39: 444–52.

[36] Granata KP, England SA. Stability of dynamic trunk movement. *Spine* 2006; 31: E271–276.

[37] England SA, Granata KP. The influence of gait speed on local dynamic stability of walking. *Gait & Posture* 2007; 25: 172–8.

[38] Dingwell JB, Cusumano JP, Cavanagh PR, Sternad D. Local dynamic stability versus kinematic variability of continuous overground and treadmill walking. *Journal of Biomechanical Engineering* 2001; 123: 27–32.

[39] Toebe MJP, Hoozemans MJM, Furrer R, Dekker J, Dieën JH van. Local dynamic stability and variability of gait are associated with fall history in elderly subjects. *Gait & Posture* 2012; 36: 527–31.

[40] Hurmuzlu Y, Basdogan C. On the measurement of dynamic stability of human locomotion. *Journal of Biomechanical Engineering* 1994; 116: 30–6.

[41] Dingwell JB, John J, Cusumano JP. Do Humans Optimally Exploit Redundancy to Control Step Variability in Walking? *PLoS Comput Biol* 2010; 6:

[42] Menz HB, Lord SR, Fitzpatrick RC. Acceleration patterns of the head and pelvis

when walking on level and irregular surfaces. *Gait & Posture* 2003; 18: 35–46.

[43] Lamoth CJC, Beek PJ, Meijer OG. Pelvis–thorax coordination in the transverse plane during gait. *Gait & Posture* 2002; 16: 101–14.

[44] Lowry KA, Smiley-Oyen AL, Carrel AJ, Kerr JP. Walking stability using harmonic ratios in Parkinson’s disease. *Movement Disorders* 2009; 24: 261–7.

[45] Costa M, Peng C-K, Goldberger A L., Hausdorff JM. Multiscale entropy analysis of human gait dynamics. *Physica A: Statistical Mechanics and Its Applications* 2003; 330: 53–60.

[46] Lamoth CJ, Deudekom FJ van, Campen JP van, Appels BA, Vries OJ de, Pijnappels M. Gait stability and variability measures show effects of impaired cognition and dual tasking in frail people. *Journal of NeuroEngineering and Rehabilitation* 2011; 8:

[47] Sylos Labini F, Meli A, Ivanenko YP, Tufarelli D. Recurrence quantification analysis of gait in normal and hypovestibular subjects. *Gait & Posture* 2012; 35: 48–55.

[48] Riley M., Balasubramaniam R, Turvey M. Recurrence quantification analysis of postural fluctuations. *Gait & Posture* 1999; 9: 65–78.

[49] Riva F, Bisi MC, Stagni R. Orbital stability analysis in biomechanics: A systematic review of a nonlinear technique to detect instability of motor tasks. *Gait & Posture* 2013; 37: 1–11.

[50] Peters A, Galna B, Sangeux M, Morris M, Baker R. Quantification of soft tissue artifact in lower limb human motion analysis: A systematic review. *Gait & Posture* 2010; 31: 1–8.

[51] Galna B, Peters A, Murphy AT, Morris ME. Obstacle crossing deficits in older adults: a systematic review. *Gait & Posture* 2009; 30: 270–5.

[52] Piriyaarasarth P, Morris ME. Psychometric properties of measurement tools for quantifying knee joint position and movement: a systematic review. *The Knee* 2007; 14: 2–8.

[53] McGinley JL, Baker R, Wolfe R, Morris ME. The reliability of three-dimensional kinematic gait measurements: a systematic review. *Gait & Posture* 2009; 29: 360–9.

[54] Arellano CJ, Layne CS, O’Connor DP, Scott-Pandorf M, Kurz MJ. Does load carrying influence sagittal plane locomotive stability? *Medicine and Science in Sports and Exercise* 2009; 41: 620–7.

[55] Arellano CJ, O’Connor DP, Layne C, Kurz MJ. The independent effect of added mass on the stability of the sagittal plane leg kinematics during steady-state human walking. *The Journal of Experimental Biology* 2009; 212: 1965–70.

[56] Bruijn SM, Dieën JH van, Meijer OG, Beek PJ. Statistical precision and

sensitivity of measures of dynamic gait stability. *Journal of Neuroscience Methods* 2009; 178: 327–33.

[57] Bruijn SM, Ten Kate WRT, Faber GS, Meijer OG, Beek PJ, Dieën JH van. Estimating dynamic gait stability using data from non-aligned inertial sensors. *Annals of Biomedical Engineering* 2010; 38: 2588–93.

[58] Dingwell JB, Kang HG, Marin LC. The effects of sensory loss and walking speed on the orbital dynamic stability of human walking. *Journal of Biomechanics* 2007; 40: 1723–30.

[59] Dingwell JB, Robb RT, Troy KL, Grabiner MD. Effects of an attention demanding task on dynamic stability during treadmill walking. *Journal of Neuroengineering and Rehabilitation* 2008; 5:

[60] Gates DH, Dingwell JB. Muscle fatigue does not lead to increased instability of upper extremity repetitive movements. *Journal of Biomechanics* 2010; 43: 913–9.

[61] Gates DH, Dingwell JB. The effects of muscle fatigue and movement height on movement stability and variability. *Experimental Brain Research. Experimentelle Hirnforschung. Expérimentation Cérébrale* 2011; 209: 525–36.

[62] Hidler JM, Rymer WZ. Limit cycle behavior in spasticity: analysis and evaluation. *IEEE Transactions on Bio-Medical Engineering* 2000; 47: 1565–75.

[63] Hurmuzlu Y, Basdogan C, Stoianovici D. Kinematics and dynamic stability of the locomotion of post-polio patients. *Journal of Biomechanical Engineering* 1996; 118: 405–11.

[64] Kang HG, Dingwell JB. Effects of walking speed, strength and range of motion on gait stability in healthy older adults. *Journal of Biomechanics* 2008; 41: 2899–905.

[65] Kang HG, Dingwell JB. Dynamic stability of superior vs. inferior segments during walking in young and older adults. *Gait & Posture* 2009; 30: 260–3.

[66] Kang HG, Dingwell JB. Dynamics and stability of muscle activations during walking in healthy young and older adults. *Journal of Biomechanics* 2009; 42: 2231–7.

[67] Marghitu DB, Hobatho M-C. Dynamics of children with torsional anomalies of the lower limb joints. *Chaos, Solitons & Fractals* 2001; 12: 2411–9.

[68] Marghitu DB, Kincaid SA, Rumph PF. Nonlinear dynamics stability measurements of locomotion in healthy greyhounds. *American Journal of Veterinary Research* 1996; 57: 1529–35.

[69] McAndrew PM, Wilken JM, Dingwell JB. Dynamic stability of human walking in visually and mechanically destabilizing environments. *Journal of Biomechanics* 2011; 44: 644–9.

- [70] Schablowski M, Gerner HJ. Comparison of Two Measures of Dynamic Stability During Treadmill Walking. In: *Fast Motions in Biomechanics and Robotics*. Berlin, Heidelberg: Springer Berlin Heidelberg. p. 345–60.
- [71] Scott-Pandorf MM, O'Connor DP, Layne CS, Josić K, Kurz MJ. Walking in simulated Martian gravity: influence of the portable life support system's design on dynamic stability. *Journal of Biomechanical Engineering* 2009; 131:
- [72] Scott-Pandorf MM, O'Connor DP, Layne CS, Josic K, Kurz MJ. Walking in simulated Martian gravity: Influence of added weight on sagittal dynamic stability. *Acta Astronautica Maggio*; 66: 1341–52.
- [73] Schooten KS van, Sloot LH, Bruijn SM, Kingma H, Meijer OG, Pijnappels M, et al. Sensitivity of trunk variability and stability measures to balance impairments induced by galvanic vestibular stimulation during gait. *Gait & Posture* 2011; 33: 656–60.
- [74] Higgins e Green. *Cochrane Handbook for Systematic Reviews of Interventions*.
- [75] Deeks JJ. Systematic reviews in health care: Systematic reviews of evaluations of diagnostic and screening tests. *BMJ* 2001; 323: 157–62.
- [76] Lohr KN, Carey TS. Assessing “best evidence”: issues in grading the quality of studies for systematic reviews. *The Joint Commission Journal on Quality Improvement* 1999; 25: 470–9.
- [77] Verhagen AP, Vet HC de, Bie RA de, Kessels AG, Boers M, Bouter LM, et al. The Delphi list: a criteria list for quality assessment of randomized clinical trials for conducting systematic reviews developed by Delphi consensus. *Journal of Clinical Epidemiology* 1998; 51: 1235–41.
- [78] Vandembroucke JP, Elm E von, Altman DG, Gøtzsche PC, Mulrow CD, Pocock SJ, et al. Strengthening the Reporting of Observational Studies in Epidemiology (STROBE): Explanation and Elaboration. *Annals of Internal Medicine* 2007; 147: W–163–W–194.
- [79] Kavanagh J, Barrett R, Morrison S. The role of the neck and trunk in facilitating head stability during walking. *Experimental Brain Research* 2006; 172: 454–63.
- [80] Alton F, Baldey L, Caplan S, Morrissey MC. A kinematic comparison of overground and treadmill walking. *Clinical Biomechanics* 1998; 13: 434–40.
- [81] Su JL-S, Dingwell JB. Dynamic stability of passive dynamic walking on an irregular surface. *Journal of Biomechanical Engineering* 2007; 129: 802–10.
- [82] Roos PE, Dingwell JB. Influence of simulated neuromuscular noise on the dynamic stability and fall risk of a 3D dynamic walking model. *Journal of Biomechanics* 2011; 44: 1514–20.

- [83] Bruijn SM, Bregman DJJ, Meijer OG, Beek PJ, Dieën JH van. The validity of stability measures: A modelling approach. *Journal of Biomechanics* 2011; 44: 2401–8.
- [84] Solomon JH, Wisse M, Hartmann MJ. Fully interconnected, linear control for limit cycle walking. *Adaptive Behavior* 2010; 18: 492–506.
- [85] Croce U della, Cappozzo A, Kerrigan DC. Pelvis and lower limb anatomical landmark calibration precision and its propagation to bone geometry and joint angles. *Medical & Biological Engineering & Computing* 1999; 37: 155–61.
- [86] Cappozzo A, Catani F, Croce UD, Leardini A. Position and orientation in space of bones during movement: anatomical frame definition and determination. *Clinical Biomechanics (Bristol, Avon)* 1995; 10: 171–8.
- [87] Aminian K, Najafi B, Büla C, Leyvraz P-F, Robert P. Spatio-temporal parameters of gait measured by an ambulatory system using miniature gyroscopes. *Journal of Biomechanics* 2002; 35: 689–99.
- [88] Kantz H, Schreiber T. *Nonlinear time series analysis*. Cambridge University Press; 2004.
- [89] Hausdorff JM, Lertratanakul A, Cudkowicz ME, Peterson AL, Kaliton D, Goldberger AL. Dynamic markers of altered gait rhythm in amyotrophic lateral sclerosis. *Journal of Applied Physiology* 2000; 88: 2045–53.
- [90] Malatesta D, Simar D, Dauvilliers Y, Candau R, Borrani F, Prefaut C, et al. Energy cost of walking and gait instability in healthy 65- and 80-yr-olds. *Journal of Applied Physiology* 2003; 95: 2248–56.
- [91] Khandoker AH, Lai DTH, Begg RK, Palaniswami M. Wavelet-based feature extraction for support vector machines for screening balance impairments in the elderly. *IEEE Transactions on Neural Systems and Rehabilitation Engineering: a Publication of the IEEE Engineering in Medicine and Biology Society* 2007; 15: 587–97.
- [92] Zijlstra W, Hof AL. Assessment of spatio-temporal gait parameters from trunk accelerations during human walking. *Gait & Posture* 2003; 18: 1–10.
- [93] Willemsen ATM, Bloemhof F, Boom HBK. Automatic stance-swing phase detection from accelerometer data for peroneal nerve stimulation. *IEEE Transactions on Biomedical Engineering* 1990; 37: 1201–8.
- [94] Lopez AM, Alvarez D, Gonzalez RC, Alvarez JC. Validity of four gait models to estimate walked distance from vertical COG acceleration. *Journal of Applied Biomechanics* 2008; 24: 360–7.
- [95] González RC, López AM, Rodríguez-Uría J, Alvarez D, Alvarez JC. Real-time gait event detection for normal subjects from lower trunk accelerations. *Gait & Posture* 2010; 31: 322–5.

- [96] Stel VS, Smit JH, Pluijm SM., Visser M, Deeg DJ., Lips P. Comparison of the LASA Physical Activity Questionnaire with a 7-day diary and pedometer. *Journal of Clinical Epidemiology* 2004; 57: 252–8.
- [97] Ganz DA, Higashi T, Rubenstein LZ. Monitoring Falls in Cohort Studies of Community-Dwelling Older People: Effect of the Recall Interval. *Journal of the American Geriatrics Society* 2005; 53: 2190–4.
- [98] Brach JS, McGurl D, Wert D, Vanswearingen JM, Perera S, Cham R, et al. Validation of a measure of smoothness of walking. *The Journals of Gerontology. Series A, Biological Sciences and Medical Sciences* 2011; 66: 136–41.
- [99] Tochigi Y, Segal NA, Vaseenon T, Brown TD. Entropy analysis of tri-axial leg acceleration signal waveforms for measurement of decrease of physiological variability in human gait. *Journal of Orthopaedic Research: Official Publication of the Orthopaedic Research Society* 2012; 30: 897–904.
- [100] Choi JM, Bae BH, Kim SY. Divergence in perpendicular recurrence plot; quantification of dynamical divergence from short chaotic time series. *Physics Letters A* 1999; 263: 299–306.
- [101] Eckmann J-P, Kamphorst SO, Ruelle D. Recurrence Plots of Dynamical Systems. *Europhysics Letters* 1987; 4: 973–7.
- [102] Savelberg HHC., Vorstenbosch MAT., Kamman EH, Weijer JG. van de, Schambardt HC. Intra-stride belt-speed variation affects treadmill locomotion. *Gait & Posture* 1998; 7: 26–34.
- [103] Guyatt GH, Sullivan MJ, Thompson PJ, Fallen EL, Pugsley SO, Taylor DW, et al. The 6-minute walk: a new measure of exercise capacity in patients with chronic heart failure. *Canadian Medical Association Journal* 1985; 132: 919–23.
- [104] McCamley J, Donati M, Grimpampi E, Mazzà C. An enhanced estimate of initial contact and final contact instants of time using lower trunk inertial sensor data. *Gait & Posture* 2012; 36: 316–8.
- [105] Riva F, Toebes MJP, Pijnappels M, Stagni R, Dieen JH van. Estimating fall risk with inertial sensors using gait stability measures that do not require step detection. Article Submitted to *Gait & Posture*.
- [106] Scheffer AC, Schuurmans MJ, Dijk N van, Hooft T van der, Rooij SE de. Fear of falling: measurement strategy, prevalence, risk factors and consequences among older persons. *Age and Ageing* 2008; 37: 19–24.
- [107] Ganz DA, Yano EM, Saliba D, Shekelle PG. Design of a continuous quality improvement program to prevent falls among community-dwelling older adults in an integrated healthcare system. *BMC Health Services Research* 2009; 9: 206.

- [108] Brennan M, Palaniswami M, Kamen P. Do existing measures of Poincaré plot geometry reflect nonlinear features of heart rate variability? *IEEE Transactions on Bio-medical Engineering* 2001; 48: 1342–7.
- [109] Takens F. Detecting strange attractors in turbulence. In: *Dynamical Systems and Turbulence*, Warwick 1980. Springer Berlin / Heidelberg; 1981. p. 366–81.
- [110] Richman JS, Moorman JR. Physiological Time-Series Analysis Using Approximate Entropy and Sample Entropy. *American Journal of Physiology - Heart and Circulatory Physiology* 2000; 278: H2039–H2049.
- [111] Liao F, Wang J, He P. Multi-resolution entropy analysis of gait symmetry in neurological degenerative diseases and amyotrophic lateral sclerosis. *Medical Engineering & Physics* 2008; 30: 299–310.
- [112] Pincus SM. Approximate entropy as a measure of system complexity. *Proceedings of the National Academy of Sciences of the United States of America* 1991; 88: 2297–301.
- [113] Bruijn SM, Dieën JH van, Meijer OG, Beek PJ. Is slow walking more stable? *Journal of Biomechanics* 2009; 42: 1506–12.
- [114] Goldberger AL, Amaral LAN, Glass L, Hausdorff JM, Ivanov PC, Mark RG, et al. PhysioBank, PhysioToolkit, and PhysioNet Components of a New Research Resource for Complex Physiologic Signals. *Circulation* 2000; 101: e215–e220.

XI. SCIENTIFIC WRITING

XI.1. PUBLICATIONS IN INTERNATIONAL JOURNALS

1. Riva F, Bisi MC, Stagni R, “*Orbital stability analysis in biomechanics: a systematic review of a nonlinear technique to detect instability of locomotor tasks*”, **Gait & Posture**, 2013; 37(1): 1-11.
2. Bisi MC, Stagni R, Riva F, “*Biomechanical and metabolic responses to seat-tube angle variation during cycling in tri-athletes*”, **Journal of Electromyography and Kinesiology** 2012; 22(6): 845-51.
3. Riva F, Bisi MC, Stagni R, “*Influence of input parameters on dynamic orbital stability of walking: in-silico and experimental evaluation*”, submitted to **Journal of Biomechanical Engineering**.
4. Riva F, Bisi MC, Stagni R, “*Reliability of stability and variability measures*”, submitted to **Gait & Posture**.
5. Riva F, Toebes MJP, Pijnappels M, Stagni R, van Dieën JH, “*Estimating fall risk with inertial sensors using gait stability measures that do not require step detection*”, **Gait & Posture**, in press, SIAMOC methodological prize 2012.
6. Riva F, Grimpampi E, Mazzà C, Stagni R, “*Are gait variability/stability measures influenced by directional changes?*”, submitted to **Gait & Posture**.
7. Riva F et al. “*Stability of walking and short-term fall history*” to be submitted to **Gait & Posture**.

XI.2. ABSTRACTS PUBLISHED IN PROCEEDINGS OF INTERNATIONAL CONFERENCES

1. Bisi MC, Riva F, Stagni R, Gnudi G, “*Energetics of movement: comparison of two different models for the estimation of muscular energy consumption*”. **Proceedings of GCMAS conference**, May 2010, Miami (Florida, USA).
2. Bisi MC, Riva F, Stagni R, Gnudi G, “*Energetics of movement: comparison of two different models for the estimation of muscular energy consumption*”. **Proceedings of the 17th congress of the European Society of Biomechanics (ESB)**, July 2010, Edinburgh (Scotland).
3. Bisi MC, Riva F, Stagni R, Gnudi G, “*Quantification of energy expended during movement starting from biomechanical information*”. **Proceedings of the IUTAM Symposium**, September 2010, Leuven (Belgium).
4. Riva F, Bisi MC, Stagni R, Cristofolini L, “*Orbital stability of step climbing: analysis of muscle activations in young subjects*”. **Proceedings of the VPH Conference**, September/October 2010, Brussels (Belgium).
5. Riva F, Stagni R, Cristofolini L, “*Orbital stability analysis of human movement: in-silico preliminary evaluation for the definition of experimental trials*”. **Proceedings of GCMAS conference**, April 2011, Bethesda (Maryland, USA).
6. Bisi MC, Riva F, Stagni R, “*A non-invasive protocol to estimate muscle tendon lengths and moment arms through ultrasound images*”. **Proceedings of GCMAS conference**, April 2011, Bethesda (Maryland, USA).
7. Stagni R, Bisi MC, Riva F, “*Subject specific muscle tendon length and moment arm quantification for muscle-skeletal modeling: non-invasive estimate using direct and ultra-sound calibration*”.

Proceedings of the XXIIIrd Congress of the International Society of Biomechanics (ISB), July 2011, Brussels (Belgium).

8. Riva F, Stagni R, Cristofolini L, “*Orbital stability analysis of human movement: in-silico and experimental preliminary evaluation on a stair climbing task*”. **Proceedings of the XXIIIrd Congress of the International Society of Biomechanics (ISB)**, July 2011, Brussels (Belgium).

XI.3. ABSTRACTS PUBLISHED IN PROCEEDINGS OF NATIONAL CONFERENCES

1. Bisi MC, Riva F, Stagni R, Gnudi G. “*Kinetics and energetics during exercise: A model evaluation*”. **Proceedings of the Secondo Congresso Nazionale di Bioingegneria (GNB)**, July 2010, Torino (Italy).
2. Riva F, Bisi MC, Stagni R, Cristofolini L, “*Orbital stability of muscle activations during step climbing in young subjects*”. **Proceedings of the Secondo Congresso Nazionale di Bioingegneria (GNB)**, July 2010, Torino (Italy).
3. Riva F, Cristofolini L, Stagni R, “*Orbital stability of walking: in-silico assessment of a walking model*”, **Proceedings of the Terzo Congresso Nazionale di Bioingegneria (GNB)**, June 2012, Roma (Italy).

XI.4. ABSTRACTS PUBLISHED IN INTERNATIONAL JOURNALS

1. Bisi MC, Riva F, Stagni R, Gnudi G. “*Kinetics and energetics during exercise: A model evaluation*”. **Proceedings of the SIAMOC conference**, October 2009, Alghero (Italy), **Gait & Posture**, 30S1, pag. S50, 2009.
2. Riva F, Bisi MC, Stagni R, Cristofolini L, “*Kinematic orbital stability during step climbing in young subjects*”. **Proceedings of the XI SIAMOC conference**, October 2010, Ferrara (Italy), **Gait&Posture** 33S1, pag. S47, 2011.
3. Bisi MC, Riva F, Stagni R, “*A non invasive protocol to estimate muscle tendon lengths and moment arms through ultrasound images*”. **Proceedings of the XI SIAMOC conference**, October 2010, Ferrara (Italy), **Gait&Posture** 33S1, pagg. S28-S29, 2011.
4. Riva F, Bisi MC, Stagni R, 2011. “*Orbital stability analysis of voluntarily altered gait pattern*”. **Proceedings of the XII SIAMOC conference**, September/October 2011, Bosisio Parini (Lecco, Italy), **Gait & Posture** 35S1, Pages S3-S4, 2012.
5. Bisi MC, Ceccarelli M, Riva F, Stagni R, 2011. “*Biomechanical and metabolic responses to seat-tube angle variation during cycling in tri-athletes*”. **Proceedings of the XII SIAMOC conference**, September/October 2011, Bosisio Parini (Lecco, Italy), **Gait & Posture** 35S1, Pages S25-S26, 2012.
6. Riva F, Stagni R, “*In-silico assessment of orbital stability analysis applied to walking*”, **Proceedings of the XVIII Congress of the European Society of Biomechanics (ESB)**, July 2012, Lisbona (Portogallo). **Journal of Biomechanics** 45S1, Page S226, 2012.
7. Riva F, Mayberry K, Stagni R, “*Comparison between model and experimental orbital stability analysis of gait*”, **Proceedings of the XVIII Congress of the European Society of Biomechanics (ESB)**, July 2012, Lisbona (Portogallo). **Journal of Biomechanics** 45S1, Page S227, 2012.
8. Stagni R, Bisi MC, Riva F, “*Quantification of subject specific muscle moment arm and muscle length: an issue for modeling*”, **Proceedings of the XVIII Congress of the European Society of Biomechanics (ESB)**, July 2012, Lisbona (Portogallo). **Journal of Biomechanics** 45S1, Page S242, 2012.
9. Bisi MC, Riva F, Stagni R, “*Measures of gait stability: evaluation of the proposed methods comparing adults with infants at the beginning of independent walking*”, **Proceedings of the XVIII Congress of the European Society of Biomechanics (ESB)**, July 2012, Lisbona (Portogallo). **Journal of Biomechanics** 45S1, Page S230, 2012.

10. Riva E, Toebes MJP, Pijnapples M, Stagni R, van Dieën JH, “*Fall history: is a minimum setup quantification possible?*”, **Proceedings of the XIII SIAMOC conference**, September 2012, Bellaria (Rimini, Italy), to be published in **Gait & Posture**.

XI.5. AWARDS

1. **SIAMOC Award 2012** for the best methodological work, “*Fall history: is a minimum setup quantification possible?*”, **XIII SIAMOC conference**, September 2012, Bellaria (Rimini, Italy)



TEMPORAL GAIT PARAMETERS DETERMINATION FROM SHANK-WORN MIMU SIGNALS RECORDED DURING HEALTHY AND PATHOLOGICAL GAIT

¹Diana Trojaniello, ¹Andrea Cereatti, ¹Gabriele Paolini, ²Andrea Ravaschio and ¹Ugo Della Croce

¹Information Engineering Unit, POLCOMING Department, University of Sassari, Sassari, Italy; email: dtrojaniello@uniss.it

²Department of Neurosciences, University of Genoa, Italy

SUMMARY

In this preliminary study, a novel method for estimating initial and final foot contacts (IC and FC) during gait for both healthy and pathological subjects using two inertial sensors attached just above the ankles is proposed and validated against the measurements obtained from an instrumented walkway. Data from five healthy and five pathological subjects walking in different conditions were acquired. The proposed method consists of a preliminary identification of trusted swing and stance phases, so that the search intervals for IC and FC could be narrowed. In the two resulting time intervals, IC and FC timings were identified from characteristics of the gyroscope and accelerometer signals. Stance and swing time were then determined. Differences with respect to the stance and swing timings obtained with the instrumented walkway are limited to an average of less than 0.01s for all walking conditions and all subjects. Additional validation work is required on gait of other pathological populations in order to safely adopt the proposed method in clinical settings.

INTRODUCTION

In recent years, wearable inertial sensors (MIMUs) have been extensively proposed as effective tools for measuring gait temporal characteristics [1-5]. In most studies the proposed techniques were applied to the gait of healthy subjects, with a few exceptions [6-8]. Discrepancies with gold standard were in the range of 0.03s - 0.04s in determining temporal events in Parkinson patients gait [6]. In this preliminary work we evaluate a novel technique for the determination of the timing of initial foot contact (IC) and final foot contact (FC) and the determination of consequent temporal gait parameters, by comparing its results to those obtained from an instrumented walkway during one-minute walking trials of both healthy and pathological subjects. The hypothesis of the study was that, by using a method able to restrict the search intervals in the MIMU signals in which gait events can be found, an adequate reliability of their estimate can be obtained for both healthy and pathological gait.

METHODS

Gait data from five Parkinson patients (three females, 75 ± 3 y.o.) and five healthy subjects (one female, 36 ± 7 y.o.) were acquired simultaneously using body worn MIMUs (Opal, APDM) and an instrumented walkway (GAITrite, CIR

System Inc). Two MIMUs were attached laterally to the shank (2cm above the lateral malleolus), using velcro straps, on both sides (x-axis pointing downward, y-axis pointing forward and z-axis pointing laterally). The MIMUs and the instrumented walkway were synchronized using a dedicated trigger output from the instrumented walkway and sampled at 128Hz and 120Hz, respectively.

Subjects were asked to walk back and forth for about one minute along a 12-meter walkway in three different walking conditions: a) self-selected, comfortable speed, b) higher speed and c) comfortable speed while performing a cognitive task (subtracting repetitively the number three from a pre-assigned number).

For every gait cycle, time intervals of trusted swing (T_{SW}) and of trusted stance (T_{ST}) were first identified and the remaining time intervals were used as IC and FC search intervals (T_{IC} and T_{FC}). T_{SW} was identified by isolating the time interval during which the gyroscope signal along the z direction (ω_z) exceeded the 20% of its maximum value. T_{ST} was obtained by isolating, at the center of the portion of the gait cycle outside the T_{SW} interval (\hat{T}_{SW}), the time interval in which ω_z showed a standard deviation 60% lower than that in \hat{T}_{SW} . Therefore, T_{IC} and T_{FC} were defined as the time intervals between T_{SW} and T_{ST} and T_{ST} and T_{SW} , respectively. For each gait cycle, IC (t_{IC}) and FC (t_{FC}) instances were identified inside T_{IC} and T_{FC} , respectively (Figure 1).

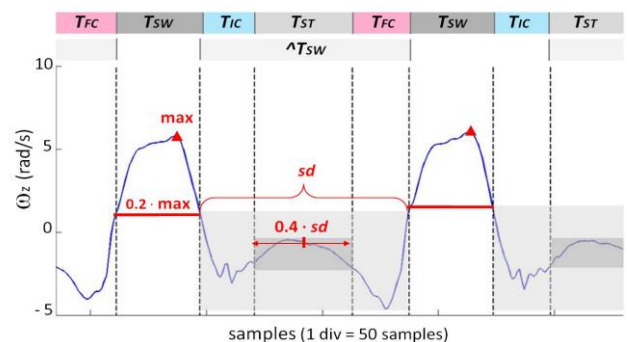


Figure 1: The gyroscope signal ω_z during approximately two gait cycles. Trusted swing (T_{SW}) and trusted stance (T_{ST}) are identified first, so that IC and FC search windows (T_{IC} and T_{FC}) result as their complement within the gait cycle.

The t_{IC} was identified as the instant of minimum ω_z [7] in the time interval between the beginning of T_{IC} and the instant of maximum anterior acceleration a_y in T_{IC} . The instant t_{FC} was defined as the occurrence of the minimum of

a_y preceding the instant of the last maximum value in T_{FC} (Figure 2). Stance time (ST_{Time}) and swing time (SW_{Time}) were obtained from t_{IC} and t_{FC} and compared against those obtained from the instrumented walkway. Therefore, only the data acquired while the subjects walked over the instrumented walkway were used for the analysis.

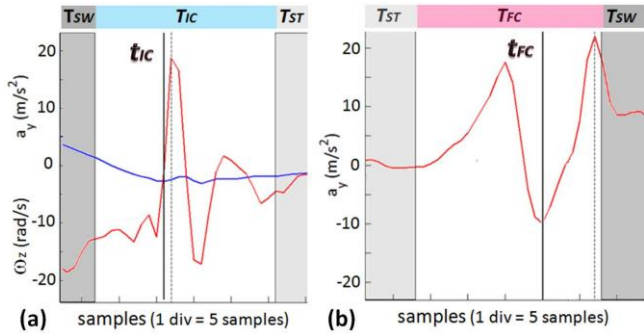


Figure 2: IC (t_{IC}) and FC timing (t_{FC}) identification. (a) The gyroscope signal ω_z (blue) and acceleration signal a_y (red) in the T_{IC} search window are shown. The vertical dashed line represents the instant of maximum a_y in T_{IC} , while the solid vertical line identifies the IC detected. (b) The acceleration a_y (red) in the T_{FC} search window is shown. The dashed vertical line represents the instant of the last a_y maximum in T_{FC} , while the solid line identifies the FC detected.

RESULTS AND DISCUSSION

In Table 1, ST_{Time} and SW_{Time} as determined by the MIMU and their difference (Δ) with respect to the values obtained with the instrumented walkway are reported for all subjects walking in the three conditions, for a total of more than 1500 measurements. Results showed extremely low values for Δ across the three walking conditions: the average absolute value of Δ was always lower than 0.01s ($sd = 0.02s$) in both healthy and pathological subjects. This result is particularly promising considering that the gait

characteristics in the same gait condition showed a remarkable variability across subjects (ST_{Time} varied from 0.62s to 0.82s at comfortable speed). Moreover, the proposed method was able to properly estimate ST_{Time} and SW_{Time} both in very regular gait ($sd = 0.01s$ in S1 comfortable walk) and in less regular gait ($sd = 0.08s$ in P2 comfortable walk).

CONCLUSIONS

The validation of the proposed method for determining temporal gait events and consequent parameters provided robust results across gait conditions and subjects. However, a wider range of pathologies should be tested in order to have a stronger validation of the method. Moreover, gait conditions could be extended to variations of gait such as obstacle negotiation and turning.

ACKNOWLEDGEMENTS

This study was carried out as part of the V-TIME project partially funded by the European Commission under the 7th Framework Program, grant #278169

REFERENCES

1. Sabatini A.M., et al. *IEEE transactions on bio-medical engineering*, **52**: 486-794, 2005
2. Selles R., et al. *IEEE transactions on neural systems and rehabilitation engineering*, **13**: 81-88, 2005
3. Hanlon M., et al. *Gait & Posture*, **30**:523-527, 2009
4. Greene B. R., et al. *Medical & biological engineering & computing*, **48**: 1251-1260, 2010
5. Mannini A., et al. *Gait & posture*, **36**: 657-661, 2012
6. Han, J. et al. *Medical & biological engineering & computing*, **47**: 1155-1164, 2009
7. Salarian A., et al., *System*, **51**: 1434-1443, 2004
8. Lau H., et al. *Gait & posture*, **27**:248-57, 2008

Table 1: Trial average (gray background) and sd (no background) values for ST_{Time} and SW_{Time} as determined from the MIMU signals and the difference (Δ) with respect to the relevant values obtained from the instrumented walkway for three different gait conditions. Numbers are reported in seconds.

	COMFORTABLE WALK				FAST WALK				COGNITIVE TASK WALK			
	ST_{TIME}	Δ	SW_{TIME}	Δ	ST_{TIME}	Δ	SW_{TIME}	Δ	ST_{TIME}	Δ	SW_{TIME}	Δ
S1	0.77	0.01	0.46	- 0.01	0.58	0	0.40	0	0.66	0.01	0.42	- 0.01
	0.01	0.01	0.01	0.01	0.02	0.01	0.01	0.01	0.03	0.02	0.02	0.02
S2	0.69	0	0.43	0	0.59	0	0.39	0	0.69	0.01	0.41	- 0.01
	0.02	0.01	0.02	0.01	0.03	0.01	0.02	0.01	0.03	0.01	0.02	0.01
S3	0.65	0.02	0.38	- 0.02	0.53	0	0.36	0	0.71	0.01	0.42	- 0.01
	0.01	0.01	0.01	0.01	0.03	0.03	0.03	0.03	0.03	0.01	0.02	0.01
S4	0.62	0	0.40	0	0.46	0	0.33	0	0.68	0	0.42	0
	0.02	0.02	0.02	0.02	0.02	0.01	0.01	0.01	0.03	0.01	0.02	0.01
S5	0.67	- 0.01	0.42	0.01	0.51	0	0.34	0	0.72	0	0.43	0
	0.03	0.03	0.03	0.03	0.02	0.02	0.02	0.02	0.04	0.02	0.04	0.02
P1	0.65	0	0.38	0	0.57	0	0.36	0	0.64	0	0.38	0
	0.02	0.02	0.01	0.02	0.04	0.02	0.02	0.02	0.03	0.02	0.02	0.02
P2	0.83	0.01	0.36	- 0.01	0.70	- 0.01	0.32	0.01	0.83	- 0.01	0.29	0.01
	0.08	0.03	0.04	0.03	0.07	0.03	0.03	0.02	0.05	0.03	0.03	0.03
P3	0.82	0.02	0.40	- 0.02	0.74	0	0.38	0	0.81	0.02	0.40	- 0.02
	0.04	0.02	0.03	0.02	0.04	0.02	0.02	0.02	0.05	0.06	0.03	0.04
P4	0.79	- 0.01	0.44	0.01	0.67	- 0.01	0.40	0.01	1.10	0	0.48	0
	0.06	0.01	0.04	0.01	0.02	0.01	0.02	0.01	0.12	0.02	0.06	0.02
P5	0.70	- 0.02	0.41	0.02	0.67	- 0.02	0.41	0.01	0.79	- 0.01	0.45	0.01
	0.02	0.01	0.01	0.02	0.03	0.01	0.01	0.02	0.04	0.01	0.02	0.01

In-Suit Sensor Systems for Characterizing Human-Space Suit Interaction

A. Anderson¹, A. Hilbert², P. Bertrand³
Massachusetts Institute of Technology, Cambridge, MA, 02139, USA

S. McFarland⁴
NASA Johnson Space Center Advanced Space Suit Lab, Houston, TX, 77058, USA

D. J. Newman⁵
Massachusetts Institute of Technology, Cambridge, MA, 02139, USA

Although the U.S. has studied space suit performance for decades, relatively little is known about how the astronaut moves and interacts within the space suit. We propose the use of in-suit sensor systems to characterize this interaction and present our results using pressure sensors and inertial measurement units (IMUs) inside the David Clark Mobility Mock-Up and the Mark III space suit from NASA's Advanced Space Suit Lab at the Johnson Space Center. A network of 12 low-pressure sensors are distributed over the arm to measure the pressure between the arm and the suit soft goods. A high-pressure sensor mat is used to detect the pressure between the shoulder and the suit hard upper torso (HUT). Finally, we place three IMUs inside directly on the person's lower arm, upper arm and torso, with three corresponding IMUs outside on the space suit to measure joint angles. We perform two human subject experiments with 5 movement tasks focusing on upper body motions. The 5 motions include 3 isolated joint movements (elbow flexion/extension, shoulder flexion/extension, and shoulder abduction/adduction) and 2 functional tasks (overhead hammering and multi-join cross body reach). We discuss the implementation of this experiment, our lessons learned, quality of the data, and follow-on work. Finally, we propose future improvements for the characterization of human biomechanics and injury mechanisms from a human-space suit perspective.

Nomenclature

ABF	= Anthropometry and Biomechanics Facility
DCCI	= David Clark Company Incorporated
EMU	= Extravehicular Mobility Unit
EVA	= Extravehicular Activity
HUT	= Hard Upper Torso
IMU	= Inertial Measurement Unit
ISS	= International Space Station
JSC	= Johnson Space Center
LCVG	= Liquid Cooling and Ventilation Garment
NASA	= National Aeronautics and Space Administration

¹ PhD. Candidate, Department of Aeronautics and Astronautics, 37-218

² Master Candidate, Department of Aeronautics and Astronautics, 37-218

³ Master Candidate, Department of Aeronautics and Astronautics, 37-218

⁴ Senior Project Engineer, Wyle: Spacesuit and Crew Survival Systems Branch, NASA-JSC

⁵ Professor of Aeronautics and Astronautics and Engineering Systems, 33-307

NBL = Neutral Buoyancy Lab
SSA = Space Suit Assembly

I. Introduction

EXTRAVEHICULAR activity (EVA) requires substantial preparation and the proper hardware to ensure the safety of the astronaut and the success of the mission. EVA has allowed us to perform the most important moments in human space flight. The space suit is a technical marvel, through design and iterative enhancements of the system assures each of the primary requirements to sustain life in the harsh vacuum of space is achieved. However, accumulated time in the suit causes fatigue, increases metabolic expenditure, and eventually may lead to injuries^[2-11].

The space suit that U.S. astronauts currently fly and train in is the extravehicular mobility unit (EMU), which causes a variety of musculoskeletal injuries. This system includes the space suit assembly (SSA), protective and comfort pieces, and the life support system. A sketch of the EMU and comfort equipment is shown in Figure 1. A comprehensive description of these systems can be found in [12] and [13]. The EMU is gas-pressurized to 29.6 kPa (4.3 psi), making the soft goods somewhat stiff and rigid, requiring the wearer to work to deform the suit itself in addition to the work required for the task he or she is performing^[5, 14-18]. As a result, astronauts experience discomfort, hot spots, skin irritation, abrasions, contusions, and over time injuries requiring medical attention. The most common types of reported suit incidences are to the hands, feet, and shoulders. The remaining reports occur primarily where the person impacts and rubs against the suit to articulate it. Although most injuries have been minor and did not affect mission success, injury incidence during EVA is much higher than injury that occurs elsewhere on-orbit^[6, 7, 9]. EVA-associated injuries have been further exacerbated with the increased number of EVAs and training sessions for the construction of the International Space Station (ISS) in the Neutral Buoyancy Lab (NBL) training pool^[18]. Astronauts and tools are made neutrally buoyant to simulate the weightlessness of microgravity, allowing for realistic mission preparation with mockups of the ISS, robotic arms, and other pieces of space hardware. Many hours of training are required for each EVA, and the injuries seen on-orbit are magnified as more time is spent inside the suit. During NBL training astronauts shift inside the suit due to gravity and hydrodynamic resistance which must be overcome, both factors likely cause new injuries not seen in flight. For example, some training positions when inverted cause the weight of the body to rest on the shoulders, causing discomfort and injury, and in some instances leading to surgical intervention. Shoulder injuries are some of the most serious and debilitating injuries astronauts face as a result of working in the suit^[7, 8, 10, 19-21].

In addition to the EMU, there are several prototype suits geared toward improving capabilities for planetary and deep space exploration. The Mark III (Figure 2B), originally built in 1987 by NASA and ILC Dover, is the most well characterized prototype suit. It incorporates some hard components and rotating bearings (rather than soft fabric pieces) over the torso and hips to improve mobility and mitigate the effects of volume change. The concept was originally designed with planetary exploration in mind, hence the focus on mobility. The suit has seen several iterations and improvements since its original design. Although the bearings reduce the joint torques required to move the suit, their designs give the suit additional programming, making movements less natural. This effect was also seen in the AX-5, a full body hard suit designed at NASA Ames^[22]. Soft suits, such as the Modified ACES, Demonstrator Suit, and the Mobility Mockup, are designed by the David Clark Company, Incorporated (DCCI). The Demonstrator Suit (Figure 2A) was designed to address launch and entry requirements and contingency EVA situations. Their Mobility Mockup allows these concepts to be implemented on a full pressure suit rapidly to determine relative success or failure of components design^[11]. Additional prototype suits include the REI-Suit and

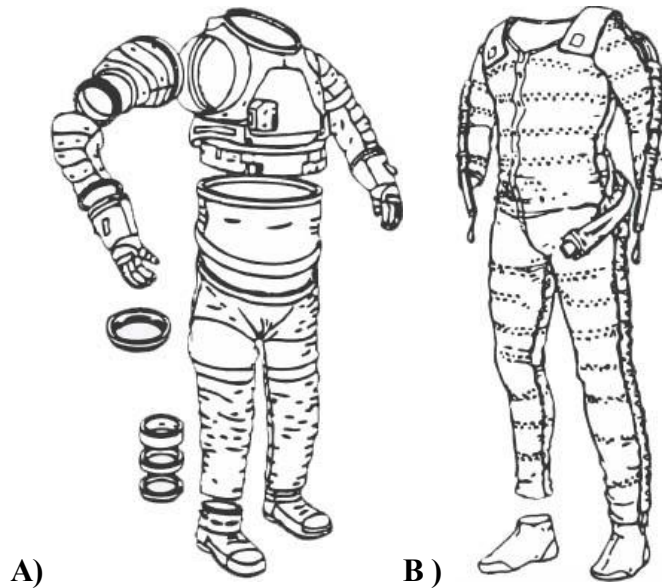


Figure 1. EMU spacesuit pieces and comfort garments. A) The EMU in an exploded view so the hard upper torso, soft pieces, sizing rings, and boots may be seen. Courtesy of Hamilton Sunstrand. B) Each of the comfort pieces, including the LCVG with padding, ventilation tubes, and boot inserts. Courtesy of "Human Spaceflight".

the Z-1 suit designed by ILC Dover for NASA. Finally, there are a few space suit concepts being developed in academia, such as the University of Maryland's MX-2, the University of North Dakota's NDX-2, and MIT's mechanical counter-pressure BioSuit™, which are test-beds for advanced space suit design and operations research [25, 26].

Relatively little is known about how the person moves inside the space suit to move the suit itself. We hypothesize that injuries occur due to improper suit fit, shifting, limited use of protective garments, and repetitive motions and contact working against the suit [8, 10, 27]. Suit fit is a critical element in preventing astronaut injury and achieving optimal comfort, but there is no universal solution for every person. Achieving the best fit is extremely individualized and discomfort "hot spots" may exist in an area for one crewmember but not for another. Even between training sessions minor adjustments are made to suit enhance fit [28]. Additionally, a person's body dimensions, especially height, change as they adjust to microgravity [29], which may necessitate further suit adjustment. No matter which environment the astronaut is working in, movement in the suit is unnatural due to each space suit's inherent programming [30] and stiffness. Astronauts learn to change their biomechanical movement strategies, rather than attempting to move as they do naturally when unsuited [28].

The difference between how a person moves as compared to the suit has not been previously quantified. The performance and movement of the space suit have been studied both experimentally and theoretically. However, evaluating how the person interacts within the space suit has not been rigorously measured. Performance is usually measured for the person and the space suit as a combined system. There have been many experiments to characterize range of motion, work envelope, reach envelope, and the strength required by a person to move the suit, especially for isolated joints. Previous studies use a variety of techniques, such as photogrammetry, motion capture, and ergonomic strength measurement [5, 14, 22, 31-36]. Results from these three techniques, however, are highly variable in that their methodologies are inherently different. Only comparison within one technique is possible and is not generalizable across subjects. Experimental evaluation of the human-space suit system gives gross metrics of performance and the upper bound of human capabilities within the environment. Modeling EVA has been used to get a sense of human-suit system performance for each of these metrics over a broad range of conditions not possible to be evaluated experimentally, such as modeling astronaut reach and work envelope over a population or modeling metabolic costs [31] [11, 14, 16, 17, 37-39]. In addition, there is currently no way to evaluate human movement within, although some work has focused on determining body joint angles within the suit [40, 41]. Knowing joint angles or where the body impacts the suit would improve performance data collection techniques through precise torque measurements, human range of motion inside the suit, and greater insight into metabolic cost data. Building from these studies could provide direct insight into resolving issues associated with EVA injury, comfort, fit, and mobility of future suit designs.

Future gas-pressurized space suit designs are governed by mobility requirements as we shift focus to planetary exploration. Surface exploration will require greater range of motion and more frequent sorties, leading to more time spent in EVA. This could potentially lead to higher injury incidence if the system is not enhanced to find long-term, healthy solutions to prevent EVA injury [18, 42, 43].



Figure 2. Advanced concept space suits for technology demonstration. A) *The David Clark Demonstrator suit. Photo credit [1]* B) *The Mark III worn during the experiment presented here in.*

The objective of this research is to develop an understanding of how the person interacts with the space suit, and use that information to assess and mitigate injury. The approach was to quantify and evaluate human-space suit interaction with two pressure sensing tools, focusing on the arm and shoulders under different loading regimes. Additionally, inertial measurement units (IMUs) were placed both internal and external to the space suit arm to assess biomechanics. Both custom and commercially produced sensors were incorporated into a modified athletic garment to realize a wearable pressure sensing system inside the suit. This experiment establishes a precedent and proof of concept, opening the doorway for

future technology development. The successes, failures, and lessons learned in performing EVA experiments are presented herein, while detailed discussion of the data and its consequences are presented elsewhere.

II. Methods

A. Sensor Systems

The human-suit interface is currently an unknown in space suit characterization. Subjectively, astronauts describe contact locations and areas of discomfort; however, there is no way to quantify the nature of that contact. Pressure measurements would allow greater insight into how these interactions occur and help characterize suit performance. Additionally, an understanding of the joint angle differences between the suit and the person would give us more information about the biomechanics of movement in the space suit. Sensors integrated into a wearable garment are shown in Figure 3. The two systems selected to measure pressure at different pressure sensing regimes and the inertial measurement units (IMUs) used to measure kinematics are shown in Figure 4.

The Polipo is the system of 12 sensors developed as part of this research effort for the low-pressure regime expected to be measured on the body under the soft goods. Full characterization of sensor performance is presented elsewhere^[44], but under dynamic loading conditions the sensors have a root mean square deviation from the applied pressure of 3 kPa, with a time constant of 0.1 seconds, and have been measured as highly repeatable. The sensors are 2.5 cm in diameter and cover the pressure range from about 0-100kPa with approximately 1kPa resolution. The sensors are molded using a hyperelastic polymer that is cured to have a microfluidic channel into which liquid conductive metal is deposited. The sensors measure normal pressure by a change in resistance of the conductive metal when the channels are deformed. These sensors are placed over the arm in a way that targets anticipated hot spots, and secondarily for uniform coverage. The Polipo is integrated into a conformal athletic garment with targets into which the sensors are mounted with Velcro. The system is detachable, allowing independent pressure sensing system to be used on many differently sized people, each donning the wearable pressure-sensing garment. The experimenter can move the sensors to desired anatomical locations and/or concentrate them over a certain region of the body. Due to limitations

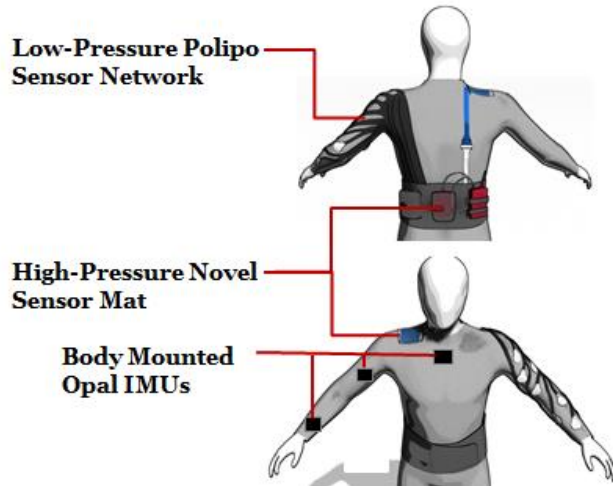


Figure 3. In-suit sensor systems. Each of the three sensor systems are attached to the person's body before donning the space suit. The two pressure sensing systems, the Polipo and Novel, are integrated to a conformal garment, while the IMUs are placed directly on the subject's body.

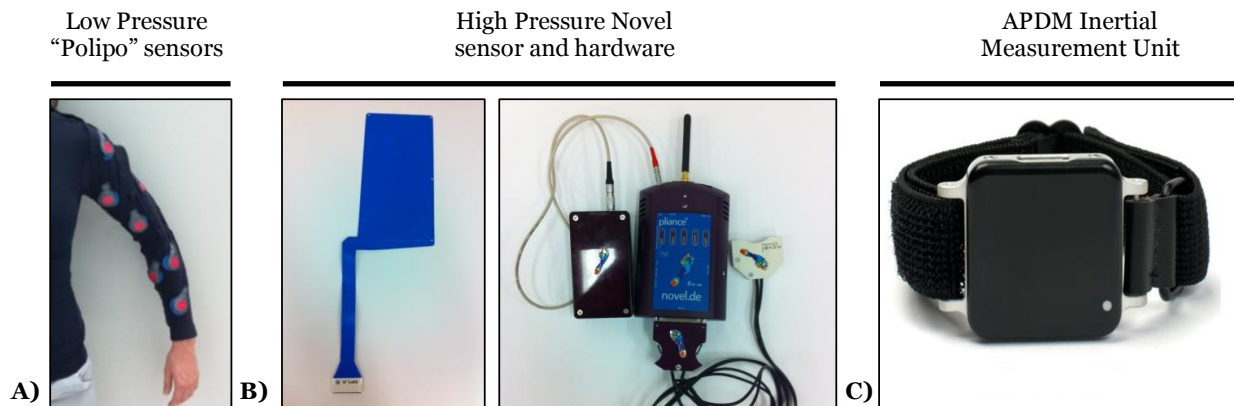


Figure 4. In-suit sensor systems. A) Polipo low-pressure sensors to measure the pressure between the arm and soft goods. B) Novel high-pressure sensor and associated hardware to measure pressure on shoulder under the HUT. C) APDM Opal inertial measurement unit with three placed internally and three placed externally to the suit to measure joint angle differences.

of power and inability to transfer data wirelessly with multiple systems, the Polipo is wearable and run with on-board data collection with electronics attached at the base of the back. An Arduino Microprocessor is used for data collection. Each sensor is powered with constant current of 0.5mA. The entire board in nominal operation with 12 sensors runs ~100mA. The system uses a commercial off-the-shelf 9V battery encased and mounted next to the electronics board, giving a 4 hour test duration limit.

The garment used to attach the Polipo sensors incorporates a pocket interface over the shoulder to house the Novel (Munich, Germany) pressure-sensing mat, which is used for the high-pressure sensing regime. The high-pressure regime is at the interface between the person's body and the hard upper torso of the suit. A Novel pressure sensing mat has been used previously in a study by the Anthropometry and Biomechanics Facility (ABF) on an Extravehicular Mobility Unit hard upper torso in unpublished work. For this experiment a modified S2073 sensor mat with 128 sensor points is used. Each sensor is 1.4cm in each dimension and has a pressure range between 20-600kPa. The Novel system uses ten 1.2V nickel metal hydride batteries with 2000 mAh. The sensor is run at 330mA. Like the Polipo, data collection hardware is mounted at the base of the back and data was stored onboard. Finally, a cover shirt slides easily over the entire sensor suite to prevent catching and to ensure proper sensor placement.

The inertial measurement units (IMUs) chosen for this experiment are the APDM Opal IMU Sensing System (Portland, OR), which are commercially available and are the highest quality sensor system offered by APDM. The IMUs can be seen in Figure 4. Each IMU consists of three accelerometers, three gyroscopes and three magnetometers. An algorithm combines the measurements of the accelerometers and the magnetometers to update the gyroscopes readings that are subject to drift. When the magnetometers measurements are perturbed by external ferro-magnetic field fluctuations, the algorithm preferentially updates the gyroscope with the accelerometers. The algorithm is described in greater details in Yun^[45], but the algorithm as implemented by APDM is proprietary. Three sensors were mounted internally on the upper arm, lower arm, and chest. The IMUs were placed in-plane with one another to optimize the output for isolated joint movements, but their relative orientations allow the detection of off-axis rotations. Three externally mounted IMU sensors on the upper and lower spacesuit arm and suit torso were attached to the suit such that they corresponded to the internal sensors. The internal sensors were attached to the body with a harness or straps and were secured with athletic tape to prevent them from moving during the experiment. The external IMUs were fixed by straps and athletic tape, or Velcro®. Each sensor is 4.8x3.6x1.3 cm and weighs less than 22g. The gyroscopes and magnetometers were recalibrated before each subject and each experiment to take into account the magnetic environment and minimize the gyroscope drift over time. They are powered by a lithium ion battery at 3.7V nominal. The maximum current through the sensor is approximately 56 mA, and battery failure is highly unlikely. The data from the IMU sensors was collected wirelessly and continuously synchronized in real time. In addition, the unsynchronized data was saved on board the sensor in the event of a wireless signal failure. The sensors had 8GB of onboard storage and a battery life of 8 hours. The data was synchronized in real time through the IMU with a resolution of 10 μ s.

Three high-resolution cameras were used to record the motions of the subjects from both the head on and profile views during the experiment. This data was helpful to review the details of the experiment and to visually track the kinematics to compare to IMU results.

B. Subject Selection

This experiment was performed on a total of four subjects. The first experiment was performed in conjunction with the DCCI where one subject was tested in their Mobility Mock-Up, which is an internal test article that was used in the development of the "Demonstrator Suit"^[11]. The same experimental protocol was performed at NASA's Johnson Space Center in the Advanced Space Suit Lab. The test was performed in the Mark III space suit. For all tests, the criteria for suited subject was: 1. Current fit-check in relevant suit, 2. Current test subject medical approval, 3. Extensive experience working in the pressurized suit to aid in comfort and consistency while performing movements. In each instance, the subjects gained their high level of experience through being a suit design engineer, and therefore had performed many testing runs inside their respective suits. Their fit inside the suit had been iterated upon multiple times before the experiments, to achieve the optimal sizing. It should be noted, however, that for the DCCI experiment, the subject's fit was noted as abnormal because the suit was not in its normal configuration. The experiment proceeded due to time constraints, and the fit improved once the suit was pressurized. Due to individual variability in the way subjects move and how the suit fits them, the data collected from the experiment cannot be directly compared across subjects. However, descriptively, it is instructive to look at each subject's data side by side to get a sense of the variability we might see in future studies beyond this baseline analysis.

Each subject was briefed on the experiment and potential hazards associated with participating prior to signing an informed consent. This protocol was reviewed and approved by both the MIT Committee on the use of Humans as Experimental Subjects and NASA Johnson Space Center’s Institutional Review Board. Additionally, each sensor system was reviewed for electrical, encumbrance, and material hazards. The experiment could be terminated by the subject at any time for any reason, or by the test conductor, suit technicians or suit engineer due to any safety or hardware concerns or concern for the suited subject.

C. Experimental Design

Subjects were asked to perform a series of upper body motions inside the space suit. Experienced subjects were selected so they would not develop new, potentially confounding movement strategies to learn the way they move best in the space suits. The pressure profiles and angle histories were recorded for each subject. The test protocol consisted of 12 repetitions of 5 motions inside the space suit. A representative schematic of the test protocol is shown in Figure 5. The selected movements engage the upper body, particularly where the sensors are placed. The 5 motions are 3 isolated joint movements (elbow flexion/extension, shoulder flexion/extension, and shoulder abduction/adduction) and 2 multi-joint functional tasks (overhead hammering, cross body reach). These tasks are described in detail in Figure 6. Prior to the test, subjects were trained on each movement and allowed to repeat it as many times as they desired before the experiment commenced to minimize the effects of learning. For each movement, the 12 repetitions were further subdivided into 3 groups of 4 repetitions each. This was done to evaluate subject fatigue or potential change of biomechanical strategies over the course of the test period. After each group of movements, the subject rested for a minimum of 5 minutes and qualitative information was gathered on subject comfort, subject fatigue, perceived contact with the suit, and perceived consistency of movement. This information was also collected prior to the experiment to determine initial contact with the suit. The experimental design was counterbalanced and each test condition randomized for each subject. Unsited data was collected after the suited test to form the baseline pressure profile used to mitigate the effects of erroneous readings caused by movement without contact with the suit. For the unsited condition, subjects were asked to perform the task matching the pace and range of motion while suited.

Outside of the experimental protocol, additional data was recorded in static positions and for additional dynamic motions for the purposes of calibrating the IMUs and determining baseline loading from the suit. This was done before the subject donned the suit, while pressurized inside the suit, and in some instances while the subject was suited, but unpressurized. Finally, measurements were performed after the experiment to determine changes from the pre-experiment data. The calibration consists of 1) a static calibration where the subject was asked to maintain two different postures for 20 seconds each, and 2) a dynamic calibration where the subject moved through 4 specific isolated joint movements. The dynamic motions included: wrist pronation/supination, elbow flexion/extension, shoulder flexion/extension and shoulder abduction/adduction. The dynamic calibration was used to check the

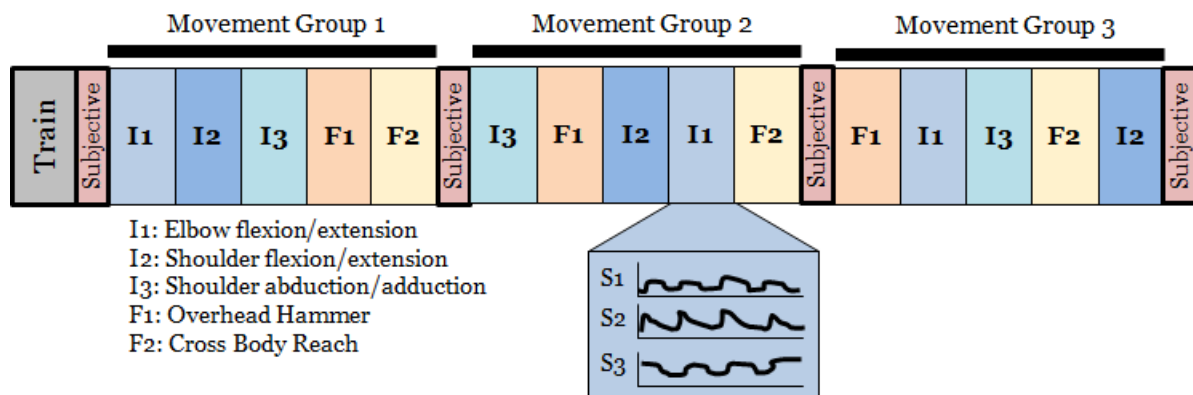


Figure 5. Experimental test protocol for a single subject. Subjects are given time to train each of the 5 movements inside the space suit. Subjective information is taken on comfort and pressure hot spots. The 5 movements are performed in 3 groups with subjective information taken after each group. The order is counterbalanced within the group and randomized between subjects and space suits. Each of the movements is repeated 4 times each. Sensor pressure profiles over time are recorded for analysis.

Elbow Flexion/Extension

The subject stands away from the donning stand supported by their own effort. Beginning with both arms relaxed at their side, palms facing anterior, the subject bends the arms at the elbow through their maximum range of motion. The subject then releases to the relaxed position.



Shoulder Flexion/Extension

The subject stands away from the donning stand supported by their own effort. Beginning with both arms relaxed at their side, the subject bends the arms at the shoulder through the sagittal plane. The subjects move through their maximum range of motion. The subject then releases to the relaxed position.



Shoulder Abduction/Adduction

The subject stands away from the donning stand supported by their own effort. Beginning with both arms relaxed at their side, the subject bends the arms at the shoulder through the coronal plane. The subject moves through his or her maximum range of motion. The subject then releases to the relaxed position.



Cross Body Reach

The subject begins in a relaxed position and reaches across their body to touch their hip on the opposite side. The subject moves their arm up to chest level and sweeps in front of their body. When the arm is extended in front of the shoulder, the subject touches the helmet on the same side. The movement is then repeated with the opposite arm.



Overhead Hammering

Subjects are given a rubber mallet to be grasped with both hands. The subject aims for a flat 7" rubberized square pad. The subject will hammer with both hands beginning the movement overhead and ending at approximately waist level at the height of the stand to which the rubber pad is attached.



Figure 6. Space suit movement tasks performed by each subject. Three isolated joint tasks are performed: *Elbow Flexion/Extension, Shoulder Flexion/Extension, and Shoulder Abduction/Adduction*. Two functional tasks were performed: *Cross Body Reach and Overhead Hammering*. Subjects were given very specific instructions on how to perform the isolated joint tasks, while subjects were given way-point markers to meet and allowed to develop their own biomechanical strategies for the functional tasks. Subject in Mark III suit is shown.

amplitude of the motions as recorded by the sensors. A steel square with level bubbles was used to ensure that subjects reached the requested 90° movement amplitude.

III. Results

A. David Clark Company Experiment

The first experiment was performed on one subject at the DCCI inside their Mobility Mockup space suit, following a pilot study in the MIT arm vacuum chamber. The DCCI Mobility Mockup suit was pressurized to 3.5 psi and used an air cooling system. The subject wore comfort garments and padding as desired for comfort and suit fit. The suit is used to evaluate new suit concepts, and therefore the upper body configuration was different for each arm/shoulder. In addition to the test protocol outlined previously, the subject also performed the experiment suited while un-pressurized.

The testing at DCCI proved extremely useful to finalize the experimental protocol for the NASA Mark III testing. Subjects were given very specific instructions as to arm orientation during the motion, when to focus on which isolated joint movements, and ensuring the subject returned to a neutral position before beginning the next repetition. This evolved over the course of the pilot and DCCI experiments based on the subject feedback and observation. We adjusted the ordering of tasks based on subject feedback, such as changing cross body reach to 4 repetitions with the right arm followed by 4 with the left. It also became clear that taking subjective feedback after each motion instead of after each movement group would improve our results. Finally, it allowed us to improve our

data collection timing-tool so we could sync the data after the experiment, without which analyzing across sensor systems would not be possible.

The Polipo system did not produce rigorous data results for the DCCI experiment. Due to technical issues, the data logged once every 7 seconds, rather than the intended 0.3 seconds. Therefore detailed results corresponding to specific movement pressures were elusive. However, DCCI test was successful in allowing us to finalize the procedural aspects for the Mark III space suit experiment. The subject was asked to evaluate the garment fit and evaluate the degree to which the system inhibited motion. Adjustments were made in real time, a practice that was used in the follow-up experiment at NASA. Additionally, it was determined that turning on and beginning data collection prior to initializing the Novel data collection system was necessary. All hardware issues were resolved prior to any additional testing.

The DCCI experiment was extremely important for evaluating the performance of the Novel pressure mat. Our ability to mimic the testing environment was limited in our laboratory pilot experiments, giving us very limited information of how the system would function in a full body pressurized suited environment. The experiment gave us a general idea of the durability of the system, as well as the range of pressure data, including localized pressure magnitudes, noise levels, and ease of identifying pressure profiles of various movements. One important aspect of the data was the occasional erroneous pressure readings that spiked to the maximum possible pressure value of the sensor. It was determined that this was likely caused by bending or folding of the sensor due to the motion of the arm with respect to the placement of the sensor on the subject's body. Also of note was that nearly every sensor in the sensor mat was loaded during each movement, indicating that the subject is broadly loaded over the entire shoulder in the DCCI suit.

The IMU sensors recorded accurate and reliable data for the DCCI experiment. The experiment demonstrated the reliability of the wireless signal through the suit. The root mean square error (RMS) was calculated for the yaw and pitch angles over 20 seconds for all IMUs under each static calibration. The average drift was 5.8° (7.1° standard deviation) for the elbow joint angle and 4.9° (standard deviation 5.5°) for the shoulder joint angle. However, prior to the final two motions of the experiment, the IMU laptop recording the data crashed, which reemphasized the need to take both wireless transmission of data and onboard data storage, allowing this portion of the experiment to be recovered in post processing. The most effective way to mount the sensors to minimize shifting was to use elastic straps (APDM, Portland, OR) with athletic tape on the back of the sensor attached directly to the subject's skin. Using the DCCI IMU data, the methodology for analyzing kinematics through quaternions was developed. However, at the time of the experiment, only five IMUs were available. The IMU located on the suit torso was not used, making it impossible to quantify the suit shoulder joint angle. For this reason, a comparison of the shoulder suit joint angle between the Mark III and the David Clark Mobility Mockup is not possible. In addition to establishing the final protocol, the analysis of the IMU data also showed statistically significant decrements in motion while suited compared to the unsuited case. A full review of the IMU data analysis can be found in "Feasibility of Spacesuit Kinematics and Human-Suit Interaction" (Bertrand et al., ICES, 2014).

B. NASA Johnson Space Center Experiment

The second experiment was performed at NASA Johnson Space Center with three subjects inside the Mark III space suit. The suit was pressurized at 4.3 psi for these experiments, but is capable of being pressurized to 8.3 psi. As per normal operation, the subjects also wore a liquid cooling garment, thermal comfort undergarment, wristlets, comfort gloves, and socks to aid in comfort and thermal control. Padding was used based on the subject's normal suit requirements, however any shoulder padding was removed to prevent interference with the Novel system located over the shoulder.

Static data taken prior to donning the suit was used to establish the zero-pressure value while on the subject's body. Once the suit was donned and pressurized, static data collected during IMU calibration was used to determine the suit loading on the person's body. After the pressurized portion of the experiment, static data collected during unsuited IMU calibration was used to determine any shifts from the baseline readings and to identify sensors that broke over the course of the experiment.

All Polipo sensors were calibrated prior to the experiment. However, any sensors replaced over the course of the experiment were calibrated upon returning to MIT. Some sensors were known to give erroneous results. Sensor 8 is excluded from the experiment because it had a wire break inside the Polipo cover. Sensors 7 and 12 were known to give jumpy responses prior to the beginning of the experiment due to internal fraying of the copper wiring inside the Polipo's fabric cover. With pressure on the wires, however, the connection could be reestablished. Therefore, these sensors were able to give responses, but their recorded profiles were treated with particular caution.

The 3 subjects performed 5 movement tasks spread over 3 movement groups. Data was collected by 11 sensors, for a total of 495 response profiles to evaluate. Each profile was examined to determine if the output was useful. Table 1 summarizes the survivability of the Polipo sensors inside the space suit environment for all subjects across all movement tasks. Figure 7 shows the location of the sensors on the arm. Of the 165 possible sensor loading regimes (3 subjects, 5 motions, 11 sensors), 44% of the profiles were useful. The integrity of the data deteriorated as the experiment progressed. Subject 1 registered a sensor response for 58% of his loading scenarios, while Subjects 2 and 3 had 44% and 29% respectively. The continual decrease in data integrity reflects deterioration of the sensor system with use, due primarily to breakage of the copper strands in the wiring.

There is a distinction to be made between sensors that broke and sensors that didn't register a response because the motion did not load it. Sensors broke for a variety of reasons. The first reason was due to losing the connection at the solder joint between the wiring and the sensor itself. This typically resulted in a total loss of signal. However, for some sensors, the movement itself would reestablish the circuit's connection, allowing some intermittent data to be used. The most common form of failure was in the slow deterioration of the wiring. Internal breakage of the copper strands in the wires caused the data to be jumpy, either increasing or decreasing the resistance as the subject moved and copper strands came in and out of contact with one another. This progressively became more problematic with each subject as wear on the system increased. Table 1 shows the breakdown of which sensors gave useful results not only because the sensor was not broken, but also because it was loaded during the movement group. Profiles are divided by subject and movement task for each sensor. The table indicates under which movement group the sensor was loaded and the profile was readable. Sensors which also gave a reading during the unsuited movement are designated with a "U".

In general, Sensor 1 did not provide useful information due to internal breakage of the wires. The response profiles were very jumpy, although occasionally a consistent response could be detected below the noise. Sensor 2 was extremely useful for Subject 1, but broke early during the experiment for Subject 2. The wiring was repaired and performed well for Subject 3, although it was only loaded during elbow flexion/extension (and therefore also cross body reach). Although Sensor 3 survived the entire experiment, it was also nearly never loaded. The sensor was located on the back side of the forearm, and seemingly rarely made contact with the suit. Sensor 4 broke early in the experiment for Subject 1 at the solder joint. It was repaired and provided useful data for Subject 2. However, over the course of the experiment the wires began to break internally, making it unusable for Subject 3. Sensor 5 was very useful for Subject 1, but broke at the solder joint late in the experiment. It broke again at the solder joint early in the experiment for Subject 2, but was repaired for Subject 3 and remained intact, providing useful profiles for the duration of the experiment. Sensor 6 remained intact for all subjects, but broke midway through the experiment for Subject 3. It provided some of the clearest profiles, but also exhibited an unsuited response due to its placement on the elbow. This artifact should be removed from the data before considering pressure magnitudes. Sensor 7 was known prior to the experiment to give erratic responses due to wire breakage, and almost no usable profiles were detected. Sensor 8 was not included in the experiment. Sensor 9 remained intact for Subject 1,

Table 1. Useful movement profiles. Summary of sensors detecting pressure over each subject, movement task, and movement group. Movement tasks are E – Elbow flexion/extension, S – Shoulder flexion/extension, A – Shoulder abduction/adduction, C – Cross body reach, and O – Overhead hammering. The movement groups are numbered 1, 2, and 3, while an unsuited profile is listed as "U".

	Subject 1					Subject 2					Subject 3				
	E	S	A	C	O	E	S	A	C	O	E	S	A	C	O
Sensor 1				1 2 3 U						1 2 3 U					
Sensor 2	1 2 3	1 2 3	1 2 3 U	1 2 3	1 2 3	1	1	1	1	1	1 2 3			1 2 3	
Sensor 3	1 2 3														
Sensor 4	1 2	1	1	2		1 2 3	1 2	1 2 3		1 2					
Sensor 5	1 2	1 2 3	1 2	1 2 3		1			1 2		1 2 3	1 2 3	1 2 3	1 2 3	1 2 3
Sensor 6	1 2 3 U	1	1 2 3	1 2 3 U		1 2 3 U	1 2 3	1 2 3	1 2 3 U	1 2 3	1 2	1 2	1	1	1 2
Sensor 7	3														
Sensor 8															
Sensor 9	3		1 2 3						1					1 2 3	
Sensor 10	2	1		1		1 2	1	1 2	1 2	1 2		1			
Sensor 11	1 2 3	1 2 3	1 2 3 U	1 2 3 U	1 2 3						1 2 3				1 2 3
Sensor 12	1 2 3				1 2		1								

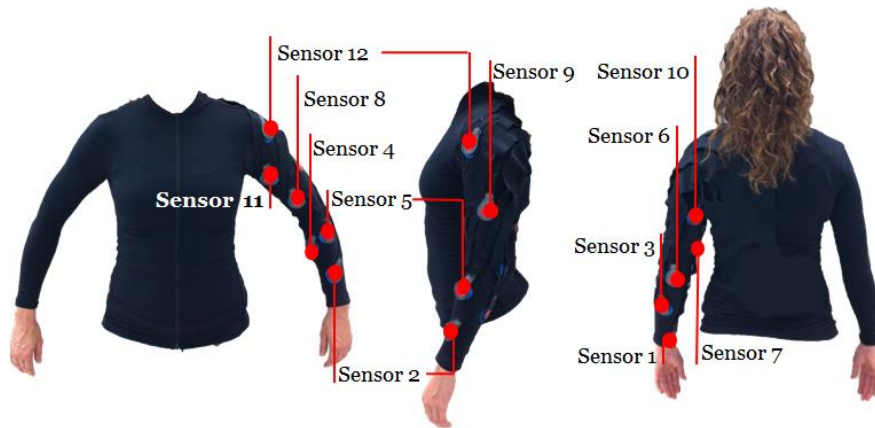


Figure 7. Polipo sensor locations. *The Polipo low-pressure sensing system is placed on the subject's left arm and is designed for anticipated pressure hot spots and for even distribution over the sleeve. Sensors 1 and 2 are located on the wrist; Sensors 3 and 4 on the forearm; Sensors 5 and 6 on the elbow; Sensors 7-9 on the upper arm, and Sensors 10-12 near the shoulder.*

however was rarely loaded against the suit. Short spikes in pressure were detected on occasion, likely due to impact with the upper arm bearing. This was confirmed with Subject 2, whose impact with the bearing caused the sensor to rupture. The sensor was replaced and Subject 3 showed similar response profiles to Subject 1. Sensor 10 was constantly loaded for all subjects in the neutral posture, due to its placement on the back of the upper arm. Therefore, the response profiles detected by this sensor are in offloading, rather than in loading. For all subjects, the sensor broke during the course of the experiment. Sensor 11 produced very useful results for Subject 1, but over the course of the experiment its responses deteriorated due to internal breakage of the wires. Finally, Sensor 12 was nearly unusable due to internal breakage, however occasionally response profiles were able to be detected through the noise.

In general, the Novel pressure sensing system proved to be very reliable in terms of quality of gathered data. While a few erroneous readings such as those that arose in the testing at DCCI also occurred for Subject 1, these were easily removed during data processing, and none occurred for Subjects 2 or 3. With regards to durability, the Novel system performed well, but by the end of all three days of testing there was noticeable damage to the sensor. Any future in-suit testing would necessitate reconditioning of the sensor. Another notable change over the course of the experiment was shifting of the Mark III shoulder straps inside the suit's HUT. As the right shoulder pad was located directly on top of the Novel sensor, any shifting would affect the measured distribution of pressure. This occurred noticeably for Subject 3, although this was likely a result of performing additional tasks involving extensive bending and reaching that were not performed with Subjects 1 or 2. Nevertheless, slight shifting could also have occurred for Subjects 1 and 2. This shifting of shoulder pads does not pose a problem for our data, as it still represents how pressures change when humans move within the suit; however, it is an observation to consider when comparing pressure distributions across subjects.

As sensor placement varied between subjects, we made a procedural adjustment during the experiment that involved locating and briefly applying localized pressure to pre-identified bony landmarks—the acromion, mid-shoulder, crux of the clavicle, and corner of shoulder blade. During data analysis, we could then determine how the sensor was oriented on each of the subjects based on where these pressure points were detected on the sensor grid. Table 2 shows representative loading maps of the Novel sensor for each subject during each movement. The percentage of sensors loaded is also given. The orientation of the sensor anatomically is shown in Figure 8. In general, Subject 1 was more broadly loaded than each of the other subjects. All subjects were loaded more broadly on the proximal end of the shoulder near the neck, which is consistent with shoulder pad placement. The results of this analysis show the sensor was well positioned for measuring load, but it is not clear how additional sensors or changes in placement would affect the results. Considering the interface between the Novel system and the internal suit architecture, the internal harness with shoulder padding prevented us from measuring the pressures that would be directly applied to the shoulder due to contact with the hard upper torso. We anticipate more concentrated and potentially higher pressure readings in the absence of such padding. However, this padding is part of the Mark III

suit design, so our measurements accurately reflect the pressures an astronaut would experience while working in the suit. It would nevertheless have contributed to the interpretation of our results if we had known the exact placement of the shoulder pad on the sensor.

The IMU system functioned well during the experiment and gave useful data for the subjects. No sample drop occurred and there was no crash from the wireless signal or the computer recording the data. The root mean square error (RMS) was calculated for the yaw and pitch angles over 20 seconds for all IMUs for all static calibrations. Subject 1 had an average drift of 1.2° (1.1°) for the elbow joint angle and 3.3° (4.8°) for the shoulder joint angle, while subject 2 had 1.2° (1.0°) for the elbow joint angle and 1.5° (1.6°) for the shoulder joint angle. Two IMUs from the first subject had a constant gyroscope offset to the raw signal due to miscalibration, causing erroneous readings. The data was recovered by removing the constant offset and reprocessing the signals through the algorithm used by APDM to calculate the orientation quaternions, but the data has yet to be analyzed. The IMUs were recalibrated and performed as reported for the other two subjects. The placement of the sensors on the subject was the same as for the DCCI experiment, with the same attachment technique. On the suit, the torso IMU was attached on the hard upper torso of the Mark III with Velcro®, and stayed fixed during all the experiment for the three subjects. The IMU located on the suit lower arm, was attached with straps, and was secured with athletic tape just above the glove bearing. It did not move significantly during the all experiments. However, this placement disturbed the measurement of the elbow flexion/extension for Subject 2. Although the subjects were asked to perform the elbow flexion/extension without wrist bending, Subject 2 bent his wrist at the top of the elbow flexion. The IMU located internally on the lower arm could not bend because it was fixed on the forearm, while the corresponding suit IMU moved with wrist flexion, giving some biased results. The IMU located on the upper arm of the suit was attached with straps and athletic tape for Subject 1. The strap and IMU slid on the bearing over the course of the experiment. For the remaining subjects, the IMU was attached with Velcro®, which resolved the problem. The data analyzed from these experiments include measuring differences between the person and the space suit, the lag between the angles the subject's move through, and the constant offset of joint angles during maxima and minima of movement. Results showed suit multi-axis rotations for the shoulder bearing, as

Table 2 . Sensor mat loading for all subjects over each movement task. Sensor mat orientation corresponds to that shown in Figure 8. Individual variability may be due to fit and shoulder pad placement, but sensor coverage appears to be adequate.

	Subject 1	Subject 2	Subject 3
Elbow Flex./Ext.	51.6%	39.8%	32.3%
Shoulder Flex./Ext.	80.5%	59.9%	76.3%
Shoulder Ab./Add.	82.3%	54.4%	57.6%
Crossbody Reach	84.1%	61.2%	50.5%
Overhead Hammer	79.4%	60.2%	58.9%

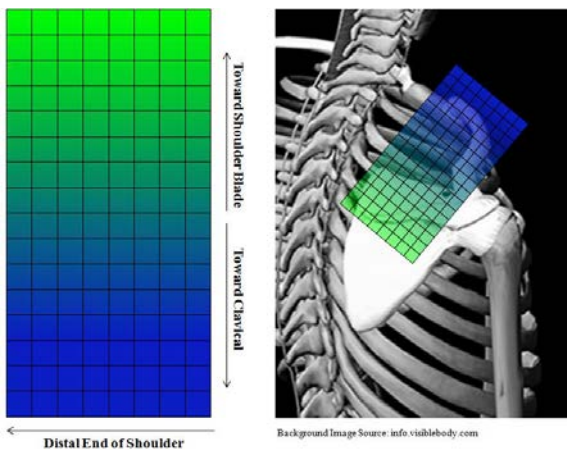


Figure 8. Orientation of the Novel sensor relative to each subject's body. This orientation corresponds to the information in Table 2.

expected. A full review of the data analysis can be found in “Feasibility of Spacesuit Kinematics and Human-Suit Interaction” by the authors here-in.

IV. Conclusions

This research is, to our knowledge, the first experiment to characterize human-space suit interaction with pressure sensors placed inside the pressurized suit environment. Unpublished work from the NASA Anthropometry and Biomechanics Facility performed a similar study and future work includes comparing results and procedures. This research builds from previous work on measuring joint angles both internal and external to the suit. It is our first glimpse “inside the space suit” and will be the baseline for future studies.

Some of the most important lessons learned from this study were regarding identifying and evaluating potential hazards to the test subjects, as evaluated in the Hazard Analysis performed prior to the JSC experiment. Materials, electrical, battery, and hardware encumbrance were each analyzed and deemed to be an acceptable level of risk with controls. These considerations should be incorporated in future iterations of suited experiments with wearable electronics. Each sensor system was designed/selected to be stand-alone and wearable in the suit environment. This allowed us to move beyond traditional barriers of creating a suit pass-through or potential movement inhibition. Demonstrating a safe, well executed experiment will allow future iterations of this work to be completed more rapidly and with a track record for implementation, reducing uncertainty.

These experiments also allowed us to evaluate the sensor systems in the suit environment. As a result of these tests, limitations of durability were identified for both pressure-sensing systems. Improvements to the Polipo for future work include developing a wiring system where friction and repeated bending will not cause internal breakage of the wire. Additionally, the solder joint between the sensors and the wires should be improved to improve system resilience. Improvements may also be made for the Novel sensor. The sensor was bent and the cover began peeling near the edges with use. Although this did not negatively impact the results, future tests should not be performed until the sensor can be reconditioned. The sensor could be housed differently to prevent the cover peel, but the bending cannot be fixed given the sensor’s size. Potentially in the future a smaller sensor or some of their newly developed stretchable sensors may be better suited for these tests. To improve the IMU results, further study beyond our cursory analysis could be performed to quantify the magnetometer perturbations and its effects on the estimation of the orientation of the IMUs. A 3D visualization tool of suit joint angles is being developed to better understand the multi-axis rotation of joints through the bearings, and will aid in comparing the human and space suit motions.

Future iterations of this experiment should improve the integration of the three data collection systems together. Due to potential concerns of interference with the communications system, not all the data was collected wirelessly. Currently, this problem is resolved by keeping individual timelines for each system, and the data is synced post-test, increasing the potential for error. Coupling the data from the kinematics sensors with the pressure sensors is ideal to determine the contact between the human and the suit. Either a new data initialization process should be developed, or the data should be collected by one central processor. Additionally, future areas of study should evaluate shifting the placement of the Polipo sensors to areas of the body we would like to target for further study. This may also include other areas of the body. Decreasing sensor size would also allow an increased density of sensor placement to collect additional pressure values against the body.

There were many successes in implementing this experiment that should be carried further into future experiments. The Polipo sensor system was built from scratch for this application. It was designed to be wearable through the full range of motion, stand alone for power and data collection, be transferrable between subjects, and was targeted at detecting pressure at the low-pressure range and resolution expected under the soft goods. Each of these design objectives was achieved. As a result, its applicability to the space suit environment was validated with this experiment. The Novel pressure sensing system also proved to be extremely useful even in the loading regime that was less than it was originally designed for. The experiment also proved that kinematics could be efficiently tracked inside the suit, wirelessly, and compared to the suit motions, with the use of inertial measurement units.

These experiments were very successful in opening the door for this type of space suit testing. Although the data is presented elsewhere, the results from the experiment provide valuable insight into how motions occur, how consistent subjects are, and how discomfort and fatigue can build up over time while working in the suit. Future planned experiments include continued collaboration with our colleagues at DCCI and the ASL to characterize new suited motions, new suit configurations, and other areas of the body. The implications of the test are valuable in finding an initial baseline of human-suit interaction and will guide future tests to optimize placement of sensors.

Acknowledgments

The authors would like to thank David Clark Company, in particular Dr. Shane Jacobs, and NASA Johnson Space Center Advanced Space Suit Lab, in particular Mrs. Amy Ross, for their support. This project is funded through NASA Grant NNX12AC09G, "Spacesuit Trauma Countermeasure System for Intravehicular and Extravehicular Activities". Additional support provided by the National Science Foundation Graduate Research Fellowship Program and the MIT Portugal Program.

References

- [1] Jacobs S, D. Tufts. Follow-On Development of the Demonstrator Suit for Post-Shuttle Operations. International Conference on Environmental Systems. Portland, OR: American Institute of Aeronautics and Astronautics, 2011. p.19.
- [2] Hochstein J. Astronaut Total Injury Database and Finger/Hand Injuries During EVA Training and Tasks. vol. M.S. Strausborg, FR: International Space University, 2008.
- [3] Jones JA, Hoffman RB, Buckland DA, Harvey CM, Bowen CK, Hudy CE, Strauss S, Novak J, Gernhardt ML. The use of an extended ventilation tube as a countermeasure for EVA-associated upper extremity medical issues. *Acta Astronautica* 2008;63:763.
- [4] Longnecker D, et al. Review of NASA's Longitudinal Study of Astronaut Health. In: *Medicine 10*, editor. Washington, D.C.: National Academies Press, 2004.
- [5] Morgan DA, Wilmington R, Pandya A, Maida J, Demel K. Comparison of Extravehicular Mobility Unit (EMU) Suited and Unsuited Isolated Joint Strength Measurements. Houston, TX: Johnson Space Center, 1996.
- [6] Opperman R. Astronaut Extravehicular Activity - Safety, Injury, and Countermeasures & Orbital Collisions & Space Debris - Incidence, Impact, and International Policy. *Aeronautics and Astronautics, Technology Policy Program*, vol. M.S. Cambridge, MA: Massachusetts Institute of Technology, 2010. p.183.
- [7] Scheuring RA, Mathers CH, Jones JA, Wear ML. Musculoskeletal injuries and minor trauma in space: incidence and injury mechanisms in U.S. astronauts. *Aviat Space Environ Med* 2009;80:117.
- [8] Strauss S. Extravehicular Mobility Unit Training Suit Symptom Study Report. Houston, TX: Johnson Space Center, 2004.
- [9] Viegas S, Jones J, Strauss S, Clark J. Physical Demands and Injuries to the Upper Extremity Associated with the Space Program. *Journal of Hand and Surgery* 2004;29:7.
- [10] Williams DR, Johnson BJ. EMU Shoulder Injury Tiger Team Report. Houston, TX, 2003. p.104.
- [11] Carr C. Bioenergetics of Walking and Running in Space Suits. *Aerospace and Astronautics*, vol. Ph.D. Cambridge: Massachusetts Institute of Technology, 2005.
- [12] Harris GL, editor *Origins and Technology of the Advanced Extravehicular Space Suit*. San Diego, CA: American Astronautical Society, 2001.
- [13] Thomas K, McMann H. *US Spacesuits*. Chichester, UK: Springer-Praxis Publishing Ltd, 2006.
- [14] Schmidt P. An Investigation of Space Suit Mobility with Applications to EVA Operations. *Aeronautics and Astronautics*, vol. PhD. Cambridge, MA: Massachusetts Institute of Technology, 2001. p.254.
- [15] Norcross J, K. Clowers, T. Clark, L. Harvill, R. Morency, L. Stroud, L. Desantis, J. Vos, M. Gernhardt. *Metabolic Costs and Biomechanics of Level Ambulation in a Planetary Suit*. Houston, TX: Johnson Space Center, 2010. p.74.
- [16] Newman D, Schmidt P, Rahn D, Badler N, Metaxes D. Modeling the Extravehicular Mobility Unit (EMU) Space Suit: Physiology Implications for Extravehicular Activity (EVA). International Conference on Environmental Systems. Toulouse, FR: SAE International, 2000.
- [17] Jaramillo MA, Angermiller B, Morency R, Rajulu S. Refinement of Optimal Work Envelope for Extravehicular Activity Suit Operations. In: *Facility AaB*, editor. Houston, TX: Johnson Space Center, 2008.
- [18] Gernhardt M, Jones J, Scheuring R, Abercromby A, Tuxhorn J, Norcross J. Risk of Compromised EVA Performance and Crew Health Due to Inadequate EVA Suit Systems. Houston, TX: Human Research Program, 2009.
- [19] Strauss S, Krog RL, Feiveson AH. Extravehicular mobility unit training and astronaut injuries. *Aviat Space Environ Med* 2005;76:469.
- [20] Opperman R, Waldie J, Newman DJ. EVA Injury, Comfort, and Protection: Improving the Plight of the Hand and Shoulder for the Constellation Program. International Conference on Environmental Systems. San Francisco, CA: AIAA, 2009.
- [21] Scheuring R, McCullough P, VanBaalen M, Minard C, Watson R, Bowen S, Blatt T. *Shoulder Injuries in US Astronauts Related to EVA Suit Design*. Aerospace Medical Association. Atlanta, GA, 2012.
- [22] Reinhardt A, Magistad J. AX-5 Space Suit Reliability Model. International Conference on Environmental Systems, vol. 99. Williamsburg, VA: SAE, 1990. p.1057.
- [23] Gilkey A. Space Suit Simulator for Partial Gravity Extravehicular Activity Experimentation and Training. Department of Aeronautics and Astronautics, vol. M.S. Cambridge, MA: Massachusetts Institute of Technology, 2012.
- [24] Jacobs S, Tufts D. Follow-On Development of the Demonstrator Suit for Post-Shuttle Operations. International Conference on Environmental Systems. Portland, OR: American Institute of Aeronautics and Astronautics 2011.

- [25] Braden JR, Akin DL. Development and Testing of a Space Suit Analogue for Neutral Buoyancy EVA Research. International Conference on Environmental Systems. San Diego, CA: Society of Automotive Engineers, 2002.
- [26] de Leon P, Harris GL. NDX-2: Development of an Advanced Planetary Space Suit Demonstrator System for the Lunar Environment. International Conference on Environmental Systems. Portland, OR: AIAA, 2011.
- [27] Benson E, Rajulu S. Complexity of Sizing for Space Suit Applications. In: Duffy VG, editor. Digital Human Modeling: Springer-Verlag, 2009. p.599.
- [28] Gast M, Moore S. A Glimpse from the Inside of a Space Suit: Whats it Really Like to Train for an EVA? Acta Astronautica 2010;2011:9.
- [29] NASA. NASA Space Flight Human System Standard Volume 2: Human Factors, Habitability, and Environmental Health. NASA-STD-3001 VOL II, 2011.
- [30] Cowley M, Margerum S, Harvill L, Rajulu S. Model for Predicting the Performance of Planetary Suit Hip Bearing Designs. In: Duffy VG, editor. Advances in Human Factors and Ergonomics. CRC Press, 2012.
- [31] Parry D, L. Curry J, D. Hanson, Towle G. A Study of Techniques and Equipment for the Evaluation of Extravehicular Protective Garments. Dayton, OH: Hamilton Standard, 1966. p.427.
- [32] Holschuh B, Waldie J, Hoffman J, Newman D. Characterization of Structural, Volume, and Pressure Components to Space Suit Joint Rigidity. International Conference on Environmental Systems. Savannah, GA: Society of Automotive Engineers, 2009.
- [33] Matty J, Aitchison L. A Method for and Issues Associated with the Determination of Space Suit Joint Requirements. International Conference on Environmental Systems. Berlin, Germany: SAE International 2009.
- [34] Valish D, Eversley K. Space Suit Joint Torque Measurement Method Validation. International Conference on Environmental Systems. San Diego, CA: American Institute of Aeronautics and Astronautics, 2012. p.14.
- [35] Meyen F, Holschuh B, Kobrick R, Jacobs S, Newman D. Robotic Joint Torque Testing: A Critical Tool in the Development of Pressure Suit Mobility Elements. International Conference on Environmental Systems. Portland, OR: AIAA, 2011.
- [36] Greenisen M. Effect of STS Space Suit on Astronaut Dominant Upper Limb EVA Work Performance. University of Houston, 1986. p.8.
- [37] Griffin B, Howard R, Rajulu S, Smitherman D. Creating a Lunar EVA Work Envelope. International Conference on Environmental Systems. Savannah, GA: Society of Automotive Engineers, 2009.
- [38] Kuznetz L. Real Time Determination of Metabolic Rate and Life Support Consumables During EVA. Houston, TX: Crew Systems Division, 1969. p.63.
- [39] Waligora J, Horrigan D. Metabolism and Heat Dissipation During Apollo EVA Periods. In: J. Parker J, editor. Biomedical Results of Apollo. Houston, TX: Johnson Space Center, 1975.
- [40] Di Capua M, Akin D. Body Pose Measurement System (BPMS): An Inertial Motion Capture System for Biomechanics Analysis and Robot Control from Within a Pressure Suit. International Conference on Environmental Systems. San Diego: American Institute of Aeronautics and Astronautics, 2012.
- [41] Kobrick R, C. Carr, F. Meyen, A. Domingues, Newman D. Using Inertial Measurement Units for Measuring Spacesuit Mobility and Work Envelope Capability for Intravehicular and Extravehicular Activities. International Astronautical Congress. Naples, Italy: International Astronautical Federation, 2012. p.9.
- [42] Newman DJ, J. Hoffman, K. Bethke, C. Carr, N. Jordan, L. Sim, N. Campos, C. Conlee, B. Smith, J. Wilcox, G. Trotti. Astronaut BioSuit System for Exploration Class Missions: NIAC Phase II Final Report. Cambridge, MA: Massachusetts Institute of Technology, 2005. p.34.
- [43] Norcross J, Lee L, Clowers K, Morency R, Desantis L, Witt J, Jones J, Vos J, Gernhardt M. Feasibility of Performing a Suited 10-km Ambulation on the Moon - Final Report of the EVA Walkback Test (EWT). Houston, TX: Johnson Space Center, 2009. p.48.
- [44] Anderson, A. "Understanding Human-Space Suit Interaction to Prevent Injury During Extravehicular Activity" Doctoral Thesis, Massachusetts Institute of Technology. Cambridge, MA, June 2014.
- [45] Yun X., Bachmann E. R., McGhee R. B., A Simplified Quaternion-Based Algorithm for Orientation Estimation from Earth Gravity and Magnetic Field Measurements, IEEE Transactions in Instrumentation and Measurement, VOL. 57, NO. 3, March 2008.),

The Effect of Window Size and Lead Time on Pre-Impact Fall Detection Accuracy Using Support Vector Machine Analysis of Waist Mounted Inertial Sensor Data

Omar Aziz, Colin M. Russell, Edward J. Park, *Senior Member, IEEE*, and Stephen N. Robinovitch

Abstract—Falls are a major cause of death and morbidity in older adults. In recent years many researchers have examined the role of wearable inertial sensors (accelerometers and/or gyroscopes) to automatically detect falls. The primary goal of such fall monitors is to alert care providers of the fall event, who can then commence earlier treatment. Although such fall detection systems may reduce time until the arrival of medical assistance, they cannot help to prevent or reduce the severity of traumatic injury caused by the fall. In the current study, we extend the application of wearable inertial sensors beyond post-impact fall detection, by developing and evaluating the accuracy of a sensor system for detecting falls prior to the fall impact. We used support vector machine (SVM) analysis to classify 7 fall and 8 non-fall events. In particular, we focused on the effect of data window size and lead time on the accuracy of our pre-impact fall detection system using signals from a single waist sensor. We found that our system was able to detect fall events at between 0.0625-0.1875 s prior to the impact with at least 95% sensitivity and at least 90% specificity for window sizes between 0.125-1 s.

I. INTRODUCTION

Falls are the leading cause of injury among older adults in Canada, including over 90% of hip fractures [2], [10] and wrist fractures [7], and a large percentage of head and spine injuries [6]. About 30% of older adults living in the community and 60% of individuals living in a residential care environment will experience at least one fall each year [11]. Hip fractures are the most significant injury related to falls, with approximately 23,000 annual cases in Canada, and medical costs in excess of \$1 billion [8].

Wearable kinematic sensors such as accelerometers and gyroscopes represent a promising technology for preventing and mitigating the effects of falls in older adults. One of the key issues in preventing fall related injuries is to detect a fall in its descending phase with a sufficient lead time in order to deploy protective equipment (such as inflatable hip protectors, helmets, etc.) to cushion the fall prior to impact [12]. Wu and Xue [13] proposed a pre-impact fall detection technique by thresholding the vertical velocity profile of the waist worn accelerometer, and showed that with vertical

velocity threshold set at -1 m/s their algorithm was able to detect all falls with at least 70 ms lead time with only three false positives found during approximately 13 hours of data. Similarly, Nyan et al. [5] showed 100% sensitivity with approximately 200 ms lead time by locating sensors at the sternum, waist and under the arm. However, Nyans threshold algorithm resulted in 16% of the activities of daily living (ADLs) being misclassified as falls.

Our study diverges from traditional threshold-based methods by using a machine-learning pre-impact fall detection method – support vector machines (SVM) – for better adaptability and reliability. Furthermore, our study uses a wide variety of fall and daily activity scenarios to more rigorously test the accuracy of our SVM algorithm across a combination of varying lead times and window sizes, using a single waist mounted tri-axial accelerometer and gyroscope.

II. METHODS

A. Participants

Ten healthy adults (ranging in age between 22 and 32 years) participated in the study. All subjects were students at Simon Fraser University (SFU), recruited through advertisements posted on university notice boards. All participants provided informed written consent and the experimental protocol was approved by the research and ethics committee at SFU.

B. Experiment Design

We examined a library of video sequences of 227 real-life falls in older adults, acquired as part of an ongoing project by our research team to examine the mechanisms of falls in long-term care facilities [9]. We found that 75% of falls were collectively due to the following seven causes: (i) slips, (ii) trips, (iii) hit or bump by an object or another person, (iv) collapse or loss of consciousness, (v) misstep or cross-step while walking and (vi-vii) incorrect shift of bodyweight while sitting down on or rising from a chair. We included all seven of these types of falls in our laboratory experiment. During all fall trials, the floor was covered with 30 cm thick gymnasium mats into which we inserted a 12 cm thick top layer of high-density ethylene acetate foam. The composite structure was stiff enough to allow for stable standing and walking while still soft enough to reduce the impact force to a safe level in case of a fall.

In addition to fall trials, eight activities of daily living (ADLs) were recorded which included: (i) walking, (ii)

O. Aziz is with the School of Engineering Science, Simon Fraser University, Burnaby, BC, V5A 1S6 Canada. oaziz@sfu.ca

C. M. Russell is with the Department of Biomedical Physiology and Kinesiology, Simon Fraser University. crussell@sfu.ca

E. J. Park is with Mechatronic Systems Engineering, Simon Fraser University. ed_park@sfu.ca

S. N. Robinovitch is with the School of Engineering Science and the Department of Biomedical Physiology and Kinesiology, Simon Fraser University. stever@sfu.ca

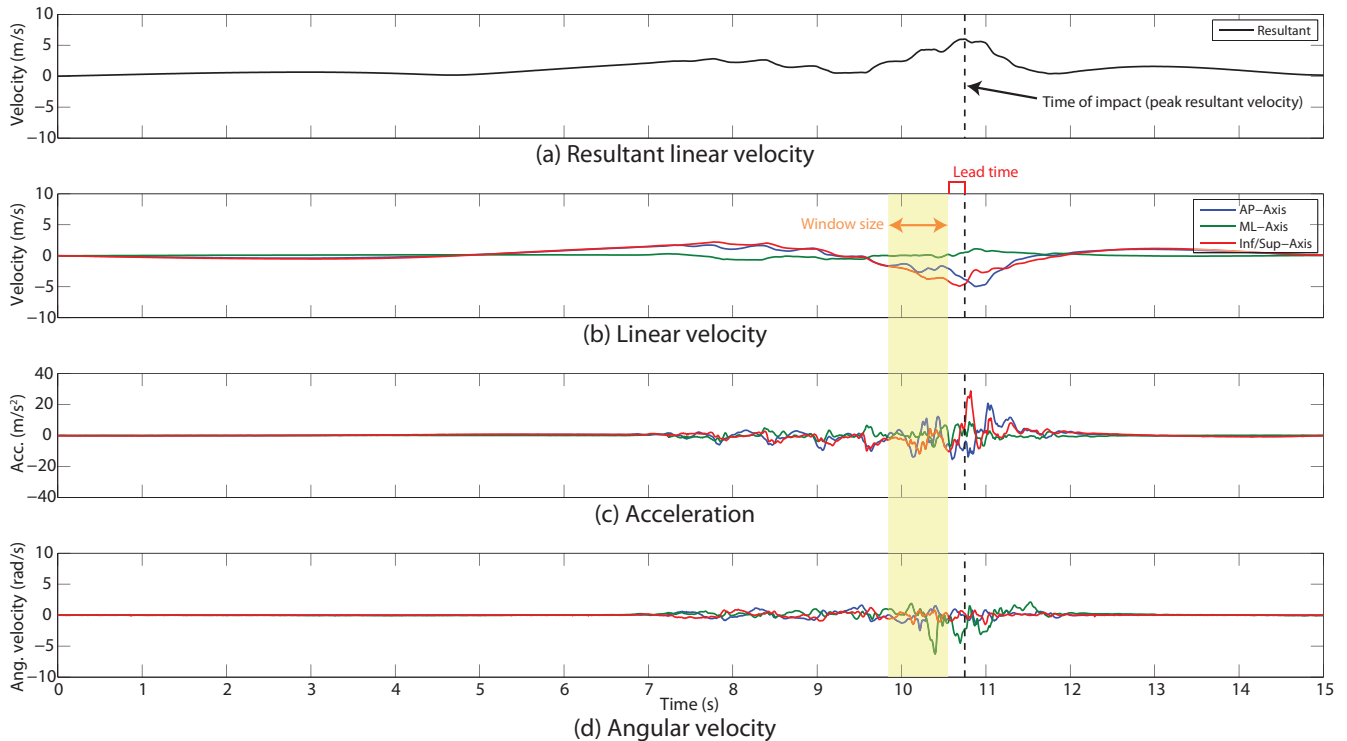


Fig. 1. Waist sensor signals for a sample slip fall trial. (a) Time of impact (dashed line) is estimated by finding the time of peak resultant linear velocity (obtained from numerical integration of the resultant acceleration signal), and the window location (shaded region, not shown to scale) is shifted by the lead time (not shown to scale) ahead of the time of impact. Mean and variance features are calculated within the window for each of the anteroposterior (AP), mediolateral (ML), and inferior-superior (Inf/Sup) axes of the (b) linear velocity, (c) acceleration and (d) angular velocity signals. Note that the peak linear velocity does not always coincide with peak acceleration.

standing quietly, (iii) rising from sitting, descending from (iv) standing to sitting and from (v) standing to lying, (vi) picking up an object from the ground, (vii) ascending and (viii) descending stairs. All participants performed each fall and ADL category three times. Accordingly, over ten participants, a total of 210 fall trials and 240 ADL trials were acquired.

C. Data Acquisition

In each trial, we recorded body kinematics using a single tri-axial accelerometer and gyroscope (ranges of ± 6 g and ± 26.18 rad/s respectively, Opal model, APDM Inc., Portland, OR) worn on a belt at the anterior aspect of the waist. Data were recorded at 128 Hz for a duration of 15 s per trial and streamed directly to a computer for storage and subsequent analysis.

D. Data Analysis

Our data analysis focused on determining how the various window size and lead time combinations influenced the accuracy of our pre-impact fall detection algorithm (Fig. 1). We used seventeen different data window sizes in combination with eighteen lead times to evaluate their effect on the sensitivity and specificity of the algorithm. The window sizes used varied from 0.125 s to 1.125 s with an increment of 0.0625 s, while the lead times varied from 0.0625 s to 1.125 s with the same increment.

In order to determine the base window location for fall trials, we estimated the instance of the body impacting the floor due to a fall by finding the time of peak resultant velocity from the waist sensor [3]. The resultant peak velocity was calculated through numerical integration of the high-pass filtered (cut-off frequency of 0.25 Hz to remove gravity signal) resultant acceleration signal. We then shifted the base window location a fixed amount back from the impact timepoint according to the chosen lead time (Fig. 1a). For increasing window sizes, we shifted the start time point of the base window back in time by the corresponding amount.

For ADL trials, we visually identified the start and end time points of activity motion from the sensor signals, and then set the base window location at a random position within that time frame. ADL window start and end time points were shifted symmetrically from that base window as window sizes were increased. Lead times were not used in the analysis of ADL trials, as they do not contain a timepoint of interest analogous to the fall impact time.

Within each window we calculated the means and variances of X-, Y- and Z-axis accelerations, velocities and angular velocities to form the 18 features for use in our Support Vector Machine (SVM) analysis (Fig. 1b-d). We used the SVM implementation in LIBSVM [1] with a Radial Basis Function (RBF) kernel for pre-impact fall detection. The features (i.e. means and variances) were then split into training and testing sets of equal size by choosing the data

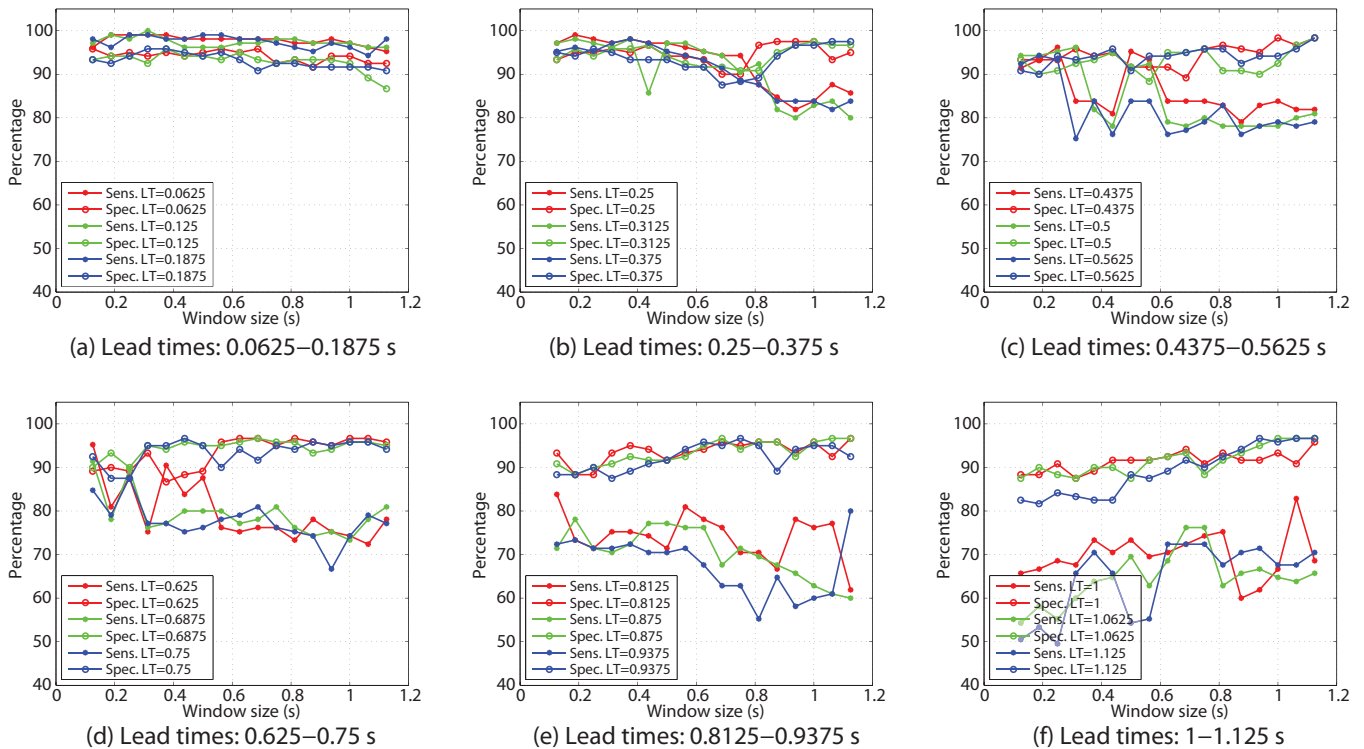


Fig. 2. Overall sensitivity and specificity of trial classification for each combination of window size and lead time. Subfigures (a-f) show results for triplets of increasing lead time size. Note that sensitivity and specificity are relatively stable across all window sizes for the three smallest lead times between 0.0625-0.1875 s (a), with sensitivity consistently above 95%. For larger lead times (b-f), sensitivity and specificity varied dramatically depending on window size, indicating the algorithm performance was less robust for these cases.

from the first five subjects for training and the following five for testing. The best combination of the two RBF kernel parameters C and γ was selected by a grid-search with exponential growing sequences (i.e. $C \in \{2^{-5}, 2^{-4}, \dots, 2^{14}, 2^{15}\}$; and $\gamma \in \{2^{-15}, 2^{-14}, \dots, 2^2, 2^3\}$). Each combination of parameter choices was tested using a 10-fold cross-validation and the parameter with the best cross-validation accuracy was picked. The final model, which was used for classifying test data, was then trained on the entire training set using the selected parameters. The process of training and testing the SVM model was repeated for every combination of window size and lead time.

After creating classification sets of test data for all window size and lead time combinations, we evaluated algorithm performance by calculating the sensitivity and specificity of each classification set. To assess typical algorithm performance per trial, we calculated the mean and standard deviation of each trial's classification sensitivity (for fall trials) or specificity (for ADLs) across all combinations of window size and the three smallest lead times (0.0625-0.1875 s).

All data analysis was performed in MATLAB (R2013a, The MathWorks Inc.).

III. RESULTS

Overall sensitivity and specificity of trial classification for each combination of window size and lead time are shown in Fig. 2. We found that our algorithm yielded relatively stable sensitivity and specificity values across all window sizes

for the three smallest lead times between 0.0625-0.1875 s (Fig. 2a), with sensitivity consistently above 95% and with specificity above 90% (for window sizes 1 s or smaller). For larger lead times (Fig. 2b-f), sensitivity and specificity varied dramatically depending on window size, indicating algorithm performance was less robust for these cases.

Table I shows the individual trial means and standard deviations (SDs) of classification sensitivity (for falls) and specificity (for ADLs), as calculated across combinations of all window sizes and the three smallest lead times. Our algorithm typically had very high classification sensitivity (means $>97\%$ and SDs $<4\%$) for all fall trials, with the exception of incorrect transfer while rising from sitting (ITRS) which had a mean sensitivity of 93.5% and SD of 7.5%. Classification specificity for ADLs was very high (means $>97\%$ and SDs $<4\%$) for rising from sitting to standing (RSS), descending from standing to sitting (DSS), and standing quietly (SQ); moderately high (means $>94\%$ and SDs $<5\%$) for normal walking (NW), ascending stairs (AS), and descending stairs (DS); but were relatively low and/or variable for descending from standing to laying (DSL, mean of 93.2% but SD of 9.1%) and picking up an object from the ground (POG, mean of 85.6% and SD of 11.3%).

IV. DISCUSSION

In this study we evaluated for the first time, to the best of our knowledge, the effect of data window size and lead time on pre-impact fall detection accuracy using data from a

TABLE I
INDIVIDUAL TRIAL MEANS AND STANDARD DEVIATIONS (SD) OF CLASSIFICATION SENSITIVITY (FALLS) AND SPECIFICITY (ADLS)^a.

	Falls							Spec. (%)	ADLS						
	CS	HB	ITDS	ITRS	LCC	Slip	Trip		NW	AS	DS	RSS	DSS	DSL	SQ
Sens. (%)	99.3	100.0	97.4	93.5	98.2	99.3	99.9	94.5	96.3	94.6	99.7	97.8	93.2	100.0	85.6
SD (%)	2.0	0.0	4.0	7.5	3.5	2.4	0.9	4.6	4.7	4.6	1.3	3.7	9.1	0.0	11.3

^aDescriptive statistics calculated by including all combinations of window sizes from 0.125-1.125 s and lead times from 0.0625-0.125 s (0.0625 s increments), as shown in Fig. 2a. CS = cross-step, HB = hit or bumped, ITDS = incorrect transfer while descending from standing, ITRS = incorrect transfer while rising from sitting, LCC = loss of consciousness or motor control, NW = normal walking, AS = ascending stairs, DS = descending stairs, RSS = rising from sitting to standing, DSS = descending from standing to sitting, DSL = descending from standing to laying down, SQ = standing quietly, POG = picking up an object from the ground.

waist-mounted inertial sensor. Furthermore, we employed a machine learning algorithm (SVM), as opposed to traditional threshold based techniques, to allow for more adaptability and robustness across subject and motion variability.

Based on the analysis of data collected in lab experiments with young adults, our system provided at least 95% sensitivity and at least 90% specificity for combinations of window size from 0.125-1 s and lead time from 0.0625-0.1875 s. However, we found that for lead times 0.25 s or greater, sensitivity and specificity varied dramatically with choice of window size, indicating poor robustness of the classification performance. Therefore, we would recommend the use of a target lead time around 0.1875 s or less, and window size 1 s or less for robust pre-impact fall detection.

Furthermore, we believe estimating the time of initial impact for fall trials based on the instant of peak resultant linear velocity is a more intuitively precise method than based on peak acceleration as done previously, since the largest accelerations would typically occur shortly after impact [3].

There are several limitations of our study. Due to safety concerns, all fall and ADL trials were performed by young adults under controlled laboratory conditions and atop gymnasium mats. While there are important differences between falling patterns from typical laboratory studies of young subjects compared to real-life falls among older adults [4], we attempted to minimize these differences by having our subjects simulate a variety of falls most commonly observed among older adults [9]. Also, our analysis did not attempt to analyse sensor signals by sliding a sampling window along the datastream, as would be necessary in a real-time implementation for triggering device deployment, however, our study design allowed for a controlled method of testing the effects of window size and lead time. Finally, our system provided relatively low overall specificity, likely due to our wide range of ADLs tested (with individual specificities ranging from 85.6%-100%) and a modest testing sample from five subjects. Future work is required to compare the accuracy of machine learning versus threshold-based approaches on the same data set. While current performance is too low for practical use in device deployment, it may be improved in the future through the use of larger training datasets of falls and ADLs recorded from older adults, or with the use of complementary signals from other physiological sensors.

Our results provide a template for future development of a robust pre-impact fall detection system, which is necessary for the development of ‘smart’ next generation inflatable hip protectors or helmets for improved force attenuation and user acceptance.

ACKNOWLEDGMENT

This work was supported by team grants from the Canadian Institutes of Health Research (funding reference numbers AMG-100487 and TIR-103945). SNR was also supported by the Canada Research Chairs program.

REFERENCES

- [1] Chih-Chung Chang and Chih-Jen Lin. Libsvm: a library for support vector machines. *ACM Trans Int Syst Technol*, 2(3):27, 2011.
- [2] J. A. Grisso, D. F. Schwarz, A. R. Wishner, B. Weene, J. H. Holmes, and R. L. Sutton. Injuries in an elderly inner-city population. *J Am Geriatr Soc*, 38(12):1326–31, 1990.
- [3] E. T. Hsiao and S. N. Robinovitch. Common protective movements govern unexpected falls from standing height. *J Biomech*, 31(1):1–9, Jan 1998.
- [4] J. Klenk, C. Becker, F. Lieken, S. Nicolai, W. Maetzler, W. Alt, W. Zijlstra, J. M. Hausdorff, R. C. van Lummel, L. Chiari, and U. Lindemann. Comparison of acceleration signals of simulated and real-world backward falls. *Med Eng Phys*, 33(3):368–373, Apr 2011.
- [5] M. N. Nyan, F. E. Tay, A. W. Tan, and K. H. Seah. Distinguishing fall activities from normal activities by angular rate characteristics and high-speed camera characterization. *Med Eng Phys*, 28(8):842–9, 2006.
- [6] L. Nyberg, Y. Gustafson, D. Berggren, B. Brannstrom, and G. Bucht. Falls leading to femoral neck fractures in lucid older people. *J Am Geriatr Soc*, 44(2):156–60, 1996.
- [7] M. Palvanen, P. Kannus, J. Parkkari, T. Pitkajarvi, M. Pasanen, I. Vuori, and M. Jarvinen. The injury mechanisms of osteoporotic upper extremity fractures among older adults: a controlled study of 287 consecutive patients and their 108 controls. *Osteoporos Int*, 11(10):822–31, 2000.
- [8] E. A. Papadimitropoulos, P. C. Coyte, R. G. Josse, and C. E. Greenwood. Current and projected rates of hip fracture in canada. *CMAJ*, 157(10):1357–63, 1997.
- [9] S. N. Robinovitch, F. Feldman, Y. Yang, R. Schonnop, P. M. Leung, T. Sarraf, J. Sims-Gould, and M. Loughin. Video capture of the circumstances of falls in elderly people residing in long-term care: an observational study. *Lancet*, 381(9860):47–54, 2013.
- [10] D. W. Spaite, E. A. Criss, T. D. Valenzuela, H. W. Meislin, and J. Ross. Geriatric injury: an analysis of prehospital demographics, mechanisms, and patterns. *Ann Emerg Med*, 19(12):1418–21, 1990.
- [11] J. A. Stevens and S. Olson. Reducing falls and resulting hip fractures among older women. *MMWR Recomm Rep*, 49(RR-2):3–12, 2000.
- [12] T. Tamura, T. Yoshimura, M. Sekine, M. Uchida, and O. Tanaka. A wearable airbag to prevent fall injuries. *IEEE Trans Inf Technol Biomed*, 13(6):910–4, 2009.
- [13] G. Wu and S. Xue. Portable preimpact fall detector with inertial sensors. *IEEE Trans Neural Syst Rehabil Eng*, 16(2):178–83, 2008.

A QUANTITATIVE EXAMINATION OF THE 20 METER SPRINT TEST IN JUNIOR WHEELCHAIR BASKETBALL BY INERTIAL SENSING

E. Bergamini (1), F. Marchetti (2), F. Paradisi (1,2), A.S. Delussu (2), C. Mazzà (1,3)

(1) Università degli Studi di Roma “Foro Italico”, Rome, Italy

(2) Fondazione Santa Lucia IRCCS, Rome, Italy

(3) Department of Mechanical Engineering, The University of Sheffield, Sheffield, UK

INTRODUCTION

Improved wheelchair design and increased attention to the enhancement of physical conditioning in athletes with disabilities have increased the popularity of wheelchair sports in general and of wheelchair basketball in particular [1]. Extensive research has been conducted to assess and improve adult players' performance [2]. However, only few papers focused on young athletes [3]. This study proposes a method for the quantitative characterization of a performance field test, the 20 m sprint test, in junior wheelchair basketball players, and aims at providing a contribution in identifying performance-related factors.

METHODS

Ten athletes (2 females, 8 males; age=16±3 years; mass=59±23 kg; functional classification score: from 0.5 to 4.5) participated in the study. Upper arms maximal muscle power was measured through arm crank ergometry to assess the athletes' physical capacity. Each participant was equipped with four Magnetic Inertial Measurement Units (MIMUs) (Opal, APDM Inc. -128 frames/s) containing 3D accelerometer, gyroscope and magnetometer and positioned with elastic belts on the sternum, and on both wrists. The fourth MIMU was attached to the backrest of the wheelchair. After a 10-minute warm up, subjects were asked to perform a 20-m sprint trial, a test validated for the assessment of specific wheelchair basketball skills in young populations [4]. The time to complete the test was recorded by means of a chronometer. MIMU data were low-pass filtered (4th-order zero-lag Butterworth, 10 Hz) and the pushing phase cycles identified, as determined from the wheelchair MIMU acceleration forward component. The following parameters were computed for the steady-state portion of the test: pushing phase frequency, from the wheelchair MIMU forward acceleration; upper limb symmetry indexes (Root Mean Square Error: S1, Pearson's Correlation Coefficient: S2) from the norm of the wrist MIMUs accelerations (Fig.1); peak-to-peak trunk inclination from the orientation of the sternum MIMU estimated with the unit built-in algorithm. The correlation between the time to complete the test, the normalized arm maximal power, and the MIMU based parameters was assessed using the Pearson's correlation coefficient (ρ).

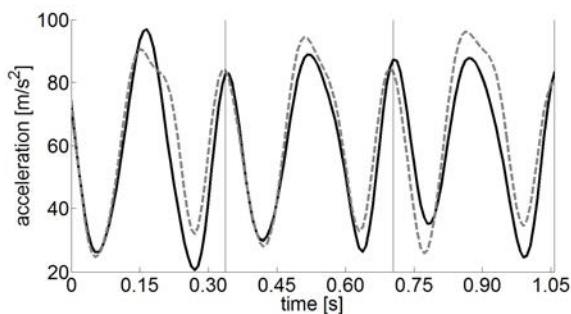


Fig. 1: Right (solid line) and left (dashed line) wrist acceleration norm for three pushing phases (vertical lines).

RESULTS

The time to complete the test was strongly correlated with the arm maximal muscle power ($\rho=-0.85$), the symmetry indexes ($\rho=0.96$ for S1 and $\rho=0.90$ for S2), as well as with the pushing frequency ($\rho=-0.88$). The symmetry indexes were also significantly correlated with the arm maximal muscle power ($\rho=-0.76$ for S1 and $\rho=0.70$ for S2), and with the pushing frequency ($\rho=0.87$ for both S1 and S2). No significant correlation was found for the peak-to-peak trunk inclination.

DISCUSSION

The proposed method allowed for a detailed characterization of a validated field test for the assessment of specific wheelchair basketball skills in young players. Better performances on the 20 m sprint are associated to adequate upper arm muscle power, higher pushing frequency and symmetry between upper limbs while pushing. The young players that better coordinate the upper arms and manage to increase the pushing frequency are the most efficient in completing the test. Control of trunk movement does not seem to be a key sprint performance factor. In conclusion, the proposed instrumented test provided quantitative information about the subject-specific player skills that allow for an optimal performance and can be used to improve wheelchair basketball training in young players.

REFERENCES

- [1] Crespo-Ruiz BM et al, *Adapted Physical Activity Quarterly* 2011; 28: 157-172.
- [2] Gil-Agudo A et al, *Physical Medicine and Rehabilitation Clinics of North America* 2010; 21: 141-156.
- [3] Starrs P et al, *Prosthetics and Orthotics International* 2012; 36: 324-331.
- [4] Delussu AS et al, *Medicina dello Sport* 2011; 64: 231-241

ACKNOWLEDGEMENTS

Funded by the SIVAM project (co-funded by the Italian Ministry of Economic Development – ICE (agreement with CRUI) – call 2010, by Letsense srl, by ITOP Officine Ortopediche spa, and by the authors' University).

Gait as a Biomarker? Accelerometers Reveal that Reduced Movement Quality while Walking is Associated with Parkinson's Disease, Ageing and Fall Risk

Matthew A. Brodie *Member, IEEE*, Nigel H. Lovell *Fellow, IEEE*, Colleen G. Canning, Hylton B. Menz, Kim Delbaere, Stephen J. Redmond *Senior Member, IEEE*, Mark Latt, Daina L. Sturnieks, Jasmine Menant, Stuart T Smith *Member, IEEE*, Stephen R. Lord

Abstract—Humans are living longer but morbidity has also increased; threatening to create a serious global burden. Our approach is to monitor gait for early warning signs of morbidity. Here we present highlights from a series of experiments into gait as a potential biomarker for Parkinson's disease (PD), ageing and fall risk. Using body-worn accelerometers, we developed several novel camera-less methods to analyze head and pelvis movements while walking. Signal processing algorithms were developed to extract gait parameters that represented the principal components of vigor, head jerk, lateral harmonic stability, and oscillation range. The new gait parameters were compared to accidental falls, mental state and co-morbidities. We observed: 1) People with PD had significantly larger and uncontrolled anteroposterior (AP) oscillations of the head; 2) Older people walked with more lateral head jerk; and, 3) the combination of vigorous and harmonically stable gait was demonstrated by non-fallers. Our findings agree with research from other groups; changes in human gait reflect changes to well-being. We observed; different aspects of gait reflected different functional outcomes. The new gait parameters therefore may be complementary to existing methods and may have potential as biomarkers for specific disorders. However, further research is required to validate our observations, and establish clinical utility.

I. INTRODUCTION

Decreased mobility levels are prevalent in older people, and the predicted aging of the world's population will increase the global burden of these conditions on morbidity and mortality [1]. Changes in gait may prelude major events [2], for example, strokes, cognitive decline, falls, or death, which may be preventable. Accelerometers have previously been connected to the head [3], pelvis [4], trunk [5, 6], and even ski boots [7] to provide an inexpensive way to monitor human movement [8]. In clinical settings, accelerometers have been used to identify between-group differences in the gait of old and young [9, 10], fallers and non-fallers [11], and

people with and without Parkinson's disease (PD) [3, 12]. Statistical associations, however, do not necessarily translate into biomarkers, if prevalence is low, as for PD, and false-positive rates are high.

Previous research with accelerometers has generally focused on the direct interpretation of acceleration [8]. Here, novel signal processing algorithms were developed to extract new measures of gait jerk, harmonic stability, and oscillation range, using accelerometers attached to the head and pelvis. We investigated if these measures revealed a high level of discrimination between groups and therefore the potential of gait as a biomarker for PD, ageing, and increased fall risk.

II. METHODS

Approval by the Human Studies Ethics Committee at the University of New South Wales was given and informed consent was obtained prior to participation. Participants were eligible if they were able to walk 20 meters unassisted, had normal hearing and vision and scored ≥ 24 on the Mini Mental State Examination [13]. With respect to people with PD, only mild idiopathic clinical stage I-II of illness according to Hoehn and Yahr [14] were assessed. Falls in the previous 12 months were recorded. Fallers (one or more falls) were compared to non-fallers (no reported falls).

Age differences in gait were investigated using data from 43 young people, mean age 29 (SD 4) years and 100 older people, mean age 80 (SD 4) years. Potential biomarkers for PD were investigated using data from 10 people with idiopathic PD, mean age 67 (SD 4) years, and 10 healthy age-

M. A. Brodie (email: matthew.brodie@neura.edu.au) K. Delbaere (email: k.delbaere@neura.edu.au) D. L. Sturnieks (email: d.sturnieks@neura.edu.au) J. Menant (email: j.menant@neura.edu.au) and S. R. Lord (email: s.lord@neura.edu.au) are with Neuroscience Research Australia, UNSW Australia, Sydney, NSW 2031.

S. J. Redmond (email: s.redmond@unsw.edu.au) and N. H. Lovell (email: n.lovell@unsw.edu.au) are with the Graduate School of Biomedical Engineering, UNSW Australia, Sydney, NSW 2052.

C. G. Canning (email: colleen.canning@sydney.edu.au) is with the Faculty of Health Sciences, University of Sydney, Lidcombe, NSW 1825.

H. B. Menz (email: h.menz@latrobe.edu.au) is with the Faculty of Health Sciences, La Trobe University, Bundoora, Victoria, Australia

Mark Latt (email: mark.latt@bigpond.com) is with Royal Prince Alfred Hospital, The University of Sydney, Sydney NSW 2006.

S. T. Smith (email: Stuart.Smith@utas.edu.au) is with the School of Health Sciences, UTAS, Launceston, TAS 7250.

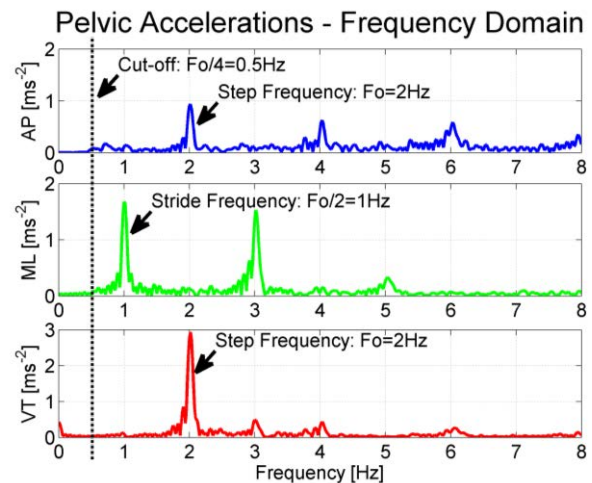


Fig. 1. Pelvic accelerations transformed into the frequency domain by discrete Fourier transform. A high-pass filter cut-off frequency of 0.25 times the step frequency (F_o) preserves most within-stride information.

matched, mean age 66 (SD 7) years. Potential biomarkers for falls were investigated using data from 96 independent-living older people: 35 fallers, mean age 79 (SD 4) years, and 61 non-fallers, mean age 80 (SD 4) years.

Tri-axial accelerometers were attached to the head and pelvis (Opal™ by APDM, sampling frequency 128 Hz). The data from the middle 15 meters of a 19 meter walkway were marked with an external trigger [15]. Results from two repeat walks were combined prior to statistical analysis.

A. Signal Processing

The acceleration signals were processed to extract parameters that represented the principal components of vigor, head jerk, harmonic stability, and oscillation range. Calculations were performed in MATLAB. Step frequency (Fo) was determined by the dominant VT peak in the frequency domain after a discrete Fourier transform (Fig. 1).

A continuously rotational correction was applied to align the vertical axes of the sensors with the global vertical (VT). Accelerations were transformed into the body centered coordinate system [16], whereby anteroposterior (AP) accelerations act in the direction of ambulation, and mediolateral (ML) accelerations act right to left in the horizontal plane. A fourth order low-pass Butterworth filter with cut-off scaled to a quarter of the step frequency (dashed line, Fig. 1) was used to obtain the changing low frequency error matrix (**R**). The corrected accelerations (**A_{Corr}**) were then obtained by rotating the raw accelerations (**A**), see equation (1).

$$\mathbf{A}_{\text{Corr}} = \mathbf{R}\mathbf{A} \quad (1)$$

The new continuous correction may provide greater reduction in gravitational ‘cross-talk’ relative to previous static methods [4].

Head and pelvic oscillations (Fig. 2) were calculated by integrating the corrected body centered accelerations with respect to time, and filtered to remove any accumulated

integration drift. A fourth order high-pass Butterworth filter with cut-off scaled to a quarter of the step frequency (dashed line, Fig. 1) was used to obtain both velocity and displacement oscillations during gait, which may be visualized as similar to the paths swept out during treadmill walking. The new scaled cut-off approach was developed to preserve most within-stride information while filtering out most accumulated integration error. Optical motion capture was used to determine any accuracy improvements.

Linear head jerk was calculated by differentiating the corrected linear acceleration with respect to time. Root Mean Square (RMS) head jerk was calculated over the AP, ML, and VT axes. The log ratio (2) of lateral to vertical ML/VT jerk was calculated in decibels (dB) creating a normally distributed and dimensionless gait parameter [18].

$$\text{Ratio} = 10 \log_{10} \left(\frac{\text{RMS ML Jerk}}{\text{RMS VT Jerk}} \right) \quad (2)$$

Lateral harmonic stability of the pelvis was calculated using spectral decomposition to identify the magnitude and dispersion of ‘stabilizing’ ML acceleration peaks. Different to previous analyses using harmonic ratios [15], overlapping eight-step data windows were used instead of two-step data windows, therefore, better adjusting for the monophasic basis of ML movements while walking, providing increased spectral resolution, incorporating measurement of between stride variability, and reducing any noise associated with taking Fourier transforms over finite data windows [19].

B. Statistical Analysis

Classification accuracy (with sensitivity equal to specificity) was assessed using two-fold cross validation boot strapped 5000 times. Group differences between young and old people, between people with PD and healthy controls, and between fallers and non-fallers were assessed using ANOVA. Subspace clusters were partitioned by medians. Principal component analysis (PCA) using the Varimax rotation method was used to investigate which gait parameters were most representative of different gait

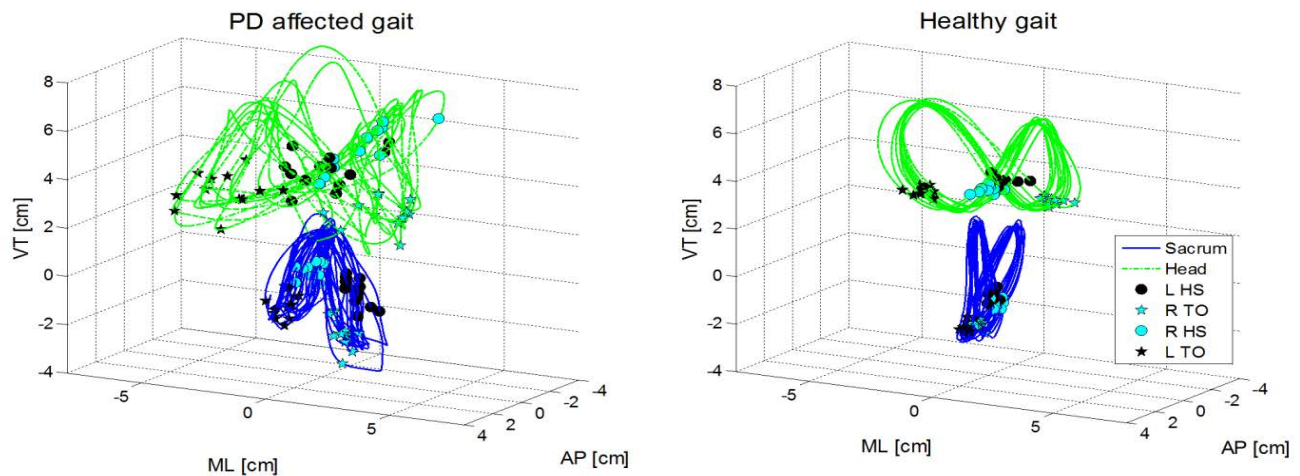


Fig. 2. Head and pelvic (sacrum) oscillations while walking for PD affected and healthy gait. Left (L) and right (R) heel strikes (HS) and toe-offs (TO) are represented by circles and stars.

constructs. Extraction of components was terminated by an Eigenvalue value below unity. Pearson’s correlations were used to assess the independence between different aspects of gait.

III. RESULTS

When pelvic movements using accelerometers were compared to the optical motion capture analysis of walking: The continuous rotational correction and new scaled filter cut-off approach reduced errors by approximately 10-fold relative to a fixed approach that used a static correction and 0.1Hz high-pass filter cut-off (Table 1).

TABLE 1. ERROR AS A PERCENTAGE OF MEASUREMENT RANGE. THE NEW SCALED APPROACH RESULTED IN AN APPROXIMATELY 10-FOLD REDUCTION IN ERROR.

	Pelvis		
	AP	ML	VT
95% Range of Movement			
Optical System [cm]	4.62	6.55	4.17
Root Mean Square Error (RMSE)			
Scaled Method [cm]	0.76	1.06	0.22
Error [%]	16%	16%	5%
Fixed Method [cm]			
Fixed Method [cm]	8.03	5.51	2.01
Error [%]	174%	84%	48%

Within our data, PCA (Table 2) revealed gait parameters reflecting vigor, for example walking speed and step length, were largely independent of gait parameters that described head or pelvic stability.

On average, older people presented increased RMS lateral head jerk and took shorter steps than younger people. ML/VT jerk correctly classified 89% of participants (Fig. 3) and was superior in this regard to all other gait parameters including step length, which was the best established gait parameter we tested. A step length of 67 cm correctly classified 71% of participants. ML/VT jerk and step length were only weakly correlated ($r^2=0.03$) suggesting they largely reflect different aspects of gait.

TABLE 2. PRINCIPAL COMPONENT ANALYSIS OF GAIT. NORMALIZED WEIGHTINGS ARE SHOWN AND SORTED FOR EACH COMPONENT. HIGHLIGHTED HAVE A WEIGHTING GREATER THAN 0.5.

Principal Components of gait	1) Gait	2) Pelvic	3) Head
	Vigor	Stability	Stability
Head Jerk VT	.88	-.03	-.21
Head Jerk ML	.77	.09	.47
Cadence	.75	.24	-.12
Speed	.74	.39	-.28
Head Jerk AP	.57	-.24	.53
Step Length	.56	.39	-.29
Harmonic Ratio AP	-.08	.87	-.00
Step Time Variability	-.20	-.82	-.09
Harmonic Ratio VT	.19	.70	-.12
ML/VT Jerk	-.08	.17	.86
AP/VT Jerk	-.20	-.25	.79

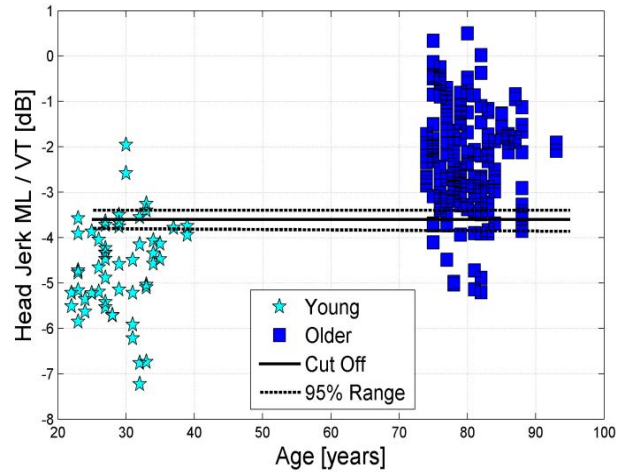


Fig. 3. Classification of age, ML/VT head jerk was 89% accurate.

People with PD presented significantly ($p=0.02$) faster AP head movements (33.2 cms^{-1}), as measured by the velocity of AP head oscillations, than the healthy age matched group (24.5 cms^{-1}), which was uncorrelated ($r^2=0.008$) with the significant ($p=0.02$) slower walking speed (1.2 ms^{-1} for PD, vs. 1.4 ms^{-1} for the healthy age matched).

With respect to falls, when different walking speeds were taken into account, a significant subspace clustering effect was observed for lateral harmonic stability (Fig. 4). The fast and stable group (top right quadrant) were 5.3 times less likely to have fallen than all other participants: relative risk 0.19, 95% confidence interval 0.06-0.57.

IV. DISCUSSION

Measurement noise was reduced 10-fold using the new method. The scaled filter cut-offs were generally around 0.5 Hz and were significantly higher than previously approaches that have used fixed cut-offs around 0.1 Hz [17]. For both methods VT position error was least because gravitational cross-talk has least effect along this axis. For measurements of head and pelvic stability in gait, we suggest scaling the filter cut-offs with step frequency is optimal because it

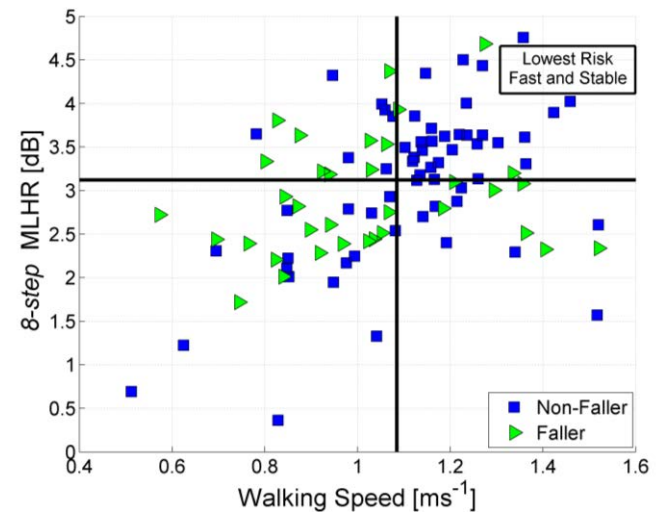


Fig. 4. Better separation, the fast and stable walkers (top right quadrant) had a 5.3 times lower risk of falls.

preserves most information about the movements of interest, within strides, while rejecting most measurement noise. Such error reduction was important for the subsequent investigation into gait as a biomarker.

In our experiments, we observed; different aspects of gait reflected health status and different functional outcomes such as fall risk. Similar to previous research [3, 8, 10-12], we observed that younger people, non-fallers, and those without PD walk faster, and take longer steps, with reduced variability of step time. However, when we assessed these established gait parameters using univariate statistical analysis, we found substantial overlap between the distributions from different groups [18, 19], which limits their utility as specific biomarkers at an individual level.

The PCA revealed that head and pelvic stability were distinct and were largely independently of walking speed. Therefore, we investigated if these new measures could provide additional information about gait impairments in different populations. Both as independent variables and through non-linear subspace clustering with walking speed, an existing measure of gait vigor. Each new parameter may quantify a different aspect of “steadiness” while walking and is different to other measures such as local dynamic stability, step time variability, or existing harmonic ratios.

Relative to traditional measures including step length [18], superior group separation, reflecting age differences in gait, was achieved using the log ratio of ML/VT head jerk. Older people presented an increased ratio, indicating greater lateral head jerk which was largely independent of reduced walking vigor. The jerkier lateral head movements therefore suggest that the older people were less able to rely on their mechanical (inverted pendulum) stability as they oscillated side-to-side in time with their stepping.

People with PD walked with increased AP head oscillations, which were uncorrelated to their decrease in walking speed. This suggests motor impairment symptoms relating to gait instability maybe distinct from hypokinetic gait symptoms. Potentially this provides separate targets for therapy.

Separation between fallers and non-fallers was significantly improved when above average walking speed was combined with above average lateral harmonic stability of the pelvis [19]. An observation that suggests fast walking alone may not always be protective of falls. Therefore, future research should investigate if interventions aimed at reducing fall risk and improving mobility should also focus on enhancing lateral stability.

V. SUMMARY

We found the new gait parameters were associated with different principal components and were sensitive to different conditions. Different measures of gait “steadiness” may quantify different aspects of gait and may be complementary to existing measures of walking speed or vigor. Combining measures using subspace clustering (Fig. 4) enables more homogeneous subgroups to be identified, which increases the potential for gait to be used as a biomarker. However, further research is required to validate our observations in larger populations, and to establish utility in clinical practice.

REFERENCES

- [1] Salomon JA, Wang H, Freeman MK, Vos T, Flaxman AD, Lopez AD, et al. Healthy life expectancy for 187 countries, 1990-2010: a systematic analysis for the Global Burden Disease Study 2010. *Lancet*. 2012;380(9859):2144-62.
- [2] Montero-Odasso M, Hachinski V. Preludes to brain failure: executive dysfunction and gait disturbances. *Neurological sciences : official journal of the Italian Neurological Society and of the Italian Society of Clinical Neurophysiology*. 2013.
- [3] Latt MD, Menz HB, Fung VS, Lord SR. Acceleration Patterns of the Head and Pelvis During Gait in Older People With Parkinson's Disease: A Comparison of Fallers and Nonfallers. *J Gerontol a-Biol*. 2009;64(6):700-6.
- [4] Moe-Nilssen R. A new method for evaluating motor control in gait under real-life environmental conditions. Part 1: The instrument. *Clinical Biomechanics*. 1998;13(4-5):320-7.
- [5] Kavanagh J, Morrison S, Barrett RS. Coordination of head and trunk accelerations during walking. *Eur J Appl Physiol*. 2005;94(4):468-75.
- [6] Wilhelmsen K, Nordahl SHG, Moe-Nilssen R. Attenuation of trunk acceleration during walking in patients with unilateral vestibular deficiencies. *Journal of Vestibular Research*. 2010;20:439-46.
- [7] Brodie M, Walmsley A, Page W. Fusion motion capture: a prototype system using inertial measurement units and GPS for the biomechanical analysis of ski racing. *Sports Technology*. 2008;1(1):17-28.
- [8] Kavanagh JJ, Menz HB. Accelerometry: A technique for quantifying movement patterns during walking. *Gait & Posture*. 2008;28(1):1-15.
- [9] Kavanagh JJ, Barrett RS, Morrison S. Age-related differences in head and trunk coordination during walking. *Human Movement Science*. 2005;24(4):574-87.
- [10] Menant JC, Steele JR, Menz HB, Munro BJ, Lord SR. Step Time Variability and Pelvis Acceleration Patterns of Younger and Older Adults: Effects of Footwear and Surface Conditions. *Res Sports Med*. 2011;19(1):28-41.
- [11] Yogev G, Plotnik M, Peretz C, Giladi N, Hausdorff JM. Gait asymmetry in patients with Parkinson's disease and elderly fallers: when does the bilateral coordination of gait require attention? *Exp Brain Res*. 2007;177(3):336-46.
- [12] Hausdorff JM. Gait dynamics in Parkinson's disease: common and distinct behavior among stride length, gait variability, and fractal-like scaling. *Chaos*. 2009;19(2):026113.
- [13] Folstein MF, Folstein SE, McHugh PR. "Mini-mental state". A practical method for grading the cognitive state of patients for the clinician. *Journal of psychiatric research*. 1975;12(3)
- [14] Hoehn MM, Yahr MD. Parkinsonism: onset, progression and mortality. *Neurology*. 1967;17(5):427-42.
- [15] Menz HB, Lord SR, Fitzpatrick RC. Acceleration patterns of the head and pelvis when walking on level and irregular surfaces. *Gait & Posture*. 2003;18(1):35-46.
- [16] Brodie MAD, Lord SR, Smith ST, Menz HB. Accuracy of postural sway in gait measured with accelerometers. XXIV Congress of the ISB Biomechanics; Natal, Brazil2013.
- [17] Zijlstra W, Hof AL. Assessment of spatio-temporal gait parameters from trunk accelerations during human walking. *Gait & Posture*. 2003;18(2):1-10.
- [18] Brodie MA, Menz HB, Lord SR. Age-associated changes in head jerk while walking reveal altered dynamic stability in older people. *Exp Brain Res*. 2013.
- [19] Brodie MA, Menz HB, Smith ST, Delbaere K, Lord SR. Good lateral harmonic stability combined with adequate gait speed is required for low fall risk. *Gerontology*. (In Press 2014).



ICTTP 2014

Stepping to the beat improves spatiotemporal characteristics of gait in stroke patients with hemiparesis: A proof of concept case study of a home-based training intervention

Briony S. Brownless^{*}, Rachel L. Wright, Alan M. Wing

Department of Psychology, University of Birmingham, Edgbaston, Birmingham, B15 2TT, United Kingdom

Abstract

Hemiparetic gait due to stroke is characterized by temporal asymmetry and variability. Research shows this can be improved by auditory cueing, whereby participants train to step in time and space with a visual or auditory cue. This particular method is effective in training a symmetrical gait and helps to improve coordination and speed. We describe a pilot study that investigates the possibility of training with an auditory rhythmical metronome embedded in music, during stepping in place within a home-based setting. Stepping in place incorporates aspects of movements that are also important for a successful gait, such as reciprocal flexion and extension of the legs in timely coordination and synchronization, creating a step frequency, a swing phase and single limb support. Stepping in place may also provide a valuable method for home-based training, as little space in the home is required and, therefore, participants are less likely to fall. This case study seeks to obtain proof of the concept that stepping in place within a home setting may be a useful tool for locomotor training after stroke.

A hemiparetic stroke patient, PF, successfully completed 6 weeks of home-based training for 15 minutes a day, 5 days a week (with 5% weekly increments in music tempo). PF (aged 58) is a male, right handed, chronic stroke survivor, who presented left sided hemiparesis. He was recruited from a local stroke club based on the inclusion criteria that he was able to walk independently without supervision (but able to use a gait aid such as a cane or walker) and was free from hearing impairments. Finally, PF was also able to complete a 3 m Timed Up and Go, which is typically used as an indicator of falls and provides an indication of the patient's ability during turns. He was assessed five times during the 12 week period of the study, which included baseline, three weeks of training, three weeks of rest (used to measure resting effects), a second three-week training period and finally after another three weeks of rest. During each assessment, PF was tested for his gait speed during a 10 m walking task. During these tests, we also captured the spatiotemporal parameters of his gait using six accelerometer sensors (OPAL, APDM). The sensors were placed around the trunk, the lumbar, and the left and right shins and feet and have been designed to measure walking. The use of such motion capture systems is intended to provide a more sensitive and objective measure of the changes in movement that might occur following gait rehabilitation, compared to the use of standard clinical measures. We also used the

^{*}Corresponding author. Tel: +44-7867-499142
E-mail address: brownless14@gmail.com

following clinical assessments: The Dynamic Gait Index (which measures balance during walking), and The Rivermead Motor Scale (measuring general walking ability).

The results showed significant improvements in all spatiotemporal aspects of PF's gait. There was a 10 s speed increase in his 10 m walking, between his baseline and final assessment. Furthermore, changes in PF's gait cycle were shown after 6 weeks of training stepping in place, suggesting improvements towards a more symmetrical gait pattern. For example, an increase in cadence was revealed, which likely follows increases in the gait speed during 10 m walking. A decrease in the overall gait cycle time, decreases in double support, and further decreases in stride length asymmetry and swing asymmetry were also observed. These findings might be expected based on previous work investigating changes in spatiotemporal parameters after gait rehabilitation and suggest that training stepping in place generalizes to walking ability. Furthermore, no changes were observed in any of the clinical assessments, suggesting the need for more sensitive measures of functional ability in capturing improvements of lower limb function after training stepping in place. These preliminary data show promising results for stepping in place in the home, as a method of training a symmetrical gait after stroke. This method also provides a cheap addition to other rehabilitation techniques such as physiotherapy, as it can be conducted within the home, without the need for a therapist and will provide patients with more intensive rehabilitation after stroke. Lastly, it is important to note, based on patient feedback that presenting the rhythmical beat in a music context was likely a key factor in motivating the patient to complete his training. As compliance is of high importance in rehabilitation, incorporating music should be taken into consideration for future investigations whereby the training provided may be repetitive in nature.

© 2014 The Authors. Published by Elsevier Ltd.

Selection and peer-review under responsibility of the Organizing Committee of the International Conference on Timing and Time Perception.

Keywords: Stroke; Intervention; Hemiparesis; Hemiparetic gait; Rehabilitation; Rhythmical auditory cues; Kinematics; Accelerometers

A Wearable System for Measuring Limb Movements and Balance Control Abilities Based on a Modular and Low-cost Inertial Unit

A. Cristiani - *IEEE Member*, G. M. Bertolotti - *IEEE Member*, M. Dainotti, P. Colagiorgio, F. Romano and S. Ramat - *IEEE Member*

Abstract— Monitoring balance and movement has proven useful in many applications ranging from fall risk assessment, to quantifying exercise, studying people habits and monitoring the elderly. Here we present a versatile, wearable instrument capable of providing objective measurements of limb movements for the assessment of motor and balance control abilities. The proposed device allows measuring linear accelerations, angular velocities and heading either online, through wireless connection to a computer, or for long-term monitoring, thanks to its local storage abilities. One or more body parts may be simultaneously monitored in a single or multiple sensors configuration.

I. INTRODUCTION

Balance control is a very complex task, involving several sensory systems and motor responses which interact dynamically. As shown by several studies, postural and balance control abilities gradually decline with age. Older people affected with balance disorders typically suffer from multiple impairments, e.g. multi-sensory loss, weakness, orthopedic constraints and cognitive impairments [1-3]. Typically, balance control is assessed by means of clinical balance scales, that consist in the scoring of a set of simple, everyday-life movements executed in sequence by the patient. The most common scales are: the Tinetti test [4,5], the Berg balance scale [6], and the BEST test [7]. The subject's performance is currently evaluated by the physiatrist or the physiotherapist, who give his/her judgment by means of a numerical score on a predefined scale. The evaluation is therefore affected by subjective factors causing possible inter- and even intra-evaluator variability of judgment. The continuing development of reduced size, weight, and cost MEMS inertial sensors has offered the possibility of using them for human activity monitoring, recognition and classification through body-worn devices [8-14]. We designed and built a novel, portable, low-cost system, embedding a three axial accelerometer, a three axial gyroscope, and a three axial magnetometer, aimed at providing objective measurements of limb movements for the assessment of motor and balance control abilities (figure 1).

The developed instrument has been conceived as a modular device which can be used in different scenarios: i) single unit wirelessly connected to a PC or handheld device

(laboratory experiments, short-term monitoring); ii) single unit capable of storing the acquired data on a local memory (patient's home, long-term monitoring); iii) body network, i.e. multiple units deployed on the subject's body and wired to a gateway unit which can have a local memory or a wireless connection to a PC or handheld device (full body monitoring of exercises, several scenarios). Although a number of wearable IMU devices that can be used for monitoring posture and movements are available on the market, we preferred to build our own IMU "platform" for having the possibility of adding custom features. This is hardly possible with commercial devices, as they generally come with their own software and, in particular, their firmware cannot be modified as needed. Among them, Lumoback (Lumo BodyTech, Inc., CA, USA) seems a very interesting system, but can only be connected to an Apple device with a proprietary application. Sapphire, Emerald and Opal wearable sensors (APDM Inc., OR, USA) come with a development kit allowing researchers to build their own applications; nevertheless, it is impossible to act on the firmware in both cases. This limits the possibility to add features to the system, e.g. an onboard custom processing or the capability of connecting the IMU to command external devices (e.g. electro stimulators).

II. SYSTEM DESCRIPTION

The electronic device described in the presented work is an autonomous system able to detect and monitor the movements of the subject. In order to obtain a system capable of acquiring inertial signals generated by the activity of the wearer without impeding his/her movement, the circuit layout and the battery were designed and selected to minimize both dimensions and weight of the final device. Also the physical magnitude of the signal has been investigated to properly choose the sensors for this type of measurement. Our instrument is based on a STM32F303VC microcontroller (by ST Microelectronics) which has a high performance ARM Cortex M4 32-bit RISC core operating at a frequency of up to 72 MHz. This microcontroller is able to interact with external devices through an extensive range of peripherals, while maintaining relatively small dimensions (7x7x1.6 mm, 48 pin package). The same package hosts also a 256 Kbytes flash memory, where data can be permanently stored, and 40 Kbytes of SRAM for temporary data storage [15]. The measurement of human body movements is made possible by means of three inertial sensors: an accelerometer; a magnetometer and a gyroscope. The three dimensional angular rate is provided by the L3G4200D (ST Microelectronics), a digital low-power three-axes angular rate sensor including a MEMS sensing element and an I2C interface capable of providing the measured angular rate to

Research supported by the Italian Ministry of Research PRIN grant 2010R277FT_004 to S. Ramat.

A. Cristiani, G. M. Bertolotti, M. Dainotti, P. Colagiorgio, F. Romano and S. Ramat (corresponding author, phone: +39 0382985745, fax: +39 0382985373) are with the Department of Electrical, Computer and Biomedical Engineering, University of Pavia, Pavia, 27100 Italy (e-mails: andrea.cristiani@unipv.it, gianmario.bertolotti@unipv.it, stefano.ramat@unipv.it).

the external world through a I2C or a Serial Peripheral Interface (SPI). Full scale values are selectable among the following: 250 °/s, 500 °/s, 2000 °/s. Sensitivity values are, respectively, 8.75 °/s/digit, 17.50 °/s/digit, and 70 °/s/digit [16]. The LSM303DLHC (ST Microelectronics) allows the measurement of the three-dimensional accelerations and magnetic field; it is a system-in-package featuring a 3D digital linear acceleration sensor (selectable full-scales from ± 2 g to ± 16 g, sensitivity from 1 mg to 12 mg, where g is the



Figure 1. The assembled device and casing: battery (left) and circuit board (right).

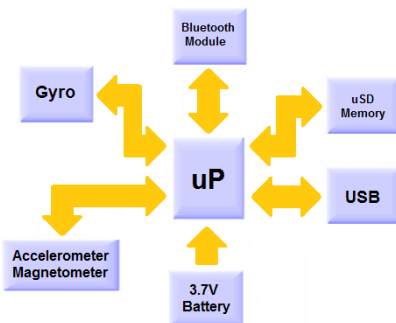


Figure 2. System architecture.

gravitational acceleration) and includes a 3D digital magnetic sensor (selectable full-scales ranging from ± 1.3 G to ± 8.1 G, and magnetic gain setting ranging from 1100 to 205 digit/G, where G is the abbreviation for gauss) embedded in a 14 lead, 3x5x1mm-sized package. Magnetic and accelerometer parts can be enabled or put into power-down mode separately, allowing to reduce the power consumption when one of these features is not required. An Inter-Integrated Circuit (I2C) serial bus interface is included, that supports standard (100 kHz) and fast (400 kHz) speed mode [17]. The microcontroller can manage these external sensors through two different kinds of synchronous serial communication internal interfaces: the I2C and SPI. The latter is a communication based on 3 digital lines and is used to send commands and receive data from the LSM303DLHC, while the I2C, that uses only two digital lines, allows to share data with the gyroscope. The SPI interface is also used to store data in ASCII files on a micro Secure Digital (μ SD) card which can then be extracted for data visualization and

processing. Otherwise, the acquired data can be sent to a remote device (such as notebook, tablet or smartphone) thanks to a RN-41 class 1 Bluetooth® radio module (by Roving Networks). This small (13.4x25.8x2mm), low power (30 mA connected, < 10 mA sniff mode) module exchanges data with the microcontroller through a Universal Asynchronous Receiver/Transmitter (UART) interface, and delivers a data rate of up to 3-Mbps for distances up to 100 meters [18]. A 4 layers, 55x30x2mm, printed circuit board allows the above listed components to work properly and to exchange data. The circuit is powered by a very small (5x25x35mm), extremely lightweight (9 g) 3.7 V Polymer Lithium Ion battery with a nominal capacity of 400 mAh, including a built-in protection against over voltage, over current, and minimum voltage. The battery can be recharged by connecting the unit via USB to a PC or a 5 V power adapter. Current consumption of the inertial unit is shown in Table I (data measured in worst case conditions). The system is currently capable of continuously acquiring and transmitting data to a PC for about 10 hours, but we are implementing power saving techniques in order to further extend the battery life. The circuit board, the Bluetooth module and the battery are enclosed in a 60x35x20 mm box, which is made in translucent plastic, in this way the LED indicators on the board are totally visible. The developed prototype is lightweight and unobtrusive, and its packaging allows to wear it on the body part to be monitored using elastic Velcro straps, and it is adaptable to different kinds of monitoring purposes: long term monitoring thanks to the μ SD card and real-time monitoring through a Bluetooth wireless connection. The device can also be used as a node of a body area network in this way it is possible to monitor the activity of more than one limb.

TABLE I. DEVICE CURRENT CONSUMPTION (WORST CASE)

Components	Current Consumption (mA)
Microcontroller	27
Accelerometer and magnetometer (measuring)	0.11
Gyroscope (measuring)	6.1
Bluetooth module (peaks data transmission)	65
Bluetooth module (average)	30
μ SD (Page Write ¹)	60

¹Page Write Time = 3ms

III. SYSTEM APPLICATION

As mentioned in the Introduction, we conceived this instrument for three kinds of scenarios.

In the first one, a single unit is exploited in a typical laboratory or clinical environment: the instrument is attached to the limb of interest or to the trunk and connected via Bluetooth to a PC, notebook, tablet, or smartphone on which the researcher can visualize in real time the acquisition signals when the subject performs a set of movements (e.g. exercises included in a clinical balance test).

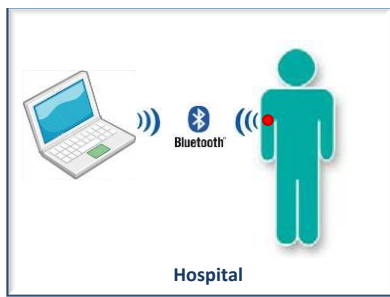


Figure 3. Application Scenario 1: the subject wears a single unit during a trial performed in a clinical environment; data are transmitted via Bluetooth to a PC/tablet/smartphone.

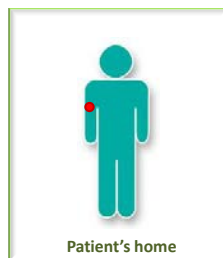


Figure 4. Application Scenario 2: the subject wears a single unit at home, the Bluetooth module is switched off and data are stored on the local memory.

In the second scenario, the basic unit is used for long-term monitoring, while the patient is at home, for instance. In this case the Bluetooth® module is not necessary, therefore it is simply switched off. Data are recorded on the local μ SD memory, where they are arranged in text spreadsheet files. When the device is returned back to the laboratory/clinic, the μ SD is extracted so that the files can be downloaded to a PC for further processing.

In the third, and most complex, scenario many basic units are positioned on the body of the subject, e.g. one at the level of L3, two on the thighs, two on the wrists or arms and one on the head. One of these devices, typically the one on L3, acts as a gateway and relay node, so that it is wired to all the other devices and collects their data. It then extracts parameters of interest if needed, and then it either stores data and computed figures on the μ SD or transmits them wirelessly to a PC. The peripheral units are connected to the gateway unit by means of a multiprocessor serial communication, implementing a single master – multiple slaves system. With our design, the body network can be composed by up to ten (9 slave and 1 master) units, with 9 signals (3 accelerations, 3 angular velocities, 3 magnetic field signals) provided by each unit, sampled at 400Hz per channel.

IV. EXPERIMENTAL TRIALS

In order to carry out preliminary tests of the system's performance, we have recorded a population of 10 control subjects performing exercises, i.e. items, drawn from the Tinetti test for balance control assessment, with the single sensor configuration attached to the subjects' back at the level of L3-L4. With this setup the sensor's data were

acquired at 100Hz sampling frequency through the Bluetooth connection to a laptop computer and saved in a text file. Subjects were simultaneously recorded using a Microsoft Kinect (30 fps recordings) system positioned at about 2.5 m in front of each subject, through a custom developed C++ application.

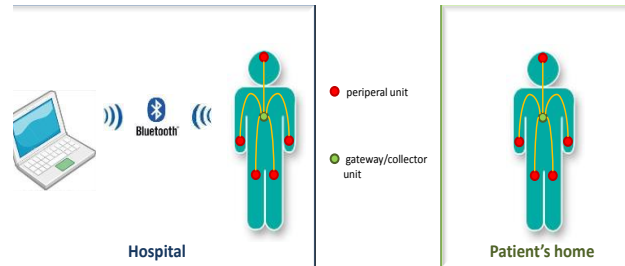


Figure 5. Application Scenario 3: the subject wears a body area network of inertial units. In a clinical environment, the gateway unit collects all units' data and transmits them wirelessly to the remote station. While the subject is at home, instead, data are gathered by the collector unit and stored locally in its μ SD memory card.

Using custom developed Matlab functions we then exploited the 3D accelerometer as an inclinometer by low-pass filtering its data with a 1Hz cutoff frequency and computing its pitch and roll angles in an gravity-referenced coordinates system. These data were then compared to the roll and pitch trunk inclination angles computed based on the 100Hz-resampled Kinect data. An example of such comparison on a representative subject performing the “Stand Up” and the “Reaching” exercises is shown in Figure 6, where the pitch angle computed from the sensor mounted on the subject's lower back is shown together with the trunk inclination computed based on the Kinect data. Table II presents the correlation coefficients between the two signals for the 10 subjects while performing the Stand Up, Sit Down and Reaching exercises.

V. CONCLUSION

The acquired data show very good correlation coefficients between the sensor's data and the Kinect, which was used here as a control instrumentation. These preliminary experimental tests prove the reliability of the proposed sensor in such configuration. The system (single unit for short-term acquisition, first scenario) is being used in an experimental campaign where both its quantitative measurements, and expert examiners' judgments are recorded while a group of patients and controls carry out motor tasks included in the most common balance scales exercises (e.g., Tinetti test, Berg Balance Scale, BESTest).

In these tests the instrument has proven to be very comfortable to the subjects and easy to use by the operators. A proper computational framework is being devised for processing the acquired signals which will provide, at the end of the experimental session, a quantitative assessment of a subject's performance in carrying out the exercises prescribed by the various clinical scales for the assessment of balance and fall risk.

REFERENCES

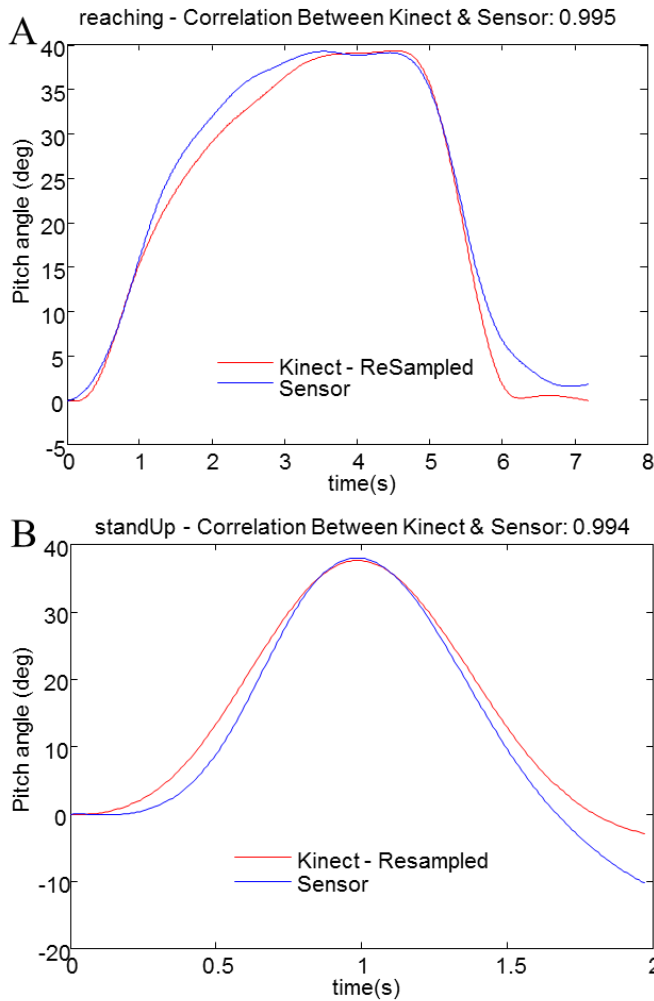


Figure 6. Comparison of trunk pitch inclination measurements performed with the developed sensor wirelessly acquired through the bluetooth connection and simultaneous Kinect recordings. Panel A: data from a representative subject performing a reaching forward exercise; Panel B: data from a representative subject performing a stand up exercise.

TABLE II. EXPERIMENTAL CORRELATION COEFFICIENTS (r)

Subject	Stand Up	Sit Down	Reaching
S1	1.000	0.894	0.989
S2	0.993	0.995	0.986
S3	0.989	0.995	0.997
S4	0.988	0.857	0.998
S5	0.995	0.976	0.998
S6	0.972	0.907	0.993
S7	0.993	0.963	0.941
S8	0.999	0.847	0.996
S9	0.986	0.988	0.987
S10	0.972	0.945	0.993

ACKNOWLEDGMENT

The authors would like to thank R. Gandolfi for providing technical support and assembling the device prototype.

- [1] C. A. Laughton et al, Aging, muscle activity, and balance control: physiologic changes associated with balance impairment, *Gait Posture.*, 18:2,101-108, 2003
- [2] S. R. Lord et al, Physiological factors associated with falls in older community-dwelling women, *J. Am. Geriatr. Soc.*, 42:10,1110-1117, 1994
- [3] M. E. Tinetti et al, Shared risk factors for falls, incontinence, and functional dependence. Unifying the approach to geriatric syndromes, *JAMA*, 273:17,1348-1353, 1995
- [4] L. Panella et al, Towards objective evaluation of balance in the elderly: validity and reliability of a measurement instrument applied to the Tinetti test, *Int. J. Rehabil. Res.*, 31:1,65-72, 2008
- [5] M. E. Tinetti, Performance-oriented assessment of mobility problems in elderly patients, *J. Am. Geriatr. Soc.*, 34:2,119-126, 1986
- [6] K. O. Berg et al, Measuring balance in the elderly: validation of an instrument, *Can. J. Public Health*, 83 Suppl 2,S7-11, 1992
- [7] F. B. Horak et al, The Balance Evaluation Systems Test (BESTest) to differentiate balance deficits, *Phys. Ther.*, 89:5,484-498, 2009
- [8] K. Altun et al, Comparative study on classifying human activities with miniature inertial and magnetic sensors, *Pattern Recognition*, 43:10,3605-3620, 2010
- [9] A. Turcato, S. Ramat, A computational framework for the standardization of motion analysis exploiting wearable inertial sensors, *Conf. Proc. IEEE Eng Med. Biol. Soc.*, 2011,4963-4966, 2011
- [10] M.J. Mathie et al, A system for monitoring posture and physical activity using accelerometers, *Proceedings of the 23rd Annual International Conference of the IEEE Engineering in Medicine and Biology Society*, 2001, vol.4, no., pp.3654,3657 vol.4, 2001
- [11] B. Ying-Wen et al, Design and implementation of a fall monitor system by using a 3-axis accelerometer in a smart phone, *2012 IEEE 16th International Symposium on Consumer Electronics (ISCE)*, pp.1,6, 4-6 June 2012
- [12] S.S. Intille et al, Design of a wearable physical activity monitoring system using mobile phones and accelerometers, *2011 Annual International Conference of the IEEE Engineering in Medicine and Biology Society, EMBC*, Aug. 30 2011-Sept. 3 2011
- [13] M. Schulze et al, Development and clinical validation of an unobtrusive ambulatory knee function monitoring system with inertial 9DoF sensors, *2012 Annual International Conference of the IEEE Engineering in Medicine and Biology Society (EMBC)*, pp.1968,1971, Aug. 28 2012-Sept. 1 2012
- [14] P. Čech et al, Head position monitoring system design, *2010 20th International Conference Radioelektronika (RADIOELEKTRONIKA)*, pp.1,4, 19-21 April 2010
- [15] STMicroelectronics (2013). RM0316 Reference manual: STM32F302xx, STM32F303xx and STM32F313xx advanced ARM-based 32-bit MCUs [Online]. Available: http://www.st.com/web/en/resource/technical/document/reference_manual/DM00043574.pdf
- [16] STMicroelectronics (2010). L3G4200D MEMS motion sensor: ultra-stable three-axis digital output gyroscope [Online]. Available: <http://www.st.com/st-web-ui/static/active/en/resource/technical/document/datasheet/CD00265057.pdf>
- [17] STMicroelectronics (2013). LSM303DLHC: Ultra-compact high-performance eCompass module: 3D accelerometer and 3D magnetometer [Online]. Available: <http://www.st.com/web/en/resource/technical/document/datasheet/DM00027543.pdf>
- [18] Roving Networks (2013). RN41/RN41N Class 1 Bluetooth Module [Online]. Available: <http://ww1.microchip.com/downloads/en/DeviceDoc/rn-41-ds-v3.42r.pdf>



Neural decoding of expressive human movement from scalp electroencephalography (EEG)

Jesus G. Cruz-Garza^{1,2†}, Zachery R. Hernandez^{1,3*†}, Sargoon Nepal⁴, Karen K. Bradley⁵ and Jose L. Contreras-Vidal^{1,3}

¹ Laboratory for Noninvasive Brain-Machine Interface Systems, Department of Electrical and Computer Engineering, University of Houston, Houston, TX, USA

² Center for Robotics and Intelligent Systems, Instituto Tecnológico y de Estudios Superiores de Monterrey, Monterrey, Mexico

³ Department of Biomedical Engineering, University of Houston, Houston, TX, USA

⁴ Department of Neurobiology, University of Maryland, College Park, MD, USA

⁵ Department of Dance, University of Maryland, College Park, MD, USA

Edited by:

Klaus Gramann, Berlin Institute of Technology, Germany

Reviewed by:

Joseph T. Gwin, University of Michigan, USA

Julie A. Onton, Institute for Neural Computation, USA

*Correspondence:

Zachery R. Hernandez, Laboratory for Noninvasive Brain-Machine Interface Systems, Department of Electrical and Computer Engineering, University of Houston, 4800 Calhoun Rd., Houston, TX 77004, USA
e-mail: zrhernandez@uh.edu

[†] These authors have contributed equally to this work.

Although efforts to characterize human movement through electroencephalography (EEG) have revealed neural activities unique to limb control that can be used to infer movement kinematics, it is still unknown the extent to which EEG can be used to discern the expressive qualities that influence such movements. In this study we used EEG and inertial sensors to record brain activity and movement of five skilled and certified Laban Movement Analysis (LMA) dancers. Each dancer performed whole body movements of three Action types: movements devoid of expressive qualities (“Neutral”), non-expressive movements while thinking about specific expressive qualities (“Think”), and enacted expressive movements (“Do”). The expressive movement qualities that were used in the “Think” and “Do” actions consisted of a sequence of eight Laban Effort qualities as defined by LMA—a notation system and language for describing, visualizing, interpreting and documenting all varieties of human movement. We used delta band (0.2–4 Hz) EEG as input to a machine learning algorithm that computed locality-preserving Fisher’s discriminant analysis (LFDA) for dimensionality reduction followed by Gaussian mixture models (GMMs) to decode the type of Action. We also trained our LFDA-GMM models to classify all the possible combinations of Action Type and Laban Effort quality (giving a total of 17 classes). Classification accuracy rates were $59.4 \pm 0.6\%$ for Action Type and $88.2 \pm 0.7\%$ for Laban Effort quality Type. Ancillary analyses of the potential relations between the EEG and movement kinematics of the dancer’s body, indicated that motion-related artifacts did not significantly influence our classification results. In summary, this research demonstrates that EEG has valuable information about the expressive qualities of movement. These results may have applications for advancing the understanding of the neural basis of expressive movements and for the development of neuroprosthetics to restore movements.

Keywords: EEG, neural classification, mobile neuroimaging, neural decoding, dance, Laban Movement Analysis

INTRODUCTION

In recent years, neural engineering approaches to understanding the neural basis of human movement using scalp electroencephalography (EEG) have uncovered dynamic cortical contributions to the initiation and control of human lower limb movements such as cycling (Jain et al., 2013); treadmill walking (Gwin et al., 2010, 2011; Presacco et al., 2011, 2012; Cheron et al., 2012; Petersen et al., 2012; Severens et al., 2012; Schneider et al., 2013), and even robotic assisted gait (Wagner et al., 2012; Kilicarslan et al., 2013). Most of these studies however have been limited to slow walking speeds and have been constrained by treadmills or the cycling or robotic devices used in the tasks, and have yet to examine more natural, and therefore less constrained, expressive movements. To address this important limitations, a mobile EEG-based brain imaging (MoBI) approach may be a valuable tool for recording and analyzing what the brain and the

body do during the production of expressive movements, what the brain and the body experience, and what or how the brain self-organizes while movements of physical virtuosity are modified by expressive qualities that communicate emotional tone and texture—the basic language of human interactions. These expressive patterns are unique to each person, and we organize them in such particular ways that they become markers for our identities, even at great distances and from behind (Williams et al., 2008; Hodzic et al., 2009; Ramsey et al., 2011).

Interestingly, studies of the so-called human action observation network, comprised of ventral premotor cortex, inferior parietal lobe, and the superior temporal sulcus, have shown dissociable neural substrates for body motion and physical experience during the observation of dance (Cross et al., 2006, 2009). Orgs et al. (2008) reported modulation of event-related desynchronization (ERD) in alpha and beta bands between 7.5 and 25 Hz in

accordance to a subject's dance expertise while viewing a dance movement. Tachibana et al. (2011) reported gradual increases in oxygenated-hemoglobin (oxy-Hb) levels using functional near-infrared spectroscopy (fNIRS) in the superior temporal gyrus during periods of increasing complexity of dance movement. While current neuroimaging research aims to recognize how the brain perceives dance, no study has described the various modes of expressive movements within a dance in relation to human scalp EEG activity. Thus, the current study focuses on extracting information about expressive movements performed during dance from non-invasive high-density scalp EEG.

The study emerged from many questions about the differences in neural engagement between functional and expressive movement in elite performers of movement; specifically, dance, and movement theatre. The questions are important, because dance has been studied primarily as elite athletic movement, located in the motor cortex. And yet, dancers train for years to express nuanced and complex qualities in order to tell a story, express an emotion, or locate a situation. Where do these various communicative messages, manifested in expressive movers, fire? Are they part of the motor functions, or are other aspects of cognition involved? The questions therefore became the basis of an emergent inquiry, using the high-density scalp EEG. Since no previous data on the differences between these two modalities of movement have been found, the study is nascent. As the investigators planned for the research, it became clear from the lack of any prior studies making these distinctions that we would be gathering baseline data and demonstrating feasibility for further studies.

Our study utilized expert analysts and performers of expressive movement, all trained in Laban Movement Analysis (LMA) (Laban, 1971; Bradley, 2009). LMA is composed of four major components: Body, Space, Effort, Shape, which make up the grammar for movement "sentences," or phrases. In this study, we focus on the Effort component, which represents dynamic features of movement, specifically the shift of an inner attitude toward one or more of four factors: *Space* (attention or focus), *Weight* (impact, overcoming resistance), *Time* (pacing), and *Flow* (on-goingness). Each factor is a continuum between two extremes: (1) *Indulging in or favoring* the quality and (2) *Condensing* or fighting against the quality. **Table 1** illustrates the Laban's Effort qualities, each factor's indulging and condensing element, respectively with textual descriptions and examples.

LMA differentiates between functional and expressive movement. Functional movement is perfunctory, task-oriented, non-expressive movement. It can be highly skill-based and technically complex, but it does not communicate an attitude or express an emotion. An example of functional movement might be cycling or treadmill walking; when such activities are primarily about the mechanics of executing the action. Expressive movement occurs through shifts in thoughts or intentions, and communicates something about the personal style of the mover. Human beings communicate in both verbal and nonverbal ways; the nonverbal expressive aspects of movement are "read" as indicators of our unique personalities and personal style. For example, movement analysts would describe individuals as "hyper" or "laid-back" based, in part, on their Effort patterns. Individuals

Table 1 | Effort factors and effort elements (Zhao, 2001; Bishko, 2007; Bradley, 2009).

Effort	Element	Description
Space	Indirect	Attention to the surroundings. "Where." Spatial orientation All-round awareness, three-dimensionality of space, flexible Example: waving away bugs, scanning room for misplaced keys
	Direct	Straight, linear action, attention to singular spatial possibility Example: pointing to a particular spot, threading a needle
Flow	Free	Amount of control. "How." Feeling of how movement progresses Uncontrolled, unable to stop in the course of movement Example: flinging a rock into a pond, waving wildly
	Bound	Rigid, controlled, restrained, resisting the flow Example: carrying an filled up of hot tea, moving in slow motion
Weight	Light	Sensing, Intention. "What." Attitude of movement Buoyant, weightless, sensitive Example: dabbing paint on a canvas, movement of feather
	Strong	Powerful, bold, forceful, determined Example: punching, pushing, wringing a towel
Time	Sustained	Intention, decision. "When." Lack or sense of urgency Leisurely, lingering Example: yawning, smelling the flowers
	Quick	Unexpected, surprising, urgent, fleeting Example: swatting a fly, grabbing child from path of danger

might have recurring moments of a Strong, Direct stance. Others may demonstrate recurring moments of Quick, Free, Light gestures that accent a sparkly or lively presence. These expressive components of movement do not occur in isolated ways from the other aspects of movement analysis (Body, Space, and Shape), but rather, modify movement events. They are capable of a wide range of such modifications, and the complex patterns of expressiveness make up unique movement signatures. In this way, familiar people can be identified from even great distances, simply from their Effort qualities. Unfortunately, prior research investigating natural expressive movement has been limited to motion capture technology (Zhao and Badler, 2005; Bouchard and Badler, 2007). The markers that track the body in movement are tantalizingly close to being able to trace movement qualities, but have not yet achieved legibility of the shift into expressive movement. Thus, the goal of

this study is two-fold: (1) Identify those efforts and individual differences in such qualities from brain activity recorded with scalp EEG, and (2) further develop MoBI approaches to the study of natural unconstrained expressive movement.

Certified Laban Movement Analysts were used as subjects because of the extensive training in distinguishing between categories of movement as both observers and performers. The five subjects were also teachers of LMA, and had extensive experience in demonstrating the differences and unique qualities of each feature of expressive movement to students of the work. One of the researchers (Bradley) is a Certified Laban Movement Analyst and has been teaching the material for 30 years. Such experienced subjects and researcher allowed for the identification (and labeling) of shifts in performance from functional to expressive moments.

MATERIALS AND METHODS

EXPERIMENTAL SETUP

Subjects

Five healthy Certified Movement Analysts (CMAs) proficient in the expressive components of LMA participated in the study after giving Informed Consent. All subjects were professional teachers and performers of movement; either dancers or movement-based actors. One man and four women were studied with ages ranging from 28–62 years. Data from subject 2 were discarded due to technical issues during the recording that resulted in missing data or data of bad quality.

Task

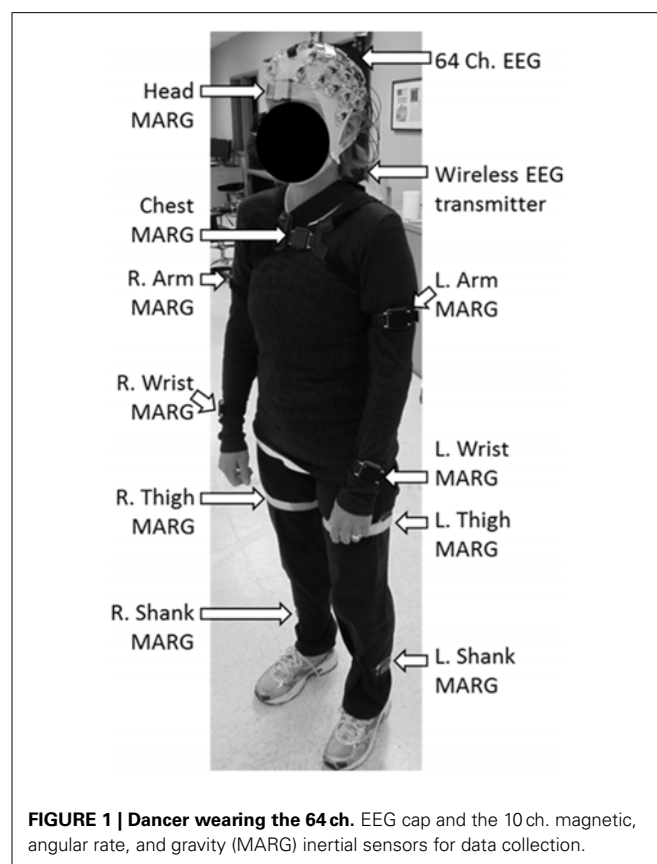
The study consisted of three-trial blocks where synchronized scalp EEG and whole-body kinematics data were recorded during a ~5 min unscripted and individualized dance performance. Each trial block consisted of three Action Types (“neutral,” “think,” “do”). During “neutral” action, subjects were directed to perform functional movements without any additional qualities of expression. This was followed by the “think” condition where subjects continued to perform functional movements, but now imagined a particular Laban Effort quality instructed by the experimenter. Lastly, subjects executed (i.e., enacted) the previously imagined expressive movement during the “do” condition. Dancers were instructed to begin and end each Laban Effort quality cued by the experimenter, a professional movement analyst, in addition to a monotone auditory trigger at the onset of each condition. The sequence of Laban Effort qualities varied from trial-to-trial as well as from subject-to-subject. Nonetheless, all efforts were arranged such that the *indulging* (*favoured*) element was preceded by *condensing* element of the Laban Effort quality. As we were interested in inferring expressive qualities, all the “neutral” instances, which were devoid of willed expressiveness, were collapsed within a superset “neutral” leaving therefore a total of 17 distinct classes of expressive movements to infer from scalp EEG (“neutral” + “think” × 8 efforts + “do” × 8 efforts).

DATA ACQUISITION AND PREPROCESSING

Brain activity was acquired non-invasively using a 64 channel, wireless, active EEG system sampled at 1000 Hz (BrainAmpDC with actiCAP, Brain Products GmbH). Electrode labeling was prepared in accordance to the 10–20 international system using FCz

as reference and AFz as ground. The kinematics of each dance’s movements were captured using 10 wireless Magnetic, Angular Rate, and Gravity (MARG) sensors (OPAL, APDM Inc., Portland, OR) sampled at 128 Hz mounted on the head, upper torso, lumbar region, arms, thighs, shanks, and feet. Each sensor contains a triaxial magnetometer, gyroscope, and accelerometer (**Figure 1**). A Kalman filter was used to estimate the orientation of each IMU with respect to the global reference frame. Using this information about sensor orientation, the tri-axial acceleration data, which had been compensated for gravitational effects, was estimated (Marins et al., 2001).

Peripheral EEG channels (FP1-2, AF7-8, F7-8, FT7-10, T7-8, TP7-10, P7-8, PO7-8, O1-2, Oz, PO9-10 in the extended 10–20 EEG system montage) were rejected as these channels are typically heavily corrupted with motion artifacts and scalp myoelectric (EMG) contamination. In addition, time samples of 500 ms before and after the onset of each condition were removed from further analysis to minimize time transition effects across conditions. EEG signals were resampled to 100 Hz, followed by a removal of low frequency trends and constrained to the delta band (0.2–4 Hz) using a 3rd order, zero-phase Butterworth band-pass filter. The EEG data were then standardized by channel by subtracting the mean and dividing by the standard deviation. Finally, a time-embedded feature matrix was constructed from $l = 10$ lags corresponding to a $w = 100$ ms window of EEG data. The embedded time interval was chosen based on previous studies demonstrating accurate decoding of movement kinematics



from the fluctuations in the amplitude of low frequency EEG (Bradberry et al., 2010; Presacco et al., 2011, 2012). The feature vector for each time sample t_n was constructed by concatenating the 10 lags ($t_n - 9, t_n - 8, \dots, t_n$) for each channel into a single vector of length $10 \times N$, where N is the number of EEG channels. To avoid the problem of missing data, the feature matrix was buffered by starting at the 10th EEG sample of the trial. All EEG channels and time lags were subsequently concatenated and standardized to form a $[t_0 - w] \times [N * I]$ feature matrix.

DIMENSIONALITY REDUCTION

Once feature matrices were generated for all trial blocks, training and testing data were randomly sampled in equal sizes for each class for cross-validation purposes, and reduced in dimensionality (Bulea et al., 2013; Kilicarslan et al., 2013). Local Fisher's Discriminant Analysis (LFDA) is deployed here to reduce the dimensionality of a sample set of classes by minimizing and maximizing samples within and between classes, respectively, while preserving the locality of the samples that form each class (Sugiyama, 2006, 2007). Details of the technique adopted here (LFDA) are described in Sugiyama (2006, 2007).

NEURAL CLASSIFIER ALGORITHM

A Gaussian mixture model (GMM), capable of representing arbitrary statistical distributions as a weighted summation of multiple Gaussian distributions, or components (Paalanen et al., 2006), was employed to classify the Laban Movement (LBM) Efforts from scalp EEG. As the name implies, GMM represents each class as a mixture of Gaussian components whose parameters and component number are approximated using the Estimation-Maximization (EM) algorithm and Bayes Information Criterion (BIC), respectively (Li et al., 2012). The two main parameters for this algorithm include the number of reduced dimensions r and k -nearest neighbors k_{nm} (from the LFDA) and thus must be optimized for this particular application of expressive movement classification (Li et al., 2012; Kilicarslan et al., 2013).

The probability density function for a given training data set $X = \{x_i\}_{i=1}^n \in \mathbb{R}^d$ is given by:

$$p(x) = \sum_{k=1}^K \alpha_k \phi_k \quad (1)$$

$$\phi_k(x) = \frac{e^{-0.5(x - \mu_k)^T \Sigma_k^{-1} (x - \mu_k)}}{(2\pi)^{d/2} |\Sigma_k|^{1/2}} \quad (2)$$

where K is the number of components and α_k is the mixing weight, μ_k is the mean, and Σ_k is the covariance matrix of the k -th component. The parameters of each GMM component K , including α_k , μ_k , and Σ_k , are estimated as those which maximize the log-likelihood of the training set given by:

$$L_k = \sum_{i=1}^n \log p_k(x_i) \quad (3)$$

where $p(x)$ is given in (1). Maximization of (3) is carried out using an iterative, greedy expectation-maximization (EM) algorithm

(Vlassis and Likas, 2002), with the initial guess of the parameters α_k , μ_k , and Σ_k established via k -means clustering (Su and Dy, 2007), until the log-likelihood reaches a predetermined threshold. The determination of K is critical to successful implementation of GMMs for classification. The BIC has been reported as an effective metric for optimizing K (Li et al., 2012).

$$BIC = -2L_{max} + 2 \log(n) \quad (4)$$

where L_{max} is the maximum log-likelihood of each model from (3). During training, the maximum value of $K = 10$ was chosen based on estimates from prior work in our lab (Kilicarslan et al., 2013). We then computed L_{max} for each value of $K \in \{1, 2, \dots, 10\}$ and estimated the optimal value of K as the model, using the minimum BIC from (4). In this manner, class-specific GMMs representing each Effort could be specified for use in a maximum-likelihood classifier. The parameters for each class-conditional GMM were specified using an optimization data set (classifier optimization). The posterior probability of each new data point was computed using the optimized model for each class, and that data point was then assigned to the class that returned the largest value.

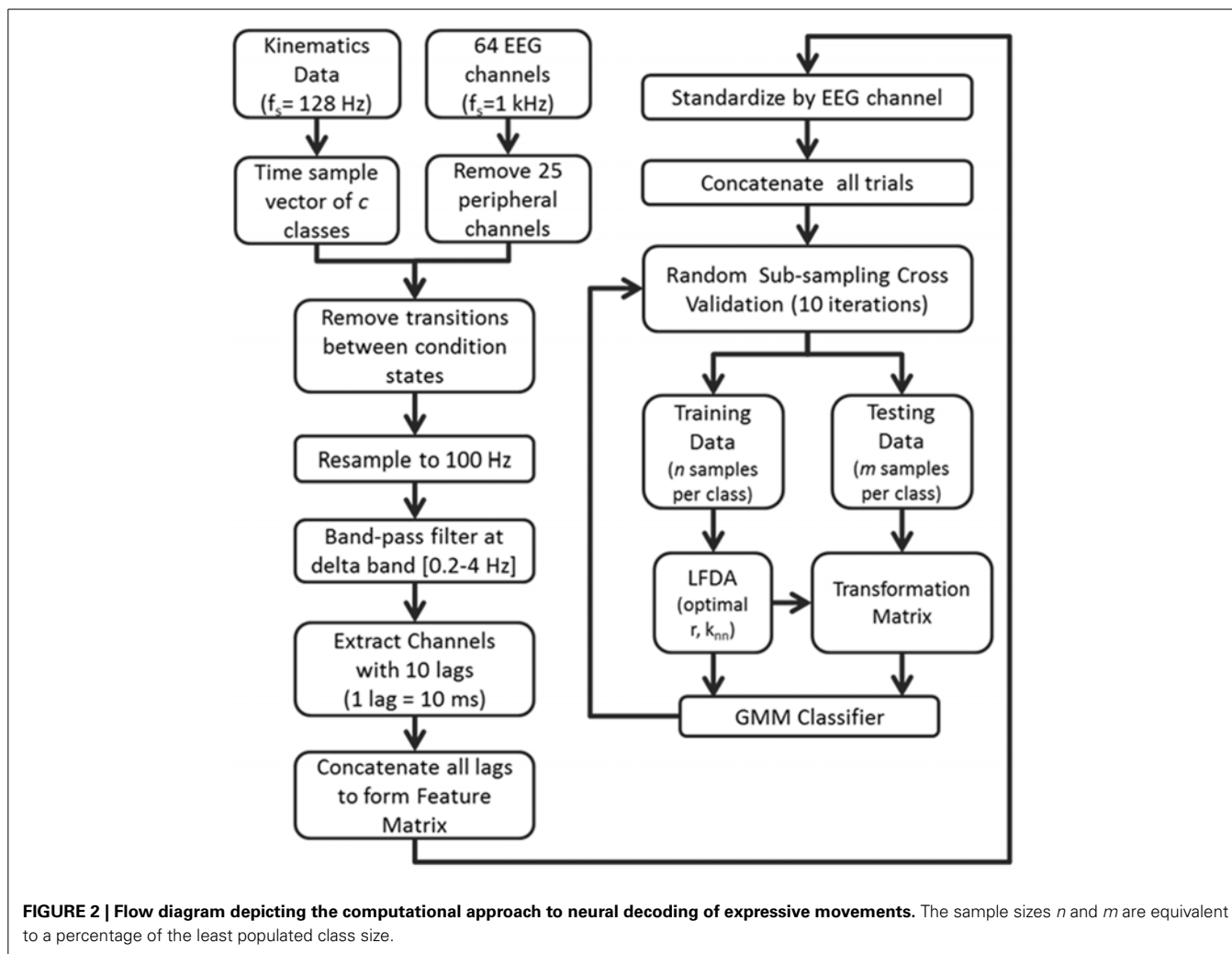
Neural classification from scalp EEG was performed using two schemes of class initialization. We defined the Scheme 1 (Action Type) as a differentiation of n time samples into one of three classes corresponding to the conditions of "Neutral," "Think," and "Do." In a similar initialization for Scheme 2 (Laban Effort quality Type), each condition of "Think" and "Do" were segregated into each of the eight Laban Effort quality elements, thereby forming an accumulation of 17 classes. The results of each classification could be observed by obtaining the confusion matrix of each classification scheme. This matrix provides the user with a detailed understanding of the overall accuracy rate in terms of the accuracy, or sensitivity and precision, for each class.

CROSS VALIDATION

Overall classification accuracy and class precision rates were averaged by implementing a random sub-sampling cross validation scheme. That is, samples from the concatenated feature matrix of three trial blocks were randomly selected and placed into an equal number of samples per class based on a percentage of samples from the least populated class. This process was then repeated 10 times (Figure 2) in order to minimize the effects of random sampling bias, avoid over-fitting, and demonstrate replicability of the algorithm. A sampling of 10 accuracies was found to be sufficient as it usually resulted in a low standard error ($\epsilon < 1$).

FORWARD SELECTION OF EEG CHANNELS

In an attempt to identify the EEG channels that contributed most to classification accuracy, the iterative process of forward selection was introduced upon the EEG channels and their corresponding lags that comprise the feature matrix. This was performed by computing the mean classification accuracy of each EEG channel independently using the LFDA-GMM algorithm, and ranking them in descending order of accuracy values. The highest ranked channel was added to the selected channels list (SCL), and tested against each of the remaining channels. The channel that ranked



highest in classification accuracy when tested along the SCL was added to the SCL for the next iteration. This procedure was repeated until all remaining non-SCL channels were exhausted.

EXAMINATION OF POTENTIAL MECHANICAL ARTIFACTS ON EEG DECODING

To assess the potential contribution of mechanical/motion artifacts to decoding, we performed a series of analyses including time-frequency analysis, cross-correlation analysis, and coherence analysis to compare the EEG signals with the motion signals acquired with the MARG sensors. First, we performed principal component analysis (PCA; Duda et al., 2012) on the acceleration data ($d = 10$ sensors). A cross-correlation analysis was then performed between the raw EEG (resampled to 100 Hz) and the first “synergy” (i.e., first PC) of acceleration data. Histograms and box plots of each EEG channel by PC1 calculated correlation values were subsequently assessed to observe differences across the distribution of each class. Second, we performed a time-frequency analysis to compare the raw EEG signals over selected frontal, lateral, central, and posterior scalp sites and the gravity-compensated accelerometer readings from the MARG

sensor placed on the head. Then, we estimated the coherence between the raw EEG signals and the accelerometer signals. Finally, we computed a whole-scalp cross-correlation of the EEG signals and the head accelerometer readings to examine the contribution of head motion to EEG.

RESULTS KINEMATIC ANALYSIS

Figure 3 depicts a sample set of EEG and motion capture recordings for Subject 4, Trial 2 comprising all Action type classes for the Laban Effort quality of Flow, which includes the opposing elements of free and bound flows. PCA was performed upon the full time series of acceleration data from all 10 MARG sensors. The PCs whose cumulative variability summed to at least 80% were also featured within the sample set of signal data in Figure 3. Time series provided for both “neutral” blocks in Figure 3 appear to be relatively “smooth” (less varying) in terms of both neural activity and kinematic movement. One exception to this includes rapid changes in acceleration around 169s as confirmed by the acceleration plots. EEG signal patterns are visually distinct between “think” time segments of free and bound flow elements, especially

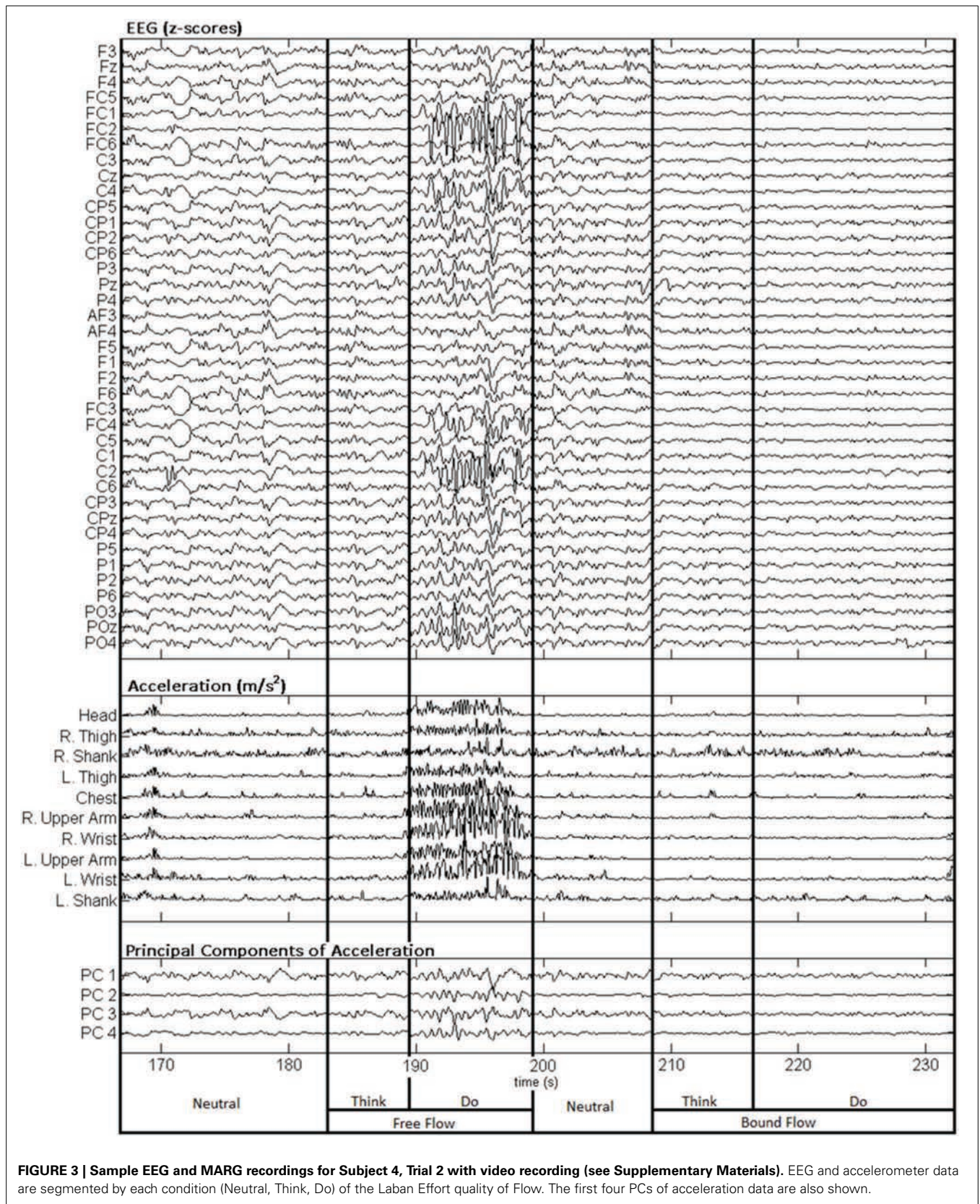
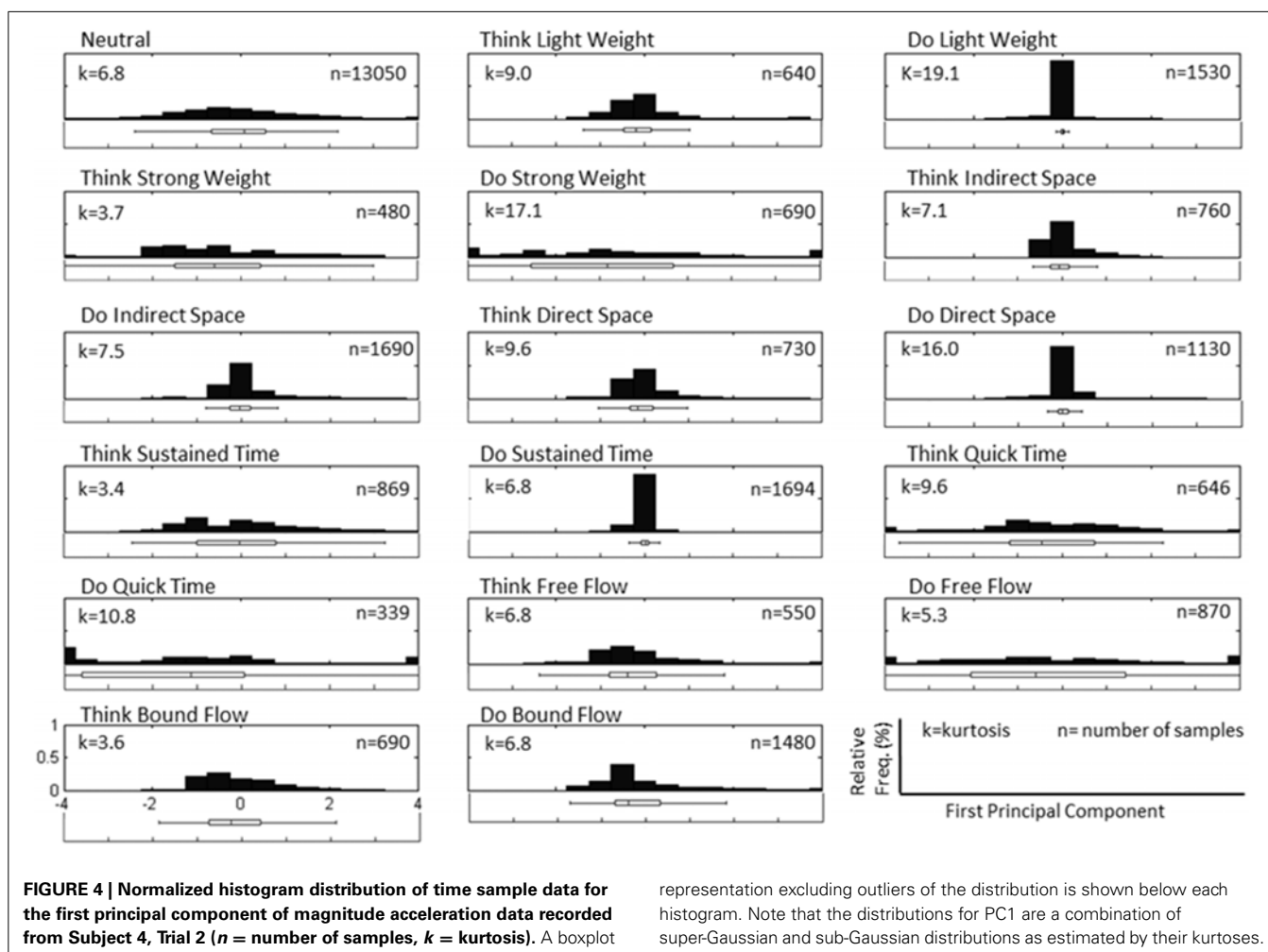
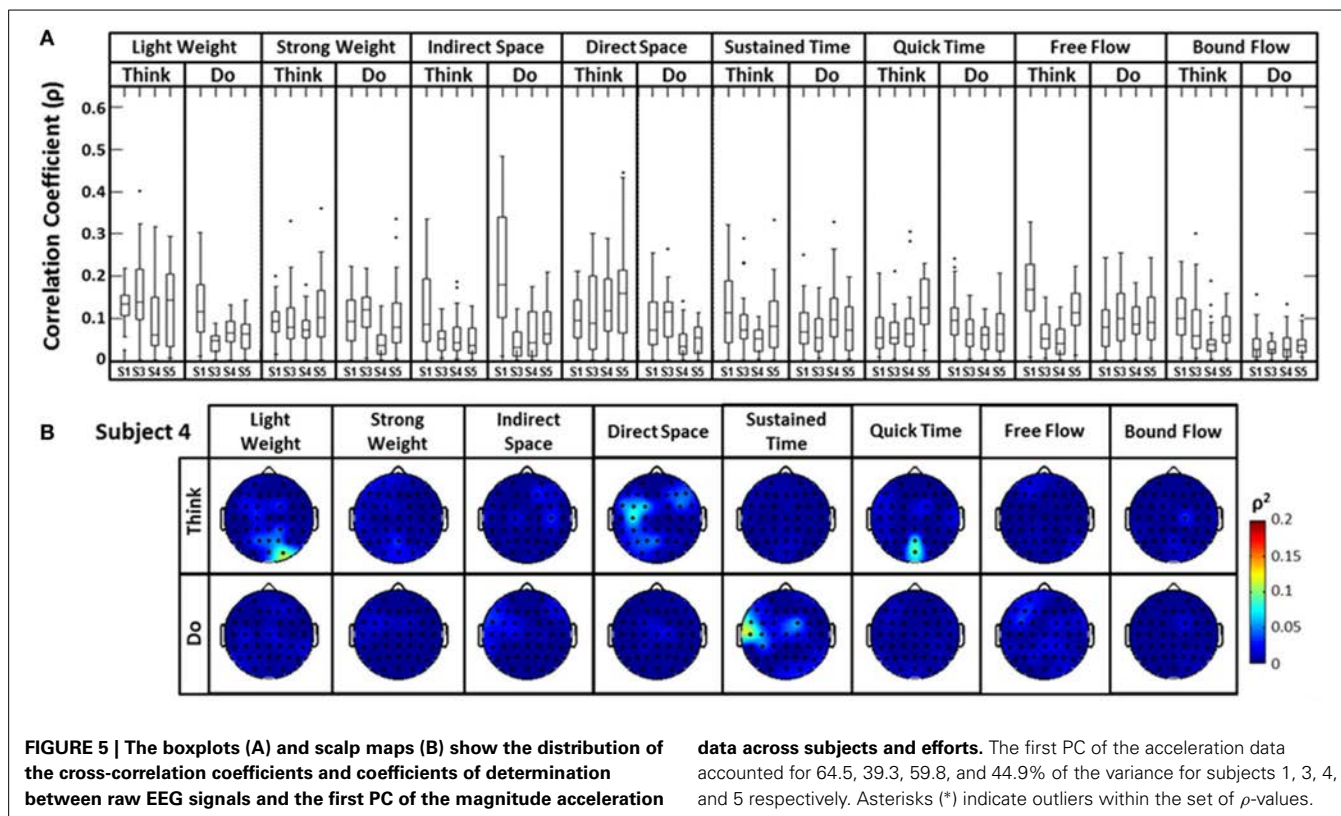


FIGURE 3 | Sample EEG and MARG recordings for Subject 4, Trial 2 with video recording (see Supplementary Materials). EEG and accelerometer data are segmented by each condition (Neutral, Think, Do) of the Laban Effort quality of Flow. The first four PCs of acceleration data are also shown.

with unique areas of modulation of neural activity at 185 s (free flow) and 209 and 214 s (bound flow) which contained little to no effect of motion artifacts, as confirmed by the kinematics signal data. By contrast, the “do” section of the Laban Effort quality of free flow was found to contain the greatest influence of motion embedded in the EEG signal data, as demonstrated by the large excursions in signal magnitude for both EEG and kinematics data. These differences between classes are more prominent when the distribution of PC values can be observed for every class in the trial, as shown in **Figure 4**. Key features to note include the small variance accounted by “Do Light Weight” and “Do Sustained Time” classes, which reflects the low movement the subject effectuated for the particular action. Other classes such as “Do Free Flow” and “Do Quick Time” have a higher variance due to the nature of these efforts as they cover a greater range of motion. Potential motion artifacts produced by the subject’s movements appear to contaminate EEG signal patterns, however the effect appears to be localized to specific classes of Laban Effort qualities (e.g., “Do Free Flow”) and thus not consistent over the entire time series. A more detailed analysis of potential mechanical/motion artifacts based on cross-correlation, coherence and time-frequency analyses are thus provided next.

The distribution of correlation values between raw EEG channels and the first PC of the raw acceleration data returned a range of median correlation coefficients between 0.02 and 0.15 across classes (**Figure 5A**). Outliers were identified for some efforts, and thus may be indicative of a close relationship between a particular EEG channel and the first PC “synergy” of acceleration. The coefficient of determination was obtained by squaring each correlation coefficient ρ . This coefficient is defined as the percent variation in the values of the dependent variable (raw EEG) that can be explained by variations in the values of the independent variable (acceleration). Coefficients of determination (ρ^2) values were generally low and ranged from ~ 0.0 to ~ 0.23 (that is, ~ 0 to 23% of the total variation of the raw EEG can be accounted for by changes in the PC1) across all subjects and electrodes. Spatial distributions of ρ^2 -values were plotted as scalp maps to indicate the relationship between the raw EEG and the head acceleration across scalp channels. Peaks of highest accounted variance (**Figure 5B**) were observed for certain Laban Effort qualities, most notably in the occipital regions for “Think Quick Time” and “Think Light Weight” and temporal regions for “Do Sustained Time” for Subject 4 (See Supplementary Material for ρ^2 data from other subjects).





A similar analysis comparing the raw EEG signals and the head accelerometer (which directly recorded EEG electrode movements), rather than the first PC “synergy,” was also conducted (Figure 6). This resulted in correlation values generally below $\rho = 0.15$, though many boxplot distributions varied by subject throughout each Laban Effort quality (Figure 6A). Although strong relationships between the accelerometer and EEG signals may be expected, the relatively low ρ^2 scores indicate otherwise. Low correlations between neural activity and head motion were observed for classes such as “Bound Flow,” which is reasonable given the rigid-like movements that this effort entails. In contrast, much higher correlation coefficients remained for “Light Weight” and “Indirect Space” time segments. Figure 6B depicts scalp maps with ρ^2 -values between head accelerometer and raw EEG data for Subject 4. In the scalp maps some classes show channels with slightly high correlation $\rho^2 = 0.1$ (which account for $\sim 10\%$ of the total variation of the EEG due to the head motion), specifically in “Think Light Weight,” “Think Direct Space,” “Think Quick Time,” and “Do Sustained Time,” for Subject 4. Overall, these analyses showed a slight contamination, for some classes of Laban Effort qualities, of EEG signals due to head movement (see Supplementary Material), but the amount of total variance in the EEG signals explained by head motion was relatively small.

Additionally, time-frequency and coherence analyses were performed upon the raw signals of three selected EEG electrodes (Cz, C6, and POz) representing a sampling of the spatial assortment of neural activity across the scalp, as well as the gravity-compensated acceleration magnitude of the head MARG sensor by generating two spectrograms, as shown in Figure 7. The spectrograms

were generated by computing the short-time Fourier transform (STFT) over a time window of samples with overlap at each PSD computation of the FFT. We used a frequency range between 0.1–40 Hz and a time window of 1024 samples with 93% overlap. The mean-squared coherence between the head acceleration and each corresponding EEG electrode at each frequency value was computed using Welch’s overlapped-segment averaging technique (Carter, 1987). From the spectrograms it can be observed that the actions “Do Quick Time,” “Do Think Free Flow,” “Do Strong Weight,” and short-lived portions of “Neutral” tasks contained higher power in the head accelerometer readings that may affect decoding. However, coherence estimates were generally low (< 0.3 ; see Figure 7) with some transient increases in coherence between EEG and head acceleration during some Laban Effort qualities. Given that relatively high levels of coherence were short-lived and localized to a few classes of Laban Effort qualities, and that random sampling of EEG signals were used for training and cross-validation of our neural classifiers, we argue that motion artifacts, if present, had only a very minor contribution to decoding. We further discuss these results below.

DECODING ACTION TYPE FROM SCALP EEG

We first examined the feasibility of inferring the action type (“neutral,” “think,” “do”), irrespective of Laban Effort quality, from scalp EEG. Analyses showed the “think” condition had the highest sensitivity than the other two action types. Based on the optimization of LFDA parameters, the mean accuracy rate (10 random subsampling cross-validation iterations were used for each subject) was $56.2 \pm 0.6\%$ by Action Type for Subject 1

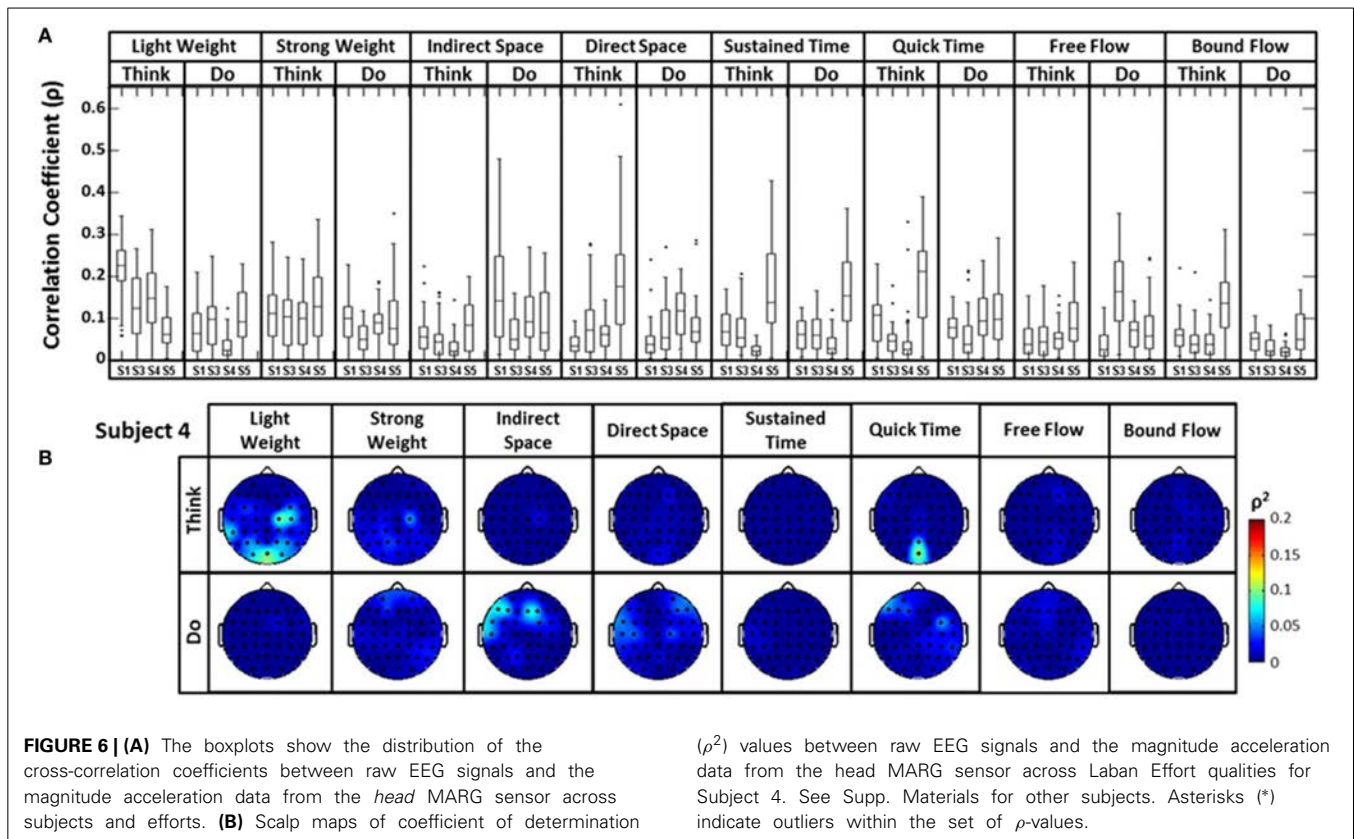


FIGURE 6 | (A) The boxplots show the distribution of the cross-correlation coefficients between raw EEG signals and the magnitude acceleration data from the head MARG sensor across Laban Effort qualities for Subject 4. See Supp. Materials for other subjects. Asterisks (*) indicate outliers within the set of ρ -values.

(ρ^2) values between raw EEG signals and the magnitude acceleration data from the head MARG sensor across Laban Effort qualities for Subject 4. See Supp. Materials for other subjects. Asterisks (*) indicate outliers within the set of ρ -values.

($r = 300$, $k_{nn} = 21$), which was well above 33% chance probability. Similar classification accuracy results were obtained for the rest of the subjects, namely $57.0 \pm 0.4\%$ for Subject 3, $62.1 \pm 0.5\%$ for Subject 4, $62.4 \pm 1.0\%$ for Subject 5. **Figure 8** shows the mean classification accuracies for the different data sets tested.

Predicted samples were summed across all four subjects and normalized by dividing each predicted sample size by the actual class sample size, as indicated by the percentages within each confusion matrix block (**Figure 9**). **Figure 9** depicts the confusion matrix for the Action Type decodes. Classification of EEG patterns corresponding to the “think” class achieved the highest classification rates (88.2%), followed by both “neutral” and “do” classes. Note that the highest misclassifications occurred for class “neutral,” which were classified as belonging to the “think” (32.9%) class. The worst performance was for the “do” class as instances of “neutral” (23.5%) and “think” (50.7%) were misclassified as “do.”

DECODING LABAN EFFORT QUALITY TYPE FROM SCALP EEG

We then examined the classification accuracy for Laban Effort quality Type (8 Think about Laban Effort quality + 8 Do Laban Effort quality + Neutral = 17 classes). In this case, nearly all test samples were accurately classified into their respective classes, which resulted in 88.2% classification accuracy across subjects. **Figure 8** (black bars) shows the mean classification accuracies for Laban Effort qualities across subjects. Interestingly, most test samples were misclassified under the “neutral” class as shown by the relatively high percentages for all non-“neutral” classes in the

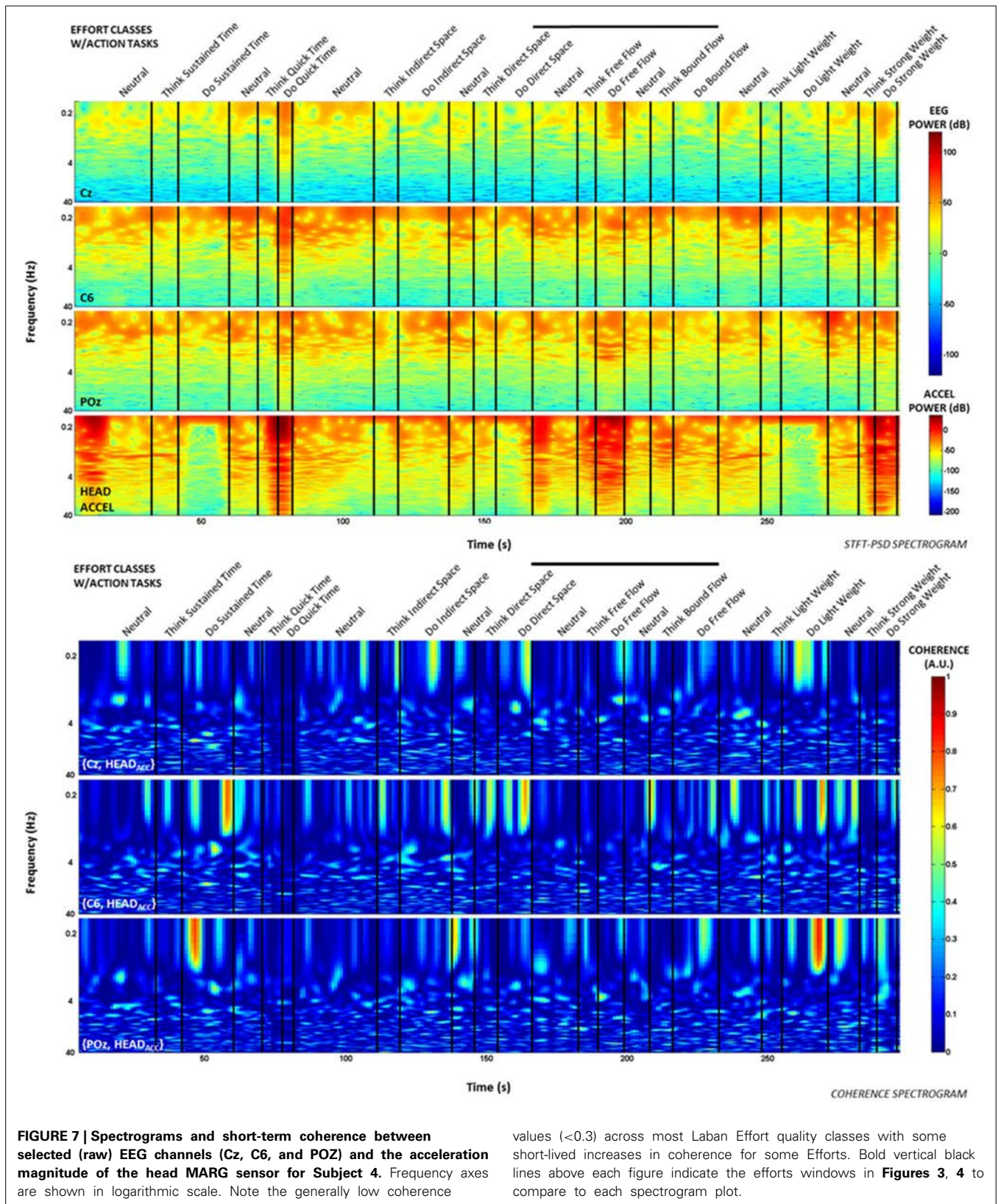
first column (**Figure 10**). Based upon **Figure 10**, classes related to actions of “do” were more difficult to classify (relative to actions of “think”) except for “Do Quick Time,” which contained the highest sensitivity rate overall (96.5%).

TRAINING SAMPLE SIZE EFFECTS ON CLASSIFICATION ACCURACY

The effect of training sample size on classification accuracy was also examined in Subject 1. The training sample size constituted a percentage (20–90) of the least populated class. Classification of Action type was not significantly affected by percentage of training samples (**Figure 11**); however, classification of Laban Effort quality type showed a non-linear increase as a function of percentage of training samples.

RELEVANT EEG CHANNELS FOR CLASSIFICATION

A forward selection approach was employed per subject in order to identify the EEG channels with the most useful information for classification (Pagano and Gauvreau, 2000). While maintaining the number of reduced dimensions (r) and k -nearest neighbors (k_{nn}) constant ($r = 10$, $k_{nn} = 7$) and operating under the Effort Type classification scheme, the mean classification accuracy was computed for all 39 channels and corresponding lags independently. The channel that yielded the highest classification accuracy (channel A) was then selected. Classification accuracies were then re-computed by adding channel A to each of the remaining 38 channels independently. The channel-pair yielding the highest accuracy was again selected and added to each of the remained channels to find the channel-triplets yielding



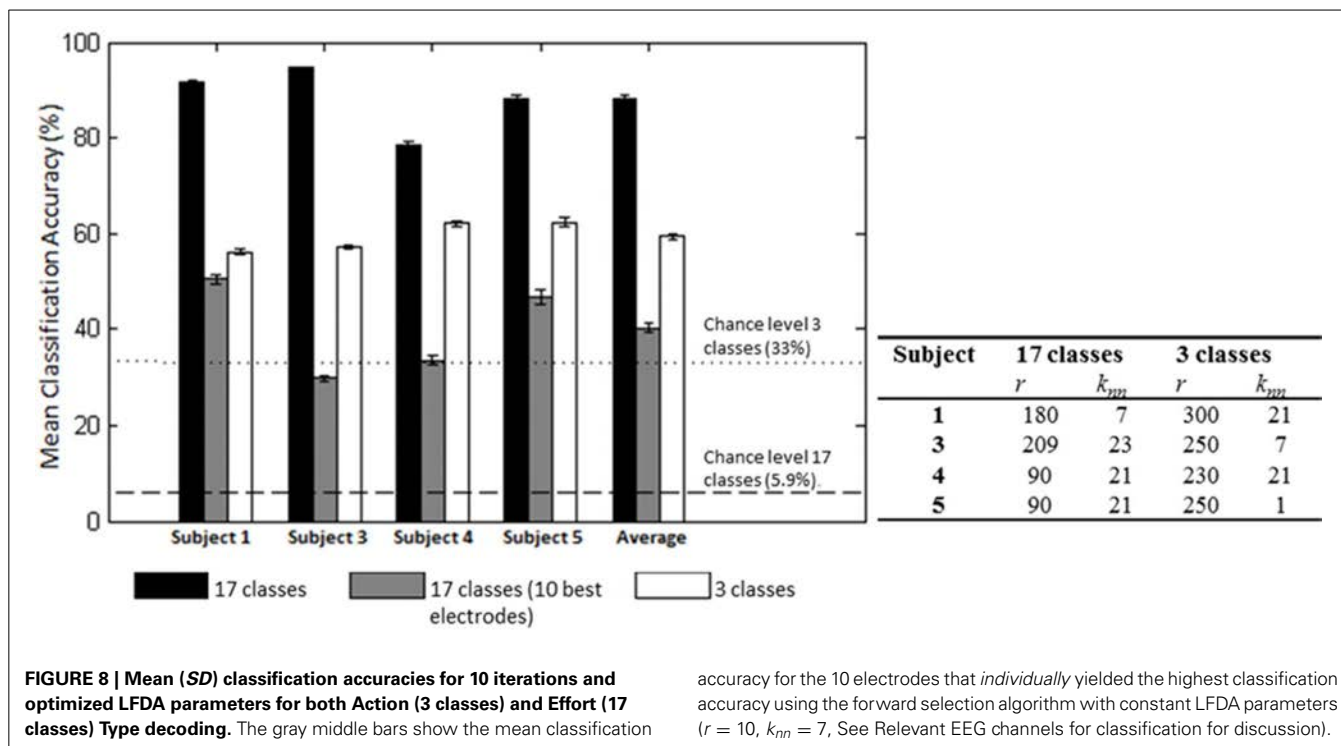


FIGURE 8 | Mean (SD) classification accuracies for 10 iterations and optimized LFDA parameters for both Action (3 classes) and Effort (17 classes) Type decoding. The gray middle bars show the mean classification

accuracy for the 10 electrodes that *individually* yielded the highest classification accuracy using the forward selection algorithm with constant LFDA parameters ($r = 10$, $k_{nn} = 7$, See Relevant EEG channels for classification for discussion).

the highest accuracy, and so on. This process continues until no channels remained, and classification accuracy was shown to stop increasing after selecting approximately 10 electrodes for each subject (shaded gray region in **Figure 12**). Hence, 10 electrodes were retained for further analysis per subject, as illustrated by the scalp maps depicted in **Figures 13A–D**. Electrodes common to at least two subjects were highlighted in **Figure 13E**, which span over scalp areas above bilateral premotor and motor cortices and dorsal parietal lobule areas. This is consistent with previous studies seeking to associate dancing movements with cortical regions (Cross et al., 2006, 2009). Though peak accuracies at 10 electrodes (**Figure 12**) were low (40–50%) relative to optimized Effort Type accuracies (**Figure 8**), this was largely due to the lower reduced dimension parameter for LDFA. This suggests that a higher-than-chance classification accuracy can be obtained by using as few as 10 electrodes. Nevertheless, relevant information within all 39 EEG channels ultimately allows the classifier to reach more than 90% decoding accuracy (**Figure 8**).

EFFECTS OF HEAD MOTION ON NEURAL CLASSIFICATION

We examined the relationship between classification performance and motion artifact contamination. Taking the ρ -values from **Figure 5A**, we compared them with each class' F1 score in classification. If classes with higher ρ -values showed a higher F1 score, this would mean that the classifier was able to better classify the classes that were modulated by motion artifacts. However, **Figure 14** shows no evidence of a correspondence between the F1 score and the correlation coefficients per class.

The F1 score (5) is a weighted average of the sensitivity and precision rates, and thus reflects the overall accuracy of a particular class (Hripcsak and Rothschild, 2005). For purposes of this

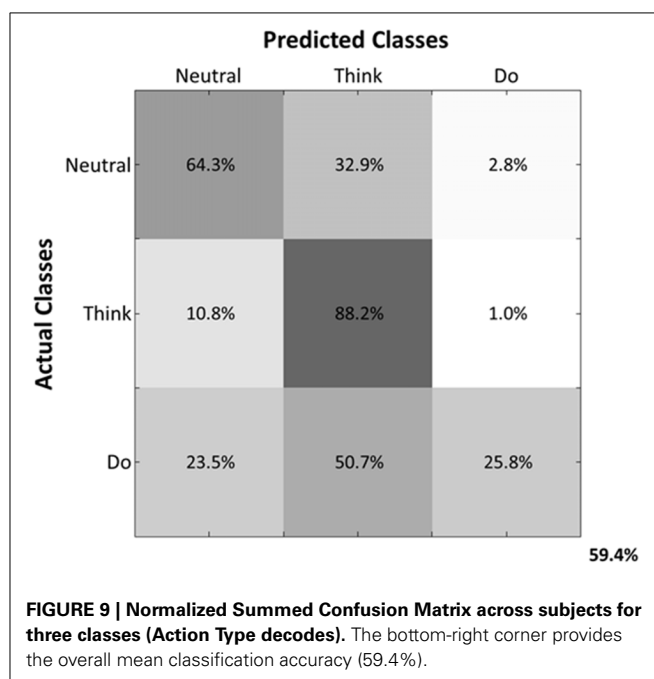
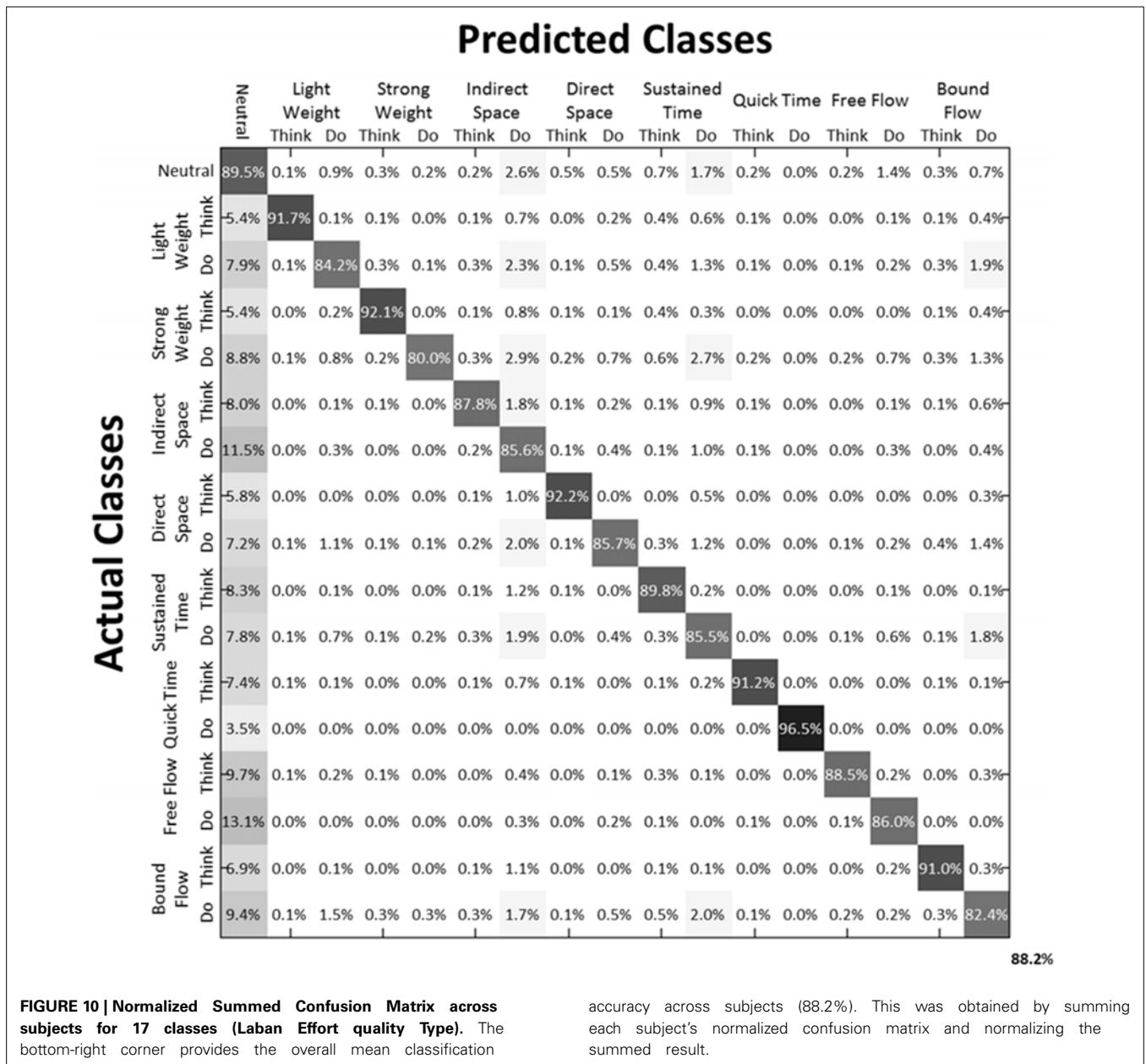


FIGURE 9 | Normalized Summed Confusion Matrix across subjects for three classes (Action Type decodes). The bottom-right corner provides the overall mean classification accuracy (59.4%).

study we use the balanced F1 score equation, defined as:

$$F = \frac{(1 + \beta^2) \times \text{sensitivity} \times \text{precision}}{(\beta \times \text{precision}) + \text{sensitivity}}, \beta = 1 \quad (5)$$

where β is used as a weighting factor between sensitivity and precision. Overall, a direct relationship between classification



success and the median correlation coefficient of EEG channels-to-acceleration data does not seem to occur, but rather a tendency exists for high successes of neural classification in classes that also contain low correlations with accelerometer data.

EFFORT TYPE CLASSIFICATION REPRESENTED IN 4D LABAN SPACE

Figure 15 illustrates the highly predictive power of the Laban Effort quality Type neural classification scheme. Using a normalized variant of the GMM probability density function, we placed weightings to the four coordinates in the Laban Effort quality space. Each axis corresponds to a Laban Effort quality of *Space*, *Flow*, *Weight*, and *Time*. Some testing samples were found to be misclassified between *Indirect Space*, *Light Weight*, and *Quick Time* axes, as shown by the ellipsis in Figure 15. This may suggest

shared characteristics between the expressive movements that cause such misclassification. Non-expressive, or non-classifiable, samples are depicted as green foci falling near the center of the plot, as indicated by the small arrows. The small amount of non-classified samples reflects the overall error of the classifier to predict Laban Effort quality using neural recordings.

DISCUSSION

CLASSIFICATION OF EXPRESSIVE MOVEMENTS FROM SCALP EEG

In this study we demonstrate the feasibility of classifying expressive movement from delta band, EEG signals. Classification rates ranged from $59.4 \pm 0.6\%$ for decoding of Action Type (“neutral,” “think,” and “do”) to $88.2 \pm 0.7\%$ for decoding of Laban Effort quality (17 classes). Surprisingly, only the “think” class was

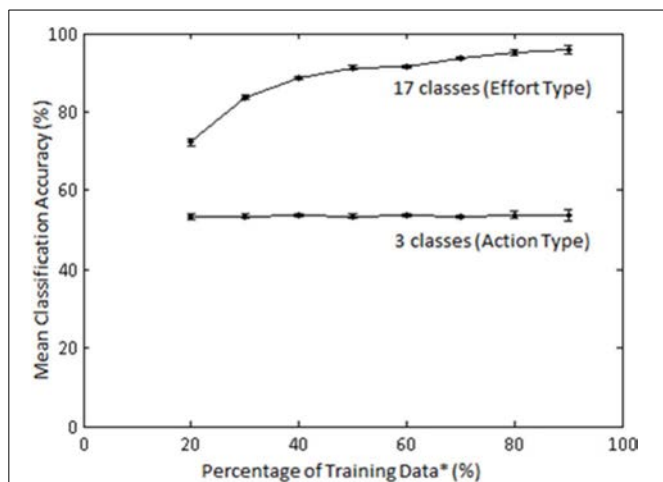


FIGURE 11 | Mean accuracies (for 10 iterations) across varying percentage of training samples for classification by Action (3 classes) and Laban Effort quality (17 classes) types for Subject 1. LFDA parameters: ($r = 180$, $k_{nn} = 7$) for both classification schemes. *Training data samples constitute a percentage of the least populated class.

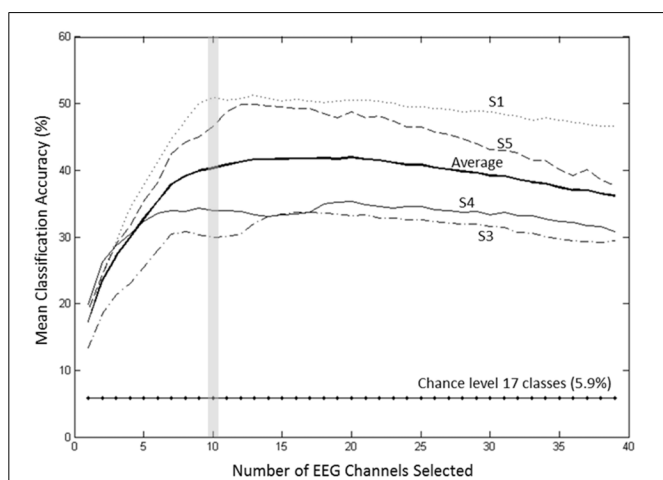


FIGURE 12 | Growth of the mean accuracy (for 30 iterations) as n channels were added to the new set for subjects 1, 3, 4, and 5 using forward selection with constant LFDA parameters ($r = 10$, $k_{nn} = 7$) and the Effort Type classification scheme. The approximate peak in accuracy rate at 10 electrodes, highlighted by the vertical gray bar, was displayed in Figure 8 to demonstrate the extent of classifying using only 10 electrodes at such a relatively low dimensionality.

reliably decoded from EEG whereas classes “neutral” and “do” were poorly decoded. It should be noted that subjects were not instructed to perform a particular pattern of movement, but rather a mode of action (“neutral,” “think,” and “do”) and Laban Effort quality as a component of LMA. Thus, subjects performed highly individualized changing movement patterns throughout the recording session irrespective of mode of action. We note that our neural decoding framework uses a within-subject approach where neural classifiers are trained for each subject. Such neural decoding approaches are subject specific (Lotte et al., 2007; Bradberry et al., 2010; Presacco et al., 2011, 2012; Wagner

et al., 2012; Bulea et al., 2013), and thus common and unique neural patterns are to be expected to influence classification. Conventional statistical analyses can therefore be difficult to interpret in the context of this framework because many factors affect the resulting estimates of significance (i.e., assumptions underlying response distribution, sample size, number of trials, data over-fitting, etc.) (Tsuchiya et al., 2008). Given the cross-validation procedure (i.e., separate random sampling of data for training and test trials) used in our methodology, the risk of over-fitting is minimized. By deploying our methodology for investigating differences in cortical EEG activity patterns, especially as a function of within-subject training, valuable information could be learned about the adaptation/learning trajectories of those patterns and their relationship to performance and training. On the other hand, the consistency of the underlying neural representations, within a subject, would be a valuable metric in longitudinal studies.

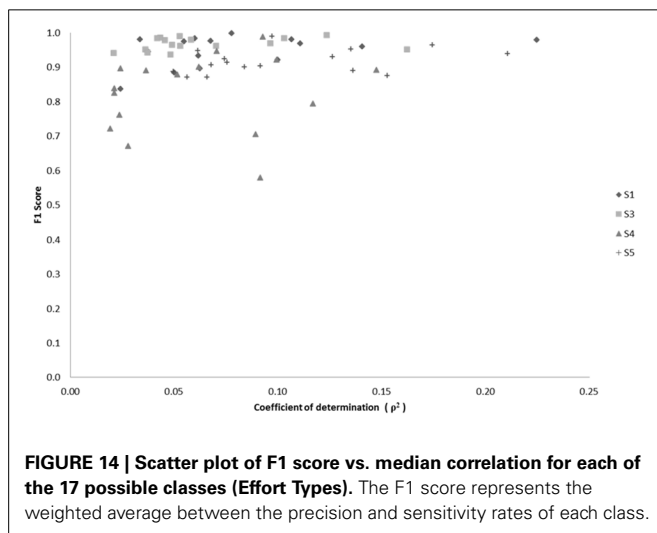
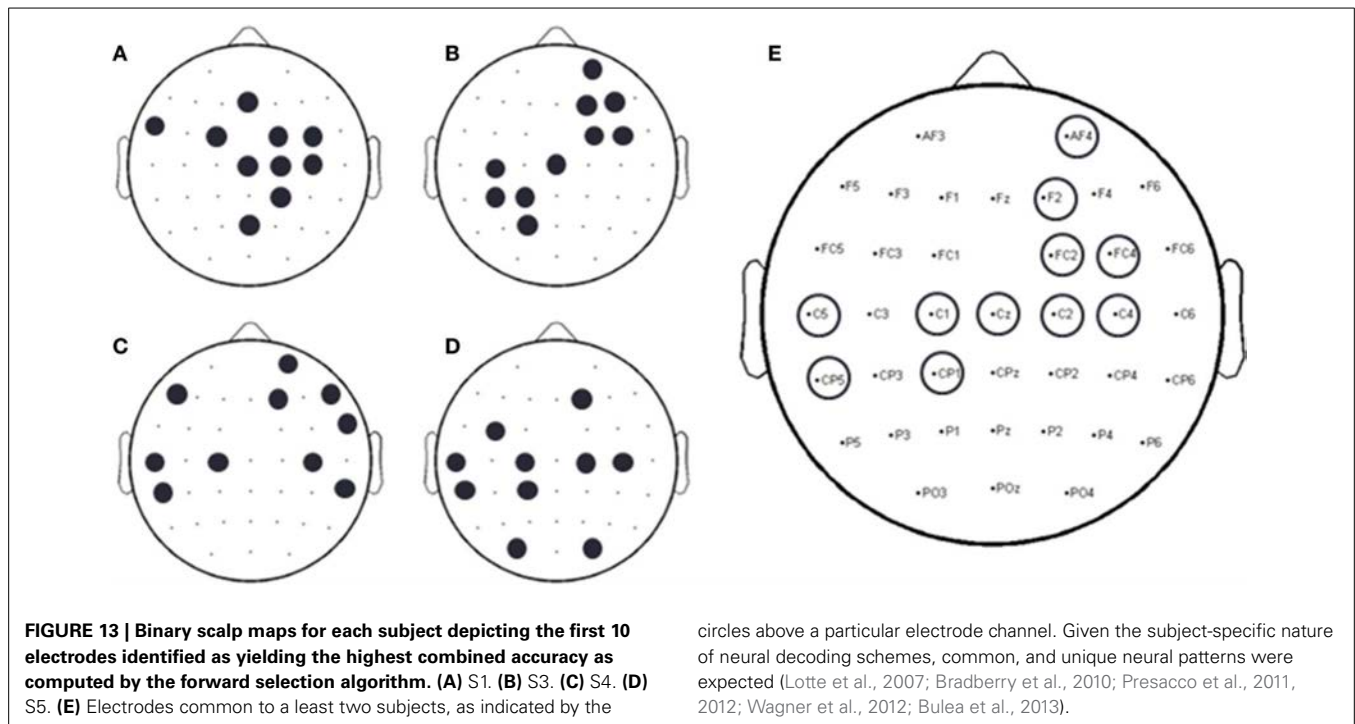
DECODING OF ACTION TYPE AND LABAN EFFORT QUALITIES

The mean decoding accuracy for action type (“neutral,” “think,” “do”) was near 60%, which was well above chance level. Interestingly, classification rate for the “think” actions was highest (88.2%), followed by “neutral” (64.3%) and “do” actions (25.8%). We note that individualized and unscripted functional movements were performed across all the three action types. Thus, the lowest classification rate for the “do” actions may reflect neural patterns that contain integrated elements of “thought” expressiveness and functional movement that were enacted by the dancers. This would have likely introduced “noise” to these patterns as diverse functional movements were performed irrespective of the Laban Effort qualities being imagined. On the other hand, the “neutral” actions, albeit unscripted and varying across time, contained separable information for the classifiers to discriminate them from the other action types. Only the “think” actions contained separable information about functional movement and Laban Effort qualities, which could be decoded by the classifiers. Thus, it is expected the “neutral” class to yield the worst classification rate given the stochastic pattern of functional movements it contains. Likewise the poor classification of the “do” class may be due to the heterogeneous mixture of functional and expressive movements co-occurring, which may introduce some neural noise within the neural activity evoked by this action.

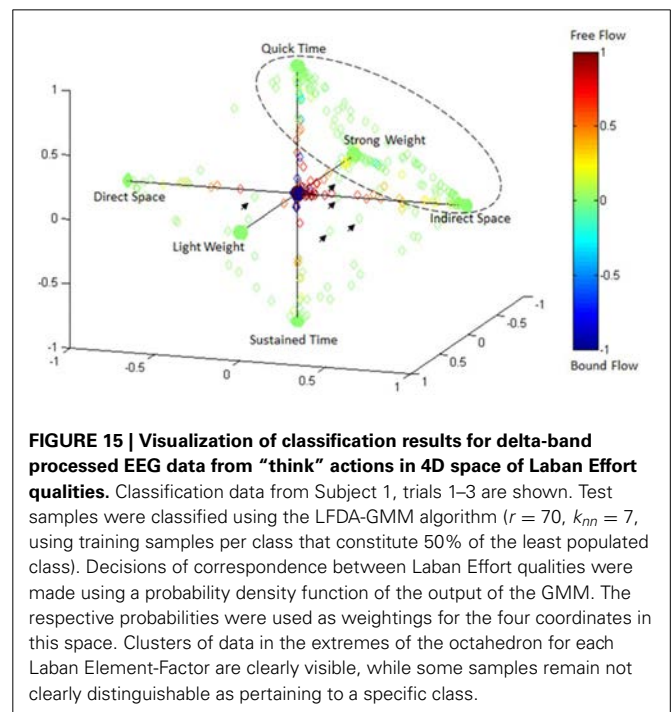
Interestingly our results demonstrate a greater predictive power toward the classification of each Laban Effort quality element rather than the aggregation of all Laban elements into a singular condition-defined class (Figures 9, 10) suggesting that the neural internal states associated with these efforts contain differentiable features, beyond the movements performed, that can be extracted from scalp EEG.

INFLUENCE OF MOTION ARTIFACTS

Given the nature of the experimental setup, it is reasonable to assert the assumption that the EEG data may be plagued with motion artifacts. To examine this possibility we performed a series of analyses to uncover any potential relationship between the EEG signals and the dancers’ body and head movements. We found that in a few instances the correlation between the raw



EEG and the dancers' movements assessed via the MARG sensors was moderately high; however these effects appear to be localized to particular segments of time (see **Figures 3, 4**). We also note that periods of intense unscripted and varying functional movements may have been responsible for the periods of higher correlation and coherence estimates. However, we hypothesize that for the same reason, neural activity related to the "thinking" of Laban Effort qualities may have occurred or modulated varying body and head movements, thus making these motions likely irrelevant for classifiers. Additionally, the relatively low coefficients of determination between EEG and kinematics data demonstrated that the % variability of EEG signals accounting for head motion was rather small. Moreover, the random sampling of both training and testing datasets would have precluded



the introduction of kinematic influences in both calibration and testing of the classifier, as the temporal nature of kinematic artifacts would have not been included in the training or testing data. This however warrants further investigation to develop better strategies of implementing MoBI approaches to capture neural mechanisms behind general movements.

Overall, our results show the feasibility of inferring the expressive component of movements (according to the

Laban categorization) from scalp EEG, especially when those components are imagined as subjects perform unscripted natural body movements. These results may have implications for the study of movement training, disease and brain-computer interfaces for restoration of expressive movements.

ACKNOWLEDGMENTS

This material is based upon work supported by the National Science Foundation under Grant # HRD-1008117 and the National Institutes of Health Award # NINDS R01 NS075889, and also in collaboration with Laboratorio de Robotica del Noreste y Centro de Mexico-CONACYT, Tecnologico de Monterrey. We would also like to express our gratitude to Thomas Bulea, Atilla Kilicarslan, and Harshavardhan Agashe for assisting with the LFDA-GMM algorithms and setting up the EEG, kinematics, and video recordings for this study.

SUPPLEMENTARY MATERIAL

The Supplementary Material for this article can be found online at: <http://www.frontiersin.org/journal/10.3389/fnhum.2014.00188/abstract>

Video Recordings to Figure 3 | Subject 4, Trial 2 EEG and kinematics data.

Recordings are included in the online manuscript submission and are titled as: Direct Space Effort (Movie 1), Free Flow Effort (Movie 2), and Bound Flow Effort (Movie 3).

Figure 5.S1 | Mapping of the coefficient of determination (ρ^2) between the first principal component of the accelerometer data and unprocessed EEG data for each Laban Effort quality performed by each subject.

Figure 6.S1 | Mapping of the coefficient of determination (ρ^2) between the head accelerometer magnitude and unprocessed EEG data for each Laban Effort quality performed by each subject.

REFERENCES

- Bishko, L. (2007). The uses and abuses of cartoon style in animation. *Animation* 2, 24–35. Available online at: <http://journal.animationstudies.org/wp-content/uploads/2007/12/ASVol2Art4LBishko.pdf>
- Boucard, D., and Badler, N. (2007). “Semantic segmentation of motion capture using laban movement analysis,” in *Intelligent Virtual Agents*, eds C. Pelachaud, J.-C. Martin, E. André, G. Chollet, K. Karpouzis, and D. Pelé (Berlin; Heidelberg: Springer), 37–44. doi: 10.1007/978-3-540-74997-4_4
- Bradberry, T. J., Gentili, R. J., and Contreras-Vidal, J. L. (2010). Reconstructing three-dimensional hand movements from noninvasive electroencephalographic signals. *J. Neurosci.* 30, 3432–3437. doi: 10.1523/JNEUROSCI.6107-09.2010
- Bradley, K. (2009). *Rudolf Laban*. New York, NY: Routledge.
- Bulea, T. C., Prasad, S., Kilicarslan, A., and Contreras-Vidal, J. L. (2013). “Classification of stand-to-sit and sit-to-stand movement from low frequency EEG with locality preserving dimensionality reduction,” in *Engineering in Medicine and Biology Society (EMBC), 2013 35th Annual International Conference of the IEEE (Osaka)*, 6341–6344. doi: 10.1109/EMBC.2013.6611004
- Carter, G. C. (1987). Coherence and time delay estimation. *Proc. IEEE* 75, 236–255. doi: 10.1109/PROC.1987.13723
- Cheron, G., Duvinage, M., De Saedeleer, C., Castermans, T., Bengoetxea, A., Petieau, M., et al. (2012). From spinal central pattern generators to cortical network: integrated BCI for walking rehabilitation. *Neural Plast.* 2012:375148. doi: 10.1155/2012/375148
- Cross, E. S., Hamilton, A. F., and Grafton, S. T. (2006). Building a motor simulation de novo: observation of dance by dancers. *Neuroimage* 31, 1257–1267. doi: 10.1016/j.neuroimage.2006.01.033
- Cross, E. S., Hamilton, A. F., Kraemer, D. J. M., Kelley, W. M., and Grafton, S. T. (2009). Dissociable substrates for body motion and physical experience in the human action observation network. *Eur. J. Neurosci.* 30, 1383–1392. doi: 10.1111/j.1460-9568.2009.06941.x
- Duda, R. O., Hart, P. E., and Stork, D. G. (2012). *Pattern Classification*. New York, NY: John Wiley and Sons.
- Gwin, J. T., Gramann, K., Makeig, S., and Ferris, D. P. (2010). Removal of movement artifact from high-density EEG recorded during walking and running. *J. Neurophysiol.* 103, 3526–3534. doi: 10.1152/jn.00105.2010
- Gwin, J. T., Gramann, K., Makeig, S., and Ferris, D. P. (2011). Electrocortical activity is coupled to gait cycle phase during treadmill walking. *Neuroimage* 54, 1289–1296. doi: 10.1016/j.neuroimage.2010.08.066
- Hodzic, A., Kaas, A., Muckli, L., Stirn, A., and Singer, W. (2009). Distinct cortical networks for the detection and identification of human body. *Neuroimage* 45, 1264–1271. doi: 10.1016/j.neuroimage.2009.01.027
- Hripsak, G., and Rothschild, A. S. (2005). Agreement, the F-Measure, and reliability in information retrieval. *J. Am. Med. Inform. Assoc.* 12, 296–298. doi: 10.1197/jamia.M1733
- Jain, S., Gourab, K., Schindler-Ivens, S., and Schmit, B. D. (2013). EEG during pedaling: evidence for cortical control of locomotor tasks. *Clin. Neurophysiol.* 124, 379–90. doi: 10.1016/j.clinph.2012.08.021
- Kilicarslan, A., Prasad, S., Grossman, R. G., and Contreras-Vidal, J. L. (2013). “High accuracy decoding of user intentions using EEG to control a lower-body exoskeleton,” in *Engineering in Medicine and Biology Society (EMBC), 2013 35th Annual International Conference of the IEEE (Osaka)*, 5606–5609. doi: 10.1109/EMBC.2013.6610821
- Laban, R. (1971). *The Mastery of Movement*. Boston, MA: Plays, Inc. (Original work published 1950).
- Li, W., Prasad, S., Fowler, J. E., and Bruce, L. M. (2012). Locality-preserving dimensionality reduction and classification for hyperspectral image analysis. *IEEE Trans. Geosci. Remote Sensing* 50, 1185–1198. doi: 10.1109/TGRS.2011.2165957
- Lotte, F., Congedo, M., Lécuyer, A., Lamarche, F., and Arnaldi, B. (2007). A review of classification algorithms for EEG-based brain-computer interfaces. *J. Neural Eng.* 4, R1–R13. doi: 10.1088/1741-2560/4/2/R01
- Marins, J. L., Yun, X., Bachmann, E. R., McGhee, R. B., and Zyda, M. J. (2001). “An extended Kalman filter for quaternion-based orientation estimation using MARG sensors,” in *Intelligent Robots and Systems, 2001. Proceedings. 2001 IEEE/RSJ International Conference on*, Vol. 4, (Maui, HI), 2003–2011. doi: 10.1109/IROS.2001.976367
- Orgs, G., Dombrowski, J. H., Heil, M., and Jansen-Osmann, P. (2008). Expertise in dance modulates alpha/beta event-related desynchronization during action observation. *Eur. J. Neurosci.* 27, 3380–3384. doi: 10.1111/j.1460-9568.2008.06271.x
- Paalanen, P., Kamarainen, J.-K., Ilonen, J., and Kälviäinen, H. (2006). Feature representation and discrimination based on Gaussian mixture model probability densities—practices and algorithms. *Pattern Recogn.* 39, 1346–1358. doi: 10.1016/j.patcog.2006.01.005
- Pagano, M., and Gauvreau, K. (2000). “Multiple Regression,” in *Principles of biostatistics*, 2nd Edn., eds C. Crockett, et al. (Pacific Grove, CA: Duxbury), 449–469.
- Petersen, T. H., Willerslev-Olsen, M., Conway, B. A., and Nielsen, J. B. (2012). The motor cortex drives the muscles during walking in human subjects. *J. Physiol.* 590, 2443–2452. doi: 10.1113/jphysiol.2012.227397
- Presacco, A., Goodman, R., Forrester, L., and Contreras-Vidal, J. L. (2011). Neural decoding of treadmill walking from noninvasive electroencephalographic signals. *J. Neurophysiol.* 106, 1875–1887. doi: 10.1152/jn.00104.2011
- Presacco, A., Forrester, L. W., and Contreras-Vidal, J. L. (2012). Decoding intra-limb and inter-limb kinematics during treadmill walking from scalp electroencephalographic (EEG) signals. *IEEE Trans. Neural Syst. Rehabil. Eng.* 20, 212–219. doi: 10.1109/TNSRE.2012.2188304
- Ramsey, R., van Schie, H. T., and Cross, E. S. (2011). No two are the same: Body shape is part of identifying others. *Cogn. Neurosci.* 2, 207–208. doi: 10.1080/17588928.2011.604721
- Schneider, S., Abeln, V., Popova, J., Fomina, E., Jacobowski, A., Meeusen, R., et al. (2013). The influence of exercise on prefrontal cortex activity and cognitive performance during a simulated space flight to Mars (MARS500). *Behav. Brain Res.* 236, 1–7. doi: 10.1016/j.bbr.2012.08.022
- Severens, M., Nienhuis, B., Desain, P., and Duysens, J. (2012). “Feasibility of measuring event Related Desynchronization with electroencephalography during walking,” in *Engineering in Medicine and Biology Society (EMBC), 2012 Annual International Conference of the IEEE (San Diego, CA)*, 2764–2767. doi: 10.1109/EMBC.2012.6346537

- Su, T., and Dy, J. G. (2007). In search of deterministic methods for initializing K-means and Gaussian mixture clustering. *Intell. Data Analysis* 11, 319–338.
- Sugiyama, M. (2006). “Local Fisher discriminant analysis for supervised dimensionality reduction,” in *Proceedings of the 23rd International Conference on Machine Learning*, (ACM), 905–912.
- Sugiyama, M. (2007). Dimensionality reduction of multimodal labeled data by local fisher discriminant analysis. *J. Mach. Learn. Res.* 8, 1027–1061.
- Tachibana, A., Noah, J. A., Bronner, S., Ono, Y., and Onozuka, M. (2011). Parietal and temporal activity during a multimodal dance video game: an fNIRS study. *Neurosci. Lett.* 503, 125–130. doi: 10.1016/j.neulet.2011.08.023
- Tsuchiya, N., Kawasaki, H., Oya, H., Howard, M. A., and Adolphs, R. (2008). Decoding face information in time, frequency and space from direct intracranial recordings of the human brain. *PLoS ONE* 3:e3892. doi: 10.1371/journal.pone.0003892
- Vlassis, N., and Likas, A. (2002). A greedy EM algorithm for Gaussian mixture learning. *Neural Process. Lett.* 15, 77–87. doi: 10.1023/A:1013844811137
- Wagner, S., Lucka, F., Burger, M., Grasedyck, L., Hauelsen, J., and Wolters, C. H. (2012). Comparison of direct and reciprocal forward modeling approaches in EEG source analysis. *Biomed. Tech. Berl.* 57:310 (Suppl. 1). doi: 10.1515/bmt-2012-4069
- Williams, G., Bregler, C., Hackney, P., Rosenthal, S., McDowall, I., and Smolskiy, K. (2008). *Body Signature Recognition*. Technical Report, TR-2008-915, New York University.
- Zhao, L. (2001). *Synthesis and Acquisition of Laban Movement Analysis Qualitative Parameters for Communicative Gestures*. PhD diss., Philadelphia, PA: University of Pennsylvania, 147.
- Zhao, L., and Badler, N. I. (2005). Acquiring and validating motion qualities from live limb gestures. *Graph. Models* 67, 1–16. doi: 10.1016/j.gmod.2004.08.002

Conflict of Interest Statement: The authors declare that the research was conducted in the absence of any commercial or financial relationships that could be construed as a potential conflict of interest.

Received: 30 November 2013; accepted: 14 March 2014; published online: 08 April 2014.

Citation: Cruz-Garza JG, Hernandez ZR, Nepal S, Bradley KK and Contreras-Vidal JL (2014) Neural decoding of expressive human movement from scalp electroencephalography (EEG). *Front. Hum. Neurosci.* 8:188. doi: 10.3389/fnhum.2014.00188 This article was submitted to the journal *Frontiers in Human Neuroscience*.

Copyright © 2014 Cruz-Garza, Hernandez, Nepal, Bradley and Contreras-Vidal. This is an open-access article distributed under the terms of the Creative Commons Attribution License (CC BY). The use, distribution or reproduction in other forums is permitted, provided the original author(s) or licensor are credited and that the original publication in this journal is cited, in accordance with accepted academic practice. No use, distribution or reproduction is permitted which does not comply with these terms.

Wearable motion sensors to continuously measure real-world physical activities

[Bruce H. Dobkin](#), MD

Bruce H. Dobkin, Professor of Neurology, University of California Los Angeles, Geffen UCLA School of Medicine, 710 Westwood Plaza, Los Angeles, CA 90095, 310-2066500;

Bruce H. Dobkin: bdobkin@mednet.ucla.edu

[Copyright notice](#) and [Disclaimer](#)

Abstract

Purpose of review

Rehabilitation for sensorimotor impairments aims to improve daily activities, walking, exercise, and motor skills. Monitoring of practice and measuring outcomes, however, is usually restricted to laboratory-based procedures and self-reports. Mobile health devices may reverse these confounders of daily care and research trials.

Recent findings

Wearable, wireless motion sensor data, analyzed by activity pattern-recognition algorithms, can describe the type, quantity, and quality of mobility-related activities in the community. Data transmission from sensors to the cell phone and Internet enable continuous monitoring. Remote access to laboratory-quality data about walking speed, duration and distance, gait asymmetry and smoothness of movements, as well as cycling, exercise, and skills practice, opens new opportunities to engage patients in progressive, personalized therapies with feedback about performance. Clinical trial designs will be able to include remote verification of the integrity of complex physical interventions and compliance with practice, as well as capture repeated, ecologically sound, ratio-scale outcome measures.

Summary

Given the progressively falling cost of miniaturized wearable gyroscopes, accelerometers, and other physiologic sensors, as well as inexpensive data transmission, sensing systems may become as ubiquitous as cell phones for health care. Neurorehabilitation can develop these mobile health platforms for daily care and clinical trials to improve exercise and fitness, skills learning, and physical functioning.

Keywords: mobile health, stroke rehabilitation, outcome assessment, physical activity, accelerometer, gyroscope, activity monitor, signal processing, telemedicine

Introduction

Mobile health or mHealth is a growing endeavor to improve healthcare services via mobile communication devices.¹ The cell phone enables continuous access to the Internet over broadband and WiFi for data

transmission of physiologic variables, physical activity, blood tests, images, social interactions, mental states, and environmental conditions.² By simultaneously assessing behavioral, physiological, and psychological states in the real world and in real-time, mHealth also aims to quantify states of health and well-being. Feedback, cues, and updated instructions via graphics and text messages can be provided in real time based on the flow of information from and back to a patient. The result will be high throughput, multi-streamed, longitudinal data sets to facilitate disease prevention, diagnostics, compliance, personalized management, and behavioral change.³ A global aim is to use this technology to reduce healthcare disparities, especially for patients with chronic diseases, and lower the long-term cost of more personalized care. This long-term management capability is especially important in neurologic rehabilitation after disabling spinal cord and traumatic brain injury, as well as in stroke, multiple sclerosis, and any progressive or neurodegenerative disease. Thus, the rehabilitation team may find remarkable opportunities in mHealth, just as it has for other assistive technologies.

Mobile health smartphone apps take advantage of external sensors and the camera, microphone, GPS, and accelerometer built into these communication devices. The phone already serves as a transmission relay for Bluetooth equipped weight scales, blood pressure and heart rate devices, equipment for exercise, and mental and social health state assessments. Bio-monitoring of blood chemistries, embedded lab-on-a-chip sensors, and tele-monitoring for remote personal health advice by professionals are moving forward as well. Evidence for efficacy is growing, if slowly.⁴ For example, the first mHealth Cochrane analysis of randomized clinical trials (RCTs) for self-management of type 2 diabetes found larger effects on glucose and HgbA1C control for cell phone-based interventions compared to conventional information and computer use.⁵ Studies of efficacy, however, are sparse. Across all health conditions at the end of 2012, 176 RCTs of mHealth technologies were listed at clinicaltrials.gov,⁶ but few have been published or relate to neurologic disability.

This review describes efforts to bring wearable, wireless sensor networks to bear on community-based assessments and treatments to improve walking, exercise, fitness, and other mobility-related activities after neurologic injuries and diseases. It addresses the challenge of a white paper⁷ from the National Institute of Child Health and Human Development, which concluded, “Advanced technology/sensors must be developed to establish better tracking of compliance and clinical outcomes, at several International Classification of Functioning, Disability, and Health levels. New, low-cost, portable sensors may ultimately replace prevailing clinical instruments used for outcome assessments.” Inexpensive smartphones and tablets are lowering the complexity of this challenge since they can communicate with multiple sensors placed on the body; initiate, store or transmit data for processing; provide a variety of user interfaces; download instructions and reminders; and remotely update applications.

Sensor Platforms

A wide range of wearable sensors ([Table 1](#)) are available commercially that provide the raw data to describe arm, trunk, and lower extremity actions outside of a motion analysis gait laboratory.⁸ The choice of sensors, number, and placement will depend on the activity and movement variables to be ascertained. Practical sensor systems must meet many complex design requirements, from cosmetic, privacy and technology acceptability by users to signal processing, data transmission, annotation, and scalability for easy use ([Table 2](#)). Especially important for motion sensing is the accuracy and speed of feature detection and classifier algorithms that turn a sequence of inertial signals into a recognizable movement pattern to measure clinically important details of gait and other purposeful activities.

Commercial devices

Recently, fitness, exercise and wellness gadgets have come to the social networking market. Can they be

used for patient care? In general, these cosmetically striking devices detect successive movements by a single biaxial or triaxial accelerometer placed in a pocket or on a wristband (e.g., FitBit, BodyMedia, FuelBand). Results are summarized by downloading data to a computer or smartphone usually via Bluetooth. Episodic and cyclical body movements are then calculated as activity or step counts or converted into calorie counts. Each swing of the arm or forward propulsion of the trunk is interpreted as a stride during repetitive exercise. Actions with low gravitational force or unusual combinations of acceleration-deceleration of short duration may be misinterpreted, however. Adventitious movements may be interpreted as the motion of interest. Reliability and validity are uncertain in healthy persons in real-world settings and yet to be studied in disabled persons. At best, a wrist-worn accelerometer may distinguish sedentary, household, walking and running as distinct activities and correctly classify intensity of activity 50% of the time.⁹ In their present configuration, these are not suitable for research on patients with neurologic impairments.

Single accelerometer-based step counters have been available for 2 decades for outpatient use (e.g., Actigraph, Pensacola FL; StepWatch Activity Monitor, Oklahoma City, OK).^{10,11} Their count of steps over time generally correlate with the degree of walking impairment for patients with stroke (e.g., slower walkers take fewer steps)¹² and other neurological diseases. Like even less sophisticated pedometers, they may not detect all steps when the cadence falls below 50/minute, walking speed slows below 0.6 m/s¹³ or the gait pattern includes irregular movements. None measure walking speed or have yet been enabled to download to a smartphone. Triaxial accelerometer systems placed posteriorly at the midline of the waist use proprietary algorithms to detect the gait cycle and walking speed (e.g., Actibelt, Munchen, Germany), but so far, tend to be less accurate in patients with greater impairment who walk slowly.¹⁴⁻¹⁶ Indeed, multi-sensor systems are significantly more accurate than any of these single accelerometers to measure activity and estimate energy expenditure.¹⁶

Research devices

An important goal for rehabilitation is to be able to remotely classify human activities and quantitatively measure the quality of their component movements outside of a motion analysis laboratory. Wireless gait laboratory systems (e.g., APDM, Portland, OR) that integrate from 2-7 accelerometers and gyroscopes worn on the wrists, ankles and chest or waist, plus additional types of sensing, are said to be accurate for revealing the gait cycle and walking speed. Combinations of accelerometers are also sufficient to detect postural imbalance,¹⁷ and may help detect or predict falls. Wheelchair activity and energy consumption measurement also requires multiple sensors, on each arm and the chair.¹⁸ These systems, due to cost and complexities in management, have primarily been used in controlled settings, but not for continuous community usage enabled by automatic downloading to a smartphone.

Comfortable, user-friendly sensor network designs compatible with the notion of mHealth are becoming available.¹⁹ In one study, low-cost, miniaturized triaxial accelerometers with electronic circuits were placed over the tibia just above both ankles in healthy and hemiplegic participants. A template walk at several speeds for 10 m was used to help train the activity-pattern-recognition algorithm for each subject.²⁰ The synchronous bilateral raw inertial signals were examined for features related to the timing of components of each stride, including heel-off, toe-off, peak swing, end of swing, and foot flat. A machine learning, Bayesian activity-recognition classifier was developed that grouped activities and set the features that distinguished them. The algorithm then recognized subsequent bouts of walking across a day's activity and calculated walking speeds in the stroke patients as low as 0.1 m/s, along with distance and duration of each bout, and limb asymmetries in stance and swing times. This protocol led to high correlation with ground truth measures during walking in the community.^{20,21} This sensor and analysis system was then used to provide feedback over the Internet about daily walking bouts in terms of speed,

duration and distance in a RCT during inpatient stroke rehabilitation at 15 sites in 12 countries.²² Over 2100 hours of activities were identified and quantified in 140 subjects, revealing the progression of walking-related measures and the actual amount of physical therapy provided for mobility. A Bluetooth connection from the sensors can download the data to a smartphone as well, then to a remote server for algorithm processing. Another research group placed bilateral accelerometers at mid-leg along with a gyroscope to try to eliminate the template walk, but their algorithm was only accurate when walking speed exceeded 0.6m/s.²³ Other sensor placements and approaches to feature extraction from the accelerometer signal have been reported for subacute stroke,²⁴ Parkinson's,²⁵ and multiple sclerosis.¹⁷

Thus, much progress is being made for personalized motion technologies. A smartphone with a continuously running software application that compresses and transmits data to a central server can be an effective hub to manage multiple streams of sensor and other physiological data.²⁶ Practical sensing for the study of patients, however, requires technical and logistical development and planning.² In addition to features listed in [Table 2](#), cultural acceptance of technologies must evolve to optimize utilization. For inexpensive, wide utilization, interoperability of software and communication systems, publicly open standards, and qualitative and quantitative evidence about what works for what population under specified conditions seems essential.^{4,27} For neurology and rehabilitation, efficacy and effectiveness trials are necessary before a final iteration of hardware, software and infrastructure should be scaled for wide usage.

Motion Sensing for Daily Care

Disabled persons, such as those after stroke, take far fewer steps daily, with fewer and shorter bouts of walking compared to healthy peers.²⁸ Critical research to understand how to reduce risk factors for vascular disease, for example, and to reduce disability and increase daily participation will benefit from the ability to quantify the type, quantity, and quality of daily activities.⁸ Sensor networks that monitor upper²⁹ and lower extremity²⁰ activities should facilitate accurate ongoing assessment during community functioning and enable frequent recommendations about how to progress exercise and skills practice from remotely located professionals. Sensors, then, may alter behavior by offering feedback and personal activity auditing that encourages self-efficacy in the form of graphics and instruction from anywhere the Internet reaches. When particular exercises and skills practice are prescribed during long-term rehabilitation efforts, both patients and caregivers may benefit from remote supervision that addresses their concerns about safety and how best to work to advance the reacquisition of skills.

Although this level of monitoring could be viewed as an invasion of privacy, disabled persons are likely to applaud the accessibility of rehabilitation supervision in the context of their home and community at low cost. Tele-neurology³⁰ and tele-rehabilitation³¹ could interface with wearable sensor technology to complement home-based care and compliance with medical recommendations.

Sensors for Clinical Trials

Having ground truth about activity levels, in terms of frequency, duration, intensity, and energy consumption, will turn assumptions about the quantity of exercise and practice during trials into certainties. For example, all of the large recent RCTs of treadmill and robotic training to improve walking after stroke,^{12,32-34} spinal cord injury,^{35,36} Parkinson's,^{37,38} and multiple sclerosis³⁹ have assigned subjects in the control and experimental groups to a specified number of hours of weekly treatment. None of the studies, however, can report with confidence how much walking and exercise occurred during planned practice sessions or whether participants practiced locomotor skills and exercised outside of formal training times.⁴⁰ Exercise trials that take place in the community are even less likely to be able to capture the quantity of practice.^{41,42} Yet a bias toward high or low levels of practice beyond what the investigative team sees may have a confounding impact on the effects of the experimental therapy. For

example, participants who practice more may gain better skills; incorrect practice could reduce the effect of the formal therapy. The quantity and quality of an experimental physical intervention may also vary across the multiple sites of an RCT or change when a new therapist replaces the one who was trained at onset of the trial. Good trial design recommends that extensive training in provision of a complex physical intervention take place before an RCT starts and that videotaping of the intervention or in-person, intermittent monitoring be part of the protocol at subsequent intervals. The conventional approach to these monitoring needs may be less reliable and cost more than intermittent remote sensor monitoring of actual practice (how much, how well) during formal training sessions and in between therapies.

Continuous monitoring of what subjects actually perform enables other benefits to trial integrity and design. Serial sensor measures can provide dose-response assessments or be used for imputation by statisticians when a participant drops out. Real-world sensing also offers ecologically sound, interval and ratio scale assessments to augment questionnaires and ordinal scales about disability, participation in fulfilling personal goals and roles, and physical functioning (Table 3). Quality of life tools for this have become a requirement as primary or secondary outcomes in neurologic trials. Most diseases have their own tool, often derived from questions developed for the Medical Outcomes Study's SF36 and now represented in the NIH's NeuroQOL toolbox.⁴³ These Likert-scaled measures of change in daily physical activity and ratings of difficulty (climbing stairs, walking 1 block, etc), however, have usually not been confirmed by real-time studies of these activities. For example, the reported level of independence by persons with SCI differed from what clinicians found on testing.⁴⁴ Wearable sensors can provide that ground truth.

Just as self-reporting scales stand as a partial surrogate for actual activity and participation, so do other commonly used walking-related outcome tools, such as the timed short-distance walk (6-15m) and the distance walked in 2-6 min in a laboratory setting. In general, improved effects on surrogates do not necessarily transfer into health benefits; indeed, the surrogate may fail as a guide to the most clinically meaningful and effective therapies.⁴⁵ In neurorehabilitation trials, a pre- to post-test gain of >20% in 10-m speed or 6-min distance often reaches statistical significance and favors one intervention over another. The clinical meaningfulness of such change, however, is uncertain. The gain may generally correlate with self-reported functional measurement tools,⁴⁶ but outliers are common, because reliability of self-reports are uncertain. The ability to serially capture walking-related variables in the home and community, to examine changes in speed and leg symmetry on varied surfaces, and capture changes in exercise capacity, for example in relation to pain, fatigue or adverse effects of medications, should provide greater insight into the effectiveness of new therapies in all patients for whom an evidence-based trial suggests efficacy.^{47,48}

The frequency at which patients might be monitored by wearable activity-sensing networks depends on the object of the study. Levels of walking activity using pedometers require about 7 days of data collection to obtain a stable and representative average for healthy persons⁴⁹ to as little as 2 days for those with incomplete SCI.⁵⁰ For a clinical trial of a walking intervention of 3 months duration, a minimal data set might include 2 weeks of daily monitoring prior to starting the comparison treatments, then for one week monthly or at the time of scheduled outcome measures. For a drug trial, activity might be measured continuously for at least a month – two weeks prior and at least 2 weeks after initiation to detect fluctuations in response to medications (e.g., dyskinesias or freezing of gait in Parkinson's disease, leg spasms in SCI). Skills practice at home might be assessed for 1-2 sessions a week to monitor quality of movements. Schedules for feedback about performance to motivate compliance will have to be empirically derived.

Conclusion

Wireless remote sensing to monitor the type, quantity, and quality of physical activities, daily

participation, and skill reacquisition offers great potential for neurologic and neurorehabilitation patient care and clinical trials. Progressive reductions in the cost, size and energy requirements of gyroscopes, accelerometers, other physiologic sensors and data transmission over the Internet, along with empirical work on activity-recognition algorithms, suggest that wearable systems may become ubiquitous tools. Efficacy and effectiveness trials are necessary, however, before clinicians can utilize sensor data for ecologically sound monitoring and outcome measures.

Acknowledgments

This review was partially supported by grants from the Dr. Miriam and Sheldon G. Adelson Medical Research Foundation and National Institutes of Health R01 HD071809. Faculty and students from the UCLA Wireless Health Institute, particularly William Kaiser, PhD, Majid Serrafzadeh, PhD, Xiaoyu Xu, PhD, Andrew Dorsch, MD, and Gregg Pottie, PhD provided valuable insights into mHealth sensing networks.

References

- **1. Free C, Phillips G, Galli L, et al. The effectiveness of mobile-health technology-based health behavior change of disease management interventions for health care consumers: a systematic review. *PLoS Med.* 2013;100:e1001362. This systematic review examined mobile technology-based health interventions that supported health care consumers in healthier behaviors and disease management. Text messaging of reminders and instructions/feedback proved most efficacious. [PMCID: PMC3548655] [PubMed: 23349621]
- **2. Clifford G, Clifton D. Wireless technology in disease management and medicine. *Annu Rev Med.* 2012;63:479–92. This detailed review of wireless medical data transmission describes many of the advantages and problems associated with these technologies and potential confounders in physiologic monitoring. [PubMed: 22053737]
3. Sarasohn-Kahn J. Making sense of sensors: How new technologies can change patient care. 2013:1–24. In: <http://www.chcf.org/~media/MEDIA>.
4. Tomlinson M, Rotheram-Borus M, Swartz L, Tsai A. Scaling up mHealth: Where is the evidence? *PLoS Med.* 2013;10:e1001382. [PMCID: PMC3570540] [PubMed: 23424286]
5. Pal K, Eastwood S, Michie S, et al. Computer-based diabetes self-management interventions for adults with type 2 diabetes mellitus. *The Cochrane Library.* 2013
6. Labrique A, Vasudevan L, Chang L, Mehl G. Hope for mHealth: More “y” or “o” on the horizon? *Int J Med Inform.* 2012;S1386-5056(12):00240–7. [PMCID: PMC3849805]
7. Barkovich A, Szeffler S, Olson E, Rymer W. White Paper: Scientific Vision Workshop on Diagnostics and Therapeutics. *NICHHD.* 2011 Mar 1-2;:13.
8. Dobkin B, Dorsch A. The promise of mHealth: Daily activity monitoring and outcome assessments by wearable sensors. *Neurorehabil Neural Repair.* 2011;25:788–98. [PMCID: PMC4098920] [PubMed: 21989632]
9. Welsh W, Bassett D, Thompson D, et al. Classification accuracy of the wrist-worn GENE A accelerometer. *Med Sci Sports Exerc.* 2013;45 epub in press. [PMCID: PMC3778030]
10. Dinesh J, Freedson P. ActiGraph and ActiCal physical activity monitors: a peek under the hood. *Med Sci Sports Exerc.* 2012;44:S86–9. [PMCID: PMC3248573] [PubMed: 22157779]

11. Gebruers N, Vanroy C, Truijen S, Engelborghs S, De Deyn P. Monitoring of physical activity after stroke: a systematic review of accelerometry-based measures. *Arch Phys Med Rehabil.* 2010;91:288–97. [PubMed: 20159136]
12. Duncan P, Sullivan K, Behrman A, et al. Body-weight-supported treadmill rehabilitation program after stroke. *N Engl J Med.* 2011;364:2026–36. [PMCID: PMC3175688] [PubMed: 21612471]
13. Carroll S, Greig C, Lewis S, McMurdo M, Scopes J, Mead G. The use of pedometers in stroke survivors: are they feasible and how well do they detect steps? *Arch Phys Med Rehabil.* 2012;93:466–70. [PubMed: 22373934]
14. Hartmann A, Murer K, de Bie R, de Bruin E. Reproducibility of spatio-temporal gait parameters under different conditions in older adults using a trunk tri-axial accelerometer system. *Gait Posture.* 2009;30:351–5. [PubMed: 19628391]
15. Motl R, Weikert M, Suh Y, Sosnoff J, Lederer C, Daumer M. Accuracy of the Actibelt accelerometer for measuring walking speed in a controlled environment among persons with multiple sclerosis. *Gait Posture.* 2011;35:192–96.
16. Van Remoortel H, Giavedoni S, Raste Y, et al. Validity of activity monitors in health and chronic disease: a systematic review. *Int J Behav Nutr Phys Activity.* 2012;9:84. [PMCID: PMC3464146]
17. Spain R, St George R, Salarian A, et al. Body-worn motion sensors detect balance and gait deficits in people with multiple sclerosis who have normal walking speed. *Gait Posture.* 2012;35:573–78. [PMCID: PMC3614340] [PubMed: 22277368]
18. Hiremath S, Ding D, Farrington J, Cooper R. Predicting energy expenditure of manual wheelchair users with spinal cord injury using a multisensor-based activity monitor. *Arch Phys Med Rehabil.* 2012;93:1937–43. [PubMed: 22609119]
- **19. Patel S, Park H, Bonato P, Chan L, Rodgers M. A review of wearable sensors and systems with applications in rehabilitation. *J Neuroeng Rehabil.* 2012;9:21. This review of wearable sensors describes enabling technologies and clever systems for physiologic, motion, and ambient sensing. It includes many potential applications for wellness, exercise, falls prevention, cardiac monitoring, and international efforts by engineers and clinicians that are relevant to neurological diseases and rehabilitation. [PMCID: PMC3354997] [PubMed: 22520559]
20. Dobkin B, Xu X, Batalin M, Thomas S, Kaiser W. Reliability and validity of bilateral ankle accelerometer algorithms for activity recognition and walking speed after stroke. *Stroke.* 2011;42:2246–50. [PMCID: PMC4337400] [PubMed: 21636815]
21. Xu X, Batalin M, Kaiser W, Dobkin B. Robust hierarchical system for classification of complex human mobility characteristics in the presence of neurological disorders *IEEE Explore 2011.* 2011 International Conference on Body Sensor Networks. :65–70. doi: 10.1109/BSN.2011.23.
22. Dorsch A, Thomas S, Xu C, Kaiser W, Dobkin B, trialists S. A multi-center, international, randomized clinical trial using wireless technology to affect outcomes during acute stroke rehabilitation. *Neurology.* 2013;80:PO4.036.
23. Yang S, Zhang JT, Novak A, Brouwer B, Li Q. Estimation of spatio-temporal parameters for post-stroke hemiparetic gait using inertial sensors. *Gait Posture.* 2013;37:354–58. [PubMed: 23000235]
24. Prajapati S, Gage W, Brooks D, SE B, Mcllroy W. A novel approach to ambulatory monitoring: investigation into the quantity and control of everyday walking in patients with subacute stroke.

- Neurorehabil Neural Repair. 2011;25:6–14. [PubMed: 20829413]
25. Weiss A, Sharifi S, Plotnik M, van Vugt J, Giladi N, Hausdorff J. Towards automated, at-home assessment of mobility among patients with Parkinson's disease using a body-worn accelerometer. *Neurorehabil Neural Repair*. 2011;25:810–8. [PubMed: 21989633]
26. Doherty S, Oh P. A multi-sensor monitoring system of human physiology and daily activities. *Telemed e-Health*. 2012;18:185–92.
27. Barbour V, Clark J, Connell L, et al. A reality checkpoint for Mobile Health: Three challenges to overcome. *PLOS Medicine*. 2013;10:e1001395. [PMCID: PMC3582561] [PubMed: 23468597]
28. Roos M, Rudolph K, Reisman D. The structure of walking activity in people after stroke compared with older adults without disability. *Phys Ther*. 2012;92:1141–7. [PMCID: PMC3432950] [PubMed: 22677293]
29. Patel S, Hughes R, Hester T, et al. Tracking motor recovery in stroke survivors undergoing rehabilitation using wearable technology. *Conf Proc IEEE Eng Med Biol Soc 2010*. 2010:6858–61.
30. Rubin M, Wellik K, Channer D, Demaerschalk B. Systematic review of teleneurology: methodology. *Front Neurol*. 2012;3:156. [PMCID: PMC3497715] [PubMed: 23162527]
31. Chumbler N, Quigley P, Li X, et al. Effects of telerehabilitation on physical function and disability for stroke patients. *Stroke*. 2012;43:2168–74. [PubMed: 22627983]
32. Chang W, Kim M, Huh J, Lee P, Kim Y. Effects of robot-assisted gait training on cardiopulmonary fitness in subacute stroke patients: A randomized controlled study. *Neurorehabil Neural Repair* 2012. 2011 Nov 15; doi: 10.1177/1545968311408916. Epub.
33. Morone G, M B, Iosa M, et al. Who may benefit from robotic-assisted gait training? A randomized clinical trial in patients with subacute stroke. *Neurorehabil Neural Repair*. 2011;25:636–44. [PubMed: 21444654]
34. Daly J, Zimbelman J, Roenigk K, et al. Recovery of coordinated gait: randomized controlled stroke trial of functionalelectrical stimulation (FES) versus no FES, with weight-supported treadmill and over-ground training. *Neurorehabil Neural Repair*. 2011;25:588–96. [PubMed: 21515871]
35. Dobkin B, Apple D, Barbeau H, et al. Weight-supported treadmill vs over-ground training for walking after acute incomplete SCI. *Neurology*. 2006;66:484–93. [PMCID: PMC4102098] [PubMed: 16505299]
36. Alcobendas-Maestro M, Esclarin-Ruiz A, Casado-Lopez R, Munoz-Gonzalez A, Martin J. Lokomat robotic-assisted versus overground training within 3 to 6 months of incomplete spinal cord lesion: randomized controlled trial. *Neurorehabil Neural Repair*. 2012;26:1058–63. [PubMed: 22699827]
37. Carda S, Invernizzi M, Baricich A, Comi C, Croquelois A, Cisari C. Robotic gait training is not superior to conventional treadmill training in Parkinson Disease. *Neurorehabil Neural Repair*. 2012;26:1027–34. [PubMed: 22623206]
38. Picelli A, Melotti C, Origano F, et al. Robot-assisted gait training in patient with Parkinson disease: a randomized controlled trial. *Neurorehabil Neural Repair*. 2012;26:353–61. [PubMed: 22258155]
39. Vaney C, Gattlen B, Lugon-Moulin V, et al. Robotic-assisted step training (Lokomat) not superior to equal intensity of over-ground rehabilitation in patients with multiple sclerosis. *Neurorehabil Neural Repair*. 2012;26:212–21. [PubMed: 22140197]
40. Dobkin B, Duncan P. Should body weight-supported treadmill training and robotic-assistive steppers

for locomotor training trot back to the starting gate? *Neurorehabil Neural Repair*. 2012;26:308–17. [PMCID: PMC4099044] [PubMed: 22412172]

41. Dean C, Rissel C, Sherrington C, et al. Exercise to enhance mobility and prevent falls after stroke: The community stroke club randomized trial. *Neurorehabil Neural Repair*. 2012;26:1046–57. [PubMed: 22544817]

42. van Wijk R, Cumming T, Churilov L, Donnan G, Bernhardt J. An early mobilization protocol successfully delivers more and earlier therapy to acute stroke patients: further results from Phase II of AVERT. *Neurorehabil Neural Repair*. 2012;26:20–6. [PubMed: 21807984]

43. Cella D, Lai J, Nowinski C, et al. Neuro-QOL: brief measures of health-related quality of life for clinical research in neurology. *Neurology*. 2012;78:1860–7. [PMCID: PMC3369516] [PubMed: 22573626]

44. Van Hedel H, Dokladal P, Holtz-Boendermaker S, Group E-SS Mismatch between investigator-determined and patient-reported independence after spinal cord injury: consequences for rehabilitation and trials. *Neurorehabil Neural Repair*. 2011;25:855–64. [PubMed: 21636830]

45. Svensson S, Menkes D, Lexchin J. Surrogate outcomes in clinical trials. *JAMA Intern Med*. 2013;173:611–12. [PubMed: 23529157]

46. Nadeau S, Wu S, Dobkin B, et al. Effects of task-specific and impairment-based training compared with usual care on functional walking ability after inpatient stroke rehabilitation: LEAPS trial. *Neurorehabil Neural Repair*. 2013;27:370–80. [PubMed: 23504552]

47. Barclay-Goddard R, Lix L, Tate R, Weinberg L, Mayo N. Health-related quality of life after stroke: does response shift occur in self-perceived physical function? *Arch Phys Med Rehabil*. 2011;92:1762–69. [PubMed: 22032211]

48. Horn S, Gassaway J. Practice based evidence: incorporating clinical heterogeneity and patient-reported outcomes for comparative effectiveness research. *Med Care*. 2010;48:S17–22. [PubMed: 20421825]

49. Hale L, Pal J, Becker I. Measuring free-living physical activity in adults with and without neurologic dysfunction with a triaxial accelerometer. *Arch Phys Med Rehabil*. 2008;89:1765–71. [PubMed: 18760161]

50. Ishikawa S, Stevens S, Kang M, Morgan D. Reliability of daily step activity monitoring in adults with incomplete spinal cord injury. *J Rehabil Res Dev*. 2011;48:1187–94. [PubMed: 22234663]

Figures and Tables

Table 1

Types of wearable sensors to assess physical activity

Triaxial accelerometer: accelerations/decelerations, velocity and displacement of a body segment in x, y, z axes.

Gyroscope: angular velocity and rotation.

Global positioning satellite (GPS) signal: location primarily outdoors; may calculate speed and distance of continuous walking with smartphone app.

Magnetometer: directional vectors of spatial orientation.

Electromyography: dry electrodes for surface EMG of timing and amount of muscle group activation.

Goniometer: joint angular range of motion.

Resistive flex and pressure sensing: fiberoptic or deformable textile across a joint detects angular change; piezoelectrode for distribution of weight on sole to define stance in the gait cycle.

Environmental context: ambient sound, light, motion-activated photo or video.

Table 2

Technical features for practical remote motion-sensing systems

Sensors:

Type, number and position depend on specific body metrics sought

Design – e.g. piezoelectric or capacitive microelectro-mechanical-system accelerometer

Cosmetic acceptability; ease and reproducibility of placement.

Raw signal structure and sensitivity to events

Firmware instructions for device components

Partial data processing on sensor chip

Platforms:

Interoperability by using common software, communication, data processing and confidentiality protocols

Open source, publically available standards

End-to-end system reliability

Data transmission:

Choice of wireless standards – Bluetooth, Zigbee, Wi-Fi, voice channels, Short Message Service, Universal Mobile Telecommunications Systems

Cost

Frequency of data sampling

Bandwidth

Power consumption; energy source

Reliability

Data time stamping

Error check

Storage capacity

Secure data at each stage of collection, transfer, and storage

Signal processing:

Temporally fuse data synchronously from multiple sensors and body sites

Analytic algorithms

Features assessed include mean of signal, peak frequency, correlation of axis, signal energy, standard deviation

Classifier models include naïve Bayes, support vector machine, decision tree, hidden Markov, neural networks, spectrum analysis, random forest

Integrate multiple layers of the classifier, e.g., activity, context, sensor location

Artifact recognition; examine outliers

Environmental context of activity

Speed of processing

Machine-learning analysis

Resolution of data:

- Software to interpret data from sensors and other sources of information to provide new insights into health states
- Normalized for matched population and sensitive to individual's daily functioning over time
- Discern trajectory of change and clinically meaningful gains and declines
- Visualize data using customizable tools and reports

Annotation:

- Describe changes in health, mood, behavior, social circumstances, environment
- Ontological encoding of data across studies, e.g., Unified Medical Language System for standard description of medical condition, treatments, responses and contexts

Methods to scale up applications:

- Simplify instructions, minimize time and effort by user; keep cognitive load low
- Minimize steps and increase automaticity in data flow during acquisition, processing, analysis and search
- Conceptualize summary data for practical uses, such as feedback, monitoring and outcome tools

Data accessibility in common databases:

- NIH or Research Electronic Data Capture (REDCap) databases
- Annotated raw data repository for data mining

Data privacy and security:

- Encryption
- HIPAA requirements

Table 3

Comparison of conventional scales and wireless, wearable sensor-derived tests of mobility-related functioning

DATA	USUAL METHOD	mHEALTH SENSORS
Type of physical activity	Self-report diary or checklist; observe in lab; video; short distance timed walk or distance walked in 2-6 min.	Activity pattern-recognition algorithms; walk, cycle, leg exercises identifiable by sensor data processing
Quantity Frequency/duration	Observation; inertial movement/step counts if accelerations high enough	Directly measure wave forms of individual components and whole actions
Quality	Laboratory motion analysis or pressure mat system	Compare each leg during step cycle in context of environs
Location of activity	Self report; lab	Anywhere; global positioning & ambient context sensing for site identification
Reliability	Inter-rater; test-retest	Ground truth measurement v. sensor-based algorithm
Validity	Content/construct for each scale	Face validity; responsiveness
Statistical testing	Ordinal scales of physical functioning	Interval / ratio scale data
Data entry	Computer	Smartphone, tablet
Human factors	Train examiners in test administration	Train participants in a culture of technology
Regulation	Local Institutional Review Board and HIPAA	Local IRB & HIPAA; possibly Food and Drug Administration

A NOVEL FEATURE EXTRACTION TECHNIQUE FOR HUMAN ACTIVITY RECOGNITION

Víctor Elvira, Alfredo Nazábal-Rentería, Antonio Artés-Rodríguez

Department of Signal Theory and Communications, Universidad Carlos III de Madrid,
Avenida de la Universidad, 30, Leganés 28911 (Spain)

ABSTRACT

This work presents a novel feature extraction technique for human activity recognition using inertial and magnetic sensors. The proposed method estimates the orientation of the person with respect to the earth frame by using quaternion representation. This estimation is performed automatically without any extra information about where the sensor is placed on the body of the person. Furthermore, the method is also robust to displacements of the sensor with respect to the body. This novel feature extraction technique is used to feed a classification algorithm showing excellent results that outperform those obtained by an existing state-of-the-art feature extraction technique.

Index Terms— Activity Classification, Ambulatory Monitoring, Features Extraction, Inertial Sensors, Magnetic Sensors, Orientation Estimation, Quaternions.

1. INTRODUCTION

The task of Human Activity Recognition (HAR) using wearable sensors has recently become a popular topic of research in context-aware monitoring applications, such as home-based rehabilitation, or ambulatory monitoring of elderly or patients with brain disorders [1]. The low cost, small size, and low energy consumption of the devices allow pervasive data acquisition without disturbing daily activities.

The most popular approach for HAR using sensors uses inertial based sensory systems (see [2] for a review). A basic Inertial Measurement Unit (IMU) consists on a 3-axis accelerometer and a 3-axis gyroscope enabling the measuring of acceleration and angular velocity, respectively. A Magnetic, Angular Rate, and Gravity (MARG) sensor is an extended IMU that also integrates a 3-axis magnetometer.

In this work, we focus on the feature extraction of the signals acquired by a MARG sensor, since it is the one that provides more information for indoor scenarios (i.e., without GPS signal). A MARG sensor provides the measurements referenced to the sensor frame. However, these raw signals are sensitive to the placement of the sensor on the body of the

person, in terms of position and orientation. Most of the classification algorithms for HAR proposed in the literature are fed with raw or mildly processed signals [2, 3]. Few of them try to extract the orientation of the sensor or the person in order to feed the classification algorithms [4]. In this paper, we propose to use as inputs of the classification algorithms the orientation of the person w.r.t. the earth frame, and the acceleration in the person frame. To that end, a novel scheme of feature extraction for HAR algorithms is presented, including an efficient algorithm based on quaternion representation that computes the orientation of the person from the measurements of the MARG sensor.

This paper is organized as follows: In Section 2, we propose the algorithm for feature extraction based on estimating the orientation of the person. In Section 3, the classification results obtained with the proposed algorithm are presented. Finally, in Section 4, conclusions and future work are discussed.

2. PROPOSED ORIENTATION ESTIMATION ALGORITHM

2.1. Quaternions and Notation

Throughout this paper we use quaternions to represent three-dimensional orientations and rotations. Quaternions retain several advantages compared to Euler rotation matrices: they do not suffer from problematic singularities such as gimbal lock [5], and they are more compact, computationally efficient, and numerically stable.

Quaternions constitute a four-dimensional space over the real numbers. They are composed by the real axis and three imaginary orthogonal axes. Here we list some relevant quaternion properties, where the \otimes operator denotes the Hamilton product, and the $\hat{\cdot}$ accent denotes a normalised vector:

1. A rotation through an angle of α around a unit vector $\hat{\mathbf{u}}$ is represented by the unit quaternion

$$\hat{\mathbf{q}} = \cos\left(\frac{\alpha}{2}\right) + \sin\left(\frac{\alpha}{2}\right) \left(u_x \hat{\mathbf{i}} + u_y \hat{\mathbf{j}} + u_z \hat{\mathbf{k}}\right). \quad (1)$$

2. Two rotation quaternions $\hat{\mathbf{q}}_1$ and $\hat{\mathbf{q}}_2$ can be combined into one equivalent quaternion, $\hat{\mathbf{q}} = \hat{\mathbf{q}}_2 \otimes \hat{\mathbf{q}}_1$ that rep-

This work has been partly supported by the Spanish government's projects COMONSENS (CSD2008-00010), ALCIT (TEC2012-38800-C03-01) and COMPREHENSION (TEC2012-38883-C02-01)

resents a rotation given by $\hat{\mathbf{q}}_1$ followed by a rotation given by $\hat{\mathbf{q}}_2$.¹

3. For any unit quaternion $\hat{\mathbf{q}}$, its inverse is equal to its conjugate $\hat{\mathbf{q}}^{-1} = \hat{\mathbf{q}}^*$.
4. If a quaternion $\hat{\mathbf{q}}$ represents a rotation, and \mathbf{v} is a three-dimensional vector, the rotated vector \mathbf{v}' can be computed as $\mathbf{p}' = \hat{\mathbf{q}} \otimes \mathbf{p} \otimes \hat{\mathbf{q}}^*$, where $\mathbf{p} = p_x \mathbf{i} + p_y \mathbf{j} + p_z \mathbf{k}$ and $\mathbf{p}' = p'_x \mathbf{i} + p'_y \mathbf{j} + p'_z \mathbf{k}$.

2.2. Coordinate Systems

Three different three-dimensional frames are described in order to compute the orientation of the person w.r.t. the earth. First, the sensor frame (S) is defined along the orthogonal axes of the physical device, $\{^S \mathbf{x}, ^S \mathbf{y}, ^S \mathbf{z}\}$. The recorded signals are referred to this frame. Secondly, the earth frame is defined by the orthonormal set of vectors $\{^E \mathbf{x}, ^E \mathbf{y}, ^E \mathbf{z}\} = \{\text{North, West, Up}\}$. Finally, we define the person frame, defined by an orthonormal set of vectors whose directions when the person is standing are aligned as $\{^P \mathbf{x}, ^P \mathbf{y}, ^P \mathbf{z}\} = \{\text{Forward, Left, Up}\}$.

We use a notation system of leading superscripts and subscripts to describe relative frame orientations and vector representations adopted from [6]. A leading subscript denotes the frame being described, and a leading superscript denotes the frame this is with reference to. For example, ${}^A_B \hat{\mathbf{q}}$ describes the orientation of frame B relative to frame A while ${}^A \mathbf{v}$ represents a vector described in frame A .

2.3. Feature Extraction Algorithm

The proposed feature extraction scheme processes the magnetic, angular rate, and accelerometer signals provided by the MARG sensors in order to excerpt

1. the orientation of the person w.r.t. the earth frame, and
2. the acceleration in the person frame, ${}^P \mathbf{a}$.

In contrast to other feature extraction schemes [4, 7], we consider that angular rate measurements provided by gyroscopes are not valuable signals any longer for the classification algorithms, since their information is incorporated to the orientation of the person.

Therefore, the main goal consists in computing ${}^P_E \hat{\mathbf{q}}$, i.e., the orientation of the earth frame (E) relative to the person frame (P). The proposed algorithm makes use of quaternion property 2., decomposing the estimation of ${}^P_E \hat{\mathbf{q}}$ as a concatenation of the estimation of the orientation of ${}^E \mathbf{z}$ w.r.t. to ${}^P \mathbf{z}$, ${}^P_E \hat{\mathbf{q}}_z$, followed by the estimation of the orientation of the plane ${}^E xy$ w.r.t. the plane ${}^P xy$, ${}^P_E \hat{\mathbf{q}}_{xy}$, i.e.,

$${}^P_E \hat{\mathbf{q}} = {}^P_E \hat{\mathbf{q}}_{xy} \otimes {}^P_E \hat{\mathbf{q}}_z, \quad (2)$$

¹Note that quaternion multiplication is not commutative

where ${}^P_E \hat{\mathbf{q}}_z$ is also decomposed as

$${}^P_E \hat{\mathbf{q}}_z = {}^S_E \hat{\mathbf{q}} \otimes {}^P_S \hat{\mathbf{q}}_z. \quad (3)$$

The orientation of the earth frame relative to the sensor frame, ${}^S_E \hat{\mathbf{q}}$, is computed by means of the gradient descent algorithm proposed in [6]. This algorithm has shown an accurate performance close to a Kalman-based algorithm [8], while remaining computationally very efficient. The algorithm updates the current orientation via integration of the provided angular rate, and corrects the gyroscope drift with accelerometer and magnetometer measurements. This correction is driven by a parameter, β , that represents the correction rate of the gyroscope drift (see [6] for more details). The authors prove that, if the sampling rate is large enough, the algorithm performs accurately just computing one gradient descent iteration per sample, which implies a very low computational cost. The convergence of the algorithm can be tuned by increasing the parameter β (see Section 3 for more details).

The second term of equation (3), ${}^P_S \hat{\mathbf{q}}_z$, corresponds to the orientation of the ${}^S \mathbf{z}$ axis w.r.t. the ${}^P \mathbf{z}$ axis. Note that, if the sensor is strongly attached to the body of the person, this orientation should remain constant. Nevertheless, considering that the sensor is fixed to the clothes (for instance bounded by a belt at the waist), ${}^P_S \hat{\mathbf{q}}_z$ may suffer from small variations. Although knowing ${}^S_E \hat{\mathbf{q}}$ during the standing position would be enough to find this orientation, with unlabelled data it is not possible to determine a priori when the person is standing. Nonetheless, walking sequences are easier to detect automatically, and while walking, the person is in average also upright; i.e., the ${}^P \mathbf{z}$ axis is aligned to the ${}^E \mathbf{z}$ axis in average. For this purpose, we have used a walking detection algorithm similar to that proposed in [4]. Therefore, ${}^P_S \hat{\mathbf{q}}_z$ can be computed by averaging ${}^S_E \hat{\mathbf{q}}$ during the walking period. Due to quaternion property 3., we obtain the second term of equation (3) as ${}^P_S \hat{\mathbf{q}}_z = {}^S_P \hat{\mathbf{q}}_z^*$. Note that although there exist several ways to average a quaternion [9], we use an unweighted mean of ${}^S_E \hat{\mathbf{q}}$ during the walking period since it provides good results while being computationally efficient. In this way, ${}^P_S \hat{\mathbf{q}}_z$ is updated every time a walking period is detected.

Finally, we compute the first term of equation (2), ${}^P_E \hat{\mathbf{q}}_{xy}$, by estimating the direction of the velocity in ${}^E xy$ plane when the person is walking. For that purpose, we integrate the acceleration in the earth frame to get the velocity [10], we remove the velocity drift [11], and we compute the angle γ of the projection of the velocity vector onto the ${}^E xy$ plane w.r.t. ${}^E \mathbf{x}$. Let ϕ be the angle between ${}^E \mathbf{x}$ and the projection of the vector ${}^P_E \hat{\mathbf{q}}_z \otimes \mathbf{i}$ onto the ${}^E xy$ plane. Then, defining $\theta = \gamma - \phi$, and according to quaternion properties 3. and 4., ${}^P_E \hat{\mathbf{q}}_{xy} = \cos(\theta/2) + \text{sen}(\theta/2)\mathbf{k}$.

Algorithm 1 summarises the process to compute ${}^P_E \hat{\mathbf{q}}[n]$, the orientation of the earth frame w.r.t. the person frame. The calculation is performed for the N available samples of magnetic field, angular rate, and acceleration measurements ac-

quired by the MARG sensor. Note that β , the key parameter of the sensor orientation algorithm [6] must be selected at the beginning, and it plays a key role in the performance of the classification algorithm, as it can be seen in Section 3.

Algorithm 1 Pseudocode of person orientation algorithm

```

Select  $\beta$ 
for  $n = 1 : N$  do
  Compute  $\hat{\mathbf{q}}_E^S[n]$  with the algorithm of [6] and  $\beta$ 
  Detect whether the person is walking
  if walking then
    Update  $\hat{\mathbf{q}}_S^P[n]$ 
    Update  $\hat{\mathbf{q}}_{xy}^P[n]$ 
  else
     $\hat{\mathbf{q}}_S^P[n] = \hat{\mathbf{q}}_S^P[n-1]$ 
     $\hat{\mathbf{q}}_{xy}^P[n] = \hat{\mathbf{q}}_{xy}^P[n-1]$ 
  end if
   $\hat{\mathbf{q}}_E^P[n] = \hat{\mathbf{q}}_{xy}^P[n] \otimes \hat{\mathbf{q}}_E^S[n] \otimes \hat{\mathbf{q}}_S^P[n]$ 
end for

```

3. EXPERIMENTS

3.1. Experimental Setting

The evaluation of the proposed method is performed using real data acquired by APDM OPAL miniature sensors [12]. These sensors provide three-axis acceleration, three-axis gyroscope, and three-axis magnetometer data. 18 data sequences have been collected, each one from a different person. A single sensor has been placed at the waist of each subject, and they have been asked to perform some of activities in no particular order. These sequences are combinations of five different activities: running, walking, standing, sitting, and lying. This data acquisition procedure has provided us with 6 hours and 21 minutes of real data samples acquired at a sampling rate of 128 Hz.

In order to randomize the testing process, we have built 25 sets of sequences. For each set, we have randomly selected 12 sequences for training from the database, and the 6 ones left have been used for testing. The 25 sets have been used to test all feature extraction algorithms, in order to maintain the consistency. The data have been processed both with the Acceleration Quaternion method (AQ) presented in this paper (using different values of β) and with the Acceleration Angular Rate method (AAR) proposed in [4]. The AAR method makes use of angular rate and acceleration signals, transforming them to a virtual sensor orientation.

For sake of simplicity and a fair comparison in terms of computational complexity, we have not made use of $\hat{\mathbf{q}}_{xy}^P$ in equation (2). Thus, we have provided the classification algorithm with the orientation of the ${}^P\mathbf{z}$ w.r.t. the earth.² We have

²We believe that most of the useful information residing in the orientation of the subject must rely on the inclination of its z-axis w.r.t. the earth.

visually checked that the processed acceleration and quaternion signals are consistent with the dynamics of the activities performed.

3.2. Training description

Although the proposed feature extraction technique is not restricted to any classification algorithm, in this paper, we evaluate its performance by applying it to an state-of-the-art hierarchical dynamic model (HDM) based on hidden Markov models (HMM). We train a different HMM for each activity independently using the Baum Welch algorithm, following the scheme of [7].

Each HMM is modelled using five states per activity, i.e., having a global model with 25 identifiable states, and a Gaussian Mixture Model (GMM) observation probability distribution with three components. We use the Forward-Backward algorithm to obtain the Maximum a Posteriori estimate of the test sequences.

3.3. Results

We compare the performance of the proposed AQ algorithm (with three different values of β) with the AAR algorithm. Table 1 shows the probability of error of both methods broken down by activity. The proposed AQ algorithm exhibits a lower error rate for all tested β , largely outperforming the AAR algorithm in some activities, and remaining very close in the others. Note that decreasing from 0.16 to 0.11 in probability of error is a remarkable reduction, since the bottleneck must presumably lie on the classification algorithm.

Activity	AAR	AQ $\beta = 1$	AQ $\beta = 3$	AQ $\beta = 5$
Running	0.38	0.18	0.19	0.20
Walking	0.02	0.05	0.02	0.05
Standing	0.03	0.06	0.05	0.05
Sitting	0.15	0.12	0.06	0.07
Lying	0.21	0.23	0.23	0.23
Mean	0.16	0.13	0.11	0.12

Table 1. Probability of error comparison of the AAR method and the proposed AQ method.

In Table 2, the feature extraction algorithms have also been compared in terms of the F-measure [13]. For all different values of β , the classification with the proposed algorithm outperforms that obtained with the AAR method. Again, the AQ method with $\beta = 3$ obtains the better results.

Finally, Figure 1 shows the F-measure range of accumulating the 6 test sequences of the 25 different sets, i.e., 150 different test sequences in total. For each method, the horizontal red line inside every box shows the median value, the

Nevertheless, further investigations will be performed.

Activity	AAR	AQ	AQ	AQ
		$\beta = 1$	$\beta = 3$	$\beta = 5$
Running	0.75	0.88	0.87	0.86
Walking	0.92	0.95	0.95	0.94
Standing	0.98	0.96	0.97	0.97
Sitting	0.81	0.76	0.81	0.79
Lying	0.82	0.84	0.86	0.85
Mean	0.86	0.88	0.89	0.88

Table 2. F-measure of the AAR method and the proposed AQ method.

upper and lower edges of the blue boxes are the 25th and 75th percentiles respectively, and the vertical black dashed lines extend to the extreme cases. It can be seen that most of the test sequences for all three values of β fall around a F-measure of 0.9 whereas for the AAR method they are around 0.85. The worst sequence with the proposed AQ method with $\beta = 3$ obtains a F-measure = 0.8 while the worst one with AAR remains at 0.75.

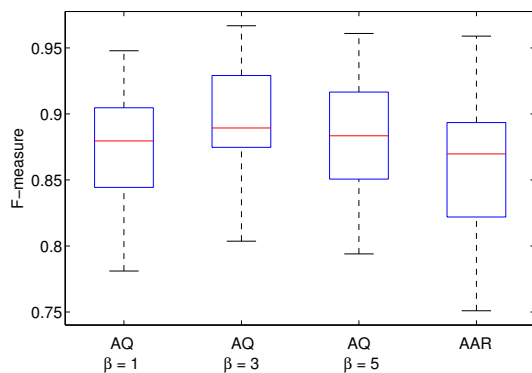


Fig. 1. F-measure results for all test sequences using the AAR method and the proposed AQ method.

4. DISCUSSION AND CONCLUSIONS

We have presented a novel feature extraction technique for human activity recognition based on quaternion representation. The proposed algorithm computes the acceleration referred to the person frame, and the orientation of the person frame with respect to the earth frame. Numerical results show a substantial improvement in the results of the classification algorithm when the feature extraction is performed with the proposed method. The computational cost of the proposed algorithm is linear with the length of the sequence and extremely low for each sample, requiring only few quaternion multiplications and additions. Moreover, the simplicity of the algorithm would also allow, with a slight adjustment, an on-line estimation of the person orientation.

5. REFERENCES

- [1] P. Bonato, “Wearable Sensors and Systems,” *Engineering in Medicine and Biology Magazine, IEEE*, vol. 29, no. 3, pp. 25–36, 2010.
- [2] O.D. Lara and M.A. Labrador, “A survey on human activity recognition using wearable sensors,” *Communications Surveys & Tutorials, IEEE*, vol. 15, no. 3, pp. 1192–1209, 2013.
- [3] S.J. Preece, J.Y. Goulermas, L.P.J. Kenney, and D. Howard, “A comparison of feature extraction methods for the classification of dynamic activities from accelerometer data,” *Biomedical Engineering, IEEE Transactions on*, vol. 56, no. 3, pp. 871–879, 2009.
- [4] B. Florentino, N. O’Mahony, and A. Artes-Rodriguez, “Long term human activity recognition with automatic orientation estimation,” in *Machine Learning for Signal Processing (MLSP), 2012 IEEE International Workshop on*. IEEE, 2012, pp. 1–6.
- [5] K. Shoemake, “Animating rotation with quaternion curves,” *ACM SIGGRAPH computer graphics*, vol. 19, no. 3, pp. 245–254, 1985.
- [6] S.O.H. Madgwick, A.J.L. Harrison, and R. Vaidyanathan, “Estimation of IMU and MARG orientation using a gradient descent algorithm,” in *Rehabilitation Robotics (ICORR), 2011 IEEE International Conference on*. IEEE, 2011, pp. 1–7.
- [7] B. Florentino, N. O’Mahony, and A. Artés-Rodríguez, “Hierarchical dynamic model for human daily activity recognition,” *Proceedings of BIOSIGNALS*, 2012.
- [8] A.M. Sabatini, “Estimating three-dimensional orientation of human body parts by inertial/magnetic sensing,” *Sensors*, vol. 11, no. 2, pp. 1489–1525, 2011.
- [9] F.L. Markley, Y. Cheng, J.L. Crassidis, and Y. Oshman, “Averaging quaternions,” *Journal of Guidance, Control, and Dynamics*, vol. 30, no. 4, pp. 1193–1197, 2007.
- [10] J.E. Bortz, “A new mathematical formulation for strap-down inertial navigation,” *Aerospace and Electronic Systems, IEEE Transactions on*, no. 1, pp. 61–66, 1971.
- [11] P.H. Veltink, P. Slycke, J. Hemssems, R. Buschman, G. Bultstra, and H. Hermens, “Three dimensional inertial sensing of foot movements for automatic tuning of a two-channel implantable drop-foot stimulator,” *Medical engineering & physics*, vol. 25, no. 1, pp. 21–28, 2003.
- [12] APDM Inc., “<http://www.apdm.com/>,” .
- [13] C.J. Van Rijsbergen, *Information retrieval*, Butterworths, 1979.

Decoding of Intentional Actions from Scalp Electroencephalography (EEG) in Freely-behaving Infants

Zachery R. Hernandez, Jesus Cruz-Garza, Teresa Tse and Jose L. Contreras-Vidal – *IEEE Senior Member*

Abstract—The mirror neuron system (MNS) in humans is thought to enable an individual’s understanding of the meaning of actions performed by others and the potential imitation and learning of those actions. In humans, electroencephalographic (EEG) changes in sensorimotor α -band at central electrodes, which desynchronizes both during execution and observation of goal-directed actions (i.e., μ suppression), have been considered an analog to MNS function. However, methodological and developmental issues, as well as the nature of generalized μ suppression to imagined, observed, and performed actions, have yet to provide a mechanistic relationship between EEG μ -rhythm and MNS function, and the extent to which EEG can be used to infer intent during MNS tasks remains unknown. In this study we present a novel methodology using active EEG and inertial sensors to record brain activity and behavioral actions from *freely-behaving* infants during exploration, imitation, attentive rest, pointing, reaching and grasping, and interaction with an actor. We used δ -band (1-4Hz) EEG as input to a dimensionality reduction algorithm (locality-preserving Fisher’s discriminant analysis, LFDA) followed by a neural classifier (Gaussian mixture models, GMMs) to decode the each MNS task performed by freely-behaving 6-24 month old infants during interaction with an adult actor. Here, we present results from a 20-month male infant to illustrate our approach and show the feasibility of EEG-based classification of freely occurring MNS behaviors displayed by an infant. These results, which provide an alternative to the μ -rhythm theory of MNS function, indicate the informative nature of EEG in relation to intentionality (goal) for MNS tasks which may support action-understanding and thus bear implications for advancing the understanding of MNS function.

I. INTRODUCTION

The discovery of mirror neurons in area F5 of the macaque monkey brain by Rizzolatti and colleagues [1] is considered one of the most influential neuroscience discoveries by challenging the notion of segregate sensory and motor functions in the brain. This suggested that action observation and action performance, by sharing the same neural network substrates, enabled individuals to understand other’s people actions and experiences. In humans, the

hypothesized MNS system has been studied extensively using scalp EEG. These studies have used changes in sensorimotor α -rhythms, also known as the μ -rhythm, to be a primary electrophysiological marker of MNS function in human infants and adults [2]. Unfortunately, several developmental (e.g., how these infants come to understand and acquire their first actions and the paucity of MNS data in infants) [3], [4] methodological [2], [5], and interpretive [6] issues need to be addressed to advance our understanding of human mirror neuron function.

Moreover, while studies are necessarily targeted to address specific questions in highly controlled lab environments, it is increasingly recognized that the processes being measured clearly do not occur in isolation and that these environments do not represent the daily behaviors of these infants at home or at play. Virtually all experimental studies in humans involve multiple cognitive components. Movement, language and memory underlie much of our existence. Subjects performing an experimental task must understand the task instructions, store them in memory, and retrieve them at the appropriate times. These processes, in turn, require executive control. Finally, competing intentions must be prioritized, sequenced, and translated into motor output, whether in the form of speech or movements. Such actions are often benefitted from extended practice and are formed and refined during development. Indeed, developmental considerations often blur these components, and thus they add to the problem. Thus, it is unclear how the above processes are accomplished in the developing infant brain. To address some of these issues, we have developed a novel experimental methodology to test freely-behaving infants while acquiring accurate information about brain activity and movement thru non-invasive means. We then deploy advanced machine learning methods to infer behavioral state or intent via scalp EEG.

The classification and prediction of movement intent using invasive ECoG and non-invasive EEG methods has long been studied, usually in research related to the fields of brain-computer interfaces and neuroprosthetics [7], [8]. However, such studies generally focus on the prediction of the kinematics of functional movements; the prediction of emotional, expressive, and contextual properties of movements has not been as well studied [8], even though such properties can affect the kinematics of a motion [9]. To the best of our knowledge, although the neural basis of the action-intention has been studied, especially during changes in μ -rhythm [10], little is known of this basis in infants. This gap in our knowledge raises many questions that could be addressed in future studies, such as how kinematics and neural activity could be used to uncover the mechanisms

Z.R. Hernandez (corresponding author, zrhernandez@uh.edu; phone: 713-743-0796; fax: 713-743-4444), T. Tse (twtse@uh.edu), and J.L. Contreras-Vidal (JLContreras-Vidal@uh.edu) are with the Non-Invasive Brain-Machine Interface Systems Laboratory at the Department of Electrical and Computer Engineering, University of Houston (UH), Houston, TX, 77004, USA.

J.G. Cruz-Garza is with the Center for Robotics and Intelligent Systems, Tecnologico de Monterrey, Monterrey Mexico.

Research supported by NIH NICHD Award PO1HD064653. We acknowledge the assistance of Yu Zhang, Michelle Edwards, Saveem Afraz, Hiba Qadri and Kathleen Bryan in the data acquisition.

behind movement intention and motor planning as well as the complexity of the intention (e.g. emotion, purpose, etc.) of the developing brain of an infant [11]. Before answering these questions, however, we must first demonstrate the feasibility of using high-density scalp EEG to decode goal-oriented movement intentions in freely-behaving infants.

In this case study, we analyzed a 15-minute session of the interactions between the infant subject and the experimenter or actor. We then segmented the infant’s actions into 6 classes: wakeful attentive rest, pointing, reach-to-grasp, reach-to-give, and manipulating an object to either explore its characteristics or to imitate an action performed by the experimenter. We first conducted an exploratory analysis of both neural and motion activity data to examine any evidence of motion artifacts. Classification of movements were further conducted using a two-step machine learning algorithm that reduces the dimensionality of our feature space of EEG data while preserving local features and then generating statistical models to fit and validate the success rate of classifying movement intentions of the infant.

II. METHODS

A. Experimental Design and Data Acquisition

Seven healthy infants (four female, three male) were recruited and given informed consent by their parent(s) or guardian as subjects for this study. Each infant’s age ranged from 6 to 24 months. Here, we focus on the analysis of a 20-month male infant. Multiple streams of data were acquired synchronously during the experiment. Neural activity was recorded using a 64-channel, active electrode EEG scalp cap sampled at 1000 Hz (BrainAmpDC with actiCAP, Brain Products, GmbH). The electrode sets were labeled according to the 10-20 international electrode montage system with FCz and AFz labeled as reference and ground, respectively. Motion was captured using four inertial measurement units (IMUs) sampled at 128 Hz (OPAL, APDM Inc., Portland, OR) attached to the head, trunk, and arms of the subject. Gravity-compensated (GC) triaxial acceleration data was estimated by applying a Kalman filter to predict IMU orientation within a global frame and removing the effects of acceleration due to gravity [12]. In order to conduct a visual inspection of the experiment and select behavioral actions of interest, we recorded the experiment with a video camera (SDR-H100, Panasonic Co.).

The subject was seated in front of the experimenter/actor with a small table. Throughout the testing session, the experimenter gave to the subject a series of 14 toys and various objects to interact and play with at random sequence. The experimenter would also interact with the toys and show the subject how to play with some of the toys (e.g. winding up a wind-up toy). After testing, the video was visually inspected and the subject’s behavioral actions were divided into six classes (shown as task {number of trials, number of samples}) described below and depicted in Fig. 1:

Attentive Rest {17 trials, 7595 samples}: A neutral state of wakeful attentive observation containing minimal to no movement.

Point {10 trials, 922 samples}: The use of the index finger to avert the other person’s (in this case, the experimenter) gaze.

Reach-Grasp {34 trials, 9077 samples}: Producing a reaching motion in order to grasp the object (toy).

Reach-Offer {24 trials, 2740 samples}: Producing a reaching motion in order to offer back the object (toy) to the experimenter.

Explore {31 trials, 16552 samples}: A brief interaction with the held object to examine its features and is usually performed instead of ‘Imitate’.

Imitate {15 trials, 1966 samples}: The successful imitation of the experimenter’s maneuver of the object.



Figure 1. Depiction of each task performed by the freely-behaving infant. Task-based classes shown are: a) Attentive Rest, b) Point, c) Reach-Grasp, d) Reach-Offer, e) Explore, and f) Imitate.

B. Pre-processing of EEG

EEG and GC-magnitude acceleration from the entire session were truncated using the start and end-session triggers synchronized to all data streams, including the video recording. Start and end time points were recorded for various trials of each task throughout the video and used to develop a target class time vector for classification analysis as illustrated in Fig. 2. The number of time samples for all classes constituted 42.25% of the total time of the truncated session. EEG electrodes, or channels, with high impedance (defined as the frequency-dependent opposition to alternating current flow at the scalp-electrode interface) values (AF7, Cz, C2, C3, C5, CP4, P2, P6, P8, PO3-4, PO7-8) [$Z > 60 \text{ k}\Omega$] and peripheral channels (FP1-2, AF7-8, F7-8, FT7-10, T7-8, TP7-10, P7-8, PO7-8, O1-2, Oz, PO9-10) were rejected from the electrode set, leaving us with 32 channels to use for further analysis. Both EEG and acceleration were then resampled to 100 Hz and compared by computing a spectrogram and short-time coherence of selected channels of data to examine any effects of motion artifacts possibly affecting the EEG signal.

Before decoding, EEG signals were then band-pass filtered within the delta frequency band (1 – 4 Hz) using a 3rd order, zero-phase Butterworth filter. A lag-based feature matrix was then constructed by selecting an initial time point (t_1) at 100 milliseconds leading the actual start time ($t_0 = t_1 - 100$) of the signal and decremented every 10 milliseconds ($t_1, t_1-90, t_1-80, t_1-70, \dots, t_0$) thus resulting in 10 lags per channel. All lags per channel were concatenated and standardized by feature to form our feature matrix for the classifier.

C. Cross Validation

To reduce bias and to minimize the potential effects of artifacts, time sample data of each class were selected separately at random for training and testing the classifier. Given the variation of samples size per class, the training set size was chosen to be a percentage of the smallest class sample size. 50% of this sample size was used for training and the remaining 50% for testing. All randomly selected samples were selected either for training or testing the classifier, hence no overlapped samples.

D. Classification Algorithm

The Local Fisher's Discriminant Analysis-Gaussian Mixture Modeling (LFDA-GMM) algorithm has been employed in multiple studies [8], [13] and shown to be a robust and proficient tool for reducing the dimensionality of the lagged-based EEG feature space into a classifiable multimodal subspace in both offline and online analyses. It operates by first executing LFDA and computing a transformation matrix to limit the number of features to a reduced set of dimensions by minimizing the variance of samples within-class and maximizing the variance between classes while maintaining the each class sample's locality. Mathematical derivations proving and testing this method are further explained in studies by Sugiyama [14].

Classification of each task was conducted by fitting a distribution of random training samples into a cumulative model of one or more Gaussian distributions, each with its own factoring weights (α_k), covariance (Σ_k), and means (μ_k), as governed by the probability density function (pdf)

$$p(x) = \sum_{k=1...K} (\alpha_k \phi_k), \quad (1)$$

where the function ϕ_k is defined as

$$\phi_k(x) = \exp\{-0.5(x-\mu_k)^T \Sigma_k^{-1}(x-\mu_k)\} / [(2\pi)^{d/2} |\Sigma_k|^{1/2}]. \quad (2)$$

An estimation-maximization (EM) algorithm was then employed to converge upon the set for each of the three pdf (1), (2) parameters and Bayes Information Criterion (BIC) used to determine the optimal set of K Gaussian distributions for a particular class [13]. Posterior probabilities were calculated for each test sample based on the class-defined

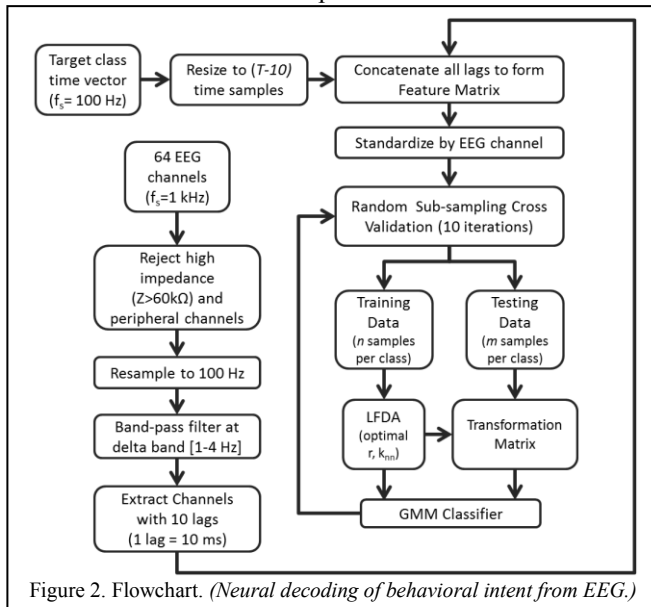


Figure 2. Flowchart. (Neural decoding of behavioral intent from EEG.)

GMM such that any given sample could contain likelihood to fall within a particular class. The maximum posterior probability was chosen per test sample to discretize each class and compute classification accuracy rates. Additional information can be provided here [8].

III. RESULTS

A. Motion Artifact Analysis

Due to the unconstrained nature of the infant's actions, we analyzed and compared the frequency content of both EEG and acceleration data from the IMUs to observe any spectral relationships between EEG and acceleration. Since any movement-related artifacts would most likely originate from head movement, only acceleration information from the head sensor was acquired for further analysis in this paper.

We computed the coherence, or relationship between two signals within the frequency domain, in a manner similar to the short-time Fourier transform in order to generate the coherence spectrogram plot displayed in Fig. 3. High coherence values indicate a strong relationship between the two analyzed signals, as is the case between the head acceleration and each corresponding EEG electrode within the 0.1 – 1 Hz range. Since this strong relationship may be a result of low frequency artifacts, only frequencies between 1 – 4 Hz (higher in the delta frequency sub-band) were band-pass filtered for further neural decoding analyses.

B. Infant Task Classification

Decoding resulted in an overall mean accuracy of $80.50 \pm 1.03\%$, which was well above the chance level of 16.67%. Ten iterations of the random sub-sampling cross validation procedure (Fig. 2) were performed to provide the mean classification

accuracies. By observing the percentage of (mis) classified samples relative to each training set size per class, a training set-normalized confusion matrix was generated as shown in Fig. 4 where each block contains a percentage of training set samples either classified or misclassified to its respective class. We note high percentages along the diagonal of this matrix indicating a high degree of accurate classification for each class. Misclassification was more apparent for 'explore' (0.8-21.1%), 'reach-grasp' (1.7-14.3%), and 'attentive rest' (0-8.2%), unlike the low misclassifications of 'point' (0%) and 'imitate' (0-0.1%) actions.

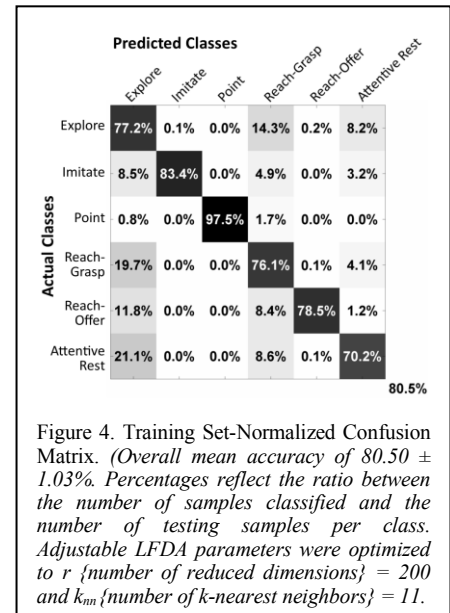


Figure 4. Training Set-Normalized Confusion Matrix. (Overall mean accuracy of $80.50 \pm 1.03\%$. Percentages reflect the ratio between the number of samples classified and the number of testing samples per class. Adjustable LFDA parameters were optimized to r {number of reduced dimensions} = 200 and k_{nn} {number of k-nearest neighbors} = 11.

The most informative channels were revealed by applying a forward selection method [15] to each channel and were located primarily in motor and premotor areas, specifically channels FC6, FC3, C1, FC4, and F5.

IV. DISCUSSION

Our results demonstrate the feasibility of decoding goal-oriented (intentional) behavioral actions from scalp EEG in freely behaving infants. These results show that scalp EEG contain valuable predictive information about the infant's intent. Though only a case study, our results already start to provide insights on how goal-oriented actions may be represented in brain activity as measured with scalp EEG. Further, goal-directed tasks such as *point* and *imitate* yielded higher classification accuracies than tasks without a clear end goal such as explore and rest. Thus, tasks such as *imitate* or *point* may have simply performed better because the infant presented a clear and direct objective/goal in his or her mind, whereas the confusion in classifying *explore* and *attentive rest* tasks may be indicative of the infant's attempts to understand the environment or the intent of the experimenter. In summary, the proposed novel methodology provides a window to study the neural activity underlying mirror neuron system (goal-oriented) tasks in freely behaving infants. It also suggests an alternative to the μ -rhythm account of MNS function by providing a predictive, network-based account of intentionality in freely behaving infants based on scalp EEG.

REFERENCES

[1] Gallese V, Fadiga L, Fogassi L, Rizzolatti G. (1996). Action recognition in the premotor cortex. *Brain* 9 (Pt 2): 593-609.
 [2] Cuevas K, Cannon EN, Yoo K, Fox NA. (2014). The infant EEG μ rhythm: methodological considerations and best practices. *Dev Rev.* 34 (1): 26-43. doi: 10.1016/j.dr.2013.12.001
 [3] Southgate V, Johnson MH, Osborne T, Csibra G. (2009). Predictive

motor activation during action observation in human infants. *Biol Lett.* 5(6): 769-772.
 [4] Woodward AL, Guajardo JJ. (2002). Infants' understanding of the point gesture as an object-directed action. *Cogn Dev.* 17: 1061-1084.
 [5] Vanderwert RE, Fox NA, Ferrari PF (2013). The mirror mechanism and μ rhythm in social development. *Neurosci Lett.* 540: 15-20. doi: 10.1016/j.neulet.2012.10.006
 [6] Hickok G. (2009). Eight problems for the mirror neuron theory of action understanding in monkeys and humans. *J Cogn Neurosci.* 2009 Jul, 21(7): 1229-43. doi: 10.1162/jocn.2009.21189
 [7] Hochberg LR, Bacher D, Jarosiewicz B, Masse NY, Simeral JD, Vogel J, Haddadin S, Liu J, Cash SS, van der Smagt P, Donoghue JP. (2012). Reach and grasp by people with tetraplegia using a neurally controlled robotic arm. *Nature* 485: 372-5.
 [8] Hernandez ZR, Cruz-Garza JG, Nepaul S, Bradley KK and Contreras-Vidal JL. (2014). Neural decoding of expressive human movement from scalp electroencephalography (EEG). *Front. Hum. Neurosci.* 8 (188). doi: 10.3389/fnhum.2014.00188
 [9] Becchio C, Sartori L, Bulgheroni M, Castiello U. (2008). The case of Dr. Jekyll and Mr. Hyde: A kinematic study on social intention. *Conscious Cogn.* 17 (3): 557-564.
 [10] Cannon EN, Yoo KH, Vanderwert RE, Ferrari PF, Woodward AL, et al. (2014). Action Experience, More than Observation, Influences μ Rhythm Desynchronization. *PLoS ONE* 9(3): e92002. doi:10.1371/journal.pone.0092002
 [11] Claxton, Laura J., Rachel Keen, and Michael E. McCarty. (2003). "Evidence of motor planning in infant reaching behavior." *Psychol Sci.* 14(4): 354-356.
 [12] Marins JL, Yun X, Bachmann ER, McGhee RB, and Zyda MJ. (2001). "An extended Kalman filter for quaternion-based orientation estimation using MARG sensors," in *Conf Proc IEEE/RSJ Intell Robot Syst.* Vol. 4, 2003-2011. doi: 10.1109/IROS.2001.976367
 [13] Li W, Prasad S, Fowler JE, and Bruce LM. (2012). Locality-preserving dimensionality reduction and classification for hyperspectral image analysis. *IEEE T Geosci Remote.* 50, 1185-1198. doi: 10.1109/TGRS.2011.2165957
 [14] Sugiyama, M. (2006). "Local Fisher discriminant analysis for supervised dimensionality reduction," in *Proc 23rd ICML.* 905-912. doi: 10.1145/1143844.1143958
 [15] Pagano M, and Gauvreau, K. (2000). "Multiple Regression," in *Principles of bio-statistics*, 2nd Ed., eds C. Crockett, et al. (Pacific Grove, CA: Duxbury), 449-469.

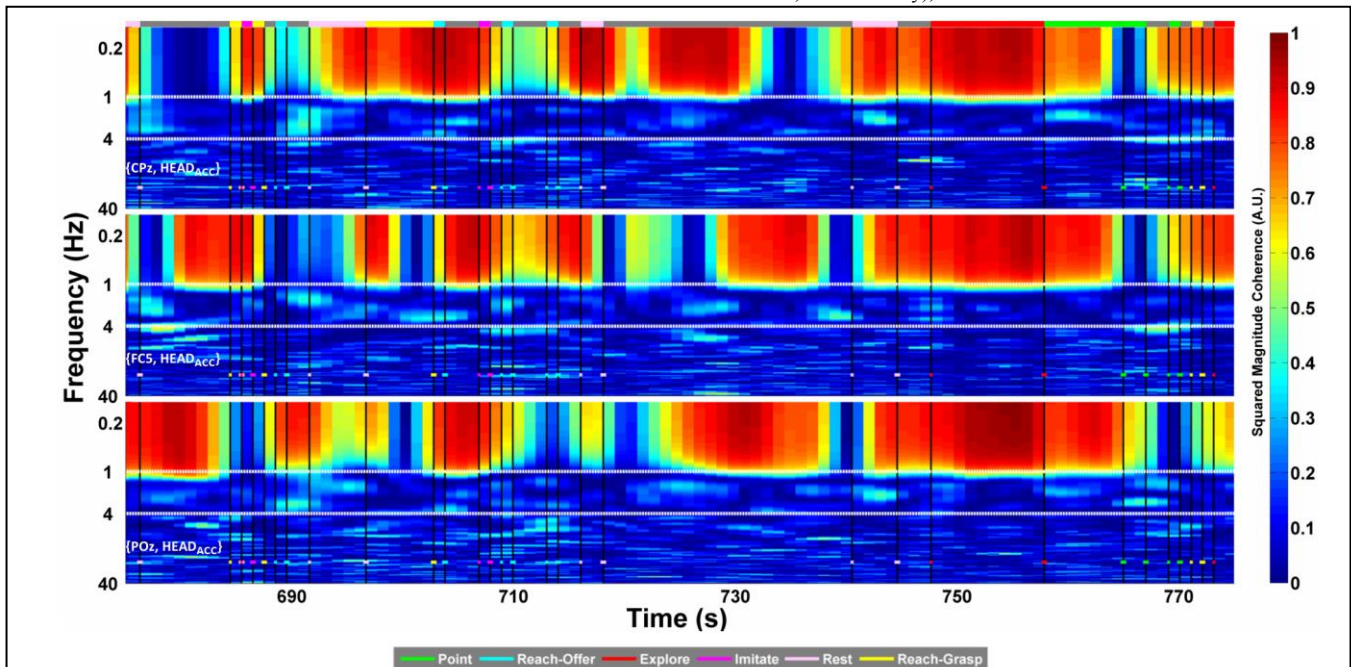


Figure 3. Coherence Spectrogram. Coherence values indicate the relationship between EEG channels and head IMU acceleration. High coherence is noticeable within the 0.1 – 1 Hz range. Dotted white lines indicate the band-pass frequency cutoffs (1 – 4 Hz) to avoid contamination of motion-related artifacts. The plot represents a subset of acquired data but all actions showed the same pattern of coherence.

DUAL-TASK GAIT BALANCE CONTROL ASSESSMENT WITH AN INERTIAL MEASUREMENT UNIT FOLLOWING CONCUSSION

David R. Howell, Louis R. Osternig, Li-Shan Chou

Department of Human Physiology, University of Oregon, Eugene, OR USA
email: dhowell@uoregon.edu, web: <http://biomechanics.uoregon.edu/MAL/>

INTRODUCTION

Despite increased awareness about the detrimental effects of concussion, injury management is currently one of the most difficult and controversial issues in clinical sports medicine (1). As balance impairments following concussion have been widely documented (2), balance control testing has been identified as a crucial component to the overall clinical management plan (3). However, many of the most sensitive measurements require expensive laboratory equipment, while many clinical assessments lack necessary objectivity and sensitivity for evaluating effects from a concussion (2).

Previous research has indicated that concussion may induce dual-task gait balance control impairments for up to two months post-injury (4). However, such deficit detection was identified using a motion analysis system. Thus, the purpose of this study was to evaluate gait balance control under dual-task conditions following concussion using a single inertial measurement unit.

METHODS

Subjects who were diagnosed with a concussion were identified and reported to the laboratory within 72 hours of injury and returned one week, two weeks, one month, and two months post-injury. Control subjects were initially assessed and then tested according to the same timeline.

Subjects walked over ground while simultaneously completing a cognitive task. Acceleration data from an IMU (Inertial Measurement Unit; APDM Inc. Opal, Portland, OR) were obtained at a sampling rate of 128 Hz while subjects completed the dual-task protocol. The IMU was placed at L5 with an elastic belt (5) and peak accelerations in frontal (Fig. 1A) and sagittal planes of motion were identified.

Retro-reflective markers were also placed on bony landmarks and whole body movement was recorded using a ten camera motion analysis system (Motion Analysis Corp., Santa Rosa, CA) at a sampling rate of 60 Hz. Peak linear center-of-mass (COM) anterior and medial-lateral (Fig. 1B) velocities were identified during the gait cycle.

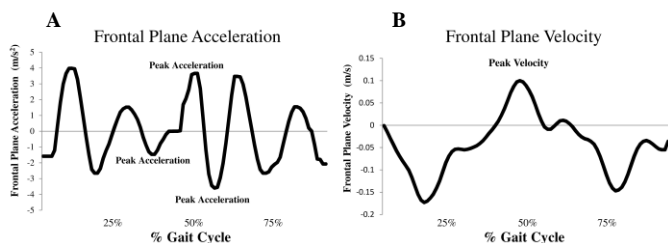


Figure 1: Exemplary frontal plane movement during a gait cycle for (A) acceleration measured by the IMU and (B) velocity measured by the motion analysis system.

The mean of 4 walking trials was computed for each dependent variable (frontal plane peak acceleration and velocity, sagittal plane peak acceleration and velocity) at each time point. Two-way mixed effects ANOVAs were used to determine the effects of group and time, and the interactions between independent variables.

RESULTS AND DISCUSSION

Ten subjects with concussion (mean age 19 ± 5 years) and 7 healthy control subjects (mean age 20 ± 5 years) completed the study protocol. Concussion subjects demonstrated significantly less mean frontal plane peak acceleration than the control group across the two months of testing (main effect of group: $p = .019$; Fig. 2A). Concussion subjects also walked with significantly less mean sagittal plane peak acceleration than the control group at the 72 hour, one week, and one month time points (time*group interaction, $p = .026$; Fig 2B).

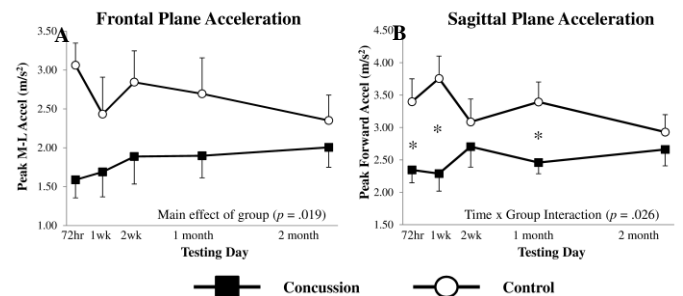


Figure 2: Results (mean \pm SE) for concussion and control groups for (A) frontal and (B) sagittal plane peak acceleration.

The results suggest that peak frontal plane acceleration may be reduced following concussion, potentially leading to increased COM medial-lateral velocity, which has been previously documented to affect adolescents with concussion for a time period of up to two months post-injury (4,6). Decreased peak forward acceleration was detected up to one month post-injury and may represent an effort to reduce forward body momentum in order to accommodate divided attention (4).

The study results indicate that a dual-task IMU assessment may be able to detect balance control difficulties following concussion. Further investigations are warranted as this tool may provide an additional way for health care professionals to objectively and sensitively track recovery from concussion.

REFERENCES

1. Doolan, AW et al., *Ann Biomed Eng.* 2012;40(1):106-13.
2. Guskiewicz KM, *Clin Sports Med.* 2011;30(1):89-102.
3. McCrory, P et al., *Br J Sports Med.* 2013;47(5):250-8.
4. Howell, DR et al., *Arch Phys Med.* 2013;94(8):1513-20.
5. King et al., *Arch Phys Med.* 2014;95(2):353-9.
6. Howell, DR et al., *Exp Brain Res.* 2014, in press.

Inertial Sensing-Based Pre-Impact Detection of Falls Involving Near-Fall Scenarios

Jung Keun Lee, *Member, IEEE*, Stephen N. Robinovitch, and Edward J. Park, *Senior Member, IEEE*

Abstract—Although near-falls (or recoverable imbalances) are common episodes for many older adults, they have received a little attention and were not considered in the previous laboratory-based fall assessments. Hence, this paper addresses near-fall scenarios in addition to the typical falls and activities of daily living (ADLs). First, a novel vertical velocity-based pre-impact fall detection method using a wearable inertial sensor is proposed. Second, to investigate the effect of near-fall conditions on the detection performance and feasibility of the vertical velocity as a fall detection parameter, the detection performance of the proposed method (Method 1) is evaluated by comparing it to that of an acceleration-based method (Method 2) for the following two different discrimination cases: falls versus ADLs (i.e., excluding near-falls) and falls versus non-falls (i.e., including near-falls). Our experiment results show that both methods produce similar accuracies for the fall versus ADL detection case; however, Method 1 exhibits a much higher accuracy than Method 2 for the fall versus non-fall detection case. This result demonstrates the superiority of the vertical velocity over the peak acceleration as a fall detection parameter when the near-fall conditions are included in the non-fall category, in addition to its capability of detecting pre-impact falls.

Index Terms—Elderly, inertial sensor, near-falls, pre-impact fall detection, vertical velocity.

I. INTRODUCTION

FALLS are the leading cause of injury-related deaths and hospitalization among older adults [1], [2]. Due to the high impact of falls on health and healthcare costs, there has been an increasing attention on automatic fall detection methods in the past decade [3]–[6]. This rapid development has been facilitated by the advent of wearable sensors, MEMS-based miniature inertial sensors (e.g., accelerometers and gyroscopes) in particular. They are rapidly shrinking in size and weight to the extent that they can be unobtrusively attached to the body [7]–[10]. In

fact, automatic fall detection methods can be categorized into the following two methods: 1) detection of a subject who has already fallen (i.e., post-impact fall detection) and 2) detection of a subject who is about to fall (i.e., pre-impact fall detection). A primary goal of the post-impact fall detection method, where the majority of existing algorithms belong to, is to minimize the time between a fall and the arrival of medical attention and prevent long lie times that are potentially fatal. However, this method has the limitation that it cannot prevent injuries from the impact. Thus, more recently, researchers have been working on body protection mechanisms such as an inflatable airbag system in order to avoid or reduce the fall-related injuries [11]–[14]. Note that an important prerequisite for the utilization of a wearable airbag system is the pre-impact fall detection to trigger the airbag inflator. While the post-impact detection method makes use of distinctive “impact” signals (e.g., peak accelerations [3], [15]) and information after falls (e.g., lying posture [16] or altitude [6]), and can be post-processed to determine the fall, the pre-impact detection should be performed in real time by relying on only some characteristic information during the descending phase of the fall as the impact and post-impact information are unavailable. This makes the latter method more challenging than the former method. Hence, to date, only a few studies have explicitly addressed the pre-impact fall detection using wearable inertial sensors (e.g., [13], [17]–[20]).

Among the existing pre-impact fall detection methods, Nyan *et al.* [19] used pretested reference templates for each type of fall by comparing the angles and angular velocities of the thigh segment between falls and normal activities. These templates were obtained from laboratory based falling experiments that try to simulate and capture the angular characteristics and patterns of the complex real-life falls. Shi *et al.* [13] and Shan and Yuan [20] used the support vector machine (SVM) through feature selection procedures among a number of raw signals from the accelerometer and gyro. However, the most popular approach to detect falls involves the threshold-based method due to its low complexity and easy implementation. Our particular interest is the works by Wu and Xue [17] and Bourke *et al.* [18] who used the downward vertical velocity as a discrimination parameter for thresholding. The vertical velocity profile represents the kinematic characteristic of falls during their descending phase. Any faller naturally experiences a certain level of downward vertical velocity that can be effectively used for the pre-impact fall detection. Both algorithms in [17] and [18] require the calculation of vertical velocity based on an inertial sensor comprising of a tri-axial accelerometer and a tri-axial gyroscope.

This work also adopts the vertical velocity profile used in [17] and [18]. Although the effectiveness of the velocity profile for

Manuscript received June 24, 2013; revised March 31, 2014 and July 06, 2014; accepted September 04, 2014. Date of publication September 19, 2014; date of current version March 05, 2015. This work was supported by team grants from the Canadian Institutes of Health Research (CIHR) under Grant AMG-100487 and Grant TIR-103945.

J. K. Lee is with the Department of Mechanical Engineering, Hankyong National University, 327 Jungangro, Anseong, Gyeonggi, 456 749, Korea (e-mail: jklee@hknu.ac.kr).

S. N. Robinovitch is with the School of Engineering Science and the Department of Biomedical Physiology and Kinesiology, Simon Fraser University, Burnaby, BC, V5A 1S6, Canada.

E. J. Park is with the School of Mechatronic Systems Engineering, Simon Fraser University, Surrey, BC, V3T 0A3, Canada.

Color versions of one or more of the figures in this paper are available online at <http://ieeexplore.ieee.org>.

Digital Object Identifier 10.1109/TNSRE.2014.2357806

the pre-impact fall detection has been proposed earlier, the calculation of the vertical velocity using the inertial sensor signals is not trivial and requires the implementation of the following two steps: i) calculation of the vertical acceleration and ii) calculation of the vertical velocity via numerical integration of the acceleration. To be practical, these two steps should be done in real time.

First, step i) needs the orientation of the sensor in order to compensate for the gravity component in the accelerometer signal and then to calculate the vertical acceleration with respect to the inertial reference frame. This implies that the orientation accuracy has a direct effect on the vertical acceleration accuracy. In [17], the orientation was obtained by a quaternion filter approach. However, the inertial sensor (with the accelerometer and gyro) without a magnetometer cannot correct the yaw (i.e., the heading direction) drift and the drifted yaw component can be fused with the quaternion components, affecting the tilt angle as well [21]. It should be noted that the required orientation for step i) is not the 3-D orientation (i.e., roll, pitch, and yaw) but only the tilt orientation (i.e., roll and pitch). In other words, only the tilt orientation is the necessary and sufficient condition, not the full 3-D orientation. Second, step ii) encounters the “boundless” drift error because the measurement errors in the acceleration will be accumulated in the estimated velocity through the integration. In order to deal with the drift issue, Kangas *et al.* [22] performed the integration only over a short period (i.e., from the beginning of the fall to the impact); Bourke *et al.* [23] used a Butterworth bandpass filter, in addition to the conditional integration (i.e., integrating only during dynamic conditions and setting the velocity to zero during static conditions); and Degen *et al.* [24] applied a damping factor in the integration to bound the drift during static conditions.

With regards to the experimental fall test protocols of the existing works, they have been focused on simulating falls and normal activities of daily living (ADLs) in laboratory settings. However, near-falls (or recoverable imbalances) are common events for many older adults and are clinically relevant markers of falls worthy of further study [25], [26]. For example, investigators have found that older adults who report multiple near falls (such as missteps or stumbles) are more likely to go on to fall [27]. One particular issue associated with the near-fall cases comes from the fact that, although near-falls are not actual falls and thus should be categorized as non-falls, they have a higher chance of causing false alarms in the detection system (i.e., classifying near-falls as falls). This is mainly due to the fact that near-falls may accompany abrupt movements that produce sensor values that go over the preset fall thresholds. Therefore, near-falls should be differentiated from falls and normal activities. In [17], three types of near-fall tests were included in the non-fall data set without discriminating them from ADLs. In [25], an automatic detection of near-falls compared to non-near-falls was investigated using treadmill walking tests under various conditions. They achieved 85.71% sensitivity and 88.02% specificity using the maximum peak-to-peak vertical acceleration derivative parameter. However, to date, the effect of the inclusion of near falls to a non-fall dataset on the fall detection performance has not been investigated yet.

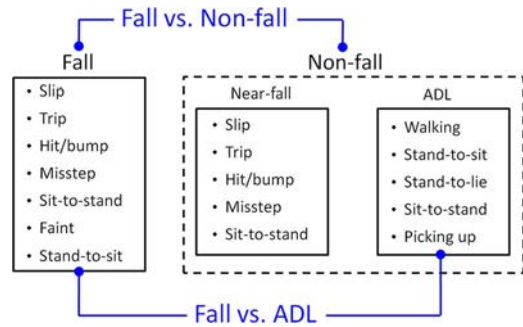


Fig. 1. Three categories of laboratory experiments (fall, near-fall, and ADL) and two classification cases (fall versus non-fall and fall versus ADL) carried out in this study.

The main contribution of this paper is therefore twofold. First, it introduces a novel vertical velocity-based pre-impact fall detection algorithm structured with a Kalman filter using a wearable inertial sensor, which can work in real-time for practical implementation. Second, this work investigates the effect of near-fall scenarios on the detection performance and the feasibility of the vertical velocity thresholding in comparison to the peak acceleration thresholding.

II. MATERIALS AND METHODS

A. Subjects and Data Collection

Eleven healthy young male adults participated in this study: mean age 27.6 (SD 4.3) years; height 176 (SD 8) cm; weight 71.3 (SD 9.7) kg. All participants were students at Simon Fraser University, recruited through advertisements and flyers on university notice boards.

We employed a wireless OPAL inertial sensor (APDM, Inc., USA) attached on the anterior side of the waist. The waist-attached inertial sensor in this study as well as in [17] is located near the body's center of gravity, providing reliable information on subject body movements [28]. The OPAL sensor includes a tri-axial accelerometer, a tri-axial gyroscope, and a tri-axial magnetometer. However, the magnetometer signals were not needed (thus not used) and only the signals from the accelerometer and gyroscope recorded at 128 Hz were used for the analysis. The experiment protocol that we carried out was approved by the Research Ethics Board at Simon Fraser University and all participants provided informed written consent.

B. Experimental Protocol

There were three categories in the experimental protocol: falls, near-falls, and ADLs (see Fig. 1). First, in the fall experiments, participants fell onto a 30-cm thick gymnasium mattress, onto which we laid a 1.3 cm top layer of high density ethylene vinyl acetate foam. The composite structure was stiff enough to allow for stable standing and walking, but soft enough to reduce the forces during impact to a safe level. In order to ensure that the falls we simulated were typical of those experienced by older adults, we selected seven types of fall experiments based on the findings in [29] conducted by our research team, which identifies major causes and activities of falls by investigating a library of video sequences of 227 real-life falls captured in local long-term care facilities (LTC). The seven types of causes

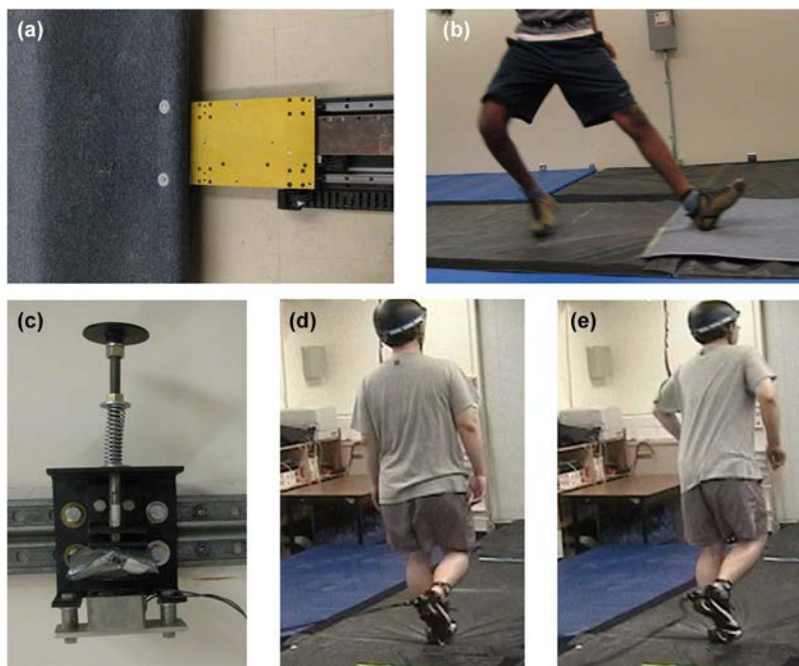


Fig. 2. Fall triggering procedures for (a) and (b) slip and (c)–(e) trip trials. (a) Translational carpet fastened to a linear motor; (b) snapshot of the sheet being translated to cause a slip; (c) tether releasing device controlled by a switch; (d) snapshot of a tether becomes taut during the swing phase of walking; and (e) snapshot of the tether being released by the device after the trip fall triggering.

we considered are: 1) *slips*; 2) *trips*, and the following five other combinations of cause and activity: 3) loss of balance after being hit/bump by another person (denoted as *hit/bump*); 4) loss of balance due to misstep or gait variability (denoted as *misstep*); 5) incorrect weight transfer while rising from sitting (denoted as *sit-to-stand* fall); 6) falls due to fainting (denoted as *faint*); and 7) incorrect weight transfer while sitting down on a chair (denoted as *stand-to-sit* fall). We conducted training sessions with each participant, where video segments of the real-life falls from our previous work [29] were used to train young participants by asking them to mimic the falling behavior of the LTC residents in the videos. In the *slip* fall trials, the participants were instructed to walk up to a carpet placed over the gym mattress, and they were made to slip backward by having the carpet translate rapidly from underneath their feet [see Fig. 2(a) and (b) and also Fig. 3(a)]. The *trip* fall trials were simulated by having a tether attached to the participants' right ankles become taut during the swing phase of walking, initiating a forward fall. Once the trip falls were triggered, the tether was quickly released so that the participants' falls were not constrained by it [see Fig. 2(c)–(e) and also Fig. 3(b)]. In the *hit/bump* falls, a sudden sideways force was applied to the participants' trunks using a soft boxing glove, initiating loss of balance and the participants were instructed to act out a sideways fall. In the *misstep* falls, the participants were instructed to walk forward with high variability in their gaits by taking a narrow step, cross-step or misstep that caused loss of balance and fall. In the *sit-to-stand* falls, the participants initially sat on a chair and were instructed to lose their balance while attempting to stand up. In the *faint* trials, the participants were instructed to act out a “collapse” or “legs giving away” by falling down [see Fig. 3(c)]. For the *hit/bump*, *misstep*,

sit-to-stand, and *faint* falls, no specific instruction was given about the direction of the fall. Lastly, in the *stand-to-sit* falls, we instructed participants to begin in a standing position and then lower the body in a controlled manner to simulate sitting down on a fictitious chair and, at the expected contact position to the chair, to lose their balance and fall backward [see Fig. 3(d)]. We acquired three trials for each fall type. Therefore, a total of 231 trials were collected for the fall test category from 11 participants.

Second, in the near-fall experiments, we conducted the following five types of near-fall trials: slip, trip, hit/bump, misstep, and sit-to-stand. The experimental procedures are equal to the fall experiments above but the participants were instructed to recover balance instead of falling. Note that the faint and stand-to-sit trials were omitted from the near-fall experiments as participants cannot recover their balances in those trials. In total, 165 trials were analyzed for the near-fall test category by acquiring three trials for each near-fall type, over 11 participants.

Third, all eleven subjects also performed three trials of the following five types of ADLs: walking 5 m, descending from standing to sitting on a chair, descending from standing to lying on the ground, rising from sitting to standing, picking an object from the ground. Again, 165 trials were obtained in total for the ADL test category.

C. Method

1) *Calculation of the Vertical Velocity*: In order to obtain the vertical velocity from the inertial sensor signals, first, we need to calculate the vertical acceleration. The sensor signals from the accelerometer (A) and the gyroscope (G) can be modeled as $\mathbf{s}_A = {}^S \mathbf{g} + {}^S \mathbf{a} + \mathbf{n}_A$ and $\mathbf{s}_G = {}^S \boldsymbol{\omega} + \mathbf{n}_G$, respectively, where \mathbf{g} is the gravitational acceleration; \mathbf{a} is the body acceleration of

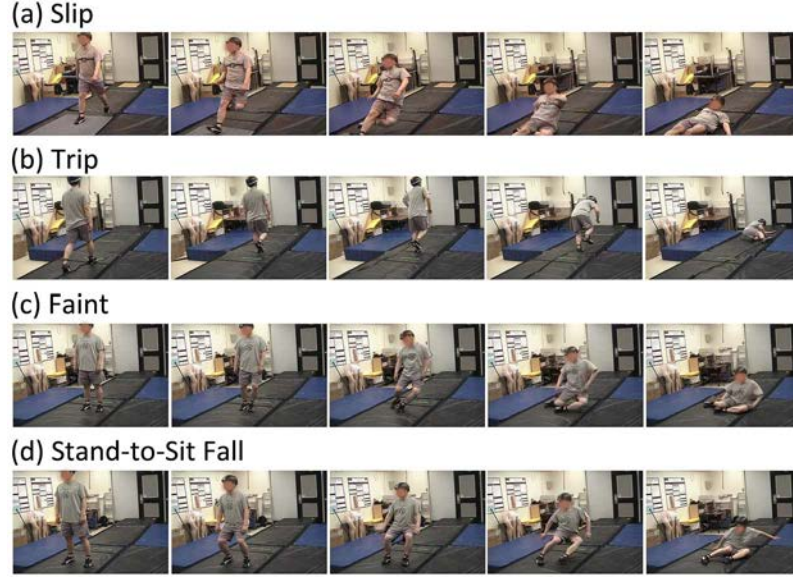


Fig. 3. Laboratory simulation of falls mimicking the falling behavior of older adults due to (a) slips, (b) trips, (c) faint, and (d) incorrect weight transfer while sitting down on a chair.

the object/body that the accelerometer is attached to; $\boldsymbol{\omega}$ is the angular velocity; and \mathbf{n} 's are the measurement noises [30]. The left superscript S implies that the corresponding vectors are expressed with respect to the sensor reference frame S , whereas the left superscript I denotes the inertial reference frame I . Note that the accelerometer signal includes not only the body acceleration that we are interested in but also the gravity component. The gravity with respect to the inertial frame (${}^I\mathbf{g}$) is a known value (i.e., ${}^I\mathbf{g} = [0, 0, g]^T$ where $g = 9.8 \text{ m/s}^2$). However, since the accelerometer reading is inherently expressed with respect to the sensor frame, S , the gravity with respect to the sensor frame (${}^S\mathbf{g}$) changes according to the changes in the sensor orientation. Thus, in order to extract the body acceleration from the accelerometer signal by compensating for the gravity component, one needs to calculate the sensor orientation.

The coordinate transformation of a 3×1 vector \mathbf{x} between the sensor frame S and the inertial frame I is ${}^I\mathbf{x} = {}^I_S\mathbf{R} {}^S\mathbf{x}$ where ${}^I_S\mathbf{R}$ is the orientation matrix of the frame S with respect to the frame I . The orientation matrix ${}^I_S\mathbf{R}$ contains the three unit column vectors of the inertial coordinate system expressed in the sensor coordinate system, i.e., ${}^I_S\mathbf{R} = [{}^S\mathbf{X} \ {}^S\mathbf{Y} \ {}^S\mathbf{Z}]^T$ where ${}^S\mathbf{X}$, ${}^S\mathbf{Y}$, and ${}^S\mathbf{Z}$ are the 3×1 unit vectors of X, Y, and Z axes of the frame I observed with respect to the frame S . Note that ${}^S\mathbf{g}$ (the gravity vector with respect to the sensor frame) can be expressed in terms of the last row of the matrix ${}^I_S\mathbf{R}$ (i.e., ${}^S\mathbf{Z}^T$) as ${}^S\mathbf{g} = g \times {}^S\mathbf{Z}$. Therefore, ${}^S\mathbf{Z}$ is sufficient information to compensate for the gravity effect in the accelerometer signal (i.e., does not require the full 3-D orientation, ${}^I_S\mathbf{R}$). In this study, the vector ${}^S\mathbf{Z}^+$ is obtained by the Kalman filter proposed recently by the authors [30], where the plus superscript denotes the *a posteriori* estimate after the filter correction and the minus superscript denotes the *a priori* estimate. The Kalman filter algorithm is summarized in the Appendix. Once the vector ${}^S\mathbf{Z}^+$ is available, the body acceleration with respect to S is ${}^S\mathbf{a}^+ = \mathbf{s}_A - g \times {}^S\mathbf{Z}^+$, and the vertical body acceleration with respect to the

inertial frame can be obtained as ${}^I a_z^+ = ({}^S\mathbf{a}^+)^T {}^S\mathbf{Z}^+$ where ${}^I\mathbf{a}^+ = [{}^I a_x^+ \ {}^I a_y^+ \ {}^I a_z^+]^T$ is used.

The vertical velocity ${}^I v_z$ is obtained through a numerical integration of the vertical acceleration. However, it is well known that the numerical integration suffers from a boundless drift. This is because the exact vertical acceleration is not available in practice and, instead, an estimated acceleration is used for the integration, i.e., ${}^I a_z^+$, which contains the measurement errors. In order to overcome this difficulty, the following conditional damping-based integration technique was used in this study:

$${}^I v_{z,t} = \begin{cases} \alpha \times {}^I v_{z,t-1}, & \text{if } |{}^I a_{z,\tau}^+| \leq \varepsilon_{\text{accel}} \text{ AND } |{}^I \dot{a}_{z,\tau}^+| \leq \varepsilon_{\text{jerk}} \forall \tau \in [t - n\Delta t, t] \\ {}^I v_{z,t-1} + \Delta t \times {}^I a_{z,t}, & \text{otherwise} \end{cases} \quad (1)$$

where α is a damping factor which slowly resets the integral to zero, and $\varepsilon_{\text{accel}}$ and $\varepsilon_{\text{jerk}}$ are the thresholds for the magnitudes of the body acceleration and its time derivative (i.e., jerk ${}^I \dot{a}_z$), respectively. The jerk is obtained from a simple numerical differentiation without noise filtering. This conditional equation is based on the assumption that a quasi-static motion (i.e., non-zero velocity with zero acceleration) is rare in human motions. Therefore, if the acceleration is near zero, the velocity begins converging to zero as well by the damping factor. It should be noted that, even during dynamic conditions, the norm of the body acceleration can shortly lie within the range designated as the static condition (i.e., $[-\varepsilon_A - \varepsilon_A]$). An example of this case would be when the accelerometer quickly alternates between acceleration and deceleration, resulting in $|{}^I a_z|$ passing in and out of the range [30]. Accordingly, the condition related to the jerk was added. Furthermore, the two conditions are assured for a certain amount of time (i.e., $n\Delta t$). In this study, the following values were experimentally chosen by trial and error and used for the data analysis: $\alpha = 0.9$, $\varepsilon_{\text{accel}} = 0.5 \text{ m/s}^2$, $\varepsilon_{\text{jerk}} = 2 \text{ m/s}^3$, and $n = 10$.

TABLE I
SENSITIVITY AND SPECIFICITY OF FALL DETECTION ALGORITHMS

Parameters	Classification	Threshold	Sensitivity	Specificity
Vertical velocity	Fall vs. ADL	- 1.2 m/s	97.4 %	99.4 %
	Fall vs. Non-fall	- 1.4 m/s	95.2 %	97.6 %
Acceleration magnitude	Fall vs. ADL	16 m/s ²	98.7 %	99.4 %
	Fall vs. Non-fall	26 m/s ²	84.0 %	85.5 %

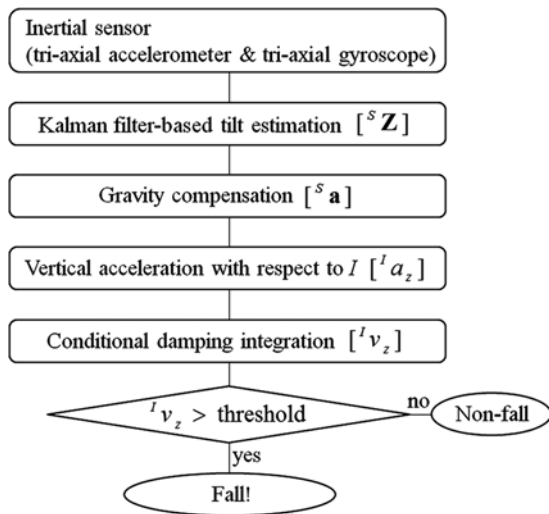


Fig. 4. Flowchart of the proposed pre-impact fall detection algorithm.

In this vertical velocity-based method (Method 1) that we are proposing, the condition in which the vertical velocity (which has a negative sign) exceeds a threshold was determined as a fall. A flowchart of the proposed method is shown in Fig. 4.

2) *Threshold-Based Fall Detections and Analysis:* For comparison purposes, the acceleration magnitude-based method (Method 2) was also used, in which the gravity-subtracted magnitude of the accelerometer signal (i.e., $\|s_A\| - g$) was used for the thresholding of the fall detection. The magnitude of the accelerometer signal (i.e., $\|s_A\|$) is one of the most commonly used fall detection parameters in low-complexity accelerometer-based fall detection methods with no gyroscope (e.g., employed by [3], [5], [8], and [15]). This parameter is related to the peak acceleration experienced mostly at the impact of the fall. Note that, while these previous works used $\|s_A\|$ as the fall detection parameter, Method 2 in this study uses $\|s_A\| - g$ to set the parameter to become zero at rest.

The classifying abilities of the two pre-impact fall detection methods were investigated in terms of the sensitivity (or true positive rate) and the specificity (or true negative rate). Also, the investigation was performed with respect to the following two classification categories: 1) “falls versus ADLs” where near-fall data were not considered and 2) “falls versus non-falls” where the near-fall data were included in the non-fall group in addition to the ADL data.

The use of the negative downward vertical velocity as a fall detection parameter in Method 1 (using both the accelerometer and gyroscope signals) is associated with the descending

TABLE II
MEAN AND ONE STANDARD DEVIATION OF
LEAD TIMES (MSEC) FOR FALL TRIALS

Fall types	Fall vs. ADL (threshold: - 1.2 m/s)	Fall vs. Non-fall (threshold: - 1.4 m/s)
Slip	206 ± 127	182 ± 79
Trip	300 ± 223	179 ± 146
Hit/bump	301 ± 100	259 ± 98
Mis-step	228 ± 112	190 ± 117
Sit-to-stand	187 ± 64	152 ± 51
Faint	226 ± 90	192 ± 92
Stand-to-sit	156 ± 68	118 ± 62
Total	231 ± 127	184 ± 104

phase of the fall before impact, while the use of the acceleration magnitude in Method 2 (using only the accelerometer signal) is related to the peak impact acceleration experienced mostly at the impact of the fall. Accordingly, only for Method 1 which has the capability of detecting falls before the impact, the lead time T_{lead} was also obtained from the fall data. The lead time was defined as $T_{lead} = T_{impact} - T_{detect}$ where T_{detect} and T_{impact} denote the time when the fall was detected and the time of the impact when the maximum negative vertical velocity was achieved, respectively [20]. The data analysis was performed using C programming.

III. RESULTS

Table I shows the classifying abilities of the resulting four cases (i.e., each of the two methods evaluated with respect to the two classification categories) and the thresholds were determined so the summation of sensitivity and specificity has the maximum value for each case. For the fall versus ADL detection, both methods produced similar accuracies but, for the fall versus non-fall detection, Method 1 showed a much higher accuracy than Method 2. This result was clearly supported by receiver operating characteristic (ROC) curves shown in Fig. 5. The ROC curves depict the classifier sensitivity versus 1-specificity at different detection thresholds and thus one can find a different sensitivity and specificity combination (e.g., specificity with 100% sensitivity).

Table II shows mean and one standard deviation of the lead times for the fall trials. The average lead times were 231 and 184 ms for the thresholds -1.2 m/s (used in the fall versus ADL classification) and -1.4 m/s (used in the fall versus non-fall

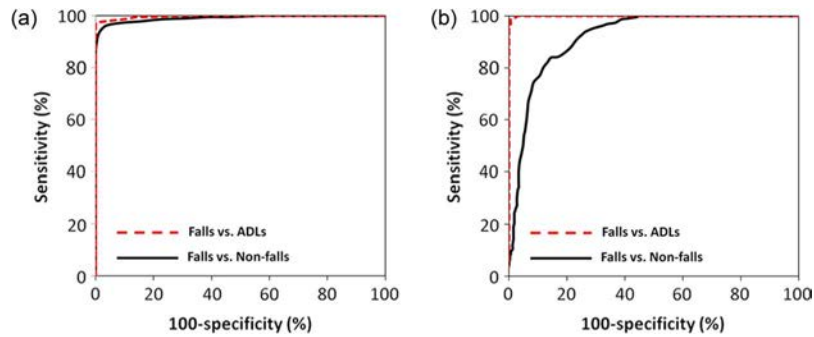


Fig. 5. ROC curves from (a) proposed vertical velocity-based method and (b) acceleration-based method.

TABLE III
COMPARISON OF PRE-IMPACT FALL DETECTION METHODS

References	Sensors and their attachment locations	Basic principles	Sensitivity / Specificity	Lead time
Wu and Xue (2008) [17]	A tri-axial accelerometers and a tri-axial gyro at anterior waist	Threshold based on a vertical velocity	100 % / See §.	70 ~ 375 ms
Bourke et al. (2008)[18]	A tri-axial accelerometers and a tri-axial gyro at anterior chest	Threshold based on a vertical velocity	100 % / 100 %	314 ms
Nyan et al. (2008) [19]	A tri-axial accelerometer and a bi-axial gyro at right thigh and a tri-axial accelerometer at waist	(i) Threshold based on the sagittal and lateral angles of the thigh segment, (ii) high correlation of angles between thigh and torso, and (iii) high correlation of angular velocities between thigh and a pre-defined template.	95.2 % / 100 %	700 ms
Shan and Yuan (2010) [20]	A tri-axial accelerometer at posterior waist	Support vector machine classifier	100 % / 100 %	203 ms

§ No information of the specificity in the reference. Three false detections during 13 hours test.

classification). For both threshold values, the stand-to-sit falls had the shortest lead time. In fall injury prevention systems using airbags, the required lead time should be longer than the inflation time of airbag system which is about 100 ms (e.g., an average of 120 ms in [14]). From the comparison of the results between Fall versus ADL and Fall versus Non-fall, it can be seen that the inclusion of the near-fall cases in the data set affects the detection accuracy (see Table I) and lead time (see Table II).

Table III summarizes the existing pre-impact fall detection methods in the literature. All of the methods except [19] in Table III achieved 100% sensitivity while our method obtained 97.4% sensitivity and 99.4% specificity for the Fall versus ADL classification. Note that our fall test protocol included the incorrect weight transfer while sitting down on a chair (denoted as *stand-to-sit fall*) based on the findings in [29]. While all of the false negatives in our results came from the stand-to-sit falls, none of the references in Table III dealt with the stand-to-sit falls. If this type of fall is excluded from our data set, our fall versus ADL detection performance also improves to 100% sensitivity and 99.4% specificity with the same threshold of -1.2 m/s.

IV. DISCUSSION

Many fall detection algorithms utilize the posture information derived from the accelerometer signals as a determinant

parameter, based on the fact that the accelerometer can be used as an inclinometer in static conditions (e.g., [5], [22], and [31]). In the case of the post-impact fall detection, the information may provide a reasonable indication whether the subject wearing the accelerometer is in lying posture. This is logical since the faller lying down after the fall would be in nearly static conditions. However, in the case of the pre-impact fall detection, we are interested in the falling phase before the impact and the accelerometer is in dynamic condition. In other words, the use of the accelerometer as an inclinometer is no longer appropriate. The addition of a gyroscope provides a solution to this problem. Even in this case, however, the use of body posture represented by the sensor orientation still needs to be paid careful attention during the interpretation of the data. Because of the interposition of the soft tissue between the target body segment and the segment-mounted sensor and the misalignment of the sensor from its initial/calibrated attachment location, there is a concern as to the extent of the error in the “surface” measurements obtained by these sensors. They may not accurately measure the underlying true segmental movements and the degree of the error may vary between subjects according to the mounting location (e.g., the waist in our case) and obesity (see, for example, [32] for artifact effects of skin-mounted inertial sensors). Due to this reason, we did not use the posture information as a fall

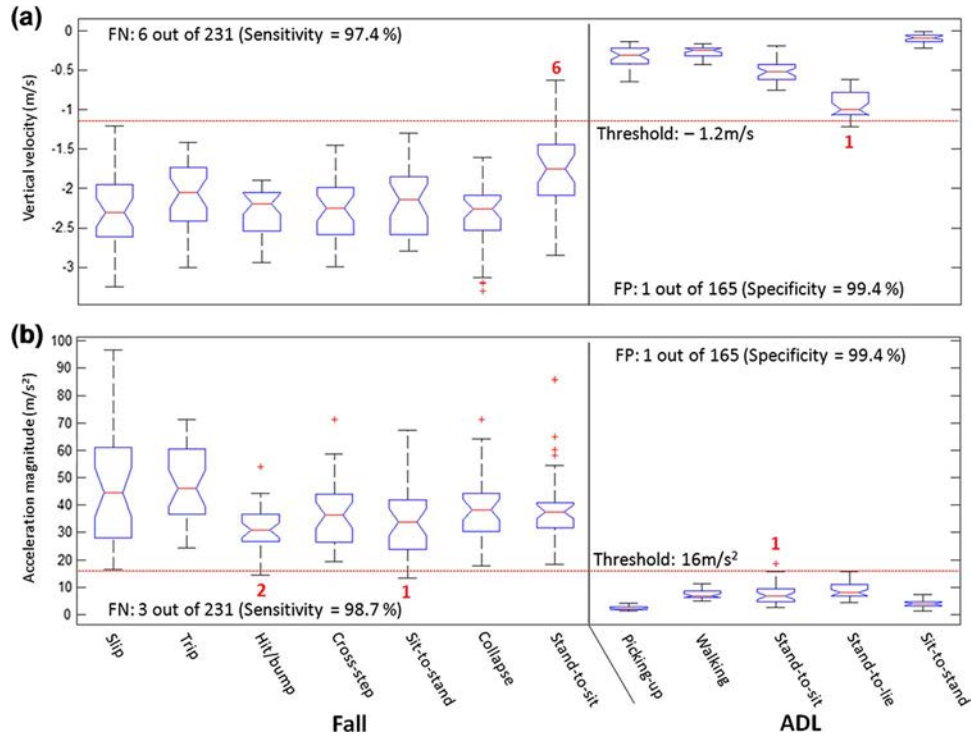


Fig. 6. Boxplots of the maximum values of (a) vertical velocity and (b) acceleration magnitude, for the discrimination of falls from ADLs. Horizontal dotted lines indicate the thresholds used. In the plots, the FN and FP indicate the false negatives and false positives, respectively, and the numbers above or below the boxes indicate the number of false detections of each trials.

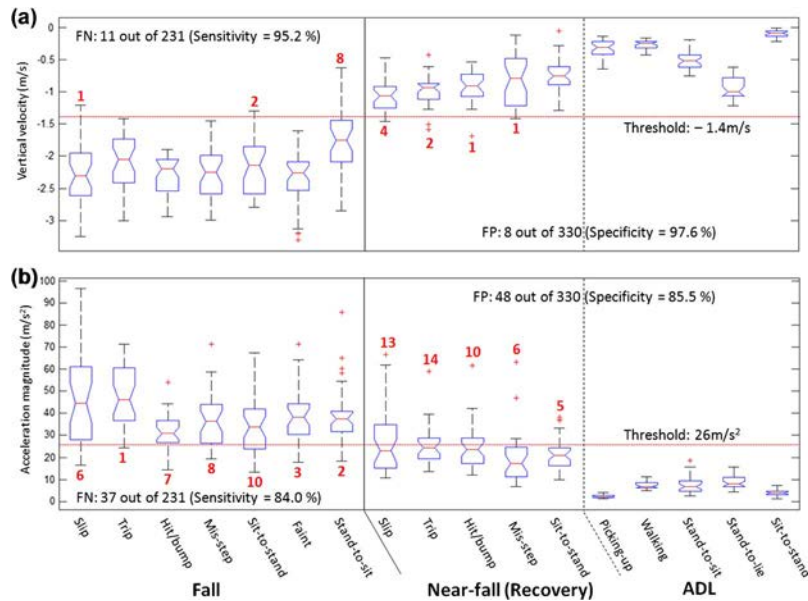


Fig. 7. Boxplots of the maximum values of (a) vertical velocity and (b) acceleration magnitude, for the discrimination of falls from non-falls. Horizontal dotted lines indicate the thresholds used. In the plots, the FN and FP indicate the false negatives and false positives, respectively, and the numbers above or below the boxes indicate the number of false detections of each trials.

detection parameter for thresholding and the proposed method is independent of this issue.

For the fall versus ADL detection (see Fig. 6), the proposed method produced six false negatives out of the 231 fall trials and one false positive out of the 165 ADL trials. Note that all of the false negatives came from the stand-to-sit falls and the only false positive came from the stand-to-lie ADLs. These results are as expected because, in the case of stand-to-sit falls,

the fall is initiated at relatively lower location and thus the time duration from the fall initiation to the impact is short and the vertical velocity may not reach to the threshold value. In contrast, the stand-to-lie ADL may accompany fast downward velocity depending on the subject. Since the false detections are concentrated on a few particular movements, the detection accuracy has much room for further improvement if those particular cases are resolved.

For the fall versus non-fall detection (see Fig. 7), Method 1 maintained a high detection accuracy (i.e., >95% in both sensitivity and specificity) but the detection accuracy of Method 2 was significantly reduced. Method 2 produced false negatives across all types of falls and false positives in all types of near-falls. During the near-fall trials, the falls were triggered experimentally or by self-generated perturbations and the participants regained their postural stability from the imbalances by quickly moving their center of mass. However, even the movements involved in these recoverable imbalances can result in a considerable increase in the peak acceleration levels, for example, in the case of Method 2. In the case of Method 1, on the other hand, since the velocity is obtained by integrating the acceleration with respect to time, it is inherently less affected by these short and abrupt movements.

We paid particular attention to the experimental protocol in order to improve the reality of the falling tests. As previously mentioned, our protocols were obtained from a detailed analysis of the real-world fall videos. Furthermore, during the participants' trials, no instruction was given about the fall direction and impact location, which can increase the complexity and variability of the falling kinematics. Nevertheless, the proposed algorithm has been evaluated using the simulated falls which may have differences with real falls as discussed in [33]. Bagala *et al.* [34] shows that the performances of the existing fall detection algorithms may be affected when real-world fall data are applied, and this may be true for our method as well. Therefore, as discussed in [34], a large, shared real-world fall database could provide an enhanced understanding of the fall process for evaluation of fall detection performance.

In conclusion, this paper proposed a novel vertical velocity-based pre-impact fall detection method using a wearable inertial sensor. The feasibility of the vertical velocity as a fall detection parameter and the detection performance of the proposed method were evaluated by comparing it with the performance of the acceleration-based method. Importantly, this paper dealt with near-fall situations in addition to the falls and ADLs. The experiments showed that both methods produced similar accuracies for the fall versus ADL detection, while Method 1 produced much higher accuracy than Method 2 for the fall versus non-fall detection. The results show the advantage of the vertical velocity over the peak acceleration in terms of the robustness for the pre-impact fall detection against both the ADL near-fall trials. The consideration of near-fall conditions for the performance evaluation of the pre-impact fall detection method may provide insight into the future development of a real-world pre-impact fall detection system.

APPENDIX

In the fall detection algorithm, a linear Kalman filter is used to estimate the unit vector ${}^S\mathbf{Z}$, in the course of calculation of the vertical acceleration. The Kalman filter can be defined by the following process and measurement models:

$$\begin{cases} {}^S\mathbf{Z}_t = \Phi_{t-1}^S \mathbf{Z}_{t-1} + \mathbf{w}_{t-1} \\ \mathbf{z}_t = \mathbf{H}^S \mathbf{Z}_t + \mathbf{v}_t \end{cases} \quad (\text{A1})$$

where ${}^S\mathbf{Z}$ is designated as the state vector; \mathbf{z} is the measurement vector that is defined as $\mathbf{s}_A - {}^S\mathbf{a}^-$ (i.e., the accelerometer signal

minus the *a priori* estimate of the body acceleration); Φ is the state transition matrix; \mathbf{H} is the observation matrix; and \mathbf{w} and \mathbf{v} are the white Gaussian process and measurement noises, respectively. Once the process and measurement models are set, the procedure of the Kalman filter is as follows.

- Step 1: Compute the *a priori* state estimate, ${}^S\mathbf{Z}_t^- = \Phi_{t-1}^S \mathbf{Z}_{t-1}^+$ where $\Phi_{t-1} = \mathbf{I} - \Delta t[\mathbf{s}_{G,t-1} \times]$ and Δt is the time sampling rate. The vector cross product operator $[\mathbf{s} \times]$ is defined as $\begin{bmatrix} 0 & -s_z & s_y \\ s_z & 0 & -s_x \\ -s_y & s_x & 0 \end{bmatrix}$ if $\mathbf{s} = [s_x \ s_y \ s_z]^T$.
- Step 2: Compute the *a priori* error covariance matrix, $\mathbf{P}_t^- = \Phi_{t-1} \mathbf{P}_{t-1}^+ \Phi_{t-1}^T + \mathbf{Q}_{t-1}$ where \mathbf{Q} is the process noise covariance matrix and is defined as $\mathbf{Q}_{t-1} = E[\mathbf{w}_{t-1} \mathbf{w}_{t-1}^T]$ where E is the expectation operator.
- Step 3: Compute the Kalman gain, $\mathbf{K}_t = \mathbf{P}_t^- \mathbf{H}^T (\mathbf{H} \mathbf{P}_t^- \mathbf{H}^T + \mathbf{M}_t)^{-1}$ where \mathbf{M} is the measurement noise covariance matrix and is defined as $\mathbf{M}_t = E[\mathbf{v}_t \mathbf{v}_t^T]$.
- Step 4: Compute the *a posteriori* state estimate, ${}^S\mathbf{Z}_t^+ = {}^S\mathbf{Z}_t^- + \mathbf{K}_t (\mathbf{z}_t - \mathbf{H}^S \mathbf{Z}_t^-)$.
- Step 5: Compute the *a posteriori* error covariance matrix, $\mathbf{P}_t^+ = (\mathbf{I} - \mathbf{K}_t \mathbf{H}) \mathbf{P}_t^-$.

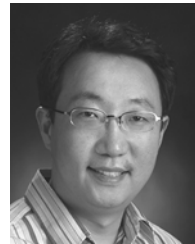
ACKNOWLEDGMENT

The authors would like to thank O. Aziz of the Simon Fraser University for supporting the data collection.

REFERENCES

- [1] J. A. Stevens, P. S. Corso, E. A. Finkelstein, and T. R. Miller, "The costs of fatal and non-fatal falls among older adults," *Inj. Prev.*, vol. 12, no. 5, pp. 290–295, Oct. 2006.
- [2] S. R. Lord, C. Sherrington, and H. B. Menz, *Falls in Older People: Risk Factors and Strategies for Prevention*. Cambridge, U.K.: Cambridge Univ. Press, 2001.
- [3] A. K. Bourke, J. V. O'Brien, and G. M. Lyons, "Evaluation of a threshold-based tri-axial accelerometer fall detection algorithm," *Gait Posture*, vol. 26, no. 2, pp. 194–199, 2007.
- [4] P. Boissy, S. Choquette, M. Hamel, and N. Noury, "User-based motion sensing and fuzzy logic for automated fall detection in older adults," *Telemed. J. E Health*, vol. 13, no. 6, pp. 683–693, 2007.
- [5] A. K. Bourke, P. van de Ven, M. Gamble, R. O'Connor, K. Murphy, E. Bogan, E. McQuade, P. Finucane, G. O'laighin, and J. Nelson, "Evaluation of waist-mounted tri-axial accelerometer based fall-detection algorithms during scripted and continuous unscripted activities," *J. Biomech.*, vol. 43, pp. 3051–3057, Nov. 2010.
- [6] F. Bianchi, S. J. Redmond, M. R. Narayanan, S. Cerutti, and N. H. Lovell, "Barometric pressure and triaxial accelerometry-based falls event detection," *IEEE Trans. Neural Syst. Rehabil. Eng.*, vol. 18, no. 6, pp. 619–627, Nov. 2010.
- [7] P. Bonato, "Wearable sensors and systems," *IEEE Eng. Med. Biol.*, vol. 29, no. 1, pp. 25–36, Mar. 2010.
- [8] D. M. Karantonis, M. R. Narayanan, M. J. Mathie, N. H. Lovell, and B. G. Celler, "Implementation of a real-time human movement classifier using a triaxial accelerometer for ambulatory monitoring," *IEEE Trans. Inf Technol. Biomed.*, vol. 10, no. 1, pp. 156–167, Jan. 2006.
- [9] S. J. Preece, J. Y. Goulermas, L. P. J. Kenney, D. Howard, K. Meijer, and R. Crompton, "Activity identification using body-mounted sensors—A review of classification techniques," *Physiol. Meas.*, vol. 30, no. 4, pp. R1–33, 2009.
- [10] J. K. Lee and E. J. Park, "3D spinal motion analysis during staircase walking using an ambulatory inertial and magnetic sensing system," *Med. Biol. Eng. Comput.*, vol. 49, pp. 755–764, 2011.
- [11] S. N. Robinovitch, S. L. Evans, J. Minns, A. C. Laing, and P. Kannus *et al.*, "Hip protectors: Recommendations for biomechanical testing—An international consensus statement (part I)," *Osteoporos Int.*, vol. 20, pp. 1977–1988, 2009.

- [12] I. D. Cameron, S. N. Robinovitch, S. Birge, P. Kannus, and K. Khan *et al.*, "Hip protectors: Recommendations for conducting clinical trials—An international consensus statement (part II)," *Osteoporos. Int.*, vol. 21, pp. 1–10, 2010.
- [13] G. Shi, C. S. Chan, W. J. Li, K. Leung, Y. Zou, and Y. Jin, "Mobile human airbag system for fall protection using MEMS sensors and embedded SVM classifier," *IEEE Sensors J.*, vol. 9, no. 5, pp. 495–503, May 2009.
- [14] T. Tamura, T. Yoshimura, M. Sekine, M. Uchida, and O. Tanaka, "A wearable airbag to prevent fall injuries," *IEEE Trans. Inf. Technol. Biomed.*, vol. 13, no. 6, pp. 910–914, Nov. 2009.
- [15] U. Lindemann, A. Hock, M. Stuber, W. Keck, and C. Becker, "Evaluation of a fall detector based on accelerometers: A pilot study," *Med. Biol. Eng. Comput.*, vol. 43, pp. 548–551, 2005.
- [16] A. K. Bourke and G. M. Lyons, "A threshold-based fall-detection algorithm using a bi-axial gyroscope sensor," *Med. Eng. Phys.*, vol. 30, pp. 84–90, 2008.
- [17] G. Wu and S. Xue, "Portable preimpact fall detector with inertial sensors," *IEEE Trans. Neural Syst. Rehabil. Eng.*, vol. 16, no. 2, pp. 178–183, Apr. 2008.
- [18] A. K. Bourke, K. J. O'Donovan, and G. ÓLaighin, "The identification of vertical velocity profiles using an inertial sensor to investigate pre-impact detection of falls," *Med. Eng. Phys.*, vol. 30, pp. 937–946, 2008.
- [19] M. N. Nyan, F. E. H. Tay, and E. Murugasu, "A wearable system for pre-impact fall detection," *J. Biomech.*, vol. 41, pp. 3475–3481, 2008.
- [20] S. Shan and T. Yuan, "A wearable pre-impact fall detector using feature selection and support vector machine," in *Proc. IEEE Int. Conf. Signal Process.*, Beijing, China, 2010, pp. 1686–1689.
- [21] X. Yun, E. R. Bachmann, and R. B. McGhee, "A simplified quaternion-based algorithm for orientation estimation from Earth gravity and magnetic field measurements," *IEEE Trans. Instrum. Meas.*, vol. 57, no. 3, pp. 638–650, Mar. 2008.
- [22] M. Kangas, I. Vikman, J. Wiklander, P. Lindgren, L. Nyberg, and T. Jamsa, "Sensitivity and specificity of fall detection in people aged 40 years and over," *Gait Posture*, vol. 29, no. 4, pp. 571–574, 2009.
- [23] A. K. Bourke, K. J. O'Donovan, and J. N. and G. M. ÓLaighin, "Fall-detection through vertical velocity thresholding using a tri-axial accelerometer characterized using an optical motion-capture system," in *Proc. IEEE 30th Annu. Int. Conf. Eng. Med. Biol. Soc.*, Vancouver, BC, Canada, 2008, pp. 2832–2835.
- [24] T. Degen, H. Jaeckel, M. Rufer, and S. Wyss, "Speedy: A fall detector in a wrist watch," in *Proc. Seventh IEEE Int. Symp. Wearable Computing*, 2003, pp. 184–187.
- [25] A. Weiss, I. Shimkin, N. Giladi, and J. Hausdorff, "Automated detection of near falls: Algorithm development and preliminary results," *BMC Res. Notes*, vol. 3, p. 62, 2010.
- [26] A. Dinh, Y. Shi, D. Teng, A. Ralhan, and L. Chen *et al.*, "A fall and near-fall assessment and evaluation system," *Open Biomed. Eng. J.*, vol. 3, pp. 1–7, 2009.
- [27] J. Teno, D. P. Kiel, and V. Mor, "Multiple stumbles: A risk factor for falls in community-dwelling elderly. A prospective study," *J. Am. Geriatr. Soc.*, vol. 38, pp. 1321–1325, 1990.
- [28] M. J. Mathie, A. C. Coster, N. H. Lovell, and B. G. Celler, "Accelerometry: Providing an integrated, practical method for long-term, ambulatory monitoring of human movement," *Physio. Meas.*, vol. 25, pp. R1–20, 2004.
- [29] S. N. Robinovitch, F. Feldman, Y. Yang, R. Schonnop, P. M. Leung, T. Sarraf, J. Sims-Gould, and M. Loughin, "Video capture of the circumstances of falls in elderly people residing in long-term care: An observational study," *Lancet*, vol. 381, pp. 47–54, 2013.
- [30] J. K. Lee, E. J. Park, and S. N. Robinovitch, "Estimation of attitude and external acceleration using inertial sensor measurement during various dynamic conditions," *IEEE Trans. Instrum. Meas.*, vol. 61, no. 8, pp. 2262–2273, Aug. 2012.
- [31] D. M. Karantonis, M. R. Narayanan, M. Mathie, N. H. Lovell, and B. G. Celler, "Implementation of a real-time human movement classifier using a triaxial accelerometer for ambulatory monitoring," *IEEE Trans. Inf. Technol. Biomed.*, vol. 10, no. 1, pp. 156–167, 2006.
- [32] A. Forner-Cordero, M. Mateu-Arce, I. Forner-Cordero, E. Alcántara, J. C. Moreno, and J. L. Pons, "Study of the motion artefacts of skin-mounted inertial sensors under different attachment conditions," *Physio. Meas.*, vol. 29, p. N21–31, 2008.
- [33] J. Klenk, C. Becker, F. Lieken, S. Nicolai, and W. Maetzler *et al.*, "Comparison of acceleration signals of simulated and real-world backward falls," *Med. Eng. Phys.*, vol. 33, pp. 368–373, 2011.
- [34] F. Bagala, C. Becker, A. Cappello, L. Chiari, and K. Aminian *K et al.*, "Evaluation of accelerometer-based fall detection algorithms on real world falls," *PLoS One*, vol. 7, no. 5, May 2012, e37062.



Jung Keun Lee (M'11) received the B.Sc. and M.Sc. degrees in mechanical engineering from Hanyang University, Seoul, Korea, in 1997 and 1999, respectively, and the Ph.D. degree in mechatronic systems engineering from the School of Engineering Science, Simon Fraser University, Surrey, BC, Canada, in 2010.

Prior to his Ph.D. study, he was a Naval Officer with the Republic of Korea Navy and, then, was a Research Engineer with the Powertrain R & D Centre, Hyundai Motor Company. He is currently an

Assistant Professor of the Department of Mechanical Engineering, Hankyong National University, Anseong, Korea. His research interests include inertial-sensing-based human motion tracking, biomechanics, wearable sensor applications, dynamics and control, and automotive engineering.



Stephen N. Robinovitch received the B.A.Sc. degree in mechanical engineering from the University of British Columbia, Vancouver, Canada, in 1988, the M.Sc. degree in mechanical engineering from Massachusetts Institute of Technology, Cambridge, MA, USA, in 1990, and the Ph.D. degree in medical engineering from MIT/ Harvard.

He is a Professor and Canada Research Chair in Injury Prevention and Mobility Biomechanics at Simon Fraser University. His research focuses on improving our understanding of the cause and prevention of fall-

related injuries (especially hip fracture) in older adults, through laboratory experiments, mathematical modeling, field studies in residential care facilities, and product design.



Edward J. Park (M'03–SM'13) received the B.A.Sc. degree from the University of British Columbia, Vancouver, BC, Canada, and the M.A.Sc. and the Ph.D. degrees from the University of Toronto, Toronto, ON, Canada, in 1996, 1999, and 2003, respectively, all in mechanical engineering.

He is currently a Professor of the School of Mechatronic Systems Engineering at the Simon Fraser University, Surrey, BC, Canada, and the Director of the Biomechatronic Systems Laboratory.

Previously, he was an Assistant Professor in the Department of Mechanical Engineering, University of Victoria, BC, Canada, from 2003 to 2008. He is also a member of the Faculty of Health Sciences. His current research interests include biomechanics, wearable technology and biomedical technology for eldercare, rehabilitation, sports science and medicine, and mechatronics applied to next generation vehicular, robotic, and space systems. He has authored/coauthored over 100 journal and conference papers in these areas.

An Accumulated Activity Effective Index for Promoting Physical Activity: A Design and Development Study in a Mobile and Pervasive Health Context

Monitoring Editor: Gunther Eysenbach

Reviewed by S.J Hsu and Pi-Chung Wang

[Chung-Tse Liu](#)¹ and [Chia-Tai Chan](#), PhD^{✉1}

¹Department of Biomedical Engineering, National Yang-Ming University, Taipei, Taiwan

Chia-Tai Chan, Department of Biomedical Engineering, National Yang-Ming University, No.155, Sec.2, Linong Street, Taipei, , Taiwan, Phone: 886 2 2826 7000 ext 7371, Fax: 886 2 2821 0847, Email: ctchan@ym.edu.tw.

[✉]Corresponding author.

Corresponding Author: Chia-Tai Chan ; Email: ctchan@ym.edu.tw

Received 2014 Feb 19; Revisions requested 2014 Jul 17; Revised 2014 Aug 21; Accepted 2014 Nov 6.

Copyright ©Chung-Tse Liu, Chia-Tai Chan. Originally published in JMIR Research Protocols (<http://www.researchprotocols.org>), 06.01.2015.

This is an open-access article distributed under the terms of the Creative Commons Attribution License

(<http://creativecommons.org/licenses/by/2.0/>), which permits unrestricted use, distribution, and reproduction in any medium, provided the original work, first published in JMIR Research Protocols, is properly cited. The complete bibliographic information, a link to the original publication on <http://www.researchprotocols.org>, as well as this copyright and license information must be included.

Abstract

Background

Increased physical activity has become a principal personal health goal worldwide because sufficient physical activity can reduce the risk of many adverse conditions. Motivating individuals to increase their levels of physical activity can increase life expectancy and contribute to a healthy life. Sharing and comparison of physical activity information by using the Internet, with fewer privacy concerns, might also help encourage people to promote and maintain sufficient physical activity. To promote and manage physical activity, an accumulated activity effective index (AAEI) is proposed in this paper.

Objective

The purpose of the AAEI design is to maintain and promote physical activity. The public can easily accept a clear indicator that reveals the current status of physical activity. The AAEI is not only an assessment and tracking tool for personal physical activity, but is also useful for goal setting and for sharing content with the Internet community.

Methods

The AAEI is derived from input in the form of accumulated physical activity, and evaluates the status of physical activities and days spent exercising. The term $AAEI(t_1, t_2)$ is an index of the accumulated physical activity in the time interval (t_1, t_2) , where the base unit of time is the day. The AAEI is determined according to accumulated physical activity and is adjusted using the previous status of physical activity. The previous status of physical activity is estimated according to the number of days spent exercising and the accumulated physical activity that has been performed. An analysis of the AAEI performance was

conducted using a simulation model and a real-world trial with 2 participants.

Results

The AAEI increased as the physical activity and days spent exercising accumulated. Conversely, the AAEI decreased with lack of physical activity and increased resting days. In simulation, the shape of the AAEI line indicated different types of exercise. The moving average AAEI represented long-term exercise. In the real-world trial, the AAEI confirmed that the simulation results were comparable to actual conditions.

Conclusions

The AAEI proposed in this paper is a method that can be used to evaluate the status of a person's physical activity. The AAEI is a simple numeric indication that is estimated by analyzing accumulated physical activity and the average number of days spent exercising. The AAEI is suitable for tracking personal physical activity, reminding the user of achievement goals, and allows data sharing by using the Internet. The results have demonstrated that the AAEI is a useful tool for physical activity management.

Keywords: accumulated activity effective index (AAEI), physical activity, activity level

Introduction

Sufficient physical activity has substantial benefits for a healthy life. Regular and moderate intensity of physical activity, such as fast walking, running, and cycling, can reduce the risk of coronary heart disease, type 2 diabetes mellitus, and depression, as well as facilitate weight control [1-3]. Moreover, physical activity increases bodily health and improves cognitive functioning. It increases resistance to neurodegenerative diseases, dementia, and related cognitive impairments [4]. Unfortunately, 31.1% of adults worldwide are physically inactive. Physical inactivity increases with age and is more prevalent in high-income countries [1]. According to previous studies, physical inactivity is the fourth leading risk factor for mortality and noncommunicable diseases, and caused 5.3 million deaths worldwide in 2008 [5]. Physical inactivity increases the risk of many adverse health conditions and threatens global health. The elimination of physical inactivity can increase life expectancy and contribute to a healthy life.

Pervasive computing technologies are well suited for health care applications and have the potential to promote a healthy lifestyle. Several well-known studies have been proposed using pervasive computing technologies to assist individuals in achieving sufficient physical activity [3,6-9]. For example, the pedometer can become a human activity sensor used to monitor physical activity and promote health because walking is a health-boosting activity and a pedometer can help motivate and track progress. Although the accuracy of pedometers can be unreliable, they have been shown to motivate individuals toward a more active lifestyle [8-10]. The progress of measuring instruments has allowed multiple sensing modules to be built which can provide information such as blood pressure and heart rate. This information is critical in health care applications; however, the professional terms and complicated interface can confuse the public and can be a barrier to the popularization model for usage of such instruments; for the public, a simple indicator is easier to accept.

Motivating individuals to increase their levels of physical activity is a critical issue in health promotion. Numerous studies have focused on the social aspects revealing that the sharing and comparison of information regarding physical activity within the community can increase interest in, and enjoyment of, exercise and can motivate people to be more active [7,9,11]. The high penetration of Internet and community websites can enhance communication in groups and can be used as a medium to motivate physical activity. However, personal context information such as time, location, and heart rate when shared using the Internet can suffer personal privacy problems. Other studies suggest that goal setting can increase self-regulatory behaviors and improve physical activity [12]. An accumulated activity effective

index (AAEI) is proposed in this paper for evaluating the status of physical activity and sharing related information with communities on the Internet. The AAEI is designed to provide a simple numeric indication of accumulated physical activity and days spent exercising, with fewer privacy concerns than personal context information. The AAEI is designed to increase awareness of physical activity by tracking physical activity, reminding the user of achievement goals, and sharing this information with the Internet community. The AAEI is also suited for self-awareness in maintaining physical activity. The performance of the AAEI was illustrated using a simulation model and a short-term real-world trial using pervasive computing tools.

Methods

Accumulated Activity Effective Index

The AAEI was designed as a simple numeral indicator that directly reveals the physical activity status of the user by estimating both accumulated physical activity and days spent exercising. The design principles of the AAEI were (1) AAEI is a simple value to reveal physical activity; (2) AAEI corresponds to physical activity; (3) AAEI increases with more physical activity, is steady in fixed physical activity, and decreases with less physical activity; (4) AAEI corresponds to days spent exercising; (5) AAEI decreases with resting days; (6) AAEI decreases more with continued resting; (7) AAEI decreases less at rest if user has exercised before; and (8) AAEI is at or near zero if the user does not exercise in 7 days. The AAEI parameters and evaluating process (Equation 1) are described in [Figure 1](#).

The term $AAEI(t_1, t_2)$ is an index of the accumulated physical activity in the time interval (t_1, t_2) , where the base unit of time is the day. The AAEI is greater than or equal to zero. The $AAEI(t_1, t_2)$ is calculated by tracking the sum of $AAEI(t_1, t_2-1)$ and the amount of physical activity in t_2 . The variable $MT(t_2)$ represents the amount of physical activity in t_2 , which is equal to the activity level multiplied by the exercise duration. The variable $E(t_2)$ is defined as the exercise expectation of physical activity in t_2 , which depends on the previous interval (t_1, t_2-1) status of physical activity include accumulated physical activity and days spent exercise. Parameter k is a constant value and is greater than zero to scale the AAEI. The design of k in a different constant or a variable can be a condition depending on $AAEI(t_1, t_2-1)$, $MT(t_2)$, or others. For example, k can increase with activity level, in which case participants exercise harder and can get a higher AAEI because AAEI increases more during vigorous activity. In another example, if k rises when $[MT(t_2) - E(t_2)] < 0$, the user needs to sustain physical activity to maintain AAEI.

The previous status of physical activity was defined as *exercise expectance*, which is greater than or equal to zero and was formulated using Equations 2 and 3 in [Figure 1](#). The notion of exercise expectation, $E(t_2)$, was that if a participant had a high AAEI, a participant was expected to require more physical activity to increase the AAEI. Otherwise, AAEI would be stable or decrease. Another design objective for exercise expectation was to reveal days spent exercising. The more days a participant rested, the more the AAEI index decreased. The variable $A(t_1, t_2-1)$ is the basic value defined as $AAEI(t_1, t_2-1)/7$. The variable C is a constant greater than zero, which adjusts the decreasing percentage of resting. In the design principle, no decreasing is defined when there is no resting. In other words, if a participant exercises every day, the AAEI does not decrease. Increasing constant C decreases the average AAEI, but does not increase the AAEI at the same amount of accumulated physical activity. Parameter α is a coefficient determined by previous accumulated physical activity. The variable W is a constant of attenuation that decreases the influence of previous physical activity. Thus, the greater the value of W , the more the previous accumulated physical activity and days spent exercising affect the exercise expectance. To achieve convergence, the absolute value of W should be less than 1 in Equation 3 in [Figure 1](#). To receive the positive AAEI, the multiplication of k and C to the power of the summation of W to the power of $(i-1)$,

where i goes from 1 to (t_2-t_1) should be less or equal to 7. In this study, for example, we set W at 0.5 causing the influence of previous accumulated physical activity to decrease 50% after 1 day. The variable t indicates the day—zero for today, 1 for yesterday, and so forth. According to the aforementioned conditions, the range of α is between -2 and infinity, and the range of $E(t_2)$ is between $A(t_1, t_2-1) \times C^2$ and zero. The initial condition of the AA EI evaluation process to be set was $AAEI(t_1, t_2)=0$, $E(t_2)=0$, and α was null because there was no physical activity recorded before. The AA EI is useful for evaluation purposes from the first time a person performs physical activity. Because $A(t_1, t_2-i)$ is null the first time to estimate AA EI, parameter α is calculated the first time after physical activity is recorded. In our prototype experiment, the defined parameters $k=1$, $W=0.5$, and $C=2$ are used to examine the performance of the AA EI.

Simulation Model

A simulation model was used to test the long-term performance of the AA EI. Based on the assumption adopted in previous analyses of human dynamics, human behavior comprises temporal statics, which are uniform and stationary. In other words, most human activities can be described using a Poisson process [13-14]. Based on these characteristics, the simulation model simulated participants partaking in exercise of various exercise durations, and the average activity level for each exercise had a Poisson distribution. The distribution of days of the week on which participants exercised was random. Different types of exercise habits were included to simulate the performance of the AA EI.

Real-World Trial

Two participants were recruited to test the AA EI performance in a real-world application. Before the AA EI evaluation, participants estimated their activity levels and exercise duration as inputs of physical activity evaluation process, as shown in Figure 2. Several methodologies were developed to estimate physical activity, such as calorimetry, double-labeled water, questionnaires, and wearable sensors. This study used a triaxial accelerometer (Opal, APDM Inc, Portland, OR, USA) to estimate activity levels because it is inexpensive, accurate, small, objective, sensitive, and suitable for the storing of personal records. Several studies have estimated activity levels by using accelerometers [15-17]. The activity level estimation methodology employed in this study was designed based on that of Liu et al [15]; the experimental results of this study showed high accuracy levels of approximately 80%. The sampling rate of the triaxial accelerometer was 40 Hz. The sensor was worn on the right side of the front of the waist. To reduce any deviation in the estimation of activity level, the exercise tasks were limited to walking, fast walking, and running, and were all performed using a running machine at various velocities. All participants were allowed to perform the tasks within their discretion during the 1-month trial period. The AA EI was estimated once per day.

Results

General Results

The ideal amount and period of physical activity was used as input to illustrate the general performance of the AA EI. A total of 100 metabolic equivalent of task (MET)-minutes were evenly distributed over 1, 3, 5, and 7 day(s) in a week (Table 1) over a period of 4 weeks as shown in Figure 3. The AA EI increased when physical activity increased, did not increase when physical activity was stable, decreased when physical activity decreased, and decreased further if continuous resting occurred. The weekly average of the AA EI over the 4 weeks is shown in Figure 3. The AA EI continued to increase in the first week, but became stable after the second week. The i -day (where $i=1, 3, 5, 7$) averages of the stable AA EI changed because of various resting days. The average percentage of the AA EI on different days of physical activity under

stable conditions is presented in [Figure 4](#).

Simulation Results

Three simulation results are presented to show the long-term performance of the AAEI. Each simulation result included different types of physical activity input to present different exercise conditions. [Figure 5](#) shows the exercise protocol proposed by the World Health Organization (WHO), which recommends exercising 5 days per week, each exercise having a 30-minute duration and 5 MET on average. These recommendations were used as parameters and entered into the simulation model. The simulation model generated an average of 718 MET-minutes per week and 4.8 days spent exercising per week over a year. The average AAEI was 663 for 1 year. The ideal ratio of AAEI to physical activity (ideal AAEI/PA), as shown in [Figure 4](#), was 0.97. The ratio of AAEI to physical activity (AAEI/PA) in the simulation was 0.92. The day line of the AAEI went up and down based on the average AAEI value. The longer-term moving averages showed smoother line changes than the average AAEI value.

Some people perform vigorous physical activity, but only for a short time interval. To simulate this condition, the simulation model set 2 days of exercise per week, each with an average duration of 20 minutes, and an average activity level of 10 MET. The simulation model generated 313 MET-minutes per week and 1.6 days spent exercising per week, on average, over a year. The average AAEI was 254. The ideal AAEI/PA was 0.80 and the AAEI/PA was 0.81. [Figure 6](#) shows the results of the simulation and the AAEI estimate. The day line of the AAEI formed a peak when physical activity was performed and formed a valley when there was a lack of physical activity.

To simulate physical inactivity, the simulation model was set at 2 days spent exercising per week, each with an average duration of 15 minutes and an average of 5 MET as parameters. The simulation model generated an average of 127 MET-minutes per week and 1.5 days spent exercising per week over a year. The average AAEI was 100. The ideal AAEI/PA was 0.78 and the AAEI/PA was 0.79. [Figure 7](#) shows the simulated results; the day line of the AAEI formed a steep shape when continuous resting occurred and the AAEI line was often low and near the zero line.

Real-World Trial Results

A total of 2 participants were recruited to take part in the real-world trial test. The participants' characteristics are listed in [Table 2](#). The recorded physical activity was measured according to observation and activity diaries. Estimated values were measured according to an accelerometer. [Table 3](#) lists the recorded and estimated total physical activity.

The average physical activity and days spent exercising shown in [Figure 8](#) were 275 MET-minutes per week and 1.2 days per week, respectively. The average AAEI was 180, the ideal AAEI/PA ratio was 0.74, and the AAEI/PA was 0.65.

The average physical activity and days spent exercising shown in [Figure 9](#) were 241 MET-minutes per week and 1.6 days per week, respectively. The average AAEI was 174, the ideal AAEI/PA ratio was 0.80, and the AAEI/PA was 0.72.

Discussion

General Performance

The AAEI was determined using the accumulated physical activity and exercise expectance. In our study, the AAEI increased when physical activity increased, did not increase when physical activity was stable, decreased when physical activity decreased, and decreased further if continuous resting occurred. The first week of ideal and periodic inputs increased because the AAEI accumulated from the first 7 days. After the

first week, the AAEI stabilized because of stationary input. Although the amount of physical activity in a week was the same, the AAEI altered on different days spent exercising. The more days participants exercised, the higher the AAEI was. The AAEI was directly proportional to the amount of physical activity accumulated in 7 days. The AAEI was primarily determined using the accumulated amount of physical activity and associated with the number of days spent exercising. The value of the AAEI was decided by accumulated physical activity more than days spent exercising. Exercise expectance, estimated using the previous physical activity status, accumulated physical activity, and number of days spent exercising, would revise the AAEI. Thus, the index usually decreased further when AAEI was high. We encouraged participants whose physical activity was low to be more active, and challenged those who performed large amounts of physical activity. A higher AAEI typically indicated more physical activity and days spent exercising; therefore, the decrease in percentage was more reasonable than fixed reducing. The constant C is used to revise the magnification of exercise expectance. A higher C value decreased the AAEI further in response to physical inactivity, but increased the AAEI little in higher physical activity situations. The setting value of the constant C can influence the average AAEI in general. Parameter k was defined as a fixed number in this study and, therefore, the AAEI directly revealed the status of physical activity. The parameter k was set to 1 because it can directly reveal the accumulated amount of physical activity. However, the setting value of k can differ depending on the status of physical activity in the Web-based application because of encouragement or challenge. The variable W is a constant of attenuation. We set W at 0.5 in this experiment causing the effect of the previous status to attenuate by 50% after each day.

Establishing a Simulation

The moving average AAEI across a range of durations revealed the varying physical activity statuses of the participants across different points in time. The long-term moving average AAEI varied slightly compared with the short-term moving average AAEI. When the short-term moving average AAEI line crossed the long-term line, it indicated that the physical activity of a participant was either higher or lower than before. We observed the index to ascertain whether the physical activity of the participant was increasing or decreasing. The simulation results reveal the phenomenon, but exhibited deviations in the amount by which physical activity decreased. Because the distribution of physical activity was not uniform in the simulation, the AAEI deviated from the estimate. The deviation of the AAEI was within 5% of the ideal situation. In the simulation model, in which the physical activity was the same as that recommended by the WHO, the achievement goal was an AAEI value of 600. If the participant reached the assigned index, he or she was likely to consider that sufficient physical activity had been performed. The other 2 simulation results exhibited insufficient physical activity in various exercise habits. The shape of the AAEI line demonstrates the different habits of the participants. A high and sharp peak of the AAEI line on the graph reveals that the participant partook in vigorous physical activity, but only over a short period. A flat and low shape of the AAEI line indicates the participant was physically inactive. The AAEI value in these 2 cases did not exceed 600; therefore, their physical activity was insufficient. An arc-shaped AAEI line with low, oscillating amplitude located at a high index (greater than 600) indicates that the participant partook in sufficient and regular physical activity. The AAEI can be used as an analysis tool for improving physical activity.

Real-World Trial

The recorded physical activity was measured through observation as well as through analysis of activity diaries, and it generally agreed with the estimated value. Although the level of accuracy of the estimated value seems considerably high, the deviation was slightly compensated by overestimating and underestimating, but it still made it possible to evaluate the AAEI in a real-world application. Both participants were physically inactive in 1 month. Generally, the results of the AAEI demonstrated the

physical activity status. The AAEI increased with increased physical activity and decreased with decreased physical activity. The AAEI decreased gradually, rather than suddenly. However, the deviation of decrease was much higher than in the simulation results, possibly because of nonuniform distribution in the short-term experiment. The AAEI did not immediately provide feedback to the participants and only showed the feasibility of real-world implementation of the AAEI. Based on previous studies [7,9,11], sharing and comparison can motivate people to be more active by increasing their interest in and enjoyment of physical activity. Goal-setting theory is based on the concept that people occasionally require a clearly defined goal to motivate them to achieve. The AAEI is not only an assessment and tracking tool for personal physical activity, but also a goal-setting and achievement-sharing tool in social contexts.

Implementation of the Accumulated Activity Effective Index

Measurement of the level of activity and the energy cost was a fundamental task before the AAEI estimates were made. Therefore, the characteristics of the measurement of activity levels were crucial to the AAEI estimates because measurement of activity level can directly reveal participants' physical activity. If the level of activity can be measured accurately, it can be useful in calculating the AAEI. One can apply preferred activity-monitoring devices and the proposed AAEI to measure physical activity for individual well-being management. Furthermore, the proposed AAEI is also useful for goal setting and for sharing content with the Internet community under the same criterion.

Conclusions

The AAEI is proposed in this paper as a means of evaluating the status of physical activity. It can track personal physical activity, remind the user of his or her achievement goals, and share this information by using the Internet. The AAEI is a simple numeric indication that is estimated by accounting for accumulated physical activity and the average number of days spent exercising. The AAEI records the accumulated physical activity that has been performed in a week and reveals any differences in exercise habits. The moving average presents a long-term value that can be used for assessment purposes. The AAEI fulfills the requirement of prompting physical activity. Based on social aspect theory, the AAEI is a useful tool that can be employed to promote physical activity.

Acknowledgments

This work is supported in part by the Ministry of Science and Technology under Grant number MOST 103-2221-E-010-013-MY2.

Abbreviations

AAEI	accumulated activity effective index
MET	metabolic equivalent of task
PA	physical activity
WHO	World Health Organization

Footnotes

Conflicts of Interest: None declared.

References

1. Hallal PC, Andersen LB, Bull FC, Guthold R, Haskell W, Ekelund U. Global physical activity levels: surveillance progress, pitfalls, and prospects. *The Lancet*. 2012 Jul;380(9838):247–257. doi: 10.1016/S0140-6736(12)60646-1.
2. Kohl HW, Craig CL, Lambert EV, Inoue S, Alkandari JR, Leetongin G, Kahlmeier S. The pandemic of physical inactivity: global action for public health. *The Lancet*. 2012 Jul;380(9838):294–305. doi: 10.1016/S0140-6736(12)60898-8.
3. Andre D, Wolf DL. Recent advances in free-living physical activity monitoring: a review. *J Diabetes Sci Technol*. 2007 Sep;1(5):760–7. <http://europepmc.org/abstract/MED/19885145>. [PMCID: PMC2769664] [PubMed: 19885145]
4. Cotman CW, Berchtold NC, Christie LA. Exercise builds brain health: key roles of growth factor cascades and inflammation. *Trends Neurosci*. 2007 Sep;30(9):464–72. doi: 10.1016/j.tins.2007.06.011. [PubMed: 17765329]
5. Lee I, Shiroma EJ, Lobelo F, Puska P, Blair SN, Katzmarzyk PT. Effect of physical inactivity on major non-communicable diseases worldwide: an analysis of burden of disease and life expectancy. *The Lancet*. 2012 Jul;380(9838):219–229. doi: 10.1016/S0140-6736(12)61031-9. [PMCID: PMC3645500]
6. Alemdar H, Ersoy C. Wireless sensor networks for healthcare: A survey. *Computer Networks*. 2010 Oct;54(15):2688–2710. doi: 10.1016/j.comnet.2010.05.003.
7. Lin RJ, Ramakrishnan S, Chang H, Spraragen S, Zhu X. Designing a web-based behavior motivation tool for healthcare compliance. *Hum. Factors Man*. 2012 Jun 25;23(1):58–67. doi: 10.1002/hfm.20519.
8. Maitland J, Sherwood S, Barkhuus L, Anderson I, Hall M, Brown B, Chalmers M, Muller H. Increasing the awareness of daily activity levels with pervasive computing. *Pervasive Health Conference and Workshops*; Nov 29–Dec 1, 2006; Innsbruck. 2006. pp. 1–9.
9. Anderson Ian, Maitland J, Sherwood S, Barkhuus L, Chalmers M, Hall M, Brown B, Muller H. Shakra: tracking and sharing daily activity levels with unaugmented mobile phones. *Mobile Netw Appl*. 2007 Aug 3;12(2-3):185–199. doi: 10.1007/s11036-007-0011-7.
10. Tudor-Locke C, Bassett DR, Swartz AM, Strath SJ, Parr BB, Reis JP, Dubose KD, Ainsworth BE. A preliminary study of one year of pedometer self-monitoring. *Ann Behav Med*. 2004 Dec;28(3):158–62. doi: 10.1207/s15324796abm2803_3. [PubMed: 15576253]
11. Frederick-Recascino CM, Schuster-Smith H. Competition and intrinsic motivation in physical activity: a comparison of two groups. *Journal of Sport Behavior*. 2003;26(3):240–254.
12. Anderson ES, Wojcik JR, Winett RA, Williams DM. Social-cognitive determinants of physical activity: the influence of social support, self-efficacy, outcome expectations, and self-regulation among participants in a church-based health promotion study. *Health Psychol*. 2006 Jul;25(4):510–20. doi: 10.1037/0278-6133.25.4.510. [PubMed: 16846326]
13. Zhou T, Han XP, Wang BH. Towards the understanding of human dynamics. In: Burguete M, editor. *Science Matters: Humanities As Complex Systems*. Singapore: World Scientific Publishing Company; 2008.
14. Chiang C-Y, Hsu SJ, Chan C-T. A resident's behavior simulation model for nursing home healthcare services. *Bio-Medical Materials and Engineering*. 2014;24:69–75. doi: 10.3233/BME-130785. [PubMed: 24211884]
15. Liu CT, Hsu SJ, Chan CT. Activity recognition and activity level estimation for context-based

prompting system of mild cognitive impairment patients. 11th International Conference on Smart Homes and Health Telematics, ICOST 2013; June 19-21, 2013; Singapore. 2013. pp. 53–60.

16. Wu W, Dasgupta S, Ramirez EE, Peterson C, Norman GJ. Classification accuracies of physical activities using smartphone motion sensors. *J Med Internet Res.* 2012;14(5):e130. doi: 10.2196/jmir.2208. <http://www.jmir.org/2012/5/e130/> [PMCID: PMC3510774] [PubMed: 23041431]

17. Bexelius C, Sandin S, Trolle Lagerros Y, Litton JE, Löf M. Estimation of physical activity levels using cell phone questionnaires: a comparison with accelerometry for evaluation of between-subject and within-subject variations. *J Med Internet Res.* 2011;13(3):e70. doi: 10.2196/jmir.1686. <http://www.jmir.org/2011/3/e70/> [PMCID: PMC3222159] [PubMed: 21946080]

Figures and Tables

Figure 1

Equations:

$$AAEI(t_1, t_2) = AAEI(t_1, t_2 - 1) + k \times [MT(t_2) - E(t_2)] \quad (1)$$

$$E(t_2) = A(t_1, t_2 - 1) \times C^{-\alpha} \quad (2)$$

$$\alpha = \sum_{i=1}^{t_2-t_1} \frac{MT(t_2 - i) - A(t_1, t_2 - i)}{A(t_1, t_2 - i)} \times W^{(i-1)} \quad (3)$$

Parameters:

AAEI: $AAEI \geq 0$, an index	(t_1, t_2) : time interval from t_1 to t_2 , unit: day
k: $k > 0$, a constant defined as 1	MT(t_2): $MT(t_2) \geq 0$, activity level multiple duration in day t_2
E(t_2): $E(t_2) \geq 0$, exercise expectation	A($t_1, t_2 - 1$): $AAEI(t_1, t_2 - 1) / 7$
C: $C > 0$, a constant defined as 2	α: $-2 \leq \alpha < \infty$, a coefficient estimated by accumulated physical activity
i: i-th days before	W: $0 < W < 1$, a constant of attenuation defined as 0.5

The accumulated activity effective index (AAEI) parameters and equations for the evaluating process (equation 1) and exercise expectance (equations 2 and 3).

Figure 2



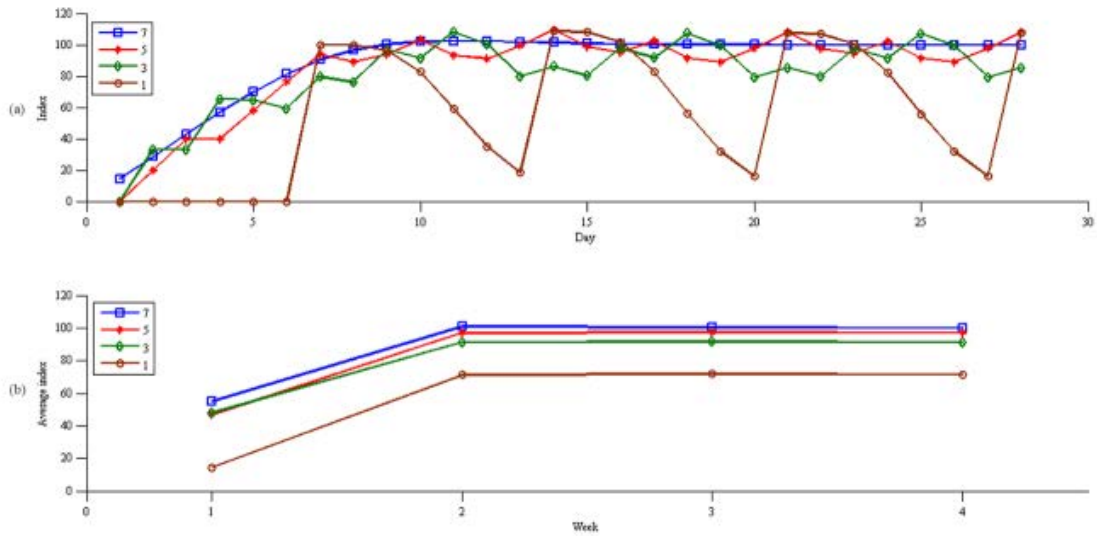
The process in a real-world trial. The first stage was activity level estimation. The second stage was AAEI estimation. The sensor data translated to activity level in first stage and then converted to AAEI in second stage.

Table 1

Input distribution of ideal and periodic physical activity in a week.

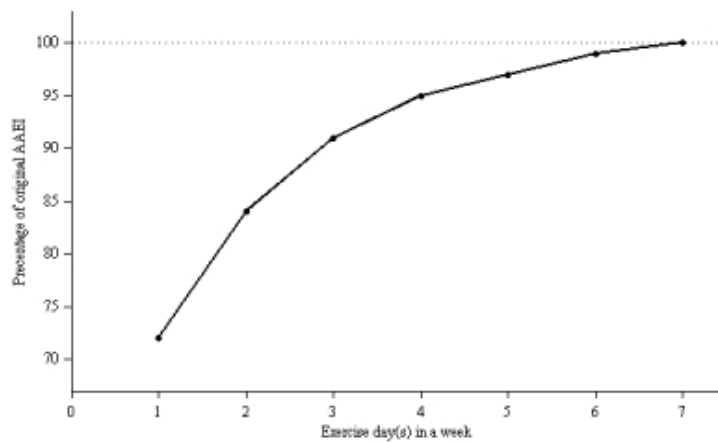
Exercise days per week	Input (MET-minutes)						
	Day 1	Day 2	Day 3	Day 4	Day 5	Day 6	Day 7
1	0	0	0	0	0	0	100
3	0	33.3	0	33.3	0	0	33.3
5	0	20	20	0	20	20	20
7	14.3	14.3	14.3	14.3	14.3	14.3	14.3

Figure 3



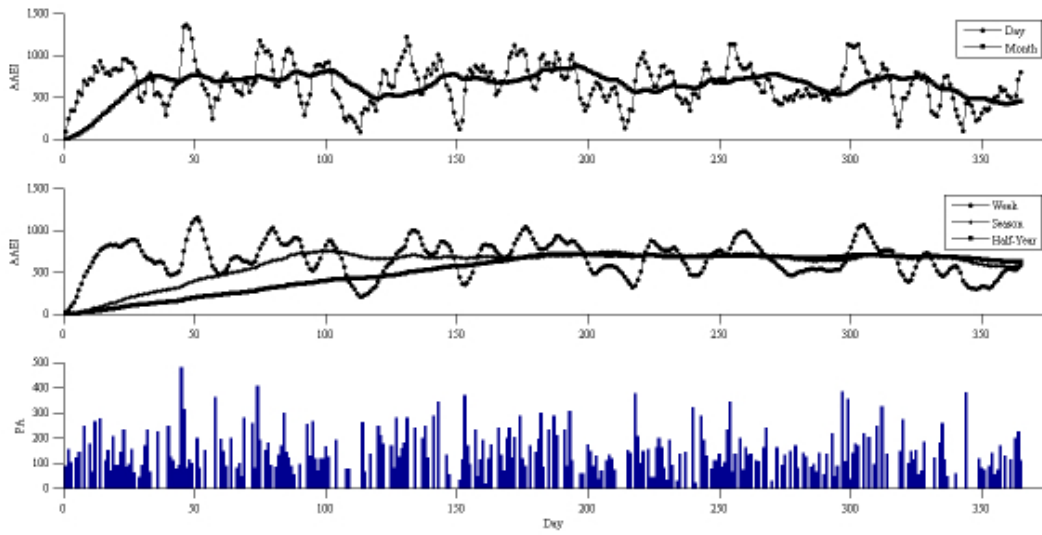
(a) AAEI of ideal and periodic physical activity input and (b) week average of AAEI.

Figure 4



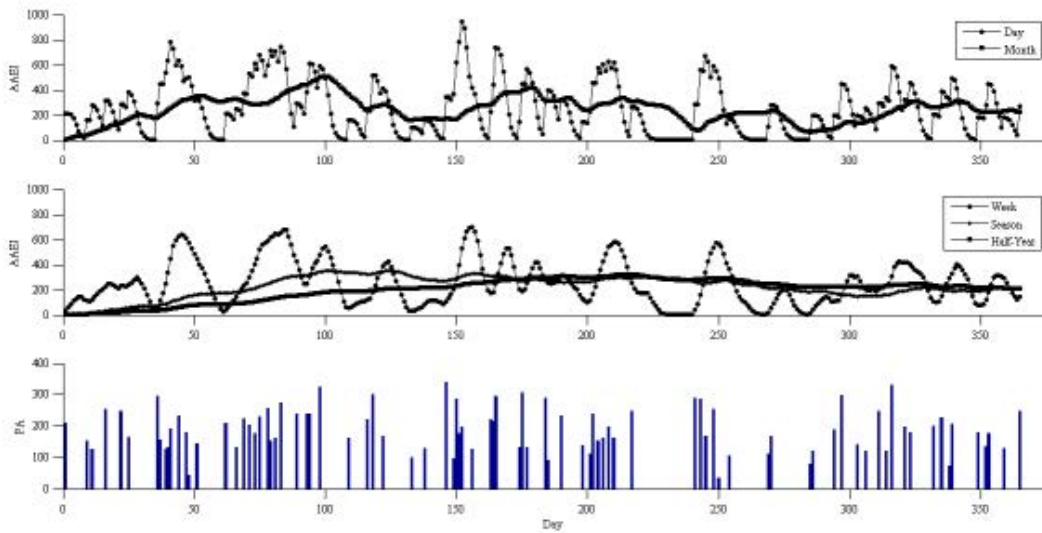
Average percentage of AAEI for different exercise days per week in an ideal situation.

Figure 5



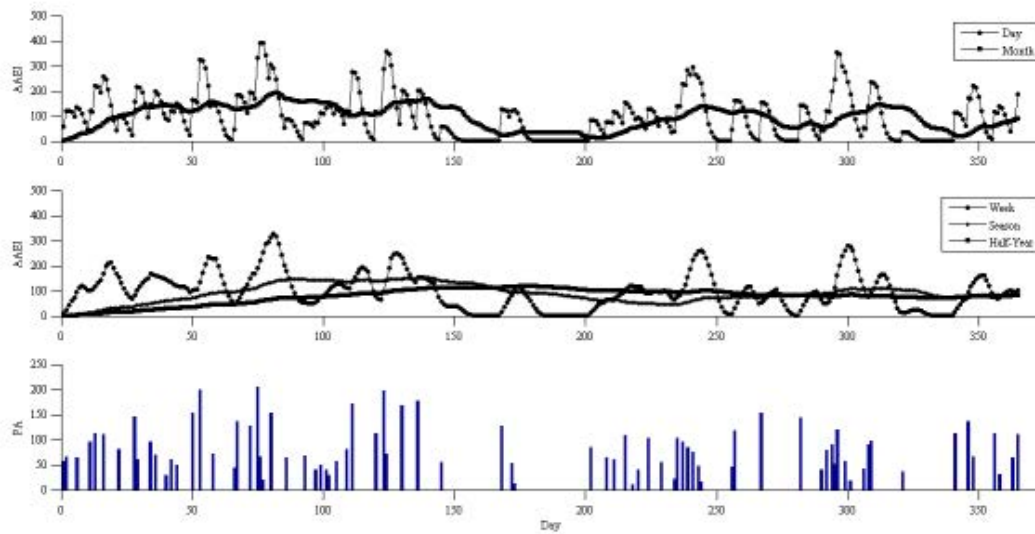
AAEI/PA simulation results with input of 5 days per week, duration of 30 minutes, and 5 MET.

Figure 6



AAEI/PA simulation results with input of 2 days per week, duration of 20 minutes, and 10 MET.

Figure 7



AAEI/PA simulation results with input of 2 days per week, duration of 15 minutes, and 5 MET.

Table 2

Participant characteristics (N=2).

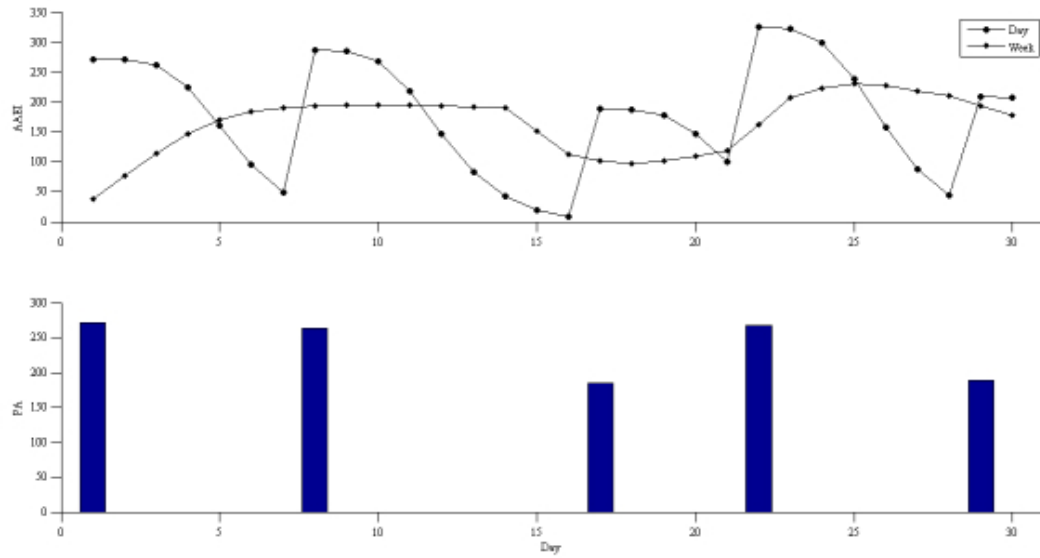
Variables	Participant 1	Participant 2
Gender	Male	Male
Age (years)	24	23
Body mass index	21.4	22.3
Medical status	Healthy	Healthy

Table 3

Result of total recorded physical activity and total estimated physical activity.

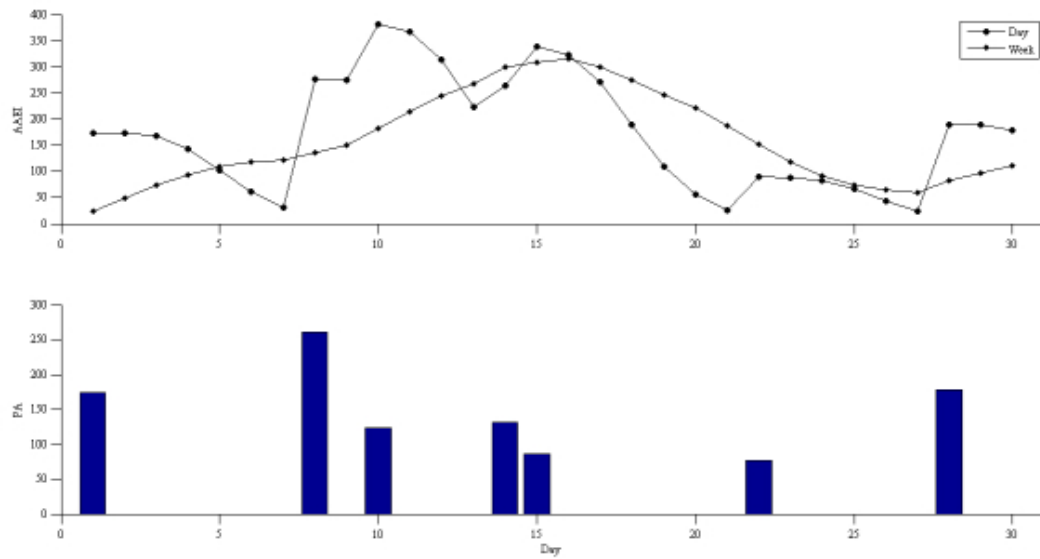
Participant	Total recorded value (MET-minutes)	Total estimated value (MET-minutes)	Ratio
Participant 1	1211	1178	0.973
Participant 2	945	1031	1.057

Figure 8



AAEI with physical activity (PA) of participant 1.

Figure 9



AAEI with physical activity (PA) of participant 2.

Swimming motion analysis: 3D joints kinematics of the upper limb using wearable inertial and magnetic sensors

Validation through dry-land simulations

Magalhães F.A.¹, Giovanardi A.², Di Michele R.³, Cortesi M.⁴, Gatta G.⁴, Fantozzi S.⁵

¹Dept. of Electrical, Electronic, and Information Engineering, University of Bologna, Bologna, Italy

²School of Pharmacy, Biotechnology and Sport Science, University of Bologna, Bologna, Italy

³Dept. of Biomedical and Neuromotor Sciences, University of Bologna, Bologna, Italy

⁴Dept. for Life Quality Studies, University of Bologna, Bologna, Italy

⁵Health Sciences and Technologies - Interdepartmental Center for Industrial Research, University of Bologna, Bologna, Italy, silvia.fantozzi@unibo.it

Abstract- The analysis of the joint kinematics during swimming plays a fundamental role both for sports conditioning and in clinical contexts. A protocol originally designed to perform the 3D kinematic analysis of the upper limbs during simple motor tasks was modified to be used in a sports setting. The performance of the modified protocol was evaluated in laboratory during simulated swimming trials performed by nine swimmers. A stereophotogrammetric system was used as gold standard. Considering both front crawl and breaststroke swimming styles and all joint degrees of freedom modeled (shoulder, elbow and wrist), the protocol implemented showed an accuracy adequate for the purposes of the research (median values of RMSE, CMC and R were 7°, 0.95 and 0.95, respectively).

Keywords- *swimming; inertial and magnetic sensors; upper limb; 3D joint kinematics*

1. INTRODUCTION

The analysis of 3D joint kinematics during swimming plays a major role for both the sports conditioning and clinical contexts. In the first case, the identification of key biomechanical factors that lead to the best propulsive efficiency is the basis for performance enhancement as well as to get valuable information for didactical purposes. In the second case, a kinematic assessment of the swimming technique would be an important tool to detect altered movement patterns that can lead to an injury or that are related to previous injuries.

To acquire swimming kinematics of the upper limbs, underwater cameras are typically used. Traditionally, markers are drawn on the skin of the swimmer and tracked [1,2]. Alternatively, a markerless approach was recently exploited [3]. However in both cases, only the 3D position of the anatomical landmarks and 2D angles were analyzed. To the knowledge of the present authors, only one study using video analysis focused on 3D joint kinematics of the shoulder and elbow during front-crawl swimming [4]. Nevertheless, all studies based on video analysis have a number of drawbacks, including the analysis being limited to underwater phases and to a single stroke due to the limited field of view (strictly associated with the number of cameras). In addition, long installation and calibration procedures, and long elaboration time are required even when an automatic tracking procedure is used [5]. Finally, quantitative video analysis can only be performed off-line, and thus it cannot be used by coaches during training sessions to make direct feedbacks about the swimming technique.

To overcome the limits of video analysis, in the last ten years, wearable inertial-magnetic measurements units (IMMUs) were exploited for the kinematic analysis of swimming. These devices, being directly fixed on the swimmer, allow a continuous data acquisition during the whole swim. Furthermore, they require a simple measurement set-up and have the potentiality to provide coaches with online performance parameters during training sessions. In literature, swimming phases, stroke frequency, time parameters, velocity profile were measured using IMMUs and validated against appropriate measurement systems [6]. More recently, sets of sensors were applied to the swimmer, on wrists, lower back, arms or legs, in order to better estimate kinematic variables referred to various body segments [7-9]. However, to the knowledge of the present authors, none of the previous studies investigated the 3D kinematics of upper limbs joints during swimming, and there are no protocols specifically designed for this kind of sports setting.

The protocols previously proposed for upper limb kinematics using inertial sensors were validated in ambulatory settings, for simple and slow movements [10-12], and thus must be extended to the sports context in order to be used for kinematic analysis of swimming. Among the different solutions available, the protocol proposed by Cutti et al. [11] was chosen for the main following reasons: (1) It was specifically designed for

being implemented with IMMUs; (2) It is suitable and accurate as a stereophotogrammetric system for the estimation of the 3D joint angles kinematics of the upper limb (shoulder, scapula, elbow) in a clinical context; (3) It can be adapted to use different IMMU systems capable to compute the orientation of the IMMUs with respect to a fixed, global system of reference; (4) It can be adapted for the use in sports contexts; (5) It has a simple and quick set-up in the acquisition phase as it requires only three calibration trials.

Therefore, the aim of the present study was to adapt the protocol proposed by Cutti et al. [11] to the swimming context, extending the kinematics analysis also to the wrist joint, and to validate the protocol in dry-land conditions using the stereo-photogrammetry as gold standard.

2. MATERIAL AND METHODS

Protocol

From a biomechanical point of view, each side was modeled as an open kinematic chain constituted by thorax, upper-arm, forearm and hand with 7 degrees of freedom. Similarly to the representation described by Cutti et al. [11], the shoulder was considered as the ball-and-socket joint between thorax and arm, while the elbow was considered as the double-hinge joint (with non-intersecting axes) between arm and forearm. The newly introduced wrist joint was modeled as the double-hinge joint formed by forearm and hand.

For each segment that formed 2 joints, both a proximal and a distal embedded anatomical reference systems (ARSs) were defined. ARSs definitions introduced by Cutti et al. [11] was adopted apart from the facts that: (1) the static calibration acquired for the definition of the thorax ARS was performed with the subject lying still, because the orientation estimation of the IMMUs was demonstrated to be more accurate in such a position; (2) the proximal forearm ARS was rotated of -90° along the Y-axis because the elbow joint during swimming is almost completely pronated in many phases of a stroke; (3) the ARS of the hand was assumed to be aligned with the distal forearm ARS during the static calibration trial. The positioning of IMMUs on body segments is shown in fig. 1 (left). The sensor on the thorax was fixed by aligning the X-axis to the longitudinal axis of the flat portion of the sternum, since the orientation of the X-axis of the IMMU is directly used for the computation of the thorax ASOR. The sensor on the humerus was fixed laterally, in order both to allow the swimmer a natural swim style, and to maximally reduce the soft tissue artifacts, thus over the central third of the humerus, slightly posterior to it [11]. The sensor on the forearm was fixed over the distal flat surface of radius and ulna, with the IMMU Z-axis pointing away from the wrist. The sensor on the hand was fixed over its dorsum, with the IMMU Z-axis pointing away from the hand.



Figure 1. Left: inertial and IMMUs positioning on body segments detailing the anatomical system of reference axes. Right: lateral and anterior views during front crawl simulation.

The protocol required three types of calibration tasks. A static trial in which the subject lied on a table keeping his arms alongside the body, and at the same time holding the dorsum of the hands aligned to the upper side of the forearms. The second and third calibration tasks were dynamic trials in which the subject was standing, and had to perform: (1) a flexion-extension of the elbow, from about 10° to 130° of flexion, keeping a constant pronation-supination (2) a full-range pronation-supination of the elbow, keeping a constant flexion-extension. In both the cases, the number of arm-stroke cycles to collect for each task was conventionally set equal to 5, 3 tasks should have been acquired, and very fast or very slow movement were not advisable.

All the axes of rotation of the elbow were modeled as mean helical axes, and computed using the algorithm defined by Woltring et al. [13]. At the end of this process, each ARS is known with respect to the corresponding IMMU technical system of reference, and can be computed frame by frame for each dynamic task. The joint angles were processed then by decomposing the relative orientation of adjacent segments. The shoulder flexion-extension, intra-extra rotation and abduction-adduction were calculated using the 'XY'Z'

Euler sequence; the elbow flexion-extension and pronation-supination were calculated using the XZ'Y'' Euler sequence; the wrists flexion-extension and ulnar-radial deviation were calculated using the XY'Z'' Euler sequence. The Euler sequence used for the shoulders was different from the one proposed by Cutti et al. [11]. The XY'Z'' sequence was chosen because it better represents the kinematics of the shoulder when it performs wide movements, and when these movements are not performed mainly around just one axis of rotation (i.e. pure flexion-extension), as usually happens in a clinical context. The carrying angle of the elbow (rotation around Z' axis) and the hypothetical internal-external rotation angle of the wrist (rotation around Y' axis) were not considered, according to the joint model adopted.

Test Validation

This test aimed to evaluate the 3D joint kinematic analysis of the upper limbs during swimming simulations using an IMMU system (Opal, APDM, Portland, Oregon, USA, 7 nodes, 128Hz). To this aim, a stereophotogrammetric system (SMART-DX 7000, BTS Bioengineering, Italy, 7 cameras, 250Hz) was used as the gold standard system. In order to be able to compare kinematic data estimated from both the IMMU and the stereophotogrammetric system, seven clusters were built and firmly fixed onto the swimmer's body. Each cluster was made of a rigid light-weighted wooden plate (width 8cm x length 15cm x depth 1cm) containing one IMMU and four retro-reflective passive markers (10 mm diameters)

Nine male swimmers (Age: 27.1 ± 0.6 years; Height 180.4 ± 5.2 cm; Weight 76.4 ± 6.2 Kg; Training 10.7 ± 3.6 years) agreed to participate and freely signed the informed consent. The inclusion criteria were the following: (1) a swimming experience at least in regional competitions; (2) no recent musculoskeletal injuries; and (3) no pain feel before or during the tests. Regarding the swimming style, 56% of the participants were specialized in the front crawl, 33% in the breaststroke and 11% in the butterfly. Concerning the swimming level, 78% of the participants were either current or former professionals, while 22% were amateurs. The swimmers were asked to swim in the same way they would have done in a swimming pool (fig.1 Right). For each trial, 10 arm-strokes cycles were requested but the participants could stop the test if they felt pain or tiredness. The main number of arm-strokes cycles was 7, so about 40 complete arm-strokes cycles were available for each swim style (front crawl and breast stroke) and for each athlete.

Data Analysis

For the computation of the orientation of each unit with respect to the global system of reference and thus of the ARSs, three Kalman-based algorithms were examined: (1) one from the Motion Studio software provided by the APDM (KBE), (2) one presented by Madgwick et al. [14] with a value of gain fixed (KMA) in all the trials, and (3) one presented by Madgwick et al. [14] with different values of gain (KMB) optimized for three different examined trials: calibration, front crawl and breaststroke. Descriptive statistics was used to summarize the characteristics of the participants. The performance of the IMMU and the SPS during simulated swimming in laboratory were compared for each joint and degree of freedom by means of root mean square error (RMSE), Pearson product-moment correlation coefficient (R), coefficient of multiple correlation (CMC) [15]. The analyses were performed using the R statistical software (version 3.0.1).

3. RESULTS

For the front crawl, the CMC was 0.94 (0.07) for KMA, 0.96 (0.06) for KMB and 0.87 (0.43) for KBE; for the breaststroke, the CMC was 0.98 (0.04), 0.98 (0.06) and 0.93 (0.25) for KMA, KMB and KBE, respectively. In both front crawl and breaststroke, as expected, the KMB showed slightly higher CMC values than the KMA, and definitely higher CMC values than the KBE. Therefore, the KMB optimized algorithm was used. Overall, there were no significant differences between the left and right sides in both front crawl and breaststroke for both the examined indices.

Analyzing the front crawl, the results showed: 1) the median value of RMSE was equal to 7.42 degrees, ranging from 3.25 degrees for the wrist ulnar-radial deviation to 14.65 degrees for the elbow flexion-extension; 2) the median value of CMC was equal to 0.95, ranging from 0.88 for the wrist ulnar-radial deviation to 0.99 for the shoulder flexion-extension, and for the internal and external rotation; 3) the median value of R was equal to 0.95, ranging from 0.90 for the wrist ulnar-radial deviation to 0.99 for the shoulder flexion-extension. Concerning the breaststroke style, the following results were found: 1) the median value of RMSE was equal to 5.39 degrees, ranging from 3.41 degrees for the shoulder internal-external rotation to 8.55 degrees for the elbow flexion-extension; 2) the median value of CMC was equal to 0.99, ranging from 0.92 for the wrist ulnar-radial deviation to 0.99 for the shoulder flexion-extension, for the abduction-adduction, for the internal and external rotation, and for the elbow flexion-extension; 3) the median value of R was equal to 0.99, ranging from 0.94 for the wrist ulnar-radial deviation to 1.00 for the shoulder flexion-extension and for the abduction-adduction. An example of the shoulder joint angles are shown in fig.2.

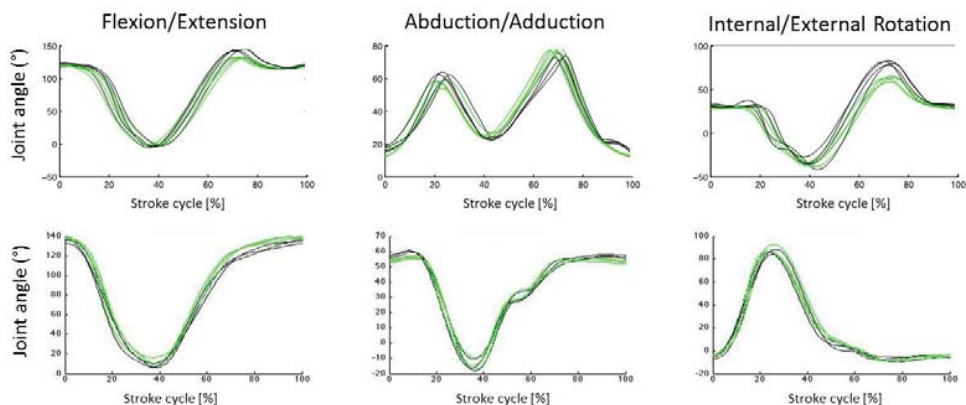


Figure 2. Shoulder joint angles estimated using IMMUs (black line) and stereophotogrammetric system (green line) for front crawl (top) and breaststroke (bottom).

4. DISCUSSION

In laboratory, simulated swimming trials were carried out in dry-land conditions, recorded by an inertial and magnetic measurement units system and simultaneously by a stereophotogrammetric system. The use of simulated arm-strokes in laboratory was chosen because: (1) it allows a better control of all procedures, (2) the gold standard is more accurate than conventional underwater video-camera systems, and (3) the complete swimming stroke cycle can be recorded, including the aerial or recovery phase. An effective movement of the trunk and upper limbs during the aerial phase is essential to place correctly the hand to use it as a rudder during the propulsive phases. Considering both the front crawl and breaststroke swimming styles and all the joint degrees of freedom modeled, the comparison between the gold standard and the inertial sensor system showed median values of RMSE (about 7°), low enough for the purposes of research, high median values of CMC (0.95), and high median values of R (0.95). Thus, the protocol implemented correctly estimated the 3D orientation of the shoulder, elbow and wrist joints during swimming with accuracy adequate for the purposes.

5. REFERENCES

- [1] McCabe, C.B., Psycharakis, S., Sanders, R., 2011. Kinematic differences between front crawl sprint and distance swimmers at sprint pace. *J Sports Sci* 29, 115-123.
- [2] P. Figueiredo, P., Sanders, R., Gorski, T., Vilas-Boas, J.P., Fernandes, R.J., 2013. Kinematic and electromyographic changes during 200m front crawl at race pace. *Int J Sports Med*, 34, 49-55.
- [3] Ceseracciu, E., Sawacha, Z., Fantozzi, S., Cortesi, M., Gatta, G., Corazza, S., Cobelli, C., 2011. Markerless analysis of front crawl swimming. *J Biomech* 44, 2236-2242.
- [4] Ceccon, S., Ceseracciu, E., Sawacha, Z., Gatta, G., Cortesi, M., Cobelli, C., Fantozzi, S., 2013. Motion analysis of front crawl swimming applying CAST technique by means of automatic tracking. *J Sports Sci* 31, 276-871.
- [5] Magalhaes, F.A., Sawacha, Z., Di Michele, R., Cortesi, M., Gatta, G., Fantozzi, S., 2013. Effectiveness of an automatic tracking software in underwater motion analysis. *J Sports Sci Med*. 12, 660-667.
- [6] Ohgi, Y., Ichikawa, H., Miyaji, C., 2002. Microcomputer-based acceleration sensor device for swimming stroke monitoring. *JSME Int J Series C Mech Syst, Mach Elem & Manufac*, 45, 960-966.
- [7] Bächlin, M., Tröster, G., 2012. Swimming performance and technique evaluation with wearable acceleration sensors. *Perv Mobile Comput*, 1574-1192.
- [8] Dadashi, F., Crettenand, F., Millet, G.P. et al., 2013. Automatic front-crawl temporal phase detection using adaptive filtering of inertial signals. *J Sports Sci* 31, 1251-60.
- [9] Hagem, R.M., Thiel, D.V., O'Keefe, S. et al., 2013. Real-time swimmers' feedback based on smart infrared (SSIR) optical wireless sensor. *Electr Lett* 49, 340-341.
- [10] Luinge, H., Veltink P., Baten C., 2007. Ambulatory measurement of arm orientation. *J Biomech* 40, 78-85.
- [11] Cutti, A.G., Giovanardi, A., Rocchi L., Davalli, A., Sacchetti R., 2008. Ambulatory measurement of shoulder and elbow kinematics through inertial and magnetic sensors. *Med Biol Eng Comp* 46, 169-178.
- [12] Picerno, P., Cereatti A., Cappozzo, A., 2008. Joint kinematics estimate using wearable inertial and magnetic sensing modules. *Gait & Post* 28, 588-595.
- [13] Woltring, H.J., Long, K., Osterbauer, P.J., Fuhr, A.W., 1994. Instantaneous helical axis estimation from 3-D video data in neck kinematics for whiplash diagnostics. *J Biomech* 27, 1415-1432.
- [14] Madgwick, S.O.H., Harrison, A.J.L., Vaidyanathan, R., 2011. Estimation of IMU and MARG orientation using a gradient descent algorithm, *IEEE International Conference on Rehabilitation Robotics*. IEEE, Zurich, Switzerland, pp. 1-7.
- [15] Ferrari, A., Cutti, A.G., Cappello, A., 2010. A new formulation of the coefficient of multiple correlation to assess the similarity of waveforms measured synchronously by different motion analysis protocols. *Gait & Post* 31, 540-542.



Visuospatial Tasks Affect Locomotor Control More than Nonspatial Tasks in Older People

Jasmine C. Menant^{1,2*}, Daina L. Sturnieks^{1,2}, Matthew A. D. Brodie¹, Stuart T. Smith^{1,3}, Stephen R. Lord^{1,2}

1 Falls and Balance Research Group, Neuroscience Research Australia, Sydney, Australia, **2** Faculty of Medicine, University of New South Wales, Sydney, Australia, **3** Faculty of Health Science, University of Tasmania, Launceston, Australia

Abstract

Background: Previous research has shown that visuospatial processing requiring working memory is particularly important for balance control during standing and stepping, and that limited spatial encoding contributes to increased interference in postural control dual tasks. However, visuospatial involvement during locomotion has not been directly determined. This study examined the effects of a visuospatial cognitive task versus a nonspatial cognitive task on gait speed, smoothness and variability in older people, while controlling for task difficulty.

Methods: Thirty-six people aged ≥ 75 years performed three walking trials along a 20 m walkway under the following conditions: (i) an easy nonspatial task; (ii) a difficult nonspatial task; (iii) an easy visuospatial task; and (iv) a difficult visuospatial task. Gait parameters were computed from a tri-axial accelerometer attached to the sacrum. The cognitive task response times and percentage of correct answers during walking and seated trials were also computed.

Results: No significant differences in either cognitive task type error rates or response times were evident in the seated conditions, indicating equivalent task difficulty. In the walking trials, participants responded faster to the visuospatial tasks than the nonspatial tasks but at the cost of making significantly more cognitive task errors. Participants also walked slower, took shorter steps, had greater step time variability and less smooth pelvis accelerations when concurrently performing the visuospatial tasks compared with the nonspatial tasks and when performing the difficult compared with the easy cognitive tasks.

Conclusions: Compared with nonspatial cognitive tasks, visuospatial cognitive tasks led to a slower, more variable and less smooth gait pattern. These findings suggest that visuospatial processing might share common networks with locomotor control, further supporting the hypothesis that gait changes during dual task paradigms are not simply due to limited attentional resources but to competition for common networks for spatial information encoding.

Citation: Menant JC, Sturnieks DL, Brodie MAD, Smith ST, Lord SR (2014) Visuospatial Tasks Affect Locomotor Control More than Nonspatial Tasks in Older People. PLoS ONE 9(10): e109802. doi:10.1371/journal.pone.0109802

Editor: Karen Lidzba, University Children's Hospital Tuebingen, Germany

Received: January 21, 2014; **Accepted:** September 13, 2014; **Published:** October 6, 2014

Copyright: © 2014 Menant et al. This is an open-access article distributed under the terms of the Creative Commons Attribution License, which permits unrestricted use, distribution, and reproduction in any medium, provided the original author and source are credited.

Funding: This work was supported by the National Health and Medical Research Council of Australia, Program Grant 350833, Partnership Grant 568975 and Capacity Building Grant 568940. The funders had no role in study design, data collection and analysis, decision to publish, or preparation of the manuscript.

Competing Interests: The authors have declared that no competing interests exist.

* Email: j.menant@neura.edu.au

Introduction

Dual task studies requiring individuals to simultaneously perform cognitive and balance tasks have shown that performance in either or both tasks is compromised [1,2], and that this interference is more marked in those with reduced sensorimotor and/or cognitive functioning due to age and disease [1,2]. These findings suggest that balance control requires higher-level cognitive functioning to selectively process information (attention) and actively maintain and manipulate it (working memory) [3].

Two models have been proposed to explain the interference between balance and secondary cognitive tasks [1]: the general capacity sharing/limited attentional resources model; and the more specific bottleneck model whereby both the primary balance task and the secondary cognitive task concurrently require similar networks. Concurrent motor timing tasks provide an example of bottleneck processing; e.g. performance of an eye blink classical conditioning task is disrupted by concurrent finger tapping,

another task requiring cerebellar processing, but not by a recognition task [4]. Some previous studies have contrasted the effects of visuospatial (VS) and nonspatial (NS) cognitive tasks on balance as a means of determining which of the two models is more apt in this context. Secondary VS cognitive tasks have been shown to reduce balance control during standing and stepping more than NS cognitive tasks in several [4–12], but not all [13] previous studies. Potential factors that might have contributed to these conflicting findings include the set order of administration of the cognitive tasks [8,9], unequal secondary task difficulty [7,9,10,13] and the inconsistent requirement of articulatory responses across trials [8,9] (a motor task that can detrimentally affect postural control) [14].

There is also some evidence that impaired VS processing is associated with gait instability and falls. Increased dual task cost of walking while completing a VS decision reaction time task was more strongly associated with recurrent falls than a simple reaction-time task to an auditory stimulus in 377 older people

[15]. In another large sample of healthy older adults, poor performance in a VS pen and paper test was significantly and independently associated with increased double-support phase variability during gait [16], as well as with increased risk of multiple falls [17]. In Parkinson's disease patients with mild cognitive impairment, impaired VS processing has been shown to be significantly associated with gait instability [18]. VS processing impairments have also been associated with stepping arrhythmicity and asymmetry in people with Parkinson's disease [19], and in contrast to tests of executive functioning, differentiate between freezers and non-freezers [19]. However, only one of the above studies has directly contrasted the effects of VS versus NS secondary tasks on gait parameters [10], and it is possible the differential effects reported may not be attributable to differences in the task type, as the difficulty of the secondary tasks were not examined or controlled for.

The aim of the present study was to compare the effects of VS and NS cognitive tasks on temporo-spatial gait parameters, smoothness and variability in older people while controlling for task difficulty. We hypothesized that if the control of walking is dependent upon VS working memory processing, walking while performing a cognitive task that requires VS processing, will disrupt one or both tasks (i.e. the bottleneck model) more so than a NS arithmetic task. While both VS and NS tasks call upon a central executive, we used the VS star-movement task [11] to involve the VS sketch pad of working memory (VS task) and a series of single digit additions and subtractions to place demands on the phonological store of working memory (NS task). Determining any differential effects of VS and NS dual tasks may provide insight into cognitive processing pathways utilized in the control of locomotion. Further, given that falls in older people frequently occur while walking [20], understanding the relative importance of secondary cognitive task types in influencing locomotor control has implications for fall risk assessments.

Methods

Ethics Statement

The study was conducted in accordance with the Declaration of Helsinki and was approved by the Human Research Ethics Committee at the University of New South Wales. Written informed consent was obtained from all participants prior to commencing the study.

Participants

Thirty-six older people (18 males; mean (SD) age: 81.4 (3.5) years) volunteered to participate in this study. All lived independently in the community and were part of a larger prospective study of falls, for which they were recruited via random selection from the electoral roll (Sydney Memory & Ageing Study) [21]. Participants had a mean Mini-Mental State Examination (MMSE) [22] score of 28.9 (SD = 1.4), were independent in activities of daily living and were able to walk 400 m without assistance. The participants had on average 14.0 (3.6) years of education. Four participants had fallen two times or more in the 12 months preceding the assessment. The exclusion criteria were medical or psychological conditions that may have prevented participants from completing assessments, i.e. a previous diagnosis of dementia or developmental disability, psychotic symptoms, Parkinson's disease, multiple sclerosis, motor neuron disease and central nervous system inflammation.

Experimental set-up

Participants completed a series of three walking trials at self-selected speed along a 20-m long walkway under four conditions presented in a block-randomised order: 1) with an easy arithmetic task (NS-easy); 2) with a difficult arithmetic task (NS-diff); 3) with an easy VS task (VS-easy); and 4) with a difficult VS task (VS-diff). Participants also performed three walking trials with no cognitive task for reference purposes. The cognitive task instructions were delivered through headphones; the instruction durations were as follows: NS-easy 4.7 s, NS-diff 6.3 s, VS-easy 7.4 s, VS-diff 8.5 s. These differences are largely due to a longer (non-informative) lead in time in the VS tasks (i.e. "the star starts in box ..."), which took 2.8 s, and no lead in time ahead of the first piece of information in the NS tasks, that being the first number of the sum (i.e. "three plus four plus one"). Instructions were given continuously throughout the walking trial; that is, a new instruction was delivered within a second of the participant answering the previous question. This procedure was identical for all dual task trials and ensured that regardless of their walking speed, participants were cognitively engaged throughout the trial. Participants were instructed to "keep walking normally" and to "give the answers as quickly as possible". Participants also completed three seated 30 s trials for each cognitive task condition that were randomly presented amongst the blocks of walking trials.

Cognitive tasks conditions

Visuospatial tasks. The VS star movement task has been previously described [11]. In brief, the VS-easy task involved participants envisaging three boxes side by side labelled A, B and C. Participants were shown the empty boxes on a visual display during the explanation of the protocol and were asked to visualise a star located in one of the boxes making three movements. They were then allowed sufficient practice with and then without the visual display until they demonstrated that they understood the test requirements and scored three consecutive correct responses. Pre-recorded instructions delivered the random starting position and the direction of the three movements, i.e. left or right. In the VS-diff task, participants were asked to visualise the star moving among four boxes arranged in a square. The pre-recorded instructions delivered the random starting position and four movements of the star, which comprised up, down, left, right and diagonal moves. As with the VS-easy task, participants practiced the task initially with and then without a visual aid.

Nonspatial tasks. The NS-easy task required participants to sum three single digit numerals. The NS-diff task involved a calculation of four single digit numerals comprising both additions and subtractions (but with a running total that was always >0). Participants practiced both easy and difficult NS tasks before commencing the data collection trials.

As the main purpose of our study was to compare the effects of different types of secondary cognitive tasks (VS versus NS) on gait parameters, the secondary tasks selected required equivalent verbal responses of mostly one syllable (eg: "nine", "ten", "a", "b", etc). Thus any confounding effect of speech on gait would be consistent across all dual task conditions.

Data collection

Pelvis accelerations were recorded by one tri-axial accelerometer (Opal, APDM Inc, Portland, OR, USA; sampling frequency 128 Hz) attached at the level of the sacrum as previously described [23]. Acceleration data collection and processing were performed in custom-written software (MATLAB R2011, Mathworks, Natick, MA, USA).

Data analysis

Gait parameters. The accelerometer data were analysed for the middle 15 m of the 20 m walkway (i.e. constant walking velocity). Heel strike was identified from the characteristic peak anterior acceleration, as reported previously [24] and used to calculate step times between successive heel-strikes and step time variability.

The following variables were computed:

- 1) Gait speed ($\text{m}\cdot\text{s}^{-1}$), step length (cm) and cadence ($\text{steps}\cdot\text{s}^{-1}$).
- 2) Step time variability (coefficient of variation of step time = (standard deviation of mean step time/mean step time) $\times 100$; %).
- 3) Vertical, anterior-posterior (AP) and medio-lateral (ML) pelvis harmonic ratios [23]. Harmonics were extracted from the pelvis acceleration data through finite Fourier series. Harmonic ratios were calculated by dividing the sum of the amplitudes of the first ten even harmonics by the sum of the amplitudes of the first ten odd harmonics over one stride for each plane, AP, ML and vertical. Harmonic ratios provide a measure of walking stability or smoothness, as they are based on the assumption that upper body oscillations are repetitive during normal walking [25]; higher harmonic ratios indicate increased stability.

Cognitive task performance. Task difficulty was assumed to be reflected in task performance measures, i.e. the time taken to respond and the accuracy of responses to the cognitive tasks. Thus, response times and percentage of correct answers were computed for each condition in the seated and walking trials. Response times were defined as the time between the delivery of the last piece of pertinent information and the verbal response.

Statistical analysis

All statistical analyses were performed using IBM SPSS (Version 21 for Windows, SPSS Science, Chicago, USA) and all significance levels were set at $p < .05$. Moderately right skewed variables (AP and ML harmonic ratios of pelvis accelerations) were log transformed and slightly right skewed variables (response times) were square-root transformed to permit parametric analyses [26]. A three-way repeated measures analysis of variance (ANOVA) with ambulation (seated, walking), task type (VS, NS) and task difficulty (easy, difficult) as within-subject factors was initially performed on cognitive task response times and revealed a significant (three-way) ambulation by task type by task difficulty interaction (see results). Subsequently two-way repeated measures ANOVAs with task type (VS, NS) and task difficulty (easy, difficult) as within-subject factors were performed on the response times for seated and walking trials separately. Two-way repeated measures ANOVAs with task type (VS, NS) and task difficulty (easy, difficult) as within-subject factors were also performed on the gait parameters. Planned contrasts were performed where main effects or interactions were identified. Due to its markedly non-normal distribution, Friedman tests (and post-hoc Wilcoxon tests) were used to compare percentage of correct answers for the cognitive tasks between the four cognitive conditions for the walking and seated trials. Wilcoxon tests were also performed to compare percentage of correct answers between seated and walking trials for each task condition. Finally, Pearson's correlations were conducted to assess the relationship between gait speed and gait variability and harmonic ratios within the four dual task conditions.

Results

Cognitive task performance

Cognitive task performance during the seated and walking trials are presented in Table 1. While seated, the percentage of correct answers differed between conditions ($\chi^2 = 22.53$, $df = 3$, $p < .001$) with participants providing significantly more correct answers in the easy compared with the difficult tasks (VS: $Z = -2.876$, $p = .004$; NS: $Z = -2.937$, $p = .003$); but no difference in the VS-easy and NS-easy tasks ($Z = -1.023$, $p = .306$) or the VS-diff and NS-diff tasks ($Z = -0.835$, $p = .404$). While walking, the percentage correct answers differed across conditions ($\chi^2 = 13.775$, $df = 3$, $p = .003$) with more correct answers provided in the NS tasks compared with the VS tasks (easy: $Z = -2.002$, $p = .045$; difficult: $Z = -2.535$, $p = .011$) but no difficulty level effects ($p > .05$). Errors made in walking and seated trials were similar ($p > .05$), except for the VS easy condition, where more errors were made while walking ($Z = -2.756$, $p = .006$).

The three-way repeated measures ANOVA revealed a significant ambulation by task type by difficulty (three-way) interaction effect ($F_{1, 29} = 7.073$, $p = .013$) on cognitive task response time. Subsequently, two-way repeated measures ANOVAs were conducted to examine task type and difficulty effects for the seated and walking trials separately. For the seated trials, there was a significant task type by difficulty interaction effect ($F_{1, 31} = 15.24$, $p < .001$) on response time resulting from a greater differential effect of increased difficulty for the NS compared with the VS cognitive tasks. There was no main effect of task type ($F_{1, 31} = 0.486$, $p = .491$) and a significant main effect of difficulty ($F_{1, 31} = 97.727$, $p < .001$) indicating slower response times in the difficult versus easy cognitive tasks.

For the walking trials, there was no significant task type by difficulty interaction effect ($F_{1, 32} = 0.947$, $p = .338$) on response time, but significant main effects for both task type ($F_{1, 32} = 16.30$, $p < .001$) and difficulty ($F_{1, 31} = 33.09$, $p < .001$). This indicated that while walking, participants had slower response times in the NS compared with VS cognitive tasks and in the difficult compared with the easy cognitive tasks. Finally, response times between the seated and walking conditions did not differ significantly ($F_{1, 29} = 1.408$, $p = .245$).

Dual task type effects: gait speed, step length and cadence

Two-way repeated measures ANOVAs showed no significant task type by difficulty interaction effects for gait speed and step length, but significant main effects for both task type and difficulty. This indicates participants walked slower and took shorter steps when concurrently performing the VS tasks compared with the NS tasks and when performing difficult cognitive tasks compared with easy cognitive tasks (Table 2). There was a significant task type by difficulty interaction effect on cadence ($F_{1, 35} = 5.132$, $p = .030$), that resulted from a reduced cadence in the VS-diff task compared with both the NS-diff ($t = -0.053$, $p = .003$) and the VS-easy tasks ($t = -0.051$, $p < .001$).

Dual task type effects: variability and smoothness

Two-way repeated measures ANOVAs showed no significant task type by difficulty interaction effects for step time variability and AP and ML harmonic ratios, but significant main effects for both task type and difficulty. This indicates participants had more variable gait and less smooth pelvis accelerations in the VS versus the NS cognitive tasks and the difficult versus easy cognitive tasks (Table 2). There was a significant task type by difficulty interaction effect on the V harmonic ratio ($F_{1, 34} = 7.599$, $p = .009$), that

Table 1. Descriptive data for the four cognitive tasks (nonspatial (NS) easy, NS difficult, visuospatial (VS) easy and VS difficult) in the seated and walking conditions for the 36 participants.

Parameter	NS cognitive task		VS cognitive task	
	Easy	Difficult	Easy	Difficult
<i>Seated trials</i>				
Number of instructions per 30 s	3.6 (0.5)	2.5 (0.5)	2.9 (0.4)	2.4 (0.6)
Percentage of correct answers	91 (89–100)	83 (67–100)	89 (86–100)	78 (67–89)
Response time (s)	4.08 (0.82)	5.89 (1.44)	4.66 (1.21)	5.21 (1.14)
<i>Walking trials</i>				
Number of instructions per trial	2.4 (0.2)	1.8 (0.1)	2.3 (0.0)	2.0 (0.0)
Percentage of correct answers	100 (83–100)	86 (75–100)	86 (67–100)	67 (50–83)
Response time (s)	4.97 (1.29)	5.93 (0.90)	4.52 (0.91)	5.56 (1.98)

Data are presented as mean (SD), except the percentage of correct answers are presented as median (interquartile range) due to non-normal distributions.
doi:10.1371/journal.pone.0109802.t001

resulted from less smooth pelvis accelerations in the VS-diff condition compared with both the NS-diff ($t = -0.204$, $p < .001$) and VS-easy ($t = -0.189$, $p < .001$) conditions.

Associations among the gait parameters

Pearson's correlations revealed that gait speed was associated with step time variability ($r = -0.541$ to -0.665 , $p \leq .001$) and harmonic ratios of pelvis accelerations (V: $r = 0.438$ to 0.687 , $p \leq .008$; AP: $r = 0.506$ to 0.590 , $p \leq .002$; ML: $r = 0.445$ to 0.670 , $p \leq .007$) in all four dual task conditions.

Discussion

In this study we compared the effects of VS and NS cognitive tasks on locomotor control in older people while controlling for task difficulty. The findings build on previous work on balance control during standing and stepping [4–6,8,9,11] by showing that VS cognitive tasks interfere with locomotor control to a greater extent than NS tasks. This differential effect was manifest in spatiotemporal parameters (reduced velocity cadence, stride length) as well as variability and smoothness measures (increased step time variability and reduced harmonic ratios).

No significant differences in either cognitive task type error rates or response times were evident in the seated conditions, suggesting equivalent task difficulty. In the walking trials, participants responded faster to the VS tasks than the NS tasks but at the cost of making significantly more cognitive task errors, i.e. they traded accuracy for speed. Thus, without specific instruction regarding which task to prioritize, healthy older people showed greater impairments in both gait and cognitive processing when performing a VS task while walking. These findings therefore support the bottleneck model of dual task interference, in that they suggest that cognitive resources required for locomotor control likely share similar pathways (i.e. the VS sketchpad of working memory [27]) to those required for performing VS tasks.

Previous studies have reported complementary findings, in that they have shown VS deficits identified in neuropsychological test batteries are associated with gait instability [16,18], freezing of gait [19] and increased risk of multiple falls in healthy populations [16,17] and people with Parkinson's disease [18,19]. They also extend knowledge that the information updating and monitoring process of executive function (working memory) is associated with gait stability (stride time variability) [28] in healthy older people,

by specifying that the VS aspect of working memory is particularly relevant for locomotor control.

In each condition, slower gait speed was significantly correlated with detrimental changes in stability, consistent with a mechanical explanation that step time variability and pelvis harmonic ratios are optimised at usual speed [29]. Slower gait speed when concurrently performing the VS cognitive task could be considered a compensatory mechanism to maintain balance, as it would increase available time to respond to hazards not seen while attention is divided, but at the apparent cost of gait smoothness. Alternatively, it could be that the maintenance of optimal speed to minimize gait variability and maximise gait smoothness requires increased levels of attention for older people. As reduced walking speed, increased step timing variability [30,31] and reduced pelvis harmonic ratios [23] during unobstructed gait are associated with an increased fall risk in older people, a gait assessment with a concomitant VS spatial task might be a useful test to include as part of a fall risk assessment.

The finding that cadence was significantly reduced in the difficult VS tasks compared with the difficult NS task is of interest given that cadence is thought to be controlled at the sub-cortical level by central pattern generators [32]. As cadence would not be expected to be affected by an increased attentional load, our findings may reflect a cortical-driven adaptation to improve walking stability or reduce speed to a further extent than that achieved by a reduction in step length.

There is neuroimaging evidence supporting the VS sketchpad working memory model [27] demonstrating that verbal and VS working memory are represented in the human brain by different domain-specific networks [33]. In addition, brain imaging studies that have examined neural correlates of either gait or spatial attention/working memory tasks in young people, point to commonalities in activated cerebral structures [34–38]. Brain areas activated during spatial attention and working memory tasks include the supplementary motor area, the premotor cortex, the cerebellum vermis and the precuneus [34,36]. Other brain imaging studies [35,38] have identified activation in these same structures (supplementary motor area, the premotor cortex, the cerebellum vermis) during gait, while conducting motor imagery of walking tasks during functional magnetic resonance imaging has identified activation of the precuneus amongst other structures [37].

It has also been documented that the hippocampus and entorhinal cortex are key cortical regions that sub-serve spatial

Table 2. Mean (SD) values for the gait parameters in normal walking (no cognitive task) and the four cognitive dual tasks conditions: nonspatial (NS) easy, NS difficult, visuospatial (VS) easy and VS difficult for the 36 participants.

Parameter	No cognitive task		NS cognitive task		VS cognitive task		Task type effects		Task difficulty effects		Task type by difficulty interaction	
	Easy	Difficult	Easy	Difficult	Easy	Difficult						
15 m walk time (s)	12.38 (1.49)	15.59 (2.99)	15.96 (3.07)	17.27 (4.25)	16.15 (3.27)	17.27 (4.25)						
Gait speed (m.s ⁻¹)	1.23 (0.15)	1.00 (0.18)	0.97 (0.17)	0.91 (0.19)	0.96 (0.17)	0.91 (0.19)	$F_{1,35} = 10.338, p = .003$	$F_{1,35} = 8.842, p = .005$	$F_{1,35} = 1.742, p = .196$			
Cadence (steps.s ⁻¹)	1.86 (0.13)	1.69 (0.21)	1.67 (0.22)	1.62 (0.25)	1.67 (0.23)	1.62 (0.25)	$F_{1,35} = 5.783, p = .022$	$F_{1,35} = 9.575, p = .004$	$F_{1,35} = 5.132, p = .030$			
Step length (cm)	66.25 (6.40)	58.85 (6.62)	57.94 (6.37)	56.04 (6.48)	57.40 (5.65)	56.04 (6.48)	$F_{1,35} = 7.429, p = .010$	$F_{1,35} = 6.733, p = .014$	$F_{1,35} = 0.416, p = .523$			
Step time variability (%)	3.92 (1.47)	4.85 (1.80)	5.17 (1.86)	5.85 (2.55)	5.34 (1.98)	5.85 (2.55)	$F_{1,35} = 5.654, p = .023$	$F_{1,35} = 4.049, p = 0.052$	$F_{1,35} = 0.516, p = .477$			
V harmonic ratio ^a	2.70 (0.53)	2.36 (0.41)	2.32 (0.46)	2.11 (0.41)	2.30 (0.42)	2.11 (0.41)	$F_{1,34} = 14.770, p = .001$	$F_{1,34} = 12.997, p = .001$	$F_{1,34} = 7.599, p = .009$			
AP harmonic ratio	2.78 (0.63)	2.43 (0.62)	2.37 (0.57)	2.25 (0.56)	2.37 (0.56)	2.25 (0.56)	$F_{1,35} = 7.380, p = .010$	$F_{1,35} = 3.264, p = .079$	$F_{1,35} = 2.787, p = .104$			
ML harmonic ratio	1.77 (0.44)	1.51 (0.34)	1.48 (0.38)	1.40 (0.33)	1.46 (0.37)	1.40 (0.33)	$F_{1,35} = 7.663, p = .009$	$F_{1,35} = 2.970, p = .094$	$F_{1,35} = 1.361, p = .251$			

ANOVA results examining main and interaction effects of task type and difficulty are also presented.

^an = 35; erroneously high data for one participant excluded from the analysis of this variable.

Note: There were also significant effects of added cognitive load ($p < 0.001$) for all gait parameters, with each dual task condition (VS-easy, VS-diff, NS-easy, NS-diff) producing significantly slower gait speeds, shorter step lengths, reduced cadence, increased step time variability and reduced harmonic ratios compared with the no cognitive task walking condition (one-way repeated measures ANOVAs with planned contrasts $p \leq 0.001$). doi:10.1371/journal.pone.0109802.t002

memory and are necessary for the sequential ordering of movement [39,40], as would be required to ensure a stable gait pattern. Atrophy in these regions is characteristic of mild cognitive impairment and Alzheimer’s Disease [41], in which patients also show early impairment in VS skills and unstable gait patterns [42]. Thus, it is possible that our VS dual task walking paradigm might have exceeded the processing capacity of the hippocampal and entohirnal regions, leading to the deteriorations in both gait and cognitive task performance.

Previous dual task balance studies [43–45] have found older adults tend to prioritize the motor tasks (i.e. postural control, and balance recovery on a moving platform) and perform significantly worse in cognitive tasks in dual task conditions. However, our study appears to show the opposite prioritization pattern, in that a greater dual task cost was evident for gait-performance, while cognitive task performance during the walking trials generally did not differ from the seated trials (one exception being the percentage of correct answers in VS-easy). This apparent difference in prioritization may be explained by the nature of the tasks; walking at self-selected speed along a flat corridor, free of obstacles is likely to be perceived as less threatening than maintaining balance on a moving platform.

This study has certain limitations. It is acknowledged that the VS instructions were longer than the NS instructions and that arithmetic tasks could involve some level of VS processing or share some common cortical networks [46]. Strictly, NS tasks such as forward digit span or verbal fluency might have been preferable with respect to not containing VS elements. However we wished to avoid the potential cross-talk between a motor rhythmic task (gait) and a verbal rhythmic task, which has been shown to lead to better performance in one or both tasks [47]. Secondly, it should be noted that we did not analyse the encoding periods (participants listening to the instructions) separately from the information maintenance periods and the retrieval period during which the participants responded [8,9]. Retrieval is assumed to be more attentionally demanding than encoding [8,9]. The participants generated more responses in the NS-easy conditions and therefore more retrieval periods could have potentially impaired walking stability. However, this was not the case as participants walked faster with a smoother and less variable gait pattern in the NS compared with the VS dual task conditions. Finally, data are presented for walking-only trials for reference purposes, and it is acknowledged that comparisons with the dual task conditions are limited by not controlling for articulatory responses.

Conclusion

This study showed that while controlling for secondary task difficulty, VS cognitive tasks led to slower, more variable and less smooth gait patterns, compared with NS cognitive tasks. These findings support the bottleneck theory of dual task interference rather than the limited attentional resources model as they suggest that the VS processing component of working memory is involved in gait control. In the future, the use of functional neuroimaging techniques allowing recording of cortical activity during gait might provide further insight into the cognitive processes relating to walking stability. At present, the clinical implications of this research are that tasks requiring VS attention during locomotion might present an additional challenge to walking stability, particularly in older people. This finding may be pertinent to persons at increased risk of falls, such as those with sensorimotor deficits and/or neuropsychological impairments.

Acknowledgments

The participants in this study were drawn from the Sydney Memory and Ageing Study of the Brain and Ageing Program, School of Psychiatry, UNSW. We thank Joanne Lo, Eunice Lim, Melissa Brodie, Mina Sarofim, Mikhail Sarofim, Mirian Garrues, Robert van Vliet for their help with data collection and Thomas Davies for his help with programming.

References

1. Woollacott M, Shumway-Cook A (2002) Attention and the control of posture and gait: a review of an emerging area of research. *Gait Posture* 16: 1–14.
2. Yogev-Seligmann G, Hausdorff JM, Giladi N (2008) The role of executive function and attention in gait. *Mov Disord* 23: 329–342.
3. Miyake A, Friedman NP, Emerson MJ, Witzki AH, Howerton A, et al. (2000) The unity and diversity of executive functions and their contributions to complex “Frontal Lobe” tasks: a latent variable analysis. *Cogn Psychol* 41: 49–100.
4. Woollacott M, Vander Velde T (2008) Non-visual spatial tasks reveal increased interactions with stance postural control. *Brain Res* 1208: 95–102.
5. Chong RK, Mills B, Dailey L, Lane E, Smith S, et al. (2010) Specific interference between a cognitive task and sensory organization for stance balance control in healthy young adults: visuospatial effects. *Neuropsychologia* 48: 2709–2718.
6. Barra J, Bray A, Sahni V, Golding JF, Gresty MA (2006) Increasing cognitive load with increasing balance challenge: recipe for catastrophe. *Exp Brain Res* 174: 734–745.
7. Kerr B, Condon SM, McDonald LA (1985) Cognitive spatial processing and the regulation of posture. *J Exp Psychol Hum Percept Perform* 11: 617–622.
8. Maylor EA, Allison S, Wing AM (2001) Effects of spatial and nonspatial cognitive activity on postural stability. *Br J Psychol* 92: 319–338.
9. Maylor EA, Wing AM (1996) Age differences in postural stability are increased by additional cognitive demands. *J Gerontol B Psychol Sci Soc Sci* 51: P143–154.
10. Nadkarni NK, Zabjek K, Lee B, McLroy WE, Black SE (2010) Effect of working memory and spatial attention tasks on gait in healthy young and older adults. *Motor Control* 14: 195–210.
11. Sturmeckis DL, St George R, Fitzpatrick RC, Lord SR (2008) Effects of spatial and nonspatial memory tasks on choice stepping reaction time in older people. *J Gerontol A Biol Sci Med Sci* 63: 1063–1068.
12. Yardley L, Gardner M, Bronstein A, Davies R, Buckwell D, et al. (2001) Interference between postural control and mental task performance in patients with vestibular disorder and healthy controls. *J Neurol Neurosurg Psychiatry* 71: 48–52.
13. Shumway-Cook A, Woollacott M, Kerns KA, Baldwin M (1997) The effects of two types of cognitive tasks on postural stability in older adults with and without a history of falls. *J Gerontol A Biol Sci Med Sci* 52: M232–240.
14. Yardley L, Gardner M, Leadbetter A, Lavie N (1999) Effect of articulatory and mental tasks on postural control. *Neuroreport* 10: 215–219.
15. Faulkner KA, Redfern MS, Cauley JA, Landsittel DP, Studenski SA, et al. (2007) Multitasking: association between poorer performance and a history of recurrent falls. *J Am Geriatr Soc* 55: 570–576.
16. Martín KL, Blizzard L, Wood AG, Srikanth V, Thomson R, et al. (2013) Cognitive function, gait, and gait variability in older people: a population-based study. *J Gerontol A Biol Sci Med Sci* 68: 726–732.
17. Martín KL, Blizzard L, Srikanth VK, Wood A, Thomson R, et al. (2013) Cognitive function modifies the effect of physiological function on the risk of multiple falls—a population-based study. *J Gerontol A Biol Sci Med Sci* 68: 1091–1097.
18. Amboni M, Barone P, Iuppariello L, Lista I, Tranfaglia R, et al. (2012) Gait patterns in Parkinsonian patients with or without mild cognitive impairment. *Mov Disord* 27: 1536–1543.
19. Nantel J, McDonald JC, Tan S, Bronte-Stewart H (2012) Deficits in visuospatial processing contribute to quantitative measures of freezing of gait in Parkinson’s disease. *Neuroscience* 221: 151–156.
20. Hill K, Schwarz J, Flicker L, Carroll S (1999) Falls among healthy, community-dwelling, older women: a prospective study of frequency, circumstances, consequences and prediction accuracy. *Aust N Z J Public Health* 23: 41–48.
21. Sachdev PS, Brodaty H, Reppermund S, Kochan NA, Trollor JN, et al. (2010) The Sydney Memory and Ageing Study (MAS): methodology and baseline medical and neuropsychiatric characteristics of an elderly epidemiological non-demented cohort of Australians aged 70–90 years. *Int Psychogeriatr* 22: 1248–1264.
22. Tombaugh TN, McIntyre NJ (1992) The mini-mental state examination: a comprehensive review. *J Am Geriatr Soc* 40: 922–935.
23. Menz HB, Lord SR, Fitzpatrick RC (2003) Acceleration patterns of the head and pelvis when walking are associated with risk of falling in community-dwelling older people. *J Gerontol A Biol Sci Med Sci* 58: M446–452.

Author Contributions

Conceived and designed the experiments: JM DS SS SL. Performed the experiments: JM DS MB. Analyzed the data: JM DS MB SL. Contributed reagents/materials/analysis tools: SS MB. Wrote the paper: JM DS SL MB SS.

24. Zijlstra W, Hof AL (2003) Assessment of spatio-temporal gait parameters from trunk accelerations during human walking. *Gait Posture* 18: 1–10.
25. Kavanagh JJ, Menz HB (2008) Accelerometry: a technique for quantifying movement patterns during walking. *Gait Posture* 28: 1–15.
26. Tabachnick BG, Fidell LS (2007) *Using multivariate statistics*. Amsterdam: Elsevier.
27. Baddeley A (1992) Working memory. *Science* 255: 556–559.
28. Beauchet O, Annweiler C, Montero-Odasso M, Fantino B, Herrmann FR, et al. (2012) Gait control: a specific subdomain of executive function? *J Neuroeng Rehabil* 9: 12.
29. Latt MD, Menz HB, Fung VS, Lord SR (2008) Walking speed, cadence and step length are selected to optimize the stability of head and pelvis accelerations. *Exp Brain Res* 184: 201–209.
30. Callisaya ML, Blizzard L, Schmidt MD, Martin KL, McGinley JL, et al. (2011) Gait, gait variability and the risk of multiple incident falls in older people: a population-based study. *Age Ageing* 40: 481–487.
31. Hausdorff JM, Rios DA, Edelberg HK (2001) Gait variability and fall risk in community-living older adults: a 1-year prospective study. *Arch Phys Med Rehabil* 82: 1050–1056.
32. Dietz V (2003) Spinal cord pattern generators for locomotion. *Clin Neurophysiol* 114: 1379–1389.
33. Gruber O, von Cramon DY (2003) The functional neuroanatomy of human working memory revisited. Evidence from 3-T fMRI studies using classical domain-specific interference tasks. *Neuroimage* 19: 797–809.
34. Alichniewicz KK, Brunner F, Klunemann HH, Greenlee MW (2012) Structural and functional neural correlates of visuospatial information processing in normal aging and amnesic mild cognitive impairment. *Neurobiol Aging* 33: 2782–2797.
35. Fukuyama H, Ouchi Y, Matsuzaki S, Nagahama Y, Yamauchi H, et al. (1997) Brain functional activity during gait in normal subjects: a SPECT study. *Neurosci Lett* 228: 183–186.
36. LaBar KS, Gitelman DR, Parrish TB, Mesulam M (1999) Neuroanatomic overlap of working memory and spatial attention networks: a functional MRI comparison within subjects. *Neuroimage* 10: 695–704.
37. Malouin F, Richards CL, Jackson PL, Dumas F, Doyon J (2003) Brain activations during motor imagery of locomotor-related tasks: a PET study. *Hum Brain Mapp* 19: 47–62.
38. Miyai I, Tanabe HC, Sase I, Eda H, Oda I, et al. (2001) Cortical mapping of gait in humans: a near-infrared spectroscopic topography study. *Neuroimage* 14: 1186–1192.
39. Heo S, Prakash RS, Voss MW, Erickson KI, Ouyang C, et al. (2010) Resting hippocampal blood flow, spatial memory and aging. *Brain Research* 1315: 119–127.
40. Smith ML, Milner B (1981) The role of the right hippocampus in the recall of spatial location. *Neuropsychologia* 19: 781–793.
41. Schott JM, Kennedy J, Fox NC (2006) New developments in mild cognitive impairment and Alzheimer’s disease. *Curr Opin Neurol* 19: 552–558.
42. Sheridan PL, Hausdorff JM (2007) The role of higher-level cognitive function in gait: executive dysfunction contributes to fall risk in Alzheimer’s disease. *Dement Geriatr Cogn Disord* 24: 125–137.
43. Brown LA, Sleik RJ, Polych MA, Gage WH (2002) Is the prioritization of postural control altered in conditions of postural threat in younger and older adults? *J Gerontol A Biol Sci Med Sci* 57: M785–792.
44. Doumas M, Smolders C, Krampe RT (2008) Task prioritization in aging: effects of sensory information on concurrent posture and memory performance. *Exp Brain Res* 187: 275–281.
45. Huang CY, Hwang IS (2013) Behavioral data and neural correlates for postural prioritization and flexible resource allocation in concurrent postural and motor tasks. *Hum Brain Mapp* 34: 635–650.
46. Zago L, Tzourio-Mazoyer N (2002) Distinguishing visuospatial working memory and complex mental calculation areas within the parietal lobes. *Neurosci Lett* 331: 45–49.
47. Beauchet O, Dubost V, Allali G, Gonthier R, Herrmann FR, et al. (2007) Faster counting while walking as a predictor of falls in older adults. *Age Ageing* 36: 418–423.



Contents lists available at ScienceDirect

Medical Engineering & Physics

journal homepage: www.elsevier.com/locate/medengphy



Objective diagnosis of ADHD using IMUs

Niamh O'Mahony^{a,*}, Blanca Florentino-Liano^b, Juan J. Carballo^b,
Enrique Baca-García^{b,c}, Antonio Artés Rodríguez^a

^a Department of Signal and Communications Theory, Universidad Carlos III de Madrid, Avda. de la Universidad, 30, Leganés 28911, Spain

^b Fundación Jiménez Díaz and Universidad Autónoma (CIBERSAM), Avda. Reyes Católicos, 2, Madrid 28040, Spain

^c Department of Psychiatry, New York State Psychiatric Institute and Columbia University, New York, NY, USA

ARTICLE INFO

Article history:

Received 12 May 2013

Received in revised form 19 January 2014

Accepted 20 February 2014

Keywords:

Objective diagnosis

Inertial sensors

Attention deficit/hyperactivity disorder

Machine learning

Classification

ABSTRACT

This work proposes the use of miniature wireless inertial sensors as an objective tool for the diagnosis of ADHD. The sensors, consisting of both accelerometers and gyroscopes to measure linear and rotational movement, respectively, are used to characterize the motion of subjects in the setting of a psychiatric consultancy. A support vector machine is used to classify a group of subjects as either ADHD or non-ADHD and a classification accuracy of greater than 95% has been achieved. Separate analyses of the motion data recorded during various activities throughout the visit to the psychiatric consultancy show that motion recorded during a continuous performance test (a forced concentration task) provides a better classification performance than that recorded during "free time".

© 2014 IPEM. Published by Elsevier Ltd. All rights reserved.

1. Introduction

Attention-deficit/hyperactivity disorder (ADHD) is one of the most common childhood psychiatric disorders and represents a significant public health problem. Several works [1–5] have illustrated a significant increase in the rates of ADHD during recent decades. Thirty years ago, reported prevalence of ADHD among schoolchildren lay between 1% and 3%, whilst recent estimates range between 3 and 10%. Rising trends do not inevitably imply changes in the prevalence of ADHD among youth [5]. These trends in ADHD diagnosis could be due to greater healthcare-seeking behaviours among families with children suffering from ADHD or to higher appreciation of this psychiatric disorder among healthcare providers, parents, and school staff [5]. However, other authors have pointed out that the criteria and rating scales used to diagnose ADHD are, by their nature, subjective and have suggested that difficulties in making an objective diagnosis of the disorder may have contributed to the secular increase in the prevalence of ADHD [6].

According to the Diagnostic and Statistical Manual of Mental Disorders (DSM IV TR) [7], ADHD is characterized by persistent inattention and/or hyperactivity-impulsivity on a more frequent or severe scale than that expected at a particular level of

development, and adversely affecting at least two areas of life (e.g. at home and at school) in terms of social, academic or occupational functioning. At present, ADHD is a clinical diagnosis. The American Academy of Child and Adolescent Psychiatry recommend the use of clinical interviews with parent(s) and patient and reports of functioning in school or day care, along with assessment for comorbid psychiatric disorders and review of medical, social and family history of the patient, in the assessment of a child for ADHD [8]. There is no mandatory requirement for psychological or neuropsychological tests [8], despite their usefulness in some cases [9]. New techniques, such as neuroimaging, are becoming a helpful research instrument in the study of ADHD but are not considered useful for the diagnosis [10].

Given that the symptoms of ADHD are non-specific and, usually, are present in some situations but not in others, difficulties in conducting a differential diagnosis exists [11]. In this sense, relying only on DSM IV criteria during the diagnostic process continues to be a subject of heated debate [12]. Not surprisingly, attempting to develop new instruments for an objective diagnosis of ADHD has become a popular research topic, in both the clinical [6,13,14] and biomedical engineering fields [15–17]. Some of the objective tools which have been investigated in the literature to date include continuous performance tests (CPTs) [14,18] and electroencephalogram (EEG) [15]. EEG and CPT testing can be costly to administer, requiring expensive equipment and specialized personnel, especially in the case of EEG.

It has previously been shown that an increased activity level is characteristic of ADHD subjects, in comparison with their

* Corresponding author.

E-mail addresses: niamh@tsc.uc3m.es (N. O'Mahony), blanca@tsc.uc3m.es (B. Florentino-Liano), jjcarballo@fjd.es (J.J. Carballo), eb2452@columbia.edu (E. Baca-García), antonio@tsc.uc3m.es (A.A. Rodríguez).

non-ADHD peers [19,20] and, in recent years, sensor technology has evolved to the point where miniature wireless inertial sensors, as small as a wristwatch, can record data for long time periods (up to 24 h). This development has paved the way for the long-term observation of subjects, in order to characterize their habitual behaviour. Recently, these advances have begun to be exploited in the literature, with a number of investigations into the use of accelerometry as an objective tool for diagnosing ADHD [17,21]. In this work, the measurement of the levels and patterns of movement in children, with and without an ADHD diagnosis, is taken one step further: instead of accelerometry, alone, inertial measurement units (IMUs), comprised of both accelerometers and gyroscopes, are used to analyze and characterize the subjects' motion. The results achieved, in fact, suggest that the inclusion of gyroscope measurements (of angular motion) provides a better discriminative ability between ADHD and non-ADHD subjects than the use of accelerometer measurements (of linear motion) alone.

This proof-of-concept study observes subjects for a duration of approximately 1 h, while they visit a psychiatric consultancy. The subjects are observed both with and without their parents and the psychiatrist, as well as during a CPT task, which requires concentration. Thus, a variety of different situations are observed, representing some of the variety in daily activities, such as school and home. The goal of the study is to determine if inertial measurements, recorded in the setting of the psychiatric consultancy, have the predictive capability to distinguish between ADHD and non-ADHD cases. To this end, machine learning tools are employed and it is shown that good predictive capability is, indeed, attained.

2. Background

2.1. State-of-the-art ADHD diagnosis

The state-of-the-art diagnostic instruments described below were employed in this study to provide the basis for comparison of the proposed method to current best-practice methods.

2.1.1. ADHD Rating Scale-IV: Home Version (ADHD RS-IV) [22]

The ADHD RS-IV consists of eighteen items that assess DSM-IV criteria for inattention and hyperactivity. Good validity, test-retest reliability and internal consistency have been demonstrated for the rating scale [23].

2.1.2. Test of variables of attention (T.O.V.A.[®]) [18]

The T.O.V.A.[®] is a CPT, consisting of a 21.6 min long test, during which subjects have to respond quickly to targets whilst withholding response to non-targets. It should be noted that the T.O.V.A. is not intended as a stand-alone factor for diagnosis. Indeed, the accuracy of the T.O.V.A.[®] alone is not sufficient for reliably distinguishing between ADHD and non-ADHD subjects, with the T.O.V.A.[®]. Clinical Manual reporting sensitivity and specificity of 84% and 89%, respectively, using a discriminant analysis method. Independent studies have shown similar or worse results, e.g. [24]. This performance is not, however, specific to the T.O.V.A.[®] and other available CPTs have a similar performance [6,25].

2.1.3. Clinical diagnosis by psychiatrist

Clinical evaluation of ADHD and other psychiatric disorders included reviewing the clinical interview and all available data, following the recommendations of the AACAP, as detailed in Section 1 [8].

In order to estimate the predictive sensitivity and specificity of any test for ADHD, the outcomes have to be compared with the outcomes of the same patients using alternative tests. Given the lack of a non-subjective and universally agreed-upon "Gold standard"

test, it is often unclear what is considered as the ground truth for a correct ADHD diagnosis. In this work, a combination of the ADHD RS-IV rating and the clinical diagnosis serves as the ground truth diagnosis for the study, such that only those patients with a positive ADHD diagnosis in the ADHD RS-IV scale and for whom this positive diagnosis was confirmed according to the psychiatrist's evaluation are considered as ADHD subjects, whilst those with a negative diagnosis in the ADHD RS-IV scale, confirmed by a negative clinical diagnosis are considered as controls. Any subject with contradictory diagnoses was eliminated from the study. Furthermore, patients who are undergoing treatment for their ADHD (i.e. pharmaceutical treatment) were not considered, as the level of effectiveness of their medication can vary and this could result in a falsely heterogeneous ADHD group.

2.2. Inertial measurements and activity

Recent advances in sensor technology have led to the widespread availability of affordable, miniature inertial sensors which can be comfortably worn by a human subject, going about normal daily activities. Currently available miniature inertial sensors typically consist of tri-axial accelerometers and tri-axial gyroscopes to measure the total inertial force and angular velocity, respectively, on mutually perpendicular axes (x , y and z). The total inertial force provides a representation of the subject's pose (inclination angle) and linear motion. The angular velocity provides a measure of the rotational characteristic of the subject's motion. As such, these sensors allow both a quantitative and qualitative characterization of the subject's motion, measuring both the level or intensity of movement and the nature (rotational, linear). This characterization of motion is exploited in this work to identify differences in movement-related behaviour between subjects who suffer from ADHD and those who do not.

For more details regarding the tri-axial accelerometers and tri-axial gyroscopes used in this work, the reader is referred to the APDM Opal sensor product information contained in [26]. These sensor modules save data directly to an on-board memory for post-processing.

2.3. Machine learning

2.3.1. Classification

In this work, the determination of the predictive capability of inertial measurements in ADHD diagnosis, is based on machine learning methods, specifically, classification methods. Many classification algorithms exist in the literature; the one used in this work is the support vector machine (SVM), a state-of-the-art learning machine, used in a wide variety of applications. For the sake of brevity, the theory of operation of the SVM will not be described here – instead the reader is referred to [27] for details. In this work, the SVM is simply used as a tool to evaluate the classification performance of features calculated from the inertial measurements.

2.3.2. Feature selection

Feature selection methods are used to reduce dimensionality of data for various reasons: to reduce computational load, to improve the generalization ability of the classifier and to improve the interpretability of the results. A good review of feature selection techniques can be found in [28]. In this work, a suboptimal forward selection method is employed as a tool to identify those features which have the best predictive capability.

3. Methods

3.1. Subjects

Forty-three children, aged 6–11 years, who were referred to the Child and Adolescent Psychiatry Unit of the Department of Psychiatry at Fundación Jiménez Díaz Hospital (Madrid, Spain), were included in this study. The experimental group consisted of children diagnosed with ADHD ($N=24$, 55.8%), and the control group consisted of children not diagnosed with ADHD ($N=19$, 44.2%). All subjects in the experimental group, but none in the control group, met DSM-IV criteria for ADHD. In the experimental group, 45.8% met criteria for the ADHD combined subtype, 41.7% for the predominantly inattentive subtype, and 12.5% for the hyperactive/impulsive subtype. In the experimental group 70.8% were male, whilst 47.4% were male in the control group. Mean age in the control group was 9.05 (± 1.39), whereas mean age in the experimental group was 8.54 (± 1.38) (t -test: $df=41$, $p=0.24$).

3.2. Ethics procedures

Parents and children were given a detailed description of the project and each subject's parent(s) or guardian(s) were required to give signed informed consent. Subjects provided assent. The consent and assent forms and the study protocol were reviewed and approved by the Institutional Review Board of Fundación Jiménez Díaz Hospital.

3.3. Monitoring procedure

The forty-three subjects were all evaluated in the same fashion. Two IMUs were used to record movement data for each subject - one attached to a belt worn at the waist and the other fixed by a velcro strap to the ankle of the "dominant" leg (the subject was asked to kick a football to identify the dominant leg). The IMU at the waist measures movement of the whole body, whilst the IMU at the foot captures local movements such as tapping the foot or other behaviour which may be associated with excess energy. Each subject wore both IMUs during the entire duration of their visit to the psychiatric consultancy (approximately 1 h). A trained employee (the "supervisor") accompanied each subject throughout the entire visit, labelling on a time-synchronized computer platform the "context" in which the data were collected, where the context refers to the "where, what and with whom" of the subject's environment. The subjects spent time in each of the following contexts:

WP	Waiting room; with parents.
WS	Waiting room; with supervisor only.
CD	Consultant's room; with psychiatrist.
CP	Consultant's room; with psychiatrist and parents.
TT	Taking the TOVA test; with supervisor only.

In both the waiting room and the consultant's room, the subjects were requested to sit in a revolving chair. While taking the TOVA test, the subjects were seated in a non-rotating chair in a room containing only a desk with the computer for administering the T.O.V.A. and nothing on the walls, to eliminate distractions.

A minimum duration of 2 min in each context was selected as valid, for the purpose of data analysis, to reduce the effects of interruptions and disruptions and to allow a fair measurement of the subjects' behaviour in each context.

3.4. Feature calculation and selection

In order to represent the recorded data in a concise form, features were calculated from the observed accelerometer and gyroscope signals. In order to exploit the most representative feature set possible, characterizing all aspects of the observed signals,

Table 1
 Number of features per category.

Category	Features
High resolution histograms [21]	35
Correlation between sensors/sensor types	8
Basic statistics: (e.g. mean, std. dev., skewness, kurtosis)	52
Frequency domain: (e.g. low/high frequency power ratio.)	8
Nonlinear features: [17] (e.g. central tendency measure)	4
Structural features: [15] (e.g. positive/negative area, slope, peak-peak value)	20
Motion features: [20] (e.g. number of movements per second)	6
Total per context	133
T.O.V.A. score, age, gender	3
Total per subject	668

features were calculated per sensor type (i.e. for gyroscope and for accelerometer), for each sensor location (waist and foot) and during each context. Features were calculated based on the modulus of the tri-axial accelerometer and gyroscope vectors, as well as on differential data (e.g. the difference between the modulus of the acceleration vector for consecutive samples). Additionally, age, gender and the achieved T.O.V.A. score were treated as additional features for each subject. The entire list of features is not included, for the sake of brevity, but the main categories, with some examples and the number of features in each category, are listed in Table 1.

A forward selection method was employed to select the subset of up to a maximum of 15 features which achieved the best classification accuracy for each context. For each context, the subset which achieved the maximum performance with the minimum number of features was selected as the final feature subset for that context. Leave-one-out validation was employed in the training and test phases of classification, due to the small number of observations available. The same forward selection procedure was also repeated, considering the set of all features calculated throughout the entire duration of the experiment (i.e. 668 features per subject).

4. Results

Two different SVMs were used to classify the subjects - one with a linear kernel and the other with a Gaussian kernel. However, despite an improved classification accuracy being achieved by the Gaussian kernel SVM, results for the linear SVM only are reported in this section, because, due to the small number of samples available in the dataset, the Gaussian SVM may be prone to overfitting the training data and giving an unrealistically elevated estimate of the classification performance.

Table 2 shows the classification performance achieved for the set of k features which resulted in the highest classification accuracy in the forward selection procedure. Results are shown for each context of the trial individually and for the entire duration of the trial ("ALL"). The following performance measures are reported: accuracy (percentage of correctly classified subjects), specificity (percentage of correctly classified non-ADHD subjects) and sensitivity (percentage of correctly classified ADHD subjects).

Table 2
 Classification performance for linear SVM with k parameters.

Context	k	Accuracy	Sensitivity	Specificity
WP	5	83.72	73.68	91.67
WS	14	85.37	89.47	81.81
CD	7	83.72	73.68	91.67
CP	5	81.40	57.89	100
TT	6	93.02	89.47	95.83
ALL	10	95.12	94.44	95.65

The performance of the SVM is seen to be good, in terms of accuracy, sensitivity and specificity, across all of the individual contexts and, particularly, during the T.O.V.A. test. The results across the entire duration (ALL) show that an increased classification performance can be achieved by the joint consideration of the subject's behaviour in multiple contexts.

For the sake of brevity, the entire list of features selected by the algorithm for each of the contexts listed in Table 2 is not included here. In summary:

- Approximately one-third of the features chosen by the feature selection procedure are gyroscope-based and the remainder are predominantly accelerometer-based (in certain contexts, gender, age and T.O.V.A. score have also been chosen).
- More than half of the selected features in all contexts came from the sensor at the child's waist.
- Of the ten features chosen by the forward selection procedure across the entire test duration, six of those came from the T.O.V.A. test context.
- More than half of the features chosen in every context were "high resolution histogram" (HRH) elements.
- The other categories of features which were selected most frequently were basic statistics, frequency domain characteristics and measures of correlation between sensors.

5. Discussion

The results, in Section 4, suggest that inertial sensors provide a promising tool for the objective diagnosis of ADHD. In the previous literature, the focus has been on acceleration measurements. Interestingly, an analysis of the features selected for each context suggests that the features calculated based on gyroscope measurements have a good predictive capability for discrimination between ADHD and non-ADHD subjects and should be considered along with accelerometer-based features. More than half of the selected features in all contexts came from the sensor at the child's waist, suggesting that "global" motion of the body is a better indicator of hyperactivity than "local" motions, such as tapping the foot, or similar habits.

Interestingly, of the ten features chosen by the forward selection procedure across the entire test duration, six of those came from the T.O.V.A. test context. Thus, it appears that the movement of a child in restrictive situations, such as carrying out a specifically defined task that requires concentration (the T.O.V.A.), provides better discriminative ability than the child's behaviour in "free time". Furthermore, it should be noted that the sensitivity and specificity of the reported method outperform the same metrics for the T.O.V.A. alone, which were 84% and 89%, respectively, as cited in Section 2.1.2.

The final observation, regarding the chosen features at the output of the forward selection, pertains to the categories to which chosen features belong. More than half of the features chosen in every context were "high resolution histogram" (HRH) elements. This does not come as a surprise, since a recent review of the state-of-the-art in extraction of features from accelerometers for the ADHD problem [17] showed that HRH features provide the best classification performance among all of the reviewed categories. However, it should be noted here that other categories of features have also been chosen in all contexts, most notable among them, basic statistics, frequency domain characteristics and measures of correlation between sensors. Thus, it can be seen that using a wide range of feature types provides improved performance over methods which rely on one single category of features.

6. Conclusions and future work

This work serves as a proof-of-concept for the use of accelerometers and gyroscopes in the diagnosis of ADHD in children between 6 and 11 years of age. Results have shown that classifiers based on a small number of features (5–10) can discriminate between ADHD subjects and control subjects with high sensitivity and specificity levels. Clearly, a more extensive follow-up study is required, with a larger number of patients, to more robustly identify the optimal set of features and the diagnostic accuracy of the system. To this end, construction of a large database has already been begun by the authors.

Furthermore, investigation into the ongoing monitoring of patients with an existing ADHD diagnosis, based on the inertial sensors and classification techniques described in this work, is also underway. The aim of that study is to use objective measures to provide feedback on the progress of the patient, their response to treatment and other indications.

Funding

This work has been partly supported by Ministerio de Educación of Spain (projects 'DEIPRO', id. TEC2009-14504-C02-01, and 'COMONSENS', id. CSD2008-00010) and partly supported by an Educational Grant to the Department of Psychiatry, Fundación Jiménez Díaz Hospital.

Ethical approval

Ethical Approval was given by the Comité Ético de Investigaciones Clínicas (equivalent to IRB). Judgements reference number is: PIC51/2011.

Conflict of interest

None declared.

References

- [1] Atladóttir HO, Parner ET, Schendel D, Dalsgaard S, Thomsen PH, Thorsen P. Time trends in reported diagnoses of childhood neuropsychiatric disorders: a Danish cohort study. *Archives of Pediatrics & Adolescent Medicine* 2007;161(2):193–8.
- [2] Robison LM, Skaer TL, Sclar DA, Galin RS. Is attention deficit hyperactivity disorder increasing among girls in the US? Trends in diagnosis and the prescribing of stimulants. *CNS Drugs* 2002;16(2):129–37.
- [3] Olfson M, Gameroff M, Marcus S, Jensen P. National trends in the treatment of attention deficit hyperactivity disorder. *American Journal of Psychiatry* 2003;160(6):1077–701.
- [4] Robison LM, Sclar DA, Skaer TL. Datapoints: trends in ADHD and stimulant use among adults: 1995–2002. *Psychiatric Services* 2005;56(12):1497.
- [5] Toh S. Datapoints: trends in ADHD and stimulant use among children, 1992–2003. *Psychiatric Services* 2006;57(8):1091.
- [6] Gualtieri CT, Johnson LG. ADHD: is objective diagnosis possible? *Psychiatry Edgmont Pa Township* 2005;2(11):44–53.
- [7] Association AP. Diagnostic and statistical manual of mental disorders DSM-IV. American Psychiatric Association; 1994.
- [8] Pliszka S. Practice parameter for the assessment and treatment of children and adolescents with attention-deficit/hyperactivity disorder. *Journal of the American Academy of Child & Adolescent Psychiatry* 2007;46(7):894–921.
- [9] Willcutt E, Doyle A, Nigg J, SV F, BF P. Validity of the executive function theory of attention-deficit/hyperactivity disorder: a meta-analytic review. *Biological Psychiatry* 2005;57(11):1336–46.
- [10] Cherkasova MV, Hechtman L. Neuroimaging in attention-deficit hyperactivity disorder: beyond the frontostriatal circuitry. *Canadian Journal of Psychiatry* 2009;54(10):651–64.
- [11] Taylor E, Dopfner M, Sergeant J, Asherson P, Banaschewski T, Buitelaar J, et al. European clinical guidelines for hyperkinetic disorder – first upgrade. *European Child & Adolescent Psychiatry* 2004;13(Suppl. 1):17–30.
- [12] Andrews G, Pine DS, Hobbs MJ, Anderson TM, Sunderland M. Neurodevelopmental disorders: cluster 2 of the proposed meta-structure for DSM-V and ICD-11. *Psychological Medicine* 2009;39(12):2013–23.
- [13] Inoue K, Nadaoka T, Oiji A, Morioka Y, Totsuka S, Kanbayashi Y, et al. Clinical evaluation of attention-deficit hyperactivity disorder by objective quantitative measures. *Child Psychiatry and Human Development* 1998;28(3):179–88.

- [14] Lis S, Baer N, Stein-en Nosse C, Gallhofer B, Sammer G, Kirsch P. Objective measurement of motor activity during cognitive performance in adults with attention-deficit/hyperactivity disorder. *Acta Psychiatrica Scandinavica* 2010;122(4):285–94.
- [15] Castro-Cabrera P, Gomez-García J, Restrepo F, Moscoso O, Castellanos-Dominguez G. Evaluation of feature extraction techniques on event-related potentials for detection of attention-deficit/hyperactivity disorder. In: Conference proceedings of the international conference of IEEE engineering in medicine and biology society, IEEE EMBS. 2010. p. 851–4.
- [16] Gómez C, Poza J, García M, Fernández A, Hornero R. Regularity analysis of spontaneous MEG activity in attention-deficit/hyperactivity disorders. In: Conference proceedings of the international conference of IEEE engineering in medicine and biology society, IEEE EMBS. 2011. p. 1765–8.
- [17] Martín-Martínez D, Casaseca-de-la Higuera P, Alberola-López S, Andrés-de Llano J, López-Villalobos J, Ardura-Fernández J, et al. Nonlinear analysis of actigraphic signals for the assessment of the attention-deficit/hyperactivity disorder (ADHD). *Medical Engineering & Physics* 2004;34(9):1317–29.
- [18] The TOVA Company. <http://www.tovatest.com/>
- [19] Tseng MH, Henderson A, Chow SMK, Yao G. Relationship between motor proficiency, attention, impulse, and activity in children with ADHD. *Developmental Medicine and Child Neurology* 2004;46(6):381–8.
- [20] Wood AC, Asherson P, Rijdsdijk F, Kuntsi J. Is overactivity a core feature in ADHD? Familial and receiver operating characteristic curve analysis of mechanically assessed activity level. *Journal of the American Academy of Child & Adolescent Psychiatry* 2009;48(10):1023–30.
- [21] Kam HJ, Lee K, Cho S-M, Shin Y-M, Park RW. High-resolution actigraphic analysis of ADHD: a wide range of movement variability observation in three school courses – a pilot study. *Healthcare Informatics Research* 2011;17(1):29–37.
- [22] Du Paul G, Power T, Anastopoulos A, Reid R. ADHD rating scales, IV: checklists, norms and clinical interpretation. NY: Guilford Press; 1998.
- [23] DuPaul GJ, Power TJ, McGoe KE, Ikeda MJ, Anastopoulos AD. Reliability and validity of parent and teacher ratings of attention-deficit/hyperactivity disorder symptoms. *Journal of Psychoeducational Assessment* 1998;16:55–68.
- [24] Preston AS, Fennell EB, Bussing R. Utility of a CPT in diagnosing ADHD among a representative sample of high-risk children: a cautionary study. *Child Neuropsychology A Journal on Normal and Abnormal Development in Childhood and Adolescence* 2005;11(5):459–69.
- [25] Bloch Y, Fixman M, Maoz H, Bloch AM, Levkovitz Y, Ratzoni G, et al. Can computerized cognitive tests assist in the clinical diagnosis of attention-deficit hyperactivity disorder? *Journal of Neuropsychiatry and Clinical Neurosciences* 2012;24(1):111–4.
- [26] APDM Inc. <http://www.apdm.com/>
- [27] Vapnik VN. *The nature of statistical learning theory*, vol. 8. New York, NY: Springer; 2000.
- [28] Guyon I, Elisseeff A. An introduction to variable and feature selection. *Journal of Machine Learning Research* 2003;3(7–8):1157–82.

Article

A New Calibration Methodology for Thorax and Upper Limbs Motion Capture in Children Using Magneto and Inertial Sensors

Luca Ricci ^{1,*}, Domenico Formica ¹, Laura Sparaci ², Francesca Romana Lasorsa ²,
Fabrizio Taffoni ¹, Eleonora Tamilia ¹ and Eugenio Guglielmelli ¹

¹ Laboratory of Biomedical Robotics and Biomicrosystems, Università Campus Bio-Medico di Roma, Via Àlvaro del Portillo 21, Rome 00128, Italy; E-Mails: d.formica@unicampus.it (D.F.); f.taffoni@unicampus.it (F.T.); e.tamilia@unicampus.it (E.T.); e.guglielmelli@unicampus.it (E.G.)

² Institute of Cognitive Sciences and Technologies (ISTC), National Research Council (CNR), Via Nomentana 56, Rome 00161, Italy; E-Mails: laura.sparaci@istc.cnr.it (L.S.); francesca.lasorsa@yahoo.it (F.R.L.)

* Author to whom correspondence should be addressed; E-Mail: l.ricci@unicampus.it;
Tel.: +39-0622-5419-610; Fax: +39-0622-5419-609.

Received: 20 November 2013; in revised form: 3 December 2013 / Accepted: 5 December 2013 /
Published: 9 January 2014

Abstract: Recent advances in wearable sensor technologies for motion capture have produced devices, mainly based on magneto and inertial measurement units (M-IMU), that are now suitable for out-of-the-lab use with children. In fact, the reduced size, weight and the wireless connectivity meet the requirement of minimum obtrusivity and give scientists the possibility to analyze children's motion in daily life contexts. Typical use of magneto and inertial measurement units (M-IMU) motion capture systems is based on attaching a sensing unit to each body segment of interest. The correct use of this setup requires a specific calibration methodology that allows mapping measurements from the sensors' frames of reference into useful kinematic information in the human limbs' frames of reference. The present work addresses this specific issue, presenting a calibration protocol to capture the kinematics of the upper limbs and thorax in typically developing (TD) children. The proposed method allows the construction, on each body segment, of a meaningful system of coordinates that are representative of real physiological motions and that are referred to as functional frames (FFs). We will also present a novel cost function for the Levenberg–Marquardt algorithm, to retrieve the rotation matrices between each sensor frame (SF) and the corresponding FF. Reported results on a group of

40 children suggest that the method is repeatable and reliable, opening the way to the extensive use of this technology for out-of-the-lab motion capture in children.

Keywords: magneto and inertial measurement unit; anatomical coordinate system; functional frame definition; calibration protocol; children motion capturing

1. Introduction

The possibility of capturing and quantitatively measuring children's motion repertoire in a daily life scenario is of great interest for a number of reasons. Clinical evaluation tools to measuring motor skills in children are, to date, able to offer qualitative, rather than quantitative, evaluation (*i.e.*, studies using standardized measures have difficulties in providing fine-grained details on children movement properties). Examples of widely used test to measure motor skills in children are the Gross Motor Function Measure, the Movement ABC or the 10 Meter Walk Test [1–3]). Therefore, the lack of reliable, objective measurements foster interest in the development of tools to accurately capture information about children's motion skills in real-life environments. For instance, it would be of key importance in the rehabilitation of children with a chronic health condition, such as cerebral palsy, to guide and evaluate interventions, to monitor progress and also to provide families with objective feedback [4]. Besides, quantitative motion evaluation can support standard clinical rating scales, providing clinicians with enriched information on patients' health [5].

Furthermore, research studies on the role of motor and communicative gesture (e.g., gestures) have highlighted the importance of assessing the motor characteristics of children's behavior [6,7]. Furthermore, in children with autistic spectrum disorder (ASD) or "at high-risk" for ASD, appropriate motion evaluation tools may be of relevance for early diagnosis and intervention [8–10].

A considerable number of systems for human motion capturing is commercially available at present. Though the technologies and the approaches are many, exhibiting different performance characteristics and operating on entirely different physical principles, no 'silver bullet' currently exists [11]. Among the plethora of choices, wearable technologies have the potential to meet the requirements for this specific application, as reported in [12,13]. Wearable motion tracking systems are based on M-IMUs, which identify a class of devices comprising tri-axial accelerometers, gyroscopes and magnetometers. Besides the information provided by the single sensor (*i.e.*, acceleration, angular velocity and magnetic flux density), M-IMUs can provide and maintain an accurate 3D-orientation estimate thanks to sensor fusion algorithms (for a comprehensive review on this topic, see [14]).

In order to obtain a precise tracking of the kinematics of human joints, the fulfillment of a calibration protocol is strictly required. The aim of our research was to define such a calibration procedure to capture the kinematics of upper limbs and thorax in children. Our method permits the construction of meaningful functional frames (FFs), in the sense of being representative of real physiological motions, on each body segment and allow for estimating of the rotation matrices between each sensor frame (SF) and the corresponding FF. A typical calibration protocol is composed of the following steps: (1)

a series of fixed reference postures and/or functional movements that the subject under experimentation is asked to perform; (2) the definition of both an FF on each body segment of interest and a mapping between each axis of the FF and each reference posture/functional movement; and (3) the computation of the transformation matrix between each FF and its corresponding SF. Despite existing literature proposing procedures for the kinematic tracking of both upper and lower limbs [15–19], no study to date has provided a calibration protocol specifically designed to be used with children. In fact, existing procedures do not take into consideration the constraints related to an use of M-IMU technology with children, e.g., the fact that particular care in the choice of movements to perform is required. Therefore an ad-hoc design is required. Based on the outcomes from a previous study [20], we have built a calibration protocol, which defines an ameliorated set of reference postures/functional movements, a new way to estimate reference axes from sensor data, and introduces a novel methodology to compute the transformation matrix. The experimental procedure has been tested in typical development (TD) children, and it has been administered by non-technicians in daily life scenarios (e.g., at school or at home), as it does not need any special expertise.

This paper is organized as follows: Section 2 provides an introduction of the motion tracking system architecture, including the hardware and software components that have been employed, and offers a detailed description of the proposed calibration protocol alongside data analysis methodology; Section 3 reports the results of the experimental session; Section 4 discusses the results and presents some conclusions.

2. Materials and Methods

2.1. System Architecture

As hardware, the experimental setup is comprised of a set of 5 wireless sensing units (SUs) chosen among the number of commercially available systems. In particular, we chose to use Opal by APDM Inc. (Portland, OR, USA), because their smaller dimension and lower weight (22 g) makes them particularly suitable for the target application. Each SU contains an M-IMU, a micro-SD for robust data logging and a radio transceiver. The orientation information is computed via the manufacturer's Kalman filter, in the form of a quaternion (\mathbf{q}_{SF}^G) relating the orientation of a global, Earth-based frame (G) to the SF. An access point is provided to gather synchronized sensor data and to make them available to a PC in real time.

As software, we developed a C++ GUI application for agile system managing and data collection, using the Qtcross-platform framework. Each M-IMU sensor can be tagged within the software application with the name of the human joint to which it is attached in order to store this information in the data logs. A complete scheme of the experimental setup is shown in Figure 1.

2.2. Calibration Protocol

This section describes the calibration protocol for the kinematic tracking of thorax and upper limb motion in children. However, before providing details and in order to clarify what will follow, we shall provide an overview of the entire procedure.

Figure 1. Experimental setup: the 5 sensing units (SUs) are attached to the body at predefined spots and data are collected and visualized via the developed software interface.



The proposed methodology was tested on a group of 40 primary school children (the average age is 6.9 ± 0.65 years old; the minimum is 6.0 and the maximum is 8.0; and the group is composed of 22 females and 18 males). Informed consent was obtained from all the children's parents, as required by the Institutional Review Board at the National Research Council (CNR). An experimentation session took place in the school, thus capturing motion in an environment familiar to the children.

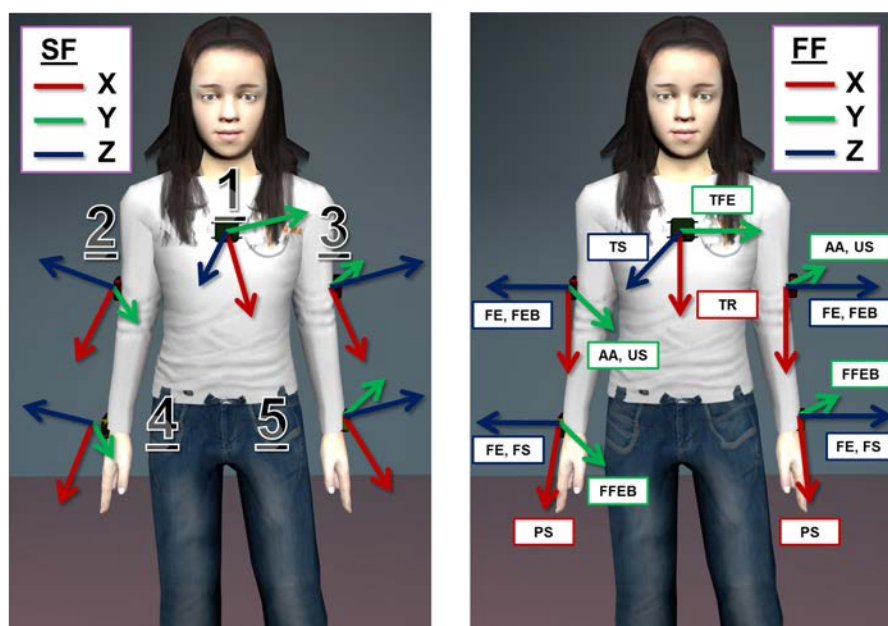
Before starting the experimentation session, being aware of the accelerometer and magnetometer calibration issues reported in [21], the calibration status of each sensor was assessed following the procedure described in [22]. Then, each sensor was fixed to the corresponding body segment of interest using Velcro straps. During the procedure, the mapping sensor-body segment was recorded in the data logs through the developed software interface.

As a preliminary step, the calibration protocol requires 5 SUs to be attached to the following body spots: central on the thorax, latero-distally on the right and left upper arm and near the wrist on the right and left forearm, as shown in Figure 2. Furthermore, each body spot is assigned an arbitrarily fixed FF, which is descriptive of the kinematic of the body spot itself, e.g., the axes of the FF on the upper arm will be related to the degree of freedom of the shoulder joint. Finally, each SU is associated with a corresponding FF. Then, the actual calibration procedure articulates in a series of 4 successive steps:

- step 1: the participant, while wearing the SUs, completes a predefined list of movements and adopts a set of stances, separately comprising the thorax, the upper limbs or the forearms. Each movement in the list is associated with an axis of the involved FFs on the body.
- step 2: the information is collected from the SUs and pre-processed (*i.e.*, normalization) in order to extract the direction of the gravity vector and of the angular velocity vector, respectively, during the stationary postures and movements.
- step 3: an estimate of each axis of the FFs, relative to the corresponding SF, is obtained from the pre-processed data, applying singular value decomposition (SVD). Moreover, associated with the estimates is a measure of the reliability of the computed axis.
- step 4: given the set of FF axes and their estimates in the SFs, a regression algorithm, namely Levenberg–Marquardt (LM), is applied to compute the transformation between each pair of systems of coordinates. Furthermore, the reliability indices computed at step 3 are used to properly condition the regression algorithm.

The final aim of the calibration procedure is then to define the transformation between each SF and the corresponding, arbitrarily fixed FF, *i.e.*, the rotation matrix, R_{SF}^{FF} . Eventually, its estimation allows for the transition from the orientation information of the SUs to the kinematic description of the upper body.

Figure 2. The figure on the left reports the position of the SUs on the body segments (1, thorax; 2, right upper arm; 3, left upper arm; 4, right forearm; 5, left forearm). On the right, a possible assignment of the functional frame (FF) on the body is reported. Note that each movement in the calibration protocol list is matched to an axis in the FFs (refer to Section 2.2.1. for the meaning of the acronyms). SF, sensor frame.



2.2.1. Calibration Movements

The first part of the calibration itself consists of a set of stationary postures and mono-axial, functional movements that the participant has to perform. This approach relies on the two procedures that are commonly referred to in the literature as the “reference” and “functional” method, respectively [19]. The aim of this first step of the protocol is to allow for the identification of, at least, a pair of non-aligned axes on each FF of the body segments of interest. These axes are representative of certain directions of interest on the body, *i.e.*, the transverse axis of a body segment, or of physiological motion, *i.e.*, the axis of rotation of the shoulder joint during flexion-extension of the upper arm. For the kinematic tracking of the thorax and upper limbs in children, we propose the following calibration movement:

- **Thorax**

TS: The gravity vector measured in supine position with arms alongside the body and palms facing down (5 s)

TR: Rotation of the thorax on the transverse plane while holding a bar (3–4 reps.), the movement is shown in Figure 3

TFE: Flexion-extension from standing position with legs opened at shoulder-width (3–4 reps.)

- **Upper arm**

US: The gravity vector measured in supine position with arms alongside the body and palms facing down ((5 s)

AA: Ab- and ad-duction from standing position with legs opened at shoulder-width (3–4 reps.); see Figure 3

FE: Flexion-extension from standing position with legs opened at shoulder-width (3–4 reps.)

FEB: Flexion-extension while holding a bar with hands at shoulder breadth with an adducted thumb grasp, as shown in Figure 3 (3–4 reps.)

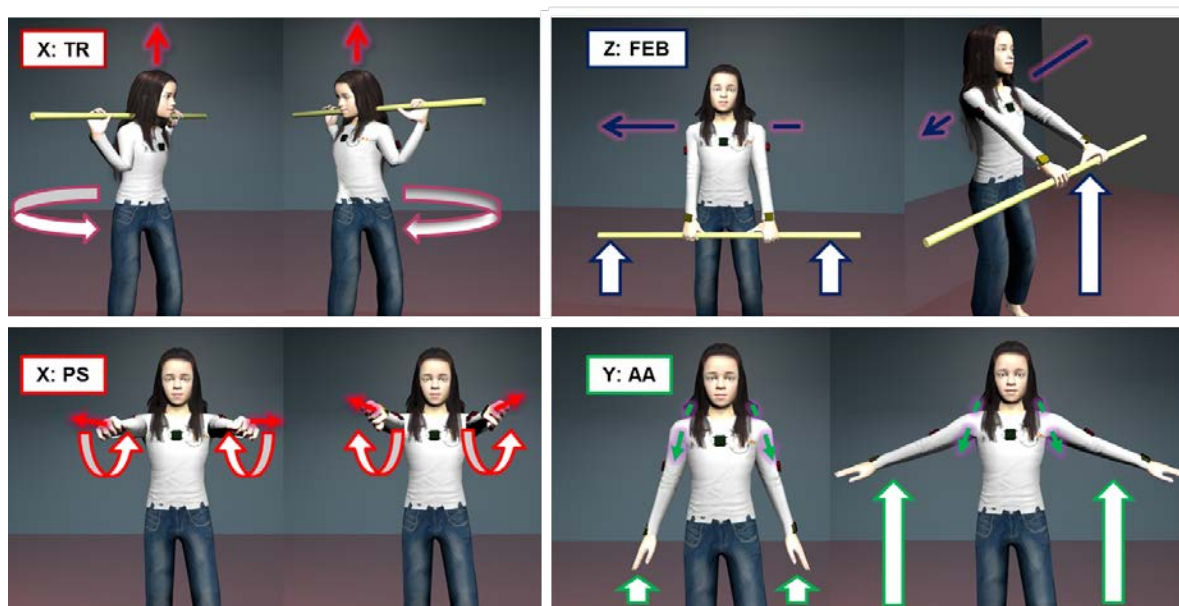
- **Forearm**

FS: The gravity vector measured in supine position with arms alongside the body and palms facing down (5 s)

PS: Pronation and supination movement with arms fully extended and hands closed (3–4 reps.) see Figure 3

FFEB: Flexion-extension while holding a bar with hands at shoulder breadth and with upper arms close to the body (3–4 reps.)

Figure 3. A subset of the calibration movements to be performed in the protocol. Clockwise from the top left we have: TR associated with the x-axis of FF_{Thorax} ; FEB of the upper arm associated with the z-axis of $FF_{Upperarm}$; AA of the upper arms associated with the y-axis of $FF_{Upperarm}$; PS of the forearms associated with the x-axis of $FF_{Forearm}$.



All calibration movements were proposed to children as a short gym exercise. An adult played the role of coach, and children were asked to observe one movement sequence before proceeding to execute the movement together with the coach. The reported list of movements and stationary postures identifies a set of no less than 3 non-aligned axes for each body segment FF. The above list describes a single trial of the calibration protocol, and the complete version will be composed of a set of 3 trials.

2.2.2. Data Collection

Aiming at identifying meaningful axes for each body segment, we are interested in collecting two kinds of information during the protocol trials, *i.e.*, accelerometer readings for the posture part and gyroscope readings for the dynamic part. In fact, accelerometers record the direction of the gravity vector while the subject is lying in supine position with palms facing down. The gyroscopes, instead, capture the angular velocity vector during movements, which allows one to identify the direction of the axis of rotation itself. Each single measurement from accelerometers or gyroscopes is a vector of data in \mathbb{R}^3 made of the three axis sensor readings. At this stage, all collected data are normalized, *i.e.*, each measurement is transformed into a unit norm vector.

2.2.3. Reference Axis Identification

We then proceeded to build the following measurements matrices, $\mathbf{A}^{SF} = [\mathbf{a}_1^{SF}, \mathbf{a}_2^{SF}, \dots, \mathbf{a}_N^{SF}]^T \in \mathbb{R}^{N \times 3}$ and $\mathbf{\Omega}^{SF} = [\boldsymbol{\omega}_1^{SF}, \boldsymbol{\omega}_2^{SF}, \dots, \boldsymbol{\omega}_N^{SF}]^T \in \mathbb{R}^{N \times 3}$, made of the N normalized readings from the accelerometers and the gyroscope, respectively. After that, we applied singular value decomposition (SVD):

$$\begin{aligned} \mathbf{A}^{SF} &= \mathbf{U} \Sigma(\sigma_i) \mathbf{V}^T \\ \mathbf{\Omega}^{SF} &= \mathbf{U} \Sigma(\sigma_i) \mathbf{V}^T \quad i = 1, 2, 3 \end{aligned} \quad (1)$$

$$\mathbf{U} \in \mathbb{R}^{N \times N}, \quad \Sigma \in \mathbb{R}^{N \times 3}, \quad \mathbf{V} \in \mathbb{R}^{3 \times 3}$$

where \mathbf{U} and \mathbf{V} are the orthogonal matrices coming out from the decomposition and containing an orthogonal basis for \mathbb{R}^N and \mathbb{R}^3 spaces, respectively. Σ is a diagonal matrix with the singular values on the main diagonal (σ_i). Based on the hypothesis of a stationary posture during the static part and a uni-axial movement during the dynamic part of the calibration protocol, the desired axis of reference will correspond to the right singular vector associated with the highest singular value ($\sigma_1 > \sigma_2 > \sigma_3$), *i.e.*, the first column of \mathbf{V} .

This result can be explained by adding the following considerations. First, in the ideal case of flawless, mono-axial movement, the angular velocity vectors will lay on a line in 3D Euclidean space, *i.e.*, they are contained in a subspace of dimension 1. Secondly, during the static part of the protocol, the projections of the gravity vectors on each axis of the SF are assumed to be constant. Again, this implies the accelerometers' readings to be confined in a subspace of dimension 1, specifically on a point. Therefore, both \mathbf{A}^{SF} and $\mathbf{\Omega}^{SF}$ are expected to be rank 1 matrices. In practice, given the objective inability for a human being to perform a perfect mono-axial joint rotation, physiological movements while lying supine (e.g., movements due to breathing) and the sensor noise, \mathbf{A}^{SF} and $\mathbf{\Omega}^{SF}$, will be full-rank. Therefore, what can be achieved with SVD is a robust discrimination between the useful information and disturbances, to identify the underlying 1-rank submatrix and its basis, *i.e.*, the axis of rotation.

In addition, we used singular values to define an index of the reliability of the computed axis, given by the following expression:

$$\rho = \frac{\sigma_1}{\sum_{i=1}^3 \sigma_i}, \quad \left[\frac{1}{3} \leq \rho \leq 1 \right] \quad (2)$$

which is a dimensionless quantity representing the ratio of the largest singular value (σ_1) and the sum of all the diagonal entries of the Σ matrix. This index provides an indication about the quality of the collected dataset, in terms of how data distributes along directions orthogonal to the computed axis of reference. In the ideal case, ρ should be the unity. In the practical one, the higher the value of ρ , the better will be the dataset collected.

By applying this procedure to all the datasets captured during steps 1 and 2, the outcome will be a set of pairs composed of axis estimates and the corresponding reliability index (\vec{v}_{SF} , ρ), for any movement in the calibration list. Further, for each FF defined on the body segments of interest, a set of at least two non-aligned axis estimates is available.

2.2.4. Transformation Matrix Computation

With the purpose of identifying the 3D rotation matrix (\mathbf{R}_{SF}^{FF}) relating each SF to its corresponding FF, the axes estimates together with their reliability indices are used in the Levenberg–Marquardt (LM) algorithm. In the following, without loss of generality, we describe the method for the case of the thorax segment ($\mathbf{R}_{SF\ Thorax}^{FF}$), where exactly 3 axis estimates are available from the protocol and will provide a means to generalize the method to the other body segments. As a first step, we construct the following vectors:

$$\vec{v}_{ref}^{FF} = \begin{bmatrix} \vec{x}^{FF} \\ \vec{y}^{FF} \\ \vec{z}^{FF} \end{bmatrix}_{9 \times 1}, \quad \vec{v}_{est}^{SF} = \begin{bmatrix} \vec{x}^{SF} \\ \vec{y}^{SF} \\ \vec{z}^{SF} \end{bmatrix}_{9 \times 1} \quad (3)$$

where \vec{v}_{ref}^{FF} is the set of canonical versors for the FF, *i.e.*, $\vec{x}^{FF} = [1 \ 0 \ 0]^T$, $\vec{y}^{FF} = [0 \ 1 \ 0]^T$, $\vec{z}^{FF} = [0 \ 0 \ 1]^T$, and \vec{v}_{est}^{SF} contains their corresponding estimates expressed in the SF. As shown in Figure 2, each versor in FF is ideally associated with a functional axis, *e.g.*, \vec{y}^{FF} represents the thorax flexion-extension movement. The vectors \vec{v}_{ref}^{FF} and \vec{v}_{est}^{SF} are related by the matrix:

$$\mathbf{Q} = \begin{bmatrix} \hat{\mathbf{R}}_{SF\ Thorax}^{FF} & & \\ & \hat{\mathbf{R}}_{SF\ Thorax}^{FF} & \\ & & \hat{\mathbf{R}}_{SF\ Thorax}^{FF} \end{bmatrix} \in \mathbb{R}^{9 \times 9} \quad (4)$$

which is a block diagonal matrix having the rotation matrix estimate repeated on the main diagonal. In the ideal case, when the estimates in \vec{v}_{est}^{SF} are orthogonal and right-handed and \mathbf{Q} contains the true \mathbf{R}_{SF}^{FF} , then the equality $\vec{v}_{ref}^{FF} = \mathbf{Q} \vec{v}_{est}^{SF}$ is verified. In the real case, the versors composing $^{SF}\vec{v}_{est}$ will most likely be not aligned, rather than orthogonal. Thus, we can define the following error function:

$$\epsilon = (\vec{v}_{ref} - \mathbf{Q}(\hat{\mathbf{R}}) \vec{v}_{est}) \quad (5)$$

where the symbol, ϵ , is the vector of residuals. In order to properly condition the LM algorithm, we used the following cost function:

$$\mathbf{C}(\hat{\mathbf{R}}) = \epsilon^T \mathbf{W} \epsilon \quad (6)$$

where we introduced a matrix, \mathbf{W} , of weights built up from the reliability indices, associated with the ${}^{SF}\vec{\mathbf{v}}_{est}$ elements, and defined as:

$$\mathbf{W} = \begin{bmatrix} \rho_x \mathbf{I}_{3 \times 3} & & \\ & \rho_y \mathbf{I}_{3 \times 3} & \\ & & \rho_z \mathbf{I}_{3 \times 3} \end{bmatrix} \quad (7)$$

If no weights are used, *i.e.*, $\mathbf{W} = \mathbf{I}$, the rotation matrix computed with the LM algorithm will be optimal in the sense of the least squares, *i.e.*, minimizing the sum of squared residuals coming from Equation (5). The advantage of introducing a matrix, \mathbf{W} , of weights, lies in the possibility to guide the optimization process in order to achieve a better fitting along the directions associated with the most reliable axes. Besides, the non-linear regression formulation will generate a rotation estimate expressed in the form of a unit norm quaternion, *i.e.*, $\hat{\mathbf{q}}_{SF}^{FF} = [w \ x \ y \ z]^T$. In order to convert the current estimate back to a rotation matrix, we used the following conversion expression:

$$\mathbf{R}(\mathbf{q}) = \begin{bmatrix} w^2 + x^2 - y^2 - z^2 & 2xy - 2zw & 2xz + 2yw \\ 2xy + 2zw & w^2 + y^2 - x^2 - z^2 & 2yz - 2xw \\ 2xz - 2yw & 2yz + 2xw & w^2 + z^2 - x^2 - y^2 \end{bmatrix} \quad (8)$$

which avoids singularity issues when computing the Jacobian of the cost function. The complete formulation of the LM regression algorithm is given by:

$$\hat{\mathbf{q}}_{k+1}^* = \hat{\mathbf{q}}_k - \Delta_k \quad (9)$$

$$\hat{\mathbf{q}}_{k+1} = \|\hat{\mathbf{q}}_{k+1}^*\|$$

where $\hat{\mathbf{q}}_{k+1}^*$ is computed from the previous quaternion ($\hat{\mathbf{q}}_k$) estimate and has to be normalized to enforce the unit-norm condition, which guarantees the estimate to be a rotation in the special orthogonal group, $\mathbb{SO}(3)$. The variable, Δ_k , represents the regression step at the k -iteration, and it is defined as:

$$\Delta_k = (\mathbf{J}^T \mathbf{W} \mathbf{J} + \lambda \text{diag}(\mathbf{J}^T \mathbf{W} \mathbf{J}))^{-1} \mathbf{J}^T \mathbf{W} \boldsymbol{\epsilon} \quad (10)$$

$$\mathbf{J} = \partial \boldsymbol{\epsilon} / \partial \mathbf{q}$$

where \mathbf{J} is the Jacobian of the error function and λ is a damping parameter, which modulates the algorithm's behavior. Note that the LM is formulated using the more efficient expression by Marquardt for the Fisher matrix ($\mathbf{F} = \mathbf{J}^T \mathbf{W} \mathbf{J} + \lambda \text{diag}(\mathbf{J}^T \mathbf{W} \mathbf{J})$), which reduces the convergence time of the algorithm. We also selected, as a convergence criterion, the percentage variation of the cost function to be under a certain threshold (ε):

$$\left| \frac{\mathbf{C}(\hat{\mathbf{R}})_k - \mathbf{C}(\hat{\mathbf{R}})_{k+1}}{\mathbf{C}(\hat{\mathbf{R}})_k} \right| < \varepsilon \quad (11)$$

Beyond the case of the thorax, the method can be scaled according to the number of vector estimates available, with the constraint of a minimum of 2 estimates in order to unambiguously identify a rotation matrix. In the general case of a number, N , of estimates, the presented matrices and vectors will have the dimension:

$${}^{FF}\vec{\mathbf{v}}_{ref} \in \mathbb{R}^{3N \times 1}, \quad {}^{SF}\vec{\mathbf{v}}_{est} \in \mathbb{R}^{3N \times 1}, \quad \mathbf{Q} \in \mathbb{R}^{3N \times 3N}, \quad \mathbf{W} \in \mathbb{R}^{3N \times 3N} \quad (12)$$

Finally, further details on the LM algorithm and its implementations can be found in [23].

3. Results

Experimental data were collected on the group of 40 children with the methodology described above. The recorded calibration movements were processed in order to extract reference axes together with their reliability measure (ρ) of the estimate. We report in Table 1 the values of our reliability index, where the reliability parameter is expressed as the mean and standard deviation on the whole group.

Table 1. The table reports the values for the reliability index, ρ , which is a dimensionless number in the range, $[\frac{1}{3}, 1]$, relative to each calibration movement. The value is expressed as a mean (± 1 SD) computed on our group of 40 children.

Calibration Movement	Thorax	Upper Arm L	Upper Arm R	Forearm L	Forearm R
Supine on the ground	0.98 \pm 0.006	0.98 \pm 0.018	0.99 \pm 0.013	0.97 \pm 0.022	0.98 \pm 0.018
Thorax rotation on the transverse plane	0.79 \pm 0.043	//	//	//	//
Thorax flexion-extension	0.78 \pm 0.050	//	//	//	//
Forearm flexion-extension with bar	//	//	//	0.74 \pm 0.044	0.74 \pm 0.046
Upper arm flexion-extension with bar	//	0.63 \pm 0.044	0.63 \pm 0.041	0.68 \pm 0.048	0.69 \pm 0.049
Upper arm flexion-extension	//	0.60 \pm 0.042	0.61 \pm 0.038	0.55 \pm 0.031	0.57 \pm 0.035
Upper arm ab-adduction	//	0.58 \pm 0.035	0.59 \pm 0.028	0.53 \pm 0.034	0.55 \pm 0.031
Forearm prono-supination	//	0.67 \pm 0.089	0.66 \pm 0.085	0.83 \pm 0.053	0.84 \pm 0.050

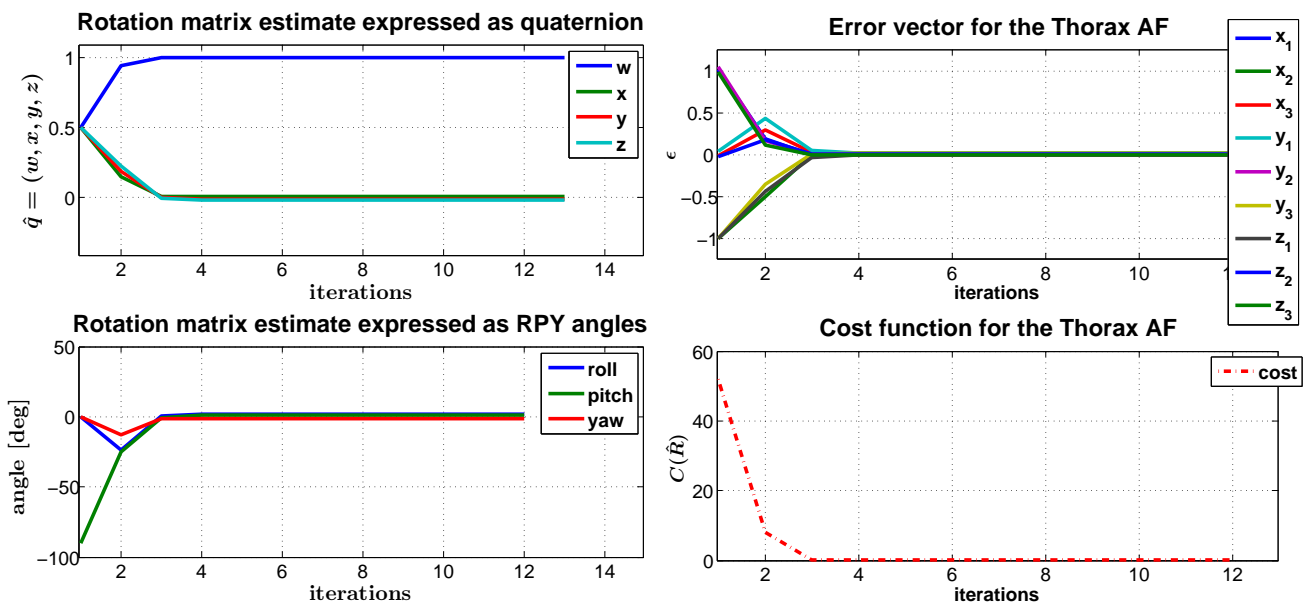
The set of axes estimates and ρ values are eventually passed as input to the LM algorithm, where they are included in the matrix of weights, defined in Equation (7). As a pre-condition to the regression, we considered the initial estimate to be the identity rotation, *i.e.*, $\hat{q}_0 = [1, 0, 0, 0]$, and we assigned $\lambda = 0.001$, which is a typical assumption for this parameter (refer to Appendix A6 in [23]). Moreover, we set the convergence criterion threshold to $\varepsilon = 10^{-4}$. Given those initialization values, the number of iterations the algorithm undergoes in the average case before attaining convergence is the following, again expressed as the mean and standard deviation:

- Thorax FF: 6.34 \pm 0.561 iterations
- Upper arm FF (left and right): 8.36 \pm 0.767 iterations
- Forearm FF (left and right): 7.30 \pm 0.863 iterations

As an example of the converging behavior of the LM algorithm, we reported the case of the thorax FF rotation matrix in Figure 4. Besides, in this particular case, we stressed that the algorithm performance

gives random initialization values as input, and we still observed the attainment of convergence after a moderate number of iterations (12 in the example).

Figure 4. The figure reports the typical converging behavior of the Levenberg–Marquardt (LM) algorithm. On the left, the trend of the \mathbf{R}_{SF}^{FF} matrix estimate relative to the FF_{Thorax} is shown, respectively expressed in the form of a unit-norm quaternion (top) and as Euler roll, pitch and yaw angles (bottom). On the right, the plots represents the error vector (top) and the cost function (bottom), respectively defined in Equations (5) and (6).



With the purpose of gaining further insight into the behavior of our regression algorithm, we focused on the error function, particularly on the vector of residuals, ϵ . As formalized in Equation (5), this vector is made of the Euclidean differences between each FF canonical axis (*i.e.*, the versors \hat{x} , \hat{y} and \hat{z}) and its corresponding estimate, both expressed in the FF system of coordinates. The aim of the regression algorithm would be that of mitigating these differences, by making matched pairs of vectors ($\vec{v}_{ref}, \vec{v}_{est}$) pointing to approximately the same directions in \mathbb{R}^3 space, *i.e.*, as close as possible, in accordance with the mathematical constraints associated with the rotation matrix, $\hat{\mathbf{R}}_{SF}^{FF}$ (e.g., the orthogonality of the column vectors). In our weighted formulation of the LM algorithm, some pairs of vectors are expected to get closer than others, depending on the value of their reliability index. In addition, the pairs that get closer are also the ones that mostly affect the computation of the transformation matrix $\hat{\mathbf{R}}_{SF}^{FF}$. In order to visualize this effect, we made a comparison of the values of these differences at the first step, when $\hat{\mathbf{R}}_{SF}^{FF} = \mathbf{I}_{3 \times 3}$, and at the convergence of the regression algorithm, $\hat{\mathbf{R}}_{SF}^{FF} = \underset{\mathbf{R}}{\operatorname{argmin}}(C(\mathbf{R}))$. As a distance metric, we considered:

$$d(\vec{v}_{ref}, \vec{v}_{est}) = \operatorname{acos}(\vec{v}_{ref}^T \vec{v}_{est}) \tag{13}$$

which is the angle between each pair of vectors. The analysis was extended to the whole set of 40 children, and we reported the results, expressed as the mean and standard deviation, for each movement, in Figure 5.

Figure 5. Comparison of the differences between pairs $(\vec{v}_{ref}, \vec{v}_{est})$ of axes estimates and their FF matches, computed at the beginning and at the end of the LM regression (refer to Section 2.2.1. for the meaning of the acronyms). As a distance metric, we considered the angle between each pair of vectors, computed as the arccosine of their dot product.

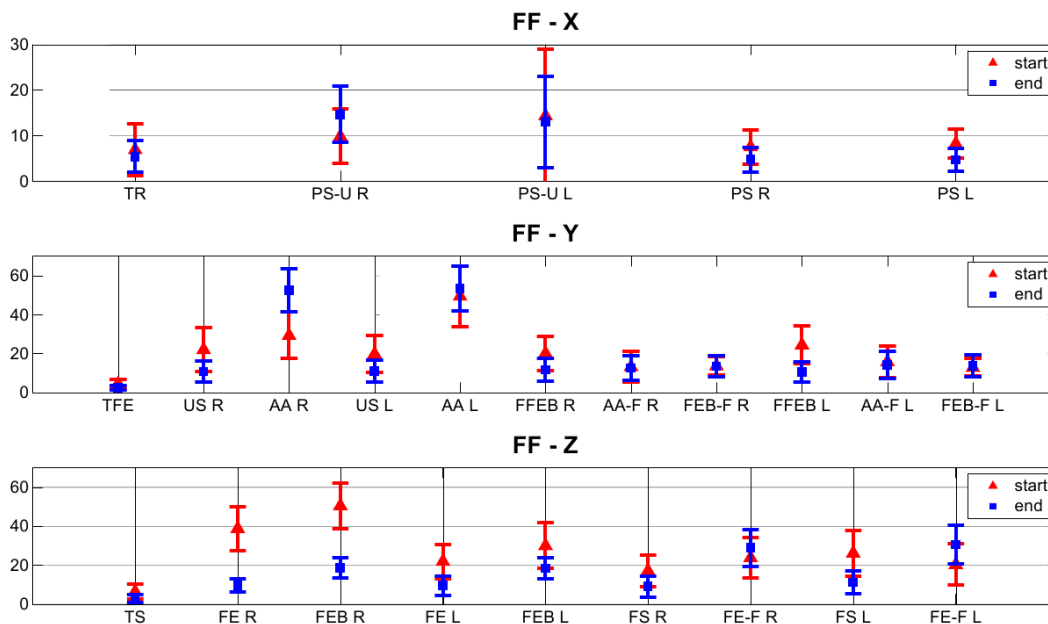
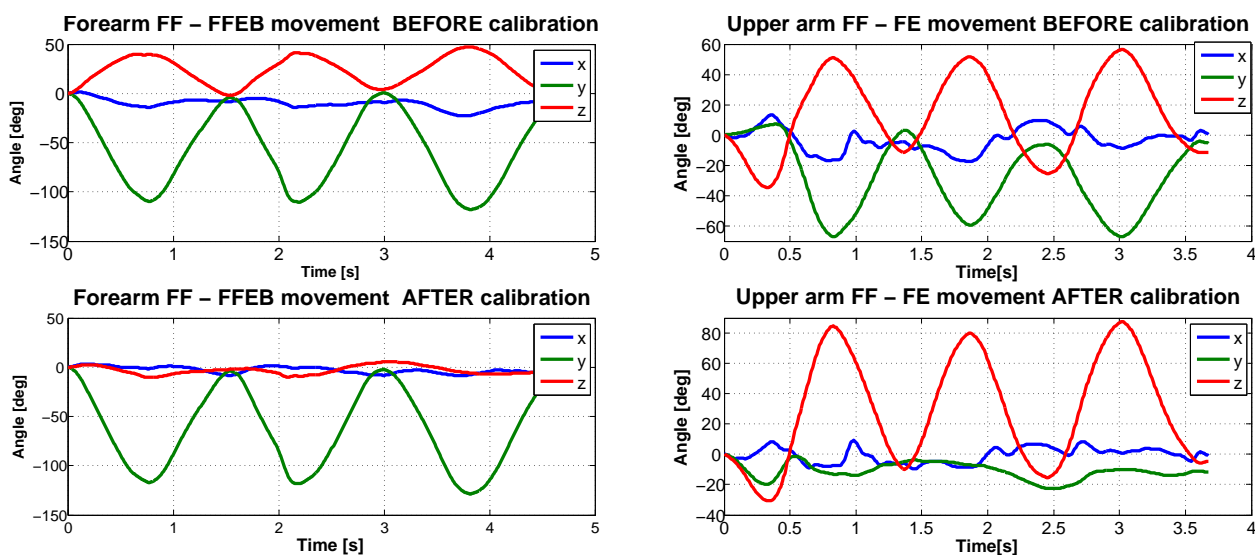


Figure 6. An example of kinematic reconstruction of the right arm during the flexion-extension (FE) movement and the supported forearm flexion-extension (FFEB) with the proposed calibration procedure.



4. Discussion and Conclusions

This paper describes a novel calibration protocol for the kinematic tracking of the thorax and upper limbs with M-IMU wearable sensors, designed to be used with children. This method allows a user to define functional coordinate systems (FF) that are fixed on the body segments and to estimate the

relation between an M-IMU sensor's frame and its corresponding body segment's FF. The proposed calibration procedure itself is made of a list of movements and a methodology to elaborate sensor data, in order to compute a rotation matrix relating each SF to the corresponding, arbitrarily-defined FF (*i.e.*, \mathbf{R}_{SF}^{FF}). Selected movements have the two-fold purpose of identifying a sufficient number of non-aligned axes on each defined FF, at least two, and conforming to the constraints of being easy to perform and short in duration, in order to avoid the fatigue of the children and to reduce the overall duration of experimental sessions.

In fact, as highlighted in our previous study [20] and as we also observed during the experimentation, some movements are easier to perform for children (6–7 yo) than others: as an example, the thorax lateral flexion, used in similar calibration protocols with adults [18], resulted in an improper choice for children. Furthermore, given the difficulty to maintain children's attention for a long time compared to adults, we tried to optimize the calibration protocol in order to limit the duration while maintaining a substantial number of functional axis estimates, as suggested in [15]. In addition, the protocol is presented as a game of imitation: an adult plays the role of the coach, and the subject is asked to mirror his movements. This experimental methodology is specific for usage with children, as it brings the two-fold benefit of: (i) making it easier for children to understand how the movements should be performed; and (ii) having an adult checking the correctness of the movement. No difficulties were encountered in the experimentation with the proposed list, and in all but the thorax case, a redundant number of functional axes were identified, referring to the minimum of a pair of non-aligned axes that is necessary in order to estimate a rotation matrix. Moreover, our novel data analysis approach eliminates the typical need of a segmentation process, which usually involves a rest period between any two phases of a rotation movement, *e.g.*, to differentiate the flexion from the extension phase, as reported in [15,16,18]. Thus, with our methodology, the duration of this part of the protocol is further reduced (*i.e.*, lasting 15 min).

In view of the necessity that may arise of pruning the list of movements to the minimum of two axes per FF, we introduced the reliability index, ρ , which is defined in Equation (2), and we used it to qualify the estimated axes, as reported in Table 1. The index of reliability is computed from measurement matrices containing repetitions (from nine to 12) of the same functional movement/reference posture and, thus, gives an indication of the precision of the child's performance. In the ideal case of a noiseless sensing unit, the maximum value of the index (*i.e.*, one) is obtained when exactly the same axis of rotation is involved in each repetition of the movement. Instead, the minimum value of the index (*i.e.*, 1/3) is mathematically obtained in the limit case when each repetition of the movement belongs to a different axis of rotation and those axes are orthogonal, *e.g.*, that would be the case in which a subject is asked to perform a flexion-extension of the upper arm three times and he instead performs a flexion-extension first, then an ab- and ad-duction and, finally, a pronosupination. Further, high precision in the execution of a movement translates into the high repeatability of the estimated reference axis.

The proposed list of movements deliberately included the same physiological movement (*i.e.*, flexion and extension) executed with or without the support of a rigid bar. The reason for that is the possibility to evaluate if, as expected from intuition, the introduction of an external support to further facilitate children's coordination improves the reliability of some movements. From the reported table, the reliability index indicates that the supported movement is better than the other. In addition, we carried out

statistical analysis using a paired t -test on the normally distributed reliability datasets, and we obtained a significant difference ($p < 0.05$) both for the forearm FFs and for the upper arm FFs.

In Figure 5, we proposed a visualization of the residual distance between vector pairs ($\vec{v}_{ref}, \vec{v}_{est}$), as defined in Equation (13), at the beginning and at the end of the LM regression and for each movement in the calibration protocol. We observed a general trend of the pairs of axes estimates and corresponding FF reference axes, to reduce their angular distance at the end of the regression. If more than one estimate for the same FF axis is available, the regression algorithm will favor the one with the higher reliability value. For instance, this is true for the case of the supine posture ($\rho = 0.98$ and $\rho = 0.99$) versus the abduction and adduction movement ($\rho = 0.58$ and $\rho = 0.59$) of the upper arms on the t-axis estimation of the associated FF. The thorax was the body segment with the overall highest reliability and with the lowest residual distance between the pairs ($\vec{v}_{ref}, \vec{v}_{est}$) in the rotation matrix estimation, respectively, 5.39° , 2.56° and 2.86° for the x, y and z component. This is due to a proper choice of the calibration movements for the thorax, with reference to both the repeatability and the fact that the set of axes estimated during each movement/reference pose is close to an orthogonal frame. Moreover, this result is in accordance with what was discussed in [18], where the functional frame built on the thorax is even proven to be the most compatible with the anatomical frame defined by the ISB recommendations [24]. The pronosupination of the forearm is the most reliable movement for the functional part of this specific FF, and its associated axis is the most repeatable, in agreement with similar studies in the literature [18,20].

Furthermore, the residual angular distance for the pairs ($\vec{v}_{ref}, \vec{v}_{est}$) amounts to 4.68° for the left and 4.72° for the right forearm.

The standard way to estimate the rotation matrix, \mathbf{R}_{SF}^{FF} , in the literature [15,16,18,24] is that of using a single pair of non-aligned axis estimates to get an orthonormal frame via successive vector products. This method is referred to in the literature as the TRIAD (Tri-axial Attitude Determination) algorithm and was originally proposed as a solution to Wahba's problem [25]. Our approach to \mathbf{R}_{SF}^{FF} estimation overcomes the known limitations of the TRIAD algorithm, in the sense that it is capable of accommodating more than two axis estimates, is not sensible to the order at which the axis estimates are considered and, more importantly, can exploit all the available information (*i.e.*, both the axis direction and its repeatability measure).

Finally, as an outcome to the method we reported in Figure 6, we present an example of the kinematic reconstruction for the right upper limb. Though evidence exists of a substantial reduction in kinematic cross-talking for single joint movements with the proposed calibration methodology, we believe that future research endeavors should focus on the comparison with data collected using optical motion capture systems, which are considered as the gold standard.

Acknowledgments

This work was partly funded by the Italian Ministry of Education, University and Research under the FIRB "Futuro in Ricerca" research program (TOUMproject, No. RBF086HEW).

Conflicts of Interest

The authors declare no conflict of interest.

References

1. Henderson, S.; Sugden, D. *Movement Assessment Battery for Children*; The Psychological Corporation: London, UK, 1992.
2. Russell, D.; Avery, L.; Rosenbaum, P.; Raina, P.; Walter, S.; Rosenbaum, P. Improved scaling of the gross motor function measure for children with cerebral palsy: Evidence of reliability and validity. *Phys. Ther.* **2000**, *80*, 873–885.
3. Crock, R.V.; Horvat, M.; McCarthy, E. Reliability and concurrent validity of the movement assessment battery for children. *Percept. Motor Skills* **2001**, *93*, 275–280.
4. Gilmore, R.; Sakzewski, L.; Boyd, R. Upper limb activity measures for 5- to 16-year-old children with congenital hemiplegia: A systematic review. *Dev. Med. Child Neurol.* **2010**, *52*, 14–21.
5. Zhang, M.; Lange, B.; Chang, C.Y.; Sawchuk, A.; Rizzo, A. Beyond the Standard Clinical Rating Scales: Fine-Grained Assessment of Post-Stroke Motor Functionality Using Wearable Inertial Sensors. In Proceedings of the 34th Annual International Conference of the IEEE EMBS, San Diego, CA, USA, 28 August–1 September 2012; pp. 6111–6115.
6. Pettenati, S.; Stefanini, S.; Volterra, V. Motoric characteristics of representational gestures produced by young children in a naming task. *J. Child Lang.* **2009**, *37*, 887–911.
7. Von Hofsten, C. An action perspective on motor development. *Trends Cognit. Sci.* **2004**, *8*, 266–272.
8. Von Hofsten, C.; Rosander, K. Perception-action in children with ASD. *Front. Integr. Neurosci.* **2012**, *6*, 1–6.
9. Taffoni, F.; Focaroli, V.; Formica, D.; Iverson, J.M.; Keller, F.; Gugliemelli, E. Sensor-Based Technology in the Study of Motor Skills in Infants at Risk for ASD. In Proceedings of the 4th IEEE RAS/EMBS International Conference on Biomedical Robotics and Biomechatronics (BIOROB 2012), Rome, Italy, 24–27 June 2012; pp. 1879–1883.
10. Campolo, D.; Taffoni, F.; Formica, D.; Iverson, J.; Sparaci, L.; Keller, F.; Gugliemelli, E. A mechatronic platform for assessing development of spatial cognition in infants. *J. Integr. Neurosci.* **2012**, *11*, 103–116.
11. Welch, G.; Foxlin, E. Motion tracking: No silver bullet, but a respectable arsenal. *IEEE Comput. Graph. Applic.* **2002**, *22*, 24–38.
12. Bonato, P. Wearable sensors/systems and their impact on biomedical engineering. *IEEE Eng. Med. Biol. Mag.* **2003**, *22*, 18–20.
13. Bonato, P. Advances in wearable technology and applications in physical medicine and rehabilitation. *J. Neuroeng. Rehab.* **2005**, *2*, doi:10.1186/1743-0003-2-2.
14. Sabatini, A.M. Estimating three-dimensional orientation of human body parts by inertial/magnetic sensing. *Sensors* **2011**, *11*, 1489–1525.
15. Luinge, H.J.; Veltink, P.H.; Baten, C.T.M. Ambulatory measurement of arm orientation. *J. Biomech.* **2007**, *40*, 78–85.

16. Cutti, A.G.; Giovanardi, A.; Rocchi, L.; Davalli, A.; Sacchetti, R. Ambulatory measurement of shoulder and elbow kinematics through inertial and magnetic sensors. *Med. Biol. Eng. Comput.* **2008**, *46*, 169–178.
17. Cutti, A.G.; Ferrari, A.; Garofalo, P.; Raggi, M.; Ferrari, A. ‘Outwalk’: A protocol for clinical gait analysis based on inertial and magnetic sensors. *Med. Biol. Eng. Comput.* **2010**, *48*, 17–25.
18. De Vries, W.H.K.; Veeger, H.E.J.; Cutti, A.G.; Baten, C.; van der Helm, F.C.T. Functionally interpretable local coordinate systems for the upper extremity using inertial & magnetic measurement systems. *J. Biomech.* **2010**, *43*, 1983–1988.
19. Kontaxis, A.; Cutti, A.G.; Johnson, G.R.; Veeger, H.E.J. A framework for the definition of standardized protocols for measuring upper-extremity kinematics. *Clin. Biomech. (Bristol, Avon)* **2009**, *24*, 246–253.
20. Ricci, L.; Formica, D.; Tamilia, E.; Taffoni, F.; Sparaci, L.; Capirci, O.; Guglielmelli, E. An Experimental Protocol for the Definition of Upper Limb Anatomical Frames on Children Using Magneto–Inertial Sensors. In Proceedings of the 35th Annual International Conference of the IEEE EMBC, Osaka, Japan, 3–7 July 2013.
21. Picerno, P.; Cereatti, A.; Cappozzo, A. A spot check for assessing static orientation consistency of inertial and magnetic sensing units. *Gait Post.* **2011**, *33*, 373–378.
22. Campolo, D.; Taffoni, F.; Formica, D.; Schiavone, G.; Keller, F.; Guglielmelli, E. Inertial-magnetic sensors for assessing spatial cognition in infants. *IEEE Trans. Biomed. Eng.* **2011**, *58*, 1499–1503.
23. Hartley, R.I.; Zisserman, A. *Multiple View Geometry in Computer Vision*, 2nd ed.; Cambridge University Press: Cambridge, UK, 2000.
24. Wu, G.; van der Helm, F.C.; (DirkJan) Veeger, H.; Makhsous, M.; van Roy, P.; Anglin, C.; Nagels, J.; Karduna, A.R.; McQuade, K.; Wang, X.; *et al.* ISB recommendation on definitions of joint coordinate systems of various joints for the reporting of human joint motionPart II: Shoulder, elbow, wrist and hand. *J. Biomech.* **2005**, *38*, 981–992.
25. Wahba, G. A least-square estimate of spacecraft attitude. *SIAM Review* **1966**, *8*, 384–386.



Gait variability and stability measures: Minimum number of strides and within-session reliability



F. Riva ^{a,*}, M.C. Bisi ^a, R. Stagni ^{a,b}

^a DEI – Department of Electrical, Electronic, and Information Engineering ‘Guglielmo Marconi’, University of Bologna, via Venezia 52, 47521 Cesena (FC), Italy

^b Health Sciences and Technologies – Interdepartmental Center for Industrial Research (HST – ICIR), University of Bologna, Italy

ARTICLE INFO

Article history:

Received 13 January 2014

Accepted 5 April 2014

Keywords:

Within-session reliability

Stride number

Gait stability

Gait variability

Inertial sensors

ABSTRACT

Background: Several methods are proposed in the literature for the quantification of gait variability/stability from trunk accelerations. Since outputs can be influenced by implementation differences, reliability assessment and standardization of implementation parameters are still an issue. The aim of this study is to assess the minimum number of required strides and the within-session reliability of 11 variability/stability measures.

Method: Ten healthy participants walked in a straight line at self-selected speed wearing two synchronized tri-axial Inertial Measurement Units. Five variability measures were calculated based on stride times namely Standard deviation, Coefficient of variation, Inconsistency of variance, Nonstationary index and Poincaré plot. Six stability measures were calculated based on trunk accelerations namely Maximum Floquet multipliers, Short term/long term Lyapunov exponents, Recurrence quantification analysis, Multiscale entropy, Harmonic ratio and Index of harmonicity. The required minimum number of strides and the within-session reliability for each measure were obtained based on the interquartile range/mean ratio. Measures were classified in five categories (namely excellent, good, average, poor, and very poor) based on their reliability.

Results: The number of strides required to obtain a reliable measure was generally larger than those conventionally used. Variability measures showed average to poor reliability, while stability measures ranged from excellent to very poor reliability.

Conclusion: Recurrence quantification analysis and multiscale entropy of trunk accelerations showed excellent reliability and a reasonable number of required strides. Based on these results, these measures should be taken into consideration in the assessment of fall risk.

© 2014 Elsevier Ltd. All rights reserved.

1. Introduction

Ageing and pathology can worsen gait performance at multiple levels and in selective ways [1], and quantitative assessment of gait pattern has been proven to be useful in the early identification and prediction of pathology or cognitive decline [2–4]. In particular, trunk acceleration-based measures of gait variability and stability are proposed in the literature aiming at quantifying subject specific gait characteristics such as gait impairment, degree of neuro-motor control and balance disorders, in pathologic and healthy subjects, and are often related to fall at risk [5–9]. However, no standard implementation procedure for these measures is defined, potentially explaining the incoherent conclusions [10], as implementation differences can affect outputs. Thus, a standardization of the

implementation parameters is necessary to perform a consistent evaluation. Moreover, these measures must reproduce the same results in the same experimental conditions.

Many strides can be required to obtain reliable measures, but treadmill walking differs significantly from over-ground walking [11]; hence, long walking trials have to be analyzed. The use of Inertial Measurement Units (IMU) allows to obtain both stride time variability and stability measures from trunk acceleration signals during long over-ground outdoor walking trials.

In order to further define implementation features for future effective exploitation of measures in research or clinical practice, an assessment of the repeatability of variability/stability measures is hence needed, together with an assessment of the number of necessary strides. The aim of the present study was to assess the minimum number of required strides and the within-session reliability of 11 temporal variability/stability measures proposed in the literature and applied to stride time and trunk accelerations during over-ground walking.

* Corresponding author. Tel.: +39 0547 33 89 53.

E-mail address: f.riva@unibo.it (F. Riva).

2. Methods

Ten healthy participants [28 ± 3 years, 174 ± 11 cm, 67 ± 13 kg] walked in a straight line at self-selected natural speed on a 250 m long dead-end road (about 180 strides), wearing two synchronized tri-axial IMU (Opal, APDM, USA) located on the trunk (at the level of the fifth lumbar vertebra) and on the right shank. Sample size was chosen in agreement with previous literature [12]. Range of accelerometers was ± 6 G and sampling rate 128 Hz. Right heel strike instants were obtained from the angular velocity measured by the sensor on the shank with a wavelet-based method [13]. Gait initiation and termination phases were excluded. The average walking speed was 1.43 ± 0.15 m/s.

Since our aim was the characterization of variability/stability measures from a strictly methodological point of view, adequately segmented data coming from the same experimental trial (long overground walk) were analyzed. This approach was adopted in order to maintain the experimental conditions unvaried, being thus able to ascribe every variation found in the results to the intrinsic variability of each measure only rather than to actual differences in gait patterns depending on specific trial analyzed.

The following variability measures were applied to stride time:

- i. Standard deviation (SD) [14];
- ii. Coefficient of variation (CV) [14];
- iii. Inconsistency of variance (IV) [15];
- iv. Nonstationary index (NI) [15];
- v. Poincaré plots (PSD1/PSD2) [16].

SD represents the standard deviation of stride time. CV is the variability of stride time normalized to the mean stride time value ($CV = 100 \times SD/\text{mean}$) [14]. IV and NI quantify the temporal “structure” of the time series (independent of the overall variance); each time series was first normalized with respect to its mean and SD and then divided into blocks of five strides each. In each segment, the local average and the local SD were computed. NI is then defined as the SD of the local averages, while IV is defined as the SD of the local SDs [15]. Stride time data plots between successive gait cycles, known as Poincaré plots, show variability of stride time data. Statistically, the plots display the correlation between consecutive stride times data in a graphical manner. PSD1 and PSD2 represent, respectively, width and length of the long and short axis describing the elliptical nature of the plots, and hence the short-term and long-term variability of stride time [16].

The following stability measures were calculated on trunk accelerations in vertical (V), medio-lateral (ML) and anterior-posterior (AP) directions:

- vi. Maximum Floquet multipliers (maxFM) [5,10];
- vii. Short term/long term Lyapunov exponents (sLE/ILE) [5];
- viii. Recurrence quantification analysis (RQA) [17];
- ix. Multiscale entropy (MSE) [18];
- x. Harmonic ratio (HR) [6];
- xi. Index of harmonicity (IH) [19].

maxFM quantify orbital stability of a periodic or pseudo-periodic dynamic system, that is the tendency of the system state to return to the periodic limit cycle orbit after small perturbations [5,10]. On the other hand, sLE and ILE quantify local dynamic stability of a system and are used for systems that do not necessarily exhibit a discernable periodic structure [5]. RQA provides a characterization of a variety of features of a given time series, including a quantification of deterministic structure and non-stationarity [17], based on the construction of recurrence plots [20]. All of these measures imply the reconstruction of the state space of the system; in this study, four different state spaces were constructed: one 3-dimensional state space composed by

acceleration signals in the V, ML and AP direction and three (one per direction) 5-dimensional state spaces composed by delay-embedding of each acceleration component (delay=10 samples). Such parameters were chosen based on previous literature, stating that an embedding dimension of 5 and a 10 samples delay are appropriate for gait data [21–23], and on a false nearest neighbors analysis performed on our data.

Several measures were extracted from RQA, namely recurrence rate (rr), determinism (det), averaged diagonal line length (avg), maximum diagonal line length (max) and divergence (diverg). In the calculation of RQA measures, a radius of 40% was chosen to make sure that recurrence rate (rr) responded smoothly and was not too high, and that determinism (det) did not saturate at the floor of 0 or the ceiling of 100, as approaching these limits would tend to suppress variance in the measure [20]. Time series derived from complex systems, like biological systems, are likely to present structures on multiple spatio-temporal scales; MSE has been introduced to quantify the complexity or irregularity of a time series [18]. MSE has been obtained calculating sample entropy (consecutive data points $m=2$, distance $r=0.2$ [24]) on six consecutively more coarse-grained (scale factor $\tau=1, \dots, 6$) time series. HR quantify the smoothness of acceleration patterns of the trunk based on amplitudes in the frequency spectra. It provides information on how smoothly subjects control their trunk during walking and it is directly related to whole body balance and coordination [6,25]. In this study, HR was not calculated stride by stride, but decomposing the whole signal into its harmonics [7]. Similarly to HR, IH assesses the contribution of the oscillating components to the observed coordination patterns by means of spectral analysis [19], quantifying the contribution of the stride frequency to the signal power relative to higher harmonics.

For the quantification of the **minimum number of strides**, measures were calculated on windows of decreasing length (from 150 to 10 strides, 1 stride resolution). Interquartile range and median value of measures were calculated for all the windows. Percent interquartile range/median ratio (*imr*) was then calculated, starting from the 150 strides window (which gave the lowest ratio) and proceeding backwards.

Adding an increasing number of strides to the calculation would cause the measure to reach a steady outcome, which represents a compromise between reliability of the measure and experimental limitations. Percent *imr* is then an indication of the variations of the measures around the median value. A low *imr* indicates small variations of the measure around its median value with the increase of the number of strides; this means that the measure reached a steady value, and it is not likely to change with the inclusion of further strides. On the contrary, a high *imr* indicates that the measure undergoes significant variation with the increase of the number of strides, and hence is still not fully reliable.

Thresholds for the *imr* were fixed at 10%, 20%, 30%, 40% and 50%. The required number of strides was defined as the smallest one at which the ratio remained below the lowest possible threshold. The minimum number of strides was calculated per index and per subject at first, and then the largest number of strides over subjects was selected for each index.

The assessment of **within-session reliability** was performed calculating variability/stability measures on a window sliding along the trial with 1 stride steps. The sliding window size was set to 85 strides, since most measures (51 out of 57) required less than 85 strides. ILE (tot, V, ML, AP) and RQA V (max, diverg) did not satisfy this criterion. Interquartile range and median values of the measures over the windows, together with the percent *imr* for each measure, were calculated. Measures were grouped in five reliability categories, ranging from very poor (*imr* > 40%) to excellent (*imr* < 10%), based on the maximum inter-subject *imr*.

Interquartile range/median ratio was chosen as a reliability measure since large magnitude variations around the median value (particularly among windows sharing a lot of data) can be potentially disruptive, and are to be considered as a sign of low repeatability and high intrinsic variability of the measure.

In addition, intra-class correlation (ICC 2,1) was calculated between two 85 strides non-overlapping windows extracted for each subject from the same walking trial (SPSS Statistics 20.0, IBM, Armonk, NY, USA).

3. Results

Measures reached steady values for different numbers of strides, depending on the threshold. For MSE V ($\tau=1, \dots, 4$) and RQA (AP rr, det, avg, ML rr and V rr, det, avg), 10 strides were sufficient to reach a 10% threshold. MSE (AP, ML, V $\tau=5,6$), RQA (ML det, avg) and sLE V reached a 20% threshold within 10 strides. Other measures showed lower stride number requirement with the increasing of the threshold. ILE required a high number of strides (> 110) even for the 50% threshold. RQA (V max, diverg) never reached steady values in the analyzed range (Table 1).

MSE and RQA (rr, det, avg) showed excellent reliability. HR and sLE demonstrated average to good reliability, with the exception of sLE (tot) that performed poorly. Temporal variability measures (SD, CV, IV, NI and PSD) showed from poor to good reliability. IH showed poor reliability, particularly in AP and V directions. ILE, maxFM and RQA (max, diverg) showed very poor reliability. Reliability results are shown in Table 2. The median values of inter-subjects medians and inter-quartiles for variability/stability measures, together with maximum *imr* values, are also shown. These values are meant as reference for the analyzed measures in healthy subjects.

ICC results showed overall coherence with *imr* values, highlighting similar correlation patterns, with the main exception of IH (AP, V) results (Table 3).

4. Discussion

While variability measures aim at quantifying the degree of variability in the stride time, stability measures directly quantify stability (maxFM, sLE, ILE) or stability-related properties of gait time-series, such as recurrence (RQA), complexity at different scales (MSE), smoothness (HR) or harmonicity (IH). Since no standard implementation procedure is defined for these measures, the aim of this study was to investigate the required minimum number of strides and the within-session reliability of a number of gait variability/stability measures.

Prior research explored similar questions [26,27], but based solely on treadmill walking. Other studies recently focused on the assessment of reliability of gait stability and variability measures [28,29], confirming that the reliability of variability parameters improves with the increase in the number of analyzed cycles.

Since data extracted from the same overground long walk were analyzed, experimental conditions were guaranteed to be the same allowing to ascribe the differences found in the results to intrinsic features of the measures only, rather than to actual differences in the gait pattern adopted by the participants.

In general, measures showed comparable performances between the reliability indication and the threshold reached for a corresponding number of strides (85). MSE (ML $\tau=1, 5$ and V $\tau=1, \dots, 4$) and RQA (AP rr, det, avg, ML rr and V rr, det, avg) reached a steady value for a 10% threshold within 10 strides. MSE and RQA (rr, det, avg) also showed excellent reliability. sLE (ML, V)

Table 1
Number of required strides for each measure at each threshold.

Variability/stability measures	Thresholds				
	10%	20%	30%	40%	50%
SD	125	59	20	15	10
CV	127	59	49	15	10
NI	143	97	89	78	70
IV	143	91	44	35	29
PSD1	127	52	16	15	10
PSD2	120	106	74	25	19
MSE AP $\tau=1$	19	10	10	10	10
MSE AP $\tau=2$	19	10	10	10	10
MSE AP $\tau=3$	18	10	10	10	10
MSE AP $\tau=4$	15	10	10	10	10
MSE AP $\tau=5$	35	10	10	10	10
MSE AP $\tau=6$	17	10	10	10	10
MSE ML $\tau=1$	10	10	10	10	10
MSE ML $\tau=2$	30	10	10	10	10
MSE ML $\tau=3$	63	10	10	10	10
MSE ML $\tau=4$	31	10	10	10	10
MSE ML $\tau=5$	10	10	10	10	10
MSE ML $\tau=6$	32	10	10	10	10
MSE V $\tau=1$	10	10	10	10	10
MSE V $\tau=2$	10	10	10	10	10
MSE V $\tau=3$	10	10	10	10	10
MSE V $\tau=4$	10	10	10	10	10
MSE V $\tau=5$	12	10	10	10	10
MSE V $\tau=6$	15	10	10	10	10
RQA AP (rr)	10	10	10	10	10
RQA AP (det)	10	10	10	10	10
RQA AP (avg)	10	10	10	10	10
RQA AP (max)	121	75	74	37	36
RQA AP (diverg)	107	95	74	74	74
RQA ML (rr)	10	10	10	10	10
RQA ML (det)	78	10	10	10	10
RQA ML (avg)	55	10	10	10	10
RQA ML (max)	136	129	73	29	29
RQA ML (diverg)	136	135	79	29	29
RQA V (rr)	10	10	10	10	10
RQA V (det)	10	10	10	10	10
RQA V (avg)	10	10	10	10	10
RQA V (max)	150	150	150	150	150
RQA V (diverg)	150	150	150	150	150
HR AP	141	26	15	10	10
HR ML	137	30	10	10	10
HR V	66	29	10	10	10
IH AP	143	141	137	75	10
IH ML	145	141	49	10	10
IH V	140	127	120	18	11
maxFM tot	137	135	23	10	10
maxFM AP	138	137	132	10	10
maxFM ML	137	131	14	10	10
maxFM V	137	51	20	10	10
sLE tot	105	70	10	10	10
sLE AP	90	17	10	10	10
sLE ML	72	10	10	10	10
sLE V	63	10	10	10	10
ILE tot	139	132	130	128	124
ILE AP	141	135	132	131	129
ILE ML	146	125	119	114	110
ILE V	138	123	121	116	113

showed that the 10% threshold could be reached for 85 strides, but inter-subject *imr* was slightly higher (0.20 and 0.28 respectively); this is likely due to the influence of the inherent variability of the trial.

SD and CV showed average reliability and quite a high number of strides (125 and 127, respectively) to undergo the 10% threshold. This confirms findings from other studies stating that a few number of strides may not be sufficient to obtain reliable measures for both young subjects and old adults [30,31].

A large number of required strides was found for ILE and RQA (V max, diverg). ILE measure required at least 110 strides to reach

Table 2
Reliability grouping of variability and stability measures. Measures have been grouped based on the maximum inter-subject *imr*. Reliabilities have been labeled as very poor (*imr* > 40%), poor (*imr* = 30–40%), average (*imr* = 20–30%), good (*imr* = 10–20%), excellent (*imr* < 10%). As an indication of reference values for the measures, median values of inter-subjects' medians and interquartiles for variability/stability measures are also shown. Units of measurement legend: MSE – unitless, RQA (rr, det) – % of points on the recurrence plot, RQA (avg, max, diverg) – number of points on the recurrence plot, HR – unitless, IH – unitless, sLE – 1/stride, ILE – 1/stride, maxFM – unitless, SD – seconds, CV – unitless, NI – unitless, IV – unitless, and PSD1/PSD2 – seconds.

	Variability/stability measures	Maximum inter-subject <i>imr</i> (%)	Median inter-subject value of the medians	Median inter-subject interquartile value
Excellent	MSE AP $\tau=1$	7	0.38	0.01
	MSE AP $\tau=2$	7	0.56	0.02
	MSE AP $\tau=3$	6	0.65	0.02
	MSE AP $\tau=4$	7	0.76	0.02
	MSE AP $\tau=5$	8	0.81	0.02
	MSE AP $\tau=6$	7	0.85	0.02
	MSE ML $\tau=1$	8	0.59	0.01
	MSE ML $\tau=2$	8	0.86	0.02
	MSE ML $\tau=3$	7	1.09	0.03
	MSE ML $\tau=4$	6	1.31	0.03
	MSE ML $\tau=5$	6	1.46	0.04
	MSE ML $\tau=6$	6	1.55	0.04
	MSE V $\tau=1$	5	0.46	0.01
	MSE V $\tau=2$	5	0.63	0.02
	MSE V $\tau=3$	7	0.74	0.02
	MSE V $\tau=4$	9	0.84	0.03
	MSE V $\tau=5$	7	0.92	0.03
	MSE V $\tau=6$	9	1.00	0.03
	RQA AP (rr)	7	15.65	0.06
	RQA AP (det)	5	69.3	1.1
	RQA AP (avg)	7	8.94	0.12
	RQA ML (rr)	3	8.50	0.12
RQA ML (det)	9	49.7	0.8	
RQA ML (avg)	7	6.67	0.12	
RQA V (rr)	6	13.76	0.22	
RQA V (det)	3	81.9	0.5	
RQA V (avg)	8	13.58	0.28	
Good	HR AP	15	3.70	0.14
	HR ML	13	2.21	0.11
	HR V	16	4.68	0.24
	PSD1	14	0.021	0.001
Average	sLE AP	26	0.67	0.14
	sLE ML	20	0.81	0.14
	sLE V	28	0.89	0.19
	SD	23	0.02	0.002
	CV	23	1.94	0.14
Poor	IH ML	37	0.15	0.02
	PSD2	34	0.021	0.002
	sLE tot	39	0.44	0.10
	NI	30	0.52	0.10
Very poor	IV	37	0.32	0.06
	maxFM tot	57	0.36	0.09
	maxFM AP	45	0.43	0.08
	maxFM ML	44	0.39	0.06
	maxFM V	44	0.48	0.08
	IH AP	50	0.04	0.01
	IH V	55	0.022	0.003
	RQA AP (max)	66	399	51
	RQA AP (diverg)	164	0.0025	0.0003
	RQA ML (max)	88	281	39
	RQA ML (diverg)	69	0.0036	0.0004
	RQA V (max)	96	1986	481
	RQA V (diverg)	176	0.0005	0.0002
	ILE tot	89	0.035	0.007
	ILE AP	112	0.035	0.008
	ILE ML	52	0.014	0.004
	ILE V	57	0.041	0.007

the 50% threshold, while RQA (V max, diverg) never reached steady values in the analyzed range. IH, maxFM, sLE and RQA (max, diverg) showed poor or very poor reliability.

ICC results showed overall coherence with *imr* values. The main exception is represented by IH (AP, V). ICC of IH (AP, V) highlighted high correlation between the two analyzed windows, whereas the analysis of *imr* showed very poor correlation. This could be partially

explained by the very small values reached by IH in AP and V directions (0.022–0.04), which could make *imr* calculation more prone to small instrumentation or numerical errors. ICC of RQA (max, diverg) was not as good as other RQA measures (rr, det, avg), but resulted slightly larger than what was obtained with *imr* observation. Coherently with the *imr* observation, ICC for some measures (maxFM, sLE tot, NI, ILE AP, ML) was very small or not significant.

Table 3

Intra-class correlation (ICC) of variability/stability measures calculated between two non-overlapping windows of 85 strides extrapolated from each experimental trial.

Measure	ICC	p-Value	Measure	ICC	p-Value
maxFM tot	-0.57	0.94	MSE V $\tau=1$	0.85	< 0.05
maxFM AP	-0.23	0.74	MSE V $\tau=2$	0.87	< 0.05
maxFM ML	-0.44	0.88	MSE V $\tau=3$	0.84	< 0.05
maxFM V	-0.47	0.89	MSE V $\tau=4$	0.85	< 0.05
HR AP	0.76	< 0.05	MSE V $\tau=5$	0.86	< 0.05
HR ML	0.90	< 0.05	MSE V $\tau=6$	0.81	< 0.05
HR V	0.95	< 0.05	RQA AP (rr)	0.91	< 0.05
IH AP	0.96	< 0.05	RQA AP (det)	0.93	< 0.05
IH ML	0.98	< 0.05	RQA AP (avg)	0.94	< 0.05
IH V	0.93	< 0.05	RQA AP (max)	0.79	< 0.05
PSD1	0.96	< 0.05	RQA AP (diverg)	0.73	< 0.05
PSD2	0.55	< 0.05	RQA ML (rr)	0.99	< 0.05
sLE tot	0.12	0.37	RQA ML (det)	0.98	< 0.05
sLE AP	0.69	< 0.05	RQA ML (avg)	0.93	< 0.05
sLE ML	0.04	0.45	RQA ML (max)	0.68	< 0.05
sLE V	0.68	< 0.05	RQA ML (diverg)	0.79	< 0.05
MSE AP $\tau=1$	0.96	< 0.05	RQA V (rr)	0.96	< 0.05
MSE AP $\tau=2$	0.97	< 0.05	RQA V (det)	0.99	< 0.05
MSE AP $\tau=3$	0.97	< 0.05	RQA V (avg)	0.97	< 0.05
MSE AP $\tau=4$	0.94	< 0.05	RQA V (max)	0.68	< 0.05
MSE AP $\tau=5$	0.94	< 0.05	RQA V (diverg)	0.51	< 0.05
MSE AP $\tau=6$	0.89	< 0.05	NI	0.35	0.15
MSE ML $\tau=1$	0.92	< 0.05	IV	0.49	< 0.05
MSE ML $\tau=2$	0.89	< 0.05	SD	0.85	< 0.05
MSE ML $\tau=3$	0.91	< 0.05	CV	0.82	< 0.05
MSE ML $\tau=4$	0.90	< 0.05	ILE tot	0.48	< 0.05
MSE ML $\tau=5$	0.89	< 0.05	ILE AP	0.42	0.08
MSE ML $\tau=6$	0.82	< 0.05	ILE ML	0.41	0.08
			ILE V	0.53	< 0.05

In conclusion, only MSE and RQA (rr, det, avg) showed excellent reliability. In a previous work [7] it was found that MSE and RQA calculated during treadmill walking correlated with fall history; these findings suggest a possible future clinical application in the definition of a more valid and robust fall risk index. Further research on the relationship of such measures with overground gait stability in old adults and pathologic subjects is highly encouraged.

In general, the number of strides necessary to obtain a reliable measure was larger than those conventionally used in the analysis of over-ground walking. Our results suggest carefulness when drawing conclusions about gait variability and stability obtained from short walking trials. A number of strides coherent with the indications illustrated in Table 1 should always be considered.

Conflict of interest statement

None declared.

Acknowledgment

This research was funded by the Project “Fall risk estimation and prevention in the elderly using a quantitative multifactorial approach” (Project ID number 2010R277FT) awarded by the Italian Ministry of Education, University and Research (Ministero dell’istruzione, dell’Università e della Ricerca).

References

- [1] S. Lord, B. Galna, L. Rochester, Moving forward on gait measurement: toward a more refined approach, *Mov. Disord.* 28 (2013) 1534–1543.
- [2] A. Mirelman, T. Gurevich, N. Giladi, A. Bar-Shira, A. Orr-Urtreger, J.M. Hausdorff, Gait alterations in healthy carriers of the LRRK2 G2019S mutation, *Ann. Neurol.* 69 (2011) 193–197.
- [3] J. Verghese, C. Wang, R.B. Lipton, R. Holtzer, X. Xue, Quantitative gait dysfunction and risk of cognitive decline and dementia, *J. Neurol. Neurosurg. Psychiatry* 78 (2007) 929–935.
- [4] G. Abellan van Kan, Y. Rolland, S. Andrieu, J. Bauer, O. Beauchet, M. Bonnefoy, et al., Gait speed at usual pace as a predictor of adverse outcomes in community-dwelling older people: an International Academy on Nutrition and Aging (IANA) Task Force, *J. Nutr. Health Aging* 13 (2009) 881–889.
- [5] J.B. Dingwell, H.G. Kang, Differences between local and orbital dynamic stability during human walking, *J. Biomech. Eng.* 129 (2007) 586–593.
- [6] H.B. Menz, S.R. Lord, R.C. Fitzpatrick, Acceleration patterns of the head and pelvis when walking on level and irregular surfaces, *Gait Posture* 18 (2003) 35–46.
- [7] F. Riva, M.J.P. Toebes, M. Pijnappels, R. Stagni, J.H. van Dieën, Estimating fall risk with inertial sensors using gait stability measures that do not require step detection, *Gait Posture* 38 (2013) 170–174.
- [8] D. Hamacher, N.B. Singh, J.H. Van Dieën, M.O. Heller, W.R. Taylor, Kinematic measures for assessing gait stability in elderly individuals: a systematic review, *J. R. Soc. Interface* 8 (2011) 1682–1698.
- [9] J.M. Hausdorff, D.A. Rios, H.K. Edelberg, Gait variability and fall risk in community-living older adults: a 1-year prospective study, *Arch. Phys. Med. Rehabil.* 82 (2001) 1050–1056.
- [10] F. Riva, M.C. Bisi, R. Stagni, Orbital stability analysis in biomechanics: a systematic review of a nonlinear technique to detect instability of motor tasks, *Gait Posture* 37 (2013) 1–11.
- [11] F. Alton, L. Baldey, S. Caplan, M.C. Morrissey, A kinematic comparison of overground and treadmill walking, *Clin. Biomech.* 13 (1998) 434–440.
- [12] S.D. Walter, M. Eliasziw, A. Donner, Sample size and optimal designs for reliability studies, *Stat. Med.* 17 (1998) 101–110.
- [13] K. Aminian, B. Najafi, C. Büla, P.-F. Leyraz, P. Robert, Spatio-temporal parameters of gait measured by an ambulatory system using miniature gyroscopes, *J. Biomech.* 35 (2002) 689–699.
- [14] J.M. Hausdorff, A. Lertratanakul, M.E. Cudkovic, A.L. Peterson, D. Kaliton, A.L. Goldberger, Dynamic markers of altered gait rhythm in amyotrophic lateral sclerosis, *J. Appl. Physiol.* 88 (2000) 2045–2053.
- [15] J.M. Hausdorff, M.E. Nelson, D. Kaliton, J.E. Layne, M.J. Bernstein, A. Nuernberger, et al., Etiology and modification of gait instability in older adults: a randomized controlled trial of exercise, *J. Appl. Physiol.* 90 (2001) 2117–2129.
- [16] A.H. Khandoker, S.B. Taylor, C.K. Karmakar, R.K. Begg, M. Palaniswami, Investigating scale invariant dynamics in minimum toe clearance variability of the young and elderly during treadmill walking, *IEEE Trans. Neural Syst. Rehabil.* 16 (2008) 380–389.
- [17] F. Sylos Labini, A. Meli, Y.P. Ivanenko, D. Tufarelli, Recurrence quantification analysis of gait in normal and hypovestibular subjects, *Gait Posture* 35 (2012) 48–55.
- [18] M. Costa, C.-K. Peng, A.L. Goldberger, J.M. Hausdorff, Multiscale entropy analysis of human gait dynamics, *Phys. A: Stat. Mech. Appl.* 330 (2003) 53–60.
- [19] C.J.C. Lamoth, P.J. Beek, O.G. Meijer, Pelvis–thorax coordination in the transverse plane during gait, *Gait Posture* 16 (2002) 101–114.
- [20] M. Riley, R. Balasubramaniam, M. Turvey, Recurrence quantification analysis of postural fluctuations, *Gait Posture* 9 (1999) 65–78.
- [21] J.B. Dingwell, J.P. Cusumano, Nonlinear Time Series Analysis of Normal and Pathological Human Walking, 10, *Chaos*, Woodbury, N.Y. (2000) 848–863.
- [22] S.A. England, K.P. Granata, The influence of gait speed on local dynamic stability of walking, *Gait Posture* 25 (2007) 172–178.
- [23] S.M. Bruijn, J.H. van Dieën, O.G. Meijer, P.J. Beek, Statistical precision and sensitivity of measures of dynamic gait stability, *J. Neurosci. Methods* 178 (2009) 327–333.
- [24] J.S. Richman, J.R. Moorman, Physiological time-series analysis using approximate entropy and sample entropy, *Am. J. Physiol. Heart Circ.* 278 (2000) H2039–H2049.
- [25] K.A. Lowry, A.L. Smiley-Oyen, A.J. Carrel, J.P. Kerr, Walking stability using harmonic ratios in Parkinson’s disease, *Mov. Disord.* 24 (2009) 261–267.
- [26] H.G. Kang, J.B. Dingwell, Intra-session reliability of local dynamic stability of walking, *Gait Posture* 24 (2006) 386–390.
- [27] T.M. Owings, M.D. Grabiner, Measuring step kinematic variability on an instrumented treadmill: how many steps are enough? *J. Biomech.* 36 (2003) 1215–1218.
- [28] K.S. van Schooten, S.M. Rispens, M. Pijnappels, A. Daffertshofer, J.H. van Dieën, Assessing gait stability: the influence of state space reconstruction on inter- and intra-day reliability of local dynamic stability during over-ground walking, *J. Biomech.* 46 (2013) 137–141.
- [29] N. König, N.B. Singh, J. von Beckerath, L. Janke, W.R. Taylor, Is gait variability reliable? An assessment of spatio-temporal parameters of gait variability during continuous overground walking, *Gait Posture* 39 (2014) 615–617.
- [30] T.M. Owings, M.D. Grabiner, Variability of step kinematics in young and older adults, *Gait Posture* 20 (2004) 26–29.
- [31] J.H. Hollman, K.B. Childs, M.L. McNeil, A.C. Mueller, C.M. Quilter, J.W. Youdas, Number of strides required for reliable measurements of pace, rhythm and variability parameters of gait during normal and dual task walking in older individuals, *Gait Posture* 32 (2010) 23–28.

The role of quantitative assessment in setting-up a gait rehabilitation tool: an experience with the Regent suit.

D. Trojaniello (1), A. Cereatti (1), G. D'Addio (2), M. Cesarelli (3), B. Lanzillo (2), U. Della Croce (1)

(1) Information Engineering Unit, POLCOMING Department, University of Sassari, Sassari, Italy

(2) S. Maugeri Foundation IRCCS, Telesse Terme, Italy

(3) Dept. of Electrical Engineering and Information Technology, University of Naples "Federico II", Naples, Italy

INTRODUCTION

Gait rehabilitation tools are gaining access to the clinical practice. Their routine use requires a setup operated by the operators customized on the patient needs and characteristics. Often, operators can only set the quantitative parameters required by the rehabilitation tool using qualitative methods based on experience and personal sensory inputs. The aim of the study was to evaluate the potential role of a quantitative assessment in setting up the Regent suit (Fig. 1). The Regent suit includes a number of elastic bands generating force fields influencing both upper and lower body movement, whose goal is to stabilize and make more symmetric the user's gait. It has been used as a gait rehabilitation tool showing positive results [1]. However, no quantitative information is available to the operators in setting up the suit. Gait asymmetry can be qualitatively evaluated by looking at the step duration and length differences between left and right, while it is often quantified by measuring asymmetries in stance and swing phase durations [2]. In this work we estimated the gait temporal parameters of six hemiparetic subjects walking with and without the suit using inertial technology with the aim of quantifying asymmetry changes introduced by the use of the suit and evaluating if the criteria used to set up the suit reflected in an actual reduction of gait asymmetry.



Figure 1. Subject wearing the Regent suit.

METHODS

Two physical therapists operating in the clinic hosting the study were asked to setup the Regent suit on six hemiparetic subjects as they would routinely. They selected the number of elastic bands and their tension level on both affected (*aff*) and non affected (*n-aff*) side based on their experience (Table 1). Inertial measurements were obtained from units (Opal, APDM) attached to the subject's ankles during walking at self selected speed (13-meter walkway with and without the suit). To get acquainted to the use of the suit, subjects walked for five minutes before data acquisition. Three trials were acquired for both conditions. A total of about 25 full gait cycles per condition were acquired for each subject. Data were processed using an algorithm previously validated on pathologic populations [3]. Step duration (*stp*), stance (*st*) and swing (*sw*) mean durations were determined for both sides. The asymmetry index (AI) was calculated as $AI = (p_{aff} - p_{n-aff}) / 0.5 \cdot (p_{aff} + p_{n-aff}) * 100$ where *p* is an above-mentioned parameter. In hemiparetic subjects, a positive AI should be expected for *stp* and *sw*.

RESULTS

In table 2 the AI (%) of *stp*, *st* and *sw* are reported for each subject and for the two walking conditions (no suit = NS, suit = S).

DISCUSSION

The qualitative evaluation of *stp* asymmetry reflected in the corresponding quantitative estimate, except for subject 6 for whom the *stp* AI slightly increased, probably due at the increased tension of both front and back elastic bands. However, *st* and *sw* AI showed that the use of the suit increased the *st* and *sw* asymmetry for subjects 2 and 6, while it did not have effects on subjects 3 and 4. A more inclusive set of quantitative data regarding the patient's gait (i.e. spatial gait parameters and EMG data from selected muscles) could improve the setting of the suit before the training.

REFERENCES

- [1] Monticone M et al. ClinRehabil. 2013; [Epubahead of print]
- [2] Robinson RO et al. J Man Manip Ther. 1987; 10:172-176
- [3] Trojaniello D et al. ISB 2013 Congress XXIV, Natal, Brazil
- [4] Patterson KK et al. Arch Phys Med Rehabil. 2008; 89:304-310

subj. id	no. of elastic bands			band tension affvs n-aff	
	front	back	side	front	back
1	2	2	2	>	=
2	2	2	2	=	>
3	2	2	2	>	>
4	2	2	2	=	=
5	2	2	0	>	>
6	2	2	0	>	>

Table 2. Regent suit main set up parameters.

subj. id	<i>stp</i>		<i>st</i>		<i>sw</i>	
	NS	S	NS	S	NS	S
1	8	4	-11	-7	24	17
2	-3	-1	1	-5	0	7
3	4	3	3	4	-4	-6
4	7	6	1	1	-1	0
5	21	14	-3	-2	7	3
6	-2	-5	1	5	0	-8

Table 2. AI of temporal parameters.

STRIDE-BY-STRIDE GAIT SPATIO-TEMPORAL PARAMETERS ESTIMATE FROM SHANK-WORN IMU RECORDINGS: VALIDATION ON PARKINSON, CHOREIC, HEMIPARETIC AND HEALTHY ELDERLY SUBJECTS

D. Trojaniello (1), A. Cereatti (1), E. Pelosin (2), A. Mirelman (3), J. M. Hausdorff (3), L. Avanzino (2), U. Della Croce (1)

(1) Information Engineering Unit, POLCOMING Department, University of Sassari, Italy

(2) Department of Neurosciences, University of Genoa, Italy

(3) Movement Disorders Unit of the Department of Neurology, Tel Aviv Sourasky Medical Center, Israel

Main topics: Analysis of clinical movement data, Analysis of gait and motor disorders

INTRODUCTION

In recent years, methods for estimating spatio-temporal parameters of gait from wearable inertial sensors (IMUs) measurements have been proposed and tested, mostly on healthy subjects, with few exceptions [1,2], which focused on single pathologies. No method was validated for the stride by stride analyses of spatial measures in various gait abnormalities. In this work, we evaluate a novel IMU based technique for the determination of both gait temporal and spatial parameters in four groups, characterized by different gait patterns.

MATERIALS and METHODS

The study included 11 hemiparetic (H) (FAC=3.6±1.5), 12 choreic (C) (UHDRS=34.9±16.9), 10 Parkinsonian (P) (UPDRS=62.7±19.1) and 10 healthy elderly (E). Data from two IMUs (Opal, APDM) attached to the subject ankles (20 mm above the malleolus) were acquired simultaneously with data from an instrumented gait mat (GAITRite, CIR System) used as gold standard (GS). Subjects walked for one minute at a self-selected speed, back and forth along a 12-meter walkway. Gait events (GEs) (initial contact - IC and final contact - FC) and resulting gait temporal parameters (stride T_{str} and stance T_{stn} duration) were estimated using an algorithm previously developed based on the preliminary identification of trusted gait phases and then of GEs search intervals in the IMU signals [3]. The stride length (L_{str}) was then estimated from the antero-posterior accelerations (i.e. along the direction of maximum average velocity in swing) by applying a modified version [3] of the OFDRI technique [4], followed by a further simple integration. The error in estimating IC, FC, T_{str} , T_{stn} and L_{str} was calculated as the difference of the IMU-based estimates and the GS estimates. Left and right side errors were averaged except for the H group (affected (A) and non-affected (NA) side). The relevant mean, standard deviation and mean absolute values (mae_s) were averaged within groups (m , sd and mae). A Kruskal–Wallis test was used to compare the mae_s among the groups.

RESULTS

In total, 1642 gait cycles (E=574, P=532, C=290, H=246) were analyzed. Two C and one H subjects were excluded from the analysis since the method could not estimate L_{str} . The descriptive statistics of the errors in estimating IC, FC, T_{str} , T_{stn} and L_{str} for all tested groups are reported in Table 1. None of the errors was significantly different among groups ($p>0.05$).

DISCUSSION and CONCLUSIONS

The method proposed was shown to be extremely accurate in estimating GEs, T_{str} and T_{stn} for all groups (Table 1). Moreover, L_{str} estimate maximum error for E and P groups was lower than those reported in previous studies [1]. The L_{str} estimation algorithm failed in one H subject probably due to the extremely low subject speed (<0.44m/s) and in two C subjects due to the excessive lateral swaying and stride-by-stride lateral deviations from the forward direction which prevented a correct signal realignment. The results are particularly promising considering the high variability of abnormal gait patterns evaluated (i.e. festinating, hyperkinetic, hemiparetic).

Table 1: Mean errors (m), standard deviation (sd) and mean absolute errors (mae) of gait parameters estimates.

	<i>speed</i> [m/s]	IC [ms]		FC [ms]		T_{str} [ms]		T_{stn} [ms]		L_{str} [mm]	
		m (sd)	mae	m (sd)	mae	m (sd)	mae	m (sd)	mae	m (sd)	mae
E	1.18 ± 0.15	0 (8)	9	-7 (14)	20	0 (12)	9	-8 (18)	21	2(20)	17
P	0.85 ± 0.15	10 (11)	13	-10 (18)	20	1 (15)	12	-9(19)	24	2(26)	19
C	1.03 ± 0.22	8 (13)	14	- 2 (15)	19	0 (18)	14	-9(19)	25	-8(30)	27
H (NA)	0.71 ± 0.19	-5 (11)	14	11 (13)	19	0 (15)	12	16(16)	23	1(30)	28
H (A)		4 (12)	17	19 (9)	20	0 (16)	13	17(14)	25	9(25)	26

ACKNOWLEDGEMENT

The study was part of V-TIME, a EC funded project (7th FP, grant #278169)

REFERENCES

- [1] A. Salarian et al., IEEE Trans. Biomed. Eng., 2004, 51:1434–1443
- [2] S. Yang et al., Gait & Posture 2013, 37:354–8
- [3] D. Trojaniello et al., Proc. XIII 3DAHM Symposium 2014, *accepted*
- [4] A. Köse et al., J. Neuroeng. Rehabil. 2012, 9:9

Head and pelvis stride-to-stride oscillations in gait: validation and interpretation of measurements from wearable accelerometers

This content has been downloaded from IOPscience. Please scroll down to see the full text.

2015 *Physiol. Meas.* 36 857

(<http://iopscience.iop.org/0967-3334/36/5/857>)

View [the table of contents for this issue](#), or go to the [journal homepage](#) for more

Download details:

IP Address: 131.252.223.50

This content was downloaded on 27/04/2015 at 19:22

Please note that [terms and conditions apply](#).

Head and pelvis stride-to-stride oscillations in gait: validation and interpretation of measurements from wearable accelerometers

Matthew A D Brodie^{1,2}, Tim R Beijer³, Colleen G Canning⁴
and Stephen R Lord¹

¹ Neuroscience Research Australia, University of New South Wales, Sydney, Australia

² Graduate School of Biomedical Engineering, University of New South Wales, Sydney Australia

³ Neurology, Canisius Wilhelmina Hospital, Nijmegen, The Netherlands

⁴ Clinical and Rehabilitation Sciences Research Group, Faculty of Health Sciences, University of Sydney, Sydney, Australia

E-mail: matthew.brodie@neura.edu.au

Received 22 April 2014, revised 22 January 2015

Accepted for publication 3 February 2015

Published 2 April 2015



CrossMark

Abstract

Unstable gait is a risk factor for falls. Wearable accelerometers enable remote monitoring of daily walking. Here, new methods for measuring stride-to-stride oscillations are validated against optical motion capture, normative data determined, and dependency on walking speed investigated. Walks by 13 young people (mean age 32 years) at fast, usual, and slow speeds were completed. Accelerometers were attached to the head and pelvis and stride-to-stride oscillation velocity and displacement were measured. Continuous tilt corrections were applied, filter cut-offs scaled by step frequency, and thresholds optimized using optical motion capture as a reference. Oscillations depended on walking speed, accelerometer placement, and measurement axis. Vertical oscillations increased with walking speed (Pearson's $r = 0.78-0.89$) and were the most accurate (1.4–2.3% error). Mediolateral or anteroposterior oscillations were less accurate (5.9–19.5% error) and had more complex relationships with walking speed (increasing, decreasing, uncorrelated, and/or 'U-shaped' minimum at usual speed). In healthy gait, the head and pelvis undergo regular oscillations, measurable with accelerometers. The results suggest head oscillations in the transverse plane are attenuated by the trunk, and there may be advantages in minimizing stride-to-stride oscillations that coincide with self-selected usual pace. These methods may prove useful for remote assessment of changing health, mental status, and/or fall risk.

Keywords: Parkinson's disease, accelerometers, oscillations, head, gait, instability, walking

(Some figures may appear in colour only in the online journal)

1. Introduction

Unstable gait is a risk factor for falls (Hausdorff *et al* 2001, Senden *et al* 2012, Brodie *et al* 2015a, Rispens *et al* 2014), and sway while walking is increased in clinical groups such as those with traumatic brain injury and Parkinson's disease (Cole *et al* 2010, Findling *et al* 2011). For higher risk individuals, health outcomes might be improved using new methods to remotely monitor stride-to-stride oscillations with wearable accelerometers. However, first measurement accuracy, normative data for people without impairment, and dependency on walking speed need to be investigated.

Previously, head, trunk, pelvis, and/or centre-of-mass translation while walking have been measured using optical motion capture (Whittle 1997, Whittle and Levine 1999, Orendurff *et al* 2004, Cole *et al* 2010, Galna *et al* 2013), extended force platforms (Cavagna *et al* 1983), instrumented treadmills (Zijlstra and Hof 1997, Tesio *et al* 2010), or shoes fitted with force platforms (Schepers *et al* 2009). However, such methods require expensive equipment and/or are limited to capturing short walks in controlled environments.

Accelerometers provide an inexpensive alternative (Kavanagh and Menz 2008), enabling up to a week of remote gait monitoring (Weiss *et al* 2013, Rispens *et al* 2014), and/or assessment by using a smart phone (Michael *et al* 2014). Accelerometers have been attached to the head (Latt *et al* 2009), the sacrum (Moe-Nilssen 1998), and the trunk (Kavanagh *et al* 2005a, Kavanagh 2009, Wilhelmsen *et al* 2010). In clinical settings gait data have been used to identify differences between young and old (Kavanagh *et al* 2005b, Menant *et al* 2011), fallers and non-fallers (Yogev *et al* 2007, Weiss *et al* 2011), and people with Parkinson's disease (Hausdorff 2009, Latt *et al* 2009).

Research has generally focused on the direct analysis of the acceleration signal (Kavanagh and Menz 2008). Measurement of velocity or displacement using accelerometers is less common and requires the data to be integrated with respect to time, which may lead to accumulating measurement errors. Data quality may be improved by static calibration, averaged tilt corrections, or sensor fusion with gyroscopes (Smidt *et al* 1971, Moe-Nilssen 1998, Menz *et al* 2003, Kavanagh *et al* 2005a, Brodie 2009). Displacement may then be obtained using a high pass filter with a fixed 0.1 Hz cut-off and/or harmonic analysis (Zijlstra and Hof 2003). However, previous efforts to improve data quality assumed fixed sensor orientation or required additional sensors. Filter cut-offs might not be optimal for remote gait monitoring; if sensor orientation changes over time, or if walking speed varies, as may occur during daily life.

In this paper, the accuracy of wearable accelerometer derived stride-to-stride oscillations, normative data for people without impairment, and effect of walking speed are investigated. Stride-to-stride oscillations are defined as head and pelvic trajectories relative to the global progression while walking over ground. Conceptually, this is similar to head and pelvic trajectories during treadmill walking if no long-term progression through space occurs. We propose a 'scaled' method to measure stride-to-stride oscillations, which is novel because: (1) continuous pitch and roll corrections are used to improve data quality; (2) filter cut-offs are scaled by step frequency; and (3) scaling constants are optimized using optical motion capture as a reference.

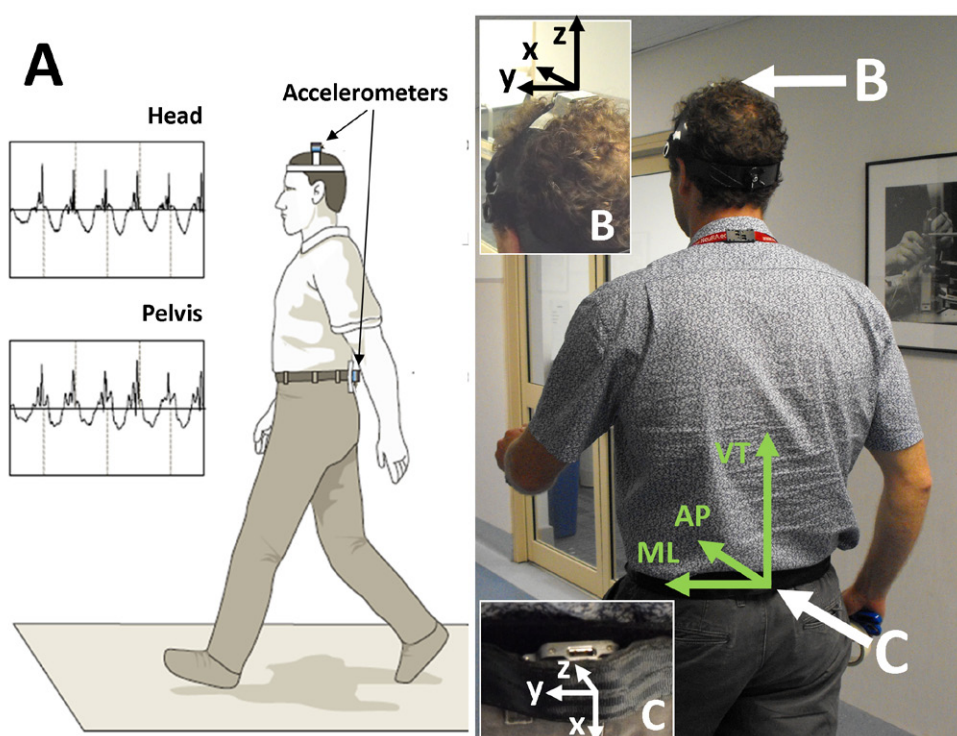


Figure 1. Accelerometer placement. (a) Schematic representation of ideal accelerometer placements. (b, c) ‘Real world’ implementation; sensors are not perfectly aligned with the global coordinate system and orientation may change over time with body movements. (b) Head accelerometer attached to plastic helmet liner. (c) Pelvic accelerometer incorporated into a belt. Insets show wearable device positions and local measurement axes enlarged. The global vertical body centred heading (GVBCH) coordinate system is visualized near the pelvis: positive VT points upwards and is fixed. In the transverse plane, AP generally points forwards and ML right to left.

2. Methods

2.1. Participants

Thirteen healthy people volunteered: 9 female and 4 male, mean age 32 years (standard deviation (SD) 6 years), height 169 cm (SD 10 cm), and weight 63 kg (SD 16 kg). Approval by the Human Studies Ethics Committee at the University of New South Wales was given for the study and informed consent was obtained from all participants prior to participation.

2.2. Collection of gait data

A tri-axial accelerometer (Opal™ by APDM, sampling frequency 128 Hz) was incorporated into a light plastic helmet liner (total mass 67 g) and secured to the participant’s head (figure 1(b)). A second tri-axial accelerometer was incorporated into an adjustable belt (figure 1(c)). Participants completed two repeated walks at self-selected fast, usual, and slow speeds over 6 m. Data were simultaneously collected with an optical motion capture system (OptiTrack® by NaturalPoint).

2.3. Accelerometer attachment and local coordinate systems

The head accelerometer's local z -axis was aligned with the global vertical (VT), the x -axis projected onto a line connecting the base of skull and tip of nose pointing forwards, and the y -axis was aligned right to left. The pelvic accelerometer's local y -axis was aligned right to left with a line connecting the posterior superior iliac spines, the x -axis pointed downward, and the z -axis pointed forward.

2.4. The global vertical, body centred heading, coordinate system

Data were reported according to the global vertical, body centred heading, coordinate system (see figure 1). For both accelerometers, VT measurements were independent of body position or sensor orientation and aligned to global VT. The anteroposterior (AP) and mediolateral (ML) axes were body fixed and could rotate in the transverse plane if the orientation of the head or pelvis changed. Within the transverse plane, AP generally pointed forwards and parallel to the floor and ML right to left across the direction of travel.

2.5. The continuous tilt correction

Prior to measuring head and pelvis oscillations from the accelerometers mathematical corrections were required to align the local sensor axes with the global coordinate system and improve data quality. Unlike the ideal sensor alignments depicted by the schematic representation (figure 1(a)), we did not assume fixed orientation with respect to the global coordinate system during gait measurements (figures 1(b) and (c)) and therefore mathematical corrections were required (Moe-Nilssen 1998). Here, a low-pass filter scaled to one quarter of the step frequency ($0.25 \times F_o \approx 0.45$ Hz, see figure 2) was used to model the continuous pitch and roll corrections.

Technical details of the continuous pitch and roll correction method used are provided in the appendix. Figure 3 demonstrates accelerations measured at the head before (left side) and after the continuous correction with gravity removed (right side). The most noticeable improvement is in the reduction of zero offset errors for the AP accelerations (top panel, right side). These errors were caused by 'head nodding' that resulted in the head sensor orientation changing as the participant looked towards the floor.

2.6. Optical motion capture measurement of stride-to-stride oscillations

The optical motion capture system (OptiTrack[®] by NaturalPoint) used six cameras in pairs, each side of the walkway, focused on the posterior aspect of the participants. A triad of markers was attached to each accelerometer. Optical data were synchronized to accelerometer data using a data acquisition board.

First the displacement data were de-trended to improve interpretation (Zijlstra and Hof 1997). A 5th order polynomial was used to separate the stride-to-stride oscillations in gait (figures 4(c)–(e)) from the global movements through the measurement space (figure 4(a)). Relative velocity was then found by differentiating displacements with respect to time.

2.7. Accelerometer measurement of stride-to-stride oscillations

The corrected accelerations (in the global vertical body centred heading coordinate system) were integrated with respect to time and high-pass filtered to obtain stride-to-stride oscillation

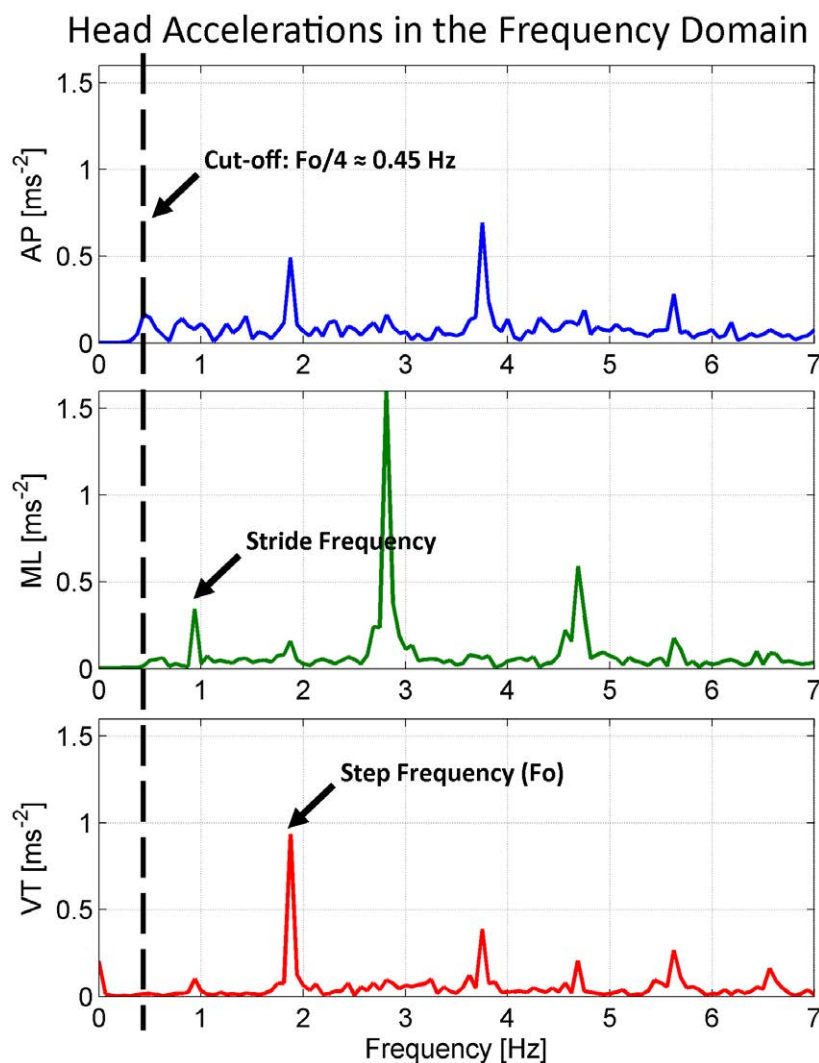


Figure 2. Head accelerations while walking in the frequency domain using discrete Fourier transform. The step frequency ($F_0 \approx 1.8$ Hz) is represented by the first peak in the AP and VT traces. The stride frequency ($0.5 \times F_0 \approx 0.90$) is represented by the first peak in the ML trace. A low-pass filter scaled to one quarter the step frequency ($0.25 \times F_0 \approx 0.45$, dashed vertical line) separates most noise caused by slow changing sensor orientation from most accelerations of interest, and was used by the continuous tilt correction to maintain vertical alignment between the local sensor axes and the global coordinate system.

velocity and displacement (figure 5). High-pass filtering was used to remove integration errors that accumulated over the walk. The calculation procedure follows:

- (a) Step frequency (F_0) was determined by identifying the dominant harmonic (see appendix).
- (b) Measured accelerations were aligned with the global coordinate system using the continuous pitch and roll correction (see appendix).

Continuous Tilt Corrections for Changing Head Orientation

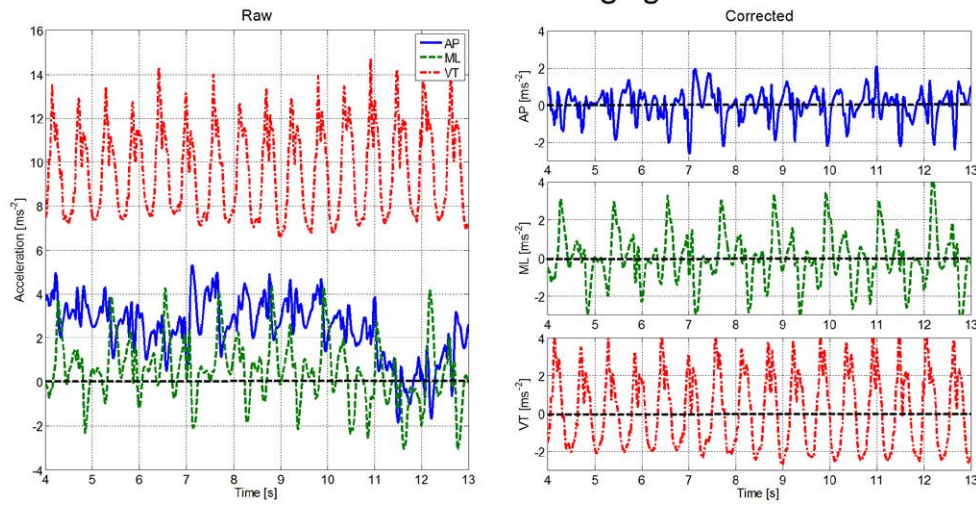


Figure 3. Head accelerations during gait. Raw data (left panel) shows the raw accelerations are offset from zero and the bias changes because of head movements. The most marked difference is in the AP channel, the corrected AP accelerations (top right panel) are properly centred about zero after the continuous tilt correction (see [appendix](#) for details).

Relative Head Oscillations from Optical Motion Capture

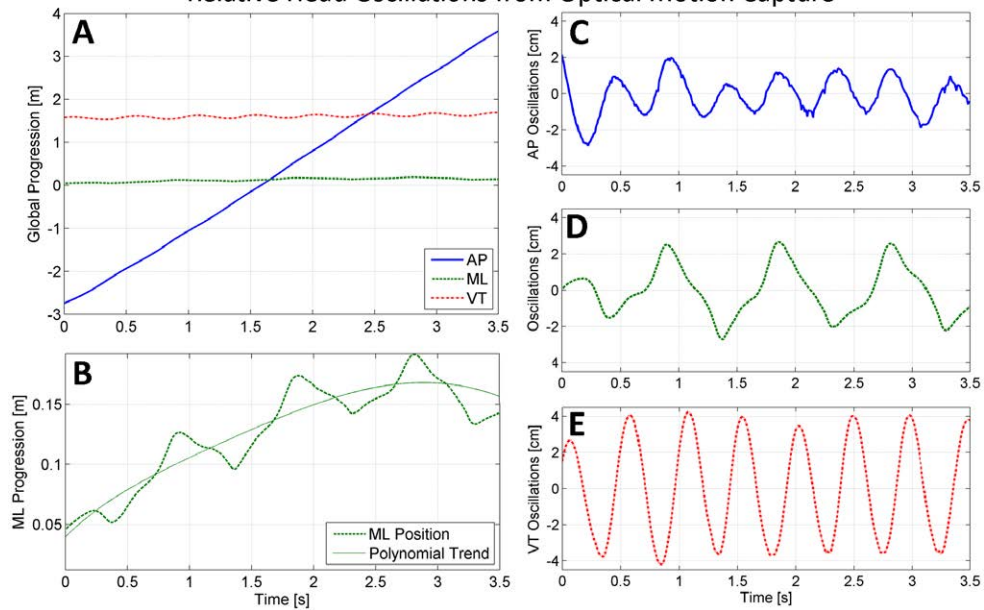


Figure 4. Head oscillation from optical motion capture data. (a) Global progression through the measurement space along the AP axis (in metres) was approximately 100 times greater than the stride-to-stride oscillations (in centimetres, panels (c)–(e)). (b) ML global displacement (dashed line) was de-trended with a 5th order polynomial (solid curve).

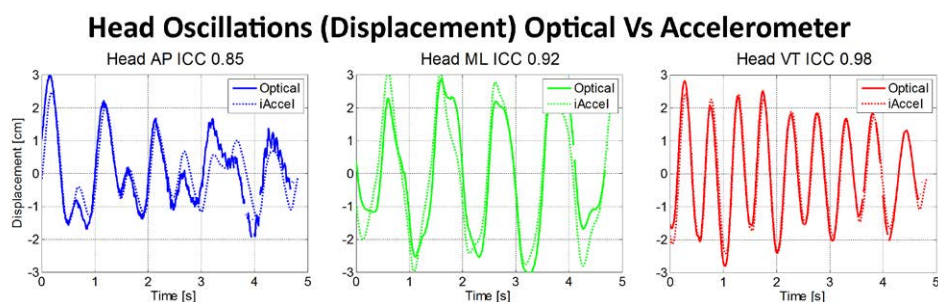


Figure 5. Head displacements relative to the global progression while walking. Optical (solid line) and accelerometer (dotted line) measurements are compared. Intra-class correlations above the panels indicate level of agreement at each epoch. Left to right represents stride-to-stride oscillations along the AP, ML, and VT axes.

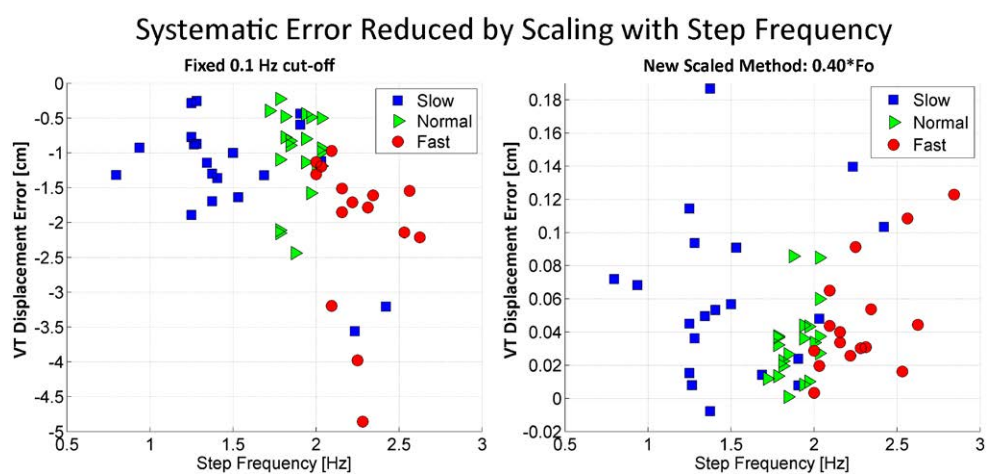


Figure 6. Reduction in systematic error was observed by both scaling, and increasing the cut-off frequency (right panel) relative to a fixed 0.1 Hz value (left panel). The negative displacement errors (left panel) indicates that the 0.1 Hz high-pass filter systematically overestimated the oscillations and the downward trends indicates that increasing errors were linked to increasing step frequency.

- (c) Corrected accelerations were integrated with respect to time to obtain velocities and displacements.
- (d) Velocities and displacements were filtered with a 4th order high-pass bi-directional Butterworth filter to obtain stride-to-stride oscillations.

2.8. Optimization of high-pass filter scaling

The high-pass filter cut-off frequency (from step four above) was scaled to step frequency (cut-off = $C \times F_0$) by a constant (C) because preliminary work indicated measurement errors were linked to step frequency (see figure 6). The scale factors for each sensor along each axis were found by a grid search that minimized the root mean squared error (RMSE) using the optical measurements as a reference. Scale factors (C) between 0.05 and 1 were searched in 0.05 steps.

Table 1. Head and pelvic oscillation ranges, optimum filter cut-offs, and errors. Optical motion capture was used as the reference. RMSE were normalized by the measurement range (NRMSE) and reported as a percent enabling comparison of errors between gait parameters with different measurement ranges using a single numerical quantity.

	Measurement range			High-pass	Errors	
	Min	Max	Range	Cut-off (Hz)	RMSE	NRMSE
Head velocity (cm s^{-1})						
RMS AP	2.82	15.68	12.86	0.50	1.36	10.6%
RMS ML	2.89	28.83	25.93	0.40	2.16	8.3%
RMS VT	3.08	42.09	39.02	0.45	0.56	1.4%
Head displacement (cm)						
RMS AP	0.22	4.15	3.93	0.45	0.56	14.2%
RMS ML	0.41	7.40	6.98	0.40	0.52	7.4%
RMS VT	0.35	2.93	2.58	0.40	0.06	2.3%
Pelvic velocity (cm s^{-1})						
RMS AP	3.97	25.88	21.91	0.25	1.30	5.9%
RMS ML	3.93	27.92	23.99	0.30	2.40	10.0%
RMS VT	2.93	43.26	40.33	0.40	0.62	1.5%
Pelvic displacement (cm)						
RMS AP	0.31	2.57	2.26	0.30	0.44	19.5%
RMS ML	0.44	4.93	4.49	0.25	0.68	15.1%
RMS VT	0.35	2.91	2.56	0.35	0.05	2.0%

2.9. Statistical analysis

Agreement between optical and accelerometer measurements of displacement and velocity at each epoch (time step) were investigated, for example see figure 5. The intra-class correlation coefficient (ICC (2,1)) was calculated. Values closer to unity indicate higher agreement.

For each walk, oscillation magnitudes along each axis were calculated using the root mean squared (RMS) statistic. Absolute errors for each walk were calculated by subtracting RMS optical measurements from RMS accelerometer measurements (figure 6). Absolute errors of all walks were then combined using the RMSE statistic. For the grid search, scale factors were selected that minimized the RMSE (table 1).

For the optimum scale factors, the normalized root mean square errors (NRMSEs) were also reported (table 1). To obtain NRMSE, along each axis, the RMSE was divided by the range (maximum–minimum) of oscillation magnitudes for that axis. Similar to Bland–Altman techniques that visualize the ratio between measurement range (on a horizontal axis) and measurement error (on a vertical axis), the percentage NRMSE reports the error as a ratio of the measurement range. This enabled the errors for the 12 new oscillation parameters to be numerically compared relative to their different measurement ranges using a single parameter.

Walking speed, step frequency, RMS oscillation velocity, and RMS oscillation displacement along each axis and at each walking speed are reported (table 2). Correlations between oscillation magnitudes and walking speed were investigated using Pearson's correlation coefficients. To prevent pseudo replication artificially inflating the number of data points used to determine statistical significance, the two repeat walks for each condition (slow, usual, and fast) were averaged before calculating the Pearson's correlation coefficients. Data were processed using MATLAB version 7.10.0 (R2010a) and SPSS version 22.

Table 2. Changes in stride-to-stride oscillation magnitudes and correlations with usual walking speed. * indicates the minimum group oscillation magnitude for each parameter. For oscillation velocity of the head, for example, AP and ML were minimized at usual speeds, and VT minimized at slow speeds.

	Walking speed						Speed correlation	
	Slow		Usual		Fast		Pearson's	
	Mean	SD	Mean	SD	Mean	SD	<i>r</i>	<i>p</i>
Walking speed (m s^{-1})	0.60*	0.17	1.33	0.14	2.06	0.30	1.00	<0.001
Step frequency (Hz)	1.51*	0.45	1.90	0.10	2.33	0.28	0.79	<0.001
Head velocity (cm s^{-1})								
RMS AP	6.61	3.44	6.12*	2.49	8.20	4.07	0.15	0.23
RMS ML	16.24	7.18	9.99*	3.82	11.14	5.48	-0.40	<0.001
RMS VT	5.99*	2.25	18.60	4.49	30.23	7.23	0.89	<0.001
Head displacement (cm)								
RMS AP	1.24	1.05	0.77*	0.37	0.78	0.45	-0.32	0.007
RMS ML	3.59	1.98	1.61	0.69	1.40*	0.87	-0.62	<0.001
RMS VT	0.63*	0.18	1.55	0.37	2.14	0.59	0.78	<0.001
Pelvic velocity (cm s^{-1})								
RMS AP	8.89*	2.95	13.04	2.23	17.39	3.69	0.80	<0.001
RMS ML	11.51	5.07	8.30*	2.34	16.70	5.38	0.40	<0.001
RMS VT	6.09*	2.92	16.70	4.46	30.31	7.00	0.89	<0.001
Pelvic displacement (cm)								
RMS AP	1.17	0.59	1.12	0.24	1.09*	0.22	-0.10	0.43
RMS ML	2.40	1.31	0.96*	0.36	1.43	0.47	-0.44	<0.001
RMS VT	0.56*	0.18	1.36	0.36	2.06	0.53	0.82	<0.001

3. Results

Stride-to-stride head oscillations while walking are presented in figure 5. At each epoch, oscillation displacements as measured by an accelerometer (dotted lines) are compared to oscillation displacements from optical motion capture (solid lines). The level of agreement along each axis is indicated using the intraclass correlation coefficient. Typically, VT displacements had the highest agreement (ICC = 0.98). Agreement was lower along the ML (0.92) and AP (0.85) axes, but the characteristics of the motion were mostly retained.

Optimum high-pass filter scaling coefficients were higher for the head (0.40–0.50 times step frequency) relative to the sacrum (0.25–0.40 times step frequency), see table 1. Oscillation velocity could be measured more accurately (NRMSE = 1.4–10.6% of measurement range) than displacement (2.0–19.5%), and VT measurements were more accurate (1.4–2.3%) than AP measurement (5.9–19.5%) or ML measurements (8.3–15.1%). Scaling by step frequency reduced the effect of step frequency on error (figure 6). Furthermore, the grid search revealed broad valleys of minimum error indicating the oscillation measurements were not sensitive to small changes in scaling coefficients.

Four different relationships were observed between oscillation magnitudes and walking speed (figure 7). Correlations were highest for VT oscillations (table 2, $r = 0.78$ – 0.89). Significant increases in oscillation with increased walking speed were also observed for AP pelvic velocity (figure 7(a), $r = 0.80$), but not for AP head velocity (figure 7(b)), which showed no significant correlation. Significant decreases in oscillation with walking speed were

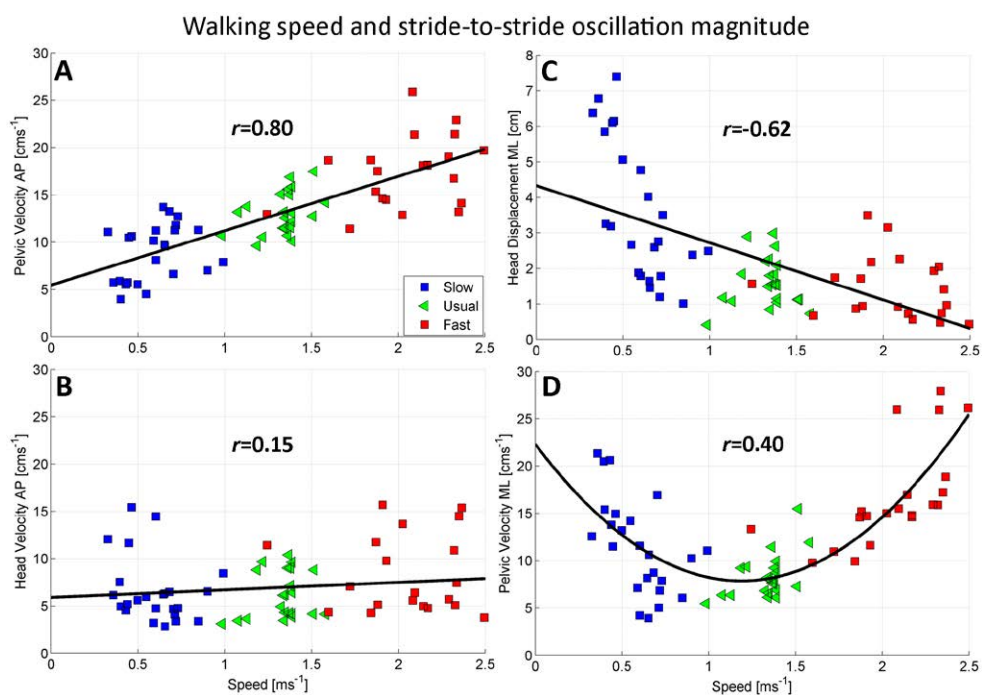


Figure 7. Oscillations in the transverse plane had varied relationships with walking speed. (a) AP pelvic velocity increased with walking speed, but in (b) AP head velocity was unchanged. (c) A negative correlation was observed for ML Head displacement. (d) ‘U-shaped’ ML pelvic velocity was minimized at usual walking speed. Pearson’s correlation coefficients (r) superimposed, significant correlations were observed for (a), (c) and (d).

also observed for ML head displacement (figure 7(c), $r = -0.62$), ML pelvic displacement ($r = -0.44$), and AP head displacement ($r = -0.32$). For five parameters, the measured oscillations were least at usual speeds relative to faster or slower speeds (table 2), suggesting U-shaped relationships may exist (see figure 7(d)), these included: ML pelvic velocity, ML pelvic position, ML head velocity, AP head velocity, and AP head position.

4. Discussion

4.1. Defining stride-to-stride oscillations

In healthy gait, the head and pelvis undergo regular oscillations that can be measured using accelerometers (figure 5). In this paper, stride-to-stride oscillations were defined as head and pelvis trajectories relative to a participants’ long-term progression over-ground. Similar to treadmill walking (Zijlstra and Hof 1997), the optical motion capture data were de-trended to aid interpretation. Polynomial de-trending was used for the optical data because for over-ground walking, global progression (figure 4(a)) may be orders of magnitude greater than stride-to-stride oscillations (figure 4(c)–(e)) and participants may not strictly maintain straight trajectories (see the curved fit for ML oscillations, figure 4(b)).

4.2. Correcting for changing sensor alignment

For the accelerometer measurement of stride-to-stride oscillations, filter cut-offs were scaled by step frequency to reduce bias. Previously, a single mean correction has been used (Moenilssen 1998). However, for our participants walking over ground, head and pelvic orientations were not constrained and could change with respect to the global coordinate system (figure 1(b)). Therefore, any slow changes in sensor orientation were modelled using a low-pass filter (see appendix). During pre-processing, the low-pass filter cut-off frequency was scaled to one quarter of the step frequency ($0.25 \times F_0 \approx 0.45$ Hz, figure 2) to improve the data quality, and may have been close to optimum; retaining most information of interest about stride-to-stride variability while rejecting most measurement noise associated with gravitational cross-talk.

4.3. Optimizing high-pass filter thresholds

Stride-to-stride oscillations were then obtained by integrating the corrected accelerations, but during integration small errors might have accumulated. These accumulated errors were likely to be low frequency in nature, and previously high-pass filtering with a 0.1 Hz cut-off threshold (Zijlstra and Hof 2003), has been used to remove 'gravitational components' (Liu *et al* 2011). However, for tracking vertical foot clearances in gait, higher frequency thresholds have been used (Lai *et al* 2008). Suggesting optimum high-pass filter thresholds may depend on both the body part and the characteristics of the movement. In this study, the high-pass filter thresholds were optimized by grid search for head and pelvic motion in gait. Filter thresholds were scaled to step frequency because participants walked over a wide range of step frequencies (0.8–2.8 Hz) and preliminary work indicated errors were linked to step frequency (figure 6).

The new scaled approach incorporated: (1) a new method for continuously aligning the accelerometer axes with the global coordinate system; (2) higher cut-off frequency thresholds, and; (3) scaling to step frequency. For remote monitoring of gait during daily life or in 'real world' scenarios (figure 1(b)) sensor alignment may be more difficult to control, and walks may be over a wide range of step frequencies; thus all three processes may be important. However, because the grid search indicated measurement errors were not sensitive to small changes in scaling coefficients, in more controlled environments (as depicted by the ideal schematic, figure 1(a)) or over a narrower range of step frequencies, the methods might be simplified.

4.4. Agreement with optical motion capture

Agreement between accelerometers and optical motion capture was generally better for oscillation velocity than oscillation displacement, probably because data were integrated only once with respect to time to obtain velocity, leading to the accumulation of fewer integration errors. Measurement accuracy was higher for VT movements that may have better approximated simple harmonic motion (figure 5) relative to ML and AP movements. Accuracy reduced as movements became more complex, suggesting the new 'scaled' method works better on relatively stable body segments such as the pelvis, head, and/or thorax, which experience limited fluctuations in orientation with respect to the vertical. For more complex movements, accuracy might be improved by the use of gyroscopes (Allum and Carpenter 2005) and sensor fusion (Brodie 2009), although gyroscopes increase cost and weight, as well as demands on battery life, which are important considerations for large scale remote monitoring applications.

4.5. Agreement with previous research

The large range of stride-to-stride oscillations we observed (0.22–7.40 cm) agrees with previous research. For example, over one stride, a 5.39 cm range of movement was measured along the VT axis and 3.33 cm along the AP axis by accelerometers attached to the lower trunk (Meichtry *et al* 2007). Vertical excursions of the centre-of-gravity from 3.88 to 5.53 cm were measured with an accelerometer attached to the L3 vertebra (Gonzalez *et al* 2009). ML pelvic amplitudes of 1.5 to 2.7 cm were measured by harmonic decomposition (Zijlstra and Hof 2003). Centre of mass excursions of 2.74 to 4.83 cm were measured along the VT axis using optical analysis (Orendurff *et al* 2004). Measurements ranges agree with those from an instrumented treadmill (Tesio *et al* 2010). Measurements also agree with optical motion capture of: pelvis motion (Zijlstra and Hof 1997), head and pelvic motion (Cole *et al* 2010), and ML centre of mass sway speeds (Galna *et al* 2013).

4.6. Interpretation of head and pelvic oscillations

VT oscillations consistently increased with walking speed (table 2), agreeing with a geometric model proposed for VT pelvic motion based on stride length (Zijlstra and Hof 1997). Similar to VT pelvic oscillations, VT head oscillations may also be governed by the walking mechanics, with little attenuation by the trunk. Similar to a model proposed for ML pelvic displacement based step frequency (Zijlstra and Hof 1997), we also observed decreasing ML head oscillation displacement with increased walking speed (figure 7(c)), which in turn was highly correlated to step frequency (table 2).

For head and pelvic oscillations in the transverse plane more complex relationships with walking speed were observed. ML pelvic oscillation velocity, for example, demonstrating a ‘U shaped’ relationship and was minimized at usual walking speed (figure 7(d)). ML pelvic position, ML head velocity, AP head velocity, and AP head position were also minimized at usual walking speeds. The ‘U shaped’ relationships suggest there might be stability, efficiency, and/or control advantages from minimizing stride-to-stride oscillations, that coincide with self-selected usual pace.

Interestingly, while AP pelvic oscillation velocity was highly correlated with walking speed ($r = 0.80$, figure 7(a)), AP head oscillation velocity was not (figure 7(b)). Furthermore, across all speeds AP pelvic oscillation velocities were faster than AP head oscillation velocities. These observations suggest that AP head oscillations are attenuated by the trunk. AP pelvic oscillations have previously been described purely by gait mechanics (Zijlstra and Hof 1997), but it appears additional control mechanisms may be involved in minimizing AP head oscillations. Our findings agree with attenuation by the trunk reported previously (Kavanagh *et al* 2005a). In healthy gait, the independence of AP head oscillation velocity from gait mechanics, variations in walking speed, and pelvic oscillations may provide a stable platform for visual and vestibular feedback mechanisms to better maintain postural stability while walking.

4.7. Limitations

We acknowledge certain limitations. This was a pilot study and focused on method development. Further research is required to determine generalizability and/or clinical usefulness in populations with known gait impairments. We measured head and pelvis oscillation displacement and velocity while walking in a healthy young population. Concurrent validity has yet to

be established in either older adults or people with unstable gait. Furthermore, gait efficiency, visual, vestibular, and/or control mechanisms were not directly measured. More research is required to better understand the complex theoretical relationships we observed between some transverse plane head oscillations and different walking speeds (see figure 7). In a companion paper, head oscillations are used to help characterize gait impairments in people with Parkinson's disease (Brodie *et al* 2015b).

5. Conclusion

Methods for remotely measuring head and pelvic oscillations while walking using wearable accelerometers were developed. In healthy gait, the head and pelvis undergo regular oscillations that can be measured with accelerometers. Consistent with previous mechanical gait models, VT oscillations of both the head and pelvis increased with walking speed, suggesting very little attenuation of VT motion by the trunk. However, some ML and AP head oscillations were uncorrelated and/or were minimized at usual speed, suggesting additional control mechanisms may be involved in the control of some transverse plane head oscillations in healthy gait. Because many consumer devices, including smart phones, already contain accelerometers, the methods presented may supplement existing gait analysis techniques and prove useful for remote assessment of changing health, mental status, and/or fall risk.

Appendix. The continuous pitch and roll correction

The continuous pitch and roll correction is visualized by figure 3 and designed to improve data quality prior to analysis by reducing errors from slow changing sensor orientation. Technical details using MATLAB commands is described in several steps below. Implementation in MATLAB and example accelerometer data from healthy and Parkinsonian gait are provided in a companion paper (Brodie *et al* 2015b).

Step frequency by fast Fourier transform

MATLAB's `fft()` function was used to transform the recorded acceleration into the frequency domain (see figure 2). The next power of 2 harmonics with relative to the data length was used. Step frequency (F_0) was determined by the peak power recorded in channels 1 and 3 of the pelvic sensor. The AP and VT harmonics were combined because step frequency was present in both axes (figure 2, top and bottom panels). The frequency of the dominant harmonic was determined using a moving average filter with a five point data window.

The continuous pitch and roll correction

The changing rotation required to correct for unintended and slow changing sensor tilt was calculated. The effects of this correction are demonstrated in figure 3. Calculation was similarly to methods used previously (Moe-Nilssen 1998), but instead of applying a one-off mean fixed correction, we calculated the low frequency error using a low-pass filter scaled to one quarter of the step frequency. The changing low frequency error was then converted into angular corrections about a floating unit vector using dot products, cross products, and a rotation matrix.

First, the complete data set, including at least two seconds of stationary data, were low-pass filtered using an 4th order Butterworth filter (CutOff = $F_0/4 \approx 0.45$ Hz, with respect to the data in figure 2) to obtain a changing low frequency acceleration (LFA) vector. MATLAB's butter() and filtfilt() functions were used.

Because steady state walking was assumed, if no orientation error were present, then the **LFA** would have been coincident to the gravitational acceleration ($\mathbf{G} = [0, 0, 9.81]'$). Slow changing sensor orientation causes the **LFA** vector to be angled away from the vertical. The continuous rotational corrections were therefore calculated by converting the LFA vector ($\mathbf{LFA} = [LFA_{AP}, LFA_{ML}, LFA_{VT}]'$) into an angular correction (θ) about a floating unit vector ($\mathbf{u} = [u_x, u_y, u_z]'$) in the XY-plane at each epoch.

The angular correction (θ , equation (A.1)) and floating axis (\mathbf{u} , equation (A.2)) at each point in time were found using dot and cross products of the **LFA** and gravitational acceleration (\mathbf{G}) vectors. For implementation refer to the supplementary material and the function. The pitch and roll corrections (θ , radians) about the unit vector (\mathbf{u}) were then put into matrix form (\mathbf{R} , equation (A.3)) and applied to the acceleration data ($\mathbf{A} = [A_{AP}, A_{ML}, A_{VT}]'$) to give acceleration corrected for pitch and roll (\mathbf{A}_{corr} , equation (A.4)).

Linear accelerations of the head and pelvis were calculated by subtracting gravity (\mathbf{G}) from the corrected acceleration (\mathbf{A}_{corr} , see figure 3, right panels). The most noticeable improvement is in the reduction of zero offset errors for the AP accelerations (figure 3, top panel, right side). Such errors may have been caused by a slow and continuous 'head nodding' that resulted in the head sensor orientation changing.

$$\theta = \cos^{-1} \left(\frac{\mathbf{LFA} \times \mathbf{G}}{\|\mathbf{LFA}\| \|\mathbf{G}\|} \right), \quad (\text{A.1})$$

$$\mathbf{u} = \frac{\mathbf{LEA} \times \mathbf{G}}{\|\mathbf{LEA} \times \mathbf{G}\|}, \quad (\text{A.2})$$

$$\mathbf{R} = \begin{bmatrix} \cos \theta + u_x^2(1 - \cos \theta) & u_x u_y(1 - \cos \theta) - u_z \sin \theta & u_x u_z(1 - \cos \theta) - u_y \sin \theta \\ u_y u_x(1 - \cos \theta) - u_z \sin \theta & \cos \theta + u_y^2(1 - \cos \theta) & u_y u_z(1 - \cos \theta) - u_x \sin \theta \\ u_z u_x(1 - \cos \theta) - u_y \sin \theta & u_z u_y(1 - \cos \theta) - u_x \sin \theta & \cos \theta + u_z^2(1 - \cos \theta) \end{bmatrix}, \quad (\text{A.3})$$

$$\mathbf{A}_{\text{corr}} = \mathbf{R}\mathbf{A}. \quad (\text{A.4})$$

References

- Allum J H J and Carpenter M G 2005 A speedy solution for balance and gait analysis: angular velocity measured at the centre of body mass *Curr. Opin. Neurol.* **18** 15–21
- Brodie M A 2009 Development of fusion motion capture for optimisation of performance in alpine ski racing *PhD Thesis* Massey University, Wellington
- Brodie M A D, Menz H B, Smith S T, Delbaere K and Lord SR 2015a Good lateral harmonic stability combined with adequate gait speed is required for low fall risk in older people *Gerontology* **61** 69–78
- Brodie M A D, Canning C G, Beijer T R and Lord S R 2015 Uncontrolled head oscillations in people with Parkinson's disease may reflect an inability to respond to perturbations while walking *Physiol. Meas.* **36** 873

- Cavagna G A, Franzetti P and Fuchimoto T 1983 The mechanics of walking in children *J. Physiol.* **343** 323–39
- Cole M H, Silburn P A, Wood J M, Worringham C J and Kerr G K 2010 Falls in Parkinson's disease: kinematic evidence for impaired head and trunk control *Mov. Disorders* **25** 2369–78
- Findling O, Schuster C, Sellner J, Ettlin T and Allum J H 2011 Trunk sway in patients with and without, mild traumatic brain injury after whiplash injury *Gait Posture* **34** 473–8
- Galna B, Murphy AT and Morris M E 2013 Obstacle crossing in Parkinson's disease: mediolateral sway of the centre of mass during level-ground walking and obstacle crossing *Gait Posture* **38** 790–4
- Gonzalez R C, Alvarez D, Lopez A M and Alvarez J C 2009 Ambulatory estimation of mean step length during unconstrained walking by means of COG accelerometry *Comput. Methods Biomech. Biomed. Eng.* **12** 721–6
- Hausdorff J M 2009 Gait dynamics in Parkinson's disease: common and distinct behavior among stride length, gait variability, and fractal-like scaling *Chaos* **19** 026113
- Hausdorff J M, Rios D A and Edelberg H K 2001 Gait variability and fall risk in community-living older adults: a 1 year prospective study *Arch. Phys. Med. Rehabil.* **82** 1050–6
- Kavanagh J J 2009 Lower trunk motion and speed-dependence during walking *J. Neuroeng. Rehabil.* **6** 9
- Kavanagh J J and Menz H B 2008 Accelerometry: a technique for quantifying movement patterns during walking *Gait Posture* **28** 1–15
- Kavanagh J, Morrison S and Barrett R S 2005a Coordination of head and trunk accelerations during walking *Eur. J. Appl. Physiol.* **94** 468–75
- Kavanagh J J, Barrett R S and Morrison S 2005b Age-related differences in head and trunk coordination during walking *Hum. Mov. Sci.* **24** 574–87
- Lai D T H, Begg R, Charry E and Palaniswami M 2008 Frequency analysis of inertial sensor data for measuring toe clearance *Issnip 2008 Proc. 2008 Int. Conf. on Intelligent Sensors, Sensor Networks, and Information Processing* pp 303–8
- Latt M D, Menz H B, Fung V S and Lord S R 2009 Acceleration patterns of the head and pelvis during gait in older people with Parkinson's disease: a comparison of fallers and nonfallers *J. Gerontol. A* **64** 700–6
- Liu Y, Redmond S J, Narayanan M R and Lovell N H 2011 Classification between non-multiple fallers and multiple fallers using a triaxial accelerometry-based system *Annual Int. Conf. of the IEEE Engineering in Medicine and Biology Society* pp 1499–502
- Meichtry A, Romkes J, Gobelet C, Brunner R and Mueller R 2007 Criterion validity of 3D trunk accelerations to assess external work and power in able-bodied gait *Gait Posture* **25** 25–32
- Menant J C, Steele J R, Menz H B, Munro B J and Lord S R 2011 Step time variability and pelvis acceleration patterns of younger and older adults: effects of footwear and surface conditions *Res. Sports Med.* **19** 28–41
- Menz H B, Lord S R and Fitzpatrick R C 2003 Acceleration patterns of the head and pelvis when walking are associated with risk of falling in community-dwelling older people *J. Gerontol. A* **58** 446–52
- Michael B D R, Kejia W, Jingjing W, Ying L, Matthew B, Kim D, Neigel H L, Stephen R L and Stephen J R 2014 A comparison of activity classification in younger and older cohorts using a smartphone *Physiol. Meas.* **35** 2269
- Moe-Nilssen R 1998 A new method for evaluating motor control in gait under real-life environmental conditions: I. The instrument *Clin. Biomech.* **13** 320–7
- Orendurff M S, Segal A D, Klute G K, Berge J S, Rohr E S and Kadel N J 2004 The effect of walking speed on center of mass displacement *J. Rehabil. Res. Dev.* **41** 829–34
- Rispens S M, van Schooten K S, Pijnappels M, Daffertshofer A, Beek P J and van Dieën J H 2015 Identification of fall risk predictors in daily life measurements: gait characteristics' reliability and association with self-reported fall history *Neurorehabil. Neural Repair* **29** 54–61
- Schepers H M, van Asseldonk E H F, Buurke J H and Veltink P H 2009 Ambulatory estimation of center of mass displacement during walking *IEEE Trans. Biomed. Eng.* **56** 1189–95
- Senden R, Savelberg H H, Grimm B, Heyligers I C and Meijer K 2012 Accelerometry-based gait analysis, an additional objective approach to screen subjects at risk for falling *Gait Posture* **36** 296–300
- Smidt G L, Arora J S and Johnston R C 1971 Accelerographic analysis of several types of walking *Am. J. Phys. Med.* **50** 285–300
- Tesio L, Rota V, Chessa C and Perucca L 2010 The 3D path of body centre of mass during adult human walking on force treadmill *J. Biomech.* **43** 938–44

- Weiss A, Brozgol M, Dorfman M, Herman T, Shema S, Giladi N and Hausdorff J M 2013 Does the evaluation of gait quality during daily life provide insight into fall risk? A novel approach using 3 d accelerometer recordings *Neurorehabil. Neural Repair* **27** 742–52
- Weiss A, Herman T, Plotnik M, Brozgol M, Giladi N and Hausdorff J M 2011 An instrumented timed up and go: the added value of an accelerometer for identifying fall risk in idiopathic fallers *Physiol. Meas.* **32** 2003
- Whittle M W 1997 3D motion of the center of gravity of the body during walking *Hum. Mov. Sci.* **16** 347–55
- Whittle M W and Levine D 1999 3D relationships between the movements of the pelvis and lumbar spine during normal gait *Hum. Mov. Sci.* **18** 681–92
- Wilhelmsen K, Nordahl S H G and Moe-Nilssen R 2010 Attenuation of trunk acceleration during walking in patients with unilateral vestibular deficiencies *J. Vestib. Res.* **20** 439–46
- Yogev G, Plotnik M, Peretz C, Giladi N and Hausdorff J M 2007 Gait asymmetry in patients with Parkinson's disease and elderly fallers: when does the bilateral coordination of gait require attention? *Exp. Brain Res.* **177** 336–46
- Zijlstra W and Hof A L 1997 Displacement of the pelvis during human walking: experimental data and model predictions *Gait Posture* **6** 249–62
- Zijlstra W and Hof A L 2003 Assessment of spatio-temporal gait parameters from trunk accelerations during human walking *Gait Posture* **18** 1–10

Uncontrolled head oscillations in people with Parkinson's disease may reflect an inability to respond to perturbations while walking

This content has been downloaded from IOPscience. Please scroll down to see the full text.

2015 Physiol. Meas. 36 873

(<http://iopscience.iop.org/0967-3334/36/5/873>)

View [the table of contents for this issue](#), or go to the [journal homepage](#) for more

Download details:

IP Address: 131.252.223.50

This content was downloaded on 27/04/2015 at 19:16

Please note that [terms and conditions apply](#).

Uncontrolled head oscillations in people with Parkinson's disease may reflect an inability to respond to perturbations while walking

Matthew A D Brodie^{1,2}, Colleen G Canning³, Tim R Beijer⁴
and Stephen R Lord¹

¹ Neuroscience Research Australia, University of New South Wales, Sydney, Australia

² Graduate School of Biomedical Engineering, University of New South Wales, Sydney Australia

³ Clinical and Rehabilitation Sciences Research Group, Faculty of Health Sciences, University of Sydney, Sydney, Australia

⁴ Neurology, Canisius Wilhelmina Hospital, Nijmegen, The Netherlands

E-mail: matthew.brodie@neura.edu.au

Received 26 November 2014, revised 28 January 2015

Accepted for publication 5 February 2015

Published 2 April 2015



CrossMark

Abstract

Fall injuries in people with Parkinson's disease (PD) are a major health problem. Increased sway while walking is a risk factor and further understanding of this destabilizing gait change may assist with rehabilitation and help prevent falls. Here, stride-to-stride head oscillations are used to help characterise different aspects of gait impairment in 10 people with PD on medication (67 years, SD 4), 10 healthy age-matched (HAM) participants (66 years, SD 7), and 10 young (30 years, SD 7). A wearable accelerometer was used to analyse head oscillations during five repeat 17 m walks by each participant.

People with PD had significantly faster transverse plane head oscillations than the HAM or young groups; both along mediolateral (PD 47.2 cm s^{-1} , HAM 32.5 cm s^{-1} , and young 32.7 cm s^{-1}) and anteroposterior axes (PD 33.3 cm s^{-1} , HAM 24.5 cm s^{-1} , and young 20.6 cm s^{-1}). These differences were uncorrelated with reduced vertical oscillation velocity (PD 15.5 cm s^{-1} , HAM 18.8 cm s^{-1} , and young 20.1 cm s^{-1}) and reduced walking speed (PD 1.2 m s^{-1} , HAM 1.4 m s^{-1} , and young 1.4 m s^{-1}).

Increased transverse plane head oscillations in people with PD may reflect motor impairment and the inability to respond sufficiently to perturbations while walking, which appears to be distinct from gait hyperkinesia, reduced vertical oscillations, step length, and walking speed.

Keywords: Parkinson's disease, head, accelerometers, sway, wearable, sensors, walking

 Online supplementary data available from stacks.iop.org/PM/36/050873

(Some figures may appear in colour only in the online journal)

1. Introduction

Approximately 68% of people with Parkinson's disease (PD) fall annually (Wood *et al* 2002). Most falls occur while moving or taking steps, provoked by postural instabilities, tripping, or freezing (Ashburn *et al* 2008). People with PD walk slowly and often with increased cadence to compensate for an inability to regulate stride length (Morris *et al* 1994). Assessments of people with PD often combine gait with postural instability, however these impairments may provide separate targets for treatment (Maetzler *et al* 2013). Typically, hypokinetic gait may be treated with medication (Rocchi *et al* 2002), physical therapy (Morris 2006), and deep brain stimulation (Johnsen *et al* 2009), but postural instabilities may respond less satisfactorily to medication (Nantel and Bronte-Stewart 2014) or deep brain stimulation (St George *et al* 2014).

Increased sway, while walking is a risk factor for falls. People with PD who fall have increased head motion while walking (Cole *et al* 2010), increased sway that is exacerbated by obstacle avoidance (Galna *et al* 2013), and increased sway velocity correlated to the severity of impairment (Galna *et al* 2013). Consensus, however, has yet to be reached about what constitutes postural instability while walking (Maetzler *et al* 2013) and research has not focused on separating this motor impairment from hypokinesia. We hypothesised that measurement of stride-to-stride oscillations using wearable accelerometers might help characterise the effects of these different motor impairments on gait in people with PD.

Accelerations measured with body worn sensors have been used to identify gait differences in old and young (Kavanagh *et al* 2005, Menant *et al* 2011), fallers and non-fallers (Yogev *et al* 2007), and people with Parkinson's disease (Hausdorff 2009, Latt *et al* 2009). Measurement of stride-to-stride oscillations (requiring accelerations to be integrated with respect to time) is less common (Brodie *et al* 2015).

In this paper, we investigate if stride-to-stride oscillations measured at the head using a wearable accelerometer might be used to help characterise both hypokinetic (slowing) and/or stability-related gait impairments in people with PD. We focused on head oscillations because according to a double inverted pendulum model of whole body balance (MacKinnon and Winter 1993), any balance perturbations may be amplified by the long lever arms connecting the supporting subtalar, hip, and cervical joint centres. Head movements may therefore be sensitive to small changes in postural instability while walking. Such insights may assist in guiding rehabilitation aimed at improving mobility and/or reducing fall injuries in people with PD.

2. Methods

Thirty participants: 10 with PD on medication, 10 healthy age-matched (HAM) controls, and 10 young participated. Participants were recruited from existing databases. Exclusion criteria were medical conditions that affect gait and impaired cognition (<24 on the Mini Mental State Examination (MMSE) (Folstein *et al* 1975)). PD participants were eligible if they had a

Table 1. Pilot study, participant background characteristics. MMSE—mini mental state examination.

Characteristics	Parkinson's disease (<i>N</i> = 10)	Healthy age-matched (<i>N</i> = 10)	Young (<i>N</i> = 10)
Age (year)	67.1 (SD 4.1)	65.6 (SD 6.9)	29.6 (SD 6.6)
Male:female (ratio)	7:3	5:5	6:4
Height (cm)	166.3 (SD 12.5)	171.5 (SD 9.7)	171.0 (SD 9.5)
Weight (kg)	72.2 (SD 15.2)	75.3 (SD 9.3)	68.2 (SD 17.1)
MMSE (0–30)	28.7 (SD 1.3)	29.9 (SD 0.3)	
Duration of PD (year)	7.1 (SD 4.2)		
Hoehn & Yahr (1–5)	1.9 (SD 1)		
# of people with stage 1 and 2	5 and 3		
# of people with stage 3 and 4	1 and 1		

diagnosis of idiopathic PD, lived in the community, were able to walk 21 m unassisted, had a clinical stage I–IV of illness according to Hoehn and Yahr (Hoehn and Yahr 1967), and had normal hearing and vision (table 1). Approval by the Human Studies Ethics Committee at the University of New South Wales was given for the study and informed consent was obtained from all participants prior to participation.

A tri-axial accelerometer (Opal™ by APDM, sampling frequency 128 Hz) was incorporated into a light plastic helmet liner (total mass 67 g) and secured to the participant's head (Brodie *et al* 2015). Data were reported according to a global vertical, body centred heading, coordinate system. Vertical (VT) measurements were independent of body position or sensor orientation and aligned to global vertical. The anteroposterior (AP) and mediolateral (ML) axes were body fixed and could rotate in the transverse plane if the orientation of the head changed. AP generally pointed forwards and parallel to the floor and ML right to left across the direction of travel (Brodie *et al* 2015). Participants completed five walks of 21 m at self-selected usual pace. The middle 17 m of data for each walk were marked with an external trigger and analysed using custom software.

Stride-to-stride oscillation velocity and displacement of the head were measured by integrating the corrected acceleration with respect to time and high-pass filtering (Brodie *et al* 2015). Head oscillations were visualised using cyclograms (Wong *et al* 2004, Tesio *et al* 2010) adapted for 3D representation (figure 1). Example data and MATLAB code to reproduce these diagrams are available as supplementary material (see appendix for details and stacks.iop.org/PM/36/050873). For all head oscillation calculations, the high-pass filter cut-off was scaled to 0.40 of step frequency for simplicity, and because previous work has shown errors were relatively insensitive to small changes in filter thresholds (Brodie *et al* 2015).

For each walk, oscillation velocity and displacement along each axis were summarised using the root mean square (RMS) statistic to define magnitude and the 95% range to define extent of oscillations. Walking speed, step length, cadence, 95% oscillation range, and RMS oscillations were recorded. The likelihood of a normal distribution for each group was determined using the Lilliefors test. Correlations with walking speed were measured using Pearson's correlation coefficients. Between test reliability between the first two repeat walks by each participant was tested using intraclass correlation coefficients ICC(2,1). Significant associations between PD and aging were investigated using the mean values across the five walking trials for each participant. ANOVA with post-hoc t-tests were used. Effect size was calculated using the difference between group means divided by the pooled standard

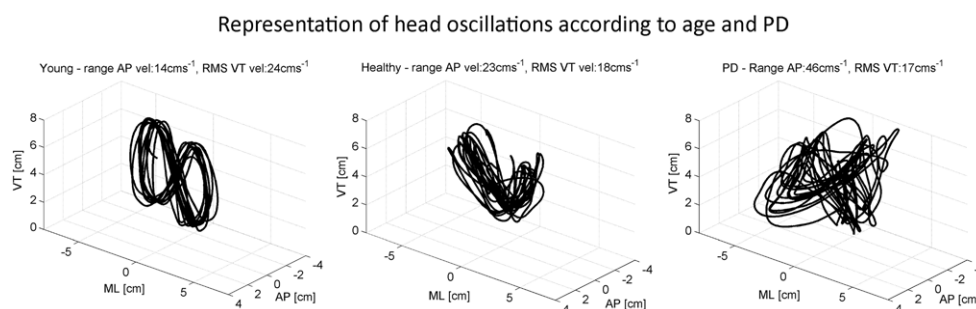


Figure 1. 3D visualisation of the effects of age and PD on head oscillations. The young person (left panel) walked with greater VT displacements. The person with PD (right panel) presented faster and less controlled transvers plane head movements. The healthy age-matched person was between.

deviation. Cluster boundaries for hypokinetic and unstable gait were determined by visual inspection. Data were processed using MATLAB (R2010a, The Mathworks Inc.) and SPSS (Version 22, IBM Corp).

3. Results

Tests for normality, between test reliability, and correlations with walking speed are summarised in table 2. No gait parameters were found to have distributions significantly different from normal (Lilliefors $p \leq 0.05$) and between test reliability was good (ICC: 0.75–0.98). Step length and all VT oscillations were all highly correlated with walking speed (0.68–0.88). AP oscillation velocity, ML oscillation velocity, and ML oscillation displacement were not significantly correlated with walking speed.

Head oscillations differed among the three groups (figure 1). Typically, young people (left panel) walked with greater VT oscillations of the head, which may be expressed as the RMS VT velocity. People with PD presented faster and less controlled transverse plane oscillations (right panel), which may be expressed as an increased 95% range of AP head velocity.

Statistical associations for people with PD, healthy age-matched and young were investigated (table 3). ANOVA revealed significant group differences for walking speed, step length, and five of the twelve head oscillation parameters investigated. Post-hoc analysis between the PD group and the healthy age-matched group revealed large effect sizes for step length (–1.28), walking speed (–1.22), the 95% range of AP head velocity (1.21) and the 95% range of ML head velocity (1.18). In summary, people with PD walked slower, took shorter steps, presented slower VT oscillations, but had faster oscillations in the transverse plane.

Interactions between walking speed, the 95% range of AP head velocity, and the RMS VT head velocity were investigated graphically with each walk plotted as a data point (figure 2). We observed strong linear correlations with walking speed for step length (panel A, $r = 0.88$), and for RMS VT head velocity (panel B, $r = 0.77$), but not for the 95% range of AP oscillation velocity (panel C), nor for the 95% range of ML oscillation velocity (panel D). According to panels A and B, hypokinetic gait in the PD group may be defined similarly by reduced VT oscillation magnitude, slower walking speed, and shorter steps. The interaction between walking speed and AP oscillation velocity (panel C) suggests that people with PD might be further separated into subgroups that have hypokinetic, unstable, and/or normal gait patterns. A

Table 2. Measuring stride-to-stride head oscillations using accelerometers, tests for normality, between test reliability, and correlations with walking speed. Lilliefors p -value ≤ 0.05 indicates the data are not normally distributed. A retest ICC(2,1) of unity indicates perfect agreement between the first two repeat walks. Pearson's r of unity indicates perfect correlation with walking speed; significant ($p \leq 0.05$) correlations marked (*).

	Lilliefors test for normality			Retest	Speed correlation	
	PD	HAM	Young	ICC(2,1)	r	p
Walking speed [ms^{-1}]	0.07	0.09	0.50	0.96		
Step length [cm]	0.25	0.11	0.50	0.97	0.88*	<0.001
Step frequency [Hz]	0.50	0.50	0.50	0.96	0.19*	0.02
Head velocity [cm s^{-1}]						
RMS AP	0.50	0.06	0.50	0.84	-0.13	0.13
RMS ML	0.50	0.5	0.14	0.81	-0.03	0.69
RMS VT	0.12	0.39	0.50	0.97	0.77*	<0.001
95% range AP	0.45	0.16	0.48	0.78	-0.16	0.06
95% range ML	0.50	0.5	0.50	0.95	-0.12	0.16
95% range VT	0.08	0.5	0.50	0.96	0.74*	<0.001
Head displacement [cm]						
RMS AP	0.50	0.5	0.14	0.80	-0.20*	0.02
RMS ML	0.50	0.34	0.44	0.95	0.03	0.71
RMS VT	0.36	0.23	0.50	0.98	0.72*	<0.001
95% range AP	0.50	0.5	0.16	0.75	-0.19*	0.02
95% range ML	0.50	0.5	0.31	0.95	0.02	0.78
95% range VT	0.12	0.1	0.32	0.98	0.68*	<0.001

similar interaction was observed for ML oscillation velocity (panel D), although the subgroup boundaries were less distinct.

4. Discussion

Measuring stride-to-stride head oscillations using wearable accelerometers provides a new way of monitoring gait in people with Parkinson's disease. The head oscillations parameters had both normal distributions and good between test reliability, which enables parametric statistics, such as ANOVA, to be used with greater confidence.

Progressive changes in head oscillations are visualised in figure 1. Increased transverse plane head oscillation velocities (as measured by the AP and ML 95% range) were significantly associated with PD (effect size: AP = 1.21 and ML = 1.18) and age (effect size: AP = 1.13), but were not significantly correlated with walking speed (Pearson's r : AP = -0.16 and ML = -0.12). Therefore, for people with PD, measurement of transverse plane oscillations during walking may provide additional information about gait impairments, which may be distinct from gait hypokinesia.

Our findings agree with previous research that found people with PD who fall have increased ML head motion (Cole *et al* 2010), increased sideways sway that is exacerbated by obstacle avoidance (Galna *et al* 2013), and increased sway speeds correlated to the severity of impairment (Galna *et al* 2013). Consistent with previous work in older people (Brodie *et al* 2013), the control of head movements, and control of walking speed may represent different gait constructs in people with PD.

Table 3. Stride-to-stride head oscillations; associations with PD and aging; significant ($p \leq 0.05$) associations marked with *, Effect—effect size.

	PD		HAM		Young		ANOVA		PD versus HAM		HAM versus Young		PD versus Young		
	Mean	SD	Mean	SD	Mean	SD	<i>p</i>	Effect	<i>p</i>	Effect	<i>p</i>	Effect	<i>p</i>	Effect	
	Walking speed [$\text{m}\cdot\text{s}^{-1}$]	1.22	0.15	1.41	0.16	1.42	0.13	0.009*	0.02*	0.02*	0.86	0.006	0.006	0.006	0.006
Step length [cm]	64.32	7.80	74.33	7.89	72.11	6.56	0.02*	0.01*	0.03	0.53	0.03	0.03	0.03	0.03	
Step frequency [Hz]	1.91	0.17	1.89	0.04	1.98	0.08	0.32	0.87	-0.08	0.02*	0.30	0.02*	0.30	-0.49	
Head velocity [$\text{cm}\cdot\text{s}^{-1}$]															
RMS AP	8.53	2.42	6.34	1.09	5.30	0.92	<0.001*	0.02*	1.14	0.04*	1.03	0.002*	1.73	1.73	
RMS ML	13.45	4.48	9.31	3.15	10.42	3.35	0.06	0.03*	1.06	0.48	-0.34	0.12	0.76	0.76	
RMS VT	15.50	4.47	18.77	3.47	20.13	4.22	0.06	0.10	-0.81	0.47	-0.35	0.03*	0.03*	-1.06	
95% range AP	33.19	9.26	24.51	3.56	20.62	3.30	<0.001*	0.02*	1.21	0.03*	1.13	0.001*	1.77	1.77	
95% range ML	47.24	13.83	32.45	11.01	32.68	8.34	0.01*	0.02*	1.18	0.96	-0.02	0.01*	1.26	1.26	
95% range VT	48.48	13.20	55.36	10.74	59.66	11.91	0.14	0.23	-0.57	0.43	-0.38	0.07	0.07	-0.89	
Head displacement [cm]															
RMS AP	1.05	0.44	0.72	0.12	0.61	0.11	0.006*	0.04*	1.01	0.08	0.90	0.01*	1.34	1.34	
RMS ML	1.89	0.83	1.44	0.54	1.64	0.57	0.35	0.18	0.64	0.45	-0.37	0.46	0.35	0.35	
RMS VT	1.31	0.38	1.57	0.28	1.63	0.34	0.11	0.10	-0.79	0.72	-0.17	0.07	-0.88	-0.88	
95% range AP	4.05	1.78	2.84	0.56	2.42	0.49	0.01*	0.07*	0.90	0.11	0.81	0.02*	1.22	1.22	
95% range ML	6.16	2.49	4.58	1.52	5.31	1.81	0.25	0.12	0.75	0.37	-0.43	0.41	0.39	0.39	
95% range VT	4.15	1.19	4.78	0.79	4.88	0.94	0.24	0.20	-0.61	0.81	-0.11	0.16	0.16	-0.67	

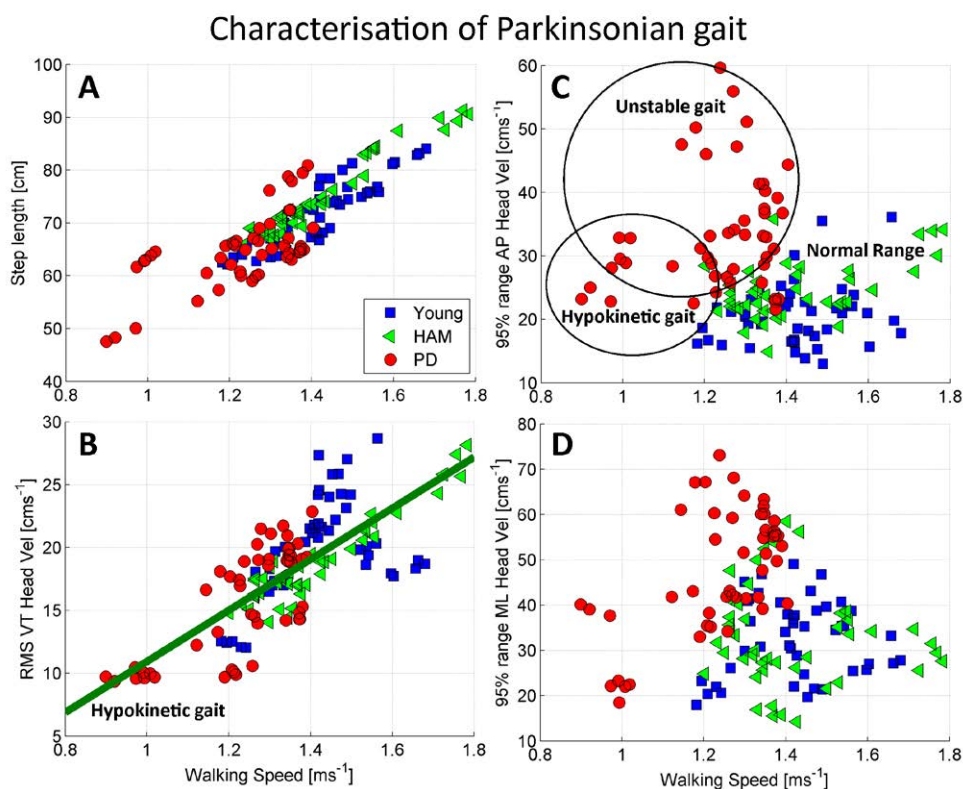


Figure 2. Head oscillations may provide one way of separating hypokinetic gait from unstable gait and/or normal range gait in people with PD. Panels A and B—walking speed, step length and vertical oscillation velocity were all highly correlated and may similarly characterise hypokinetic gait as slower, with shorter steps, and reduced VT oscillation. Panels C and D—increased transverse plane oscillation velocity may help characterise unstable gait patterns in people with PD, independent of reduced walking speed and related hypokinetic gait symptoms.

Interactions between walking speed and head oscillations were identified by visual inspection (figure 2). Three subgroups were observed. The first group comprised people with PD who walked slowly and generally also had reduced step length and VT oscillation (figures 2(a) and (b)). This ‘hypokinetic’ subgroup generally presented transverse plane oscillations within the normal range (figures 2(c) and (d)). The second group comprised people with PD who were ‘unstable’ in that they had increased transverse plane oscillations. The third group included people with ‘normal range’ gait and appeared to be neither hypokinetic nor unstable.

This observation of hypokinetic and unstable subgroups is consistent with previous research that found people with PD walk slower (Morris *et al* 1994), and also present postural instability that may respond poorly to treatment (Nantel and Bronte-Stewart 2014, St George *et al* 2014). However, additional studies, with larger sample sizes are required to determine if transverse plane head oscillations can categorise gait impairment in all people with PD. Such information may aid rehabilitation or fall prevention interventions and help provide greater distinction between hypokinesia and postural instability while walking as has been advocated (Maetzler *et al* 2013).

One method of assessing postural instability is to observe responses to rapid external perturbations in standing (Oude Nijhuis *et al* 2014). In gait, heel-strikes may provide alternative 'self-induced' perturbations and therefore an alternative way to define postural instability while walking. At the pelvis, heel-strikes can be identified by changes in AP acceleration (Zijlstra and Hof 2003) caused by rapid pelvic breaking after falling forward onto the lead foot. AP pelvic oscillations have been shown to depend primarily on step length and walking speed in gait mechanics studies (Zijlstra and Hof 1997). In healthy gait, however, AP head oscillation velocity is consistently lower than pelvic oscillation velocity and not correlated to walking speed, which suggests AP head oscillations may be controlled by additional processes and attenuated by the trunk (Brodie *et al* 2015). Therefore, we propose that the faster AP head oscillations observed in people with PD may quantify an inability to respond sufficiently to 'self-generated' perturbations caused by heel-strikes, but further research is required to confirm this hypothesis.

We acknowledge certain limitations. First, because this was an exploratory study, unadjusted *p*-values were reported (Perneger 1998). Further, because of the small group sizes, and because only people with mild PD on medication (mean Hoehn & Yahr 1.9, table 1) comprised the study participants, further research is required to determine if our findings can be generalised to all people with PD including those with more severe disease, both on and off medication. Second, as hypokinetic and unstable clusters were determined through visual inspection, further studies are required to confirm the validity of this classification and the clinical significance of identifying these subgroups. Third, based on the inverted pendulum model, we focused on head oscillations only. The assumption that head oscillations are more sensitive than pelvic oscillations to postural instability in people with PD requires confirmation. Finally, additional work is required to better characterise postural instability while walking for people with PD, and might include the full kinematic and kinetic assessment of the whole body movements recorded in a motion capture laboratory and more detailed neurological examination.

5. Conclusion

Control of head oscillations in the transverse plane appears to be compromised in people with Parkinson's disease. Increased transverse plane oscillations may reflect motor impairment and the inability to respond sufficiently to perturbations while walking, which appears to be distinct from gait hypokinesia, reduced vertical oscillations, step length, and walking speed. In the future, this distinction could be further explored using miniaturised wearable technology which may provide insights for rehabilitation and fall prevention. Further research could also focus on remotely collecting data from larger samples and investigating oscillation changes associated with medication, severity of PD, and/or increased fall risk.

References

- Ashburn A, Stack E, Ballinger C, Fazakarley L and Fitton C 2008 The circumstances of falls among people with Parkinson's disease and the use of falls diaries to facilitate reporting *Disabil. Rehabil.* **30** 1205–12
- Brodie M A, Menz H B and Lord S R 2014 Age-associated changes in head jerk while walking reveal altered dynamic stability in older people *Exp. Brain Res.* **232** 51–60
- Brodie M A D, Beijer T R, Canning C G and Lord S R 2015 Head and pelvis stride-to-stride oscillations in gait: validation and interpretation of measurements from wearable accelerometers *Physiol. Meas.* **36** 857

- Cole M H, Silburn P A, Wood J M, Worringham C J and Kerr G K 2010 Falls in Parkinson's disease: kinematic evidence for impaired head and trunk control *Mov. Disord.* **25** 2369–78
- Folstein M F, Folstein S E and McHugh P R 1975 'Mini-mental state'. A practical method for grading the cognitive state of patients for the clinician *J. Psychiatr. Res.* **12** 189–98
- Galna B, Murphy A T and Morris M E 2013 Obstacle crossing in Parkinson's disease: mediolateral sway of the centre of mass during level-ground walking and obstacle crossing *Gait Posture* **38** 790–4
- Hausdorff J M 2009 Gait dynamics in Parkinson's disease: common and distinct behavior among stride length, gait variability, and fractal-like scaling *Chaos* **19** 026113
- Hoehn M M and Yahr M D 1967 Parkinsonism: onset, progression and mortality *Neurology* **17** 427–42
- Johnsen E L, Mogensen P H, Sunde N A and Ostergaard K 2009 Improved asymmetry of gait in Parkinson's disease with DBS: gait and postural instability in Parkinson's disease treated with bilateral deep brain stimulation in the subthalamic nucleus *Mov. Disord.* **24** 590–7
- Kavanagh J J, Barrett R S and Morrison S 2005 Age-related differences in head and trunk coordination during walking *Human Mov. Sci.* **24** 574–87
- Latt M D, Menz H B, Fung V S and Lord S R 2009 Acceleration patterns of the head and pelvis during gait in older people with Parkinson's disease: a comparison of fallers and nonfallers *J. Gerontol. A-Biol.* **64** 700–6
- MacKinnon C D and Winter D A 1993 Control of whole body balance in the frontal plane during human walking *J. Biomech.* **26** 633–44
- Maetzler W, Nieuwhof F, Hasmann S E and Bloem B R 2013 Emerging therapies for gait disability and balance impairment: promises and pitfalls *Mov. Disord.* **28** 1576–86
- Menant J C, Steele J R, Menz H B, Munro B J and Lord S R 2011 Step time variability and pelvis acceleration patterns of younger and older adults: effects of footwear and surface conditions *Res. Sports Med.* **19** 28–41
- Morris M E 2006 Locomotor training in people with Parkinson disease *Phys. Ther.* **86** 1426–35
- Morris M E, Iansek R, Matyas T A and Summers J J 1994 The pathogenesis of gait hypokinesia in Parkinson's disease *Brain* **117** 1169–81
- Nantel J and Bronte-Stewart H 2014 The effect of medication and the role of postural instability in different components of freezing of gait (FOG) *Parkinsonism Relat. Disord.* **20** 447–51
- Oude Nijhuis L B, Allum J H, Nanhoe-Mahabier W and Bloem B R 2014 Influence of perturbation velocity on balance control in Parkinson's disease *PLoS one* **9** e86650
- Perneger T V 1998 What's wrong with Bonferroni adjustments *BMJ* **316** 1236–8
- Rocchi L, Chiari L and Horak F 2002 Effects of deep brain stimulation and levodopa on postural sway in Parkinson's disease *J. Neurol. Neurosurg. Psychiatry* **73** 267–74
- St George R J, Carlson-Kuhta P, Nutt J G, Hogarth P, Burchiel K J and Horak F B 2014 The effect of deep brain stimulation randomized by site on balance in Parkinson's disease *Mov. Disord.* **29** 949–53
- Tesio L, Rota V, Chessa C and Perucca L 2010 The 3D path of body centre of mass during adult human walking on force treadmill *J. Biomech.* **43** 938–44
- Wong A M K, Chen C L, Chen C P C, Chou S W, Chung C Y and Chen M J L 2004 Clinical effects of botulinum toxin A and phenol block on gait in children with cerebral palsy *Am. J. Phys. Med. Rehab.* **83** 284–91
- Wood B H, Bilclough J A, Bowron A and Walker R W 2002 Incidence and prediction of falls in Parkinson's disease: a prospective multidisciplinary study *J. Neurol. Neurosurg. Psychiatry* **72** 721–5
- Yogev G, Plotnik M, Peretz C, Giladi N and Hausdorff J M 2007 Gait asymmetry in patients with Parkinson's disease and elderly fallers: when does the bilateral coordination of gait require attention? *Exp. Brain Res.* **177** 336–46
- Zijlstra W and Hof A L 1997 Displacement of the pelvis during human walking: experimental data and model predictions *Gait Posture* **6** 249–62
- Zijlstra W and Hof A L 2003 Assessment of spatio-temporal gait parameters from trunk accelerations during human walking *Gait Posture* **18** 1–10

Research Article

Attenuation of Upper Body Accelerations during Gait: Piloting an Innovative Assessment Tool for Parkinson's Disease

Christopher Buckley,^{1,2} Brook Galna,³ Lynn Rochester,³ and Claudia Mazzà^{1,2,4}

¹MRC-Arthritis Research UK Centre for Integrated Research into Musculoskeletal Ageing (CIMA), Pam Liversidge Building, University of Sheffield, Sheffield S1 3JD, UK

²Department of Mechanical Engineering, University of Sheffield, Sir Frederick Mappin Building, Sheffield S1 3JD, UK

³Institute of Neuroscience/Newcastle University Institute for Ageing, Newcastle University, Clinical Ageing Research Unit, Campus for Ageing and Vitality, Newcastle upon Tyne NE4 5PL, UK

⁴INSIGNEO Institute for in Silico Medicine, University of Sheffield, Pam Liversidge Building, Sheffield S1 3JD, UK

Correspondence should be addressed to Christopher Buckley; cjbuckley1@sheffield.ac.uk

Received 21 November 2014; Accepted 21 January 2015

Academic Editor: Angelica Alonso

Copyright © 2015 Christopher Buckley et al. This is an open access article distributed under the Creative Commons Attribution License, which permits unrestricted use, distribution, and reproduction in any medium, provided the original work is properly cited.

The objective of the current investigation was to explore whether upper body accelerations obtained during gait provide sensitive measures of postural control in people with Parkinson's disease (PD). Thirteen people with PD (70 ± 11 years) and nineteen age-matched controls (70 ± 7 years) walked continuously for two minutes while wearing three inertial sensors located on their lower back (L5), shoulder level (C7), and head. Magnitude (root mean square (RMS)), attenuation (attenuation coefficient), and smoothness (Harmonic ratios, HR) of the accelerations were calculated. People with PD demonstrated greater RMS, particularly in the mediolateral direction, but similar harmonic ratio of head accelerations compared to controls. In addition, they did not attenuate accelerations through the trunk and neck as well as control participants. Our findings indicate that measuring upper body movement provides unique information regarding postural control in PD and that poor attenuation of acceleration from the pelvis to the head contributes to impaired head control. This information is simple to measure and appears to be sensitive to PD and, consequently, is proposed to benefit researchers and clinicians.

1. Introduction

People with Parkinson's disease (PD) walk with a gait pattern that is characterised by slowness (bradykinesia), muscle rigidity, and postural instability [1–3]. As the disease progresses, postural control deteriorates and predisposes people with PD to falls [4–6]. Current measures of postural control, based on the ability to maintain upright balance during quiet stance, poorly reflect real life situations when people with PD are at risk of falling. Consequently, researchers and clinicians are promoting the measurement of postural control during gait [7, 8].

The recent development of small and inexpensive wireless inertial sensors has helped facilitate routine measurement of postural control during gait in the clinic, laboratory, and the community. Emerging evidence suggests that measuring upper body acceleration during gait using inertial sensors

can objectively quantify differences in gait patterns between those with and without PD [9, 10]. It has also been shown that upper body accelerations are sensitive to differences between PD fallers and nonfallers [11]. Specifically, these studies have revealed a deterioration of the smoothness of trunk accelerations in people with PD as measured by harmonic ratios, which was more pronounced in those with a history of falls.

Despite emerging evidence that maintaining head stability during gait is a key determinant of postural control [12–16], accelerations of the head have been neglected in these previous studies examining upper body acceleration in PD. One potential reason head stability is important is that the head contains the visual and vestibular systems, which are critical for navigation and preplanning of adaptive motor strategies [13]. Head stability may have added importance for people with PD because they rely heavily on vision to

maintain their postural control [5]. Recent evidence suggests that vision during gait is affected in PD [17] and that the smoothness of trunk accelerations is also altered [9, 10]. However, it has not yet been established whether PD affects the stability of the head during gait. A key mechanism in maintaining head stability is the attenuation of accelerations through the trunk. People with PD often develop axial rigidity, which may impair their ability to attenuate the accelerations that are applied to the lower limbs during gait from impacting on head stability. The measurement of attenuation of accelerations through the upper body has previously been investigated as a strong postural control indicator for children, adults, and elderly individuals [18–21] but has not yet been examined in people with PD.

The objective of the current investigation was to explore whether upper body accelerations obtained during gait provide sensitive proxy measures of postural control in people with Parkinson's disease (PD). More specifically, the aims of this study were to assess the magnitude, attenuation, and smoothness of upper body accelerations in people with PD compared to age-matched controls. We tested the hypotheses that: people with PD would demonstrate impaired smoothness and attenuation of accelerations. To address these aims, accelerations of the head, trunk, and pelvis were assessed during gait in a cohort of people with PD and an age-matched control group.

2. Materials and Methods

2.1. Participants. A subsection of community dwelling older adults and people with PD were tested as part of the ongoing ICICLE-PD (Incidence of Cognitive Impairment in Cohorts with Longitudinal Evaluation—Parkinson's Disease) Gait study [22, 23]. Participants were excluded if they had any neurological (other than PD), orthopaedic, or cardiothoracic conditions that may have markedly affected their walking or safety during the testing sessions. In addition, PD participants had to be diagnosed with idiopathic PD according to the UK Parkinson's Disease Brain Bank criteria and were excluded if they presented with significant memory impairment (Mini Mental State Exam (MMSE) ≤ 24 [24]), dementia with Lewy bodies, drug induced parkinsonism, "vascular" parkinsonism, progressive supranuclear palsy, multiple system atrophy, corticobasal degeneration, or poor command of English. This study was conducted according to the Declaration of Helsinki and had ethical approval from the Newcastle and North Tyneside research ethics committee. All participants signed an informed consent form.

2.2. Experimental Protocol. All participants walked for two minutes at their preferred pace around a 25 m circuit, fully described in [27]. Spatiotemporal gait variables (walking speed, step time, step length, and step width) were measured using a 7 m long Gaitrite pressure activated electronic walkway (Platinum model Gaitrite, software version 4.5, CIR systems, United States of America). Upper body accelerations were measured using three OPAL inertial sensors sampling at 128 Hz (APDM Inc, Portland, OR, USA) located at 5th lumbar vertebra to represent the pelvis level (P), the 7th cervical

vertebra to represent the shoulder level (S) and upon the back of the head (H). The Gaitrite and the OPAL system were synchronised and the data was collected using the same A/D converter.

2.3. Data Analysis. To ensure only steady-state, straight-line walking was analysed, only the portion of the acceleration data recorded while participants who were in contact with the Gaitrite walkway was used. As detailed in Mazzà et al. [20], prior to collecting the gait data, a calibration trial was captured using a sensor placed on the floor to create a global reference frame for the laboratory. Thereafter, the local reference frame of each sensor was reoriented for each time sample to the newly established global reference frame [19, 28]. Following, the acceleration data was further segmented based upon the foot contact and foot off values obtained from the Gaitrite walkway. Then, the mean value of the signal was removed and a low-pass fourth order Butterworth filter with a cut-off frequency of 10 Hz was applied [19]. Data for each stride was normalised to 100 data points using linear interpolation. All signals were processed using MATLAB (version 8.1.0).

2.4. Magnitude of Acceleration. The magnitude of accelerations was calculated using the root mean square (RMS) of the accelerations, measured by each sensor for each stride in the Anteroposterior (AP), Mediolateral (ML), and Vertical (V) directions.

2.5. Attenuation of Acceleration. The ability to attenuate accelerations through the upper body was quantified using the attenuation coefficient. The attenuation coefficient describes the ability to reduce accelerations from inferior to the superior anatomical locations and was calculated using the RMS values for each stride.

The attenuation coefficients were computed using the RMS values of the head (RMS_H), shoulder (RMS_S), and pelvis (RMS_P) as follows [18–20]:

$$\begin{aligned} C_{PH} &= \left(1 - \frac{RMS_H}{RMS_P}\right) \times 100, \\ C_{PS} &= \left(1 - \frac{RMS_S}{RMS_P}\right) \times 100, \\ C_{SH} &= \left(1 - \frac{RMS_H}{RMS_S}\right) \times 100 \end{aligned} \quad (1)$$

with C_{PH} representing the attenuation from the pelvis to the head, C_{PS} representing the attenuation from the pelvis to the shoulder, and C_{SH} representing the attenuation from the shoulder to the head. Each equation provides a percentage representing the amount of acceleration that is attenuated from the inferior sensors to the superiorly located sensor. A positive coefficient indicates reduced acceleration at the superiorly located sensor relative to the inferiorly located sensor. A negative coefficient value indicates a greater acceleration at the superiorly located sensor.

Table 1: The mean (\pm SD) participant characteristics and spatial-temporal gait variables for the PD and control group.

	PD ($n = 13$)	Control ($n = 19$)	P (t -test)
Age (years)	69.7 \pm 11.1	70.2 \pm 6.7	0.90
Height (m)	1.70 \pm 0.10	1.72 \pm 0.10	0.99
Mass (Kg)	77.9 \pm 13.3	83.2 \pm 14.2	0.30
BMI	26.1 \pm 3.3	28.0 \pm 4.5	0.20
MDS UPDRS III	35.6 \pm 12.6	NA	NA
Hoehn and Yahr stage	HY II: 11;HY III: 2	NA	NA
Gait speed (m/s ²)	1.22 \pm 0.22	1.32 \pm 0.15	0.14
Step time (s)	0.54 \pm 0.21	0.54 \pm 0.44	0.97
Step length (cm)	0.66 \pm 0.12	0.71 \pm 0.07	0.15
Step width (cm)	0.09 \pm 0.03	0.09 \pm 0.02	0.46

*Significant difference at $P < 0.05$.

BMI: body mass index.

MDS UPDRS III: Movement Disorders Society Revised Unified Parkinson's Disease Rating Scale–Movement Subsection [25].

HY: Hoehn and Yahr stage [26].

2.6. Smoothness of Accelerations. We quantified the smoothness of upper body accelerations using the harmonic ratio (HR). The HR accurately describes the step-to-step symmetry within a stride but for upper body gait analysis is also commonly referred to as a measure smoothness [29]. The HR was calculated via discrete Fourier transform for each of the acceleration components measured at the H, S, and P levels in the AP, ML, and V directions [30]. The fundamental frequency was set equal to the stride frequency.

For the AP and V Components, the HR Was Defined as:

$$HR = \frac{\sum \text{Amplitudes of even harmonics}}{\sum \text{Amplitudes of odd harmonics}} \quad (2)$$

For the ML Component, the HR Was Defined as:

$$HR = \frac{\sum \text{Amplitudes of odd harmonics}}{\sum \text{Amplitudes of even harmonics}} \quad (3)$$

Higher values of HR are associated with a higher similarity between the pattern of the upper body movements occurring during the right and left steps and are therefore favourable [9, 31]. Following calculation, the HR's were normalised to each participant's gait speed [9, 14].

2.7. Statistical Analysis. A series of two-tailed paired t -tests were used to test the difference between groups for the magnitude, attenuation, and smoothness of accelerations. The level of significance was set at $P = 0.05$. Given the exploratory nature of this study, the P value was not adjusted for multiple comparisons.

3. Results

The characteristics of the participants are reported in Table 1. All the participants with PD were tested within 18–54 months post diagnosis. No significant differences were found between the two groups in terms of anthropometric characteristics or spatiotemporal gait values.

3.1. Magnitude of Acceleration. Significantly higher ML head accelerations were observed in people with PD compared to controls (1.08 ± 0.29 m/s² versus 0.86 ± 0.21 m/s², $P = 0.024$) but not at the pelvis or the shoulder level. There were no other significant between-group differences although AP and V head accelerations tended to be greater in the PD group (Table 2).

3.2. Attenuation of Acceleration. People with PD did not attenuate AP or ML accelerations as well as controls (Figure 1). For C_{PH} , a significant difference existed between PD and the control participants in the ML direction ($0.12 \pm 34.7\%$ versus $33.8 \pm 21.3\%$, $P = 0.003$). For C_{PS} , a significant difference existed between PD and controls in the AP ($16.0 \pm 15.6\%$ versus $33.1 \pm 12.4\%$, $P = 0.002$), as well as the ML direction ($5.5 \pm 24.5\%$ versus $27.7 \pm 18.6\%$, $P = 0.009$). For C_{SH} , a significant difference existed between the PD and the control group in the ML direction ($-3.6 \pm 15.5\%$ versus $9.4 \pm 15.3\%$, $P = 0.031$).

3.3. Harmonic Ratio. The HRs normalised to gait speed showed no significant differences between the PD and control participants (Table 3).

4. Discussion

Our current investigation provides evidence that upper body accelerations obtained during gait provide sensitive measures of postural control in people with Parkinson's disease (PD). As hypothesised, the results of this study showed that people with PD walked with altered upper body accelerations compared to age-matched controls. In particular, people with PD walked with greater magnitude of ML head accelerations and demonstrated impaired attenuation of accelerations from the pelvis and neck to the head. In contrast to our hypothesis, smoothness of upper body accelerations as measured by the HR was not significantly affected in this sample of PD.

To our knowledge, this is the first study to show impaired head stability in people with PD using inertial sensors. A greater magnitude of ML head acceleration was found for

Table 2: The mean (\pm SD) root mean square (RMS) for the PD and the control participants calculated at the head (H), shoulder (S), and the pelvis (P) levels.

Sensor location	Component	PD	Control	P (t -test)
H	AP	1.02 ± 0.24	0.92 ± 0.20	0.22
	ML	1.08 ± 0.29	0.86 ± 0.21	0.02*
	V	2.15 ± 0.74	2.41 ± 0.47	0.26
S	AP	1.03 ± 0.18	0.96 ± 0.16	0.31
	ML	1.05 ± 0.24	0.96 ± 0.17	0.25
	V	2.04 ± 0.64	2.28 ± 0.46	0.24
P	AP	1.28 ± 0.38	1.47 ± 0.33	0.14
	ML	1.17 ± 0.36	1.41 ± 0.42	0.11
	V	2.16 ± 0.70	2.35 ± 0.47	0.37

*Significant difference at $P < 0.05$.

H: head; S: shoulder level; P: pelvis.

AP: anterior/posterior; ML: medial/lateral; V: vertical.

Table 3: The mean (\pm SD) Harmonic ratios normalised to gait speed for the PD and the control participants calculated at the head (H), shoulder (S), and the pelvis (P) levels.

Sensor location	Component	PD	Control	P (t -test)
H	AP	0.71 ± 0.36	0.53 ± 0.23	0.11
	ML	1.22 ± 0.56	1.02 ± 0.38	0.27
	V	2.03 ± 0.57	2.18 ± 0.60	0.50
S	AP	0.70 ± 0.23	0.66 ± 0.22	0.64
	ML	0.80 ± 0.50	0.80 ± 0.22	0.95
	V	2.34 ± 0.77	2.51 ± 0.72	0.55
P	AP	1.22 ± 0.38	1.13 ± 0.48	0.61
	ML	1.05 ± 0.69	0.80 ± 0.38	0.22
	V	2.02 ± 0.60	2.17 ± 2.17	0.58

H: head; S: shoulder level; P: pelvis.

AP: anterior/posterior; ML: medial/lateral; V: vertical.

the PD group. This was interpreted as a result of poor postural control for the PD participants and a failure to stabilise their head in space [18, 21]. High values for the head accelerations have been previously described as a reduced ability to stabilise the head in space. This is particularly crucial for people with PD because of their aforementioned increased dependence upon visual input for correcting postural control [5]; higher accelerations are likely disturbing their visual system, leading to an impaired ability to preplan effective motor strategies [13], causing an increased likelihood to fall. Although they might be a useful measure of postural control, RMS values of head accelerations are known to be dependent upon step length and gait speed [31]. Despite no significant differences being observed for these parameters between the PD and the control group in this sample, it is common that PD affects both gait speed and step length [1-3]. As a result, the magnitude of accelerations may lack sensitivity when used for

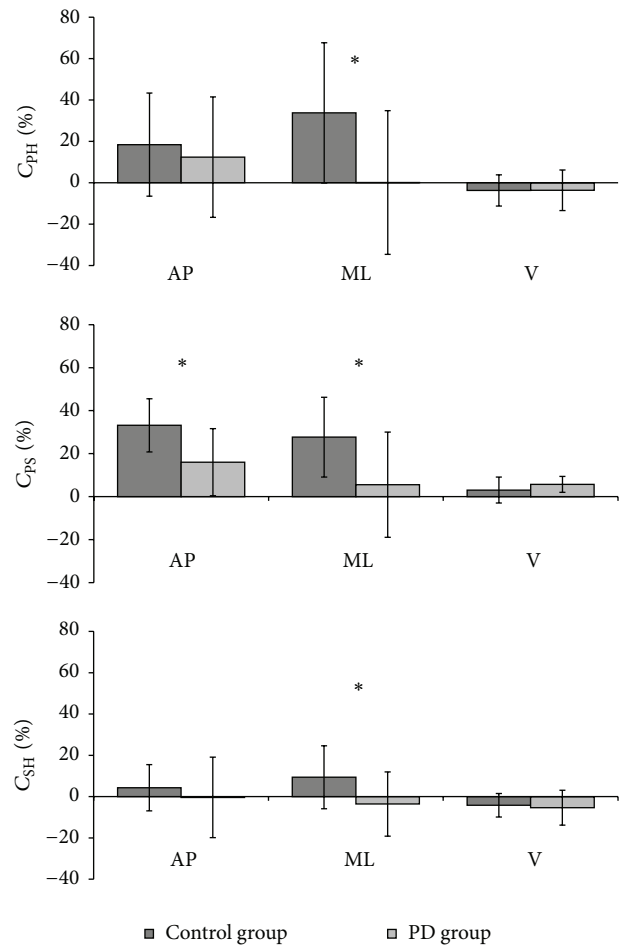


Figure 1: Mean (\pm SD) values of the attenuation coefficients (C_{PHI} , C_{PS} , and C_{SH}) of the three acceleration components (AP = anterior/posterior, ML = medial/lateral; V = vertical), computed for the control and group with PD. * $P < 0.05$.

discriminating PD patients, which in other studies have been shown to possess a decreased step length and gait speed, when compared to age-matched controls.

Alternatively, being computed as a ratio between accelerations measured during the same trial [18], the coefficients of attenuation do not suffer from being speed dependent. In the current investigation; the coefficients of attenuation provided insight into why the PD participants demonstrated greater accelerations at the head. Participants with PD were less able to attenuate accelerations through the trunk, as shown by impaired pelvis-shoulder attenuation coefficients, which were reduced on average by at least a half in the PD cohort, both in the AP and in the ML direction. It is not possible to fully explain why the people with PD did not attenuate accelerations well through the upper body; however, it may be associated with *en bloc* movement and axial rigidity. It has previously been stated that increased rigidity may cause underlying changes in the physiological and mechanical functioning of the axial muscles which results in *en bloc* movement, where the head, trunk and pelvis move together

as one rigid unit [12, 32]. It might be assumed that the same mechanisms could be responsible for poor attenuation of accelerations through the spine in PD. However, more research is certainly needed to test this hypothesis and explain the mechanisms ruling altered head accelerations and poor attenuation in PD, as well as the implications of poor head stability on vision and postural control.

Interestingly, the findings regarding attenuation coefficients were strongest in the ML direction. Similar results were found even when analysing healthy elderly subjects [21]. The fact that instability was predominantly found in the ML direction, suggests that when utilising a coefficient of attenuation, the ML direction is potentially most informative of an impaired walking stability. Consequently, assessments in the ML direction may be best for proxy measures of postural control in PD.

In contrast with our hypothesis and previous studies [9], the smoothness of upper body accelerations (harmonic ratios) was not significantly affected in our sample of PD participants. The discrepancy with previous studies is unlikely due to methodological differences, as the studies were similar in design. It is possible, however, that we were statistically underpowered to detect group difference, as suggested by a 25% reduction of AP HRs and 16% reduction of ML HRs at the head in the PD group that did not reach statistical significance ($P = 0.106$). Further research is required to determine the effectiveness of harmonic ratios as a sensitive measure to PD at different stages of their disease progression, as well as its ability to predict future falls.

Clinicians require objective measures to assess postural control during locomotion in people with PD to supplement standard clinical assessments and conventional rating scales which are not sensitive to subtle postural control disturbance [31, 33, 34]. Our findings indicate that it is feasible to measure the magnitude, attenuation, and smoothness of upper body accelerations in people with PD using body worn sensors. The rapid technological development of inertial sensors may afford a quick, clinically appropriate, and cost effective method to measure postural control in the clinic and community settings [5]. Specifically, the attenuation coefficient is a promising measure that is sensitive to PD; however, larger longitudinal studies are needed to assess its ability to monitor disease progression, determine intervention efficacy, and inform clinical management [5, 34, 35].

5. Conclusion

The current investigation suggests that assessing upper body acceleration offers additional and unique information about postural control during gait in people with PD. In particular, the magnitude of ML head accelerations and attenuation of upper body acceleration appear sensitive to PD and consequently hold promise as useful proxy measures that can be utilised in clinical and community settings.

Conflict of Interests

The authors declare that there is no conflict of interests regarding the publication of this paper.

Acknowledgments

The authors would like to thank the MRC-Arthritis research UK Centre for Integrated Research into Musculoskeletal Ageing (CIMA) for their part in funding the project and for allowing for the collaboration with the contributing members from the Clinical Ageing Research Unit (CARU). The authors would also like to acknowledge all participants for their time and interest into the project. ICICLE-GAIT is supported by the National Institute for Health Research (NIHR) Newcastle Biomedical Research Unit based at Newcastle upon Tyne Hospitals NHS Foundation Trust and Newcastle University. The research was also supported by NIHR Newcastle CRF Infrastructure funding. The views expressed are those of the authors and not necessarily those of the NHS, the NIHR, or the Department of Health.

References

- [1] J. Barth, J. Klucken, P. Kugler et al., "Biometric and mobile gait analysis for early diagnosis and therapy monitoring in Parkinson's disease," in *Proceedings of the 33rd Annual International Conference of the IEEE Engineering in Medicine and Biology Society (EMBS '11)*, pp. 868–871, September 2011.
- [2] R. E. A. van Emmerik, R. C. Wagenaar, A. Winogrodzka, and E. C. Wolters, "Identification of axial rigidity during locomotion in parkinson disease," *Archives of Physical Medicine and Rehabilitation*, vol. 80, no. 2, pp. 186–191, 1999.
- [3] M. H. M. Cole, P. A. P. Silburn, J. M. Wood, C. J. Worringham, and G. K. Kerr, "Falls in Parkinson's disease: kinematic evidence for impaired head and trunk control," *Movement Disorders*, vol. 25, no. 14, pp. 2369–2378, 2010.
- [4] F. B. Horak and M. Mancini, "Objective biomarkers of balance and gait for Parkinson's disease using body-worn sensors," *Movement Disorders*, vol. 28, no. 11, pp. 1544–1551, 2013.
- [5] M. Mancini, F. B. Horak, C. Zampieri, P. Carlson-Kuhta, J. G. Nutt, and L. Chiari, "Trunk accelerometry reveals postural instability in untreated Parkinson's disease," *Parkinsonism and Related Disorders*, vol. 17, no. 7, pp. 557–562, 2011.
- [6] M. D. Latt, S. R. Lord, J. G. L. Morris, and V. S. C. Fung, "Clinical and physiological assessments for elucidating falls risk in Parkinson's disease," *Movement Disorders*, vol. 24, no. 9, pp. 1280–1289, 2009.
- [7] A. L. Adkin, B. R. Bloem, and J. H. J. Allum, "Trunk sway measurements during stance and gait tasks in Parkinson's disease," *Gait and Posture*, vol. 22, no. 3, pp. 240–249, 2005.
- [8] H. J. Yack and R. C. Berger, "Dynamic stability in the elderly: identifying a possible measure," *Journal of Gerontology*, vol. 48, no. 5, pp. M225–M230, 1993.
- [9] K. A. Lowry, A. L. Smiley-Oyen, A. J. Carrel, and J. P. Kerr, "Walking stability using harmonic ratios in Parkinson's disease," *Movement Disorders*, vol. 24, no. 2, pp. 261–267, 2009.
- [10] K. A. Lowry, A. J. Carrel, J. M. McIlrath, and A. L. Smiley-Oyen, "Use of harmonic ratios to examine the effect of cueing strategies on gait stability in persons with Parkinson's disease," *Archives of Physical Medicine and Rehabilitation*, vol. 91, no. 4, pp. 632–638, 2010.
- [11] M. M. D. Latt, H. H. B. Menz, V. S. Fung, and S. R. Lord, "Acceleration patterns of the head and pelvis during gait in older people with Parkinson's disease: a comparison of fallers and

- nonfallers,” *Journals of Gerontology A: Biological Sciences and Medical Sciences*, vol. 64, no. 6, pp. 700–706, 2009.
- [12] S. Mesure, J. P. Azulay, J. Pouget, and B. Amblard, “Strategies of segmental stabilization during gait in Parkinson’s disease,” *Experimental Brain Research*, vol. 129, no. 4, pp. 573–581, 1999.
- [13] T. Pozzo, A. Berthoz, and L. Lefort, “Head stabilization during various locomotor tasks in humans. I. Normal subjects,” *Experimental Brain Research*, vol. 82, no. 1, pp. 97–106, 1990.
- [14] H. B. Menz, S. R. Lord, and R. C. Fitzpatrick, “Acceleration patterns of the head and pelvis when walking on level and irregular surfaces,” *Gait and Posture*, vol. 18, no. 1, pp. 35–46, 2003.
- [15] J. J. Kavanagh, S. Morrison, and R. S. Barrett, “Coordination of head and trunk accelerations during walking,” *European Journal of Applied Physiology*, vol. 94, no. 4, pp. 468–475, 2005.
- [16] J. J. Kavanagh and H. B. Menz, “Accelerometry: a technique for quantifying movement patterns during walking,” *Gait and Posture*, vol. 28, no. 1, pp. 1–15, 2008.
- [17] B. Galna, S. Lord, D. Daud, N. Archibald, D. Burn, and L. Rochester, “Visual sampling during walking in people with Parkinson’s disease and the influence of environment and dual-task,” *Brain Research*, vol. 1473, pp. 35–43, 2012.
- [18] C. Mazzà, M. Iosa, F. Pecoraro, and A. Cappozzo, “Control of the upper body accelerations in young and elderly women during level walking,” *Journal of NeuroEngineering and Rehabilitation*, vol. 5, article 30, 2008.
- [19] C. Mazzà, M. Iosa, P. Picerno, and A. Cappozzo, “Gender differences in the control of the upper body accelerations during level walking,” *Gait and Posture*, vol. 29, no. 2, pp. 300–303, 2009.
- [20] C. Mazzà, M. Zok, and A. Cappozzo, “Head stabilization in children of both genders during level walking,” *Gait and Posture*, vol. 31, no. 4, pp. 429–432, 2010.
- [21] T. Doi, T. Asai, S. Hirata, and H. Ando, “Dual-task costs for whole trunk movement during gait,” *Gait and Posture*, vol. 33, no. 4, pp. 712–714, 2011.
- [22] S. Lord, B. Galna, J. Verghese, S. Coleman, D. Burn, and L. Rochester, “Independent domains of gait in older adults and associated motor and nonmotor attributes: validation of a factor analysis approach,” *Journals of Gerontology, Series A: Biological Sciences and Medical Sciences*, vol. 68, no. 7, pp. 820–827, 2013.
- [23] L. Rochester, B. Galna, S. Lord, and D. Burn, “The nature of dual-task interference during gait in incident Parkinson’s disease,” *Neuroscience*, vol. 265, pp. 83–94, 2014.
- [24] M. F. Folstein, S. E. Folstein, and P. R. McHugh, “‘Mini-mental state’: A practical method for grading the cognitive state of patients for the clinician,” *Journal of Psychiatric Research*, vol. 12, no. 3, pp. 189–198, 1975.
- [25] C. G. Goetz, S. Fahn, P. Martinez-Martin et al., “Movement disorder society-sponsored revision of the unified Parkinson’s disease rating scale (MDS-UPDRS): process, format, and clinimetric testing plan,” *Movement Disorders*, vol. 22, no. 1, pp. 41–47, 2007.
- [26] C. Goetz, W. Poewe, O. Rascol et al., “Movement disorder society task force report on the Hoehn and Yahr staging scale: status and recommendations,” *Movement Disorders*, vol. 19, pp. 1020–1028, 2004.
- [27] B. Galna, S. Lord, and L. Rochester, “Is gait variability reliable in older adults and Parkinson’s disease? Towards an optimal testing protocol,” *Gait & Posture*, vol. 37, no. 4, pp. 580–585, 2013.
- [28] A. Godwin, M. Agnew, and J. Stevenson, “Accuracy of inertial motion sensors in static, quasistatic, and complex dynamic motion,” *Journal of Biomechanical Engineering*, vol. 131, no. 11, Article ID 114501, 2009.
- [29] J. L. Bellanca, K. A. Lowry, J. M. VanSwearingen, J. S. Brach, and M. S. Redfern, “Harmonic ratios: a quantification of step to step symmetry,” *Journal of Biomechanics*, vol. 46, no. 4, pp. 828–831, 2013.
- [30] F. Pecoraro, C. Mazzà, A. Cappozzo, E. E. Thomas, and A. Macaluso, “Reliability of the intrinsic and extrinsic patterns of level walking in older women,” *Gait and Posture*, vol. 26, no. 3, pp. 386–392, 2007.
- [31] M. D. Latt, H. B. Menz, V. S. Fung, and S. R. Lord, “Walking speed, cadence and step length are selected to optimize the stability of head and pelvis accelerations,” *Experimental Brain Research*, vol. 184, no. 2, pp. 201–209, 2008.
- [32] J. Spildooren, S. Vercruyse, E. Heremans et al., “Head-pelvis coupling is increased during turning in patients with Parkinson’s disease and freezing of gait,” *Movement Disorders*, vol. 28, no. 5, pp. 619–625, 2013.
- [33] P. Vieregge, H. Stolze, C. Klein, and I. Heberlein, “Gait quantitation in Parkinson’s disease—locomotor disability and correlation to clinical rating scales,” *Journal of Neural Transmission*, vol. 104, no. 2-3, pp. 237–248, 1997.
- [34] M. Mancini, L. King, A. Salarian, L. Holmstrom, J. McNamee, and F. B. Horak, “Mobility lab to assess balance and gait with synchronized body-worn sensors,” *Journal of Bioengineering & Biomedical Science*, supplement 1, article 007, 2012.
- [35] M. Iosa, A. Fusco, G. Morone et al., “Assessment of upper-body dynamic stability during walking in patients with subacute stroke,” *Journal of Rehabilitation Research and Development*, vol. 49, no. 3, pp. 439–450, 2012.



Hindawi

Submit your manuscripts at
<http://www.hindawi.com>



Research Article

Assessment of Movement Patterns during Intubation between Novice and Experienced Providers Using Mobile Sensors: A Preliminary, Proof of Concept Study

Jestin N. Carlson,¹ Samarjit Das,² Stephanie Spring,¹ Adam Frisch,³
Fernando De la Torre,² and Jessica Hodgins²

¹Department of Emergency Medicine, Allegheny Health Network, Erie, PA 16544, USA

²The Robotics Institute, Carnegie Mellon University, Pittsburgh, PA 15213, USA

³Department of Emergency Medicine, Albany Medical Center, Albany, NY 12208, USA

Correspondence should be addressed to Jestin N. Carlson; jcarlson@svhs.org

Received 17 December 2014; Revised 9 February 2015; Accepted 12 February 2015

Academic Editor: Hideo Inaba

Copyright © 2015 Jestin N. Carlson et al. This is an open access article distributed under the Creative Commons Attribution License, which permits unrestricted use, distribution, and reproduction in any medium, provided the original work is properly cited.

Background. There are likely marked differences in endotracheal intubation (ETI) techniques between novice and experienced providers. We performed a proof of concept study to determine if portable motion technology could identify the motion components of ETI between novice and experienced providers. **Methods.** We recruited a sample of novice and experienced providers to perform ETIs on a cadaver. Their movements during ETI were recorded with inertial measurement units (IMUs) on the left wrist. Their signals were assessed visually between novice and experienced providers to identify areas of differences at key steps during ETI. We then calculated spectral smoothness (SS), a quantitative measure inversely related to movement variability, for all ETI attempts. **Results.** We enrolled five novice and five experienced providers. When visually inspecting the data, we noted maximum variability when inserting the blade of the laryngoscope into the mouth and while visualizing the glottic opening. Novice providers also had greater overall variability in their movement patterns (SS novice 6.4 versus SS experienced 26.6). **Conclusion.** Portable IMUs can be used to detect differences in movement patterns between novice and experienced providers in cadavers. Future ETI educational efforts may utilize portable IMUs to help accelerate the learning curve of novice providers.

1. Introduction

Endotracheal intubation (ETI) is an advanced airway procedure that is defined by a series of movements that result in a tube passing through the glottic opening into the trachea to allow for oxygenation and ventilation. Unsuccessful or prolonged ETI efforts can lead to multiple complications including hypoxia, brain damage, and even death [1–3]. The complications may be magnified when performing ETI in acute care settings including the emergency department and out-of-hospital environments [1, 3, 4]. As a result, learning ETI in acute care settings is challenging and often the learning curve for ETI in these settings is prolonged [5, 6]. Procedural competency is essential for low-frequency and high-consequence procedures such as ETI and therefore it is essential to accelerate the learning curve for emergent ETI.

While there are educational programs for teaching ETI, there are few objective metrics available to assess procedural competency, specifically the kinematics involved in ETI. An improved understanding of the motions involved in ETI and their connections with airway exposure and visualization could impact airway education practices, shedding light on the unrecognized actions needed to accomplish ETI and improve patient outcomes. Previous work with motion capture has identified differences in movement patterns between novice and experienced providers [7]. This work has been restricted to mannequin models due to limited portability of motion analysis technology. Portable inertial measurement units (IMUs) have been used in other clinical settings, but their utility in ETI is unknown [8, 9].

We demonstrate proof of concept that ETI motions can be recorded by portable IMUs. We hypothesize that portable

IMUs can identify movement patterns that differentiate novice from experienced providers when performing ETI outside of mannequins.

2. Methods

2.1. Study Design and Setting. We performed an interventional, observational study examining the movement patterns of providers while performing intubation on a cadaver. After providing informed consent, participants were outfitted with IMUs (Emerald Model, APDM Inc, Portland, OR) on the left wrist. Participants then performed one intubation attempt on a cadaver using the CMAC video laryngoscope (Model 8402, Karl Storz Corp., Tuttlingen, Germany) with a #4 Macintosh blade. Participants used the CMAC as a direct laryngoscope; however, their ETI attempts were recorded for offline review. All intubation attempts were made with the cadaver on the anatomy table (fixed height of 89.5 cm). The providers' movements were recorded with the IMUs. Prior to each ETI attempt, providers were instructed to clap three times, pick up the laryngoscope with their left hand, move the laryngoscope up and down three times, lay the laryngoscope back down, and rest their hands on the table. This provided a unique signal, allowing us to synchronize the videos from the CMAC and the movement patterns from the IMUs to identify the beginning of the intubation attempt. Providers' movements, as recorded by the IMUs, were then compared offline between experienced and novice providers. This study was approved by our Institutional Review Board.

2.2. Selection of Participants. We recruited a convenience sample of five providers from a pool of attending physicians and fourth year emergency medicine residents with each having over 100 ETIs in the clinical setting, and defined these as "experienced" providers. We also recruited a convenience sample of five third and fourth year medical students with each having <10 ETIs in the clinical setting and defined these as "novice" providers. All providers had previous formal airway training. We defined "previous formal airway training" as having attended a structured airway didactics of ≥ 1 hour in length for experienced providers (emergency medicine resident or attending physician). Novice providers must have attended a structured airway didactics of ≥ 1 hour in length or completed a rotation in anesthesia. No participants reported significant experience with the CMAC prior to this study. We excluded providers who had performed between 10 and 100 ETIs or if they had no formal airway training.

2.3. Cadaver Preparation. All intubations were made on a single, embalmed, male human cadaver. The cadaver had no oral, pharyngeal, or neck trauma, craniofacial abnormality, or a known history of tracheostomy. We recorded anatomic measurements related to airway placement including thyromental distance (6 cm), thyrohyoid distance (2 cm), and neck circumference (56 cm) at the level of the thyroid cartilage [10]. Initially, a 2-inch incision was made through the skin over the area of the zygomatic arch down towards the jaw line. The skin was reflected inferiorly to expose the underlying

structures. The parotid gland and subcutaneous tissues were removed in order to expose the masseter and its origins on the zygomatic arch. The superficial and deep heads of the masseter were detached from the zygomatic arch and retracted inferiorly in order to expose the mandible. In order to permit more free motion of the jaw, the temporalis muscle was then detached from its insertion on the coronoid process of the mandible. This allowed providers to instrument anatomic structures during ETI attempts and created a grade 3 Cormack-Lehane view as assessed by the investigators. We created a grade 3 Cormack-Lehane view as we felt this would allow for greater discrimination between the movement patterns of novice and experienced providers.

2.4. Methods and Measurements. We collected provider demographics and recorded both the movement patterns of the IMUs using the IMU integrated software along with video of the intubation attempt using the integrated CMAC software. Placement of the endotracheal tube (trachea versus esophagus) was assessed by visual inspection by the investigators after each ETI attempt. We defined an intubation attempt each time the blade of the laryngoscope entered the mouth. We defined attempt time as the time in seconds from when the blade of the laryngoscope entered the mouth until it was fully withdrawn from the mouth after placement of the endotracheal tube (either successful placement in the trachea or unsuccessful in the esophagus).

2.5. Outcomes. Our primary outcome was variability in movement patterns assessed by spectral smoothness and visual accelerometer patterns between novice and experienced providers during ETI.

2.6. Analysis. Providers had their movements recorded during ETI using an IMU placed on the posterior aspect of the left wrist. We collected accelerometer data in the x -, y - and z -axes (Figure 1). We visualized the data to identify the IMU and axis with maximum variability and utilized these data for analysis. We segmented the IMU data into portions of the ETI attempt based on previous ETI motion analysis: laryngoscope entering the mouth, obtaining the view of the vocal cords, placing the endotracheal tube, and removing the laryngoscope [7]. We computed 16-point Fast Fourier Transform (FFT) on the segmented signal [11, 12]. A quantitative measure of spectral smoothness (SS) was computed over all trials corresponding to each group (novice and experienced). The SS measure was computed from the FFT of accelerometer data as follows [13]:

- (1) X is the FFT vector;
- (2) $SS = \sigma(\delta[X]) / \|m(\delta[X])\|$, where $\|\cdot\|$ is the absolute value, $\sigma(\cdot)$ is the standard deviation, $\delta[\cdot]$ is first order differential, and $m(\cdot)$ is the mean function.

SS is a nonnegative (>0) measure, which is inversely proportional to the absolute value of the mean of signal differential. Therefore, the choppier the signal (e.g., greater variability or less smooth), the lower the SS value. This is due to larger differences in successive signal samples and thus

Table 1: Provider characteristics. EM: emergency medicine.

	Novice ($n = 5$)	Experienced ($n = 5$)
Age in years, (SD)	27 (2.8)	31.4 (1.3)
Sex: male (n)	80% (4)	80% (4)
Handedness: right	100% (5)	100% (5)
Experience	Fourth year medical student: 4 Third year medical student: 1	Fourth year EM resident: 4 EM attending: 1
First attempt success (n)	20% (1)	40% (2)
Attempt time in seconds (mean, SD)	38.3 (9)	33 (5.5)



Figure 1: Inertial measurement unit on the left wrist. Blue arrow, x -axis. Red arrow, y -axis. Green arrow, z -axis.

high absolute value of the mean of differential signal. A smooth signal results in low absolute mean value of the differential signal, thereby increasing the SS value. Thus, the SS measure represents the extent of redundant motion variations (i.e., choppiness) associated with ETI attempts [13]. The computations were completed with MATLAB, release 2012b (version 8.0, MathWorks, Inc, Natick, MA).

We also sought to identify patterns that may exist in the movement signals between novice and experienced providers. Movement patterns consist of two aspects, the dispersion or distance traveled and the acceleration or quickness. Dispersion in the x -, y -, and z -axes is not simple straight lines, but it represents complex mathematical signals. As a result, dispersion is often difficult to represent as a single sinusoidal equation. However, each ETI dispersion signal can be represented as a collection of simpler sinusoidal waves with different frequencies (as measured in hertz or Hz) that combine to form the overall sinusoidal equation. The second movement component, acceleration, can be measured by the accelerometers in the IMUs, and expressed as force (in gravitational constants or g). To directly compare the overall movement patterns between novice and experienced providers, we graphed the net value of force, in g^2 , by the various simpler sinusoidal frequencies that constitute the overall complex sinusoidal equation for dispersion [11-12].

Based on the computed 16-point Fast Fourier Transform (FFT) of the overall complex signal, the components can be equally transformed into 16 discrete units representing simpler sinusoidal waves between -60 Hz and 60 Hz. (11, 12) This allowed us to visually compare the movement components, both dispersion and force, between experienced and novice providers.

3. Results

We enrolled five novice (one third year and four fourth year medical students), and five experienced providers (four fourth year emergency medicine residents and one attending physician) (Table 1). Due to troubles with recording, one provider in each group did not have their IMU signal available for analysis and was thus excluded from the study. The IMU data corresponding to the laryngoscope insertion and glottis visualization was then segmented out for further analysis (Figure 2). We compared the IMU data to the videos recorded during the intubation attempt and identified the four segments of the kinematic signals: laryngoscope entering the mouth, obtaining the view of the vocal cords, placing the endotracheal tube, and removing the laryngoscope [7]. The orange box (Figure 2) represents the steps where the laryngoscope entered the mouth and a view of the vocal cords was obtained. Visually, there appeared to be the greatest movement variability during this step; thus, this area is magnified in Figure 3.

After transforming the data via the FFT, the spectral analysis of the Z -component from these sections had a parabolic curve for both novice and experienced providers (Figure 4). This curve was smoother for experienced providers both on visual inspection and when analyzed by spectral smoothness (SS novice 6.4 versus SS experienced 26.6).

When the complex movement patterns in the z -axis were broken down into simpler frequencies, there appeared to be a unique, parabolic relationship between these sinusoidal waves (the description of movement) and force with experienced providers (Figure 4). Experienced providers had a bimodal distribution of forces, where greater forces were noted at lower frequency signals and then again at higher frequency signals.

4. Limitations

There are several limitations to this study. Our study was limited to a small sample. Initially, we sought to compare five

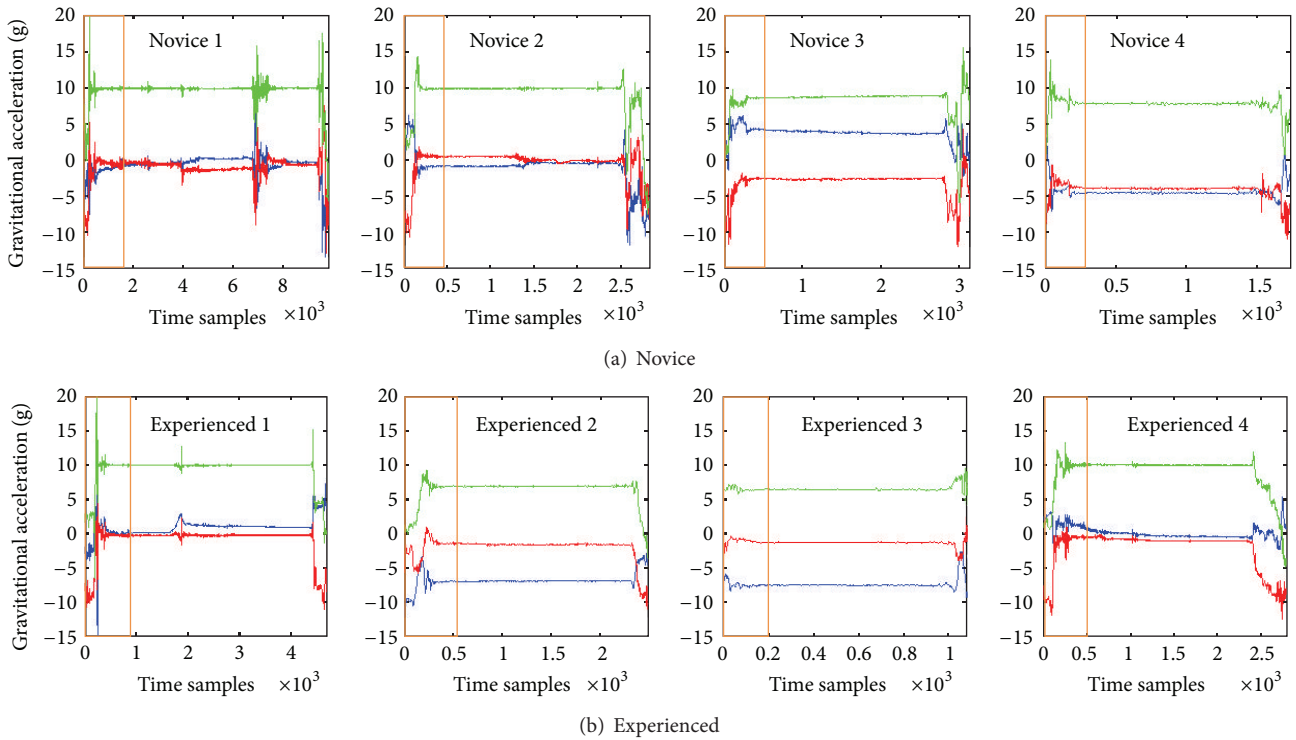


Figure 2: Complete movement patterns in the x -, y -, and z -axes for the four novice (a) and experienced (b) providers. The blue line represents movement in the x -axis. The red line represents movement in the y -axis. The green line represents movement in the z -axis. The orange box represents the laryngoscope entering the mouth and obtaining the view of the vocal cords (magnified in Figure 3).

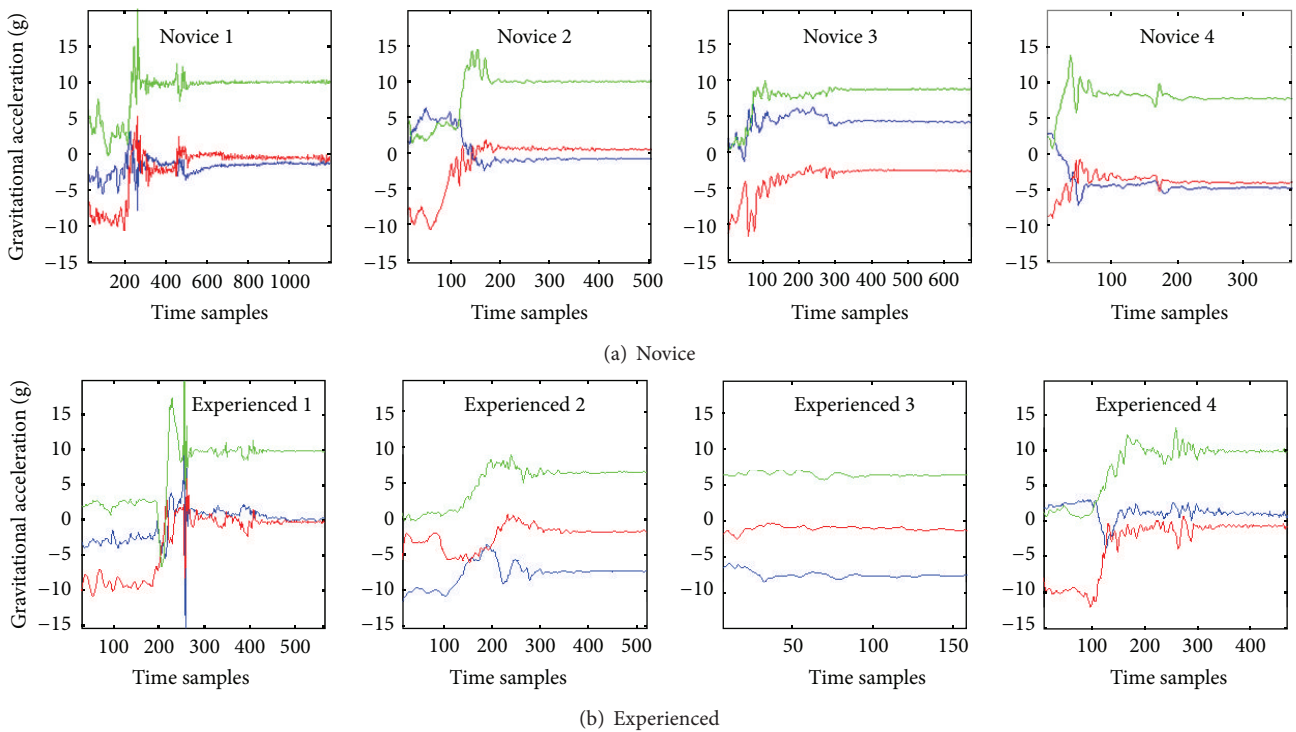


Figure 3: Complete movement patterns in the x -, y -, and z -axes for the four novice (a) and experienced (b) providers from blade insertion until glottic visualization. The blue line represents movement in the x -axis. The red line represents movement in the y -axis. The green line represents movement in the z -axis.

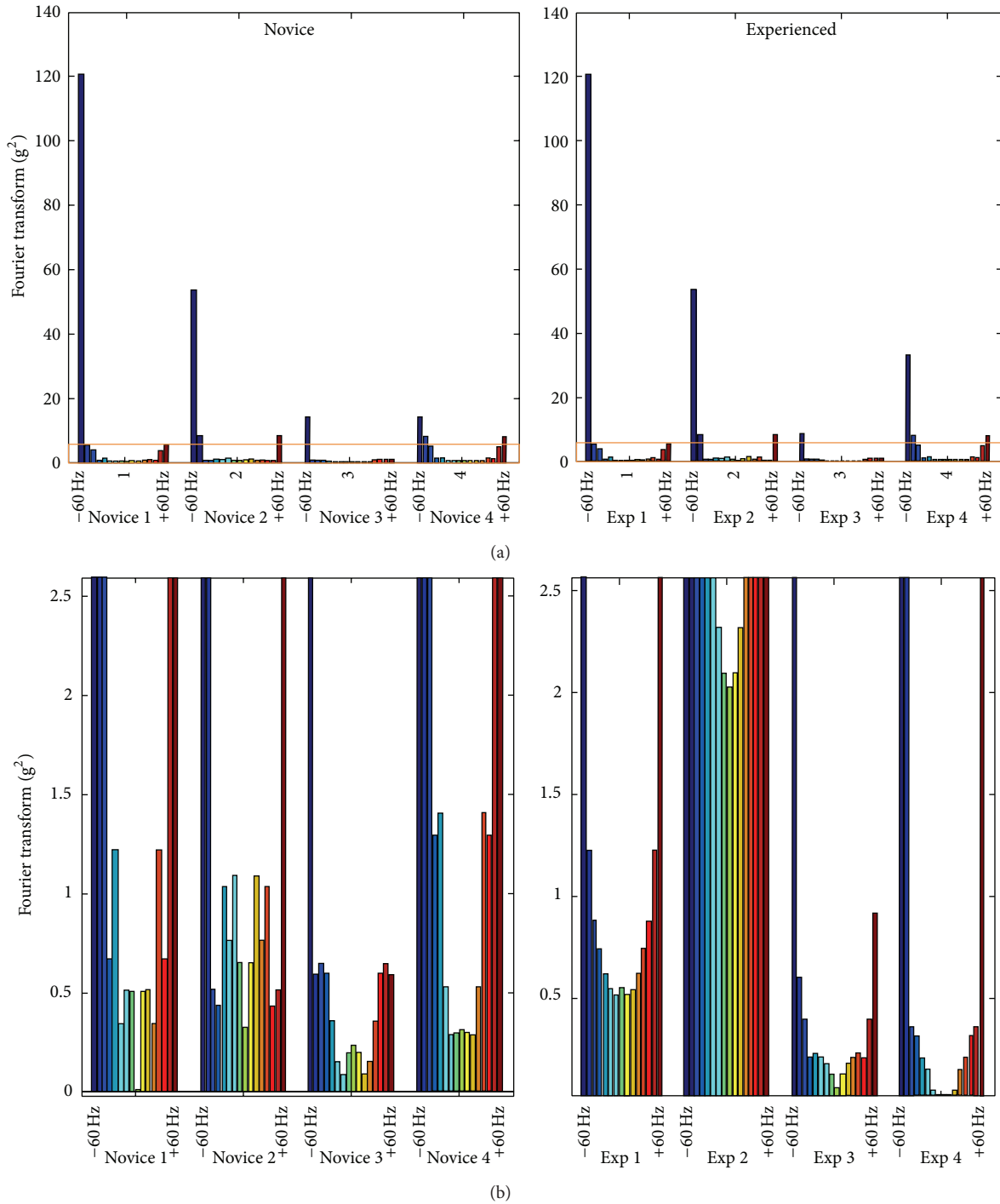


Figure 4: Spectral analysis of the Z-component of IMU signal from insertion until glottic visualization for the four novice and experienced providers. Spectral range (blue to red) for each subject is ± 60 Hz divided into 16 equal segments. The overall signals are shown in the top graphs. The orange box represents the areas magnified in the lower graphs. Exp: experienced.

novice and five experienced providers but had to limit the study size to four providers in each group due to incomplete recording of the data. Second, this study was performed in a cadaver model with a difficult airway (grade 3 Cormack-Lehane). The cadaver underwent a modified dissection of tissue, masseter, and temporalis muscle detachment to allow for a grade 3 Cormack-Lehane view. We felt a difficult

airway (Cormack-Lehane grade 3) would allow for greater discrimination between the movement patterns of novice and experienced providers. As Cormack-Lehane grade 3 views are infrequently encountered in emergency airway management, we focused our efforts on the cadaver model [14-16]. Also, from a patient safety and research ethics standpoints, we did not feel it was in patients' best interest to perform

multiple intubation attempts on a patient or patients with a difficult airway, especially with novice providers, for a proof of concept study. The cadaver allowed us to standardize the intubation attempts as all attempts could then be made on one airway. While we are able to show proof of concept that IMUs are able to collect data and differentiate between novice and experienced providers in ETI using human tissue, future efforts will be needed to assess IMUs in the clinical setting with varying glottic views. Studies involving comparison between cadaver and human subjects would provide further insight with the kinematics involved in ETI. Other movement patterns that may be critical to ETI success were not investigated. As we were only able to analyze left wrist movement patterns, future investigations may examine other joints (elbow, shoulder, right wrist, etc.) to provide a more complete analysis of the kinematics involved in ETI.

5. Discussion

We were able to identify differences between experienced and novice providers using IMUs in a cadaver model. By identifying these key differences, future work may provide further quantification and impactful feedback during ETI instruction. Eventually, this may be incorporated with a model that allows real-time feedback via instruction and correction while performing the task of ETI in a clinical setting. ETI proficiency is associated with procedural experience with this skill [6]. If we are able to further accelerate the learning curve of providers, competency may be achieved at a faster rate, thus reducing the potential harmful of the learning curve.

In a multicenter analysis including over 6,000 ETIs, the first attempt success rates varied by provider experience with the first year emergency medicine residents having success rate of only 72% compared to 82% and 88% in the second year and third year, respectively [17]. First attempt success also decreases with Cormack-Lehane view where grade 3 views have first attempt success rates near 40%, similar to those noted in our study [16]. Complications occur more frequently in cases where multiple ETI attempts are made [3]. Accelerating the learning could directly address the complications related to multiple attempts in novice providers in the acute setting.

We chose to evaluate the movements of the left wrist in novice and experienced providers during intubation. While there is not yet a clear link between wrist movements and intubation success or side effects, there are distinct differences in the movement patterns of the left wrist between novice and experienced providers [7]. As providers gain experience with emergency airway management, they demonstrate greater intubation success and lower rates of complication related to intubation [17, 18]. Examining the link between these movement patterns and intubation outcomes may provide insight into why these differences in intubation success exist and identify opportunities for improvement in ETI techniques.

To our knowledge, ours is the first study using portable movement mapping technology to evaluate intubation. The benefits of portable sensors have yet to be fully realized

in the acute care setting. Portable sensors may not be limited to the use of IMUs but may also make use of other technologies such as smartphones with incorporated cameras and accelerometers. Previous work has shown that smartphones may help with ETI and can even monitor chest compression during cardiopulmonary resuscitation [19–21]. The ubiquitous nature of the technologies incorporated into smartphones represents an ideal tool for capturing information and providing feedback.

While our study was designed as a proof of concept, we believe that portable sensors may be able to identify movement patterns between providers with different levels of experience. The technologies can identify patterns of force that may vary with different components of the overall dispersion signal (i.e., there might be dispersion differences between not only novice and experienced providers measured in space, but also the force with which these actions take place). Despite our small sample size, there appear to be differences in the combination of dispersion and force between novice and experienced providers where experienced providers had a bimodal distribution of forces, where greater forces were noted at lower frequency signals and then again at higher frequency signals while this was not seen with novice providers (Figure 4).

Interpreting these findings can be challenging but may be contextualized more easily using an example outside of medicine. When assessing how someone may swing a golf club, there are two components to the swing, the dispersion (or measurement of the distance moved) and the acceleration or force. The golfer needs the ideal “mechanics” or dispersion combined with the proper force at the correct time during the swing. Representing the relationship between the dispersion and force allows for the identification of key differences within the movement pattern. Identifying the unique interaction between dispersion and force may also help to explain the differences in ETI success rates between providers and allow for focused feedback to novice providers.

6. Future Directions

The clinical implications of this line of work are broad. Future work with portable sensors may help to track the movements of novice providers, compare these movements to those of experienced providers, and provide real-time, objective feedback to trainees on their movement patterns. While we have focused on ETI, similar educational models could be developed for other medical procedures. The successful development of these models requires multiple steps:

- (1) identify portable sensors that can objectively track movement patterns in the clinical setting;
- (2) classify movement patterns that differentiate novice from experienced providers;
- (3) incorporate analysis algorithms that will allow for rapid assessment of movement patterns and recognize areas that require focused educational attention (e.g., what portion of the ETI attempt differed from that of previously analyzed experienced ETI attempts);

- (4) develop teaching curriculum that incorporates these measurements to allow for impactful, timely feedback.

While we have shown proof of concept that ETI motions can be recorded by portable IMUs (step (1)), future work will be needed to effectively develop this technology into an educational modality (steps (2)–(4)).

Ericsson's model of deliberate practice presents a framework for this information to be leveraged [22, 23]. Ericsson states that deliberate practice must provide immediate feedback, correction, remediation, and repetition [6, 22, 23]. The inclusion of additional feedback to the student from the kinematic data allows for more precise and immediate feedback beyond a simple yes/no of success with the performance of ETI. While kinematic feedback may require a better understanding of the whole body movements of the provider during ETI, we chose to focus our preliminary efforts on the left wrist as there are distinct differences in the movement patterns of the left wrist between novice and experienced providers [7]. Experienced providers also have greater intubation success and lower rates of complication indicating a potential link between movement patterns and intubation success [17, 18]. A more nuanced understanding of the entire ETI process presents additional opportunity for the practitioner to receive immediate feedback on these movement differences and accelerate the learning curve.

Specific to simulation and mannequin based learning, prior studies including Hall et al. have also shown increased skill acquisition with the combination of simulated and mannequin based training [24]. With the additional data gleaned from a more complex mapping of the novice versus experienced movements made during ETI, we may further enhance skill acquisition outside of clinical practice. Segmenting the steps and breaking down the process of ETI may also allow for more precise practice with cadavers and mannequins.

Movement sensor analysis provides valuable, objective data and has been used in a variety of clinical settings. Other studies have used portable sensors to track progression after stroke [8, 9]. This line of work has shown that motion sensor analysis presents a linear relationship with subjective measures of stroke severity. In a similar manner, motion sensor analysis in the use of ETI may provide a more objective measure of techniques utilized in successful ETI beyond subjective feedback of an instruction practitioner. Future efforts are needed to advance the kinematic analysis process and provide subjects with real-time feedback.

7. Conclusion

IMUs can be used to identify the kinematics of both novice and experienced providers in a cadaver model. By further understanding movement patterns for ETI and quantitatively analyzing ETI kinematics, we are better able to understand the mechanics of intubation. These are the first steps in designing a real-time feedback system to accelerate the learning curve of ETI.

Conflict of Interests

The authors declare that there is no conflict of interests regarding the publication of this paper.

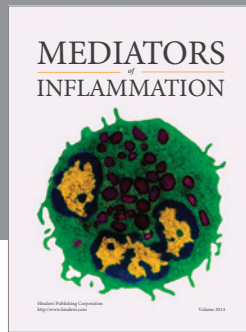
Acknowledgments

The authors would like to thank Ms. Kaitlyn Blackburn for her assistance with dissecting the cadaver along with Dr. Randy Kulesza and the anatomy lab staff at the Lake Erie College of Osteopathic Medicine for their assistance with the cadaver. They would like to thank the Lake Erie College of Osteopathic Medicine (LECOM/LECOMT) for funding this research and Dr. Arvind Venkat for his assistance in proof-reading this paper.

References

- [1] A. C. Heffner, D. S. Swords, M. N. Neale, and A. E. Jones, "Incidence and factors associated with cardiac arrest complicating emergency airway management," *Resuscitation*, vol. 84, no. 11, pp. 1500–1504, 2013.
- [2] T. C. Mort, "The incidence and risk factors for cardiac arrest during emergency tracheal intubation: a justification for incorporating the ASA Guidelines in the remote location," *Journal of Clinical Anesthesia*, vol. 16, no. 7, pp. 508–516, 2004.
- [3] T. C. Mort, "Emergency tracheal intubation: complications associated with repeated laryngoscopic attempts," *Anesthesia and Analgesia*, vol. 99, no. 2, pp. 607–613, 2004.
- [4] H. E. Wang, J. R. Lave, C. A. Sirio, and D. M. Yealy, "Paramedic intubation errors: isolated events or symptoms of larger problems?" *Health Affairs*, vol. 25, no. 2, pp. 501–509, 2006.
- [5] H. E. Wang, S. R. Seitz, D. Hostler, and D. M. Yealy, "Defining the learning curve for paramedic student endotracheal intubation," *Prehospital Emergency Care*, vol. 9, no. 2, pp. 156–162, 2005.
- [6] P. G. Tarasi, M. P. Mangione, S. S. Singhal, and H. E. Wang, "Endotracheal intubation skill acquisition by medical students," *Medical Education Online*, vol. 16, article 7309, 2011.
- [7] J. N. Carlson, S. Das, F. de la Torre, C. W. Callaway, P. E. Phrampus, and J. Hodgins, "Motion capture measures variability in laryngoscopic movement during endotracheal intubation: a preliminary report," *Simulation in Healthcare*, vol. 7, no. 4, pp. 255–260, 2012.
- [8] E. V. Olesh, S. Yakovenko, and V. Gritsenko, "Automated assessment of upper extremity movement impairment due to stroke," *PLoS ONE*, vol. 9, no. 8, Article ID e104487, 2014.
- [9] H. Zhou, H. Hu, and N. Harris, "Application of wearable inertial sensors in stroke rehabilitation," in *Proceedings of the 27th Annual International Conference of the Engineering in Medicine and Biology Society (IEEE-EMBS '05)*, pp. 6825–6828, IEEE, Shanghai, China, September 2005.
- [10] M. Naguib, F. L. Scamman, C. O'Sullivan et al., "Predictive performance of three multivariate difficult tracheal intubation models: a double-blind, case-controlled study," *Anesthesia and Analgesia*, vol. 102, no. 3, pp. 818–824, 2006.
- [11] L. R. Rabiner and R. W. Schafer, *Introduction to Digital Speech Processing*, Now Publishers, Boston, Mass, USA, 2007.
- [12] A. V. Oppenheim, A. S. Willsky, and S. H. Nawab, *Signals & Systems*, Prentice Hall, Upper Saddle River, NJ, USA, 2nd edition, 1997.

- [13] A. P. Klapuri, "Multipitch estimation and sound separation by the spectral smoothness principle," in *Proceedings of the IEEE International Conference on Acoustics, Speech, and Signal Processing*, vol. 5, pp. 3381-3384, May 2001.
- [14] J. N. Carlson, J. Quintero, F. X. Guyette, C. W. Callaway, and J. J. Menegazzi, "Variables associated with successful intubation attempts using video laryngoscopy: a preliminary report in a helicopter emergency medical service," *Prehospital Emergency Care*, vol. 16, no. 2, pp. 293-298, 2012.
- [15] F. X. Guyette, K. Farrell, J. N. Carlson, C. W. Callaway, and P. Phrampus, "Comparison of video laryngoscopy and direct laryngoscopy in a critical care transport service," *Prehospital Emergency Care*, vol. 17, no. 2, pp. 149-154, 2013.
- [16] C. A. Graham, A. J. Oglesby, D. Beard, and D. W. McKeown, "Laryngoscopic views during rapid sequence intubation in the emergency department," *Canadian Journal of Emergency Medicine*, vol. 6, no. 6, pp. 416-420, 2004.
- [17] M. J. Sagarin, E. D. Barton, Y.-M. Chng, R. M. Walls, and National Emergency Airway Registry Investigators, "Airway management by US and Canadian emergency medicine residents: a multicenter analysis of more than 6,000 endotracheal intubation attempts," *Annals of Emergency Medicine*, vol. 46, no. 4, pp. 328-336, 2005.
- [18] J. Toda, A. A. Toda, and J. Arakawa, "Learning curve for paramedic endotracheal intubation and complications," *International Journal of Emergency Medicine*, vol. 6, no. 1, article 38, 2013.
- [19] A. Frisch, S. Das, J. C. Reynolds, F. De la Torre, J. K. Hodgins, and J. N. Carlson, "Analysis of smartphone video footage classify chest compression rate during simulated CPR," *The American Journal of Emergency Medicine*, vol. 32, no. 9, pp. 1136-1138, 2014.
- [20] G. A. Hawkes, C. P. Hawkes, C. A. Ryan, and E. M. Dempsey, "The demand for an educational smartphone app," *Resuscitation*, vol. 84, no. 10, p. e139, 2013.
- [21] C. P. Hawkes, B. H. Walsh, C. A. Ryan, and E. M. Dempsey, "Smartphone technology enhances newborn intubation knowledge and performance amongst paediatric trainees," *Resuscitation*, vol. 84, no. 2, pp. 223-226, 2013.
- [22] K. A. Ericsson, "Deliberate practice and acquisition of expert performance: a general overview," *Academic Emergency Medicine*, vol. 15, no. 11, pp. 988-994, 2008.
- [23] K. A. Ericsson, "Deliberate practice and the acquisition and maintenance of expert performance in medicine and related domains," *Academic Medicine*, vol. 79, no. 10, supplement, pp. S70-S81, 2004.
- [24] R. E. Hall, J. R. Plant, C. J. Bands, A. R. Wall, J. Kang, and C. A. Hall, "Human patient simulation is effective for teaching paramedic students endotracheal intubation," *Academic Emergency Medicine*, vol. 12, no. 9, pp. 850-855, 2005.



Hindawi
Submit your manuscripts at
<http://www.hindawi.com>



Human Joint Angle Estimation with Inertial Sensors and Validation with A Robot Arm

Mahmoud El-Gohary, and James McNames

Abstract—Traditionally, human movement has been captured primarily by motion capture systems. These systems are costly, require fixed cameras in a controlled environment, and suffer from occlusion. Recently, the availability of low-cost wearable inertial sensors containing accelerometers, gyroscopes, and magnetometers have provided an alternative means to overcome the limitations of motion capture systems. Wearable inertial sensors can be used anywhere, cannot be occluded, and are low cost. Several groups have described algorithms for tracking human joint angles. We previously described a novel approach based on a kinematic arm model and the Unscented Kalman Filter (UKF). Our proposed method used a minimal sensor configuration with one sensor on each segment. This article reports significant improvements in both the algorithm and the assessment. The new model incorporates gyroscope and accelerometer random drift models, imposes physical constraints on the range of motion for each joint, and uses zero-velocity updates to mitigate the effect of sensor drift. A high-precision industrial robot arm precisely quantifies the performance of the tracker during slow, normal, and fast movements over continuous 15 minute recording durations. The agreement between the estimated angles from our algorithm and the high-precision robot arm reference was excellent. On average, the tracker attained an RMS angle error of about 3° for all six angles. The UKF performed slightly better than the more common Extended Kalman Filter (EKF).

Index Terms—Inertial Measurement Units, Inertial sensors, Kinematics, Joint Angle Tracking, Shoulder, Elbow.

I. INTRODUCTION

THE need to characterize normal and pathological human movement has consistently driven researchers to develop new rigorous tracking systems. These systems need to be accurate, unobtrusive, and suitable for continuous monitoring over long periods while subjects perform normal daily activities.

Magnetic resonance imaging-based methods for measuring the mechanics of human joints have been successfully applied to evaluate biomechanics in different human joints [1], [2]. Bey *et al.* developed and validated a tracking technique for measuring glenohumeral joint translations during shoulder motion from x-ray images [3]. These systems require a dedicated laboratory, trained staff to operate the systems, and are restricted to static or very slow and limited range of motion. Tracking of bone pins has also been used, but this is an invasive technique which limits the number of subjects who might be willing to participate in these studies [4], [5]. Motion capture systems have been successfully used to quantify joint kinematics by tracking the position of reflective

surface markers during dynamic activities [6]. However, these systems are costly, restricted to controlled laboratory settings, suffer from occlusion, and are susceptible to skin movement artifact; all of which limit their usage [7].

To overcome many of the limitations associated with conventional motion measurement techniques, inertial measurement units (IMU) consisting of triaxial accelerometers were used to estimate thigh, shank and knee pitch and yaw angles [8], [9]. These studies were limited to measuring only 2 degrees of freedom (DOFs) movement during limited activities.

Most studies using IMU's, combine accelerometers and gyroscopes in wearable sensor systems [10], [11]. Traditionally, the orientation of a segment has been estimated by integrating the angular velocities measured by gyroscopes and position is obtained by double integration of the translational acceleration measured by accelerometers. A significant problem with integration, however, is that inaccuracies inherent in the measurements quickly accumulate and rapidly degrade accuracy. Roetenberg showed that integration of noisy gyroscope data resulted in a drift between $10 - 25^\circ$ after one minute [12]. Roetenberg *et al.* argued that errors due to magnetic field disturbance may be compensated by adequate model-based sensor fusion [13]. They developed a Kalman filter that operated on two inputs: the difference between inclination from the accelerometer and gyroscope, and from the magnetometer and gyroscope. The states of the model included the gyroscope bias error, orientation error, and magnetic disturbance. The filter was tested with ferromagnetic materials close to the sensor for less than a minute. The results show that the orientation estimates improved significantly when the magnetic interference correction was used. However, the accuracy could decrease if the magnetic disturbance was due to varying sources that are present during longer periods of testing.

To reduce the effect of gyroscope drift on orientation estimates, accelerometers and magnetic sensors have been used to compensate the drift about the horizontal plane, and the vertical axis respectively [14], [15]. Favre *et al.* integrated angular velocity data and corrected angle estimates based on known joint anatomical constraints and inclination data from accelerometers during static periods [16]. Luinge *et al.* used physical constraints in the elbow to measure the forearm orientation relative to upper arm [17], [18]. They minimized the error around the vertical axis by using the knowledge that the elbow joint does not permit abduction/adduction movement. Although they reported an improvement in estimating the orientation, the average orientation error was 20° . Cooper *et al.* also used biomechanical constraints to estimate knee joint flexion/extension with 2 IMU's with triaxial accelerometers and gyroscopes attached to the thigh and shank. The performance of the algorithm was evaluated with data obtained from

El-Gohary (mahmoud@apdm.com), McNames and PSU have a significant financial interest in APDM, a company that may have a commercial interest in the results of this research and technology. The potential individual and institutional conflicts of interest have been reviewed and managed by PSU.

Copyright (c) 2014 IEEE. Personal use of this material is permitted. However, permission to use this material for any other purposes must be obtained from the IEEE by sending an email to pubs-permissions@ieee.org.

7 healthy subjects during walking and running over 5 minute periods. The average measurement error ranged from 0.7° for slow walking to 3.4° for running [19]. However, the algorithm only used a simplified model of a single hinge knee joint.

In other studies, systems with accelerometers, gyroscopes and magnetometers were used to measure the orientation of different body segments [20]–[24]. Accelerometer and gyroscopes were used to estimate inclination and orientation. Magnetometers were used to measure orientation around the vertical axis, assuming uniform local magnetic field. Bachmann *et al.* investigated the effect of magnetic disturbance on the accuracy of orientation tracking systems and observed errors that ranged from 12° to 16° [25]. Yun *et al.* presented a simplified algorithm for orientation estimation using only accelerometers and magnetic field measurements [26]. The gyroscope-free system was only suitable for tracking slow movements. Cutti *et al.* used inertial and magnetic data to measure arm kinematics in one subject performing tasks involving shoulder and elbow single-joint-angle movements [27] and obtained an average RMSE $\leq 3.6^\circ$.

In summary, other groups have used accelerometers and magnetometers to compensate for the orientation error that occurs when integrating the angular rate from gyroscopes, but all of these methods were only applicable under limited circumstances. Some groups restricted the application to simple tasks and short tracking periods. In other studies, the estimation was accurate for only brief periods when the acceleration measurements were only due to gravity. Others reported large orientation errors due to magnetic field disturbances.

In a previous study [28], we combined kinematic models designed for control of robotic arms with state space methods to estimate human joint angles using two wearable inertial measurement units. Each IMU consisted of triaxial gyroscopes and accelerometers. We used the unscented Kalman filter (UKF) to estimate shoulder and elbow joint angles from eight subjects performing prescribed and free arm articulation for an average of 2 minutes. Compared to angles obtained from an optical reference system, we achieved an RMS angle error of less than 8° . Although errors between optical and inertial angle estimates are minimal, some of these errors might be attributed to markers moving independently of each other, especially during fast movements [29]. Tracking performance is also limited by the noise and drift of MEMS inertial sensors.

In this study, we incorporate sensor random drift models, prior knowledge of physical constraints and human natural range of motion to obtain better joint angle estimates, and to mitigate the effect of sensors drift on the estimated angles during long periods of movement. We also employ zero-velocity updates to mitigate the effect of gyroscope drift on the estimated heading angles. We quantify the performance of our UKF-based method by comparing the angle estimates to those obtained directly from a 6-axis high-precision robot during 15-minute recordings for slow, regular and fast-speed arm movement. We evaluate the performance of the extended Kalman filter (EKF) compared to that of the UKF in estimating the joint angles, given the nonlinear relationship between the joint angles and the sensor measurements.

II. THEORY

To describe angles and movements of an arm segment relative to its neighboring segments, we use an established method of biomechanical modeling based on a sequence of links connected by joints. This method was proposed by Denavit and Hartenberg in 1955, and has been used in the analysis and control of robotic manipulators [30]. The method is based on characterizing the relationship between links and joints with a (4×4) homogeneous transformation matrix. The matrix depends on four parameters associated with each link. The first parameter is the link length a_i which is the distance from the rotation axis Z_i to Z_{i+1} measured along their common normal axis X_i . The link twist α_i , is the angle from Z_i to Z_{i+1} measured about the X_i axis. The distance from X_{i-1} to X_i measured along the Z_i axis is known as the link offset d_i . The fourth parameter is the joint angle θ_i , which is the angle from X_{i-1} to X_i measured about the Z_i axis. These four parameters are known as the Denavit-Hartenberg (D-H) parameters and will be specified for the 6 DOFs arm model in the following section. To describe the kinematics of each link relative to its adjacent link, it simplifies this description to attach a frame to each link. The convention of attaching frames to the arm was detailed in [31].

A. Arm joint angles

We present a model for an arm movement with six degrees of freedom. Typically, the shoulder joint is modeled as a ball-and-socket joint with three DOFs. However, for the purpose of quantifying the performance of our algorithm, we model the shoulder with only two DOFs to match those of the industrial robot used in this study for comparison. Fig. 1 shows the arm model with static base reference frame 0 at the center of the shoulder joint. Frame 1 represents shoulder internal/external

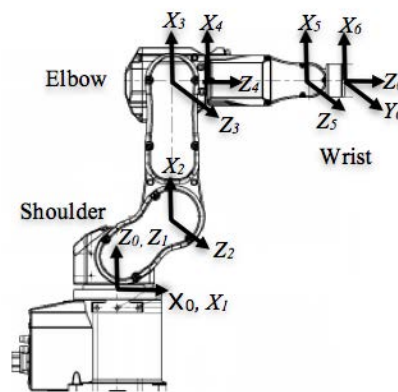


Fig. 1. Kinematics diagram of the arm model with Frame 0 as the static reference at the base. Frames 1 and 2 represent shoulder internal/external rotation, and flexion/extension, respectively. Frame 3 represents elbow flexion/extension. Frame 4 represents forearm pronation/supination. Wrist flexion/extension, and wrist twist are represented by frames 5 and 6, respectively.

rotation, and frame 2 represents shoulder flexion/extension. The elbow joint is a hinge joint that allows movement in one plane, flexion/extension, represented by frame 3. The fourth joint is a pivot joint that allows for the forearm pronation/supination, and is represented by frame 4. Frames 5 and 6 represent wrist flexion/extension, and twist respectively.

Table I shows the D-H parameters of the arm model, where l_u is the length of the upper arm, l_f is the length of the forearm, and θ_i is the i^{th} angle of rotation.

TABLE I
DENAVIT-HARTENBERG PARAMETERS FOR THE 6 DOFS ARM MODEL.

Frame	α_{i-1}	a_{i-1}	d_i	θ_i
1	0	0	0	θ_1
2	$\pi/2$	a_1	0	$\theta_2 + \pi/2$
3	0	l_u	0	θ_3
4	$\pi/2$	0	0	$\theta_4 + \pi/2$
5	$-\pi/2$	0	l_f	$\theta_5 - \pi/2$
6	$\pi/2$	0	0	θ_6

We used three inertial measurement units (IMUs) to track the arm movement. Two IMUs, with triaxial gyroscopes and accelerometers, were secured with Velcro straps to the robot upper arm and forearm, and a third unit was secured inside a box on the wrist; see Fig. 2.

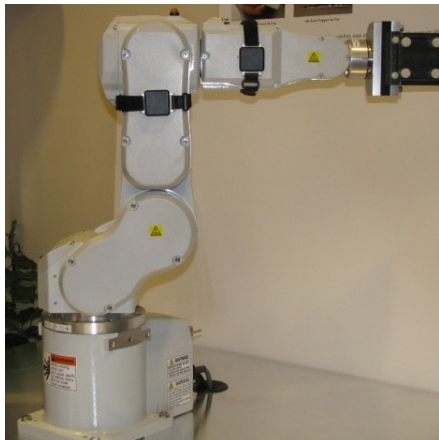


Fig. 2. Two IMUs were secured with Velcro straps to the robot upper arm and forearm, and a third unit was secured inside a box on the wrist

B. Propagation of velocity and acceleration

To formulate the dynamic equations for arm sensor measurement, including gyroscope and accelerometer data, we use three of the Newton-Euler equations of motion. Each link of the arm in motion has some angular velocity, angular and linear acceleration $(\omega, \dot{\omega}, \dot{v})$. The velocity ${}^{i+1}\omega_{i+1}$ of link $i+1$ is that of link i plus the new velocity component added by joint $i+1$. Similarly, the angular and linear acceleration of each link are related by the following recursive equations:

$${}^{i+1}\omega_{i+1} = {}^{i+1}R {}^i\omega_i + \dot{\theta}_{i+1} {}^{i+1}Z_{i+1} \quad (1)$$

$${}^{i+1}\dot{\omega}_{i+1} = {}^{i+1}R {}^i\dot{\omega}_i + {}^{i+1}R {}^i\dot{\omega}_i \times \dot{\theta}_{i+1} {}^{i+1}Z_{i+1} + \ddot{\theta}_{i+1} {}^{i+1}Z_{i+1} \quad (2)$$

$${}^{i+1}\dot{v}_{i+1} = {}^{i+1}R [{}^i\dot{\omega}_i \times {}^iP_{i+1} + {}^i\omega_i \times ({}^i\omega_i \times {}^iP_{i+1}) + {}^i\dot{v}_i] \quad (3)$$

where ${}^{i+1}R$ is the rotation matrix between the i^{th} and $(i+1)^{th}$ link, \times represents the cross product operation, ${}^iP_{i+1}$ is the position vector of frame $i+1$, which is the upper right 3×1 vector of the D-H matrix. The rotation matrices R , can be obtained by taking the transpose of the upper left 3×3 transformation matrix and the D-H parameters shown

in Table I. The single and double dot notation represents the first and second derivatives with respect to time. We initialize $\omega_0 = \dot{\omega}_0 = (0, 0, 0)^T$. Effect of gravity is included in the model at no extra cost by setting $\dot{v}_0 = (g_x, g_y, g_z)^T$, where g is gravity along each of the three axes. These forward recursive equations are used to propagate angular velocity, and angular and linear acceleration from the reference coordinate system through the links of upper arm, forearm and wrist.

C. State Space Model

The general discrete time state-space model is of the form,

$$x(n+1) = f_n[x(n), u(n)] \quad (4)$$

$$y(n) = h_n[x(n), v(n)] \quad (5)$$

where $x(n)$ is the unobserved state of the system, $y(n)$ is the observed or measured data, $f_n[\cdot]$ and $h_n[\cdot]$ are nonlinear state and observation equations, $u(n)$ and $v(n)$ are the state and observation white noise with zero mean. Our state model equations which describe the evolution of the states with time are given by

$$\theta_i(n+1) = \theta_i(n) + T_s \dot{\theta}_i(n) + \frac{1}{2} T_s^2 \ddot{\theta}_i(n) \quad (6)$$

$$\dot{\theta}_i(n+1) = \dot{\theta}_i(n) + T_s \ddot{\theta}_i(n) \quad (7)$$

$$\ddot{\theta}_i(n+1) = \alpha \ddot{\theta}_i(n) + u_{\ddot{\theta}_i}(n) \quad (8)$$

where $i = \{1, \dots, 6\}$ of the six angles, $\theta_i(n)$ is the i^{th} angle at time n , $\dot{\theta}_i$ is the angular velocity, $\ddot{\theta}_i$ is the angular acceleration, $u_{\ddot{\theta}_i}(n)$ is a white noise process with zero mean, α is a process model parameter, and $T_s = 1/f_s$ is the sampling period. These are standard equations for a physical object traveling at a constant acceleration. The model assumes the acceleration is constant for the duration of a sampling interval. This is sufficient for our data, which was acquired with a sample rate of $f_s = 128$ Hz. The angular acceleration is modeled as a first-order autoregressive process with zero mean. Depending on the choice of the parameter α , this represents process models ranging from a random walk model ($\alpha = 1$) to a white noise model ($\alpha = 0$). For values of $\alpha < 1$ the estimated angular accelerations are biased towards 0. Typically, the value of α is assigned an intermediate value that represents typical patterns of constrained human joint rotation, which does not grow unbounded. It is one of the filter parameters tuned to improve the tracking performance. Its value and other parameter used in the tracker are described in Table II.

The observation model describes the measurement obtained by the triaxial gyroscope for the angular rate and the triaxial accelerometer for the translational acceleration

$$y(n) = \begin{bmatrix} \omega(\mathbf{n}) \\ \dot{\mathbf{v}}(\mathbf{n}) \end{bmatrix} + \begin{bmatrix} \mathbf{v}_g(\mathbf{n}) \\ \mathbf{v}_a(\mathbf{n}) \end{bmatrix}$$

where $\omega = \{\omega_x, \omega_y, \omega_z\}^T$ is the angular velocity along the X , Y and Z axes. The gyroscope noise is described by the 3D vector \mathbf{v}_g . Similarly, the translational accelerations and their noise along the three axes are $\dot{\mathbf{v}} = \{\dot{v}_x, \dot{v}_y, \dot{v}_z\}^T$. It should be noted that the acceleration measurement vector includes translational accelerations and the effect gravity.

D. Modeling Sensor Random Drift

To reduce the effect of random drift on shoulder rotation angle estimates, we model the bias of the sensors placed on the shoulder. Bias is modeled as a random walk, adding 6 more dimensions to the process model:

$$\begin{aligned}\theta_i(n+1) &= \theta_i(n) + T_s \dot{\theta}_i(n) + \frac{1}{2} T_s^2 \ddot{\theta}_i(n) \\ &\vdots \\ \mathbf{b}_\omega(n+1) &= \mathbf{b}_\omega(n) + \mathbf{u}_{\mathbf{b}_\omega}(n) \\ \mathbf{b}_a(n+1) &= \mathbf{b}_a(n) + \mathbf{u}_{\mathbf{b}_a}(n)\end{aligned}$$

The 3D gyroscope bias \mathbf{b}_ω and 3D accelerometer bias \mathbf{b}_a are random walk with zero-mean white noise $\mathbf{u}_{\mathbf{b}_\omega}$ and $\mathbf{u}_{\mathbf{b}_a}$. The observation equation for the inertial measurement unit placed on the upper arm is given below:

$$\omega_x(n) = \dot{\theta}_1 \cos(\theta_2) + b_{\omega_x} \quad (9)$$

$$\omega_y(n) = -\dot{\theta}_1 \sin(\theta_2) + b_{\omega_y} \quad (10)$$

$$\omega_z(n) = \dot{\theta}_2 + b_{\omega_z} \quad (11)$$

$$\begin{aligned}\dot{v}_x(n) &= a_1 \sin(\theta_2) \dot{\theta}_1^2 + g \cos(\theta_2) - \dot{\theta}_1^2 a_2 \sin(\theta_2)^2 \\ &\quad - \dot{\theta}_2^2 a_2 + b_{ax}\end{aligned} \quad (12)$$

$$\begin{aligned}\dot{v}_y(n) &= a_1 \cos(\theta_2) \dot{\theta}_1^2 - g \sin(\theta_2) - \dot{\theta}_1^2 a_2 \cos(\theta_2) \sin(\theta_2) \\ &\quad + \ddot{\theta}_2 a_2 + b_{ay}\end{aligned} \quad (13)$$

$$\begin{aligned}\dot{v}_z(n) &= a_1 a_2 \cos(\theta_2) \dot{\theta}_1 \dot{\theta}_2 + \ddot{\theta}_1 a_2 \sin(\theta_2) \\ &\quad + \dot{\theta}_1 \dot{\theta}_2 a_2 \cos(\theta_2) - a_1 \ddot{\theta}_1 + b_{az}\end{aligned} \quad (14)$$

where θ_i is the i^{th} angle at time n , $\dot{\theta}_i$ is the angular velocity, and $\ddot{\theta}_i$ is the angular acceleration. The distance between elbow flexion joint and the device is a_2 . The time index n was dropped from right-side of the equations for ease of readability. Observation equations for the forearm and wrist sensors are too large to be shown here.

E. Anatomical Constraints in The Shoulder And Elbow

The state model equations provide an elegant and convenient mean of incorporating prior knowledge of physical constraints on state estimates to obtain accurate estimation. Human shoulder rotation around the humerus bone cannot exceed 90° . Similarly, shoulder cannot attain more than 180° of abduction or flexion [32]. The natural range of elbow flexion is between zero and 145° . The range of forearm supination is between zero and 85° , and between zero and 80° for the forearm pronation. The wrist flexion/extension natural range is $\pm 75^\circ$. There are many ways to incorporate state constraints into the nonlinear state estimators [33]. In this study, the constraints information are incorporated in the UKF algorithm during the time update, by restricting the sigma points within the natural range of motion region. The constrained sigma points are then used to in the measurement update, Kalman gain calculation, and state updates. During the measurement update, the constraints may be violated due to the linearization. However, these violations are rare and small in magnitude.

F. Zero-Velocity Updates

To mitigate the effect of gyroscope drift on the estimated heading angles during long periods of movement, we employ the zero-velocity updates. Zero-velocity updates has been used in ambulatory gait analysis and pedestrian navigation. During walking cycles, human feet alternate between a moving stride phase and a stationary stance phase when the foot is on the ground. In their tracking algorithm, Feliz *et al.* detected the stationary phase when the total angular rate was below $1^{rad}/sec$ [34] to reset the angular rate to zero. Resetting the inertial data to zero is referred to as hard update. Foxlin detected the stationary phase when gyroscope and accelerometer data stayed below a prescribed threshold for at least 0.15 seconds. He applied zero-velocity updates as pseudo-measurements in an EKF navigation error corrector [35]. This is classified as soft zero-velocity updates [36]

In this study, we only apply zero-velocity to update estimates of the gyroscope bias around the vertical axis. Since our algorithm uses gravity to estimate the attitude and we only lack an absolute reference for heading about the vertical axis. When the rotational rate around the vertical axis stays below $3^\circ/sec$ for at least 0.25 sec, movement is considered static. During this static period, the measurement equation is augmented with a pseudo-measurement of gyroscope vertical axis random bias. Putting pseudo-measurements into the UKF filter, instead of applying a hard update by resetting the velocity to zero, provides additional benefits. Firstly, the filter provides an estimate of the gyroscope bias, and corrects rotational rate estimates. Thus, the filter corrects estimates of heading angle, and consequently other distal arm angles.

G. Nonlinear state estimator

The model introduced above has a nonlinear relationship between the angles and sensor measurements. The EKF is the most common method of nonlinear state estimation. It is based on linearizing the state and observation models with a first-order Taylor series expansion. It models the state variables with first and second order moments, which is most appropriate when the distribution is Gaussian. The linearization leads to poor performance if the dynamics are highly nonlinear and the local linearization insufficiently characterizes the relationship. The EKF also requires calculation of Jacobian matrices, which can be difficult, tedious, error prone, and time consuming.

Sequential Monte Carlo methods, also known as particle filters, can overcome the performance and implementation limitations of the EKF [37]. These algorithms can be applied to highly nonlinear and non-Gaussian estimation problems, but they have computational requirements that are often orders of magnitude larger than the EKF or UKF. The UKF has nearly the same computational requirements as the EKF, but uses a more accurate method to characterize the propagation of the state distribution through the nonlinear models [38]. While the methods described in this article could be implemented with any of these nonlinear state space tracking algorithms, in our tracker we used the UKF. We also implement the tracker with the EKF to compare its performance versus UKF.

Q and R , are user-specified parameters to represent the process and the measurement noise covariance. Since we assume

white Gaussian noise, we set the off-diagonal entries of the two matrices to zeros. The diagonal elements of R are determined empirically and account for the uncertainty in the measurement data. We approximate the measurement noise based on short static periods at both ends of sensor measurements. Q is the process noise covariance matrix, and its diagonal elements are used as tuning parameters. These parameters control the tradeoff between certainty in the process model representing accurate motion dynamics, and how precisely the model tracks the sensor measurements. Table II lists the different parameters used to generate the tracking results.

TABLE II
 USER-SPECIFIED PARAMETERS AND SAMPLE RATE FOR THE UKF- AND EKF-BASED TRACKER. I REPRESENTS AN IDENTITY MATRIX.

Name	Symbol	Value
Variance of gyroscope measurement white Gaussian noise	σ_{vg}^2	.0001
Variance of accelerometer measurement white Gaussian noise	σ_{va}^2	.0064
Variance of process white Gaussian noise	σ_u^2	1.00
Initial state covariance matrix	P	I
Angular acceleration process parameter	α	0.90

H. Performance assessment

To evaluate the performance of the inertial tracking system in monitoring arm movement, we compared the joint angles calculated by the inertial tracker with those obtained from an industrial Epson C3 robot arm (Epson Robots, California) with six degrees of freedom. The arm is a high speed, and a very high precision industrial robot, that is normally used for medical device and parts assembly. Three Opal sensors (APDM, Portland, OR), each containing triaxial accelerometers and gyroscopes were placed on the upper arm, forearm and wrist as shown in Fig. 2. Table III shows the Epson C3 range of motion and operating speed of the six joints.

TABLE III
 MAXIMUM OPERATING SPEED AND MOTION RANGE FOR THE ROBOT ARM.

Task	Rate	Max. Motion Range
Shoulder Internal/External Rotation	450°/sec	±180°
Shoulder Flexion/Extension	450°/sec	-160°, +65°
Elbow Flexion/Extension	514°/sec	-51°, +225°
Forearm Supination/Pronation	553°/sec	±200°
Wrist Flexion/Extension	553°/sec	±135°
Wrist Twist	720°/sec	±360°

Inertial sensor and robot data were synchronized by calculating the lag time using cross-correlation analysis.

$$\hat{r}_{yx}(\ell) \approx E[y(n)x(n-\ell)] \quad (15)$$

If $\max(\hat{r}_{yx})$ is significant at lags $|\ell| > 0$, then ℓ gives information about the delay between the signals. In this study, inertial sensors were started before the robot arm. Hence, the robot data was lagging. The lagging robot data was augmented with ℓ zeros to synchronize it with the leading sensor data.

The majority of the tracking algorithms discussed in the introduction limit their performance assessment to movement performed with slow articulation. To verify the performance of our inertial algorithm in tracking normal and fast movement, we collected planar and complex arm movement at three different rotational rates. The first data set was of the arm movement at slow speed, which was defined as one fourth of

the arm maximum rotational rate. The second and third data sets were of the arm movement at medium and fast speed, which were defined as one half and full range of the maximum arm rotational rate, respectively.

Another limitation of previous systems, is the brief time duration of correct tracking or assessment. In this study, each data set lasted at least 15 minutes. Each recording started with a stationary period of 3 seconds at the initial pose. This period was used to estimate the gyroscope deterministic bias offset. The mean of each gyroscope-axis stationary measurement was removed from gyroscope data before calculating the joint angles. The rest of the recording was designed to include simple planar movement around each of the six joints. Each planar movement, explained in Table III, was repeated four times. This was followed by a second of stationary movement, and ended with a complex joints movement that involved the three joint simultaneously to mimic regular arm movement for about two minutes. This arm trajectory was repeated a few times to obtain 3 continuous 15-minute recordings of robot arm movements at slow, medium and fast rotation rate.

III. RESULTS

We used two different trackers to compare the performance of the EKF to that of the UKF in estimating the joint angles. The assessment of the tracking performance is based on the entire 15-minute duration of recording of arm movement.

A. Baseline Performance Results

In this section, we present baseline performance results of the tracker before employing the modified model to account for sensor drift, physical constraints and zero-velocity updates. The baseline results will be used to assess the performance improvement introduced by employing the drift reduction techniques. We calculated the correlation coefficient r , and the average root mean squared error (RMSE) between angle estimates from the inertial tracker and true arm angles. Table IV shows the baseline RMSE for the three data sets.

TABLE IV
 BASELINE RMSE BETWEEN TRUE ROBOT ANGLES AND ESTIMATED USING THE UKF OF THE THREE DATA SETS.

Task	Slow (°)	Medium (°)	Fast (°)
Shoulder Internal/External Rotation	25.0	8.1	9.6
Shoulder Flexion/Extension	1.1	2.4	2.5
Elbow Flexion/Extension	1.1	2.6	3.3
Forearm Supination/Pronation	1.4	2.1	2.4
Wrist Flexion/Extension	1.2	2.2	2.9
Wrist Twist	1.8	3.9	3.8
Rotational Rate	≤ 180°/s	≤ 360°/s	≤ 720°/s

B. UKF Performance with Modified Arm Model

We combined the three techniques discussed above into one modified arm model to account for sensor drift, and to employ physical constraints and zero-velocity updates. Fig. 3 show the last two minutes of the wrist true angles (dotted red lines) and their estimates (solid blue lines) using the UKF-based inertial tracking system during slow rotation rate up to 180°/sec. Fig. 4 shows the last two minutes of shoulder internal/external rotation, and flexion/extension angles and

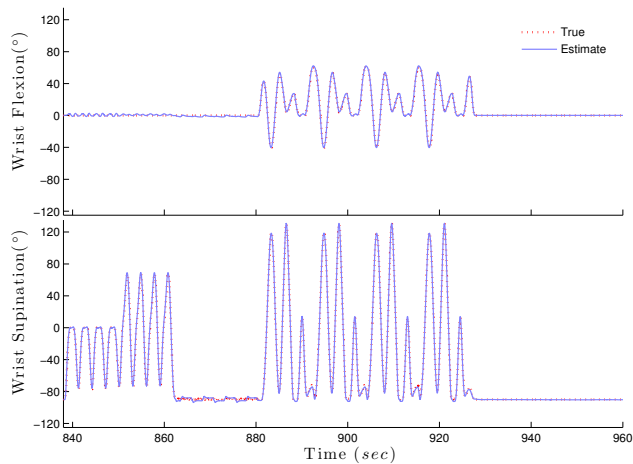


Fig. 3. True (dotted red line) and estimated (solid blue line) wrist angles during the last 2 minutes of slow arm movement.

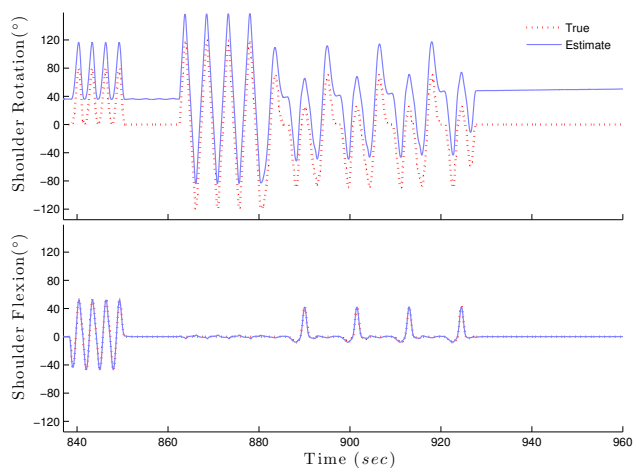


Fig. 4. Baseline shoulder angle estimates compared to the true angles during the last 2 minutes of slow arm movement.

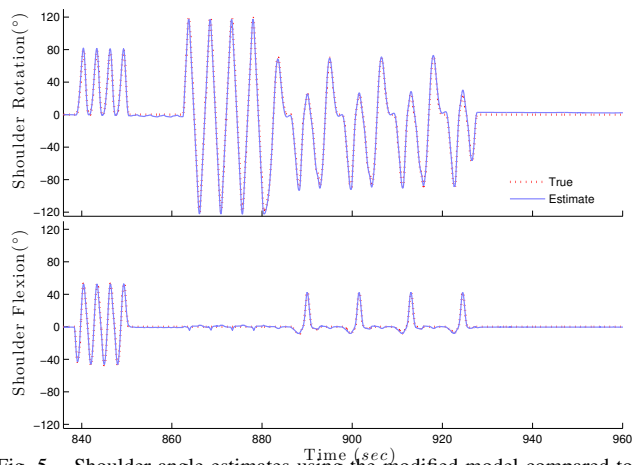


Fig. 5. Shoulder angle estimates using the modified model compared to the true angles during the last 2 minutes.

their baseline estimates during slow rotation. Fig. 5 shows the same angles estimated using the modified model.

Table V shows that the new modified model dramatically decreased shoulder internal/external rotation angle error from 25.0° to 7.8° ; an error reduction of 69% compared to baseline estimates around the vertical axis. The modified model also resulted in an increased average correlation

TABLE V
RMSE BETWEEN ANGLE ESTIMATES AND TRUE ROBOT ARM ANGLES DURING SLOW, MEDIUM AND FAST SPEED MOVEMENT USING UKF.

Task	Slow ($^\circ$)	Medium ($^\circ$)	Fast ($^\circ$)
Shoulder Internal/External Rotation	7.8	3.0	5.9
Shoulder Flexion/Extension	0.8	1.6	2.5
Elbow Flexion/Extension	0.9	2.0	2.8
Forearm Supination/Pronation	1.3	1.2	1.1
Wrist Flexion/Extension	1.1	1.5	1.8
Wrist Twist	1.7	2.8	2.2
Error reduction	69%	63%	39%

from 0.92 to 0.98 for slow movement. Consistent with the results for slow arm movement, tracking errors between inertial angle estimates and true robot joint angles were $\leq 3.0^\circ$ during medium-speed movement, and $\leq 5.9^\circ$ during fast-speed movement. Error in shoulder internal/extension rotation estimates was still higher than the joint angle error, although it dropped from 8.1° to 3.0° during medium movement, and from 9.6° to 5.9° during fast movement. Error in the other five arm angles were consistently lower than estimation error the shoulder rotation, with a maximum error of 2.8° in elbow flexion/extension during fast arm movement.

C. EKF Performance

We implemented the inertial tracker with the EKF using the modified arm model, and the same user-specified parameters which were used with the UKF-based tracker. Fig. 6 shows the last two minutes of the robot shoulder during medium internal/external rotation around the vertical axis at a rotational rate of $225^\circ/\text{sec}$. We obtained consistent agreement between the true arm angles and their inertial estimates.

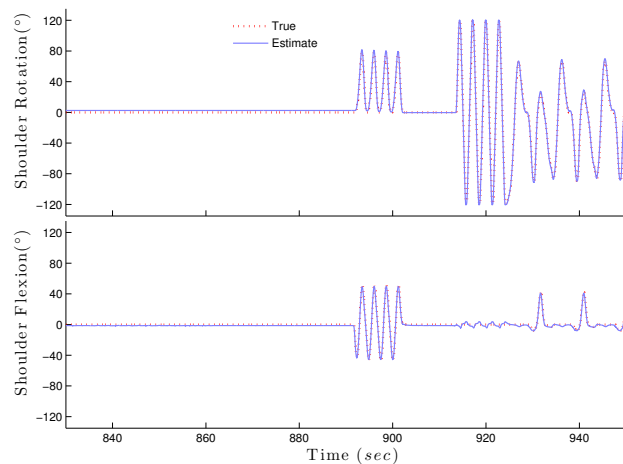


Fig. 6. True shoulder angles and their estimates of the last 2 minutes at an average rotation rate of $225^\circ/\text{s}$. Angles were estimated using the modified arm model with the EKF-based tracker.

TABLE VI
RMSE BETWEEN ANGLE ESTIMATES AND TRUE ROBOT ARM ANGLES DURING SLOW, NORMAL AND FAST SPEED MOVEMENT USING EKF.

Task	Slow	Regular	Fast
Shoulder Internal/External Rotation	8.8	8.6	9.7
Shoulder Flexion/Extension	1.2	1.9	2.5
Elbow Flexion/Extension	1.3	2.1	3.1
Forearm Supination/Pronation	0.8	1.4	1.4
Wrist Flexion/Extension	1.2	1.9	2.9
Wrist Twist	1.8	3.7	3.4

IV. DISCUSSION

In this study, we combined kinematic models with state space methods to estimate human joint angles using wearable inertial measurement units. The state model equations provide elegant and efficient means of incorporating sensor bias model, prior knowledge of physical constraints on state estimates, and zero-velocity updates to obtain accurate estimation of continuous long recordings. Besides the rotational rate data, the state space model includes both the translational and gravitational components of acceleration. This enables the system to provide state estimates during both fast and slow movements with consistent accuracy. States estimates included joint angles, angular rotation and acceleration. This framework could easily be extended to estimate joint segment lengths and segment positions, to provide full human body kinematics during spontaneous daily activities.

We used the unscented Kalman filter (UKF) to estimate shoulder, elbow and wrist joint angles from an industrial robot arm with 6 DOFs. Despite the different characteristics of human movement from the movement of robots, we argue that using a robot arm for assessment has many advantages over the traditional optical systems. The different characteristics are mainly due to the type of joints. According to [32], the human arm mechanism is composed of 7 DOFs, with shoulder joint as a ball-and-socket joint with 3 DOFs. However, the robot shoulder has only 2 DOFs, which limits the comparison to only 6 DOFs. Despite this limitation, using the robot arm for assessment provides many advantages. Unlike motion capture systems, which require estimation of joint angles from marker positions and interpolation during marker occlusions, the robot system provides direct angle measurements with high precision. The arm movement rate can be controlled to a desired rate ranging from slow to very fast, up to $720^\circ/\text{sec}$. The robot provides a wide range of motion that can easily mimic human movement in performing various tasks.

A stationary calibration period of 3 seconds at the initial pose preceded each data set served multiple purposes. The first was to align the inertial sensors and the robotic reference system. The second was to calculate the variance of sensor measurement noise. The stationary period was also used to calculate the gyroscope constant bias. This bias was removed from the gyroscope data before calculating the joint angles.

Compared to joint angles obtained from the robot reference system, we achieved an average RMS angle error $\leq 3^\circ$ during slow arm movement at a rotational rate $\leq 180^\circ/\text{sec}$. As expected, a maximum error of 7.8° was obtained for heading angles around the vertical axis. Estimation error accumulates around the vertical axis during slow or static periods. In absence of changes in acceleration, gravity alone does not provide any complementary data to that of the gyroscope. Shoulder angle estimates around the vertical axis rely only on gyroscope data, therefore error accumulates due to gyroscope drift after 15 minutes. This, however, is a very reasonable error range compared to what was reported by Roetenberg who showed that integration of noisy gyroscope data resulted in a drift between $10\text{--}25^\circ$ after one minute [12].

In contrast to many studies discussed in the introduction, we

validated the performance of our tracking algorithm during different speeds, over 15 minutes. Angle estimates during arm movement at medium rotation rate $\leq 360^\circ/\text{sec}$ are very similar to those obtained during slow movement. On average, the RMS angle error was 2.0° , with a maximum error of 3.0° between true and estimated shoulder internal/external rotation. The error slightly increased during fast movement with an average RMS angle error of 2.7° , and a maximum error of 5.9° between true and estimated shoulder internal/external rotation. Besides the effect of gyroscope drift on the accuracy of the estimated angles, there was another source of noise that contributed to the larger error. That was the effect of fast arm movement on the table on which the arm is mounted. Due to the very fast movement, the table was vibrating strongly, especially during rotation around the vertical axis, adding more noise to the sensor measurements. Despite the slightly higher estimate error during fast movement, we maintained a very reasonable error range compared to what was achieved by other studies which reported error range of $12^\circ - 16^\circ$ [25].

The combined effect of imposing physical constraints, modeling sensor bias, and employing zero-velocity updates resulted in a considerable decrease in tracking error. The RMSE dropped from 25.0° of the baseline heading angle to 7.8° for estimates during slow rotation; an error reduction of 69%. Similarly, the RMSE dropped from 8.1° with the baseline heading angle to 3.0° ; an error reduction of 63% for joint angles during medium-speed rotation. Estimation error of fast shoulder rotation around the vertical axis was reduced also from 9.6° to 5.9° . The combined effect of using the modified model in reducing the error due to sensor drift can be observed especially during the last few minutes of the recording in Fig. 4. With the prior knowledge that the arm rotation cannot exceed a certain limit, the effect of gyroscope drift on angle estimates was reduced to a very reasonable range of errors. This eliminates the need to using magnetic sensors which leads to large errors due to magnetic field disturbances [25].

Results for the EKF-based tracker shows that the UKF performs slightly better. On average, the RMSE was 2.5° , 3.3° , and 3.8° during slow, regular and fast arm movement respectively. As in the UKF case, maximum error was obtained for heading angles around the vertical axis. Shoulder internal/external rotation ranged from 8.6° to 9.7° . The additional complexity of the EKF in deriving a Jacobian matrix, besides the UKF better performance, leads to the conclusion that the UKF is a better choice for estimating Joint angles.

Natural resting positions of the human arm could be detected, and used to correct long-term drift during the day. We are currently collecting continuous data from human subjects performing daily life activities. We plan to study the effect of employing drift-correction to shoulder joint angles during these resting positions.

V. CONCLUSION

The results presented here demonstrate that wearable inertial sensors have the potential to achieve a level of accuracy that facilitates the study of normal and pathological human movement. We combined kinematic models designed for control of

robotic arms with state space methods to directly and continuously estimate human joint angles using wearable inertial sensors. These algorithms can be applied to any combination of synchronized sensors and can be generalized to track any limb movement. The state space framework enables one to efficiently impose physical constraints on state estimates, and to track in real-time or with improved accuracy offline. The agreement with a high-precision robot arm reference system was excellent. Unlike other motion systems, which require fixed cameras in a controlled environment and suffer from problems of occlusion, wearable inertial sensors can be used anywhere, cannot be occluded, and are low cost. Our proposed method used a minimal sensor configuration with one sensor on each segment. In addition, our method is very accurate during long periods of movements at various rotational rates.

REFERENCES

- [1] H. Graichen, S. Hinterwimmer, R. von Eisenhart-Rothe, T. Vogl, K. Englmeier, and F. Eckstein, "Effect of abducting and adducting muscle activity on glenohumeral translation, scapular kinematics and subacromial space width in vivo," *J Biomech.*, vol. 38, no. 4, pp. 755–760, 2005.
- [2] R. J. de Asla, L. Wan, H. E. Rubash, and G. Li, "Six DOF in vivo kinematics of the ankle joint complex: Application of a combined dual-orthogonal fluoroscopic and magnetic resonance imaging technique," *Journal of Orthopaedic Research*, vol. 24, pp. 1019–1027, May 2006.
- [3] M. J. Bey, S. K. Kline, R. Zauel, T. R. Lock, and P. A. Kolowich, "Measuring Dynamic In-Vivo Glenohumeral Joint Kinematics: Technique And Preliminary Results," *Journal of Biomechanics*, vol. 41, no. 3, pp. 711–714, November 2008.
- [4] J. B. Lunden, J. P. Braman, R. F. LaParade, and P. M. Ludewig, "Measuring Dynamic In-Vivo Glenohumeral Joint Kinematics: Technique And Preliminary Results," *Journal of Shoulder and Elbow Surgery*, vol. 19, no. 2, pp. 216–223, March 2010.
- [5] C. E. Draper, T. F. Besier, M. Fredericson, J. M. Santos, G. S. Beaupre, S. L. Delp, and G. E. Gold, "Differences in patellofemoral kinematics between weight-bearing and non-weight-bearing conditions in patients with patellofemoral pain," *Journal of Orthopaedic Research*, vol. 29, no. 3, pp. 312–317, March 2011.
- [6] E. Roux, S. Bouilland, A. Godillon-Maquinghen, and D. Bouttens, "Evaluation of the global optimization method within the upper limb kinematics analysis," *J Biomech.*, vol. 35, no. 9, pp. 1279–1283, 2002.
- [7] G. Welch and E. Foxlin, "Motion Tracking: No Silver Bullet, but a Respectable Arsenal," *IEEE Computer Graphics and Applications*, vol. 22, no. 6, pp. 24–38, Nov-Dec 2002.
- [8] K. Liu, T. Liu, K. Shibata, Y. Inoue, and R. Zheng, "Novel approach to ambulatory assessment of human segmental orientation on a wearable sensor system," *Journal of Biomechanics*, vol. 42, no. 16, pp. 2747–2752, September 2009.
- [9] F. Bagal, V. L. Fuschillo, L. Chiari, and A. Capello, "Calibrated 2D angular kinematics by single-axis accelerometers: From inverted pendulum to N-Link chain," *IEEE Sensors Journal*, vol. 12, no. 3, pp. 479–486, March 2012.
- [10] H. Dejnabadi, B. M. Jolles, E. Casanova, P. Fua, and K. Aminian, "Estimation and Visualization of Sagittal Kinematics of Lower Limbs Orientation Using Body-Fixed Sensors," *IEEE Transactions on Biomedical Engineering*, vol. 53, no. 7, pp. 1385–1393, July 2006.
- [11] J. Bregmann, R. Mayagoitia, and I. Smith, "A portable system for collecting anatomical joint angles during stair ascent: a comparison with an optical tracking device," *Dynamic Medicine*, vol. 8, no. 3, 2009.
- [12] D. Roetenberg, "Inertial and Magnetic Sensing of Human Motion," Ph.D. dissertation, University of Twente, The Netherlands, 2006.
- [13] D. Roetenberg, H. Luinge, C. Baten, and P. Veltink, "Compensation of magnetic disturbances improves inertial and magnetic sensing of human body segment orientation," *IEEE Transactions on Neural Systems and Rehabilitation Engineering*, vol. 13, no. 3, pp. 395–405, 2005.
- [14] K. O'Donovan, R. Kamnik, D. O'Keefe, and G. Lyons, "An inertial and magnetic sensor based technique for joint angle measurement," *Journal of Biomechanics*, vol. 40, no. 16, pp. 2604–2611, March 2007.
- [15] W. H. K. de Vries, H. E. J. Veeger, A. G. Cutti, C. Baten, and F. C. T. van der Helm, "Functionally interpretable local coordinate systems for the upper extremity using inertial and magnetic measurement systems," *Journal of Biomechanics*, vol. 43, pp. 1983–1988, 2010.
- [16] J. Favre, B. M. Jolles, R. Aissaoui, and K. Aminian, "Ambulatory measurement of 3D knee joint angle," *Journal of Biomechanics*, vol. 41, no. 5, pp. 1029–1035, January 2008.
- [17] H. Luinge, P. Veltink, and C. Baten, "Ambulatory Measurement of Arm Orientation," *Journal of Biomechanics*, vol. 40, pp. 78–85, 2007.
- [18] H. Luinge, D. Roetenberg, and P. Slycke, "Motion tracking system," U.S. Patent 2008/0285805 A1, November 2008.
- [19] G. Cooper, L. Sheret, and L. et al. . McMillan, "Inertial sensor-based knee flexion/extension angle estimation," *Journal of Biomechanics*, vol. 42, no. 16, pp. 2678–2685, 2009.
- [20] E. R. Bachmann and R. B. McGhee, "Inertial and magnetic posture tracking for inserting humans into networked virtual environments," in *ACM Symposium on Virtual Reality Software and Technology*. ACM: New York, NY, 2001, pp. 9–16.
- [21] H. Zhou and H. Hu, "Inertial motion tracking of human arm movements in stroke rehabilitation," in *Proceedings of the IEEE International Conference on Mechatronics and Automation*, 2005, pp. 1306–1311.
- [22] X. Yun and E. Bachmann, "Design, Implementation, and Experimental Results of a Quaternion-Based Kalman Filter for Human Body Motion Tracking," *IEEE Transaction on Robotics*, vol. 22, pp. 1217–1227, 2006.
- [23] D. Roetenberg, P. Slycke, and P. Veltink, "Ambulatory Position and Orientation Tracking Fusing Magnetic and Inertial Sensing," *IEEE Transactions on Biomedical Engineering*, vol. 54, no. 5, pp. 883–890, May 2007.
- [24] H. Zhou and H. Hu, "Upper limb motion estimation from inertial measurements," *International Journal of Information Technology*, vol. 13, no. 1, pp. 1–14, 2007.
- [25] E. R. Bachmann, X. Yun, and C. Peterson, "An investigation of the effects of magnetic variations on Inertial/Magnetic orientation sensors," in *Proceedings of the 2004 IEEE International Conference on Robotics and Automation*, 2004, pp. 1115–1122.
- [26] X. Yun, E. Bachmann, and R. McGhee, "A Simplified Quaternion-Based Algorithm for Orientation Estimation From Earth Gravity and Magnetic Field Measurements," *IEEE Transactions on Instrumentation and Measurement*, vol. 57, no. 3, pp. 638–650, 2008.
- [27] A. G. Cutti, A. Giovanardi, L. Rocchi, A. Davalli, and R. Sacchetti, "Ambulatory measurement of shoulder and elbow kinematics through inertial and magnetic sensors," *Medical & biological engineering & computing*, vol. 46, pp. 169–178, February 2008.
- [28] M. El-Gohary and J. McNames, "Shoulder And Elbow Joint Angle Tracking with Inertial Sensors," *IEEE Transactions on Biomedical Engineering*, vol. 59, no. 9, pp. 577–585, July 2012.
- [29] A. G. Cutti, C. Troncosi, A. Davalli, and R. Sacchetti, "Soft tissue artefact assessment in humeral axial rotation," *Gait Posture*, vol. 21, pp. 341–349, April 2005.
- [30] J. J. Craig, *Introduction to Robotics, Mechanics and Control*, ser. Electrical and Computer Engineering: Control Engineering. Addison-Wesley, 1989.
- [31] M. El-Gohary, L. Holmstrom, J. Huisinga, E. King, and J. McNames, "Upper limb joint angle tracking with inertial sensors," in *Engineering in Medicine and Biology Society, EMBC, 2011 Annual International Conference of the IEEE*, 2011, pp. 5629–5632.
- [32] A. Forner-Cordero, J. L. Pons, E. A. Turowska, and A. Schiele, "Kinematics and dynamic of wearable robots," in *Wearable Robots: Biomechatronic Exoskeletons*, 2nd ed., J. L. Pons, Ed. West Sussex, England: John Wiley & Sons Ltd, 2008, ch. 3, pp. 47–85.
- [33] D. Simon, "Kalman filtering with state constraints: a survey of linear and nonlinear algorithms," *Control Theory & Application*, vol. 4, no. 8, pp. 1303–1318, August 2010.
- [34] R. Feliz, E. Zalama, and J. G. Garcia-Bermejo, "Pedestrian tracking using inertial sensors," *Journal of Physical Agents*, vol. 3, no. 1, pp. 35–42, January 2009.
- [35] E. Foxlin, "Pedestrian Tracking with Shoe-Mounted Inertial Sensors," *IEEE Computer Graphics and Applications In Computer Graphics and Applications*, vol. 25, no. 6, pp. 38–46, November 2005.
- [36] I. Skog, P. Händel, J.-O. Nilsson, and J. Rantakokko, "Zero-Velocity Detection – An Algorithm Evaluation," *IEEE Transaction on Biomedical Engineering*, vol. 57, no. 11, pp. 2657–2666, November 2010.
- [37] O. Cappé, S. Godsill, and E. Moulines, "An overview of existing methods and recent advances in sequential monte carlo," in *Proceedings of the IEEE*, vol. 95, May 2007, pp. 899–924.
- [38] S. Julier and J. Uhlmann, "Unscented filtering and nonlinear estimation," in *Processings of The IEEE*, vol. 92, 2004, pp. 401–422.

Accuracy of Femur Angles Estimated by IMUs during Clinical Procedures used to Diagnose Femoroacetabular Impingement

Ryan S. McGinnis, Stephen M. Cain, Sui Tao, David Whiteside, Grant C. Goulet, Elizabeth C. Gardner, Asheesh Bedi, Noel C. Perkins

Abstract—We present a novel method for quantifying femoral orientation angles using a thigh-mounted inertial measurement unit (IMU). The IMU-derived femoral orientation angles reproduce gold-standard motion capture angles to within mean (standard deviation) differences of 0.1 (1.1) degrees on cadaveric specimens during clinical procedures used for the diagnosis of Femoroacetabular Impingement (FAI). The method, which assumes a stationary pelvis, is easy to use, inexpensive and provides femur motion trajectory data in addition to range of motion measures. These advantages may accelerate the adoption of this technology to inform FAI diagnoses and assess treatment efficacy. To this end, we further investigate the accuracy of hip joint angles calculated using this methodology and assess the sensitivity of our estimates to skin motion artifact during these tasks.

Index Terms—Inertial Measurement Unit, Femoroacetabular Impingement, Hip Angles

I. INTRODUCTION

FEMOROACETABULAR impingement (FAI) is one of the most common mechanical precursors to the development of osteoarthritis of the non-dysplastic hip [1]. FAI is caused by surfeit acetabular coverage and/or asphericity of the femoral head, leading to repetitive microtrauma to the labrum and/or the acetabular cartilage [2], resulting in hip pain for patients of all ages [2]–[4]. Diagnosis of FAI often proceeds from standard clinical range of motion (ROM) tests (i.e.

FABER, FADIR, etc.) used to identify abnormal deficits in terminal joint motion and/or specific, pain inducing hip angles [2]. The ROM values in these tests are often estimated visually or from goniometers [2], both of which exhibit poor intertester reliability [5]. Moreover, goniometric and visual assessments provide only an end measure of hip ROM in each motion plane and not the hip motion trajectory that achieves that end position. Without trajectory information, clinicians potentially lose valuable diagnostic data. Significant benefits would follow from the development of a precise, non-invasive method for measuring hip angles (ROM and motion trajectory) in clinical settings to reveal pathology.

Optical motion capture (MOCAP) is a common tracking modality used to quantify joint angles [6]. MOCAP typically employs an array of high-speed cameras arranged around the perimeter of a measurement volume. The cameras record three-dimensional position coordinates of a set of markers which are often reflective targets (e.g., [6]–[8]). To estimate hip joint angles, markers are affixed to bony anatomical landmarks which are then used to construct anatomical reference frames for the pelvis and femur [9]. The relative orientation of these reference frames can be decomposed into joint angles following standard Euler decomposition [10]. These joint angle estimates are susceptible to artifacts due to the additional movement of markers affixed to soft tissue [11]. MOCAP systems are expensive, and the associated marker placement, calibration, data collection, and data processing require considerable time and expertise. For these reasons, MOCAP has not been widely adopted in clinical settings.

Fortunately, many of these shortcomings are addressable by advancing an alternative technology for calculating joint angles, namely miniaturized inertial measurement units (IMUs). Miniature IMUs, which incorporate microelectromechanical systems (i.e., MEMS accelerometers and angular rate gyros), measure the angular velocity and linear acceleration of any rigid body to which they are attached. When deployed on body segments adjacent to a joint, miniature IMUs provide data which can be used to calculate joint angles [7], [8], [12]–[17]. Moreover, IMUs are highly portable and can be deployed in the clinic for a small fraction of the cost of MOCAP [18], [19]. These advantages provide substantial motivation for advancing IMUs for quantifying joint angles in clinical settings.

Manuscript submitted for review on July 3, 2014.

R.S. McGinnis was with the School of Kinesiology and the Department of Mechanical Engineering, University of Michigan, Ann Arbor, MI 48109 USA (e-mail: ryanmcg@umich.edu). He is now with MC10, Inc. Cambridge, MA 02140 USA.

S.M. Cain is with the School of Kinesiology and the Department of Mechanical Engineering, University of Michigan, Ann Arbor, MI 48109 USA (e-mail: smcain@umich.edu).

S. Tao is with the Department of Mechanical Engineering, University of Michigan, Ann Arbor, MI 48109 USA (e-mail: suitao@umich.edu).

D. Whiteside is with the School of Kinesiology, University of Michigan, Ann Arbor, MI 48109 USA (e-mail: dwhites@umich.edu).

G.C. Goulet is with the School of Kinesiology, University of Michigan, Ann Arbor, MI 48109 USA (e-mail: gcgoulet@umich.edu).

E.C. Gardner is with the Department of Orthopedic Surgery, Yale University, New Haven, CT 06520 USA.

A. Bedi is with the Department of Orthopedic Surgery, University of Michigan, Ann Arbor, MI 48109 USA (e-mail: abedi@umich.edu).

N.C. Perkins is with the Department of Mechanical Engineering, University of Michigan, Ann Arbor, MI 48109 USA (e-mail: ncp@umich.edu).

Recent studies have investigated the validity of IMU-technology for estimating joint angles. For example, [12], [13], [16], [17], [20], [21] employ IMUs for calculating knee angle during gait and address the effects of drift error on the estimated joint angles by fusing separate estimates from accelerometer, gyro, and magnetometer data (if available). The accuracy of orientation drift correction methods are evaluated in [7] by comparing IMU and MOCAP estimates of pelvis, thigh, and shank orientation during maximal hip flexion and abduction, walking, squatting, and standing on one leg. The accuracy of a commercially available IMU system (Xsens MVN BIOMECH, Enschede, Netherlands) for estimating rotations across the hip, knee, and ankle during level walking, stair ascent, and stair descent is revealed in [8]. Excellent agreement in flexion/extension is observed with poor agreement in abduction/adduction and internal/external rotation. Interestingly, few studies report inaccuracies due to the relative motion between soft tissue and the underlying bony anatomy which remains a potential source of error. One excellent example [16] explores the error in IMU-derived knee angles during gait trials from a transfemoral amputee, and cites skin motion as the primary source for larger errors in the intact leg knee angle estimates as compared to the prosthetic. However, no studies investigate the level of accuracy achievable from this technology in the clinical tests used for the diagnosis of FAI or how soft tissue motion may impact the clinical relevance of these measurements.

We build upon this body of research by presenting a novel IMU orientation drift correction technique for estimating hip joint angles using optimization during the clinical tests used to diagnose FAI, we establish the validity of this technique compared to gold standard MOCAP, and specifically investigate the effects of soft tissue motion on angle estimates. The promising results presented herein may accelerate the adoption of this technology to inform FAI diagnoses and assess treatment efficacy.

II. METHODS

Two fresh-frozen human cadaveric hemi-pelvises (one male and one female, ages 55 and 76 years, respectively) were harvested for testing following a protocol approved by The University of Michigan Institutional Review Board. Specimens with a history of illness, injury, or treatment affecting the hip or pelvis were excluded. Specimens were stored at -29°C and thawed for a minimum of 24 hours prior to testing. The intact pelvis of each specimen was affixed to a custom base using external fixator constructs (Smith and Nephew, Stryker Hoffman II) positioned at the bilateral iliac wings, and further secured with tensioned nylon straps to restrict pelvis motion (Fig. 1). Prior to testing, care was taken to ensure that fixation did not interfere with rotation across the hip joint.

A. Dynamic Testing Protocol

Hips were pre-cycled 10 times in flexion, abduction, adduction, and internal and external rotation prior to data collection. The right hip of each specimen was then taken

through two movement sequences designed to exercise the hip through its full range of motion. All hip manipulation was performed by the same experienced clinician. In the first sequence, referred to as the ‘combined’ test, the hip was moved in isolated flexion, abduction and adduction in approximately 0° flexion (leg flat on table), as well as internal and external rotation in both 0° flexion and 90° flexion. In the second sequence, referred to as the ‘clinicians’ test, the hip

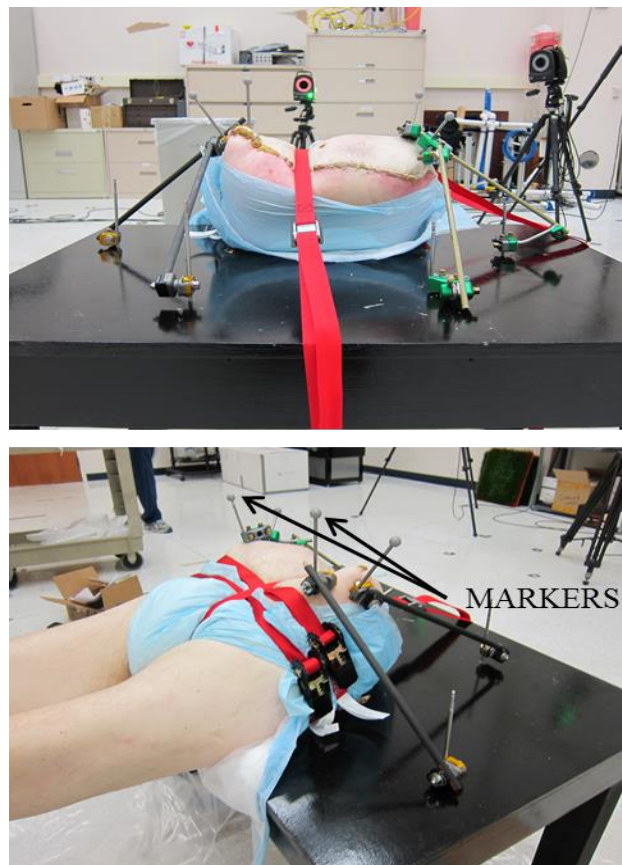


Fig. 1. Hemi-pelvis specimen mounted to testing base using bilateral external fixator constructs and tensioned nylon straps. MOCAP markers mounted to bone pins inserted into the pelvis.

was placed into a position of simultaneous maximum flexion, abduction and external rotation (FABER), and subsequently simultaneous maximum flexion, adduction and internal rotation (FADIR) to replicate two commonly used clinical tests for the diagnosis of FAI [2]. In both motion sequences, the hip was exercised to the point of terminal motion and held in this position for at least 2 seconds. Each hip was taken through the protocol three times in succession, before the hip joint capsule was surgically altered for a separate, but related study. Four capsular conditions were investigated for each hip, yielding 12 ‘combined’ and 12 ‘clinicians’ tests. Issues with MOCAP and IMU data precluded the use of two trials, resulting in 46 tests for analysis (24 ‘combined’ and 22 ‘clinicians’). Following testing, anatomical hip angles and femoral orientation angles were calculated using data from two motion sensing technologies: 1) optical motion capture, and 2) a femur-mounted inertial measurement unit.

B. Anatomical Hip Angles from Motion Capture

Twenty-six retro-reflective markers (7 calibration; 19 tracking), 12-mm in diameter, were affixed to each specimen. A 12-camera VICON MX system (VICON Motion Systems, Oxford, UK) operating at 240 Hz tracked three-dimensional (3D) marker trajectories. To eliminate the effect of soft tissue artifact, pelvis motion was derived from three markers affixed to pins surgically inserted into the ilia (Fig. 1). Similarly, a pin was inserted into the femoral shaft and mounted with a frame containing four markers (Fig. 2) that were used to record the motion of the underlying bone. An identical frame was superficially mounted on the skin of the thigh using elastic, self-adhesive athletic tape, congruent with typical in-vivo motion capture conditions. In previous and current studies, we have found that mounting devices to the skin in this fashion is simple and provides adequate hold even for highly dynamic motions (e.g. running, cutting, jumping). The markers on each frame were used to create arbitrary ‘bone-mounted’ and ‘skin-mounted’ segmental reference frames from which hip joint kinematics were subsequently derived.

Prior to the dynamic protocol, a static trial was collected in accordance with the calibrated anatomical systems technique

TABLE I

Segment	Definition
<i>Pelvis</i>	
Origin	3D midpoint of ASIS markers
x-axis	Unit vector directed from mid-PSIS to pelvis origin
y-axis	Cross product of z and x axes
z-axis	Unit vector directed from left ASIS to right ASIS
<i>Femur</i>	
Origin	Hip joint center
x-axis	Cross product of y and z axes
y-axis	Unit vector directed proximally from knee joint center to hip joint center
z-axis	Unit vector directed from medial to lateral femoral condyles

Anatomical reference frame definitions for the pelvis and femur.

[22]. The bilateral anterior superior iliac spines (ASIS) and the midpoint of the posterior superior iliac spine (PSIS) markers were stored in the reference frame created by the surgically attached iliac markers. Likewise, the medial and lateral femoral condyles were stored in the arbitrary femoral reference frames. The knee joint center was considered as the 3D midpoint of the femoral condyle markers. Hip joint center was calculated for each motion using a ‘‘pivoting’’ algorithm [23]. The abovementioned landmarks and joint centers were then used to define the anatomical reference frames in each trial according to the standards outlined in [10](Table 1).

Gaps in the raw marker trajectories were identified automatically within the VICON Nexus software (VICON Motion Systems, Oxford, UK). These gaps were infrequent, persisted for no more than 15 frames and were ultimately interpolated using a cubic spline. Data were subsequently filtered using a Woltring filter [24] with the optimal mean squared error of 1 mm determined by a residual analysis. In accordance with [10], anatomical hip joint rotations were expressed using the Euler ZXY decomposition yielding flexion/extension, adduction /abduction, and internal/external rotation angles.

C. Anatomical Hip Angles from an Inertial Sensor

The femur-mounted IMUs were commercially available YEI 3-Space sensors (Yost Engineering, Portsmouth, Ohio). Prior to use, the IMUs were calibrated following the procedure detailed in [25]. Data was sampled at approximately 300 Hz, written to flash memory on the device, and subsequently downloaded to a computer via USB after each data collection session. The devices were secured to the motion capture marker frames used to define the ‘bone-mounted’ and ‘skin-mounted’ segmental reference frames (Fig 2). The IMUs were

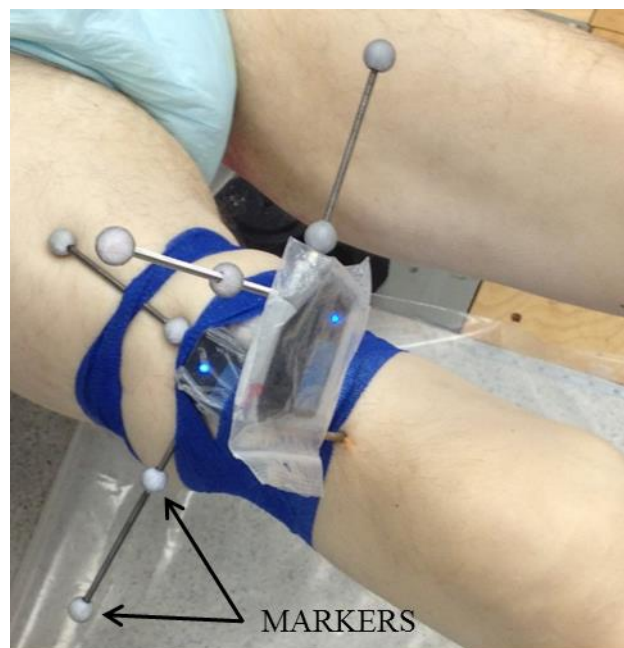


Fig. 2. Mounting location of the two inertial sensors on MOCAP marker frames affixed to each subject. The pin sensor is secured to an ex-fix pin inserted into the femoral shaft while the skin sensor is secured to the soft tissue of the thigh.

calibrated while attached to the marker frames to ensure alignment between the sense axes of each IMU and the reference directions of the attached frame.

Defining anatomical hip angles poses a challenge for inertial sensor based measurement techniques as the anatomical angles rely on reference frames defined by the location of bony anatomical landmarks—locations the IMU has no means of sensing. As an alternative, one can identify these reference frames using functional ‘calibration’ motions before the anatomical hip angles are calculated [12], [20]. Calibration motions were performed prior to each round of the dynamic protocol, where the hip was moved in isolated internal and external rotation with 0° flexion. A principle component analysis of the measured angular velocity yields the primary rotation axis during this motion. This axis is assumed to define the mechanical axis of the femur thereby establishing the relationship between the ‘bone-mounted’/‘skin-mounted’ frames and the y-axis of the anatomical femoral reference frame. This direction is then held fixed in the femur for the following round of the dynamic protocol. The remaining anatomical reference directions are established by considering the initial orientation of the mechanical axis of the femur. Specifically, we assume that the femur is at rest at the beginning of each test, the

anatomical femoral and pelvic reference frames are aligned, and the z -axis of each lies in the horizontal plane. Since the accelerometer measures translational acceleration as well as gravity, when the IMU is at rest, the accelerometer establishes the direction of gravity in the sensor frame of reference. The cross product of this direction with the mechanical axis of the femur establishes the relationship between the ‘bone-mounted’/‘skin-mounted’ frames and the z -axes of the anatomical frames. Finally, the x -axes of the anatomical frames follow from right-handed frame convention. This procedure establishes the (constant) direction cosine matrix between the femoral anatomical frame (F) and either the ‘bone-mounted’ frame (B) or the ‘skin-mounted’ frame (S) ($C_{F/B}$ and $C_{F/S}$, respectively). Acceleration and angular velocity data from each IMU are then used to calculate the direction cosine matrix between the pelvic and femoral anatomical frames C_F^P for the duration of the trial beginning from an initially aligned state as follows.

Assuming the pelvis is fixed, the evolution of the direction cosine matrix is governed by the differential equation

$$\frac{d}{dt} C_{P/F} = C_{P/F} \bar{\omega}_m \Big|_F^\times \quad (1)$$

where $\bar{\omega}_m \Big|_F^\times$ is the measured angular velocity vector of the femur, resolved in the femoral anatomical frame (e.g., $\bar{\omega}_m \Big|_F^\times = (C_{F/B} \bar{\omega}_m \Big|_B)^\times$), in skew symmetric form, and $C_{P/F}$ is the direction cosine matrix describing the orientation of the anatomical frame of the femur relative to the fixed pelvis (P). Numerical solution to Eq. (1) following [26] yields $C_{P/F}$ at every sampled time during the trial using the trivial (3x3 identity) initial condition. This solution for $C_{P/F}$ is subject to drift error, a well-known phenomenon with inertial sensors [27], [28]. To provide the best estimates of femur orientation, and therefore hip angle, this error needs to be estimated and removed. This is often accomplished by fusing drift-prone orientation estimates from the gyro with drift-free but noisy or incomplete orientation estimates from the accelerometer and/or magnetometer (e.g., [27], [29]). Because of the possibility of locally changing magnetic fields in clinical settings, we utilize orientation estimates from the accelerometer alone to correct for orientation drift. This correction is accomplished via a novel optimization approach, which uses estimates of the direction of gravity from the accelerometer and rate gyros throughout the test to define small corrections to the angular velocity data. The corrected angular velocity is defined according to

$$\bar{\omega} = \begin{bmatrix} 1+s_x & 0 & 0 \\ 0 & 1+s_y & 0 \\ 0 & 0 & 1+s_z \end{bmatrix} \bar{\omega}_m - \begin{bmatrix} b_x \\ b_y \\ b_z \end{bmatrix} \quad (2)$$

where s_x , s_y , and s_z are small adjustments to the scale factor values for each sense axis, and b_x , b_y , and b_z are corresponding small adjustments to the bias values identified for each trial. To identify these six unknowns, we consider instances during the trial when the femur is held at rest, which is readily indicated when the magnitude of the measured angular velocity falls within the device noise floor, and the measured acceleration differs from 1 g by less than the magnitude of its noise floor. At these sampled times (t_i), the gyro-derived direction of gravity predicted by integration of Eq. (1) follows from

$$\bar{g}_g(t_i) = C_{P/F}^T(t_i | s_x, s_y, s_z, b_x, b_y, b_z) \bar{g}_a(0) \Big|_P \quad (3)$$

where $\bar{g}_g(t_i)$ is the gyro-derived direction of gravity at time t_i resolved in the femoral anatomical frame, $C_{P/F}^T(t_i | s_x, s_y, s_z, b_x, b_y, b_z)$ is the transpose of the direction cosine matrix at time t_i parameterized by the six unknown gyro corrections, and $\bar{g}_a(0) \Big|_P$ is the direction of gravity determined from the accelerometer while the femur was held at rest at the start of the trial, resolved in the pelvic anatomical frame. The accelerometer-derived direction of gravity is defined according to

$$\bar{g}_a(t_i) = C_{F/B} \bar{a}_m(t_i) \quad (4)$$

where $\bar{g}_a(t_i)$ is resolved in the femoral anatomical frame, and $\bar{a}_m(t_i)$ is the measured acceleration at time t_i . Equation (4) is written for an acceleration measured by the ‘bone-mounted’ IMU, one could also construct the analogous equation for the ‘skin-mounted’ sensor. The angular difference between these two vectors is defined by the dot-product

$$e(t_i | s_x, s_y, s_z, b_x, b_y, b_z) = \cos^{-1} \left(\frac{\bar{g}_a(t_i) \cdot \bar{g}_g(t_i)}{|\bar{g}_a(t_i)| |\bar{g}_g(t_i)|} \right) \quad (5)$$

where $e(t_i | s_x, s_y, s_z, b_x, b_y, b_z)$ is the angular difference at time t_i parameterized by the six unknown gyro corrections. Drift, being a one-sided error, increases monotonically in time. Thus, as t_i increases, the contribution of drift error to $e(t_i | s_x, s_y, s_z, b_x, b_y, b_z)$ increases and overwhelms contributions from all other sources (i.e. noise in the accelerometer gravity estimate, small calibration misalignments, etc.). Accordingly, we minimize the objective function

$$E(s_x, s_y, s_z, b_x, b_y, b_z) = \sum_{i=1}^n \left(e(t_i | s_x, s_y, s_z, b_x, b_y, b_z) \cdot t_i \right)^2 \quad (6)$$

for all ($n > 2$) sampled “still” times to solve for the six unknown gyro corrections. Here $E(s_x, s_y, s_z, b_x, b_y, b_z)$ denotes the sum squared angle difference between gyro and accelerometer gravity directions weighted by the sampled “still” time to consider differences primarily due to drift. This non-linear minimization is accomplished in Matlab (MathWorks, Natick, MA, USA) using the *lsqnonlin* function with the Levenberg-Marquardt (i.e. damped least squares) algorithm. Following convergence of this numerical optimization, the corrected angular velocity follows from Eq. (2). The method of [26] is used with this corrected angular velocity to define a corrected direction cosine matrix $C_{P/F}$ via numerical solution of Eq. (1). As with MOCAP, the anatomical hip joint rotations are then calculated via an Euler decomposition yielding flexion/extension, adduction/abduction, and internal/external rotation angles for comparison.

D. Comparing Femoral Orientation Angles from IMU and Motion Capture Data

As stated above, the definition of anatomical hip angles poses a challenge for inertial sensor based measurement techniques because of difficulties identifying anatomical reference frames. Significant errors in adduction/abduction and internal/external rotation angles arise from small misalignments in the anatomical frames [8], [30]. To demonstrate the accuracy of the proposed IMU orientation drift correction, we must first correct for misalignment in the IMU anatomical reference frames. To this end, we define the femoral orientation angles (X, Y, Z) as the IMU estimates of the anatomical hip angles defined above (flexion/extension, adduction/abduction, and internal/external rotation). To calculate these same angles from MOCAP data, we construct the direction cosine matrix $C_{P/F}$ by considering the orientation of the ‘bone-mounted’ or ‘skin-mounted’ frames defined using the attached reflective markers, which we denote as ${}^M C_{P/F}$. Specifically, the three-dimensional position data for each of the four markers is used to construct the direction cosine matrix which defines the orientation of the ‘bone-mounted’ or ‘skin-mounted’ frame relative to the ground frame (G) of the motion capture system (${}^M C_{G/B}$ for bone-mounted and ${}^M C_{G/S}$ for skin-mounted) established during system calibration. The fixed rotation from the ‘bone-mounted’ or ‘skin-mounted’ frame to the femur anatomical frame ($C_{F/B}$ for bone-mounted and $C_{F/S}$ for skin-mounted), established by the IMU-based methodology, is then used to define the orientation of the femur anatomical frame relative to the ground motion capture frame per

$${}^M C_{G/F} = {}^M C_{G/B} C_{F/B}^T \quad (7)$$

where ${}^M C_{G/F}$ defines the orientation of the femoral frame relative to the motion capture ground frame. Since the pelvic and femoral frames are aligned at the beginning of each test, ${}^M C_{G/F}(0)$ defines the fixed rotation (${}^M C_{P/G}$) between the MOCAP ground frame and the IMU-defined pelvis frame. Finally, the orientation of the IMU-defined femoral frame relative to the pelvis frame is determined via

$${}^M C_{P/F} = {}^M C_{P/G} {}^M C_{G/B} C_{F/B}^T \quad (8)$$

where ${}^M C_{P/F}$ defines the orientation of the femoral frame relative to the IMU-defined pelvic frame. Equations (7) and (8) have been written for the ‘bone-mounted’ frame, but analogous equations can be developed for the ‘skin-mounted’ frame as well. The matrix ${}^M C_{P/F}$ can then be decomposed multiple ways, but we follow the convention in [10]; namely, a ZXY decomposition, yielding X, Y, and Z femoral orientation angles for direct comparison with those from the IMU-based method.

III. RESULTS

To establish the accuracy of the IMU orientation measurements, we report differences between 1) IMU and MOCAP estimates of anatomical hip angles, 2) IMU and MOCAP estimates of femoral orientation angles, and 3) pin and skin IMU estimates of femoral orientation angles.

A. Anatomical Hip Angles

Fig. 3 illustrates flexion/extension (Flex/Ext), adduction/abduction (Ad/Ab), and internal/external rotation (Ir/Er) angles as estimated from IMU (gray) and MOCAP (black) data during representative ‘combined’ (Fig. 3A) and ‘clinicians’ (Fig. 3B) tests. Consistent with previous studies [8], [13], the results of Fig. 3 confirm that, for both the ‘combined’ and ‘clinicians’ tests, there is excellent agreement between IMU and MOCAP estimates of Flex/Ext angle, but poorer agreement in Ad/Ab and Ir/Er. These facts are further revealed in the correlation plots of Fig. 4 where IMU anatomical angles are plotted against their MOCAP counterparts during the example ‘clinicians’ test reported in Fig. 3B. A reference (black) line with unit slope and zero intercept is added. Table 2 provides summary results of the full dataset (N=46) including the mean (SD) of the mean and standard deviation of the difference in the anatomical angles, as well as the mean (SD) of the slope, intercept, and R^2 of best-fit lines to the correlation plot data. These results reveal that the IMU estimates for the Flex/Ext, Ad/Ab, and Ir/Er hip angles exhibit mean (SD) differences of -1.0 (1.1), 5.7 (5.8), and 3.4 (3.6) degrees, respectively, relative to those estimated using MOCAP. The differences in the anatomical angles derive from misalignment between IMU and MOCAP anatomical reference frames as evidenced by the accuracy of the femoral orientation angles reported next.

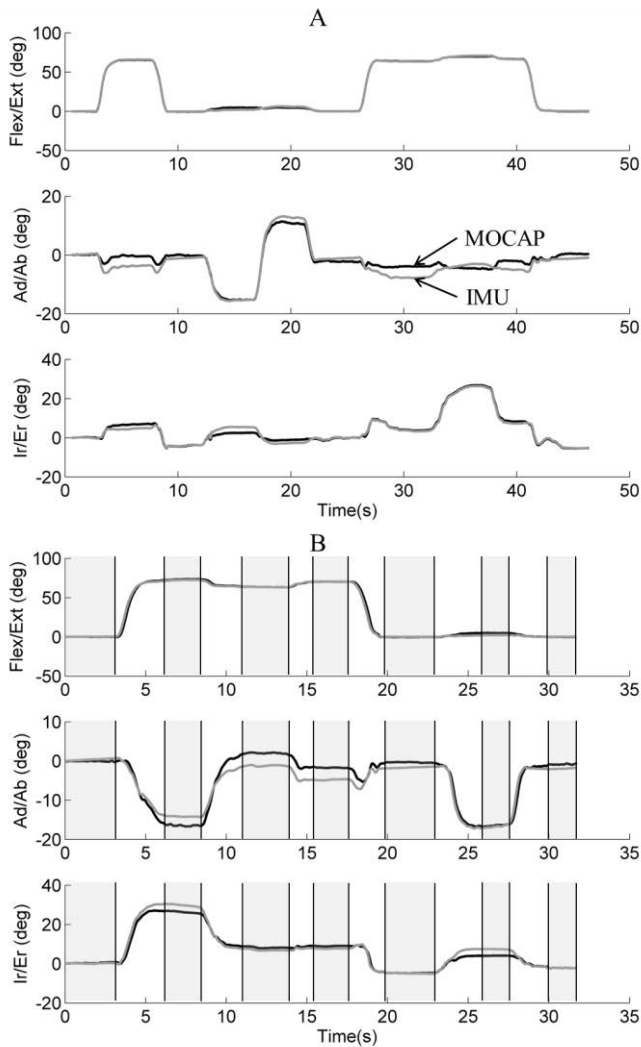


Fig. 3. Example flexion/extension (Flex/Ext), adduction/abduction (Ad/Ab), and internal/external rotation (Ir/Er) angles as estimated from IMU (gray) and MOCAP (black) data during the ‘combined’ (A) and ‘clinicians’ (B) tests. Example still phases used to correct for drift error indicated by gray shading in (B).

TABLE II

Angle	Mean (deg)	SD (deg)	Slope	Intercept	R ²
Flex/Ext	-1.00(1.12)	2.64(1.12)	1.01(0.03)	0.63(0.58)	1.00(0.00)
Ad/Ab	5.72(4.64)	5.78(2.77)	0.96(0.16)	-5.62(4.56)	0.74(0.13)
Ir/Er	3.42(2.07)	3.58(1.82)	0.83(0.12)	-2.26(1.71)	0.92(0.09)

Agreement between IMU and MOCAP estimates of the flexion/extension (Flex/Ext), adduction/abduction (Ad/Ab), and internal/external rotation (Ir/Er) angles of the hip summarized by the mean (SD) of the mean and SD of the difference, and the slope, intercept, and R2 of the best-fit line to the correlation plot data.

TABLE III

Angle	Mean (deg)	SD (deg)	Slope	Intercept	R ²
X	-0.06 (0.32)	0.53 (0.18)	1.00 (0.01)	-0.03 (0.24)	1.00 (0.00)
Y	0.02 (1.39)	0.96 (0.49)	0.99 (0.04)	0.00 (1.35)	0.99 (0.02)
Z	-0.09 (0.85)	1.12 (0.68)	0.99 (0.06)	0.18 (0.63)	0.99 (0.01)

Agreement between IMU and MOCAP estimates of the X, Y, and Z femoral orientation angles summarized by the mean (SD) of the mean and SD of the difference, and the slope, intercept, and R2 of the best-fit line to the correlation plot data.

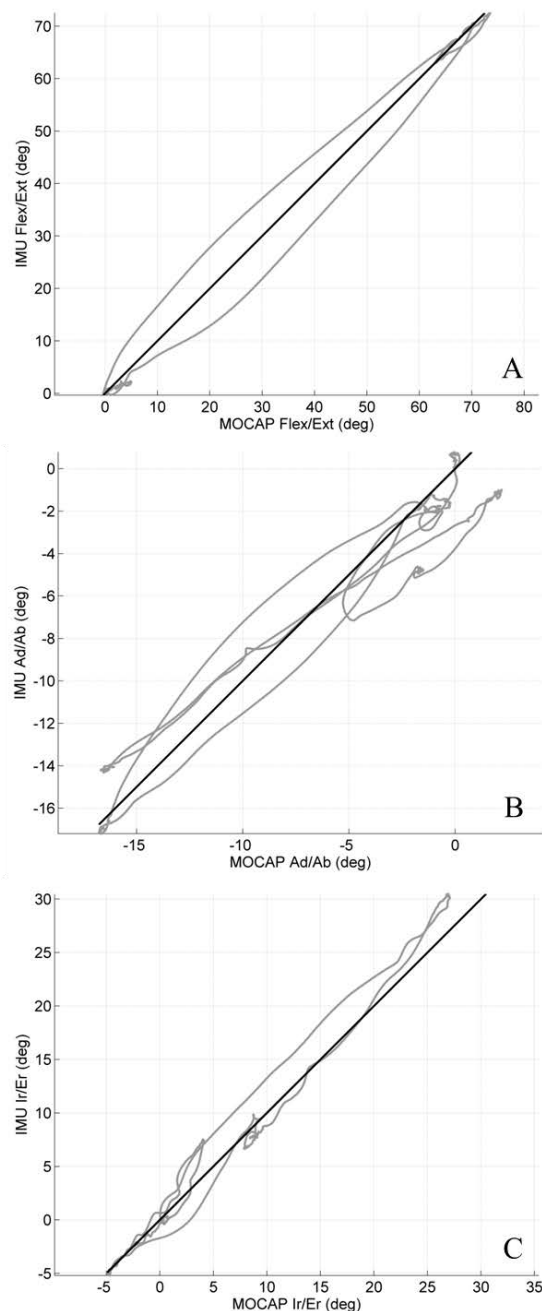


Fig. 4. Correlation plots of flexion/extension (A), adduction/abduction (B), and internal/external rotation (C) angles during the example ‘clinicians’ test reported in Fig. 3. A reference (black) line with unit slope and zero intercept is added.

B. Femoral Orientation Angles

Fig. 5 illustrates example X, Y, and Z femoral orientation angles as calculated from IMU (gray) and MOCAP (black) data from representative ‘combined’ (A) and ‘clinicians’ (B) tests. For reference, the X angle is nearly flexion/extension, the Y is nearly adduction/abduction, and the Z is nearly internal/external rotation. The close agreement for all angles evident in Fig. 5 is further confirmed by the correlation plots for the ‘clinicians’ test (Fig. 5B) presented in Fig. 6A-C, where IMU X, Y, and Z angles are plotted against their MOCAP counterparts. Again a reference (black) line with unit slope and zero intercept is added for comparison. This

agreement is consistent across all trials considered (92 total: 46 pin and 46 skin) as evidenced by average mean (SD) differences in the X, Y, and Z angles of $-0.06(0.53)$, $0.02(0.96)$, and $-0.09(1.12)$ degrees, respectively. Table 3 summarizes the results for the 92 tests by reporting the mean (SD) of the mean and standard deviation of the difference in the three orientation angles, as well as the mean (SD) of the slope, intercept, and R^2 of best-fit lines to the correlation plot data.

C. Influence of Skin Artifact

Consider next possible differences between the pin- and skin-mounted IMU estimates of the femoral orientation angles due to soft tissue artifact. Fig. 7 illustrates representative X, Y, and Z femoral orientation angles as calculated from the pin (black) and skin (gray) IMUs during the ‘combined’ (A) and ‘clinicians’ (B) tests. For the X femoral orientation angle, the pin and skin estimates are nearly identical. By contrast, there are observable discrepancies in the Y and Z angles due to skin artifact. These discrepancies are further revealed in the correlation plots for the ‘clinicians’ test (Fig. 7B) presented in Fig. 8A-C,

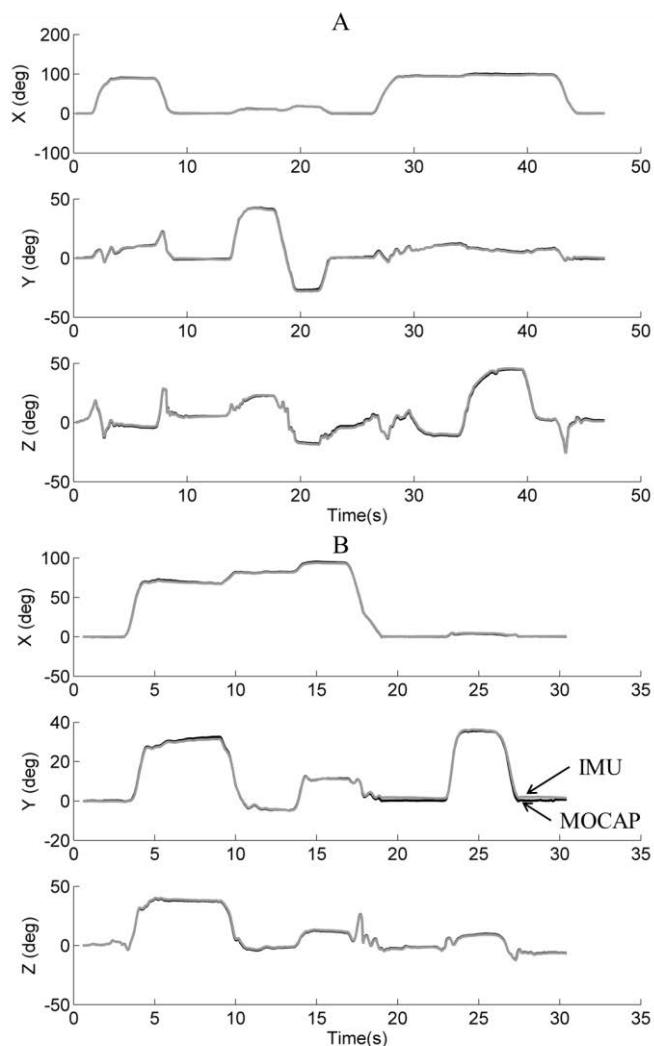


Fig. 5. Representative X, Y, and Z femoral orientation angles estimated from IMU (gray) and MOCAP (black) data during the ‘combined’ (A) and ‘clinicians’ (B) tests.

where skin X, Y, and Z angles are plotted against the corresponding pin angles. As before, a reference (black) line with unit slope and zero intercept is added. It is evident from the correlation plots in Fig. 8, as well as from the time history plots in Fig. 7, that soft tissue artifact influences the femoral orientation angles, particularly in the frontal and transverse planes. This influence is consistent across all trials ($N=46$) as evidenced by average mean (SD) differences in the X, Y, and Z orientation angles of $-1.68(2.35)$, $-2.63(3.13)$, and $6.41(6.44)$ degrees, respectively, reported with other summary results in Table 4.

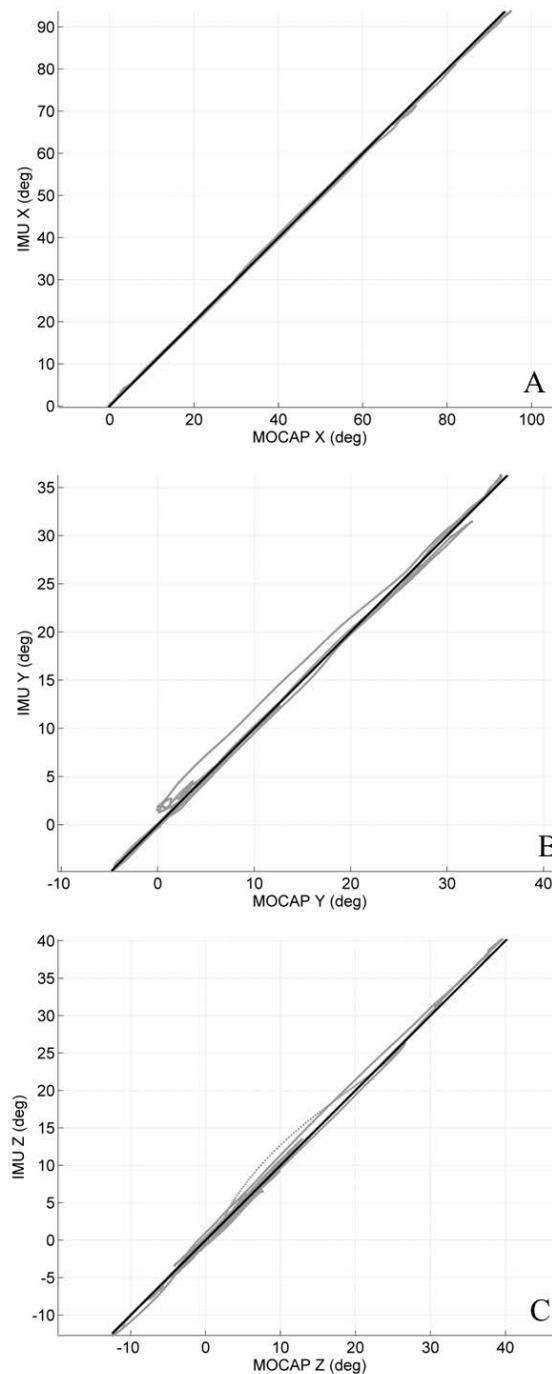


Fig. 6. Correlation plots (IMU vs. MOCAP) of X (A), Y (B), and Z (C) femoral orientation angles during the representative ‘clinicians’ test reported in Fig. 5. A reference (black) line with unit slope and zero intercept is added for comparison.

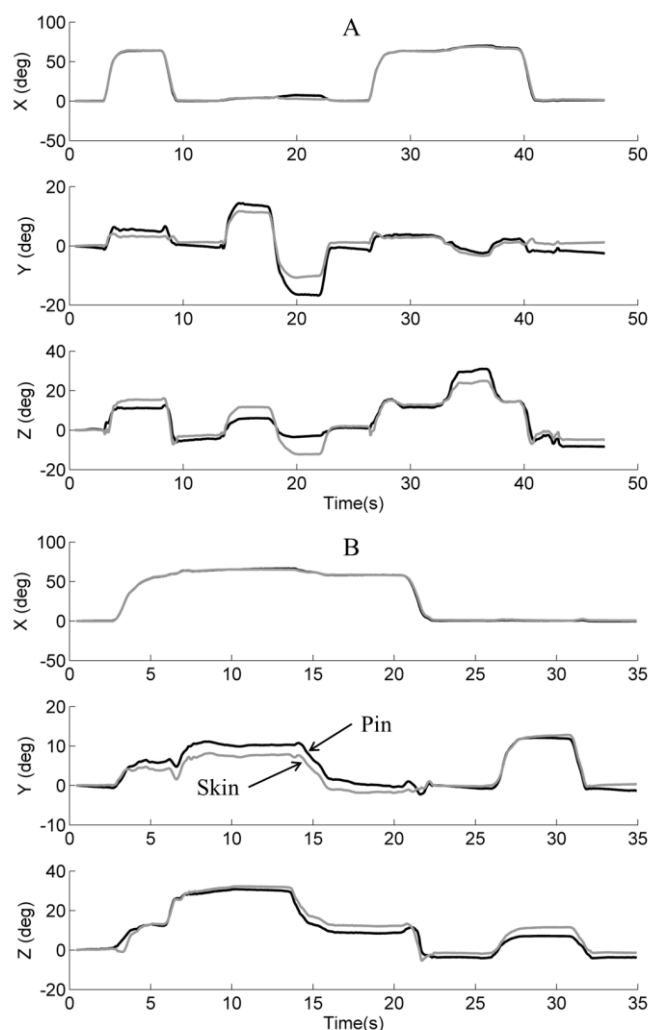


Fig. 7. Representative X, Y, and Z femoral orientation angles as estimated from the pin (black) and skin (gray) IMU data during the ‘combined’ (A) and ‘clinicians’ (B) tests.

TABLE IV

Angle	Mean (deg)	SD (deg)	Slope	Intercept	R ²
X	-1.68 (1.92)	2.35 (1.04)	1.03 (0.05)	0.45 (0.50)	1.00 (0.00)
Y	-2.63 (3.04)	3.13 (1.17)	1.02 (0.12)	2.52 (3.21)	0.89 (0.07)
Z	6.41 (4.71)	6.44 (2.83)	0.83 (0.22)	-3.82 (2.70)	0.80 (0.15)

Difference between pin and skin IMU estimates of the X, Y, and Z femoral orientation angles summarized by the mean (SD) of the mean and SD of the difference, and the slope, intercept, and R² of the best-fit line to the correlation plot data.

IV. DISCUSSION

A new IMU orientation drift correction algorithm is proposed herein for quantifying the angular displacement of the femur during common clinical tests used for the diagnosis of FAI and other morphological abnormalities of the pre-arthritic hip (e.g., [2]). The validity of IMU-based hip angle measurements in these clinical tests has not previously been reported. Below, we discuss the validity of 1) the estimated anatomical hip joint angles, followed by 2) the estimated femoral orientation angles. In so doing, we also comment on orientation estimates reported in the literature. Finally, we discuss how soft tissue motion influences the estimated

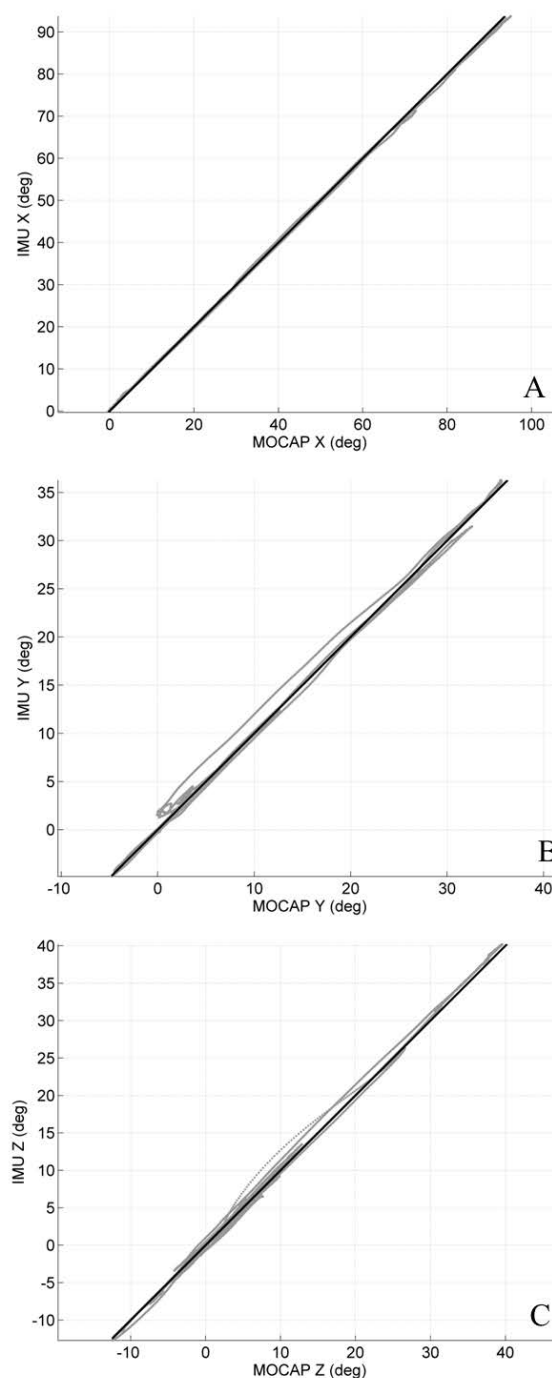


Fig. 8. Correlation plots (Skin vs. Pin) of X (A), Y (B), and Z (C) angles during the example ‘clinicians’ test reported in Fig. 7. A reference (black) line with unit slope and zero intercept is added..

femoral orientation angles and the potential implications for clinical diagnosis of FAI.

A. Validity of Anatomical Hip Angles

The validity of IMU-based measurements of anatomical hip angles has previously been explored in the literature in the context of gait analysis (e.g., [8], [17], [31]). However, no studies have investigated the validity of IMU-based measurements for estimating hip angles during the common clinical tests for FAI. Despite the simplification of a fixed pelvis, these tests exercise the hip through very large ranges in

each motion plane, which is distinct from the gait-induced hip motions (largely restricted to the sagittal plane) considered in related studies [7], [30]. According to [30], this increased range of motion can significantly amplify slight misalignments in the IMU anatomical frame, and yield erroneous joint angle estimates. The proposed functional calibration seeks to reduce this misalignment error, yet its success is also limited as evidenced by the average mean (SD) differences in the anatomical hip angles across all trials (N=46) of -1.0 (1.1) degrees in flexion/extension, 5.7 (5.8) degrees in adduction/abduction, and 3.4 (3.6) degrees in internal/external rotation. The effects of misalignment are further revealed by considering the average slope and coefficient of determination (R^2) of the best-fit lines from the correlation plot data (IMU versus MOCAP angles), which are 1.01 (1.00), 0.96 (0.74), and 0.83 (0.92), for the flexion/extension, adduction/abduction, and internal/external rotation angles, respectively. These results suggest that, on average, the IMU overestimates the MOCAP flexion/extension angle by 1%, and underestimates the adduction/abduction and internal/external rotation angles by 4% and 17%, respectively, relative to the MOCAP angle. Moreover, the IMU-derived estimates explain nearly 100% of the variance in the flexion/extension angle, 92% of the variance in the internal/external rotation angle, but only 74% of the variance in the adduction/abduction angle. Simple correction for anatomical frame misalignment yields the femoral orientation angles reported next having significantly improved levels of agreement.

B. Validity of Femoral Orientation Angles

The accuracy of the hip angle drift correction algorithm is revealed after first correcting for the misalignment between the IMU and MOCAP anatomical reference frames. Doing so allows a direct comparison of femoral orientation angles (X, Y, Z) calculated from IMU and MOCAP data to within a small residual misalignment error due to construction of the MOCAP marker frames. The resulting X, Y, and Z orientation angles correspond to IMU-estimated flexion/extension, adduction/abduction, and internal/external rotation angles since the MOCAP anatomical frame is now aligned with the IMU anatomical frame at the start of each test. Across all trials (N=92), the average mean (SD) differences between the X, Y, and Z angles estimated from IMU and MOCAP data remain far below one degree and are -0.06(0.53), 0.02(0.96), and -0.09(1.12) degrees, respectively. This outstanding consistency is superior (by an order of magnitude) to the reported accuracies of two widely used IMU systems, the Xsens MVN and APDM Opal, which advertise static (dynamic) orientation accuracies of 1.00(2.00) and 1.50(2.80) degrees, respectively. These commercial systems fuse orientation estimates from accelerometers and rate gyros, as well as magnetometers. In contrast, the algorithm presented herein achieves superior results while fusing estimates from accelerometers and rate gyros alone. A recent study [7] also compares IMU-derived orientation angles (fusing gyro and accelerometer estimates) to MOCAP-derived orientation angles for quasi-static functional tasks, including maximum hip flexion and adduction, gait, two leg squats, and one leg standing. However, the most successful drift error correction algorithm reported only achieves mean and standard deviation

errors of 2-3 degrees in the most successful task. Thus, the drift correction algorithm reported herein may well set a new standard for accuracy for the clinical tests for FAI considered.

When compared to the orientation drift algorithms presented in [7], the algorithms above succeed by using data from the entire clinical tests for FAI. Specifically, during the clinical tests for FAI, a device mounted to the femur is held stationary when each of its three sense axes nearly aligns with gravity for some subset of the test. Data from these time periods provide the measurements that enable identification of the optimal drift correction constants (scale factor and bias) for each of the gyro sense axes as defined in Eq. (6). Doing so accounts for drift present in all coordinate directions, including yaw, a limitation noted for several of the tests and methodologies presented in [7].

It is important to note that the accuracy of the algorithm described herein is accompanied by the loss of several generalities maintained by the commercial IMU systems as well as the algorithms tested in [7]. Specifically, the described drift correction algorithm relies on data collected over the entire duration of a given test, and therefore cannot be applied in real time. Moreover, the tests considered herein exercise each femur-mounted device through its entire ROM, so these results may not extend to general applications where a more limited ROM is expected.

C. Influence of Skin Artifact and Clinical Implications

The effects of skin artifact on measured hip angles during clinical tests for FAI have not previously been investigated. In this study, the differences between skin- and pin-mounted IMU estimates of femur orientation were -1.68(2.35), -2.63(3.13), and 6.41(6.44) degrees about the X, Y, and Z axes, respectively (Table 4). The average slope and coefficient of determination (R^2) of the best-fit lines to the correlation plot data (skin-mounted versus pin-mounted orientation angles) were 1.03(1.00), 1.02(0.89), and 0.83(0.80), in the X, Y, and Z directions, respectively. These results reveal that the skin mounted IMU overestimates the X and Y orientation angles by only 3% and 2%, respectively, but underestimates the Z orientation angle by 17% relative to the MOCAP angle estimates. Moreover, based on the R^2 results, the skin mounted IMU explains nearly 100% of the variance in the X orientation angle, 89% of the variance in the Y angle, and only 80% of the variance in the Z angle, on average, for the 46 trials considered.

The differences in femoral orientation angle trajectories translate to range of motion (ROM) differences that have direct clinical significance. For the 46 tests analyzed, the mean (SD) range of motion differences are 1.68 (3.12), 0.76 (4.15), and -2.40 (9.18) degrees in the X, Y, and Z angles, respectively. As illustrated in Fig. 2, the skin-mounted IMU is secured approximately at mid-thigh using self-adhesive, elastic, athletic tape. While this location is convenient, it likely induces considerable skin artifact. Smaller skin artifact, and therefore smaller ROM differences, would follow from mounting and indexing the IMU against the iliotibial band or the proximal end of the lateral femoral condyle [32]. Regardless, normative (flex/ext: 110-120°; Ir/Er: 30-40°) [33] and surgically-confirmed FAI (flex/ext: 97(9)°; Ir/Er: 9(8)°) [34] cohorts have been shown to exhibit considerable

discrepancies in hip ROM. Thus, *any* mounting location would be expected to resolve the large differences in ROM (13-23 and 21-31 degrees for flexion/extension and internal/external rotation, respectively) between healthy and FAI afflicted hips, irrespective of any likely skin artifact.

V. CONCLUSION

This study presents compelling evidence of the validity of the proposed IMU-based method for quantifying femoral orientation angles during the common clinical tests used to diagnose Femoroacetabular Impingement. This method provides levels of accuracy and precision superior to those advertised in commercial IMU systems and previously published IMU-based methods. Even after accounting for expected skin motion artifact, the method will likely discriminate between healthy and FAI afflicted hips. The method is easy to use, inexpensive and provides hip motion trajectory data in addition to range of motion measures. These advantages may accelerate the adoption of this technology to inform FAI diagnoses and assess treatment efficacy.

ACKNOWLEDGMENT

Many thanks to Alex Brunfeldt for preparation of the cadaveric specimens.

REFERENCES

- [1] M. Leunig and R. Ganz, "[FAI - concept and etiology]," *Orthop.*, vol. 38, no. 5, pp. 394–401, May 2009.
- [2] C. Ratzlaff, J. Simatovic, H. Wong, L. Li, A. Ezzat, D. Langford, J. M. Esdaile, C. Kennedy, P. Embley, D. Caves, T. Hopkins, and J. Cibere, "Reliability of Hip Examination Tests for Femoroacetabular Impingement," *Arthritis Care Res.*, vol. 65, no. 10, pp. 1690–1696, 2013.
- [3] A. Rimmasch and P. Ravert, "Femoroacetabular Impingement: A Guide to Diagnosis in Primary Care," *J. Nurse Pract.*, vol. 9, no. 9, pp. 606–611, Oct. 2013.
- [4] M. R. Safran, "Hip Arthroscopy: The Next Frontier in Orthopaedic Surgery and Its Challenges," pp. 21–22, Jan. 2009.
- [5] F. Dobson, Y. M. Choi, M. Hall, and R. S. Hinman, "Clinimetric properties of observer-assessed impairment tests used to evaluate hip and groin impairments: A systematic review," *Arthritis Care Res.*, vol. 64, no. 10, pp. 1565–1575, 2012.
- [6] J. M. Moreside and S. M. McGill, "Quantifying normal 3D hip ROM in healthy young adult males with clinical and laboratory tools: Hip mobility restrictions appear to be plane-specific," *Clin. Biomech.*, vol. 26, no. 8, pp. 824–829, Oct. 2011.
- [7] F. Öhberg, R. Lundström, and H. Grip, "Comparative analysis of different adaptive filters for tracking lower segments of a human body using inertial motion sensors," *Meas. Sci. Technol.*, vol. 24, no. 8, p. 085703, Aug. 2013.
- [8] J.-T. Zhang, A. C. Novak, B. Brouwer, and Q. Li, "Concurrent validation of Xsens MVN measurement of lower limb joint angular kinematics," *Physiol. Meas.*, vol. 34, no. 8, p. N63, Aug. 2013.
- [9] J. E. Langenderfer, P. J. Laz, A. J. Petrella, and P. J. Rullkoetter, "An efficient probabilistic methodology for incorporating uncertainty in body segment parameters and anatomical landmarks in joint loadings estimated from inverse dynamics," *J. Biomech. Eng.*, vol. 130, no. 1, p. 014502, Feb. 2008.
- [10] G. Wu, S. Siegler, P. Allard, C. Kirtley, A. Leardini, D. Rosenbaum, M. Whittle, D. D. D'Lima, L. Cristofolini, H. Witte, O. Schmid, and I. Stokes, "ISB recommendation on definitions of joint coordinate system of various joints for the reporting of human joint motion—part I: ankle, hip, and spine," *J. Biomech.*, vol. 35, no. 4, pp. 543–548, Apr. 2002.
- [11] A. Leardini, L. Chiari, U. Della Croce, and A. Cappozzo, "Human movement analysis using stereophotogrammetry. Part 3. Soft tissue artifact assessment and compensation," *Gait Posture*, vol. 21, no. 2, pp. 212–225, Feb. 2005.
- [12] J. Favre, R. Aissaoui, B. M. Jolles, J. A. de Guise, and K. Aminian, "Functional calibration procedure for 3D knee joint angle description using inertial sensors," *J. Biomech.*, vol. 42, no. 14, pp. 2330–2335, Oct. 2009.
- [13] J. Favre, B. M. Jolles, R. Aissaoui, and K. Aminian, "Ambulatory measurement of 3D knee joint angle," *J. Biomech.*, vol. 41, no. 5, pp. 1029–1035, 2008.
- [14] H. Rouhani, J. Favre, X. Crevoisier, and K. Aminian, "Measurement of Multi-segment Foot Joint Angles During Gait Using a Wearable System," *J. Biomech. Eng.*, vol. 134, no. 6, pp. 061006–061006, Jun. 2012.
- [15] A. V. Dowling, J. Favre, and T. P. Andriacchi, "A Wearable System to Assess Risk for Anterior Cruciate Ligament Injury During Jump Landing: Measurements of Temporal Events, Jump Height, and Sagittal Plane Kinematics," *J. Biomech. Eng.*, vol. 133, no. 7, pp. 071008–7, Jul. 2011.
- [16] T. Seel, J. Raisch, and T. Schauer, "IMU-Based Joint Angle Measurement for Gait Analysis," *Sensors*, vol. 14, no. 4, pp. 6891–6909, Apr. 2014.
- [17] S. Šlajpah, R. Kamnik, and M. Munih, "Kinematics based sensory fusion for wearable motion assessment in human walking," *Comput. Methods Programs Biomed.*, vol. 116, no. 2, pp. 131–144, Sep. 2014.
- [18] E. Jovanov, A. Milenkovic, C. Otto, and P. C. de Groen, "A wireless body area network of intelligent motion sensors for computer assisted physical rehabilitation," *J. NeuroEngineering Rehabil.*, vol. 2, no. 1, p. 6, Mar. 2005.
- [19] W. Y. Wong, M. S. Wong, and K. H. Lo, "Clinical Applications of Sensors for Human Posture and Movement Analysis: A Review," *Prosthet. Orthot. Int.*, vol. 31, no. 1, pp. 62–75, Mar. 2007.
- [20] A. Brennan, J. Zhang, K. Deluzio, and Q. Li, "Quantification of inertial sensor-based 3D joint angle measurement accuracy using an instrumented gimbal," *Gait Posture*, vol. 34, no. 3, pp. 320–323, Jul. 2011.
- [21] R. Williamson and B. J. Andrews, "Detecting absolute human knee angle and angular velocity using

- accelerometers and rate gyroscopes,” *Med. Biol. Eng. Comput.*, vol. 39, no. 3, pp. 294–302, May 2001.
- [22] A. Cappozzo, F. Catani, U. Della Croce, and A. Leardini, “Position and orientation in space of bones during movement: anatomical frame definition and determination,” *Clin. Biomech.*, vol. 10, no. 4, pp. 171–178, Jun. 1995.
- [23] R. A. Siston and S. L. Delp, “Evaluation of a new algorithm to determine the hip joint center,” *J. Biomech.*, vol. 39, no. 1, pp. 125–130, 2006.
- [24] H. J. Woltring, “A Fortran package for generalized, cross-validatorspline smoothing and differentiation,” *Adv. Eng. Softw.* 1978, vol. 8, no. 2, pp. 104–113, Apr. 1986.
- [25] K. W. King, “The design and application of wireless MEMS inertial measurement units for the measurement and analysis of golf swings,” PhD, University of Michigan, Ann Arbor, MI, 2008.
- [26] R. S. McGinnis and N. C. Perkins, “A highly miniaturized, wireless inertial measurement unit for characterizing the dynamics of pitched baseballs and softballs,” *Sensors*, vol. 12, no. 9, pp. 11933–11945, Aug. 2012.
- [27] J. Favre, B. M. Jolles, O. Siegrist, and K. Aminian, “Quaternion-based fusion of gyroscopes and accelerometers to improve 3D angle measurement,” *Electron. Lett.*, vol. 42, no. 11, pp. 612–614, May 2006.
- [28] H. J. Luinge, P. H. Veltink, and C. T. M. Baten, “Ambulatory measurement of arm orientation,” *J. Biomech.*, vol. 40, no. 1, pp. 78–85, 2007.
- [29] H. M. Schepers, D. Roetenberg, and P. H. Veltink, “Ambulatory human motion tracking by fusion of inertial and magnetic sensing with adaptive actuation,” *Med. Biol. Eng. Comput.*, vol. 48, no. 1, pp. 27–37, Jan. 2010.
- [30] A. Brennan, K. Deluzio, and Q. Li, “Assessment of anatomical frame variation effect on joint angles: A linear perturbation approach,” *J. Biomech.*, vol. 44, no. 16, pp. 2838–2842, Nov. 2011.
- [31] P. Picerno, A. Cereatti, and A. Cappozzo, “Joint kinematics estimate using wearable inertial and magnetic sensing modules,” *Gait Posture*, vol. 28, no. 4, pp. 588–595, Nov. 2008.
- [32] A. Cappozzo, F. Catani, A. Leardini, M. G. Benedetti, and U. D. Croce, “Position and orientation in space of bones during movement: experimental artefacts,” *Clin. Biomech. Bristol Avon*, vol. 11, no. 2, pp. 90–100, Mar. 1996.
- [33] D. J. Magee, *Orthopedic Physical Assessment*. Elsevier Health Sciences, 2008.
- [34] J. C. Clohisy, E. R. Knaus, D. M. Hunt, J. M. Leshner, M. Harris-Hayes, and H. Prather, “Clinical Presentation of Patients with Symptomatic Anterior Hip Impingement,” *Clin. Orthop.*, vol. 467, no. 3, pp. 638–644, Jan. 2009.

Investigation of Sensor-based Quantitative Model for Badminton Skill Analysis and Assessment

Chew Zhen Shan^a, Sim Lee Sen^a, Yeong Che Fai^{b*}, Eileen Su Lee Ming^a

^aFaculty of Electrical Engineering, Universiti Teknologi Malaysia, 81310 UTM Johor Bahru, Johor, Malaysia

^bCentre for Artificial Intelligence and Robotics, Faculty of Electrical Engineering, Universiti Teknologi Malaysia, 81310 UTM Johor Bahru, Johor, Malaysia

*Corresponding author: cfyong@fke.utm.my

Article history

Received :15 June 2014
Received in revised form :
15 September 2014
Accepted :15 October 2014

Graphical abstract



Abstract

Badminton is one of the most popular sports in Malaysia. The main aim of this project is to investigate sets of movements in badminton training using sensors, to identify the good movement that enhance badminton performance. In addition, this project also aims to identify measurable parameters to quantify badminton skill levels. The performance of elite players will be studied to identify benchmark values for these measurable parameters. A quantitative model will be proposed using these measurable parameters to help in the objective assessment of skill levels. Findings of this project will help badminton players to improve their techniques, as well as providing an objective measurement to assess badminton skills.

Keywords: Badminton; skill assessment; wireless sensor; inertia measurement unit; movement analysis

© 2015 Penerbit UTM Press. All rights reserved.

1.0 INTRODUCTION

The Badminton World Federation estimated about 150 million people play badminton worldwide and more than 200 players participate in international competition [1]. Badminton is listed as top three of Malaysian most popular game. Most of Malaysian grown up playing Badminton, but only less than 10 Badminton athletics listed in top 100 players in BWF (Badminton World Federation) ranking [2]. Studies have shown that exercises using different joints surprisingly showed similar muscle activation and that strength training was not helpful for functional tasks that involved multiplanar movements [3]. Therefore, it is crucial to study specific exercises for specific type of sports.

A research on several movement-based or “functional” exercises has been carried out to assess their effect on technique change [4]. The exercises investigated included walkout in sagittal plane, overhead cable pushes, lateral cable walkouts, the good morning exercise and the bowler’s squat. It was found that despite the activities being rather strenuous, muscle activation levels were relatively modest. In addition, the exercises uses similar joint moments but the patterns of activity between muscles were different. The study further conclude that strength training muscles may not help in functional multiplanar tasks. Data from this study indicated that selection of exercise and movements are crucial for performance enhancement. In the context of badminton players, those at their beginning of training may require different sets of exercises from those who are at the intermediate level or subsequent higher levels.

Researches had been carried out to analyze the movement by athletics through the years. Efforts at player motion tracking have traditionally involved a range of data collection techniques from live observation to post-event video analysis where player movement patterns are manually recorded and categorized to determine performance effectiveness [5]. Two most popular solutions are highlighted here. Firstly, a precise system that required high speed video camera and markers to record the athletics’ motion like Marker Instrumented Player [6]. Secondly, wireless inertial measurement unit that is portable and usable at any environment like Opal sensor from APDM, Inc [7]. There are custom-made products such as Zepp Tennis [8] for tennis players, developed by Zepp US Inc to track the useful data like power, spin, court time and connect with APPLE I-Pad to get the instant feedback. At the same time, Sony Corporation had announced the prototype of smart tennis sensor [9] at CES2014 which can detect the speed of the ball hit on the racket.

A review of vision-based motion analysis in sport study by Sian Barris had mention that problem of current motion analysis system by using video recording or motion capture such as TRAKUSTM, SoccerManTM, TRAKPERFORMANCETM, PfinderTM and ProzoneTM is hard to apply at crowded place, often compounded by the quality of video capture, the relative size and occlusion frequency of people, and also changes in illumination [5]. Besides that, Inertial measurement unit or IMU had the advantage of high sample rate, tiny size and weight so it wouldn’t affect player’s performance much, no hidden spot, portable, low cost and suitable to use at real training condition. IMU is widely

used on vibration and impact detection, low velocity movement like gait and jogging, and detect orientation.

Hassan Ghasemzadeh had introduce a sensor-based quantitative model which takes into consideration signal processing techniques on the collected data and quantifies the correctness of the performed actions by a Golf player [10]. Linear projection methods, PCA and LDA which used as classification and dimension reduction technique used in this project to build a regression model which can provide feedback on quality of movements for the purpose of training. The model is able to provide information on quality of golf swing with respect to angle of wrist rotation. This model is good for gather the information on quality of swinging movements with the player wrist rotation which is suitable to apply on Badminton game but this method required at least five sensors to collect enough data for accurate analysis.

Thomas Jaitner and Wolf Gawin had develop a mobile device to quantify the influence of variables that describe movement of arm on parameters of racket acceleration and shuttlecock speed by using Pearson's correlation analysis [11]. He stated that about 70% of the variance of the shuttle velocities can be explained by the acceleration of the racket. And the remaining 30% might be explained by racket properties such as string stiffness and string gauge. Gowitzke also stated that around 53% of shuttle velocity can be explained by the last rotation performed by shoulder and elbow [12].

El-Gohary proposed to combine kinematic models designed for control of robotic arms with state-space methods to directly and continuously estimate human joint angles from inertial sensors [13]. They developed an inertia tracking algorithm and compare with unscented Kalman filter (UKF) based method. These algorithms can be applied to any combination of synchronized sensors and suitable for both regular and fast speed movement.

Despite sensor for motion analysis being widely available, sensor-based assessment for badminton skill is currently unavailable. Since badminton is one of the most thriving sports in Malaysia, it is reasonable to investigate methods to make it easier to train more badminton players without being too dependent on the availability of expert coaches. Players who do not have coaches to train them could use these sensors to rate their own performance, improve their skills while avoiding movements that will lead to long term injuries. Even players with coaches sometimes have to train on their own without supervision and these sensors could help record their data for real-time feedback or post-analysis.

The main aim of this project is to investigate and create a database of sets of movements in badminton training to differentiate the good movements that enhance performance from the bad movements which potentially lead to musculoskeletal injuries. Besides investigation sets of movements in badminton training, this project also aims to identify crucial kinematics parameters to quantify badminton skill levels. The performance of elite players will be studied to identify benchmark values for these measurable parameters. A quantitative model will be proposed using these measurable parameters to help in the objective assessment of skill levels. This will help badminton players to improve their techniques and prevent some sports injuries, as well as providing an objective measurement to assess badminton skills.

2.0 METHODOLOGY

2.1 Interview Section

Interview had been conducted for three badminton players comprising a state elite player, a coach and a casual player. Some useful information had been obtained about training and expectation on modern techniques. From these interviews, we found that the conventional badminton training is focused on skill and stamina training. The badminton coach stated that the modern training technology should be able to track the position of shutter lock and player location to determine the agility and skill of a player. Several algorithms need to be proposed and tested in producing the most precise and accurate evaluation of badminton players movements. The best way to achieve this is through collaboration with BAM (Badminton Association Malaysia), sports center, players and coach where pilot study can be conducted and feedbacks can be obtained from groups of interest.

2.2 Hardware sourcing

An inertial measurement unit, or IMU, is an electronic device that measures and reports on a craft's velocity, orientation, and gravitational forces, using a combination of accelerometers and gyroscopes, sometimes also magnetometers. IMUs are typically used to manoeuvre aircraft, including unmanned aerial vehicles (UAVs), among many others, and spacecraft, including satellites and landers. Recent developments allow for the production of IMU-enabled GPS devices. An IMU allows a GPS receiver to work when GPS-signals are unavailable, such as in tunnels, inside buildings, or when electronic interference is present. In this project, a wireless IMU device will be used to collect data from athletics.

Opal sensor from APDM INC. [9] had been selected in this project. Opal sensor is a miniature, wireless inertial measurement unit that can both log kinematic data and stream it in real-time continuously for over 8 hours. A wireless network of up to 24 Opals is possible, maintaining time-synchronization of ≤ 1 ms between Opals. WIMU like Opal sensor is useful to collect the kinematics value from athletics. Zepp Tennis sensor and X-IMU sensors also been considered in this project to validate the Opal sensor.

2.3 Experiment Setup

Experiments had been conducted for the purpose to validate the selected sensor and for data collection for smash performance. Figure 1 shows the axis of selected WIMU.

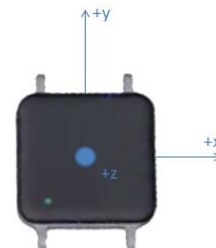


Figure 1 Axis of APDM Opal sensor

Then the sensors are attached on wrist and right arm of the subject as shown in Figure 2 where sensor A is attached on the arm and sensor B is attached on the wrist.

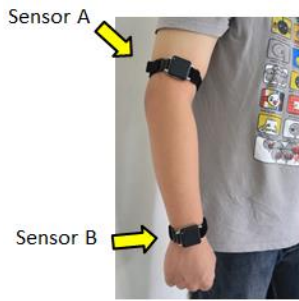


Figure 2 Opal sensor are attached on subject's arm and wrist

2.3.1 Experiment 1–Swing hand 180° upward

The objective of this experiment is to provide a simple movement that can be used as references for other complicated Badminton stroke like smashing. This experiment also aims to validate the Opal sensor. Figure 3 shows that the subject swinging hand upwards around 180°. The swinging are repeated 4 times.



Figure 3 Flow of Experiment 1

3.0 RESULTS AND DISCUSSIONS

In this project, the Opal sensors which are attached on subject's body are used to measure the kinematics parameters like acceleration, rotational velocity, magnetic force, temperature and orientation. Then, there are a APDM station that play the role to collect data via Bluetooth technique and transfer it to a PC application called APDM Motion Studio.

3.1 Data Analysis

The collected data during Experiment 1 is shown in Figure 4 where Sensor A represent the Arm Sensor and Sensor B represent the wrist sensor. From the graph, we can observe that there are total 4 minor changes for all accelerometer, gyroscope and magnetometer which show that the 4 swinging performed by subject in experiment 1.

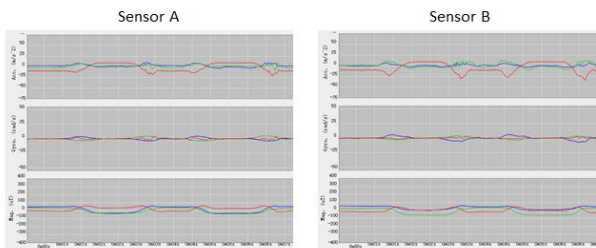


Figure 4 Acceleration, rotational velocity and magnetic impact of sensor A and sensor B

Then, from the collected orientation value, Euler angle had been calculated by using MATLAB. From Figure 5, we can clearly observe that there are around 180° swinging for 4 times in the graph.

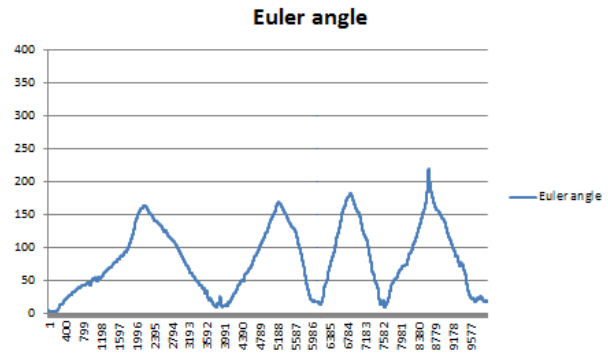


Figure 5 Euler angle of Experiment 1

From this experiment, we observed that the sensor is stable and validate for further study and experiments in this project due to its accuracy and the data of this experiment will become the references of future experiment such as smashing movement and etc.

4.0 CONCLUSIONS

From this stage of study, the most expected outcome is to identify the benchmark value of crucial parameters that affected player's skill performance, an objective assessment is expected in this project. A study and review of investigation of sensor-based quantitative model for badminton skill analysis and assessment need to be continuing more in depth. The full training model for the purpose of improve player skill is expected in the future research. Other experiments which is focus on Badminton stroke like smashing, clear, drop and service will be conducted among larger population of sample subject who involve various level Badminton player from casual player to professional player. Position of player on the game court should be detected in future research to obtain a more completed automatic Badminton skill evaluation system.

Acknowledgement

The authors would like express their gratitude to Universiti Teknologi Malaysia. This work is supported by the Universiti Teknologi Malaysia Research grant 04H66 and 08J91.

References

- [1] Badminton World Federation. Players worldwide. In: Badminton World Federation [online]. Available at: old.internationalbadminton.org/players.asp. Accessed April 10, 2014.
- [2] Badminton Association Malaysia [online]. Available at: http://www.bam.org.my/index.php?option=com_content&view=article&id=4373:2014tahun-transformasi-buat-bam&catid=46:latest-news&Itemid=181 Accessed November 25, 2014.
- [3] Shariff, A H., George, J. and Ramlan, A. 2009. Musculoskeletal Injuries Among Malaysian Badminton Players. *Singapore Med J.* 50(11): 1095
- [4] McGill, S., Karpowicz, A., Fenwick, C. and Brown, S. 2009. Exercises for the Torso Performed in a Standing Posture: Spine and Hip Motion and Motor Patterns and Spine Load. *Journal of Strength and Conditioning Research.* 23: 455–464.

- [5] Sian, B. and Chris, B. 2008. A Review of Vision-Based Motion Analysis in Sport. *Sports Medicine*. 38(12): 1025–1043.
- [6] Michael, T. L. 2008. A Wearable, Wireless Sensor System for Sports Medicine. Massachusetts Institute of Technology.
- [7] OPAL, APDM, INC, [online] 2014, <http://apdm.com/Wearable-Sensors/Opal> (Accessed: 10 April 2014).
- [8] ZEPP TENNIS, ZEPP, INC, [online] 2014, <http://www.zepp.com/tennis>.
- [9] Sony Tennis Sensor, Trusted reviews [online] 2014, http://www.trustedreviews.com/sony-tennis-sensor_Gadget_review.
- [10] Hassan Ghasemzadeh, Vitali Loseu, Eric Guenterberg, Roozbeh Jafari, Sport Training Using Body Sensor Networks: A Statistical Approach to Measure Wrist Rotation for Golf Swing, /ICST.BODYNETS2009.6035.
- [11] T. Jaitner, W. Gawin. (2010). A Mobile Measure Device for the Analysis of Highly Dynamic Movement Techniques. *Procedia Engineering* 2. 3005–3010.
- [12] Gowitzke, B. A. and Waddell, D. B. 1977. The Contributions of Biomechanics in Solving Problems in Badminton Stroke Production. *International Coaching Conference Malmo*.
- [13] El-Gohary, Mahmoud, McNames, James. 2012. Shoulder and Elbow Joint Angle Tracking With Inertial Sensors. *IEEE Transactions on Bio-medical Engineering*. 2635–2641.

Objective and personalized longitudinal assessment of a pregnant patient with post severe brain trauma

Elizabeth B. Torres^{1*} and Brian Lande²

¹ Department of Psychology, Computational Biomedicine Imaging and Modeling Center, Computer Science, Neuroscience and Rutgers Center for Cognitive Science, Rutgers the State University of New Jersey, New Brunswick, NJ, USA,

² Department of Computer Science, University of California, Santa Cruz, CA, USA

OPEN ACCESS

Edited by:

Marta Olivetti,
Sapienza University of Rome, Italy

Reviewed by:

Jorge V. Jose,
Indiana University, USA
Joaquin Santolaya,
Robert Wood Johnson Medical
School, USA

*Correspondence:

Elizabeth B. Torres,
Department of Psychology,
Computational Biomedicine Imaging
and Modeling Center, Computer
Science, Neuroscience and Rutgers
Center for Cognitive Science, Rutgers
the State University of New Jersey,
Rutgers University-Psychology Dept.
Busch Campus., 152 Frelinghuysen
Rd, New Brunswick, NJ 08854, USA
ebtorres@rci.rutgers.edu

Received: 06 December 2014

Paper pending published:

04 February 2015

Accepted: 24 February 2015

Published: 17 March 2015

Citation:

Torres EB and Lande B (2015)
Objective and personalized
longitudinal assessment
of a pregnant patient with post
severe brain trauma.
Front. Hum. Neurosci. 9:128.
doi: 10.3389/fnhum.2015.00128

Background: Following severe trauma to the brain (whether internally generated by seizures, tumors or externally caused by collision with or penetration of objects) individuals may experience initial coma state followed by slow recovery and rehabilitation treatment. At present there is no objective biometric to track the daily progression of the person for extended periods of time.

Objective: We introduce new analytical techniques to process data from physically wearable sensors and help track the longitudinal progression of motions and physiological states upon the brain trauma.

Setting and Participant: The data used to illustrate the methods were collected at the hospital settings from a pregnant patient in coma state. The patient had brain trauma from a large debilitating seizure due to a large tumor in the right pre-frontal lobe.

Main Measures: We registered the wrist motions and the surface-skin-temperature across several daily sessions in four consecutive months. A new statistical technique is introduced for personalized analyses of the rates of change of the stochastic signatures of these patterns.

Results: We detected asymmetries in the wrists' data that identified in the dominant limb critical points of change in physiological and motor control states. These patterns could blindly identify the time preceding the baby's delivery by C-section when the patient systematically brought her hand to her abdominal area. Changes in temperature were sharp and accompanied by systematic changes in the statistics of the motions that rendered her dominant wrist's micro-movements more systematically reliable and predictable than those of the non-dominant wrist.

Conclusions: The new analytics paired with wearable sensing technology may help track the day-by-day individual progression of a patient with post brain trauma in clinical settings and in the home environment.

Keywords: coma, pregnancy, brain trauma, wearable sensors, analytics, statistics

Introduction

According to the Centers for Disease Control (CDC) severe trauma to the brain is a contributing factor to a third (30%) of all injury-related deaths in the US (Carroll et al., 2012; Centers for Disease Control and Prevention (CDC), 2013), thus posing a large societal and economic toll (Finkelstein et al., 2006). Non-fatal brain trauma may result in immediate unconsciousness (coma) and amnesia states followed by slow recovery with subsequent extended periods of impairments in one or more general functional areas. Trauma may be due to internal insult caused by seizures, tumors, among other factors. Trauma may also be due to collision with an external object (static or in motion). Different prognosis and subsequent states emerge from different types of injuries to the brain. These may include impaired cognitive and/or motor functions as well as impaired sensations and/or emotional responses. Physicians and researchers now generally recognize that the spectrum of disorders related to coma can be more broadly defined as a range of disorders of consciousness (DOC) that can be mapped onto a multi-dimensional space primarily defined by cognitive and motor impairments.

In many cases the initial coma state may evolve towards improved levels of consciousness and physical function such as a minimally conscious state (MCS). To assess coma and impaired consciousness in the early stages of post brain trauma there are several clinical tools based on reports from observation. These include the Glasgow Coma Scale (GCS), Coma Recovery Scale—Revised (CRS-R), the Abbreviated Injury Scale (AIS) and the Trauma Score or Abbreviated Trauma Score, among others. These observational tools can also be used to track progress while at the hospital or during subsequent visits, in cases where the patient improves and undergoes rehabilitation at home. Other tools used in the hospital settings include objective assessments of the brain condition using imaging techniques. The use of these techniques is however limited to a few times per year, due primarily to their cost and regional availability.

Upon recovery from the initial coma state, many patients undergo rehabilitation and eventually return home to be looked after by a caregiver and to continue receiving therapy. At that stage there are presently no objective tracking tools to help the caregivers, and/or the occupational and physical therapists assess the daily progression of the patient in response to treatments. The current assessments to track physical progress rely primarily on observation (e.g., the use of inventories such as the Western Neuro Sensory Stimulation Profile, WNSSP among others). Yet the human eye has limited capacity to detect subtle changes in physical motions that could signal improvement, or call for immediate attention to some sharp change in physiological states. For example, physicians and therapists look for eye opening to detect changes in arousal and behavioral command following and/or changes in spontaneous/reflexive movement to detect changes in awareness. Diagnoses of changes in states of awareness or arousal based on clinical observation alone have high rates of diagnostic error, approximately 40% (Schnakers et al., 2009). There is no way to objectively track the longitudinal

rate of change of the person's patterns so critical information is being missed that could help the patient and caregivers cope. In particular health insurance companies require evidence-based improvements for coverage of therapies but under the present observational methods it is a challenge to report accurate and reproducible results.

With the advent of wearable sensing technology it may be possible to use motion tracking in combination with other physiologically relevant signals (temperature, electrodermal activity, heart beat variability, etc.) to help medical personnel and care givers assess the patient's mental and physical states daily, as they fluctuate, both during the hospitalization period and after discharge, when the patient goes into rehabilitation.

Wearable sensors are now ubiquitous in our lives. They are present in our smart phones, smart tablets, wellness and fitness bracelets, etc. Yet the current analytical techniques embedded in such devices have been recently called into question as somewhat inaccurate and occasionally misleading. Such methods may be acceptable to track fitness and wellness, but they may lack the reliability necessary to be adopted as standard metrics in the clinical domain. New analytical techniques to be embedded in wearable sensors are needed to help caregivers and medical personnel track the evolution of patients with severe post trauma to the brain. In this paper we introduce new personalized statistical methods that may be of help in tracking the progression of patients with brain trauma (independent of the type of trauma involved). We illustrate the methods with data from a pregnant patient who underwent severe brain trauma, slipped into a coma and had her baby successfully delivered by C-section.

Methods

All methods and measurements presented in this study have been approved by the Rutgers IRB Committee in accordance with the Helsinki Act.

Patient

Timeline of the Patient as Reported by Her Doctors

AB is a 39-year-old, right handed woman who was pregnant when diagnosed with a grade 2 oligoastrocytoma on 03/05/14 after worsening headaches, fatigue, nausea and some degree of confusion which prompted an MRI scan. The MRI revealed on 03/07/14 a right frontal lobe mass lesion (8.5×5) with characteristics suggestive of oligodendroglioma. Surgical excision was recommended by the neurologist and scheduled for 03/12/14 in consultation with her high-risk Ob/Gyn. On the morning of 03/13/14 AB suffered an acute neurological decompensation with loss of consciousness and nonreactive dilated right pupil, sluggishly responsive pupil and decorticate posturing. It was thought that she had a seizure. She was intubated and given Mannitol and hyperventilated for probable increased intracranial pressure. A STAT CT of the brain revealed cerebral edema with uncal herniation. She underwent surgical decompression, a right hemicraniectomy with tumor debulking (see **Figure 1** showing brain after surgical removal of the

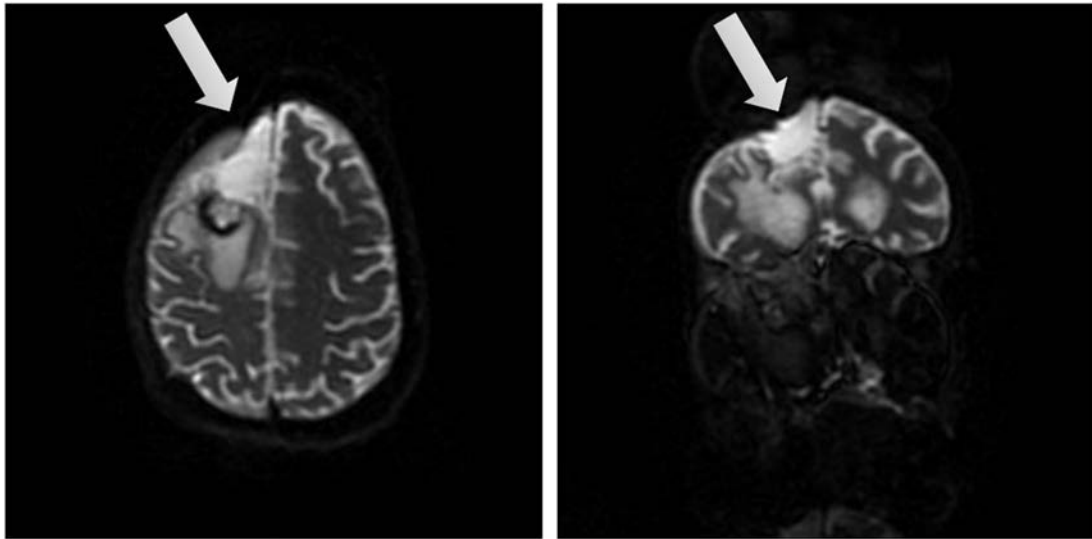


FIGURE 1 | Brain views after tumor removal. Two different views of the right frontal lobe upon removal of the tumor (affected area marked by arrow).

tumor). EEG upon surgery did not reveal seizure activity. Postoperative exams included decerebrate posturing, CT and MRI. These tests revealed extensive hemorrhagic infarct or cytotoxic edema involving multiple vascular territories in the bilateral parietal temporal and occipital lobes, as well as bilateral (right more than left) thalami. Small foci of ischemia were also found on the right mid-brain, pons and right cerebellar hemisphere.

During the first week post-operation, AB remained unconscious. Her GCS was 3. Even under comatose state she displayed spontaneous eye opening and movements in the extremities. Some examiners reported hand movement on command on 03/20/14, but subsequent reports have been inconclusive, possibly due to delays in response and inconsistencies in responses. On 03/20/14 an external ventricular drain was camped. An MRI on 03/23/14 revealed interval development of a large pseudomeningocele at the right hemicraniectomy site. The external ventricular drain was removed on 03/24/14.

On 05/22/14 AB underwent a C-section delivery of a healthy baby boy. On 05/28/14 a percutaneous endoscopic jejunostomy tube was placed. She was transferred from the hospital to a rehabilitation hospital for neurorehabilitation.

At the hospital she had fever on 06/25/14 due to an infection. She underwent a course of antibiotics. A clot in her IVC was revealed by ultrasound on 06/26/14. She was fully anticoagulated prophylactically and fully anticoagulated with Lovenox.

Patient AB is on a trach collar. Her ABG on 06/30/14 showed adequate oxygenation. Her weekly scores on the WNSSP from June 4th 2014 till October 8th 2014 are reported on **Table 1**. The discharge medications are reported below.

Discharge Medications

Medications administered per feeding tube: Amantadine 150 mg, 50 mg in the AM and 100 mg noon; Desmopressin 0.1 mg

TABLE 1 | Weekly scores from the Western Neuro Sensory Stimulation Profile (WNSSP) commonly used to track changes in neural sensory processing.

Month	(Day) WNSSP				
June	(4) 11	(11) 10	(18) 26	(25) 27	
July	(2) 27	(10) 22	(17) 22	(24) 22	(31) 29
August	(6) 13	(13) 14	(20) 5	(27) 17	
September	(3) 7	(10) 3	(17) 10	(24) 3	
October	(1) 9	(8) 14			

per day; Docusate 2 mg per day; Ferrous sulfate 300 mg; Folic acid 1 mg; Glycopyrrolate 0.5 mg; Keppra 1000 mg; Multivitamin (1 tablet); Potassium chloride 20 mEq; Senna two tabs; Vitamin D3 2000 IU; Aquatears to both eyes four times a day; Chlorhexidine 15 ml for oral care 4 times daily; Meropenem 1 g IV q 8.

Medications administered by subcutaneous bid: Enoxaparin 50 mg and Vancomycin 1 g IV.

Measurements

The wrist motions of patient AB were continuously captured in various daily sessions across the months of April till July 2014 using inertial measurement units IMU (APDM opal, Portland, OR). These IMU register linear and angular acceleration, a signal related to surface skin temperature, gyroscopic data, and magnetometer data at 128 Hz. The units are synchronized and operate through wireless technology in live streaming mode and also in robust logging mode. The former enables real time visualization of the synchronous data with no loss of data, while the latter allows the same without visualization of the recordings streamed in real time. We report data from the right and left wrists of the patient, synchronously recorded in robust logging mode (no data loss). Each session comprises several hours.

TABLE 2 | Number of hours recorded by the APDM sensors per each day session across the 4 months.

	Day, hours		Day, hours		Day, hours		Day, hours		Day, hours		Day, hours			
April	24	7.09	25	7.22	26	7.16	29	6.41						
May	3	9.45	6	12.56	8	12.28	11	3.45	13	6.26	17	6.74	27	12.24
June	5	3.57	8	11.33	12	7.32	20	13.29						
July	1	9.34	9	7.06	12	9.43	15	4.32	17	5.37	19	7.14		

Table 2 provides information on the number of hours per session when the data were registered. We describe statistical features of the data using new biometrics that connect acceleration-dependent motion and temperature-dependent data.

Biometrics

The motion patterns were analyzed along with those of the temperature values, both registered simultaneously by the sensors. We focus our analyses on the linear acceleration obtained from the tri-axial linear accelerometers. To this end we first express the linear acceleration as the time series of the norm of the three-dimensional vector of accelerations expressed as a function of the temperature range in each section. The patterns of variability of the maximal instantaneous deviations of the acceleration from the overall mean acceleration across the session were examined using distributional analyses previously described in other work involving velocity- and acceleration dependent signals (Torres, 2011, 2013a,b; Torres et al., 2013, 2014). **Figure 2** shows representative data from the patient's wrists. The location of the sensors is circled on the patient's wrists in **Figure 2A**. **Figure 2B** shows the plots of the tri-axial acceleration profiles over several hours obtained on April 24th 2014 (see also **Table 2**). **Figure 2C** shows the profiles of temperature registered by the sensors while **1D** shows the acceleration profiles. These are built as the time series of the instantaneous norm of the acceleration vector, $accel = \sqrt{(\vec{a}_1)^2 + (\vec{a}_2)^2 + (\vec{a}_3)^2}$ in a given session. Here the a_i are the tri-axial components along the x , y , and z axes.

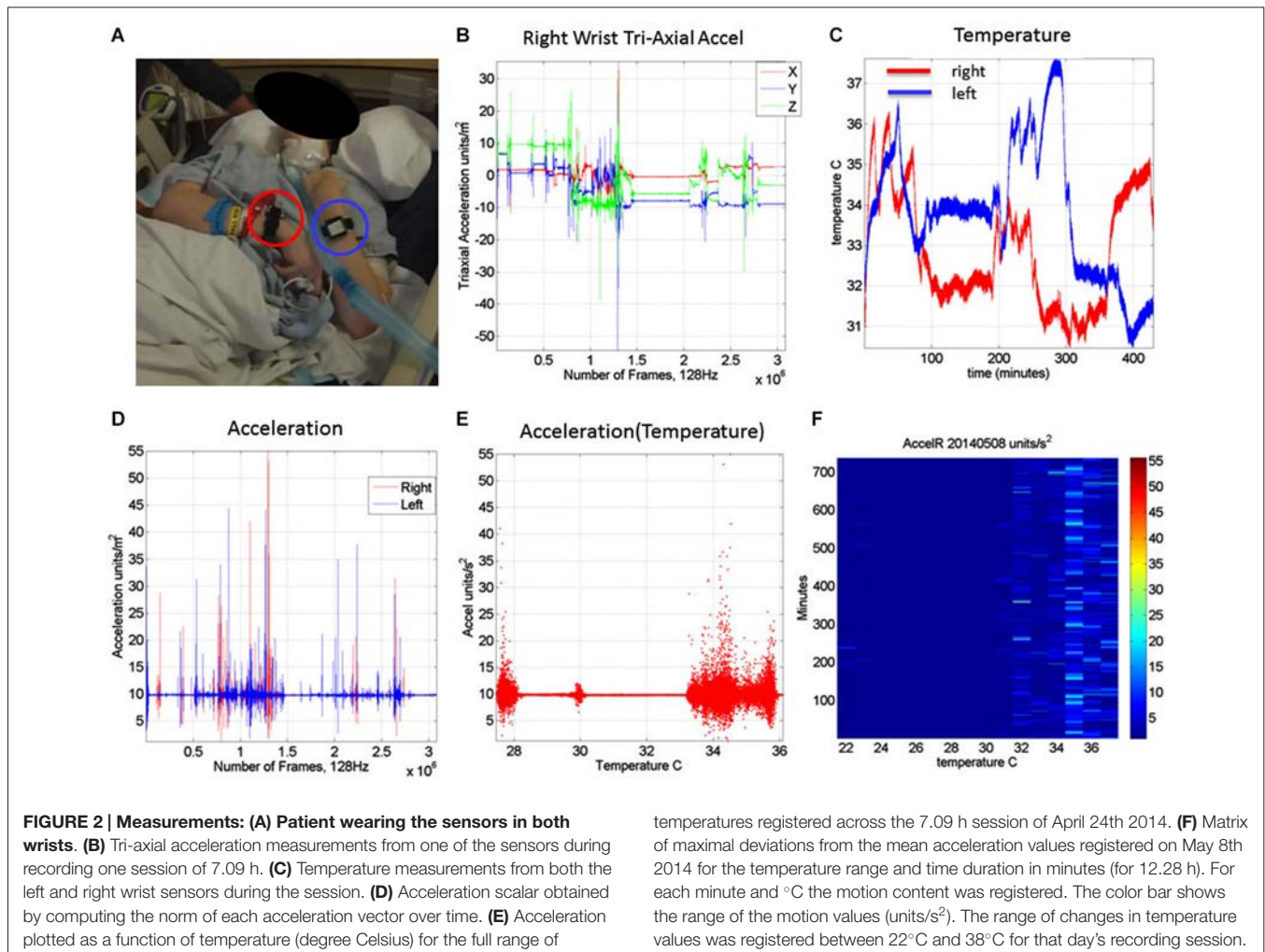
Figure 2E shows the scalar acceleration expressed as a function of the temperature range registered by the sensors. We take the mean acceleration value and the instantaneous maximal deviation from the overall mean of the session. These profiles are then obtained as a function of temperature. For each minute of the session all samples of the maximal deviation from the mean acceleration are obtained and plotted in matrix form in **Figure 2F** (shown for a session in May 8th 2014) for 12.28 h (739.6 min shown along the rows). The columns of the matrix show one-degree Celsius intervals spanning the range of temperatures for that session. Notice that the temperature output includes the skin surface temperature, the ambient temperature and the internal temperature of the sensors' battery as it drains when motions are being registered. The color of each entry in the matrix reflects for each minute and degree interval the maximal amount of motion deviating from the mean acceleration (see color bar) in units/s². **Figure 3** illustrates the steps followed to build these matrices. The acceleration and temperature data is first harnessed in one-minute-long intervals (128 Hz × 60 s, 7,680 registered frames). For each

degree the range of motion registered is obtained over time. The example in **Figure 3** shows this for the 34–35°C-interval. All motion data occurring in that interval is harnessed (inset in right panel). Then for each minute and each °C the maximal deviation from the mean acceleration is obtained. Across the minutes and degrees, these are the entries of the matrix depicted in **Figure 3**. The color indicates the amount of motion maximally deviating from the mean acceleration of the session on May 8th.

In **Figure 4** we continue to use the May 8th matrix to further illustrate the methods. We use the range from 33–35°C to show the statistics of the motion. For each °C we count the number of maximal deviations (peaks) across the session (6.26-h or 375 min along the rows of the matrix) and gather them in a frequency histogram. For each of the histograms representing the motions for each °C-interval we then fit a probability distribution function. Using maximum likelihood estimation (MLE) we obtain estimates of the shape (a) and the scale (b) parameters of the Gamma probability distribution with 95% confidence intervals. (We have used the continuous Gamma family of probability distributions in previous work to characterize the range of human motion variability across a range of neurological disorders and typical motions). From the Gamma estimated parameters we obtain the Gamma statistical parameters (mean and variance) and plot them on a (μ , σ)-plane. Each point represents the Gamma statistical parameters of the acceleration-dependent motions for a temperature °C-interval taken across the time length of the session.

Noise-to-Signal Ratio Analyses

We also use for each minute (comprising the 60 s × 128 Hz frames per minute) the above mentioned approach to obtain for each entry in the matrix the Fano Factor. This is the variance divided by the mean, the noise to signal ratio. The resulting noise-to-signal ratio matrix corresponding to the motion matrix for the May 8th session is shown in **Figure 5A** bottom panel. Notice here that at 25°C the highest noise-to-signal level is revealed. **Figure 5B** shows the frequency histograms for each of the 11 columns of the matrix corresponding to each °C-interval. We mark the regimes with the highest (blue star) and lowest (red star) noise levels detected at 25°C and 32°C respectively. This immediately alerts us that not all motion from the accelerometers is physiologically relevant. At 25°C for example this session reveals a pattern of motion whereby the motion noise registered by these accelerometers overpowers the signal. The range from 33–35°C used in **Figure 4** to illustrate the methods are also



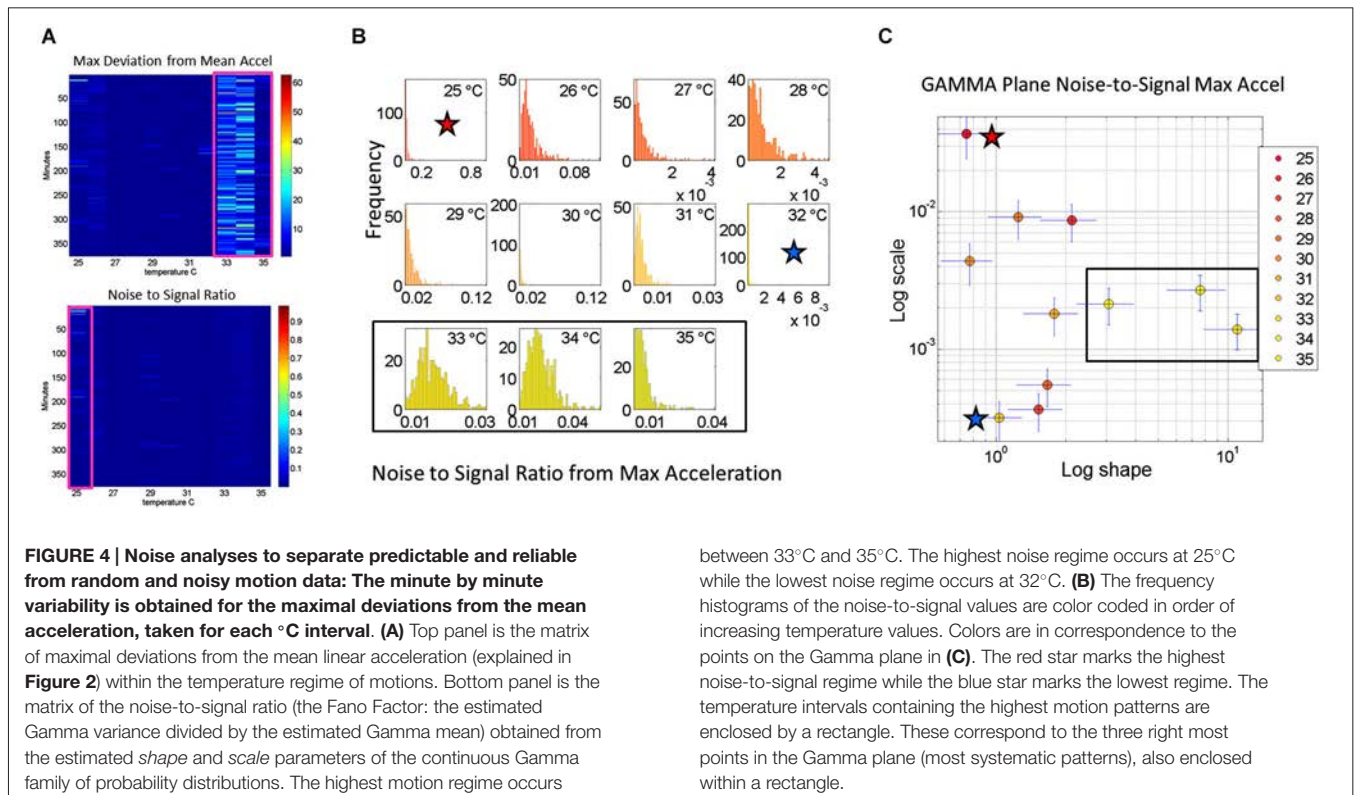
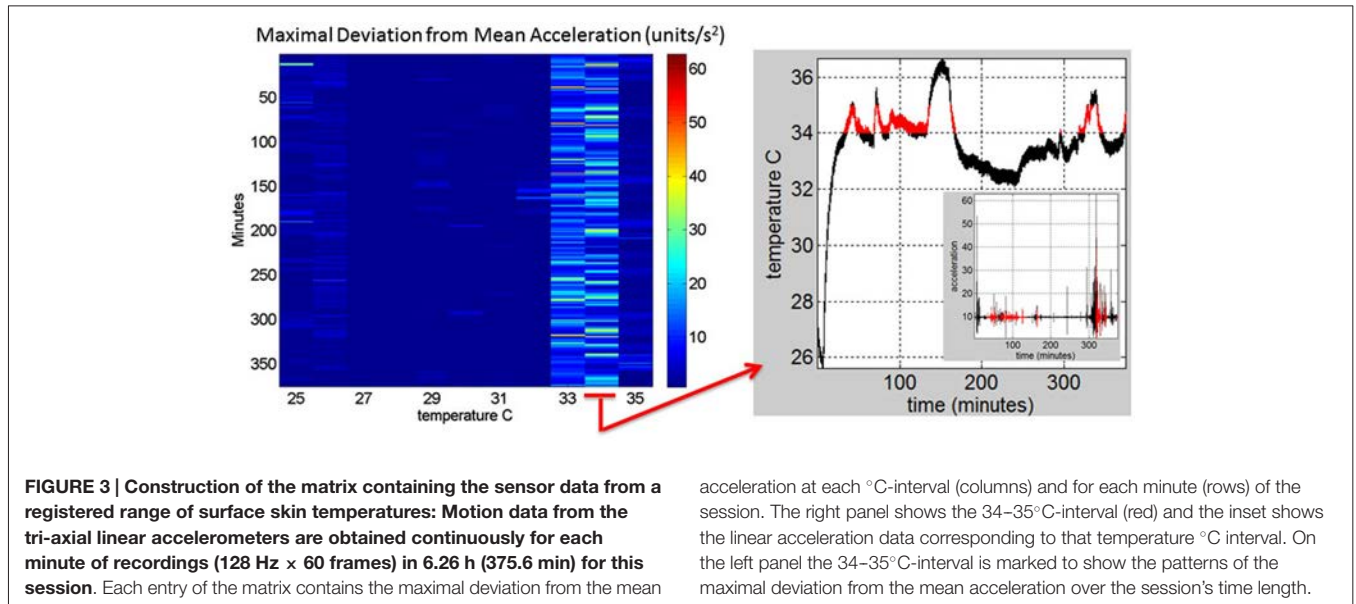
marked here to show their range of noise-to-signal. Using the MLE procedure we estimate the Gamma distribution shape and scale parameters of the distributions corresponding to the noise-to-signal values. This was done to determine the physiologically appropriate statistical regimes in the motion data to further analyze that data. These are regimes of temperature where the motion maintains minimal noise-to-signal ratios across the session, as opposed to the signal being overpowered by instrumentation noise. We plot the estimated shape and scale parameters on the Gamma plane with 95% confidence intervals in **Figure 5C**. The color code corresponds to the frequency histograms of **Figure 5B** and the legend reflects the corresponding temperature °C-interval for this May 8th session. The points corresponding to the shape value of 1 (log-log plot along the horizontal axis is 10°) are at the most random noise-to-signal levels. Those towards the right correspond to statistically more predictable (systematic) regimes of noise-to-signal levels (towards symmetric shapes of the distribution of the noise-to-signal ratios). Along the scale axis, higher values indicate higher levels of noise (highest marked by blue star in correspondence with the frequency histogram in **Figure 5B**). We also mark the 33–35°C temperature interval

used in **Figure 4B** to illustrate the methods to isolate the physiologically relevant motion regimes and in correspondence with the frequency histograms of the noise-to-signal ratio in **Figure 5B**.

In summary we first examine the motion statistical regimes for each minute and °C-interval (**Figure 4**) and then examine the noise-to-signal ratios corresponding to each of these acceleration-dependent motion entries (**Figure 5**). By combining temperature and motion of these sensors we automatically extract the range of physiologically relevant motion data to discriminate noise from signal. Then we can further perform our longitudinal activity tracking analyses to blindly detect relevant changes in skin surface temperature and to distinguish systematic from spontaneous acceleration-dependent motion patterns. **Figure 6** summarizes in matrix form the separation between relevant data and noisy data using the May 8th session as an example.

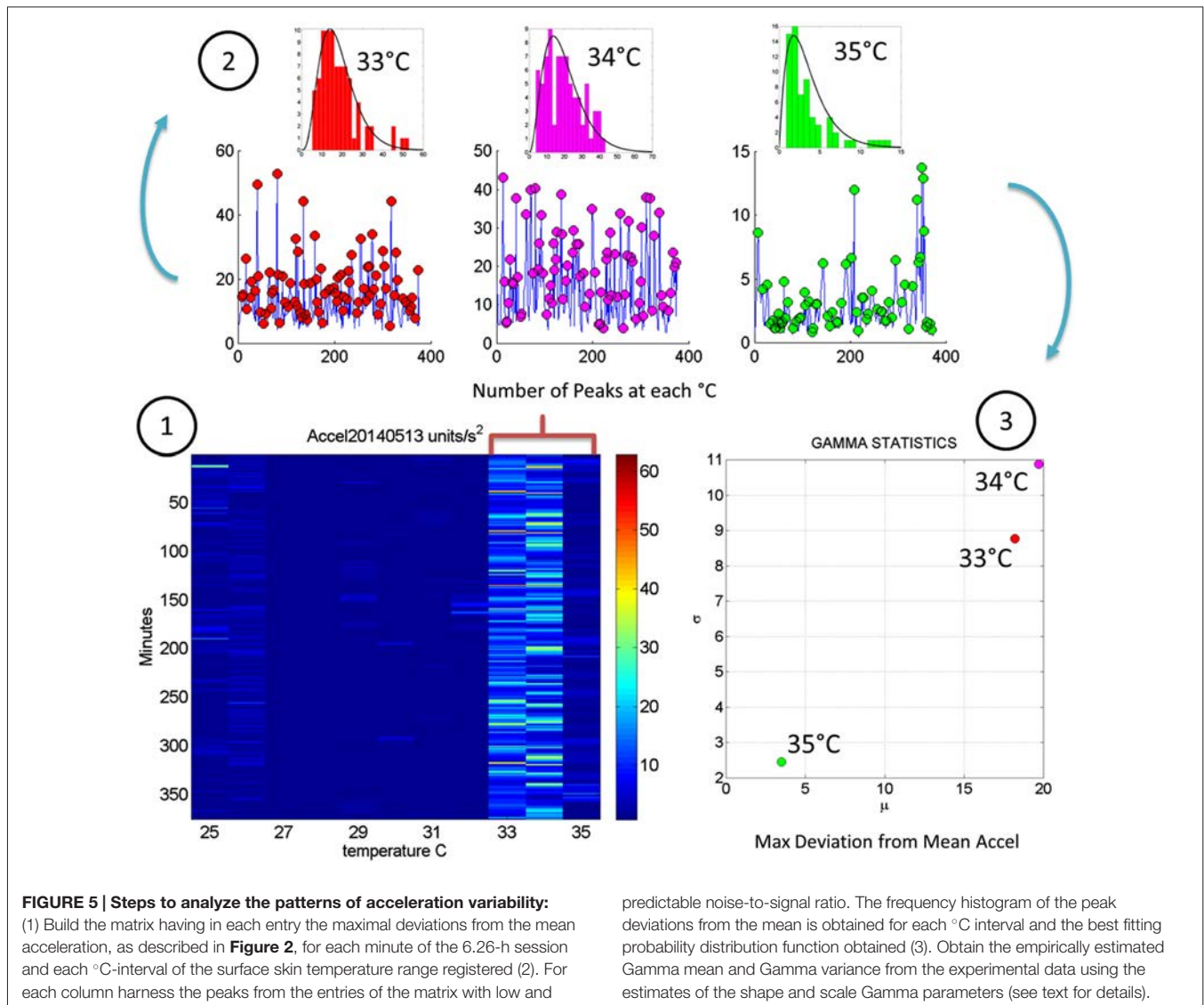
Automatic Blind Identification of Relevant Periods in the Longitudinal Data

The analyses of the evolution in the patterns of noise-to-signal ratio for one session can be extended to each of the sessions to



assess the *longitudinal* evolution of the physiologically relevant data in each session. Recall that these are the data combining the minimal noise-to-signal ratios across the various °C-intervals. **Figure 7** depicts the longitudinal stochastic trajectory of the noise-to-signal ratios extracted from the motion data across all sessions. There are 124 measurements automatically extracted from 21 sessions registered across 4 months (spanning from

April to July). In each session several temperature °C-intervals of low noise data were extracted and their shift in Gamma (*b*)-scale parameter levels obtained for each °C-interval along with their shift in the Gamma (*a*)-shape parameter corresponding to the frequency histogram of the motion's noise-to-signal ratio and estimated using MLE. We point here that the Gamma (*b*)-scale parameter relates to the Fano Factor, the



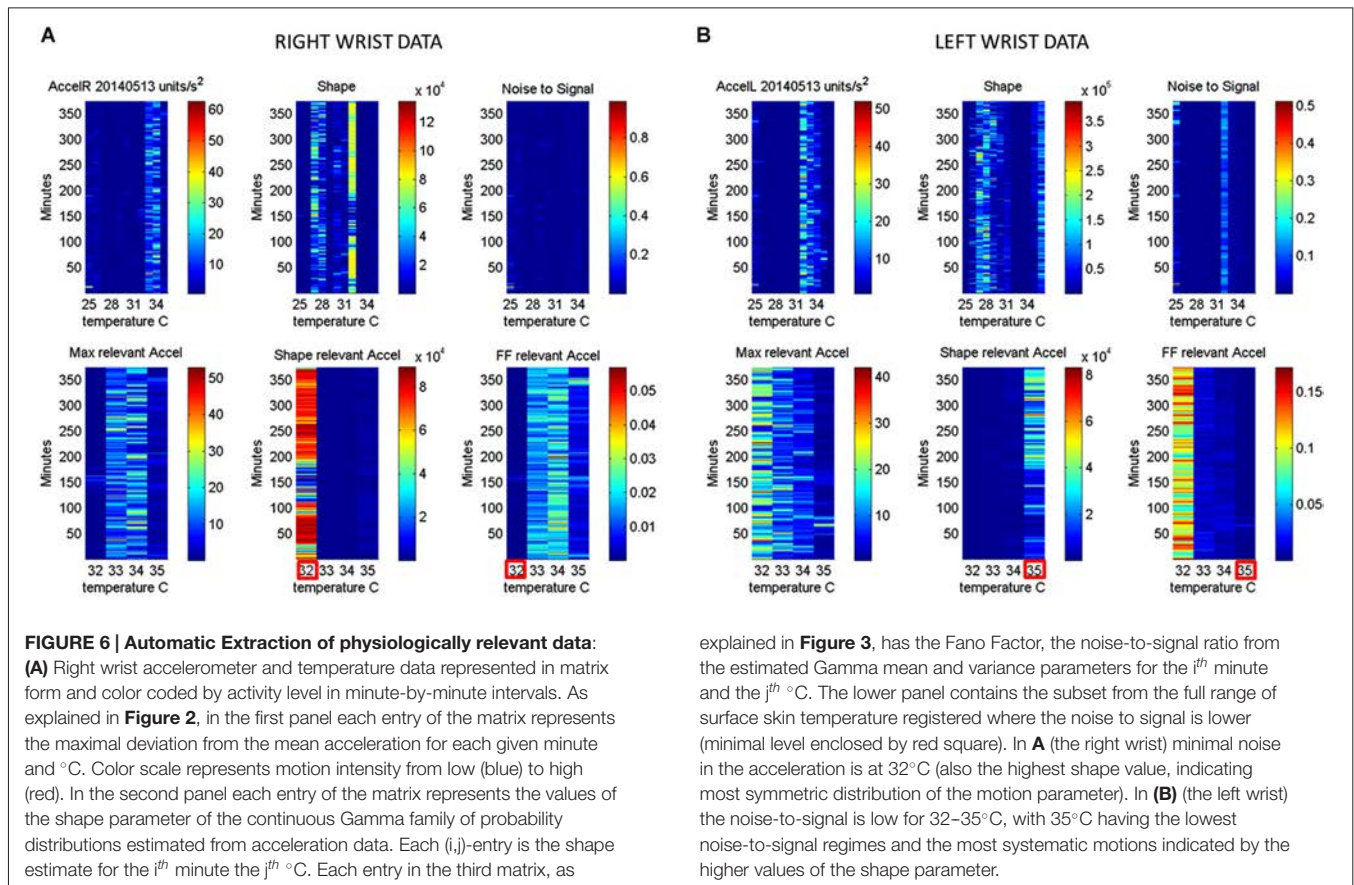
Gamma estimated variance divided by the Gamma estimated mean value. The former is $a.b$ while the latter is $a.b^2$. The Fano Factor is then b , which is the scale parameter. Thus we are examining the rate of change of the noise-to-signal ratio from the acceleration-dependent motions as they turn more or less random, and/or as they turn more or less systematic.

Figure 7A (right wrist) and **Figure 7B** (left wrist) show the 3-dimensional trajectories of the changes in these Gama parameters (X-Y log-log plane) along the temperature ranges (Z-axis °C) registered by the sensors. The vector field (black arrows) indicates the direction and the magnitude of the change in the reliability and predictability of the changes in the noise-to-signal ratio from the motion data. Low changes in values vs. high changes in values are better appreciated in **Figures 7C,D** along the surface fitted through the 124 points of physiologically relevant (low noise) data across all sessions. Along the Z-axis of these surfaces are the changes in temperature level. Notice that

the right wrist had a dramatically sharp change in the month of May, while the left wrist had a gradual change in temperature from June onwards. We come back to this observation in the discussion section below. Points along the 0-change lines of temperature, scale and shape are steady states in each session.

Identification of and Further Distributional Analyses in Critical Sessions

Once the proper regimes of noise-to-signal levels are determined from the motion-temperature data, and their rates of change obtained, we go back to the stochastic analyses of the acceleration data. The prior methods allow us to zoom in the month of highest (or lowest) change in activity across the longitudinal data. **Figure 8** shows the frequency histograms of the right and left wrists data involving the maximal deviations from the mean acceleration obtained within the proper temperature intervals (those identified with the lowest noise-to-signal levels). The



explained in Figure 3, has the Fano Factor, the noise-to-signal ratio from the estimated Gamma mean and variance parameters for the i^{th} minute and the j^{th} °C. The lower panel contains the subset from the full range of surface skin temperature registered where the noise to signal is lower (minimal level enclosed by red square). In A (the right wrist) minimal noise in the acceleration is at 32°C (also the highest shape value, indicating most symmetric distribution of the motion parameter). In B (the left wrist) the noise-to-signal is low for 32–35°C, with 35°C having the lowest noise-to-signal regimes and the most systematic motions indicated by the higher values of the shape parameter.

figure focuses on the month of May which Figure 7 identified as critical for the dominant hand. Notice the changes in the shape and width of these frequency histograms across the various sessions in May.

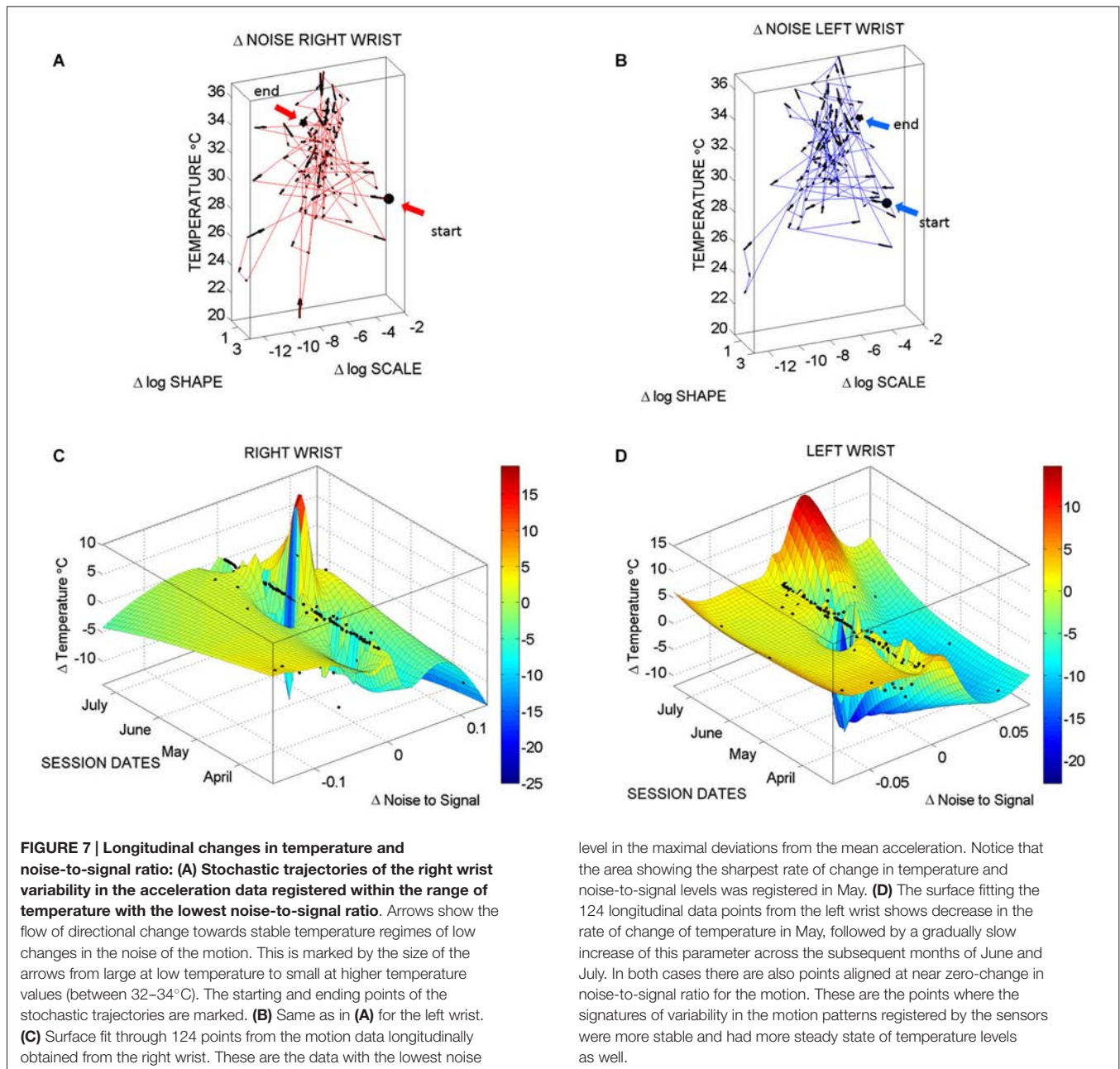
Figure 9A tracks the stochastic trajectories of the estimated Gamma parameters for each wrist (corresponding to the acceleration-dependent motions) and identifies (with a star) in each case the session with the largest rate of change towards the regimes of lowest variability (most reliable) and most symmetric shape, towards systematic motions, away from the (most random) Exponential distribution regimes of the Gamma plane. The starting and ending points of the trajectories are also highlighted. Figure 9B shows for each day the Gamma estimated statistics (mean and variance) highlighting in the legend the dates of the sessions and the largest change in statistical regimes. Other analyzes of the rates of change in these estimated parameters were performed for the month of May and for other months as well. We report the results in the next section of the paper.

Results

Identification of the motion regimes with the lowest noise-to-signal ratio per session enabled us to focus on the physiologically relevant motion data and examine the rates of change of the width and the shape of the frequency distributions of

the maximal deviation from the mean acceleration. Given that there are many spontaneous motions in the patient, the purpose of these analyses was to discriminate random from systematic changes in shape and scale parameters, as well as to establish possible relations between motion and temperature data indicative of emerging volition in the movements.

Figure 10A shows the result of the analyses corresponding to the stochastic changes in the shape of the distribution estimated for each of the sessions of each month where the noise-to-signal was at its minimum. The frequency distribution of the rate of change of the shape parameter in each session was well fit by the Gamma family. The estimated shape and scale parameters are plotted with 95% confidence intervals on the (log-log) Gamma Plane. This plane shows a clear separation in the clustering of the points corresponding to the sessions in the month of May for the right wrist. This separation is consistent with the overall behavior of the changes in temperature and motion data identified in Figures 7C,D. The upward shift in this cluster along the vertical axis indicates an increase in the variability (the width) of the shapes of the distributions of the acceleration-dependent motion parameter. The rightwards shift of this cluster along the horizontal axis indicates systematic changes towards more symmetric shapes. More symmetric shapes indicate Gaussian-like behavior with a build up in the expected value of the parameters while shifts away from these regimes (towards the left

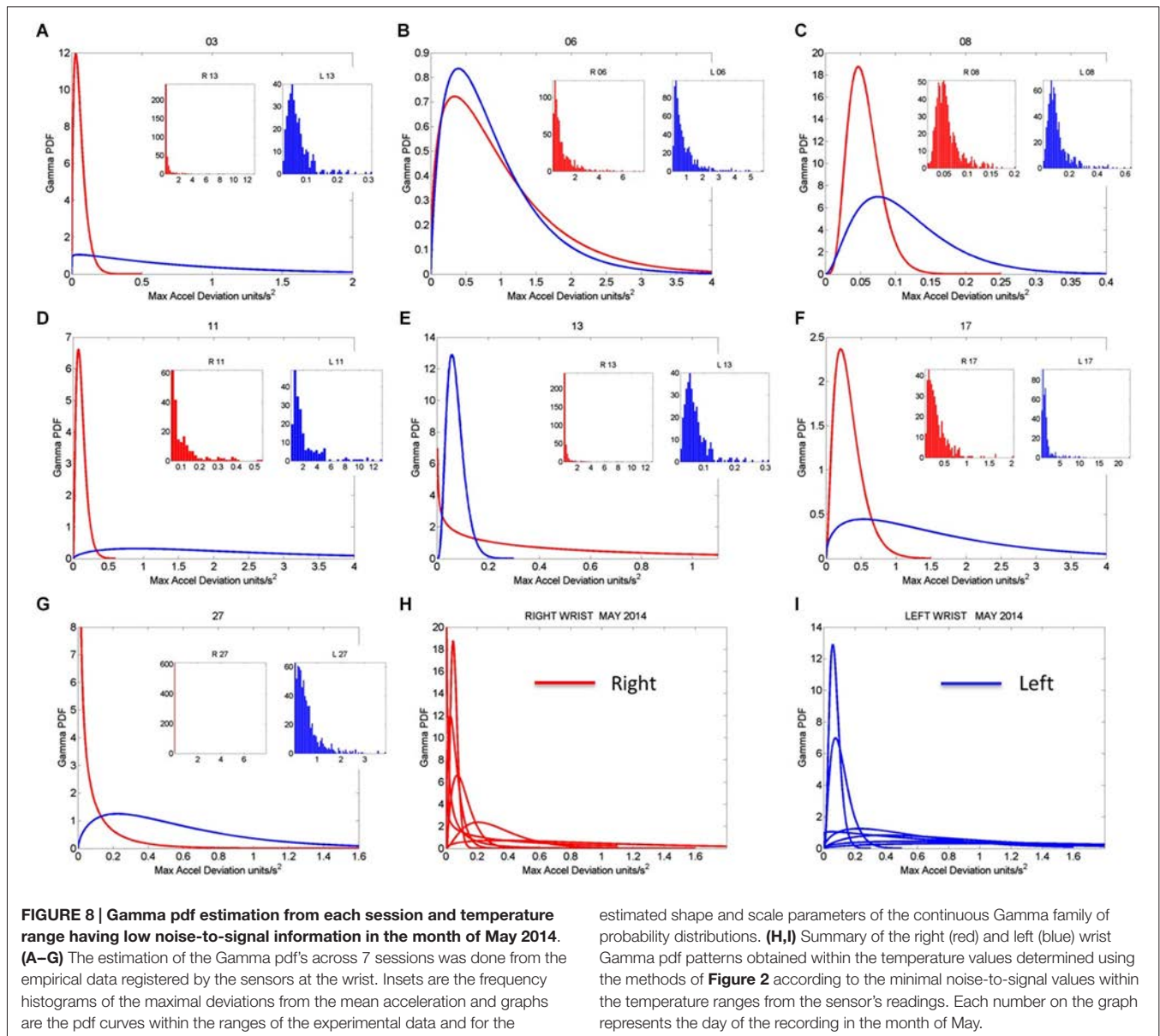


of the shape axis) mark increase in randomness and total lack of volition.

In summary these analyses revealed that the rate of change of the shape parameter estimated from the linear accelerations with the lowest noise-to-signal values singled out May as the critical month. This was the month with highest variability in the change of the shape parameter of the maximal deviations from the mean acceleration, but it was also the month when these changes were the most systematic, predictive of a reliable expected value. In other words, the variability in the acceleration-dependent motion of the dominant hand was not random during the month of May. These motions were not spontaneous in

nature as those with random patterns are. The rate of change in the stochastic patterns was highly systematic, as quantified by the shifts in the shape of the probability distribution of the acceleration dependent parameters.

Figure 10B shows the results from similar analyses as in **Figure 10A** but this time corresponding to the rate of change of the noise-to-signal levels in the surface skin temperature. The frequency distributions of the rate of change of surface skin temperature noise followed the Gamma distribution as well. We estimated the shape and scale parameters of each session with minimal acceleration-dependent motion noise and plotted the point from each session on the (log-log) Gamma plane

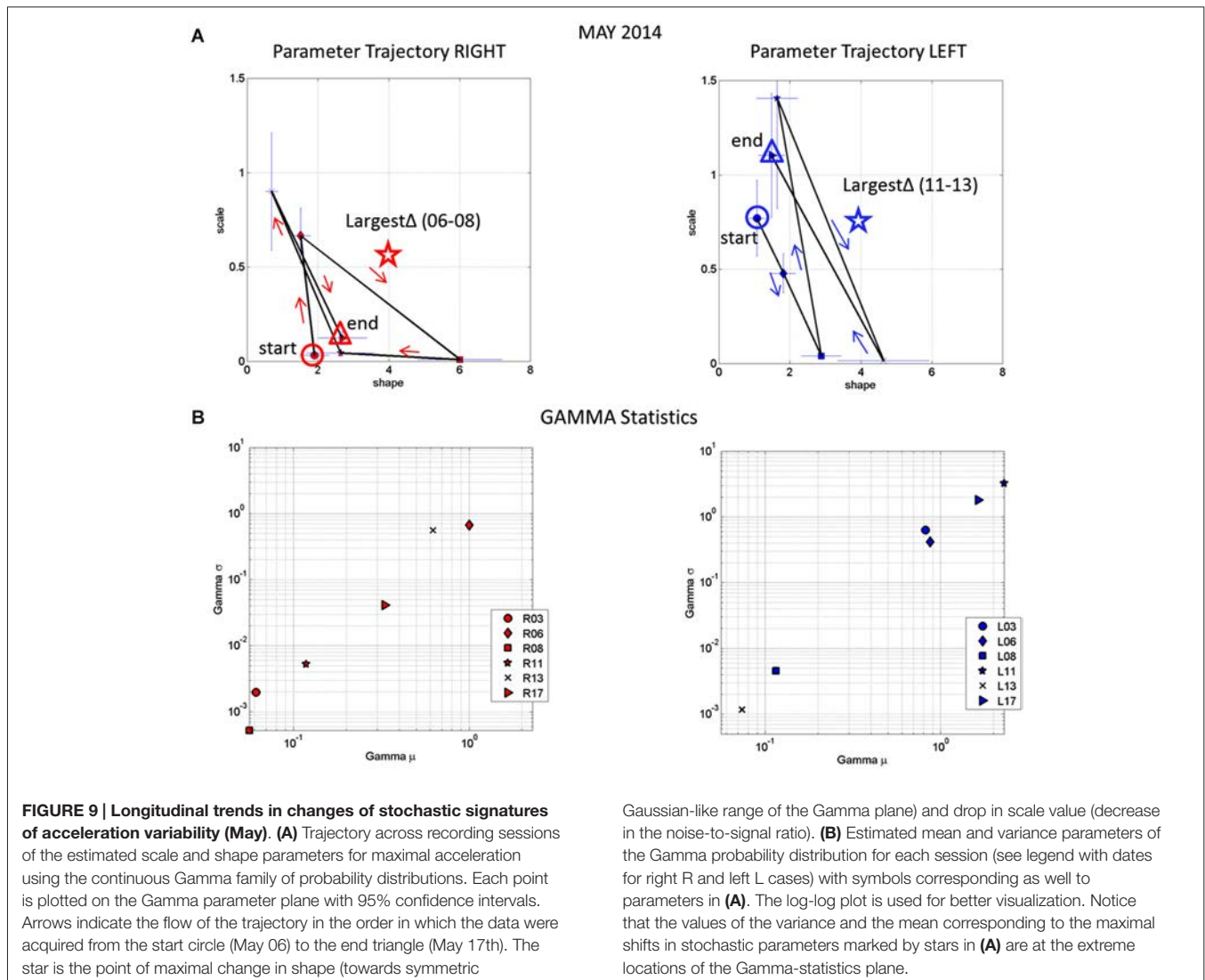


with 95% confidence interval. The month of May once again stood out as a separate cluster with systematic shifts downwards towards regimes of reliable measurements (low noise) and shifts rightwards towards more systematic regimes tending towards symmetric (Gaussian) shapes of the distribution of the rate of change in temperature noise. These patterns were not present in the values registered by the left wrist. In the left wrist the points from the sessions in the month of May did not cluster apart from those estimated from the measurements taken in the other months. Unlike in the right wrist, no reliable and systematic changes were revealed in the motions of the left wrist during the month of May.

Figure 10C shows the patterns corresponding to the rate of change in the shape parameter discussed in **Figures 10A,B** for the acceleration-dependent motion as a function of the

temperature. The points representing the month of May cluster apart from the rest. Here, in relation to the other months, May had larger values for the change in the shape of the acceleration-dependent distribution corresponding to larger values in the change of the shape of the temperature-dependent distribution. This indicates a systematic change in the shapes of these distributions towards more symmetric shapes: as the changes in the shape of the distributions of temperature became more systematic, so did the changes in the shape of the distributions of the maximal deviations from the mean acceleration. This means that in May the changes in the motions of the right wrist as a function of surface skin temperature were not random.

While **Figure 10C** speaks of systematic changes in the shapes of the parameters' distributions, **Figure 10D** speaks of the



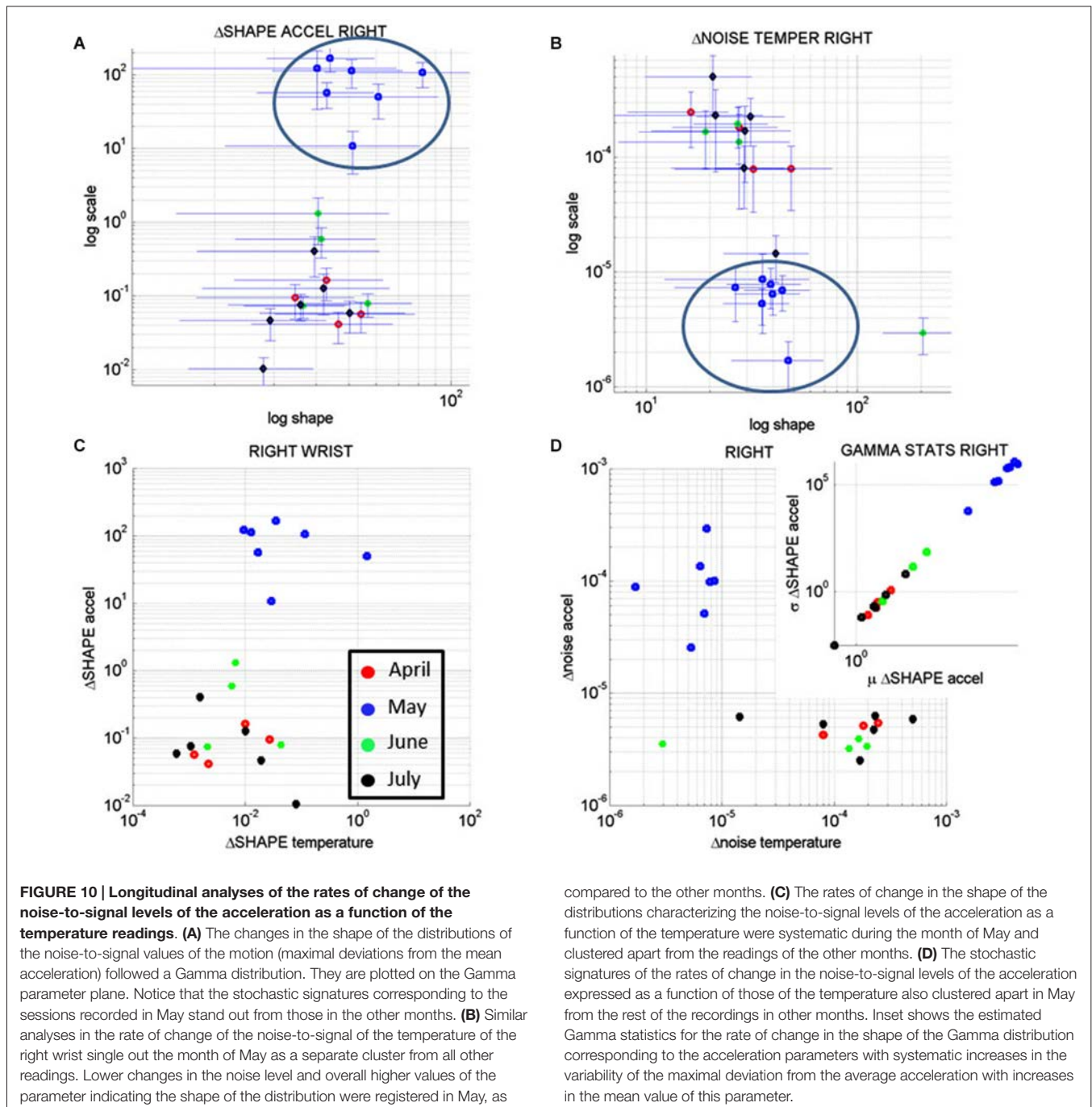
changes in their noise-to-signal levels. There we see that in relation to other months, the measurements in the month of May stood out with lower changes in temperature noise and higher changes in acceleration noise. The rates of change in noise levels in temperature were steady, while the rates of change in the acceleration noise increased. There was more variability in the motion for steady temperature ranges. Yet this variability was systematic according to the statistics of the shape values of the distribution of motion parameters shown in the inset.

The inset zooms in the Gamma statistics of the changes in the shape of the distributions of maximal deviation from the mean acceleration. The figure shows that in May the motions were more systematic than in the other months and their variability in the shape of the distribution was higher. In particular, by May 17th the changes in surface skin temperature were steadier as the changes in motion patterns turned more systematic (as revealed by the higher values of the shape of the distribution of the relevant acceleration and temperature dependent parameters).

Patient AB had the C-section delivery of her baby boy on May 22, 2014. All the data preceding that date indicated patterns of systematic variability in her motions from the dominant (right) hand that were absent in the motions from her non-dominant (left) hand. Furthermore, the medical records indicated the formation of a blood clot in the right arm after May. **Figure 7D** shows a slow gradual increase in the changes in surface skin temperature for the left wrist that also coincided with higher levels of motion. These motions from the left wrist however had no discernable patterns of systematic changes in variability levels as those observed in May. The motions registered in the left wrist were truly spontaneous in nature (random) whereas those of the right wrist were reliably predictable of an expected value.

Discussion

This paper introduces new methods to assess in a personalized manner the day-by-day longitudinal progression of body



motions as a function of surface skin temperature using wearable sensors. The statistical metrics introduced here may permit the continuous longitudinal assessment of patients as they move and as they undergo changes in physiological states. We have used a particular case of a patient with severe brain trauma to illustrate the methods. Yet these methods can be generally extended and used in other patients as well. These methods do not assume population statistics or expected values of the parameters of interest. Instead, they empirically estimate the probability distributions most likely underlying the changes in motion and

physiologically relevant parameters registered in tandem within each daily session and longitudinally over months. The methods focus on the rates of change of these parameters' statistics along a continuum.

A surprising revelation from these analyses was that not all motions recorded by wearable sensors were physiologically relevant. We found a great deal of instrumentation noise that we had to separate from the signal in order to perform appropriate analyses on the motion data. This is important in light of the general use of wearable sensors in the market to track activity,

wellness and fitness. Here we found high levels of noise-to-signal ratio in the acceleration data under unrealistic regimes of skin surface temperature. We were able to further use the surface skin temperature as a natural filter to help us separate the random rates of change of the noise levels in the motion from systematic rates of change. We also distinguished systematic from random changes in the shape of the distributions of these parameters.

These data analyses suggest that in general more motion registered by accelerometers does not imply that there is more neural control of movements. The registration of higher acceleration values should not be associated with more volitional control or intent in the motions. Instead, one should separate the noisy data and assess the levels of reliable and systematic changes in the motion data with low noise-to-signal ratio. In these sensors a layer of noise, particularly at low levels of temperature rendered irrelevant a large portion of high levels of motions registered by the tri-axial linear accelerometers. The lower temperature regimes coincided with motion data that was predominantly noisy. This was consistently the case across all sessions of recordings.

We note here that Newtonian mechanics concerned with acceleration estimations has no known relation to thermodynamics. The laws of mechanics governing physical motions were derived for inanimate objects and rigid bodies, rather than for biological bodies in motion undergoing physiological changes that impact the motions' variability. Such changes are guided by feedback from sensory nerves conducting information from the peripheral to the central nervous system about pain, temperature and motion/touch/pressure. Although the field of neural control of movement employs primarily Newtonian mechanics in the analyses and modelings of behavioral states (Shadmehr and Wise, 2005), it may be important to introduce new ways of examining motion data in tandem with physiologically relevant measurements (such as temperature, heartbeat, breathing patterns, etc.) of use in clinical settings. An approach such as the one introduced here would then enable us to better understand the nature of motion data that is also governed by a nervous system under volitional control, rather than exclusively described by the physical laws of motion. The motor output variability registered in tandem with the surface skin temperature helped us unambiguously distinguish random (spontaneous) patterns from systematic, reorganized (predictable) patterns. We may have characterized a degree of volition in the dominant wrist as the patient repeatedly touched her abdomen during the contractions preceding the day of the C-section.

While analyses and modeling of motion data is the exclusive focus of the field of neural control of movements without regards of physiological data, the medical field follows a complementary approach to patient assessment. In the clinical settings, measurements of physiological data such as temperature, breathing, heartbeat, blood pressure, etc. are routinely taken from the patient. These measurements are taken in isolation, without considering possible relationships to bodily motion patterns.

The human body is in constant motion in tandem with other physiological patterns of the person. Such patterns fluctuate and change over time. In clinical settings the absolute values of the parameters of interest are often registered, but very little is said about the trends and fluctuations of their rates of change over time. Here we have shown that the rates of change of those parameters over time contained information predictive of a relevant upcoming event. In particular we were able to blindly identify May as the month of highest relevance in these longitudinal data sets. A dramatic and sharp change in the patterns of motion and surface skin temperature of this patient's dominant hand manifested in May preceding the birth of her baby boy by C-section.

These metrics may be of use to monitor critical events during pregnancy and foretell (and possibly prevent) potential problems. It is possible that we may have even captured and characterized here in this patient the patterns of noise-to-signal corresponding to the painful contractions that are known to precede birth, as her hand moved to her abdominal area. It will be interesting to repeat this study systematically in a large number of pregnant women of different ages. We would be able to characterize with unprecedented precision the risk of miscarriage as a function of age, as well as various individualized physiological scales of painful contractions as a function of temperature and motion profiles, among other symptoms during pregnancy.

The critical task of characterizing longitudinally the individualized profiles of various physiological stages of pregnancy in an objective, non-invasive manner would be highly feasible now using our new analytics in tandem with a broad range of wearable sensors available in the market. The current market offers sensors that capture heart rate variability, electro dermal activities, and blood-volume levels, among others. The various outcomes of these biomarkers are currently examined in isolation during visits to the clinic. These new analytics offer the possibility of integrating the physiological signals with the motion's temporal profiles to provide a multi-dimensional profile tractable longitudinally at home and during the visits to the clinic. Pregnant patients increase their visits to the clinicians during the last trimester and other techniques are used to monitor their progress (Reece and Hobbins, 2007). It would be ideal to team up with an antenatal and perinatal expert to be able to compare and combine the methods presented here with currently used neuroimaging techniques, ultrasound among others.

We also suggest that in the future by combining the motion and the physiological measures (registered in tandem) we could better and continuously monitor patients with post trauma to the brain (independent of the type of trauma). We could better understand the course of individual changes in their motions and body physiology as the patient receives therapies and as the patient undergoes drug treatments. We could find new ways to objectively track the progress of patients as they recover from brain trauma, identify critical points along the evolution of the person and assess the effectiveness of treatments in non-invasive ways. We could do all of this continuously at home or in the clinic

by simply using off-the-shelf wearable sensing technology broadly available today.

In summary these sensor's physiological data were able to blindly forecast what without a doubt would be considered the most important day in a woman's biological lifecycle. They did so even under a coma state. The information revealed by this new analytical technology could be potentially of use to individually track the longitudinal patterns of other patients with post trauma to the brain and tailor

their treatments accordingly. These new metrics may bring us a step closer towards true personalized medical practices.

Acknowledgments

Acknowledgments, Credits, or Disclaimers Torres EB. These methods are IP protected by the Rutgers University Office of Technology Transfer.

References

- Carroll, C. P., Cochran, J. A., Guse, C. E., and Wang, M. C. (2012). Are we underestimating the burden of traumatic brain injury? Surveillance of severe traumatic brain injury using centers for disease control international classification of disease, ninth revision, clinical modification, traumatic brain injury codes. *Neurosurgery* 71, 1064–1070; discussion 1070. doi: 10.1227/NEU.0b013e31826f7c16
- Centers for Disease Control and Prevention (CDC). (2013). CDC grand rounds: reducing severe traumatic brain injury in the United States. *MMWR Morb. Mortal. Wkly. Rep.* 62, 549–552.
- Finkelstein, E., Corso, P. S., and Miller, T. R. (2006). *The Incidence and Economic Burden of Injuries in the United States*. Oxford, New York: Oxford University Press.
- Reece, E. A., and Hobbins, J. C. (2007). *Clinical Obstetrics: The Fetus and Mother*. 3rd Edn. Malden, Mass.: Blackwell Pub.
- Schnakers, C., Vanhaudenhuyse, A., Giacino, J., Ventura, M., Boly, M., Majerus, S., et al. (2009). Diagnostic accuracy of the vegetative and minimally conscious state: clinical consensus versus standardized neurobehavioral assessment. *BMC Neurol.* 9:35. doi: 10.1186/1471-2377-9-35
- Shadmehr, R., and Wise, S. P. (2005). *The Computational Neurobiology of Reaching and Pointing: A Foundation for Motor Learning*. Cambridge, Mass.: MIT Press.
- Torres, E. B. (2011). Two classes of movements in motor control. *Exp. Brain Res.* 215, 269–283. doi: 10.1007/s00221-011-2892-8
- Torres, E. B. (2013a). The rates of change of the stochastic trajectories of acceleration variability are a good predictor of normal aging and of the stage of Parkinson's disease. *Front. Integr. Neurosci.* 7:50. doi: 10.3389/fnint.2013.00050
- Torres, E. B. (2013b). Signatures of movement variability anticipate hand speed according to levels of intent. *Behav. Brain Funct.* 9:10. doi: 10.1186/1744-9081-9-10
- Torres, E. B., Brincker, M., Isenhower, R. W., Yanovich, P., Stigler, K.A., Nurnberger, J.I., et al. (2013). Autism: the micro-movement perspective. *Front. Integr. Neurosci.* 7:32. doi: 10.3389/fnint.2013.00032
- Torres, E. B., Cole, J., and Poizner, H. (2014). Motor output variability, deafferentation and putative deficits in kinesthetic reafference in Parkinson's disease. *Front. Hum. Neurosci.* 8:823. doi: 10.3389/fnhum.2014.00823

Conflict of Interest Statement: The authors declare that the research was conducted in the absence of any commercial or financial relationships that could be construed as a potential conflict of interest.

Copyright © 2015 Torres and Lande. This is an open-access article distributed under the terms of the Creative Commons Attribution License (CC BY). The use, distribution and reproduction in other forums is permitted, provided the original author(s) or licensor are credited and that the original publication in this journal is cited, in accordance with accepted academic practice. No use, distribution or reproduction is permitted which does not comply with these terms.

Characterization of inertial measurement unit placement on the human body upon repeated donnings

Morris Vanegas
Department of Aeronautical and
Astronautical Engineering
Massachusetts Institute of Technology
Cambridge, MA 02139
mvanegas@mit.edu

Leia Stirling
Department of Aeronautical and
Astronautical Engineering
Massachusetts Institute of Technology
Cambridge, MA 02139
leia@mit.edu

Abstract—Accurate estimations of variability in multiple donnings of sensor suites may aid algorithm development for wearable motion capture systems that make use of Inertial Measurement Units (IMUs). The accuracy of any algorithm incorporating these sensors is limited by the accuracy of the sensor to segment calibration. When either sensor placement (use by a non-expert) or limb motion during calibration (natural human variation) vary, the estimations are affected. In this study, 22 participants self-placed IMUs on three locations and performed six prescribed motions during each of these five donnings. For absolute placement of the sensors, the chest location mean was less than the forearm, which was less than the bicep. For sensor orientation, the opposite ordering of location was found. No difference in sensor rotation was found between the bicep and forearm, but both locations differed from the chest location. Results were analyzed at the beginning of prescribed motions.

Keywords—Variability, Inertial Measurement Unit, Sensor Suites, Donning, Doffing.

I. INTRODUCTION

According to the 2014 IHS MEMS & Sensors for Wearable Report [1], consumers will be wearing close to 500 million sensors by 2019. This estimate includes devices for motion measurement, user interfaces, and health industry products, with an emphasis on personal devices that are used daily by non-experts. A necessary requirement to enable such portable and continually-used consumer systems that are reliable, self-sufficient, and require minimal-logistical needs is to understand and appropriately incorporate the variability of humans during repeated use in the system architecture. This study specifically considers wearable technology systems for estimating human motion.

A common method for estimating rigid body motion is the use of Inertial Measurement Units (IMUs), which are small electronic sensor suites of accelerometers, rate gyros, and magnetometers that measure linear acceleration, angular velocity, and local magnetic field. Compared to other motion capture technologies like optical, image-based, and magnetic, IMUs provide an inexpensive and portable solution. Recent technological advances have improved the energy consumption, cost, and availability of these sensors [2]. Whereas optical

and acoustic devices require a source emission to track objects, IMUs do not, which simplifies system integration and increases portability.

Despite these benefits, IMUs have disadvantages. Accelerometers measure the sum of linear acceleration and gravity. In a quasi-static movement, linear acceleration can be neglected. In a dynamic situation, it is difficult to decouple the two measures and may lead to difficulty calculating attitude accurately [3]. Angular velocity measurements by gyroscopes are prone to sensor drift over time, and magnetometers are susceptible and influenced by ferrous material. With an estimated orientation for a given IMU, there is still a need to calibrate individual sensors to the global body coordinate system every time the sensor suite is donned.

To overcome these individual sensor disadvantages, fusion techniques have been implemented. Starting in 1970, Bortz [4] computed sensor orientation by integrating angular velocity. Since then, others have extended fusion methods and examined Kalman Filter algorithms to obtain dynamic orientations of IMUs by implementing an Euler angle representation [5][6]. To avoid singularities in Euler angles and to limit the need for linearizing, quaternion-based Extended Kalman Filters (EKF) have been implemented [7][8], although this method still requires an embedded physical model linearization and is limited to slow motions due to the computation time.

Results of the use of IMUs on robotic hinges rather than on humans [9] show that if accelerometers can be placed exactly on the joint center, a simpler algorithm (common-mode rejection algorithm) can accurately predict joint-angles without the need for computationally heavy filters. The need for the IMU to be placed exactly on the joint center indicates that the variability of sensor placement by humans during repeated use may be a large cause of motion estimation errors. As Luinge et al. [10] also conclude, the accuracy of any method is limited by the accuracy of the sensor to segment calibration.

IMU calibration can be either static or dynamic (e.g. [11], [12], respectively). The most common pose held for a static calibration is a “T” pose in which both arms are held straight out to each side. Dynamic calibration motions vary but may include simple one degree of freedom motions for relevant

segments. Wu et al. [13] developed a self-calibration process incorporating sensor misplacement for in-plane orientation misalignment, but it was not able to aid misalignment in rotations along local body curvature. All these calibrations relate the local coordinate system of the IMU to the global placement of the IMU on the body. Calibration poses increase preparation time for a system and are also only as accurate as the ability of a human to perform a specified motion.

The literature suggests that a motion capture system using IMUs where both sensor placement and calibration poses and motions are exact and repeatable provide good estimates of the system state. However, when either sensor placement (non-expert) or limb motion during calibration (natural human variation) vary, the estimations are affected. This study will test the hypotheses that initial placement (defined as distance, orientation, and rotation) of IMUs located at the chest, bicep, and forearm by a non-expert are affected by (1) the number of times the sensors are donned, (2) the type of functional motions performed, and (3) the location of the IMU. Here, the uncertainty in IMU placement when donned by a non-expert user is characterized. These data will aid in algorithm development to minimize and compensate for the donning and doffing variability measured in relevant motions.

II. METHODS

A. Participants

The study included 22 subjects (6 female) aged 23.3 ± 3.0 years. The study was carried out in the Man-Vehicle Laboratory within the Department of Aeronautics and Astronautics at the Massachusetts Institute of Technology. Procedures were approved by the MIT Committee on the Use of Humans as Experimental Subjects (COUHES) and participants provided written consent. Participants received a \$20 gift card as compensation.

B. Experimental Protocol

Participants were instructed to self-place four IMUs (APDM, Opal 425) during the study to analyze the variability in placement on the upper body for two mounting configurations, straps and garment based. In this paper, the straps mounting configuration is highlighted.

Prior to data collection, researchers placed 24 passive reflective markers (12 9.5mm diameter markers on the participant and 12 6.4 mm diameter markers on the IMUs) to permit standard motion capture analysis (Vicon 10-camera Bonita system) (Fig. 1).

For data collection, all subjects were asked to perform five donnings and doffings of each of the two IMU configurations. During each donning, one calibration pose was performed prior to the six predetermined motions (Fig. 2) that were performed randomly a total of six times each (total of 36 motions during each donning). The motions were randomized to prevent learning effects.

An instructional donning was performed during the first mounting configuration, in which all straps were adjusted for fit and comfort using the participant's feedback. This instructional donning was purely for fit and none of the predetermined motions were performed. The participants were also fitted for

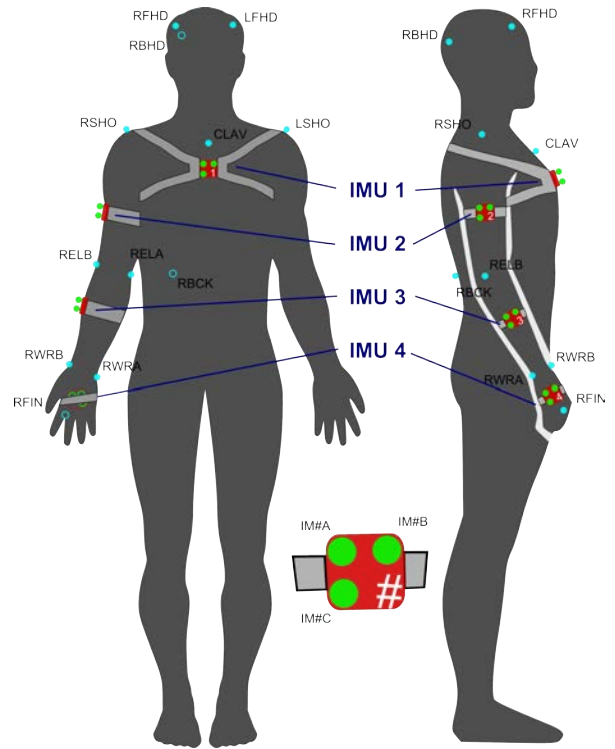


Fig. 1: Recommended sensor placement (boxes on straps) and researcher placed optical motion capture markers. Sensor placement labelling scheme is shown in the bottom of the figure.

fabric arm braces, placed on the right forearm and bicep, to prevent subjects from using the imprint of the IMU on the skin as a reference for placement during repeated donnings. The braces were not removed during the multiple donnings of the IMUs. During the garment fit, the second configuration, a trace of the silhouette of the participant was created and used as a guide to participants when they repeated the calibration pose, limiting variability. The strap and garment configurations were not resized after this instructional donning.

C. Data Acquisition

1) *Donning Configuration*: The IMU strap configuration utilized Velcro straps (APDM) to independently mount the four IMUs (Fig. 1). One single hoop strap was used for each IMU placed on the hand, forearm, and bicep. A chest strap with two connection points, two snap buttons on one side of the IMU, and hoops for each arm was used to secure an IMU to the chest.

2) *Motion Capture*: Vicon data were sampled at 120 Hz. The IMU data were sampled at 128 Hz and wirelessly logged in real-time and synchronized to enable comparison of the optical and inertial data. In addition, all participants were video recorded during the trials.

3) *Motions*: Six predetermined motions were described to the participants prior to data collection through text and visual descriptions (Fig. 2). The motions were chosen to include a range of single and multiple (more than one) degrees of freedom. Motions included elbow, wrist, and shoulder flexion

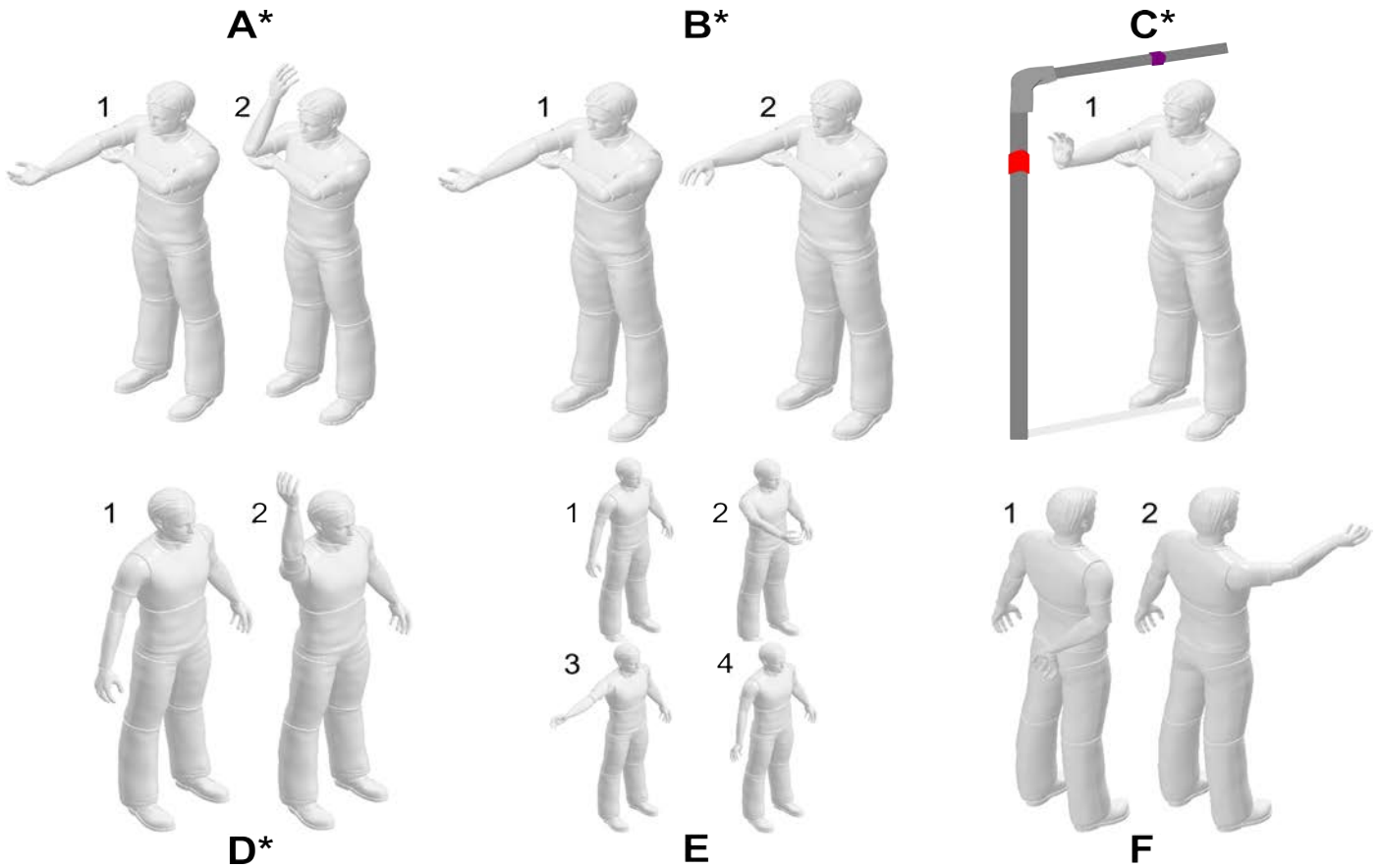


Fig. 2: Predetermined motions showing relevant degrees of freedom (A = elbow flexion and extension; B = forearm pronation and supination; C = wrist ulnar and radial deviation, wrist flexion and extension; D = Lifting arm upwards, which included elbow flexion and extension, shoulder flexion and extension; E = Lifting arm forward and to the side, which included shoulder abduction, flexion and rotation; F = Lifting arm forward from a behind the back starting position, which included wrist, elbow, and shoulder flexion and extension, shoulder abduction, and forearm pronation and supination). Motions have numbered figures to indicate sequence of poses. Subjects performed the sequence in a motion, and then returned to the first pose in the sequence. Target Apparatus only shown in Motion C but was used by four motions (A * indicates the motion used a guide).

and extension; forearm pronation and supination; wrist ulnar and radial deviation; and shoulder abduction and rotation. The visual descriptions of the motions were within eye sight of the participants during data gathering for reference. During 4 of the 6 motions, a target apparatus was used to determine the starting and ending positions (Fig. 2). The apparatus was created out of 3/4" PVC pipe and consisted of two poles at 90 degrees, one vertical at arms reach of the participant and one horizontal above the head of the participant. The vertical bar had a red target at shoulder height. The horizontal bar had a purple target above the participant, at a height just above the reach of the participant. The apparatus was adjusted to the height of each participant and was not adjusted during data collection.

D. Data Processing

Vicon Nexus software was used to reconstruct, label markers, fill in gaps, and export the optical data. A Biomechanical Toolkit was used to import these data to Matlab. In-house code was used to calculate IMU position, orientation, and rotation. Here, data for IMUs 1, 2, and 3 are presented.

As shown in Fig. 1, each IMU had a triad of markers labeled A, B, and C corresponding to the top left, top right, and bottom left markers, respectively. The centroid of each IMU was defined as the midpoint between markers B and C. IMU position was defined as the distance between the IMU's centroid and a pre-specified body-fixed marker for each IMU (Fig. 3). IMU orientation was defined as the angle (in degrees) the IMU had rotated along the plane of initial placement. A vector from the IMU centroid to the pre-specified body-fixed marker defined zero degrees. The angle between this vector, and a vector created from marker C to A on each IMU, defined the IMU orientation (Fig. 3).

IMU rotation was defined as the angle about the local body curvature (Torso, bicep, and forearm for IMU 1, 2, and 3, respectively). IMU rotation was calculated as the dot product of a normal vector to the IMU plane and a normal vector created from surrounding body-fixed markers (Fig. 3). An example of IMU 2 rotation being calculated can be found in Fig. 4. IMU 1, 2, and 3 distance, orientation, and rotation were scaled by torso, bicep, and forearm length, respectively, for each subject. These normalized values then had the overall

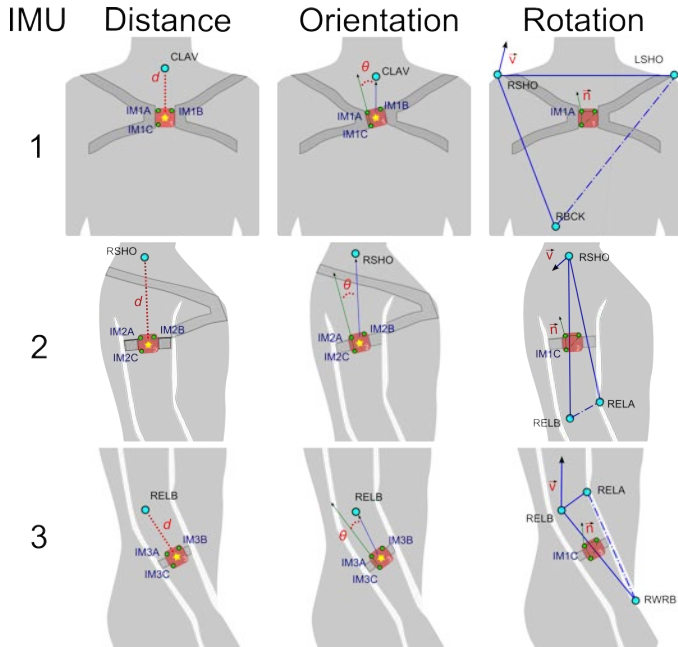


Fig. 3: Definition of the three IMU measurements for each of the three IMUs and associated markers. IMUs had three markers, labeled A, B, and C, used to define the local IMU coordinate system. Each subfigure shows the surrounding markers used in the IMU’s measurement calculation.

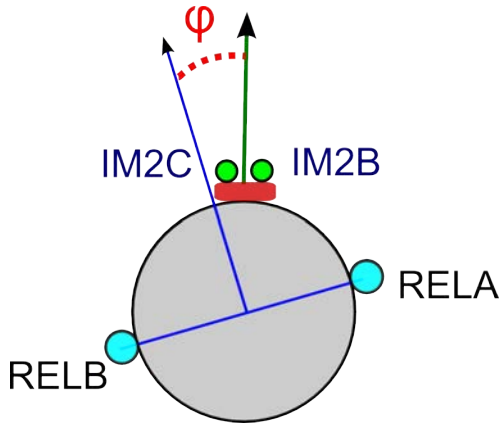


Fig. 4: Example of how rotation is calculated on IMU 2. This view is from the elbow looking towards the shoulder. The rotation angle is the angle between the IMU normal vector and the surrounding body markers’ normal vector. From this view, markers IM2A and RSHO are masked.

means by IMU number subtracted such that comparisons between IMUs could be made.

E. Statistical Analysis

Data are presented as scaled IMU distance, orientation, and rotation. ANOVAs were performed to examine the main and interaction effects of the independent variables (location, donning, and motion). A p value <0.05 was used to indicate statistical significance. The Tukey Difference test and the Student-Newman-Keuls test were used for post-hoc comparisons. Levene’s test was used to assess the equality of variances. SYSTAT software was used for calculations.

III. RESULTS

A three-factor ANOVA was conducted for each dependent variable (distance, orientation, and rotation) to test for main and interaction effects of location, donning, and motion. Significant effects were found for all main effects, two-way, and three-way interactions ($p <0.0005$) for all three IMU dependent measurements.

Post-hoc pairwise comparisons of the IMU location using Tukey’s Difference Test showed significant differences between all three locations for IMU distance ($p <0.0005$). For IMU orientation, significant differences were found between locations 1 and 2 ($p <0.0005$), and locations 1 and 3 ($p <0.0005$), but not between locations 2 and 3 ($p = 0.554$). Similarly, for IMU rotation, significant differences were found between locations 1 and 2 ($p <0.0005$), and locations 1 and 3 ($p <0.0005$), but not for locations 2 and 3 ($p = 0.837$). Pairwise comparisons for donning showed no significant difference between donnings 1 and 3 ($p = 0.225$), 1 and 5 ($p = 0.485$), and 3 and 5 ($p = 0.995$). Donnings 2 and 4 were significantly different from the other donnings ($p <0.0005$). Student-Newman-Keuls post-hoc tests were used to group similar motions. For IMU distance and orientation, there were 3 groupings: motion A, motions B and C, and motions D, E, and F. For IMU rotation, there were also three groupings: motion B, motions A and C, and motions D, E, and F.

Since no consistent trend in any dependent variable was found with consecutive donnings, the donnings were pooled and interaction effects of motion with location were analyzed. Fig. 5 shows the significant difference within motions for all IMUs.

Levene’s test showed significant differences in the variances for the distance ($p <0.0005$) and orientation ($p <0.0005$) for all three IMU locations (Table I). For distance, location 2 was the most variable and location 1 was the least variable. For orientation, location 1 was the most variable while location 2 was the least variable. There was no significant difference in rotation variance between locations 2 and 3.

IV. DISCUSSION

This study aimed to characterize the uncertainty in IMU distance, orientation, and rotation during donning by a non-expert. Participants performed five donnings of self-placed IMUs on the chest, bicep, and forearm. Within each donning, participants performed six repetitions each of six prescribed motions. This study tested the hypotheses that initial distance,

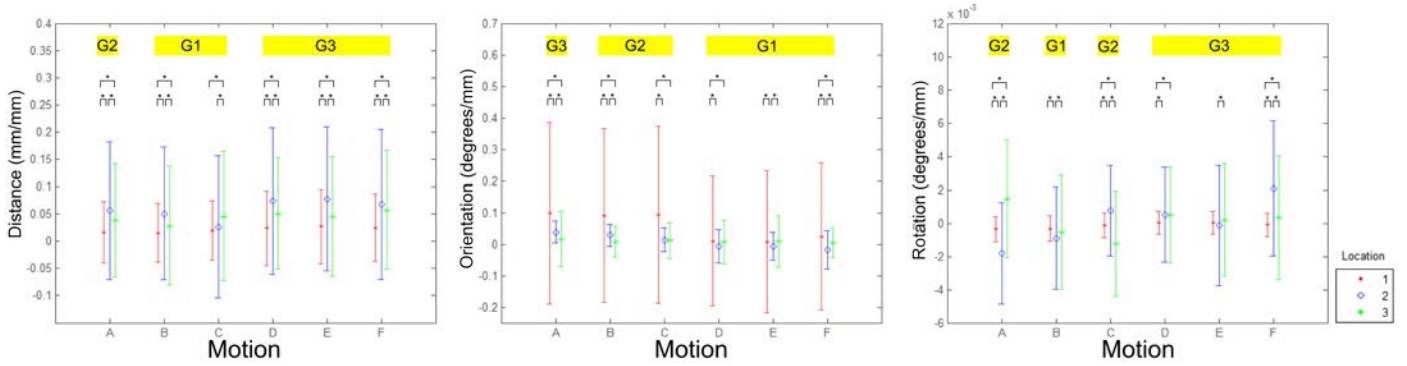


Fig. 5: Shown are the within motion interaction effects between location. Additional significant effects across motions are not shown. Main effect groupings are shown in horizontal bars above graphs in the order of group means from smallest (G1) to largest (G3). Bars show one standard deviation from the mean. Above each graph, asterisks (*) indicate significant difference according to Tukey’s Difference Test ($p < 0.05$).

TABLE I: Normalized and mean shifted location variances for all independent variables

Variable	Variance		
	IMU 1	IMU 2	IMU 3
Distance (mm/mm)	0.0038 *◇	0.0172 *◁	0.0119 ◁◇
Orientation (degrees/mm)	0.0646 *◇	0.0024 *◁	0.0044 ◁◇
Rotation (degrees/mm)	5.5×10^{-7} *◇	1.24×10^{-5} *	1.21×10^{-5} ◇

*, ◇, and ◁ indicate significance ($p < 0.0005$) between IMUs 1 and 2, 1 and 3, and 2 and 3, respectively.

orientation, and rotation of IMUs are affected by (1) the number of times the sensors are donned, (2) the type of functional motions performed, and (3) the location of the IMU.

While hypothesis 1 was confirmed, that there were significant main effects of donning, no consistent trend in any dependent variable with consecutive donnings were found. This implies that multiple donnings do not show learning effects. For initial placement, multiple donnings did not lead to more or less accurate placement.

Hypothesis 2 suggested that prescribed motions may affect the dependent measurements. Although motions A and B had the same starting position, the dependent measures were significantly different from each other. Motions D, E, and F were consistently grouped together for all IMU dependent variables. These three motions had different starting positions than motions A, B, and C, but similar starting positions to each other. It is clear that the starting point has an effect on the dependent variables. Relative placements are important because the relationship between the local and global coordinate system is defined in the calibration pose.

Hypothesis 3 suggests that location of IMU may affect the dependent variables. IMU distance showed significant differences across all locations, with the group mean lowest for location 1. This is consistent as the torso enabled the most precise placement of the IMU centroid due to having more constraints than the straps on IMUs 2 and 3 (Fig. 1). IMU 1 orientation was also found to be significantly different from

IMUs 2 and 3. The similarity in orientation between IMUs 2 and 3 is consistent with the strap configurations. For the attachment method evaluated, the location of the IMU had an effect on IMU placement. There is a component of IMU placement that may be due to the user’s natural placement variability, but there is also a portion that can be influenced by the strap type.

As a component may be attributed to strap type, it is important to consider how the straps were implemented. The straps associated with IMU 1 were constrained by four incoming straps with two connection points while IMUs 2 and 3 had two incoming straps and two connection points (Fig. 1). The loop on IMUs 2 and 3 that secured the IMU to the bicep and forearm allowed for more freedom of movement along the limb as well as movement along the local body curvature. In order to don these straps, the Velcro was looped through a buckle that was the same width as the IMU. This fixture limited changes in orientation of the IMU because the Velcro was as wide as the buckle, causing the IMU to align with the strap more consistently. The strap on IMU 1 was donned by looping each arm (much like a sweater is put on) and then snapping two buttons on one side of the IMU. Since the strap lengths were not changed, the chest strap was expected to provide consistent placement of the IMU centroid and to limit rotation about the torso. However, each of the two buttons had snaps that allowed some pivot, and thus small changes in strap location on the shoulder and under the armpit induced changes in IMU orientation. The data were consistent with these strap types and showed IMU 1 variance to be highest for orientation, but lowest for distance and rotation as compared to the other two IMUs.

This study made use of strap mounting configurations for the IMUs and understands that not all sensors are mounted in this manner. These results, however, can inform sensor attachment design. While an arm brace was used to limit the imprint on the skin, participants still had proprioceptive feedback which could aid in re-alignment of the IMU.

All these results were analyzed at the initial time point of the six motions studied. However, calibrations affect estimations throughout a time trajectory so it is important to

study how these relationships change throughout the entire motion. When the data are studied across time points, different similarity groupings may arise due to the changes in orientation of the limb. Future work will present the effect of IMU distance, orientation, and rotation changes across each motion. The data collected on the garment, which has fewer attachments points, will also be analyzed. From the current analysis, the hypothesis is that garments, which have less embedded structure, may show increased placement variability. Next steps are to understand how the effect size of these distance, orientation, and rotation variations affect motion estimations using current algorithms.

V. CONCLUSION

The accuracy of rigid body motion estimation is dependent on sensor placement and calibration. Therefore, characterization of sensor placement is needed to aid in development of algorithms and sensor attachment design for wearable motion capture systems. The results presented in this study examined the effects of self-donning on IMU distance, orientation, and rotation at the chest, bicep, and forearm. This study made use of off-the-shelf strap mounting configurations for the IMUs and found that the chest mount varied the least in initial placement in terms of distance and rotation, but its orientation varied more than when the IMUs were placed on the bicep and forearm.

This research was the first to characterize the way users vary placement of sensors on the human body. Relating mounting locations, motions, and number of donnings to IMU placement provides data to assist in designs for housing sensors and can aid the development of quick don and doff sensor suites that can be reliably used by a non-expert for real-time decision making.

ACKNOWLEDGMENT

The authors would like to thank Alan Natapoff for discussions on the statistical analysis, Jeff Hoffman for guidance in determination of relevant motions, and Sarah Schneider for assistance with troubleshooting Vicon.

REFERENCES

- [1] S. Nissilia, J. Bouchaud, and M. Boustany, "MEMS & sensors for wearables report - 2014" IHS Technology, Tech. Report., 2014
- [2] H. Fourati, N. Manamanni, L. Afilal, and Y. Handrich, "Complementary observer for body segments motion capturing by inertial and magnetic sensors," *IEEE Transactions on Mechatronics*, vol. 19, pp.149-157, 2014
- [3] H. Luinge and P. Veltink, "Inclination Measurement of human movement using a 3-D accelerometer with autocalibration," *IEEE Transactions on Neural Systems and Rehabilitation Engineering*, vol. 12, no. 1, pp.112-121, 2004.
- [4] J. Bortz, "A new mathematical formulation for strap-down inertial navigation," *IEEE Transactions on Aerospace and Electronic Systems*, vol. 7, no. 1, pp. 6166, 1971.
- [5] R. Zhu and Z. Zhou, "A real-time articulated human motion tracking using tri-axis inertial/magnetic sensors package," *IEEE Transactions on Neural Systems and Rehabilitation Engineering*, vol. 12, pp. 295-302, 2004.
- [6] D. Roetenberg, H. Luinge, C. Baten, and P. Veltink, "Compensation of magnetic disturbances improves inertial and magnetic sensing of human body segment orientation," *IEEE Transactions on Biomedical Engineering*, vol. 13, pp. 395-405, 2005.

- [7] X. Yun and E. Bachmann, "Design, implementation, and experimental results of a quaternion based kalman filter for human body motion tracking," *IEEE Transactions on Robotics*, vol. 22, pp. 1216-1227, 2006.
- [8] AM. Sabatini, "Quaternion-based extended kalman filter for determining orientation by inertial and magnetic sensing," *IEEE Transactions on Biomedical Engineering*, vol. 53, pp. 1346-56, 2006.
- [9] P. Cheng and B. Oelmann, "Joint-angle measurement using accelerometers and gyroscopesA survey," *IEEE Transactions on Instrumentation and Measurement*, vol. 59, no. 2, pp. 4044-14, 2010.
- [10] H. Luinge, P. Veltink, and C. Baten, "Ambulatory measurement of arm orientation," *Journal of Biomechanics*, vol. 40, pp. 78-85, 2007.
- [11] I. Prayudi and D. Kim, "Design and implementation of imu-based human arm motion capture system," *Proceedings of the IEEE International Conference on Mechatronics and Automation*, (Chengdu, China), August 2012.
- [12] H. Yang and J. Ye, "A calibration process for tracking upper limb motion with inertial sensors," *Mechatronics and Automation (ICMA), 2011 International Conference on*, pp.618,623, 7-10 Aug. 2011
- [13] X. Wu, Y. Wang, C. Chien, G. Pottie, "Self-calibration of sensor misplacement based on motion signature," *IEEE Body Sensor Networks*, vol. 1, 2013.